VISIT…

LANZAROTE
Caliente.com

Opto-Mechanical Systems Design

Third Edition

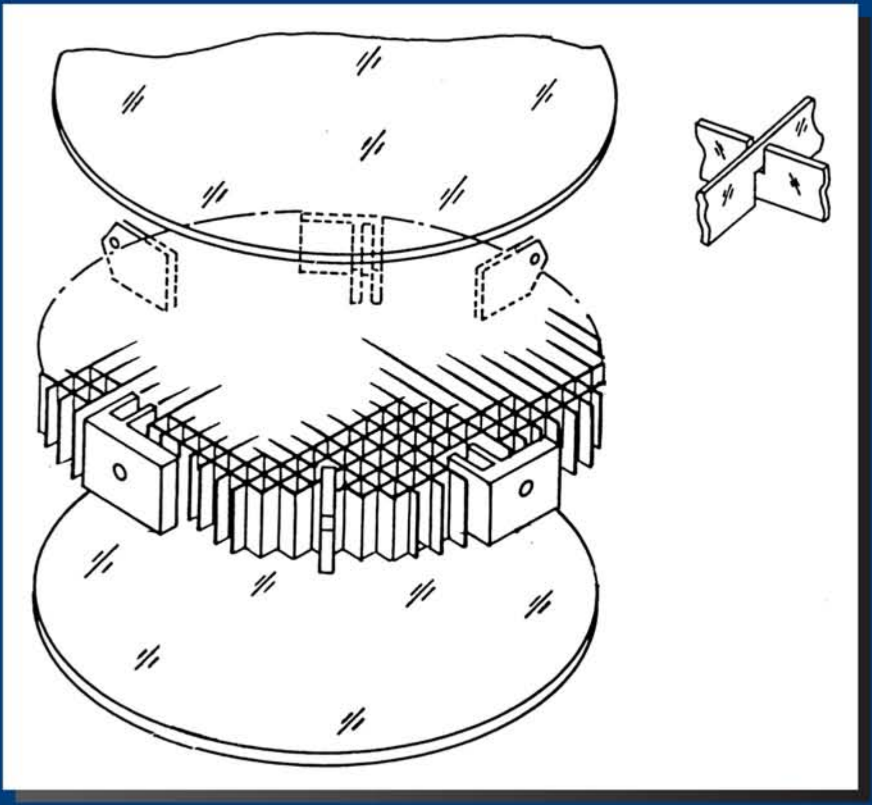

Paul R. Yoder, Jr.

Taylor & Francis
Taylor & Francis Group

Opto-Mechanical Systems Design

Third Edition

OPTICAL SCIENCE AND ENGINEERING

Founding Editor
Brian J. Thompson
University of Rochester
Rochester, New York

1. Electron and Ion Microscopy and Microanalysis: Principles and Applications, *Lawrence E. Murr*
2. Acousto-Optic Signal Processing: Theory and Implementation, *edited by Norman J. Berg and John N. Lee*
3. Electro-Optic and Acousto-Optic Scanning and Deflection, *Milton Gottlieb, Clive L. M. Ireland, and John Martin Ley*
4. Single-Mode Fiber Optics: Principles and Applications, *Luc B. Jeunhomme*
5. Pulse Code Formats for Fiber Optical Data Communication: Basic Principles and Applications, *David J. Morris*
6. Optical Materials: An Introduction to Selection and Application, *Solomon Musikant*
7. Infrared Methods for Gaseous Measurements: Theory and Practice, *edited by Joda Wormhoudt*
8. Laser Beam Scanning: Opto-Mechanical Devices, Systems, and Data Storage Optics, *edited by Gerald F. Marshall*
9. Opto-Mechanical Systems Design, *Paul R. Yoder, Jr.*
10. Optical Fiber Splices and Connectors: Theory and Methods, *Calvin M. Miller with Stephen C. Mettler and Ian A. White*
11. Laser Spectroscopy and Its Applications, *edited by Leon J. Radziemski, Richard W. Solarz, and Jeffrey A. Paisner*
12. Infrared Optoelectronics: Devices and Applications, *William Nunley and J. Scott Bechtel*
13. Integrated Optical Circuits and Components: Design and Applications, *edited by Lynn D. Hutcheson*
14. Handbook of Molecular Lasers, *edited by Peter K. Cheo*
15. Handbook of Optical Fibers and Cables, *Hiroshi Murata*
16. Acousto-Optics, *Adrian Korpel*
17. Procedures in Applied Optics, *John Strong*
18. Handbook of Solid-State Lasers, *edited by Peter K. Cheo*
19. Optical Computing: Digital and Symbolic, *edited by Raymond Arrathoon*
20. Laser Applications in Physical Chemistry, *edited by D. K. Evans*
21. Laser-Induced Plasmas and Applications, *edited by Leon J. Radziemski and David A. Cremers*
22. Infrared Technology Fundamentals, *Irving J. Spiro and Monroe Schlessinger*
23. Single-Mode Fiber Optics: Principles and Applications, Second Edition, Revised and Expanded, *Luc B. Jeunhomme*
24. Image Analysis Applications, *edited by Rangachar Kasturi and Mohan M. Trivedi*
25. Photoconductivity: Art, Science, and Technology, *N. V. Joshi*

26. Principles of Optical Circuit Engineering, *Mark A. Mentzer*
27. Lens Design, *Milton Laikin*
28. Optical Components, Systems, and Measurement Techniques, *Rajpal S. Sirohi and M. P. Kothiyal*
29. Electron and Ion Microscopy and Microanalysis: Principles and Applications, Second Edition, Revised and Expanded, *Lawrence E. Murr*
30. Handbook of Infrared Optical Materials, *edited by Paul Klocek*
31. Optical Scanning, *edited by Gerald F. Marshall*
32. Polymers for Lightwave and Integrated Optics: Technology and Applications, *edited by Lawrence A. Hornak*
33. Electro-Optical Displays, *edited by Mohammad A. Karim*
34. Mathematical Morphology in Image Processing, *edited by Edward R. Dougherty*
35. Opto-Mechanical Systems Design: Second Edition, Revised and Expanded, *Paul R. Yoder, Jr.*
36. Polarized Light: Fundamentals and Applications, *Edward Collett*
37. Rare Earth Doped Fiber Lasers and Amplifiers, *edited by Michel J. F. Digonnet*
38. Speckle Metrology, *edited by Rajpal S. Sirohi*
39. Organic Photoreceptors for Imaging Systems, *Paul M. Borsenberger and David S. Weiss*
40. Photonic Switching and Interconnects, *edited by Abdellatif Marrakchi*
41. Design and Fabrication of Acousto-Optic Devices, *edited by Akis P. Goutzoulis and Dennis R. Pape*
42. Digital Image Processing Methods, *edited by Edward R. Dougherty*
43. Visual Science and Engineering: Models and Applications, *edited by D. H. Kelly*
44. Handbook of Lens Design, *Daniel Malacara and Zacarias Malacara*
45. Photonic Devices and Systems, *edited by Robert G. Hunsberger*
46. Infrared Technology Fundamentals: Second Edition, Revised and Expanded, *edited by Monroe Schlessinger*
47. Spatial Light Modulator Technology: Materials, Devices, and Applications, *edited by Uzi Efron*
48. Lens Design: Second Edition, Revised and Expanded, *Milton Laikin*
49. Thin Films for Optical Systems, *edited by Francoise R. Flory*
50. Tunable Laser Applications, *edited by F. J. Duarte*
51. Acousto-Optic Signal Processing: Theory and Implementation, Second Edition, *edited by Norman J. Berg and John M. Pellegrino*
52. Handbook of Nonlinear Optics, *Richard L. Sutherland*
53. Handbook of Optical Fibers and Cables: Second Edition, *Hiroshi Murata*
54. Optical Storage and Retrieval: Memory, Neural Networks, and Fractals, *edited by Francis T. S. Yu and Suganda Jutamulia*
55. Devices for Optoelectronics, *Wallace B. Leigh*
56. Practical Design and Production of Optical Thin Films, *Ronald R. Willey*
57. Acousto-Optics: Second Edition, *Adrian Korpel*
58. Diffraction Gratings and Applications, *Erwin G. Loewen and Evgeny Popov*
59. Organic Photoreceptors for Xerography, *Paul M. Borsenberger and David S. Weiss*

60. Characterization Techniques and Tabulations for Organic Nonlinear Optical Materials, *edited by Mark G. Kuzyk and Carl W. Dirk*
61. Interferogram Analysis for Optical Testing, *Daniel Malacara, Manuel Servin, and Zacarias Malacara*
62. Computational Modeling of Vision: The Role of Combination, *William R. Uttal, Ramakrishna Kakarala, Spiram Dayanand, Thomas Shepherd, Jagadeesh Kalki, Charles F. Lunskis, Jr., and Ning Liu*
63. Microoptics Technology: Fabrication and Applications of Lens Arrays and Devices, *Nicholas Borrelli*
64. Visual Information Representation, Communication, and Image Processing, *edited by Chang Wen Chen and Ya-Qin Zhang*
65. Optical Methods of Measurement, *Rajpal S. Sirohi and F. S. Chau*
66. Integrated Optical Circuits and Components: Design and Applications, *edited by Edmond J. Murphy*
67. Adaptive Optics Engineering Handbook, *edited by Robert K. Tyson*
68. Entropy and Information Optics, *Francis T. S. Yu*
69. Computational Methods for Electromagnetic and Optical Systems, *John M. Jarem and Partha P. Banerjee*
70. Laser Beam Shaping, *Fred M. Dickey and Scott C. Holswade*
71. Rare-Earth-Doped Fiber Lasers and Amplifiers: Second Edition, Revised and Expanded, *edited by Michel J. F. Digonnet*
72. Lens Design: Third Edition, Revised and Expanded, *Milton Laikin*
73. Handbook of Optical Engineering, *edited by Daniel Malacara and Brian J. Thompson*
74. Handbook of Imaging Materials: Second Edition, Revised and Expanded, *edited by Arthur S. Diamond and David S. Weiss*
75. Handbook of Image Quality: Characterization and Prediction, *Brian W. Keelan*
76. Fiber Optic Sensors, *edited by Francis T. S. Yu and Shizhuo Yin*
77. Optical Switching/Networking and Computing for Multimedia Systems, *edited by Mohsen Guizani and Abdella Battou*
78. Image Recognition and Classification: Algorithms, Systems, and Applications, *edited by Bahram Javidi*
79. Practical Design and Production of Optical Thin Films: Second Edition, Revised and Expanded, *Ronald R. Willey*
80. Ultrafast Lasers: Technology and Applications, *edited by Martin E. Fermann, Almantas Galvanauskas, and Gregg Sucha*
81. Light Propagation in Periodic Media: Differential Theory and Design, *Michel Nevière and Evgeny Popov*
82. Handbook of Nonlinear Optics, Second Edition, Revised and Expanded, *Richard L. Sutherland*
83. Polarized Light: Second Edition, Revised and Expanded, *Dennis Goldstein*
84. Optical Remote Sensing: Science and Technology, *Walter Egan*
85. Handbook of Optical Design: Second Edition, *Daniel Malacara and Zacarias Malacara*
86. Nonlinear Optics: Theory, Numerical Modeling, and Applications, *Partha P. Banerjee*
87. Semiconductor and Metal Nanocrystals: Synthesis and Electronic and Optical Properties, edited by *Victor I. Klimov*

88. High-Performance Backbone Network Technology, *edited by Naoaki Yamanaka*
89. Semiconductor Laser Fundamentals, *Toshiaki Suhara*
90. Handbook of Optical and Laser Scanning, *edited by Gerald F. Marshall*
91. Organic Light-Emitting Diodes: Principles, Characteristics, and Processes, *Jan Kalinowski*
92. Micro-Optomechatronics, *Hiroshi Hosaka, Yoshitada Katagiri, Terunao Hirota, and Kiyoshi Itao*
93. Microoptics Technology: Second Edition, *Nicholas F. Borrelli*
94. Organic Electroluminescence, *edited by Zakya Kafafi*
95. Engineering Thin Films and Nanostructures with Ion Beams, *Emile Knystautas*
96. Interferogram Analysis for Optical Testing, Second Edition, *Daniel Malacara, Manuel Sercin, and Zacarias Malacara*
97. Laser Remote Sensing, *edited by Takashi Fujii and Tetsuo Fukuchi*
98. Passive Micro-Optical Alignment Methods, *edited by Robert A. Boudreau and Sharon M. Boudreau*
99. Organic Photovoltaics: Mechanism, Materials, and Devices, *edited by Sam-Shajing Sun and Niyazi Serdar Saracftci*
100. Handbook of Optical Interconnects, *edited by Shigeru Kawai*
101. GMPLS Technologies: Broadband Backbone Networks and Systems, *Naoaki Yamanaka, Kohei Shiomoto, and Eiji Oki*
102. Laser Beam Shaping Applications, *edited by Fred M. Dickey, Scott C. Holswade and David L. Shealy*
103. Electromagnetic Theory and Applications for Photonic Crystals, *Kiyotoshi Yasumoto*
104. Physics of Optoelectronics, *Michael A. Parker*
105. Opto-Mechanical Systems Design: Third Edition, *Paul R. Yoder, Jr.*

Opto-Mechanical Systems Design

Third Edition

Paul R. Yoder, Jr.
Consultant in Optical Engineering
Norwalk, Connecticut, U.S.A.

SPIE
PRESS
Bellingham, Washington USA
SPIE.org

CRC Taylor & Francis
Taylor & Francis Group
Boca Raton London New York

A CRC title, part of the Taylor & Francis imprint, a member of the
Taylor & Francis Group, the academic division of T&F Informa plc.

Published in 2006 by
CRC Press
Taylor & Francis Group
6000 Broken Sound Parkway NW, Suite 300
Boca Raton, FL 33487-2742

© 2006 by Taylor & Francis Group, LLC
CRC Press is an imprint of Taylor & Francis Group

No claim to original U.S. Government works

Printed in the United States of America on acid-free paper
10 9 8 7 6 5 4 3 2 1

International Standard Book Number-10: 1-57444-699-1 (Hardcover)
International Standard Book Number-13: 978-1-57444-699-9 (Hardcover)
Library of Congress Card Number 2005050575

This book contains information obtained from authentic and highly regarded sources. Reprinted material is quoted with permission, and sources are indicated. A wide variety of references are listed. Reasonable efforts have been made to publish reliable data and information, but the author and the publisher cannot assume responsibility for the validity of all materials or for the consequences of their use.

No part of this book may be reprinted, reproduced, transmitted, or utilized in any form by any electronic, mechanical, or other means, now known or hereafter invented, including photocopying, microfilming, and recording, or in any information storage or retrieval system, without written permission from the publishers.

For permission to photocopy or use material electronically from this work, please access www.copyright.com (http://www.copyright.com/) or contact the Copyright Clearance Center, Inc. (CCC) 222 Rosewood Drive, Danvers, MA 01923, 978-750-8400. CCC is a not-for-profit organization that provides licenses and registration for a variety of users. For organizations that have been granted a photocopy license by the CCC, a separate system of payment has been arranged.

Trademark Notice: Product or corporate names may be trademarks or registered trademarks, and are used only for identification and explanation without intent to infringe.

Library of Congress Cataloging-in-Publication Data

Yoder, Paul R.
Opto-mechanical systems design / Paul R. Yoder, Jr.-- 3rd ed.
p. cm. -- (Optical engineering ; 105)
Includes bibliographical references and index.
ISBN 1-57444-699-1 (alk. paper)
1. Optical instruments--Design and construction. 2. Mechanics, Applied. I. Title. II. Optical engineering (Marcel Dekker, Inc.) ; v. 105.

TS513.Y63 2005
681'.4--dc22 2005050575

T&F informa
Taylor & Francis Group
is the Academic Division of T&F Informa plc.

Visit the Taylor & Francis Web site at
http://www.taylorandfrancis.com

and the CRC Press Web site at
http://www.crcpress.com

This book is proudly dedicated to the memory of the two men who most strongly influenced my professional career in optics: my father, Paul R. Yoder, Professor of Physics at Juniata College, Huntingdon, Pennsylvania, who filled my young mind with the wonders of science, and Professor David H. Rank, my mentor in graduate school at Pennsylvania State University, University Park, Pennsylvania, who introduced me to geometric optics, lens design, and optical systems engineering.

Preface to the Third Edition

Building upon the success of the two prior editions, this third edition of *Opto-Mechanical Systems Design* updates the techniques used in opto-mechanics by emphasizing many important old and new technology developments. Most of these are discussed in depth while others are simply mentioned so readers interested in those particular topics can access the original documents for more details. Each of the 15 chapters treats its subject matter in sufficient detail for the reader to apply the technology to real-world problems. Numerical examples are employed to illustrate applications of theory and of the numerous equations provided herein. Many new references — some as recent as mid-2005 — make available key advances in opto-mechanical design of the past decade.

The field of opto-mechanics continues to grow, seemingly at an ever-increasing rate. Workers in the field are becoming much more willing to share their accomplishments with the community at large. To a large extent, this growth can be attributed to the continuing success of the International Society for Optical Engineering (SPIE), in attracting participation in its conferences and short courses and in publishing key technical papers in proceedings and journals as well as in books, CD-ROMs, videos, and other publications. By far, the SPIE's symposium proceedings represent today's most significant sources of information about new optical technology, about new tools and techniques for designing, building, and testing hardware, and about the performance of major systems such as astronomical telescopes and spaceborne scientific payloads. Since the publication date (1992) of this work's second edition, more than thirty-three SPIE conferences with papers contributing to opto-mechanical technology have been held. These papers describe, in significant detail, a large share of the new technology reported here.

The entire text of *Opto-Mechanical Systems Design* has been rewritten in an attempt to clarify certain technical details and to correct inadvertent errors that appeared in the earlier versions. In this new edition:

- In Chapter 1, coverage of the progress of the International Organization for Standards (ISO) and of the U.S. Optics and Electro-Optics Standards Council (OEOSC) relative to adoption of revised, broad-based standards in optics has been expanded and charts depicting the flow of activities during the conceptual, preliminary design, final design, manufacturing, and verification phases of optical instrument development have been added. The influences of computers and the Internet are noted.
- Information has been added to Chapter 2 on characteristics of the space environment, vibration criteria for sensitive equipment, ways to minimize contamination, and laser damage to optics.
- In Chapter 3 the list of optical glasses for which opto-mechanical characteristics are tabulated has been updated. This list reflects recent thinking by lens designers on "preferred" glass types. Several other tables of materials properties have also been updated and a table of coefficients of thermal defocus and thermo-optical coefficients for a variety of optical materials has been added.
- Sections have been added to Chapter 3 on special coatings for opto-mechanical materials and techniques for manufacturing opto-mechanical parts. These include discussions of protective finishes, optical black coatings, platings that improve surface smoothness of metal mirrors, and methods for making optical and mechanical components, including those made of composites.
- Details have been added to Chapter 4 on mounting lenses with retaining rings, flanges, and on flexures, effects of tightening tolerances on lens costs, calculating lens weights and center of gravity locations, and ways to align single lenses to their mounts.

- The discussion of catadioptric systems in Chapter 5 has been expanded and sections have been added on liquid coupling of lens elements and techniques for aligning multiple lenses in their mounts.
- New general considerations of windows and hardware design examples for domes and conformal windows have been added in Chapter 6.
- The discussions in Chapter 7 have been extended to include equations for designing 26 types of prisms and prism assemblies, and coverage on semikinematic mountings for prisms and techniques for bonding prisms to their mounts has been expanded.
- A new Chapter 8 on design and mounting of small mirrors, gratings, and pellicles has been added. Considerations of individual mirror designs and mirror system design, ghost image formation by second-surface mirrors, and numerous examples of typical component mounting designs are included.
- Chapter 9, which deals with lightweight, nonmetallic mirrors, has been expanded to include discussions of modeling built-up substrate structures, techniques for spin casting large (8 m class) mirror substrates, and estimating weight of contoured-back solid mirrors.
- The considerations of techniques for designing large mirrors and mountings for such mirrors in fixed horizontal axis, fixed vertical axis, and variable axis orientation applications have been expanded in Chapter 10 through Chapter 12. State-of-the-art design examples include the 2.49-m (98-in.)-diameter primary for the Hubble Space Telescope, the 2.7 m (106 in.) primary for the SOFIA Telescope, the 8.1 m (319 in.) primaries for the Gemini Telescopes, and the aspherical grazing incidence cylindrical mirrors that range in diameters from 0.68 m (27 in.) to 1.2 m (47 in.) for the Chandra X-ray Telescope.
- Prior chapters on design and mounting of metal mirrors have been consolidated into a single expanded Chapter 13. Considerations of such topics as metal matrix materials for mirrors, foam core construction, platings, single-point diamond turning (SPDT), and flexure mountings have been enhanced.
- Descriptions of several new optical instruments to illustrate favorable structural design principles have been added to Chapter 14. Considerations of modular design techniques have also been expanded. Athermalization techniques are discussed at length, and many new hardware examples are explained.
- In a new Chapter 15, discussions have been added about the effects of surface damage on the strength of optics, statistical methods for estimating optical component time to failure, and the basis for a rule-of-thumb tolerance for tensile stress in components made of common optical glasses, some optical crystals, and some nonmetallic mirror materials. The previously scattered discussions of techniques for analyzing stresses at optic-to-mount interfaces for lenses, prisms, and small mirrors have been consolidated in this chapter. Coverage of key effects such as temperature gradients and differential expansion/shrinkage effects from temperature changes in cemented and bonded joints have been significantly expanded. Prior investigations of the rate of change of axial preload with temperature (a parameter known as K_3) have been revisited and extended to allow preload at any temperature to be estimated much more confidently than previously possible. Discussions of axially and radially compliant mounts that can compensate for residual thermal expansion mismatches have been added, along with several representative hardware examples of such designs.
- An Appendix D has been added containing a glossary of terms and symbols used in this book.

Once again I acknowledge with thanks the support of many individuals, companies, and governmental agencies worldwide that provided much of the technical information included here. In particular, I acknowledge the superb assistance of Daniel Vukobratovich, Alson E. Hatheway, Roger A. Paquin, David Crompton, Victor L. Genberg, Keith B. Doyle, and William A. Goodman, who provided guidance, reviewed drafts of portions of the manuscript, identified sources of additional technical information, helped me understand some complex design issues, and checked some of the new theories and equations provided in this work. I trust that this information has been accurately conveyed and that credit has been given where appropriate. I take full responsibility for and deeply regret any misstatements, technical inaccuracies, or omissions. I hope that this book will enhance understanding of opto-mechanics by its readers, that it will prove useful in the workplace, and that future optical instruments and other hardware systems designed and developed as recommended here perform as intended.

Preface to the Second Edition

Since the first edition of this book appeared in 1986, the multifaceted discipline of opto-mechanical systems design has received increased attention, and a wealth of new literature on related subjects has been published. This is due, in part, to recent advancements in the degree of sophistication of analytical techniques for evaluating mechanical structures and the optic-to-mount interface, to the availability of new and improved materials, and to more complete information on the mechanical properties of existing materials.

Through this revised and expanded version of *Opto-Mechanical Systems Design*, I have attempted to bring as much of this new technology as is reasonably possible into the context of this work. Approximately 300 new literature references have been added, some as current as mid-1992. Many more hardware examples are examined for new and unique design approaches, the coverage of environmental influences on optical instruments is expanded, a summary of preferred techniques for evaluating optical hardware under adverse environmental conditions has been added, and our considerations of the effects of mounting forces on optical components have been broadened. Wherever feasible, both SI and U.S. customary units are employed in tables and quantified examples.

I acknowledge with thanks the assistance of the many individuals who so graciously contributed technical information to this new edition or allowed their published works to be described. I sincerely hope that this new edition will serve its readers well and that it will foster continued growth of this important discipline.

Preface to the First Edition

In the preface to his book on *Fundamentals of Optical Engineering* (McGraw Hill, 1943), Donald H. Jacobs wrote of his conviction that "in the design of any optical instrument, optical and mechanical considerations are not separate entities to be dealt with by different individuals but are merely two phases of a single problem." I have seen the truth of this statement many times during the design, development, and production of a variety of optical instruments — many of these being highly sophisticated systems intended for military and/or aerospace applications. The close interrelationship of the optical and mechanical disciplines cannot be ignored or left to chance encounters when the performance and reliability of the end item are vital to an important mission, such as photographing the farthest reaches of space with a spaceborne optical observatory. At the other extreme, the designers of even the simplest of optical instruments can benefit from a coordinated approach to the design problem.

This book is intended to be a compilation of opto-mechanical systems design guidelines and experiences. It tells how certain design tasks, such as the mounting of critical optical components in high-performance instruments, have been accomplished. The logic underlying those designs is outlined and, wherever possible, the success of the configuration used is evaluated. Included are considerations of analytical methods for predicting how a particular system or subsystem will react if exposed to specified environmental conditions. The mathematics of complete systems optimization is not stressed simply because the subject matter addressed here is so broad. A thorough analytical treatment of but a few of the design problems considered would fill a volume this size. Instead, this work concentrates on qualitative descriptions and references the optimization techniques explained elsewhere.

While many books on lens design and several on the design of mechanical structures and mechanisms have appeared in print since Jacobs first tried to tie together these topics, no author has given more that a fleeting consideration to them as an integrated topic. Indeed, Rudolph Kingslake specifically excluded considerations of the mechanical aspects of instrument design from the first five volumes of *Applied Optics and Optical Engineering* (Academic Press, 1965–1969), which he edited. It was not until 1980 when Robert E. Hopkins wrote on "Lens Mounting and Centering" in Volume VIII that an opto-mechanical topic was presented in any depth in that series.

The importance of the topic has been recognized, however, since many technical papers on opto-mechanical subjects have appeared in the *Journal of the Optical Society of America, Applied Optics, Journal of Scientific Instruments, Optical Engineering,* the *Soviet Journal of Optical Technology*, and similar publications. The subject has also been addressed by several professional society symposia, including OSA seminars, OSA workshops on optical fabrication and testing, and SPIE seminars on such topics as "Optics in Adverse Environments," "Opto-Mechanical Design," "Optical Specifications," and "Optical Systems Engineering." In assembling material for this book, I have unhesitatingly drawn on many available sources to provide pertinent information. The above-listed journals and symposia proceedings are heavily referenced. Lens design per se is intentionally not stressed here.

One of the most significant problems in developing a reference book such as this was the determination of how to organize the material to be covered. I chose to supply information that should be useful to individuals involved in developing optical instrument designs and carrying those designs to completion of operational hardware. Usually, such assignments include an optical design phase in which a collection of related optical elements is defined, and a mechanical design phase, which incorporates the optics into a suitable mechanical surround. The goal of the total effort is to create an instrument capable of doing a specific job within specific constraints of size, weight, cost, physical packaging, and environment.

The discussion begins with a summary of the total opto-mechanical systems design process from conceptualization to end item evaluation and documentation. This introduces us to the major steps that must be taken to achieve a successful design. Next, we examine environmental influences and the traditional, as well as some newer, materials from which we can fabricate the optics and the mechanical parts of the instrument. Techniques for mounting various typical optical elements and groupings thereof, ranging in aperture size from a few centimeters to several meters, are considered next. Included are design and mounting considerations for individual lenses, mirrors, and prisms; refracting and catadioptric subassemblies; lightweight mirror substrates; mountings for mirrors with axis horizontal, vertical, or in variable orientation; and design, fabrication, and mounting of metallic mirrors. We close with considerations of the structural design of optical instruments.

Familiarity on the part of reader with geometric optics, the functions of optical systems, and the fundamentals of mechanical engineering is assumed. Theory and analytical aspects of opto-mechanical engineering are minimized in favor of descriptions of past and current design approaches.

It is expected that this work will be of interest to a wide range of readers including optical instrument designers, developers, and users; optical and mechanical systems engineers; structural and materials engineers, and students of the optical sciences. It is hoped that the material presented here will serve as a useful guide in the conception, design, development, evaluation, and use of optical instrumentation in military, space, and commercial applications.

Many people have helped in the preparation of this book by providing information, photographs, comments and suggestions, and permissions to use previously published material. Hopefully, credits have been given properly in all cases; I express here my thanks to these individuals and to any whose contributions have inadvertently been omitted. Of great importance was the assistance of the following associates at Perkin-Elmer: Richard German and Ross Gelb, who prepared many of the illustrations, and Jessica Monda, Helen Ryan, Jo Anne Gresham, and Stephanie Shearer, who typed much of the manuscript. I am especially indebted to Richard Babish, Peter Mumola, and Julianne Grace of Perkin-Elmer, Brian Thompson of the University of Rochester, the staff of Marcel Dekker, Inc., and my wife, Elizabeth, for providing the encouragement that kept this project moving to completion.

The Author

Paul R. Yoder, Jr. serves the optical community as a consultant in optical engineering. For 55 years he has designed and analyzed optical instruments and managed optical technology development projects. He held various technical and engineering management positions with the U.S. Army's Frankford Arsenal, Perkin-Elmer Corporation, and Taunton Technologies, Inc. The author or coauthor of 65 technical papers on optical engineering topics and *BASIC-Programme fur die Optik* (Oldenbourg, 1986), he also wrote chapters for the OSA's *Handbook of Optics,* 2nd ed., Vol. I (McGraw-Hill, 1995) and for the *Handbook of Optomechanical Engineering* (CRC Press, 1997) as well as *Mounting Lenses in Optical Instruments* (SPIE Press, 1995); *Design and Mounting of Prisms and Small Mirrors in Optical Instruments* (SPIE Press, 1998); *Mounting Optics in Optical Instruments* (SPIE Press, 2002), and the two previous editions of the present work. He is listed as inventor or co-inventor on 15 U.S. and foreign patents.

Yoder received his B.S. and M.S. degrees in physics from Juniata College (1947) and Pennsylvania State University (1950), respectively. He is a Fellow of OSA, a Fellow of SPIE, a member of Sigma Xi and a founding member of the SPIE's Optomechanical/Instrument Working Group. He previously served as book reviews editor for *Optical Engineering*, as a topical editor for *Applied Optics*, as a member of the U.S. Advisory Group for the ISO's Technical Committee T172, *Optics and Optical Instruments*, and as a member of the U.S. Committee for the ICO. He also has taught numerous short courses on optical engineering and opto-mechanical design for SPIE, industry, and U.S. government agencies; graduate-level courses for the University of Connecticut; and two courses for the National Technological University Network.

Table of Contents

Chapter 1

The Opto-Mechanical Design Process

1.1 Introduction 1
1.2 Conceptualization 2
1.3 Performance Specifications and Design Constraints 5
1.4 Preliminary Design 12
1.5 Design Analysis and Computer Modeling 14
1.6 Error Budgets and Tolerances 21
1.7 Experimental Modeling 27
1.8 Finalizing the Design 30
1.9 Design Reviews 31
1.10 Manufacturing the Instrument 32
1.11 Evaluating the End Product 33
1.12 Documenting the Design 34
References 34

Chapter 2

Environmental Influences

2.1 Introduction 37
2.2 Parameters of Concern 38
  2.2.1 Temperature 39
  2.2.2 Pressure 43
  2.2.3 Static Strains and Stresses 44
  2.2.4 Vibration 45
  2.2.5 Shock 52
  2.2.6 Humidity 54
  2.2.7 Corrosion 54
  2.2.8 Contamination 55
  2.2.9 Fungus 59
  2.2.10 Abrasion and Erosion 60
  2.2.11 High-Energy Radiation and Micrometeorites 63
  2.2.12 Laser Damage to Optical Components 66
    2.2.12.1 Fundamental Mechanisms 66
    2.2.12.2 Surfaces and Mirrors 67
    2.2.12.3 Materials and Measurements 67
    2.2.12.4 Thin Films 69
2.3 Environmental Testing of Optics 69
References 71

Chapter 3

Opto-Mechanical Characteristics of Materials

3.1 Introduction 77
3.2 Materials for Refracting Optics 77
  3.2.1 General Considerations 77

- 3.2.2 Optical Glass 79
- 3.2.3 Optical Plastics 89
- 3.2.4 Optical Crystals 95
  - 3.2.4.1 Alkali and Alkaline Earth Halides 97
  - 3.2.4.2 Glasses and Other Oxides 100
  - 3.2.4.3 Semiconductors 100
  - 3.2.4.4 Chalcogenides 105
  - 3.2.4.5 Coefficients Related to Optical Material Thermal Behavior 105
- 3.3 Materials for Reflecting Optics 105
  - 3.3.1 Smoothness 105
  - 3.3.2 Stability 113
  - 3.3.3 Rigidity 115
- 3.4 Materials for Mechanical Components 115
  - 3.4.1 Aluminum 116
    - 3.4.1.1 Alloy 1100 116
    - 3.4.1.2 Alloy 2024 118
    - 3.4.1.3 Alloy 6061 118
    - 3.4.1.4 Alloy 7075 118
    - 3.4.1.5 Alloy 356 118
  - 3.4.2 Beryllium 118
  - 3.4.3 Copper 121
    - 3.4.3.1 Alloy C10100 122
    - 3.4.3.2 Alloy C17200 122
    - 3.4.3.3 Alloy C360 122
    - 3.4.3.4 Alloy C260 122
    - 3.4.3.5 Glidcop™ 122
  - 3.4.4 Invar and Super Invar 122
  - 3.4.5 Magnesium 123
  - 3.4.6 Carbon Steel 123
  - 3.4.7 Corrosion-Resistant Steel 123
  - 3.4.8 Titanium 123
  - 3.4.9 Silicon Carbide 124
  - 3.4.10 Composite Materials 124
- 3.5 Adhesives 128
  - 3.5.1 Optical Cements 128
    - 3.5.1.1 Solvent Loss Cements 129
    - 3.5.1.2 Thermoplastic Cements 129
    - 3.5.1.3 Thermosetting Cements 129
    - 3.5.1.4 Photosetting Cements 130
  - 3.5.2 Physical Characteristics 131
  - 3.5.3 Transmission Characteristics 131
  - 3.5.4 Cementing Optical Surfaces 132
  - 3.5.5 Structural Adhesives 133
    - 3.5.5.1 Epoxies 134
    - 3.5.5.2 Urethane Adhesives 134
    - 3.5.5.3 Cyanoacrylate Adhesives 137
- 3.6 Sealants 137
- 3.7 Special Coatings for Opto-Mechanical Materials 140
  - 3.7.1 Protective Coatings 140
    - 3.7.1.1 Paints 140
    - 3.7.1.2 Platings and Anodic Coatings 141
    - 3.7.1.3 Proprietary Coatings 141

3.7.2 Optical Black Coatings 141
3.7.3 Coatings to Improve Surface Smoothness 143
3.7.3.1 Nickel 143
3.7.3.2 Alumiplate® 143
3.8 Techniques for Manufacturing Opto-Mechanical Parts 143
3.8.1 Manufacturing Optical Parts 143
3.8.2 Manufacturing Mechanical Parts 146
3.8.2.1 Machining Methods 146
3.8.2.2 Casting Methods 147
3.8.2.3 Forging and Extrusion Methods 147
3.8.2.4 Fabricating and Curing Composites 149
3.8.3 General Comments Regarding Manufacturing Processes 150
References 151

Chapter 4
Mounting Individual Lenses

4.1 Introduction 157
4.2 Considerations of Centered Optics 157
4.3 Cost Impacts of Fabrication Tolerances 167
4.4 Lens Weight and Center of Gravity Location 173
4.4.1 Lens Weight Estimation 174
4.4.2 Lens Center of Gravity Location 177
4.5 Mounting Individual Low-Precision Lenses 178
4.5.1 Spring Mountings 178
4.5.2 Burnished Cell Mountings 179
4.5.3 Snap Ring Mountings 180
4.6 Mountings for Lenses with Curved Rims 183
4.7 Mountings Interfacing with Spherical Surfaces 184
4.7.1 General Considerations 184
4.7.2 The Threaded Retaining Ring Mounting 187
4.7.3 Continuous Flange Mounting 192
4.7.4 Multiple Cantilevered Spring Clip Mounting 194
4.7.5 Opto-Mechanical Interface Types 197
4.7.5.1 Sharp Corner Interface 197
4.7.5.2 Tangential Interface 197
4.7.5.3 Toroidal Interface 198
4.7.5.4 Spherical Interface 198
4.7.5.5 Interfaces on Bevels 198
4.8 Elastomeric Mountings for Lenses 202
4.9 Mounting Lenses on Flexures 204
4.10 Alignment of the Individual Lens 207
4.11 Mounting Plastic Lenses 222
References 226

Chapter 5
Mounting Multiple Lenses

5.1 Introduction 229
5.2 Multielement Spacing Considerations 229
5.3 Examples of Lens Assemblies with No Moving Parts 235
5.3.1 Military Telescope Eyepiece 235
5.3.2 Military Telescope Objective 237

5.3.3 Fixed-Focus Relay Lens 237
5.3.4 Aerial Photographic Objective Lens 239
5.3.5 Low-Distortion Projection Lens 240
5.3.6 Motion Picture Projection Lens 241
5.3.7 Collimator Designed for High-Shock Loading 241
5.3.8 Large Astrographic Objective 243
5.3.9 Infrared Sensor Lens 245
5.4 Examples of Lens Assemblies Containing Moving Parts 245
5.4.1 Objectives Designed for Mid-IR Applications 245
5.4.2 Internally Focusing Photographic Lenses 247
5.4.3 Binocular Focus Mechanisms 248
5.4.4 Zoom Lenses 252
5.5 Lathe Assembly Techniques 259
5.6 Microscope Objectives 264
5.7 Assemblies Using Plastic Parts 267
5.8 Liquid Coupling of Lenses 270
5.9 Catadioptric Assemblies 272
5.10 Alignment of Multi-Lens Assemblies 282
5.11 Alignment of Reflecting Telescope Systems 297
References 298

Chapter 6
Mounting Windows and Filters

6.1 Introduction 301
6.2 Conventional Window Mounts 302
6.3 Special Window Mounts 303
6.4 Mounts for Shells and Domes 310
6.5 Conformal Windows 315
6.6 Filter Mounts 320
6.7 Windows Subject to a Pressure Differential 323
6.7.1 Survival 323
6.7.2 Optical Performance Degradation 327
References 329

Chapter 7
Designing and Mounting Prisms

7.1 Introduction 331
7.2 Geometric Relationships 331
7.2.1 Refraction and Reflection at Prism Surfaces 331
7.2.2 Aberrations Caused by Prisms and Plates 332
7.2.3 Beam Displacements Caused by Prisms and Plates 332
7.2.4 Tunnel Diagrams 333
7.2.5 Total Internal Reflection 336
7.3 Designs for Typical Prisms 337
7.3.1 The Right-Angle Prism 338
7.3.2 The Beam Splitter (or Beam Combiner) Cube Prism 338
7.3.3 The Amici Prism 338
7.3.4 The Porro Prism 339
7.3.5 The Abbe Version of the Porro Prism 339
7.3.6 The Porro Erecting System 342

7.3.7 The Abbe Erecting System 344
7.3.8 The Rhomboid Prism 345
7.3.9 The Dove Prism 346
7.3.10 Double-Dove Prism 346
7.3.11 The Penta Prism 347
7.3.12 The Roof Penta Prism 348
7.3.13 The Amici/Penta and Right-Angle/Roof Penta Erecting Systems 349
7.3.14 The Reversion, Abbe Type A, and Abbe Type B Prisms 349
7.3.15 The Delta Prism 350
7.3.16 The Pechan Prism 352
7.3.17 The Schmidt Prism 355
7.3.18 The 45° Bauernfeind Prism 358
7.3.19 The Frankford Arsenal Prisms Nos. 1 and 2 358
7.3.20 The Leman Prism 359
7.3.21 An Internally Reflecting Axicon Prism 359
7.3.22 The Cube-Corner Prism 359
7.3.23 An Ocular Prism for a Coincidence Rangefinder 361
7.3.24 A Biocular Prism System 365
7.3.25 Dispersing Prisms 366
7.3.26 Thin-Wedge Prism Systems 368
7.3.26.1 The Thin Wedge 368
7.3.26.2 The Risley Wedge System 368
7.3.26.3 The Longitudinally Sliding Wedge 370
7.3.26.4 A Focus-Adjusting Wedge System 370
7.3.27 Anamorphic Prism Systems 371
7.4 Kinematic and Semikinematic Prism Mounting Principles 373
7.5 Mounting Prisms by Clamping 375
7.5.1 Prism Mounts: Semikinematic 375
7.5.2 Prism Mounts: Nonkinematic 384
7.6 Mounting Prisms by Bonding 387
7.7 Flexure Mounts for Prisms 396
References 399

Chapter 8

Design and Mounting Small, Nonmetallic Mirrors, Gratings, and Pellicles

8.1 Introduction 401
8.2 General Considerations 402
8.2.1 Mirror Applications 402
8.2.2 Geometric Configurations 402
8.2.3 Reflected Image Orientation 402
8.2.4 Beam Prints on Optical Surfaces 405
8.2.5 Mirror Coatings 408
8.2.6 Ghost Image Formation by Second-Surface Mirrors 411
8.3 Semikinematic Mountings for Small Mirrors 415
8.4 Mounting Mirrors by Bonding 425
8.5 Flexure Mounts for Mirrors 428
8.6 Multiple-Mirror Mounts 433
8.7 Mountings for Gratings 441
8.8 Pellicle Design and Mounting 444
References 446

Chapter 9

Lightweight Nonmetallic Mirror Design

9.1 Introduction 449
9.2 Material Considerations 450
9.3 Core Cell Configurations 451
9.4 Cast Ribbed Substrates....................453
9.5 Slotted-Strut and Fused Monolithic Substrates 456
9.6 Frit-Bonded Substrates....................463
9.7 Low-Temperature Bonded Substrates 465
9.8 Machined-Core Substrates 466
9.9 Contoured-Back Solid Mirror Configurations 470
9.10 Thin Face Sheet Mirror Configurations....................472
9.11 Scaling Relationships for Lightweight Mirrors 473
References 477

Chapter 10

Mounting Large, Horizontal-Axis Mirrors

10.1 Introduction 481
10.2 General Considerations of Gravity Effects 481
10.3 V-Type Mounts....................482
10.4 Multipoint Edge Supports 489
10.5 The Ideal Radial Mount 491
10.6 Mercury Tube Mounts 492
10.7 Strap and Roller-Chain Mounts 493
10.8 Push–Pull Mounts 498
10.9 Comparison of Dynamic Relaxation and Finite-Element Analysis Techniques 499
References 501

Chapter 11

Mounting Large Vertical-Axis Mirrors

11.1 Introduction 503
11.2 Ring Mounts....................503
11.3 Air Bag (Bladder) Mounts 506
11.4 Multiple-Point Supports....................509
    11.4.1 Three-Point Mounts 509
    11.4.2 Hindle Mounts 512
    11.4.3 Counterweighted Mounts....................515
    11.4.4 Pneumatic/Hydraulic Mounts....................516
11.5 Metrology Mounts 518
    11.5.1 A 36-Point Pneumatic Metrology Mount 519
    11.5.2 A 27-Point Hydraulic Metrology Mount 519
    11.5.3 A 52-Point Spring Matrix Metrology Mount....................520
    11.5.4 Lateral Constraints during Polishing 524
References 525

Chapter 12

Mounting Large, Variable-Orientation Mirrors

12.1 Introduction 527
12.2 Mechanical Flotation Mounts 527

12.3 Hydraulic/Pneumatic Mounts....534
  12.3.1 Historical Background....534
  12.3.2 Gemini Telescopes....537
  12.3.3 New Multiple Mirror Telescope....545
12.4 Center-Mounted Mirrors....548
12.5 Mounts for Double-Arch Mirrors....553
12.6 Bipod Mirror Mounts....557
12.7 Thin Face Sheet Mirror Mounts....561
  12.7.1 General Considerations....561
  12.7.2 The Keck Telescopes....566
  12.7.3 Adaptive Mirror Systems....571
    12.7.3.1 The Advanced Electro-Optical System Telescope....574
    12.7.3.2 The MMT Adaptive Secondary Mirror....575
12.8 Mounts for Large Space-Borne Mirrors....577
  12.8.1 The Hubble Space Telescope....577
  12.8.2 The Chandra X-Ray Telescope....579
References....582

Chapter 13
Design and Mounting of Metallic Mirrors

13.1 Introduction....585
13.2 General Considerations of Metal Mirrors....585
13.3 Aluminum Mirrors....587
  13.3.1 Cast Aluminum Mirrors....593
  13.3.2 Machined Aluminum Mirrors....593
  13.3.3 Welded Aluminum Mirrors....595
13.4 Beryllium Mirrors....598
13.5 Mirrors Made from Other Metals....607
  13.5.1 Copper Mirrors....607
  13.5.2 Molybdenum Mirrors....607
  13.5.3 Silicon Carbide Mirrors....608
13.6 Mirrors with Foam and Metal Matrix Cores....611
13.7 Plating of Metal Mirrors....623
13.8 Single-Point Diamond Turning of Metal Mirrors....625
13.9 Conventional Mountings for Metal Mirrors....636
13.10 Integral Mountings for Metal Mirrors....638
13.11 Flexure Mountings for Larger Metal Mirrors....642
13.12 Interfacing Multiple SPDT Components to Facilitate Assembly and Alignment....648
References....652

Chapter 14
Optical Instrument Structural Design

14.1 Introduction....659
14.2 Rigid Housing Configurations....659
  14.2.1 Military Binoculars....659
  14.2.2 Commercial Binoculars....662
  14.2.3 Tank Periscopes....663
  14.2.4 Space-Borne Spectro-Radiometer Cameras....666
  14.2.5 Large Aerial Camera Lens....669
  14.2.6 A Thermally Stable Optical Structure....674

14.3 Modular Design Principles and Examples 675
  14.3.1 Injection-Molded Plastic Modules 676
  14.3.2 A Modular Military Binocular 677
  14.3.3 A Modular Spectrometer for Space Application 682
  14.3.4 A Dual-Collimator Module 685
14.4 A Structural Design for High Shock Loading 687
14.5 Athermalized Structural Designs 689
  14.5.1 Instruments Made from a Single Material 689
    14.5.1.1 The IRAS Telescope 689
    14.5.1.2 The Spitzer Space Telescope 690
    14.5.1.3 A Telescope with Optical and Inter-Component Interfaces Processed by SPDT 693
  14.5.2 Active Control of Focus 694
  14.5.3 Instruments Athermalized with Metering Sructures 695
    14.5.3.1 The Orbiting Astronomical Observatory 696
    14.5.3.2 The Geostationary Operational Environmental Satellite 698
    14.5.3.3 The Deep Imaging Multi-Object Spectrograph 702
    14.5.3.4 Athermalization of the Multiangle Imaging Spectro-Radiometer 703
    14.5.3.5 Athermalization of the Hubble Space Telescope Truss Structure 706
    14.5.3.6 Athermalization of the Galaxy Evolution Explorer 709
  14.5.4 Athermalization of Refracting Optical Systems 712
14.6. Geometries for Telescope Tube Structures 716
  14.6.1 The Serrurier Truss 716
  14.6.2 The New Multiple-Mirror Telescope 718
  14.6.3 The N-Tiered Truss 721
  14.6.4 The Chandra Telescope 721
  14.6.5 Truss Geometries for Minimal Gravitational and Wind Deflections 724
  14.6.6 Determinate Space Frames 725
References 729

Chapter 15

Analysis of the Opto-Mechanical Design

15.1 Introduction 733
15.2 Failure Predictions for Optics 733
  15.2.1 General Considerations 733
  15.2.2 Testing to Determine Component Strength 735
  15.2.3 The Weibull Failure Prediction Method 740
  15.2.4 The Safety Factor 742
  15.2.5 Time-to-Failure Prediction 743
  15.2.6 Rule-of-Thumb Stress Tolerances 744
15.3 Stress Generation at Opto-Mechanical Interfaces 748
  15.3.1 Point Contacts 748
  15.3.2 Short Line Contacts 751
  15.3.3 Annular Contacts 756
    15.3.3.1 The Sharp Corner Interface 758
    15.3.3.2 The Tangential Interface 759
    15.3.3.3 The Toroidal Interface 759

        15.3.3.4 The Spherical Interface 761
        15.3.3.5 The Flat Bevel Interface 762
15.4 Parametric Comparisons of Annular Interface Types 762
15.5 Bending Effects Due to Offset Annular Contacts 764
    15.5.1 Bending Stress in the Optical Component 765
    15.5.2 Change in Surface Sagittal Depth of a Bent Optic 767
15.6 Effects of Temperature Changes 767
    15.6.1 Radial Effects at Reduced Temperature 768
        15.6.1.1 Radial Stress in the Optic 768
        15.6.1.2 Tangential (Hoop) Stress in the Mount Wall 769
    15.6.2 Radial Effects at Increased Temperature 770
    15.6.3 Changes in Axial Preload Caused by Temperature Changes 770
        15.6.3.1 General Considerations 770
        15.6.3.2 Approximation of K_3 Considering Bulk Effects Only 772
        15.6.3.3 Approximation of K_3 Considering Effects Other Than Bulk Effects 778
            15.6.3.3.1 Glass and Metal Surface Deflection Effects 779
            15.6.3.3.2 Retainer Deflection Effects 779
            15.6.3.3.3 Shoulder Deflection Effects 780
            15.6.3.3.4 Radial Dimension Change Effects 780
        15.6.3.4 Illustrative Examples of K_3 Estimation 780
    15.6.4 Estimation of Tensile Contact Stresses in the Lens at Various Temperatures 781
    15.6.5 Advantages of Providing Controlled Axial Compliance in the Lens or Mirror Mount 784
15.7 Effects of Temperature Gradients 795
    15.7.1 Radial Temperature Gradients 798
    15.7.2 Axial Temperature Gradients 800
15.8 Stresses in Cemented and Bonded Optics Due to Temperature Changes 800
15.9 Some Effects of Temperature Changes on Elastomerically Mounted Lenses 803
References 806

Appendix A

Units and Their Conversion 809

Appendix B

Summary of Methods for Testing Optical Components and
Optical Instruments under Adverse Environmental Conditions

B.1 Cold, Heat, Humidity Testing 811
B.2 Mechanical Stress Testing 811
B.3 Salt Mist Testing 812
B.4 Cold, Low Air Pressure Testing 812
B.5 Dust Testing 812
B.6 Drip, Rain Testing 812
B.7 High-Pressure, Low-Pressure, Immersion Testing 813
B.8 Solar Radiation 813
B.9 Combined Sinusoidal Vibration, Dry Heat, or Cold Testing 813
B.10 Mold Growth Testing 813
B.11 Corrosion Testing 814

B.12 Combined Shock, Bump, or Free Fall, Dry Heat, or Cold Testing 814
B.13 Dew, Hoarfrost, Ice Testing 815

Appendix C
Hardness of Materials

References 817

Appendix D
Glossary

D.1 Units of Measure and Abbreviations Used 819
D.2 Prefixes 820
D.3 Greek Symbol Applications 820
D.4 Acronyms, Abbreviations, and Other Terms 820

Index 827

1 The Opto-Mechanical Design Process

1.1 INTRODUCTION

Opto-mechanical design of optical instruments is a tightly integrated process involving many technical disciplines. It begins with a statement of need for a particular hardware item and a definition of goals and firm requirements for that item's configuration, physical characteristics, performance in a given application environment, etc. The design effort proceeds through a logical sequence of major steps and concludes only when the instrument is awarded a pedigree establishing its ability to meet its specifications and to be produced in the required quantity — whether that is as a "one off" (such as the Chandra X-Ray Telescope) or as a very large number (such as a lens for the ubiquitous "point-and-shoot" camera).

As pointed out by Petroski (1994) in one of his interesting series of books on engineering design, "Design problems arise out of the failure of some existing thing, system, or process to function as well as might be hoped, and they arise also out of anticipated situations wherein failure is envisioned." Existing hardware designs that prove to be deficient or that may fail in some future, significantly more demanding application and the availability of new technology that makes a new design feasible can lead to a desire or a genuine need for a new hardware design that does a particular task better than the previously available designs.

In this chapter, we treat each major design step in a separate section. Admittedly, our approach is idealized since few designs develop as smoothly as planned. We endeavor to show how the process *should* occur and trust that those planning, executing, reviewing, and approving the design will have the ingenuity and resourcefulness to cope with the inevitable problems and bring errant design activities back into harmony.

Driving forces behind the methodology applied in the design process include schedule constraints, availability of properly trained personnel; facilities, equipment, and other resources; perceived demands from the marketplace; and the inherent costs of accomplishing and proving the success of the design. These we consider to lie within the province of project management, a subject clearly beyond the scope of this book.

A great influence on the opto-mechanical design process is the degree of maturity of the technology to be applied. For example, not many years ago the design of the 2.4 m (94.5 in.) aperture Hubble Space Telescope (HST) capable of being lifted into Earth's orbit by the space shuttle would have been virtually impossible for a variety of reasons. One mechanical reason was the then nonavailability of structural materials with the required blend of high stiffness, low density, and ultralow thermal expansion characteristics. To have used aluminum, titanium, or Invar in the telescope truss structure *in lieu* of the less familiar but promising new types of graphite epoxy (GrEp) composites actually employed would have severely limited the performance of the instrument in the varying operational thermal environment.* Further, the strict telescope weight limitations imposed by NASA would have been difficult to meet. The achievement of a successful state-of-the-art instrument design utilizing new materials requires more theoretical synthesis and analysis, experimentation, and qualification testing than would a design involving the application only of tried and proven materials and technologies. Applying a higher level of technology or entirely new technology to make a system perform better, weigh less, or last longer may increase cost over less capable, but available technology. Paraphrasing Sarafin (1995a), who spoke from the vantage point of much aerospace experience, we should not ask "Can we make the system do …?" because the answer probably is, "Yes, we can." More appropriate questions are "At what cost can we make the system do …, what are the technical risks of failure, and what would it cost in time and dollars to recover if we fail?" Careful consideration of these issues will help balance the advantages and disadvantages of such alternate pathways.

---

*According to Krim (1990), temperature stabilization requirements for the HST would have been ± 0.027°C, ± 0.06, and ± 0.35°C with Al, Ti, or Invar structures, respectively. The actual athermalized telescope structure (involving a GrEp truss) was designed to maintain optical performance over a more realistic temperature range as large as ± 13°C.

Key elements that minimize risk and facilitate completion of assignments in the opto-mechanical design process are expedited communication between all involved individuals and easy access to required technical information. The former is greatly facilitated today by electronic means such as E-mail, teleconferencing, facsimile transmission, and the use of cellular telephones, while the latter is facilitated by worldwide access to a vast number of excellent reference libraries and technical data files via the Internet. The detailed design itself can now be computer-based rather than in the form of paper drawings and other documents. Computer-aided design and engineering (CAD and CAE) technologies allow access throughout a network for information exchange yet limits design change privileges to the proper authorities. Communication between design or engineering groups and manufacturing groups can be accomplished by electronic means, thereby reducing transit time and enhancing accuracy of data transmittal. Data entry directly into a machine's computer, i.e., computer-aided manufacture (CAM), then facilitates making parts by eliminating many manual machine setup chores and reducing the possibility of human errors during data entry. Testing also can often be facilitated by computer control of the test sequence and automatic data storage, retrieval, and analysis.

Complex opto-mechanical systems generally consist of many subsystems; each has a unique set of design problems with its own specifications and constraints. Subsystems usually consist of several major assemblies that, in turn, consist of subassemblies, components, and elements. By dividing the overall design problem into a series of related but independently definable parts, even the most complex system will yield to the design process.

No one design can be cited in this chapter to illustrate all the various steps of the opto-mechanical design process. We therefore utilize a variety of unrelated examples involving military and aerospace instruments for this purpose. In real life, the magnitude of the effort required in any given step would be tailored to that appropriate to the specific design problem. The general approach to each step and to the overall design process would, however, be expected to follow the guidelines established here.

1.2 CONCEPTUALIZATION

The first step in the evolution of the design of an opto-mechanical system is recognition of the need for a device to accomplish a specific purpose. Usually, the mere definition of a need brings to the minds of inventive engineers one or more vague concepts of instrumentation that might meet that need. Knowledge of how similar needs were met by prior designs plays an important role at this point. Experience indicates not only how the device might be configured, but also how it should *not* be configured.

Functional block diagrams relating major portions of the system are valuable communication tools. Figure 1.1 shows one such diagram for a high-performance, long-focal-length panoramic camera system to be applied in a downward-looking, aerial reconnaissance application from an aircraft flying at high altitude. This system consists of three major assemblies: a camera assembly consisting primarily of imaging optics and scene scanning mechanisms, film supply and take-up magazines, film transport mechanisms, exposure and focus controls, a velocity–height sensor, an image motion compensator, temperature control devices, and a suitable structure; a control subsystem assembly to

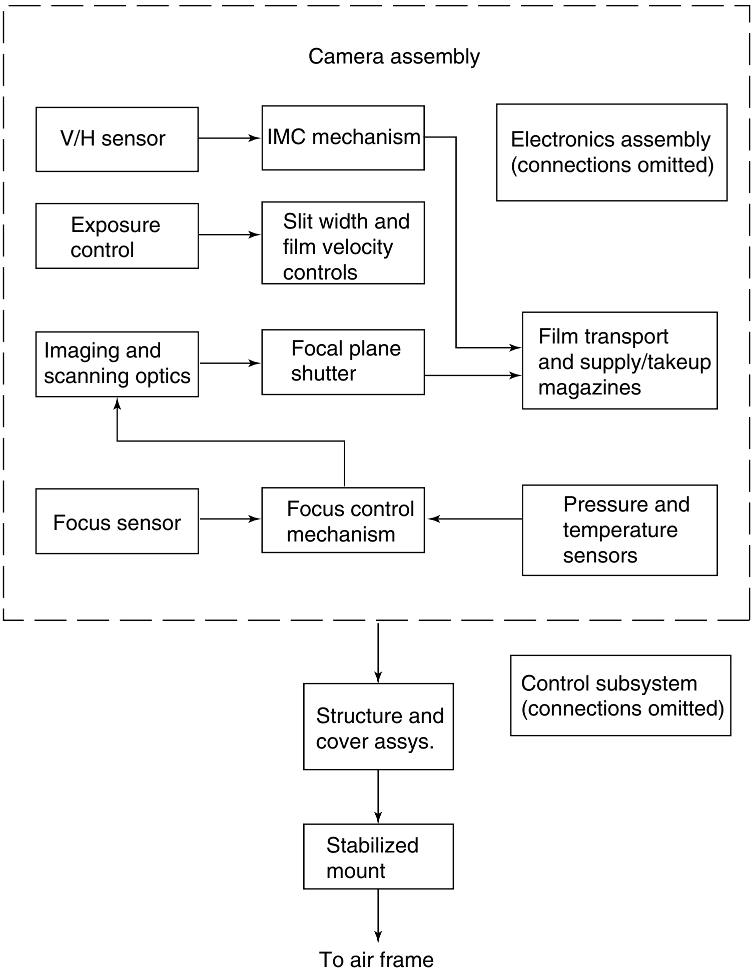
Camera assembly
V/H sensor
IMC mechanism
Electronics assembly (connections omitted)
Exposure control
Slit width and film velocity controls
Imaging and scanning optics
Focal plane shutter
Film transport and supply/takeup magazines
Focus sensor
Focus control mechanism
Pressure and temperature sensors
Structure and cover assys.
Control subsystem (connections omitted)
Stabilized mount
To air frame

FIGURE 1.1 Top-level functional block diagram for a high-performance panoramic aerial reconnaissance camera system using film as the storage medium.

provide the required operational functions; and a stabilized mount assembly. At this stage in the design conceptualization, the detailed configurations of the individual blocks making up this system would not be known.

The opto-mechanical makeup of one concept for the imaging and scanning optics block of Figure 1.1 is defined in Figure 1.2. Here we see a lower level block diagram indicating that the optical system consists conceptually of three separated lens groups, two fold mirrors to deviate the line of sight, a scanning prism, and a window. The lens groups and fold mirrors are mounted into cells or mounts that attach, along with the prism and its mechanisms, to a support structure. The window is mounted in a housing that encloses the optical system and forms the lens cone. This housing interfaces, in turn, to the camera assembly and to the airframe through the stabilized mount.

If a catadioptric Newtonian-type optical system concept were to be advanced for this same application, one might expect an opto-mechanical block diagram of the form shown in Figure 1.3 to apply. Here it is assumed that the main image-forming component is a spherical primary mirror, and that two full-aperture corrector plates and a field lens group are required for image quality reasons. A single full-aperture folding mirror is to be provided to scan the light path and a derotation system is employed in image space to maintain an erect image on the film.

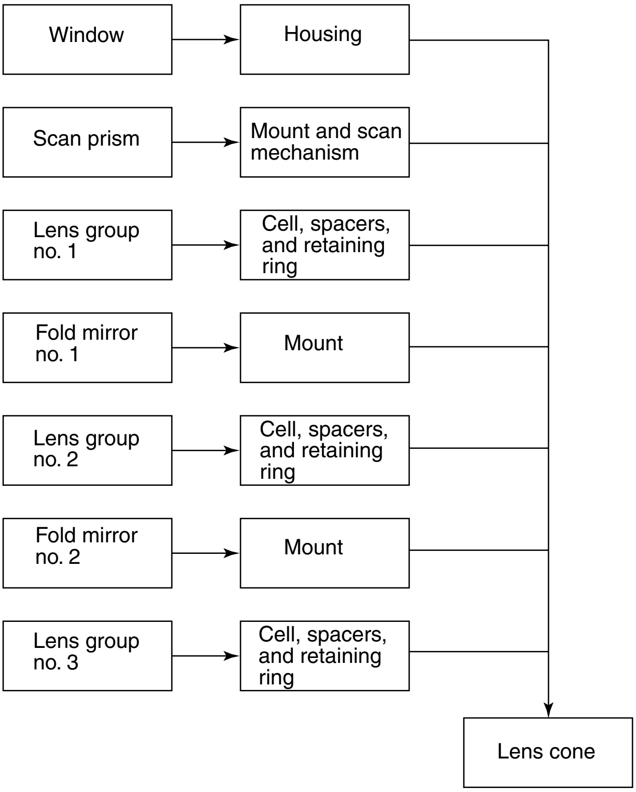
Window
Housing
Scan prism
Mount and scan mechanism
Lens group no. 1
Cell, spacers, and retaining ring
Fold mirror no. 1
Mount
Lens group no. 2
Cell, spacers, and retaining ring
Fold mirror no. 2
Mount
Lens group no. 3
Cell, spacers, and retaining ring
Lens cone

FIGURE 1.2 Lower level block diagram of the Imaging and scanning optics block shown in Figure 1.1 here configured as a refracting optical system with an object-space scanning prism.

As the function of the device to be designed is examined in more detail and the technical specifications begin to take form, the relative advantages and disadvantages of the suggested concepts can be established and weighed. Parametric trade-off analyses are often performed at this time in order to develop approximate interrelations between design variables. This helps disclose incompatibilities between specific requirements such as optical system specification combinations that would violate the Lagrange invariant (see Kingslake, 1983) in moving from object space to image space. Rough estimates of the physical size and weight of the instrument if built along alternative lines also may prove helpful in identifying inconsistencies and in pointing out the more favorable of alternative concepts. Preliminary material choices made at this time need be no more specific than to assume that optical glass would be used in lenses and windows, that reflective components would be glass or ceramic or metal, that refractive and reflective optical component thicknesses would be 10 and 20% of their diameters respectively, that the system's relative aperture and field of view would be some reasonable but specific values, and that the number of optical components required in the optical system would lie between two reasonable extremes. From the mechanical viewpoint, it would be appropriate to make a tentative choice between alternative structural concepts such as a lightweight truss covered by a thin protective skin (appropriate to some spaceborne scientific payloads), a cast aluminum housing (appropriate to a photographic lens assembly or a binocular), or a tubular stainless-steel housing (appropriate to a submarine periscope). Conceptual layouts of the most viable concept(s) can then be prepared for evaluation, comparison, and choice of the best configuration. This then would serve as the starting point for a detailed preliminary design.

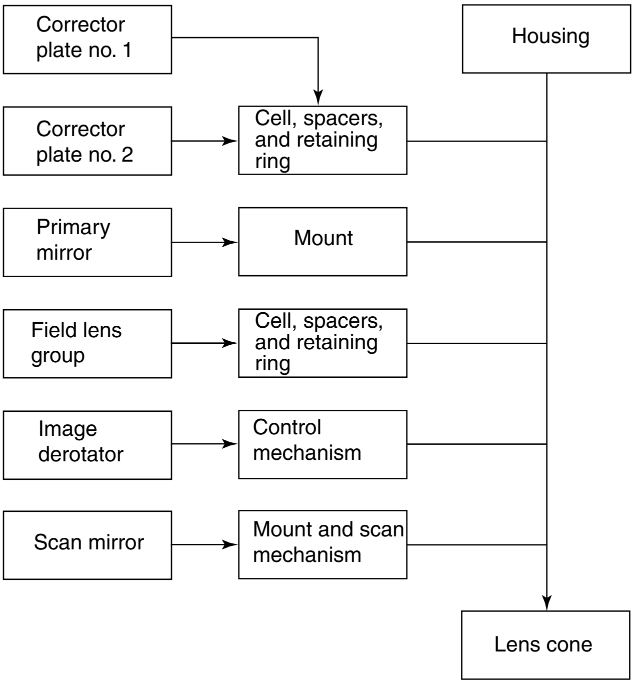

FIGURE 1.3 Lower level block diagram of the Imaging and scanning optics block shown in Figure 1.1 here configured as a catadioptric Newtonian-type optical system with an object–space scanning mirror and image derotation system.

1.3 PERFORMANCE SPECIFICATIONS AND DESIGN CONSTRAINTS

Two of the most important inputs to the design process are the performance specification and the definition of imposed constraints. The former sets forth the user's definition of what the end item must do and how well it must work to be judged acceptable, whereas the latter defines the physical limitations, such as size, weight, configuration, environment, and resource consumption that affect opto-mechanical and electrical interfaces with the surround. In the case of a scientific payload for a space probe, these generally would consist of many separate, complex, and lengthy documents. In the simplest cases, the specification could consist of one short document giving a few general requirements and parameters would be left to the discretion of the optical and mechanical designers and engineers. In almost all cases, the preparation of at least one drawing to specify the item's opto-mechanical interfaces would be appropriate.

A suggested list of items to be considered in the typical performance specification and constraint definition for an opto-mechanical system may be found in Table 1.1. These items are not necessarily in order of importance nor all-inclusive. Careful consideration of these features (and others that may be unique to the design in question) should help the design teams create a satisfactory end item or product. It is advisable also to indicate clearly the intended purpose of the instrument at the beginning of the specification.

Figure 1.4 illustrates an *opto-mechanical interface drawing*. This drawing defines the required external configuration for a particular 9 in. (22.9 cm) focal length, *f*/1.5 objective lens assembly with coaxial laser output and image-forming input channels that is discussed in more detail in Section 5.5. The drawing also sets limits on overall package size, defines critical dimensions, states requirements for perpendicularity of the optical axis of the imaging system (datum -A-) and of the image plane to the mounting flange (datum -C-), and establishes tolerances for critical dimensions and angles. The technical performance specification for this lens defines the optical characteristics

TABLE 1.1
Checklist of General Design Features Typically Included in Specifications and Constraint Definitions for Optical Instruments

- Performance requirements such as resolution, MTF at specified spatial frequencies, radial energy distribution, encircled or ensquared energy at specific wavelengths, or numerical aperture
- Focal length, magnification (if system is afocal), magnification and object-to-image track length (if system has finite conjugates)
- Angular or linear field of view (in specified meridians if anamorphic)
- Entrance and exit pupil sizes and locations
- Spectral transmission requirements
- Image orientation for a given object
- Sensor characteristics such as dimensions, spectral response, element size and spacing, and/or frequency response
- Size, shape, and weight limitations
- Survival and operating environmental conditions
- Interfaces (optical, mechanical, electrical, etc.)
- Thermal stability requirements
- Duty cycle and useful life requirements
- Maintenance and servicing provisions (access, fits, clearances, torquing, etc.)
- Emergency or overload conditions
- Center of gravity (CG) location and lifting provisions
- Human-instrument interface requirements and restrictions (including safety aspects)
- Electrical requirements and restrictions (power consumption, frequency, phase, grounding, etc.)
- Material selection recommendations and limitations
- Finish/color requirements
- Corrosion, fungus, rain, sand/dust, and salt spray erosion protection requirements
- Inspection and test provisions
- Electromagnetic interference restrictions and susceptibility
- Special markings or identifications
- Storage, packaging, and shipping requirements

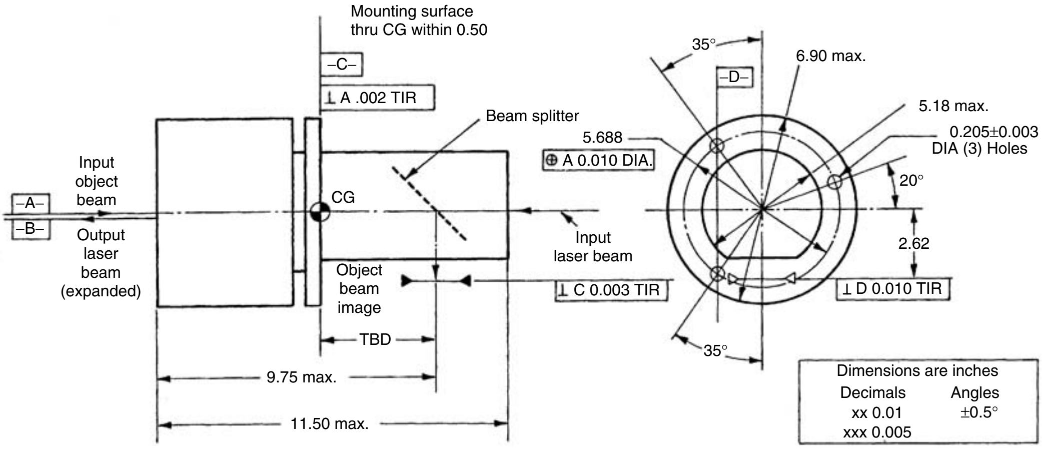
Mounting surface
thru CG within 0.50
–C–
⊥ A .002 TIR
Beam splitter
5.688
⊕ A 0.010 DIA.
Input
object
beam
–A–
–B–
CG
Output
laser
beam
(expanded)
Input
laser beam
Object
beam
image
⊥ C 0.003 TIR
TBD
9.75 max.
11.50 max.
35°
–D–
6.90 max.
5.18 max.
0.205±0.003
DIA (3) Holes
20°
2.62
⊥ D 0.010 TIR
35°
Dimensions are inches
Decimals
Angles
xx 0.01
±0.5°
xxx 0.005

FIGURE 1.4 Example of an opto-mechanical interface drawing showing the configuration, critical dimensions and their tolerances, and key features of a lens assembly.

(focal length, relative aperture, field of view, image quality, vignetting, transmission, etc.) as well as constructional features needed for the assembly to accomplish its intended function in a specific environment.

One aspect of optical instrument performance specification preparation worthy of special consideration here is the quantification of what is really needed from the equipment once it has been designed and built. Smith (1989) advised us that specifications should ask for just enough to accomplish the intended purpose and no more. Technical requirements should be clear and concise; not overburdened with details, yet not so general as to foster confusion on the part of the designers trying to determine what is wanted. For example, although it is easy to say that a new photographic lens is to be "diffraction-limited," it is not so easy to prove that some lower level of performance would not suffice. It has become a common practice for those wishing a device to be developed to ask first for an analysis of the trade-offs between performance and cost. The time and cost of such analyses, if properly conducted and documented, are usually worthy expenditures. It has often been said that requirements are not absolute and performance is not always the most important attribute of a system. For instance, life cycle cost is sometimes the most vital aspect of new hardware. An affordable system that works adequately may be better in the long run than a more expensive version that offers a small technical advantage, but requires more maintenance. Strict schedule constraints such as having a new space payload ready to meet a specific launch window that will not occur again for years also might lead to acceptable compromises in performance because some scientific information from the mission would be better than no information at all. Above all, the project team must understand what the user (read customer) really wants — not just what the initial specification reads! In this case, understanding requires communication and willingness on the part of all parties to examine all aspects of the application to see if the "requirements" are realistic.

Price (1985) went a bit further by defining a trade-off as a "balancing of factors or conditions, all of which are not attainable at the same time." He cited and then discussed three useful viewpoints, one or more of which is generally applicable to almost any system:

1. The hardware system including all components from the object to the final output (e.g., a video recording or display system comprising object, illumination, atmosphere, lens, camera, detector, electronics, recorder, tape, player, monitor, and observer's eye).
2. The product-user system including the interaction between the person and the apparatus (e.g., controls, platforms, handles, switches, eye position, eye-hand coordination requirements, time delays between actions and reactions, etc.).
3. The manufacturing system including raw materials, materials handling, parts manufacture, assembly, quality control, optics-to-product interfaces and tests, and the attendant costs, schedules, processes, and personnel utilization.

Price's paper concluded with the profound statement: "a well prepared analysis is an essential, but not necessarily sufficient, condition to obtaining acceptance of a proposed system design."

The extent to which the cost of an optical system can be reduced or the product can be made more attractive to prospective buyers for other reasons is often intimately related to the allowable degradation from "perfect" operation. Customers faced with the predicted cost of buying state-of-the-art aerial reconnaissance camera systems built to a given specification have been known to ask for a "shopping list" of alternative designs showing system costs in large quantities as a function of resolution in line pairs per millimeter. Although a reliable relationship between these factors is quite difficult to derive, its serious consideration would surely help all parties understand the importance of compromise. Shannon (1979) illustrated this point by pointing out the magnitude of optical distortion introduced by the curved windshields of modern automobiles that is tolerated for style and cost reasons. Walker (1979) dealt at length with the compromises appropriate in the design of visual systems such as telescopes, binoculars, or periscopes. Parameters particularly amenable to trade-off in such instruments are image quality, vignetting, and light transmission. To a lesser degree, one might trade field of view, pupil diameter, or exit pupil distance against system complexity, size, and cost. At the end of his paper, Walker provided his version of the dictionary definition of a specification as follows: "A detailed and exact statement prescribing materials, dimensions, workmanship and performance, arrived at after careful and cooperative consideration of the system application and the realistic needs of the end user." This seems to express accurately the viewpoint of many of us active in opto-mechanical system design.

For many years, specifications for optical instruments procured for U.S. government use referred to military specifications, standards, and other government publications. These documents defined general requirements and provided guidance for the selection of materials, design, inspection, and testing of a variety of equipment items. In 1994, the U.S. Armed Services issued a directive stating that all future military procurement contracts should refer to national and international commercial standards rather than military specifications. As of this writing, of the many military specifications that relate to optical products, several have been canceled and others have been declared inactive. Inactive specifications can be applied to existing procurement contracts, but not to new ones. Specifications for optical coatings can be replaced by the international standard ISO 9211 "Optics and optical instruments — Optical coatings," but other U.S. military specifications are being reviewed for relevancy to current manufacturing techniques. It is expected that many of these will be rewritten as new voluntary optical standards. Standards applicable to commercial products are usually prepared by voluntary standard bodies and distributed through the standard organizations of the various countries producing and/or procuring those products.

Work on international voluntary optical standards began in 1979 under the auspices of the International Organization for Standards (ISO) headquartered in Geneva, Switzerland. This effort is conducted within ISO/TC (Technical Committee) 172, Optics and Optical Instruments. The Deutsches Institut fur Normung (DIN) of Germany functions as secretariat for this Committee. Currently 13 nations are actively participating in this work through their national standards bodies. The latter bodies are listed in Table 1.2. In addition, 27 nations are observers. Another international organization involved in standardization efforts is the International Electrotechnical Commission (IEC). It is the leading global organization that prepares and publishes international standards for all electrical, electronic, and related technologies, including electronics, magnetics and electro-magnetics, electro-acoustics, multimedia, telecommunication, and energy production and distribution.

ISO/TC 172 was established to promote standardization of terminology, requirements, interfaces, and test methods in the field of optics. This includes complete systems, devices, instruments, optical components, auxiliary devices and accessories, as well as materials. Its scope excludes standardization efforts relative to specific items in the field of cinematography (the responsibility of ISO/TC 36), photography (the responsibility of ISO/TC 42), eye protectors (the responsibility of ISO/TC 94), micrographics (the responsibility of ISO/TC 171), fiber optics for telecommunication (the responsibility of IEC/TC 86), and electrical safety of optical elements.

TABLE 1.2
International Organizations Involved in the Development of Voluntary Standards Related to Optics and Optical Instrumentation under ISO TC172

- Association française de normalisation (AFNOR) from France
- American National Standards Institute (ANSI) from the United States
- Asociatia de Standardizare din România (ASRO) from Romania
- British Standards Institution (BSI) from the United Kingdom
- Deutsches Institut für Normung (DIN) from Germany (Secretariat)
- State Committee of the Russian Federation for Standardization and Metrology (GOST R) from Russia
- Japanese Industrial Standards Committee (JISC) from Japan
- Korean Agency for Technology and Standards (KATS) from Korea
- Österreichisches Normungsinstitut (ON) from Austria
- State Administration of China for Standardization (SACS) from China
- Standards Australia International Ltd. (SAI) from Australia
- Swiss Association for Standardization (SNV) from Switzerland
- Ente Nazionale Italiano di Unificazione (UNI) from Italy

To facilitate the development of optical standards and fill the void left by the absence of the U. S. military specifications, a consortium made up of seven professional societies, trade associations, and companies sponsored the incorporation of the Optics and Electro-Optics Standards Council (OEOSC), which acts as the administrator of national optical standards for the United States.[†] OEOSC has received accreditation from the American National Standards Institute (ANSI) for a committee called ASC/OP "Optics and Electro-Optical Instruments." ASC/OP is now authorized to develop U.S. national standards. OEOSC is also responsible for supporting ISO/TC 172 through a U.S. Technical Advisory Group (TAG). This group is a committee made up of U.S. optical experts whose primary responsibility is to review drafts of proposed international optical standards so that it can formulate U.S. opinions regarding the suitability of those drafts to become international standards, and then to transmit those opinions, through ANSI, to the ISO technical committee. The TAG also is responsible for reviewing U.S. national optical standards to determine which of them should be offered as drafts for new voluntary international standards.

Within ISO/TC 172, seven subcommittees (SC) have been established to address different major topics. Under each active SC, there are several working groups (WG) that do the actual writing. Table 1.3 depicts the organizational structure to WG level as of mid-2002. Draft international standards prepared and adopted by the various ISO technical committees are circulated to the international members of ISO for approval before the ISO Council formally approves them. Approval requires at least 75% acceptance by the member bodies voting.

Most U.S. optical companies and the Department of Defense have long based their engineering drawings for mechanical and optical parts on ANSI Specification Y14.5M-1982, "Dimensioning and Tolerancing," and ASME/ANSI Specification Y14.18M-1986, "Optical Parts," respectively. One result of activity by ISO/TC 172 that is particularly germane to this practice is the promulgation of ISO 10110, "Optics and optical instruments — Preparation of drawings for elements and systems," written by WG 2 of SC 1. This standard is expected eventually to replace ASME/ANSI Y14.18M. One important feature of this standard is that it expresses as many concepts as possible in terms of symbols to minimize the need for notes that would require translation for the drawing to be understood in the languages of various countries. Default tolerances are given in the standard for cases in which a specific tolerance is not required. This simplifies the appearance of drawings in those cases.

ISO 10110 has 13 parts as listed in Table 1.4. A few of these parts are worthy of special attention here. The following descriptions are based largely on Parks (1991) and Willey and Parks (1997). The first part deals with the mechanical aspects of optical drawings including lists of items to check for completeness of system layouts, subassemblies, and individual optical element drawings. Only such items as are unique to optics are included. All strictly mechanical aspects of optical drawings are covered by ISO standards on technical drawings, as contained in ISO Handbooks 12 and 33.[‡] These ISO standards are largely compatible with ANSI Y14.5M. In cases where there are differences, wording is included to permit usage of national standards so long as they are called out on the pertinent drawings.

The next three parts of ISO 10110 deal with optical material specifications and are straightforward adaptations of glass catalog specifications for stress birefringence, bubbles and inclusions, and inhomogeneity (including striae).

Part 5 of ISO 10110 deals with optical surface figure errors. Either a visual test plate assessment of figures or computer reduction of interferometric fringe or phase data can be employed. Centering tolerances are the subject of Part 6. It shows how to specify centering relative to various datum surfaces. Part 7 covers surface imperfections or cosmetic defects such as those commonly

---

[†] Information concerning the activities, membership, and progress of this council can be found on the OEOSC web site: *www.optstd.org*.

[‡] It is customary for the ISO to issue groupings of published standards dealing with various aspects of a related subject in the form of a handbook. For example, ISO Standards Handbook 33, *Applied Metrology—Limits, Fits and Surface Properties* was published in 1988 to bring together under one cover 58 standards developed within 7 different TCs; all are related to the science of measurement. The handbook includes terminology; indication of mechanical tolerances and surface conditions on technical drawings, limits and fits, and properties of surfaces and measuring instruments.

TABLE 1.3
Listing of Subcommittees and Working Groups under ISO/TC 172, "Optics and Optical Instruments." Secretariat/Convener for each is Shown in Parentheses (See Table 1.2 for definitions of acronyms)

Subcommittee	Title/Working Group
SC1	Fundamental standards (DIN)
	WG1 General optical test methods (DIN)
	WG2 Preparation of drawings for optical elements and systems (AFNOR)
	WG3 Environmental test methods (DIN)
	WG4 Electronic data transfer (BSI)
SC3	Optical materials and components (AFNOR)
	WG1 Raw optical glass (DIN)
	WG2 Coatings (ANSI)
	WG3 Characterization of IR materials (AFNOR)
SC4	Telescopic systems (GOST R)
	WG1 Binoculars, monoculars, and spotting scopes (GOST R)
	WG3 Astronomical telescopes (JISC)
	WG4 General test methods (DIN)
	WG5 Night vision devices (GOST R)
SC5	Microscopes and endoscopes (DIN)
	WG3 Terms and definitions (BSI)
	WG6 Endoscopes (JISC)
	WG7 Infinity corrected optics (DIN)
SC6	Geodetic and surveying instruments (SNV) (WG not formalized)
SC7	Ophthalmic optics and instruments (DIN)
	WG1 Terminology (BSI)
	WG2 Spectacle frames (BSI)
	WG3 Spectacle lenses (AFNOR)
	WG6 Ophthalmic instruments and test methods (ANSI)
	WG7 Ophthalmic implants (SIS)
	WG8 Data interchange (ANSI)
	WG9 Contact lenses (ANSI)
SC9	Electro-optical systems (DIN)
	WG1 Terminology and test methods for lasers (DIN)
	WG2 Interfaces and system specifications for lasers (AFNOR)
	WG3 Safety (ANSI)
	WG4 Laser systems for medical applications (ANSI)
	WG5 Laser systems for general applications (BSI)
	WG6 Optical components and their test methods (DIN)
	WG7 Electro-Optical systems other than lasers (JISC)

called "scratches and digs." Either of the two techniques may be used to evaluate these defects. The defect areas can be measured directly or their visibility assessed against an appropriately illuminated background. Baker (2002) has described a simple and inexpensive apparatus for quantifying these types of defects. Baker (2004) is a definitive reference on this subject.

Part 8 of ISO 10110 concerns ground and polished surface texture while part 9 tells how to indicate that a surface is to be coated. It does not specify what type of coating is to be applied nor what the coating's characteristics and performance should be. These details are covered in another standard, ISO 9211, *Optical Coatings*.

Part 10 of ISO 10110 outlines ways to specify simple optical elements in tabular form without preparing a drawing. This is useful, as it allows the opto-mechanical designer to communicate

TABLE 1.4
Subject Matter of the 11 parts of ISO Standard 10110, "Optics and optical instruments—Preparation of drawings for elements and systems"

- Part 1: General
- Part 2: Material imperfections — stress birefringence
- Part 3: Material imperfections — bubbles and inclusions
- Part 4: Material imperfections — inhomogeneity and striae
- Part 5: Surface form tolerances
- Part 6: Centering tolerances
- Part 7: Surface imperfection tolerances
- Part 8: Surface texture
- Part 9: Surface treatment and coating
- Part 10: Table representing data of a lens
- Part 11: Non-toleranced data
- Part 12: Aspheric surfaces
- Part 13: Laser irradiation threshold

manufacturing requirements by computer link. Part 11 of the ISO standard gives a table of default tolerances applicable to dimensions of manufactured elements for which no tolerances have been given on the drawing. For example, when not otherwise specified, elements from 10 to 30 mm in diameter are expected to have diameters within 0.5 mm of the specified nominal value. If this level of accuracy is adequate for the application, the drawing can be simplified by simply omitting the tolerance.

Part 12 tells us how to specify an aspheric surface in a widely understood and accepted manner. Finally, Part 13 describes how to specify a threshold for laser damage to optics. The subject of laser damage is considered in Section 2.2.12.

To assist designers and engineers in the interpretation and application of ISO 10110, the Optical Society of America prepared a *Handbook of Optical Standards*. This handbook (Kimmel and Parks, 2002) facilitates the preparation of optical element and systems drawings and the inclusion therein of appropriate notations and symbology.

Several other ISO standards are of interest here. Listed in Table 1.5, these cover measurement, inspection, and testing of optics. The first of these (ISO 9022) is considered further in Chapter 2 and Appendix B. Willey and Parks (1997) pointed out that the four parts of ISO 9211 deal with pertinent subjects in more detail than any other generally available document. Part 1 clarifies coating terminology and defines ten coating types by function. It also illustrates many kinds of coating imperfections. Part 2 deals with optical properties of typical coatings and tells how to specify them. Examples are given to facilitate understanding of this topic. Part 3 covers environmental durability of coatings in terms of their intended applications. These range from the relatively benign environment of a sealed instrument to severe outdoor conditions. The consequences of unsupervised (and perhaps improper) cleaning of optical surfaces are also discussed. Part 4 specifies methods for environmental testing.

The reader interested in obtaining copies of these or other published ISO standards or who wishes to learn the status of ISO standards in preparation should contact the ANSI directly. Activities of ANSI, the SPIE, the OSA, and OEOSC pertinent to standards can be easily accessed through their respective websites.[§]

[§] American National Standards Institute, 1819 L St., NW, Washington, DC 20036, Tel. (202) 293-8020, *http://www.ansi.org*. SPIE, The International Society for Optical Engineering, P.O. Box 10, Bellingham, WA 98227-0010, Tel. (360) 676-3290, *http://www.spie.org*. The Optical Society of America, 2010 Massachusetts Avenue, NW, Washington, DC 20036-1023, Tel. (800) 762-6960 or (202) 223-1096, *http://www.osa.org*. The Optical and Electro-Optical Standards Council can be contacted through Mr. Gene Kohlenberg, Administrator TAG/ISO/TC172 c/o OEOSC, P.O. Box 25705, Rochester, NY 14625. Tel/Fax: (585) 377-2540, *http://www.optstd.org*.

TABLE 1.5
List of ISO Standards Dealing with Measurement, Inspection, and Testing of Optics

- ISO 9022: "Environmental test methods" (20 parts)
- ISO 9039: "Determination of distortion"
- ISO 9211: "Optical coatings" (4 parts)
- ISO 9335: "OTF, camera, copier lenses, and telescopes" (3 parts)
- ISO 9336: "Veiling glare, definition and measurement"
- ISO 9802: "Raw optical glass, vocabulary
- ISO 10109: "Environmental test requirements" (7 parts)
- ISO 10934: "Microscopes, terms" (3 parts)
- ISO 10935: "Microscopes, interface connections"
- ISO 10936: "Microscopes, operation"
- ISO 10937: "Microscopes, eyepiece interfaces"
- ISO 11254: "Laser damage thresholds"
- ISO 114211: "OTF measurement accuracy"
- ISO 11455: "Birefringence determination"
- ISO 12123: "Bubbles, inclusions: test methods and classification"

When all inputs to the technical specifications and interface requirements are believed to have been established, it is time for the first design review (see Section 1.9). During this review, experts critique those documents for adequacy and completeness. Only after approval should the activity proceed into the preliminary design phase. In some cases, approval is granted subject to correction of the requirements or constraints documents along specific lines or completion of further trade-off studies and minor modifications of the concept(s).

1.4 PRELIMINARY DESIGN

Given the sets of specifications and constraints as well as one or more concepts for an opto-mechanical system, the idealized design process proceeds into the preliminary design phase. Here the optical designer, optical engineer, mechanical engineer, and other concerned individuals strive cooperatively to define an approximate assemblage of parts that have a high probability, once finalized, of meeting the system's design goals and requirements. These individuals must be given sufficient time to sort through design alternatives, scrutinize details, analyze data, and, on occasion, invent new ways to solve problems. Otherwise, under pressure to finish by the quickest route, the design team may produce instruments that reincarnate weaknesses of earlier designs. At the earliest stage of preliminary design, the optics may be represented as thin lenses or mirrors that possess focal lengths, apertures, and axial separations, but have no specific radii, thicknesses, or material types. The locations, sizes, and orientations of images and pupils should be correct to a first-order approximation in such representations.

Figure 1.5(a) shows a thin-lens optical schematic for a periscopic sight with characteristics as listed in the legend. The paths of the marginal rays entering the system parallel to the axis at the rim of the entrance pupil and the principal rays at maximum plus and minus semifield angles are shown. In order to provide a lateral offset in the optical path, flat mirrors or prisms can be inserted into the air spaces to fold the system. It must be remembered, of course, that appropriate space will be needed later to convert the thin lenses into thick ones and, in some cases, into multiple-element groups. For this reason, it is common practice to assume the thin-lens system length to be somewhat shorter than that of the required thick-lens system.

The mechanical layout of the housings, cells, mirror brackets, etc, for an optical instrument known only for thin-lens approximation would not be of much value. Hence, any serious consideration of mountings usually follows completion of the preliminary thick-lens design. At this point, the number and approximate shapes of the optics are known, their separations are nearly final, and

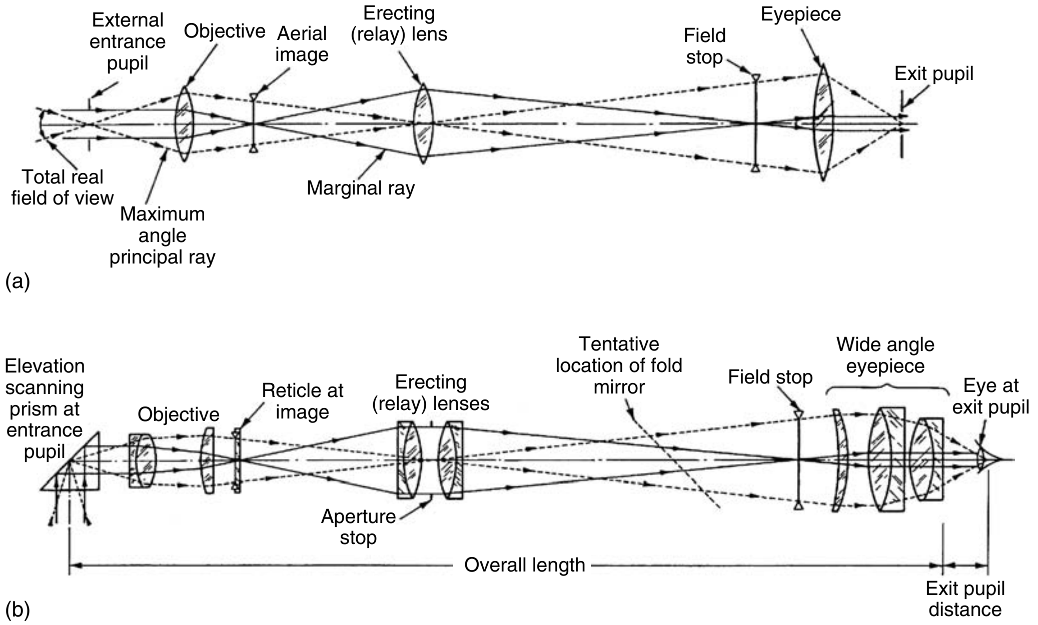
External entrance pupil
Objective
Aerial image
Erecting (relay) lens
Field stop
Eyepiece
Exit pupil
Total real field of view
Maximum angle principal ray
Marginal ray
(a)
Elevation scanning prism at entrance pupil
Objective
Reticle at image
Erecting (relay) lenses
Tentative location of fold mirror
Field stop
Wide angle eyepiece
Eye at exit pupil
Aperture stop
Overall length
Exit pupil distance
(b)

FIGURE 1.5 Optical schematic diagrams for a lens-erecting periscopic sight with the following characteristics: magnification = 2×, total object space field of view = 35°, exit pupil diameter = 0.2 in. (5.08 mm), exit pupil distance = 0.68 in. (17.3 mm), and overall length = 13 in. (330 mm). (a) Thin-lens version; (b) preliminary thick-lens design.

all apertures are known approximately. Figure 1.5(b) illustrates a preliminary thick-lens schematic of the periscope shown in Figure 1.5(a). We do not have space to consider here how the lens designer creates the final optical design. This topic is well covered in other publications such as Smith (1992, 2000, 2004), Kingslake (1978, 1983), O'Shea (1985), Laikin (2001), Shannon (1997), Walker (1998), and Fischer and Tadic-Galeb (2000).

The parameters most responsible for driving the optical design in the type of system shown in Figure 1.5 are overall length, magnification, entrance and exit pupil diameters, and field of view. The use of a lens-erecting system instead of prisms to erect the image is appropriate since the objective and eyepiece focal lengths should be kept short. Longer focal lengths that would be required to accommodate the added path length of prisms would cause the image of a given field of view to grow proportionately in diameter. The field of view and exit pupil diameter determine the diameter of the eyepiece for a given exit pupil distance. The overall length influences the diameters of the erecting lenses and, hence, that of the entire telescope. In order to provide adequate image quality over a large field of view with external pupils, the objective and eyepiece should both be wide-angle types. An Erfle-type eyepiece and an objective styled after a Kellner-type eyepiece are shown. These configurations are described in many optics texts (e.g., Rosin 1965; Smith 2000).

Comparison of the thin- and thick-lens designs for this periscope shows the significant change in system length that occurs when real lenses are substituted. The original focal lengths of the thin-lens system are preserved in the thick-lens version. Given a preliminary (or final) thick-lens optical design, the mechanical engineer can begin a layout of the metal parts for the instrument. An important input at this time is a preliminary definition of the set of adjustments that should be provided to take care of manufacturing variations in parts at assembly. Knowledge of the predicted sensitivity of the optical design to mispositioned and dimensionally off-nominal components is needed for this determination. Sensitivity data are also needed to assign appropriate tolerances to both optical and mechanical part dimensions and physical properties in the mechanical design. This aspect of the design process is addressed in Section 1.6.

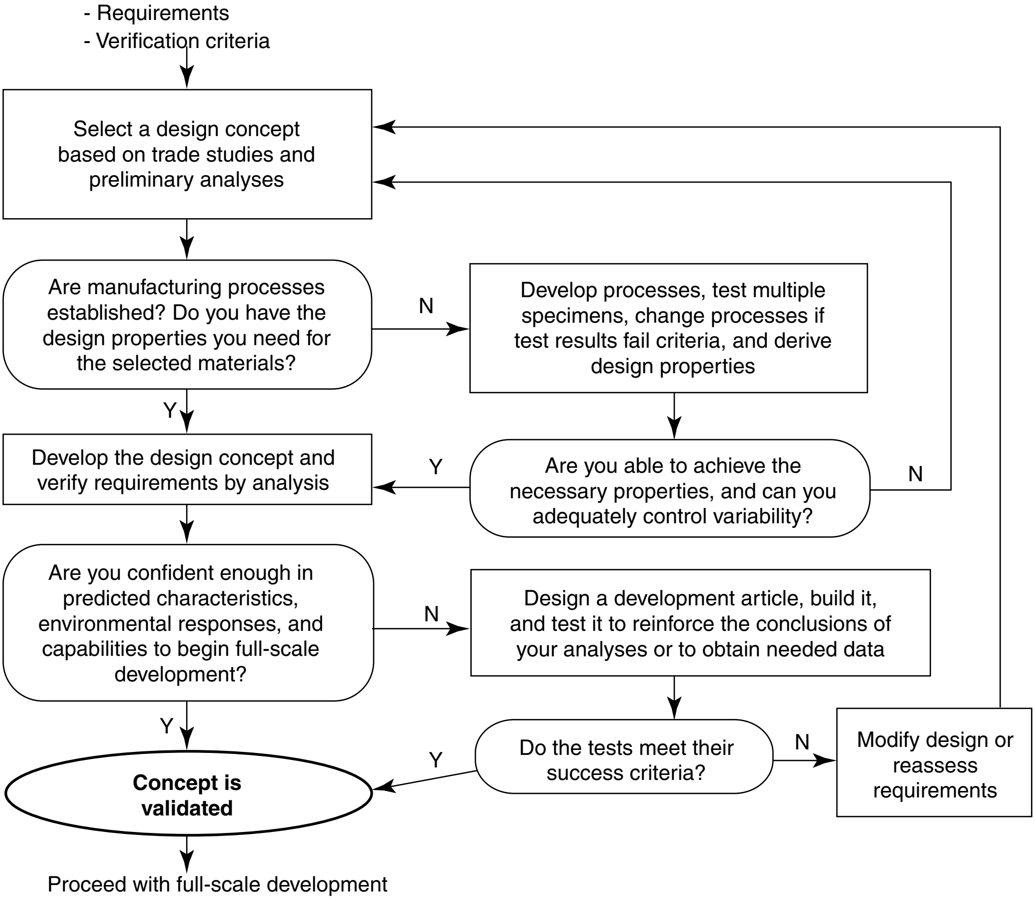
- Requirements
- Verification criteria
Select a design concept based on trade studies and preliminary analyses
Are manufacturing processes established? Do you have the design properties you need for the selected materials?
N
Develop processes, test multiple specimens, change processes if test results fail criteria, and derive design properties
Y
Develop the design concept and verify requirements by analysis
Y
Are you able to achieve the necessary properties, and can you adequately control variability?
N
Are you confident enough in predicted characteristics, environmental responses, and capabilities to begin full-scale development?
N
Design a development article, build it, and test it to reinforce the conclusions of your analyses or to obtain needed data
Y
Concept is validated
Y
Do the tests meet their success criteria?
N
Modify design or reassess requirements
Proceed with full-scale development

FIGURE 1.6 Flow diagram for design/material/process verification steps during conceptual and preliminary design phases of the project. (From Sarafin, T.P., in *Spacecraft Structures and Mechanisms*, Sarafin, T.P., and Larson, W.J., Eds., Microcosm, Torrance and Kluwer Academic Publishers, Boston, 1995b, chap. 11.)

Establishing confidence that a proposed preliminary design will really work when finalized entails answering several key questions. Figure 1.6 shows a flow diagram for such an evaluation. Starting with the existing requirements and criteria for verifying capability of the design to meet them, we develop the design concept. The first set of questions deals with issues of adequacy of manufacturing processes and availability of materials with suitable properties. If these are answered "yes," we proceed with the preliminary design. If answered "no," we fill in the missing information and show that we can control variability of materials and processes. Hopefully, analysis and modeling (Section 1.5) then confirm that we are ready to begin full-scale development. If this is not the case, we design, build, and test models to obtain the needed data. If successful, the concept proceeds to the detailed design step (Section 1.6). If not, we modify the design or change the requirements and repeat the evaluation process. Eventually, the improved preliminary design is accepted (at a preliminary design review; see Section 1.9), and then we go ahead into detailed design.

1.5 DESIGN ANALYSIS AND COMPUTER MODELING

At this point in the design, the materials for all major parts of the instrument would have been chosen, at least tentatively, so the thermal and dynamic (shock and vibration) characteristics of the design when exposed to the anticipated environment can be analyzed. Any apparent inadequacy of the preliminary design revealed by these analyses should be carefully assessed to determine whether redesign is necessary. The changes might be as simple as substitution of stainless steel for aluminum to reduce the coefficient of thermal expansion of the parts determining a particularly critical air space. Glass choices might need reconsideration if, for example, analysis indicates that cemented doublets may not survive thermal shock due to the widely differing expansion properties in the elements or if focal length changes with temperature are excessive. More complex changes in structural design may be found necessary if analytical simulations of shock or vibration loads indicate excessive deformations or even the possibility of structural failure.

In simple instruments, it may be sufficient to estimate the perturbed system's mechanical behavior using classical beam and shell theory to quantify component deflections (i.e., strains) and stresses as well as classical heat transfer theory to quantify temperature effects. In such cases, limited knowledge of temperature distributions, component deformations, and displacements may be adequate to estimate these effects on system performance. Roark (1954) and later versions of that work (such as Young, 1989) provided a general set of equations for deflections, internal moments, shears, and stresses of a large variety of geometrical bodies. Roark's equations form the basis for many of the analyses of various types of opto-mechanical components and assemblies in Chapter 15.

No value calculated with the aid of closed-form equations from reference books can be considered to be exact. The equations are based on certain assumptions on the applicability and behavior of a mathematical model of the hardware, the uniformities of key properties of materials within extended pieces of these materials, uniformities of geometric forms, and applied boundary conditions that are not necessarily absolutely true. Further, they are derived by mathematical procedures that often involve additional approximations. Fortunately, extremely high accuracy is not generally required in engineering design or analysis so calculations made with these equations are adequate in most cases. More elaborate, but not necessarily more accurate, calculations related to structural design problems are usually accomplished with finite element analysis (FEA) methods. Even in simple instruments, the calculations may be complex if one has to deal with temperature-dependent material properties, three-dimensional spatial variations of temperature, temporal variations (such as thermal shock due to rapid temperature changes or development of gradients), and alternative material or configuration trade-offs.

FEA methods have been developed over many years and are the generally accepted tools for design and analysis of mechanical structures. They have great applicability to static, dynamic, and heat transfer analyses of opto-mechanical instruments. In a typical FEA analysis, a model of the structure is created as a two- or three-dimensional continuum of small elements. It is assumed that deformations (i.e., strains) within these elements are elastic, uniform, and distributed according to some known relationship. The elements usually have triangular, rectangular, or trapezoidal faces and are assumed to be connected by frictionless pins at their vertices or nodes. Elastic-body relationships are utilized to derive polynomial representations of deformations of the structure under applied disturbances. Temperature distributions can be applied to the model to determine thermal effects. Optical components are typically modeled as structures since we are interested in surface deformations as well as stress distributions. Many equations must be solved to describe the behavior of the entire structure, so matrix operations, complex software programs, and high-speed, large-capacity computers are employed. The results are recognized as approximations. They approach truth, i.e., converge, as the assumed model analyzed becomes more complex and greater numbers of smaller elements (i.e., a finer mesh in the model) are considered.

Hatheway (2003) illustrated this convergence property of the FEA method with the following example. A 16-in.-square and 32-in.-long aluminum beam was cantilevered from one end. Its distributed weight caused the free end to droop under gravity. The proportions of the beam were chosen to require consideration of shear effects as well as elastic deformation. The deflection was predicted by a linear elastic computation and by FEA assuming different numbers of nodes. Figure 1.7 shows five models having progressively finer meshes and hence more nodes. Table 1.6 lists the characteristics of these models. Figure 1.8 plots the variation of the deflection at the free end of the beam calculated by

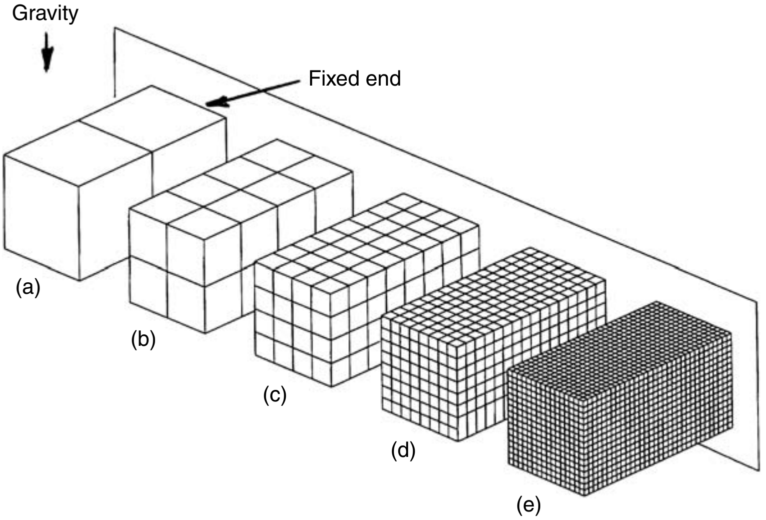

FIGURE 1.7 Five FEA models used to illustrate the effect of convergence on complexity of the model. (Adapted from Hatheway, A.E., *Proc. SPIE*, 5178, 1, 2003.)

TABLE 1.6
Characteristics of FEA Models of Beam Shown in Figure 1.7

View	(a)	(b)	(c)	(d)	(e)
n=number of elements on edge of square face	1	2	4	8	16
Element size (in.)	1	0.5	0.25	0.125	0.062
Total nodes in model=$(n+1)^2(2n+1)$	12	45	225	1377	9537

Source: Adapted from Hatheway, A.E., *Proc. SPIE,* 5178, 1, 2003.

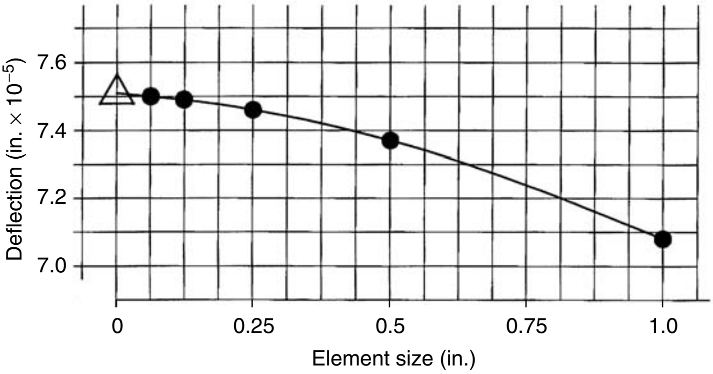

FIGURE 1.8 Convergence of calculated beam deflections as the sizes of the FEA elements decrease and the number of nodes increases. (Adapted from Hatheway, A.E., *Proc. SPIE*, 5178, 1, 2003.)

the linear equation (triangle) and by FEA (solid circles) for different numbers of nodes. The curve shows the FEA approximation approaching the linear value, as the elements grow smaller, i.e., the number of nodes increases. This characteristic can be used to estimate the degree of accuracy of an FEA analysis by testing a given calculation with an increased number of nodes. If the calculation result changes by only a small amount, convergence is occurring and the result can be considered reasonably accurate.

Several computerized structural analysis codes such as NASTRAN, ANSYS, STARDYNE, etc., have been developed to facilitate these computations (and especially parametric recomputations with small modifications of various mechanical parameters). The structural analysis codes compute the elastic deflections of structures under an assumed set of imposed loads, either static or dynamic (time-varying) as well as the localized stresses in those structures. Stress computations are frequently used to estimate the potential for structural damage under extreme environmental conditions. Doyle et al. (2002) gave very specific explanations of the basic considerations involved in the use of FEA methods to model and analyze optical instruments.

FEA codes are very effective from the systems viewpoint if used in combination with other codes. Figure 1.9 shows a representation of the interaction between various types of analyses. Mechanical and thermal analysis models utilize many different types of codes. When optics are involved, we add optical analysis models and codes. The most powerful of these are general-purpose lens-design and analysis codes such as Code V, OSLO, ZEMAX, etc. These codes calculate multiple-ray trajectories and intercepts using the laws of reflection, refraction, and diffraction. Optical performance is usually evaluated in terms of geometrical aberrations, modulation transfer functions, point and line spread functions, and Zernike polynomial representations of aberrations and/or optical surface distortions. Optical system performance degradation usually results from rigid-body component tilts, displacements from nominal orientation and location, and from surface deformations.

Most sophisticated applications, such as the design and analysis of complex instruments for space exploration or large ground based astronomical telescopes, involve disciplines other than optics and mechanics. Control systems, fluid mechanics, electro-magnetics, electronic signal processing, communications, etc., may need to be considered. All the disciplines that comprise the total system may need to share data in order to permit analysis of the instrument's performance.

Contemporary CAD packages (such as AutoCad, SolidWorks, and Pro/Engineer) are very powerful tools for formatting models of opto-mechanical systems and for graphically portraying computational results. Optical design codes and structural or thermal analysis codes use different techniques for solving their equations, and their input/output data formats are not generally identical, so the computational routines may not be directly compatible. In order to evaluate the optical

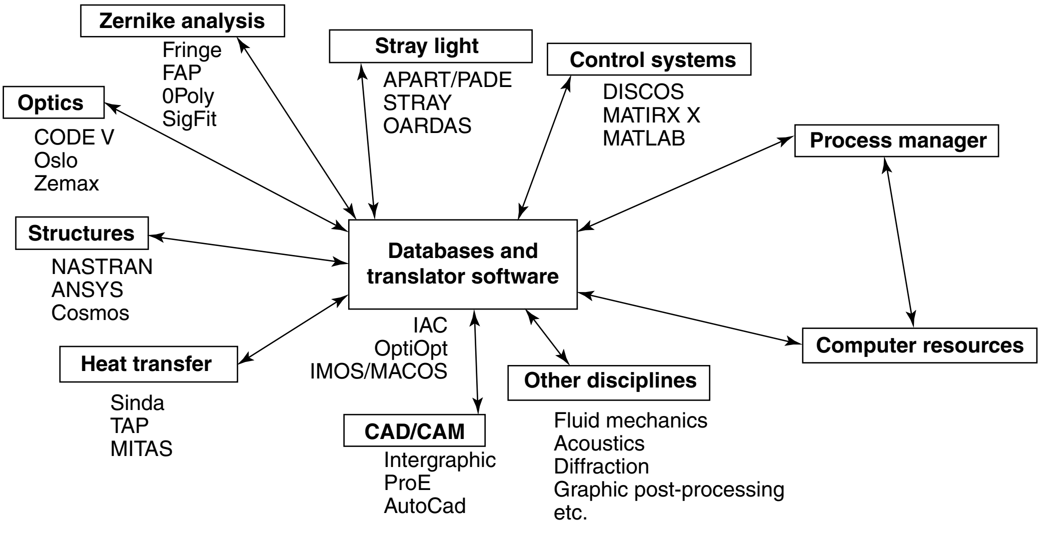
Zernike analysis
Fringe
FAP
0Poly
SigFit
Stray light
APART/PADE
STRAY
OARDAS
Control systems
DISCOS
MATIRX X
MATLAB
Optics
CODE V
Oslo
Zemax
Process manager
Structures
NASTRAN
ANSYS
Cosmos
Databases and translator software
IAC
OptiOpt
IMOS/MACOS
Heat transfer
Sinda
TAP
MITAS
Computer resources
Other disciplines
Fluid mechanics
Acoustics
Diffraction
Graphic post-processing
etc.
CAD/CAM
Intergraphic
ProE
AutoCad

FIGURE 1.9 Interactions between various disciplines in opto-mechanical analysis. (From Hatheway, A.E., *Proc. SPIE*, 5178, 1, 2003.)

effects of mechanical or thermal disturbances, it has become common practice to evaluate the optical performance of the unperturbed system, compute the elastic deformations due to external influences such as vibration or temperature change, and then to input those results into the optical design code where the optical performance is recomputed. Coronato and Juergens (2003) described a technique for accomplishing this transfer using Zernike circular polynomials.

In what is called an *integrated analysis method*, each technical discipline uses its own software, and a database manager moves data from code to code and reformats (or translates) the output of each code to serve as the input to the next code. Data values are interpolated or extrapolated to fit the unique requirements of the various codes as they are transferred. Figure 1.9 depicts this method. Errors introduced in the data transfer steps may be large and are difficult to quantify. Validation of results may require checking with a more rigorous procedure or by experimental test. In some cases, solving problems for which the results are already known from prior closed form calculations or tests can validate the calculation routines.

The method diagrammed in Figure 1.9 has all the individual software codes available to the database managing and translating software (DBM/TS) that uses a central computer or system of computers programmed to interface and control all the computational steps. Once required input files (models) for each code have been prepared, the DBM/TS can run the appropriate problems and direct the output from each code to the proper next recipient. If the indicated recipient is another code, the DBM/TS automatically processes the data into the proper format for input to that code. For example, data-processing algorithms may convert data from a cylindrical to a rectangular coordinate system or interpolate temperature distribution data to a finer grid than originally computed. This represents a very sophisticated operating system for the software codes that it is designed to integrate.

Figure 1.10 shows an expanded representation of the integrated analysis method with potential pathways for complex flow of design data between various software programs during the idealized design or development process. Solid lines imply direct influences while dashed lines indicate data flow that may form the basis for manual design changes. Data exchange between programs is facilitated if they all use standard formats. Examples of existing data exchange formats are listed in Table 1.7. The reader's attention is drawn especially to the last entry in that table (STEP), which is an attempt by ISO at producing and applying an international standard for product data representation and exchange. It is intended, in part, to address the need for data exchange throughout

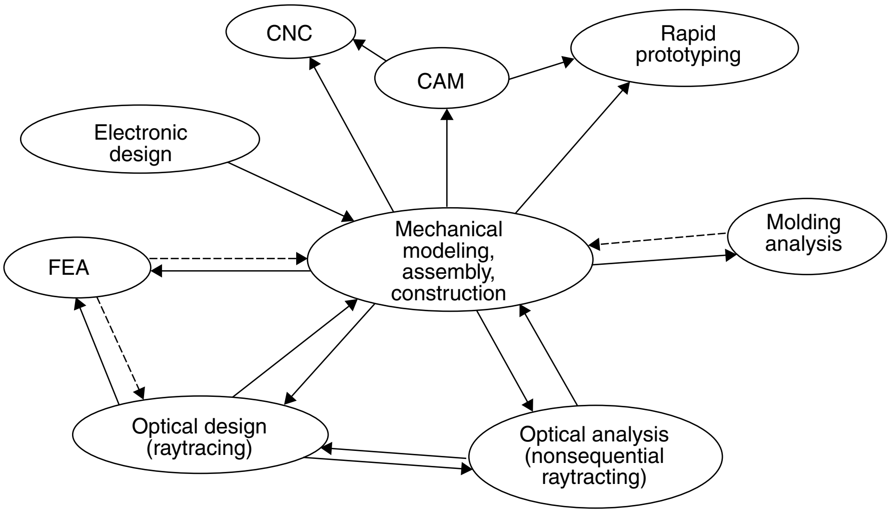
CNC
CAM
Rapid prototyping
Electronic design
FEA
Mechanical modeling, assembly, construction
Molding analysis
Optical design (raytracing)
Optical analysis (nonsequential raytracing)

FIGURE 1.10 Potential pathways for design data flow between software packages. The dashed-line arrows represent paths wherein analysis data can be used as a basis for design changes, but the analysis program does not modify the design data directly. (From Shackelford, C.J., and Chinnock, R.B., *Proc. SPIE*, 4198, 148, 2000.)

TABLE 1.7
Some CAD and Graphics File Formats for Electronic Data Exchange

Format	Name	Maintained by	Comments
BMP	Windows **B**it**M**a**P**	Microsoft Corp.	Graphics file format used by Windows. File with array of RBG graphics data for each image pixel.
DXF	**D**rawing e**X**change **F**ormat	Autodesk	Vector-based 3D Format
IGES	**I**nternational **G**raphics **E**xchange **S**pecification	National Computer Graphics Association	Set of protocols for transfer display of graphical data
JPEG	**J**oint **P**hotographic **E**xperts **G**roup	C-Cube Microsystems	JPEG is a compression algorithm for encoding bitmap data and not a file format.
JFIF	**J**PEG **F**ile **I**nterchange **F**ormat	C-Cube Microsystems	JFIF is the de-facto standard Internet JPEG format.
STL	**ST**ereo **L**ithography **I**nterface **F**ormat	3D Systems	ASCII or binary files allow CAD data to be read by stereolithography apparatus.
VDA-FS	**V**erband **D**er **A**utomobil-industrie **F**laschen **S**nittstelle	Verband Automobil-industrie	German international standard
STEP	**ST**andard for the **E**xchange of **P**roduct	International Standards Organization	ISO 10303 Industrial automation systems – Product representation and exchange

Source: Adapted from Shackelford, C.J., and Chinnock, R.B., *Proc. SPIE*, 4198, 148, 2000.

the life cycle of a product. This time period may extend well beyond the lifetime of the computer program used to design the product. During this period, proprietary programs may become obsolete or lose their ability to communicate with other needed programs. STEP also provides a neutral data model (NDM) that allows data to be stored on any database platform and to be accessed from any application through a standard interface. The STEP technique is in limited use at this time.

A different approach to solving multidisciplinary computational problems related to opto-mechanics is to develop a mathematical analogy between the discipline of interest and the FEA code being used. Hatheway (1988, 2003) defined this as a *unified analysis method*. In almost all cases, one relies on linearized versions of equations for each discipline involved, such as thermal, elasticity, and optics. By linearizing the equations used in the analogy, the solution often requires only one software code, thus avoiding the interpolations, extrapolations, format changes, truncations, and data expansions, and contractions that might otherwise be required to move the problem solution back and forth among software codes en route to the desired result.

To illustrate this technique, Figure 1.11(a) shows an FEA model of the structure supporting the primary and secondary mirrors of an afocal telescope. This telescope was not performing well because of mechanical strains introduced into the primary mirror by its mounting structure. Direct evaluation was complicated by the smallness of the distortions relative to the rigid-body motions of the mirror. In an FEA simulation, an optical analog of an interferometer was applied to the mirror surface. This interferometer was considered mathematically to move with the mirror surface when the structure was deformed as shown in Figure 1.11(b). Then, only relative motions appeared in the output data. Plots of simulated interferograms at appropriate scales (in wavelengths) allowed the determination of the disturbing effects of minute particles trapped under the mirror's mounting flange. In Figure 1.11(c), mirror deformations resulting from a single, hard, 0.005-in. (125-μm)-diameter particle located under the mounting flange for the primary mirror at a particular grid location were represented by contour lines separated by 1/2 wave at 450 nm wavelength. The total deflection range equaled 0.71 wave at 633 nm wavelength and explained why the system did not perform properly.

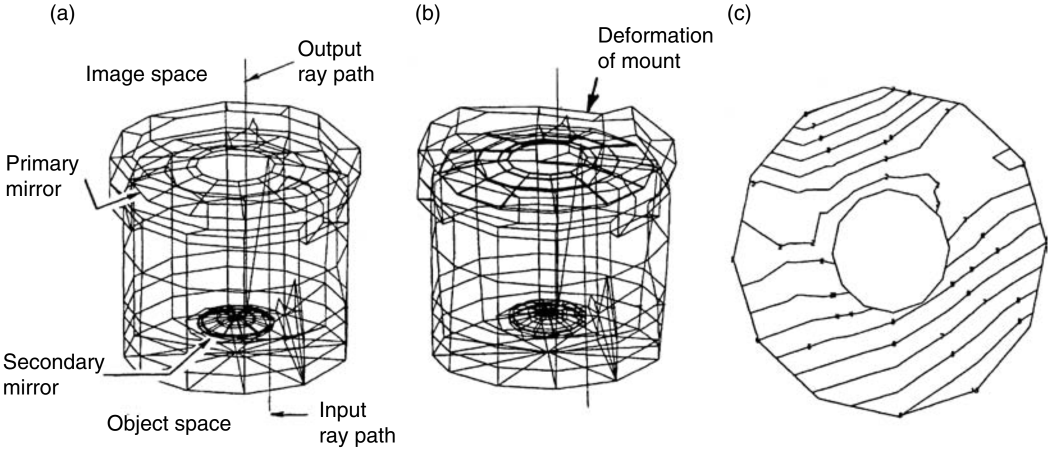

FIGURE 1.11 Representation of a FEA graphical output showing: (a) an undeformed telescope structure, (b) the same structure with a deformed flange, and (c) an analog interferogram of the distorted primary mirror in the telescope of (b) scaled in waves of 450-nm wavelength light to show detailed surface figure errors. Note that the unresolved symbols on the fringes of (c) are numbers identifying the fringe sequence. (From Hatheway, A.E., Computers in Engineering, American Society of Medical Engineering, New York, 1988, p. 3. Reprinted with permission from the American Society of Mechanical Engineers.)

The capability of properly applied FEA programs to perform analyses such as those just described may lead some analysts to believe computed results without adequately questioning the validity of the assumptions and modeling inputs to the program or the accuracy limits of the selected model. The design engineer must never lose sight of the fact that the FEA model may, under certain circumstances, neglect important characteristics of the structure analyzed or be improperly applied. It will then give misleading results. As mentioned earlier, by carefully applying selected classical methods of elastic structure behavior analysis (such as Roark, 1954 or Roark's formulas as presented by Young, 1989) along with the FEA program as synergistic tools of the trade, greater confidence in the results can be generated. Genberg et al. (2002) indicated that FEA results should be considered "guilty until proven innocent." Those authors also indicated that the engineer must accept the burden of understanding the underlying theory of structural/thermal/finite element analysis; understand the working details of the FEA program, including its pre- and post-processor features; make and verify modeling decisions and assumptions; interpret the results and draw the appropriate conclusions; and properly document the analysis.

No matter what form the analysis of a design may take, it is imperative that records be kept as the design progresses. Items such as the reasons for choosing particular materials, the basis for concluding that a design (or a portion thereof) will or will not work reliably, and the logic behind the choice of specific commercial parts for incorporation into the design are important enough to document. These records serve as valuable backup information for design reviews (see Section 1.9). Experience has shown that these records also are well worth the trouble of preparation if they are needed for future reference in the solution of unanticipated problems, for support of patent applications, or for protection from product liability claims. These documents should become part of the formal design files and not reside in the individual designer's or engineer's mind or files, where they are likely to become lost with time.

If, as is generally the case, production cost and maintainability of the instrument through its life cycle are critical to the intended application, analyses of these aspects of the design would be appropriate. Trade-off studies of alternative versions of cost-driving features should help indicate the most cost-effective design. Maintainability analyses may lead to design improvements that reduce the number of spare parts to be inventoried, eliminate needs for special tooling, or facilitate (or eliminate needs for) manual adjustments by highly trained personnel. Willey (1983, 1989), Fischer (1990), Willey and Durham (1990, 1992), and Smith (2000) have contributed many examples of good and bad designs as well as excellent technical guidelines for avoiding production or testing problems by proper instrument design and thoughtful selection of materials and processes before finalizing the drawings.

1.6 ERROR BUDGETS AND TOLERANCES

Closely related to the performance specifications and constraint definitions considered in Section 1.3 are the multilevel budgets on allowable deviations from perfection of component dimensions and alignments relative to other components in the instrument. Tolerances strongly influence how an opto-mechanical system will perform and the life cycle cost of that instrument. For example, let us consider an electro-optical star sensor system intended for use as a precision attitude reference on a spaceborne platform as described by Cassidy (1982) and discussed in Section 5.9. The achievement of pointing accuracies of the order of 1 part in 58,000 (0.5 arcsec over an 8° field of view) required uniform symmetry and encircled energy consistency of the star images over the full field of view. Analysis showed that, for proper function, the actual spot diameter at, for instance, the 75% encircled energy level should be considerably larger than the diffraction limit corresponding to the chosen fast (f/1.5) system relative aperture. In order for the designer of this lens system to do his or her job effectively, a target energy distribution in the axial image produced by the lens and a budget on permitted perturbation of that distribution due to aberrations as a function of semifield angle were specified as design parameters. Once it was determined that this performance was easily achievable in a properly built and aligned system, an error analysis indicated how tilt, decentration, and despace of the individual optical components were related to image degradation. A portion of the total error budget was then assigned to individual and ensemble internal component misalignments and the detailed mechanical design was allowed to proceed. Since the ability of technicians to assemble a lens to meet component decentration, tilt, and despace budgets depends in part on their ability to detect small errors, portions of the error budget were assigned to instrumental and random errors in the measurement processes used. Inherent in this budgeting process is the assumption that the focus of the lens system remains perfect during operation. Obviously, temperature changes could affect focus, so a portion of the mechanical design error budget was allocated to uniformly distribute thermal effects. Thermal gradients across the lens affect symmetry of the image so they also received due attention and were assigned another portion of the budget. As a result of careful manufacture and assembly closely monitored by quality control inspectors who ensured that the design was followed in the hardware, the system met all requirements for its application.

Smith (1985) pointed out that since many potential sources of error unique to any particular design situation need consideration, the allocation of error budgets should be systematized in order to ensure a successful design. Ginsberg (1981) outlined a technique used successfully for this purpose. He stated that the purpose of the process was “to determine the loosest tolerances that can be specified for optical and mechanical parts and assemblies which will still provide adequate performance.” Acting on the assumption that this purpose logically fits most applications facing the reader, we summarize Ginsberg’s process. A simplified block diagram relating various steps is shown in Figure 1.12. We have already discussed blocks 1 to 6. Block 7 represents a preliminary cooperative decision by the design team as to the general tolerancing approach, i.e., whether parts should be held close to nominal dimensions and little adjustment flexibility be designed into the assembly, or vice versa. Obviously, the preliminary optical schematic and the opto-mechanical layout should be consulted to determine which variables can easily be controlled and which elements can be adjusted to compensate for the adverse effects of other variations. Table 1.8 lists typical “loose” and “tight” tolerances on specific parameters of interest in building common optical instruments as well as approximate limits of capability of current manufacturing technology.

Figure 1.13 shows the example of a simple laser beam expander (telescope) used in Ginsberg’s 1981 paper to illustrate the application of tolerancing to a typical assembly. The telescope is to be

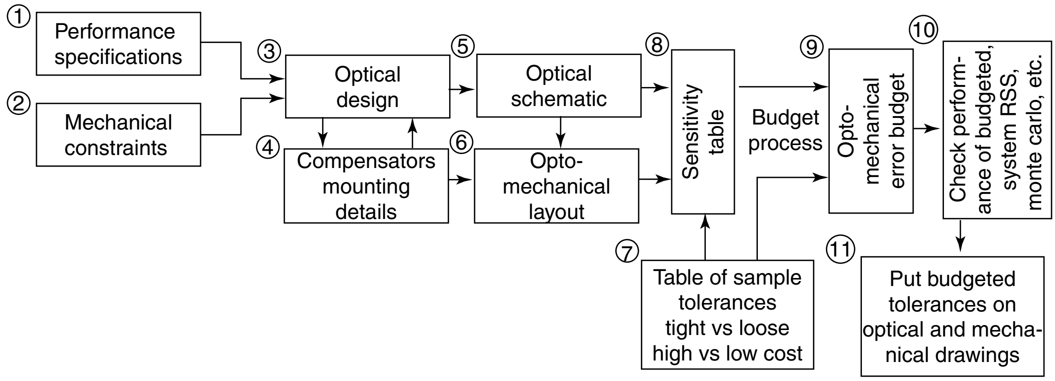
①
Performance specifications
②
Mechanical constraints
③
Optical design
④
Compensators mounting details
⑤
Optical schematic
⑥
Opto-mechanical layout
⑦
Table of sample tolerances tight vs loose high vs low cost
⑧
Sensitivity table
Budget process
⑨
Opto-mechanical error budget
⑩
Check performance of budgeted, system RSS, monte carlo, etc.
⑪
Put budgeted tolerances on optical and mechanical drawings

FIGURE 1.12 Block diagram showing the initial steps in one type of opto-mechanical error budgeting and tolerancing process. (From Ginsberg, R.H., *Opt. Eng.*, 20, 175, 1981.)

TABLE 1.8
Sample Tolerances Applicable to Opto-Mechanical Parameters

Parameter	Units	Tolerance		Approximate limiting value
		Loose	Tight	
Index of refraction	—	0.003	0.0003	0.00003[a]
Radius departure from test plate	fringes[b]	10	3	1
Departure from spherical or flat	fringes[c]	4	1	0.1
Element diameter	mm	0.5	0.075	0.005
Element thickness	mm	0.25	0.025	0.005
Lens wedge angle	arcmin	3	0.5	0.25
Air space thickness	mm	0.25	0.025	0.005
Decenter, mechanical	mm	0.1	0.010	0.005
Tilt, mechanical	arcmin	3	0.3	0.1
Dimensional errors of prisms	mm	0.25	0.010	0.005
Angle errors: prisms and windows	arcmin	5	0.5	0.1

[a] Depends upon piece size.

[b] One fringe equals 0.5 wavelength at 0.546 μm (mercury green). Fringes are specified over the maximum dimension of the clear aperture.

[c] Depends on the manufacturing process.

Source: Adapted, in part, from Ginsberg, *Opt. Eng.*, 20, 175, 1981 and Plummer, J. and Lagger, W., *Photon.*, *Spectra*, Dec, 65, 1982 as updated by Fischer, R.E. and Tadic-Galeb, B., *Optical System Design*, McGraw-Hill, New York, 2000.

flange-mounted at datum -A- and located laterally with respect to a pilot diameter (datum -B-). It is assumed that the laser beam will enter perpendicular to datum -A- and will be centered with respect to the pilot diameter. The larger lens is to be used as a compensator for focusing the output beam and also for aligning that beam normal to datum -A- (by sliding the lens mount on surface -C-). Because the first lens registers to its first polished surface, an assembly clearance between its outer diameter and the metal inner diameter will allow the lens to tilt slightly about the center of curvature of that surface. The second lens, on the other hand, is referenced to a plane surface so it cannot tilt, but can only decenter. The first lens will tilt if the shoulder against which it is mounted is tilted with respect to surface -A-. Because the larger lens' cell rotates in its threads for focus adjustment, its centering relative to the cell should be controlled by tolerancing the concentricity of the threads and the fit between the

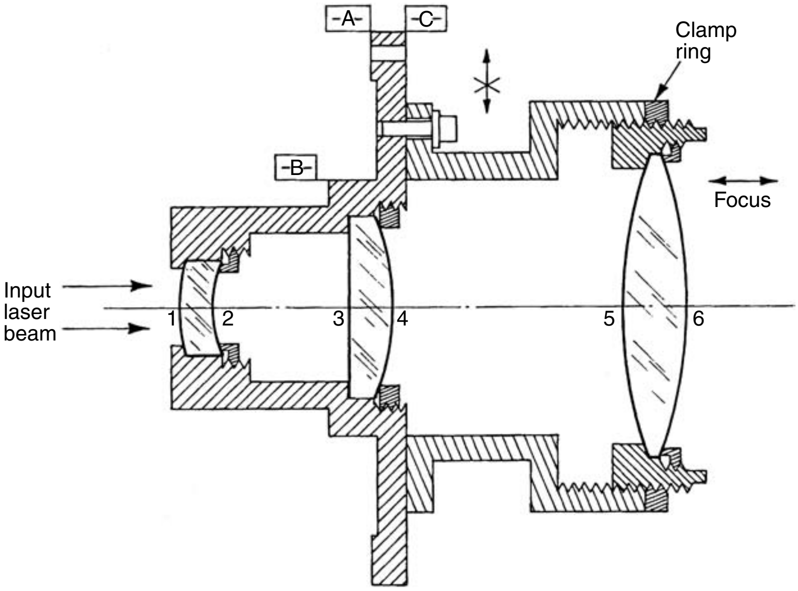

FIGURE 1.13 Opto-mechanical layout of a simple laser beam expander telescope used as an example in considerations of a process for budgeting error tolerances. (From Ginsberg, R.H., *Opt. Eng.*, 20, 175, 1981.)

mating threads. Other design features requiring tolerances include the parallelism of surfaces -A- and -C- and the fit of the threads that seat retainers against curved lens surfaces. More will be said about lens-to-metal interfaces in Chapter 4 so we need not elaborate here on that aspect of the design.

To prepare data for the sensitivity table of block 8 in Figure 1.12, the maximum reasonable magnitudes for all potential errors are approximated and then each parameter is changed by a convenient small step. The corresponding change in performance in terms of some merit function or aberration that are agreed upon is computed and entered into the blank spaces on a previously prepared table such as that shown in Figure 1.14. Linearity with small parameter changes is assumed.

The sensitivity data in Figure 1.14 apply to the hardware example of Figure 1.13. The performance characteristic of interest here is the output beam divergence, Δdiv (in μrad), due to the changes listed in the column headed "change." Footnote "A" states that adjustment of the third lens element compensates for defocus or change in direction of the output beam before the change in divergence is calculated. The magnitudes of these adjustments are computed and entered into the final two columns. Additional columns could be added to the table to record sensitivities of other performance criteria as appropriate. If the error-to-performance relationship is not linear, different tables should be prepared for errors of different magnitudes.

The actual error budget (see block 9 of Figure 1.12) is developed from the sensitivities and table of approximated maximum errors. Environmentally induced errors during operation may be considered. Figure 1.15 shows a budget applicable to the example considered by Ginsberg. All parameters of interest for each component are listed together to facilitate transferring the information to the optical and mechanical drawings. The applicable tolerances must, of course, be considered as an ensemble. If the errors are reasonably independent, we may estimate their overall effect as the root sum square of those errors. This should be compared with the total allowable system error. A "worst-case" budget would allow the errors to add. This is not a reasonable representation of actual hardware.

Since application of this process to even the simplest of optical instruments can result in an unacceptable "first-cut" error budget, it is usually necessary to iterate the process until a satisfactory distribution is achieved. One benefit of such recomputations may be the relaxation of cost-driving tight tolerances on one or more parameters. Usually, but not always, the magnitudes of the allowable errors

Sensitivity table

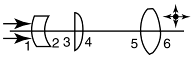

	Surface element or group	Change	Parameter and comments	Δdiv. µrad. Ⓐ	Req'd refocus 5-6 inches	Req'd DCNTR 5-6 inches
	1-2	0.001	Index of refraction			☒
	3-4	0.001	-do-			☒
	5-6	0.001	-do-			☒
	1-2	0.00001	Homogeneity		☒	☒
	3-4	0.00001	-do-		☒	☒
	5-6	0.00001	-do-		☒	☒
	1-2	0.001"	Thickness or Air space			☒
	2-3	0.001"	-do-			☒
	3-4	0.001"	-do-			☒
	4-5	0.001"	-do- (without compensation)		☒	☒
	5-6	0.001"	-do-			☒
	1	0.1%	Radius			☒
	2	0.1%	-do-			☒
	4	0.1%	-do-			☒
	5	0.1%	-do-			☒
	6	0.1%	-do-			☒
	3	1 Frng	Non-flat over " ϕ			☒
	1	1 Frng	Irregty over " ϕ		☒	☒
	2	1 Frng	-do- " ϕ		☒	☒
	3	1 Frng	-do- " ϕ		☒	☒
	4	1 Frng	-do- " ϕ		☒	☒
	5	1 Frng	-do- " ϕ		☒	☒
	6	1 Frng	-do- " ϕ		☒	☒
	1-2	1 Frng	Wedge @ 2		☒	
	3-4	1mr	Wedge @ 4		☒	
	5-6	1mr	Wedge @ 6		☒	
	1-2	0.001"	Roll @ 1		☒	
	5-6	0.001"	Roll @ 5		☒	
	1-2	0.001"	Decenter		☒	

(A) After refocusing output beam with lens 5 - 6, or correcting output beam direction with lens 5-6.

Sensitivity table

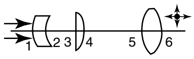

	Surface element or group	Change	Parameter and comments	Δdiv. µrad. Ⓐ	Req'd refocus 5-6 inches	Req'd DCNTR 5-6 inches
	3-4	0.001"	Decenter		☒	
	5-6	0.001"	-do- (without compensation)		☒	
	1-2	1mr	Tilt @ 1 C.A		☒	
	3-4	1mr	Tilt @ 3		☒	
	5-6	1mr	Tilt @ 5 C.A		☒	
	☒	☒	Axial displacement Ⓑ	☒	☒	☒
	☒	0.010"	Laser decenter			
	☒	1mr	Laser tilt @ 1			
	☒	10mr	Laser tilt @ 1			

(B) Information available from air space changes.

FIGURE 1.14 Typical sensitivity table applicable to the opto-mechanical assembly shown in Figure 1.13. (From Ginsberg, R.H., *Opt. Eng.*, 20, 175, 1981.)

Error budget

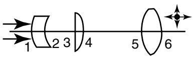

	Surface element or group	Change	Parameter and comments	Δdiv. µrad. Ⓐ	Req'd refocus inches	Req'd DCNTR inches
	1-2		Index of refraction			☒
			Homogeneity			☒
		"	Thickness			☒
	1	"	Radius error FR. %			☒
	2	"	Radius error FR. %			☒
	1	FR	Irregty over . " ϕ		☒	☒
	2	FR	Irregty over . " ϕ		☒	☒
	@ 2	mr	Wedge		☒	
	@ 1	"	Roll		☒	
			Decenter, RSS of all causes		☒	
		"	Axial displacement, RSS			☒
	@ 1C.A.	mr	Tilt, RSS			
	3-4		Index of refraction			☒
			Homogeneity			☒
		"	Thickness			☒
	3	FR	Non-flat over . "ϕ			☒
	4	"	Radius error FR . %			☒
	3	FR	Irregty over . "ϕ		☒	☒
	4	FR	Irregty over . "ϕ		☒	☒
	@ 4	mr	Wedge		☒	
		~~"~~	~~Roll~~		☒	
		"	Decenter, RSS of all causes		☒	
		"	Axial displacement, RSS			☒
	@ 3	mr	Tilt, RSS			
		"	Laser decenter		☒	☒
		mm	Laser tilt		☒	☒

(A) After refocusing output beam with lens 5 - 6, or correcting output beam direction with lens 5-6.

Error budget

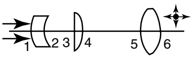

	Surface element or group	Change	Parameter and comments	Δdiv. µrad. Ⓐ	Req'd refocus inches	Req'd DCNTR inches
	5-6		Index of refraction			☒
			Homogeneity			☒
		"	Thickness			☒
	5	"	Radius error FR. %			☒
	6	"	Radius error FR. %			☒
	5	FR	Irregty over . " ϕ		☒	☒
	6	FR	Irregty over . " ϕ		☒	☒
	@ 6	mr	Wedge		☒	
	@ 5	"	Roll		☒	
		~~"~~	~~Decenter, RSS of all causes~~		☒	
		"	Axial displacement, RSS			☒
	@5 CA	mr	Tilt, RSS			
			Index of refraction			
			Homogeneity			
		"	Thickness			
		FR	Irregty over . "ϕ			
		FR	Irregty over . "ϕ			
		mr	Wedge			
		"	Roll			
		"	Decenter, RSS of all causes			
		"	Axial displacement, RSS			
		mr	Tilt, RSS			
			Σ			
			RSS			

FIGURE 1.15 Typical error budget derived from the sensitivity table of Figure 1.14. (From Ginsberg, R.H., *Opt. Eng.*, 20, 175, 1981.)

will be adjusted so that the parameters easiest to control are given the tightest tolerances. Smith (2000) suggested as a rational approach to budget optimization that the tolerances on the most sensitive parameters be tightened, while the tolerances on those parameters that are relatively insensitive be loosened. If no acceptable budget can be achieved, it may be necessary to modify the optical design or the mechanical system and develop a new budget.

Figure 1.16 is a more complete version of the earlier block diagram (see Figure 1.12). This version shows many of the decisions and possible loops involved in achieving the most acceptable error budget for a given system. One aspect of design that is frequently forgotten (or ignored until problems are discovered in the hardware phase) involves the producibility of the optical and mechanical subsystems. Figure 1.17 shows additional loops that may be inserted appropriately into the design process to make sure that critical producibility factors are adequately analyzed. Early consultation with those individuals who will later be asked to fabricate, coat, assemble, test, and maintain the system will allow their feedback to be incorporated into the design while it is still relatively fluid.

Optical systems with required performance higher than that expected of the simple example just considered should be treated differently. We can specify optical surfaces to be known (close) fits to calibrated test plates. In such cases, the actual radii in a particular optical system are well established. We can obtain measured index of refraction data for each melt of glass used in the system from the manufacturer. We can also measure actual axial thicknesses of lenses, prisms, spacers, etc. With this information, we can then reoptimize the nominal optical design (usually by adjusting air spaces) and assemble the system accordingly. This is generally a cost-effective means for achieving required system performance.

In complex systems, it may be necessary to consider error budgets for individual lenses in subassemblies and then higher level error budgets for those subassemblies acting as rigid bodies relative to the balance of the system. This just adds complexity to the process. The basic process at each level remains as considered here. Some designs lend themselves to fabrication of parts with accuracy sufficient that assembly can proceed without adjustment. Unless the performance requirements are quite lenient, this may require critical (i.e., optical and mechanical interfacing) surfaces of those parts to be machined by single-point diamond turning (SPDT) because of the inherent degree of perfection

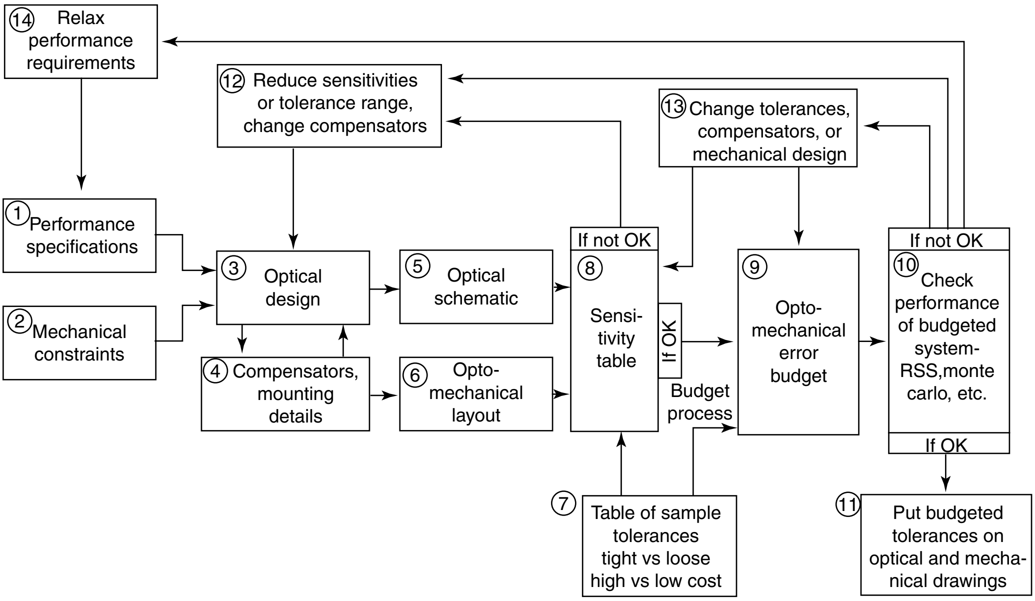
⑭ Relax performance requirements
⑫ Reduce sensitivities or tolerance range, change compensators
⑬ Change tolerances, compensators, or mechanical design
① Performance specifications
② Mechanical constraints
③ Optical design
④ Compensators, mounting details
⑤ Optical schematic
⑥ Opto-mechanical layout
If not OK
⑧ Sensitivity table
If OK
Budget process
⑨ Opto-mechanical error budget
If not OK
⑩ Check performance of budgeted system-RSS,monte carlo, etc.
If OK
⑦ Table of sample tolerances tight vs loose high vs low cost
⑪ Put budgeted tolerances on optical and mechanical drawings

FIGURE 1.16 Expanded version of the error budget process from Figure 1.12 showing recomputation loops used to optimize the tolerance distribution. (From Ginsberg, R.H., *Opt. Eng.*, 20, 175, 1981.)

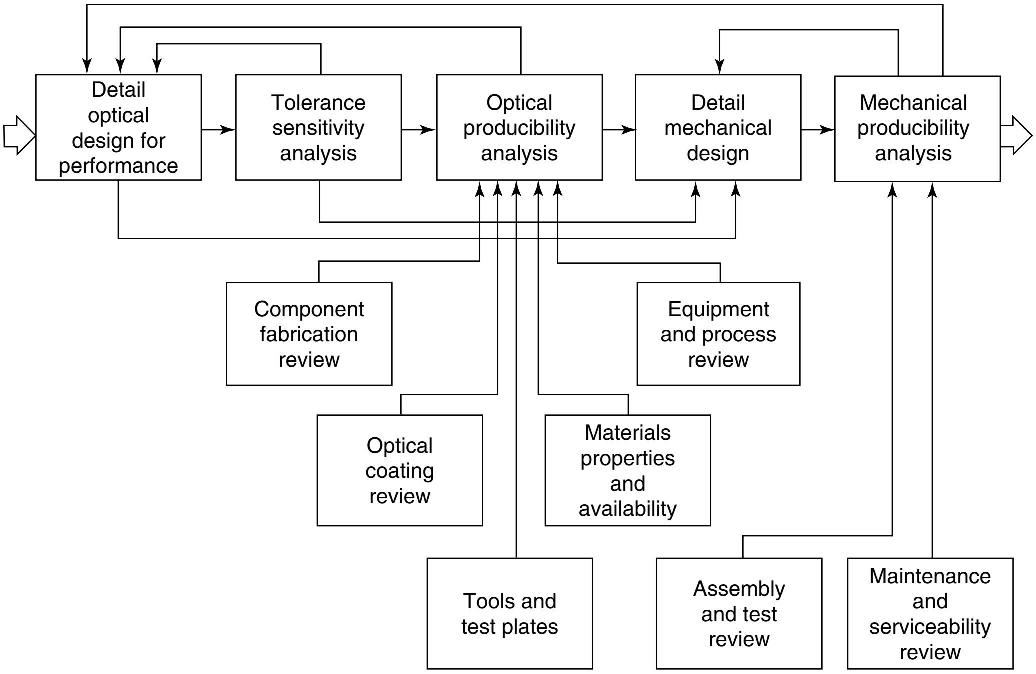
Detail optical design for performance
Tolerance sensitivity analysis
Optical producibility analysis
Detail mechanical design
Mechanical producibility analysis
Component fabrication review
Equipment and process review
Optical coating review
Materials properties and availability
Tools and test plates
Assembly and test review
Maintenance and serviceability review

FIGURE 1.17 Additional loops that should be incorporated into the design process to ensure producibility of the optical and mechanical systems. (From Willey, R.R., *Proc. SPIE*, 399, 371, 1983.)

achievable by that technique. In other cases, even essentially perfect components cannot perform adequately without at least a few adjustments. Part of the opto-mechanical design task is to achieve a good balance between tightness of tolerances (and hence cost) and the need for adjustments. The reader is undoubtedly aware that adjustments add mechanical complexity and metrology instrumentation for determining when the adjustments are adequately achieved. In addition, one must plan for labor expenditure to accomplish the adjustments.

A workable methodology for assigning tolerances to optics used in relatively simple systems so as to minimize production costs was described by Willey (1983, 1984, 1989), Willey et al. (1983), and Willey and Durham (1992). That methodology predicts system costs from a database of estimated costs to achieve various levels of perfection in parameters common to all optical instruments. In Section 4.3, we describe the method in some detail.

The tolerances discussed in this section apply primarily to errors in dimensions, locations, and orientations of optical components. Mechanical part designs also need tolerances in order to fabricate, inspect, and assemble those parts. In general, broad tolerances mean lower production costs because less expensive fabrication methods can be used and fewer inspections are required. In some cases, broad tolerances on alignment and positioning of mechanical components reduce labor during assembly. On the other hand, broad tolerances introduce greater variability into the parts and their compatibility during assembly. These factors may also reduce performance of the completed instrument.

Some instances in which tight tolerances on mechanical part designs are advisable include dimensions of holes for shear-carrying fasteners (to maintain in-plane stiffness and distribute loads), interfaces for bearings (to provide proper preloads and minimize entry of contaminants), key dimensions of structural parts that control optical alignment and focus in high-performance instruments, and fits between optical and mechanical parts in applications involving very high accelerations (such as sensors in gun-fired projectiles).

A general philosophy of holding tolerances reasonably tight wherever the resulting cost appears acceptable, relaxing tolerances where achievement thereof appears difficult, and providing a minimal number of adjustments in the design for performance optimization at assembly should apply to mechanical as well as optical components. A trade-off sometimes forgotten during design is that the sensitivity analysis and budgeting process for determining which tolerances can be loose and which should be tight adds time and labor to the project. These costs may not be recovered in production unless the quantity involved is large. For small hardware quantities, it may be cost-effective to bias the tolerances toward the tight side and forego the analysis steps.

1.7 EXPERIMENTAL MODELING

Although analyses tell much about how a given paper design will function in use, a more direct indication is derived from tests of hardware made to that design. This hardware may be called a functional mock-up, breadboard, brassboard, engineering model, or preproduction prototype, depending on the degree of approximation allowed. The decision about the appropriate form of the model may depend on allowable costs and schedule limitations. It would also be influenced by the degree of maturity of the technology utilized in the design. A very sophisticated design involving state-of-the-art technology and materials would demand a closer representation than the one involving well-understood technology and materials.

Thorough testing of models is especially important if the total cost of developing the system and placing it in operation is large. For example, before grinding and polishing began on the primary mirror that is now part of NASA's HST, a subscale mirror of 60 in. (1.52 m) diameter (see Figure 1.18) was built and evaluated. The materials, fabrication and test techniques, and support (metrology mount) configuration were similar to those that would later be used to make the 94.5-in. (2.4-m)-diameter flight version. Details of this preliminary activity, which resulted in an aspheric

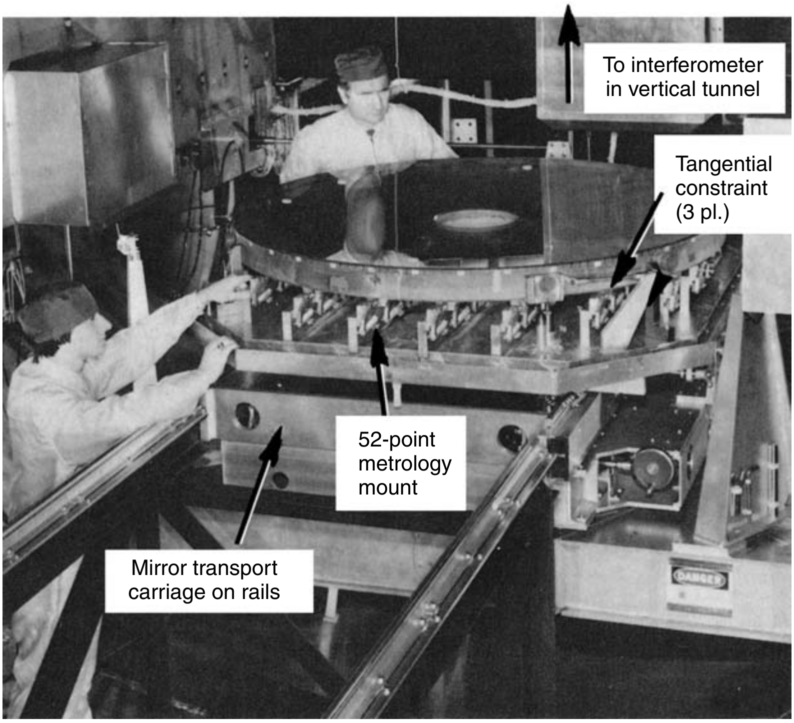
To interferometer in vertical tunnel
Tangential constraint (3 pl.)
52-point metrology mount
Mirror transport carriage on rails

FIGURE 1.18 The 60-in. (1.52-m)-diameter $\lambda/61$ rms figure quality aspheric mirror fabricated and tested as a subscale experimental model of the larger mirror to be built later for the Hubble Space Telescope. (From Montagnino, L.A., Arnold, R., Chadwick, D., Grey, L., and Rogers, G., *Proc. SPIE*, 183, 109, 1979.)

mirror of the required (and unprecedented) $\lambda/61$ rms figure quality at $\lambda = 0.6328$ μm wavelength, were given by Babish and Rigby (1979) and Montagnino et al. (1979). Successful completion of this preliminary experiment provided a sound technical basis for building the full-size mirror. That the null lens to be used to test the latter mirror would accidentally be misaligned prior to use was certainly not anticipated during the building and testing of this model.

Another reason for building experimental models is to permit hardware evaluation in operational and storage environments before the commitment is made to mass produce an optical instrument to a given design. An example of this occurred during the development of the 7 × 50 Binocular M19 by the U.S. Department of Defense. The size of the experimental design (known then as the Binocular T14) is graphically compared with the prior standard 7 × 50 M17 version (of World War II vintage) in Figure 1.19. The T14 design was unique in that it featured a modular design for improved low-cost maintainability (Brown and Yoder, 1960). Prototypes of this design (see Figure 1.20) were extensively evaluated by military personnel and subjected to rigorous environmental testing in the laboratory and in the simulated battlefield. Although found to be excellent in optical performance and to provide the required improvements in size, weight, and maintainability over prior 7 × 50 instruments, its durability in the military environment was judged to need improvement.

A new version of this binocular with a more rugged mechanical design and only very slightly increased size and weight was developed at the U.S. Army's Frankford Arsenal during the 1960s. The highly favored modular design feature was retained. This improved binocular, called the Binocular T14EI, was successfully tested by the intended users and adopted in the 1970s as the standard binocular to replace the M17. With a few further changes, it was produced in large quantity as the Binocular M19 (Trsar et al., 1981). This instrument is shown in Figure 1.21 and is discussed from a structural viewpoint in Chapter 14. Although the total time span (1956 to 1975) of the cycle from initiation of development to initial production was unusually long in this case (owing primarily to the then adequate inventory of M17 equipment), the design evolution was greatly facilitated by the availability of two generations of experimental models for evaluation. The M19 Binocular is described in detail in Section 14.3.2.

Before concluding the subject of experimental models, a few words are appropriate regarding the use of catalog optics instead of optics custom fabricated for the purpose. Many suppliers offer lenses,

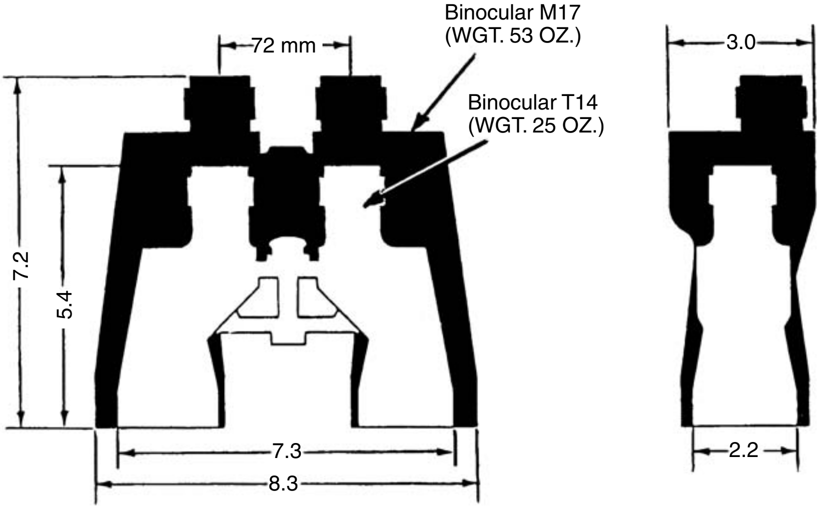

FIGURE 1.19 Size comparison of the experimental Binocular T14 developed as a reduced-size, lightweight 7 × 50 military instrument to replace the military standard Binocular M17. Dimensions are in inches except as noted. The Binocular M19 produced later was essentially the same size as the T14. (From Yoder, P.R., Jr., *J. Opt. Soc. Am.*, 50, 491, 1960.)

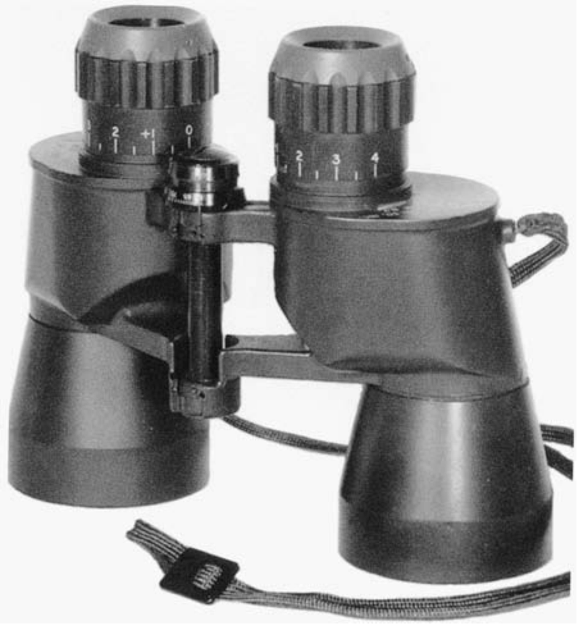

FIGURE 1.20 The first prototype Binocular T14. (Courtesy of the U.S. Army.)

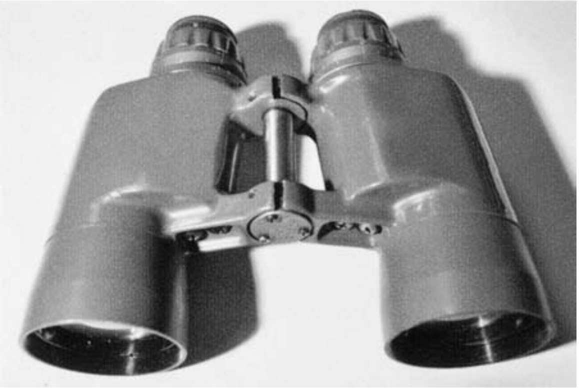

FIGURE 1.21 The modular 7 × 50 Binocular M19 developed as a ruggedized production version of the prototype Binocular T14 shown in Figure 1.20.

prisms, mirrors, windows, filters, etc., of fine quality at competitive prices. The radii of singlet elements with equal radii or one plano surface can be easily computed from the catalog focal lengths and thicknesses if the design wavelengths and materials are known. Equations from texts such as Smith (2000) are useful for this purpose. Exact designs for simple elements and doublets such as achromats from suppliers, for example, Edmund Optics, Opto-Sigma, Melles Griot, or Spindler and Hoyer, are available as catalog designs in the resident libraries of some lens design programs. The designs for more complex commercial lens assemblies are generally not available to the public, so exact performance computations are virtually impossible. In some cases, standard designs from sources such as Smith (1992, 2004) or Laikin (2001) can be used to approximate the design of an off-the-shelf assembly of similar type. Such a design may be adequate for computer modeling of a system containing the assembly or to serve as a starting point for custom design of a new assembly.

In order to build a working model of some types of optical systems, such as the periscope shown in Figure 1.5(b), a group of cemented doublets and singlets selected from commercial suppliers' catalogs on the basis of focal length, aperture, a 90° prism, and a flat mirror would probably suffice. A suitable eyepiece could probably be purchased as a subassembly. These components could be mounted in a crude or more elaborate mechanical surround, depending upon the degree of realism to be provided. Performance of the optical system so created would, of course, not be optimum, but should allow for demonstration, preliminary evaluation, and approximate packaging study.

It would be impractical to construct even a functional mock-up of any but the very simplest of photographic objectives using anything other than customized parts because of the intricate dependence of aberrations on lens configurations. A commercial objective of focal length and relative aperture approximating the desired version may be available. It may suffice for preliminary evaluation purposes while a customized version is developed.

Among the factors that must be considered in making the choice between catalog and custom optics are the availability of parts of the appropriate dimensions and materials, the adequacy of the quality of the catalog parts, and the types and quality of coatings available. In some cases, uncoated optics will suffice. For lenses, it is usually important to know the wavelengths and conjugate distances for which the designs have been optimized. A lens achromatized for the "F" to "C" (blue-green to red) spectral region will probably work fairly well for many visual applications or with red helium-neon laser light. Other factors deserving consideration when deciding between catalog and custom optics are the conjugates for which the off-the-shelf lens has been designed. For example, a photographic objective type lens designed for an object at infinity may not work well with finite conjugates whereas an enlarging lens assembly would perform better at finite conjugates than with an object at infinity. In some applications, such as in a telescope, field lenses may be needed in the experimental system to locate the entrance and exit pupils properly.

1.8 FINALIZING THE DESIGN

Once the preliminary design has been confirmed by analysis or experimentation with models, it is time to prepare, check, review, revise as required, and approve the detailed design. Release of the design for fabrication usually follows a critical design review (CDR), as discussed in Section 1.9. The final design comprises drawings or electronic data files. The latter might well be CAE documentation or CAM files representing the individual parts and assembly and alignment documents. Technical reports regarding analyses should also be prepared, reviewed, and preserved for future reference. Assembly and alignment procedures are then finalized, as are the detailed procedures for in-process and final testing of the system. Special and standard test equipment and fixtures required to accomplish all these tasks must be defined and fabricated and procured on a timely basis. If project formality warrants, the latter equipment and fixtures should be certified to established standards traceable to the National Institute of Standards and Technology (NIST).

In-process verification of the final design is an iterative process following steps such as those shown in Figure 1.22. As the details are developed, each is evaluated to see if it meets all criteria established through the specifications and constraint documents. If so, we are ready for the CDR (see Section 1.9).

No matter how carefully the design of an instrument is produced, the need for revisions in released drawings and procedures is almost a certainty. These may be necessitated by errors that were overlooked at prior design and review stages, or they may reflect design improvements implemented as the hardware takes form. Each proposed design change must be reviewed carefully to make sure it is necessary and appropriate. If completed or in-process hardware is involved, the effectivity of the changes must be determined. This may be based on model and serial number, production date, or some other method as appropriate. In any case, it is advisable to keep complete records of design change effectivity for any hardware produced in quantities greater than one unit. For major systems, complete records are frequently required even if only one is built. This record keeping is usually called "configuration management" and is greatly facilitated by computer-based, "as built" documentation of each unit. This documentation serves to keep all parties who need to know of changes fully advised in order to minimize later inconsistencies.

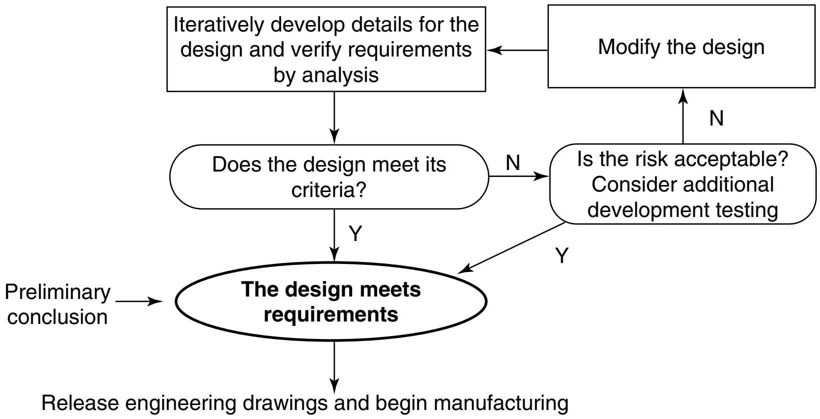
Iteratively develop details for the design and verify requirements by analysis
Modify the design
N
Does the design meet its criteria?
N
Is the risk acceptable? Consider additional development testing
Y
Y
Preliminary conclusion
The design meets requirements
Release engineering drawings and begin manufacturing

FIGURE 1.22 Flow diagram for design verification steps during the detail (final) design phase of the project. (From Sarafin, T.P., in *Spacecraft structures and Mechanisms*, Sarafin, T.P. and Larson, W.J., Eds., Microcosm, Torrance and Kluwer Academic Publishers, Boston, 1995b, chap. 11.)

1.9 DESIGN REVIEWS

An important aspect of the design process not yet discussed is that of design reviews. We use the plural here since any but the simplest design projects will need as many as four technical reviews. These are timed to occur at logical points during the evolution of the design as follows:

1. *Systems Requirements Review* prior to initiation of design
2. *Preliminary Design Review* following conceptual and preliminary design
3. CDR following detailed design
4. *First Article Configuration Review* following an initial production run

The collective purpose of these reviews is to reduce the risk associated with the introduction of new or improved products into the marketplace. They apply equally to military, aerospace, and commercial equipment, and to large- and modest-quantity production. Each review brings together specialists from all pertinent disciplines with the prime purpose of optimizing the design from various viewpoints including, but not limited to, function, cost, reliability, appearance, marketability, and interfaces with associated equipment and the operation personnel.

Participants in these reviews might well include, but need not be limited to, knowledgeable representatives of the design engineering, manufacturing, design assurance, quality assurance, reliability engineering, human factors engineering, purchasing, marketing, and field service disciplines. In government or prime-subcontractor procurement situations, representation from the procuring organization is appropriate. The chairperson is generally a high-level member of the engineering group who has a broad understanding of the overall technical situation. Ideally, this individual would not be in the direct line of authority over the design team.

It is generally advantageous for the project team to allow adequate time for preparation in the planning stages of any technical review. Table 1.9 lists key steps leading to and through such a review. The use of modern communication and information-transfer methods such as E-mail and electronic data and drawing transfer facilitate preparation by the reviewers as well as those who will present the design for approval and those who will handle the logistics of the meetings. For maximum effectiveness, the presentations would include background information on the product and its intended application, the design goals and requirements that the product is to satisfy, the technical approach to the design (including trade-off studies conducted and the rationale behind conclusions reached), descriptive summaries of major technical problems encountered and resolved, definitions

TABLE 1.9
Key Steps in the Planning Schedule for a Technical Design Review

- Schedule design review
- Publish agenda, assign personnel to prepare topics, invite participants
- Preliminary presentation materials available, distribute review packages
- Dry runs as appropriate
- Final presentation materials available
- Final dry run (if needed)
- Design review
- Receive critiques from all reviewers
- Issue summary report, including all action items and completion schedule

Source: Adapted from Burgess, J.A., *Mach. Des.*, 90, 1968.

of technical problems yet to be solved and plans for achieving their solutions, and a clear factual demonstration that the design is satisfactory at the then current stage of its development. Teleconferencing techniques may allow the review to proceed without face-to-face participation by attendees. Following each design review, it is important for a report of the meeting to be prepared and distributed promptly. These reports should document all action items and unresolved questions with clear assignments of responsibility for their resolution.

1.10 MANUFACTURING THE INSTRUMENT

The manufacturing process includes acquisition of raw materials, materials handling, parts manufacture, parts inspection, assembly, quality control, optics-to-product interfaces and tests, and the attendant costs, schedules, processes, and personnel utilization. Manufacturing personnel should, of course, have been involved throughout the design process because the product is not properly designed if it cannot be produced. Ease of manufacture, including assembly, enhances reliability of the hardware. Most instruments will experience some level of disassembly before they are finished. Ease of disassembly not only facilitates access to fix some internal problem that shows up late, but makes maintenance during use much easier.

The most common ways to make metal parts are machining, chemical milling, sheet-metal forming, casting, forging, extruding, and SPDT. Generating, grinding, polishing, edging, coating, cementing, and bonding glass or crystalline materials are the processes most often used to make optical parts. Some parts can be made by SPDT methods if the materials are compatible with that process. Assembly entails mounting the optics and aligning them with respect to other optical and mechanical components and mechanisms. In-process inspection and testing at various points during the overall manufacturing process play very important roles in building a successful product. Processes used to produce optical and mechanical components for optical instruments are discussed further in Section 3.8.

Optical systems involving conventional light sources, light-emitting diodes, lasers, detectors, actuators, figure or image quality sensors, analog-to-digital converters, thermal control subsystems, etc., must also involve electronics devices such as electrical power delivery and control subsystems. These need to be fabricated, tested, and integrated into the instrument at appropriate times during the manufacturing process.

Verification is a very important part of manufacture. Questions such as those depicted in Figure 1.23 need to be asked and answered. Processes, individual parts, assemblies, and the complete instrument should be considered. Analyses and inspections conducted during manufacture serve to verify fit and function. Inevitably, tests are required to prove the adequacy of the design from the engineering and environmental qualification viewpoints, as well as acceptability of hardware for

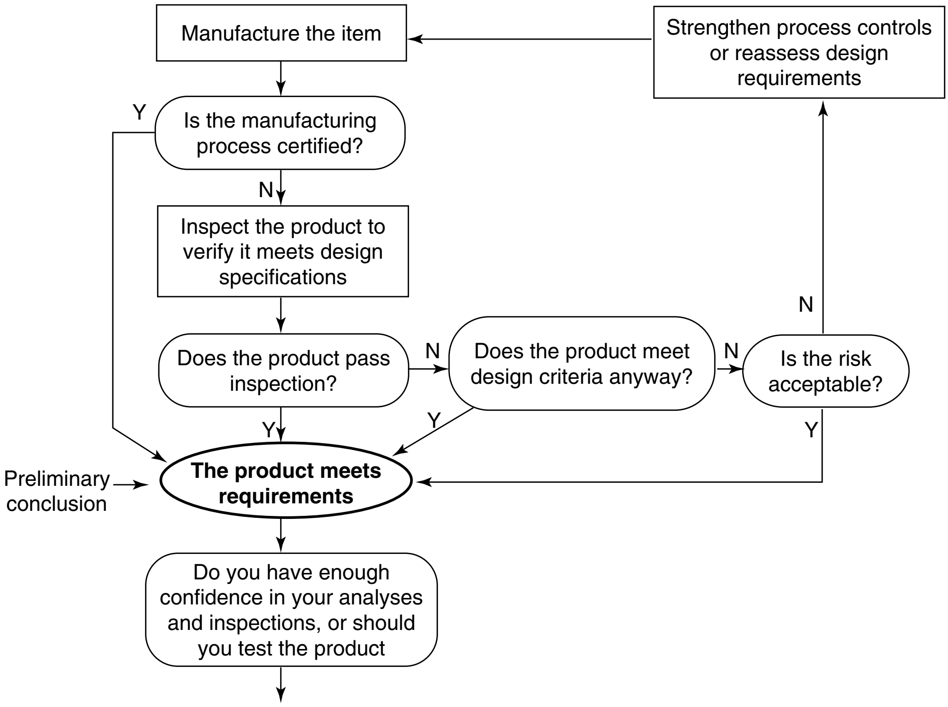
Manufacture the item
Strengthen process controls or reassess design requirements
Is the manufacturing process certified?
Y
N
Inspect the product to verify it meets design specifications
Does the product pass inspection?
N
Does the product meet design criteria anyway?
N
Is the risk acceptable?
N
Y
Y
Y
Preliminary conclusion
The product meets requirements
Do you have enough confidence in your analyses and inspections, or should you test the product

FIGURE 1.23 Flow diagram for design/process verification steps during the manufacturing phase of the project. The advisability of testing may be indicated. (From Sarafin, T.P., in *Spacecraft structures and Mechanisms*, Sarafin, T.P., and Larson, W.J., Eds., Microcosm, Torrance and Kluwer Academic Publishers, Boston, 1995b, chap. 11.)

delivery. In some cases, lack of correlation between analysis results and test results or significant problems uncovered during manufacture lead to requirements for additional analyses, testing, or even redesign and retrofit of hardware. A significant responsibility of the design team is to prevent, or at least minimize, these troublesome events.

1.11 EVALUATING THE END PRODUCT

Engineering testing of early units of the finished product has long been used as a method for checking the adequacy of a new design. Test results are tangible and, when the tests have been performed carefully and intelligently, give reliable insights. The testing conducted on experimental models, as discussed in Section 1.7, provides early indications of design success. Extrapolation from those tests to the final product may, however, not always be justified. Repetition of all major tests conducted on earlier hardware versions is good engineering practice whenever the design has changed significantly. Tests of especially critical aspects of the design should be conducted to failure to indicate the safety margins built into that design. These tests should be conducted as early in the production cycle as possible in order to minimize tooling and hardware redesign, repair, or replacement costs if problems are discovered.

Acceptance testing of deliverable hardware is a common way to confirm the adequacy of the design. It goes beyond the design and verifies adequacy of the production methods, materials, and inspection processes. Usually, an end item that has been subjected to thorough engineering and environmental qualification testing programs needs only a few functional tests and workmanship inspection on each production unit prior to delivery.

Figure 1.24 summarizes key questions that need to be answered during the late stages of the instrument design and development process. Positive answers to these questions verify the design

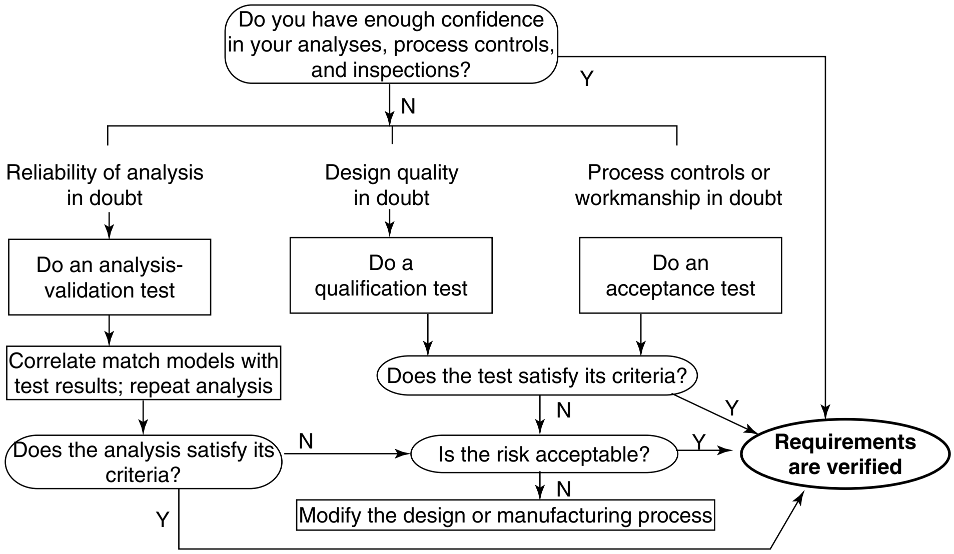
Do you have enough confidence in your analyses, process controls, and inspections?
Y
N
Reliability of analysis in doubt
Design quality in doubt
Process controls or workmanship in doubt
Do an analysis-validation test
Do a qualification test
Do an acceptance test
Correlate match models with test results; repeat analysis
Does the test satisfy its criteria?
N
Y
Does the analysis satisfy its criteria?
N
Is the risk acceptable?
Y
Requirements are verified
N
Modify the design or manufacturing process
Y

FIGURE 1.24 Flow diagram for possible analysis/quality/process/workmanship verification steps during final testing phase of the project. (From Sarafin, T.P., in *Spacecraft structures and Mechanisms*, Sarafin, T.P., and Larson, W.J., Eds., Microcosm, Torrance and Kluwer Academic Publishers, Boston, 1995b, chap. 11.)

and enhance confidence that the end item will achieve all required performance requirements and interface constraints.

Another valuable source of information on the adequacy of an instrument's design is a compilation, over time, of a database comprising factory and field problem reports from service personnel and customer complaint follow-up reports. Analysis of this database will provide the design engineer with a means of verifying his or her analyses and tests and, if necessary, will provide guidance concerning design improvements needed.

1.12 DOCUMENTING THE DESIGN

The final step of the design process is to record as completely as possible all information needed to produce, test, and maintain the end item throughout its life cycle. Files of engineering and production drawings; CAD, CAE, and CAM files; and related documentation (specifications, procedures, reports of analyses and tests, etc.) should be created and maintained. All design changes should be fully documented and "as built" configuration records kept for an appropriate time period. Given a complete file on any design, the solution of production problems and the evolution of that design into later improved versions (or even entirely different designs using only certain successful features from the former one) will be greatly facilitated.

REFERENCES

ANSI Y14.5M. *Dimensioning and Tolerancing*, American National Standards Institute, New York, 1982.

ANSI Y14.18M. *Optical Parts*, American National Standards Institute, New York, 1987.

Babish, R.C. and Rigby, R.R., Optical fabrication of a 60-inch mirror, *Proc. SPIE*, 183, 105, 1979.

Baker, L., Surface damage metrology: precision at low cost, *Proc. SPIE, 4779*, 41, 2002.

Baker, L., *Metrics for High-Quality Specular Surfaces*, Tutorial Text TT65, SPIE Press, Bellingham, 2004.

Brown, E.B. and Yoder, P.R., Jr., Lightweight binoculars, *ORDNANCE*, Jan.–Feb, 1960.

Burgess, J.A., Making the most of design reviews, *Mach. Des.,* 90, 1968.

Cassidy, L.W., Advanced stellar sensors — a new generation, *Proc. AIAA/SPIE/OSA Technology for Space Astrophysics Conference:The Next 30 Years*, Danbury, 164, 1982.

Coronato, P.A. and Juergens, R.C., Transferring FEA results to optics codes with Zenrikes: a review of techniques, *Proc. SPIE*, 5176, 1, 2003.

Doyle, K.B., Genberg, V.L., and Michels, G.J., *Integrated Optomechanical Analysis*, TT58, SPIE Press, Bellingham, 2002.

Fischer, R.E., Optimization of lens designer to manufacturer communications, *Proc. SPIE*, 1354, 506, 1990.

Fischer, R.E. and Tadick-Galeb, B., *Optical System Design*, McGraw-Hill, New York, 2000.

Genberg,V., Michels,G., and Doyle,K., Integrated opto-mechanical analysis, *SPIE Short Course SC254 Notes*, *SPIE*, Bellingham, 2002.

Ginsberg, R.H., Outline of tolerancing (from performance specification to toleranced drawings), *Opt. Eng*., 20, 175, 1981.

Hatheway, A.E., Optics in the finite element domain, in *Computers in Engineering*, American Society of Mechanical Engineering, New York, 1988, p. 3.

Hatheway, A.E., Error budgets for optomechanical modeling, *Proc. SPIE*, 5178, 1, 2003.

ISO 9211–1:1994. Optics and optical instruments - Optical coatings, ISO Central Secretariat, Geneva.

ISO 10110–14:2003. Optics and optical instruments - Preparation of drawings for optical elements and systems, ISO Central Secretariat, Geneva.

ISO Standards Handbook 12, Technical Drawings, 1991, ISO Central Secretariat, Geneva.

ISO Standards Handbook 33, Applied Metrology - Limits, Fits and Surface Properties, 1988, ISO Central Secretariat, Geneva.

Kimmel, R.K., and Parks, R.E., *ISO 10110 Optics and Optical Instruments -Preparation of drawings for optical elements and systems.- A User's Guide*, 2nd. ed., Optical Society of America, Washington, DC, 2002.

Kingslake, R., *Lens Design Fundamentals*, Academic Press, New York, 1978.

Kingslake, R., *Optical System Design*, Academic Press, New York, 1983.

Krim, M., Athermalization of optical structures, *SPIE Short Course Notes SC2*, SPIE Press, Bellingham, 1990.

Laikin, M., *Lens Design*, 3rd ed., Marcel Dekker, New York, 2001.

Montagnino, L.A., Arnold, R., Chadwick, D., Grey, L., and Rogers, G., Test and evaluation of a 60-inch test mirror, *Proc. SPIE*, 183, 109, 1979.

O'Shea, D.C., *Elements of Modern Optical Design*, Wiley, New York, 1985.

Parks, R.E., private communication, 1991.

Petroski, H., *The Evolution of Useful Things*, Vintage Press, a division of Random House, New York, 1994, 231.

Price, W.H., Trade-offs in optical system design, *Proc. SPIE*, 531, 148, 1985.

Plummer, J. and Lagger, W., Cost-effective design — a prudent approach to the design of optics, *Photon., Spectra*, Dec, 65, 1982.

Roark, R.J., *Formulas for Stress and Strain*, McGraw-Hill, New York, 1954.

Rosin, S., Eyepieces and magnifiers, in *Applied Optics and Optical Engineering*, Vol. III, Kingslake, R., Ed., Academic Press, New York, 1965, chap. 9.

Sarafin, T.P., Developing mechanical requirements and conceptual designs, in *Spacecraft Structures and Mechanisms*, Sarafin, T.P., and Larson, W.J., Eds., Microcosm, Torrance and Kluwer Academic Publishers, Boston, 1995a, chap. 2.

Sarafin, T.P., Developing confidence in mechanical designs and products, in *Spacecraft Structures and Mechanisms*, Sarafin, T.P., and Larson, W.J., Eds., Microcosm, Torrance and Kluwer Academic Publishers, Boston, 1995b, chap. 11.

Shackelford, C.J., and Chinnock, R.B., Making software get along: integrating optical and mechanical design programs, *Proc. SPIE*, 4198, 148, 2000.

Shannon, R.R., Making the qualitative quantitative — a discussion of the specification of visual systems, *Proc. SPIE*, 181, 42, 1979.

Shannon, R.R., *The Art and Science of Optical Design*, Cambridge University Press, New York, 1997.

Smith, W.J., Fundamentals of establishing an optical tolerance budget, *Proc. SPIE*, 531, 196, 1985.

Smith, W.J., How to design a lens specification, *Proc. OSA How-to Program, Orlando*, Optical Society of America, Washington, DC, 1989.

Smith, W.J., *Modern Lens Design*, 2nd. ed., McGraw-Hill, New York, 1992.

Smith, W.J., *Modern Optical Engineering*, 3rd ed., McGraw-Hill, New York, 2000.

Smith, W.J., *Modern Lens Design*, 3rd. ed., McGraw-Hill, New York, 2004.

Trsar, W.J., Benjamin, R.J., and Casper, J.F., Production engineering and implementation of a modular military binocular, *Opt. Eng*., 20, 201, 1981.

Walker, B.H., Specifying the visual optical system, *Proc. SPIE*, 181, 48, 1979.

Walker, B.H., *Optical Engineering Fundamentals*, SPIE Press, Bellingham, 1998.

Willey, R.R. Economics in optical design, analysis and production, *Proc. SPIE*, 399, 371, 1983.

Willey, R.R., George, R., Odell, J., and Nelson, W., Minimized cost through optimized tolerance distribution in optical assemblies, *Proc. SPIE*, 389, 12, 1983.

Willey, R.R., The impact of tight tolerances and other factors on the cost of optical components, *Proc. SPIE*, 518, 106, 1984.

Willey, R.R., Optical design for manufacture, *Proc. SPIE*, 1049, 96, 1989.

Willey, R.R., and Durham, M.E., Ways that designers and fabricators can help each other, *Proc. SPIE*, 1354, 501, 1990.

Willey, R.R., and Durham, M.E., Maximizing production yield and performance in optical instruments through effective design and tolerancing, *Proc. SPIE*, CR43, 76, 1992.

Willey, R.R. and Parks, R.E., Optical fundamentals, in *Handbook of Optomechanical Engineering*, CRC Press, Boca Raton, FL, 1997, chap. 1.

Yoder, P.R., Jr., Two new lightweight military binoculars, *J. Opt. Soc. Am*., 50, 491, 1960.

Young, W.C., *Roark's Formulas for Stress and Strain*, McGraw-Hill, New York, 1989.

2 Environmental Influences

2.1 INTRODUCTION

An extremely important factor influencing the design of any opto-mechanical system is the environment to which that system is to be exposed during its lifetime. Generally, that environment has different embodiments for operation, storage, and shipment conditions. It also differs according to the intended use of the system since an instrument to be used in a home or laboratory with a controlled environment would be expected to experience a different set of conditions than one designed for military use worldwide or space applications.

For military applications not involving space environments, general information about expected extreme and typical values of natural climatic conditions such as temperature, humidity, wind speed, rainfall, snowfall, atmospheric pressure, ozone concentration, sand, and dust for hot, basic, cold, severe cold, and sea surface or coastal regions of the Earth may be derived from MIL-STD-210, *Climatic Information to Determine Design and Test Requirements for Military Systems and Equipment*.* Much of the data contained in that standard are also applicable to nonmilitary, i.e., commercial and consumer, equipment to be used in outdoor environments. Guidelines for planning and conducting environmental tests to determine the ability of military equipment to withstand the anticipated climatic exposures may be found in MIL-STD-810, *Environmental Engineering Considerations and Laboratory Tests*. These guidelines also apply, within limits, to the testing of commercial and consumer products.

The environmental conditions encountered in space vary in severity, depending on spacecraft location relative to the Sun, Earth, Moon, and other celestial bodies. Table 2.1 classifies key Earth orbits while Figure 2.1 depicts these graphically. The Low-Earth-Orbit (LEO) environment is well known, having been explored through instrumented probes and manned missions (Musikant and Malloy, 1990; Wendt et al., 1995; Shipley, 2003). Higher orbits are also fairly well defined. Ventures to nearby planets have revealed harsh environments that challenge payload designers to select materials and configure hardware so as to protect sensors long enough to accomplish the mission. Detailed considerations of the problems of designing optical instruments to cope with such environments are beyond the scope of this book.

In this chapter, we identify key environmental parameters of concern and discuss some considerations related to the task of designing optical hardware. Potential deployment scenarios should be defined as completely as possible and the duration of exposure estimated. Potential failure modes should be identified, and the likelihood of revealing hidden design weaknesses during planned testing evaluated. Early consideration of these points plus continued review of such issues throughout the design process would improve the probability of success.

---

*As pointed out in Section 1.3, U.S. military specifications are in the process of being revised or replaced by voluntary or international standards. Because they contain useful information and replacement documents may not as yet be readily available, we here cite key selected military documents for general guidance.

TABLE 2.1
Earth Orbit Classifications

Orbit	Altitude (km)	Period	Applications
Low-Earth (LEO)	200–700	60–90 min	Military Earth/weather monitoring Space shuttle missions
Middle-Earth (MEO)	3000–30,000	Several orbits per day	Military Earth observation Weather monitoring
Geosynchronous (GEO)	35,800	1 day	Communications Mass-media Weather monitoring
Highly elliptical (HEO)	Perigee <3000 Apogee >30,000	Wide range in hours	Communications Military
L1 Halo[a] about Sun/Earth/Moon	"Halo" about L1 ~150,000,000 from Earth	80–90 days	Solar observations Global observations
L2 Halo[a] about Sun/Earth/Moon	"Halo" about L2 ~150,000,000 from Earth	Days–months	Scientific observations Global observations

[a] Lagrange points 1 and 2 are 1% of Sun–Earth separation from Earth.

Source: From Shipley, A.F., Optomechanics for Space Applications, *SPIE Short Course Notes SC561*, 2003.

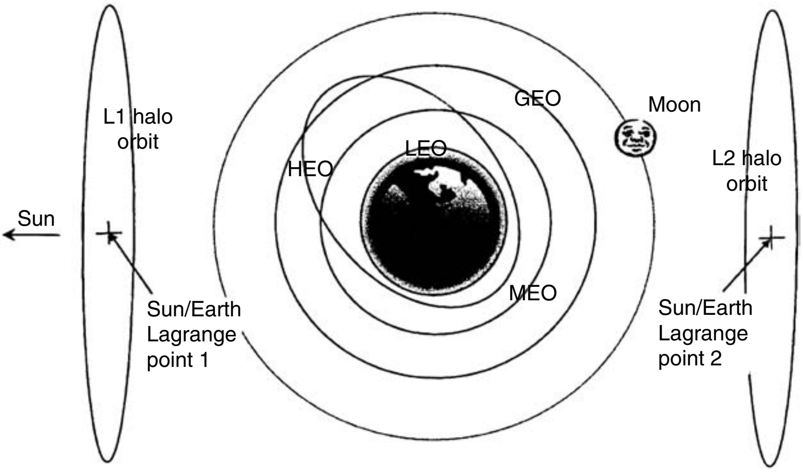

FIGURE 2.1 Space environments as a function of orbital altitude. Note: not to scale. (Adapted from Shipley, A.F., *SPIE Short Course Notes SC561*, 2003).

2.2 PARAMETERS OF CONCERN

Table 1.1 in the preceding chapter identified several general design factors for optical instruments pertaining to the environment. For the convenience of the reader we repeat them here:

- Temperature
- Pressure
- Vibration
- Shock

- Humidity
- Corrosion
- Contamination
- Fungus
- Abrasion/Erosion
- Radiation

Each of these factors must be considered at one or more times during instrument design. Some may be instantly dismissed as not relevant owing to the nature and intended application of the instrument. Others may become major design drivers. We will next look briefly at each factor.

2.2.1 TEMPERATURE

This is perhaps the most ubiquitous of environmental parameters. Historically, James Clerk Maxwell defined it as "the thermal state of a body considered with reference to its ability to communicate heat to other bodies." We measure temperature with a variety of thermometers that measure change with temperature of some property (volume, length, electrical resistance, etc.) of a substance. In this book, we express temperature in the Celsius (°C), Kelvin (K), or Fahrenheit (°F) scale as appropriate to the context of other units employed. Values in any one of these scales are converted into another scale using relationships found in Appendix A.

The temperature of a body may be identified with the level of its internal molecular energy. Modes of heat transfer are *conduction*, the direct communication of molecular disturbance through a substance or across interfaces between different substances by molecular or atomic collisions; *convection*, transfer by actual motion of the hotter material; and a combination of *radiation* and *absorption*. In the last process, heat is emitted by material at a given temperature (i.e., a "source"), transmitted through adjacent media or space, and absorbed by another material (i.e., a "sink"). The common effect of all modes of heat transfer is to change the temperatures of both the heat source and heat sink until a state of thermal equilibrium is attained.

All three modes of heat transfer are of vital importance in opto-mechanical design because it is virtually impossible for any real object to be completely in thermal equilibrium with its environment. Temperature gradients are common and cause nonuniform expansion or contraction of integral or connected parts. A commonplace contemporary example is the "hotdog" effect on orbiting spacecraft structures constantly receiving solar radiation on one side and radiating heat into outer space on the other. The hotter side expands more than the cooler side and the shape of the structure tends to bend toward the familiar shape of a cooked frankfurter. The laws of thermomechanics determine how differential expansion occurs within parts at different temperatures or within parts made of different materials but at the same temperature.

The four sources of external thermal radiation reaching spacecraft components include the aforementioned solar radiation, albedo radiation reflecting from a nearby planetary body, emissions from a nearby planetary body, and emissions from other parts of the spacecraft itself. Figure 2.2(a) illustrates these sources. The direct radiant flux (or flow of energy per unit time across a unit area) from the Sun for an Earth-orbiting satellite varies from ~ 415 Btu/h ft^2 (1309 W/m^2) when the Earth is farthest from the Sun (aphelion) in July to about 444 Btu/h ft^2 (1400 W/m^2) when the Earth is closest to the Sun (perihelion) in January (Wendt et al., 1995). The resulting heat load on the satellite is obtained by multiplying the flux by the irradiated surface area. If the irradiated area is flat, the heat load must be factored by the cosine of the angle of inclination θ_S of the surface normal relative to the incoming solar radiation.

Albedo radiation (see Figure 2.2[b]) is a function of the albedo (reflectance) of the reflecting surface (average of ~0.3 for the Earth), the Sun's direct flux, the cosine of the angle γ(shown in the figure), and a dimensionless modification factor k_a that is a function of spacecraft altitude and the angle of incidence θ_e between the irradiated surface normal and the line connecting the satellite to the

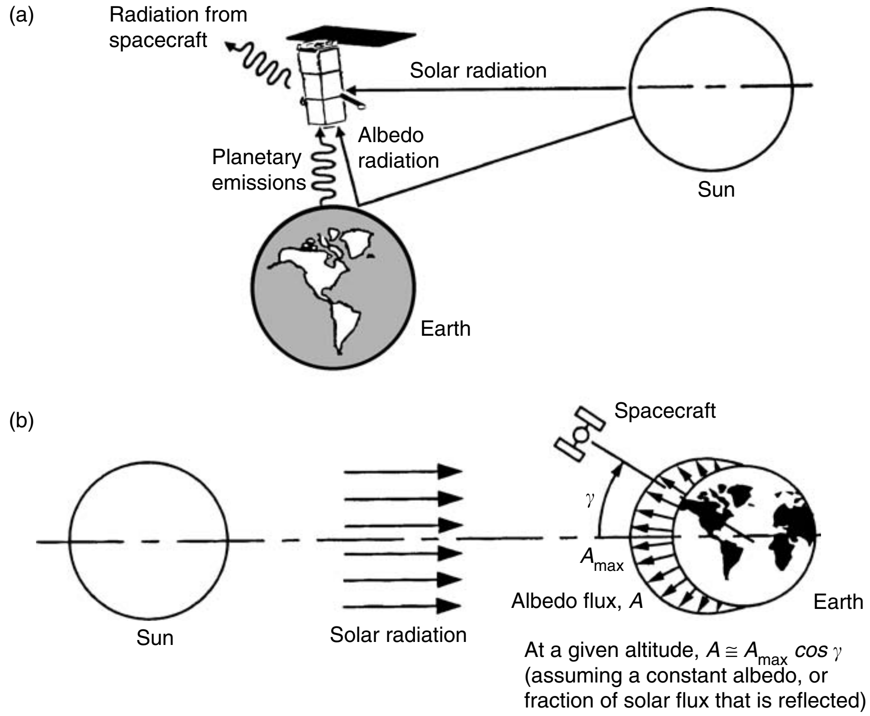
(a)
Radiation from spacecraft
Solar radiation
Albedo radiation
Planetary emissions
Sun
Earth
(b)
Spacecraft
γ
A_{max}
Albedo flux, A
Earth
Sun
Solar radiation
At a given altitude, $A \cong A_{max} \cos\gamma$
(assuming a constant albedo, or fraction of solar flux that is reflected)

FIGURE 2.2 (a) The four sources of thermal radiation for an orbiting spacecraft; (b) approximate variation of albedo flux from the Earth. (From Wendt, R.G. et al., in *Spacecraft Structures and Mechanisms*, Sarafin, T.P. and Larson, W.J. (Eds.), Microcosm, Torrance and Kluwer Academic Publishers, Boston, 1995, p. 37.)

center of the reflecting body (Earth, Moon, etc.). This modification factor is plotted in Figure 2.3(a). Note that there is no albedo for $\gamma > \pm 90°$. Albedo effects from a body other than the Earth are estimated in a manner similar to that just described with the albedo factor as appropriate for that body.

Planetary emissions depend upon the planet's temperature so are Infrared (IR) radiation in the range 1 to 100 μm. The radiant source flux from the Earth ranges from 60 to 83 Btu/h ft^2 (189 to 262 W/m^2). The effects of this radiation are significant only for orbits lower than 7000 nmi. The flux from such a source incident on a flat surface can be estimated as the product of the flux received from the planet and a dimensionless modification factor k_P. The latter is illustrated in Figure 2.3(b).

Thermal irradiation effects may be cyclic or otherwise time varying or transient, as when a spacecraft in LEO moves in and out of the Earth's shadow, or when a high-powered, pulsed laser beam temporarily irradiates an optical surface. Differential expansions of the involved components that are made of different materials or are at different temperatures may cause optical misalignments of sufficient magnitude to affect system performance. Finite element analysis (FEA) techniques are frequently used to predict these misalignments under specific thermal loadings.

Thermal shock typically occurs when an instrument is taken from the cold outdoors into a warm room or when an aerial reconnaissance system is carried aloft in the camera bay of an aircraft with imperfectly stabilized temperature. This is an important consideration affecting the design of the exposed instrument (Geary, 1980; Friedman, 1981). A more extreme case of thermal shock could occur upon ejection of a protective cover from the window of an electro-optical sensor in a ballistic missile during high-altitude hypersonic flight as the missile enters its terminal (guided) phase. Au (1989) analyzed the heating effects when magnesium oxide, diamond, sapphire, and germanium forward-looking infrared (FLIR) windows at 300 K were suddenly exposed to 800 K shock wave

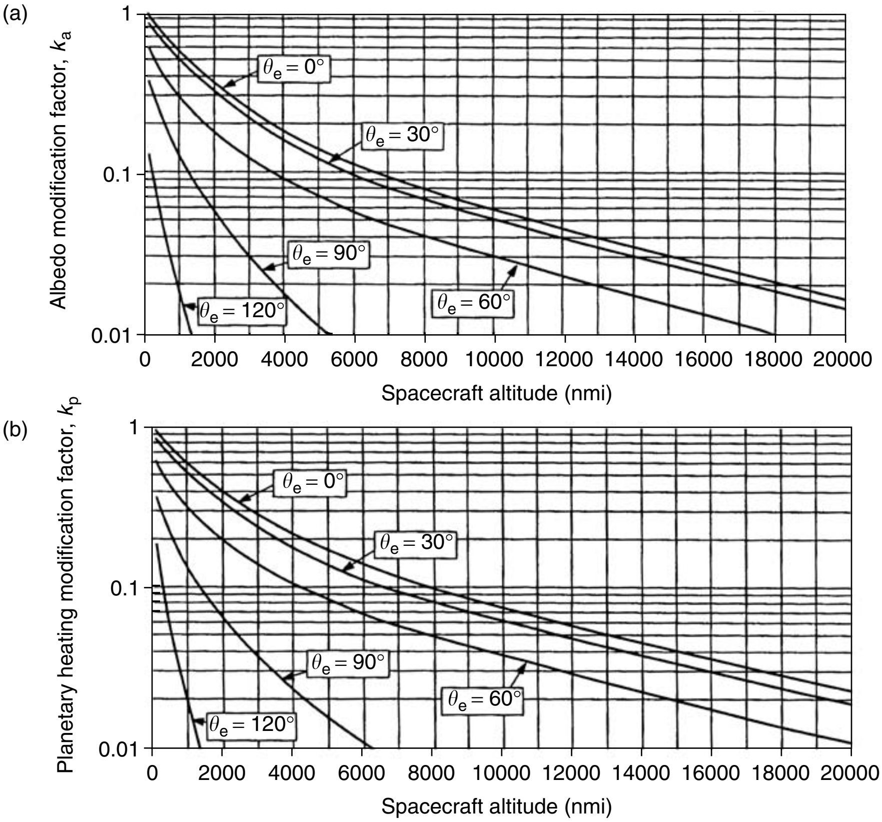

FIGURE 2.3 (a) Albedo modification factor for Earth; (b) planetary emission modification factor for Earth. (From Wendt, R.G. et al., in *Spacecraft Structures and Mechanisms*, Sarafin, T.P. and Larson, W.J. (Eds.), Microcosm, Torrance and Kluwer Academic Publishers, Boston, 1995, p. 37.)

air temperature at a 65,000 ft (19.8 km) altitude. It was reported that rapid temperature rise could rupture some of the windows. Even if not damaged, a hot window material could saturate the sensor's infrared detector with stray radiation unless that window is adequately cooled during the exposed time period. Techniques for laboratory simulation of extreme thermal effects upon sensor windows during such hypersonic flight were reported by Kalin and Clark (1989), Kalin et al. (1990), and Harris (1999). Stubbs and Hsu (1991) reported on the design of a special lens cell intended to cool a germanium lens from room temperature to about 120 K in less than 5 min. This design is discussed in Section 15.6.1.

Other examples of situations that pose significant thermal shock potential include laser systems with high intrinsic power beams incident on optics or lower power ones in which optics are near focused images of the beam. Similar effects can occur with high-intensity incoherent sources such as arc lamps. Even "ghost" reflections from antireflection-coated refracting surfaces can concentrate sufficient energy from an intense light beam to overheat or thermally shock and perhaps damage coatings or optical materials if focused into a small enough spot at or near those surfaces.

Temperature extremes encountered by optical instruments on the Earth generally range from about −62°C (−80°F) to 71°C (160°F). If manual operation is involved, the temperatures usually range from −54°C (−65°F) to 52°C (125°F). Specifications frequently reflect these temperature ranges for the storage and operational use, respectively, of optical equipment. Equipment intended for home or laboratory use should be designed for the conditions of shipment that may involve temperature extremes of at least −32°C (−25°F) to 52°C (125°F).

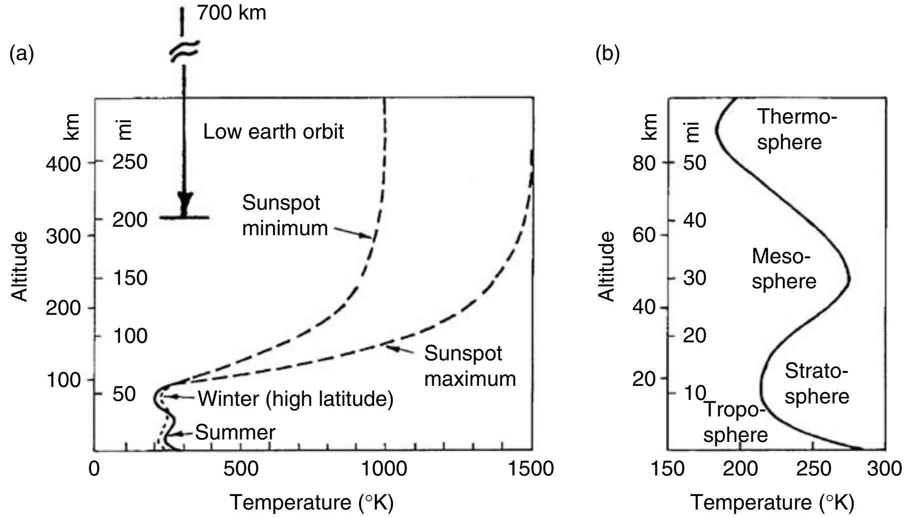

FIGURE 2.4 Temperature of the Earth's atmosphere at different altitudes: (a) to 250 mi, (b) to 50 mi on a larger scale. (Adapted from Glasstone, S., *Sourcebook on the Space Sciences*, Van Nostrand, New York, 1965.)

The variation of temperature with altitude in the Earth's atmosphere and beyond would be of interest if an optical instrument were to be designed for exposure to that environment. Figure 2.4(b) approximates this variation to an altitude of about 96 km (60 mi). Within the lower portion of the innermost layer (the *troposphere*), the temperature drops at about 6.5°C/km (18°F/mi). It levels off at about −60°C (−76°F) at 8 to 16 km (5 to 10 mi) depending on latitude and season. It then rises to about 0°C (32°F) in the *mesosphere* and drops again at about −90°C (−130°F) at the interface between the mesosphere and the *thermosphere* at about 80 km (50 mi) (see McCartney [1976]). In the latter region, extending to about 400 km (250 mi) (see Figure 2.4[a]), the temperature rises again, reaching perhaps 1250°C (2280°F) during maximum sunspot activity. As pointed out by Tribble (1995), the high temperature represents the thermal velocity and, hence, the kinetic energy of the rarefied gas present and not the temperature acquired by an exposed object such as a spacecraft. That temperature depends largely on energy absorption from the four radiation sources discussed above and reradiation characteristics of the object. Heat loss is primarily through radiation.

Basic material thermal properties of interest from the opto-mechanical engineering viewpoint include thermal conductivity, emissivity, absorptance, specific heat, and coefficient of thermal expansion. Key properties are tabulated in Chapter 3 for materials of prime importance here.

To illustrate the significance of a seemingly small temperature change on the performance of optical systems, consider an example of an 8 in. (203.2 mm) focal length, *f*/2, thin, germanium lens used at 10.6 μm wavelength in a variable temperature environment. Applying athermalization theory explained in Section 15.6.1 and appropriate material data, this lens would change its focal length by $\Delta f = (\delta_G)(f)(\Delta T) = (124.87 \times 10^{-6})(203.2)(1.00) = 0.025$ mm/°C temperature change. The quarter-wave optical path difference (OPD) Rayleigh tolerance on defocus for this lens is $\pm(2)(\text{wavelength})(f\text{-no})^2 = \pm(2)(0.0106)(2)^2 = \pm 0.085$ mm (0.003 in.). If some form of athermalization is not employed, the temperature would need to be controlled to ±3.4°C to keep the lens in focus to this tolerance. This level of temperature control would be difficult to achieve in the real world without expenditure of energy. A thermally compensated (i.e., passively athermal) opto-mechanical design for this lens system would, on the other hand, be quite simple to achieve. Examples of athermalized opto-mechanical designs for simple cases such as this one are given in Section 14.5.4.

Methods for temperature testing of optical instruments are summarized in Appendix B.

2.2.2 PRESSURE

This parameter is a measure of force acting on a unit area. Typical units are the pascal (N/m^2) in the metric system and pounds per square inch ($lb/in.^2$) in the USC system.* Fluid pressure is sometimes expressed in terms of the height in millimeters or inches of a column of water or mercury supported at a specific temperature. This latter concept is utilized in defining the normal or standard atmospheric pressure. This is the pressure exerted by a column of mercury 76 cm (29.921 in.) high at sea level, at 0°C, and at standard acceleration of gravity. It equals 101.324 kPa and is used extensively in engineering literature. In USC units, the standard atmospheric pressure (1 atm) is 14.7 $lb/in.^2$. Pressures in vacuum environments are frequently defined in millimeters of mercury or torr (T) where $1\ T = 1\ mm\ Hg = 0.0013\ atm$.

Most optical instruments are designed for use at ambient pressure in the Earth's atmosphere. Exceptions are those for use in a pressurized region (such as a periscope used in a submarine) or in a vacuum (such as an evacuated ultraviolet spectrometer on the Earth or a vented camera in space).

Glasstone (1965) defined the Earth's atmosphere as the layer of mixed gases immediately surrounding the Earth. It has no definite upper limit, but blends gradually into the very low-density gaseous medium that pervades the solar system. From the viewpoint of its composition, the atmosphere can be divided into the *homosphere*, extending up to an altitude of about 100 km (60 mi), and the *heterosphere*, extending farther outward. Mixing occurs within the former region, but there is little mixing in the latter region. Composition of the heterosphere therefore changes with altitude under the influence of gravity, with its innermost layer containing primarily molecular nitrogen and oxygen and its outermost layer having atomic hydrogen as its main constituent. Within the homosphere, the atmospheric density decreases with altitude in accordance with the expression $\ln(d_1/d_2) = h/4.3$, where ln designates a natural logarithm (Naperian base e) and d_1 and d_2 are the atmospheric densities at two altitudes separated by the distance h (in miles). The variation of pressure with altitude in the range ~0 to ~10,000 km (~6214 mi) is plotted in Figure 2.5. In Geosynchronous Earth orbit (GEO) the ambient pressure is approximately $2 \times 10^{-17}\ lb/in.^2\ (10^{-15}\ T)$.

An important consequence of the change in ambient pressure with altitude is the "pumping" action that occurs when an imperfectly sealed optical instrument is exposed to altitude changes. These changes can cause air, water vapor, dust, or other constituents of the atmosphere to seep

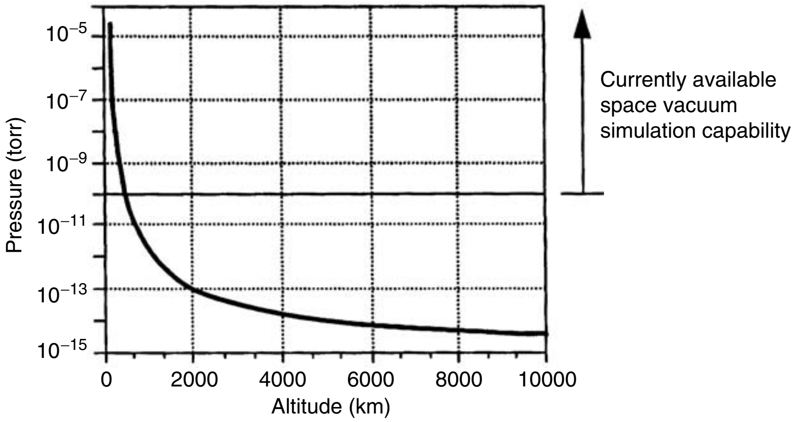

FIGURE 2.5 Variation of pressure with altitude. (From Wendt, R.G. et al., in *Spacecraft Structures and Mechanisms*, Sarafin, T.P. and Larson, W.J. (Eds.), Microcosm, Torrance and Kluwer Academic Publishers, Boston, 1995, p. 37.)

---

* We here refer to the British system of units as the "U.S. Customary" (USC) system.

through leaks. This may contaminate the instrument and lead to condensation, corrosion, light scatter, and other problems.

Decreasing pressure in the environment surrounding the imperfectly sealed optical instrument can lead to extraction of air or other gases from various chambers such as those between lenses, those between the rims of lenses and their mechanical mounts, or those within blind holes partially blocked by screw threads. If these chambers are sealed, pressure differentials of sufficient magnitude to distort optical and mechanical surfaces may develop. Honeycomb cores in mirrors and structures as well as blind screw holes should be vented to prevent such problems.

As discussed in Section 2.2.8, decreasing pressure can also cause some composites, plastics, paints, adhesives, and sealants, as well as some materials used in welded and brazed joints, composites, gaskets, O-rings, bellows, shock mounts, etc., to outgas or offgas, especially at elevated temperatures. The effluents from these materials can be harmful to coatings or they may deposit as contaminants on optical surfaces. Some materials absorb water from humid environments on Earth and desorb that moisture in vacuum. This may cause contamination problems as well as dimensional changes for sensitive components.

Instruments moving within the Earth's atmosphere and under water will experience an overpressure owing to aerodynamic or hydrodynamic forces exerted on exposed optical surfaces. Fluid flow over these surfaces may be turbulent or laminar, depending on design and environmental factors such as temperature, velocity, fluid density, ambient pressure, viscosity, etc. Frictional skin heating of windows and domes due to rapidly flowing air may affect the thermal balance of related optical instruments in high-speed aircraft and missiles. The use of special coatings and temperature-insensitive materials in such exposed optical components may be required to minimize thermal problems.

A very important consequence of pressure occurs when an optic supports a pressure differential and deforms. These effects are of least significance if the optic is a window configured as a plane-parallel plate and the transmitted beam is collimated, but should be considered potential problems if they occur in high-performance optical systems. This type of problem is addressed quantitatively in Chapter 6.

In applications such as the optical lithography of microcircuits, the temperature of the apparatus is usually controlled to perhaps $\pm 0.1°C$, but generally no attempt is made to control barometric pressure. Weather-induced pressure variations can change the index of refraction of the air surrounding the optics sufficiently to degrade focus and image quality and vary the system's magnification so as to introduce alignment (overlay) errors between successive mask exposures. Measurement of pressure changes and compensating adjustment of the optical system would then be needed to minimize these adverse effects. The pressure environments of future extremely high-resolution lithography systems will undoubtedly need to be tightly controlled. These systems will probably operate in a vacuum.

Methods for pressure testing of optical instruments are summarized in Appendix B.

2.2.3 STATIC STRAINS AND STRESSES

In this book, we are particularly interested in the changes in dimensions and configurations (i.e., strains) of structural components made of mechanical materials (metals, plastics, composites, etc.) and of optical components (lenses, mirrors, prisms, windows, etc.) produced by forces imposed either externally or internally on these bodies. Generally, we assume that all materials are elastic, isotropic, homogeneous, and infinitely divisible without change in properties, and that they obey Hooke's law, which requires stress (force exerted over a unit area) to be proportional to strain (deflection) in an elastic body. We recognize that each of these assumptions holds only to a certain extent and that theoretical and experimental analyses are only approximations. Even so, the predictions that can now be made during engineering design regarding the behavior of opto-mechanical systems under specific conditions are remarkably reliable.

Roark and Young (1975) identified four types of loading that develop stress within a body. Quoting in part,* these are:

1. *Short-time static loading* — The load is applied so gradually that at any instant all parts are essentially in equilibrium. In testing, the load is increased progressively until failure occurs, and the total time required to produce failure is not more than a few minutes. In service, the load is increased progressively up to its maximum value, is maintained at that maximum value for only a limited time, and is not reapplied often enough to make fatigue a consideration. The ultimate strength, elastic limit, yield point, yield strength, and modulus of elasticity of a material are usually determined by short-term static testing at room temperature.
2. *Long-time static loading* — The maximum load is applied gradually and maintained. In testing, it is maintained for a sufficient time to enable its probable final effect to be predicted; in service, it is maintained continuously or intermittently during the life of the structure. The creep, or flow characteristics, of a material and its probable permanent strength are determined by long-time static testing at the temperatures prevailing under service conditions.
3. *Repeated loading* — Typically, a load or stress is applied and wholly or partially removed or reversed repeatedly. This type of loading is important if high stresses are repeated for a few cycles or if relatively lower stresses are repeated many times.
4. *Dynamic loading* — The circumstances are such that the rate of change of momentum of the parts must be taken into account. One such condition may be that the parts are given definite accelerations corresponding to a controlled motion, such as the repeated accelerations suffered by a portion of a connecting rod (of an engine). As far as stress effects are concerned, these loadings are treated as virtually static and the inertia forces are treated exactly as though they were ordinary static loads.

In this book, we will concentrate on static loading effects such as component deformations under gravity and a few generalities regarding critical dynamics. Detailed treatment of critical dynamic environments, although vital to the detailed design of optical instruments undergoing extreme vibration, acoustic disturbances, and shock, will be left to other works.

2.2.4 VIBRATION

Vibrational disturbances to opto-mechanical instruments may be periodic or nonperiodic in nature. The oscillatory motion of an elastic body in response to a periodic forcing function (loading type 3 above) may be termed *natural* if the force results only in a displacement of the body or parts thereof. An example is gravitational deflection of a telescope housing or of a mirror. The motion would be termed *forced* if the body is continually driven externally. Figure 2.6 shows some types of periodic forcing functions while Figure 2.7 shows some typical nonperiodic forcing functions. In the case represented in view (d) of Figure 2.7, the motion is damped by some resistance offered by, for example, friction or viscous effects.

Sources of vibration-inducing forces include unbalanced rotary or reciprocating motion of some mass directly or indirectly coupled to the body, certain types of fluid flow, and disturbances to the body's uniform motion (such as a tracked armored vehicle's motion over rough terrain, a helicopter disturbed by the rotor's action, or a spacecraft jittering from attitude control thruster firing). Amplitude, frequency, and direction of vibratory motion are variables of importance in the opto-mechanical design of any component or assembly.

---

[*] Reproduced from Roark and Young (1975) *Formulas for Stress and Strain*. Copyright © 1975 by McGraw-Hill, New York.

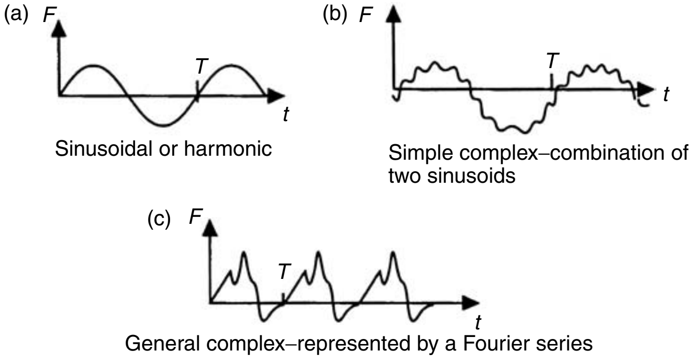
(a) F
T
t
Sinusoidal or harmonic
(b) F
T
t
Simple complex–combination of two sinusoids
(c) F
T
t
General complex–represented by a Fourier series

FIGURE 2.6 Examples of periodic forcing functions. F, force; t, time; and T, the period of one cycle. (From Feldman, H.R. et al., in *Spacecraft Structures and Mechanisms*, Sarafin, T.P. and Larson, W.J. (Eds.), Microcosm, Torrance and Kluwer Academic Publishers, Boston, 1995, p. 95.)

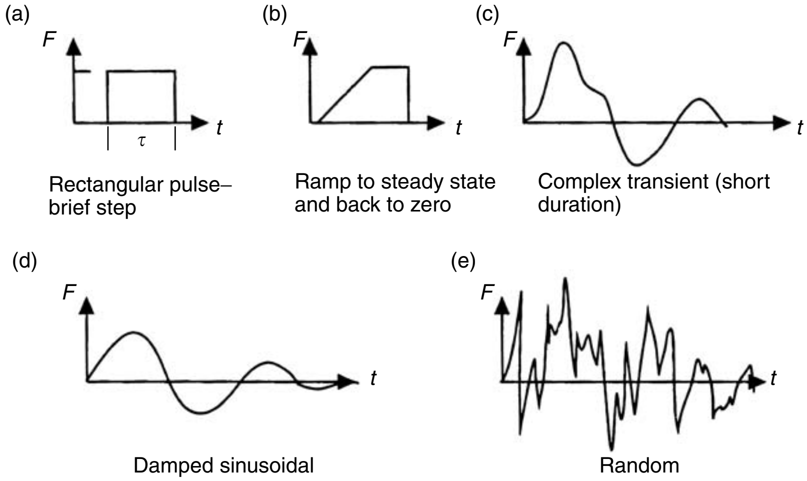
(a)
F
τ
t
Rectangular pulse–brief step
(b)
F
t
Ramp to steady state and back to zero
(c)
F
t
Complex transient (short duration)
(d)
F
t
Damped sinusoidal
(e)
F
t
Random

FIGURE 2.7 Examples of nonperiodic forcing functions: F, force; t, time; τ, pulse duration; T, the period of one cycle. (From Feldman, H.R. et al., in *Spacecraft Structures and Mechanisms*, Sarafin, T.P. and Larson, W.J. (Eds.), Microcosm, Torrance and Kluwer Academic Publishers, Boston, 1995, p. 95.)

A particularly important condition occurs when the frequency of the periodic force nearly or exactly corresponds to the natural or fundamental frequency of the driven body. Unless effectively damped, the resulting resonance induces vibratory amplitudes exceeding those that would be produced by the same force if applied at a lower or higher frequency. This natural frequency f_n depends only on the mass m of the vibrating body and the stiffness k associated with the vibrating system. It is given by

$$f_n = (0.5/\pi)(k/m)^{1/2} \tag{2.1}$$

The success of engineering design of opto-mechanical instruments depends to a significant extent on the engineer's ability to predict and compensate for resonance problems. This may be accomplished by designing parts to have high stiffness so that their natural frequencies are safely higher than those of the anticipated driving forces. Compensating forces produced by strategically designed and located auxiliary damping mechanisms may also be employed to reduce resonances.

A system exposed to random vibration as in view (e) of Figure 2.7 experiences all frequencies within a given range of interest. The effect is expressed statistically in terms of the "root-mean-square" (rms) acceleration response of the driven body. We will abbreviate this response as ξ. All six degrees of freedom (DOF) should be considered, but the mathematics of so doing is complex, requiring the application of matrix methods. Frequently, opto-mechanical engineers treat each DOF separately. Figure 2.8(a) illustrates schematically a simple single degree of freedom (SDOF) system in which a force $F(t)$ is applied directly to the mass m supported from a fixed rigid platform by some structure with spring stiffness k and a viscous damper having a damping factor c. An example of direct driving force is acoustic loading.

Most often, a force acts on an optical instrument through one or more adjacent component(s). For example, a telescope secondary mirror is attached to a mount that is attached to a spider that is attached to the telescope tube or truss and so on. A simple case addressing part of this chain is shown in Figure 2.8(b). The connections between any two components are always somewhat flexible and can be represented by a spring and an associated damping factor. Vibrational force is delivered from the base through the connecting spring and damper c. Motions of the base (X_2 in the figure) cause motions X_1 of m. The right-hand view in the same figure shows the forces acting on m. At the top we see Newton's law that says force equals mass times acceleration. The spring delivers a force equal to the spring stiffness (or spring constant) multiplied by the difference between the two displacements. The damper exerts a force equal to the damping factor multiplied by the difference between the two velocities. All forces vary with time.

The characteristic transmissibility TR or ratio of the spring's response force to the peak input force for the SDOF system depicted in Figure 2.8(b) is shown in Figure 2.9. The different curves correspond to different damping factors ζ. The term Ω is the driving frequency while ω_n is the natural frequency of m. When the frequency ratio Ω/ω_n equals $\sqrt{2}$, the transmissibility is unity. When the same ratio is greater than $\sqrt{2}$, the response is smaller than the input, i.e., attenuated. When it is smaller than $\sqrt{2}$, the response is amplified. The effect of resonance is seen when ζ is very small. The transmissibility then approaches $1/(2\zeta)$.

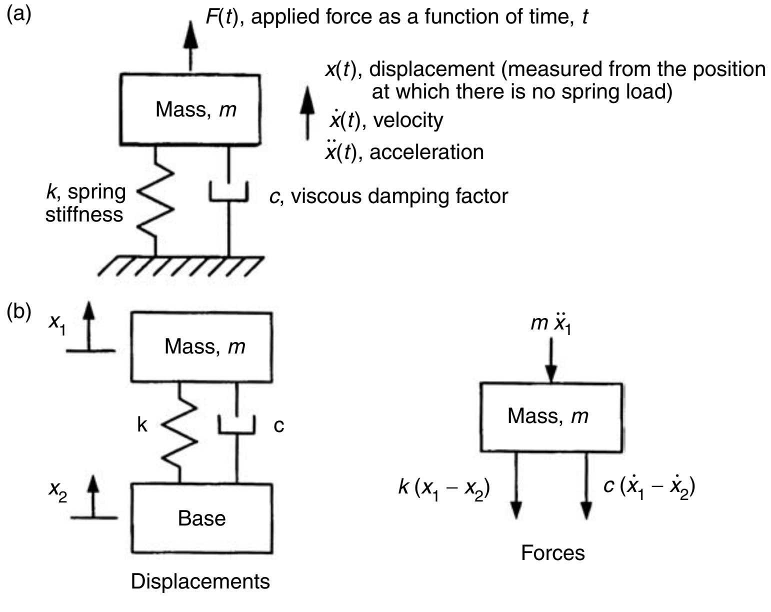
(a)
F(t), applied force as a function of time, t
Mass, m
x(t), displacement (measured from the position at which there is no spring load)
ẋ(t), velocity
ẍ(t), acceleration
k, spring stiffness
c, viscous damping factor
(b)
x1
Mass, m
k
c
x2
Base
Displacements
m ẍ1
Mass, m
k (x1 − x2)
c (ẋ1 − ẋ2)
Forces

FIGURE 2.8 Schematics of an idealized single degree of freedom system undergoing an applied force: (a) applied directly to the body and relative to a fixed base structure, (b) applied through an externally driven base. (From Feldman, H.R. et al., in *Spacecraft Structures and Mechanisms*, Sarafin, T.P. and Larson, W.J. (Eds.), Microcosm, Torrance and Kluwer Academic Publishers, Boston, 1995, p. 95.)

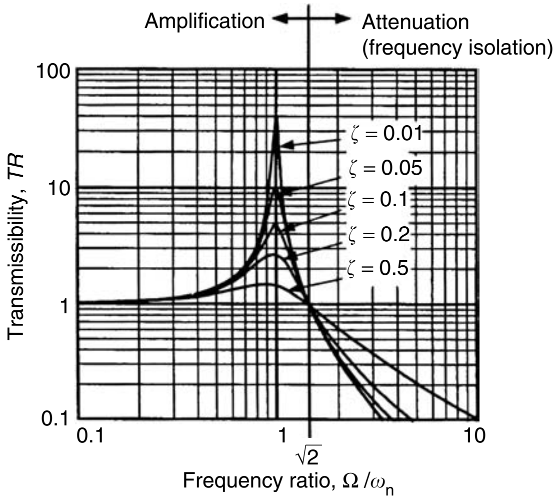

FIGURE 2.9 Transmissibility of a base-driven harmonic system for various damping functions. (From Feldman, H.R. et al., in *Spacecraft Structures and Mechanisms*, Sarafin, T.P. and Larson, W.J. (Eds.), Microcosm, Torrance and Kluwer Academic Publishers, Boston, 1995, p. 95.)

For an SDOF system of the type shown in Figure 2.8(b), the rms acceleration response ξ is given by[†]

$$\xi = [\pi f_n \mathrm{PSD_a}/(4\zeta)]^{1/2} \tag{2.2}$$

where ξ is the damping factor for the system at a given frequency f, f_n the fundamental frequency, and $\mathrm{PSD_a}$ the input acceleration power spectral density expressed in dimensionless units of g^2/Hz. Vukobratovich (1997) gave representative values for the $\mathrm{PSD_a}$s of typical military and aerospace environments including warships, aircraft, several space launch rockets, and the space shuttle (see Table 2.2). These range from 0.001 to 0.17 g^2/Hz over the frequency range 1 to 2000 Hz. The $\mathrm{PSD_a}$ for these and other applications are determined by measurement.

During vibration testing of components, assemblies, or complete instruments, the oscillatory motion is typically induced by attaching the equipment to be tested to a vibrator capable of forcing the specified motion of that item. Measurements of vibration levels at the hardware to determine the effectiveness of its design are usually made with calibrated accelerometers. Methods for vibration testing of optical instruments are summarized in Appendix B.

To illustrate the use of Eqs. (2.1) and (2.2), let us consider a simple example similar to the model shown in Figure 2.8. We assume that a mirror is the mass m while its mount is the base. During random vibration testing, a single-axis acceleration is to be delivered normal to the mirror's back by the mount. The mirror and mount assembly has a stiffness of $k = 1.5 \times 10^5$ N/m and a damping factor of $\zeta = 0.05$. The mass of the mirror is 2.00 kg. From the system specification, the input PSD_a at the mount is to be 0.1 g^2/Hz over a frequency range of 30 to 1000 Hz. We need to know what rms acceleration ξ the mirror will experience during testing and what vibration level that assembly should be designed for. Using Eq. (2.1), we find that $f_n = (0.5/\pi)(1.5 \times 10^5/2.00)^{1/2} = 43.6$ Hz. From Eq. (2.2), $\xi = \{\pi(43.6)(0.1)/[(4)(0.05)]\}^{1/2} = 8.3$ times gravity. Vukobratovich (1997) indicated that it is common practice in opto-mechanical vibration engineering to assume that most structural damage is done by the *3-sigma acceleration*. Hence, instrument design should be based on acceleration levels of 3ξ for each structural component. Applying these criteria, we learn that the mirror should be designed to withstand random vibration of (3)(8.3) = ~ 25 times gravity.

[†] This equation is attributed to J.W. Miles, so is frequently called *Miles' equation*.

TABLE 2.2
Vibration Power Spectral Densities for Typical Military and Aerospace Environments

Environment	Frequency (f) (Hz)	Power spectral density
Navy warships	1–50	0.001 g^2/Hz
Minimum integrity test	20–1000	0.04 g^2/Hz
per MIL-STD-810E	1000–2000	−6 dB/octave
Typical aircraft	15–100	0.03 g^2/Hz
	100–300	+4 dB/octave
	300–1000	0.17 g^2/Hz
	≥ 1000	−3 dB/octave
Thor-Delta launch vehicle	20–200	0.07 g^2/Hz
Titan launch vehicle	10–30	+6 dB/octave
	30–1500	0.13 g^2/Hz
	1500–2000	−6 dB/octave
Ariane launch vehicle	5–150	+6 dB/octave
	150–700	0.04 g^2/Hz
	700–2000	−3 dB/octave
Space shuttle	15–100	+6 dB/octave
(orbiter keel location)	100–400	0.10 g^2/Hz
	400–2000	−6 dB/octave

Source: From Vukobratovich, D., in *Handbook of Optomechanical Design*, CRC Press, Boca Raton, FL, 1997, p. 65, chap 2.

Another aspect of designing optical instruments for vibration resistance is the environment afforded by the facility in which vibration-sensitive instruments are used. Although perhaps not always noticeable to people, the ambient vibration levels for surfaces (floors and walls) as well as the acoustic inputs from air-circulating systems, process equipment, and support systems within a given facility impose limitations on the degree of precision achieved in use of instruments such as visual microscopes, projection lithography equipment, and scanning electron microscopes. If the vibration environment is too severe for the instrument to provide its required performance, we may need to design vibration isolation mechanisms into the instrument or into the interface between the instrument and the facility. One example of the latter approach is to support an optical table or a workstation on low-friction air springs with damping tuned to reduce particularly troublesome frequencies to acceptable levels. Very few existing facilities can provide an environment suitable for work at an extremely small scale, even with vibration isolation. Research, development, production, and applications of nanotechnology require facilities designed especially for those purposes.

General guidance as to the allowable vibration level for specific types of activities has been developed in the form of vibration criterion (VC) curves published in facility design documents such as a Recommended Practice Document RP-CC012.2, *Considerations in Clean Room Design*, currently being prepared by the Institute of Environmental Sciences and Technology (IEST).[‡] Figure 2.10 from that document shows the latest VC curves and indicates their applications. Here, the vibration is expressed as an rms velocity (as opposed to displacement or acceleration). This is because studies (see, for example, Gordon, 1991, 1999) have indicated that some equipment and people are sensitive at different frequencies and that these points of sensitivity lie on curves of constant velocity. The abscissa of the graph is a proportional bandwidth equal to 23% of the band center frequency.

[‡] Institute of Environmental Sciences and Technology, 5005 Newport Drive, Suite 506, Rolling Meadows, IL 60008-3841, Tel. (847) 255-1561, www.iest.org.

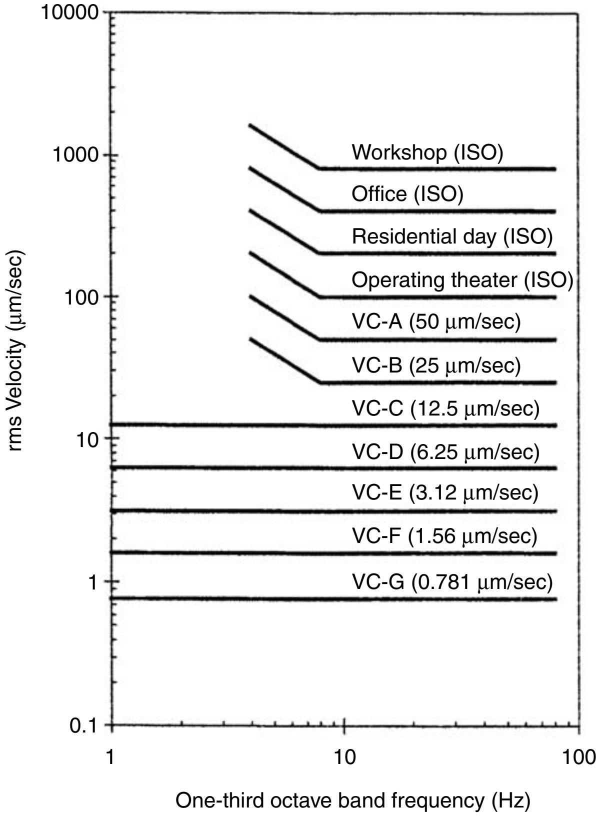

Criterion	Definition
VC-A	256 μg between 4 and 8 Hz; 50 μm/sec (2000 μin./sec) between 8 and 80 Hz
VC-B	128 μg between 4 and 8 Hz; 25 μm/sec (1000 μin./sec) between 8 and 80 Hz
VC-C	12.5 μm/sec (500 μin./sec) between 1 and 80 Hz
VC-D	6.25 μm/sec (250 μin./sec) between 1 and 80 Hz
VC-E	3.12 μm/sec (125 μin./sec) between 1 and 80 Hz
VC-F	1.56 μm/sec (62.5 μin./sec) between 1 and 80 Hz
VC-G	0.78 μm/sec (31.3 μin./sec) between 1 and 80 Hz

FIGURE 2.10 Graphical and numerical definitions of vibration criterion curves for vibration sensitive applications. (Courtesy of the Institute of Environmental Science and Technology, Rolling Meadows, IL, USA.)

This is based on an observation that random vibrations rather than periodic ones dominate most environments. For a site to comply with a particular equipment category, the measured one-third octave band velocity spectrum must lie below the appropriate criterion curve of the figure. The curves are considered conservative and apply to the most sensitive equipment within the specified category. The criteria assume that bench-mounted equipment is supported on rigid benches and damped so amplification from resonances is limited. Table 2.3 correlates the various criteria curves of Figure 2.10 to amplitude levels, sizes of details involved, and descriptions of the applications.

Manufacturers of vibration-sensitive equipment sometimes specify siting requirements in terms of the frequency domain in which their devices are designed to operate. For example, Figure 2.11 shows vendor specifications for four types of electro-optical equipment superimposed upon the corresponding VC curves VC-A through VC-E. Another factor potentially influencing future

TABLE 2.3
Application and Interpretation of the Generic Vibration Criterion (VC) Curves Shown in Figure 2.10

Criterion curve	Amplitude[1] (µm/s) (µm/a)	Detail size[2] (µm)	Description of use
Workshop (ISO)	800 (32,000)	N/A	Distinctly perceptible vibration. Appropriate to workshops and nonsensitive areas
Office (ISO)	400 (16,000)	N/A	Perceptible vibration. Appropriate to offices and nonsensitive areas
Residential day (ISO)	200 (8,000)	75	Barely perceptible vibration. Appropriate to sleep areas in most instances. Usually adequate for computer equipment, probe test equipment, and microscopes less than 40x
Operating theatre (ISO)	100 (4, 000)	25	Vibration not perceptible. Suitable in most instances for microscopes to 100x and for other equipment of low sensitivity
VC-A	50 (2,000)	8	Adequate in most instances for optical microscopes to 400x, microbalances, optical balances, proximity and projection aligners, etc
VC-B	25 (1,000)	3	Appropriate for inspection and lithography equipment (including steppers) to 3 µm line widths
VC-C	12.5 (500)	1–3	Appropriate standard for optical microscopes to 1000x, lithography and inspection equipment (including moderately sensitive electron microscopes) to 1 µm detail size
VC-D	6.25 (250)	0.1–0.3	Suitable in most instance for demanding equipment, including many electron microscopes (SEMs and TEMs) and e-beam systems
VC-E	3.12 (125)	<0.1	A challenging criterion to achieve. Assumed to be adequate for the most demanding of sensitive systems including long path, laser-based, small target systems, E-beam lithography system working at nanometer scales, and other systems requiring extraordinary dynamic stability
VC-F	1.56 (62.5)	N/A	Appropriate for extremely quiet research spaces; generally difficult to achieve in most instance, especially cleanrooms. Not recommended for use as a design criterion, only for characterization
VC-G	0.78 (31.3)	N/A	Appropriate for extremely quiet research spaces; generally difficult to achieve in most instances, especially cleanrooms. Not recommended for use as a design criterion, only for characterization

Notes: (1) As measured in one-third octave bands of frequency over the range 8 to 80 Hz (VC-A and VC-B) or 1 to 100 Hz (VC-C through VC-G).

(2) The detail size refers to linewidth in the case of microelectronics fabrication, the particle (cell) size in the case of medical and pharmaceutical research, etc. It is not relevant to imaging with probe technologies, atomic force microscopy, and nanotechnology.

Source: Courtesy of the Institute of Environmental Sciences and Technology, Rolling Meadows, IL, USA.

versions of vibration criteria is the desirability of considering frequencies below 4 Hz and above 100 Hz. Further, the descriptions of the applications in Table 2.3 are subject to revision as new technology is developed.

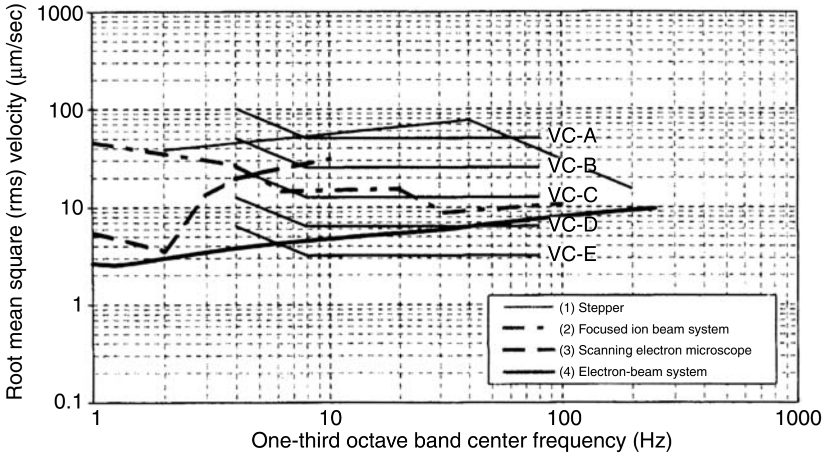

FIGURE 2.11 Examples of vendor's environmental vibration specifications for four types of high performance optical instruments. Note: The VC curves do not exactly correspond to those in Figure 2.10. (From Gordon, C.G., *Proc. SPIE.*, 3786, 22, 1999.)

2.2.5 SHOCK

A force applied suddenly and briefly to a complete instrument or, more typically, to a portion thereof, introduces a series of dynamic conditions into its structural members. Elastic (or perhaps inelastic) deformations generally occur, and inadequately supported parts dislocate relative to their surroundings. Optical alignment may be impaired temporarily or permanently and fragile components (such as some optics) may be overstressed and fail — especially if internal strain is present because of inadequate annealing or strain relieving during fabrication. Shock resistance of opto-mechanical systems is increased by (1) use of isolation subsystems (shock mounts), (2) design so that anticipated loads are spread over as large an area as possible, (3) favorable choice of materials and fabrication processes, and (4) design for minimum mass of the driven body and adequacy of physical strength and rigidity of all components.

Specifications generally define shock in terms of acceleration in multiples of gravity applied in a specified direction or in three mutually orthogonal directions. We here specify the level of acceleration in terms of a dimensionless multiplying factor a_G. The shock level associated with normal manual handling of optical instruments is generally thought to be $a_G = 3$.

Shipping often entails the worst shock conditions that an instrument will ever encounter. Structural loads are normally higher during transportation by truck than by rail. A truck typically encounters transient forces such as hitting a pothole, speed bump, or some other abrupt change in pavement height and may have to move over rough pavements such as found with older, poorly maintained roadways (Wendt et al., 1995). A vehicle with an air-ride suspension will reduce the severity of the disturbance. In cases where shock during transportation is likely to be severe, the specification may distinguish between conditions with and without shipping containers and shock mountings. Without a container or with a direct path for force to pass from the vehicle to the instrument, the shock level may exceed $a_G = 25$. Suitably designed packaging should attenuate transportation shocks to no more than $a_G = 15$. Transient forces are also encountered in air transportation because of wind gusts and landing forces while more sustained forces (vibration) result from air turbulence. Note that pressure and temperature variations also occur frequently during shipping.

Defining the value for a_G is necessary, but not sufficient when preparing a shock specification for an instrument or portion thereof. Traditionally, specifications have also defined shock duration and pulse shape. For example, the method for shock testing given in Paragraph 2 of Appendix B for ISO 9022 requires "3 shocks in each direction along each axis to 1 of 8 degrees of severity ranging from 10 to 500 g's acceleration with half-sine wave pulse durations of 6 to 16 msec." Space payloads can encounter severe shocks during launch, stage separation, orbital changes using thrusters, activation of pyrotechnic devices, upon reentry, and during shuttle landings. Because these shocks can have drastic effects if poorly specified or designed systems are involved, especially for man-rated systems, more definitive requirements are now specified for space-borne equipment. A plot of acceleration in *g*'s vs. time such as that shown in Figure 2.12 is specified. Duration of the "pulse" is a small fraction of a second. Frequencies from about 20 to 10,000 Hz are typically included. The intent of such a specification is to define the requirement in terms of the effect of the shock or its damage potential.

The peak acceleration for a shock pulse (such as that from an explosive bolt–see NAS5–15208, Aerospace Systems Pyrotechnic Shock Data) passing through a structure such as a spacecraft typically attenuates with distance from the disturbance and with the number of joints encountered. From tests and analyses, attenuation with distance is generally as indicated in Figure 2.13. We see that the peak acceleration is reduced by 50% in about 20 in. while the ramp portion of the spectrum is reduced to about 64% in the same distance. Further attenuation of about 40% occurs per mechanically fastened (not welded or bonded) structural joint for up to three joints. Usually, after passing through three joints, no further attenuation is observed. The shock pulse delivered through two joints to a point 20 in. from a shock source would then be about $(1-0.4)^2(0.5) = 18\%$ as intense as the peak input pulse.

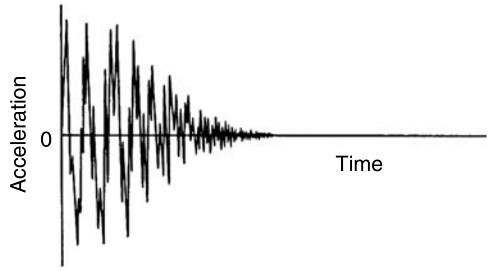

FIGURE 2.12 Schematic acceleration time history for a shock pulse. (From Sarafin, T.P. et al., in *Spacecraft Structures and Mechanisms*, Sarafin, T.P. and Larson, W.J. (Eds.), Microcosm, Torrance and Kluwer Academic Publishers, Boston, 1995.)

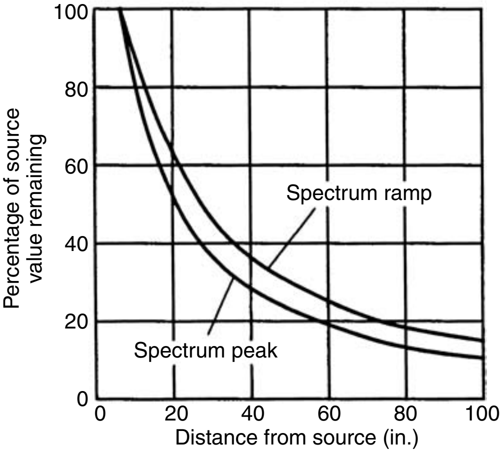

FIGURE 2.13 Representation of how the peak and ramp of a shock pulse attenuate with distance. (From Sarafin, T.R. et al., in *Spacecraft Structures and Mechanisms*, Sarafin, T.R. and Larson, W.J. (Eds.), Microcosm, Torrance and Kluwer Academic Publishers, Boston, 1995.)

Obviously, we must design a given optical instrument to withstand the shock pulse that we expect to be delivered to the instrument from the external environment. Shock testing performed in accordance with MIL-STD-1540B must be at a level 5 dB (1.78 times) above the estimated mean value. Traditional methods for shock testing of optical instruments are summarized in Appendix B.

2.2.6 HUMIDITY

The atmosphere encountered in most applications of opto-mechanical systems is a mixture of gases and vapors, including superheated water vapor, saturated water vapor, and perhaps unvaporized water, as in clouds, fog, or rainfall. The absolute humidity of that atmosphere is the amount of vapor actually present — expressed typically as weight per unit volume. Relative humidity (RH), on the other hand, is the ratio of the density of water vapor actually present in the mixture to the density of saturated vapor at the temperature of the mixture. It also corresponds to the ratio of the actual partial pressure of the vapor to its saturated pressure at the given temperature. In all cases, saturation of the atmosphere corresponds to an RH of 100%. The RH of an atmosphere containing a specific (assumed constant) amount of water vapor rises as the temperature drops (at constant pressure) until saturation and condensation occur at the dew point.

Devices that determine the humidity of gas-vapor mixtures are known as hygrometers or psychrometers. The wet or dry-bulb hygrometer measures the temperature depression due to evaporative cooling as the gas mixture circulates across a thermometer bulb whose wick is saturated with the liquid that is present as a vapor in the atmosphere. The theory of measuring device function, applicable equations, and nomographs for use are found in a variety of texts and engineering handbooks.

The presence of water as liquid or vapor inside an optical instrument can lead to deterioration of optical surfaces, oxidation of ferrous metals, and obscuration of transmitted or reflected radiation due to absorption or scatter. These instruments are generally designed to be reasonably watertight through the application of sealants, gaskets, O-rings, etc. Flushing and pressurization of optical instruments with dry purified gas (such as nitrogen or helium) are common techniques for minimizing internal damage due to humidity. Instruments can also be vented through desiccators to keep their internal atmospheres dry without sealing them to pressure changes. Most plastics, many composites, and water-soluble crystals (such as rock salt or fluorite) must be protected from humid conditions to preserve their optical function.

A particularly troublesome constituent of some atmospheres that frequently accompanies high humidity is common salt (NaCl). High salt content in moisture deposited on optics such as lenses, prisms, and mirrors can lead rapidly to failure of coatings and eventually to corrosion of some optical substrate and structural materials. This subject is considered in the next section.

Methods for humidity testing of optical instruments are summarized in Appendix B.

2.2.7 CORROSION

Corrosion is a chemical or electrochemical reaction between materials and their environment. Its most common form occurs when two dissimilar materials combine in the presence of a fluid, such as water. The reaction involves oxidation (which is the formation of metallic ions and liberation of electrons) and reduction (which is the consumption of free electrons). The electrons transfer through the fluid.

The most effective means of preventing the adverse effects of corrosion on materials used in opto-mechanical instruments is to keep the parts free from corrosive agents. Although generally impossible, this is still a valid goal. Certain protective coatings or platings can, of course, be applied to sensitive materials in some cases, but these may deteriorate and lose their protective nature with time or under mechanical or thermal stress.

Some of the most common forms of corrosion are *fretting*, in which impact between surfaces from vibration causes the breakdown of protective coatings such as oxide layers; *galvanic attack*, in which electrons flow from one metal to a less noble (i.e., less active) metal; *hydrogen embrittlement*, in which hydrogen diffuses into a metal and makes it susceptible to brittle fracture; and *stress-corrosion cracking*, in which defects such as pits in the surface of a material grow under sustained tensile stress in the presence of moisture and lead to brittle fracture (Wendt et al., 1995). A plausible explanation for the mechanism of stress-corrosion-accelerated failure in mechanically stressed metals, given by Souders and Eshbach (1975), is that pits or notches formed by corrosion are opened up as the material's surface deforms under tension and becomes filled with rust or other contaminants. When the tension is released and the openings close over the foreign material, wedge action tends to increase the stress within the part and to induce additional and more severe cracks. The situation grows progressively worse until the part fatigues and failure occurs.

Metals differ considerably with regard to their inherent resistance to corrosion. Aluminum and its alloys, for example, are reasonably immune to corrosion if kept in a dry atmosphere. Moisture, alkalis, and salt cause these materials to corrode. Anodic oxide coatings offer considerable protection. Titanium is commonly used if corrosion resistance as well as a high structural strength-to-weight ratio is needed; magnesium, on the other hand, is quite susceptible to damage from atmospheric contaminants such as salt in the presence of moisture. The stainless steels[§] offer varying degrees of resistance to corrosion owing to their inherent passive nature as a class. This results from a surface characteristic or passive film formed naturally in air or other oxidizing atmospheres. Type-410 CRES, for example, forms a superficial oxide film after a few weeks of exposure to air. All other factors being equal, Type-316 CRES is best for resistance to salt atmosphere (Mantell, 1958; Elliott and Home Dickson, 1960).

Techniques to minimize corrosion of metals include avoiding contact between noncompatible types, careful cleaning to remove corrosive residues during processing, applying protective coatings, and controlling exposure to high humidity.

Zito (1990) reported observation of corrosive effects on aluminum mirror surfaces at the Lick Observatory on Mt. Hamilton, California surrounding small particles of soot from nearby grass fires that reacted with moisture from the humid atmosphere. Antireflection coatings for refracting optics also suffer from environmental exposure (Baumeister, 1965).

Chemical vapor deposition (CVD) and plasma-assisted CVD (PACVD) provide techniques for applying polycrystalline diamond films to optics. These films are known as diamond-like coatings (DLCs). They help to protect vulnerable surfaces such as germanium, zinc selenide, and zinc sulfide from corrosive and abrasion effects (see Willey, 1996). Some DLC films possess a structure with grains about 10 μm in diameter and such rough surfaces that excessive scatter results. Some reductions in surface roughness result from postdeposition polishing of the coating by abrasive, chemical, or ion/sputter techniques (Snail, 1990; Moran et al., 1990). All DLC films exhibit compressive stress, and most adhere fairly well to properly prepared substrates.

Other coatings that improve the corrosion resistance and durability of infrared optics include PACVD germanium carbide (GeC), PACVD boron phosphide, and multilayer coatings comprising GeC, Ge, and DLC. The last, described by Monachan et al. (1989), are especially designed for use on germanium at the 3 to 5 μm and 8 to 12 μm wavelengths and on zinc sulfide at 8 to 12 μm wavelengths.

Methods for testing corrosion resistance of optical instruments are summarized in Appendix B.

2.2.8 CONTAMINATION

All optical instruments are subject to some level of contamination by particulate and molecular matter during fabrication, storage, and use. Early in the development of any instrument, the importance of contamination should be determined from an assessment of its critical importance in achieving performance goals. For simple, modest-performance systems used by humans in normal ground environments, common sense tells us that the parts should be clean at the time of assembly and that the instrument should be protected from dirty and wet environments. Typically, occasional external cleaning of such hardware is necessary. At the other extreme are instruments such as optical projection systems for deep-UV microlithography applications. Here, minute particles of optical substrates, grinding and polishing media, and residues of cleaning solvents may adhere to the optical surfaces in spite of careful cleaning (Keski-Kuha et al., 1994). These reduce system performance by contaminating the coatings or reducing light transmission by scattering, reflection, and absorption. In extremely high-power laser systems, such as the National Ignition Facility (NIF) currently being assembled and tested at Lawrence Livermore National Laboratory, the interaction of the beam fluences with contamination on glass surfaces can lead to surface damage and progressive obscuration of the beam. This would decrease energy delivered to the target and threaten the survival of the optical components. Pumping flashlamp fluence can also progressively damage slab laser glass components.

[§] In this book, a stainless steel is designated as *corrosion-resistant steel* (CRES).

Honig (2004) indicated that tests show that the NIF is "the cleanest large-scale laser built to date." Measurement of cleanliness in such systems is accomplished in accordance with U.S. Federal Standard 209 for airborne cleanliness and U.S. Military Standard 1246C for surface cleanliness. Special equipment in the form of a large format flatbed scanner with custom software was developed at NIF for measuring cleanliness of laser slabs. To avoid these problems, optics must be fabricated, cleaned, coated, assembled, and maintained with care under conditions of the utmost cleanliness.

Although antireflection and reflection-enhancing thin-film coatings applied to refracting and reflecting surfaces, respectively, by reputable suppliers are generally durable, cleaning unavoidably tends to degrade the characteristics of those coatings to some extent. Repeated or unnecessary cleaning should be avoided. When cleaning optics, approved procedures and materials should be used. The most common sources of contamination are smoke, fingerprints, oil from the skin, contaminants dissolved in cleaning solutions, condensation of moisture and chemical vapors, dust, and the by-products of corrosive action of the atmosphere on the coatings or nearby components. The specific conditions applicable to contamination of a surface, the nature of the coating and substrate materials, and the environment under which the cleaning is to be accomplished will affect the success of a cleaning operation. Karow (1989) and Schaick et al. (1989) described in some detail the types of contaminants typically found on optics and various methods, materials, and apparatus used to remove them. Zito (1990) described techniques for *in situ* cleaning of large optics such as the mirrors of astronomical telescopes with CO_2 snow. Problems encountered using this process caused by contamination of the gaseous CO_2 with oil from the compressor have been investigated and solved by using improved filters to purify the gas (Zito, 2000).

Facey and Nonnenmacher (1988) reported that during thermal-vacuum testing of the Hubble Space Telescope (HST) before launch, the measured temperature of the primary mirror was found to be lower than expected and an axial temperature gradient through the mirror was found to exist. Evidently, an excessive amount of heat was being lost through the front surface of the mirror. This represented an anomaly in the sense that the computer simulation model did not predict it.

Even though the mirror had continuously been kept in a protected environment after removal from the coating chamber, it was known that over a 2- to 3-year period, a small amount of particulate contamination (covering 2 to 3% of the mirror's surface) had accumulated. Careful use of a custom-built "vacuum cleaner" held near the mirror's coated surface and moved over the entire area had succeeded in removing a significant portion of the contaminating particles from the surface (Facey, 1985, 1987). It was theorized that the small remaining particulate coverage (0.6% of the area) and additional contamination accumulated during the intervening 2 years of integration and testing were the cause of a significant increase in the effective emissivity of the surface coating. Laboratory tests were conducted in vacuum with a thoroughly instrumented, small, surrogate fused-silica mirror with its coated surface clean and with five different amounts of particulate matter intentionally distributed thereon. Total hemispherical emissivity of the surface was calculated from the rate of temperature change, and the particle size distribution and mirror area obscuration measured by microdensitometer analysis of photographs of the contaminated surface. The results confirmed that the contaminating dust did cause an increase in effective emissivity and could explain the unexpected heat loss from the mirror. The emissivity of the mirror surface was not subsequently reevaluated prior to launch, but no problems have been encountered in orbit that could be attributed to surface contamination (Facey, 1991).

Military and commercial optical equipment may be exposed to lubricants, silicones, coolants, de-icing solvents, fire-fighting foam, Halon, salt fog and spray, cleaning fluids, acids, and other chemicals. Special care is required during operation of such equipment to keep it operational. Space payloads may be exposed to some, if not all, of these potential contaminants, as well as x-rays, protons, electrons, micrometeorites, man-made space debris, or rocket exhaust products from the prelaunch, launch, and orbital correction environments (Thornton and Gilbert, 1990; Tribble, 1995; Shipley, 2003). Some of these may be corrosive, whereas others may simply contaminate surfaces and degrade performance. For complex, state-of-the-art instruments destined for operation in space, it is usually appropriate for a detailed contamination-control process to be initiated at a very early stage of the design and for provisions to be made to protect all the parts and the finished instrument throughout its useful life. Knowledge of the nature and effects of the stressful environments of space are also important to finding means to preserve system performance in orbit. Musikant and Malloy (1990) briefly summarized the LEO contamination environment. More details were provided by Tribble (1995).

Atomic oxygen is a particularly troublesome agent for long-duration space missions, especially in LEO. Polymeric materials (such as Teflon, Kapton, Mylar, and adhesives), graphite epoxy and other carbon-based composites, organically based paints, coatings and films (including indium tin oxide and Chemglaze — a thermal control white paint), and some metals (aluminum, silver) react with atomic oxygen and should be protected along the direction of spacecraft motion. Shipley (2003) reported that degradation of some materials is accelerated by simultaneous exposure to atomic oxygen, UV radiation, and the LEO environments.

When exposed to vacuum, many materials *outgas*, i.e., release substances in gaseous form. Outgassing products can be organic constituents of the materials or gases previously absorbed such as oxygen, nitrogen, or carbon dioxide (Wendt, 1995). In space payloads, outgassing can cause important properties of materials to degrade or outgassed products to condense on optical and thermal control surfaces. Outgassed products can also cause mechanisms and bearings to stick or jam (Phinney and Britton, 1995). Desorption in vacuum of gases or moisture previously collected on the surfaces of materials is called *offgassing*. This can cause problems similar to those resulting from outgassing.

It is obvious that the use of durable, low-outgassing and nonshedding materials in the design of space-borne instruments is vital. Processes used in the manufacture and assembly phases need to be carefully selected and controlled. Assembly, ground testing, and packaging for shipping are normally done in clean, dry environments with the in-process accumulation of contaminants, including moisture, carefully monitored. Table 2.4 summarizes the budgeted cleanliness levels for particulate matter on various critical surfaces in a typical space scientific instrument, the Cryogenic Limb Array Etalon Spectrometer (CLAES), as described by Steakley et al. (1990). Maintenance of such an instrument usually involves periodic internal and external cleaning as well as testing to make sure the device is adequately clean. Testing may take the form of visual examination under magnification, chemical or spectroscopic analysis, or measurement of transmission, surface reflectance, scatter, and bidirectional reflectance distribution function (BRDF).

Contamination by silicones is especially difficult to remove. It is recognized that the adequate cleanliness of optical instruments cannot always be preserved throughout long-duration space missions, such as those of Space Station Freedom, so on-orbit inspection and optics-cleaning techniques may be needed. If possible, allowances should be made for thermal and optical performance degradation due to contamination sources during orbit.

Uy et al. (1998) reported evidence that multilayer insulation used in space-borne payloads as thermal insulation can be a source of moisture contamination during temperature cycling of cryogenic instruments. They also indicated that residual particulate matter carried into orbit can also be

TABLE 2.4
Example of a Contamination Control Summary Budget for a Typical Spaceborne Scientific Instrument (Cryogenic Limb Array Etalon Spectrometer [CLAES])

Contamination: Particles in sensor

Effect:
1. Degrade BRDF and increase off-axis scatter
2. Absorb incident radiation, changing surface radiative properties
3. Obscure transmissive surfaces, resulting in performance loss

Critical hardware:	LAAM[a]	Primary mirror	Secondary mirror	Internal spectrometer	Focal plane internal	Baffling internal	Baffling external	CLAES exterior
Derived cleanliness level goals (A) (per MIL-STD-1246):								
	100	100	100	300	300	200	300	500
Obscuration allowances:								
To delivery (%)	3	1.5	1.5	9	15			
Total (%)	6	3	3	13	3			
BRDF allowances ($\times 10^{-3}$):								
To delivery	0.75	0.75	2					
Total	2.5	2.5	5					
Clean facilities (per FED-STD-209):								
Preclean	10,000	10,000	10,000	10,000	10,000	10,000	10,000	10,000
Precision clean	100	100	100	100	100	100	100	1,000
Assembly	100	100	100	100	100	100	100	1,000
Test	1,000	1,000	1,000	1,000	1,000	1,000	1,000	1,000
Package	10,000	10,000	10,000	10,000	10,000	10,000	10,000	10,000

[a] Limb acquisition and adjustment mirror.

Source: Adapted from Steakley, B.C., et al., *Proc. SPIE*, 1329, 31, 1990.

redistributed within instruments by vibrations caused by the activation of mechanisms such as doors or by temperature changes.

Chemical warfare agents (CWAs) are a serious consideration in the design of military optical instruments. These are aggressive organic chemicals designed to incapacitate or kill personnel. They can degrade performance of optical devices or cause them to be inoperable safely even with protective apparel because they are contaminated (Krevor et al., 1993). The latter situation can also occur if the instruments are exposed to biological warfare agents or the by-products of a nuclear explosion. Any of these contaminants may reside in or on the hardware for extended periods of time and render it useless because decontamination is extremely difficult or impossible.

Complex optical systems such as the NIF are susceptible to contamination problems in part because they have so many optical surfaces; the cumulative effect of a little foreign matter on each of many surfaces therefore becomes very significant (Stowers, 1999). Losses in energy occur owing to obscuration and scatter in such systems. Elaborate cleaning and inspection as well as strict control of environmental conditions in the facility help minimize the problems.

A special form of contamination in optical lithography systems poses severe problems for semiconductor manufacturers in their efforts to produce advanced memory and logic devices. This is the photon absorption of air constituents including O_2, CO_2, and water vapor. In order to achieve features on chips with sizes smaller than 70 nm, the wavelength of the light employed must be pushed far into the UV. Systems working at 157 nm may soon replace current systems using lasers operating at 193 nm, while developments for the longer term involve extreme ultraviolet radiation (EUV) sources operating at 126 nm or shorter wavelengths. The absorption of air at 157 nm is several orders of magnitude greater than that at 193 nm, so 157 nm systems require thorough purging with dry filtered N_2 or He. EUV systems will have to be evacuated in order to have sufficient throughput. Nonoutgassing materials are needed in all UV systems to prevent molecular condensation on optical surfaces that would drastically lower transmission or reflection characteristics as a function of operating time. Evacuated instruments will probably need to be modular with the modules isolated in order to avoid long pump-down times after maintenance.

To keep lithography photomasks ultraclean requires either extreme cleanliness of the entire instrument interior along the optical path or the introduction of thin windows (pellicles) near the photomasks to shield them from particulate contamination. These pellicles would be located far enough from the image plane for deposits thereon to not excessively degrade the system's imagery. In some systems under development, extremely thin (< 10 μm thick) pellicles are used. These are called "soft" pellicles. Thicker, so-called "hard," pellicles ($\sim$800 μm thick) can be made and used if their high unit costs are acceptable and if their influences on system performance are compensated for in the optical design. Some developmental system designs provide means for the pellicles to be moved out of the optical path during operation. This feature adds considerably to instrument complexity and cost.

2.2.9 FUNGUS

When optical instruments such as telescopes, binoculars, cameras, or microscopes are exposed for long periods to warmth and high humidity, films and localized deposits of fungus (or mold) may develop. Particularly troublesome in tropical climates, these organic contaminants degrade performance by introducing scatter at early stages of development. Later, they may permanently damage optical surfaces by etching patterns into the material.

Mold fungi have been found to germinate and grow on glass surfaces even though the surfaces had been thoroughly cleaned to remove fingerprints, dust particles, and lubricants (Theden and Kerner-Gang, 1965). The microscopic spores are ubiquitous and seem to be able to supply sufficient nutrients internally to support limited growth. Some glasses with high resistance to climate and acid seem to resist fungus as well. Others (such as KzFS4) seem to impede mold growth, at least at high humidity levels, although they are otherwise susceptible to climatic and acid conditions. This contradictory behavior indicates that the chemical composition of the glass plays a role in mold susceptibility.

Sprouse and Lawson (1974) reported evidence from tests conducted in the tropics (Panama Canal region) to the effect that natural organic compounds present on surfaces of glass and steel could serve as nutrient sources for fungal growth. It was thought that in the tropics, organic compounds (hydrocarbons) could come from vegetation effluents. Monoterpenes (empirical formula $C_{10}H_{16}$) previously thought to play a role in tropical fungal accumulation were not found in any significant quantity in the tropical atmosphere sampled. An aliphatic ester common to certain tropical grasses was found to be present in significant quantity in that atmosphere.

Baker (1967) evaluated some fungicides as fungus preventive agents on optics. Later, he described possible adverse effects of two fungicides (Baker, 1968). Baigozhin et al. (1977) reported experiments with some chemically unstable optical glasses that had been protected by fungicidal coatings that did not alter the glasses' optical properties. Optics protected with silicone films containing arsenic, mercury, or tin resisted fungus tests for 3 to 4 months, whereas unprotected optics of the same glasses were overgrown with fungus within 1 month of the same test. Harris and Towch (1989) described a series of environmental tests conducted on several types of infrared windows intended for use in FLIR systems. They included fungus growth in this program, expecting to find the materials to be impervious to this damage hazard. After 28 days, the test results indicated that a zinc sulfide sample had lost most of its rain-resistant coating and a monocrystalline germanium window showed coating damage. Transmission losses for these samples exceeded what would be expected if the coatings were completely removed. Similar control samples did not incur any damage or transmission loss, so the degradation was attributed to the effects of fungus.

Methods for fungus testing of optical instruments are summarized in Appendix B.

2.2.10 ABRASION AND EROSION

Exposure to abrasive action from wind-driven particles is a distinct hazard to optics such as ground-based telescopes and solar energy collectors located in desert regions as well as to windshields and optical instruments used in military vehicles operating at or near ground level. Typical examples of the latter are the driver's periscope for an armored ground vehicle and night-vision equipment for helicopters. Generally, replaceable windows are used as the exposed optics in these instruments to minimize maintenance costs. Durability is usually stressed in choosing antireflection coatings for these optics.

Covers are frequently provided to protect the expensive windows used on aerial reconnaissance aircraft while taxiing, during takeoff or landing, and during low-level flight. These are retracted or discarded prior to use of the sensors. Items of optical equipment used in space-borne payloads frequently have no windows; rather, they may have on-orbit ejectable, protective covers or remotely actuated doors that cover the open aperture (and hence the internal optics) during ground preparations, launch, and nonoperational periods in orbit.

Particulate erosion can be a serious problem for optics and radomes on aircraft and missiles. The particulate environments include airborne dust, rain, and ice. Flight through these environments can affect windows and other exposed optics resulting in loss of transmission due to obscuration of the beam and surface scattering and possibly cracking or catastrophic failure of the components. Particulate erosion effects on radomes can cause reduced wall thickness that would introduce boresight error or localized cracking of the radome. Cracking could result in catastrophic failure.

Since many of the operational requirements for military sensor systems exceed the particulate erosion resistance afforded by existing materials, these environmental problems have to be viewed in a broader context than the simple qualification tests that were used for many years. A general approach for utilizing laboratory test results to estimate the damage for actual flight scenarios was formulated by Adler (1987, 1991a). This general approach has been implemented with computational analyses of in-flight particle impact conditions, computational analyses of the impact damage, development of improved testing capabilities, generation of meaningful test data, and predictive modeling of the cumulative particle impact damage effects.

Water drop impact experimentation involves rotating-arm facilities (for velocities below Mach 1), ballistic ranges (for subsonic and supersonic impact velocities), and rocket sleds (for supersonic impact conditions). The rotating-arm facilities can produce a sustained multiple-water drop impact capability (Adler, 1989), whereas a ballistic range typically affords impacts with a single or small number of drops (Adler, 1991b). Rain-erosion testing using a rocket sled provides a multiple water drop environment. The cost of this type of testing places some limitations on the scope of the test conditions. A multiple-impact water jet device developed at the University of Cambridge has been used to simulate the damaging effects of a water drop collision (Seward et al., 1994).

A number of efforts have been directed toward simulating the effects of water drop impacts using solid particles. The advantage of this test procedure is that the target is stationary and the projectiles are propelled into it. Adler and Boland (1990) described a system for achieving multiple simulated water drop impacts using soft polymeric beads. Particles with diameters from 1 to 10 mm (0.04 to 0.4 in.) could be propelled at velocities from Mach 0.6 to Mach 4. Typical damage to a CVD ZnS window due to multiple 2-mm (0.08-in.)-diameter nylon beads impacting at normal incidence and simulating rain erosion at 462 m/sec (Mach 1.35) is shown in Figure 2.14. Davies and Field (2001) reported erosion tests of CVD diamond using 300- to 600-µm quartz sand particles. Field et al. (1994) reported on sand erosion tests of ZnS, calcium lanthanum sulphide ($CaLa_2S_4$), CVD diamond, and natural diamond.

Multiple polymeric bead impacts over a broad range of impact conditions have been used to generate data for predictive modeling (Adler et al., 1992). A three-dimensional, high-fidelity, dynamic finite element computational model has been developed to describe the impact of a rain drop on a structured target (Adler and Mihora, 1994). This approach allows the interaction between the drop and the target to be described for both normal and oblique impacts. The computer model allows parametric variations in the geometric and material properties of a target such as a window to be carried out to determine the most productive directions for improving its rain erosion resistance. The computer analyses minimize the need for fabricating and testing numerous material iterations to optimize a candidate window design.

Seward et al. (1990) described a means for firing single and multiple water jets at material samples and briefly compared test results on zinc sulfide with *in situ* flight tests on the same material. Blackwell and Kalin (1990) presented the results of small-particle impacts on sapphire windows,

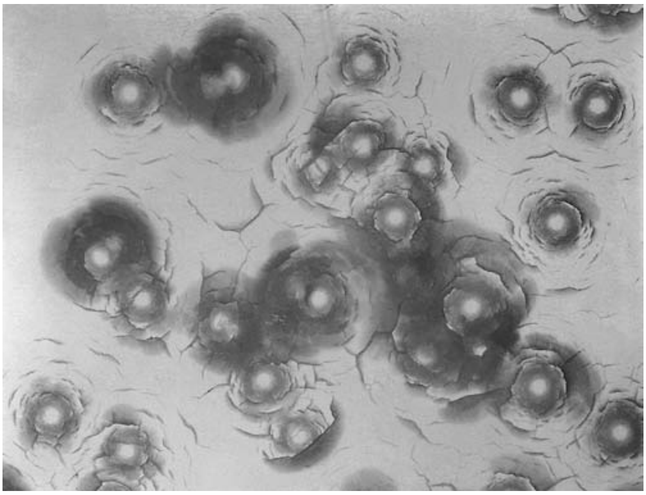

FIGURE 2.14 Photograph of impact damage from 2-mm-diameter Nylon beads on CVD zinc sulfide substrate at normal incidence simulating rain erosion at 462 m/sec velocity. (From Adler, W.F. et al., *Proc. SPIE.*, 1760, 303, 1992.)

whereas Weiskopf et al. (1990) reviewed the results of erosion modeling and tests on slip-cast fused silica radomes.

Field et al. (1974, 1979, 1983, 1989) and Adler and co-workers (Adler and Mihora, 1992; Adler et al., 1991) have used the postimpact strength of brittle materials as a quantitative measure of particulate impact damage. A bursting technique in which the specimen is hydraulically loaded to failure was developed at the University of Cambridge (Seward et al., 1992). In this technique, a uniform biaxial stress field is generated over a large part of the specimen surface so as to ensure that all flaws extended by the impact are sampled equally. Only very low stresses are felt by the edges of the specimen, so "edge" failures are almost entirely eliminated.

A typical series of burst tests reported by Seward et al. (1992) involved several 25-mm (1-in.)-diameter, 3-mm (0.12-in.)-thick disks of different IR-transmitting materials. Each was subjected to multiple-jet impacts normal to one surface. The impact velocity varied between 80 and 200 m/sec and the number of impacts varied from 1 to > 100. Figure 2.15 shows typical results for ZnS samples. At each velocity, a critical number of impacts have to be experienced before damage occurs. The solid line indicates this number. The small dots below the line represent tests in which no damage was observed, while the open circles above the line indicate tests in which damage did occur. Higher velocity impacts require fewer impacts, while more impacts are needed for damage to occur at lower velocities. These authors reported similar results for magnesium fluoride, spinel, and sapphire.

Adler (1991a) and Adler et al. (1992) obtained residual strength measurements for windows using a concentric-ring biaxial flexure test. This test was accurately characterized using detailed FEA. One advantage of the concentric ring configuration over the burst test is its applicability to testing at elevated temperatures representative of the aerodynamic heating for high-velocity flight conditions.

The preexposure surface finish condition of an optical material has a lot to do with its ability to withstand catastrophic damage under stress. The presence of subsurface cracks or grinding damage not completely removed by polishing significantly reduces the material's strength. This was demonstrated

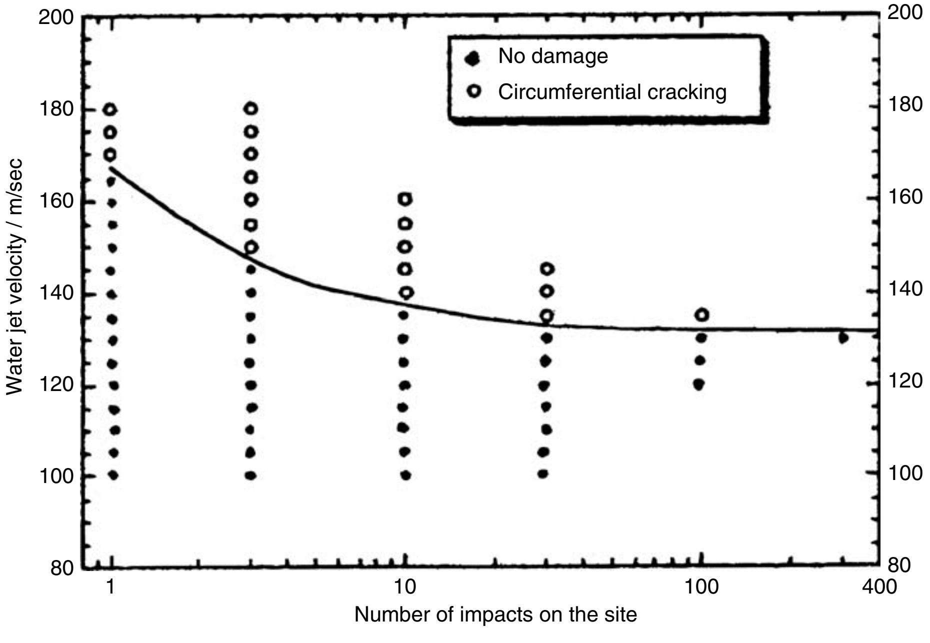

FIGURE 2.15 Graphical summary of damage vs. velocity data for different numbers of water drop impacts from a water jet normal to the surface of ZnS samples. The solid curve represents the threshold for damage. Dots below the curve are tests without damage while open circles above the curve are tests with damage. (Adapted from Seward, C. R., et al., *Proc. SPIE.*, 1760, 280, 1992.)

by van der Zwagg and Field (1982) for zinc sulfide. Others have found similar results with other optical materials (see Section 15.2).

Stover (1990) reported measurements of scatter in the form of the bidirectional transmittance distribution function (BTDF) from rain-impact-damaged germanium, zinc selenide, and gallium arsenide windows. His analysis predicted the corresponding performance reduction of an electro-optical sensor.

In attempts to counter the rain-erosion problem on soft materials, optical coating suppliers have developed protective coatings with good optical properties. Both hard and elastic coatings have been investigated (Matthewson and Field, 1980; van der Zwaag and Field, 1982; van der Zwaag et al., 1986). Hard, multilayer coatings such as DLC may introduce stress into the substrate owing to a mismatch of thermal expansion properties, especially if the coatings are more than a few micrometers thick. Coatings may tend to delaminate.

More elastic and thicker coatings of materials such as PACVD GeC appear to be suitable for increasing rain-erosion resistance (Mackowski et al., 1992). Monachan et al. (1989) found success with PACVD GeC and boron phosphide, both of which can be deposited in thicknesses of tens of micrometers without developing excessive stress. The absorption of 8 to 12 μm radiation by boron phosphide coatings is lower than that of DLC coatings. Combinations of DLC with GeC and Ge layers have proven effective for 8 to 12 μm band coatings for germanium (Monachan et al., 1989; Waddell and Monachan, 1990). Klocek et al. (1992) reported increased rain-erosion resistance in germanium, gallium arsenide, and zinc sulfide windows with polycrystalline or epitaxial gallium phosphide (GaP) coatings in thicknesses of about 20 μm using a metal-organic chemical vapor deposition (MOCVD) process.

Hasan (1990) described a multilayer coating for zinc sulfide windows and domes made of zinc selenide, thorium fluoride (ThF_4), and cerium fluoride (CeF_3) that had a reflectance less than 1% in the 8 to 12 μm band and that performed well under environmental stress, including rain erosion. A durable, multilayer, gradient-index, antireflection coating for zinc sulfide and zinc selenide windows having multispectral transmission capability from visible to IR wavelengths was described by Hasan and Bui (1992). Layers of ZnSe and ThF_4 were co-evaporated to produce the desired index profile. An external CeF_3 layer was added to improve durability. This coating has been applied to ZnSe windows as large as 32 in. (0.81 m). The coating passed rain erosion tests with only minor damage at velocities of 134 m/s. This velocity would be adequate for helicopter flight applications.

2.2.11 HIGH-ENERGY RADIATION AND MICROMETEORITES

In an overview of the effects of high-energy radiation on transparent optical components, Treadaway and Passenheim (1977) stated, in part:

> One of the adverse environments in which optical sensor systems are required to operate is the high-energy radiation environment. This environment is found in space, in commercial and research nuclear reactors, as well as in accelerator and radioisotope sources. In these environments, one finds various combinations of gamma rays, x-rays, neutrons, protons, and electrons. The mechanisms by which these types of radiation interact with matter are of two types: *displacement* and *ionization*. Displacement refers to the interaction by which an atom is displaced from its original site in the lattice to another site. Ionization refers to the mechanism by which the various types of radiation interact with the atomic electrons in a material and thus deposit energy through the material.
>
> If one considers the passive optical components in an optical sensor, the radiation effects are most readily observed in the transparent materials such as filter substrates, lenses, and windows. The effects on these materials that are of importance to the performance of optical sensors are radiation-induced absorption and radiation-induced luminescence. Radiation-induced absorption decreases the signal that reaches the detector while radiation-induced luminescence results in an increase in optical noise at the detector. Both effects degrade performance by reducing the signal-to-noise ratio.
>
> … Since glasses are naturally disordered materials, displacement effects, which only tend to slightly increase the amount of disorder, generally have no impact upon the performance of glasses. As a result, ionization effects dominate the response of optical glasses in radiation environments.

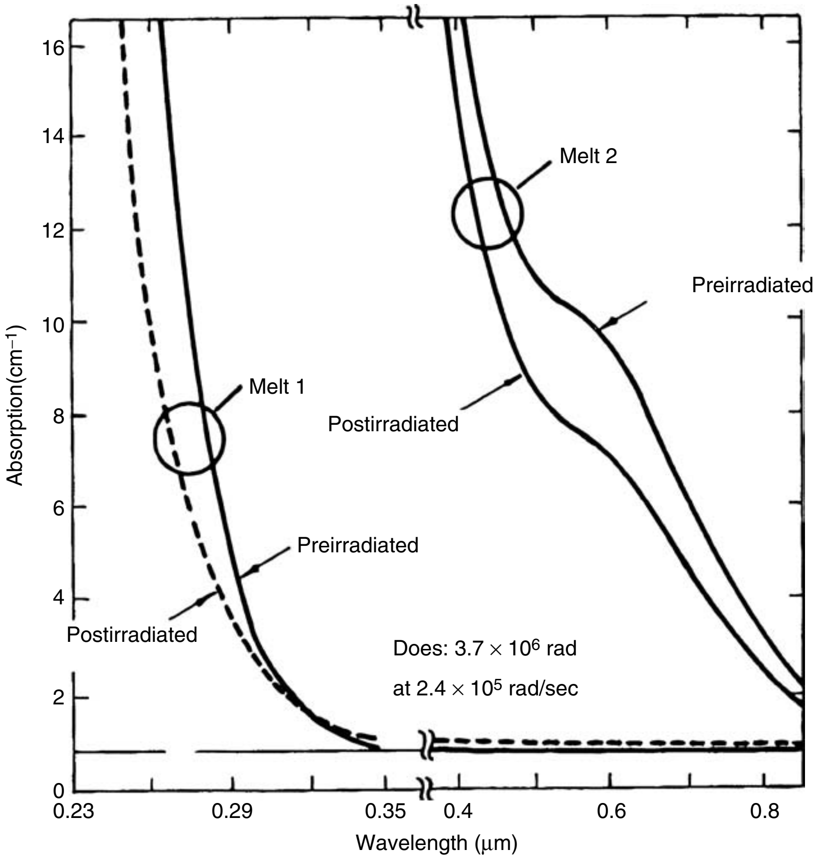

FIGURE 2.16 Absorption characteristics of two samples from different melts of Schott SK14 glass before and after exposure to the radiation doses listed. (Adapted from Treadaway, M. J., and Passenheim, B. C., *Proc. SPIE.*, 121, 67, 1977.)

The same authors also showed experimentally (see Figure 2.16) that the behavior of a given type of glass can vary from melt to melt, so predictions of radiation effects must be considered approximations unless confirmed by tests of samples from each melt to be used in a particular application. Further, they showed that the absorption variations of a given glass sample as a function of cumulative radiation doses at various wavelengths have the same shape (linear region followed by saturation). It follows that a measurement of the full absorption spectrum after exposure to one dose is sufficient to characterize the absorption growth at any dose and wavelength. In the long term, some fading or bleaching of the coloration may occur. Owing to thermal annealing, bleaching tendencies vary with material type and temperature. Treadaway and Passenheim (1977) indicated that bleaching occurs faster for glasses with lower Abbe numbers and that the rates do not vary greatly from melt to melt.

Some optical materials are naturally more resistant to high-energy radiation than others. Pure fused silica is a prime example of a material with good resistance to γ radiation, as shown in Figure 2.17(a). For comparison, Figure 2.17(b) shows the slight darkening that occurred in a sample of one type of "radiation-protected" glass (Schott BK7G14, containing 1.4% by weight of cerium dioxide) when exposed to 10^6 Gy¶ of γ radiation. The UV transmittances of CeO_2-doped glasses are significantly

---

¶The unit for radiation dose in the SI system is the gray (Gy). It equals 100 rad, where 1 rad is the dose needed to deposit energy of 100 erg into 1 g of irradiated material (Curry et al., 1990).

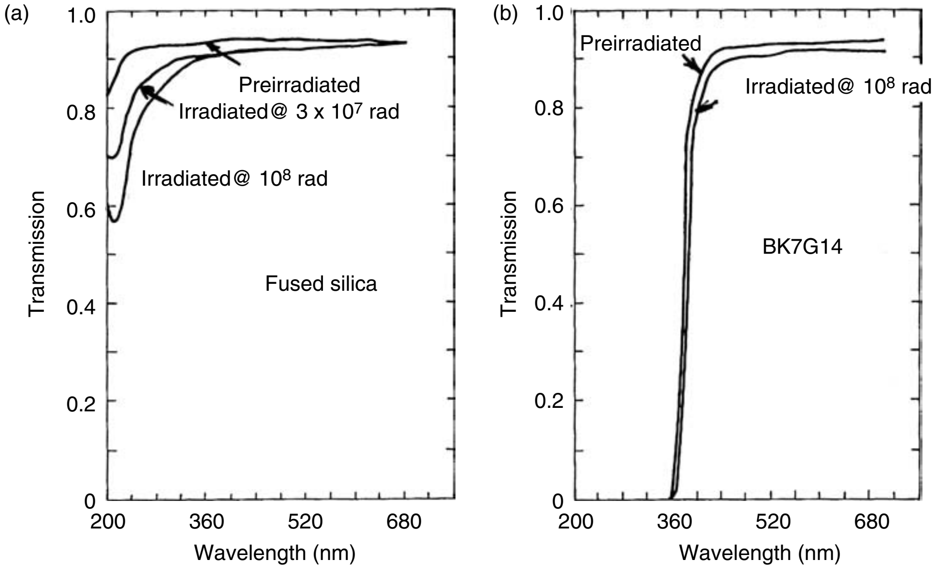

FIGURE 2.17 Transmission as a function of wavelength for (a) a fused silica sample and (b) a Schott BK7-G14 cerium-doped glass after being exposed to different γ radiation levels of (0 to 10^8 rad). (Adapted from Shetter, M. T. and Abreu, V. J., *Appl. Opt.*, 18, 1132, 1979.)

changed from those of the equivalent standard glasses (Marker et al., 1991). Their mechanical properties are essentially the same as those of the standard versions of the same glasses.

As is indicated in Section 3.2.2, the efficiency with which CeO_2 reduces discoloration in glasses is dependent on glass composition and radiation type. Some doped glasses are more resistant to electron radiation, whereas others are more resistant to neutron radiation, and still others are more resistant to γ radiation. Fortunately, several types of radiation-resistant optical glasses are now available so an appropriate choice to resist a given anticipated radiation environment can be made more easily.

The performance of spaceborne optical instruments in MEO may be affected by the high-energy radiation (protons and electrons) found in the Van Allen belts and by cosmic radiation (protons, electrons, and some heavy particles). The energy spectrum of this radiation is dependent on time, location, and energy source. Primary cosmic radiation originates outside the solar system and consists of light and heavy elements that have been accelerated to great velocity by galactic fields. Chua and Johnson (1991) characterized the average flux reaching the Earth's atmosphere each second as about 1 particle/cm^2 and its kinetic energy level as ranging from < 1 MeV to > 10 GeV. The composition of this radiation is approximately 88.4% H, 10.6% He, 0.51% C, 0.46% O, and 0.03% miscellaneous elements (Emiliani, 1987).

A hostile radiation environment is also created by detonation of nuclear weapons. Near the event, an instrument would receive significant doses of thermal, neutron, and γ radiation as well as experience an electromagnetic pulse that could damage electronic devices. If such an event occurs in space, charged particles would be trapped by the Earth's magnetic field and create a radiation belt that would endure for many years.

A series of tests of radiation effects on selected optical glasses, filter glasses, birefringent crystals, glass, plastic, and silica fibers was reported by Pellicori et al. (1979). Lowry and Iffrig (1990) reported more recent radiation tests on certain types of optical filters and unprotected Schott BK7 prisms. Spacecraft-shielding provisions also have significant effects on the dose received by optical payloads. Haffner (1967), Kase (1972), and Holzer and Passenheim (1979) gave examples of the effects of radiation in the presence of various amounts of shielding for various mission parameters.

Specific guidance regarding the effectiveness of various radiation-shielding materials and techniques may also be obtained from references such as Stevens and Trubey (1972).

Micrometeorites with masses typically 10^{-12} to 1 g and speeds as great as 72 km/sec (Cour-Palais, 1969), and space debris of comparable or larger masses, pose a significant hazard to astronauts, instruments, and spacecraft alike when in the Earth's orbit. The hazards from these objects and radiation are somewhat reduced on the lunar surface owing to the natural shielding provided by the Moon itself. The potential for problems due to dust on the lunar surface is also significant. Particles disturbed by micrometeorite impact or human or machine activity follow long ballistic trajectories owing to the low gravity and reduced atmospheric drag in that environment. Deposits of these particles on optics, solar cells, and mechanisms as well as obscuring dust clouds in optical paths may be expected (Johnson and Dietz, 1991).

2.2.12 LASER DAMAGE TO OPTICAL COMPONENTS

The interaction of intense coherent radiation with optical materials has been the topic of numerous technical studies and publications almost from the time that the laser was invented. The chief forum for deliberations in this field since 1969 is the continuing series of international conferences called the *Boulder Damage Symposia*, which are held each year at the National Institute of Science and Technology in Boulder, CO. Recurring topics for contributed papers include definitions of laser-induced damage (LID), thresholds for onset of damage, means for predicting damage onset, methods for testing, protocols for data reduction, formats for reporting, and techniques for modeling the interactions. In addition to sessions for oral presentations and poster sessions, these symposia have, over the years, included several mini-symposia on vital technology issues such as mirror contouring by diamond turning, damage to lithographic optics, contamination effects, damage to optical fibers, laser diode developments, and optics for deep-UV.

Through the cooperative efforts of thousands of symposia participants, immense progress has been made in improving the purity, homogeneity, thermal conductivity, surface quality, etc., of substrates and coatings (thereby reducing absorption and increasing damage thresholds); in understanding the mechanisms for component failures; and in finding ways to evaluate materials and increase lifetime by minimizing damage. These improvements have enhanced the performance of instruments involving all types of lasers ranging from the smallest diodes to immense inertial confinement fusion systems.

The list of publications resulting from the Boulder Damage Symposia has grown immensely; this indicates the importance of and interest in this rapidly advancing technology. According to Guenther (1998), a total of about 15,000 proceedings pages were published between 1969 and 1998. The interested reader is referred to a three-volume set of CD-ROMs entitled *Laser-Induced Damage in Optical Materials*, published by the SPIE in 1999, that contains all the papers[‖] from the 30-year period ending in 1998. These papers are categorized into four general areas: *Fundamental Mechanisms*, *Surfaces and Mirrors*, *Materials and Measurements*, and *Thin Films*. Some information gleaned from representative papers in each category is summarized briefly below.

2.2.12.1 Fundamental Mechanisms

In this category, we find analyses, reports, discussions, and assessments of the basic photon–matter interaction, of nonlinear effects, of techniques for modeling observed phenomena, and of laser performance in a variety of applications.

Early theoretical and modeling work dealt primarily with failures in continuous wave (CW) and long pulse laser applications resulting from heating of the bulk material, impurities (such as traces of platinum in glasses), and the presence of contamination sites on interfaces (Bennett, 1971; Hellwarth,

---

[‖] Some manuscripts not available at the time of proceedings publication are represented by abstracts only.

1972; Gulati and Grannemann, 1976; Palmer and Bennett, 1983). Interest in this area continues in conjunction with laser weapon development and other applications (Feit et al., 1996; Dijon et al., 1998; Poulingue et al., 1998; Shah et al., 1998). More recently, efforts have concentrated on extremely short pulses (Stuart et al., 1995; Efimov et al., 1996; Koldunov and Manenkov, 1998).

Important aspects of laser damage modeling are the determination of relationships between material parameters, such as the dependence of thresholds with refracting material refractive index (Bettis et al, 1974), and how to scale results from one analysis or a series of tests to other situations (Guenther and McIver, 1994).

The significance of the fundamental mechanisms underlying LID in the achievement of success in a variety of laser applications is indicated in papers such as Jollay (1995) and Ghita et al. (1998), which deal with laser diodes, and Newnam (1992), which focuses on EUV projection lithography systems. Influences of LID on larger systems are represented by papers on the optics for NIF (Schwartz et al., 1998; Feit et al., 1998) and on the proposed use of high-power laser systems to project intense laser beams into space to power satellites or remove orbital space debris (Bennett, 1995).

2.2.12.2 Surfaces and Mirrors

This category includes presentations on refracting and reflecting substrate material properties affecting damage thresholds, optical surface preparation, subsurface damage, roughness and scattering, and environmental degradation and aging.

Subsurface mechanical damage (microscopic fractures) to optics has long been known to affect the survivability of the optics in adverse thermal and mechanical environments. It also tends to increase scatter from the damaged surface and is important with regard to the LID of optical and semiconductor materials (Tesar et al., 1991). One means for reducing subsurface damage is "controlled grinding," in which successively finer grades of abrasive are used during the final stages of grinding and early stages of polishing with the depth of material removal at each stage at least three times the diameter of the abrasive particles used previously (Stoll et al., 1961). Reicher et al. (1991) indicated that the use of a "float polishing" technique has also been useful in enhancing component resistance to LID.

Optics with flawed surfaces are easily fractured under mechanical stress, see Section 15.2. Research involving fused silica vacuum windows for inertial confinement fusion applications has indicated that the parameters controlling failure are the tensile stress in the component, the ratio of window thickness to flaw depth, and secondary crack propagation (Campbell et al., 1996). The surface flaws can result from LID during system testing or operation. The researchers concluded that a properly mounted window would fail in a controlled or "safe" manner (i.e., crack, but not implode) if the window thickness to flaw depth ratio is 6 or more, and if the tensile stress in the window does not exceed 500 lb/in.^{2} (3.4 MPa) — allowing for a safety factor of ~2. An additional requirement is that the air leak through the crack must be rapid enough to reduce the stress before secondary cracks appear. The latter cracks can occur because the tensile stresses in the broken window pieces increase after the first fracture occurs and the sizes of those pieces may be smaller than six times the critical flaw dimension for the material. Implosion occurs if the multiplicity of window pieces cannot support the residual vacuum load.

2.2.12.3 Materials and Measurements

Investigations into and results of measurements of the basic properties of bulk materials are reported in this LID category.

Schuhmann (1998) discussed the general requirements for optical components to be used for laser applications. He considered image quality, surface scatter, absorptance, and laser-induced damage threshold (LIDT) for commercially produced uncoated and coated optics such as windows, mirrors, lenses, polarizers, prisms, and beam splitters. Reference is made in Schuhmann's paper to

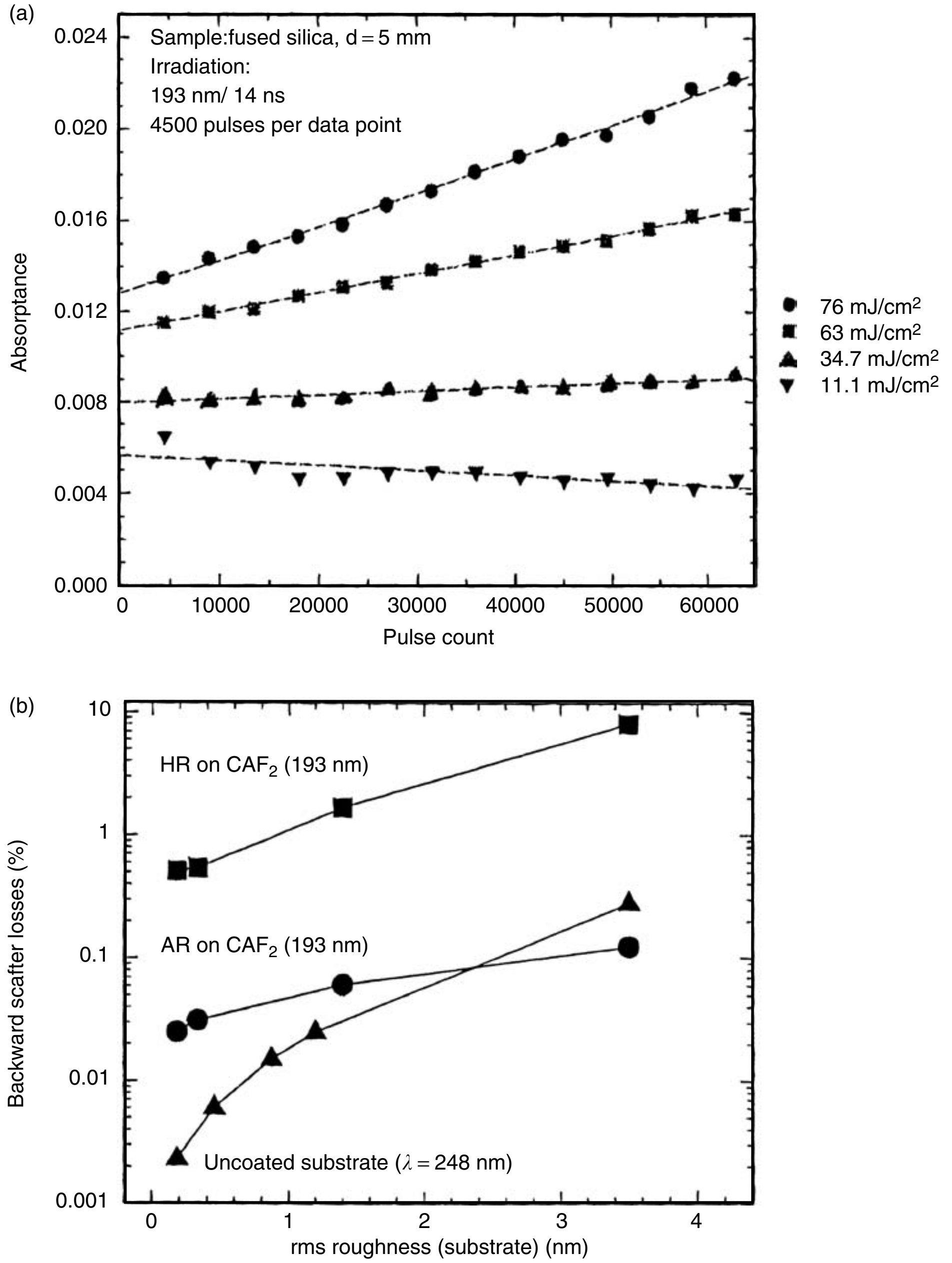

FIGURE 2.18 (a) Degradation of high-grade fused silica due to color center formation under irradiation with 193 nm laser pulses of various energy densities. (b) Backward scatter losses from uncoated, antireflection coated, and high reflectance coated CaF_2 samples with different surface roughness. The coatings here are MgF_2/LaF_3 layers designed for normal incidence at 193 nm wavelength. (Adapted from Mann, K., et al., *Proc. SPIE.*, 3578, 1999.)

ISO/DIS 11151, *Laser and Laser-Related Equipment — Standard Optical Components* for standard tolerances applicable to commercial products and typical test results for optics made of several materials in regard to surface microroughness, total surface scatter, and LIDT with 1064 and 248 nm wavelength laser exposures.

Custom optics for laser applications are of major interest with regard to LID. For example, Mann et al. (1999) discussed absorptance and scatter effects for coated and uncoated optics used in deep-UV laser systems at 193 nm and 248 nm wavelengths. Characteristics such as color center formation and their effects on light transmission and losses due to scattering were considered. Figure 2.18(a) illustrates the measured degradation that occurs in high-grade fused silica when irradiated with increasing numbers of 193 nm pulses of various energy densities. Figure 2.18(b) shows the impact of surface microroughness on backward scatter from uncoated, antireflection-coated, and high-reflection-coated samples of CaF_2 under normal incidence irradiation at 193 nm wavelength. The results depicted in Figures 2.18(a) and (b) are as expected and qualitatively typical of other materials as well.

The experiments just described were obtained at one laboratory with one set of measuring apparatus. In the LID field, it is customary to conduct the same tests at several laboratories using different apparatus, the same (i.e., mutually agreed upon) procedures, and either the same samples or samples manufactured identically. If the results correlate, one can draw more meaningful conclusions. These test programs are called “round-robin tests.” Typical examples are reported by Riede et al. (1998) and Ristau et al. (1998). The methods used in these experiments were in accordance with ISO/DIS 11254-1 (pertaining to LID using linear regression of damage probability data) and ISO 11551 (pertaining to absorptance), respectively.

An overview of means for delivering laser power through fibers and the resultant damage considerations thereof was given by Harrington (1996). He discussed fibers made of silica, heavy metal and chalcogenide glasses, and sapphire as well as hollow waveguides. The effects of bending these flexible components and of typical defects were explained.

2.2.12.4 Thin Films

In this LID category, we find research into the sensitivity of thin films to radiation, damage thresholds, film structure, deposition technology, contamination and other environmental effects, and measurement techniques for all the above as applicable to optical coatings.

The interactions of laser radiation with optical components have been investigated ever since the first laser was constructed because it undoubtedly damaged its optics. The use of coatings to enhance transmission and reflectance and thus improve the performances of lasers in general as well as the performances of the systems in which the lasers were used followed immediately. Structural defects, internal stresses, and contamination were soon identified as sources of coating failure (see, for example, Austin et al., 1972). Some of the later publications in this area include Steiger and Brausse (1994), Reichling et al. (1994), Fornier et al. (1996a, b) and Callahan and Flint (1998). As laser wavelengths have grown shorter, the LID problems have grown more serious and harder to solve.

2.3 ENVIRONMENTAL TESTING OF OPTICS

The fundamental purpose of environmental testing of equipment is to ensure, through laboratory simulation, that it has been designed and manufactured to withstand all pertinent environmental conditions to which it might reasonably be subjected, alone or in combination, throughout its planned life cycle. Whenever practical, the test item should be the final equipment configuration and interfaced, as appropriate, with related support structure(s). This ideal situation frequently cannot be realized, especially with new designs. In such cases, the test item and related structure should represent the final configuration as closely as possible. Military, national, and international standards generally allow the test item to be functionally dissimilar to the equipment’s final configuration if construction, materials, and manufacturing processes are representative of that configuration. The severity of conditioning during a given test is often increased over the normally expected level to obtain meaningful results in a relatively short time period.

In Appendix B, we briefly summarize methods for testing individual optical components and complete optical instruments in 13 types of adverse environmental conditions. These considerations are based primarily on International Standard ISO 9022, *Methods for Testing Optical Components and Optical Instruments under Adverse Environmental Conditions* since it is directly applicable to optical instruments. In many cases, the tests specified in ISO 9022 are similar to those specified in U.S. military standard MIL-STD-810, *Environmental Test Methods and Engineering Guidelines*, and similar documents used in other countries. Some tests defined in the ISO standard were derived from related standards prepared by the International Electrotechnical Commission (IEC) and suitably modified to apply to optical instruments. Each test is categorized by a nonconsecutive "method number" beginning with 10 and ending with 89; the applicable numbers are indicated in Appendix B. During each environment test, the specimen is to be in one of the following states of operation:

0: In transport/storage container
1: Unprotected, ready for operation, power off
2: Operating

Unless otherwise required, the test sequence includes the following steps:

Preconditioning: Here, the test specimen is prepared for test and temperature stabilized to within ±3 K of ambient.

Initial test: The specimen is tested per specifications and examined for conditions that could affect results of environmental tests.

Conditioning: Exposure to conditioning method at specified severity and state of operation. Note that under operational state 2, the instrument is functionally tested during exposure.

Recovery: Specimen is brought back to within ±3 K of ambient temperature and otherwise prepared for functional test.

Final test: Examine and test specimen per specifications.

Evaluation: Results are reviewed to determine pass/fail.

For space applications, MIL-STD-1540B recommends functional testing of optical equipment as indicated in Table 2.5. The listed tests are performed during qualification testing or acceptance testing as indicated. Some tests are shown as optional. The decision as to the need for such tests is determined on the merits of the design and the application. This author has observed that certain tests not listed as required in MIL-STD-1540B for optical equipment are often appropriate for many spaceborne optical instruments. These include thermal cycling, sinusoidal vibration, handling/transportation-level

TABLE 2.5
Testing Specified by MIL-STD-1540B for Spaceborne Optical Equipment before and after Environmental Exposure

Test type	Performed during: qualification	Acceptance	Optional
Thermal vacuum	X	X	
Sinusoidal vibration			X
Random vibration	X	X	
Pyro shock			X
Acceleration	X		
Humidity			X
Life			X

Source: Adapted from Sarafin, T. P., in *Spacecraft structures and Mechanisms*, Sarafin, T. P. and Larson, W. J. (Eds.), Microcosm, Torrance and Kluwer Academic Publishers, Boston, 1995b.

shock, pressure, and leak testing. The detailed methods and levels for such additional testing might well follow the guidance offered in Appendix B.

REFERENCES

Adler, W.F., Development of design data for rain impact damage in infrared-transmitting windows and radomes, *Opt. Eng.*, 26, 143, 1987.

Adler, W.F., Rain erosion testing, *Proc. SPIE*, 1112, 275, 1989.

Adler, W.F., Supersonic water drop impact on materials, *Proceedings of the 6th European Electromagnetic Structure Conference*, Friedrichshafen, FRG, p. 237 September 4–6, 1991a.

Adler, W.F., Dynamic behavior of materials and structures, General Research Corporation, Santa Barbara, California, 1991b (Capabilities Summary).

Adler, W.F. and Boland, P.L., Multiparticle supersonic impact test program, *Proc. SPIE*, 1326, 268, 1990.

Adler, W.F., Boland, P.L., Flavin, J.W., and Richards, J.P., Multiple simulated water drop impact damage in zinc sulfide at supersonic velocities, *Proc. SPIE*, 1760, 303, 1992.

Adler, W.F. and Mihora, D.J., Biaxial flexure testing: analysis and experimental results, in *Fracture Mechanics of Ceramics*, Vol. 10, Bradt, R. C., Hasselman, D. P. H., Munz, D., Sakai, M., and Ya Shevchenko, V., Eds., Plenum, New York, 1992.

Adler, W.F. and Mihora, D.J., Analysis of water drop impacts on layered window constructions, *Proc. SPIE*, 2286, 264, 1994.

Adler, W.F., Mihora, D.J., and Ritchey, G., Biaxial flexure evaluation of germanium, *Proceedings of the 4th DoD Electromagnetic Windows Symposium*, p. 203 November 19–21, 1991.

Au, R.H., Optical window materials for hypersonic flow, *Proc. SPIE*, 1112, 330, 1989.

Austin, R.R., Michaud, R.C., Guenther, A.H., Putman, J.W., and Harniman, R., Influence of structural effects on laser damage thresholds of discrete and inhomogeneous thin films and multilayers, *Damage in Laser Materials: 1972, Spec. Publ. 372*, Nat. Bur. Stand., Washington, DC, 1972.

Baigozhin, A., Rodionova, M.S., Panfilenok, E.I., Bereznikovskaya, L.V., and Belova, I.V., Methods of protecting optical components made out of chemically unstable glasses from biological overgrowths, *Sov. J. Opt. Technol.*, 44, 416, 1977.

Baker, P.W., An evaluation of some fungicides for optical instruments, *Int. Biodeterioration Bull.*, 3, 59, 1967.

Baker, P.W., Possible adverse effects of ethyl-mercury chloride and meta-cresyl-acetate if used as fungicides for optical/electronic equipment, *Int. Biodeterioration Bull.*, 4, 59, 1968.

Baumeister, P., Interference and optical interference coatings, in *Applied Optics and Optical Engineering,* Vol. 1, Kingslake, R. Ed., Academic Press, New York, 1965, chap. 8.

Bennett, H.E., Minimizing susceptibility to damage in CO_2 laser mirrors, *Damage in Laser Materials: 1971, Spec. Publ. 356*, Nat. Bur. Stand., Washington, DC, 1971.

Bennett, H.E., Segmented adaptive optic mirrors for laser power beaming and other space applications, *Proc. SPIE*, 2714, 240, 1995.

Bettis, J.R., Guenther, A.H., and Glass, A.J., The refractive index dependence of pulsed laser induced damage, *Damage in Laser Materials: 1974, Spec. Publ. 414*, Nat. Bur. Stand., Washington, DC, 1974.

Blackwell, T.S. and Kalin, D.A., High-velocity, small particle impact erosion of sapphire windows, *Proc. SPIE*, 1326, 291, 1990.

Callahan, G.P. and Flint, B.K., Characteristics of deep UV optics at 193 nm and 157 nm, *Proc. SPIE*, 3578, 45, 1998.

Campbell, J.H., Hurst, P.A., Heggins, D.D., Steele, W.A., and Bumpas, S.E., Laser induced damage and fracture in fused silica vacuum windows, *Proc. SPIE*, 2966, 106, 1996.

Chua, K.M. and Johnson, S.W., Foundation, excavation and radiation shielding concepts for a 16-m large lunar telescope, *Proc. SPIE*, 1494, 119, 1991.

Cour-Palais, B.G., Meteoroid environment model-1969, near earth to lunar surface, *NASA SP-2013*, 1969.

Curry, T.S., Dowdey, J.E., and Murry, R.C., *Christensen's Physics of Diagnostic Radiology*, 4th ed., Lae and Febiger, Philadelphia, PA, 1969, p. 374.

Davies, A.R. and Field, J.E., Damage mechanisms involved in the solid particle erosion of CVD diamond, *Proc. SPIE*, 4375, 171, 2001.

Dijon, J., Ravel, G., and André, B., Thermomechanical model of mirror laser damage at 1.06 μm. Part 2: flat bottom pits formation, *Proc. SPIE*, 3578, 398, 1998.

Efimov, O.M., Gabel, K., Garnov, S.V., Glebov, L.B., Grantham, S., Richardson, M., and Soileau, M.J., *Proc. SPIE*, 2966, 65, 1996.

Elliott, A. and Home Dickson, J., *Laboratory Instruments — Their Design and Application*, Chemical Pub. Co., New York, 1960.

Emiliani, C., *Dictionary of Physical Sciences*, Oxford Univ. Press, New York, 1987.

Facey, T.A., A study of surface particulate contamination on the primary mirror of the Hubble Space Telescope, *Proc. SPIE*, 525, 140, 1985.

Facey, T.A., Particulate contamination control in the optical telescope assembly for the Hubble Space Telescope, *Proc. SPIE*, 777, 200, 1987.

Facey, T.A., Private communication, 1991.

Facey, T.A. and Nonenmacher, A., Measurement of total hemispherical emissivity of contaminated mirror surfaces, *Proc. SPIE*, 967, 308, 1988.

Feit, M.D., Rubenchik, A,M., Faux, D.R., Riddle, R.A., Shapiro, A., Eder, D.C., Penetrante, B.M., Milam, D., Génin, F.Y., and Kozlowski, M.R., Modeling of laser damage initiated by surface contamination, *Proc. SPIE*, 2966, 417, 1996.

Feit, M.D., Rubenchik, A.M., Kozlowski, M.R., Génin, F.Y., Schwartz, S., and Sheehan, L.M., Extrapolation of damage test data to predict performance of large-area NIF optics at 355 nm, *Proc. SPIE*, 3578, 226, 1998.

Feldman, H.R., Demchak, L.J., and MacCoun, J.L., Loads analysis for single degree of freedom systems, in *Spacecraft Structures and Mechanisms*, Sarafin, T.P. and Larson, W.J., Eds., Microcosm, Torrance and Kluwer Academic Publishers, Boston, 1995, p. 95, chap. 5.

Field, J.E., Camus, J.J., Gorham, D.A., and Rickerby, D.G., Impact damage produced by large water drops, *Proceedings of the 4th International Symposium*, *Rain Erosion and Associated Phenomenon*, Royal Aeronautical Establishment, Farnborough, 1974.

Field, J.E., Gorham, D.A., Hagan, J.T., Matthewson, M.J., Swain, M.V., and van der Zwagg, S., Liquid jet impact and damage assessment for brittle solids, *Proceedings of the 5th International Conference on Erosion by Liquid and Solid Impact*, Univ. of Cambridge, 1979.

Field, J.E., van der Zwagg, S., and Townsend, T.T., Liquid impact damage assessment for a range of IR materials, *Proceedings of the 6th International Conference on Erosion by Liquid and Solid Impact*, Univ. of Cambridge, 1983.

Field, J.E., Hand, R.J., Pickles, C.J., and Seward, C.R., Rain erosion studies of IR materials, *Proc. SPIE*, 1191, l00, 1989.

Field, J.E., Sun, Q., and Gao, H., Solid particle erosion on infrared transmitting materials, *Proc. SPIE*, 2286, 301, 1994.

Fornier, A., Cordillot, C., Bernardino, D., Lam, O., Roussel, A., Amra, C., Escoubas, L., Albrand, G., Commandré, G., Roach, P., Cathelinaud, M., and Gatto, A., Characterization of optical coatings: damage threshold/local absorption correlation, *Proc. SPIE*, 2966, 292, 1996a.

Fornier, A., Cordillot, C., Bernardino, D., Lam, O., Roussel, P.B., Geenen, B., Leplan, H., and Alexandre, W., Characterization of HR coatings for the megajoule laser transport mirrors, *Proc. SPIE*, 2966, 327, 1996b.

Friedman, I., Thermo-optical analysis of two long focal-length aerial reconnaissance lenses, *Opt. Eng*., 20, 161, 1981.

Geary, J.M., Response of long focal length optical systems to thermal shock, *Opt. Eng*., 19, 233, 1980.

Ghita, R.V., Cengher, D., Lazanu, S., and Cimpoca, V., Contribution to the failure analysis of AlGaAs/GaAs laser diodes, *Proc. SPIE*, 3578, 359, 1998.

Glasstone, S., *Sourcebook on the Space Sciences*, Van Nostrand, New York, 1965.

Gordon, C.G., Generic criteria for vibration-sensitive equipment, *Proc. SPIE*, 1619, 71, 1991.

Gordon, C.G., Generic vibration criteria for vibration-sensitive equipment, *Proc. SPIE*, 3786, 22, 1999.

Guenther, A.H., Symposium welcome, on the occasion of the thirtieth boulder damage symposium, *Proc. SPIE*, 3578, xv, 1998.

Guenther, A.H. and McIver, J.K., To scale or not to scale, *Proc. SPIE*, 2114, 488, 1994.

Gulati, S.K. and Granneman, W.W., Laser damage to semiconductor materials from 10.6 μm CW CO_2 laser radiation, *Damage in Laser Materials, Spec. Publ. 462A*, Nat. Bur. Stand., Washington, 1976.

Haffner, J., *Radiation and Shielding in Space*, Academic Press, New York, 1967.

Harrington, J.A., An overview of power delivery and laser damage in fibers, *Proc. SPIE*, 2966, 536, 1996.

Harris, D.C., *Materials for Infrared Windows and Domes*, SPIE Press, Bellingham, 1999.

Harris, R.D. and Towch, A.W., Window evaluation program for an airborne FLIR system: environmental and optical aspects, *Proc. SPIE*, 1112, 244, 1989.

Hasan, W., Rain erosion resistance coating for ZnS domes, *Proc. SPIE*, 1326, 157, 1990.

Hasan, W. and Bui, Broadband durable anti-reflection coating for an E-O system window having multiple wavelength applications, *Proc. SPIE*, 1760, 253, 1992.

Hellwarth, R., Fundamental absorption mechanisms in high-power laser window materials, Damage in Laser Materials, Spec. Publ. 372A., Nat. Bur. Stand., Washington, DC, 1972.

Holzer, J.A. and Passenheim, B.C., Performance of laser systems in radiation environments, *Opt. Eng.*, 18, 562, 1979.

Honig, J., Cleanliness improvements of National Ignition Facility amplifiers as compared to previous large-scale lasers, *Opt. Eng.*, 43, 2904, 2004.

ISO 9022, (1991). *Optics and Optical Instruments — Environmental Test Methods*, ISO Central Secretariat, Geneva.

ISO/DIS 11151, *Laser and Laser-Related Equipment — Standard Optical Components*, ISO Central Secretariat, Geneva.

ISO/DIS 11254-1, *Test Method for Laser Induced Damage of Optical Surfaces,* ISO Central Secretariat, Geneva.

Johnson, C.L. and Dietz, K.L., Effects of the lunar environment on optical telescopes and instruments, *Proc. SPIE*, 1494, 208, 1991.

Jollay, R., Manufacturing experience in reducing environmental induced failures of laser diodes, *Proc. SPIE*, 2714, 679, 1995.

Kalin, D.A. and Clark, R.L., Tabletop experimental simulation of hypersonic aero-optical effects, *Proc. SPIE*, 1112, 377, 1989.

Kalin, D.A., Mullins, S.F., Couch, L.L., Blackwell, T.S., and Saylor, D.A., Experimental investigation of high-velocity mixing/shear layer aero-optic effects, *Proc. SPIE*, 1326, 178, 1990.

Karow, H. H., Cleaning Technology Review, in *Technical Digest of How-to Program*, *Orlando*, Optical Society of America, Washington, DC, 1989, p. 123.

Kase, P., The radiation environments of outer-planet missions, *IEEE Trans. Nucl. Sci.*, NS-19, 141, 1972.

Keski-Kuha, R.A.M., Ostantowski, J.F., Blumenstock, G.M., Gum, J.S., Fleetwood, C.M., Leviton, D.B., Saha, T.T., Hagopian, J. G., Tveekrem, J.L., and Wright, G. A., High reflectance coatings and materials for the extreme ultraviolet, *Proc. SPIE*, 2428, 294, 1994.

Klocek, P., Hoggins, J.T., and Wilson, M., Broadband IR transparent rain erosion protection coating for IR windows, *Proc. SPIE*, 1760, 210, 1992.

Koldunov, M.F. and Manenkov, A.A., Recent progress in theoretical studies of laser-induced damage (LID) in optical materials: fundamental properties of LID threshold in the wide pulse width range from microseconds to femtoseconds, *Proc. SPIE*, 3578, 212, 1998.

Krevor, D.H., Hargovind, N.V., and Xu, A., Effects of military environments on optical adhesives, *Proc. SPIE*, 1999, 36, 1993.

Lowry, J.H. and Iffrig, C.D., Radiation effects on various optical components for the Mars Observer Spacecraft, *Proc. SPIE*, 1330, 132, 1990.

Mackowski, J.M., Cimma, B., Pignard, R., Colardelle, P., and Laprat, P., Rain erosion behavior of germanium carbide (GeC) films, *Proc. SPIE*, 1760, 201, 1992.

Mann, K., Apel, O., and Eva, E., Characterization of absorption and scatter losses on optical components for ArF excimer lasers, *Proc. SPIE*, 3578, 614, 1999.

Mantell, C.L., Ed., *Engineering Materials Handbook*, McGraw-Hill, New York, 1958.

Marker, A.J., III, Hayden, J.S., and Speit, B., Radiation resistant optical glasses, *Proc. SPIE*, 1485, 160, 1991.

Matthewson, M.J. and Field, J.E., An improved strength measurement technique for brittle solids, *J. Phys. Eng.*, 13, 355, 1980.

McCartney, E.J., *Optics of the Atmosphere*, Wiley, New York, 1976.

MIL-STD-210C, *Climatic Information to Determine Design and Test Requirements for Military Systems and Equipment*, U.S. Dept. of Defense, Washington, DC, 1997.

MIL-STD-810F, *Environmental Engineering Considerations and Laboratory Tests,* U.S. Dept. of Defense, Washington, DC, 2003.

MIL-STD-1540D, *Product Verification Requirements for Launch, Upper Stage, and Space Vehicles*, U.S. Dept. of Defense, Washington, DC, 1999.

Monachan, B.C., Kelly, C.J., and Waddell, E.M., Ultrahard coatings for IR materials, *Proc. SPIE*, 1096, 129, 1989.

Moran, M.B., Johnson, L.F., and Klemm, K.A., Diamond films for IR applications, *Proc. SPIE*, 1326, 137, 1990.

Musikant, S. and Malloy, W.J., Environments stressful to optical materials in low earth orbit, *Proc. SPIE*, 1330, 119, 1990.

NAS5-15208. *Aerospace Systems Pyrotechnic Shock Data (Ground test and Flight)*, Vol. VI, NASA Goddard Space Flight Center.

Newnam, B.E., Optical degradation issues for XUV projection lithography systems, *Proc. SPIE*, 1848, 474, 1992.

Palmer, J.R. and Bennett, H.E., A predictive tool for evaluating the effect of multiple defects on the performance of cooled laser mirrors, *Damage in Laser Materials: 1981, Spec. Publ. 638*, Nat. Bur. Stand., Washington, DC, 1983.

Pellicori, S.F., Russell, S.F., and Watts, L.A., Radiation induced transmission loss in optical materials, *Appl. Opt.*, 18, 2618, 1979.

Phinney, D.D. and Britton, W.R., Developing mechanisms, in *Spacecraft Structures and Mechanisms*, Sarafin, T.P. and Larson, W.J., Eds., Microcosm, Torrance and Kluwer Academic Publishers, Boston, 1995, p. 665, chap. 19.

Poulingue, M., Dijon, J., Garrec, P., and Lyan, P., 1.06 μm laser irradiation on high reflection coatings inside a scanning electron microscope, *Proc. SPIE*, 3578, 188, 1999.

Reicher, D.W., Kranenberg, C.F., Stowell, R.S., Jungling, K.C., and McNeil, J.R., Fabrication of optical surfaces with low subsurface damage using a float polishing process, *Proc. SPIE*, 1624, 161, 1992.

Reichling, M., Bodemann, A., and Kaiser, N., A new insight into defect-induced laser damage in UV multilayer coatings, *Proc. SPIE*, 2428, 307, 1994.

Riede, W., Willamowski, U., Dieckmann, M., Ristau, D., Broulik, U., and Steiger, B., Laser-induced damage measurements according to ISO/DIS 11 254-1: results of a national round robin experiment in Nd:YAG laser optics, *Proc. SPIE*, 3244, 96, 1998.

Ristau, D., Willamowski, U., and Welling, H., Measurement of optical absorptance according to ISO 11551: parallel round-robin test at 10.6 μm, *Proc. SPIE*, 3578, 657, 1999.

Roark, R.J. and Young, W.C., *Formulas for Stress and Strain*, McGraw-Hill, New York, 1975.

Sarafin, T.P., Structural mechanics, in *Spacecraft Structures and Mechanisms*, Sarafin, T.P. and Larson, W.J., Eds., Microcosm, Torrance and Kluwer Academic Publishers, Boston, 1995a, chap. 4.

Sarafin, T.P., Developing confidence in mechanical designs and products, in *Spacecraft Structures and Mechanisms*, Sarafin, T.P. and Larson, W.J., Eds., Microcosm, Torrance and Kluwer Academic Publishers, Boston, 1995b, chap. 11.

Sarafin, T.P., Harmel, T.A., and Webb, R.W., Jr., Verification criteria, in *Spacecraft Structures and Mechanisms*, Sarafin, T.P. and Larson, W.J., Eds., Microcosm, Torrance and Kluwer Academic Publishers, Boston, 1995, chap. 12.

Schaick, R., Smith, R., and Weese, C., Classical methods of cleaning, handling and storage of optical components, in *Technical Digest of How-to Program, Orlando,* Optical Society of America, Washington, DC, 1989, p. 165.

Schuhmann, R., Quality of optical components and systems for laser applications, *Proc. SPIE*, 3578, 672, 1999.

Schwartz, S., Feit, M.D., Kozlowski, M.R., and Mouser, R.P., Current 3ω large optic test procedures and data analysis for the quality assurance of National Ignition Facility optics, *Proc. SPIE*, 3578, 314, 1999.

Seward, C.R., Pickles, C.S., and Field, J.E., Single- and multiple-impact jet apparatus and results, *Proc. SPIE*, 1326, 280, 1990.

Seward, C.R., Pickles, C.S.J., Marrah, R., and Field, J.E., Rain erosion data on window and dome materials, *Proc. SPIE*, 1760, 280, 1992.

Seward, C.R., Coad, E.J., Pickles, C.S., and Field, J.E., Rain erosion resistance of diamond and other window materials, *Proc. SPIE*, 2286, 285, 1994.

Shah, R.S., Bettis, J.R., Stewart, A.F., Bonsall, L., Copland, J., Hughes, W., Echeverry, J.C., Finite element thermal analysis of multispectral coatings for the ABL, *Proc. SPIE*, 235, 3578, 1999.

Shetter, M.T. and Abreu, V.J., Radiation effects on the transmission of various optical glasses and epoxies, *Appl. Opt.*, 18, 1132, 1979.

Shipley, A.F., Optomechanics for Space Applications, *SPIE Short Course Notes SC561*, 2003.

Snail, K.A., CVD diamond as an optical material for adverse environments, *Proc. SPIE*, 1330, 46, 1990.

Souders, M. and Eshbach, O.W., Eds., *Handbook of Engineering Fundamentals*, 3rd ed., Wiley, New York, 1975.

Sprouse, J.F. and Lawson, W.F., III, *Ambient Organic Compounds in the Tropics and their Relationship to Microbial Effects*, Rept. 7409001, U.S. Army Tropic Test Ctr, 1974.

Steakley, B.C., King, A.D., and Rigney, T.E., Contamination control of the Cryogenic Limb Array Etalon Spectrometer, *Proc. SPIE*, 1329, 31, 1990.

Steiger, B. and Brausse, H., Interaction of laser radiation with coating defects, *Proc. SPIE*, 2428, 559, 1994.

Stevens, P.N. and Trubey, D.K., Methods for calculating neutron and gamma ray attenuation, in *Weapons Radiation Shielding Handbook, DNA-1892-3*, Rev. 1, Defense Nuclear Agency, Washington, DC, 1972, chap. 3.

Stoll, R., Forman, P.F., Edelman, J., The effect of different grinding procedures on the strength of scratched and unscratched fused silica, *Proceedings of the Symposium on the Strength of Glass and Ways to Improve it*, Union Scientifique Continentale du Verre, Florence, Italy, 1961.

Stover, J C., Practical measurement of rain erosion and scatter from IR windows, *Proc. SPIE*, 1326, 321, 1990.

Stowers, I.F., Optical cleanliness specifications and cleanliness verification, *Proc. SPIE*, 3782, 525, 1999.

Stuart, B.C., Feit, M.D., Herman, S., Rubenchik, A.M., Shore, B.W., and Perry, M.D., *Proc. SPIE*, 2714, 616, 1995.

Stubbs, D.M. and Hsu, I.C., Rapid cooled lens cell, *Proc. SPIE*, 1533, 36, 1991.

Tesar, A.A., Brown. N.J., Taylor, J.R., and Stolz, C.J., Subsurface polishing damage of fused silica: nature and effect on laser damage of coated surfaces, *Proc. SPIE*, 1441, 154, 1991.

Theden, G. and Kerner-Gang, W., Results of investigations on the contamination of optical glass by fungi, originally published in 1964 in *Glastec. Ber.* 37: 200, 1965. (Translation published by U.S. Defense Documentation Ctr. in 1965 as *Document AD458907.*)

Thornton, M.M. and Gilbert, C.C., Spacecraft contamination database, *Proc. SPIE*, 1329, 305, 1990.

Treadaway, M.J. and Passenheim, B.C., Radiation effects on optical components, *Proc. SPIE*, 121, 67, 1977.

Tribble, A.C., *The Space Environment*, Princeton University Press, Princeton, 1995.

U.S. Military Standard MIL-STD-1246C, *Product cleanliness levels and contamination control program*, U.S. Department of Defense, Washington, DC, 1994.

U.S. Federal Standard 209E, *Airborne particulate cleanliness classes in cleanrooms and clean zones*, Institute of Environmental Sciences and Technology, Rolling Meadows, IL, 1992.

Uy, O.M., Benson, R.C., Erlandson, R.E., Silver, D.M., Lesho, J.C., Galica, G.E., Green, B.D., Boies, M.T., Wood, B.E., and Hall, D.F., Contamination lessons learned from the Midcourse Space Experiment, *Proc. SPIE*, 3427, 28, 1998.

van der Zwagg, S. and Field, J.E., Liquid jet impact damage on zinc sulphide, *J. Mat. Sci.*, 17, 2625, 1982.

van der Zwagg, S., Dear, J.P., and Field, J.E., The effect of double-layer coatings of high modulus on contact stresses, *Phil. Mag.*, A 53, 101, 1986.

Vukobratovich, D., Optomechanical design principles, in *Handbook of Optomechanical Design*, CRC Press, Boca Raton, FL, 1997, chap. 2.

Waddell, E.M. and Monachan, B.C., Rain erosion protection of IR materials using boron phosphide coatings, *Proc. SPIE*, 1326, 144, 1990.

Weiskopf, F.B., Lin, J.S., Drobnick, R.A., and Feather, B.K., Erosion modeling and test of slip-cast fused silica, *Proc. SPIE*, 1326, 310, 1990.

Wendt, R.G., Miliauskas, R.E., Day, G.R., MacCoun, J.L., and Sarafin, T.P., Space mission environments, in *Spacecraft Structures and Mechanisms*, Sarafin, T.P. and Larson, W.J., Eds., Microcosm, Torrance and Kluwer Academic Publishers, Boston, 1995, chap. 3.

Willey, R.R., *Practical Design and Production of Optical Thin Films*, Marcel Dekker, New York, 1996.

Zito, R.R., Cleaning large optics with CO_2 snow, *Proc. SPIE*, 1236, 952, 1990.

Zito, R.R., CO_2 snow cleaning of optics: curing the contamination problem, *Proc. SPIE*, 4096, 82, 2000.

3 Opto-Mechanical Characteristics of Materials

3.1 INTRODUCTION

The major classes of raw materials from which optical instruments are created include glasses, plastics, crystals, semiconductors, ceramics, metals, thin films of all the above, composites, adhesives, sealing compounds, and special finishes. In this chapter, we consider for each of these classes the general characteristics of importance in opto-mechanical systems design and tabulate typical values for selected parameters and materials. Sources in the literature for more detailed information regarding these and other materials of interest are cited. Just as Wolfe (1990) reported for refractive properties of infrared materials, the mechanical properties of most types of materials used in optical instruments can vary slightly from lot to lot and from one source to another. Numerical values cited here are approximate and may not be adequate for final design purposes. Materials manufacturers should be contacted for specific values pertaining to their products, and if adequate data are not available, measurements should be made on representative samples.

3.2 MATERIALS FOR REFRACTING OPTICS

3.2.1 General Considerations

The most obvious characteristic of a refractive material such as glass is its ability to transmit electromagnetic radiation in some part or parts of the spectral region ranging, from UV to IR. This ability is not perfect, for the resultant intensity I of a beam just after entering the material must decrease from the incident value I_0 as the radiation penetrates farther into the body of the material. Losses accrue owing to absorption and scattering, with the former usually playing the major role. In both cases, the intensity decrease with distance is exponential, as indicated in the following equation:

$$\frac{I}{I_0} = \exp[-(a_\mathrm{a} + a_\mathrm{s})t] \tag{3.1}$$

Here, the beam traverses a distance t inside the material having absorption coefficient a_a and scattering coefficient a_s.

Generally, absorption within transparent materials is spectrally dependent; some wavelengths are absorbed more than others. Owing to this selective process, the transmitted radiation assumes the "color" of the incident radiation minus the absorbed part. Similarly, the energy scattered by molecules, internal discontinuities, or included matter will, in general, be wavelength dependent; therefore, the color of the directly transmitted beam is further altered by subtraction of wavelengths scattered from the propagating beam. For a given size of scattering element, longer wavelengths are scattered less effectively than shorter ones. Equation (3.1) applies only monochromatically since both a_a and a_s vary with wavelength.

For an uncoated refracting surface, an additional amount of the incident beam is diverted owing to Fresnel reflection at the surface. The relative intensity I of a normally incident beam I_0 actually entering the material can be determined from

$$\frac{I}{I_0} = 1 - \frac{(n_2 - n_1)^2}{(n_2 + n_1)^2} \tag{3.2}$$

Here, n_1 and n_2 are the refractive indices relative to air at a given wavelength for the two materials separated by the interface. More complex equations applying at oblique incidence are given in optics texts such as Smith (2000). The state of polarization of the radiation must then be taken into account.

As implied in Eq. (3.2), a key optical parameter that usually changes as the radiation passes from one medium into another is the refractive index. We define two forms of this parameter. The *absolute* refractive index n_{abs} is the ratio of the velocity of light in a vacuum to that in the material. In most engineering applications, we use the *relative* refractive index n or n_{rel}, which is the ratio of the absolute refractive index of the material to the absolute refractive index of air (~1.00029 at standard temperature and pressure for visible wavelengths). Owens (1967) discussed the variation of the index of air with temperature, pressure, humidity, and carbon dioxide content. Optical glass catalogs list the relative refractive index.

In most optically transparent solids, n lies between 1.3 and 4.1; in optical glasses, the range is from about 1.4 to 2.1. Wolfe (1978, 1990), Wolfe and Zissis (1978), and Tropf et al. (1995) provide extensive tables of values for this parameter.

Optical glass manufacturers give average relative refractive index values for their products at several specific wavelengths (most corresponding to Fraunhofer absorption lines) in their catalogs and can supply measured values (called test certificates or "melt data") for a given production lot, or melt, at a few wavelengths for purchased quantities of those materials. At added cost, measured values at other wavelengths can usually be obtained.

The variation of refractive index with wavelength is called dispersion. It is depicted in Figure 3.1 for a few representative materials transmitting in the visible range. Study of these curves reveals that

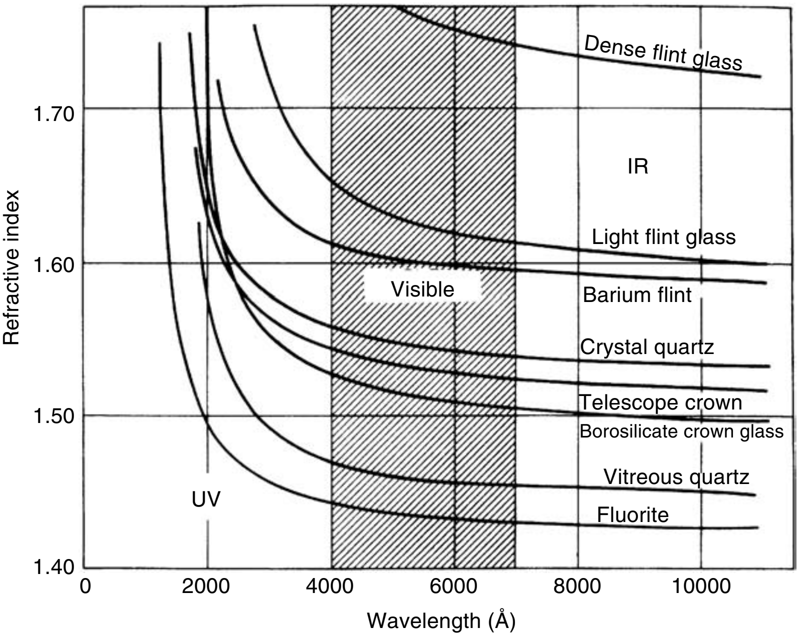

FIGURE 3.1 Dispersion curves for several materials commonly used for refracting optical components. (Adapted from Jenkins, F.A. and White, H.E., *Fundamentals of Optics*, McGraw-Hill, New York, 1957.)

(1) the index decreases with increasing wavelength; (2) the rate of change of n is greatest at the short wavelength end; and (3) the slopes of the curves at a given wavelength are steeper for higher-index materials. Not so obvious is the fact that (4) the shape of the dispersion curve for one material cannot be accurately derived from that for another material simply by changing scale or transforming the coordinate system.

The refractive index of optical materials also varies with the temperature of that material. Such changes induce changes in optical path length and the focusing properties of refracting components. Glass catalogs generally define the changes in absolute and relative index per degree temperature change, dn/dT, at several wavelengths spaced over the useful transmission range of the material for each of their products. Typically, these changes are a few parts in the sixth decimal place per °C. Most glasses have a positive index change for an increase in temperature, but a few, such as Schott N-FK5, have negative dn/dT values. Since the rate of change dn/dT varies with temperature, the catalog values are averaged over temperature ranges such as -40 to -20°C or $+20$ to $+40$°C.

Passage of light from one more or less transparent material into another follows Eq. (3.3), which is Snell's law, relating the angles of incidence and refraction I_1 and I_2 and the refractive indices n_1 and n_2 of the media immediately preceding and following the interface:

$$n_1 \sin I_1 = n_2 \sin I_2 \tag{3.3}$$

The ray angles are determined with respect to an imaginary line locally normal to the interface at the point of incidence.

The refractive properties of some transmitting optical materials that might be considered homogeneous may actually suffer from slight spatial index variations because of natural causes or, in the case of man-made materials, residual effects of the manufacturing process, such as inadequate annealing. They may also display internal stress from external influences such as temperature changes or imposed mechanical forces. When afflicted by any of these perturbations, the material is said to be birefringent, i.e., possessive of slightly different values of refractive index for different states of polarization of the transmitted light. This subject is considered further with regard to optical glasses in the next section. Natural birefringence is frequently found in some crystals; this can significantly affect the way polarized light refracts through the material.

The suitability of any optical material for use in opto-mechanical systems is dependent on many mechanical properties as well as optical ones. Of particular interest here are density, Young's modulus, Poisson's ratio, linear thermal expansion coefficient, specific heat, thermal conductivity, hardness (typically measured against Knoop or Vickers scales), and transformation temperature. All but the last are common parameters to the opto-mechanical engineer and are defined in standard engineering texts and handbooks. Parker (1979) gave a particularly useful discussion of these properties as applicable to glass.

Transformation temperature refers to the elevated temperature at which a distinct change in thermal expansion coefficient of a glass or other material occurs. Softening takes place near this temperature. A brief discussion of hardness and an approximate comparison of various scales for quantifying this property may be found in Appendix C.

3.2.2 OPTICAL GLASS

The Sellmeier equation is commonly used to determine the value of relative refractive index at normal room temperature (68°F or 20°C) and normal air pressure (14.7 lb/in.^{2} or 0.10133 MPa) for optical glasses at intermediate wavelengths other than those given by measurements or taken from the literature (Tropf et al., 1995). A common form of this equation is used by Schott Glass Technologies (Mainz, Germany and Duryea, PA.) to provide this information from coefficients B_1 to B_3 and C_1 to C_3 as given in their optical glass catalog. This equation is as follows:

$$n_\lambda^2 - 1 = \frac{B_1\lambda^2}{\lambda^2 - C_1} + \frac{B_2\lambda^2}{\lambda^2 - C_2} + \frac{B_3\lambda^2}{\lambda^2 - C_3} \tag{3.4}$$

The variable λ is the wavelength expressed in μm. The manufacturer of any given melt of glass can provide measured values for the coefficients upon request.

A commonly used measure of dispersion of an optical glass is the Abbe number v_λ (frequently called the v or *nu* value). Two forms of this parameter are computed as follows:

$$v_{\mathrm{d}} = \frac{n_{\mathrm{d}} - 1}{n_{\mathrm{F}} - n_{\mathrm{C}}} \tag{3.5a}$$

$$v_{\mathrm{e}} = \frac{n_{\mathrm{e}} - 1}{n_{\mathrm{F}} - n_{\mathrm{C}}} \tag{3.5b}$$

Here, the subscripts d, e, F, and C identify the parameters as refractive index values for the specific colors of light corresponding to spectral emission lines of helium at 587.5618 nm, mercury at 546.0740 nm, and hydrogen at 486.1327 and 656.2725 nm, respectively. Other dispersive parameters of interest to lens designers are the partial dispersions such as

$$P_{\mathrm{g,F}} = \frac{n_{\mathrm{g}} - n_{\mathrm{F}}}{n_{\mathrm{F}} - n_{\mathrm{C}}} \tag{3.6a}$$

$$P_{\mathrm{C,s}} = \frac{n_{\mathrm{C}} - n_{\mathrm{s}}}{n_{\mathrm{F}} - n_{\mathrm{C}}} \tag{3.6b}$$

Values for these and some similar quantities are listed for each material in optical glass catalogs. The partial dispersions indicate how the material's refractive properties change in a specific small spectral range as compared with the change over a larger spectral range.

The Sellmeier-type equation used by Schott to compute the rate of change of index with temperature, d*n*/d*T*, in a vacuum as a function of wavelength (in μm) and temperature T (in °C) for optical glass is as follows:

$$\frac{\mathrm{d}n_{\mathrm{abs}}(\lambda,T)}{\mathrm{d}T} = \frac{n_{\mathrm{rel}}^2(\lambda,T_0) - 1}{2n_{\mathrm{rel}}(\lambda,T_0)}\left(\mathrm{D}_0 + 2\mathrm{D}_1\Delta T + 3\mathrm{D}_2\Delta T^2 + \frac{E_0 + 2E_1\Delta T}{\lambda^2 - \lambda_{\mathrm{TK}}^2}\right) \tag{3.7}$$

where n_{abs} and n_{rel} are glass indices as previously defined, T_0 is a reference temperature (usually 20°C), D_{i}, E_{i}, and λ_{TK} are coefficients specific to the glass, and $\Delta T = T - T_0$.*

Figure 3.2(a) is a "glass map" showing the large number of optical glasses produced by Schott a few years ago. Each symbol represents a specific material type. Several other manufacturers produce essentially the same glasses. The glasses are plotted by refractive index (ordinate) and Abbe number (abscissa) for yellow (helium) light of wavelength 587.5618 nm. The symbols fall into basic groups (labeled) based on chemical constituents. Generally, these regions lie on a diagonal from lower left to upper right, indicating that practical glasses exist only near that diagonal. Abbe showed that glasses with "normal" dispersive properties lie along a straight line connecting the points $n_{\mathrm{d}} = 1.511$, $v_{\mathrm{d}} = 60.5$ and $n_{\mathrm{d}} = 1.620$, $v_{\mathrm{d}} = 36.3$. Glasses located off this line display more or less abnormal dispersions and are used to correct secondary spectrum, a form of chromatic aberration in refractive optical systems. A lens corrected (i.e., has the same focal length) for two wavelengths is called *achromatic* while one corrected also for secondary spectrum has the same focal length for three wavelengths and is called *apochromatic*.

Kumler (2004) pointed out a serious challenge facing lens designers and opto-mechanical engineers today. The number of types of optical glass now available routinely (i.e., without special order in large quantity) is decreasing and the characteristics of some glasses are changing. Figure 3.2(b) shows the smaller number of "preferred" glass types that are currently readily available from Schott. A similar population shrinkage situation exists with other manufacturers. Newer versions of

---

[*] Refractive index shown as n without a subscript should be considered to be the relative index n_{rel}.

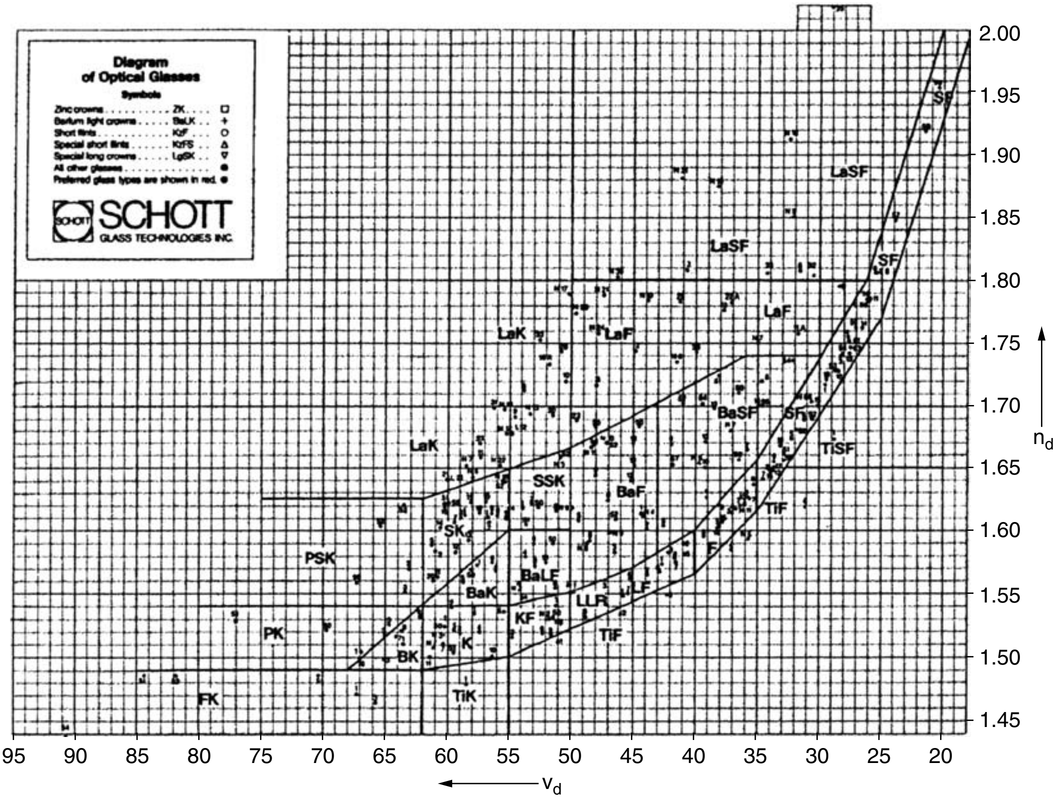

FIGURE 3.2(a) "Glass map" showing the variety of optical glasses produced just a few years ago by one major supplier.

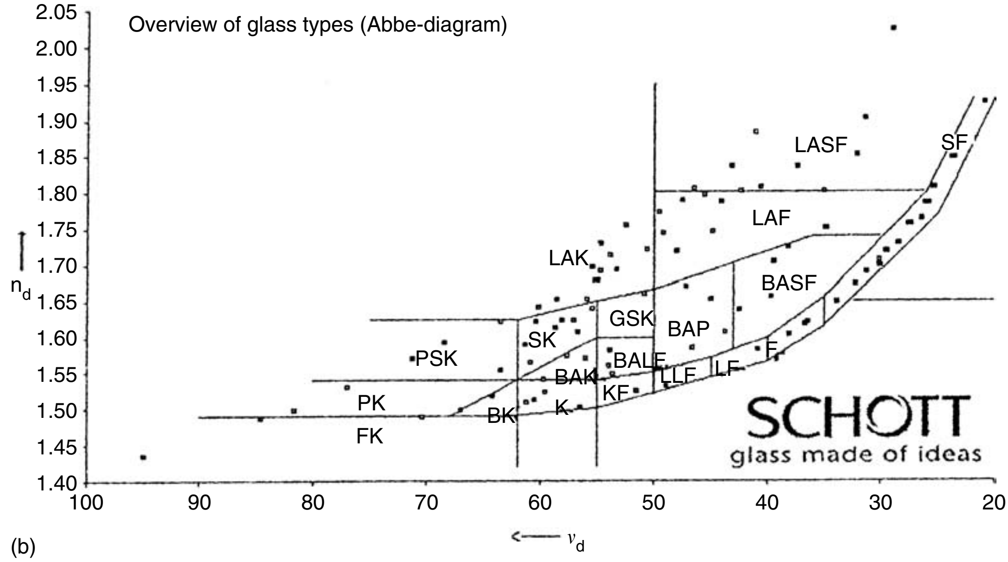

FIGURE 3.2(b) More recent "glass map" indicating the "preferred types" currently readily available by the same supplier as in Figure 3.2(a). (Courtesy of Schott Glass Technologies, Inc., Duryea, PA.)

traditionally used glasses are better in that they are free of lead and arsenic, but their optical and mechanical characteristics are not always the same as the older types located at or very near the same point on the map. Lens design software has not always kept up with these changes. Outdated glasses may still be listed for use in designs, but the materials cannot be found when the time comes to manufacture optical elements. To be sure of the parameters for any glass type, measurements should be made on representative samples rather than accepting the values listed in a catalog or in the design program.

Figure 3.3 is a reproduction of a page from the Schott optical glass catalog, which we will use to illustrate the types of information provided by glass manufacturers for optical design and engineering purposes. The optical properties of interest shown here are the refractive indices (measured values averaged for several melts) at as many as 23 wavelengths, Abbe numbers v_d and v_e, 12 relative partial dispersion values, constants B_i and C_i for the index vs. wavelength equation (Eq. [3.4]) temperature variation coefficients D_i, E_i, and λ_{TK} for refractive indices, and average values for internal transmittance τ_i of 10 and 25 mm thicknesses of the material at many wavelengths between 250 and 2500 nm.

Other parameters of interest from the optical viewpoint are homogeneity; variations of nominal refractive indices and Abbe numbers from the catalog values; and the presence of localized, threadlike, vitreous inclusions (striae), bubbles, inclusions, and residual stress (perhaps resulting in birefringence). These parameters are not listed on the individual catalog pages but rather in the general specifications for the various material quality levels available for purchase. Special controls on manufacturing processes and selected materials with specific properties may be available at premium prices. Parks (1980) provided valuable guidelines on the selection and specification of material quality.

All the above-named mechanical and thermal properties for optical glasses are generally given in glass catalogs. For example, they are given for Schott N-BK7 glass in Figure 3.3. Table 3.1 lists the symbols used by Schott for each of these parameters since they are not otherwise identified in the tabular data.

In order to point out the more desirable of the many types of optical glass available from the prime glass suppliers throughout the world, Walker (1993) designated 68 glasses as the types he considered most useful to lens designers. His list included glasses in “the most common range of refractive index and dispersion and [that] have the most desirable characteristics in terms of price, bubble content, staining characteristics, and resistance to adverse environmental conditions.” Zhang and Shannon (1995) reported a study conducted to identify the “minimum number of glasses needed for most lens designs.” Using the double Gauss lens form as a model and three commonly used lens design libraries — CodeV Reference Manual (1994), Laikin (1991), and Cox (1964) — as specific design sources, they created a list of 15 most commonly used glasses and a subset of 9 recommended glasses. Many of the glasses in the list of 15 are not included in Walker’s list. This is due, in part, to Walker’s omission of glasses that he felt had less desirable mechanical or environmental resistance properties, whereas Zhang and Shannon considered only optical properties while choosing their candidates.

Table 3.2 lists the 49 glasses currently supplied by Schott as “preferred” types that appear in the combined lists by Walker and Zhang and Shannon. These should suffice for many new designs for either commercial or noncommercial applications. It should be noted that exceptional design requirements would, of course, demand the use of other, less-standard glass types. Many older glass types can be found in existing inventories or produced on special order. Some special orders are subject to the condition that a full melt must be purchased.

For each of the glasses listed in Table 3.2, the reader will find the glass name and type or international code ($n_d - 1$ followed by 10 times v_d), the Young’s modulus, the Poisson’s ratio, a constant K_G that is used to estimate contact stress under mounting forces (see Section 15.3), the thermal expansion coefficient, and the density. Values are given in both USC and metric units. The extreme high or low values for each parameter are identified in the table by the symbols “H” and “L.” This is intended to highlight the general magnitudes of the changes that occur in these parameters throughout this group of selected glass types. At the bottom of each column, the ratio of the maximum to

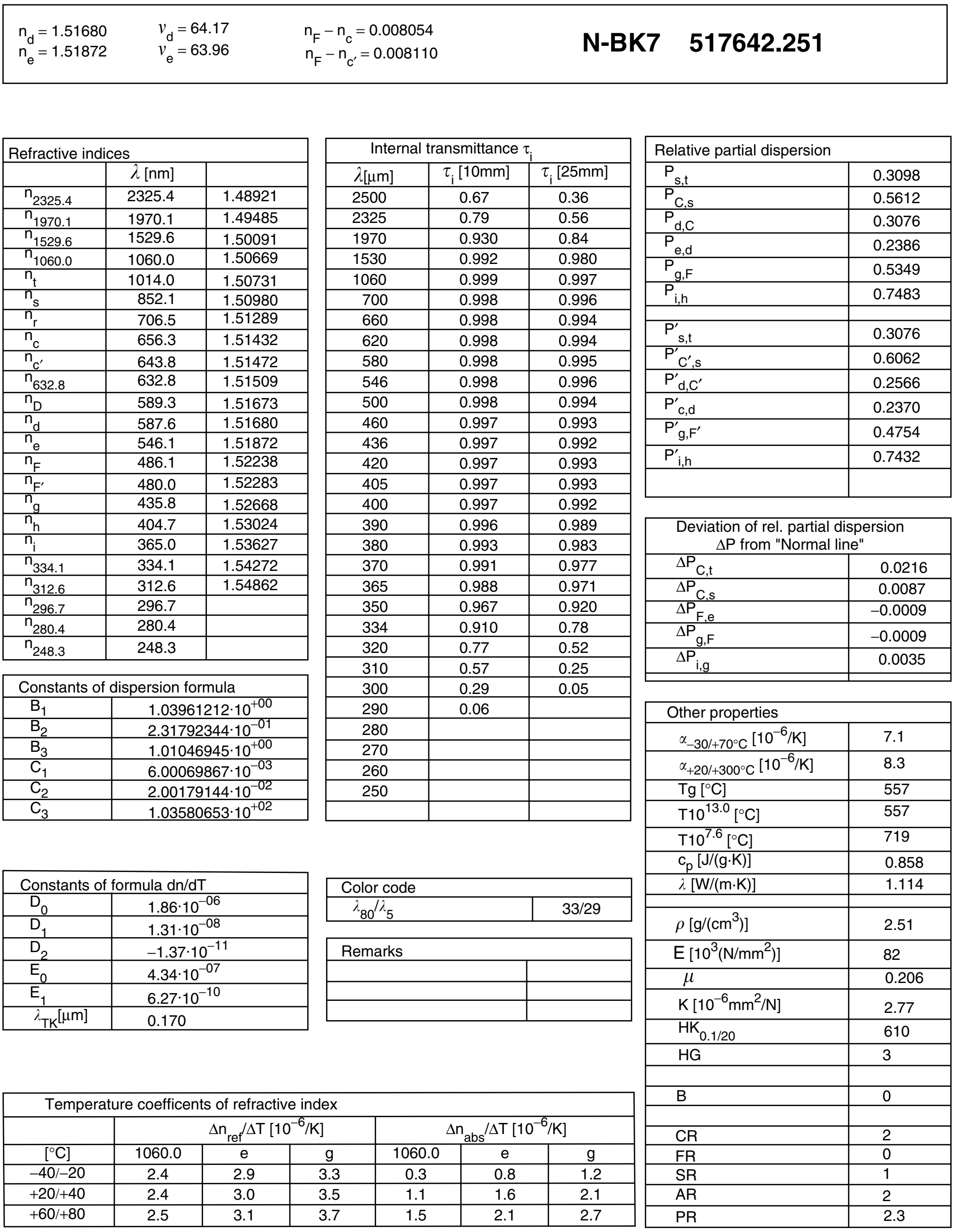

$n_d = 1.51680$ $\nu_d = 64.17$ $n_F - n_C = 0.008054$

$n_e = 1.51872$ $\nu_e = 63.96$ $n_F - n_{C'} = 0.008110$

N-BK7 517642.251

Refractive indices		
	λ [nm]	
$n_{2325.4}$	2325.4	1.48921
$n_{1970.1}$	1970.1	1.49485
$n_{1529.6}$	1529.6	1.50091
$n_{1060.0}$	1060.0	1.50669
n_t	1014.0	1.50731
n_s	852.1	1.50980
n_r	706.5	1.51289
n_C	656.3	1.51432
$n_{C'}$	643.8	1.51472
$n_{632.8}$	632.8	1.51509
n_D	589.3	1.51673
n_d	587.6	1.51680
n_e	546.1	1.51872
n_F	486.1	1.52238
$n_{F'}$	480.0	1.52283
n_g	435.8	1.52668
n_h	404.7	1.53024
n_i	365.0	1.53627
$n_{334.1}$	334.1	1.54272
$n_{312.6}$	312.6	1.54862
$n_{296.7}$	296.7	
$n_{280.4}$	280.4	
$n_{248.3}$	248.3	

Constants of dispersion formula	
B_1	$1.03961212 \cdot 10^{+00}$
B_2	$2.31792344 \cdot 10^{-01}$
B_3	$1.01046945 \cdot 10^{+00}$
C_1	$6.00069867 \cdot 10^{-03}$
C_2	$2.00179144 \cdot 10^{-02}$
C_3	$1.03580653 \cdot 10^{+02}$

Constants of formula dn/dT	
D_0	$1.86 \cdot 10^{-06}$
D_1	$1.31 \cdot 10^{-08}$
D_2	$-1.37 \cdot 10^{-11}$
E_0	$4.34 \cdot 10^{-07}$
E_1	$6.27 \cdot 10^{-10}$
λ_{TK}[μm]	0.170

Internal transmittance τ_i		
λ[μm]	τ_i [10mm]	τ_i [25mm]
2500	0.67	0.36
2325	0.79	0.56
1970	0.930	0.84
1530	0.992	0.980
1060	0.999	0.997
700	0.998	0.996
660	0.998	0.994
620	0.998	0.994
580	0.998	0.995
546	0.998	0.996
500	0.998	0.994
460	0.997	0.993
436	0.997	0.992
420	0.997	0.993
405	0.997	0.993
400	0.997	0.992
390	0.996	0.989
380	0.993	0.983
370	0.991	0.977
365	0.988	0.971
350	0.967	0.920
334	0.910	0.78
320	0.77	0.52
310	0.57	0.25
300	0.29	0.05
290	0.06	
280		
270		
260		
250		

Color code	
λ_{80}/λ_5	33/29

Remarks	

Relative partial dispersion	
$P_{s,t}$	0.3098
$P_{C,s}$	0.5612
$P_{d,C}$	0.3076
$P_{e,d}$	0.2386
$P_{g,F}$	0.5349
$P_{i,h}$	0.7483
$P'_{s,t}$	0.3076
$P'_{C',s}$	0.6062
$P'_{d,C'}$	0.2566
$P'_{e,d}$	0.2370
$P'_{g,F'}$	0.4754
$P'_{i,h}$	0.7432

Deviation of rel. partial dispersion ΔP from "Normal line"	
$\Delta P_{C,t}$	0.0216
$\Delta P_{C,s}$	0.0087
$\Delta P_{F,e}$	−0.0009
$\Delta P_{g,F}$	−0.0009
$\Delta P_{i,g}$	0.0035

Other properties	
$\alpha_{-30/+70°C}$ $[10^{-6}/K]$	7.1
$\alpha_{+20/+300°C}$ $[10^{-6}/K]$	8.3
Tg [°C]	557
$T10^{13.0}$ [°C]	557
$T10^{7.6}$ [°C]	719
c_p [J/(g·K)]	0.858
λ [W/(m·K)]	1.114
ρ $[g/(cm^3)]$	2.51
E $[10^3(N/mm^2)]$	82
μ	0.206
K $[10^{-6}mm^2/N]$	2.77
$HK_{0.1/20}$	610
HG	3
B	0
CR	2
FR	0
SR	1
AR	2
PR	2.3

Temperature coefficents of refractive index						
	$\Delta n_{ref}/\Delta T$ $[10^{-6}/K]$			$\Delta n_{abs}/\Delta T$ $[10^{-6}/K]$		
[°C]	1060.0	e	g	1060.0	e	g
−40/−20	2.4	2.9	3.3	0.3	0.8	1.2
+20/+40	2.4	3.0	3.5	1.1	1.6	2.1
+60/+80	2.5	3.1	3.7	1.5	2.1	2.7

FIGURE 3.3 A page from an optical glass catalog dated 2/2001 showing opto-mechanical parameters for a typical glass (N-BK7). (Courtesy of Schott Glass Technologies, Inc., Duryea, PA.)

minimum values listed is given for each parameter. This indicates the approximate range of those parameters throughout this limited population. Note that most of these ratios are about 2.0, and so we generalize that all optical glasses are approximately equal from a mechanical viewpoint.

The prefix "N" in some of the glass names indicates a newer version of that glass now produced by Schott. These have essentially the same refractive properties as the older versions thereof, but their mechanical properties generally differ from those of older versions. Three digits added to the glass code for Schott glasses represent density divided by ten. On nine occasions in Table 3.2, both

TABLE 3.1
Identification of Symbols Used in the Schott Optical Glass Catalog to Represent Mechanical, Thermal, and Other Properties

Glass code	International designation of (n_d–1) plus (10 v_d) plus (density divided by 10). See Note (1)
$\alpha_{-30/+70}$ (ppm/K)	Linear thermal expansion coefficient in the temperature range −30 to + 70°C. See Note (2)
$\alpha_{20/300}$ (ppm/K)	Linear thermal expansion coefficient in the temperature range +20 to + 300°C. See Note (3)
T_G (°C)	Transformation temperature
$T_{10}{}^{13.0}$ (°C)	Temperature of glass, at a viscosity of $10^{13.0}$ dPa·sec (sometimes called the upper annealing point)
$T_{10}{}^{7.6}$ (°C)	Temperature of glass, at a viscosity of $10^{7.6}$ dPa·sec (sometimes called the softening point)
c_P (J/g·K)	Average specific heat capacity
λ (W/m·K)	Thermal conductivity, at 90°C
ρ (g/cm^3)	Density
E (10^3 N/mm^2)	Young's modulus
μ	Poisson's ratio
K	Stress optic coefficient in nm/cm at 589.3 nm and 21°C
HK	Knoop hardness
HG	Grindability code
B	Bubble class: total cross-section of bubbles, stones, and crystals based on 100 cm^3 glass volume
CR	Climatic resistance class
FR	Stain resistance class
SR	Acid resistance class
AR	Alkaline resistance class
PR	Phosphate resistance class

Notes: (1) Schott's density suffix is sometimes omitted from glass type designation elsewhere in this book for simplicity. (2) This parameter is used for design and analysis purposes. (3) This parameter is used by glass manufacturers in the annealing process.

Source: Adapted from Schott, *Schott Optical Glass Catalog* (CD Version 1.2 USA). Schott Glass Technologies, Inc., Duryea, Pennsylvania, 2001.

older and newer versions of the same glass are listed. Mechanical differences are apparent, especially in terms of density where elimination of lead from the chemistry of the newer versions has reduced that parameter. It should be noted that Schott claims that all "N" glasses are essentially free of arsenic and radioactive materials such as thorium oxide.

Stress introduced into optical glasses during cooling (i.e., annealing) of the melt can cause problems during subsequent component fabrication. Typically, a piece of poorly annealed glass has surfaces under compressive stress and an interior under tensile stress. As the piece is cut or when material is removed from one surface, these stresses are at least partially relieved and the piece warps slightly. Response to the various steps in fabrication would then be unpredictable. Residual permanent stress after fabrication or temporary stress introduced by thermal or mechanical causes may affect the optical performance of the finished component. This stress can be detected and estimated as birefringence by polarimetry and the resultant variation in refractive index measured by interferometry. Stress-related problems can be greatly reduced in magnitude by specifying the permitted residual birefringence of the raw material and the finished optical component, and by minimizing external (i.e., mounting) forces applied to the component. Analysis of birefringence effects and determination of appropriate tolerance values for that attribute during optical system design can by accomplished using the methods described by Doyle and Bell (2000), Doyle et al. (2002a), and Doyle et al. (2002b).

Tolerances on birefringence are usually expressed in terms of the permitted optical path difference (OPD) for the parallel (||) and perpendicular (⊥) states of polarization of transmitted light at a

TABLE 3.2
Key Mechanical Properties of 49 Schott Optical Glasses Ranked in Order of Increasing Value of n_d

Rank (and ref.)	Glass Name	Glass Code	Young's Modulus (E_G)		Poisson's Ratio	$K_G=(1-\nu_G^2)/E_G$		Thermal Exp. Coef. (α_G)		Density (ρ)	
			(lb/in.^{2})	(MPa)	(ν_G)	(in.^{2}/lb)	(1/Pa)	(1/°F)	(1/°C)	(lb/in.^{3})	(g/cm^3)
1(b)	N-FK5	487704	9.0e+6	6.2e+4	0.232	1.05e–7	1.53e–11	5.1e–6	9.2e–6	0.088L	2.45L
2(a)	K10	501564	9.4e+6	6.5e+4	0.190 L	1.02e–7	1.48e–11	3.6e–6	6.5e–6	0.091	2.52
3(a)	N-ZK7	508612	1.0e+7	7.0e+4	0.214	9.54e–8	1.34e–11	2.5e–6L	4.5e–6L	0.089	2.49
4(a)	K7	511604	1.0e+7	6.9e+4	0.214	9.52e–8	1.38e–11	4.7e–6	8.4e–6	0.091	2.53
5(a)	N-BK7	517642	1.2e+7	8.2e+4	0.206	8.05e–8	1.17e–11	3.9e–6	7.1e–6	0.090	2.51
6(a)	N-K5	522595	1.0e+7	7.1e+4	0.224	9.24e–8	1.34e–11	4.6e–6	8.2e–6	0.093	2.59
7(a,b)	N-LLF6	532489	1.0e+7	7.2e+4	0.211	9.15e–8	1.33e–11	4.3e–6	7.7e–6	0.090	2.51
8(a)	N-BaK2	540597	1.0e+7	7.1e+4	0.233	9.18e–8	1.33e–11	4.4e–6	8.0e–6	0.103	2.86
9(a)	LLF1	548459	8.7e+6	6.0e+4	0.208	1.10e–7	1.59e–11	4.5e–6	8.1e–6	0.106	2.94
10(a)	N-PSK3	552635	1.2e+7	8.4e+4	0.226	7.85e–8	1.14e–11	3.4e–6	6.2e–6	0.105	2.91
11(a)	N-SK11	564608	1.1e+7	7.9e+4	0.239	8.23e–8	1.19e–11	3.6e–6	6.5e–6	0.111	3.08
12(a)	N-BAK1	573575	1.1e+7	7.3e+4	0.252	8.84e–8	1.28e–11	4.2e–6	7.6e–6	0.115	3.19
13(a)	N-BaLF4	580538	1.1e+7	7.7e+4	0.245	8.42e–8	1.22e–11	3.6e–6	6.5e–6	0.112	3.11
14(a)	LF5	581409	8.6e+6	5.9e+4	0.223	1.11e–7	1.61e–11	5.0e–6	9.1e–6	0.116	3.22
15(a)	N-BaF3	583466	1.2e+7	8.2e+4	0.226	8.00e–8	1.16e–11	4.0e–6	7.2e–6	0.100	2.79
16(a)	F5	603380	8.4e+6	5.8e+4	0.220	1.13e–7	1.64e–11	4.4e–6	8.0e–6	0.125	3.47
17(a)	N-BaF4	606437	1.2e+7	8.5e+4	0.231	7.68e–8	1.11e–11	4.0e–6	7.2e–6	0.104	2.89
18(a)	F4	617366	8.1e+6	5.6e+4	0.222	1.17e–7	1.70e–11	4.6e–6	8.3e–6	0.129	3.58
19(a)	N-SSK8	618498	1.2e+7	8.4e+4	0.251	7.69e–8	1.12e–11	4.0e–6	7.2e–6	0.118	3.27
20(a)	F2	620364	8.3e+6	5.7e+4	0.220	1.15e–7	1.67e–11	4.6e–6	8,2e–6	0.130	3.61
21(a)	N-F2	620364	1.2e+7	8.2e+4	0.228	7.97e–8	1.16e–11	4.3e–6	7.8e–6	0.095	2.65
22(b)	N-SK16	620603	1.3e+7	8.9e+4	0.264	7.21e–8	1.04e–11	3.5e–6	6.3e–6	0.129	3.58
23(a)	SF2	648339	8.0e+6L	5.5e+4L	0.227	1.19e–7H	1.72e–11H	4.7e–6	8.4e–6	0.139	3.86
24(a)	N-LaK22	651559	1.3e+7	9.0e+4	0.266	7.12e–8	1.03e–11	3.7e–6	6.6e–6	0.134	3.73
25(b)	N-BaF51	652450	1.3e+7	9.1e+4	0.262	7.06e–8	1.02e–11	4.7e–6	8.4e–6	0.120	3.33
26(b)	N-SSK5	658509	1.3e+7	8.8e+4	0.278	7.23e–8	1.05e–11	3.8e–6	6.8e–6	0.133	3.71
27(a)	N-BaSF2	664360	1.2e+7	8.4e+4	0.247	7.71e–8	1.12e–11	3.9e–6	7.1e–6	0.113	3.15
28(a)	SF5	673322	8.1e+6	5.6e+4	0.233	1.16e–7	1.69e–11	4.6e–6	8.2e–6	0.147	4.07
29(a)	N-SF5	673322	1.3e+7	8.7e+4	0.237	7.48e–8	1.08e–11	4.4e–6	7.9e–6	0.103	2.86
30(a)	N-SF8	689313	1.3e+7	8.8e+4	0.245	7.23e–8	1.07e–11	4.8e–6	8.6e–6	0.152	2.90

TABLE 3.2 (*Continued*)

Rank (and ref.)	Glass Name	Glass Code	Young's Modulus (E_G)		Poisson's Ratio	$K_G=(1-\nu_G^2)/E_G$		Thermal Exp. Coef. (α_G)		Density (ρ)	
			(lb/in.^{2})	(MPa)	(ν_G)	(in.^{2}/lb)	(1/Pa)	(1/°F)	(1/°C)	(lb/in.^{3})	(g/cm^3)
31(a)	SF15	699301	8.7e+6	6.0e+4	0.235	1.09e–7	1.57e–11	4.4e–6	7.9e–6	0.146	4.06
32(a)	N-SF15	699302	1.3e+7	9.0e+4	0.243	7.21e–8	1.04e–11	4.4e–6	8.0e–6	0.105	2.92
33(a)	SF1	717295	8.1e+6	5.6e+4	0.232	1.16e–7	1.69e–11	4.5e–6	8.1e–6	0.160	4.46
34(a)	N-SF1	717296	1.3e+7	9.0e+4	0.250	7.18e–8	1.04e–11	5.1e–6	9.1e–6	0.109	3.03
35(b)	N-LaF3	717480	1.4e+7H	9.6e+4H	0.286	6.66e–8	9.66e–12	4.2e–6	7.6e–6	0.149	4.14
36(a)	SF10	728284	9.3e+6	6.4e+4	0.232	1.02e–7	1.48e–12	4.2e–6	7.5e–6	0.154	4.28
37(a)	N-SF10	728285	1.3e+7	8.7e+4	0.252	7.42e–8	1.08e–11	5.2e–6	9.4e–6	0.110	3.05
38(b)	N-LaF2	744449	1.4e+7H	9.6e+4H	0.288H	6.73e–8	9.76e–12	4.5e–6	8.1e–6	0.155	4.30
39(b)	LaFN7	750350	1.2e+7	8.0e+4	0.280	7.94e–8	1.15e–11	2.9e–6	5.3e–6	0.157	4.38
40(b)	N-LaF7	749348	1.4e+7H	9.6e+4H	0.271	6.65e–8	9.65e–12	4.0e–6	7.3e–6	0.134	3.73
41{b)	SF4	755276	8.1e+6	5.6e+4	0.241	1.15e–7	1.68e–11	4.4e–6	8.0e–6	0.172	4.79
42(b)	N-SF4	755274	1.3e+7	9.0e+4	0.256	7.16e–8	1.04e–11	5.3e–6H	9.5e–6H	0.113	3.15
43(a)	SF14	762265	9.4e+6	6.5e+4	0.231	1.00e–7	1.45e–11	3.7e–6	6.6e–6	0.163	4.54
44(a)	SF11	785258	9.6e+6	6.6e+4	0.235	9.87e–8	1.43e–11	3.4e–6	6.1e–6	0.170	4.74
45(a)	SF56A	785261	8.3e+6	5.7e+4	0.239	1.14e–7	1.65e–11	4.4e–6	7.9e–6	0.177	4.92
46(a)	N-SF56	785261	1.3e+7	9.1e+4	0.255	7.08e–8	1.03e–11	4.8e–6	8.7e–6	0.118	3.28
47(a)	SF6	805254	8.0e+6L	5.5e+4L	0.244	1.18e–7	1.71e–11	4.5e–6	8.1e–6	0.186H	5.18H
48(a)	N-SF6	805254	1.3e+7	9.3e+4	0.262	6.90e–8	1.00e–11	5.0e–6	9.0e–6	0.121	3.37
49(a)	LaSFN9	850322	1.6e+7H	1.1e+5H	0.286	5.76e–8L	8.35e–12L	4.1e–6	7.4e–6	0.159	4.44
Ratio (high/low)			1.75		1.51	2.07		2.12		2.11	

Sources: Glass selection is from: (a) Walker, B.H., in *The Photonics Design and Applications Handbook*, Lauren Publishing, Pittsfield, H-356, 1993 and (b) Zhang, S. and Shannon, R.R., *Opt. Eng.*, 34, 3536, 1995. Data (except for K_G) is from Schott, *Schott Optical Glass Catalog* (CD Version 1.2, USA). Schott Glass Technologies, Inc., Duryea, Pennsylvania, 2001.

Note: "L" indicates extreme low value and "H" indicates extreme high value for this parameter in this group.

specified wavelength. According to Kimmel and Parks (1995), birefringence of components for various instrument applications should not exceed 2 nm/cm for polarimeters or interferometers, 5 nm/cm for precision applications such as photolithography optics and astronomical telescopes, 10 nm/cm for camera, visual telescope, and microscope objectives, and 20 nm/cm for eyepieces and viewfinders. Lower quality materials can be used in condenser lenses and most illumination systems. In all cases, the material's stress optic coefficient K_S determines the relationship between the applied stress and the resulting OPD:

$$\mathrm{OPD} = (n_{\parallel} - n_{\perp})t = K_s S t \tag{3.8}$$

where t is the light path length in the material in cm, K_S is expressed in mm^2/N, and S is the tensile or compressive stress in N/mm^2. Table 3.3 lists the values of K_S at a wavelength of 589.3 nm and a temperature of about 21°C for the glasses listed in Table 3.2. Note that the variability ratio of K_S within this group is relatively large at 5.58. All values are positive for the listed glasses. Some glasses, such as Schott SF58, SF66, and SF59 (not listed in Tables 3.2 or 3.3), have negative K_S values (-0.93×10^{-6}, -1.20×10^{-6}, and -1.36×10^{-6} mm^2/N, respectively). Another older, but still available Schott glass, SF57, has an extremely low K_S value of 0.02×10^{-6} mm^2/N. Use of the latter material in critical optical components might be appropriate if externally induced birefringence must be minimized. Figure 3.4 illustrates the relative insensitivity of the stress optic coefficient of some optical glasses to changes in wavelength throughout the visible range.

The excellent light transmission characteristics of optical glasses are prime reasons for their success in optical systems applications. Not all such materials are exactly equivalent in transmission throughout the UV to near-IR spectral regions. Figure 3.5 illustrates this point. The crowns generally tend to cut on at shorter wavelengths than the flints, whereas the latter types tend to transmit farther into the near-IR. In the green to red regions, all common optical glasses are approximately equal with regard to internal transmission. In the absence of antireflection (A/R) coatings, the higher index glasses suffer greater Fresnel losses. Simple A/R coatings such as a quarter-wave-thick MgF_2 film are more efficient with the flint-type glasses because of their higher refractive indices.

Special glasses offering enhanced transmission in the near-UV region between 200 and 350 nm include Schott Ultran 30, which transmits as indicated in Figure 3.6. Fused silica and a few crystals (discussed later in this chapter) also transmit well in this region.

It is well known that all standard optical glasses tend to lose transmission (i.e., to darken or "brown") when exposed to high levels of particle or photon radiation. Exposure to 10 gray (Gy)[†] is sufficient to cause perceptible transmission loss in most of these glasses. Figure 3.7 illustrates the change that occurs in standard BK7 glass when subjected to a γ radiation level of 10^4 Gy. This darkening tends to fade slightly over time as indicated by the curve labeled "fading." The time period involved here was 30 d. Although detectable, this fading does not restore the original transmission capability of the material.

It has been shown (Stroud, 1961, 1962, 1965; Stroud et al., 1965; Volf, 1984) that chemically stabilizing (doping) optical glasses with cerium in the form of CeO_2 inhibits darkening when the material is exposed to certain kinds of radiation. This doping process lowers the transmission of the material slightly throughout the transmission range and significantly in the near-UV region, but effectively reduces the darkening effect of radiation. Figure 3.8 (from Marker et al., 1991) shows this effect for 10 mm thicknesses of two types of Schott radiation-resistant glasses, BK7GI8 and BK7G25. The number added to the glass name is ten times the percentage content of CeO_2. Table 3.4 indicates the internal transmissions of 10 mm thicknesses of standard BK7 and BK7G25 before and after exposure to specified doses of proton, electron, neutron, and gamma radiation. The advantage of these radiation-resistant glasses under these conditions is apparent.

[†] The *gray* (Gy) is the SI unit for the absorbed radiation dose. It is defined as the radiation necessary to deposit 1 J of energy in 1 kg of tissue (Curry et al., 1990). It equals 100 rad (an earlier unit for dose).

TABLE 3.3
Stress Optic Coefficients K_S at 589.3 nm and 21°C for the Glasses Listed in Table 3.2

Rank	Glass Name	Stress Optic Coefficient (10^{-6} mm^2/N)	Rank	Glass Name	Stress Optic Coefficient (10^{-6} mm^2/N)
1	N-FK5	2.91	26	N-SSK5	1.90
2	K10	3.12	27	N-BaSF2	3.04
3	N-ZK7	3.63 H	28	SF5	2.28
4	K7	2.95	29	N-SF5	2.99
5	N-BK7	2.77	30	N-SF8	2.95
6	N-K5	3.03	31	SF15	2.20
7	N-LLF6	2.93	32	N-SF15	3.04
8	N-BaK2	2.60	33	SF1	1.80
9	LLF1	3.05	34	N-SF1	2.72
10	N-PSK3	2.48	35	N-LaF3	1.53
11	N-SK11	2.45	36	SF10	1.95
12	N-BaKl	2.62	37	N-SF10	2.92
13	N-BaLF4	3.01	38	N-LaF2	1.42
14	LF5	2.83	39	LaFN7	1.77
15	N-BaF3	2.73	40	N-LaF7	2.57
16	F5	2.92	41	SF4	1.36
17	N-BaF4	2.58	42	N-SF4	2.76
18	F4	2.84	43	SF14	1.62
19	N-SSK8	2.36	44	SF11	1.33
20	F2	2.81	45	SF56A	1.10
21	N-F2	3.03	46	N-SF56	2.87
22	N-SK16	1.90	47	SF6	0.65 L
23	SF2	2.62	48	N-SF6	2.82
24	N-LaK22	1.82	49	LaSFN9	1.76
25	N-BaF51	2.22			

Ratio (high/low) = 5.58

Note: “L” indicates extreme low value and “H” indicates extreme high value in this group.

In the recent past, manufacturers such as Schott have offered many types of radiation-resistant optical glasses. Some are frequently made while others can be manufactured upon request for special applications. Figure 3.9 shows 31 types made by Schott arranged in the form of a “radiation-resistant glass map.” Figure 3.10 is a data sheet for one of these glasses (BK7G25). This may be compared with Figure 3.3, which provides similar information for the currently produced undoped version of that glass (N-BK7). The mechanical properties of the doped glass are virtually the same as the standard version.

Not all radiation-resistant glasses behave the same when exposed to different types of radiation because of their differing inherent chemical compositions. Marker et al. (1991) indicated that LF5GI5 glass transmits relatively well after exposure to γ radiation, but poorly after exposure to electrons. Another glass, Schott SF6G05, transmits poorly after exposure to γ radiation, but its transmission holds up well after exposure to electrons. The differences are attributed to the manner in which lead is constrained within one material and not constrained in the other.

Another concern in some applications of optical glasses is the effect of exposure to intense UV radiation. This effect is sometimes called *solarization*. Setta et al. (1988) and Marker et al. (1991) discussed the effects of UV exposure on various types of standard and CeO_2-doped glasses. Some of the latter have inferior transmission characteristics compared with the undoped versions of the same materials after UV exposure. Liepmann et al. (1988) discussed the variations in UV cut-on

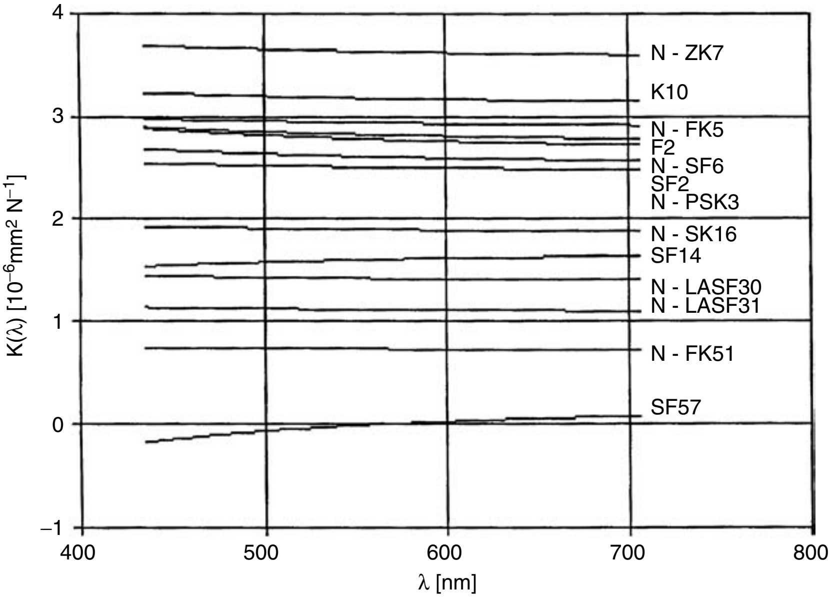

FIGURE 3.4 Variation of stress optical coefficient K_S for several glasses as a function of wavelength. (From Schott, *Schott Optical Glass Catalog*, (CD Version 1.2, USA). Schott Technologies, Inc., Duryea, Pennsylvania, 2001. With permission.)

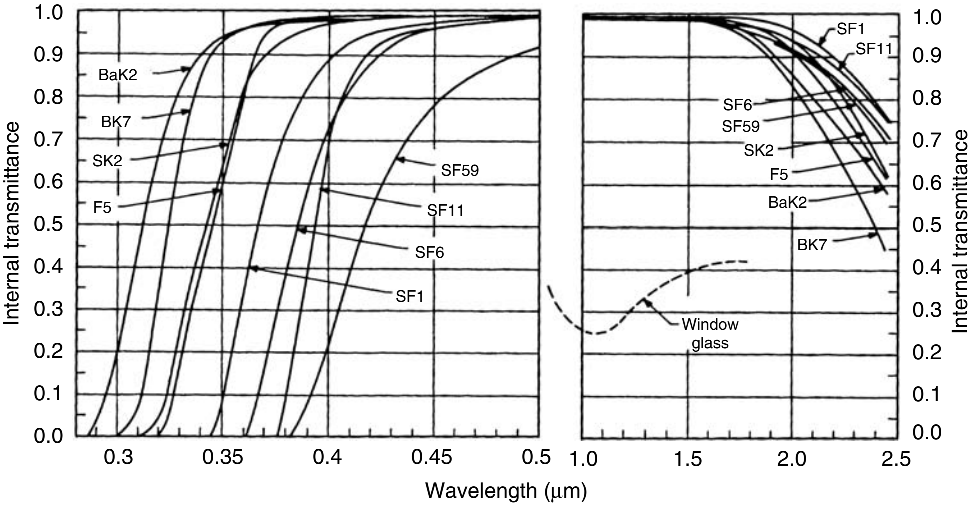

FIGURE 3.5 Internal transmittances of several representative optical glasses and of common window glass, all for thicknesses of 25 mm. (From Smith, W.J., *Modern Optical Engineering*, 3rd ed., McGraw-Hill, New York, 2000. With permission.)

performance of a fluor crown glass (UVFK54) and of a heavy metal fluoride glass (ZBLAN) when exposed to both broadband UV and excimer laser radiation at 248 nm wavelength.

3.2.3 OPTICAL PLASTICS

Certain plastics are utilized for some types of refracting optics because of the low cost of their raw material, ease of fabrication by molding, lightness of weight, resistance to mechanical shock, and

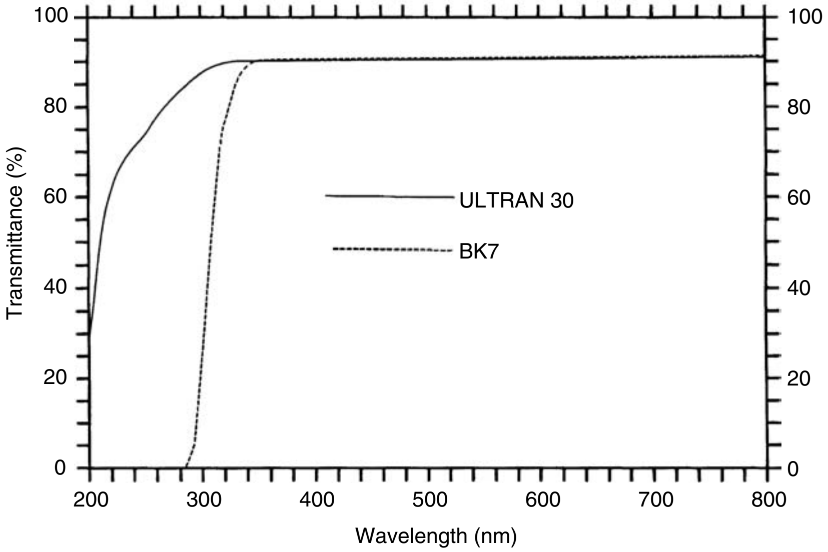

FIGURE 3.6 Transmittances in the near-UV and visible regions of 5 mm (0.197 in.) thick samples of Schott Ultran 30 glass as compared with that of Schott BK7 glass. (From Schott, *Product Information, No. 2105/90, ULTRAN 30-548743, UV Transmitting Glass*, Schott Glass Technologies, Inc., Duryea, Pennsylvania, 1990b. With permission.)

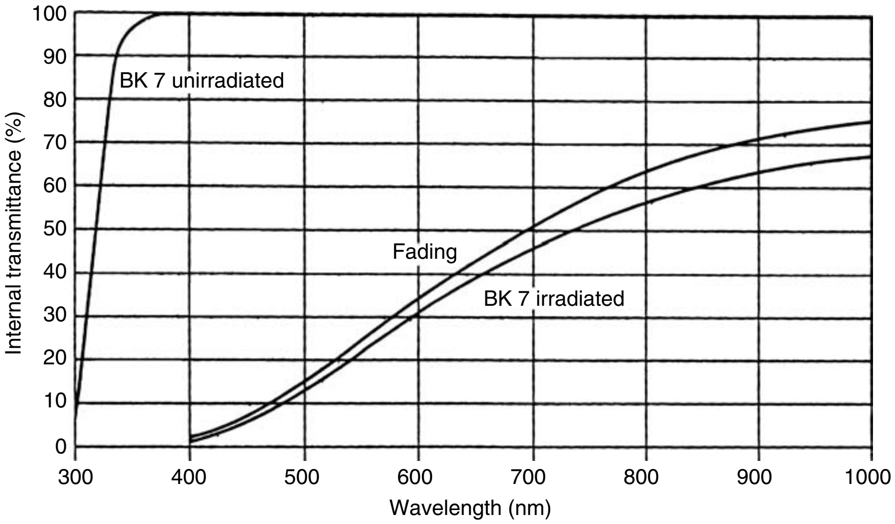

FIGURE 3.7 Internal transmittances of unirradiated 10 mm (0.394 in.) thick samples of standard BK7 glass vs. wavelength before and after exposure to 10^4 Gy (10^6 rad) doses of gamma radiation from a Co60 source. Curve marked "fading" depicts the partial recovery after 30 d. (From Schott, *Technical Information, No. 10017e, Radiation Resistant Glasses*, Schott Glass Technologies, Inc., Duryea, Pennsylvania, 1990a. With permission.)

ease of providing nonspherical surfaces and integral mounting features. On the negative side, we note their low abrasion resistance, d*n*/d*T* and CTE much larger than those of glass, low softening temperature (perhaps as low as 60°C), difficulty in coating, high cost of molding, tooling, hygroscopic tendency, possible birefringence due to stresses from the molding process, and surface and internal scattering greater than those of glass (see Tanaka and Miyamae, 1990; Lytle, 1995; and Pfeffer, 2005). These factors limit the usefulness of plastics in optics to lower precision applications such as

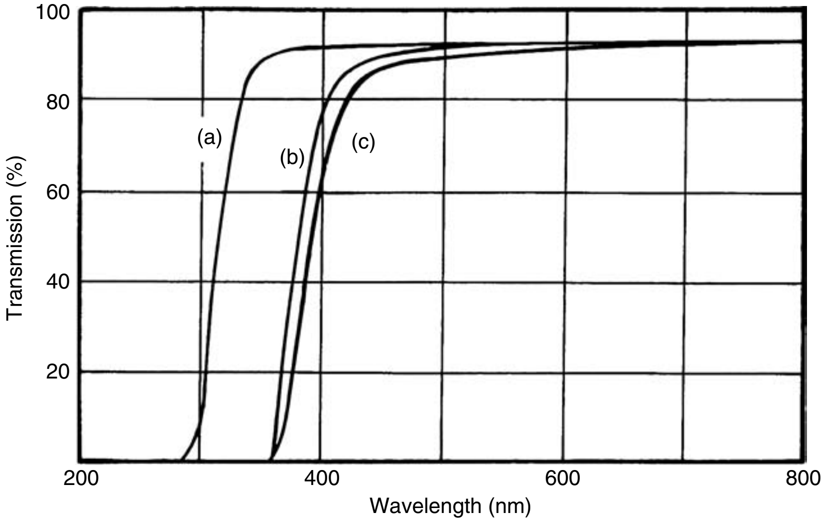

FIGURE 3.8 Internal transmittances of 10 mm (0.394 in.) thick samples of (a) standard BK7 glass, (b) BK7G18 protected glass, (c) BK7G25 protected glass as functions of wavelength, particularly in the near-UV region. (From Marker, A.J., III, Hayden, J.S., and Speit, B., Radiation resistant optical glasses, *Proc. SPIE*, 1485, 55, 1991. With permission.)

TABLE 3.4

Spectral Variations of Internal Transmission of 10 mm Thicknesses of Un-irradiated Standard BK7 and BK7G25 Glasses After Irradiation With Electrons, Protons, Neutrons, and γ Radiation. Exposures are as Indicated by Notes.

Wave Length (nm)	Standard BK7 w/o Radiation	Transmission of: BK7G25 w/o Radiation	BK7G25 w/ Electrons[a]	BK7G25 w/ Protons[b]	BK7G25 w/ Neutrons[c]	BK7G25 w/ γ[d]	BK7G25 w/ γ[e]	BK7G25 w/ γ[f]
400	0.991	0.68	0.56	0.59	0.14	0.66	0.63	0.75
450	0.994	0.93	0.84	0.89	0.65	0.93	0.93	0.90
500	0.996	0.95	0.87	0.93	0.75	0.95	0.94	0.93
550	0.996	0.97	0.90	0.95	0.95	0.97	0.96	0.95
600	0.997	0.97	0.91	0.96	0.85	0.97	0.97	0.96
650	0.997	0.98	0.92	0.98	0.98	0.98	0.98	0.97
700	0.998	0.99	0.93	0.99	0.90	0.99	0.99	0.98

[a] Electrons: fluence = 8.8×10^{21} e$^-$/m^2; energy = 0.05 MeV; irradiation time = 20.6 h.

[b] Protons: energy = 7 to 50 MeV; dose = 1.4×10^{18} MeV/m^2· sec.

[c] Neutrons: fluence < 0.15×10^{21} N/m^2.

[d] γ radiation: 10^4 Gy (10^6 rad).

[e] γ radiation: 10^5 Gy (10^7 rad).

[f] γ radiation: 10^6 Gy (10^8 rad).

Source: Adapted from Schott, *Technical Information, No. 10017e, Radiation Resistant Glasses*, Schott Glass Technologies, Inc., Duryea, Pennsylvania, 2001.

inexpensive cameras, telescopes, and binoculars; some simple military devices such as nonimage-forming prismatic periscopes (sometimes called *vision blocks*); eyeglasses, contact lenses, and intraocular lenses; devices in which optical, electrical, and mechanical functions must be combined

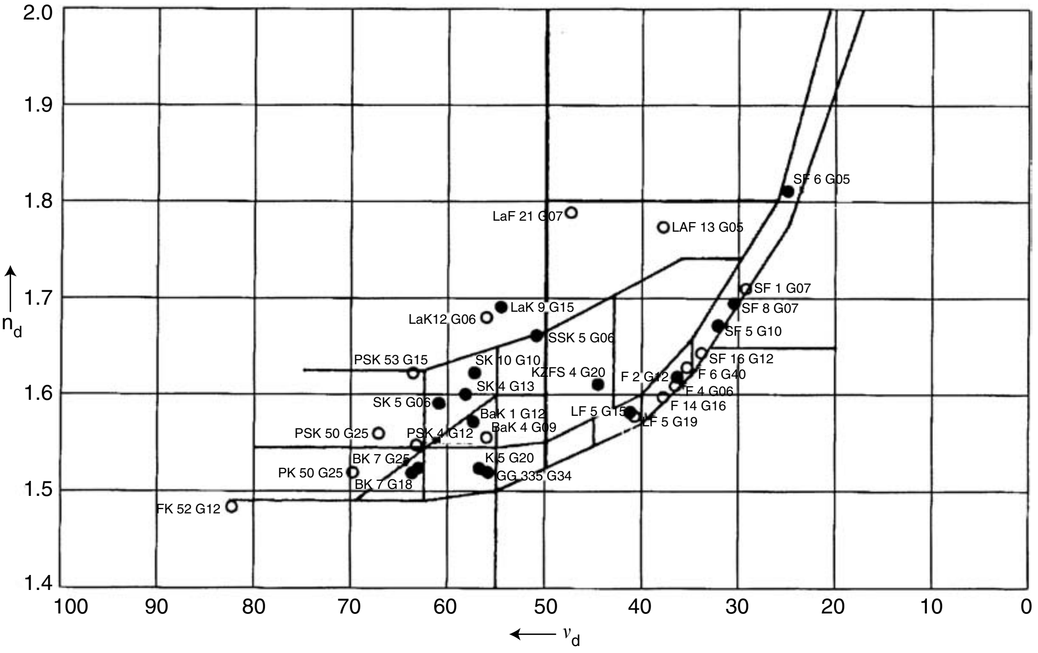

FIGURE 3.9 The "radiation-resistant optical glass map" showing CeO_2-protected glasses available in stock and by special order as of 1990. The types currently available may differ. (From Schott, *Technical Information, No. 10017e, Radiation Resistant Glasses*, Schott Glass Technologies, Inc., Duryea, Pennsylvania, 1990a. With permission.)

in a single part for packaging and cost reasons (Lytle, 1995), in miniature lenses and microlens arrays used for fiber optic coupling, in wavefront sensors, and in data storage (Milster, 1995), and in single use (Pfeffer, 2005, Bäumer, 2005).

The number of available types of optical plastics (polymers) is severely restricted. Figure 3.11 is the plastics equivalent of the glass map discussed above and shows materials most commonly used in optics. The few plastics that have been characterized sufficiently for meaningful optical applications lie outside and below the regions containing the optical glasses as designated in the figure by the traditional Schott glass type designations along the FK-to-SF boundary line. Lytle (1995) gave index values to three or four decimal places for polymethylmethacrylate (492574),[‡] polystyrene (590309), polycarbonate (585299), copolymer styrene–acrylonitrile (SAN) (567348), polyetherimide (660183), and polycyclohexylmethacrylate (505561). These data are not guaranteed since the materials may change properties during the heating/curing cycle inherent in the manufacturing process and since refractive properties depend significantly upon often unidentified additives used to facilitate that process. Since no high-index optical plastic varieties exist at this time, the curvatures of lenses made of these materials are generally stronger than those of their glass counterparts. Thicknesses thus tend to be greater for a given focal length.

Typical transmission vs. wavelength curves for two types of polymethylmethacrylate, polystyrene, and polycarbonate for the spectral region 0.2 to 2.2 μm are given in Figure 3.12. With a few exceptions, transmission of optical plastic as a class is low in the near-UV and near-IR regions. Absorption bands around 1150 nm and 1350 nm are characteristic of the carbon-based material structures.

From the mechanical viewpoint, plastic materials offer some advantages over glass materials. The abilities to mold surfaces of practically any contour (including aspherics) and to provide integral

---

[‡] Numbers in parenthesis are international glass codes comprising $(n_d - 1)$ plus 10 times ν_d.

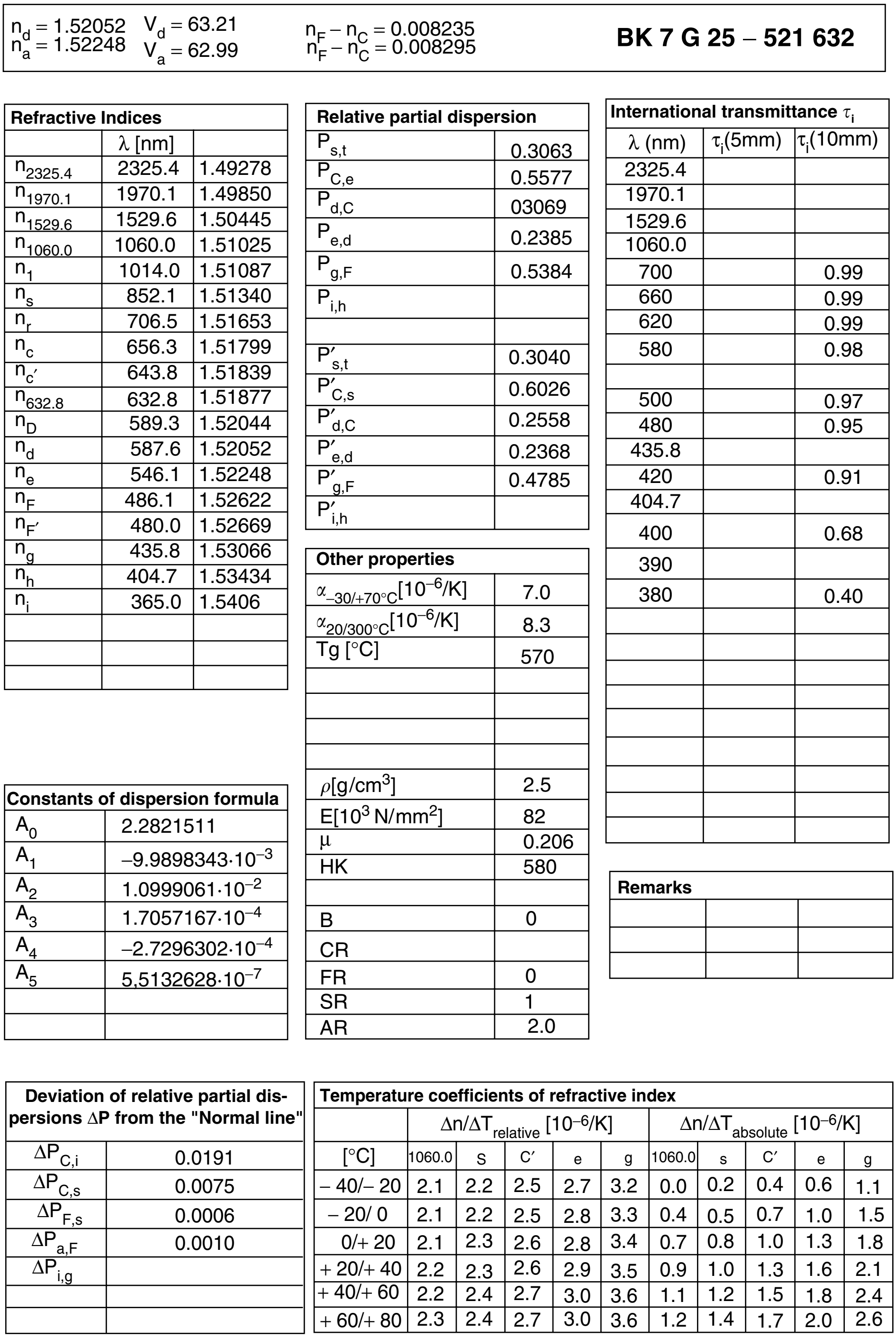

$n_d = 1.52052$ $V_d = 63.21$ $n_F - n_C = 0.008235$
$n_a = 1.52248$ $V_a = 62.99$ $n_F - n_C = 0.008295$

BK 7 G 25 – 521 632

Refractive Indices		
	λ [nm]	
$n_{2325.4}$	2325.4	1.49278
$n_{1970.1}$	1970.1	1.49850
$n_{1529.6}$	1529.6	1.50445
$n_{1060.0}$	1060.0	1.51025
n_1	1014.0	1.51087
n_s	852.1	1.51340
n_r	706.5	1.51653
n_c	656.3	1.51799
$n_{c'}$	643.8	1.51839
$n_{632.8}$	632.8	1.51877
n_D	589.3	1.52044
n_d	587.6	1.52052
n_e	546.1	1.52248
n_F	486.1	1.52622
$n_{F'}$	480.0	1.52669
n_g	435.8	1.53066
n_h	404.7	1.53434
n_i	365.0	1.5406

Relative partial dispersion	
$P_{s,t}$	0.3063
$P_{C,e}$	0.5577
$P_{d,C}$	03069
$P_{e,d}$	0.2385
$P_{g,F}$	0.5384
$P_{i,h}$	
$P'_{s,t}$	0.3040
$P'_{C,s}$	0.6026
$P'_{d,C}$	0.2558
$P'_{e,d}$	0.2368
$P'_{g,F}$	0.4785
$P'_{i,h}$	

Other properties	
$\alpha_{-30/+70°C}[10^{-6}/K]$	7.0
$\alpha_{20/300°C}[10^{-6}/K]$	8.3
Tg [°C]	570
$\rho[g/cm^3]$	2.5
$E[10^3\ N/mm^2]$	82
μ	0.206
HK	580
B	0
CR	
FR	0
SR	1
AR	2.0

International transmittance τ_i		
λ (nm)	τ_i(5mm)	τ_i(10mm)
2325.4		
1970.1		
1529.6		
1060.0		
700		0.99
660		0.99
620		0.99
580		0.98
500		0.97
480		0.95
435.8		
420		0.91
404.7		
400		0.68
390		
380		0.40

Remarks		

Constants of dispersion formula	
A_0	2.2821511
A_1	$-9.9898343 \cdot 10^{-3}$
A_2	$1.0999061 \cdot 10^{-2}$
A_3	$1.7057167 \cdot 10^{-4}$
A_4	$-2.7296302 \cdot 10^{-4}$
A_5	$5,5132628 \cdot 10^{-7}$

Deviation of relative partial dispersions ΔP from the "Normal line"	
$\Delta P_{C,i}$	0.0191
$\Delta P_{C,s}$	0.0075
$\Delta P_{F,s}$	0.0006
$\Delta P_{a,F}$	0.0010
$\Delta P_{i,g}$	

Temperature coefficients of refractive index										
	$\Delta n/\Delta T_{relative}$ $[10^{-6}/K]$					$\Delta n/\Delta T_{absolute}$ $[10^{-6}/K]$				
[°C]	1060.0	s	C′	e	g	1060.0	s	C′	e	g
– 40/– 20	2.1	2.2	2.5	2.7	3.2	0.0	0.2	0.4	0.6	1.1
– 20/ 0	2.1	2.2	2.5	2.8	3.3	0.4	0.5	0.7	1.0	1.5
0/+ 20	2.1	2.3	2.6	2.8	3.4	0.7	0.8	1.0	1.3	1.8
+ 20/+ 40	2.2	2.3	2.6	2.9	3.5	0.9	1.0	1.3	1.6	2.1
+ 40/+ 60	2.2	2.4	2.7	3.0	3.6	1.1	1.2	1.5	1.8	2.4
+ 60/+ 80	2.3	2.4	2.7	3.0	3.6	1.2	1.4	1.7	2.0	2.6

FIGURE 3.10 Data sheet for Schott BK7G25 radiation-protected glass. (From Schott, *Technical Information, No. 10017e, Radiation Resistant Glasses*, Schott Glass Technologies, Inc., Duryea, Pennsylvania, 1990a. With permission.)

mounting means are prime examples. Examples of mountings for plastic lenses are discussed in Chapter 4. Shrinkage (typically on the order of 0.2 to 0.6%) can often be compensated for in mold

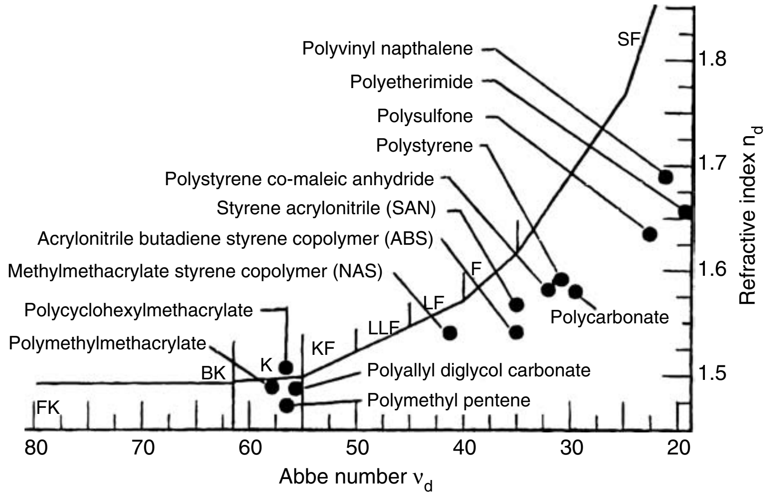

FIGURE 3.11 The "optical polymer map" showing varieties used for plastic optics referenced to adjacent optical glass types. (Adapted from Lytle, J.D., in *OSA Handbook of Optics*, 2nd ed. Vol. II, Bass, M., Vanstryland, E., Williams, D.R., and Wolfe, W.L., Eds., McGraw-Hill, Inc., New York, 1995, chap. 34.)

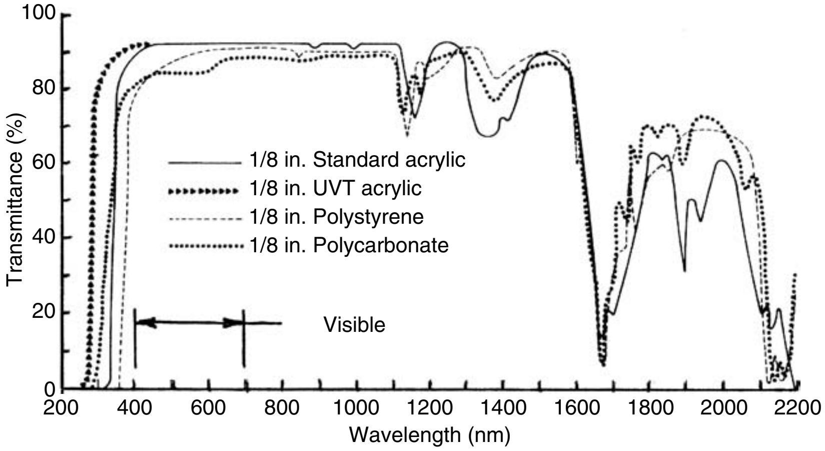

FIGURE 3.12 Curves of transmittance vs. wavelength for four commonly used optical polymers. (Adapted from Welham, B., in *Applied Optics and Optical Engineering*, Shanon, R.R. and Wyant, J.C., Eds. Vol. VII, Academic Press, New York, 1979, chap. 3. With permission.)

design. Musikant (1985) reported that focal lengths of lenses made in multicavity molds can be held to 2%, whereas those made in single-cavity molds can be held to 1%. Further, he stated that the surface figures of flats and some spherical optics can be held to 5 fringes (2.5 waves), whereas aspherics can be controlled to about 10 fringes (5 waves). Wolpert (1989) provided general tolerances for injection-molded lenses (see Table 3.5). Lytle (1995) and Pfeffer (2005) both indicated that some of these parameters can be held more precisely because of improvements in mold-making techniques and a better understanding of shrinkage effects.

Welham (1979), U.S. Precision Lens, Inc. (1983), and Pfeffer (2005) discussed the optical, mechanical, chemical, and fabrication properties of selected plastics. Table 3.6 lists optical and mechanical characteristics of six commonly used materials. All those data should be considered

TABLE 3.5
Common Tolerances for Injection-Molded Plastic Lenses

	Low Cost	Commercial	Precision
Focal length	±3% to 5%	±2% to 3%	±0.5% to 1%
Radius of curvature	±3% to 5%	±2% to 3%	±0.8% to 1.5%
Figure			
Spherical power	6 to 10 fr.[a]	5 to 2 fr.	1 to 0.5 fr.
Irregularity (per 10 mm)	4 to 2.4 fr.	2.4 to 0.8 fr.	1.2 to 0.8 fr.
Surface quality (scratch/dig)	80/50	60/40	40/20
Centration (min)	±3	±2	±1
Vertex thickness (in.)	±0.004	±0.002	±0.0006
Diameter (in.)	±0.004	±0.002	±0.0006
Repeatability tolerances, lens-to-lens (%)	1 to 2	0.5 to 1	0.3 to 0.5
Vertex-to-edge thickness ratio		Ability to mold	
5:1		Difficult	
3:1		Moderate	
2:1		Easy	

[a] Fringes of visible light

Sources: Adapted from Wolpert, H.D., *The Photonics Design and Applications Handbook*, Lauren Publishing, Pittsfield, H-321, 1989; Milster, T.D., in *OSA Handbook of Optics*, 2nd ed., Vol. II, Bass, M., Van Stryland, E., Williams, D.R., and Wolfe, W.L., Eds., McGraw-Hill, New York, 1995, chap. 7; and Pfeffer, M., in *Handbook of Plastic Optics*, Baumer, S.M.B., Ed., Wiley Interscience, New York, 2005, chap. 7.

approximations. Lytle (1995) listed a few physical properties of additional plastic materials. Pfeffer (2005) pointed out that water absorption of optical plastics causes dimensional changes and affects refractive index.

Most of the authors cited in this section as contributors to the field of plastic optics have stressed the need for more detailed and more reliable information from the material manufacturers regarding their products and greater control over the properties important for use in opto-mechanical design. Since only an extremely small fraction of the millions of pounds of plastics produced each year end up in optics, the motivation for increased variety and better optical properties is relatively small.

Some applications of plastics in lenses and their mounts are considered in Sections 4.9 and 5.7.

3.2.4 OPTICAL CRYSTALS

Synthetic crystalline materials are often used instead of natural minerals (such as rock salt [NaCl], fluorite [CaF_2], sylvite [KCl], and quartz [SiO_2]) in optical applications. Applications are primarily in the UV and IR spectral regions where optical glasses do not transmit (see Figure 3.13). Optical crystals are grouped under the following four general categories: alkali and alkaline earth halides, glasses and other oxides, semiconductors, and calcogenides.

The following sections provide brief descriptions and tables of key opto-mechanical characteristics of each of these groups of materials. For more detailed information, the reader should consult references such as the *American Institute of Physics Handbook* (Gray, 1972), the *Infrared Handbook* (Wolfe and Zissis, 1978), the *OSA Handbook of Optics* (1995), Wolfe (1978), Parker (1979), Musikant (1985), Taylor and Goela (1986), Savage (1990), Browder et al. (1991), Harris (1999), and the data sheets and catalogs offered by various manufacturers. Wolfe (1990) summarized the available data on

TABLE 3.6
Opto-Mechanical Properties of Commonly Used Optical Plastics

Properties[a]	**ASTM Test Method**	**Methyl methacrylate (Acrylic)**	**Poly-styrene**	**Poly-carbonate**	**Methyl methacrylate styrene co-polymer (NAS)**	**Styrene acryloni-trile (SAN)**	**Allyl diglycol carbonate (CR39)**
Refractive index n_D	D542	1.492	1.590	1.585	1.564	1.567	1.504
Abbe value ν_D	D542	57.4	30.9	29.9	34.8	38	56
dn/dT($\times 10^{-5}$)	(°C)$^{-1}$	−8.5	−12.0	−14.3	−14.0		−14.3
Haze	D1003 (%)	< 2	< 3	< 3	< 3	3	3
Deflection temperature $\times 10^{-5}$ (°F)$^{-1}$	D648-56						
3.6°F/min., 264 psi		198	180	280		99–104	—
3.6°F/min., 66 psi		214	230	270	212	100	
CTE $\times 10^{-5}$ (°C)$^{-1}$	D696-44	6.0	6.4–6.7	6.7	5.6	6.4	6.3 at 25–75°C
Young's modulus (Gpa)		3	2.89	2.4	2.34	3.3	3
Recommended maximum continuous service temperature (°C)		85	80	120	85	75	100
Water absorption (immersed 24 h at 73°F) (%)	D570-63	0.3	0.03	0.2–0.3	0.15	0.28	
Density (ρ)	D792	1.18	1.05	1.25	1.13	1.07	1.32
Mohs scale hardness (0.25 in. sample)	D785-62	M97	M90	M70	M75		
Thermal conductivity (k) (cal/sec · cm ·°C)		4–6	2.4–3.3	4.75	4.5	2.8	4.9

[a] Material formulation and characteristics data should be confirmed prior to design and specification.

Sources: Adapted from U.S. Precision Lens, Inc., *The Handbook of Plastic Optics*, 2nd ed., Cincinnati, Ohio, 1983; Wolpert, H.D., *The Photonics Design and Applications Handbook*, Lauren Publishing, Pittsfield, H-321, 1989., Lytle, J.D., in *OSA Handbook of Optics*, 2nd ed., Vol. II, Bass, M., Van Stryland, E., Williams, D.R., and Wolfe, W.L., Eds., McGraw-Hill, New York, 1995, chap. 34; and Pfeffer, M., in *Handbook of Plastic Optics*, Baumer, S.M.B., Ed., Wiley Interscience, New York, 2005, chap. 2.

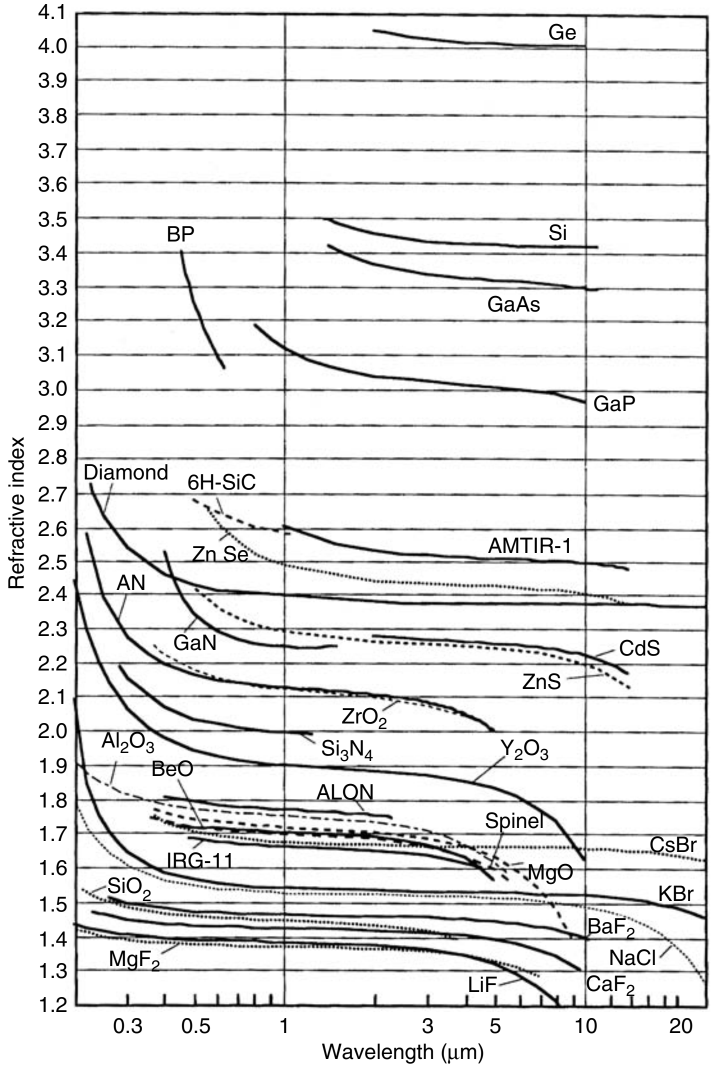

FIGURE 3.13 Refractive index variation with wavelength for several optical materials that transmit in the IR as well as in the visible region. (From Harris, D.C., *Materials for Infrared Windows and Domes*, SPIE Press, Bellingham, 1999. With permission.)

the key properties of a variety of IR-transmitting materials and commented on the reliability of much of that data. Hoffman and Wolfe (1991) reported measured refractive indices for three commonly used IR-transmitting materials (ZnSe, Ge, and Si) at a 10.6 μm wavelength over the extended temperature range of 20 to 300 K. The rates of change of index through this range were also reported for these materials and the random and systematic errors of the experimental and curve-fitting methods analyzed.

3.2.4.1 Alkali and Alkaline Earth Halides

These crystals are readily available, have reasonably good transmission, and are relatively inexpensive. They are used in applications where relatively poor mechanical and thermal characteristics can be tolerated (see Table 3.7). Manufacturing techniques for the alkali halides (KBr, KCl, LiF, NaCl, and

TABLE 3.7
Opto-Mechanical Properties of Selected Alkali Halides and Alkaline Earth Halides

Material Name (Symbol)	Refractive Index n at λ (μm)	dn/dT at λ (μm) ($\times 10^{-6}$/°C)	CTE α ($\times 10^{-6}$/°C)	Young's Modulus E ($\times 10^{10}$ Pa)	Poisson's Ratio ν	Density ρ (g/cm^3)	Knoop Hardness (kg/mm^2)	$K_G = (1-\nu_G^2)/E_G \times 10^{-11}$ (Pa^{-1})
Barium fluoride (BaF_2)	1.463 at 0.63	−16.0 at 0.6	6.7 at 75 K	5.32	0.343	4.89	82	1.659
	1.458 at 3.8	−15.9 at 3.4	18.4 at 300 K			(500 g load)		
	1.449 at 5.3							
	1.396 at 10.6	−14.5 at 10.6						
Calcium fluoride (CaF_2)	1.431 at 0.7	−10.4 at 0.66	18.9 at 300 K	9.6	0.29	3.18	160–178	0.954
	1.420 at 2.7							
	1.411 at 3.8	−8.1 at 3.4						
	1.395 at 5.3							
Potassium bromide (KBr)	1.555 at 0.6		25.0 at 75 K	2.69	0.203	2.75	7	3.564
	1.537 at 2.7	−41.9 at 1.15				(200 g load)		
	1.529 at 8.7	−41.1 at 10.6						
	1.515 at 14							
Potassium chloride (KC1)	1.474 at 2.7	−36.2 at 1.15	36.5	2.97	0.216	1.98	7.2	3.210
	1.472 at 3.8					(200 g load)		
	1.469 at 5.3							
	1.454 at 10.6	−34.8 at 10.6						
Lithium fluoride (LiF)	1.394 at 0.5	−16.0 at 0.46	5.5 at 77 K	6.48	0.225	2.63	102–113	1.465
	1.367 at 3.0	−16.9 at 1.15	~37 at 20°C			(600 g load)		
	1.327 at 5.0	−14.5 at 3.39						

TABLE 3.7 (*Continued*)
Opto-Mechanical Properties of Selected Alkali Halides and Alkaline Earth Halides

Material Name (Symbol)	Refractive Index n at λ (μm)	dn/dT at λ (μm) (× 10^{-6}/°C)	CTE α (× 10^{-6}/°C)	Young's Modulus E (× 10^{10} Pa)	Poisson's Ratio ν	Density ρ (g/cm³)	Knoop Hardness (kg/mm²)	$K_G = (1-\nu_G^2)/E_G \times 10^{-11}$ (Pa⁻¹)
Magnesium	1.384 at 0.46o[a]		14.0 (‖) 8.9(⊥)	16.9	0.269	3.18	415	0.549
fluoride	1.356 at 3.8o	+0.88 at 1.15	–					
(MgF_2)	1.333 at 5.3o	+1.19 at 3.39						
Sodium	1.525 at 2.7	−36.3 at 0.39	39.6	4.01	0.28	2.16	15.2	2.298
chloride	1.522 at 3.8					(200 g load)		
(NaCl)	1.517 at 5.3							
Thallium	2.602 at 0.6	−254 at 0.6	58	1.58	0.369	7.37	40.2	5.467
bromo-	2.446 at 1.0	−240 at 1.1				(200 g load)		
iodide	2.369 at 10.6	−233 at 10.6						
(KRS5)	2.289 at 30	−152 at 40						

[a] Birefringent material, o = ordinary axis.

Source: Adapted from Yoder, P.R., Jr., *Mounting Optics in Optical Instruments*, SPIE Press, Bellingham, 2002.

KRS5) and the alkaline earth halides (BaF_2, CaF_2, MgF_2, Irtran 1, and Irtran 3) were summarized and numerous literature references cited by Savage (1990). Higher-quality, low-loss, scatter-free crystals of some materials (notably CaF_2) have been made by reactive atmosphere processing (Miles, 1976 and Savage, 1990). Efforts to make CaF_2 characterized by extremely high standards of homogeneity, freedom from impurities, and extremely low birefringence have evolved recently in order to improve its usability in advanced state-of-the-art optical lithography applications in the UV spectral region at 193 and 157 nm and shorter wavelengths. See McCay et al. (2001). Wang (2002) briefly described a new technique using a photoelastic modulator as an alternative to the traditional crossed-polarizer method to measure birefringence in materials such as CaF_2 at high speed and high accuracy.

Hot forging of melt-grown crystals has been found to increase the fracture resistance of some alkaline halides. Anderson et al. (1981) reported success in replicating KBr lenses by hot isostatic pressing (HIP) a water-polished monocrystal substrate into an optically figured Pyrex die to form an objective for a thermal imager.

The two, hot-pressed, polycrystalline materials (Irtran 1 [MgF_2] and Irtran 3 [CaF_2]) included in this category were among six types of such materials developed by Eastman Kodak Co., Rochester, NY, in the 1960s for use in low-power IR windows, lenses, and domes that could tolerate scatter from particulates. Wolfe and Zissis (1978) provided transmittance curves for these materials at room temperature. Of particular concern for many applications were the density and scatter variations in curved substrates due to uniaxial pressing during manufacture (Savage, 1990). These materials are no longer manufactured, but some pieces and components may still exist.

3.2.4.2 Glasses and Other Oxides

The long-wavelength transmission cutoff of amorphous optical glasses containing silicon is typically about 3.7 μm. To reach farther into the IR region, it is customary to replace the silicon with higher atomic weight molecules. Key materials of this type are listed in Table 3.8. Included are some oxides and oxynitrides that are good candidates for the optics to be used in severe environments.

Quartz in its natural or artificially grown form is birefringent, so its uses are somewhat limited. Two forms of amorphous fused silica, also called vitreous silica (Laufer, 1965), are made from the natural material by direct fusion of quartz crystals and flame fusion of powdered quartz. The latter process is sometimes called the Heraeus process. The material produced by the first of these processes has the lower UV transmittance since metallic impurities of the natural material are present. It has the higher IR transmittance because it contains the least water, which absorbs heavily at about 3 mm. In the second type, many natural impurities are removed but the water absorption is significant.

A synthetic fused silica is commonly made by vapor-phase hydrolysis of an organosilicon product such as $SiCl_4$. It has high purity and hence high UV transmittance. Varieties with normal and reduced water absorption characteristics are available. Figure 3.14 compares the short- and long-wavelength transmittances of these forms of fused silica. When compared with optical glasses, synthetic fused silica shows superior resistance to discoloration due to x-ray, UV, and γ radiation, as well as to neutron, proton, and electron bombardment. Table 3.9 lists the qualitative changes observed in two types of synthetic fused silica manufactured by Heraeus Amersil, Inc. Fairfield, NJ, after exposure to specified radiation doses. One of these materials, T19 Suprasil 1, was selected for use in the laser ranging retroreflectors placed on the moon during an Apollo mission partly because of its inherent resistance to radiation. The radiation sensitivities of synthetic fused silica materials are significantly reduced at elevated temperatures.

3.2.4.3 Semiconductors

The semiconductor materials useful in IR-transmitting optics (see Table 3.10) have high refractive indices and reasonably good thermal and mechanical properties. Transmission is generally lower than the IR crystals and glasses of Tables 3.7 and 3.8, especially after short exposures to elevated

TABLE 3.8
Opto-Mechanical Properties of Selected IR-Transmitting Glass and Other Oxides

Material Name (Symbol)	Refractive Index n at λ (μm)	dn/dT at λ (μm) ($\times 10^{-6}$/°C)	CTE α ($\times 10^{-6}$/°C)	Young's Modulus E ($\times 10^{10}$ Pa)	Poisson's Ratio ν	Density ρ (g/cm^3)	Knoop Hardness (kg/mm^2)	$K_G = (1-\nu_G^2)/E_G \times 10^{-11}$ (Pa^{-1})
Aluminum oxynitride (ALON)	1.793 at 0.6 1.66 at 4.0		5.8	32.2	0.24	3.71	1970	0.293
Calcium alumino–silicate (Schott IRG11)	1.684 at 0.55 1.635 at 3.3 1.608 at 4.6		8.2 at 293–573 K	10.8	0.284	3.12	608	0.851
Calcium alumino–silicate (Corning 9753)	1.61 at 0.5 1.57 at 2.5		6.0 at 293–573 K	9.86	0.28	2.798 (500 g load)	600	0.935
Calcium alumino–silicate (Schott IRGN6)	1.592 at 0.55 1.562 at 2.3 1.521 at 4.3		6.3 at 293–573 K	10.8	0.284	3.12	608	0.851
Fluoride glass (Ohara HTF1)	1.51 at 1.0 1.49 at 3.0	−8.19	16.1	6.42	0.28	3.88	311	1.436
Fluoro-phosphate glass (Schott IRG9)	1.488 at 0.55 1.469 at 2.3 1.458 at 3.3		16.1 at 293–573 K	7.7	0.288	3.63	346 (200 g load)	1.191
Germanate (Corning 9754)	1.67 at 0.5 1.63 at 2.5 1.61 at 4.0		6.2 at 293–573 K	8.41	0.290	3.581	560 (100 g load)	1.089
Germanate (Schott IRG2)	1.899 at 0.55 1.841 at 2.3		8.8 at 293–573 K	9.59	0.282	5.00	481 (200 g load)	0.960

TABLE 3.8 (*Continued*)

Material Name (Symbol)	Refractive Index n at λ (μm)	dn/dT at λ (μm) ($\times 10^{-6}$/°C)	CTE α ($\times 10^{-6}$/°C)	Young's Modulus E ($\times 10^{10}$ Pa)	Poisson's Ratio ν	Density ρ (g/cm^3)	Knoop Hardness (kg/mm^2)	$K_G = (1-\nu_G^2)/E_G \times 10^{-11}$ (Pa^{-1})
Lanthanum dense flint (Schott IRG3)	1.851 at 0.55 1.796 at 2.3 1.776 at 3.3		8.1 at 293–573 K	9.99	0.287	4.47	541 (200 g load)	0.918
Lead silicate (Schott IRG7)	1.573 at 0.55 1.534 at 2.3		9.6 at 293–573 K	5.97	0.216	3.06	379	1.597
Sapphire[a] (Al_2O_3)	1.684 at 3.8 1.586 at 5.8	13.7	5.6 (‖) 5.0(⊥) –	40.0	0.27	3.97	1370 (1000 g load)	0.232
Fused silica (Corning 7940)	1.561 at 0.19 1.460 at 0.55 1.433 at 2.3 1.412 at 3.3	10–11.2 at 0.5–2.5	0.6 at 73 K 0.58 at 273–473 K	7.3	0.17	2.202 (200 g load)	500	1.333

Notes: [a] Birefringent material.

Source: Adapted from Yoder, P.R., Jr., *Mounting Optics in Optical Instruments*, SPIE Press, Bellingham, 2002.

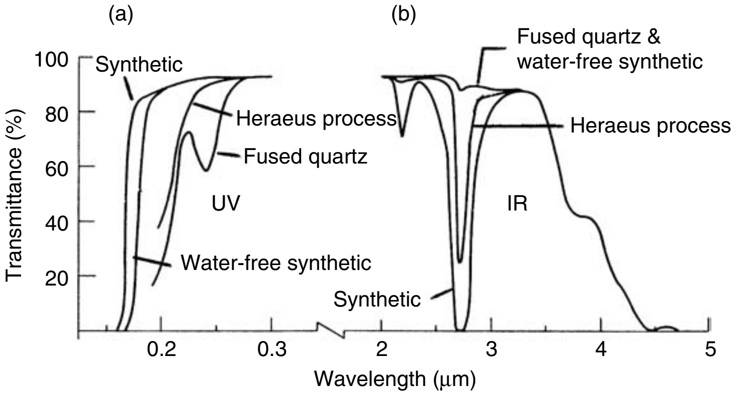

FIGURE 3.14 Approximate UV and IR transmittances of four types of vitreous silica as noted: (a) thickness 10 mm, (b) thickness 5 mm. (Adapted from Parker, C.J., in *Applied Optics and Optical Engineering*, Vol. VII, Shannon, R.R. and Wyant, J.C., Eds., Academic Press, New York, 1979, chap.2.)

TABLE 3.9
Typical Radiation Resistance of Synthetic Fused Silica

Material	**Radiation Dose**	**Observed Results**
X-ray radiation (50 kV source)		
Suprasil	3 × 10^6 rad	No decline in optical transmission
Optosil	1 × 10^5 rad	Slight loss in optical transmission; weak discoloration in violet; absorption band at 300 nm
UV radiation (20 kW Xenon lamp)		
Suprasil	0.4 kWh/cm^2	No decline in optical transmission
Optosil	0.4 kWh/cm^2	Slight decline in optical transmission below 300 nm; no visible discoloration
Protons		
Suprasil	8 × 10^{10} p/cm^2 at 4.6 MeV	No decrease in optical transmission over 200 to 3500 nm region
Optosil	1 × 10^{14} p/cm^2 at 3 MeV	Slight decline in optical transmission below 800 nm
Electrons		
Suprasil	5 × 10^{15} e/cm^2 at 0.75 MeV	Weak absorption at 215 nm; otherwise, no change in optical transmission
Optosil	1 × 10^{15} e/cm^2 at 1 MeV	Weak violet discoloration in visible range; absorption band at 215 nm
Neutrons		
Suprasil	4 × 10^6 n/cm^2	Slight decline in optical transmission below 300 nm; absorption band at 215 nm
Optosil	4 × 10^6 n/cm^2	Decline in optical transmission with visible dark violet discoloration

Source: Adapted ftom Heraeus Publication 40-1015-079.

temperatures. The usefulness of germanium for high-power laser applications or as domes for high-velocity missiles traveling in the atmosphere is limited by a large decrease in light transmission when it is heated above 500 K (440°F). This phenomenon, called "thermal run-away," may also lead to the self-destruction of the optical component (see Wilner et al., 1982).

TABLE 3.10
Opto-Mechanical Properties of Diamond and Selected IR-Transmitting Semiconductor Materials

Material Name (Symbol)	Refractive Index n at λ (μm)	dn/dT at λ (μm) ($\times 10^{-6}$/°C)	CTE α ($\times 10^{-6}$/°C)	Young's Modulus E ($\times 10^{10}$ Pa)	Poisson's Ratio ν	Density ρ (g/cm^3)	Knoop Hardness (kg/mm^2)	$K_G = (1-\nu_G^2)/E_G \times 10^{-11}$ (Pa^{-1})
Diamond (C)	2.382 at 2.5 2.381 at 5.0 2.381 at 10.6		−0.1 at 25 K 0.8 at 293 K 5.8 at 1600 K	114.3	0.069 (for CVD)	3.51	9000	0.094
Indium antimonide (InSb)	3.99 at 8.0	4.7	4.9	4.3	5.78	225		
Gallium arsenide (GaAs)	3.1 at 10.6	1.5	5.7	8.29	0.31	5.32	721	1.090
Germanium (Ge)	4.055 at 2.7 4.026 at 3.8 4.015 at 5.3 4.00 at 10.6	424 at 250–350 K	2.3 at 100 K 5.0 at 200 K 6.0 at 300 K	10.37	0.278	5.323	800	0.890
Silicon (Si)	3.436 at 2.7 3.427 at 3.8 3.422 at 5.3 3.148 at 10.6	130	2.7–3.1	13.1	0.279	2.329	1150	0.704

Source: Adapted from Yoder, P.R., Jr., *Mounting Optics in Optical Instruments*, SPIE Press, Bellingham, 2002.

3.2.4.4 Chalcogenides

The materials listed in Table 3.11 all contain a chalcogen (oxygen, sulfur, selenium, or telurium). These materials have high refractive indices, moderately low absorption coefficients, and fair mechanical and thermal characteristics. Some materials (notably ZnS and ZnSe) offer wide bandpass properties extending from the long-wave visible well into the IR. The transmission cutoff of ZnSe occurs farther out in the IR than that of ZnS, but the latter is harder and more resistant to mechanical surface damage. If uncoated, the high refractive indices of these materials lead to higher Fresnel losses than with other IR-transmitting materials. The internal absorption coefficient of ZnSe is comparatively low (4×10^{-4} cm^{-1} at 3.8 and 5.25 mm), so it is highly regarded as a material for the optics to be used in moderate-energy laser applications. When manufactured by a CVD process, higher quality, lower scatter substrates can be made. This process depends on the chemical reactions of gases in a controlled environment where the thermal, pressure, and flow conditions induce deposition of the desired material on a substrate.

3.2.4.5 Coefficients Related to Optical Material Thermal Behavior

Table 3.12 presents values for the coefficient of thermal defocus δ_G and thermo-optical coefficient γ_G of 185 Schott optical glasses, 14 crystals, 4 plastics, and 4 index-matching liquid materials. δ_G is used in passive athermalization of optical systems using refracting optical components as discussed in Section 15.7.1.2, while δ_G is used in estimating the optical effect of radial temperature gradients as discussed in Section 15.8.1. The numerical data in Table 3.12 and much of the theory underlying its application were derived from Jamieson (1992).

3.3 MATERIALS FOR REFLECTING OPTICS

Mirrors are commonly used in optical systems where large apertures, absence of light dispersion, folding of the light path, and a convenient means for introducing an aspheric surface are required. In essence, a mirror consists of two parts: the reflecting surface (a single-layer thin film or a multiple-layer stack of dielectric or dielectric/metallic thin films), and a more or less rigid substrate. Usually, only the very thin front reflecting surface serves an optical purpose since transmission of the incident radiation through the substrate then is not directly involved. Mechanically, the substrate then serves primarily only to hold the reflecting surface in place and in the proper contour. In second-surface mirrors, the substrate transmits the radiation.

Selected mechanical characteristics of the principal nonmetallic, metallic, and composite materials used as mirror substrates are given in Table 3.13 and Table 3.14. In the sections that follow, we consider some of the most important general properties of mirror substrate materials.

3.3.1 SMOOTHNESS

Practically all mirrors used in optical instruments are polished to a high degree of smoothness. The exceptions, which are of degree and not of principle, are mirrors intended for use in the IR region, where rougher surfaces can be tolerated because of the long wavelengths.

Three categories of surface irregularities exist in most mirrors. The coarsest are called figure errors; they introduce various forms and orders of common optical aberrations, such as spherical, coma, and astigmatism, into the reflected wave front. Full-aperture interferometry is commonly used to measure figure errors. Parks (1983) indicated that these errors can be characterized by the first 24 or 36 terms of a two-dimensional Zernike polynomial and correspond to spatial frequencies up to eight cycles per aperture diameter radially and four cycles per azimuthal rotation about the optic axis.

At the other end of the spatial frequency spectrum lie the high-frequency errors, sometimes called surface microroughness. These act primarily to scatter some of the incident radiation at angles $> 1°$. Techniques such as profilometry, fringes of equal chromatic order (FECO) interferometry, and

TABLE 3.11
Opto-Mechanical Properties of Selected IR-Transmitting Chalcogenide Materials

Material Name (Symbol)	Refractive Index n at λ (μm)	dn/dT at λ (μm) ($\times 10^{-6}$/°C)	CTE α ($\times 10^{-6}$/°C)	Young's Modulus E ($\times 10^{10}$ Pa)	Poisson's Ratio ν	Density ρ (g/cm^3)	Knoop Hardness (kg/mm^2)	$K_G = (1-\nu_G^2)/E_G \times 10^{-11}$ (Pa^{-1})
Arsenic trisulfide (AsS_3)	2.521 at 0.8 2.412 at 3.8 2.407 at 5.0	85 at 0.6 17 at 1.0	26.1	1.58	0.295	3.43	180	5.778
$Ge_{33}As_{12}Se_{55}$ (AMTIR-1)	2.605 at 1.0 2.503 at 8.0	101 at 1.0 72 at 10.0	12.0	2.2	0.266	4.4	170	4.224
Zinc Sulfide (ZnS)	2.36 at 0.6 2.257 at 3.0 2.246 at 5.0 2.192 at 10.6	63.5 at 0.63 49.8 at 1.15 46.3 at 10.6	4.6	7.45	0.29	4.08	230	1.229
Zinc selenide (ZnSe)	2.61 at 0.6 2.438 at 3.0 2.429 at 5.0 2.403 at 10.6	91.1 at 0.63 59.7 at 1.15 52.0 at 10.6	5.6 at 163 K 7.1 at 273 K 8.3 at 473 K	7.03	0.28	5.27	105	1.311

Source: Adapted from Yoder, P.R., Jr., *Mounting Optics in Optical Instruments*, SPIE Press, Bellingham, 2002.

TABLE 3.12 Coefficients of Thermal Defocus and Thermo-Optical Coefficients for 185 Schott Optical Glasses, 14 Crystals, 7 Plastics, and 4 Index-Matching Liquids

Material	Coefficient of Thermal Defocus δ_G ($\times 10^{-6}$/°C)	Thermo-Optical Coefficient γ_G ($\times 10^{-6}$/°C)	Material	Coefficient of Thermal Defocus δ_G ($\times 10^{-6}$/°C)	Thermo-Optical Coefficient γ_G ($\times 10^{-6}$/°C)	Material	Coefficient of Thermal Defocus δ_G ($\times 10^{-6}$/°C)	Thermo-Optical Coefficient γ_G ($\times 10^{-6}$/°C)
Optical Glasses			LAKN7	−7.86	6.34	BK10	−1.49	10.11
			LAK10	−1.15	10.25	K3	−7.08	9.52
FK3	−11.66	4.74	LAKN13	−11.03	5.77	K7	−8.03	9.52
FK52	−30.68	−1.88	LAK21	−7.63	5.97	K50	−2.18	11.82
PK3	−4.58	9.62	LAK28	−0.73	10.67	ZKN7	6.07	15.07
PK51A	−28.12	−2.72	LLF6	−3.53	11.47	BAK4	−3.00	11.00
PSK50	−11.64	5.56	BAF5	−2.74	11.26	BAK50	8.99	16.39
BK1	−6.54	8.86	BAF50	−7.17	9.43	SK4	−4.22	8.58
BK7	−4.33	9.87	BAF54	−1.96	10.44	SK9	−0.26	11.74
BALKN3	−5.82	9.98	LF5	−6.75	11.45	SK12	−3.54	9.26
K5	−7.76	8.64	F2	−3.82	12.58	SK16	−5.68	6.92
K11	−2.31	10.49	F5	−2.48	13.52	SK20	−3.38	9.42
ZK5	−6.80	10.60	FN11	−3.93	11.07	SK55	−3.05	8.95
BAK2	−6.96	9.04	BASF1	−5.11	11.89	KF50	−1.63	12.97
BAK6	−4.91	9.69	BASFI0	−5.38	11.82	BALF6	−2.03	11.37
SK2	−0.67	11.33	BASF52	4.51	14.91	BALF51	−6.75	9.45
SK6	−0.94	11.46	BASF56	−2.36	13.84	K3	−1.84	11.36
SK11	−3.51	9.49	LAF2	−9.02	7.18	SSK51	−6.86	8.34
SK15	−5.89	7.91	LAF9	3.11	17.51	LAK8	−1.07	10.13
SK19	−4.14	8.66	LAF22	−4.24	9.76	LAK11	−7.96	6.44
SK52	0.34	12.34	FK5	−14.89	3.51	LAKN14	−2.27	8.73
KF9	−1.42	12.18	FK54	−30.66	−1.46	LAKL21	−3.28	8.92
BALF5	−7.27	8.93	PK50	−11.42	6.18	LLF1	−5.01	11.19
BALF50	−8.19	8.41	PSK2	−3.97	8.83	BAF3	−4.09	11.51
SSK2	−1.51	10.89	PSK52	−11.55	5.45	BAF8	−1.69	12.31
SSKN8	−4.94	9.26	BK3	1.81	12.41	BAF52	−8.00	8.80

TABLE 3.12 ***(Continued)***

Material	Coefficient of Thermal Defocus δ_G ($\times 10^{-6}/°C$)	Thermo-Optical Coefficient γ_G ($\times 10^{-6}/°C$)	Material	Coefficient of Thermal Defocus δ_G ($\times 10^{-6}/°C$)	Thermo-Optical Coefficient γ_G ($\times 10^{-6}/°C$)	Material	Coefficient of Thermal Defocus δ_G ($\times 10^{-6}/°C$)	Thermo-Optical Coefficient γ_G ($\times 10^{-6}/°C$)
LF1	−6.45	10.55	SK5	−1.67	9.33	BASF51	6.32	17.12
LF8	−6.76	10.24	SK10	−5.03	8.97	BASF55	5.63	15.83
F3	−2.58	13.42	SK14	−3.60	8.40	BASF64	−3.68	10.92
F6	−3.79	13.21	SKN18	0.18	12.98	LAFN7	3.46	14.06
F14	−2.36	13.44	SK51	−12.69	5.11	LAF21	−1.90	9.90
BASF5	6.36	22.16	KF3	−3.96	12.24	LAFN24	0.85	11.65
BASF13	−2.17	12.03	BALF4	0.26	13.06	LAF25	2.79	14.39
BASF54	−0.06	14.54	BALF8	−6.50	10.10	LASF3	0.66	11.66
BASF57	−2.21	11.99	SSK1	−1.40	11.20	LASF13	3.10	15.50
LAF3	−7.33	7.87	SSK4	−3.46	8.74	LASFN31	−2.64	10.96
LAFN10	−0.15	11.25	SSK52	−3.53	9.87	SF2	−3.33	13.47
LAFN23	−9.08	7.12	LAK9	−2.89	9.71	SF5	−2.18	14.22
FK51	−29.35	−2.15	LAKN12	−9.69	5.51	SF7	−1.82	13.98
PK2	−3.95	9.85	LAKN16	1.25	11.85	SFI1	8.01	20.21
PK51	−31.82	−5.62	LAK23	−11.19	4.61	SF14	5.75	18.95
PSK3	−3.58	8.82	LLF4	−5.73	10.67	SF18	1.02	17.22
PSK53	−15.37	3.43	BAF4	−4.04	11.76	SF53	0.42	16.82
BK6	−5.88	9.72	BAF9	−0.60	12.40	SF56	−0.10	15.70
BALK1	−10.94	7.26	BAF53	−1.92	11.08	SF58	4.09	22.09
K4	−3.01	11.59	LF3	−5.07	11.13	SF63	0.82	17.22
K10	−1.04	11.96	F1	−5.32	12.08	TIF2	−9.87	7.33
K51	5.75	14.35	F4	−4.37	12.23	KZFS1	−2.01	7.99
BAK1	−5.72	9.48	F9	−2.20	13.20	KZFSN5	2.04	11.04
BAK5	−6.73	8.87	F15	−3.26	12.94	KZFS8	3.30	13.90
SK1	−1.62	10.58	BASF6	−3.69	11.11	LAF26	3.35	14.55

TABLE 3.12 *(Continued)*

Material	Coefficient of Thermal Defocus δ_G ($\times 10^{-6}$/°C)	Thermo-Optical Coefficient γ_G ($\times 10^{-6}$/°C)	Material	Coefficient of Thermal Defocus δ_G ($\times 10^{-6}$/°C)	Thermo-Optical Coefficient γ_G ($\times 10^{-6}$/°C)	Material	Coefficient of Thermal Defocus δ_G ($\times 10^{-6}$/°C)	Thermo-Optical Coefficient γ_G ($\times 10^{-6}$/°C)
LASFN9	−3.18	11.62	SFL6	−9.61	8.39	GaAs	58.56	70.36
LASFN15	−2.33	10.67	SF10	1.05	16.05	KRS5	−233.22	−111.22
LASF32	−4.37	11.43	SF13	2.96	17.16	KC1	−99.25	−27.25
SF3	0.33	17.13	SF16	−3.01	13.79	KBr	−106.44	−51.24
SF6	3.72	19.92	LASF11	−0.14	11.46	NaCl	−97.44	−9.44
SF9	0.97	17.32	SF50	−8.73	11.47	CsBr	68.84	164.64
SF12	−1.89	13.71	SF55	0.64	17.04	CsI	−174.05	−74.05
SF15	−1.15	14.65	SF57	4.81	21.41	**Plastics**		
SF19	−0.27	15.13	SF62	−1.17	15.23			
SF54	1.69	17.09	TIKI	−17.85	2.75	Acrylic	−278.4	−154.4
SFL56	−8.36	9.04	KZFSN2	−1.54	10.66	Polycarbonate	−253.4	−117.4
SF61	1.62	17.42	KZFSN4	1.89	10.89	Polystyrene	−289.7	−189.7
SFN64	−7.30	9.70	KZFSN7	2.61	12.21	SAN	−246.5	−146.5
KZFN1	−3.39	10.81	**Infrared Crystals**			**Liquids**		
KZFSN2	1.82	10.82						
KZFS6	−0.96	9.24	Germanium	124.87	136.27	CG305974	−1076.26	1076.26
LGSK2	−20.31	3.89	Silicon	61.93	66.93	CG505257	−923.66	−923.66
LAFN28	−1.18	10.42	ZnSe	34.12	49.32	CG710209	−926.27	−926.27
LASFN30	−2.04	10.36	ZnS	26.17	41.97	CG810184	−1113.27	−1113.27
SF1	0.11	16.31	CdTe	52.46	61.46			
SF4	2.51	18.51	AMTIR1	33.47	59.47			

Source: Adapted from Jamieson, T.H., *Proc. SPIE*, CR43, 141, 1992.

TABLE 3.13
Mechanical Properties of Selected Nonmetallic Mirror Substrate Materials

Material Name and Symbol	Source	CTE α ($\times 10^{-6}$/°C; $\times 10^{-6}$/°F)	Young's Modulus E ($\times 10^{10}$ Pa; $\times 10^{6}$ lb/in.^{2})	Poisson's Ratio ν	Density ρ (g/cm^3; lb/in.^{3})	Specific Heat c_p (J/kg · K ; Btu/lb ·°F)	Thermal Conductivity k (W/m · K ; Btu/h · ft ·°F)	Knoop Hardness	Best Surface Smoothness (Å rms)
Duran 50	Schott	3.2 (1.8)	6.17 (8.9)	0.20	2.23 (0.081)	835 (0.20)	1.02 (0.59)		~5
Pyrex 7740	Corning	3.3 (1.86)	6.30 (9.1)	0.2	2.23 (0.081)	1050 (0.25)	1.13 (0.65)		~5
Borosilicate crown E6	Ohara	2.8 (1.5)	5.86 (8.5)	0.195	2.18 (0.079)				
Fused Silica 7940	Corning	0.58 (0.32)	7.3 (10.6)	0.17	2.205 (0.080)	741 (0.177)	1.37 (0.8)	500	~5
ULE 7971	Corning	0.015 (0.008)	6.76 (9.8)	0.17	2.205 (0.080)	766 (0.183)	1.31 (0.76)	460	~5
Zerodur	Schott	0 ± 0.05 (0 ± 0.03)	9.06 (13.6)	0.24	2.53 (0.091)	821 (0.196)	1.64 (0.95)	60	~5
Zerodur-M	Schott	0 ± 0.05 (0 ± 0.03)	28.9 (12.9)	0.25	2.57 (0.093)	810 (0.194)	1.6 (0.92)	540	~5
Cer-Vit C-101[a]	Owens-Illinois	0 ± 0.03 0 ± 0.02	9.18 (13.3)	0.25	2.50 (0.090)	840 (0.20)	1.70 (1.0)	540	~5

[a] Obsolete material. Included here for historical purposes.

Source: Adapted from Yoder, P.R., Jr., *Mounting Optics in Optical Instruments*, SPIE Press, Bellingham, 2002.

TABLE 3.14
Mechanical Properties of Selected Metallic and Composite Mirror Substrate Materials

Material Name and Symbol	CTE α ($\times 10^{-6}$/°C; $\times 10^{-6}$/°F)	Young's Modulus E ($\times 10^{10}$ Pa; $\times 10^{6}$ lb/in.^{2})	Poisson's Ratio ν	Density ρ (g/cm^3; lb^2/in.^{3})	Specific Heat c_p (J/kg · K; Btu/lb ·°F)	Thermal Conductivity k (W/m · K; Btu/h · ft ·°F)	Hardness	Best Surface Smoothness (Å rms)
Aluminum (6061-T6)	23.6 (13.1)	6.82 (9.9)	0.332	2.68 (0.100)	960 (0.23)	167 (96)	30–95 Brinell	~200
Beryllium (I-70H)	11.3 (6.3)	28.9 (42)	0.08	1.85 (0.067)	1820 (0.436)	216 (125)		60–80 (sputtered)
Beryllium (S-200-FH)	11.3 (6.3)	30.3 (44)	0.08	1.85 (0.067)	1820 (0.436)	216 (125)		
Beryllium (O-30H)	11.46 (6.37)	30.3 (44)	0.08	1.85 (0.067)	1820 (0.436)	215/365[a] (125/211)	80 Rockwell B	15–25
Copper (OFHC[b])	16.7 (9.3)	11.7 (17)	0.35	8.94 (0.323)	385 (0.092)	392 (226)	40 Rockwell F	40
Glidcop™	18.4 (10.3)	13.0 (18.9)	0.33	8.84 (7.40)	380 (211)	216 (125)		
Molybdenum (TZM)	5.0	31.8 (2.8)	0.32 (46)	10.2	272 (0.368)	146 (0.065)	200 (84.5)	10 Vickers
Silicon	2.6 (1.4)	13.1 (19.0)	0.42	2.33 (1.95)	710 (0.170)	137 (79)		4 to l
Silicon carbide (RB-30% Si)	2.64 (1.47)	31.0 (45)		2.92 (0.106)	660 (0.16)	158 (91)		
Silicon carbide (RB-12% Si)	2.68 (1.49)	37.3 (54.1)		3.11 (0.112)	680 (0.16)	147 (85)		
Silicon carbide CVD	2.4 (1.3)	46.6 (67.6)	0.21	3.21 (0.116)	700 (0.17)	146 (84)	2540 Knoop (500 g)	

TABLE 3.14 (*Continued*)

Material Name and Symbol	CTE α ($\times 10^{-6}$/°C; $\times 10^{-6}$/°F)	Young's Modulus E ($\times 10^{10}$ Pa; $\times 10^{6}$ lb/in.^{2})	Poisson's Ratio ν	Density ρ (g/cm^3; lb^2/in.^{3})	Specific Heat c_p (J/kg · K; Btu/lb ·°F)	Thermal Conductivity k (W/m · K; Btu/h · ft ·°F)	Hardness	Best Surface Smoothness (Å rms)
CESIC®	2.6 at 300 K (1.4 at 68°F) < 0.5 at 90 to 20 K	23.5 (34.1)		2.65	660 (0.16)	~135 (~78)		
SXA metal matrix of 30% SiC in 2124 Al[c]	12.4 (6.9)	11.7 (17)		2.90 (0.105)	770 (0.18)	130 (75)		
AlBeMet 162	13.9 (7.7)	19.3 (28)		2.10 (0.076)	1560 (0.373)	(210) (121)		
Berylcast191	13.3 (7.4)	20.1 (29.3)		2.15 (0.078)	1454 (0.34)	178 (103)		
AlBeCast 910	13.8 (7.7)	19.2 (28.0)		2.09 (0.076)	1539 (0.36)	104 (60)		
Al-Si alloy 393-T6 (22% Si)	16.1 (9.0)	10.3 (15)		2.64 (0.096)	898 (0.21)	15.6 (9.0)		
Graphite epoxy GY-70/x30	0.02 (0.01)	9.3 (13.5)		1.78 (0.064)		35 (20)		

[a] Measured at 25°C/–166°C.

[b] Oxygen free, high conductivity.

[c] With SiC particles of mean size 3.5 µm (0.014 in.) per Advanced Composite Materials Corp., Greer, SC.

Source: Adapted from Paquin, R.A., Advanced materials: an overview, *Proc. SPIE*, CR67, 3, 1997a.; Ahmad, A., Wright, R., and Baker, T., *Proc. SPIE*, 306, 66, 1981.; Yoder, P.R., Jr., *Mounting Optics in Optical Instruments*, SPIE Press, Bellingham, 2002.; Muller, C., Papenburg, U., Goodman, W.A., and Jacoby, M., *Proc. SPIE*, 4198, 249, 2001.; Parsonage, T., *Proc. SPIE*, 5494, 39, 2004. Brush Wellman Literature.

heterodyne microinterferometry are commonly used to measure these errors. They may have frequencies as high as 50 cycles/mm. Elson and Bennett (1979) provided an excellent theoretical discussion of scatter from surfaces with this type of defect.

Between the coarse and fine extremes are the midfrequency errors. They are best measured by subaperture interferometry. In a paper on the methodology of specifying performance requirements for large mirrors, Patterson and Crout (1982) defined these midfrequency irregularities as those at frequencies of 0.01 to 0.25 cycles/mm. Noll (1979), Wetherell (1982), and Parks (1983) are good sources of information on these errors and their effects on image quality.

Although all the materials considered here are generally compatible with achievement of the typical levels of surface figure required in contemporary optical systems — at least over reasonable-sized apertures — not all can be polished to the same degree of smoothness. For example, extremely smooth surfaces can be produced on fused silica or Zerodur mirrors. Consequently, those materials are frequently used for x-ray optics where the short wavelength emphasizes scatter effects. At the other extreme, mirrors made of metals such as aluminum or beryllium usually have rough surfaces suitable only for IR applications. Coatings of electroless nickel (ELN), sputtered beryllium, or proprietary forms of aluminum have been applied to these metals to provide an amorphous layer that accepts a better polish. Typical coatings applied for this purpose are discussed in Section 3.7.3. One technique for producing optically smooth surfaces on aluminum without plating or coating was described by Lyons and Zaniewski (2002). This technique utilizes new materials as agents applied during optical shop polishing with a specially prepared lap. The aluminum surface is first prepared by diamond turning, or lapping with fine diamond particles to a roughness of < 100 Å and optical figure within one-half wave of the desired final value. It then is polished with a pitch lap using a polishing agent comprising certain proportions of carbon black, ammonium hydroxide, phenol, ethylene glycol, and water. According to the authors, 6061-T6 aluminum mirror surfaces with roughness < 5 Å and optical figure errors < 0.5 wave have been produced with this method.

It is difficult to rank mirror materials between these two extremes. In general, the harder materials polish better than soft ones. Any isotropic material that does not contain many inclusions, bubbles, or voids can be polished to an acceptable degree of smoothness if sufficient time is spent in that operation. The achievement of the ultimate in smoothness on any given material may, however, require the optician to apply tools and techniques that tend to disrupt the figure of the surface. This is particularly true of wide-aperture (i.e., fast) aspheric surfaces, for which subaperture tools must be used to accommodate significant changes in surface radius of curvature from axis to rim. Midfrequency errors generally result in surfaces polished with subaperture tools. Larger flexible tools tend to reduce these errors. Barnes and McDonough (1979) described techniques for achieving low-scatter surfaces on aspheric mirrors made to three types of material (fused silica, ULE*, and Cer-Vit).

3.3.2 STABILITY

Once an optical surface has been ground and polished into a mirror substrate, it is important for the figure not to change as a result of environmental exposure, temperature changes, or (as is most common) release of internal stress. Well-annealed glass and glass–ceramic materials usually do not exhibit such stress. Figure 3.15 shows typical variations of CTE with temperature for a variety of low-expansion materials. Figure 3.16 shows temporal variations of dimensions for the same materials. If regular Zerodur is subjected to temperatures above 130°C during fabrication or use, followed by cooling to that particular temperature at a rate other than that originally used by the manufacturer during annealing, relaxation effects may cause small changes in component dimensions and CTE (Shaffer and Bennett, 1984; Jacobs et al., 1984; Jacobs, 1992; Lindig and Pannhorst, 1985). The latter changes would manifest themselves as permanent changes in the thermal expansion behavior of the material, as compared with its original form. This form of hysteresis can be avoided if the material is cooled at or below a particular rate or reannealed after exposure to high temperature. A newer product, Schott Zerodur-M, does not exhibit this

---

* ULE is Corning's ultra low expansion material.

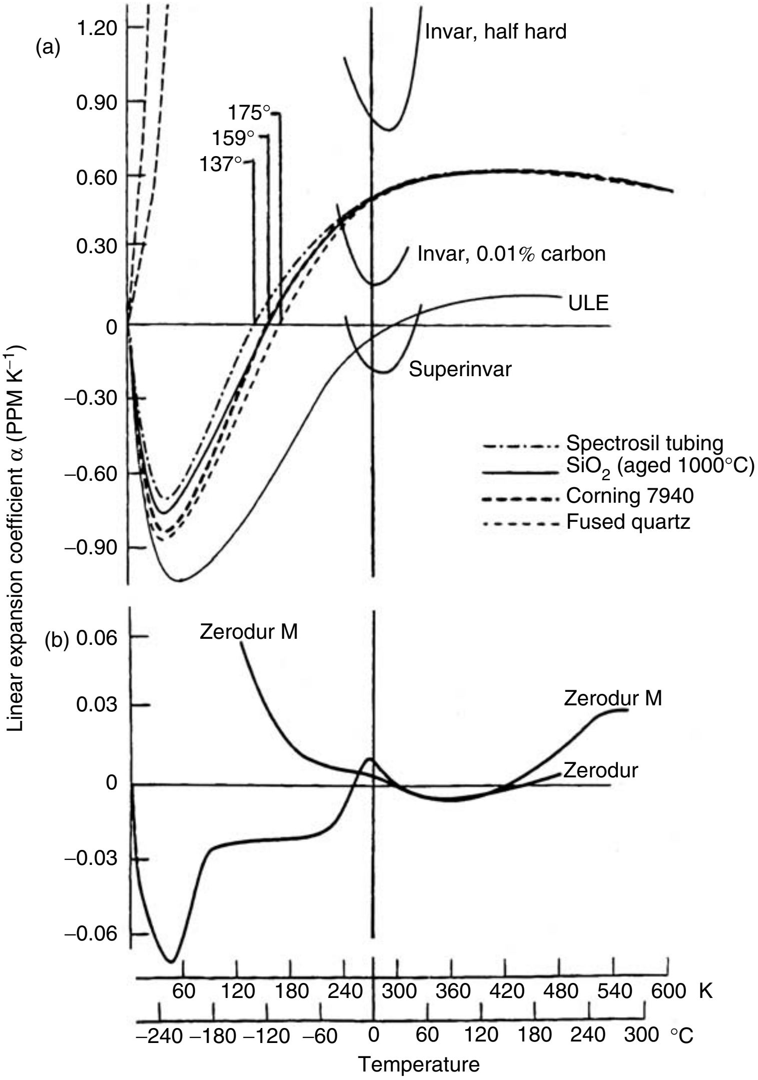

FIGURE 3.15 Variations of CTE with temperature for: (a) various low-expansion materials, (b) for Zerodur and Zerodur M. (Adapted from Jacobs, S.F., Variable invariables — dimensional instability with time and temperature, *Proc. SPIE*, CR43, 181, 1992.)

hysteresis effect and is recommended for use whenever the component must undergo temperatures in excess of 130°C.

Another effect, that of small, but significant, delayed elastic deformation of Zerodur at room temperature upon release of external forces applied for a significant time interval, was reported by Pepi and Golini (1991a, b). This phenomenon, repeatably experienced during fabrication of segments of the first Keck 10 m telescope primary mirror, was confirmed by an independent test and attributed to rearrangement of ion groups within the material structure. Theory due to Murgatroyd and Sykes (1947) indicated that this behavior occurs in materials with alkali oxide content. Tests of ULE by Pepi and Golini reported in the above 1991 references showed no delayed elastic effects. This was attributed to the absence of alkali oxides in ULE.

If transparent, materials can be tested for stress by observing them in transmission between crossed polarizers. Unfortunately, this cannot be done with metals and other opaque materials. In those cases, the manufacturer can reduce the likelihood of excessive residual stress by thermal

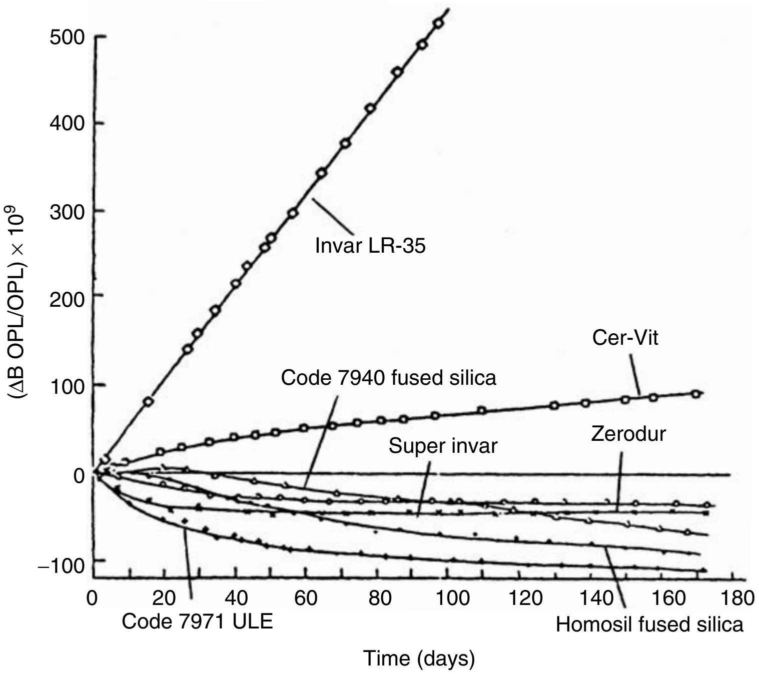

FIGURE 3.16 Temporal changes of sample length for a number of low-expansion materials. (Adapted from Berthold, J.W., Jacobs, S.F., and Norton, M.A., Dimensional stability of fused silica, Invar and several ultralow thermal expansion materials, *Appl. Opt.* 15, 1898, 1976.)

cycling the mirror at selected stages during processing. Procedures for doing this with metal mirrors are discussed in Chapter 13.

Paquin (1990, 1992), Marschall (1990), and Hagy (1990) each discussed temporal dimensional stability in nonmetallic and metallic materials. Although too lengthy to be repeated here, these documents would make informative reading for the opto-mechanical engineer interested in optical instrument design. Paquin (1995) provided details regarding the variation with temperature of the CTEs, thermal conductivities, and specific heats for aluminum, beryllium, copper, gold, silver, iron, stainless steel, nickel, molybdenum, silicon, and α- and β-silicon carbide. CTE changes for these materials over the range 5 to 700 K are summarized in Table 13.3.

3.3.3 RIGIDITY

The inherent stiffness of the substrate material has a significant effect on the suitability of the finished and installed mirror. A more rigid material with low density tends to resist deformations due to polishing, mounting, gravity, and vibration during operation. The specific stiffnesses E/ρ of various candidate substrate materials are listed in Table 3.15. A large number is desirable. Beryllium and silicon carbide lead the list in this regard. Cer-Vit (an obsolete material) and Zerodur have the highest values for the nonmetals. Rigidity and other factors of importance in choosing a material for mirrors are discussed by Kishner et al. (1990). Other figures of merit for mirror materials are summarized in Table 3.16.

3.4 MATERIALS FOR MECHANICAL COMPONENTS

The following sections provide brief descriptions of metals commonly used as housings, lens barrels, cells, retainers, structural members, covers, springs, metering rods, etc., in optical instruments. Key properties are as given in Tables 3.14 through 3.17 for metals used in mirrors and in Table 3.18 for metals used in mechanical parts of optical instruments. For more detailed information regarding

TABLE 3.15
Specific Stiffnesses of Candidate Mirror Materials

Material	Specific stiffness E/ρ (10^4 N · m/g)
Nonmetallics	
Duran 50	2.77
Borosilicate crown E6	2.69
Fused silica	3.33
ULE 7971	3.08
Zerodur	3.58
Zerodur-M	3.46
Cer-Vit C-101	3.67
Metallics	
Beryllium 1–70	15.6
Aluminum 6061-T6	2.55
OFHC copper	1.31
TZM molybdenum	3.12
Silicon carbide RB-30% Si	10.6
Silicon carbide RB-12% Si	11.99
Silicon carbide CVD	12.2
SXA metal matrix	4.03
Graphite epoxy GY-70/x3O	5.22

specific materials, the reader is referred to handbooks such as Boyer and Gall (1985), to manufacturers' literature, and to Paquin (1995, 1997a, b) as well as the many references in the latter publications. As mentioned earlier, some of these materials are used in mirror substrates; further discussion of that application may be found in Chapter 13.

3.4.1 ALUMINUM

The pure form of aluminum is seldom used in optical instrument mechanical parts; aluminum alloys have better properties for such applications. These materials are light and strong, readily available at low cost in either cast or wrought forms, and are easily machined. Cast aluminum parts are frequently used for instrument housings. Cast billets can be rolled, extruded, or forged to make wrought aluminum stock. Parts made from this material are stronger, more ductile, and have fewer defects than cast parts. Wrought materials are usually heat treated to increase strength. Brief descriptions of common tempering conditions are given in Table 3.19.

All surfaces of aluminum parts should be protected by a chemical film (such as Iridite or Alodine) or an anodic coating. The exception to this rule is that reference surfaces for locating mating parts are not protected in some high-precision applications or if electrical contact is required. Black anodized coatings provide increased wear resistance and some degree of light-reflection reduction. Both these attributes may be needed in optical applications.

General descriptions of key aluminum materials follow.

3.4.1.1 Alloy 1100

This is a low-strength alloy (the principal alloying composition is 0.12% copper) with excellent formability and high corrosion resistance. It is not heat treatable. Its primary use is for spinning and deep-drawn parts. Cold working can strengthen this alloy. It machines well, has excellent weldability, and can be brazed with or (in vacuum) without flux.

TABLE 3.16
Comparison of Material Figures of Merit Especially Pertinent to Mirror Design

	Weight and Self-Weight Deflection Proportionality Factors				Thermal Distortion Coefficients	
	$(E/\rho)^{1/2}$ Resonant Frequency for same Geometry	ρ/E Mass or Deflection for same Geometry	ρ^3/E Deflection for same Mass	$(\rho^3/E)^{1/2}$ Mass for same Deflection	α/k Steady State	α/D Transient
Preferred value	**Large**	**Small**	**Small**	**Small**	**Small**	**Small**
Pyrex	5.3	3.54	1.76	0.420	2.92	5.08
Borosilicate crown E6	5.2	3.72	1.71	0.420		
Fused silica	5.7	3.04	1.46	0.382	0.36	0.59
ULE	5.5	3.30	1.61	0.401	0.02	0.04
Zerodur	6.0	2.78	1.78	0.422	0.03	0.07
Zerodur M	5.9	2.89	1.91	0.437	0.03	
A1 6061	5.0	3.97	2.90	0.538	0.13	0.33
Metal matrix 30% SiC-Al	6.3	2.49	2.11	0.459	0.10	0.22
Be I-70H or I-220H	12.5	0.64	0.22	0.149	0.05	0.20
Cu, OFHC	3.6	7.64	61.1	2.471	0.04	0.14
Glidcop™	3.8	6.80	53.1	2.305	0.05	0.17
Invar 36	4.2	5.71	37.0	1.923	0.10	0.38
Super Invar	4.3	5.49	36.3	1.905	0.03	0.12
Molybdenum	5.6	3.15	32.8	1.812	0.04	0.09
Silicon	7.5	1.78	0.97	0.311	0.02	0.03
SiC HP alpha	11.9	0.70	0.72	0.268	0.02	0.03
SiC CVD beta	12.0	0.69	0.71	0.267	0.01	0.03
SiC RB-30% Si	10.7	0.88	0.73	0.270	0.02	0.03
CRES 304	4.9	4.15	26.5	1.629	0.91	3.59
CRES 416	5.3	3.63	22.1	1.486	0.34	1.23
T1 6A14V	5.1	3.89	7.63	0.873	1.21	3.03

Source: Adapted from Paquin R.A., *Proc. SPIE.*, CR67, 3, 1997a.

TABLE 3.17
Characteristics of Aluminum Matrix Composites

Property	Instrument Grade	Optical Grade	Structural Grade
Matrix alloy	6061-T6	2124-T6	2021-T6
Volume % SiC	40	30	20
SiC form	Particulate	Particulate	Whisker
CTE ($\times 10^6$ K^{-1})	10.7	12.4	14.8
Thermal conductivity (W/m·K)	127	123	
Young's modulus (MPa)	145	117	127
Density (g/cm^3)	2.91	2.91	2.86

Source: Adapted from Mohn, W.R. and Vukobratovich, D., *Opt. Eng*., 27, 90, 1988.

3.4.1.2 Alloy 2024

This is a high-strength, heat-treatable structural alloy (the principal alloying composition is 4.5% copper, 0.6% manganese, and 1.5% magnesium). It is commonly used in the T4 or T351 condition. Resistance to stress corrosion is poor. In bar or rod form tempered to T8 condition, it is more corrosion-resistant. Machinability is good, but it is difficult to weld.

3.4.1.3 Alloy 6061

This is the best general-purpose structural aluminum alloy. Its principal alloying composition is 0.6% silicon, 0.25% copper, 1.0% magnesium, and 0.2% chromium. It is usually tempered to the *T*6 condition. With moderate strength, 6061 has good dimensional stability, good machinability, and excellent weldability. It can also be brazed.

3.4.1.4 Alloy 7075

This is a high-strength alloy, especially in the T6 condition. It is susceptible to stress corrosion. Resistance to this problem is maximized in the T73 condition. It machines well, but welding is not recommended. The principal alloying composition is 1.6% copper, 2.5% magnesium, 0.3% chromium, and 5.6% zinc.

3.4.1.5 Alloy 356

This alloy has good castability by sand, permanent mold, and die-casting methods, and moderate to high strength. It is highly recommended for general-purpose optical instrument applications. The principal alloying composition is 7% silicon and 0.3% magnesium. Machinability is good. Castings can be repaired by welding.

3.4.2 BERYLLIUM

This lightweight, high-stiffness, high-thermal conductivity material offers many structural advantages in opto-mechanical applications, especially those involving cryogenic temperatures. It is more expensive than most other metals. Dimensional stability is excellent. Thermal expansion characteristics differ significantly in the different directions of the hexagonal crystal structure of the elemental material. Corrosion resistance is generally excellent at room temperature (except for susceptibility to certain acids and alkalis) because of the thin layer of beryllium oxide that forms on surfaces exposed to air. Machinability at best is poor. The material is quite brittle. Welding is not recommended, although electron beam methods have had some success. Some varieties of the material can

TABLE 3.18
Mechanical Properties of Selected Metals and Composites used for Mechanical Components

Material	CTE α ($\times 10^{-6}$/°C; $\times 10^{-6}$/°F)	Young's Modulus[a] E_M ($\times 10^{10}$ Pa; $\times 10^{6}$ lb/in.^{2})	Yield Stress[a] S_Y ($\times 10^{7}$ Pa; $\times 10^{3}$ lb/in.^{2})	Poisson's Ratio ν_M	Density ρ (g/cm^3; lb/in.^{3})	Thermal Conductivity[a] k (W/m·K; Btu/h·ft ·°F)	Hardness[a]	$K_M = (1-\nu_M{}^2)/E_M$ ($\times 10^{-11}$ m^2/N; $\times 10^{-8}$ in.^{2}/lb)
Aluminum	23.6	6.89	3.4–15.2		2.71	218–221	23–44	
1100	(13.1)	(10.0)	(5–22)		(0.098)	(126–128)	Brinell	
Aluminum	22.9	7.31	7.6–39.3	0.33	2.77	119–190	47–130	1.22
2024	(12.7)	(10.6)	(11–57)		(0.100)	(69–110)	Brinell	(8.41)
Aluminum	23.6	6.82	5.5–27.6	0.332	2.68	167	30–95	1.30
6061	(13.1)	(9.9)	(8–42)		(0.097)	(96.5)	Brinell	(8.99)
Aluminum	23.4	7.17	10.3–50.3		2.79	142–176	60–150	
7075	(13.0)	(10.4)	(15–73)		(0.101)	(82–102)	Brinell	
Aluminum	21.4	7.17	17.2–20.7		2.68	150–168	60–70	
356	(11.9)	(10.4)	(25–30)		(0.097)	(87–97)	Brinell	
Beryllium	11.5	27.6–30.3	20.7		1.85	220	80–90	
S-200	(6.4)	(40–44)	(30)		(0.067)	(127)	Rockwell-B	
Beryllium	11.5	27.6–30.3	34.5	0.08	1.85	220	100	1.63
I-400	(6.4)	(40–44)	(50)		(0.067)	(127)	Rockwell-B	(2.37)
Beryllium	11.3	28.9		0.08	1.85	194		1.63
I-70A	(6.3)	(42)			(0.067)	(112)		(2.37)
Copper	16.9	11.7	6.9–36.5	0.343	8.94	391	10–60	3.56
C10100 (OFHC)	(9.4)	(17)	(10–53)		(0.323)	(226)	Rockwell-B	(5.16)
Copper	17.8	12.7	107–134	0.35	8.25	107–130	27–42	0.691
C17200 (BeCu)	(9.9)	(18.5)	(155–195)		(0.298)	(62–75)	Rockwell-C	(4.76)
Copper	20.5	9.65	12.4–35.9		8.50	116	62–80	
360 (brass)	(11.4)	(14.0)	(18–52)		(0.307)	(67)	Rockwell-B	
Copper	20.0	11.0	7.6–44.8		8.52	121	55–93	
C260	(11.1)	(16)	(11–65)		(0.308)	(70)	Rockwell-B	

TABLE 3.18 (*Continued*)

Material	CTE α ($\times10^{-6}$/°C; $\times10^{-6}$/°F)	Young's Modulus[a] E_M ($\times10^{10}$ Pa; $\times10^6$ lb/in.^{2})	Yield stress[a] S_Y ($\times10^7$ Pa; $\times10^3$ lb/in.^{2})	Poisson's Ratio ν_M	Density ρ g/cm^3; lb/in.^{3}	Thermal Conductivity[a] k (W/m · K ; Btu/h · ft ·°F)	Hardness[a]	$K_M = (1-\nu_M{}^2)/E_M$ ($\times10^{-11}$ m^2/N; $\times10^{-8}$ in.^{2}/lb)
Glidcop™	16.6	13.1	30.3	0.33	8.75	365		0.680
	(9.23)	(19.1)	(44)		(0.316)	(211)		(4.69)
Invar	1.26	14.1	27.6–41.4	0.259	8.05	10.4	160	0.662
36	(0.7)	(21.4)	(40–60)		(0.291)	(6.0)	Brinell	(4.57)
Super	0.31	14.8	30.3	0.29	8.13	10.5	160	0.629
Invar	(0.17)	(21.5)	(44)		(0.294)	(6.1)	Brinell	(4.34)
Magnesium	25.2	4.48	14.5–25.5	0.35	1.77	97	73	1.95
AZ-31B-H241	(14)	(6.5)	(21–37)		(0.064)	(56)	Brinell	(13.5)
Magnesium	25.2	4.48	12.4–17.9		1.77	138	42–54	
MIA	(14)	(6.5)	(19–26)		(0.064)	(79.8)	Brinell	
Steel	11.9	20.7	28.3–31.0	0.287	7.75		111–126	0.44
1015 (low carbon)	(6.6)	(30)	(41–45)		(0.28)		Brinell	(3.05)
CRES	14.7	19.3	51.7–103	0.27	8.0	16.2	83 Rockwell-B	0.48
304	(8.2)	(28)	(75–150)		(0.29)	(9.4)	42 Rockwell-C	(3.31)
CRES	9.9	20.0	27.6–103	0.283	7.8	24.9	82 Rockwell-B	0.46
416	(5.5)	(29)	(40–150)		(0.28)	(14.4)	42 Rockwell–C	(3.17)
Titanium	8.8	11.4	82.7–106	0.34	4.43	7.3	36–39	0.79
6A14V	(4.9)	(16.5)	(120–154)		(0.16)	(4.2)	Rockwell-C	(5.47)
SXA Metal Matrix	12.4	11.7			1.78	35	Variable within	
(SiC & 2124 Al)	(6.9)	(17)			(0.064)	(20)	sample	
AlBeMet	13.8	19.9	19.3		2.10	(210)		
162	(7.7)	(29)	(28)		(0.076)	(121)		
CESIC®	2.6 at 300 K	23.5			2.65	135		
	(1.4 at 68°F)	(34.1)				(~78)		
	<0.5 at 90 to 20 K							

[a] Range of values pertains to various tempers.

Sources: Adapted from Yoder, P.R., Jr., *Mounting Optics in Optical Instruments*, SPIE Press, Bellingham, 2002; Paquin, private communication, 2003, Muller, C., Papenburg, U., Goodman, W.A., and Jacoby, M., *Proc. SPIE*, 4198, 249, 2001.

TABLE 3.19
Common Temper Conditions for Aluminum Alloys

Condition	Description
F	*As fabricated.* Applies to products shaped by cold working, hot working, or casting processes in which no special control over thermal conditions or strain hardening is employed
O	*Annealed.* Applies to wrought products that are annealed to obtain lowest strength temper, and to cast products that are annealed to improve ductility and dimensional stability
H	*Strain-hardened (wrought products only).* Applies to products that have been strengthened by strain hardening, with or without supplementary heat treatment
W	*Solution heat-treated.* An unstable temper applicable only to alloys that naturally age (spontaneously at room temperature) after solution heat treatment
T	*Heat-treated to produce stable tempers other than F, O, or H.* Applies to products that are thermally treated, with or without supplementary strain hardening, to produce stable tempers. The T is followed by one or more digits

Source: Adapted from Boyer, H.E. and Gall, T.L., Eds., *Metals Handbook-Desk Edition*, Am. Soc. For Metals, Metals Park, Ohio, 1985.

TABLE 3.20
Beryllium Grades and Some of Their Properties

	Beryllium Grade				
Property	**O-30-H**	**I-70-H**	**I-220-H**	**I-250**	**S-200-FH**
Maximum beryllium oxide content (%)		0.7	2.2	2.5	1.5
Grain size (μm)	7.7	10	8	2.5	1.5
2% offset yield strength (MPa)	295–300	207	345	544	296
Microyield strength (MPa)	24–25	21	41	97	34
Elongation (%)	3.5–3.6	3.0	2.0	3.0	3.0

Source: Adapted from Paquin (1997a), Parsonage, T., *Proc. SPIE*, 5494, 39, 2004; Parsonage, T., private communication, 2005.

be brazed. Beryllium powder is toxic. Machining must be done in a controlled environment and chips and dust must be handled and disposed of as hazardous waste. Characteristics of three varieties are listed in Table 3.18. Additional information is given in Table 3.20.

The most common forms of supply for structural beryllium are vacuum hot-pressed block, hot-extruded billet, and cross-rolled sheet. The highest uniformity of characteristics results from manufacture by HIP techniques. The latter process is used for optical components (scanners, mirrors, etc.) and some critical structural parts. Beryllium mirrors are discussed in Section 13.3.

3.4.3 COPPER

Copper and its alloys are used in applications requiring excellent electrical or thermal properties, resistance to corrosion, ease of fabrication, good strength and fatigue resistance, and nonmagnetic properties. Easily soldered, brazed, and plated, copper is frequently used in heat exchangers, tubing, valves, and heat transfer straps as well as wire and electrical parts. Beryllium copper is frequently used for springs, whereas alloys containing up to 6% lead and brass are widely used for screw-machine parts and mounting hardware (bolts, rivets, etc.). Table 3.18 gives typical characteristics of copper-based materials. Descriptions of these materials follow.

3.4.3.1 Alloy C10100

This high-purity copper alloy is designated *oxygen-free*, *high conductivity* (OFHC) or *oxygen-free*, *electronic grade*. It is at least 99.95% copper and is frequently used for mirrors in applications involving high thermal irradiance of the optical surface (see Chapter 13), or in electronic tubes, vacuum seals, and parts to be assembled by hydrogen brazing. Machinability is fair; solderability and weldability are good.

3.4.3.2 Alloy C17200

This high-strength beryllium copper is used primarily for springs, clips, washers, and in electrical and electronic equipment. Machinability is good. It can be welded and brazed (with some difficulty). Soldering requires use of activated flux. The machining of parts must be completed before aging or heat treating.

3.4.3.3 Alloy C360

This alloy is the industry standard free-cutting brass for ease of machining of screw-machine products. It solders and brazes well, but welding is not recommended.

3.4.3.4 Alloy C260

This brass has excellent cold workability so it is widely used for deep-drawn shells, sheet metal stampings, pins, rivets, etc. Machinability is excellent as are its soldering and brazing characteristics. Weldability is only fair.

3.4.3.5 Glidcop™

This proprietary material is a dispersion-strengthened, relatively pure, copper alloy designed to provide thermal conductivity nearly equal to that of OFHC copper, but with the ability to maintain strength after brazing at temperatures as high as 1000°C. It is available in three grades depending upon Al_2O_3 content. When fully annealed, one grade, AL-15 UNS C15715 with 0.3% (by weight) Al_2O_3, is used in cooled mirrors for synchrotron and other applications (Howells and Paquin, 1997; Paquin, 2003).

3.4.4 INVAR AND SUPER INVAR

Low-expansion alloys of iron and nickel are used when control of thermally induced dimensional changes is required by the application. One iron alloy, Invar 36, contains 36% nickel with 0.35% manganese, 0.2% silicon, and 0.02% carbon. It has a virtually invariable (hence the name) and low CTE over a limited temperature range (typically 40 to 100°F [4 to 38°C]). The CTE changes relatively rapidly outside this range as shown in Figure 3.15. The actual value of CTE in a given Invar 36 part depends on its temperature and machining history. For maximum stability, parts should be annealed as described by Howells and Paquin (1997). The characteristics of Invar are included in Table 3.18.

Super Invar alloy (Fe/31% Ni/5% Co) can have near-zero CTE with special heat treatment processing (Lement et al., 1950), but this is true over only a very limited temperature range (Jacobs, 1990, 1992) (see Figure 3.15). The slower change of CTE with change of temperature of standard Invar 36 may make it preferable to Super Invar in some applications involving significant temperature changes. Further, Super Invar undergoes a phase change when cooled below −50°C, so it is not a good material of choice when exposure to such low temperatures is anticipated. On the other hand, Berthold et al. (1976) showed that Invar 36 is much less stable over extended time (typical dimensional change 2 ppm/yr) than Super Invar or several nonmetallic low-expansion materials (see Figure 3.16). Patterson (1990) attributed the high stability of Super Invar to the amount of mechanical work performed on the material during its manufacture. It is sometimes desirable to plate Invar or Super Invar parts with nickel or chromium to reduce their tendency to oxidize.

3.4.5 MAGNESIUM

Reasonable strength and lightness of weight make magnesium a good candidate material for many opto-mechanical applications in which it can be protected from corrosion by coating or anodizing. It is not as strong as aluminum, but its strength-to-weight ratio is about the same. Parts can be made by casting; by machining from wrought bars, plates, or sheets; and by forging. Because of its low wear resistance, inserts of harder materials are generally installed (by heat shrinking or threading) in magnesium parts such as rollers and wheels. Properties of two commonly used magnesium types are listed in Table 3.18. A proprietary coating that improves corrosion resistance of magnesium parts is described in Section 3.7.

It is well known that parts made of dissimilar materials should be chemically compatible, separated physically, or protected by appropriate intermediate materials so that they cannot form a galvanic couple. Stainless steels, titanium, copper, and aluminum alloys are particularly active from a corrosion resistance viewpoint if in contact with magnesium. Organic films such as baked vinyl plastisols, epoxies, and high-temperature-resistant fluorinated hydrocarbon resin coatings can be used as corrosion insulation between these dissimilar metals.

Magnesium alloy MIA is nearly pure magnesium. Because of its good damping properties, it can be useful for vibration isolation of critical components.

3.4.6 CARBON STEEL

Because of the almost universal demand for lightweight in optical instruments, the use of conventional steel products as differentiated from the corrosion-resistant and low-expansion varieties is generally limited to test and support equipment. Exceptions occur, of course, when high strength, high endurance, good wear, magnetic properties, or other special requirements apply that can best be met by steel. The most commonly used types are low-carbon and high-carbon (spring) steels. Most types machine and weld well. Painting, coating or plating is required for corrosion resistance. The characteristics of one variety of low-carbon steel are listed in Table 3.18.

3.4.7 CORROSION-RESISTANT STEEL

Corrosion-resistant (CRES) or stainless steels contain at least 12% chromium by weight and owe their corrosion-resisting properties to a film of chromium oxide that forms on their surfaces. Their ductility and hardness values are higher than those of carbon steels. The 300 series or austentitic stainless steels are not magnetic, but the 400 series ferritic varieties are magnetic. As a class, these metals are difficult to machine owing to their high work-hardening nature. A few varieties (including type 416 described in Table 3.18) are more easily machined because they contain additives such as sulfur or selenium. The corrosion resistances of such free-machining varieties are somewhat reduced.

Stainless steels may be heat treated for annealing, hardening, or stress-relieving purposes, depending on the application requirements. All types can readily be welded to the same or other types of CRES steels. Brazing in a vacuum or hydrogen atmosphere is preferred for attaching stainless steel to other metals. The 300-series CRES types can lose their corrosion resistance after welding owing to a change called *sensitization*, which is the forming of chromium-free regions near the welds. This change does not occur in a CRES variety that has an “L” designation, such as 304L, (Sarafin et al., 1995.) The 400-series CRES varieties can become brittle at low temperatures.

3.4.8 TITANIUM

Titanium is a medium-density, nonmagnetic metal that can be highly strengthened by alloying and deformation processing. It is resistant to corrosion because of a tenacious layer of titanium dioxide that readily forms on its surfaces. It has a CTE compatible with many common, crown-type, optical glasses. Hence, it is frequently used in cells and lens barrels for high-performance optical systems exposed to large temperature variations. The variety (Ti6Al4V) described in Table 3.18 has 6% aluminum and 4% vanadium by weight. Its favorable properties include fair workability and castability. During machining, cutters wear rapidly. Joining by brazing is routine; welding can be accomplished, but may cause changes in material properties because of reaction with oxygen at high temperatures (above 600°F [315°C]). Good welds can be made by electron beam and laser techniques, or by employing inert cover gases (such as nitrogen or argon). Titanium parts can also be made by powder metallurgy methods including HIP.

Vukobratovich (2004) indicated that a suitable heat treatment for stress-relieving titanium (especially the 6Al-4V version) has been defined in a handbook by Wood and Favors (1972). The handbook says that stress relief in titanium is exponential with respect to time and also depends upon temperature. Specifically, at 500, 700, 900, and 1100°F, about 10, 15, 60, and 95%, respectively, of the stress is relieved in 1 h. For most practical purposes, about 2 h at 1100°F would suffice. Heat treating should be accomplished in a vacuum furnace with the temperature reduced to about 700°F before air is admitted into the chamber for final cooling. This treatment also produces good dimensional stability in titanium; increasing the temperature, on the other hand, does not significantly improve that property of the material.

3.4.9 SILICON CARBIDE

Silicon carbide (SiC) is a composite ceramic material produced in many types and grades by several methods, including reaction bonding or sintering, CVD, hot pressing, and HIP. As a class, SiC has high strength, stiffness, thermal conductivity, and hardness. Density is moderate, as is its CTE. Compared to Be, it has a lower CTE and only slightly lower specific stiffness. It is less fragile than glass, can withstand high heat loads, and has low thermal distortion characteristics. SiC has an advantage over other materials in that it can be tailored to some extent by varying the composition. Key mechanical characteristics of three versions of SiC are given in Table 3.14. Additional information about materials made by four production techniques may be found in Table 3.21.

An important application of SiC is in mirrors. This topic is considered in depth in Section 13.5.3.

3.4.10 COMPOSITE MATERIALS

A composite material is one in which two or more materials are bonded together. Four general classes of these are polymer (resin) matrix composites (PMCs), metal matrix composites (MMCs), ceramic matrix composites (CMCs), and carbon matrix composites, including carbon/carbon matrices (CCCs). They all offer the advantage over single-component materials in that their characteristics, notably CTE, can be adjusted by varying the composition during fabrication. The reinforcements may be continuous (aligned fibers) or discontinuous (chopped fibers, whiskers, particles). Typical continuous reinforcement materials are graphite, glass, and aramid (Kevlar™ and Spectra™) fibers. Zweben (1999) provided tables of physical properties of a variety of composites. One of these is shown here as Table 3.22. Some other types of fibers are used for optical instrument applications, but these are primarily proprietary materials, so their characteristics are not readily available.

The most important types of composites for optical instrument applications are PMCs and MMCs, so we will concentrate on those types here. Table 3.23 compares several varieties for aerospace applications. Much of this information applies to opto-mechanical components and structures. Note that this table distinguishes between carbon and graphite fibers. Manufacturing processes for each type are described by Lubin (1982). Carbon fibers have higher ultimate tensile strengths but lower Young's moduli (i.e., are less stiff) than graphite fibers.

The resins used in polymer matrix composites may be thermosetting or thermoplastic. The former are most widely used. They cure by reaction linking of long polymer chains. Once cured, these resins cannot be reconstituted or melted. Included in this type are epoxies, bismaleimides, polyimides,

TABLE 3.21
Characteristics of Major Silicon Carbide Types

SiC type	Composition	Density	Fabrication Process	Properties[a]	Remarks
Hot pressed (HP)	$>$ 98% alpha plus others	$>$ 98%	Powder pressed in heated dies	High E, ρ, K_{ic}, MOR; lower k	Simple shapes only; size limited
Hot isostatic pressed (HIP)	$>$ 98% alpha/beta plus others	$>$ 99%	Hot gas pressure on encapsulated preform	High E, ρ, K_{ic}, MOR; lower k	Complex shapes possible, size limited
Chemically vapor deposited (CVD)	100% beta	100%	Deposition on hot mandrel	High E, ρ, k; lower K_{ic}, MOR	Thin shells or plates, built-up shapes
Reaction bonded (RB)	50–92% alpha plus silicon	100%	Cast prefired or porous preform fired with silicon infiltration	Lower E, ρ, MOR, k; lowest K_{ic}	Complex shapes readily formed, large sizes, properties are silicon-content-dependent

[a] MOR = modulus of rupture, K_{ic} = plane strain fracture toughness.

Source: Adapted from Paquin (1997a).

TABLE 3.22
Physical Properties of Selected Unidirectional Polymer Matrix Composites

Fiber Type[a]	Density (g/cm³; lb/in.³)	Axial CTE (10⁻⁶/K; 10⁻⁶/°F)	Transverse CTE (10⁻⁶/K; 10⁻⁶/°F)	Axial Thermal Conductivity (W/m · K; Btu/h · ft ·°F)	Transverse Thermal Conductivity (W/m · K; Btu/h · ft ·°F)
E-glass	2.1 (0.075)	6.3 (3.5)	22 (12)	1.2 (0.7)	0.6 (0.3)
Aramid	1.38 (0.050)	−4.0 (−2.2)	58 (32)	1.7 (1.0)	0.1 (0.08)
Boron	2.0 (0.073)	4.5 (2.5)	23 (13)	2.2 (1.3)	0.7 (0.4)
Standard carbon (PAN)[b]	1.58 (0.057)	0.9 (0.5)	27 (15)	5(3)	0.5 (0.3)
Ultrahigh modulus carbon (PAN)	1.66 (0.060)	−0.9 (−0.5)	40 (22)	45 (26)	0.5 (0.3)
Ultrahigh modulus carbon (pitch)	1.80 (0.065)	−1.1 (−0.6)	27 (15)	380 (220)	10 (6)
Ultrahigh thermal conductivity (pitch)	1.80 (0.065)	−1.1 (−0.6)	27 (15)	660 (380)	10 (6)

[a] Fiber volume fraction of 60% is assumed.

[b] PAN is polyacrilonitrile.

Source: From Zweben, C., *Proc. SPIE*, 3786, 148, 1999.

cyanate esters, thermosetting polyesters, vinyl esters, and phenolics. These differ significantly with regard to their ability to withstand high temperatures; epoxies are usable to about 120°C (250°F), bismaleimides to about 200°C (390°F), polyimides to about 250°C (500°F), and cyanate esters to about 205°C (400°F). All tend to absorb moisture and outgas in a vacuum. Cyanate esters perform best and are increasingly replacing epoxies as the preferred type of resin for optical applications. Thermoplastics intertwine during curing, but do not link. This allows the thermoplastic varieties to be melted, solidified, and remelted.

Composite materials with continuous fiber reinforcements are multilayer assemblies of laminae or plies that are tape-like or like woven cloth. The fibers in stacks may all be aligned in one direction or aligned in different directions. The orientation makes them orthotropic (unidirectional) or quasi-isotropic (multidirectional) with regard to resistance to in-plane (shear) loading. The former arrangement is used to create tubes and axially loaded structures while the latter arrangement is used in panels or face sheets for sandwich structures. Figure 3.17 shows two forms of quasi-isotropic lay-ups. In view (a), there are eight plies of unidirectional cloth at various orientations. In view (b) we see four plies of bidirectional cloth. Typically, each unidirectional ply has a thickness between 0.00125 and 0.01 in. (0.032 to 0.254 mm) with 0.005 in. (0.127 mm) the most commonly used value. Multidirectional plies usually are 0.0025 to 0.01 in. (0.064 to 0.254 mm). Once again, the most common value is 0.005 in. (0.127 mm).

It is a relatively straightforward task to create a structure with near-zero CTE from composites. One such application using a carbon-reinforced epoxy composite was in the trusses that form the main structural members of the Hubble Space Telescope. This application is discussed in Section 14.5.2.

Mechanical characteristics of three grades of aluminum MMCs are given in Table 3.17. An example of one metal matrix composite (MMC) is SXA,[§] which is produced by powder metallurgy techniques using a type of aluminum alloy such as 2124-T6 reinforced with an ultrafine dispersion

---

[§] SXA is a trademark of Advanced Composite Materials Corporation, Greer, SC.

TABLE 3.23
Comparison of Metal Matrix and Polymer Matrix Composite Materials

Material	Advantages	Disadvantages	Typical Applications
Metal Matrix			
SiC/Al (Discontinuous SiC particles)	Isotropic Large database 1.5 times the modulus and strength of aluminum alloys at the same mass density	Most are not weldable Machinable, but high tool wear Lower ductility than conventional aluminum alloys Limited flight heritage	Truss fittings Brackets Mirrors and optical benches
B/Al (Continuous boron fiber)	High strength vs. weight Low coefficient of thermal expansion	Anisotropic Expensive	Truss members Shuttle payload doors
Polymer Matrix			
Aramid/Epoxy (e.g., Kevlar™ or Spectra™ fibers with epoxy matrix)	Impact resistant Lower density than graphite/epoxy High strength vs. weight	Absorbs water Outgasses Low compressive strength Negative coefficient of thermal expansion	Solar array structures Radio frequency (RF) antenna covers (Radomes)
Carbon/Epoxy (High-strength fiber)	Very high strength vs. weight High modulus vs. weight Low coefficient of thermal expansion Flight heritage	Outgasses (matrix-dependent) Absorbs water (matrix-dependent)	Truss members Face sheets for sandwich panels Optical benches Monocoque cylinders
Graphite/Epoxy (high-modulus fiber)	Very high modulus vs. weight High strength vs. weight Low coefficient of thermal expansion High thermal conductivity	Low compressive strength Ruptures at low strain Absorbs water and outgasses (matrix-dependent)	Truss members Antenna booms Face sheets for sandwich panels: Optical benches Monocoque cylinders
Glass/Epoxy (Continuous glass fiber)	Low electrical conductivity Well-established manufacturing processes	Higher density than graphite/epoxy Lower strength and modulus than graphite/epoxy	Printed circuit boards Radomes

Source: From Sarafin, T.P., Heymans, R.L., Wendt, R.G., Jr., and Sabin, R.V., in *Spacecraft Structures and Mechanisms*, Sarafin, T.P., Ed., Microcosm, Inc., Torrance and Kluwer Academic Publishers, Boston, 507, 1995, chap. 15. With Permission.

of silicon carbide whiskers or particles. The SiC tends to strengthen and stiffen the aluminum and increase the material’s resistance to creep. Available in structural, instrument, and optical grades, the CTE of SXA can, within limits, be adjusted to match that of interfacing materials or coatings such as nickel. Components such as mirror substrates or structural members can have thinner cross

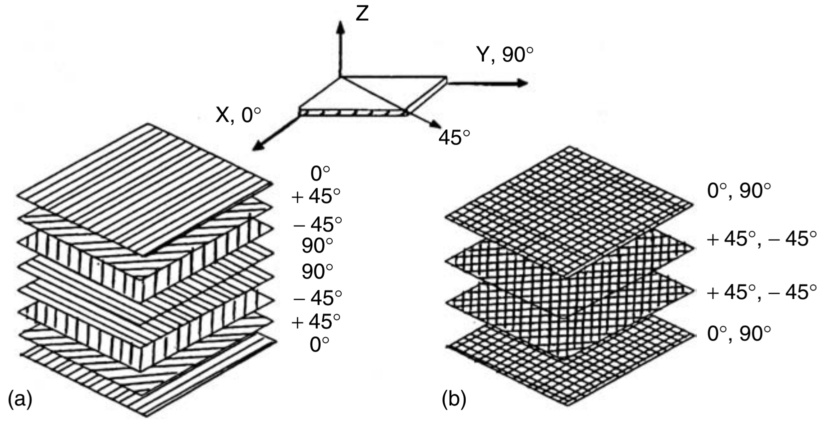

FIGURE 3.17 Examples of quasi-isotropic laminated composite sheets comprising (a) eight unidirectional plies and (b) four bidirectional plies arranged at the indicated angles. (Adapted from Sarafin, T.P., Heymans, R.L., Wendt, R.G., Jr., and Sabian, R.V., in *Spacecraft Structures and Mechanisms*, Sarafin, T.P., Ed., Microcosm, Inc., Torrance and Kluwer Academic Publishers, Boston, 507, 1995, chap. 15.)

sections or be lightweighted by machining pockets or holes without sacrificing stiffness, in contrast to the unreinforced base material. It can also be produced as foam to give good structural properties with very low weight. Applications of SXA to optical instruments, aircraft structural parts, guidance systems, etc., have been described by Ulph (1988), Mohn and Vukobratovich (1988), Pellegrin et al. (1989), Vukobratovich (1989), and Vukobratovich et al. (1995). Some uses of SXA in mirrors and structures are discussed in Chapters 13 and 14, respectively.

AlBeMet162^R is a proprietary material manufactured by BrushWellman of Elmore, OH. By weight, it contains 62% commercially pure beryllium and 38% commercially pure aluminum, and is ~22% lighter, ~3 times stiffer, and more thermally stable than aluminum. The material is available as rolled sheet, HIPed bar, extruded bar, and near net shape forms. It can be welded, brazed, and coated like aluminum.

Parsonage (2005) reported that this material appears to be well suited for use in mirror substrates. Tests conducted in 1998 on a 15 cm (5.90 in.) diameter mirror with ELN plating that had been polished to 20 nm rms optical figure and < 10 Å surface roughness retained its figure when cycled from −50°F to +150°F (−45°C to +65°C). When retested after 4 years, the mirror's figure quality remained the same, so the material's stability is also good. Testing of other mirrors of this type is continuing in an attempt to determine its maximum useful temperature range.

3.5 ADHESIVES

Two general classes of adhesives are widely used in opto-mechanical instruments: optical cements are used to hold together refracting surfaces (as in a cemented doublet lens or in interconnects between optical fibers), while structural adhesives are used to hold together mechanical members or to attach optical components to mechanical components. In the former class, the adhesive must be transparent and homogeneous in the spectral region of interest, whereas in the latter, transmission through the adhesive is not essential. We consider both classes of adhesives in this section.

3.5.1 Optical Cements

The desired properties of optical cements were listed by Hunt (1967) and Mahe et al. (1979) in detailed assessments of the available types. Table 3.24 is an adaptation of those lists for a generic product. The thrust of the historical evolution of cement varieties from natural resins (tree sap) to sophisticated polymers has been to improve product characteristics along these lines (see Magyar,

TABLE 3.24
Desirable Properties of Optical Cements

Optical Properties

- High light transmission in the spectral region of interest
- Colorless (i.e., minimum spectral variation of transmission)
- Refractive index matching interfacing optical materials
- Minimal fluorescence
- Homogeneous and free of strain after curing

Mechanical Properties

- Minimal shrinkage on curing
- Resistant to vibration and mechanical and thermal shock
- Stable over an extended temperature range
- Resistant to UV and high-energy radiation (including lasers)
- Resistant to moisture
- Adequate adhesion in thin layers

Chemical and Biological Properties

- Chemically stable
- Inert to interfacing materials
- Nontoxic
- Resistant to fungal attack

Operational Properties

- Easily prepared to desired cleanliness and viscosity
- Compatible with alignment of freshly cemented elements within a reasonable time period
- Capable of decementing, if necessary
- Easily transported, stored, and used

Sources: Adapted from Hunt, P.G., *Optica Acta*, 14, 401, 1967.; Mahe, C., Nicolay, N., and Marioge, J.P., J. Opt. (Paris), 10, 41, 1979.

1991). The four basic types of optical cements available today provide refractive indices in the range ~1.47 to ~1.61. Descriptions of each type follow.

3.5.1.1 Solvent Loss Cements

These viscous solutions of high-molecular-weight natural or synthetic substances cure by elimination of solvent at an elevated temperature. Considerable volume shrinkage occurs on curing, so annealing is required to minimize strain. Canada balsam is an example. Its refractive index (n_D) is ~1.53. Adhesion is poor. Cemented components can be separated by application of dry heat or heating in an organic solvent such as trichloroethylene or xylene.

3.5.1.2 Thermoplastic Cements

These are clear or lightly colored solids that liquefy on heating to about 120°C (248°F). Slow cooling is essential. Cellulose caprate is an example. Its refractive index (n_D) is ~1.48. The cure process is reversible, so cemented elements can be separated by reheating.

3.5.1.3 Thermosetting Cements

These are basically two-component systems with a short useful life after mixing. Cementing and alignment of the elements are done at room temperature. One product that is widely used is

Summers Type C59 Lens Bond. Its refractive index at 25°C (77°F) is ~1.55. It cures in less than 2 h at 70°C (160°F), but the actual time depends on the catalyst ratio. Room-temperature cure of this cement requires 3 to 6 d. Cleanup of excess cement can be accomplished with acetone. Exposure of the joint edge to excess solvent should be avoided. Boiling in a proprietary solvent available from the manufacturer can separate cured elements.

A two-component cement formulated with a plasticizer ingredient so as not to cause excessive stress in thin optical elements upon curing is Summers RD3-74 Lens Bond. Room-temperature cure for 24 to 36 h, depending on the catalyst ratio, is recommended, although cure at 70°C (160°F) can be accomplished in 30 min after a 30 min precure at room temperature. The refractive index of this cement also is ~1.55 at 25°C (77°F). U.S. military specification MIL-A-3920 prescribes physical parameters, method of application, and procedures for testing thermosetting optical cements. Commercially available cements that reportedly meet this specification include Norland NOA 61 and Summers C-59, M-62, and F-65.

3.5.1.4 Photosetting Cements

These are colorless, one-component adhesives that are cured by exposure to UV light. Maximum absorption is in the wavelength range of 0.254 to 0.378 μm. Application and cure are at room temperature. Norland NOA 61 is a typical example of such adhesives. Its refractive index is ~1.56. Another example is Summers UV-69 Lens Bond, which has a refractive index of ~1.55 at 25°C (77°F). Generally, curing of this type of cement is done in two steps: a short exposure (typically to a UV sunlamp at 12 in. [30.5 cm] for 20 min) followed by a 90 min exposure to the same lamp at the same distance. With a long-wave UV (366 nm wavelength) fluorescent-tube light source, 10 min first exposure followed by 60 min second exposure, both at 1 in. (2.5 cm), is recommended. Cemented parts can be handled carefully after first exposure. For maximum stability, the joint should experience a full cure before handling.

Various companies make UV photosetting cements that cure sufficiently for gentle handling of the cemented elements after even shorter exposures to UV light. This allows removal of the assembly from the holding fixture and cleaning. For example, Summers UV-74 Lens Bond precures with only a 20 sec exposure to a source such as a General Electric 15-W F-15-T8 fluorescent tube at 1 in. (2.5 cm). Full cure is accomplished by an additional exposure of 60 min duration under the same irradiation conditions. Although U.S. military specification MIL-A-3920 applies to thermosetting adhesives, Summers Laboratories claim that their Type UV-74 Lens Bond will also meet the requirements of that specification.

For the minimum effect of cement-induced mechanical distortion on the transmitted wave front, exposure of the entire joint area to uniform UV illumination for the full cure cycle duration before removing the unit from the cementing fixture is advisable. Wimperis and Johnston (1984) reported interferometric quality results (< 0.1 wave peak-to-peak wave front distortion at 0.546 μm) with 20-μm (0.0008-in.) thick layers of NOA 61 adhesive between quartz flats cured by exposure to illumination uniform to $< 10\%$ spatial variation over a 10 cm (3.9 in.) diameter.

The solvent resistance of photosetting cements is high, especially after aging for about 3 weeks. Separation can usually be accomplished only after the initial cure, but before the final cure. Soaking overnight in methylene chloride has occasionally proven successful. It is important to check alignment of cemented elements after the first cure.

Although the bond strength of UV-cured cements is adequate for many optical element-bonding applications, it is not as high as that of two-component thermosetting varieties. Magyar (1991) explained this, in part, to be a result of the incomplete acid–base reaction between the more alkaline glasses and the more acid cement after the UV cure. He indicated that subjecting the UV-cured cemented assemblies to an elevated temperature of perhaps 60 min duration at 40°C (104°F) would improve intermolecular linking and enhance the strength of the bond.

TABLE 3.25
Typical Physical Characteristics of a Generic Optical Cement

Refractive index n after cure	1.48 to 1.55
Thermal expansion coefficient (27 to 100°C)	63 ppm/°C (35 ppm/°F)
Young's modulus E	43×10^{10} Pa (62×10^6 lb/in.^{2})
Shear strength	36×10^6 Pa (5200 lb/in.^{2})
Specific heat c_p	837 J/kg · K (0.3 Btu/lb · °F)
Water absorption (bulk material)	0.3% after 24 h at 25°C
Shrinkage during cure	< 6%
Viscosity	200 to 320 cps
Density	1.22 g/cm^3 (0.044 lb/in.^{3})
Hardness (shore D)	Approximately 90
Total mass loss in vacuum	3 to 6%

3.5.2 PHYSICAL CHARACTERISTICS

Since most modern adhesives used for cementing optical surfaces together are basically the same, except for additives such as promoters and initiators, their physical characteristics are similar. If more specific information regarding a particular type of cement is not available, the general characteristics listed in Table 3.25 can be used for engineering purposes, at least through the preliminary stages of design.

3.5.3 TRANSMISSION CHARACTERISTICS

The optical cements discussed above are usable only in the near-UV to near-IR region because of transmission limitations. Figure 3.18 shows the spectral transmittance of a typical cement, Norland NOA 61 photosetting polymer. Its absorptance in the UV is representative of many synthetic cements.

Pellicori (1964) showed that Canada balsam and cellulose caprate transmit to slightly shorter wavelengths (typically ~50% transmission at 0.30 and 0.24 μm, respectively). He also indicated that some silicone elastomers have favorable characteristics as cements for use in the UV region. Later, Pellicori (1970) reported tests of five silicone elastomers, one of which (Dow Corning DC93-500) transmitted > 50% in a 0.066-mm (0.0026-in.) thick layer for wavelengths longer than ~0.23 μm, even 7 months after having been irradiated with 2×10^6 rad of 10 MeV electrons. At longer wavelengths, $0.32 < \lambda < 2.2$ μm, these elastomers displayed negligible absorption in 0.060 mm (0.0002 in.) thicknesses. Sedova et al. (1982) described the use of catalyzed polydimethyl siloxane rubber as the basis for a UV-transmitting cement, called UF-215, that transmitted to 0.215 μm.

Since cured silicone-based cements tend to be somewhat flexible, they have found favor as bonding agents for materials with widely differing thermal expansion coefficients (see, e.g., Ivanova et al., 1973). In Chapter 5, we report the use of Sylgard XR-63-489 silicone compound in such an application. We also note there that this adhesive resists intense, transmitted, laser radiation at 1.06 μm. Unfortunately, this material is no longer available. Similar materials may exist.

Pellicori (1991) reported the successful use of the above-mentioned Dow Corning compound (DC93-500) to bond calcite crystals that later survived the adverse thermal and high-energy particulate radiation exposure of a journey beyond Jupiter without degradation. This sealing compound was sufficiently flexible to tolerate the crystal's asymmetric thermal expansion characteristics. The application required transmission of UV radiation and the chosen cement met this requirement. It has an extremely low (0.25%) weight loss in vacuum and is considered suitable for space application as an encapsulant or for bonding cover glasses to solar cells.

Packard (1969) reported the transmission of Araldite 6010, a liquid epoxy resin, over the spectral region 2 to 14 μm. This adhesive has been used to cement infrared detectors to optical substrates (such

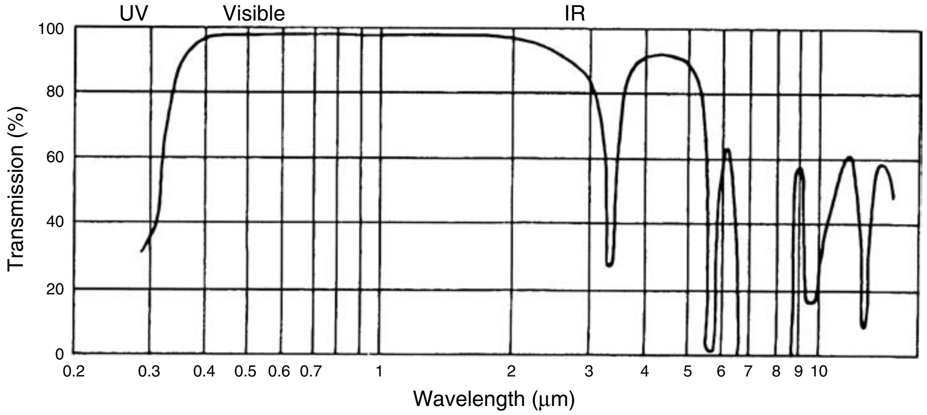

FIGURE 3.18 Spectral transmittance vs. wavelength of a typical photosetting optical cement (Norland NOA 61) over the range 0.2–17 µm. (Courtesy of Norland Products, Inc., Cranbury, NJ.)

as lenses) made of Irtran 2 or barium fluoride. Ishmuratova and Sergeyev (1967) reported the infrared transmission of an organosilicone resin, with a transmission of 82.1% in the spectral range 1 to 8 µm.

Turtle (1987) found that very thin layers (typically < 0.5 µm) of adhesive would reduce absorption effects in the IR to acceptable values, but that tiny particles in the layer or surface irregularities could cause excessive stress concentrations in such thin layers. Because these layers lack flexibility, a thermal expansion mismatch of the elements bonded would cause high-stress conditions at extreme temperatures.

Korniski and Wolfe (1978) described refractive index measurements of eight adhesives over the 1 to 5 µm spectral range. Such information is needed to estimate the Fresnel losses at interfaces between the cement layer surfaces and the element surfaces being bonded for IR applications. These losses can be high with high-index materials. Typically, the reflection coefficient for a cement-to-germanium interface would be about 20% owing to the large index mismatch. An approach to reducing index mismatch effects is to add thin-film coatings of intermediate-index materials to the element surfaces and bond the coated elements. Willey (1990) gave specific examples of this technique to reduce the visible light reflection from high-index glasses at cement layers. He reported the use of aluminum oxide (index ~1.64 at 550 nm) as the intermediate coating. Pellicori (1991) reported a similar advantage of coating germanium with zinc sulfide or zinc selenide before cementing with an epoxy or other adhesive.

Pellicori (1991) suggested the use of compounds such as Epo-Tek 301 (an epoxy), Eastman 910 (a cyanoacrylate), or Eastman HE-S-1 (a modified butyl methacrylate) as possible adhesives for use in the 3 to 5 µm region. He also indicated the possible, but not highly successful, use of high-index materials such as arsenic trisulfide or selenide in relatively thick melted layers to bond IR materials.

3.5.4 CEMENTING OPTICAL SURFACES

A method for cementing optical surfaces together has been prescribed by Sharp et al. (1980). It applies to curved surfaces of essentially the same radius of curvature and to flats. The same general techniques apply to glass and plastic elements. Essential to the method's success is the thorough cleaning of the mating surfaces in a clean room or laminar-flow hood using clean lens tissue with pure solvents such as alcohol, followed by pure acetone immediately before cementing. Sharp et al. (1980) suggested that the mating surfaces, once cleaned, be carefully touched together without cement and the interference fringes examined for evidence of dust. If clean, the surfaces should be left in contact until all preparations have been made for cementing to minimize the chance of contamination. The authors also indicated that cementing should be done within 20 min of final cleaning.

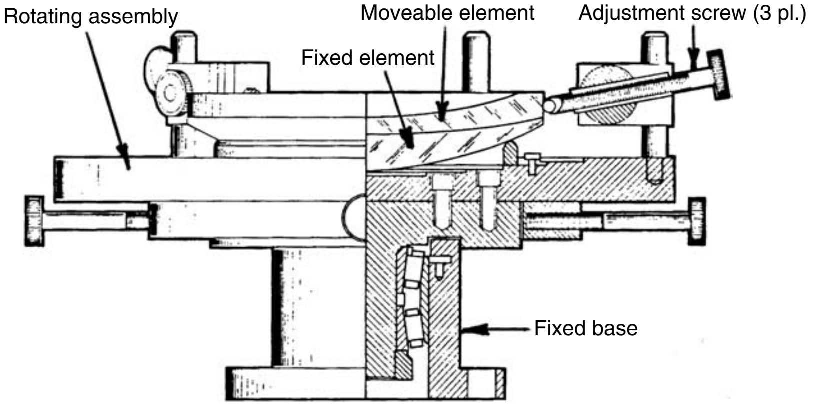

FIGURE 3.19 Diagram showing a fixture for transverse (centering) alignment of lens elements during cementing. (Adapted from Horne, D.F., *Optical Production Technology*, Adam Hilger Ltd., Bristol, England, 1972.)

The cementing procedure is essentially as follows. The upper element of the mated lens pair is raised sufficiently to allow a drop or a few drops of adhesive (determined by the size of the bond) to be placed near the center of the exposed (concave) surface of the lower element. The upper element is then lowered slowly and moved slightly in lateral directions until the cement spreads over the entire lens area. Bubbles of air can be eased out of the cement layer by this procedure. Care must be exercised with less viscous cements to avoid squeezing the layer too thin. Typically, the layer should be 8 to 13 μm (0.0003 to 0.0005 in.) thick. Procedures for cementing components of different configurations with different types of cements are given by Horne (1972). Cement manufacturers may also distribute detailed instructions for use of their products.

It is important in nearly all cemented components that the adhesive layer not be wedged. If the edge thicknesses of both the elements have been measured at three (marked) points around the rim, a wedge introduced into the cement can be detected by measurement of the edge dimensions of the unit after cementing. If the index of refraction differences between the glasses and cement are sufficiently large, interference fringes between the supposedly parallel glass surfaces can be seen under monochromatic illumination. With proper instrumentation, alignment can be checked by this method as the cemented unit cures.

The chamfers around the peripheries of edged elements such as lenses play an important role in achieving a proper bond between their surfaces. These chamfers provide a small reservoir for excess cement around the edge of the cement layer. As the cement cures, its shrinkage draws a small amount of cement from the bevel into the joint. If insufficient cement is squeezed into the bevel or the design does not specify a large enough bevel, improper bonding may occur near the rim of the cemented assembly.

Precision alignment of the mated elements is generally accomplished in a jig or fixture with mechanisms arranged to give three-point, equispaced contact on one spherical surface and to apply lateral forces independently on each element. Standard practice is for the contacts on the upper and lower elements to be 60° out of phase azimuthally. A fixture of this general type is shown in Figure 3.19. Adjustable spring loading of the rim contacts is a desirable feature of the cementing fixture. If UV-curing cements are to be used, the fixture must be designed to facilitate uniform irradiation of the entire cemented aperture.

3.5.5 STRUCTURAL ADHESIVES

Various adhesives have found welcome places in optical instrument design and manufacture as replacements for screws, rivets, clamps, and other forms of fasteners. When used in structural bonding applications, they always function as integral components in the ensemble rather than as separate entities. Bonded structures are often lighter in weight, lower in cost, and easier to assemble than those made by mechanical methods. They also distribute stresses more uniformly than mechanical fasteners and are more or less flexible. This is a highly desirable feature in some applications involving high mechanical forces or when damping is needed. Silicone elastomers are not normally used as adhesives because of their low joint strength, but they are especially useful for sealing and damping, as discussed in the next section.

Most adhesives function by interlocking with microroughnesses on the adherand's surfaces and perform best in compression or shear. Resistance to tensile stress may be slightly lower than resistance to shear. Peel and cleavage should be avoided, if possible. Techniques for cleaning, priming, and bonding with common adhesives are given by Grandilli (1981) and in manufacturers' data sheets. Table 3.26 summarizes key physical characteristics of representative structural adhesives. The selected materials are typical of different types of compounds that might be used for different applications. No attempt was made to include all varieties or all parameters that might be of interest in a particular application. Manufacturers should be contacted for more detailed information prior to use. Testing of chosen materials to confirm or supplant manufacturers' data is advisable for critical applications.

Many of the same adhesives discussed below for structural (i.e., metal-to-metal) applications are usable for securing optical components to mechanical mounts. Typical hardware examples are discussed later in this work. Some silicone elastomers and a few epoxies are useful for cementing optical elements (glass or plastic) to each other, as discussed in the next section. U.S. military specification MIL-A-48611 applies to adhesive systems for glass to metal bonds for military applications. The method for use of these bonding systems is specified in MIL-B-48612.

Adhesives generally contain ingredients that are not chemically integrated into the molecular structure and that may be volatile. Surfaces exposed to vacuum and elevated temperature may release these substances in a process called outgassing, degassing, or "smoking." The volatized material may condense as contaminating films on nearby cooler surfaces. Especially vulnerable are spaceborne optical surfaces, solar cells, thermal control surfaces, and electrical contacts. Some manufacturers' data sheets give the percentage of mass loss at elevated temperature or in vacuum as an indication of the suitability of their products for space applications.

We consider below some of the adhesive materials commonly used for opto-mechanical applications.

3.5.5.1 Epoxies

Epoxy resins are versatile thermosetting resins. As a class, they are strong, have outstanding thermal and adhesive properties, and are formulated as liquid, paste, tape, film, and powdered resins. The liquid and paste forms are widely available as one- and two-component types. Some can be cured at room temperature. Better thermal and mechanical properties result if they are cured at temperatures up to (typically) 350°F (175°C). Some types contain powdered metals or other fillers to improve their properties for particular uses. For example, silver powder increases electrical conduction, aluminum oxide enhances thermal conduction, and silica powder serves as a thickening agent.

3.5.5.2 Urethane Adhesives

Available in one- and two-component forms, the urethane (or polyurethane) adhesives form strong, durable bonds to many types of substrates. Because of their inherent flexibility, they are especially appropriate for use in bonding nonrigid components or ones with differing CTEs. Environmental resistance is inferior to that of the epoxies. The upper temperature limit is 100°C (212°F). They perform well at reduced temperatures.

TABLE 3.26
Typical Mechanical Characteristics of Representative Structural Adhesives

Material (Mfr. code)[a]	Recommended curing time at °C	Uncured Viscosity (cP)	Shear strength MPa (lb/in.^{2}) at °C	Temperature Range of Use (°C; °F)	CTE (α) ($\times10^{-6}$/°C; $\times10^{-6}$/°F)	Joint Thickness (mm; in.)	Young's modulus E (MPa; lb/in.^{2})	Poisson's Ratio ν
One-Part Epoxies								
2214 Regular Gray (3M)	60 min at 121	Thixotropic paste (aluminum filled)	20.7 (3,000) at −55 31.0 (4,500) at 24 31.0 (4,500) at 82 10.3 (1,500) at 121 2.7 (400) at 177	−53 to 121 (−67 to 250)	49 (27) at 0–80°C		~5170 (~7.5 × 10^5)	
Two-Part Epoxies								
Milbond 1:1 (bywt) mix ratio (SO)	3 h at 71 7 d at 25		17.7 (2,561) at −50 14.5 (2,099) at 25 6.8 (992) at 70	−54 to 70 (−65 to 158)	62 at −54 to 20 72 at 20 to 70	0.381 ± 0.025 (0.015 ± 0.001)	592 (8.6 × 10^4) at −50°C 158 (2.3 × 10^4) at 20°C	
2216 B/A Gray 2:3 (by vol.) mix ratio (3M)	30 min at 93 2 h at 66 7 d at 24	~80,000	13.8 (2,000) at −55 17.2 (2,500) at 24 2.7 (400) at 82 1.3 (200) at 121	−55 to 150 (−67 to 302)	102 (57) at 0 to 40°C 134 (74) at 40 to 80°C	0.102 ± 0.025 (0.004 ± 0.001)	~689 (~1.0 × 10^5)	~0.43
2216 B/A Translucent 1:1 (by vol.) mix ratio (3M)	60 min at 93 4 h at 66 30 d at 24	~10,000	20.7 (3,000) at −55 13.8 (2,000) at 24 1.4 (200) at 82 0.7 (100) at 121	−55 to 150 (−67 to 302)	81 (45) at –50 to 30°C 207 (115) at 60 to 150°C	0.102 ± 0.025 (0.004 ± 0.001)	(~6.9 × 10^4) (~1.0 × 10^5)	~0.43
Urethanes								
3532 B/A Brown 1:1 (by vol.) mix ratio (3M)	24 h at 24	30,000	13.8 (2,000) at −40 13.8 (2,000) at 24 2.1 (300) at 82		~0.127 (~0.005)			
U-05FL off-white 2:1 (by vol.) mix ratio (L)	24 h at 25 & 50% RH		5.2 (7.50) at 25			0.076 to 0.229 (0.003 to 0.009)		

TABLE 3.26 (*Continued*)

Material (Mfr. code)[a]	Recommended curing time at °C	Uncured Viscosity (cP)	Shear strength MPa (lb/in.^{2}) at °C	Temperature Range of Use (°C; °F)	CTE (α) ($\times 10^{-6}$/°C; $\times 10^{-6}$/°F)	Joint Thickness (mm; in.)	Young's modulus E (MPa; lb/in.^{2})	Poisson's Ratio ν
UV Curing								
349 Single component (L)	UV Cure at 100 mW/cm^2 Fix: < 8 sec at ~0 gap Full: 36 sec at 0.25 gap	~9,500	11.0 (1,600)	−54 to 130 (−65 to 266)	80 (44)	< 0.35 (< 0.014)		
OP-30 Single-component low stress (DY)	UV Cure at 200 mW/cm^2 10 to 30 sec	400	5.2 (750)	<150 (<302)	111 (62) at 125°C		17.2 (2,500)	
OP-60-LS Single-component <0.1% cure shrinkage (DY)	UV Cure at < 300 mW/cm^2 5−30 sec	80,000	31.7 (4,600)	−45 to 180 (−50 to 350)	27 (15) at < 50°C 66 (37) at > 50°C		6,900 (1.0×10^6)	
Cyanoacrylates								
460 (L)	Fix: 1 min at 22 Full: 24 h at 22 at 50% RH	45	11.7 (1,700)		80 (44)	Very small		

[a] Mfr. code/website: (3M) = 3M/www.3m.com, (SO) = Summers Optical/www.emsdiasum.com, (DY) = Dymax Corp/www.dymax.com, (L) = Loctite/www.loctite.com.

Source: Adapted from Yoder, P.R. Jr., *Mounting Optics in Optical Instruments*, SPIE Press, Bellingham, 2002.

3.5.5.3 Cyanoacrylate Adhesives

These are single-component adhesives that cure by exposure to the alkaline moisture and ionic substances found on most surfaces. For best adhesion to inert or acidic surfaces, a surface activator, or primer, may be applied to speed polymerization. Since they have low viscosity, they work best on smooth, closely spaced surfaces. Cure time to fixate is usually very short, typically less than 30 sec under favorable conditions. Some varieties contain elastomers that increase flexibility and gap-filling capability. Additives of this sort tend to increase cure time. Care in application is advisable since the adhesive will quickly bond skin. Full eye protection should be worn during application.

The limitations of such adhesives include a potential for failure at temperatures above 71°C (160°F), especially at high humidity. The strength of the bond on glass or ceramics may decrease with time. Vapor emitted by uncured adhesive can deposit on adjacent surfaces, leaving a white residue. A typical U.S. military specification applicable to cyanoacrylate adhesives is MIL-A-46050.

3.6 SEALANTS

Silicone rubber elastomers are polymers that are chemically inert and generally function well over temperature ranges of −80 to 204°C (−112 to 400°F). Short exposures to higher temperatures can be tolerated by some varieties. They are compounded to cure at room or elevated temperatures. The room-temperature vulcanizing (RTV) form is especially popular because of its ease of application. The priming of metal surfaces before applying RTV compounds is generally recommended. These elastomers are used primarily to fill voids, seal gaps, and protect surfaces or components from moisture or corrosive reactions with atmospheric compounds. They are generally not considered to be structural adhesives, although lightweight components can in some cases be bonded in place with these materials. Uncured material viscosity varies among different products from free-flowing consistency (sometimes called "self-leveling") to thick paste. Some uncured materials are *thixotropic*, that is, they are gel-like when undisturbed, but become fluid when stirred or shaken. Volatile ingredients may be released from some products during cure or post cure if exposed to a vacuum. This process is referred to as *outgassing*. Special formulations such as Dow Corning DC93-500, have low volatility and, hence, minimum mass loss in vacuum. They are generally used in space applications.

Curing times generally depend on temperature, with the following as typical characteristics: 1 to 2 d at 25°C (77°F), 4 h at 65°C (149°F), 1 h at 100°C (212°F), and 15 min at 150°C (302°F). Those varieties depending on reaction with atmospheric moisture for curing need about 50% relative humidity. Higher humidity reduces cure time slightly. Since these materials cure from the surface inward, full cure at the center of deep volumes may require extended time. Some room-temperature-curing varieties require catalysts to be added. The choice of catalyst determines the cure time. These varieties will cure in any thickness and confined spaces.

Curing may be inhibited by exposure of the elastomer to or contamination of the surfaces to be sealed by sulfur-containing or organo-metallic salt-containing compounds such as butyl or chlorinated organic rubbers or other nonidentical elastomer compounds. The careful selection of materials and equally careful cleaning of surfaces are essential to proper bonding of the sealant to components.

Some varieties of these materials are available in various colors (such as white, black, red, green, etc.) as well as clear and translucent. The thermal conductivity of most materials is about 8.4 $W/m^2 \cdot K$, but a few types are filled so as to increase their conductivities to about five times that value. This improves their usefulness as a flexible potting or encapsulating compound for electronic or other types of components that need to be temperature stabilized.

Table 3.27 summarizes the key physical characteristics of representative sealants. These materials are typical of different types of compounds that might be used for different applications. No attempt was made to include all varieties or all parameters that might be of interest in a particular application. Manufacturers should be contacted for more detailed information prior to use in a design.

TABLE 3.27
Typical Mechanical Characteristics of Representative Sealants

Material (Mfr. Code)[a]	Suggested Curing Time at °C	Uncured Viscosity[b]	Cured Hardness (Shore A)	Temperature Range of Use (°C; °F)	Shrinkage % after 3 d at 25°C	Effluent or mass loss % after hours at °C	CTE (α) ($\times 10^{-6}$/°C; $\times 10^{-6}$/°F)	Tensile Strength (MPa)
One-Part Silicone Products								
732 (DC)	24 h at 25 and 50% RH (0.125 in. bead)	320 g/min 0.125 in. ID orifice at 90 lb/in.^{2} air pressure	25	−60 to 177 (−76 to 350) continuous < 204 (400) intermittent		Acetic acid		2.2 (325)
RTV112 (GE)	24 h at 25 for 3 mm thickness	200 P	25	< 204 (400) continuous < 260 (500) intermittent	1.0	Acetic acid	270 (150)	2.2 (325)
Two-Part Silicone Products								
93–500 10:1 mix by weight (DC)	7 d at 77 and 50% RH		40	−65 to 200 (−85 to 392)	nil	0.16 at 24 h and 125 and < 10^{-6} Torr	300 (167)	
RTV88 200:1 mix by weight (GE)	24 h at 25 and 50% RH	8800 P	58	−54 to 260 (−65 to 500) continuous < 316 (600) intermittent	0.6	Alcohol	210 (117)	5.7 (830)

TABLE 3.27 ***(Continued)***

Material (Mfr. Code)[a]	Suggested Curing Time at °C	Uncured Viscosity[b]	Cured Hardness (Shore A)	Temperature Range of Use (°C; °F)	Shrinkage % after 3 d at	Effluent or mass loss % after	CTE (α) ($\times10^{-6}$/°C; $\times10^{-6}$/°F)	Tensile Strength (MPa)
RTV560 200:1 mix by weight (GE)	24 h at 25 and 50% RH	300 P	55	−115 to 260 (−175 to 500)	1.0		200 (110)	4.8 (690)
RTV8111 ~33/1 mix by weight[c] (GE)	< 72 h at 25 and 50% RH	99 P	45	−54 to 204 (−65 to 400)	1.0	Alcohol	250 (140)	2.4 (350)
Other products								
EC801B/A polysulfide (3M)	tack free: < 72 h at 25 full cure: 1 wk at 25	viscous liquid	>35 to 60 (40 Rex)	–54 to 82 (–65 to 180)				

[a] Mfr. code/website: (3M) = 3M/www.3m.com, (SO) = Summers Optics/www.emsdiasum.com, (DY) = Dymax Corp/www.dymax.com, (L) = Loctite/www.loctite.com.

[b] Units: g/min = grams per minute extrusion rate; P = poise; cP = centipoise.

[c] Vacuum deaerate before use.

Source: From Yoder, P.R., Jr., *Mounting Optics in Optical Instruments*, SPIE Press, Bellingham, 2002.

According to Valente and Richard (1994), Young's modulus E and Poisson's ratio ν for a typical space-grade sealant (Dow Corning DC93-500) are 500 lb/in.^{2} (3.45×106 Pa) and $\sim$0.50, respectively. Vukobratovich (2001) suggested the use of 0.43 for Poisson's ratio of some elastomers. Because of the variability of curing and test conditions as well as lot-to-lot variations, manufacturers do not generally specify opto-mechanical properties for elastomers. The values given in Table 3.27 should be used as "rule-of-thumb" values for preliminary design purposes. More precise values applicable to a particular material in a particular environment should be determined experimentally for high-performance instrumentation applications.

A typical U.S. military specification applicable to silicone sealants is MIL-A-46106. Specification MIL-S-11030 applies to polysulfide elastomers such as 3M EC-801, which is a brushable two-part material customarily used today as a fuel tank sealant. This material was widely used in the United States as a sealant for military optical instruments before the introduction of RTV-type compounds. It is still used occasionally to seal optical components into their mechanical mounts.

3.7 SPECIAL COATINGS FOR OPTO-MECHANICAL MATERIALS

When coatings are mentioned in the context of optical instrument design, one normally thinks first of thin films applied to optical substrates to change the spectral intensity distribution or polarization state of transmitted or reflected radiation incident upon those components. Those types of coatings are not discussed here. Rather, we define a "coating" as a layer of some material or a finish added externally to the surfaces of optical and mechanical parts for the purposes of (a) protecting those parts from damage or degradation of performance due to adverse environmental exposure; (b) of performing a special function such as reducing or increasing absorptivity or emissivity of a component's surface — usually for stray light suppression or thermal reasons; or (c) of providing a more suitable surface for diamond turning or polishing an optic such as a metal mirror to a smooth microroughness condition. For information regarding the design of the traditional thin film optical coatings, the interested reader is referred to other publications such as Macleod (1986), Rancourt (1987), and Willey (1996).

3.7.1 PROTECTIVE COATINGS

As mentioned in Chapter 2, corrosion is a common reaction between a material and its environment. It may exist in the form of *fretting* (due to small relative motions of parts that break down protective oxides on surfaces), *galvanic attack* (due to electron flow between dissimilar materials — usually in the presence of moisture), *hydrogen embrittlement* (due to diffusion of atomic hydrogen into a metal making it susceptible to brittle fracture), or *stress-corrosion cracking* (due to growth of a corrosion pit into a crack under tensile stress). To reduce the effects of corrosion, we apply various types of coatings to exposed surfaces of particularly susceptible materials. Common coatings are discussed here.

3.7.1.1 Paints

Most paints are a mixture of a film-forming binder (for continuity) and pigment (to provide color and opacity). Common types are oil- or water-based paints, varnish (a blend of resin and drying oil), enamel (using varnish or synthetic resin as the binder), or polymers such as acrylic or vinyl. For optical instruments, enamels and polymers are most commonly used, especially in production where fast drying is important. Powder coatings are solids applied to the surface and heated to form a continuous film. Ingredients such as aluminum flakes, zinc dust, glass beads, fungicides, silicones, or catalysts are sometimes added. Proper surface preparation (cleaning and sometimes roughening) and the use of multiple layers, including primers, are typically required for durability.

3.7.1.2 Platings and Anodic Coatings

Cadmium, chromium, and nickel platings are frequently added to other metals to protect their surfaces from corrosion. Ferrous metals can be *galvanized* by dipping in molten zinc, by heating and tumbling in zinc dust (the Sherardizing process), by electrolytic deposition, or by flame spraying with atomized powdered metal (metalizing). Cadmium applied by electroplating is also used on iron parts, but its durability may be impaired by the presence of sulfur in the atmosphere. Carbon steels and the Invars are frequently protected by chrome plating. Usually, a nickel undercoat is applied before coating with chromium. The chromium layer coating is hard, and so serves as a protection against wear and abrasion.

Aluminum alloys are usually protected by a thin aluminum oxide layer formed by making the part serve as the anode in a bath of chromic, sulfuric, or oxalic acid electrolyte. The so-called *anodized* surface so formed adds slightly to the dimensions of the part, so precision positioning and alignment of joined parts must take this into account. The anodic coating is non-conducting and must not be applied to surfaces where electrical contact is required. Some stray light suppression is achieved at other than grazing incidence by a black anodized coating. Some other colors can also be achieved in the anodic coating for cosmetic effects.

To enhance the natural corrosion resistance of stainless steel parts, they may be passivated by making the part the cathode of a low-voltage circuit in a weak acidic electrolyte.

3.7.1.3 Proprietary Coatings

Certain proprietary coatings have become available for application to metals in optical instruments and other applications in recent years. Two such coatings are described here.

The first is a room temperature alkaline electrolytic process that imparts a hard coating to titanium. This coating reduces the tendency for a titanium surface to gall when rubbed on another titanium surface and, in general, improves its wear resistance. In this *Tiodize*® process, produced by Tiodize Co., Inc., Huntington Beach, CA, the coating penetrates the surface and causes no dimensional buildup when a soft outer layer is removed by ultrasonic cleaning or burnishing. This process was used in the manufacture of a high-performance lens system involving interference-fit assembly of titanium lens cells in a titanium barrel as described in Section 5.3.

The second proprietary coating is the *Magnadize*® process by General Magnaplate Corp., Huntington Beach, CA. It increases the corrosion resistance and hardens the surfaces of magnesium parts. After cleaning, the part surfaces are converted chemically to a thin layer of hydrated magnesium oxide, a porous ceramic. This layer is then infused with a polymer or sealant to form the protective coating. This coating is hard, displays low friction, and protects the otherwise vulnerable magnesium surface. Dimensional buildup on the surface is typically 0.0003 to 0.0020 in. (0.008 to 0.051 mm).

Lytle (1995) described special coatings that can be applied to plastic optics to make them reflective. These are usually vacuum-deposited metals such as aluminum or chromium plated onto the optical surface. To make the surface more durable, a dielectric overcoat may be applied over the metal. This is done by vacuum deposition over aluminum films or by spraying or dipping an organic material over chromium. Lytle (1995) also described techniques for applying antireflection, antiabrasion, and antistatic coatings to refracting surfaces of polymer optics such as optical instrument lenses and eyeglasses. These coatings are vacuum deposited or applied by dipping, spraying, or spinning.

3.7.2 OPTICAL BLACK COATINGS

The interior surfaces of many optical devices are blackened to reduce stray light reflections within the system. Absorbing finishes are also needed on baffles and on some structural members such as spiders and vanes as well as on the sensitive surfaces of radiometric detectors and solar collectors and temperature control surfaces of space borne systems. A broad summary of the many types of paints, coatings, and surface finishes available for such purposes, typical measurements, and a large number of references to other pertinent publications may be found in Pompea and Breault (1995). For simplicity, here we define all these surface treatments as *optical black coatings*.

An optical black coating has a combination of characteristics that determine its function. These are (1) inclusion of a light-absorbing material such as a black dye, carbon black particles, or silicon carbide particles; (2) multiple reflections within cavities, craters, or cracks; (3) scattering of the radiation from surface irregularities; and (4) interference of radiation in a multilayer structure. Each of these characteristics is somewhat wavelength dependent, so the optical black coating must be tailored to the specifics of the application. Absorption of energy at one wavelength may also cause reradiation at another wavelength, thereby disturbing the thermal balance of the system.

One widely used type of optical black coating is Martin Black, a dyed anodized coating with protuberances and cavities that works well on aluminum over a broad spectral range (see Figure 3.20). The textures created in some other optical black coatings are similar to that of Martin Black, while others resemble arrays of overlapping elongated particles or arrays of vertical tubular structures. All have characteristic features with lateral dimensions measuring a few micrometers in size.

Important considerations in the choice of type of optical black coating include sensitivity to temperature extremes and changes, to vibration and shock, to solar and nuclear radiation, to abrasion, and to moisture. For space applications, the potential exists for micrometeorite damage, outgassing, problems related to gravity release, weight loss due to exposure to atomic oxygen, and aging. A variation of Martin Black (called Enhanced Martin Black) has been created to enhance its durability when exposed to atomic oxygen in low Earth orbit. Most optical black coatings are fragile and hard to clean when they pick up dust or other debris. Some coatings are especially sensitive to damage during application or from subsequent handling. These coatings sometimes fail from flexure of the substrate, so structural stiffness is important. Pike and Mehrotra (1999) described a rugged proprietary coating originally developed for thermographic applications in the 8 to 14 μm spectral band that has been found to be useful as a stray visible light suppressant in optical instruments.

A common measurement of performance of an optical black coating is its bidirectional reflectance distribution function (BRDF), which is defined as the ratio of reflected radiance to incident irradiance. This function typically varies with angle of incidence and wavelength of the radiation. The various sources of attenuation mentioned above tend to diffuse incident radiation at any given localized area on the coated surface so that the usual specular reflection from the surface is converted into a three-dimensional lobe of finite lateral extent ranging from fractions of a degree to tens of degrees. The surface therefore becomes more Lambertian as it reduces radiance.

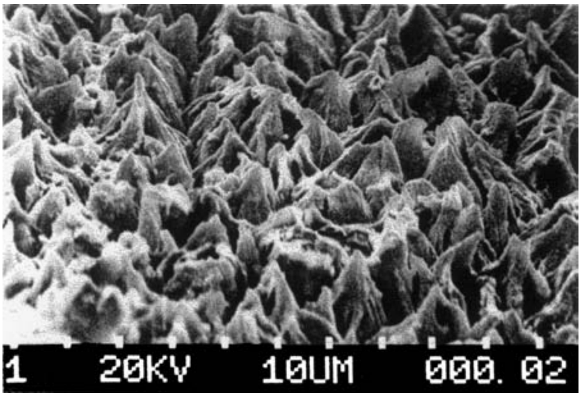

FIGURE 3.20 Scanning electron micrgraph of Martin Black, a dyed anodized aluminum surface for UV, visible, and IR light attenuation applications. (Photo courtesy of Stephen M. Pompea, Pompea and Associates, Tucson, AZ.)

Pompea and Breault (1995) correctly pointed out that selection of the appropriate optical black coating for any application is a systems issue and should be considered early in the design process. All aspects, including location in the system, substrate materials, spectral requirements, availability of information needed for design, performance requirements, effects elsewhere in the system, manufacturability, environmental degradation, maintenance, cost, and schedule should be thoroughly examined.

3.7.3 COATINGS TO IMPROVE SURFACE SMOOTHNESS

3.7.3.1 Nickel

The optical surfaces of metal mirrors are sometimes plated with electrolytic nickel (EN) or, more frequently, with electroless nickel (ELN). The latter plating is Ni with 8 to 11% phosphorus. Both platings produce a smoother surface than can be produced on the bare substrate. This reduces the radiation scattering characteristics of the surface. Typical requirements for mirror surface roughness for infrared applications are about 40 Å rms. This can only be achieved by plating, followed by diamond turning and polishing of the nickel surface. These platings are discussed further in Section 13.7.

Because the CTE of nickel, 13.5×10^{-6} °C^{-1}, is significantly different from that of typical metals used for mirrors, such as aluminum with a CTE of 20.3×10^{-6} °C^{-1} or beryllium with a CTE of 11.5×10^{-6} °C^{-1}, bimetallic effects can occur as the temperature changes. Vukobratovich et al. (1997) and Moon et al (2001) analyzed these effects for a 180 mm-diameter 6061-T651 aluminum alloy mirror of different configurations to be used at 65 K. As discussed further in Section 13.7, a previous contention that plating both sides of the mirror with the same type and thickness nickel coating would eliminate the bimetallic effect was not found to be universally true. Nor was it found that increasing mirror thickness would prevent mirror distortion. Finite element analysis is needed to accurately define the magnitude of the problem for any given design.

3.7.3.2 Alumiplate®

This proprietary coating is 99.9+% amorphous aluminum plated onto aluminum parts, such as mirror substrates, to form a layer that can be diamond turned or polished to extremely fine microroughness. It is produced by AlumiPlate, Inc., Minneapolis, MN. The layer is about 0.005 in. (0.125 mm) thick. Because there is minimal bimetallic effect, the coating works well at cryogenic temperatures (see Vukobratovich et al., 1998).

3.8 TECHNIQUES FOR MANUFACTURING OPTO-MECHANICAL PARTS

Creation of an economically producible optical instrument design requires that the design team fully understand the capabilities and limitations of candidate ways in which all opto-mechanical components can be fabricated, as well as the characteristics and idiosyncrasies of candidate materials for those components. In this section, we summarize the most commonly used techniques for making optical and mechanical parts.

3.8.1 MANUFACTURING OPTICAL PARTS

Table 3.28 from Englehaupt (2002) summarizes common methods for shaping, surface finishing, and coating optical components using most of the materials considered in this chapter. In choosing the appropriate combination of methods, it is important that no process, including plating or coating, introduces excessive internal or surface stress into the finished part. One method for making a special kind of optical component not mentioned in Table 3.28 is electroforming reflective surfaces by depositing metal onto a precision mandrel. Nickel, copper, silver, and gold are the most common metals used. Thicknesses up to a few millimeters can be deposited. By careful control of chemistry and the process,

TABLE 3.28
Techniques for Machining, Finishing, and Coating Materials for Optical Applications

Material	Machining Method[a]	Surface Finish Control Method	Coatings
Al alloys 6061, 2024	SPDT, SPT, CS, CM, EDM, ECM, IM	ELN + SPDT + PL Polish with oil distillates + diamond	MgF_2, SiO, SiO_2, AN, AN + Au, ELNiP and most others
Al matrix Al or Al + SiC	HIP, CS, EDM, ECM, GR, PL, IM, CM, SPT	ELN + SPDT + PL	MgF_2, SiO, SiO_2, AN, EN + Au
Low silicon Al castings A-201, 520	SPDT, SPT, CS, CM, EDM, ECM, IM	ELN + SPDT + PL Polish with oil + diamond	MgF_2, SiO, SiO_2, AN, EN + Au and most others
Al silicon hypereutectic 393.2 Vanasil + lower silicon A-356.0	CS, EDM, CE, IM, SPDT, SPT, GR, CM, CM - easier than composite Al-SiC	ELN + SPDT + PL	ELN or ELNIP followed by most others
Beryllium alloys	CM, EDM, ECM, EM, GR, HIP, not SPDT	ELN + SPDT + PL Polish with oil +diamond	None or coat ELN
Magnesium alloys	SPDT, SPT, CS, CM, EDM, ECM, IM	GR, PL with oil + diamond	Similar to Al, ELN
SiC Sintered, CVD, RB, carbon +	HIP/mandrel + GR, CVD/mandrel + GR, molded carbon + reaction with Silane to SiC[b]	GR + PL	Vacuum processes

TABLE 3.28
Techniques for Machining, Finishing, and Coating Materials for Optical Applications *(Contd.,)*

Si	HIP/mandrel, GR, CVD/mandrel	GR + PL	Vacuum processes
Steels	CM, EDM, ECM, Gr, not SPDT	ELN or ELNiP + SPDT + PL	ELN, ELNiP, and most others
Austenitic	CM, EDM, ECM, GR		
PH - 17-5, 17-7	not SPDT		
Ferritic 416			
Titanium alloys	CM, HIP, ECM, EDM, GR not SPDT	PL, IM	ELN + most others Cr/Au
Glass, quartz, Low expansion ULE, Zerodur	CS, GR, IM, PL, CE, SL	PL, IM, CMP, GL (laser or flame)	Vacuum processes Cr/Au, Cr, Ti-W, Ti-W/Au SiO, SiO_2, MgF_2, Ag/Al_2O_3.

[a] Method code - AN = anodize, CE = chemical etch, CM = conventional machine, CMP = chemical mechanical polish, CS = cast, CVD = chemical vapor deposit, ECM = electrochemical machine, EDM = electrode discharge mill, ELNiP = electrolytic nickel phosphorus plate (can replace ELN), ELN = electroless nickel (usually ~11% phosphorus by weight), GL = glaze, GR = grind, HIP = hot isostatic press, IM = ion mill, PL = polish, SPDT = single-point diamond turn, SPT = precision turn with tool other than diamond, SL = slump casting over mold.

[b] An interesting new process by POCO Graphite, Inc., Decatur, TX.

Source: Adapted from Englehaupt, D., private communication, Center for Applied Optics, University of Alabama, in Huntsville, Huntsville, AL, 2002. (a revision and expansion of information from Englehaupt, D., in *Handbook of Optomechanical Engineering*, Ahmad, A., Ed., CRC Press, Boca Raton, FL, 1997, chap. 10.)

internal stress can be minimized. Typical applications for the electroforming process are small mirrors, conical reflectors used to concentrate energy onto detectors, and larger mirrors for x-ray telescopes and microscopes. Details as to the process may be found in Englehaupt (1997).

As mentioned in our discussions of tolerancing optical system dimensions and conducting design reviews in Chapter 1, participation by optical manufacturing, metrology, and quality control personnel in those important elements of the design process is vital to success of the project.

Optical shop methods and processing materials have been described by such authors as Malacara (1978), DeVany (1981), Karow (1995), and Englehaupt (1997). Numerous conferences and workshops dealing with optical fabrication and testing have been sponsored over the years by the Optical Society of America (OSA), the International Society for Optical Engineering (SPIE), the European Optical Society (EOS), the Deutschen Gesellschaft für angewandte Optik (DGaO), the International Commission for Optics (ICO), and other organizations. Proceedings from such events provide guidance in those areas. In addition, technical papers on related subjects (too many to list here) have been published in the technical journals of the international optical communities.

3.8.2 MANUFACTURING MECHANICAL PARTS

With regard to designing mechanical components for production, Phinney and Britton (1995) encouraged design teams to consult manufacturing people — machinists, assembly technicians, welders, etc. — early in the design phase to promote mutual understanding of potential fabrication problems and to find ways to alleviate, or at least reduce, the magnitude of these problems. Making the hardware easier to build through this cooperative effort will also increase the reliability of the product. Anticipating the need for and making provisions in the design for easy disassembly will facilitate fixes of internal problems discovered during assembly or even after the instrument is fully assembled and under test.

Table 3.29 describes the basic ways to make mechanical parts. All are used from time to time in optical instrument fabrication, but the ones most frequently employed are machining, casting, and forging or extrusion. The latter two usually involve the first, since parts roughly shaped by casting or forging generally need to be finished by machining, at least to create interfaces with other parts or to remove excess material. Here, we summarize some important aspects of these three key fabrication methods. We also consider the manufacturing processes used to fabricate and cure parts made of composite materials.

3.8.2.1 Machining Methods

Machining is the process of removing material by cutting or grinding. It includes such processes as sawing, milling, filing, boring, drilling, reaming, broaching, threading, grinding, polishing, honing, and buffing. The part being machined may be stationary and the tool rotates or translates or the tool is stationary and the workpiece rotates or translates (see Boothroyd and Knight, 1989). It is important to design the part so that it can be machined with a minimum number of setups and operations, with as few tools as possible, and so it can easily be inspected. The choice of material for a given part should take into consideration the compatibility of that material with the machining process. For example, Figure 3.21 shows the variability of time required to machine an equal amount of material from a given part if it is made of different metals. Assuming that the function of the resulting part is the same for each case, time generally equates with cost and should influence material choice. The dimensions of each part (such as wall thickness) should be adequate to ensure stability during machining, and features such as fillets at intersections of milled surfaces should have generous radii to accommodate cutting with the same tool that is used to shape the surfaces. In some cases, the design of a given part can be created in such a way that will allow it to be made by more than one standard method. This would give the machinist more flexibility in choosing the method that best applies available tools or machines.

TABLE 3.29
Basic Processes for Fabrication of Metal Mechanical Parts

Process	Description	Advantages	Disadvantages
Machining	Remove material by cutting or grinding	Can achieve many shapes and virtually any dimensional tolerance and surface finish; does not degrade material strength; can be automated with numerical control programs	Can be expensive (machining time and material waste); can require expensive tools; can result in detrimental residual stresses
Chemical milling (etching)	Remove material by immersing the part into a chemical solution	Can achieve thinner walls than machining; can remove material from parts with two axes of curvature	Very limited part intricacy; rough surface finish; difficult to control lateral dimensions accurately; machining costs less for flat cuts
Sheet-metal forming	Form shapes by bending; usually sheet metal, but sometimes plate stock	Low cost; economical for low-quantity production	Suitable only for ductile materials; thick parts require large bend radii, which can limit applicability
Casting	Pour molten material into a mold and allow it to solidify	Versatile; many processes at different costs	Depends on the casting process
Forging	Force hot metal into a die by pounding	High strength and fatigue resistance in the direction of the material grain	Lower strength and fatigue resistance in nongrain directions; expensive for low-quantity production
Extruding	Squeeze hot metal through a die to make a part of uniform cross section	Economical; good surface finish; many standard shapes available	Poor transverse properties

Source: Habicht, W.F., Sarafin, T.D., Palmer, D.L., and Wendt, R.G., Jr., in *Spacecraft Structures and Mechanisms*, Sarafin, T.P., Ed., Microcosm, Inc., Torrance and Kluwer Academic Publishers, Boston, 735, 1995, chap. 20.

3.8.2.2 Casting Methods

Casting involves molding metal into particular shapes by melting it, pouring it into a mold, and allowing it to solidify upon cooling. Table 3.30 shows the six common methods for casting mechanical parts. Dimensions and tolerances apply to aluminum parts. The methods differ significantly with regard to their suitability for making various quantities of the same part, sizes that can be accommodated, and cost or labor for acquiring the molds or patterns. Quality is harder to control by casting than with machining methods. Cast parts must have looser dimensional tolerances and are more prone to imperfections such as porosity or inhomogeneities than if bar or sheet stock is used as the raw material for machining.

3.8.2.3 Forging and Extrusion Methods

In both of these processes, the desired part shape is obtained by the application of high pressure to hot, malleable material. Repeated impacts (pounding) creates the pressure when a part is forged. In

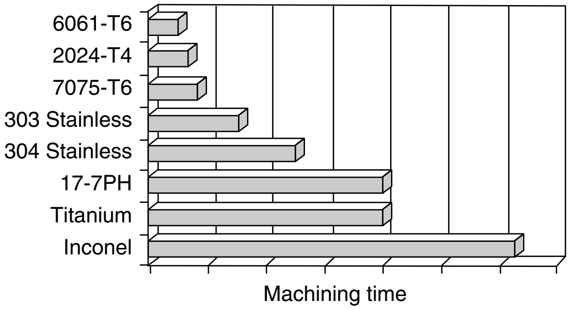

FIGURE 3.21 Variation of machining time required to machine the same amount of material from a given part if that part is made of different metals. (From Habicht, W.F., Sarafin, T.D., Palmer, D.L., and Wendt, R.G., Jr., in *Spacecraft Structures and Mechanisms*, Sarafin, T.P., Ed., Microcosm, Inc., Torrance and Kluwer Academic Publishers, Boston, 735, 1995, chap. 20. With permission.)

TABLE 3.30
Comparison of Casting Processes

Process	Advantages	Disadvantages and Limits	Best Lot Size
Sand casting	Suitable for almost any metal and size; low cost	Rough surfaces; relatively broad dimensional tolerances; minimum section thickness: 0.09–0.19 in.; high labor cost; almost always requires subsequent machining	Varies widely
Plaster-mold casting	Smooth surfaces; can hold tight tolerances; low porosity; part complexity is almost unlimited	Restricted to nonferrous (no iron) metals; usually for parts <15 lb; takes a relatively long time to make a mold, and a new mold is required for each part; minimum thickness: 0.01–0.06 in.	Very small to several hundred
Investment casting	Very smooth surfaces; can hold tight tolerances; good for almost any metal; part complexity is almost unlimited	High cost of labor; moderate cost of patterns and molds; usually for parts <10 lb; minimum thickness: 0.01–0.05 in.	Varies widely
Permanent-mold casting	Smooth surface; can hold tight tolerances; can use a mold up to 25,000 times; fast rate of production; low porosity	The molds are expensive; part complexity and size are limited; minimum thickness; 0.094–0.125 in.; restricted to aluminum, bronze, brass, and some iron	Thousands
Die casting	Very smooth surface and excellent dimensional accuracy; can use a die many times; fast rate of production	The dies are expensive; restricted to nonferrous metals; part complexity and size are limited; minimum thickness: 0.03–0.08 in.	Large
Centrifugal casting	Can maintain relatively close tolerances; fast rate of production	The mold can be expensive, as is the spinning equipment; the shape of the part is limited (typically for cylindrical parts); minimum thickness: 0.1–0.25 in.	Large

Source: Habicht, W.F., Sarafin, T.D., Palmer, D.L., and Wendt, R.G., Jr., in *Spacecraft Structures and Mechanisms*, Sarafin, T.P., Ed., Microcosm, Inc., Torrance and Kluwer, Academic Publishers, Boston, 735, 1995, chap. 20.

the simplest form of forging, the craftsman manipulates a piece of hot metal between flat dies on a mechanical or hydraulic press and pounds it into the rough shape of the desired part. It then needs considerable machining to achieve final shape and dimensions. More precise forging methods pound the hot metal into single impression or multiple impression shaped dies to create the desired shape. Either process strengthens the material in one direction and closes voids.

An extruded part is made by forcing a quantity of hot metal under high pressure through a shaped orifice in a die. The emerging material has a uniform cross section, and so this method is usually used to make parts shaped as elongated rods, bars, I-sections, channels, or angles. Extrusion is a good method for creating strips of raw material that are later cut into shorter lengths for subsequent machining to finished part shapes and dimensions. Quantity production of precision parts by forging and any quantity of parts made by extruding requires use of expensive dies.

3.8.2.4 Fabricating and Curing Composites

Structural components of optical instruments are increasingly made from polymer matrix composite materials (fibers and resins) because of the ability of the manufacturer to create items with high stiffness and specific (usually quite low) CTE. Table 3.31 lists the four basic methods for making these components as well as the advantages and disadvantages of each method. The raw materials for each process (generally called precursors) can be single fibers bundled together, tapes of unidirectional

TABLE 3.31
Basic Processes for Fabricating Composite Components

Process	Description	Advantages	Disadvantages
Filament winding	Dispense dry or prepreg fibers onto a rotating mandrel; used for large tubular and conic structures	Repetitive fiber-angle control for all layers Smooth internal surface Mandrel is reusable Automated	Mandrels are often costly and must be designed for easy removal of the composite part Rough external surface
Manual lay-up	Place tape or fabric prepreg onto (or into) a tool by hand	Requires no expensive equipment Can form localized buildups or doublers	Time consuming Difficult to orient fibers accurately Properties vary from build to build
Resin-transfer molding	Inject liquid resin at low pressure into a closed mold containing fiber preform; used for complex shapes	Often cost-effective for high-volume production Low vapor emissions No reinforcement at part edges is necessary Can vary fiber volume and angles with a single part	Equipment and mold are costly Part and mold must be designed for part removal Limited resins Resin distribution not uniform
Braiding	Weave dry or prepreg fibers, tows, or tapes onto an axi-symmetrical mandrel; used for complex shapes	Can produce outward curvature Can manufacture preforms at a high rate Interlaced fibers result in stronger joints	Low fiber/resin ratios Limited fiber angles Mandrel must be removable

Source: Habicht, W.F., Sarafin, T.D., Palmer, D.L., and Wendt, R.G., Jr., in *Spacecraft Structures and Mechanisms*, Sarafin, T.P., Ed., Microcosm, Inc., Torrance and Kluwer Academic Publishers, Boston, 735, 1995, chap. 20.

TABLE 3.32
Techniques for Curing Composite Components

Process	Description	Advantages	Disadvantages
Vacuum bagging	Place a bag around the part and seal it to the tool. Apply vacuum at controlled levels to achieve pressure up to 14.7 psi	Applies high pressure over a large area. Vacuum removes air from the part	Vacuum may be uneven on part Several vacuum ports may be required
Room temperature	Apply vacuum bag or weights and allow to cure at room temperature	Requires no special equipment	Room-temperature cure resins are usually less stable environmentally Vapor is released Requires long cure times
Oven	Apply vacuum bag or weights and cure in an oven	Equipment is readily available	Part size limited by oven; large ovens are expensive Relatively large parts see nonuniform temperatures
Autoclave	Apply vacuum bag and cure in an autoclave	High pressure results in low volume of voids Can usually control the curing cycles with a computer	Expensive equipment An autoclave requires maintenance and ASME certification as a pressure vessel

Source: Habicht, W.F., Sarafin, T.D., Palmer, D.L., and Wendt, R.G., Jr., in *Spacecraft Structures and Mechanisms*, Sarafin, T.P., Ed., Microcosm, Inc., Torrance and Kluwer Academic Publishers, Boston, 735, 1995, chap. 20.

fibers, or woven (fabric) sheets. Multiple-fiber precursors are usually impregnated with resin when they are made; the resulting products are called “prepregs.”

The process listed first, filament winding, is a good way to make cylindrical or conical parts. It involves dispensing continuous fibers or tapes onto a rotating mandrel from a translating feed arm. The feed can be adjusted to give a lay angle between about 5° and 90° from the axis of rotation. Subsequent layers, or plies, can be applied at different angles to create specific stiffness characteristics of the resulting part. Square or other flat-sided shapes are created by applying the fibers or tape at 0° onto a stationary mandrel.

Flat panels and more complex shapes can be created on composite parts by applying prepregs to a shaped mandrel. This is usually done by hand, hence the name “manual lay-up” for the second process. The process listed third is resin-transfer molding. Here, preformed assemblies of dry fibers are inserted into a closed mold. Resin is injected into the mold and cured in place. This process is used when more complex shapes need to be made.

Processes for curing composites are listed in Table 3.32. Generally, the part to be cured (on its mandrel or inside a closed mold) is sealed into a bag and the bag is evacuated. Atmospheric pressure compresses the material onto the mandrel or forces the mold into uniform contact with the precursor. Cure can be at room temperature or at elevated temperature in an oven or autoclave.

3.8.3 GENERAL COMMENTS REGARDING MANUFACTURING PROCESSES

It is vital that all processes for manufacturing and assembly of both optical and mechanical parts are documented completely and followed. Revision of these documents based on practical experience as they are used should be allowed and encouraged. One should not perpetuate erroneous instructions simply because it takes time and effort to correct them or because it may be somewhat embarrassing to admit that there might be a better way to do some task.

Whenever hardware is assembled (or disassembled and reassembled) there is the potential for internal contamination. For example, soldering electrical connections or machining operations such as drilling and reaming holes for mechanical pins to preserve component alignment can introduce flux, solder droplets, metal chips, dust, or traces of lubricants into the instrument. Care must be exercised to minimize performance loss or mechanism failure from mechanical jamming from such contamination sources.

Finally, involvement of the design team during manufacture and testing of the instrument will enhance the prospects of anticipating potential problems that were not obvious during the design phases. These problems frequently can easily be eliminated if discovered early enough. Those most familiar with the details of the design, the intended assembly sequence, and the interactions and interfaces between the various components are the people — designers and engineers — who created and analyzed the design. Their involvement in post-design phases of the project can also be thought of as a form of extended practical training; a process of learning how one might avoid creating similar problems in future designs.

REFERENCES

Ahmad, A., Wright, R., and Baker, T., Design of a lightweight telescope with highly stable line of sight, *Proc. SPIE*, 3786, 323, 1999.

Anderson, R.H., Leung, K.M., Schmit, F.M., and Ready, J.F., Contemporary methods of optical fabrication, *Proc. SPIE*, 306, 66, 1981.

Ballard, S.S., Browder, J.S., and Ebersole, J.F., Refractive index of special crystals and certain glasses, in *American Institute of Physics Handbook*, 3rd ed., McGraw-Hill, New York, 1972, p. 6.

Barnes, W.P., Jr. and McDonough, R.R., Low scatter finishing of aspheric optics, *Opt. Eng.*, 18, 143, 1979.

Bäumer, S., *Handbook of Plastic Optics*, Wiley Interscience, New York, 2005, chap. 1.

Berthold, J.W., Jacobs, S.F., and Norton, M.A., Dimensional stability of fused silica, Invar, and several ultralow thermal expansion materials, *Appl. Opt.*, 15, 1898, 1976.

Boothroyd, G. and Knight, W.A., *Fundamentals of Machines and Machine Tools*, 2nd ed., Marcel Dekker, New York, 1989.

Boyer, H.E. and Gall, T.L., Eds., *Metals Handbook-Desk Edition*, Am. Soc. for Metals, Metals Park, Ohio, 1985.

Browder, J.S., Ballard, S.S., and Klocek, P., Physical properties of infrared optical materials, in *Handbook of Infrared Optical Materials*, Marcel Dekker, New York, 1991.

Browder, J.S., Ballard, S.S., and Klocek, P., Physical properties of infrared optical materials, in *American Institute of Physics Handbook*, 3rd ed., McGraw-Hill, New York, 1972.

CodeV Reference Manual, Optical Research Associates, Pasadena, CA, 1994.

Cox, A., *A System of Optical Design: The Basics of Image Assessment and of Design Techniques with a Survey of Current Lens Types*, Focal Press, Woburn, 1964.

Curry, T.S., III, Dowdey, J.E., and Murry, R.C., *Christensen's Physics of Diagnostic Radiology*, 4th ed., Lea and Febiger, Philadelphia, 1990.

DeVany, A.S., *Master Optical Techniques*, Wiley, New York, 1981.

Doyle, K.B. and Bell, W.M., Thermo-elastic wavefront and polarization error analysis of a telecommunication optical circulator, *Proc. SPIE*, 4093, 18, 2000.

Doyle, K.B., Genberg, V.L., and Michels, G.J., Numerical methods to compute optical errors due to stress birefringence, *Proc. SPIE*, 4769, 34, 2002a.

Doyle, K.B., Hoffman, J.M., Genberg, V.L., and Michels, G.J., Stress birefringence modeling for lens design and photonics, *Proc. SPIE*, 4832, 436, 2002b.

Elson, J.M. and Bennett, J.M., Relation between the angular dependence of scattering and the statistical properties of optical surfaces, *J. Opt. Soc. Am.*, 69, 31, 1979.

Englehaupt, D., Fabrication methods, in *Handbook of Optomechanical Engineering*, Ahmad, A., Ed., CRC Press, Boca Raton, FL, 1997, chap. 10.

Englehaupt, D., private communication, Center for Applied Optics, University of Alabama in Huntsville, Huntsville, AL, 2002.

Grandilli, P.A., *Technician's Handbook for Plastics*, Van Nostrand Reinhold, New York, 1981.

Gray, D.C., Ed., *American Institute of Physics Handbook*, 3rd ed., McGraw-Hill, New York, 1972.

Habicht, W.F., Sarafin, T.D., Palmer, D.L., and Wendt, R.G., Jr., Designing for producibility, in *Spacecraft Structures and Mechanisms*, Sarafin, T.P., Ed., Microcosm, Inc., Torrance and Kluwer Academic Publishers, Boston, 735, 1995, chap. 20.

Hagy, H.E., Dimensional instabilities in glasses and glass ceramics, *Proc. SPIE*, 1335, 230, 1990.

Harris, D.C., *Materials for Infrared Windows and Domes*, SPIE Press, Bellingham, 1999.

Heraeus (undated), Fused Quartz and Fused Silica for Optics, Publication 40-1015-079, Herasil Amersil, Inc., Buford, Georgia.

Hoffman, J.M. and Wolfe, W.L., Cryogenic refractive indices of ZnSe, Ge and Si at 10.6 μm, *Appl. Opt.*, 30, 4014, 1991.

Horne, D.F., *Optical Production Technology*, Adam Hilger Ltd., Bristol, England, 1972.

Howells, M.R. and Paquin, R.A., Optical substrate materials for synchrotron radiation beam lines, *Proc. SPIE*, CR67, 339, 1997.

Hunt, P.G., Optical cements — a laboratory assessment, *Optica Acta*, 14, 401, 1967.

Ishmuratova, M.S. and Sergeyev, L.V., Optical cements transparent in the infrared, *Sov. J. Opt. Technol.*, 34, 801, 1967.

Ivanova, V.G., Vydrova, I.S., and Sergeyev, L.V., Optical cements for joining glasses with a large TEC difference, *Sov. J. Opt. Technol.*, 40, 497, 1973.

Jacobs, S.F., Unstable Optics, *Proc. SPIE*, 1335, 20, 1990.

Jacobs, S.F., Variable invariables — dimensional instability with time and temperature, *Proc. SPIE*, CR43, 181, 1992.

Jacobs, S.F., Johnston, S.C., and Hansen, G.A., Expansion hysteresis upon thermal cycling of Zerodur, *Appl. Opt.*, 23, 3014, 1984.

Jamieson, T.H., Athermalization of optical instruments from the optomechanical viewpoint, *Proc. SPIE*, CR43, 131, 1992.

Jenkins, F.A. and White, H.E., *Fundamentals of Optics*, McGraw-Hill, Inc., New York, 1957.

Karow, H.K., *Fabrication Methods for Precision Optics*, Wiley, New York, 1993.

Kimmel, R.K. and Parks, R.E., *ISO 10110 Optics and Optical Instruments — Preparation of drawings for optical elements and systems: A User's guide*, Optical Society of America, Washington, DC, 1995.

Kishner, S., Gardopee, G., Magida, M., and Paquin, R., Large stable mirrors — a comparison of glass, beryllium and silicon carbide, *Proc. SPIE*, 1335, 127, 1990.

Korniski, R.J. and Wolfe, W.L., Infrared refractometer measurements of adhesives, *Appl. Opt.*, 17, 3138, 1978.

Kumler, J., Changing glass catalogs, *oemagazine*, 4, 30, 2004.

Laikin, M., *Lens Design*, Marcel Dekker, New York, 1991.

Laufer, J.S., High Silica Glass, Quartz, and Vitreous Silica, *J. Opt. Soc. Am.*, 55, 458, 1965.

Lement, B.S., Averbach, B.L., and Cohen, M., The dimensional stability of Invar, *Trans. ASM*, 43, 1072, 1950.

Liepmann, M.J., Marker, A.J., and Sowada, U., Ultraviolet radiation effects on UV-transmitting fluor crown glasses, *Proc. SPIE*, 970, 170, 1988.

Lindig, O. and Pannhorst, W., Thermal expansion and length stability of Zerodur in dependence upon temperature and time, *Appl. Opt.*, 24, 3330, 1985.

Lubin, G., Ed., *Handbook of Composites*, Van Nostrand Reinhold, New York, 1982.

Lyons, J.J., III and Zaniewski, J.J., High quality optically polished aluminum mirror and process for producing, U.S. Patent 6,350,176, 2002.

Lytle, J.D., Polymeric optics, in *OSA Handbook of Optics*, 2nd ed., Vol. II, Bass, M., Van Stryland, E., Williams, D.R., and Wolfe, W.L., Eds., McGraw-Hill, New York, 1995, chap. 34.

Macleod, H.A., *Thin Film Optical Filters*, 2nd ed. Macmillan, New York, 1986.

Magyar, J.T., History and potential for optical bonding agents in the visible, *Proc. SPIE*, 1535, 55, 1991.

Mahe, C., Nicolay, N., and Marioge, J.P., Study of the qualities of optical cements, *J. Opt. (Paris)*, 10, 41, 1979.

Malacara, D., *Optical Shop Testing*, Wiley, New York, 1978.

Marker, A.J., III, Hayden, J.S., and Speit, B., Radiation resistant optical glasses, *Proc. SPIE*, 1485, 55, 1991.

Marschall, C.W., Sources and solutions for dimensional stability, *Proc. SPIE*, 1335, 217, 1990.

McCay, J., Fahey, T., and Lipson, M., Challenges remain for 157-nm lithography, *Optoelectronics World, Supplement to Laser Focus World*, 23, S3, 2001.

MIL-A-3920 C. *Adhesive, Optical Thermosetting*, U.S. Dept. of Defense, Washington, DC, 1997.

MIL-A-46050 C. *Adhesives, Cyanoacrylate, Rapid Room-Temperature Curing, Solventless*, U.S. Dept. of Defense, Washington, DC, 1998.

MIL-A-46106B. *Adhesive—Sealants, Silicone, RTV, One-Component*, U.S. Dept. of Defense, Washington, DC, 1992.

MIL-A-48611A. *Adhesive System, Epoxy-Elastomeric, for Glass to Metal*, U.S. Dept. of Defense, Washington, DC, 1997.

MIL-B-48612A. *Bonding with Epoxy-Elastomeric Adhesive System, Glass to Metal*, U.S. Dept. of Defense, Washington, DC, 1997.

Miles, P., High transparency infrared materials — a technology update, *Opt. Eng.*, 15, 451, 1976.

MIL-S-11030F. *Sealing Compound, Single Component, Non Curing, Polysilfide Base*, U.S. Dept. of Defense, Washington, DC, 1998.

Milster, T.D., Miniature and Micro-Optics, *OSA Handbook of Optics*, 2nd ed., Vol. II, Bass, M., Van Stryland, E., Williams, D.R., and Wolfe, W.L., Eds., McGraw-Hill, New York, 1995, chap. 7.

Mohn, W.R. and Vukobratovich, D., Recent applications of metal matrix composites in precision instruments and optical systems, *Opt. Eng.*, 27, 90, 1988.

Moon, I.K., Cho, M.K., and Richadr, R.R., Optical performance of bimetallic mirrors under thermal environment, *Proc. SPIE*, 4444, 29, 2001.

Müller, C., Papenburg, U., Goodman, W.A., and Jacoby, M., C/SiC high precision lightweight components for optomechanical applications, *Proc. SPIE*, 4198, 249, 2001.

Murgatroyd, J.B. and Sykes, R.F.R., The delayed elastic effect in silicate glasses at room temperature, *J. Soc. Glass Tech.*, 31, 17, 1947.

Musikant, S., *Optical Materials: An Introduction to the Selection and Application*, Marcel Dekker, New York, 1985.

Noll, R., Effect of mid- and high-spatial frequencies on optical performance, *Opt. Eng.*, 18, 137, 1979.

OSA Handbook of Optics, 2nd ed., Vol. II, Bass, M., Van Stryland, E., Williams, D.R., and Wolfe, W.L., Eds., McGraw-Hill, New York, 1995.

Owens, J.C., Optical refractive index of air: dependence on pressure, temperature, and composition, *Appl. Opt.*, 6, 51, 1967.

Packard, R.D., A bonding material useful in the 2–14 μm spectral range, *Appl. Opt.*, 8, 1901, 1969.

Paquin, R.A., Dimensional stability: an overview, *Proc. SPIE*, 1335, 2, 1990.

Paquin, R.A., Dimensional instability of materials: how critical is it in the design of optical instruments?, *Proc. SPIE*, CR43, 160, 1992.

Paquin, R.A., Properties of metals, in *OSA Handbook of Optics*, 2nd ed., Vol. II, Bass, M., Van Stryland, E., Williams, D.R., and Wolfe, W.L., Eds., McGraw-Hill, New York, 1995, chap. 35.

Paquin, R.A., Advanced materials: an overview, *Proc. SPIE*, CR67, 3, 1997a.

Paquin, R.A., Metal mirrors. in *Handbook of Optomechanical Engineering*, Ahmad, A., Ed., CRC Press, Boca Raton, FL, 1997b, chap. 4.

Paquin, R.A., private communication, 2003.

Parker, C.J., Optical materials-refractive, in *Applied Optics and Optical Engineering*, Vol. VII, Shannon, R.R., and Wyant, J.C., Eds., Academic Press, New York, 1979, chap. 2.

Parks, R., Optical specifications and tolerances for large optics, *Proc. SPIE*, 406, 98, 1983.

Parks, R.E., Optical component specifications, *Proc. SPIE*, 237, 455, 1980.

Parsonage, T., JWST beryllium telescope: Material and substrate fabrication, *Proc. SPIE*, 5494, 39, 2004.

Parsonage, T., private communication, 2005.

Patterson, J.S. and Crout, R.R., Optical quality requirements for large mirror systems, *Proc. SPIE*, 389, 18, 1982.

Patterson, S.R., Dimensional stability of Super Invar, *Proc. SPIE*, 1335, 53, 1990.

Pellegrin, P., Stenne, E., Ulph, E., Geiger, A., and Hood, P., Design, manufacturing and testing of a two-axis servo-controlled pointing device using a metal matrix composite mirror, *Proc. SPIE*, 1167, 318, 1989.

Pellicori, S.F., Transmittances of some optical materials for use between 1900 and 3400 Å, *Appl. Opt.*, 3, 361, 1964.

Pellicori, S.F., Optical bonding agents for severe environments, *Appl. Opt.*, 9, 2581, 1970.

Pellicori, S.F., Optical bonding agent for IR and UV refracting elements, *Proc. SPIE*, 1535, 48, 1991.

Pepi, J. and Golini, D., Delayed elastic effects in the glass ceramics Zerodur and ULE at room temperature, *Appl. Opt.*, 30, 3087, 1991a.

Pepi, J. and Golini, D., Delayed elastic effects in Zerodur at room temperature, *Proc. SPIE*, 1533, 212, 1991b.

Pfeffer, M., Optomechanics of plastic optical components, in *Handbook of Plastic Optics*, Baumer, S.M.B., Ed., Wiley Interscience, New York, 2005, chap. 2.

Phinney, D.D. and Britton, W.P., Developing mechanisms, in *Spacecraft Structures and Mechanisms*, Sarafin, T.P., Ed., Microcosm, Inc., Torrance and Kluwer Academic Publishers, Boston, 665, 1995, chap. 19.

Pike, J.N. and Mehrotra, Y., Durable coating for suppressing stray infrared radiation inside optical instruments, *Proc. SPIE*, 3786, 256, 1999.

Pompea, S.M. and Breault, R.P., Black surfaces for optical sytems, in *OSA Handbook of Optics*, 2nd. ed., Vol. II, Bass, M., Van Stryland, E., Williams, D.R., and Wolfe, W.L., Eds., McGraw-Hill, New York, 1995, chap. 37.

Rancourt, J.D., *Optical Thin Films — Users Handbook,* Macmillan, New York, 1987.

Sarafin, T.P., Heymans, R.L., Wendt, R.G., Jr., and Sabin, R.V., Conceptual design of structures, in *Spacecraft Structures and Mechanisms*, Sarafin, T.P., Ed., Microcosm, Inc., Torrance and Kluwer Academic Publishers, Boston, 507, 1995, chap. 15.

Savage, J.A., Crystalline optical materials for ultraviolet, visible, and infrared applications, in *Optical Materials: A Series of Advances*, Vol. 1, Musikant, S., Ed., Marcel Dekker, New York, 1990, chap. 3.

Schott, *Technical Information, No. 10017e, Radiation Resistant Glasses*, Schott Glass Technologies, Inc., Duryea, Pennsylvania, 1990a.

Schott, *Product Information, No. 2105/90, ULTRAN 30-548743, UV Transmitting Glass*, Schott Glass Technologies, Inc., Duryea, Pennsylvania, 1990b.

Schott, *Schott Optical Glass Catalog* (CD Version 1.2, USA). Schott Glass Technologies, Inc., Duryea, Pennsylvania, 2001.

Sedova, V.I., Shepurev, E.I., Sergeev, L.V., Shumilova, T.V., and Kompalova, L.A., Optical polymerizing cement, transparent in the UV, *Sov. Opt. Technol.*, 49, 392, 1982.

Setta, J.J., Scheller, R.J., and Marker, A.J., Effects of UV-solarization on the transmission of cerium-doped optical glasses, *Proc. SPIE*, 970, 179, 1988.

Shaffer, J.J. and Bennett, H.E., Effect of thermal cycling on dimensional stability of Zerodur and ULE, *Appl. Opt.*, 23, 2852, 1984.

Sharp, R., Hunt, P.G., and Webber, J.M.B., *A User's Guide for Optical Cements*, Sira Institute Ltd., Chislehurst, England, 1980.

Smith, W.J., *Modern Optical Engineering*, 3rd ed., McGraw-Hill, New York, 2000.

Stroud, J.S., Photoionization of Ce^{3+} in glass, *J. Chem. Phys.*, 25, 844, 1961.

Stroud, J.S., Color centers in cerium-containing silicate glass, *J. Chem. Phys.*, 37, 836, 1962.

Stroud, J.S., Color center kinetics in cerium-containing glass, *J. Chem. Phys.*, 42, 2442, 1965.

Stroud, J.S., Schreves, J.W.H., and Tucker, R.F., Charge trapping and the electronic structure of glass, *7th International Congress on Glass*, Brussels, Belgium, 1965.

Tanaka, Y. and Miyamae, H., Analysis on image performance of a moisture absorbed plastic singlet for an optical disk, *Proc. SPIE*, 1354, 395, 1990.

Taylor, R.L. and Goela, J.S., Specification of infrared optical materials for laser applications, *Proc. SPIE*, 607, 22, 1986.

Tropf, W.J., Thomas, M.E., and Harris, T.J., Properties of crystals and glasses, in *OSA Handbook of Optics*, 2nd ed., Vol. II, Bass, M., Van Stryland, E., Williams, D.R., and Wolfe, W.L., Eds., McGraw-Hill, New York, 1995, chap. 33.

Turtle, R.R., Thin optical bonds for infrared uses, *Appl. Opt.*, 26, 4346, 1987.

Ulph, E., Fabrication of a metal-matrix composite mirror, *Proc. SPIE*, 966, 116, 1988.

U.S. Precision Lens, Inc., *The Handbook of Plastic Optics*, 2nd ed., Cincinnati, OH, 1983.

Valente, T. and Richard, R., Interference fit equations for lens cell design using elastomeric lens mountings, *Opt. Eng.*, 33, 1223, 1994.

Volf, M.B., *Chemical Approach to Glass*, Elsevier, New York, 1984.

Vukobratovich, D., Lightweight laser communications mirrors made with metal foam cores, *Proc. SPIE*, 1044, 216, 1989.

Vukobratovich, D., Design and fabrication of an astrometric astrograph, *Proc. SPIE*, 1752, 245, 1992.

Vukobratovich, D., private communication, 2001.

Vukobratovich, D., private communication, 2004.

Vukobratovich, D., Don, K., and Sumner, R.E., Improved cryogenic aluminum mirrors, *Proc. SPIE*, 3435, 9, 1998.

Vukobratovich, D., Gerzoff, A. and Cho, M.K., Therm-optic analysis of bimetallic mirrors, *Proc SPIE*, 3132, 12, 1997.

Vukobratovich, D., Valenti, T. and Ma, G., Design and construction of a metal matrix composite ultra-lightweight optical system, *Proc. SPIE*, 2542, 142, 1995.

Walker, B.H., Select optical glasses, in *The Photonics Design and Applications Handbook*, Lauren Publishing, Pittsfield, H-356, 1993.

Wang, B., Studying birefringence in calcium fluoride, *oemagazine*, 2, 48, 2002.

Welham, B., Plastic optical components, in *Applied Optics and Optical Engineering*, Shannon, R.R., and Wyant, J.C., Eds., Vol. VII, Academic Press, New York, 1979, chap. 3.

Wetherell, W.B., Effects of mirror surface ripple on image quality, *Proc. SPIE*, 332, 335, 1982.

Willey, R.R., Antireflection coating for high index cemented doublets, *Appl. Opt.*, 29, 4540, 1990.

Willey, R.R., *Practical Design and Production of Optical Thin Films*, Marcel Dekker, New York, 1996.

Wilner, K., Klinger, E., and Wild, W.J., Thermal runaway in germanium laser windows, *Appl. Opt.*, 21, 1796, 1982.

Wimperis, J.R. and Johnston, S.F., Optical cements for interferometric applications, *Appl. Opt.*, 23, 1145, 1984.

Wolfe, W.L., Properties of optical materials, in *Handbook of Optics*, Driscoll, W.G., Ed., McGraw-Hill, New York, 1978, sec. 7.

Wolfe, W.L., The status and needs of infrared optical property information for optical designers, *Proc. SPIE*, 1354, 696, 1990.

Wolfe, W.L. and Zissis, G.J., Eds., *The Infrared Handbook*, Environ. Res. Inst. of Michigan/U.S. Naval Res. Lab., Washington, 1978.

Wolpert, H.D., Optical plastics: properties and tolerances, *The Photonics Design and Applications Handbook*, Lauren Publishing, Pittsfield, H-321, 1989.

Wood, R.A. and Favors, R.J., *Titanium Alloys Handbook MCIC-HB-02*, Metals and Ceramics Information Center, Battelle Columbus Laboratories, Columbus, 1972.

Yoder, P.R., Jr., *Mounting Optics in Optical Instruments*, SPIE Press, Bellingham, 2002.

Zhang, S. and Shannon, R.R., Lens design using a minimum number of glasses, *Opt. Eng.*, 34, 3536, 1995.

Zweben, C., Overview of composite materials for optomechanical, data storage, and thermal management systems, *Proc. SPIE*, 3786, 148, 1999.

4 Mounting Individual Lenses

4.1 INTRODUCTION

In this chapter, we consider a variety of ways to mount individual rotationally symmetric lenses in the size range of ~10 to 250 mm (0.4 to 10 in.) in diameter. Multiple-lens assemblies are discussed in Chapter 5. Some mountings for larger lenses and for image-forming mirrors are discussed in later chapters. Mountings for individual non-image-forming optics (prisms, flat mirrors, windows, etc.) are considered in Chapters 6 and 7.

We deal here with the means for securing the optic to its mechanical surround, and the design of that surround to ensure the proper function of the assembled parts in the intended environment. It should be noted at the outset that the universally preferred design is one in which the manufacturing and assembly tolerance buildup is minimal, the location and orientation of the optic are benign to the environment, and the optic is not unduly affected by the influences of the mechanical surround. These conditions are hard to achieve in many designs.

Following a brief discussion of what is meant by "centered" optics, the cost impacts of tightening tolerances are explored. We then describe how to estimate the weight of a lens element and locate its center of gravity (CG). Techniques for mounting individual refracting elements are addressed next. In general, we progress from simple, low-precision designs (i.e., those requiring no better than, say, 30 arcmin angular and 0.25 mm [0.01 in.] lateral positional alignment of any element relative to a given reference) to more complex and higher precision versions. A variety of designs providing mounting constraints at glass-to-metal interfaces with the rim of the lens and with its polished surfaces are considered. Different mechanical shapes of the interface touching the lens surfaces are described. Some techniques for aligning the individual lens in its mount are then summarized.

The emphasis in this chapter is on optics made of glass-type materials, although most mounting techniques discussed are also applicable to crystalline and plastic lenses. Some mounting features specific to plastic optics are described at the end of this chapter.

In Chapter 15, we present analytical means for estimating the stress levels within a lens when it is held mechanically by external forces applied at the mounting interfaces. Typical designs using that theory and the consequences of those stresses are evaluated in that chapter.

4.2 CONSIDERATIONS OF CENTERED OPTICS

Because of the inherent rotational symmetry of spherical surfaces and their aberrations, it is axiomatic for a lens designer to start a design by defining a straight line in space and locating all surfaces having optical power symmetrically about that line. If the centers of curvature of an ensemble of such surfaces lie on this same line, we define the line as the optical axis and that system as centered. Figure 4.1(a) illustrates a perfectly centered biconvex lens element. The centers C_1 and C_2 of the surfaces R_1 and R_2 define the optical axis of the lens. The ground rim of the lens is cylindrical with the axis of that cylinder coincident with the optical axis.

A lens with a plano (i.e., flat) surface is shown in Figure 4.1(b). Here, the plano-convex lens is tilted with respect to an arbitrarily oriented line A-A′ (dashed line). This line may be the mechanical axis of a cell into which the lens is to be mounted. The optical axis of the lens in view (b) is designated as the line passing through the center C_1 of R_1 and perpendicular to R_2. Symmetry exists

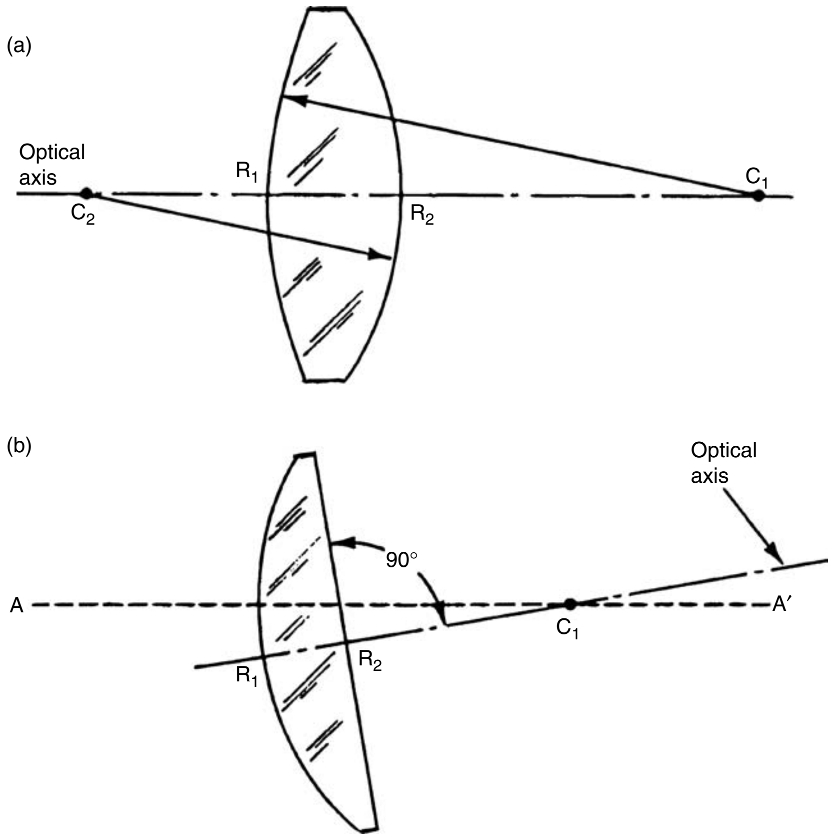

FIGURE 4.1 (a) A perfectly centered biconvex lens. Centers C_1 and C_2 of surfaces R_1 and R_2 define the optical axis of the lens. (b) A plano-convex lens tilted with respect to the mechanical reference line A-A′ passing through the surface center C_1. The optical axis of the lens passes through C_1 and is perpendicular to the plano surface.

only about this axis. Systems with intentionally tilted surfaces such as wedges or those that need asymmetry for aberrational correction reasons cannot be considered to be centered or rotationally symmetric. These asymmetric systems are not discussed here.

The above definition of a centered system applies, of course, to folded assemblies and systems in which the optical axis is deviated through a constant angle by reflection from one or more intentionally tilted mirror surface(s). An example of an optical instrument with such a fold is a visual astronomical telescope of the Newtonian form. The folding mirror is generally located a distance X inside the focus of the primary mirror, as indicated in Figure 4.2. The optical axis of the parabolic primary passes through the center C of its vertex sphere and the mirror's optical vertex A, as defined by the symmetry of its aspheric contour. The optical axis after reflection is defined as the line connecting the reflected location A′ of the primary vertex (serving as a virtual object) and the reflected location C′ of the primary's center of curvature. If the optical surfaces of the eyepiece are centered about this reflected optical axis, we may define the entire optical system as centered.

Figure 4.3 shows an unobscured-aperture Cassegrainian telescope in which the optical surfaces of the mirrors are made from aspheric parent surfaces. The latter surfaces are centered to the optical axis so that the system is centered. The entrance pupil of the system is located off the optical axis, so the design can be called an *eccentric-pupil* system or an *off-axis* system.

Practically all lens elements have cylindrical rims produced by edge-grinding the element after the surfaces are polished. This cylinder defines a mechanical axis of the lens that may or may not coincide with the lens' optical axis, depending on how the latter axis is oriented while the rim is being

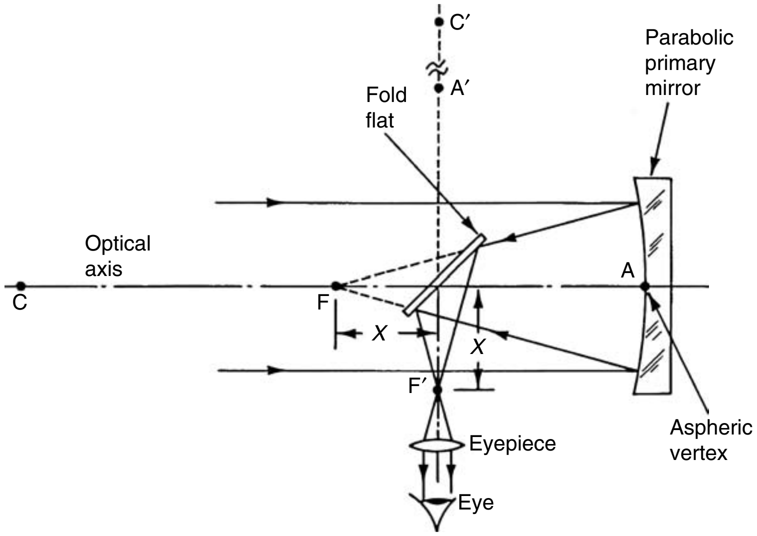
C′
A′
Fold flat
Parabolic primary mirror
Optical axis
C
F
A
X
X
F′
Eyepiece
Eye
Aspheric vertex

FIGURE 4.2 The Newtonian telescope, an example of a folded optical system with centered optics.

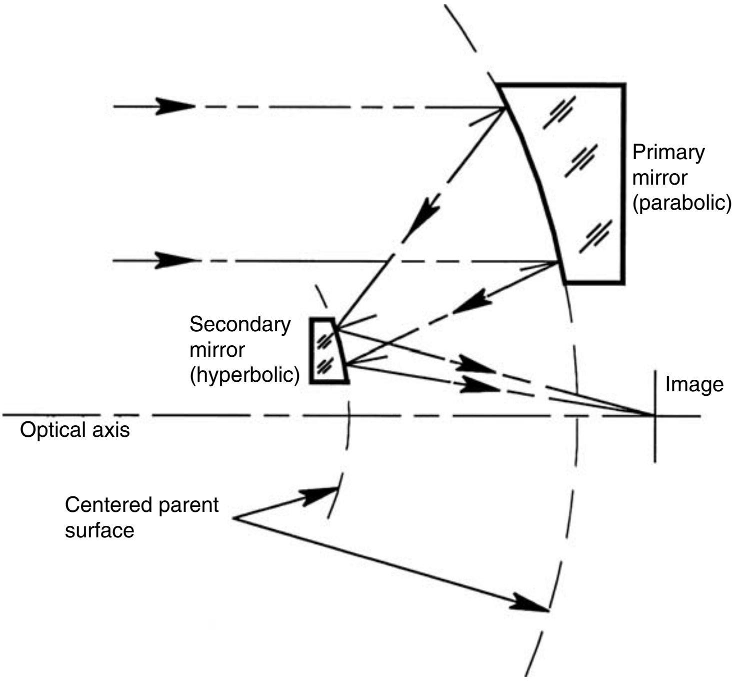
Primary mirror (parabolic)
Secondary mirror (hyperbolic)
Image
Optical axis
Centered parent surface

FIGURE 4.3 An unobscured-aperture Cassegrainian telescope with mirror segments made from centered aspheric parent surfaces. This is sometimes called an *eccentric-pupil* or *off-axis* system.

ground. Figure 4.4 shows a biconvex lens mounted on the bell (or chuck) of one type of precision lens-edging machine. The lip of the bell is rounded and the lens is generally secured to the bell with an adhesive such as wax or pitch, as shown in the detail view. The lens is held with a vacuum chuck in some machines. Warming the adhesive to soften it or partially releasing the vacuum and judiciously pushing the lens sideways until it is centered aligns the lens to the machine's rotational axis.

Care must be exercised to ensure that the glass remains in contact with the bell during the alignment process. Once the lens is aligned and secured in place, the cylindrical rim is ground to the appropriate outside diameter (OD). The mechanisms locating the grinding wheel provide the means for linear travel of the cutting edge parallel to the axis of rotation, as well as radial travel of that edge.

Figure 4.5 illustrates two common cases of misalignment of the lens during edging. In Figure 4.5(a), surface center C_1 is on the mechanical axis, whereas surface center C_2 is displaced from that axis. Surface R_2 will then wobble as it rotates, and a mechanical indicator touching the lens at the distance Y from the axis will measure a full indicator movement (FIM)[*] as shown. If edged under this condition and mounted so that its cylindrical rim is in intimate contact with the inside surface of a cylindrical recess in a cell or housing (here defined as a *rim-contact mounting*), the lens may be considered to have an integral optical wedge of angle $\theta = \text{(FIM)}/2\text{Y}$ and will deviate a transmitted beam approximately by an angle $\delta = (n - 1)\,\theta$. Both δ and θ are in radians. To convert these angles into minutes of arc, we will divide by 0.00029.

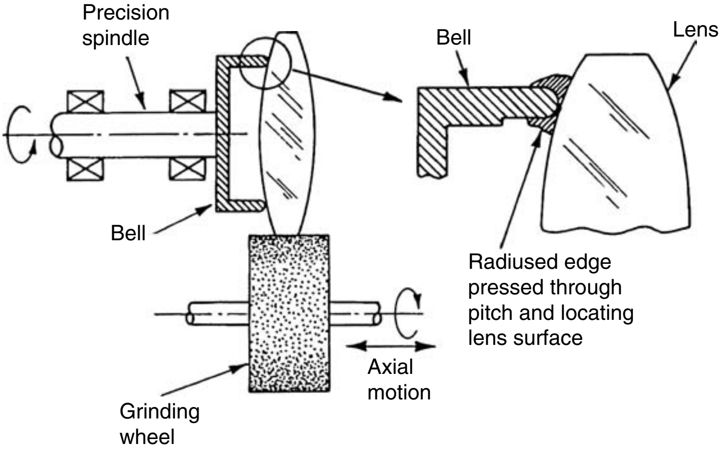
Precision spindle
Bell
Lens
Bell
Radiused edge pressed through pitch and locating lens surface
Axial motion
Grinding wheel

FIGURE 4.4 Typical setup for edging a lens element. The detail view shows one means for attaching the lens to the bell of the machine.

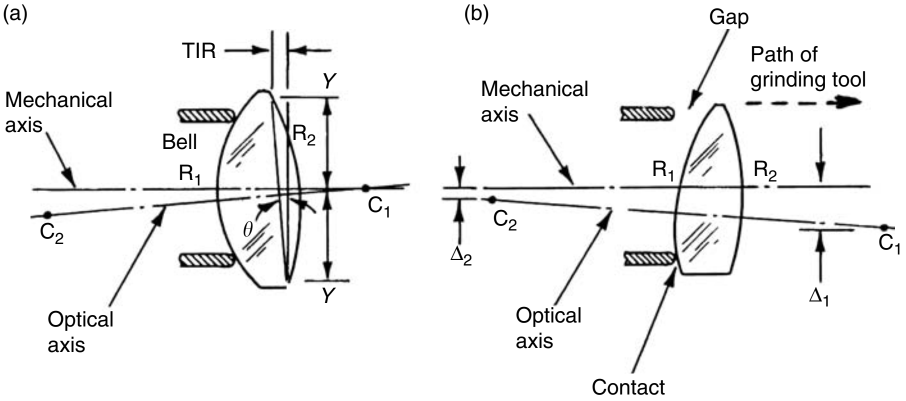
(a)
TIR
Y
Mechanical axis
Bell
R2
R1
C1
C2
θ
Y
Optical axis
(b)
Gap
Path of grinding tool
Mechanical axis
R1
R2
C2
Δ2
C1
Δ1
Optical axis
Contact

FIGURE 4.5 Typical (exaggerated) misalignments of the lens during edging. (a) C_1 on and C_2 off the rotational axis; (b) C_1 and C_2 off the rotational axis by unequal amounts in the plane of the figure.

---

[*] FIM has replaced the formerly used term "total indicator runout" (TIR) in common usage and in ANSI Y14.5M, *Dimensioning and Tolerancing*.

In Figure 4.5(b), the surface centers are off the mechanical axis by distances Δ_1 and Δ_2 in the plane of the figure. The gap shown at the top of the bell may occur because of a raised defect (burr) on the bell edge, a particle of dust lodged between the surfaces of the bell and the lens, or adhesive (pitch) that hardened while the two surfaces were not in full contact. Again, we may consider a wedge to exist inside the lens if edged under this condition. This wedge has a magnitude in radians of approximately (Δ_1/R_2)-(Δ_2/R_2) if the displacements are as shown. In general, the centers will lie off the mechanical axis in arbitrary directions and by arbitrary amounts. If $\Delta_1=\Delta_2$ in the same direction, the optical axis of the lens is decentered from, but parallel to, the axis of rotation, which is also the mechanical axis of the ground rim. In each of these three possible cases, the lens is said to be wedged, and its edge thickness is not uniform around the rim.

A wedge built into a lens element during the edging process is a very undesirable attribute for a rim-contact-mounted lens. It is frequently possible to configure the lens-to-mount interface so that alignment of the lens to its mount is determined by contacting the polished optical surfaces themselves and not any secondary, i.e., ground, reference surface such as the rim, an annular flat, or a bevel. We define this as a *surface-contact mounting*. This type of mounting is discussed in the next section. Many of the higher precision mounting methods described later in this chapter utilize this principle.

When a lens is mounted by way of secondary (ground) surfaces, an appropriate level of care must be exerted in creating those reference surfaces to control centering errors within allowable limits of the particular design. Achievement of the highest precision in centering requires the use of an air-bearing spindle to obtain the minimum possible instrumental error due to spindle-axis wobble. In all such cases, precision error-detection (i.e., metrology) instrumentation must be provided for measuring the misalignment of the particular element being edged.

Figure 4.6 illustrates a typical setup, the tools used, and the sequence of operations in edging, centering, and chamfering a typical double-concave lens that has multiple secondary mounting surfaces (three flat bevels and two cylindrical surfaces), as well as three protective chamfers. The machine represented here is a precision, automatic, computer numerically controlled (CNC) centering machine; two multiple-surface, diamond-coated grinding wheels are used to speed operations. The lens is clamped between opposing centering bells on spindles, so no adhesive or vacuum is needed to hold it in place. An axial compressive force exerted on the lens' curved surfaces around its periphery creates radial force components that tend to squeeze the lens toward its centered position, as illustrated schematically in Figure 4.7.

When centering a lens with this type of apparatus, the factor Z in the following equation should exceed 0.56 (Karow, 1993):

$$Z = (2y_C/R)_1 - (2y_c/R)_2 \tag{4.1a}$$

where y_C is the bell contact height from the axis and R the absolute values of the surface radii. Shannon (1990) indicatd that the centration capability of a lens can be included in the merit function for optimization in automatic lens design software. Lenses with long radii that cannot be adequately centered by the opposing bell process (i.e., those with $Z < 0.56$) must be aligned manually or automatically by external mechanisms applying radial force to slide the lens on the bell.

Hopkins (1980) described three general methods for detecting alignment errors of a lens during edging. These involve measurement, while the lens is rotated slowly on the spindle, of (1) the wobble (angular deviation) of a light beam passing through the center of the lens, (2) the wobble of images reflected from one or both surfaces of the lens or of interference fringes formed by the two lens surfaces, and (3) the mechanical runout of one or both surfaces at a selected radius from the axis.

The apparatus shown in Figure 4.8 illustrates Hopkins' first two methods. It allows measurement of the deviation of a laser beam reflected from one or both surfaces of the lens as well as the deviation of the transmitted portion of that laser beam while the lens is rotating on the spindle of a

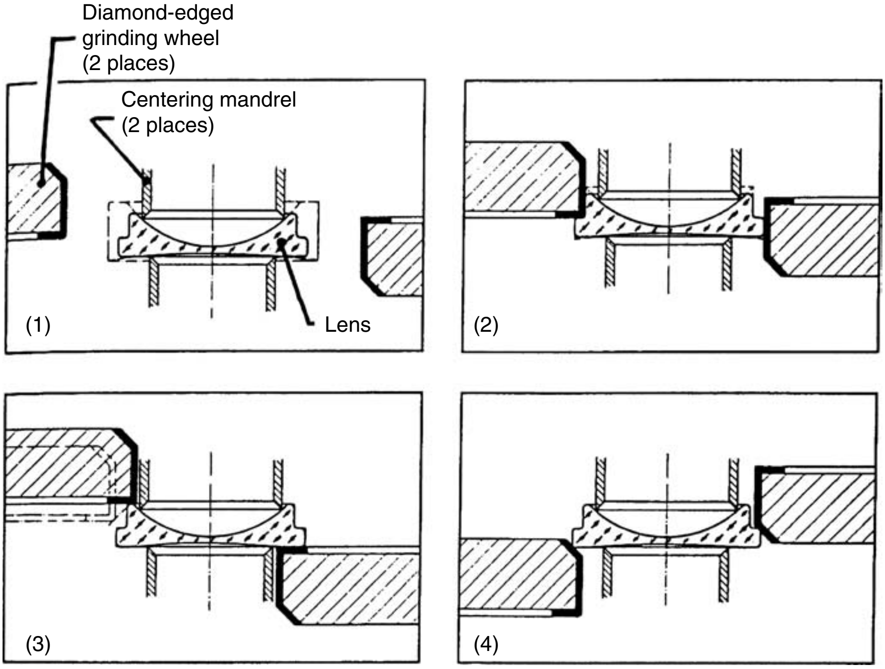
Diamond-edged grinding wheel (2 places)
Centering mandrel (2 places)
Lens
(1)
(2)
(3)
(4)

FIGURE 4.6 Lens installed in a typical opposing-bell centering machine for computer numerically controlled (CNC) centering, edging, beveling, and chamfering. Sequence of operations: (1) start position (Note: Excess material to be removed is shown by the dashed outline.), (2) machining two cylinders and one plano bevel, (3) machining two plano bevels and one protective chamfer, (4) machining two additional protective chamfers. (Courtesy of LOH Optical Machinery, Inc., Milwaukee, WI.)

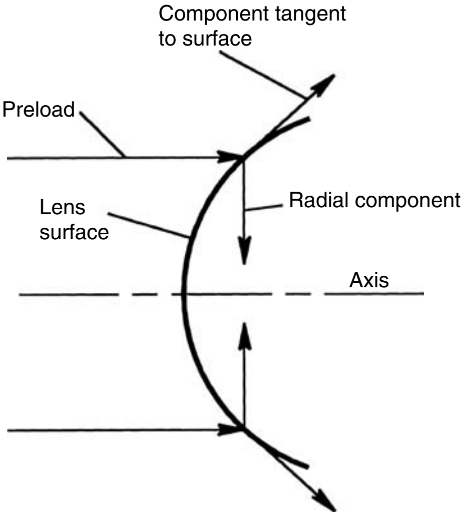
Component tangent to surface
Preload
Lens surface
Radial component
Axis

FIGURE 4.7 Schematic representation of the formation of radial (i.e., centering) force components by axial forces (preload) applied to a curved lens surface. The lens will tend to slide toward the centered condition until the difference between the opposing radial components is insufficient to overcome friction at the glass-to-metal interface.

centering machine. The output of the selected sensor is depicted graphically for ease of interpretation by the operator. The use of a beam-splitting roof prism to double the sensitivity of the reflected light method was mentioned by Hopkins.

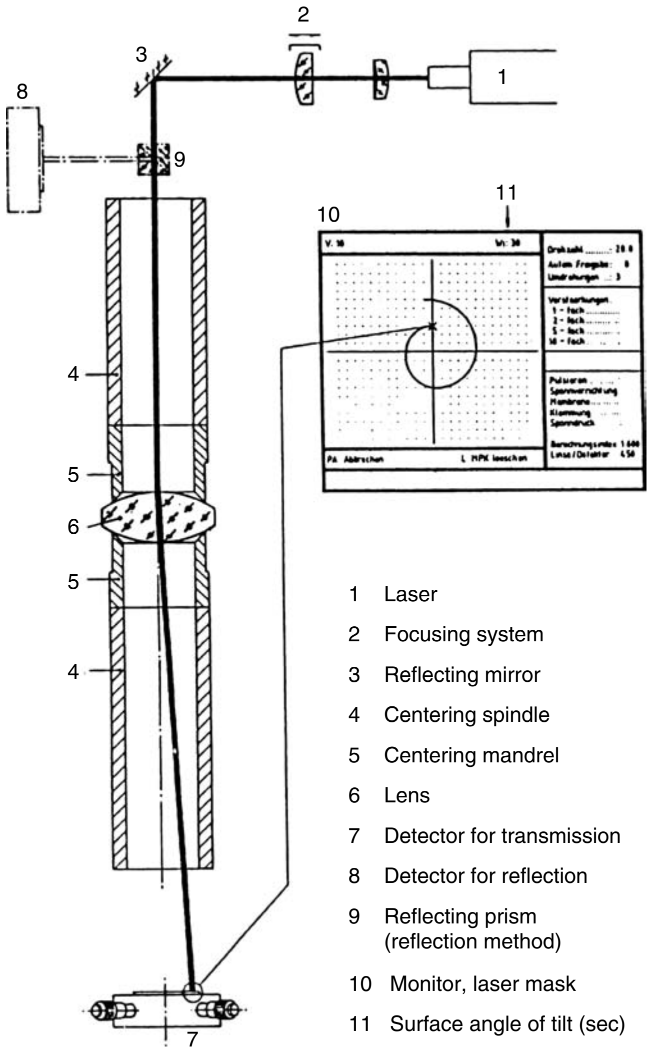
2
3
8
1
9
11
10
4
5
6
5
4
7
1 Laser
2 Focusing system
3 Reflecting mirror
4 Centering spindle
5 Centering mandrel
6 Lens
7 Detector for transmission
8 Detector for reflection
9 Reflecting prism (reflection method)
10 Monitor, laser mask
11 Surface angle of tilt (sec)

FIGURE 4.8 Opto-mechanical configuration of a commercial sensor used to measure lens centration errors by reflection or transmission during edging. (Courtesy of Loh Optical Machinery, Inc., Milwaukee, WI.)

In the third measurement method described by Hopkins (1980), precision mechanical, capacitive, or inductive sensors are arranged about the periphery of the lens being centered and edged so as to measure the mechanical runout (change in edge thickness [ΔET]) as the lens rotates between these sensors. Parks (1980) indicated that a ΔET of about 0.005 mm (0.0002 in.) could reasonably be measured with sensors available at the time.

Using the 0.005 mm value of ΔET as an upper limit, Parks (1980) estimated the optical beam deviation δ and decentration Δy that would result for lenses of various diameters and focal lengths. Equations for these parameters and the results of his parametric analysis are shown in Figure 4.9. Parks noted that the optical deviation depends on diameter, but is independent of focal length, whereas decentration corresponding to the limiting ΔET depends on both parameters. Parks also noted that an optical deviation of 3 arcmin meets the centration requirements of U.S. Military Specification MIL-O-13830.

With currently available sensors and applying standard optical workshop practices, ΔET of moderate-size optics can be controlled to $<$ 0.005 mm (0.0002 in.). Erickson et al. (1992) indicated that the high-precision techniques give ΔET values as small as 1.3 μm (50×10^{-6} in.). For a lens of diameter 60 mm (2.36 in.), these values of ΔET correspond to geometric wedge angles of 17.2 and 4.5 arcsec, respectively. Larger lenses having the same ΔET values would have proportionately smaller wedge angles. Centration and wedge errors for precision ground bevels are only slightly larger than these values.

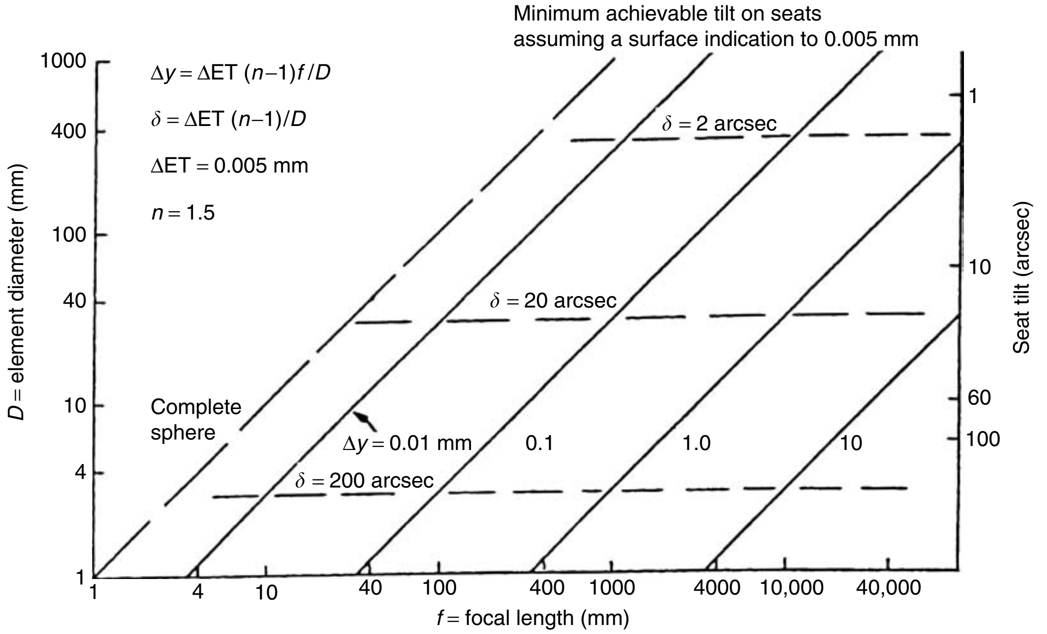

FIGURE 4.9 Limits on lens centering by controlling wedge or ET. (From Parks, R.E., *Proc. SPIE*, 237, 455, 1980.)

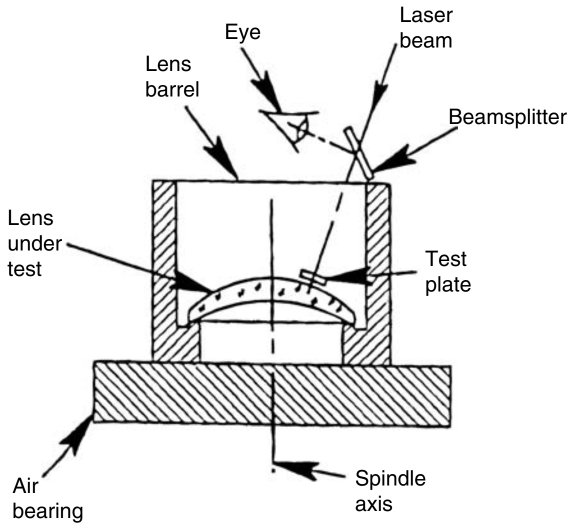
Eye
Laser beam
Lens barrel
Beamsplitter
Lens under test
Test plate
Air bearing
Spindle axis

FIGURE 4.10 A technique for testing alignment of a lens on a rotating air-bearing spindle by observing movement of Fizeau interference fringes due to surface wobble.

Interferometric lens-centration error-measuring techniques were described by Carnell et al. (1974), Reavell and Welford (1980), and Bayar (1981). Zaltz and Christo (1982) described a variety of centering error-measuring instruments and quantified their performance. Figure 4.10 illustrates schematically one type of interferometric technique in which a meniscus-shaped lens is resting on a mechanical surface in a barrel. This surface has been adjusted or machined *in situ* to run true to the axis of an air-bearing spindle. A test plate with spherical radius approximately equal to that of the exposed lens surface is held near the latter surface. As the spindle is rotated slowly, decentration or tilt of the lens surface will cause it to wobble with respect to the test plate, and Fizeau interference fringes formed between those adjacent surfaces will move. These fringes are observed by eye (with appropriate filtering) or with a video camera by means of a beamsplitter oriented as shown in the figure. Proper lens alignment is achieved when the lens has been adjusted laterally so the fringes appear to remain stationary as the spindle rotates. The lens is then secured in place to maintain that alignment.

One type of interferometric alignment error-sensing instrumentation that measures the performance of a lens or of a complete optical system as the position and orientation of an optical component is adjusted during final assembly is discussed in Section 5.10.

If a perfectly centered and edged lens is rim-mounted in a perfect cell, the image of a distant axial object point will be centered on the axis as shown in Figure 4.11(a). Axial location of the lens is usually controlled by forces applied to the spherical surfaces (as indicated by the arrows in the figure) by clamping the lens between retainers, shoulders, and spacers,. If, on the other hand, the lens has a wedge or is edged in a decentered manner as shown in Figures 4.11(b) and (c), the image of the distant on-axis object point will be deviated to an off-axis location when mounted in the perfect cell. In

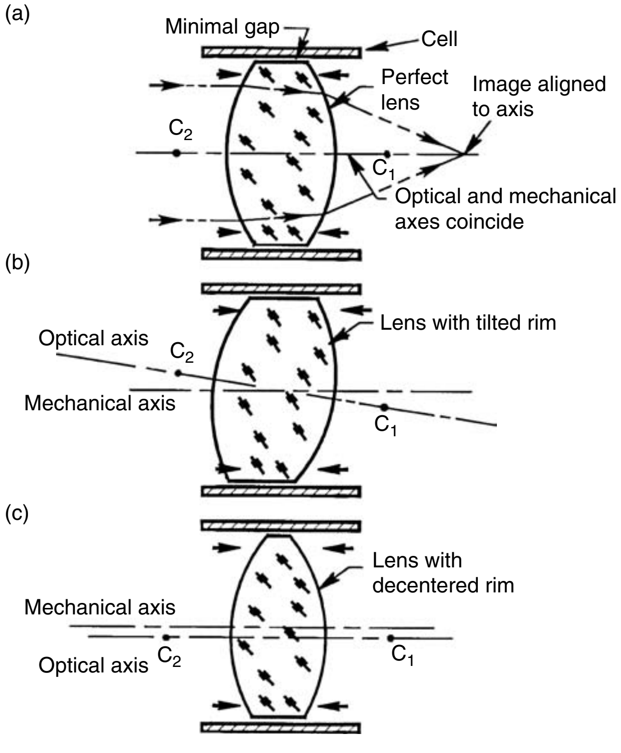

FIGURE 4.11 Holding a wedged lens (view [b]) or decentered lens (view [c]) in a rim-contact mount will deviate the image of a distant on-axis point object from the ideal condition shown in view (a) and will tend to introduce nonsymmetrical aberrations into that image. Axial preload is indicated by the symmetrical set of four horizontal arrows in each view.

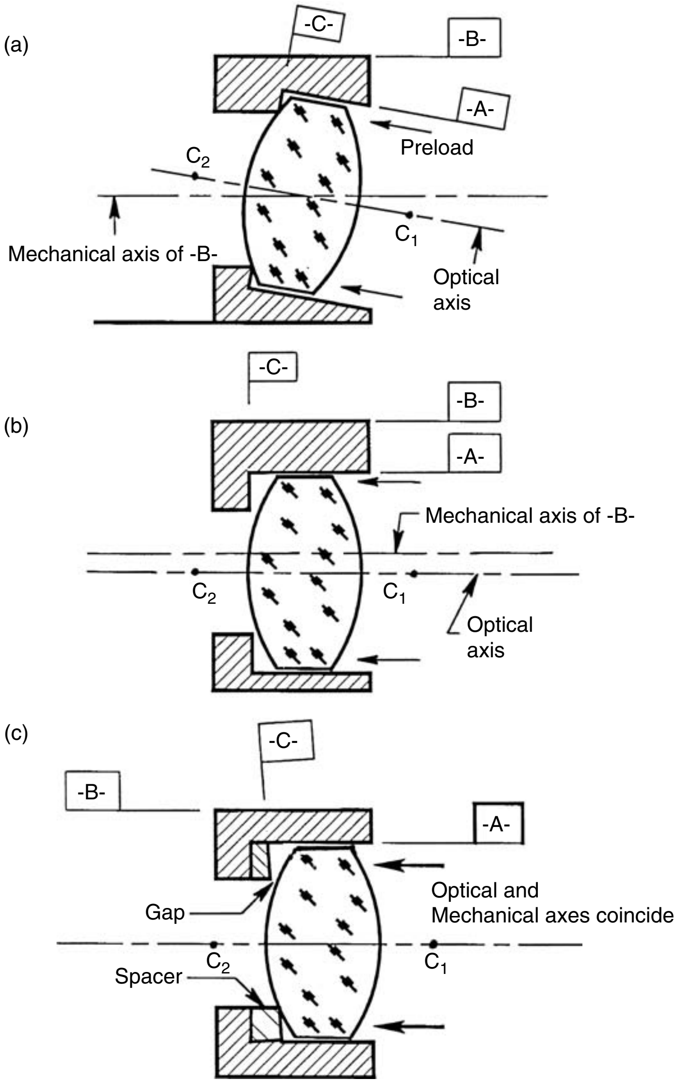

FIGURE 4.12 A perfect lens in an imperfect rim-contact mount will introduce alignment errors relative to a mechanical reference such as datum -B- as shown in (a) for a tilted bore and shoulder or (b) for a decentered bore. A wedged spacer, as in (c), will cause nonuniform distribution of preload and unsymmetrical stress buildup.

either of these cases, axial forces exerted by conventional clamping means will not be symmetrical, and excess stress may be introduced locally into the lens material.

Alignment problems would also be expected if the lens is perfectly centered and edged, but the associated mechanical parts for a rim-contact mount are not correctly made. Figure 4.12 illustrates this situation for three common machining errors. In view (a), the lens is tilted with respect to the cell OD (datum -B-) because the cylindrical bore (datum -A-) and shoulder face (datum -C-) are tilted. In view (b), a spacer used to locate the lens axially is wedged. In view (c), the cylindrical bore (datum -A-) is decentered with respect to datum -B-. The presence of a localized gap between a lens surface and the interfacing mechanical part (as in view [b]) would allow unsymmetrical, localized, stress buildup owing to axial forces exerted by the clamping means. Adequate control of dimensions and surface relationships in both optical and mechanical parts is obviously desirable.

There is no basic difference in the use of the mounting techniques described later in this chapter if the element to be mounted is a flat or curved (i.e., image-forming) mirror, as long as its external configuration has rotational symmetry. The optical consequences of centering errors are, however, significantly more pronounced in the case of a mirror since the deviation of a reflected beam due to a mirror surface being tilted through the angle θ is 2θ rather than $(n - 1)\theta$ as it is for refraction through a lens element wedged by the angle θ.

4.3 COST IMPACTS OF FABRICATION TOLERANCES

The assignment of tolerances to lens dimensions and other parameters significantly affects the cost of a lens, especially when produced in large quantities. If the tolerances for a given lens are loose enough that the standard fabrication and inspection methods cause no special labor, tooling, or test equipment costs in a given optical shop, then the unit cost will be minimal. This is defined as the base cost. If, however, the tolerances are tightened, the cost of that lens made in the same shop would be expected to rise. The rate of increase as the tolerance is tightened is not linear; cost increases more rapidly as the tolerances are made more demanding. Over a period of many years, several workers have endeavored to correlate lens unit cost to the specified tolerance for a variety of lens dimensions and parameters (Plummer, 1979; Kojima, 1979; Parks, 1980, 1983; Smith, 1985; Willey, 1983, 1984, 1989; Willey et al., 1983; Adams, 1988; Willey and Durham, 1990, 1992; Fischer, 1990; Willey and Parks, 1997). We here summarize the cumulative results of those efforts, as presented by Willey and Parks (1997), in the hope that they will serve as a guide to the cost-effective design and tolerancing of future opto-mechanical instruments. The cost impacts of specifying and tolerancing different types of coatings are not included here.

Figure 4.13 shows an empirically derived graph for the increase in cost of a lens above the base grind and polish cost as a function of glass choice, expressed in terms of its susceptibility to staining when exposed to lightly acidic water during processing. The abscissa is the Schott stain code (FR in Table 3.1). A lower number on a scale of 0 to 5 represents a more resistant glass type, so increasing the number has the same type of effect on cost as tightening a dimensional tolerance. The equation shown in the figure is a reasonably good fit to data from Fischer (1990) and to Willey's prior data for FR≤4.

Figure 4.14 shows empirically derived graphs for the increase in cost of a lens above the base grind and polish cost as a function of diameter-to-thickness ratio *D*/*T*. This parameter affects the flexibility of the substrate and may be related to the increase in surface temperature during polishing. The upper curve represents prior data obtained by Willey, while the lower curve reflects data

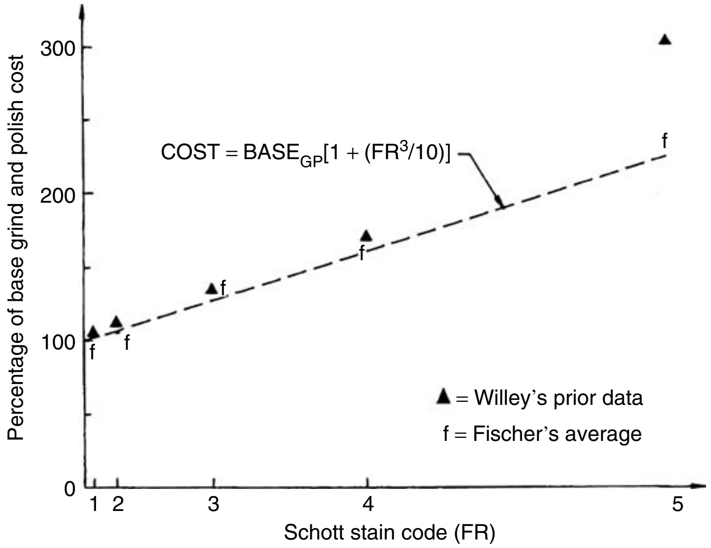

FIGURE 4.13 Relative cost of glass stain characteristics according to various authors. (Reprinted with permission from Willey, R.R. and Parks, R.E., in *Handbook of Optomechanical Engineering*, Ahmad, A., Ed., CRC Press, Boca Raton, FL, 1997, chap.1. Copyright CRC Press, Boca Raton, FL.)

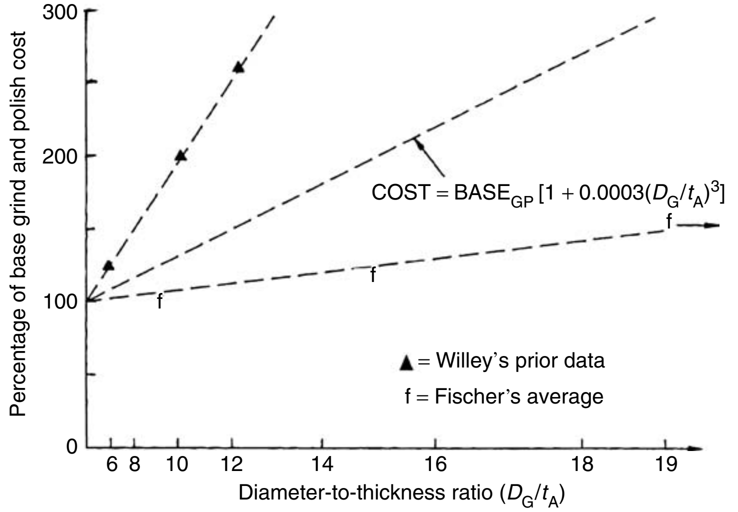

FIGURE 4.14 Relative cost vs. reciprocal tolerance according to various authors concerning lens diameter-to-thickness ratio. (Reprinted with permission from Willey, R.R. and Parks, R.E., in *Handbook of Optomechanical Engineering*, Ahmad, A., Ed., CRC Press, Boca Raton, FL, 1997, chap. 1. Copyright CRC Press, Boca Raton, FL.)

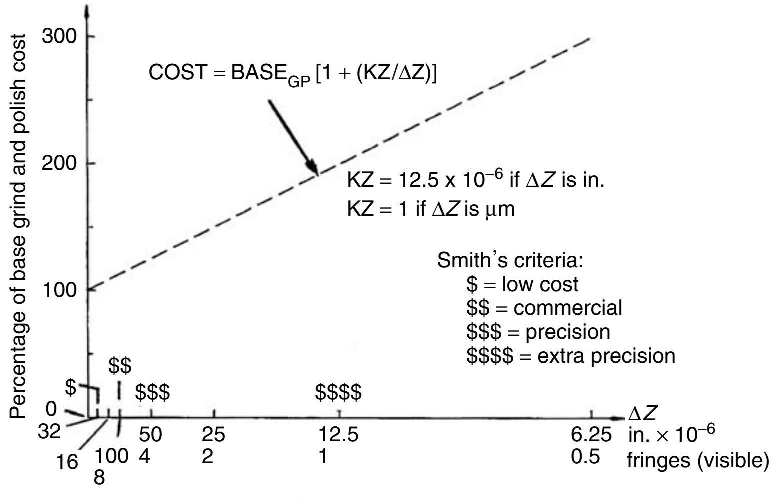

FIGURE 4.15 Relative cost vs. reciprocal tolerance according to various authors concerning radius of curvature expressed as sagittal error. (Reprinted with permission from Willey, R.R. and Parks, R.E., in *Handbook of Optomechanical Engineering*, Ahmad, A., Ed., CRC Press, Boca Raton, FL, 1997, chap. 1. Copyright CRC Press, Boca Raton, FL.)

from Fischer (1990). The wide disparity between these results has not yet been explained, so Willey and Parks (1997) recommended the middle curve and the related equation as temporary compromises pending further investigation.

Figure 4.15 shows an empirically derived graph for the increase in cost of a lens above the base grind and polish cost as a function of radius of curvature tolerance expressed as sagittal depth error. Sagittal depth is measured with a spherometer or interferometer. The relationship between the error in sagittal depth and the error in radius is given by

$$\Delta Z/\Delta R = (D_G/R)^2/8 \tag{4.1b}$$

where ΔZ and ΔR are the depth error and the radius error, respectively. As pointed out by Willey and Parks (1997), it might be more appropriate to apply tolerance to sagittal depth directly, but optical technicians expect to see the tolerance applied to radius, as represented by the graph in Figure 4.15.

Figure 4.16 shows the effect of tightening the tolerance on axial thickness t_A of a lens. It is well known that, during fine grinding and polishing, opticians will try to keep the lens on the thick side of the nominal value so that material is available in case a scratch or other defect is discovered and rework is required. If the thickness tolerance is tight, rework may become impossible, the damaged part must be scrapped, and the unit cost of the lot increases. Data from Plummer and Fischer are shown. The curve does not fully reflect Plummer's or Fischer's results for $\Delta t_A > 0.001$ in. (25 μm). Smith's criteria for costs at various quality levels are also represented.

Figure 4.17 depicts the growth of unit cost as the tolerance on surface figure error is tightened. The curve is biased toward Plummer's data rather than Willey's because average opticians obtained the former results, while the latter were obtained by highly skilled specialists (Willey, 1983). The variational limits for Willey's data (vertical error bars) indicate that polishing time varies from block to block. The variation tends to decrease as the tolerance becomes the driving force for cost.

Figure 4.18 shows the effect of specifying a more rigorous surface finish (scratch/dig) as defined in U.S. military specification MIL-O-13830. The graph reflects the fact that it is fairly easy to achieve an 80/50 finish on modest-sized lenses, whereas "reticle quality" of 10/5 or better is much more difficult. "Laser quality" surfaces are usually in the range of 40/20 or better.

Figure 4.19 shows the cost effect of tightening lens diameter tolerances. This does not have a particularly strong influence on cost up to the limiting capability of the edging apparatus and process. Note that the agreement between the results from various workers is better than in most of the other relationships discussed here.

Figure 4.20 deals with tolerancing eccentricity of the lens, expressed in terms of its residual wedge angle in milliradians or the light deviation expressed in arcminutes resulting from that wedge. The data attributed to Fischer apply to a 2-in. (50.8-mm)-diameter lens. The deviation values are based on a refractive index of 1.5 and can be scaled for other indices.

Another factor that influences the cost of a lens is the "polishability" of the glass or other material in the substrate. Table 4.1 from Willey and Parks (1997) lists this factor for a variety of common

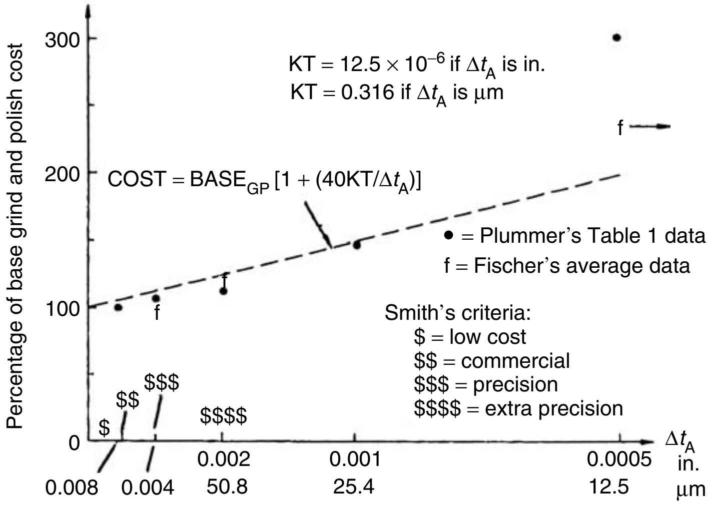

FIGURE 4.16 Relative cost vs. reciprocal tolerance according to various authors concerning lens center or axial thickness. (Reprinted with permission from Willey, R.R. and Parks, R.E., in *Handbook of Optomechanical Engineering*, Ahmad, A., Ed., CRC Press, Boca Raton, FL, 1997, chap.1. Copyright CRC Press, Boca Raton, FL.)

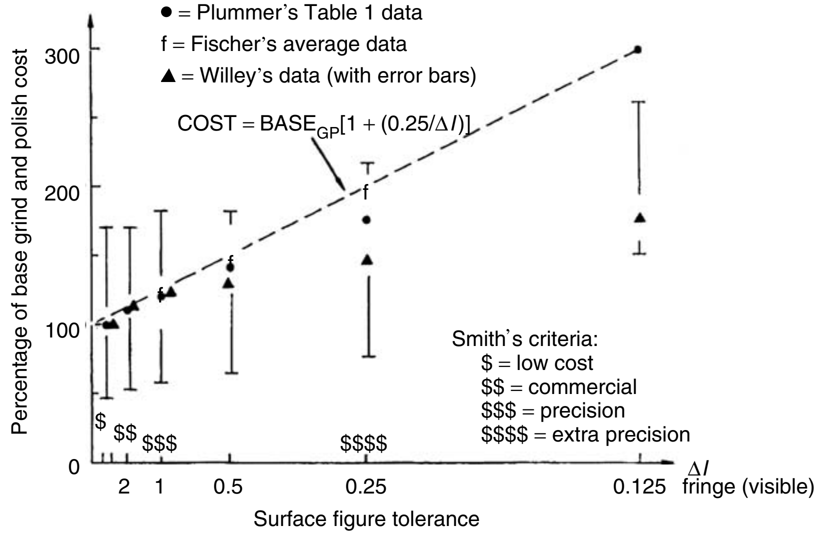

FIGURE 4.17 Relative cost vs. reciprocal tolerance according to various authors concerning lens figure irregularity. (Reprinted with permission from Willey, R.R. and Parks, R.E., in *Handbook of Optomechanical Engineering*, Ahmad, A., Ed., CRC Press, Boca Raton, FL, 1997, chap.1. Copyright CRC Press, Boca Raton, FL.)

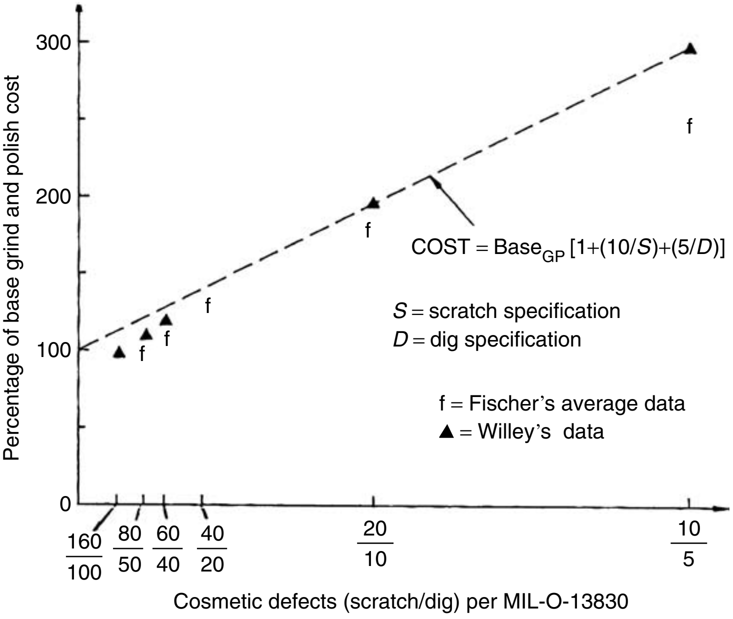

FIGURE 4.18 Relative cost vs. reciprocal tolerance according to various authors concerning lens surface finish (scratch and dig). (Reprinted with permission from Willey, R.R. and Parks, R.E., in *Handbook of Optomechanical Engineering*, Ahmad, A., Ed., CRC Press, Boca Raton, FL, 1997, chap.1. Copyright CRC Press, Boca Raton, FL.)

materials. A large value means that the material is hand to polish. The values shown are best personal estimates by those authors based on their experience. Other workers in the field may use different factors that reflect experience in other shops. Graphs of the types shown earlier regarding tolerance

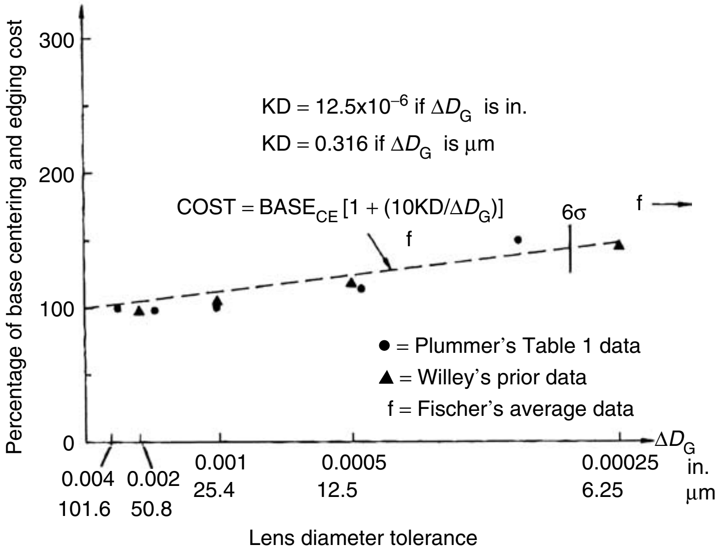

FIGURE 4.19 Relative cost vs. reciprocal tolerance according to various authors concerning lens diameter. (Reprinted with permission from Willey, R.R. and Parks, R.E., in *Handbook of Optomechanical Engineering*, Ahmad, A., Ed., CRC Press, Boca Raton, FL, 1997, chap.1. Copyright CRC Press, Boca Raton, FL.)

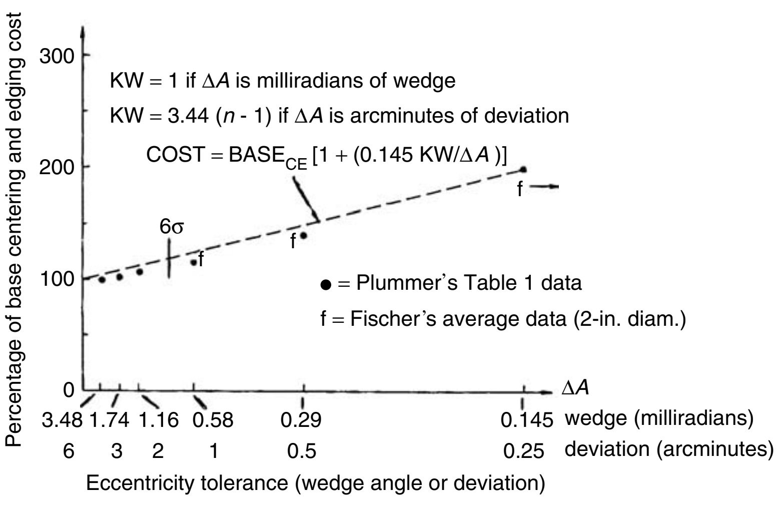

FIGURE 4.20 Relative cost vs. reciprocal tolerance according to various authors concerning eccentricity (wedge or deviation). (Reprinted with permission from Willey, R.R. and Parks, R.E., in *Handbook of Optomechanical Engineering*, Ahmad, A., Ed., CRC Press, Boca Raton, FL, 1997, chap.1. Copyright CRC Press, Boca Raton, FL.)

effects on costs cannot be prepared because polishability is not universally related to some single physical property, such as hardness or Young's modulus, of the materials. The table is included here to indicate the approximate potential production cost (and schedule) impacts of choosing different materials for a given optical component.

As indicated in Figure 4.12, errors in mechanical parts can affect lens orientation and location. From the system viewpoint, the tolerances applied to dimensions and other parameters of the mount components need to be considered when total production cost of an instrument is to be estimated. To illustrate this point, consider Figure 4.21, which shows the effect of tightening the tolerance on

TABLE 4.1
Polishability Factor for Various Materials

Material	Factor (%)	Material	Factor (%)
BK7	100	LaKN9, LaFN21	200
SF56	120	Electroless nickel	250
Pyrex	125	CaF_2, LiF	275
Germanium	130	MgF_2, Si	300
Fused silica	140	Electrolytic nickel	350
Zerodur	150	Ruby	700
ZnS, ZnSe	160	Sapphire	800
FK2, BaF_2, AMTIR	170		

Source: From Willey, R. R. and Parks, R.E. in *Handbook of Optomechanical Engineering*, Ahmad, A., Ed., CRC Press, Boca Raton, FL, 1997, chap.1.

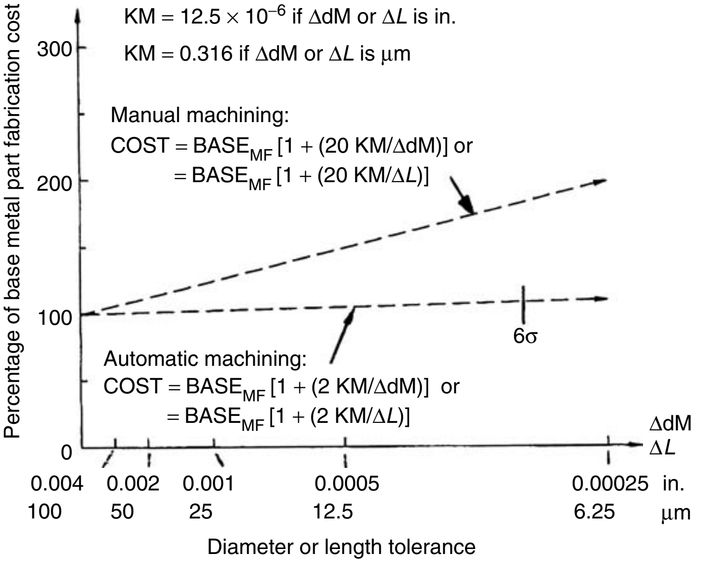

FIGURE 4.21 Relative cost vs. reciprocal tolerance concerning lens mounting bore diameters and lengths. (Reprinted with permission from Willey, R.R. and Parks, R.E., in *Handbook of Optomechanical Engineering*, Ahmad, A., Ed., CRC Press, Boca Raton, FL, 1997, chap.1. Copyright CRC Press, Boca Raton, FL.)

diameter or length of the bore into which a lens is to be mounted. The two lines represent manual and automatic machining methods. Obviously, significantly more labor is required to manually setup and machine the part if the tolerances become more demanding. The cost impact for setup and machining is smaller with automatic techniques because, once the machine is set up, the operations repeat within the capability of the machine almost regardless of tolerance. An input to this cost (and to all other relationships described in this section) is the amount and difficulty of inspection required to determine acceptability of the resulting parts when tolerances are tight.

Figure 4.22 shows another cost vs. tolerance relationship pertaining to mechanical parts. Here, the cost is seen to vary with tolerances on concentricity (ΔCE) or runout along the length of the bore (ΔLE) created to hold a lens. Two lines are shown: the upper line assumes that the part must be removed from the machine after cutting one surface, reinstalled in the machine, and realigned

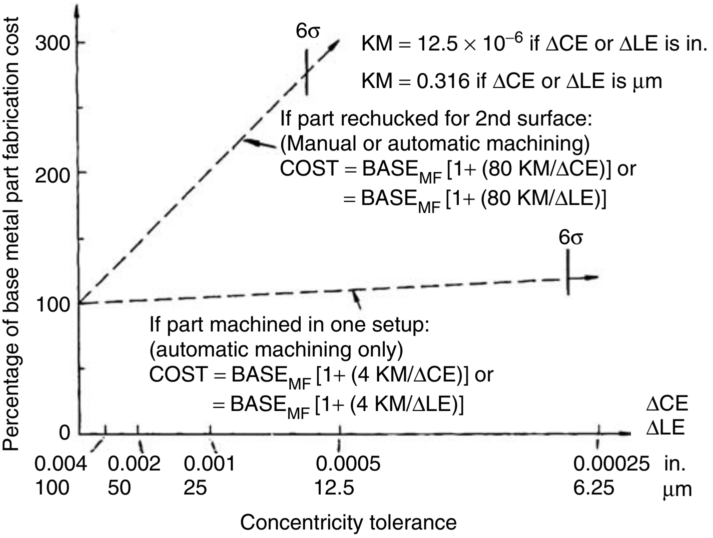

FIGURE 4.22 Relative cost vs. reciprocal tolerance concerning lens mounting bore concentricity (ΔCE) and tilt and length runout (ΔLE). (Reprinted with permission from Willey, R.R. and Parks, R.E., in *Handbook of Optomechanical Engineering*, Ahmad, A., Ed., CRC Press, Boca Raton, FL, 1997, chap.1. Copyright CRC Press, Boca Raton, FL.)

before a second surface can be cut, while the lower line assumes that all machining can be done in one setup. The big difference between the slopes of the two lines indicates the extra labor (and cost) to accomplish the second setup. The desirability of designing the mechanical part so as to allow it to be machined in one setup is apparent from the graph. This same principle should be applied whenever possible in the design of other mechanical parts.

Each parameter and dimension for a given part has a standard deviation (σ) from the nominal (read design) value. Each manufacturing process also has a standard deviation from its nominal capability. The collective effect of all deviations associated with an opto-mechanical instrument is a measure of variability in that end item. Excessive variability increases its costs and decreases its reliability. A production philosophy for reducing variability is called *Six Sigma* (6σ). Here, personnel assignments and manufacturing and testing processes are optimized to improve product quality, so a higher percentage conforms to requirements. At the same time, drawing tolerances for all components of each end item are made as lenient as possible while ensuring that they meet performance requirements in all specified operating environments throughout the useful life of the item. In Figures 4.19–4.22, Willey and Parks indicated the most stringent tolerance that allows 6σ results to be achieved. The basis for this was not explained.

Willey and Parks (1997) described how to apply the graphs of Figures 4.13–4.22 in predicting the unit production cost of lenses. They gave several equations pertinent to such calculations and illustrated the estimating process by applying it to the optical system for a multi-focal-length tracking telescope. Their goal was to establish a tolerance budget for those optics that would meet system performance requirements yet minimize cost. The interested reader should find this example quite enlightening.

4.4 LENS WEIGHT AND CENTER OF GRAVITY LOCATION

Important aspects of the design of an optical instrument are the estimation of the weights of its optical, mechanical, and other components and the locations of the CGs of those components. With this and other design information, one can predict the weight of the complete instrument and locate the

CG of the ensemble before any of the parts are available for these properties to be measured. Here, we will summarize the procedures for making these calculations for lenses or mirrors with shapes similar to the common forms of lenses. We will treat all these components as if they were lenses.

4.4.1 LENS WEIGHT ESTIMATION

Any lens can be divided into a combination of any of three basic parts: a spherical segment, a right circular cylinder, and a truncated cone. We will here refer to these as *cap*, *disk*, and *cone*, respectively. Figure 4.23 shows section views of nine basic lens configurations. The weight of a convex cap is considered to be positive while that of a concave cap is taken to be negative. Hence, for a biconvex lens, we would add the weights of the two caps to that of the disk. For a meniscus lens,

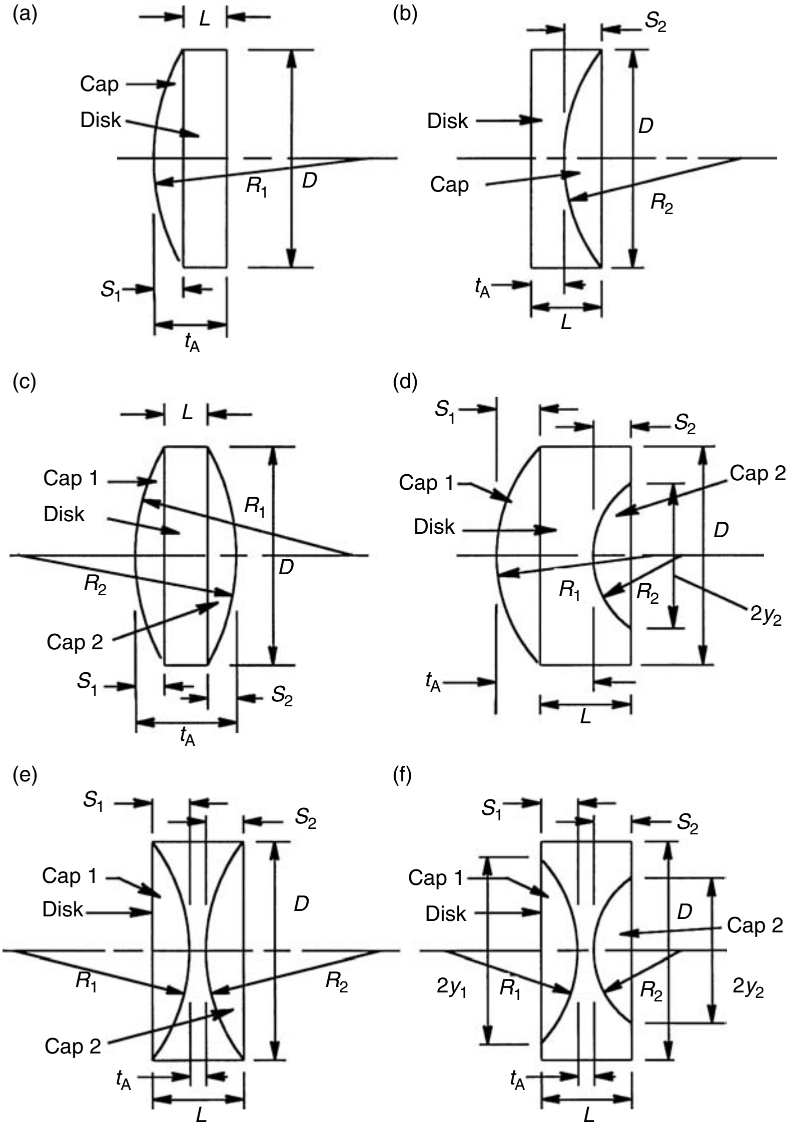
(a)
L
Cap
Disk
R_1
D
S_1
t_A
(b)
S_2
Disk
D
Cap
R_2
t_A
L
(c)
L
Cap 1
Disk
R_1
D
R_2
Cap 2
S_1
S_2
t_A
(d)
S_1
S_2
Cap 1
Cap 2
Disk
D
R_1
R_2
$2y_2$
t_A
L
(e)
S_1
S_2
Cap 1
Disk
D
R_1
R_2
Cap 2
t_A
L
(f)
S_1
S_2
Cap 1
Disk
D
Cap 2
$2y_1$
R_1
R_2
$2y_2$
t_A
L

FIGURE 4.23 Schematic sectional views of nine lens configurations dimensioned as required to estimate lens weights: (a) plano-convex, (b) plano-concave, (c) biconvex, (d) meniscus, (e) biconcave, (f) biconcave with dual flat bevels (continued on next page)

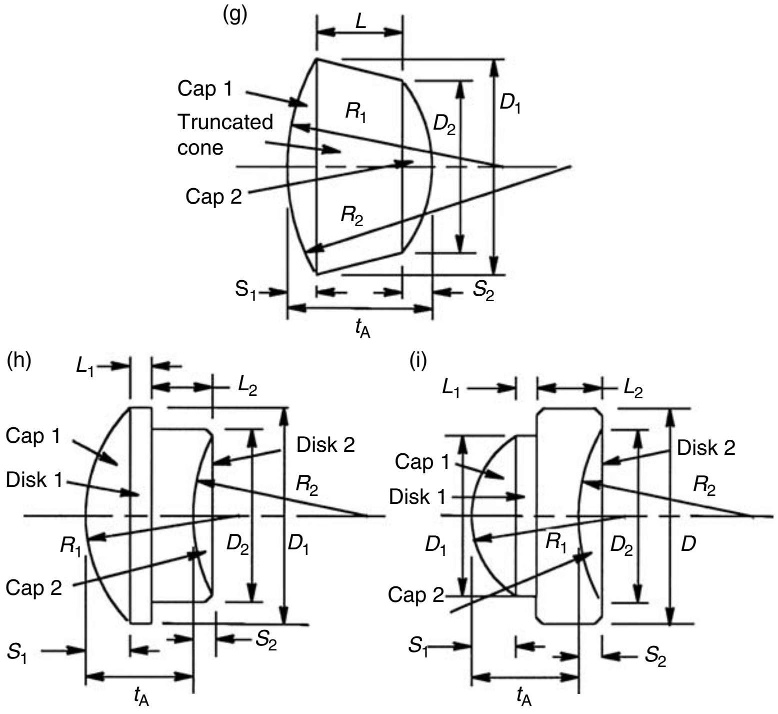
(g)
L
Cap 1
Truncated cone
Cap 2
R_1
R_2
D_2
D_1
S_1
S_2
t_A
(h)
L_1
L_2
Cap 1
Disk 1
Disk 2
R_2
R_1
D_2
D_1
Cap 2
S_1
S_2
t_A
(i)
L_1
L_2
Cap 1
Disk 1
Disk 2
R_2
D_1
R_1
D_2
D
Cap 2
S_1
S_2
t_A

FIGURE 4.23 (continued) (g) biconvex with conical section, (h) cemented meniscus with larger plano-convex element, and (i) cemented meniscus with larger plano-concave element.

we would add the weight of the convex cap to that of the disk and subtract that of the concave cap. For simplicity, lens shapes are considered to extend to sharp corners, so weight reductions from bevels (such as those shown in views [h] and [i]) are ignored. For this reason, such calculations may tend to slightly overestimate weights. Weights for cemented doublets and more complex configurations are obtained by adding the contributions from the individual elements.

The weight W_{DISK} of a disk is

$$W_{\mathrm{DISK}} = \pi \rho L D^2/4 \tag{4.2}$$

where ρ is density, L the axial length of the disk, and D its diameter.

The weight W_{CONE} of a cone is

$$W_{\mathrm{CONE}} = \pi \rho L(D_1{}^2+D_1D_2+D_2{}^2)12 \tag{4.3}$$

where L is the axial length of the cone, D_1 the diameter of the larger end of the cone, and D_2 the diameter of the smaller end of the cone.

The sagittal depth S and weight W_{CAP} of a cap are

$$S = R - [R^2 - (D^2/4)]^{1/2} \tag{4.4}$$

$$W_{\mathrm{CAP}} = \pi \rho S^2[R-(S/3)] \tag{4.5}$$

Here we may consider the algebraic signs of all radii to be positive.

To illustrate the use of these equations, consider the following four examples:

1. A biconvex lens as shown in Figure 4.23(c) has dimensions of $D = 4.0$ in. (101.6 mm), $t_A = 1.0$ in. (25.4 mm), $R_1 = R_2 = 6.0$ in. (152.4 mm). The lens is made of NBK7 glass with $\rho = 0.090$ lb/in.^{3} (2.51 g/cm^3). From Eq. (4.4), $S_1 = S_2 = 6.0 - [6.0^2 - [(4.0^2/4)]^2 = 0.343$ in. (8.716 mm). From the geometry of the figure, $L = t_A - S_1 - S_2 = 0.314$ in. (7.976 mm). From Eq. (4.2), the weight W_D of the disk is $(\pi)(0.090)(0.314)(4.0)^2/4 = 0.355$ lb (0.161 kg). From Eq. (4.5), the weight W_{CAP} of each cap is $(\pi)(0.090)(0.314^2)[6.0 - (0.314/3)] = 0.164$ lb (0.075 kg). The total lens weight W_{LENS} is $W_D + 2W_{CAP} = 0.355 + (2)(0.164) = 0.683$ lb (0.310 kg).

2. A biconcave lens as shown in Figure 4.23(e) has the same diameter and radii and is made of the same glass as in the last example. Now t_A is 0.25 in. (6.35 mm). The values for S_1 and S_2 are 0.343 in. (152.4 mm) as before so the cap weights are both 0.164 lb (0.075 kg). L is $t_A + S_1 + S_2 = 0.936$ in. (23.774 mm). The disk weight W_D is $(\pi)(0.090)(0.936)(4.0)^2/4 = 1.058$ lb (0.480 kg). The total lens weight W_{LENS} is $W_D - 2W_{CAP} = 1.058 - (2)(0.164) = 0.730$ lb (0.331 kg).

3. A lens shaped as shown in Figure 4.23(g) has radii of $R_1 = 6.0$ in (152.4 mm) and $R_2 = 4.0$ in. (101.6 mm). Its largest diameter is 2.0 in. (50.8 mm), its smallest diameter is 1.75 in. (44.45 mm), and its axial thickness is 0.88 in. (22.353 mm). It is made of F2 glass with $\rho = 0.130$ lb/in.^{3} (0.361 g/cm^3). From Eq. (4.4), $S_1 = 6.0 - [6.0^2 - (2.0^2/4)]^{1/2} = 0.084$ in. (2.132 mm) and $S_2 = 4.0 - [4.0^2 - (1.75^2/4)]^{1/2} = 0.097$ in. (2.461 mm). L is then $t_A - S_1 - S_2 = 0.88 - 0.084 - 0.097 = 0.699$ in. (17.755 mm). From Eq. (4.3), the weight W_{CONE} of the truncated cone $= (\pi)(0.130)(0.699)(2.0^2 + (2.0)(1.75) + 1.75^2)/12 = 0.251$ lb (0.114 kg). From Eq. (4.5), the weight W_{CAP1} of the larger cap is $(\pi)(0.130)(0.084^2)[6.0 - (0.084/3)] = 0.017$ lb (0.008 kg). From the same equation, the weight W_{CAP2} of the smaller cap is $(\pi)(0.130)(0.097^2)[4.0 - (0.097/3)] = 0.015$ lb (0.007 kg). The total lens weight W_{LENS} is $W_{CONE} + W_{CAP1} + W_{CAP2} = 0.251 + 0.017 + 0.015 = 0.283$ lb (0.128 kg).

4. A cemented lens configured as shown in Figure 4.23(h) has a plano-convex first element with a cylindrical rim of length $L_1 = 0.1$ in. (2.54 mm), a diameter D_1 of 1.18 in. (29.972 mm), and a radius of 1.85 in. (46.99 mm). Its glass type is NBK7. The second element has a cylindrical rim of length $L_2 = 0.35$ in. (8.89 mm), a diameter of 0.93 in. (23.622 mm), and a radius of 1.95 in. (49.53 mm). It is made of SF4 glass. From Table 3.2, ρ_1 is 0.090 lb/in.^{3} (2.51 g/cm^3) and ρ_2 is 0.172 lb/in.^{3}(4.79 g/cm^3). From Eq. (4.4), $S_1 = 1.85 - [1.85^2 - (1.18^2/4)]^{1/2} = 0.0966$ in. (2.4537 mm) and $S_2 = 1.95 - [1.95^2 - (0.93^2/4)]^{1/2} = 0.0562$ in. (1.4288 mm). The weight W_{CAP1} of the first cap is $(\pi)(0.090)(0.097^2)[1.85 - (0.097/3)] = 0.0048$ lb (0.0022 kg) and the weight W_{D1} of the first disk is $(\pi)(0.090)(0.1)(1.18^2/4) = 0.0098$ lb (0.0045 kg). The weight W_{D2} of the second disk is $(\pi)(0.172)(0.35)(0.93^2/4) = 0.0409$ lb (0.0185 kg) and the weight W_{CAP2} of the second cap is $(\pi)(0.172)(0.056^2)[1.95 - (0.056/3)] = 0.0033$ lb (0.0015 kg). The total lens weight W_{LENS} is $W_{CAP1} + W_{D1} + W_{D2} - W_{CAP2} = 0.0522$ lb (0.0237 kg).

It should be noted that the shape of a simple solid convex mirror is typically the same as that of a plano-convex lens while that of a simple solid concave mirror is typically that of a plano-concave lens. The above equations are used to estimate their weights. Techniques for estimating the weights of solid mirrors with contoured backs are summarized in Section 9.8. The weights of lightweighted mirrors made from solid blanks with cavities of various shapes and sizes created in the mirror backs can be estimated by subtracting the total weights of all the cavities (assuming them to be filled with the same material as the mirror) from the weights of the solid substrates. The weights of mirrors with built-up construction are best estimated by dividing the structure into groups of parts of the same sizes and shapes, estimating the total weight of each group, and summing these to get the aggregate mirror weight.

In general, we treat caps with aspheric surfaces as spherical ones unless the asphericity is strong, as in the case of a very deep paraboloid. In such a case, we can determine the volume (and the weight) by calculating the cross-sectional area of the aspheric volume and multiplying that by 2π times the height from the axis of symmetry of the centroid of the area. This technique is used in Section 9.8 to calculate the weight of contoured backs for arched mirrors. Appropriate equations for parabolic sections are given there. Most general aspherics can be approximated by conics. One can obtain the area and centroid height equations for conic sections other than the parabola from standard solid analytic geometry texts.

4.4.2 LENS CENTER OF GRAVITY LOCATION

Figure 4.24 shows the cross sections of the three basic shapes that make up lenses. The dimensions X indicate the locations of their CGs relative to the left side. The following equations from Vukobratovich (1993) allow us to determine X for each shape using the dimensions shown in the figures:

$$X_{\mathrm{DISK}} = L/2 \tag{4.6}$$

$$X_{\mathrm{CAP}} = S(4R - S)/[4(3R - S)] \tag{4.7}$$

$$X_{\mathrm{CONE}} = 2L[(D_1/2) + D_2]/[3(D_1 + D_2)] \tag{4.8}$$

The location of the CG of any lens comprising N parts and weighing W_{LENS} can be estimated from

$$X_{\mathrm{LENS}} = \sum_{i=1}^{i=N} (X_i' W_{\mathrm{i}})/W_{\mathrm{LENS}} \tag{4.9}$$

In this equation, X_{LENS} and all values of X_i' are measured from the same point on the axis of the lens. For example, in view (a) of Figure 4.23, if we choose the left vertex as the reference and remember that X_{CAP} is always measured from the plano side, $X'_{\mathrm{CAP1}} = S_1 - X_{\mathrm{CAP1}}$, $X'_{\mathrm{DISK}} = S_1 + X_{\mathrm{DISK}}$, and $X'_{\mathrm{CAP2}} = S_1 + L + X_{\mathrm{CAP2}}$.

We will next solve an example to illustrate the use of these equations. We assume a lens of the type shown in Figure 4.23(h) having the dimensions and weights listed in Example 4 in the last subsection. The parameters from that example needed here and the calculations of the X_{i} terms are as follows:

$$W_{\mathrm{LENS}} = 0.0522 \text{ lb}$$

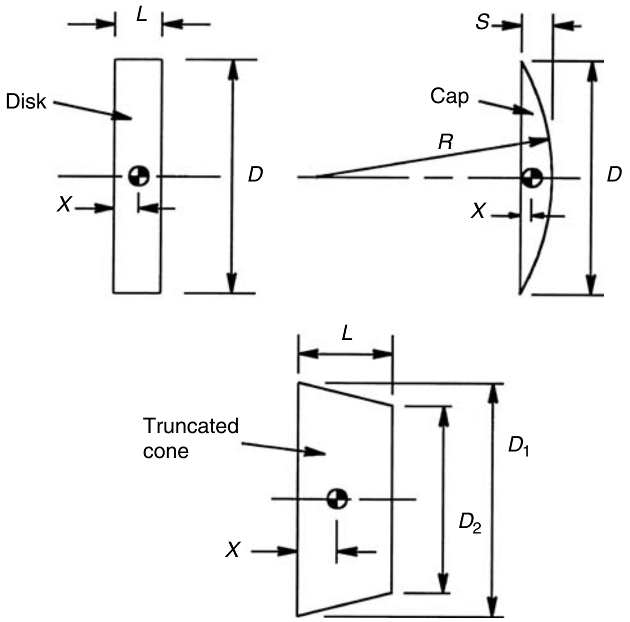

FIGURE 4.24 Schematic sectional views of basic solid shapes from which lenses are formed. The location of the center of gravity (CG) for each shape is shown.

For Cap 1, $S_1 = 0.0966$ in., $R = 1.85$ in., and $W_{\mathrm{CAP1}} = 0.0048$ lb. From Eq. (4.7), $X_{\mathrm{CAP1}} = \{0.0966\,[(4)(1.85) - 0.0966]\}/\{4[(3)(1.85) - 0.0966]\} = 0.0323$ in. Then, $X'_{\mathrm{CAP1}} = 0.0966 - 0.0323 = 0.0643$ in. Hence, $(W_iX'_i)_{\mathrm{CAP1}} = 3.086 \times 10^{-4}$ lb-in.

For Disk 1, $L_1 = 0.1$ in. and $W_{\mathrm{DISK1}} = 0.0098$ lb. From Eq. (4.6), $X_{\mathrm{DISK}} = 0.1/2 = 0.05$ in. So, $X'_{\mathrm{DISK1}} = S_1 + X_{\mathrm{DISK1}} = 0.1466$ in. and $W_iX'_i = 1.437 \times 10^{-3}$ lb-in.

For Disk 2, $L_2 = 0.35$ in. and $W_{\mathrm{DISK2}} = 0.0409$ lb. From Eq. (4.6), $X_{\mathrm{DISK2}} = 0.35/2 = 0.175$ in. Hence, $X'_{\mathrm{DISK2}} = S_1 + L_1 + X_{\mathrm{DISK2}} = 0.3716$ in. and $(W_iX'_i)_{\mathrm{DISK1}} = 1.520 \times 10^{-2}$ lb-in.

For Cap 2, $S_2 = 0.0562$ in., $R = 1.95$ in. and $W_{\mathrm{CAP2}} = 0.0033$ lb. From Eq. (4.7), $X_{\mathrm{CAP2}} = \{0.0562\,[(4)(1.95) - 0.0562]\}/\{4[(3)(1.95) - 0.0562]\} = 0.0188$ in. Hence, $X'_{\mathrm{CAP2}} = S_1 + L_1 + L_2 - X_{\mathrm{CAP2}} = 0.5278$ in. and $(W_iX'_i)_{\mathrm{CAP2}} = 1.742 \times 10^{-3}$ lb-in.

From Eq. (4.9), $X_{\mathrm{LENS}} = (3.086 \times 10^{-4} + 1.437 \times 10^{-3} + 1.520 \times 10^{-2} - 1.742 \times 10^{-3})/0.0522 = 0.2913$ in. so the CG is this distance from the left vertex of the lens.

We can check this computation in the following manner. We find the distances from each part CG to the lens CG (called moment arms) and multiply these dimensions by the respective part weights. The products are moments. Those parts whose CGs lie to the left of the lens CG cause counterclockwise (CCW) moments while those to the right of that CG cause clockwise (CW) moments. For the CG of the lens to be properly located, the sum of the CCW moments must equal the sum of the CW moments. In the example just considered, the CCW moment sum is $(0.2913 - 0.0643)(0.0048) + (0.2913 - 0.1466)(0.0098) = 2.507 \times 10^{-3}$ lb-in. and the CW moment sum is $(0.3716 - 0.2913)(0.0409) - (0.5278 - 0.2913)(0.0033) = 2.504 \times 10^{-3}$ lb-in. These moments are equal, so the lens CG location is confirmed.

4.5 MOUNTING INDIVIDUAL LOW-PRECISION LENSES

A low-precision lens is defined here rather arbitrarily as one requiring each surface to be centered to no better than, say, 30 arcmin deviation due to residual optical wedge or 0.25 mm (0.01 in.) maximum lateral decentration relative to a common optical axis. The discussion of opto-mechanical designs for securing a single-element lens in a mechanical housing or cell in this section progresses from a low to a high degree of centration. The simplest designs involve springs that constrain the lens. Reasonably simple lens-mounting designs with higher precision have been described by Jacobs(1943), Richey (1974), and Yoder (1983, 2002). All these designs can be classified as "drop-in" subassemblies in that the glass-to-metal interfaces in the mount are premachined to within some reasonable tolerances on inside diameter (ID) and squareness to the mechanical axis. The OD of the lens is dimensioned and toleranced to allow some radial clearance under all temperature conditions. The shape, or bending, of the lens is not of prime concern here. We are interested in the means for retaining the glass element so that it remains fixed with respect to its mechanical surround. For simplicity, we will call that surround a cell and assume that it is made of metal unless otherwise designated.

4.5.1 SPRING MOUNTINGS

Typical optical mountings requiring a low level of precision are those for the condensing lens and heat-absorbing filter used in the illumination system of a projector. The design is driven to a large extent by the need for low cost, ease of maintenance, and free air circulation so that the optics can survive high temperatures from the nearby light source. Figure 4.25(a) shows a very simple mounting in which a lens made of heat-resistant glass such as Pyrex is held by three springs that engage the rim of the lens. The springs are located at 120° intervals. The symmetry of the mounting tends to keep the lens centered. Flexibility of the springs reduces danger of breakage, but alignment is uncertain unless the axial locations and shapes of the detents on the springs are closely controlled. A slightly more complex version of this design has two plano-convex lenses held with the convex surfaces facing each other in three springs with double detents to separate the lenses axially.

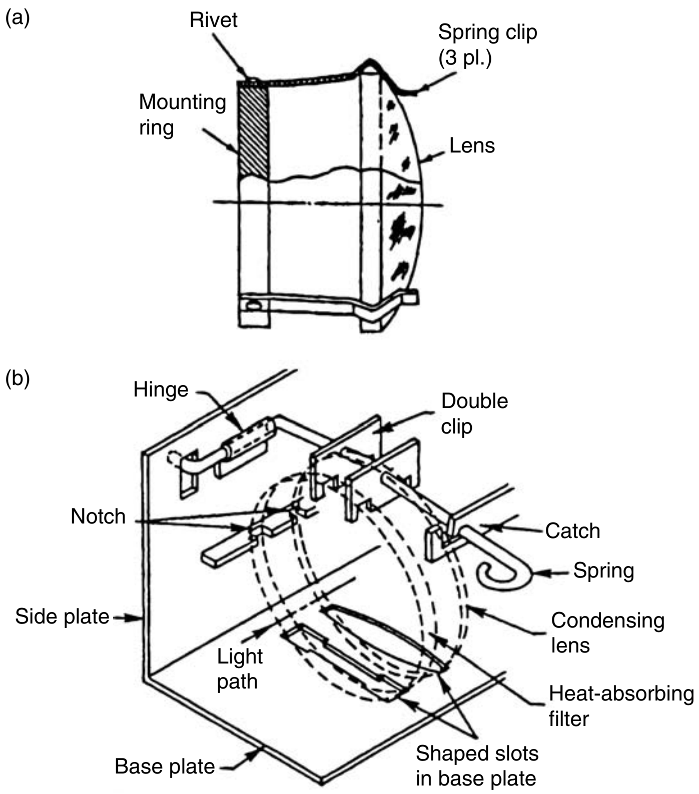

FIGURE 4.25 Spring mountings for lenses. (a) Concept using three leaf springs at 120° intervals around the lens rim, (b) a mounting for a filter and lens as used in a Kodak Ektagraphic slide projector. (From Yoder, P.R. Jr., *Mounting Optics in Optical Instruments*, SPIE Press, Bellingham, 2002.)

Figure 4.25(b) is a schematic of a low-cost, spring-loaded mounting for a heat-absorbing filter and a biconvex condensing lens as used in a Kodak Ektagraphic slide projector. The rims of the optics fit into cutouts in the sheet-metal baseplate and into detents cut into a metal strip attached to the side of the subassembly. The cutout in the baseplate is shaped such that a lens with different first and second curvatures cannot be inserted backward. The spring holding the optics in place allows for ease of engagement and disengagement to facilitate assembly and servicing. Air from the cooling fan is directed across the optical surfaces to minimize temperature rise during use.

4.5.2 BURNISHED CELL MOUNTINGS

Burnishing of a lens into its cell is illustrated by Figure 4.26 and is accomplished by deforming the metal lip from the condition shown in view (a) to that shown in view (b) after the lens is inserted. The burnished mounting is most frequently used with small lenses such as those in microscope objectives, endoscopes, or short-focal-length camera objectives. It is inexpensive, compact, and requires a minimum number of parts. Preload is uncertain. The mounting is permanent; removal of the lens without damaging it is extremely difficult.

The cell material must be malleable rather than brittle. Either brass or a soft aluminum alloy is appropriate for this reason. A radial clearance of 0.005 in. (0.125 mm) between the lens rim and the cell ID is common. One method for burnishing is performed by chucking the cell in a lathe, inserting the lens, slowly rotating the cell, and bringing three or more hardened cylindrical tools inclined at an angle against the projecting lip, forcing it over against the lens. Care must be exercised not to

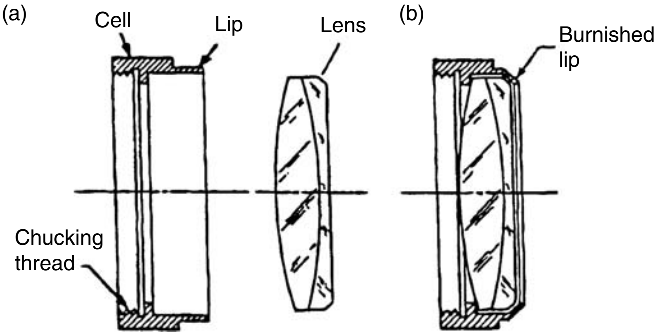

FIGURE 4.26 A lens burnished into a cell made of a malleable metal. (a) Cell and lens configurations, (b) completed subassembly. (From Yoder, P.R. Jr., *Mounting Optics in Optical Instruments*, SPIE Press, Bellingham, 2002.)

excessively strain the lens during the burnishing operation. The lens must be held firmly against its seat while the oblique force is exerted on the metal so as not to decenter the lens within its radial clearance at the early stage of the process before the lens is restrained.

Another burnishing technique that produces similar results is illustrated conceptually in Figure 4.27(a). Here, the cell is located with its axis vertical on the baseplate of a mechanical press. The lens rests on a shoulder in the cell and is centered in the cell ID with shims or by relying on a close radial fit into that ID. A tool, or die, with an internal conical surface is lowered over the cell lip and forced downward by means of the lever that actuates a rack and pinion drive mechanism so as to bend the lip over the lens (see view [b]). Alternatively, the die can be shaped more or less as indicated in view (c) so that the innermost edge of the lip is bent progressively toward the lens clear aperture rather than remaining conical.

As a minor variation on either of these methods, a thin, narrow washer of slightly resilient material such as Nylon or Neoprene is sometimes inserted against the exposed surface of the lens and the metal burnished over that washer rather than directly contacting the glass. This tends to seal the glass-to-metal interface and can offer a slight spring action to hold the glass axially against the seat at higher temperatures when the metal lip tends to expand away from the glass.

Another version of the burnished cell mounting design is shown in Figure 4.28. Here a coil spring is inserted between the lens and the cell shoulder and slightly compressed as the lip is spun over. Jacobs (1943) suggested that this method is useful when the assembly is to be subjected to severe shock or when a low-cost means of avoiding stress in the lens is needed. Yet another version has the spring between the lens and the burnished lip. This allows the lens to be registered directly against the shoulder, thereby enhancing location and alignment accuracy. A thin brass tube with staggered lateral slots can be used as the spring in either design. This avoids stress concentration at localized contacts between high points on the end of a coil spring and the lens that can occur even if the spring's end is ground flat as shown in the figure. The spring must be stiffer than the lip so the latter is bent rather than just compressing the spring during the operation.

4.5.3 SNAP RING MOUNTINGS

A snap ring that drops into a groove machined into the cell's inside surface is sometimes used to hold lenses in a cell. Figure 4.29 shows such a design with a ring of circular cross section. The ring is cut through at some point on its periphery to allow it to spring into place. This mounting is used only in low-performance applications. Simplicity and low cost are its chief virtues. Yoder (2002) provided equations for designing such a mount to interface with convex and flat beveled concave surfaces. The preload, if any, exerted by the ring onto the lens is very unpredictable because variations in lens thickness, groove location and depth, and snap ring dimensions affect the interface between the lens and ring.

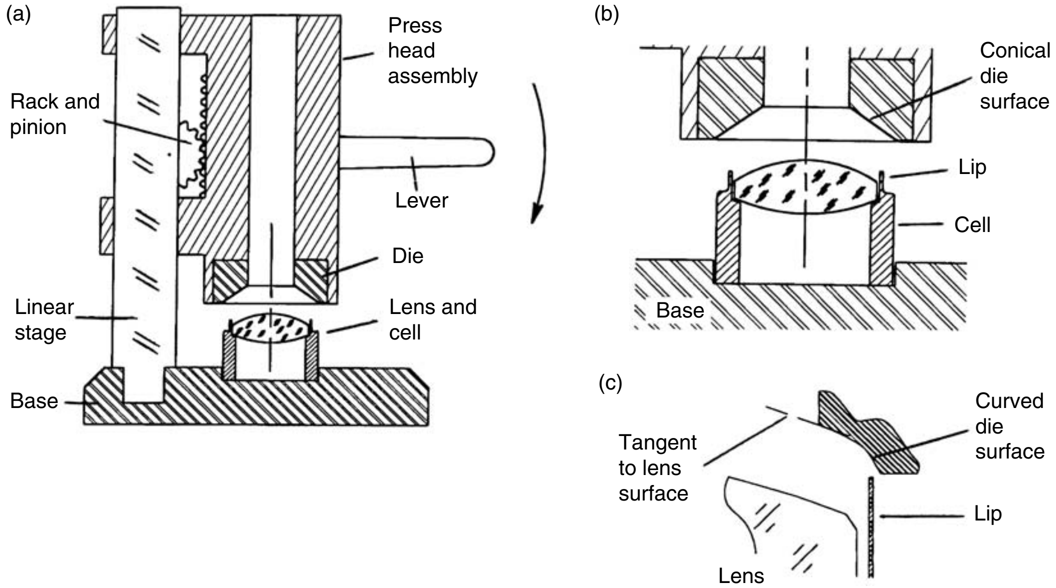
(a)
Press head assembly
Rack and pinion
Lever
Die
Linear stage
Lens and cell
Base
(b)
Conical die surface
Lip
Cell
Base
(c)
Curved die surface
Tangent to lens surface
Lip
Lens

FIGURE 4.27 An alternate method for burnishing a lens into a cell using a mechanical press to bend the cell lip without rotating the cell and lens. (a) Conceptual view, (b) enlarged view of the die, lens, and cell, and (c) alternative shape for die shaped to progressively bend the lip onto the lens.

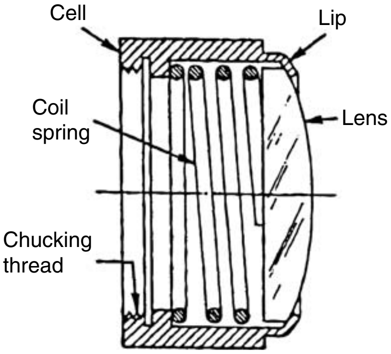
Cell
Lip
Coil spring
Lens
Chucking thread

FIGURE 4.28 Variation of the burnished-in lens mounting with a spring to axially load the lens against a shoulder. (Adapted from Jacobs, D.H., *Fundamentals of Optical Engineering*, McGraw-Hill, New York, 1943.)

A configuration for a ring-constrained lens mounting with a different form of groove is shown in Figure 4.30. Here, a continuous circular snap ring with a circular cross section is pressed into a tapered or ramped inside surface of the mount wall. The mount is made of plastic and is quite resilient. The ramped groove is molded into the mount. Spring action of the wall holds the ring against both the lens surface and the ramp. This design is less sensitive to dimensional errors than those with metal mounts and conventional grooves. It is, however, hard to establish a particular preload with this technique

A continuous ring may be used without a grooved cell if dimensioned and toleranced so that an interference fit is achieved between the ring and the inner wall of the cell when the ring is pressed in place. Figure 4.31 illustrates this technique. If the assembly is to be exposed to large temperature changes, the ring and cell materials should have reasonably close thermal expansion coefficients to prevent loosening caused by differential expansion. This is a permanent assembly technique because it is virtually impossible to remove the pressed-in ring without damaging the optic.

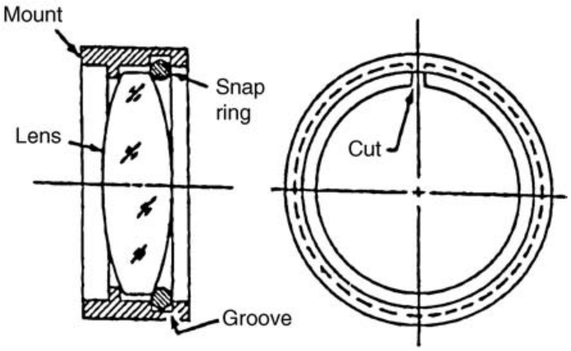

FIGURE 4.29 Technique for holding a lens in a cell with a circular cross section snap ring located in a groove in the cell ID.

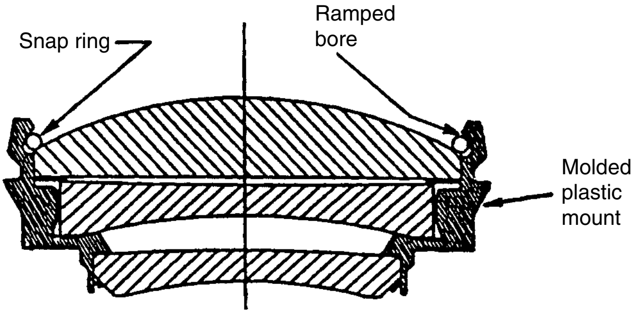

FIGURE 4.30 A lens mounting involving a circular cross section continuous ring that snaps into a ramped groove in a molded plastic mount. (Adapted from Plummer, W.T., Proceedings of the First World Automation Congress (WAC'94), Man, 193, 1994.)

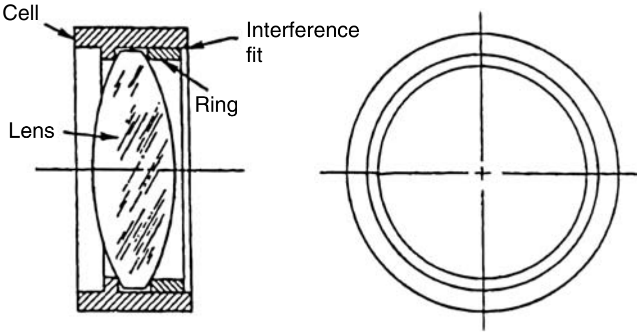

FIGURE 4.31 Technique for holding a lens in a cell with a pressed-in continuous ring. An interference fit between the ring OD and cell ID is essential.

The worst problem with this design may be deciding when to stop pushing the ring against the glass since contact is difficult to detect. In a preferred method of assembly, the cell is heated and the ring cooled sufficiently for the ring to slide easily into contact with the lens. When the temperature stabilizes, the desired radial interference fit is achieved. In both cases, the axial preload against the lens is unpredictable. Baldo (1987) indicated that Publication B4.1-1967 of the American

National Standards Institute (ANSI) defines the appropriate dimensions for force/shrink fits using parts with thin sections.

4.6 MOUNTINGS FOR LENSES WITH CURVED RIMS

In Section 4.2, we defined the rim-contact mounting for lenses as one with a close radial fit between the lens rim and the mount ID. The optical axis decentration is then essentially the error in centration of the cylindrical rim established during edging. Figure 4.32 illustrates a design feature described by Yoder (1986) that minimizes a potential problem sometimes encountered in installing lenses in cells when radial clearances are small. Here, the lens rim is fine-ground as a sphere with the radius equal to one half the lens diameter. The rim is then a short, centralized section of the surface of a ball that fits easily into the cell at any angular orientation. With this technique, a lens can be inserted into an opening that is only a few micrometers larger than the lens diameter without jamming in place from unavoidable tilt before it is properly seated. Close radial fits such as these might be appropriate for applications in which the lens will experience high, lateral acceleration loading. Ideally, the high point on the spherical rim should be in the plane normal to the axis and containing the lens' CG.

A variation of the spherical rim principle is to provide a lens with a *crowned* rim. Here, the radius of the rim is longer than one half the diameter. The allowable range of tilt without jamming is smaller with this type of rim than with the spherical one, but considerably larger than would obtain with a cylindrical rim. Spacers for high- precision lens assemblies also are frequently made with crowned rims.

Although the spherical or crowned rim requires some special optical fabrication steps, the cost of tooling and labor are increased only slightly since the contour of either surface contour does not need to be precise. The tolerances on lens OD and mount ID are, of course, relatively tight. An exception to this requirement is the case of the lathe-assembled lens in which the cell ID is machined at assembly to match the OD of the specific lens being mounted. This technique is described in Section 5.5. Curving the rim would be a worthwhile design feature as a means for preventing damage such as chipping of lens edges or jamming the lens in place at assembly when the lenses have maximum value and replacement could be expensive and affect production schedule. This is especially true if the lens is part of a matched set, i.e., lenses made to a design optimized for specific glass-melt parameters, for as-manufactured thicknesses of other components in the system, or if the cell ID has been customized for the particular lens being installed.

Another desirable feature of the design shown in Figure 4.32 is the provision for injecting elastomer such as RTV through several (minimum of three) holes equally spaced around the lens rim

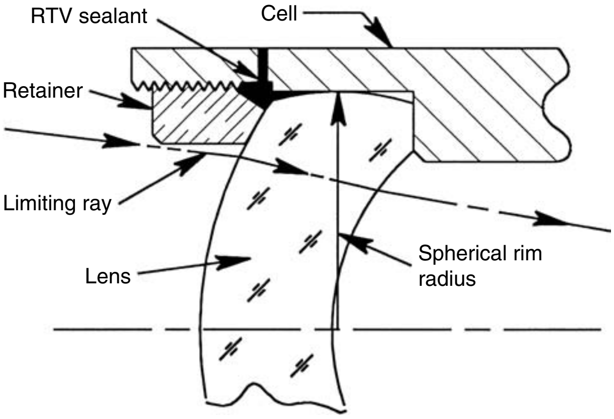

FIGURE 4.32 A spherical-rim lens in a cell. (Adapted from Yoder, P.R. Jr., *Proc. SPIE*, 656, 225, 1986.)

to seal the lens to the cell and to add extra insurance that the lens will not shift under extreme shock or vibration. The sealant also helps prevent the retainer from turning. During installation of the RTV, the lens axis is horizontal and the sealant is injected into the lowest hole(s) first. Displaced air escapes through the higher holes. If the sealant is colored (e.g., black) it can be observed through a refracting face of the lens as it rises around the lens rim. When it starts to emerge from higher holes, the injection point can shift to those holes and additional sealant can be added. If a hole has been provided at the top of the mount, it is easy to ascertain when the annular space around the lens is filled, because the material emerges from that last hole. The seal should be inspected visually through the lens faces to detect voids due to trapped air bubbles. After the sealant has cured, the subassembly should be pressure tested to ensure a complete seal.

4.7 MOUNTINGS INTERFACING WITH SPHERICAL SURFACES

4.7.1 GENERAL CONSIDERATIONS

Delgado and Hallinan (1975), Hopkins (1976), Bayar (1981), and Yoder (1983, 1991, 2002) have emphasized the advantages of contacting lens elements on their polished (generally spherical) surfaces. Some radial clearance is provided between the lens rim and the mount ID. Axial preload that holds the lens against a mechanical reference surface, such as a shoulder in the mount or a spacer, is provided by tightening a threaded retaining ring, attaching a continuous flange, or by applying some other mechanical clamping technique. A typical mounting configuration is shown in Figure 4.33. Here, a single biconvex lens is held against a cell shoulder by a threaded retainer. The chief variables in such designs are the magnitude of the applied preload and the shapes of the opto-mechanical interfaces between the glass and the metal parts. These variables are considered later in this section. This mounting can be assembled and disassembled relatively easily; it accommodates axial thickness variations of the element; it lends itself easily to environmental sealing with a formed-in-place elastomeric seal or with an O-ring; and it is compatible with mounting multiple elements in the same cell or housing.

Another distinct advantage of this so-called "surface contact" lens-mounting design is that tolerances on location and orientation of secondary references surfaces such as the lens rim, bevels, and chamfers can be relaxed since they are not contacted by the cell. Figure 4.34(a) shows a case in which the lens rim is tilted considerably while Figure 4.34(b) shows a decentered rim. These errors would have no effect on the lens alignment. The diameter of the lens is not critical with this type mounting.

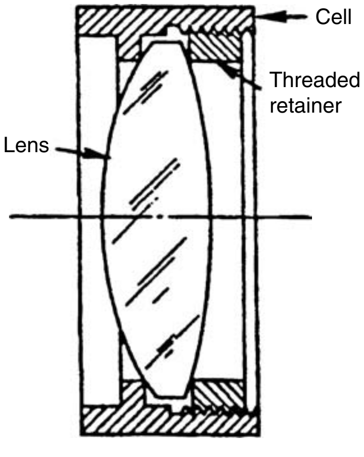

FIGURE 4.33 Common configuration for mounting a double-convex lens with a threaded retaining ring. Interfaces with the glass are generic 90° sharp corner interfaces. (From Yoder, P.R., Jr., *Proc. SPIE*, 389, 2, 1983.)

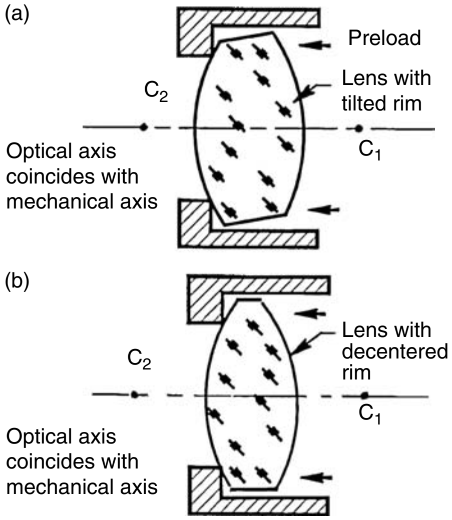

FIGURE 4.34 With interfaces directly on the spherical surfaces of a lens, errors in edging the lens and in lens diameter are not critical. (a) Tilted rim and (b) decentered rim.

In applications allowing decentrations or residual deviation due to geometric wedge in the ranges of 0.075 to 0.025 mm (0.003 to 0.001 in.) and 3 to 0.75 arcmin, respectively, it is common practice to premachine the optic and cell to radial dimensions and tolerances that will preclude damage to the glass under the most extreme temperature conditions. The lens is then inserted and clamped in place. This is sometimes called a *drop in* assembly. Its advantages include simplicity and ease of disassembly.

Neglecting the effects of temperature changes (discussed in Chapter 15), the total nominal axial force (preload), P, in lb, that should be exerted on the lens at assembly to hold it in place by any means of constraint, may be calculated as

$$P = W\Sigma a_{\mathrm{G}} \tag{4.10a}$$

where W is the weight of the lens and Σa_{G} the sum of the maximum anticipated externally applied accelerations acting in the axial direction, such as those due to constant acceleration, random vibration (3σ), amplified resonant vibration (sinusoidal), acoustic loading, and shock. These accelerations are here expressed as multiples, a_{G}, of ambient gravity. Since all types of external accelerations do not generally occur simultaneously, the summation term does not need to be taken literally. In some cases, it may be appropriate to root-sum-square (rss) the accelerations occurring in orthogonal directions. For simplicity, we here consider a_{G} to be a single-valued, worst-case number. Friction and moments imposed at the interfaces are ignored. Hence

$$P = Wa_{\mathrm{G}} \tag{4.10b}$$

Note that if the lens weight is expressed in kilograms, Eq. (4.10b) must include a multiplicative factor of 4.448 to convert units. The preload is then in newtons (N).

An axial preload applied to a curved surface of a lens tends to center the lens to the mechanical axis of the interfacing mount. This effect was illustrated by Figure 4.7 in conjunction with self-centering of a lens in preparation for edging. If the curvature of the surface is sufficiently large, the difference between the opposing radial components of the axial force pressing against a decentered lens will overcome sliding friction, and the lens will self-center to the extent possible, given the geometry and frictional resistance.

Axial preload also can resist decentration of a lens with curved surfaces in a surface-contact mounting if it is exposed to radial acceleration. In the presence of such a preload, the centered lens is nominally clamped symmetrically between the mechanical interfaces on opposite sides of the optic. Radial acceleration of magnitude a_G applied to a lens of weight W will exert a radial force of Wa_G that tends to force the mechanical interfaces apart by the wedging effect of the curved lens surface or surfaces trying to move in the direction of the acceleration. If the mechanical mount is sufficiently stiff, the interfaces will not separate axially and radial motion of the lens is prevented. The optical material would, of course, be stressed locally by this constraint.

Extreme cases occur when the optical component's surface curvature is zero, as for a plane parallel plate (window or glass reticle) or for a lens with flat bevels registered on both sides against flat mechanical surfaces oriented perpendicular to the axis. If radial clearance exists between the rim of the optic and the ID of the mount, decentration of that optic under radial acceleration is opposed only by friction. An axial preload of magnitude P creates a frictional component in the radial direction of P times μ at the interface, where μ is the effective coefficient of friction at the interface. For $P > Wa_G/\mu$, the lens will not decenter under a radial acceleration of a_G.

To illustrate this situation, consider a simple double-concave lens with flat bevels that weighs 0.085 lb (0.039 kg). Let us assume μ to be 0.15. If exposed to a radial acceleration of $a_G = 50$, the minimum preload required to prevent lens decentration is (0.086)(50)/0.15 = 28.67 lb (127.51 N). The preload required to prevent the lens from lifting off of one of its mechanical interfaces under axial acceleration of $a_G = 50$ directed away from that interface is, from Eq. (4.12b), (50)(0.085) = 4.25 lb (18.90 N). We see that the radial acceleration predominates for this example.

Another design problem related to radial acceleration occurs when the temperature rises above the assembly temperature and the mount expands more than the lens, with the result that the axial preload decreases from the value applied at assembly. This happens for the usual case in which the coefficient of thermal expansion (CTE) of the mount exceeds that of the optic. If the temperature rise is sufficient for the preload to be completely dissipated, the lens is free to move axially within any axial gap generated by a further temperature rise. It can also move radially within any radial clearance existing at that time. This situation is discussed in detail in Section 15.7.

To maintain the previously established alignment of the lens when the mount is axially compliant, the axial preload should not drop below some value that preserves glass-to-metal contact at the opto-mechanical interfaces. Figure 4.35 shows the technical basis for a way to estimate the preload required for this purpose. A plano-convex lens with radius R_1 represents a generic component that is to be constrained radially. The mechanical interfaces with the flat and curved surfaces are annular regions located at the radial distances y_1 and y_2 from the axis on opposite sides of the optic. In the case depicted in the figure, radial acceleration equal to a_G tends to drive the component of weight W downward wedging it between the mechanical interfaces. This wedging action tends to move and to compress the adjacent mechanical parts and the optical part microscopically. Those parts tend to resist these effects.

The effective downward force component at the curved interface is indicated in the figure as $-Wa_G$. This force acts through the lens CG, so it generates a moment about the contact point on the curved surface. Rotation about this point is prevented by reactions at the contacts with the flat surface. The downward force is opposed by an equal and upwardly directed reaction force Wa_G exerted by the mount. As shown in the detail view, this force has a component tangential to the lens surface equal to $Wa_G \cos \theta$. The angle θ is given by

$$\theta = \arcsin(y_1/R_1) \tag{4.11}$$

Associated with the tangential component is a component normal to the lens surface of magnitude equal to $(Wa_G/\mu)\cos \theta$, where μ is as defined earlier. The latter component has a component in the axial direction that constitutes the axial preload required to create the upwardly directed force that opposes the downward (acceleration-induced) force, and constrains the lens from moving in the radial direction. This preload is equal to

$$P = (Wa_0/\mu)\cos^2 \theta \tag{4.12}$$

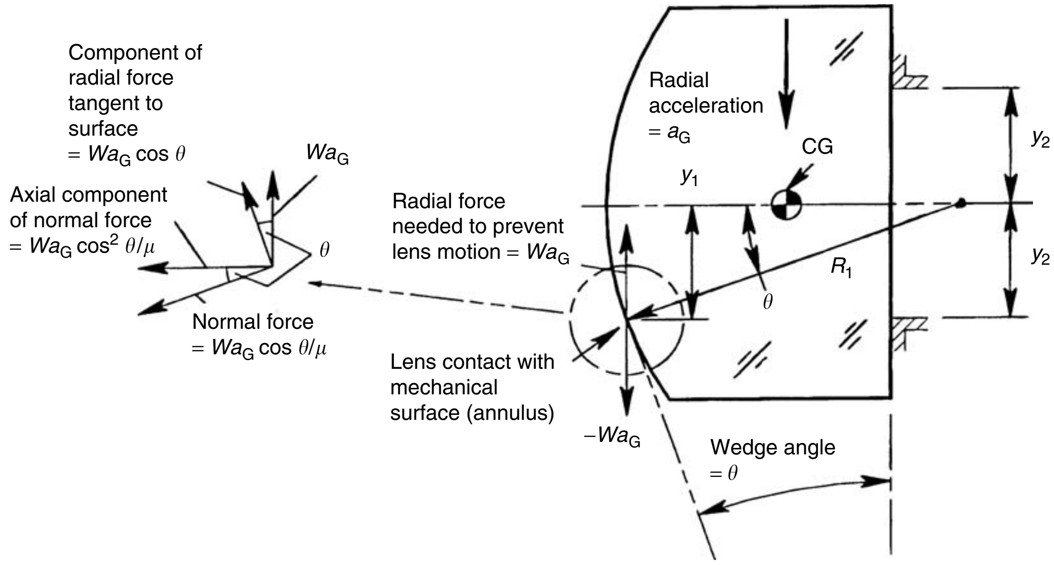
Component of radial force tangent to surface = $Wa_G \cos \theta$
Wa_G
Axial component of normal force = $Wa_G \cos^2 \theta/\mu$
θ
Normal force = $Wa_G \cos \theta/\mu$
Radial force needed to prevent lens motion = Wa_G
Lens contact with mechanical surface (annulus)
$-Wa_G$
Radial acceleration = a_G
CG
y_1
R_1
θ
y_2
y_2
Wedge angle = θ

FIGURE 4.35 Geometry for estimating preload required to prevent a surface contact lens from decentering under radial acceleration.

This equation applies to lenses of different shapes. For ones that have surface contacts at two curved surfaces, θ is the sum of the individual angles for each surface as derived from Eq. (4.11). Figure 4.36 shows this for four common lens shapes. Note that the interfaces that oppose lateral movement of the lens are on opposite sides of the axis in the case of the meniscus (Figure 4.36[b]). Note further that θ would have a zero value for the mounting interface on a plane parallel plate optic (such as a window or reticle) or on a lens mechanically referenced to two flat bevels. In those cases, P is simply Wa_G/μ, as explained above.

To illustrate the use of this equation, let us consider a lens of the type shown in Figure 4.36(a). We assume its parameters to be as follows: D_G = 4.0 in. (101.6 mm), $y_1 = y_2$ = 1.9 in. (48.26 mm), $R_1 = R_2$ = 6.0 in. (152.4 mm), W = 0.683 lb (0.31 kg), a_G = 15 (along all three axes), and μ = 0.15. By Eq. (4.11), $\theta_1 = \theta_2 = 18.46°$. Hence, $\theta = 36.92°$. From Eq. (4.12), $P = [(0.683)(15)/0.15][0.7995^2]$ = 43.66 lb (194.20 N). Note that the axial preload determined for this lens from Eq. (4.10b) is 10.24 lb (45.5 N), so once again the radial effect predominates.

4.7.2 THE THREADED RETAINING RING MOUNTING

Figure 4.37(a) shows schematically the functional aspects of the threaded retaining ring design depicted in Figure 4.33. Torque applied to the ring is converted into axial force by the thread. Sets of holes or transverse slots are usually machined into the exposed face of the retainer to accept pins or rectangular lugs on the end of a cylindrical wrench that is used to tighten the retainer (see Figure 4.37[b]). Adjustable spanner wrenches are also used (see Figures 4.37 [c] and [d]). Alternatively, a flat, plate-type tool that spans the retainer can be used as the wrench. Such a tool should be shaped so as to clear the polished surface of the lens to prevent damage to that surface. The cylindrical wrench is easier to use and is more conducive to measurement of torque applied to the ring. Figure 4.38 is a partial drawing of an actual retainer.

The axial preload clamps the lens against the cell shoulder shown to the left of Figure 4.37(a). To minimize bending of the lens due to axial force, the heights of contact y_C on both sides of the lens should be essentially the same. Means for estimating bending stress in the lens if this is not the case are described in Section 15.5.

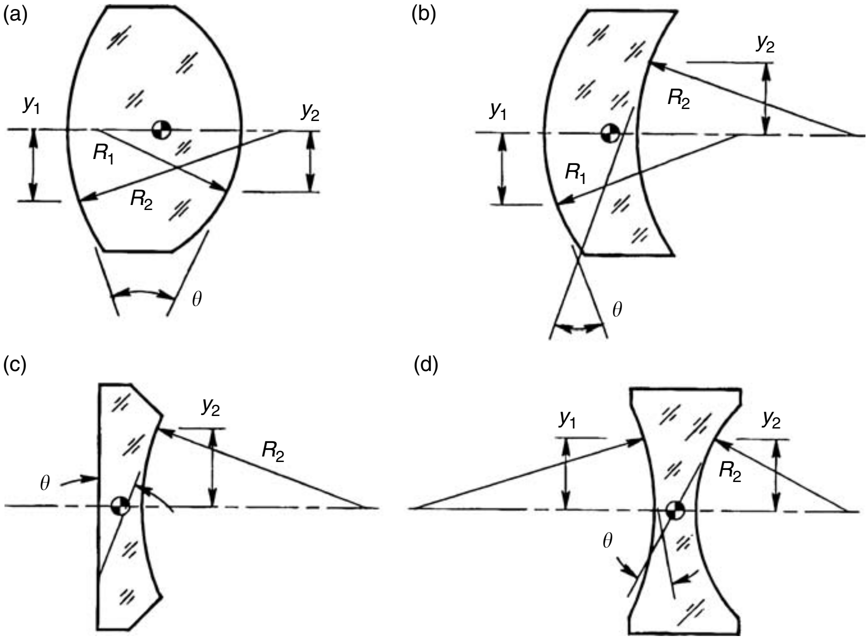
(a)
y_1
y_2
R_1
R_2
θ
(b)
y_1
y_2
R_1
R_2
θ
(c)
y_2
R_2
θ
(d)
y_1
y_2
R_2
θ

FIGURE 4.36 Determining the angle θ of four types of lenses: (a) biconvex, (b) meniscus, (c) plano-concave, and (d) biconcave.

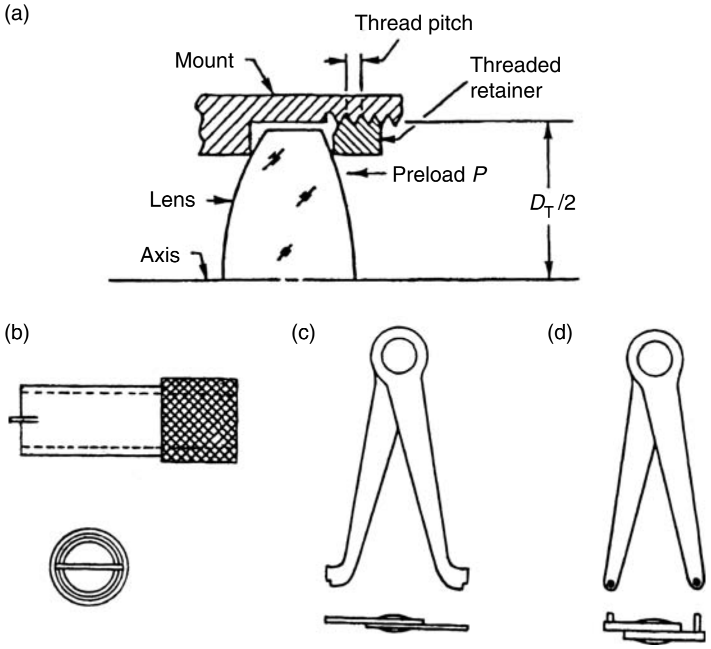
(a)
Thread pitch
Mount
Threaded retainer
Preload P
Lens
$D_T/2$
Axis
(b)
(c)
(d)

FIGURE 4.37 (a) Geometry for relating torque applied to a threaded retainer to the resulting axial preload on a lens, (b) tubular wrench of a type used to turn threaded retainers, (c) adjustable wrench for engaging slots on the ring ID, (d) adjustable pin wrench for engaging holes on the end of the ring.

The fit of the ring threads into the cell threads should be loose (Class-1 or −2 per ASME Publication B1.1-1989 [R2001]) so that the ring can tilt slightly, if necessary, to accommodate residual wedge angle in the lens or in the retainer when the lens is properly centered optically. This

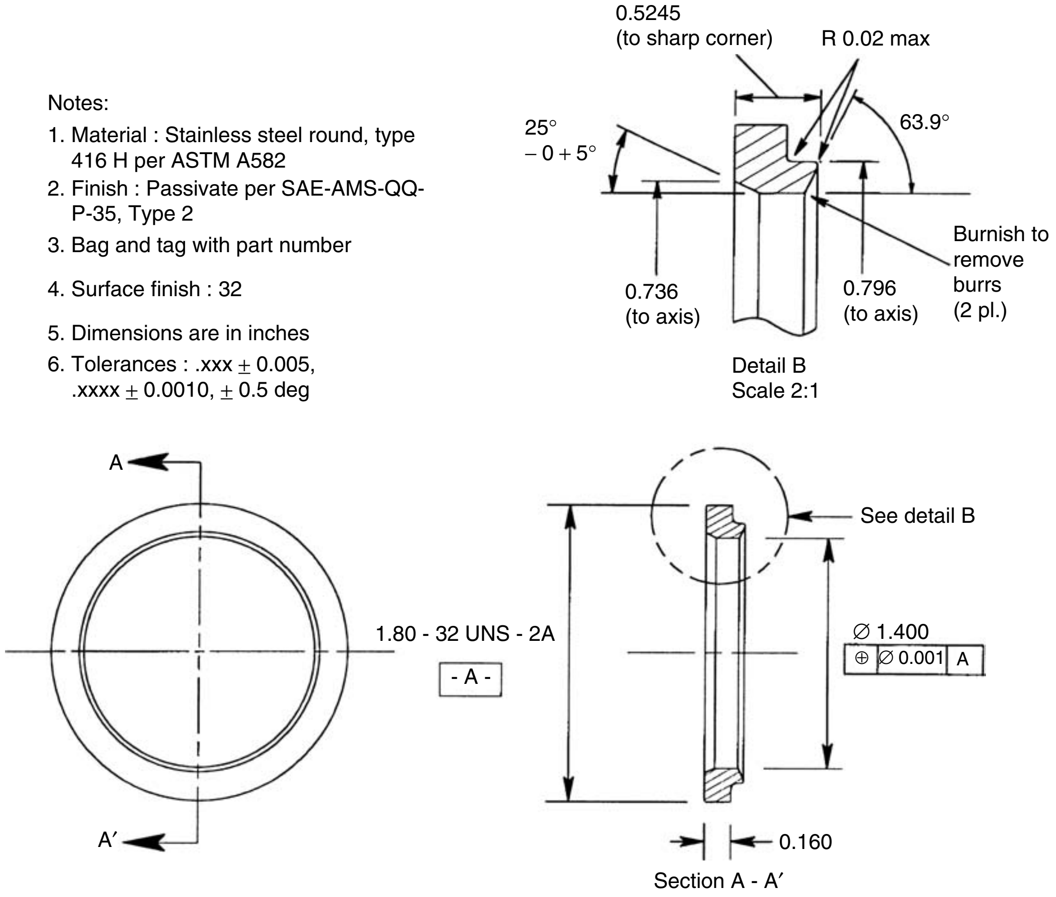

Notes:

1. Material : Stainless steel round, type 416 H per ASTM A582
2. Finish : Passivate per SAE-AMS-QQ-P-35, Type 2
3. Bag and tag with part number
4. Surface finish : 32
5. Dimensions are in inches
6. Tolerances : .xxx ± 0.005, .xxxx ± 0.0010, ± 0.5 deg

FIGURE 4.38 Representation of a typical threaded retaining ring as shown in an engineering drawing. The right end of this part has a conical surface for contacting a convex spherical lens surface with a radius of 1.671 in. (42.44 mm) at a height of 0.748 in. (19.00 mm).

helps to ensure that the preload is distributed uniformly around the lens periphery. A rule-of-thumb criterion for suitability of the fit of the threaded version is to assemble the ring in the mount without an optic in place, hold it to the ear, and shake it. You should be able to hear the ring rattle gently in the mount.

Equation (4.13a) for the approximate magnitude of the axial preload (P) produced by tightening a threaded retainer with thread pitch diameter D_T with a torque Q against a lens surface was derived by Yoder (2002). The first term in the denominator results from the classical equation for a body sliding slowly with metal-to-metal frictional constraint on an inclined plane (i.e., the thread), while the second represents the friction effects at the circular interface between the lens surface and the end of the rotating retainer:

$$P = Q/[D_T(0.577\mu_M + 0.500\,\mu_G)] \tag{4.13a}$$

where μ_M is the coefficient of sliding friction of the metal-to-metal interface and μ_G that of the glass-to-metal interface. In some designs, a thin metal slip ring is placed between the lens and the retainer to reduce the tendency for rotation of the lens as the retainer is tightened. Assuming that this ring does not move, μ_M would be used in both terms of Eq. (4.13a).

Equation (4.13a) is an approximation because of small factors neglected in the derivation and significantly larger uncertainties in the values of μ_M and μ_G. The latter values depend strongly on the smoothness of the metal surfaces (which depends, in part, upon the machined finish as well as how many times the thread has been tightened) and whether the surfaces are dry or moistened by water or a lubricant. Yoder (2002) indicated that μ_M may be about 0.19 while μ_G about 0.15. Substituting these values into Eq. (4.13a), we obtain $P = 5.42Q/D_T$. This corresponds to within about 8% with the commonly accepted approximation of the P to Q relationship (see Kowalskie, 1980 or Vukobratovich, 1993), which is

$$P = 5Q/D_T \tag{4.13b}$$

To illustrate the use of Eq. (4.13b), let us assume that a 2.1-in. (53.3-mm)-OD lens is to be clamped with a total preload of 12.5 lb (55.60 N) delivered by a retainer screwed into a cell on a thread of pitch diameter 2.2 in. (55.88 mm). Using Eq. (4.13b), the applied torque Q should be $PD_T/5 = (12.5)(2.2)/5 = 5.5$ lb-in. (0.62 N-m).

Note that like metals (such as aluminum and aluminum) should never be in contact in a threaded joint without some form of lubrication or some form of hard coating or plating on the mating parts because the surfaces may gall and seize. These surface preparations can significantly alter the coefficient of friction, making Eq. (4.13b) even more inaccurate.

Intuitively, we believe that a coarse thread should withstand axial force better than a fine one. Dimensional or "packaging" constraints might, on the other hand, require the use of fine threads in order to minimize wall thickness and overall diameter of the mount. It is well known that extreme care must be exercised in assembling a fine-threaded retainer to prevent "crossing" the threads and rendering the parts unusable. Yoder (2002) pointed out a relationship that can be used to estimate how fine a thread should be used on a threaded retaining ring to produce this preload without damaging the threads. The derivation of that relationship is summarized here.

Figure 4.39(a) shows the commonly used terminology for screw threads, while Figure 4.39(b) shows the basic profile of a thread as defined by Shigley and Mischke (1989). The dimension designations apply to a metric bolt (i.e., the retainer's threads) and its matching nut (i.e., the internal thread in the mount). The profile of a thread with inch dimensions is essentially the same as that shown in Figure 4.39(b). These apply to the unified thread system, with two major series called "UNC" and "UNF" for coarse and fine pitches, respectively.

The average stress in the threads is the total axial preload divided by the total annular area over which that force is distributed. We compare that stress with the yield stress of the materials used since damage to the threads is the chief concern. From the geometry of Figure 4.39(b), the crest-to-root thread height, H, is related to the thread pitch, p, by the following equation:

$$H = 0.5p\sqrt{3} \tag{4.14}$$

We also see from the figure that the annular area actually in contact has a radial dimension of $(5/8)H$. Hence, the annular area per thread is

$$A_T = 5\pi D_2 H/8 = 1.700pD_T \tag{4.15}$$

where D_T is the pitch diameter of the thread.

It is well known that the first few (typically three) threads on a machine screw carry most of the tensile load developed when the screw is tightened. Assuming this is also the case for a threaded lens retainer, the total annular area in contact is $3A_T$. Hence, the stress in the threads, S_T, is approximately

$$S_T = P/(3A_T) = 0.196P/(pD_T) \tag{4.16}$$

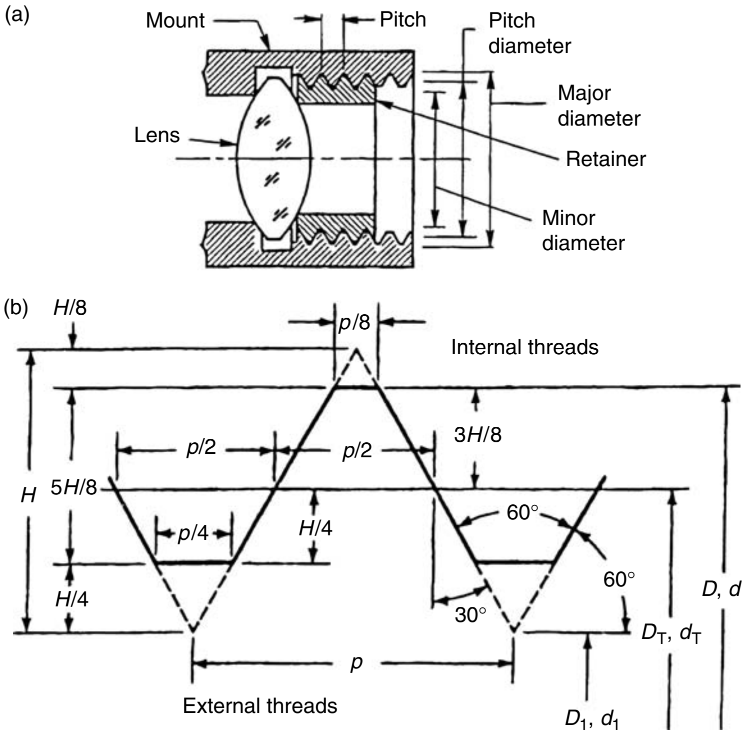

FIGURE 4.39 (a) Schematic showing terminology for retainer screw threads. (b) Basic thread profile where D (d) is the major diameter, D_1 (d_1) the minor diameter, D_T (d_T) the pitch diameter and p the thread pitch. Capital and lower case letters represent external and internal threads respectively. (Adapted from Shigley, J.E., and Mischke, C.R., in Mechanical Engineering Design, 5th ed., McGraw-Hill, New York, 1989.)

In order for this stress not to exceed the yield stress of the metal S_Y divided by an appropriate safety factor f_S, the thread pitch p should be no smaller than that given by the following equation:

$$p = 0.196 f_s P/(D_T S_Y) \tag{4.17}$$

It is common engineering practice to define a thread in terms of the number of threads per unit length rather than the linear dimension from crest to crest. This parameter is $1/p$.

For the usual designs in which the mount has a higher CTE than the lens, the thread stress should be estimated at the lowest survival temperature since the preload is the greatest then, which represents a worst-case situation. In Section 15.6, we show how to estimate the preload change in typical lens-mounting configurations as the temperature drops to its minimum expected value.

As an exercise in the use of Eq. (4.17), let us estimate the stress in the threads of a retainer holding a 2.1-in. (53.3-mm)-OD lens and the applicable safety factor if the thread size is 32 threads per inch (tpi) (1.26 threads/mm) at minimum temperature when the preload increases to 935 lb (4161 N). Assume that the retainer and cell are 6061-T6 aluminum with minimum yield strength of 40,000 lb/in.^{2} (276 MPa). Let the thread pitch diameter be 2.2 in. (55.88 mm). With Eq. (4.16) we find that $S_T = (0.196)(935)/[(1/32)(2.2)] = 2666$ lb/in.^{2} (18.4 MPa). The design's safety factor is 40,000/2666 = 15. Since a safety factor of 2.0 should be sufficient, we easily calculate from Eq. (4.17) that the finest thread that produces this safety factor for the specified low-temperature condition is $1/p = (2.2)(40{,}000)/[(0.196)(2)(935)] = 240$ tpi (9.45 threads/mm).

4.7.3 CONTINUOUS FLANGE MOUNTING

Typical designs for a lens mounting with a flange-type retainer are shown in Figures 4.40(a) and (b). These differ only in that the flange in view (a) is constrained by multiple screws threaded into the cell while, in view (b), it is held with a threaded cap. With screws, a stiffening ring might need to be added to minimize bending of the flange between the screws. This is not necessary with the cap design. Flange retainers are most frequently used with large-aperture lenses (i.e., those with diameters exceeding about 6 in. [15.4 cm]), where manufacture and assembly of a threaded retaining ring would be difficult. Their functions are essentially the same as that of the threaded retaining ring described earlier.

The magnitude of the force produced by a given axial deflection Δ of the flange shown in either of the figures can be approximated by considering the flange to be a perforated circular plate with its outer edge fixed. An axially directed load is applied uniformly along the flange's inner

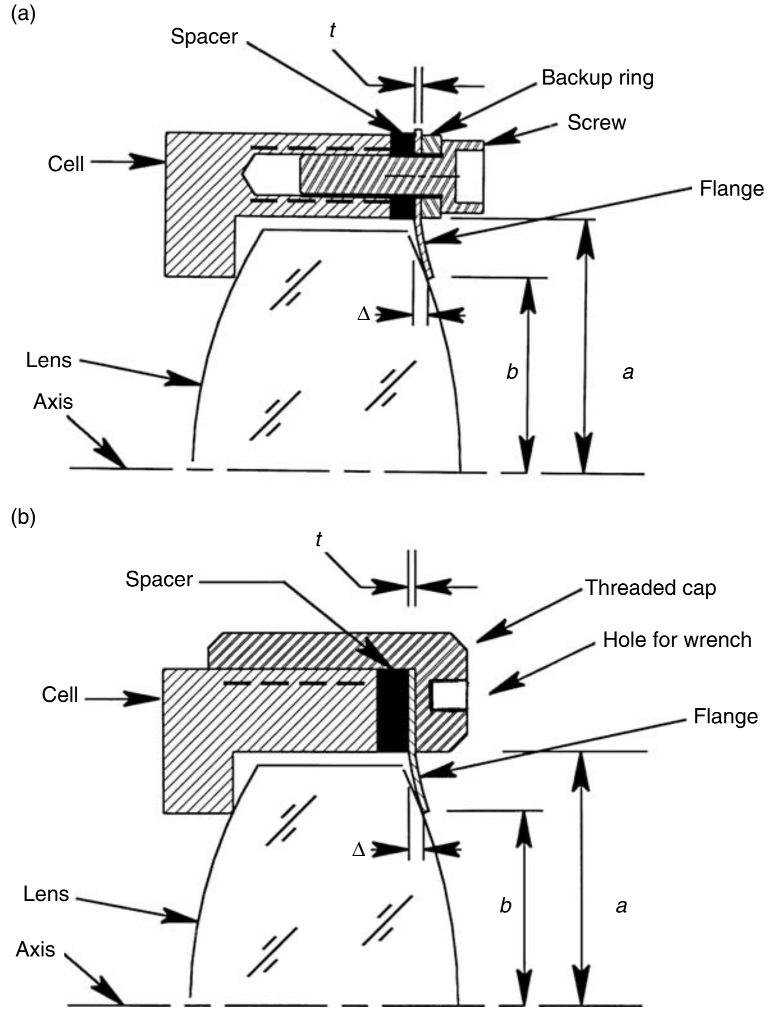

FIGURE 4.40 (a) Schematic configuration of a flange-type retainer that axially constrains a lens in a cell. The flange is stiffened with a back-up ring and secured with multiple screws. (b) Schematic of an alternative design for the flange-type lens retainer that uses a threaded cap to secure the flange to the cell. (From Yoder, P.R. Jr., *Mounting Optics in Optical Instruments*, SPIE Press, Bellingham, 2002.)

edge to deflect that edge. The applicable equation relating Δ to total preload as adapted from Roark (1954) is as follows:

$$\Delta = (K_A - K_B)\,(P/t^3) \tag{4.18}$$

where

$$K_A = 3(m^2 - 1)\,[a^4 - b^4 - 4a^2b^2\ln(a/b)]/(4\pi m^2 E_M a^2) \tag{4.19a}$$

$$K_B = \frac{3(m^2 - 1)(m + 1)[2\ln(a/b)] + (b^2/a^2) - 1][b^4 + 2a^2b^2\ln(a/b) - a^2b^2]}{4\pi m^2 E_M[b^2(m + 1) + a^2(m - 1)]} \tag{4.19b}$$

and P is the total preload, t the thickness of the cantilevered section of the flange, a the outer radius of the cantilevered section, b the inner radius of the cantilevered section, m the reciprocal of Poisson's ratio (ν_M) of the flange material, and E_M the Young's modulus of the flange material. The compliance of the flange is $\Delta/P = (K_A - K_B)/t^3 = 1/$flange spring constant.

The spacer between the cell and the flange can be ground at assembly to the particular thickness that produces the predetermined flange deflection when firm metal-to-metal contact is achieved by tightening the clamping screws or cap. Customizing the spacer accommodates variations in as-manufactured lens thicknesses. The flange material and thickness are the prime design variables. The dimensions a and b, and hence the annular width (a-b), can also be varied, but these are usually set primarily by the lens aperture, mount wall thickness, and overall dimensional requirements.

The design of a flange retainer is not complete until we determine the stress S_B built up in the bent portion of the flange. It must not exceed the yield stress S_Y of the material. A factor of safety f_S of 2.0 with regard to that limit might be advisable. The following equation adapted from Roark (1954) applies:

$$S_B = K_C P/t^2 = S_Y/f_s \tag{4.20}$$

where

$$K_c = \left[\frac{3}{2\pi}\right]\left[1 - \frac{2mb^2 - 2b^2(m + 1)\ln(a/b)}{a^2(m - 1) + b^2(m + 1)}\right] \tag{4.21}$$

The use of these equations is illustrated by the following example.

A 15.75-in. (400.05-mm)-diameter telescope corrector plate is to be held in place with a total preload P of 120 lb (534 N) distributed uniformly around and near the edge of the plate by a titanium (Ti6Al4V) flange. The ID and OD of the cantilevered portion of the flange are $a = 7.885$ in. (200.279 mm) and $b = 7.750$ in. (196.850 mm). Assume that $\nu_M = 0.340$, $E_M = 16.5 \times 10^6$ lb/in.^{2} (11.4×10^{10} Pa), and $S_Y = 120{,}000$ lb/in.^{2} (827 MPa): (a) What should be the flange thickness for a safety factor of 2.0, and (b) what deflection is required?

(a) From Eqs. (4.21) and (4.20),

$$K_C = (3/2\pi)\left[1 - \frac{(2)(2.941)(7.750^2) - (2)(7.750^2)(2.941 + 1)(\ln(7.885/7.750))}{(7.885^2)(2.941 - 1) + (7.750^2)(2.941 + 1)}\right] = 0.0164$$

$$t = [(2)(0.0164)(120)/120{,}000]^{1/2} = 0.0057 \text{ in. } (0.1455 \text{ mm})$$

(b) From Eqs. (4.19a), (4.19b), and (4.18),

$$K_A = \frac{(3)((2.941^2 - 1)(7.885^4 - 7.750^4 - (4)(7.885^2)(7.750^2)(\ln(7.885/7.750)))}{(4\pi)(2.941^2)(7.885^2)(16.5 \times 10^6)}$$

$$= 1.0556{\times}10^{-11} \text{ in.}^4/\text{lb}$$

$$K_B = \frac{\begin{array}{c}(3)(2.941^2 - 1)(2.941 + 1)(2\ln(7.885/7.750)) + (7.750^2/7.885^2) - 1)\\(7.750^4 + (2)(7.885^2)(7.750^2)(\ln(7.885/7.750)) - (7.885^2)(7.750^2))\end{array}}{(4\pi)(2.941^2)(16.5 \times 10^6)((7.750^2)(2.941 + 1) + (7.885^2)(2.941 - 1))}$$

$$= 1.8321 \times 10^{-13} \text{ in.}^4/\text{lb}$$

$$\Delta = (1.0556 \times 10^{-11} - 1.8321 \times 10^{-13})(120/0.0057^3) = 0.0067 \text{ in. } (0.1707 \text{ mm})$$

A major advantage of the flange-type constraint over the threaded retainer is that it can be calibrated. We can then know quite precisely what preload will be delivered when the flange is deflected by a particular amount. This measurement of the behavior of the flange can be done offline using a load cell or other means to measure the force produced by various deflections. This refines the flange deflection vs. force prediction made during design using the above equations. Since the test is nondestructive, we can safely assume that, during actual use, the hardware will behave as measured. For reliable measurement of Δ using conventional micrometers or height gauges, its value should be at least ten times the resolution of the measuring device.

4.7.4 MULTIPLE CANTILEVERED SPRING CLIP MOUNTING

A simple way to clamp a lens into its mount is illustrated by Figure 4.41. Here the lens rests against three thin Mylar pads (shown with exaggerated thickness) attached to a shoulder in the cell. The pads are located at 120° intervals and serve as semikinematic registration surfaces. Three metal clips that act as cantilevered springs apply preload. The outermost ends of the clips are attached to the cell with screws and washers. Spacers between the clips and the cell are machined to produce specific deflections of the clips, thereby providing axial preload. The clips are located such that preload is directed through the lens directly toward the Mylar pads. These locations are chosen because they minimize bending moments that could otherwise be applied to the optic. The use of the Mylar pads reduces the need to machine the shoulder as a geometrically accurate and smooth surface.

A shortcoming of this design occurs when the optical surface contacted by the clips is convex (as shown in Figure 4.41). The contacts with the flat springs are then at points rather than lines, and excessive localized stress can be created. This does not happen if the contacted lens surface is flat or if the contact occurs on the flat surface of a step bevel ground into a convex lens surface or on a flat bevel on a concave surface. For these cases, the clip must be tilted at its support in order for the free end to lie flat on the lens surface and provide intimate contact. Note that this requirement is alleviated if a spherical pad is added at the free end of each clip. Then, point contact will occur even if the lens surface is convex and the bent spring is attached as indicated in Figure 4.42. Another shortcoming of this design is that preload is discontinuous on the lens surface so stress is concentrated locally.

In some lens-mounting designs, more than three clips are used; they are usually spaced equally around the lens periphery. By doing so, the portion of the total preload derived from each clip is reduced. This tends to reduce the bending stress developed within each clip and the contact stress at the lens-to-spring interface.

In some optical systems, such as laser diode beam collimators, optical correlators, anarnorphic projectors, and some scanning systems, the natural aperture shapes of some lenses, windows, prisms,

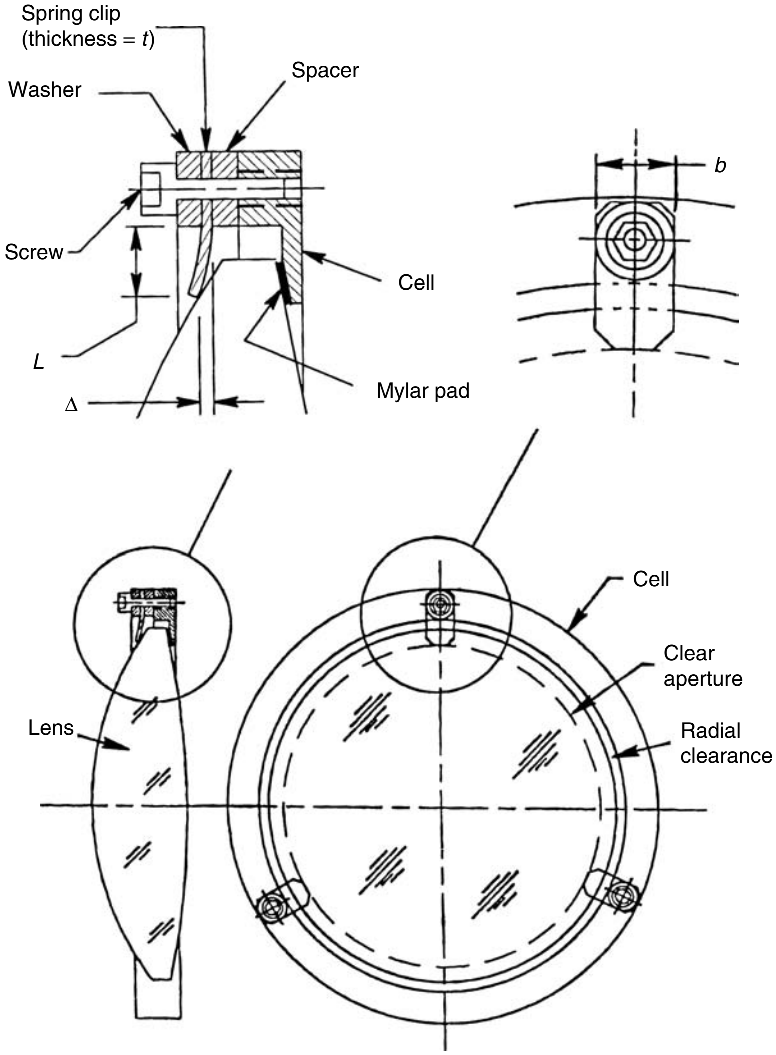

FIGURE 4.41 Concept for a lens mounting using three radially oriented cantilevered springs to locally preload a lens against pads on a cell shoulder. (From Yoder, P.R. Jr., *Mounting Optics in Optical Instruments*, SPIE Press, Bellingham, 2002.)

and mirrors are rectangular, racetrack, trapezoidal, etc., because their beams or fields of view are different in the vertical and horizontal meridians. Cylindrical, toroidal, and nonrotationally symmetrical aspheric optical surfaces are frequently used in such optical systems to create other desired beam shapes or to introduce different magnifications in orthogonal directions. These lenses have nonrotationally symmetrical surface shapes and may have noncircular apertures, so they cannot be mounted conventionally in circular cells or held in place by threaded retainers since the surface sagittas at a given distance from the axis are not equal. Mounts for these optics are usually customized for the particular needs of the component under consideration.

A simple example of such a mounting design is shown in Figure 4.42. The lens is a plano-concave cylindrical lens with a 2:1 aperture aspect ratio. The lens is clamped with four spring clips into a rectangular recess machined into a flat plate. The plate is circular, so it can be attached conventionally to the structure of the instrument. Note that a slot is provided to align the lens to the system axis as represented by a pin or key (not shown). The clips provide localized preload to hold the

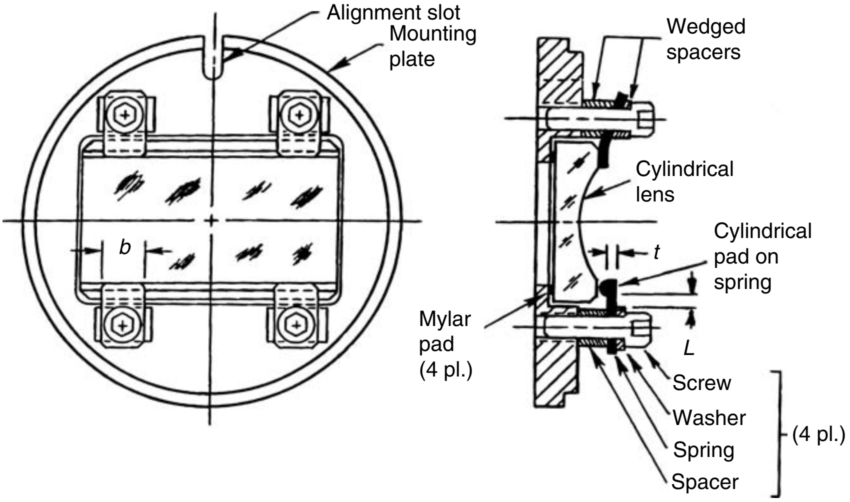

FIGURE 4.42 Schematic diagram of a mounting for a rectangular aperture lens. Note two different spring attachments are shown. One spring is tilted while the other has a cylindrical pad. (Adapted from Yoder, P.R. Jr., *Mounting Optics in Optical Instruments*, SPIE Press, Bellingham, 2002.)

lens in the recess under the anticipated acceleration forces. Because the spring must bend to provide force, it is necessary to prevent the spring from bearing against the bevel on the lens rim. One way to do this is illustrated at the top of the section view of Figure 4.42. Here the fixed end of the spring is clamped between a wedged spacer and a wedged washer. The free end of the spring rests flat against the lens bevel. Another way to accomplish the same goal is to add a curved (spherical or cylindrical) pad to the end of the spring. Then, the special spacers and washers are not needed. This design feature is shown at the bottom of the section view.

Four pads are located directly opposite the clips on the mount shoulder interface with the flat side of the lens. These pads must be accurately coplanar in order not to bend the lens by overconstraint from the clips, so the shoulder must be accurately machined flat. In some cases, thin Mylar shims can serve as the pads. With small stiff optics, three pads would probably provide enough constraint for the lens and would function semikinematically.

The following equation (adapted from Roark, 1954) can be used to calculate the deflection Δ required of each of N identical clips from its relaxed (undeflected) condition to provide a specific total preload:

$$\Delta = (1 - \nu_M^2)(4PL^3)/(E_M bt^3 N) \tag{4.22}$$

where ν_M is Poisson's ratio for the clip material, P the preload, L the free (cantilevered) length of the clip, E_M Young's modulus for the material, b the width of the clip, t the thickness of the clip, and N the number of clips.

Equation (4.23) quantifies the bending stress S_B in the clip material that is due to the deflection imposed when the optic is held in place with the preload, P:

$$S_B = 6PL/(bt^2 N) \tag{4.23}$$

Once again, this stress should not exceed about one half the yield strength of the material used (i.e., a safety factor, f_S, of about 2.0 applies). According to Roark (1954), the bending stress from Eq. (4.23) could be reduced by a factor of about 3 if the fixed end of the clip were clamped in place rather than perforated for attachment to the mount with screws. The following example will serve to illustrate the use of Eqs. (4.22) and (4.23).

A lens is to be constrained axially with a preload of 60 lb (267 N) by three titanium spring clips with dimensions $L = 0.3125$ in. (7.937 mm), $b = 0.375$ in. (9.525 mm), and $t = 0.0408$ in. (1.036 mm). Assume that $\nu_M = 0.34$ and $E_M = 16.5 \times 10^6$ lb/in.^{2} (1.14×10^5 MPa). (a) How much should each clip be deflected and (b) what is the safety factor for bending the springs?

(a) From Eq. (4.22), $\Delta = (1 - 0.34^2)(4)(60)(0.3125^3)/[(16.5 \times 10^6)(0.3750)(0.0408^3)(3)] = 0.0051$ in. (0.1295 mm).

(b) From Eq. (4.23), $S_B = (6)(60)(0.3125)/[(0.3750)(0.0408^2)(3)] = 60{,}073$ lb/in.^{2} (414 MPa).

From Table 3.18, the minimum yield strength of titanium is approximately 120×10^3 lb/in.^{2} (82.7×10^7 Pa). Therefore the safety factor f_S is about 2.0.

4.7.5 OPTO-MECHANICAL INTERFACE TYPES

4.7.5.1 Sharp Corner Interface

A sharp corner interface is created by the intersection of a cylindrical or conical hole in a lens mount and a flat surface machined perpendicular to the axis of that hole. It is the interface easiest to produce and is used in a vast majority of optical instruments. In reality, the sharp corner is not actually a knife edge. Following a series of tests in which many parts designed to have sharp corners were made by different machine shops and then measured, Delgado and Hallinan (1975) quantified the annular contact as one in which the intersection of the machined surfaces on the metal part has been burnished in accordance with good shop practice to a radius on the order of 0.002 in. (0.05 mm). This small radius surface contacts the glass at a height y_C. Figure 4.43(a) illustrates typical interfaces on convex spherical lens surfaces while Figure 4.43(b) shows typical interfaces with concave lens surfaces.

4.7.5.2 Tangential Interface

If the mechanical surface contacting the spherical lens surface is conical, the design is said to have a tangent cone interface or, more simply, a tangential interface (see Figure 4.44). The cone half-angle, ψ, is determined by the following equation:

$$\psi = 90^\circ - \arcsin(y_c/R) \tag{4.24}$$

The tangential interface is not feasible with a concave lens surface, but it is generally regarded as the nearly ideal interface for convex lens surfaces. Easily made by modern machining technology,

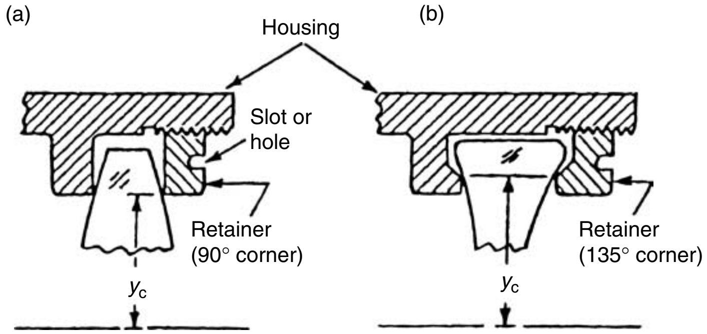

FIGURE 4.43 Typical "sharp corner" interfaces (a) with convex lens surfaces and (b) with concave lens surfaces.

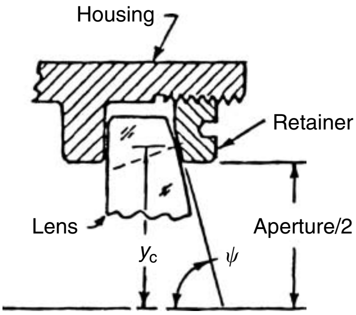

FIGURE 4.44 The tangential (conical) interface with a convex spherical lens surface. ψ is the half-angle of the cone.

the conical interface tends to produce smaller contact stress in the lens for a given preload than the sharp corner interface. This attribute of the tangential interface is discussed in Section 15.3. A retaining ring with a conical surface is shown in Figure 4.38.

4.7.5.3 Toroidal Interface

Figure 4.45(a) shows a toroidal or donut-shaped mechanical surface contacting a convex spherical lens surface of radius *R* while Figure 4.45(b) shows a similar interface on a concave lens surface. Contact nominally occurs at the center of the toroidal land in both cases. We define the height of contact as y_C. Figures 4.46(a) and (b) show families of toroids interfacing with convex and concave lens surfaces of radii *R*. The toroid radii vary from -*R*/2 to -*R*/32 in each case. This type of interface is particularly useful on concave lens surfaces where the tangent interface cannot be used. The reasons for this (which have to do with minimizing contact stress) are explained in Section 15.3.

4.7.5.4 Spherical Interface

Figures 4.47(a) and (b) show, respectively, spherical lands interfacing with convex and concave spherical lens surfaces. Contacts occur over the entire spherical lands.

The spherical interface surfaces of the mechanical parts must be accurately ground and lapped to match the radii of the lenses within a few wavelengths of light. Each mechanical part that is to touch a lens surface must be designed with access for lapping. The final stages of manufacture of these surfaces are usually conducted in the optical shop using tools equivalent to those used to make the corresponding glass surfaces. Since the manufacture and testing of these surfaces are expensive, the spherical interface mounting technique is hardly ever used. This type interface does have the distinct advantage that axial forces are distributed over large areas, so they cause relatively low contact stresses under high preloads, and high acceleration loads can be survived. They also facilitate heat transfer through the interface.

4.7.5.5 Interfaces on Bevels

It is standard optical shop practice to lightly bevel all sharp edges of optics. This minimizes the danger of chipping, so such bevels are called protective bevels. Larger bevels, or chamfers, are used to remove unneeded material when weight is critical or packaging constraints are tight, and to provide mounting surfaces. Usually all these secondary surfaces are ground with progressively finer abrasives. If the lenses are likely to have to endure severe stress, the bevels and the lens rims may also be given a crude polish by buffing with polishing compound on a cloth or felt-covered tool. These grinding and polishing procedures tend to strengthen the lens material by removing subsurface damage resulting from the grinding operations.

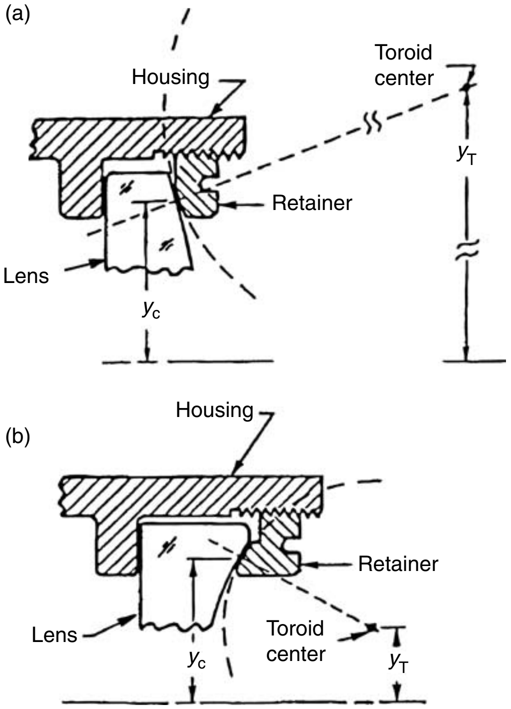
(a)
Housing
Toroid center
y_T
Retainer
Lens
y_c
(b)
Housing
Retainer
Lens
Toroid center
y_c
y_T

FIGURE 4.45 The toroidal (donut) interface: (a) contacting a convex spherical lens surface and (b) contacting a concave lens surface.

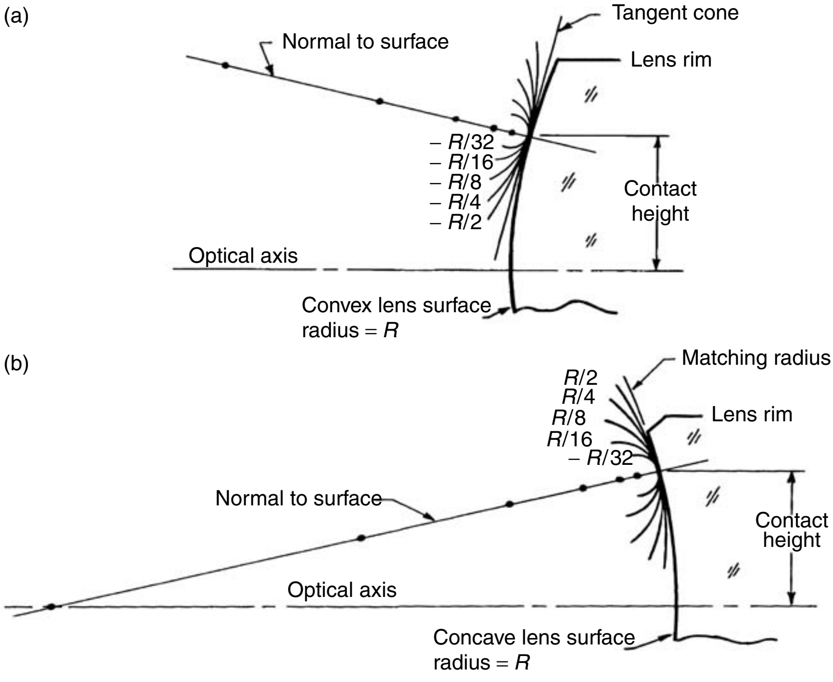
(a)
Tangent cone
Normal to surface
Lens rim
– R/32
– R/16
– R/8
– R/4
– R/2
Contact height
Optical axis
Convex lens surface radius = R
(b)
Matching radius
R/2
R/4
R/8
R/16
– R/32
Lens rim
Normal to surface
Contact height
Optical axis
Concave lens surface radius = R

FIGURE 4.46 (a) A convex lens surface of radius R interfacing with convex toroidal surfaces of differing radii. The tangent cone is a limiting case. (b) A concave lens surface of radius R interfacing with convex toroidal surfaces of differing radii. The "matching radius" or spherical interface is a limiting case. (From Yoder, P.R., Jr., *Proc. SPIE*, 1533, 2, 1991.)

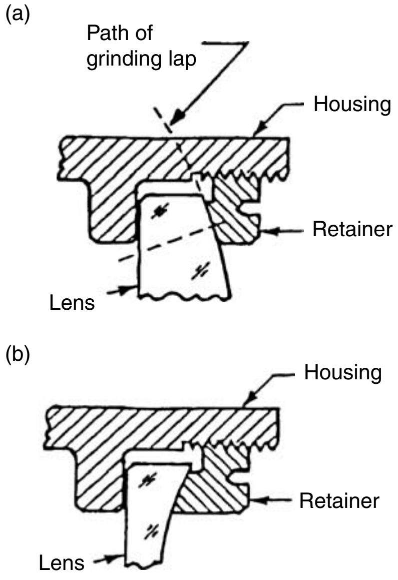

FIGURE 4.47 The spherical interface with (a) a convex spherical surface and (b) a concave surface.

Figures 4.48(a)–(c) shows three lenses with bevels. The plano-convex element of view (a) has minimum protective bevels that typically might be specified as "0.5 mm maximum face width at 45°" or " 0.4 ± 0.2-mm face width symmetric to surfaces." Each surface of the biconcave lens of view (b) has a wider annular bevel oriented perpendicular to the lens' optical axis. Applying axial preload cannot center this lens; some external means must be utilized. Tight tolerances on perpendicularity must be specified for such bevels if both centers of curvature of the lens surfaces are to be brought to the mount's mechanical axis simultaneously by lateral translation of the lens. Tolerances for this 90° angle of ±30 arcsec or less are common for precision lenses.

Figure 4.48(c) shows a meniscus lens with a wide 45° bevel on the concave side and a step bevel ground into the rim on the other (convex) side to form a flat surface recessed into the lens. A conventional retainer or a spacer can be brought to bear against the latter surface (see Figure 4.48[d]). A 45° bevel or radius should be built into the inner leading edge of the retainer so that it does not interfere with a rounded inside corner that usually is created in a step bevel during manufacture. It is not good practice to apply an axial preload directly against an angled bevel since that surface may not be precisely located. A toroidal surface-contact interface would be preferable on the concave surface of the lens. Protective bevels should be provided at the edges of all bevels.

Cemented doublet and triplet lenses are sometimes configured so that the rim of one element extends radially beyond the other element(s). The interface with the mechanical surround then occurs on just that larger element. Two designs with this type construction are shown in Figure 4.49 and Figure 4.50. There are at least two advantages to both designs: the weight of one element is reduced and any geometrical wedges in the cantilevered element or in the cement joint will not affect the symmetry of the mounting interface. The thread fits for the retainers are loose so they can register against the lens surface in spite of residual wedges in the clamped elements.

In Figure 4.49, the crown element is the larger. The mechanical interface on the convex surface is at a conical surface on the retainer while that on the concave surface is a toroidal surface machined into a shoulder in the cell. For clarity, the toroid radius is shown shorter than true scale in the figure. The lens rim OD is slightly smaller than the ID of the cell so that rim does not contact the cell wall.

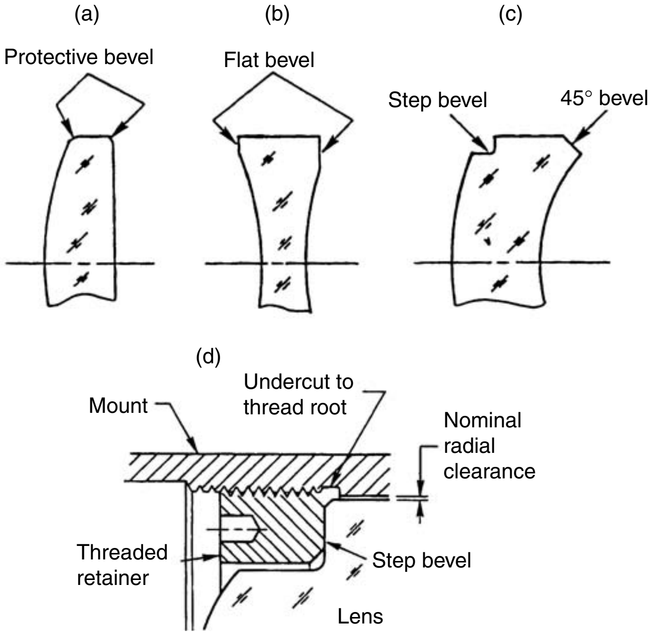
(a)
Protective bevel
(b)
Flat bevel
(c)
Step bevel
45° bevel
(d)
Mount
Undercut to thread root
Nominal radial clearance
Threaded retainer
Step bevel
Lens

FIGURE 4.48 Types of flat bevels as applied to lenses: (a) protective bevels, (b) flat bevels, (c) step and 45° bevels, and (d) details of a step bevel on a convex surface.

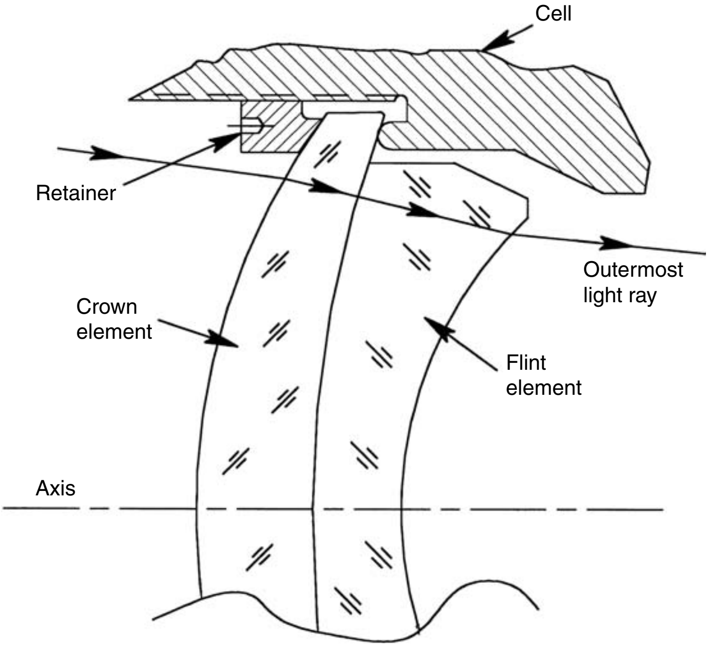
Cell
Retainer
Outermost light ray
Crown element
Flint element
Axis

FIGURE 4.49 Mounting for a cemented doublet lens with the crown element larger in diameter than the flint element.

In Figure 4.50, the flint element is the larger. It has precision flat bevels on both sides that interface with flat sides of a shoulder in the cell and a threaded retainer. Any wedge in the cement joint has no effect on the mounting. The shoulder face is accurately perpendicular to the mechanical axis of the cell. The rim of the flint element is spherical so it can fit closely into the ID of the lens barrel. The high point on the rim lies approximately in the plane of the lens' CG for maximum stability under shock and vibration.

4.8 ELASTOMERIC MOUNTINGS FOR LENSES

A simple technique for mounting lenses in cells is illustrated schematically in Figure 4.51. This figure shows a typical design for a lens constrained by an annular ring of a resilient elastomeric material within a cell. Typically, RTV sealing compounds such as Dow Corning RTV732, Dow Corning RTV93-500, or General Electric RTV8112 are used. EC2216B/A epoxy has been used for this purpose and is representative of that type of elastomer. Characteristics of the sealants are given in Table 3.27. The epoxy is described in Table 3.26.

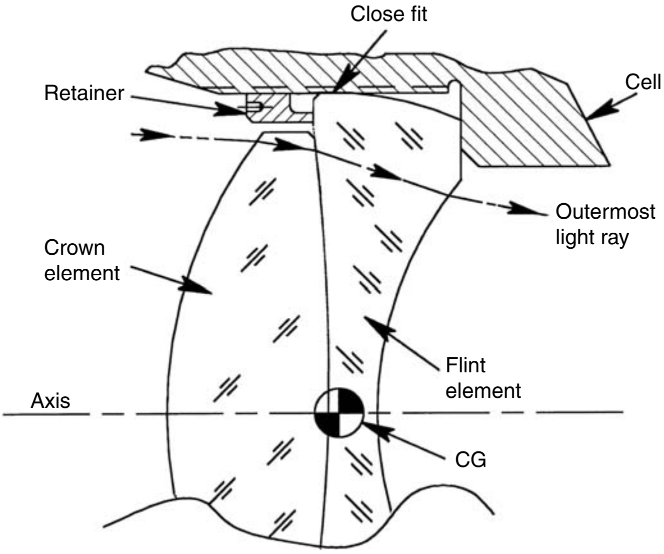

FIGURE 4.50 Mounting for a cemented doublet lens with the flint element larger in diameter than the crown element. In this rim-contact type mounting, the rim of the flint element is spherical.

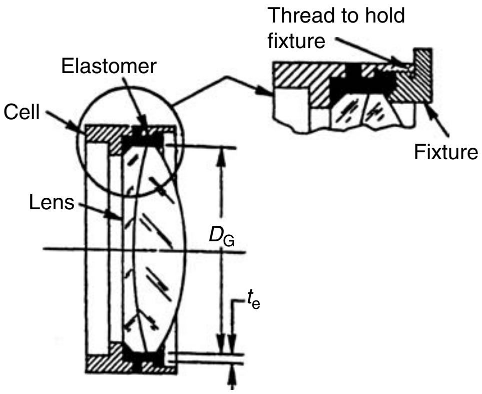

FIGURE 4.51 Technique for mounting a lens with an annular ring of cured-in-place elastomer. The detail view shows one means for holding the lens and constraining the elastomer during curing. (From Yoder, P.R. Jr., *Mounting Optics in Optical Instruments*, SPIE Press, Bellingham, 2002.)

One side of the elastomeric ring is intentionally exposed, so the material can deform under compression or tension caused by temperature changes. Registry of one optical surface against a machined mounting surface aligns the lens within the mount. Centration can be established prior to curing and maintained throughout the curing cycle with shims or external fixturing. The detail view of Figure 4.51 shows one means for holding the lens in place and constraining the elastomer during curing. The fixture, which is made of Teflon or a similar plastic or metal coated with a release compound, can be removed after curing. The elastomer is typically injected with a hypodermic syringe through radially oriented holes in the mount until the space around the lens is filled. Shims or calibrated pins can be used to center the lens. They are removed after curing and the voids filled.

If the annular elastomer layer has a particular thickness, t_e, the assembly will, to a first-order approximation, be athermal in the radial direction. This minimizes stress buildup within the optomechanical components that is caused by differential radial expansion or contraction of the lens, cell, and elastomer under temperature changes. According to Bayar (1981), this thickness is

$$t_e = (D_G/2)(\alpha_M - \alpha_G)/(\alpha_e - \alpha_M) \tag{4.25}$$

where α_G and α_M are the CTEs of the lens and mount. Data from Genberg (1997) suggests that α_e for a thin layer may be 2.52 to 3.00 times larger than the bulk value over the range $0.43 \leq \nu_e \leq 0.50$. We call this the effective CTE, or α_e^*. This value would then be used in Eq. (4.25).

The axial length of the elastomer layer usually equals the edge thickness of the lens. Because Eq. (4.25) neglects the effects of this length, it should be considered an approximation. The design is not athermal in the axial direction. When the temperature changes, the same nominal lengths of mounting wall, elastomer, and lens change at different rates that are proportional to the applicable CTEs. Some amount of shear is then introduced into the elastomer layer.

The following equation for athermal elastomer layer thickness was developed by R. Vanbezooijen and T. Muench of Lockheed Martin. It assumes ν_e is 0.43. The bulk α_e is used here.

$$t_e = \frac{(D_G/2)(1-\nu_e)(\alpha_M-\alpha_G)}{\alpha_e - \alpha_M - (\nu_e)(\alpha_G - \alpha_e)} \tag{4.26}$$

The use of Eqs. (4.25) and (4.26) is illustrated in the following example.

A 2.051-in. (52.095-mm)-diameter lens is to be mounted by an annular elastomeric ring in an aluminum cell. We would like to (a) apply Eq. (4.25) to determine the approximate value for the athermal thickness t_e assuming the material properties to be: $\alpha_G = 3.33 \times 10^{-6}$ °F^{-1} (6.0×10^{-6} °C^{-1}), $\alpha_M = 12.78 \times 10^{-6}$ °F^{-1} (23.0×10^{-6} °C^{-1}), $\alpha_e = 138 \times 10^{-6}$ °F^{-1} (248.0×10^{-6} °C^{-1}), and $\nu_e = 0.43$. Then, α_e^* would be (2.52) (138×10^{-6}) or 348×10^{-6} °F^{-1}. As example (b), we then recalculate t_e using Eq. (4.26) and compare the results.

(a) From Eq. (4.25), $t_e = (2.051/2)(12.78 - 3.33)(10^{-6})/[(348 - 12.78)(10^{-6})] = 0.029$ in. (0.734 mm).

(b) From Eq. (4.26),

$$t_e = (2.051/2)\left(\frac{(1 - 0.43)(12.78 - 3.33)(10^{-6})}{(138 - 12.78 - (0.43)(3.33 - 138))(10^{-6})}\right) = 0.030 \text{ in. } (0.762 \text{ mm})$$

This thickness agrees with that obtained from Eq. (4.25).

Valente and Richard (1994) reported an analytical technique for estimating the decentration, δ, of a lens mounted in a slightly compliant ring of elastomer when subjected to radial gravitational loading. Their equation is extended very slightly here to include more general radial acceleration forces by adding an acceleration factor a_G as follows:

$$\delta = \frac{2a_G W t_e}{\pi D_G t_E \{[E_e/1 - \nu_e^2] + S_e\}} \tag{4.27}$$

where

$$S_e = E_e/[(2)(1 + \nu_e)] \tag{4.28}$$

and W is the lens weight, t_e the elastomer layer thickness, D_G the lens diameter, t_E the lens edge thickness, ν_e the elastomer Poisson's ratio, E_e the elastomer Young's modulus, and S_e the shear modulus of the elastomer.

The decentrations of modest-sized optics corresponding to normal gravity loading are usually quite small, but may grow significantly under shock and vibration loading. A resilient elastomer is naturally elastic and so will tend to restore the lens to its unstressed location and orientation when the acceleration force dissipates.

As an example of pertinent calculations, consider a BK7 lens with diameter $D_G = 10.0$ in. (254.0 mm), thickness $t_E = 1.0$ in. (25.4 mm), and weight $W = 7.147$ lb (3.242 kg) mounted in a DC RTV3112 elastomeric ring inside a titanium cell. Assume the following properties for the materials: $\alpha_G = 3.94 \times 10^{-6}\,°\mathrm{F}^{-1}$ ($7.1 \times 10^{-6}\,°\mathrm{C}^{-1}$), $\alpha_M = 4.90 \times 10^{-6}\,°\mathrm{F}^{-1}$ ($8.8 \times 10^{-6}\,°\mathrm{C}^{-1}$), $\alpha_e = 167 \times 10^{-6}\,°\mathrm{F}^{-1}$ ($300.6 \times 10^{-6}\,°\mathrm{C}^{-1}$), $E_e = 500$ lb/in.^{2} (3.447 MPa), and $\nu_e = 0.499$. What deflection can be expected under conditions of transverse a_G = (a) 1.0 and (b) 250?

From Eq. (4.28), $S_e = 500/[(2)(1 + 0.499^2)] = 167$ lb/in.^{2} (1.151 MPa)

From Eq. (4.26),

$$t_e = (10.0/2)\left(\frac{(1 - 0.499)(4.90 - 3.94)(10^{-6})}{[167 - 4.90 + (0.499)(3.94 - 167)](10^{-6})}\right) = 0.030 \text{ in. } (0.762 \text{ mm})$$

From Eq. (4.27), for $a_G = 1.0$ and 250,

$$\delta_1 = \frac{(2)(1.0)(7.147)(0.030)}{(\pi)(10.0)(1.0)\{[500/(1 - 0.499^2)] + 167\}} = 1.6 \times 10^{-5} \text{ in. } (4.1 \times 10^{-4} \text{ mm})$$

$$\delta_{250} = (250)(1.6 \times 10^{-5}) = 0.004 \text{ in. } (0.102 \text{ mm})$$

Vukobratovich (2003) provided an equation for the natural frequency f_N of vibration for a body that deflects under its own weight when supported on a spring or other resilient mount. This body could be a mirror whose optical surface sags when its axis is parallel to gravity or a lens mounted in a ring of elastomer with its axis horizontal. This equation is

$$f_N = (0.5/\pi)\sqrt{g/\delta} \tag{4.29}$$

where g is the gravitational constant of 32.2 ft/sec^2 (9.807 m/sec^2) and δ is the self-weight deflection. In the case of the elastomeric-mounted lens, the radial deflection is given by Eq. (4.27). Applying this equation to the last example, we find that $f_N = (0.5/\pi)\,\{32.2/[(1.6 \times 10^{-5})/12)]\}^{1/2} = 783$ Hz.

4.9 MOUNTING LENSES ON FLEXURES

Very high-performance lenses must be assembled to extremely tight axial (or despace), tilt, and decentration tolerances relative to other lenses in an optical assembly or to one or more mechanical reference(s). Alignment must then be retained under operational levels of shock, vibration, pressure, and temperature variations. Furthermore, misalignments occurring during exposure to survival levels of these environments must be reversible. For these applications it may be advantageous to attach the lens to symmetrically disposed flexures so that differential expansion of materials caused by temperature changes does not affect lens tilt or centration.

Although they may be similar in appearance, a flexure is not the same as a spring. A flexure is an elastic element that bends to provide controlled relative motion of components, while a spring provides controlled force through elastic deformation. In the present context, the lens is supported on flexures in the manner depicted conceptually in Figure 4.52.

The equal compliances of the three radially oriented flexures keep the lens centered in spite of differential expansion with temperature changes, and allow the lens to decenter during extreme (survival level) shock and vibration exposure, yet return to the correct location and orientation after these dynamic disturbances have subsided. They also minimize stress within the optic during such exposures. The symbols C_R and C_T in Figure 4.52 represent the spring constants (stiffnesses) of the radial and tangential flexures. Typically, the flexures are stiff tangentially and soft radially. They also are stiff axially (perpendicular to the plane of the figure). We next describe several configurations of flexure mounts designed to maintain radial alignment of an individual lens.

Figure 4.53 shows a design by Ahmad and Huse (1990) in which the rim of the lens is bonded with an adhesive such as epoxy to the ends of three thin blades that are parts of flexure modules. Those blades are compliant radially, but stiff in all other directions. When the dimensions of the mount (here shown as a simple cell) and lens change with temperature, any mismatch in CTEs of those parts causes the flexures to bend. Since this action is symmetrical with respect to the axis, the lens stays centered.

The detail view in Figure 4.53 shows one flexure module. It is manufactured separately and attached to the mount with screws, so the bonded subassembly comprising the lens and the three flexures can be removed and replaced without damage. Since they are separate, the flexure modules can be made from a material appropriate for the application, such as titanium or stainless steel with high yield stress, while the mount can be made of a different material, such as aluminum. The metal surface adjacent to the lens rim can be shaped as a concave cylinder to approximate the curvature of that rim, or localized flats can be ground onto the lens rim to match the flexure shape. In either case, the thickness of the adhesive layer must be uniform over the joint. This provides maximum strength of the bond. To ensure against movement with respect to the cell, the flexure modules can be mechanically pinned in place or secured with epoxy applied around the edges of those modules after they are screwed in place.

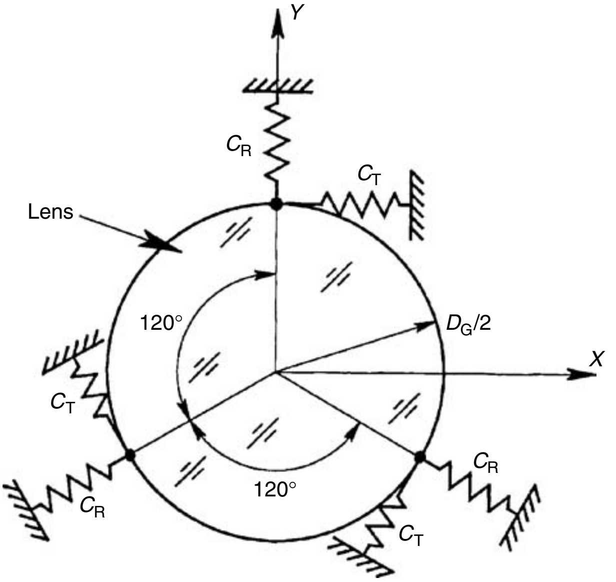

FIGURE 4.52 Schematic for a “three-point” flexure support for a lens. (Adapted from Vukobratovich, D., *Proc. SPIE*, 959, 18, 1988.)

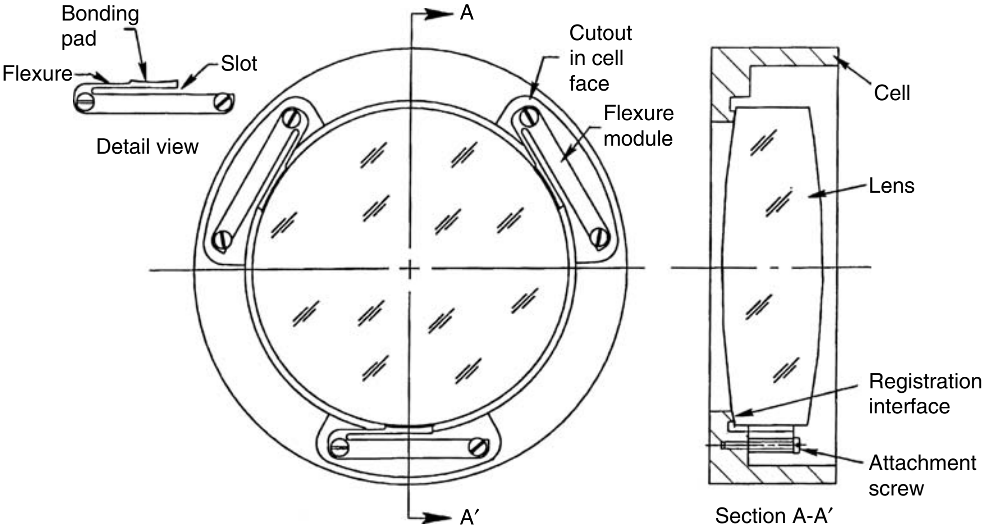

FIGURE 4.53 A mounting concept in which the rim of a lens is bonded to three removable flexure modules. The detail view shows an alternative configuration for the flexure module. (Adapted from Ahmad, A. and Huse, R.L., U.S. Patent 4,929,054,1990.)

Another configuration for a flexure mounting, from Bacich (1988), is shown in Figure 4.54. Here, the flexure blades are formed integrally with the cell, so they cannot be removed. The cell material must be chosen in part so the integral flexures function reliably throughout the many temperature cycles inherent in the desired useful life of the instrument. Slots of precisely controlled thickness and shape are easily created by the electric discharge milling (EDM) process.

Two versions of the basic mount design are depicted in Figure 4.54. In views (a) and (b), the rim of the lens is bonded to the flexures in the same general manner as in the design of Figure 4.53. Views (c) and (d) show the bottom surface of the lens bonded to small "shelves" built into the flexure blades. Machining the ID of the cell is more complicated in the latter, as more material must be removed, and the contour is more complex.

Bruning et al. (1995) built upon the technology just described in several ways. One new technique is illustrated schematically in Figure 4.55(a). Here, a cell with solid rectangular cross section has three elongated curved slots cut through the ring so as to create an inner ring that is attached to the outer ring only by way of three narrow flexures. These flexures isolate the inner ring from the outer ring, so minute distortions of the latter, which can occur when it is mechanically attached to an external structure by screws passing through the indicated recessed mounting holes, will not be transferred to the inner ring. A lens (not shown) with OD substantially the same as the ID of the slots that is mounted on top of the inner ring with adhesive will then not be subjected to stress from the distortions of the outer ring. View (b) of the same figure shows details of one flexure from Figure 4.55(a). It has two blind holes bored into the flexure blade from top and bottom faces of the rings to weaken that flexure in the direction perpendicular to the figure. The holes also allow the flexure to twist slightly. Bruning et al. (1995) described this feature as a means for further isolation of the inner ring and lens from mounting disturbances.

Alternative flexure arrangements for the ring mount of Bruning et al. (1995) are illustrated in Figures 4.56(a) and (b). In view (a), the ring is slotted along an arc so as to provide radial flexibility for a seat protruding inward from the inside surface of the ring at the midpoint of the slot. Three such slot/flexure/seat features at 120° intervals provide attachment points for a lens that would be secured with adhesive on the tops of the three seats. In view (b), a more complex slotting arrangement provides dual flexures as indicated. The long slots conform to the general design shown in Figure 4.55 in that they isolate an inner ring from the outer ring.

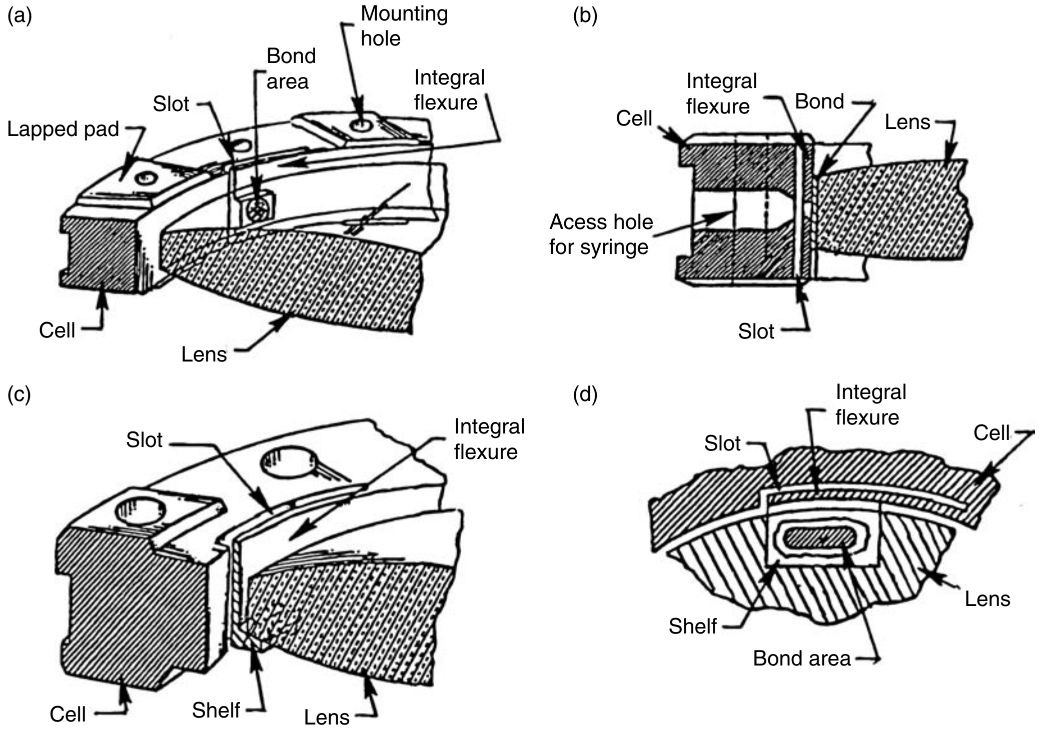

FIGURE 4.54 Lens mountings with the lens bonded to flexures machined integrally with the cell. In views (a) and (b), the bonds are on the rim of the lens while in views (c) and (d), they are on local areas of the lens' face. (Adapted from Bacich, J.J., U.S. Patent 4,733,945,1988.)

Figure 4.57(a) is a plan view of a lens/mount subassembly incorporating the flexure configuration of Figure 4.56(a). The lens is attached to the three pads as described earlier and shown in side view in Figure 4.57(b). Distortions of the ring lens mount by forces exerted by the five screws that attach the ring to the structure are prevented from reaching the lens in this design.

Another flexure mounting with integral flexure blades is shown in Figure 4.58. The flexures are formed in a box-section cell by locally machining the corners from the top and bottom rims of the box in the region where each flexure is to be located. This mounting was described by Steele et al. (1992). A design variable was the angular subtense φ of the bonded region at the center of each flexure. Using finite element analysis, 30 and 45° angles were compared. The larger angle was selected because it resulted in a smaller degree of distortion of the lens surfaces at the extreme operational temperature, had a higher natural frequency, and produced less stress in the cell and adhesive joint. These attributes of the design were all within the tolerances allowed by the application.

4.10 ALIGNMENT OF THE INDIVIDUAL LENS

In all the lens mountings so far discussed in this chapter, it is assumed that the lens has been properly centered before it was secured in place. The required accuracy of centering is dependent largely on the level of performance demanded by the application. In some cases, simple measurement and adjustment of the radial gap between the lens OD and the mount ID are sufficient. In higher performance cases, considerable care must be exercised in the centering process, and the instrumentation required is generally complex. In general, one cannot rely on radial components of an axial force to center the surface-contacted lens perfectly because friction is hard to overcome when the differences between the opposing radial forces become small. Experience has shown that very accurate centering can be achieved if the lens is held in a fixture of some sort and adjusted to the proper

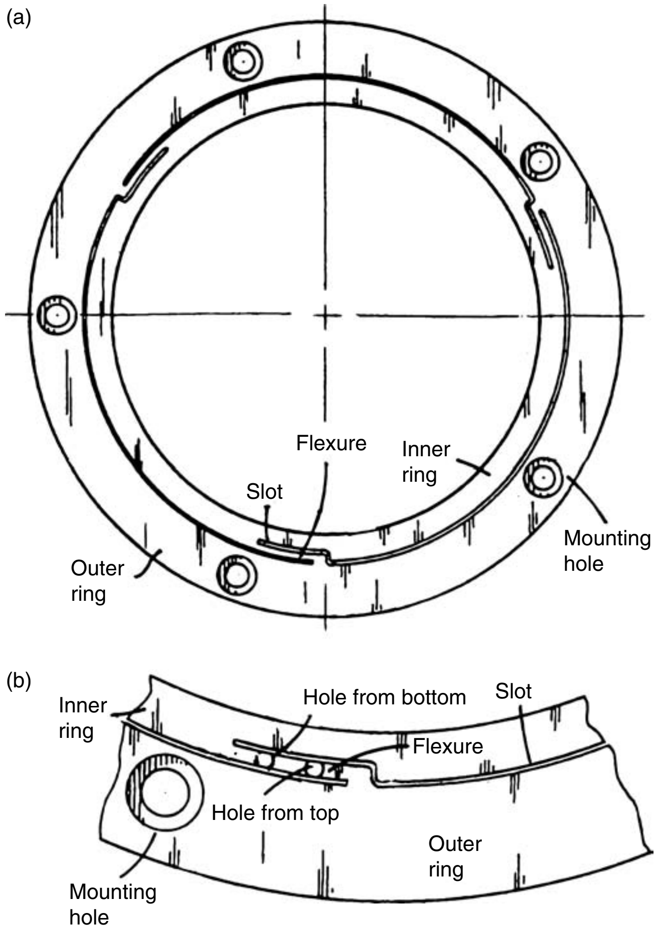
(a)
Flexure
Inner ring
Slot
Mounting hole
Outer ring
(b)
Inner ring
Hole from bottom
Slot
Flexure
Hole from top
Outer ring
Mounting hole

FIGURE 4.55 A flexure mounting in which a lens (not shown) is bonded to an inner ring that is mechanically isolated from the outer ring by three flexures. (Adapted from Bruning, J.H. et al., U.S. Patent 5,428,482,1995.)

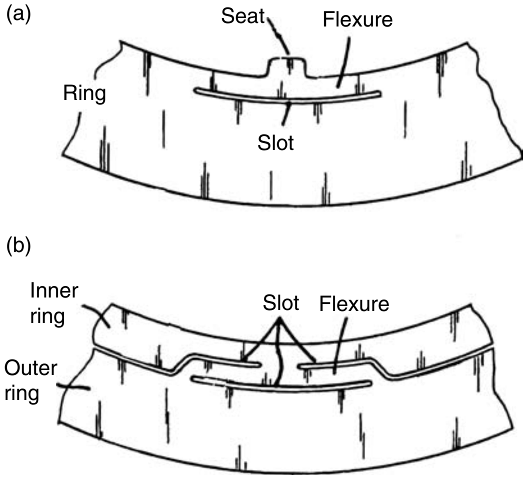
(a)
Seat
Flexure
Ring
Slot
(b)
Inner ring
Slot
Flexure
Outer ring

FIGURE 4.56 Two design variations for flexures to be used to support a lens in its mount. (Adapted from Bruning, J.H. et al., U.S. Patent 5,428,482,1995.)

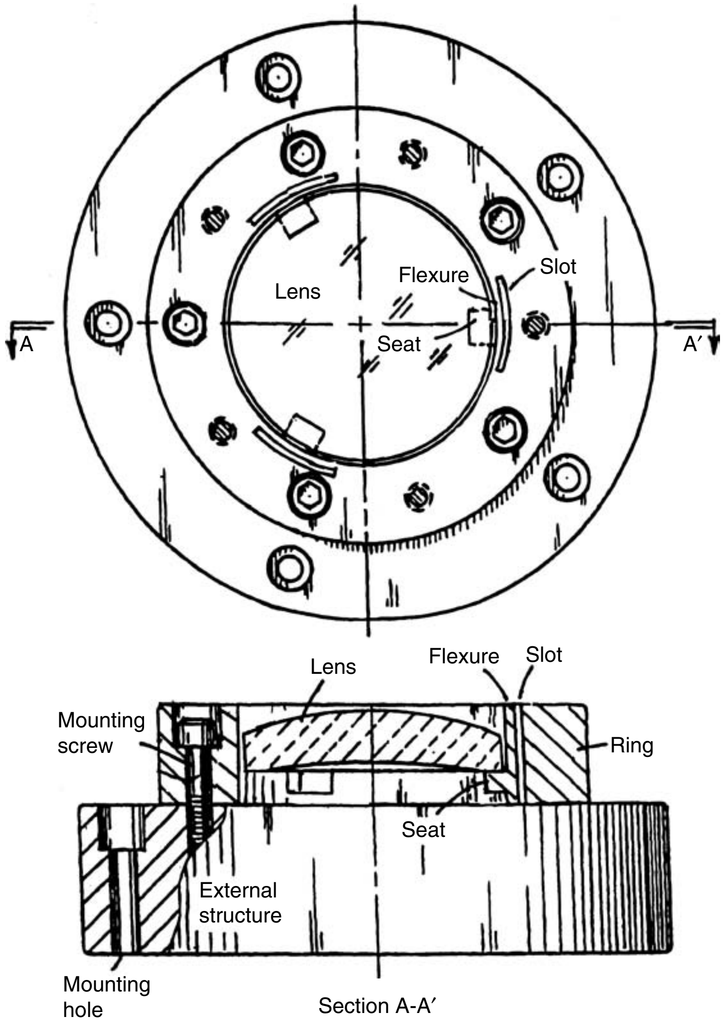

FIGURE 4.57 Top and side views of a flexure lens mounting using the flexure design of Figure 4.56(a). (Adapted from Bruning, J.H. et al., U.S. Patent 5,428,482,1995.)

orientation and location relative to some reference such as a precision mechanical surface, a prealigned light beam, or an interferometer cavity. Once the associated measurement instrumentation verifies that the lens is adequately aligned, it is clamped mechanically, potted into the mount with elastomer, or bonded to flexures to preserve that alignment. The fixture can then be removed.

We will briefly consider here four basic techniques for precision centering of individual lenses, as described by Yoder (2002). Figure 4.59(a) illustrates the first alignment technique. Here, the lens is mounted directly onto an interface provided in an instrument and adjusted so that it is centered and squared onto some feature of the mount, such as the mechanical axis of the barrel. The meniscus lens shown is to be mounted with the concave spherical surface touching a toroidal interface machined into the barrel. The barrel is positioned on a precision vertical axis spindle (such as one with an air bearing) so that the premachined toroidal surface runs true as the spindle is slowly rotated. A high-quality mechanical or electronic indicator can be used as the testing means for this adjustment. Bayar (1981) reported that lens edge runout of 5 μin. (0.13 μm) can be measured with an "electronic" gauge. Alternatively, the barrel OD can be positioned relative to the spindle axis and a finish cut made on the toroidal surface to true it to the rotation axis. A single-point diamond turning (SPDT)

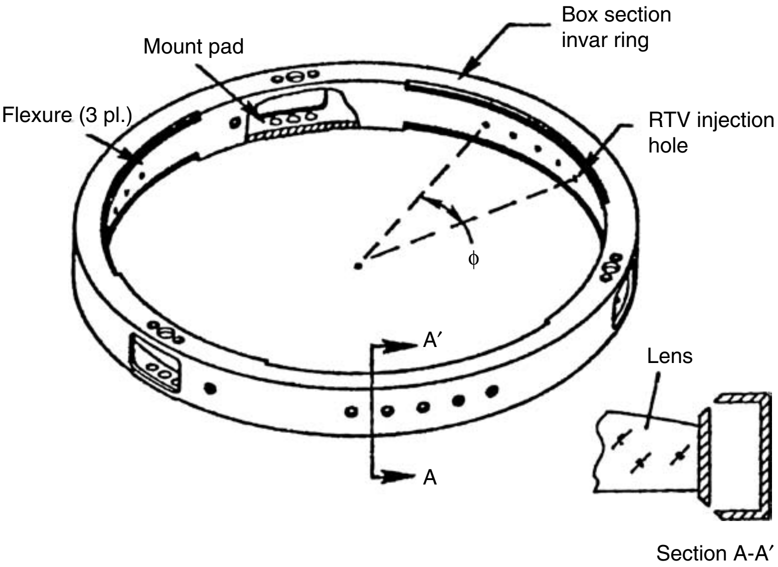
Box section invar ring
Mount pad
Flexure (3 pl.)
RTV injection hole
ϕ
A′
Lens
A
Section A-A′

FIGURE 4.58 A flexure-type lens mounting in which the lens rim is bonded to three flexure blades machined into a box-section cell. (Adapted from Steele, J.M. et al., *Proc. SPIE,* 1690, 387, 1992.)

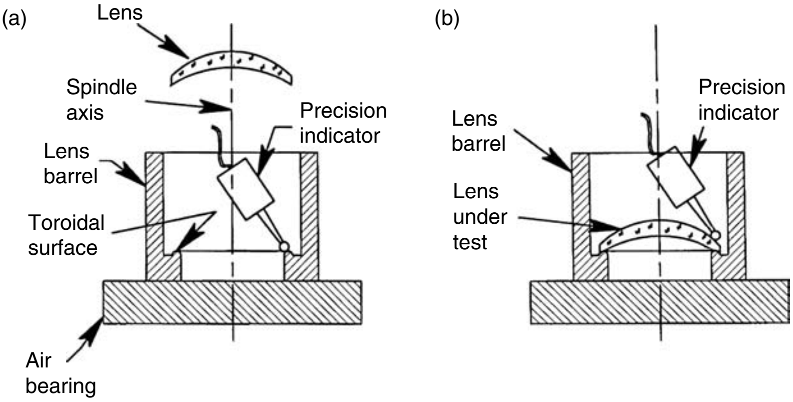
(a)
Lens
Spindle axis
Precision indicator
Lens barrel
Toroidal surface
Air bearing
(b)
Precision indicator
Lens barrel
Lens under test

FIGURE 4.59 Schematics of a technique for aligning a lens to an interface within a lens barrel or cell as in alignment technique 1 in the text. (From Yoder, P.R. Jr., *Mounting Optics in Optical Instruments*, SPIE Press, Bellingham, 2002.)

method produces the most accurate surfaces. Machines for SPDT and techniques for their use are summarized in Section 13.8.

The lens is inserted as indicated in Figure 4.59(b). Note that the lower surface is now automatically aligned to the spindle axis. The lens is moved laterally (by means not shown) while maintaining contact with the interface until the indicator shows that the top spherical surface runs true as the spindle rotates. The lens is then secured to the mount by clamping or with adhesive. In many cases where the latter technique is employed, success has been achieved by first securing the lens with a few, small, localized dabs of UV-curing epoxy and, following quick curing of that adhesive, more permanently bonding the lens with room-temperature-curing epoxy. This two-step bonding technique allows the lens and barrel to be carefully removed from the spindle before the second application of epoxy has fully cured, thus freeing the spindle for another use.

The mechanism used to move the lens laterally during alignment may be simple — as shown in Figure 4.60(a) — or slightly more complex — as shown conceptually in Figure 4.60(b). In both cases, radially directed push screws provide the desired motion. Ball-tipped setscrews are frequently used to ensure a smooth interface with the moveable component. Four screws arranged orthogonally instead of three at 120° intervals minimize cross talk between movements. Greater precision can be achieved if ball-tipped micrometers are substituted for the screws. Springs may be used in lieu of two of the screws or micrometers to provide restoring forces in opposition to the two remaining orthogonal adjustments. Commercial spring-loaded ball-plunger setscrews are sometimes used as the restoring devices. After radial alignment is completed, the lens is secured in position and the screws are removed.

An accurate means for sensing optical surface runout on a precision spindle similar to one described by Carnell et al. (1974) was shown in Figure 4.10. There, a plano-concave "test plate" with nearly the same radius of curvature as the surface to be tested is mounted near the latter's surface. Fizeau fringes formed between the adjacent surfaces move as the spindle is rotated. When the lens is properly centered, the fringes will appear stationary.

Figure 4.61 shows an autocollimation technique for sensing centration error of a lens to be mounted in a barrel on a rotating spindle. The arrows represent the interface between the lens and the barrel. Here, the beam from back-illuminated crosshair reticle$_1$ passes through a beamsplitter, is collimated by lens$_1$, and focused by lens$_2$ toward the center of curvature C_1 of the surface R_1 of lens$_3$ that is to be centered. The portion of the beam reflected from R_1 is recollimated and focused by lens$_2$ and lens$_1$, respectively and reflected by the beamsplitter to form an image of reticle$_1$ at crosshair reticle$_2$. The eyepiece then recollimates this beam so that the eye can observe it. If the surface R_1 wobbles as it turns, the image of reticle$_1$ will move with respect to the fixed reticle$_2$, thereby indicating a centration error.

In yet another means for judging proper lens alignment, a target is imaged through the lens and the motion of that image is observed under magnification as the spindle is rotated (see Figure 4.8). Note that a hollow shaft type of air-bearing table is needed if the beam is to pass through that component.

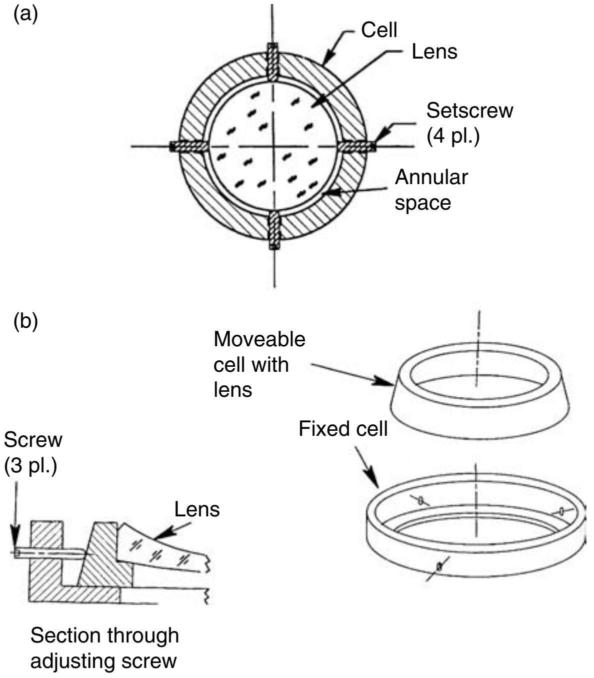

FIGURE 4.60 Techniques for using radially oriented setscrews to center a lens. (a) A simple design and (b) a more complex design. (Adapted from Yoder, P.R. Jr., *Mounting Optics in Optical Instruments*, SPIE Press, Bellingham, 2002.)

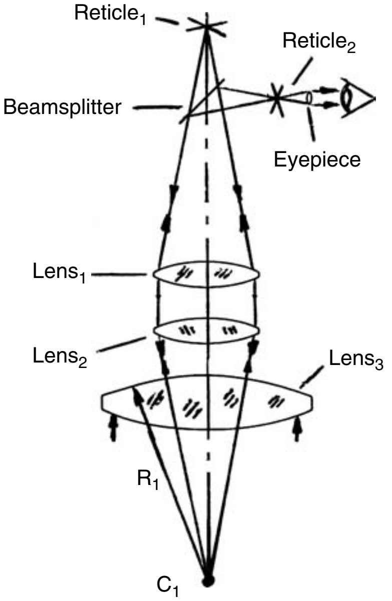

FIGURE 4.61 An autocollimation setup for sensing centration errors of a lens. (Adapted from Bayar, M., *Opt. Eng.*, 20, 181, 1981.)

Yet another technique passes an appropriately converged or diverged interferometer beam symmetrically through the lens under test. That lens does not need to rotate. The quality of the transmitted wave front is evaluated to detect alignment errors. A calibrated null lens may be needed in this test setup in order to compensate for the inherent aberrations of the test lens.

Figure 4.62 shows a setup that might be employed in aligning a lens and then bonding it to three flexure blades in a lens barrel–again using the basic alignment method just described. The flexure design of Figure 4.53 might work well here. The alignment fixture with a linear stage attached is secured to the table. The orientation of this fixture must be such that the stage motion is parallel to the spindle's axis. The lens barrel is aligned mechanically so its centerline is aligned to the spindle's axis and is then secured to the spindle table. The lens is placed on the vacuum chuck, the chuck is activated, and the chuck and lens subassembly is attached to the fixture with two springs. Two orthogonal adjustment mechanisms are needed. Only one is shown in the figure. Initially, the lens will not be aligned to the flexures nor to the tangent interface in the barrel. With the lens supported above the barrel interface, and using a centration monitor such as the Fizeau interferometer shown in the figure, the lens is moved with the orthogonal adjustment screws until it runs true as the spindle is rotated back and forth through its free range of motion, which is limited by the presence of the alignment mechanisms. When this adjustment is completed, the lens is lowered with the stage until it is properly located axially with respect to the flexures. The centration is then checked and refined as necessary.

At this point, the lens rim should be located symmetrically in the radial direction with respect to the flexure blades and a short distance away from each bonding pad. If the spacing is not quite right to provide the proper adhesive layer thickness, the flexure modules can be released and moved so this spacing becomes acceptable. Adhesive is injected into these spaces through holes in the flexure blades (not shown) and allowed to cure. After the alignment is checked once more, the vacuum can be released and the fixture removed. The barrel and the attached lens can then be removed from the table.

Note that if the flexure blades are not provided as separable (and therefore adjustable) modules, the alignment of the barrel to the spindle axis becomes more difficult. Proper clearances between the bonding pads and the lens rim can be provided only by holding manufacturing tolerances closely on the ID of the flexure pads and the lens' OD.

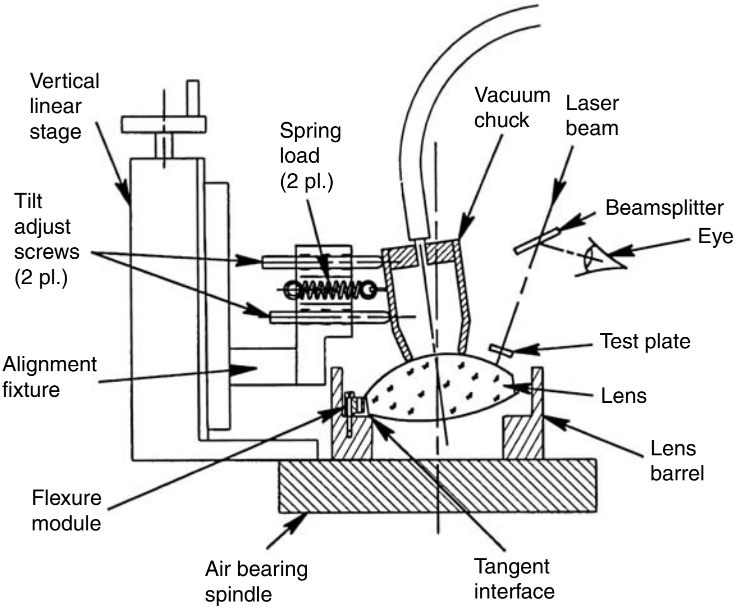

FIGURE 4.62 Schematic of a technique for aligning and bonding a lens to flexures in a barrel using alignment technique 1 in the text. (From Yoder, P.R. Jr., *Mounting Optics in Optical Instruments*, SPIE Press, Bellingham, 2002.)

To illustrate Yoder's second alignment technique, the lens is first mounted conventionally in an individual cell and then that subassembly is inserted into the lens barrel, which is in turn attached to an air-bearing spindle as shown in Figure 4.63(a). Three pins arranged at 120° intervals around the barrel and oriented parallel to the barrel axis protrude through three holes provided in the cell. One pin and one hole are shown. The ID of each hole is slightly larger than the OD of the corresponding pin. The lens and cell subassembly is adjusted laterally and tilted within the clearances between the pins and their holes until both lens surfaces run true to the spindle's axis (see Figure 4.63[b]). The axial location of the lens can also be adjusted at this time using the linear slide. Note that is not essential that the lens and cell subassembly be held on a vacuum chuck. A mechanical tool attached directly to the cell and configured to interface with the adjusting screws and springs would serve the same purpose.

Centration testing is best done optically in this case since the lower surface of the lens is not accessible for contact with an indicator. When alignment is satisfactory, the spaces around the pins are filled with epoxy and the epoxy is cured. The pinning process described here is sometimes called *liquid pinning* or *plastic dowelling*. It achieves the same result as mechanical pinning, in which holes are drilled and reamed and pins are pressed in place, but it does not involve the potential hazards of contamination and disruption of alignment characteristic of those operations. A possible modification of this concept uses three threaded rods (studs) instead of smooth pins and threads on the inside surfaces of the three holes into which these rods protrude. The annular ring of cured epoxy would then lock into the opposing threads and provide greater strength in resisting axial movement of the adjusted subassembly.

In the third lens-alignment technique described by Yoder (2002), a cell is premachined to close tolerances on its OD, circularity of the OD, and perpendicularity of both the top and bottom cell faces to the mechanical axis of the OD. A suitable interface for the lens is machined into the cell in the same machine setup as was used to finish the OD. SPDT is best for these machining operations because of its inherent precision. Figure 4.64(a) shows the premachined cell with its OD centered to the rotation axis of the spindle using a precision indicator and secured to the spindle table. The

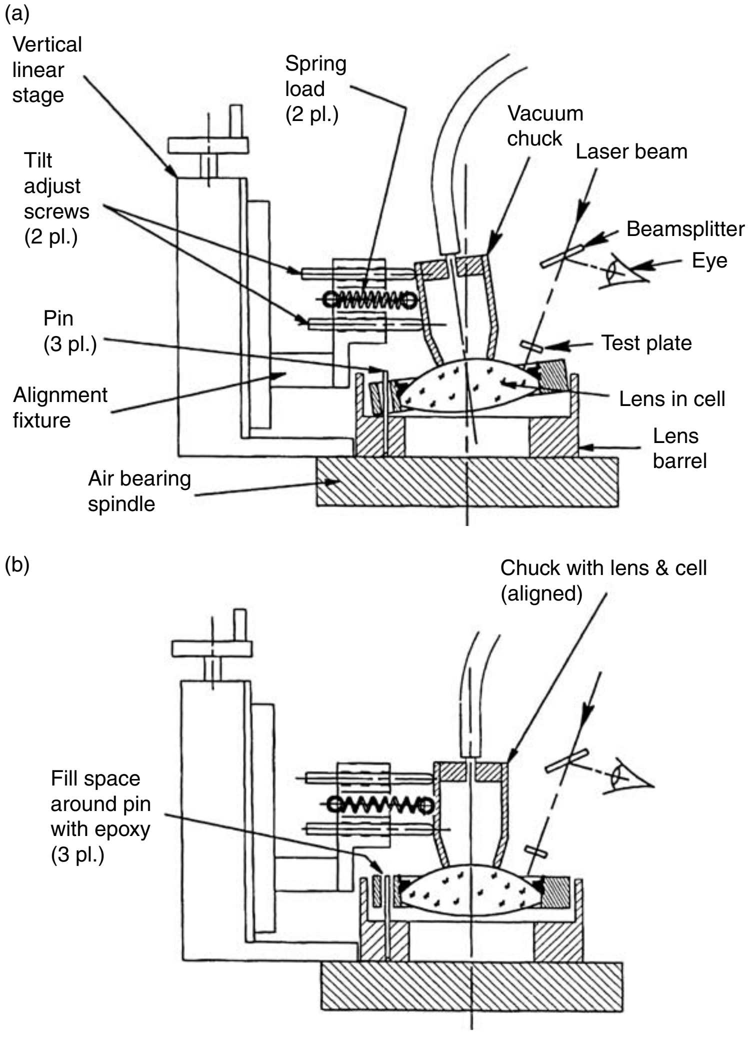
(a)
Vertical linear stage
Spring load (2 pl.)
Vacuum chuck
Laser beam
Tilt adjust screws (2 pl.)
Beamsplitter
Eye
Pin (3 pl.)
Test plate
Alignment fixture
Lens in cell
Lens barrel
Air bearing spindle
(b)
Chuck with lens & cell (aligned)
Fill space around pin with epoxy (3 pl.)

FIGURE 4.63 Schematics of an alignment setup for centering a lens and cell subassembly to a barrel as in alignment technique 2 in the text. (a) Initial step, (b) cell aligned and ready for "liquid pinning." (From Yoder, P.R. Jr., *Mounting Optics in Optical Instruments*, SPIE Press, Bellingham, 2002.)

convex surface of the meniscus lens is to be interfaced with the mechanical surface of the cell. The latter surface is shown as toroidal, but it could be conical. The lens is to be secured with a threaded retainer (shown in view [b]) or by any other suitable means. The lens is moved on the interface with adjustment screws (not shown) until the top surface runs true as the table is rotated. The retainer is then carefully clamped down and the alignment checked again.

Once the lens is properly clamped, the lens and cell subassembly can be removed from the spindle table and inserted into the lens barrel (see Figure 4.64[c]). This barrel has a carefully machined ID that is very slightly larger than the OD of the lens cell. This ensures that the lens will be aligned to the axis of that barrel.

A fourth alignment technique is illustrated by Figure 4.65(a). Here the lens cell is premachined so its top and bottom faces are parallel, flat, and separated by a specific thickness "*y*." A surface with shape appropriate to interface with the lens is also machined into the cell so as to be parallel to the cell faces and at dimension "x" from surface -A-. The cell is placed on a precision plane-parallel

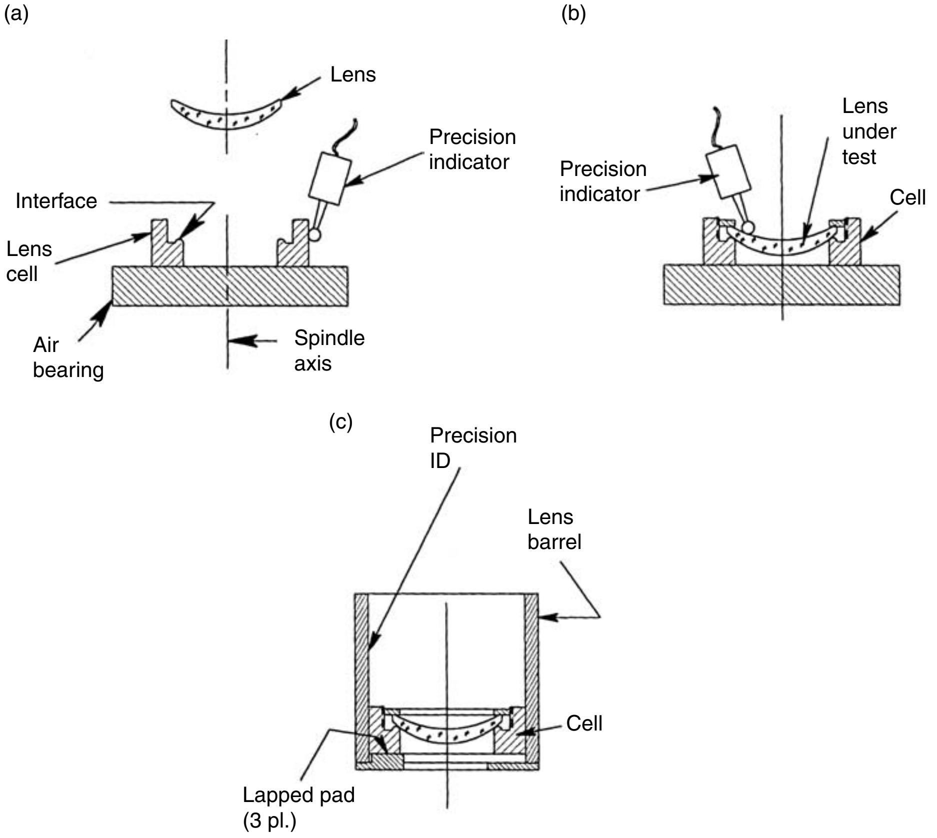

FIGURE 4.64 Schematics of an alignment setup for centering a lens and cell subassembly to a barrel as in alignment technique 3 in the text. (From Yoder, P.R. Jr., *Mounting Optics in Optical Instruments*, SPIE Press, Bellingham, 2002.)

spacer attached to an air-bearing table. The lens is inserted against the interface provided in the cell (see Figure 4.65[b]). The lens is adjusted laterally until it is aligned to the rotation axis and secured in place. The rim of the cell is then machined *in situ* to have the proper OD and to make that OD cylindrical and perpendicular to surface -A-. The lens and cell subassembly can then be removed and inserted into a barrel that has a cylindrical bore with ID only very slightly larger than the cell OD. To minimize the possibility that the cell might jam in the barrel ID if tilted slightly during insertion, the rim of the cell might be machined as a curved surface in the manner described in Section 4.6 for lens rims. The subassembly is secured to complete the alignment and assembly operation.

Extremely high-dimensional and alignment precision can be achieved by applying SPDT methods when mounting a lens. In the SPDT process (described in more detail in Section 13.8), extremely fine cuts are taken on the surface in work using a specially prepared and oriented diamond crystal as the cutting tool. The work piece is supported and rotated on a highly precise spindle (air or hydrostatic bearing). The tool is moved slowly across the surface on highly precise linear or rotary stages. Real-time interferometric control systems are used to ensure location and orientation accuracy of the cutting tool at all times. Details regarding the SPDT process as employed for assembling a lens into its mount are provided in Erickson et al. (1992), Rhorer and Evans (1994), and Arriola (2003).

As an example of this use of the SPDT method in assembling, aligning, and finish-machining of a typical lens and cell subassembly, consider the case of a meniscus-shaped fused BK7 lens that

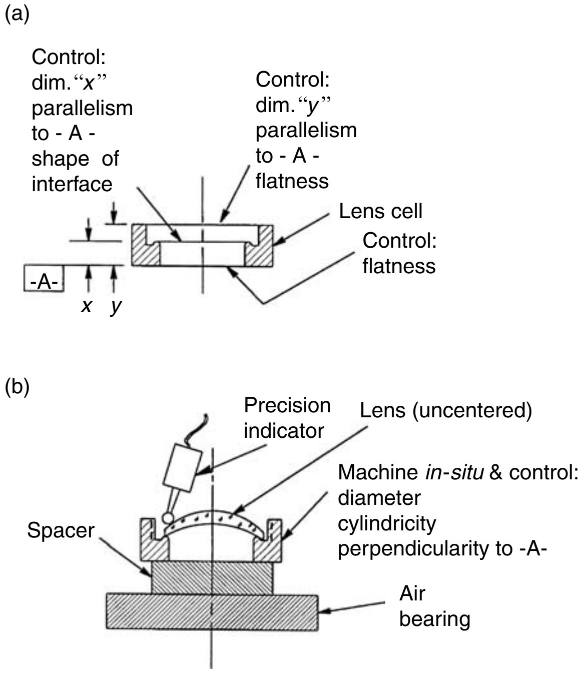

FIGURE 4.65 Schematics of an alignment setup for centering a lens in a partially premachined cell, installing and aligning the lens, and completing the cell machining as in alignment technique 4 in the text. (From Yoder, P.R. Jr., *Mounting Optics in Optical Instruments*, SPIE Press, Bellingham, 2002.)

is to have a minimum clear aperture diameter of 3.000 in. (76.200 mm), axial thickness of 0.667 ± 0.004 in. (16.9418 ± 0.1016 mm), and radii of 6.375 ± 0.001 in. (161.925 ± 0.025 mm) and 10.200 ± 0.002 in. (259.080 ± 0.050 mm). The completed lens is to be mounted athermally in a 6061-T6 aluminum cell by the elastomeric "potting" method described in Section 4.8. The cell is to be machined so its OD is concentric with the optical axis within 0.0005 in. (0.0127 mm) and parallel to that axis within 10 arcsec. The axial thickness of the cell is to be 1.1510 ± 0.0002 in. (29.2354 ± 0.0051 mm) and the front and back surfaces of the cell are to be parallel within 1.0 arcsec. The ODs of the rings on its rim are to be 4.0000 ± 0.0002 in. (101.6000 ± 0.0051 mm). The desired subassembly is illustrated in Figure 4.66. Surfaces to be finish-machined by SPDT are indicated. It is believed that only by applying this process can the tolerances required for this subassembly be met.

Key to the success of this process (based on that described by Erickson et al., 1992) is the use of a centering chuck such as that shown in Figure 4.67. This device is usually made of brass because it can be easily SPDT-machined to precise dimensions. The surfaces to be made in this manner are indicated in the figure. They can be cut in the same setup, thus ensuring high accuracy relative to each other. Other surfaces require only conventional machining. The conical interface is cut to the proper angle to interface properly with the convex surface of the lens.

The centering chuck is made so as to fit snugly into a receptacle on a base plate attached to the SPDT machine spindle. It seats against a surface having air path recesses for pulling a vacuum to secure the chuck in place. The finished lens is attached to the chuck with blocking wax (or a temporary UV-curing adhesive) (see Figure 4.68). The lens is moved laterally to center its axis to the spindle axis before the wax solidifies (or the adhesive is cured). Initial alignment can be accomplished mechanically using precision indicators and then finalized using interferometric means, such as the Fizeau technique described earlier. Measurement of the vertex distance indicated in the figure provides information useful in establishing the axial location of a machined surface on the cell in a later step.

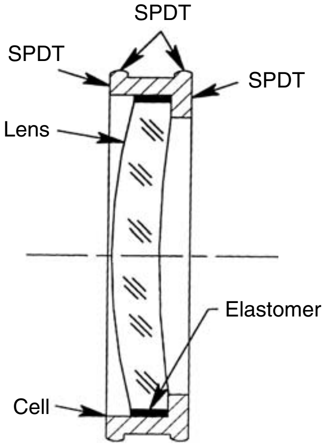

FIGURE 4.66 High precision lens-cell subassembly assembled, aligned, and final-machined by SPDT as described in the text.

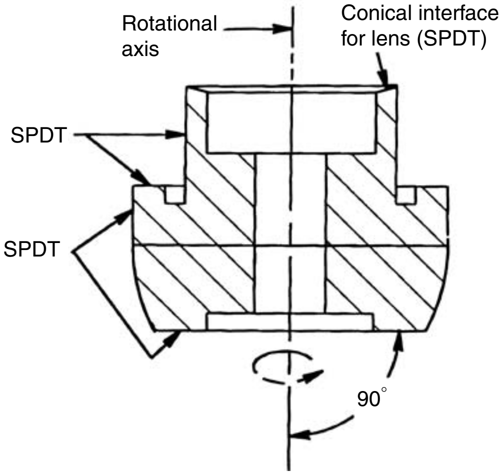

FIGURE 4.67 Removable centering chuck designed to interface a lens to the spindle of a SPDT machine. Surfaces marked SPDT are machined in one setup for maximum precision.

The cell into which the lens is to be mounted is placed over the rim of the lens as indicated in Figure 4.69. This cell has finished dimensions on all surfaces except those indicated by SPDT labels in the figure. The cell is aligned mechanically to the spindle axis and waxed to the lens as shown.

The next step in the process is to remove the chuck and lens subassembly from the spindle, invert it onto a horizontal surface as shown in Figure 4.70, and inject elastomer (typically RTV) into the annular cavity between the lens OD and the cell ID. Four radially directed holes are used for this purpose to ensure complete filling of the cavity. Note that this operation cannot be accomplished without inverting the subassembly because the elastomer must be constrained while curing. The use of the removable chuck allows the SPDT machine to be used for other purposes while the elastomer cures.

After the elastomer has completely cured, the subassembly is returned to the spindle baseplate and the exposed cell surfaces are turned to final dimensions (see Figure 4.71). As a precaution, it would be

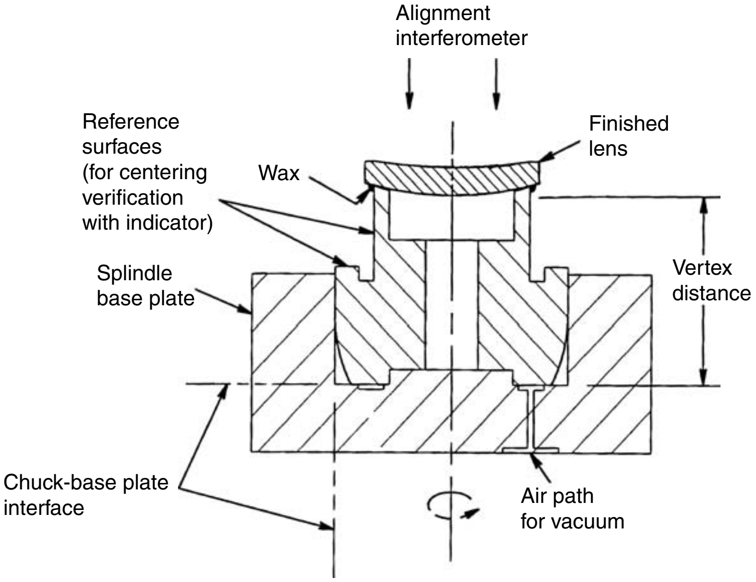
Alignment interferometer
Reference surfaces (for centering verification with indicator)
Wax
Finished lens
Splindle base plate
Vertex distance
Chuck-base plate interface
Air path for vacuum

FIGURE 4.68 Centering chuck installed on the spindle base plate of a SPDT machine with lens waxed in place and centered interferometrically.

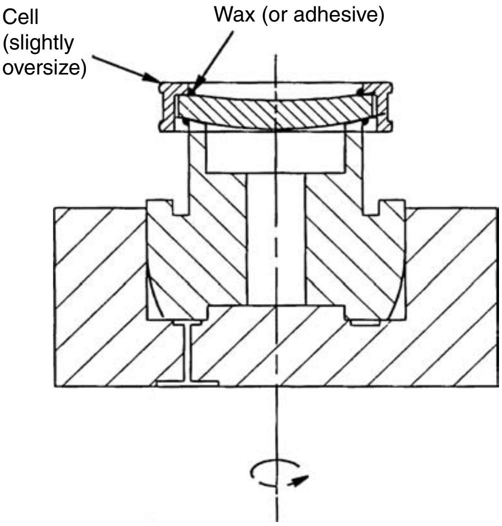
Cell (slightly oversize)
Wax (or adhesive)

FIGURE 4.69 Partially machined cell centered mechanically to spindle and attached to lens.

advisable to verify the centration of the lens interferometrically before the subassembly is removed from the chuck. Removal is accomplished by heating gently to melt the wax or by applying a solvent to dissolve the temporary adhesive. Finally, the subassembly is cleaned, inspected, and bagged for future use.

If the lens material is compatible with SPDT processing, its' finished surfaces can be processed by SPDT methods. These materials are most generally crystals used in infrared applications and a few plastics (see Table 4.2). Very important advantages of the process as compared with traditional grinding and polishing methods for optical component surface finishing are (1) that multiple faces of the component can be machined in a single setup on the machine so the relative orientations and

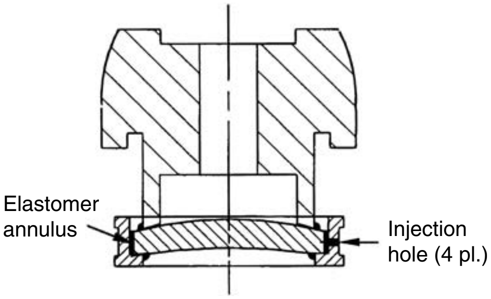

FIGURE 4.70 Chuck and lens removed from spindle and inverted for injection of elastomer.

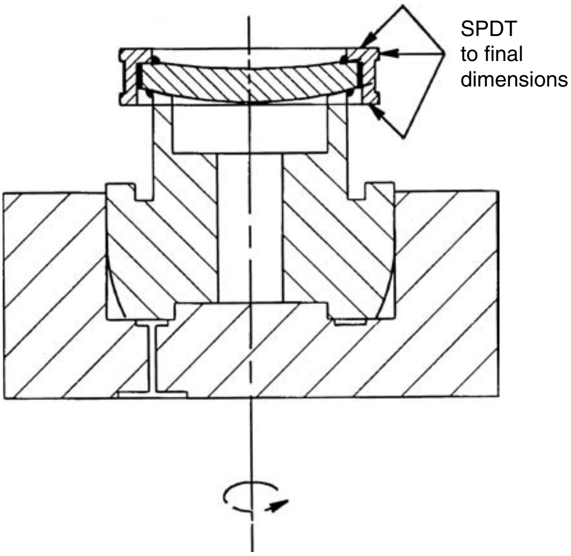

FIGURE 4.71 Chuck and lens returned to spindle for final machining of mechanical interfaces.

TABLE 4.2
Crystalline Materials that can be Diamond Turned

Calcium fluoride	
Magnesium fluoride	Germanium
Cadmium telluride	Strontium fluoride
Zinc selenide	Sodium fluoride
Zinc sulfide	KDP
Gallium arsenide	KTP
Sodium chloride	Silicon?

Note: Materials with (?) cause rapid diamond wear.

Source: Adapted from Rhorer R.L. and Evans C. I., in *Handbook of Optics*, 2nd ed. Bass, M., Van Stryland E.W., Williams, D.R., and Wolfe, W.L., Eds., McGraw-Hill, New York, 1994.

locations of optical and mounting surfaces can be accurately controlled, (2) the ability to create aspheric surfaces, and (3) the speed with which all surfaces can be created.

Figure 4.72(a) shows a cylindrical blank of the optical material attached with blocking wax to a chuck on the spindle of a SPDT machine. The outline of the desired finished lens is indicated in the figure. The convex surface of the lens (broken line) is machined to the proper radius and surface finish. The blank is then removed from the chuck and attached to a centering chuck as indicated in Figure 4.72(b). The concave surface and the lens rim can then be turned and the lens inspected for the required centration and surface quality. The completed lens can be removed from the chuck, cleaned, inspected, and bagged.

Guyer et al. (1998) described the use of SPDT-made crystalline lenses in a cryogenically cooled, dual-field IR-(4–5 μm spectral range) imaging missile tracker. The optical system of the tracker is illustrated in Figure 4.73. It was designed to be nearly athermal by distributing optical power so as to utilize the temperature variations of material properties and dimensions favorably and keep optical performance above the diffraction limit. The system included a magnification-changer subsystem that rotated about a transverse axis to change the field of view between

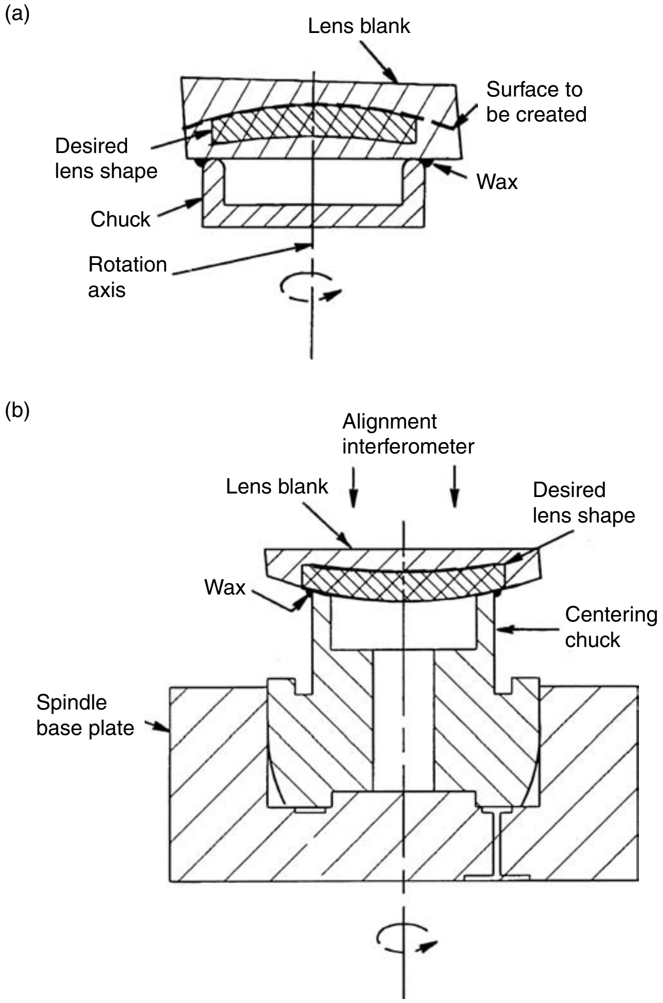

FIGURE 4.72 (a) A crystalline lens blank mounted on the spindle of a SPDT machine for cutting the initial spherical surface. (b) The partially machined blank from view (a) mounted on the SPDT machine for centering and final shaping.

the acquisition and tracking modes. A rotary solenoid drove the changer from one position to the other.

Each lens in the system had diamond-turned surfaces. The lenses in the magnification-changer subsystem each had one aspheric surface. Table 4.3 shows the tolerances assigned as results of a sensitivity analysis for tilt and axial and radial displacements of the magnification changer portion of this design. The tolerance budget allowed the larger lenses (E7 and E8) in the magnification changer to be mounted conventionally with a metal spacer as indicated in Figure 4.74. A fillet of elastomer constrained these lenses axially. The air-spaced triplet at the other end of the subassembly (lenses E4–E6) needed more precise centering, so the lens' mechanical mounting interfaces were diamond-turned in the same machine setup as the optical surfaces. These lenses were nested together and mounted as a group to minimize centration errors. In addition, the mechanical interfaces for those lenses in the aluminum housing were diamond-turned to accept the lenses. Radial clearance at lens E6 was ~ 2.5 μm. The group was held in place with elastomer injected into the three access holes indicated in Figure 4.74. The special precautions taken during design and fabrication resulted in successful production and use of the sensors.

TABLE 4.3
Results of a Mounting Sensitivity Analysis for the Magnification Changer of Figure 4.74

Element	Tilt (arcsec)	Axial displacement (μm)	Axial displacement (in.)	Transverse displacement (μm)	Transverse displacement (in.)
E4	6	10	0.0004	15	0.0006
E5	6	5	0.0002	10	0.0004
E6	6	10	0.0004	10	0.0004
E7	10	15	0.0006	20	0.0008
E8	10	15	0.0006	20	0.0008

Source: From Guyer, R.C. et al., *Proc. SPIE*, 3430, 109, 1998.

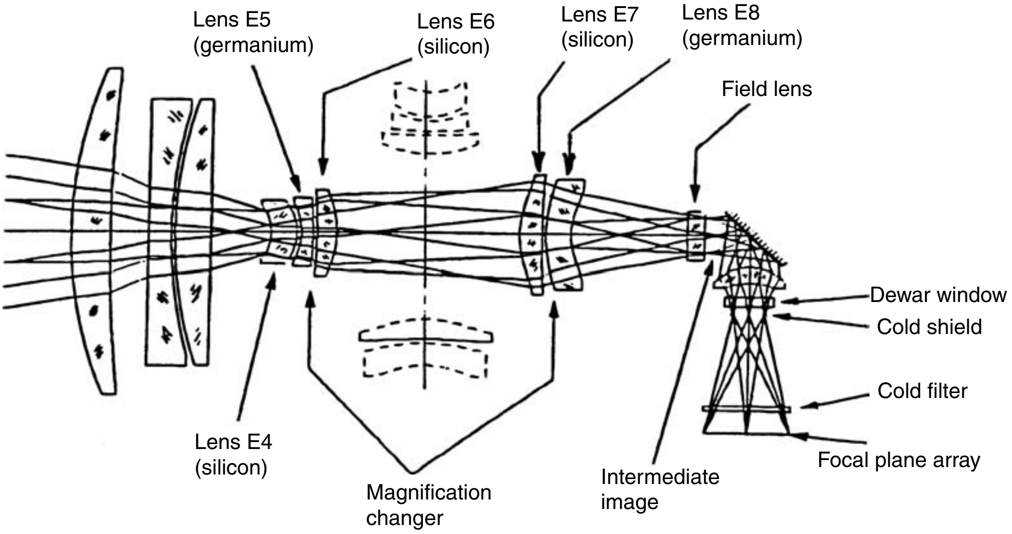

FIGURE 4.73 Optical system schematic for a dual-field IR tracker assembly. (From Guyer, R.C. et al. *Proc. SPIE*, 3430, 109, 1998.)

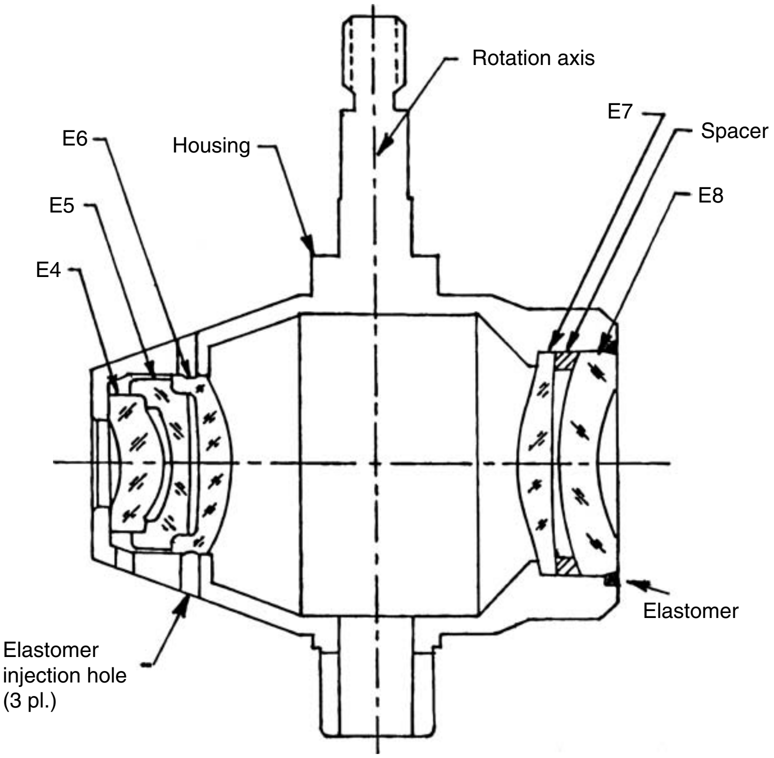

FIGURE 4.74 Opto-mechanical configuration of the magnification changer subsystem for the IR tracker. (From Guyer, R.C. et al., *Proc. SPIE*, 3430, 109, 1998.)

4.11 MOUNTING PLASTIC LENSES

Most of the development work enabling plastics to be used in refractive optics has occurred since 1936 and has been financed by private industry with the goal of fulfilling specific, high-volume product requirements. Polymethyl methacrylate (acrylic) (492574),[†] polysytrene (styrene) (590309), polycarbonate (Lexan) (585299), methyl methacrylate–styrene copolymer (NAS) (562335), copolymer styrene-acrylonitrile (SAN) (567348), and allyldiglycol carbonate (CR39) are the materials most commonly used for optical applications (Welham, 1979; Altman and Lytle, 1980; Lytle, 1995). These materials, and others, are discussed in Chapter 3.

Three basic techniques are employed in fabricating plastic lenses: conventional grinding and polishing, molding, and precision diamond turning. The material type determines the best process to be used. For example, CR39 is normally cast in a mold and cured under controlled environmental conditions. It is then ground and polished, usually for ophthalmic applications.

Injection and compression-molding are by far the most common methods for fabricating nonophthalmic plastic optics. These techniques can, of course, produce lenses configured exactly as are most glass lenses, that is, with cylindrical rims, chamfers, and annular flats. Figure 4.75 shows a set of molded plastic lenses for a 28 mm (1.10 in.) focal length, *f*/2.8 photographic objective. Each of these lenses is configured for more or less conventional mounting, as described earlier in this chapter.

Fortunately, molded plastic lenses are not constrained by requirements for rotational symmetry and ease of access to each machined surface with grinding and polishing tools. They can be provided with integral mounting flanges, locating pins, orienting tabs, spacers, and strategically located holes. These features can greatly simplify mounting the element and reduce the number and complexity of ancillary mechanical parts required. Assembly by solvent bonding, heat staking, and sonic welding techniques is feasible and economical. Other design freedoms unique to molded plastic optics were discussed by Lytle (1980, 1995) and include such approaches as nesting plastic lenses into one another to form air-spaced doublets that center and space automatically at assembly. Figure 4.76 shows a plastic lens molded into a square configuration. It has rectangular flat tabs extending beyond the optical aperture on two edges to facilitate insertion into a mechanical assembly. The tabs have unequal thicknesses to discourage incorrect installation.

[†] Index-Abbe number code as used in optical glass type designation.

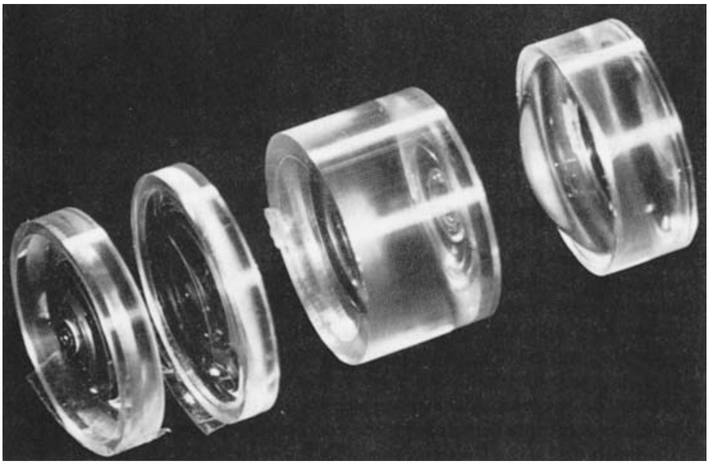

FIGURE 4.75 Isometric view of a four-element plastic objective with elements configured for conventional mechanical mounting. (From Lytle, J.D., *Proc. SPIE*, 181, 93, 1979.)

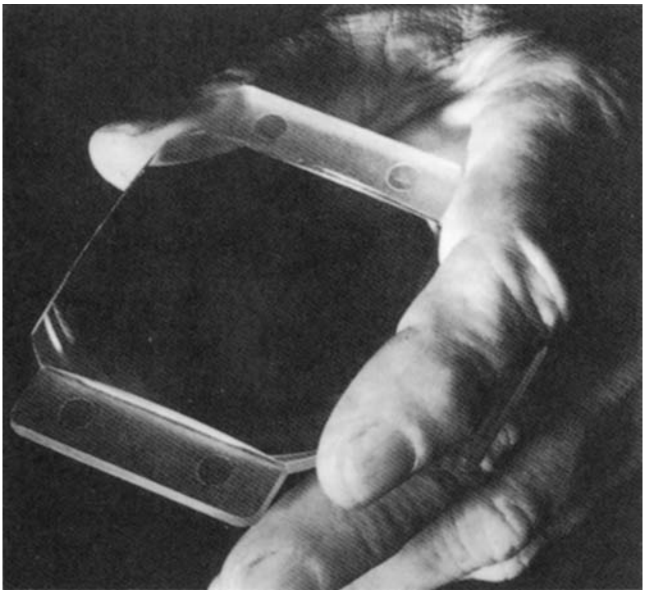

FIGURE 4.76 A plastic lens element of square configuration having integral mechanical mounting features. (From Lytle, J.D., *Proc. SPIE*, 181, 93, 1979.)

In designing optical systems to use molded plastic optics, it is especially important for the lens designer, mechanical engineer, and fabricator to work closely together so that the advantages of the materials and fabrication processes can be fully realized. Proper design of the tooling and molding equipment is essential to economical producibility. For example, Figure 4.77 from Altman and Lytle (1980) illustrates some good and bad lens configurations that may occur in typical applications. The element shown in view (a) is a simple meniscus lens configured as it might be formed in glass. The equivalent plastic version of the same lens is shown in view (b). The axial thickness is here increased to allow the use of more liberal gate cross sections for introducing plastic material into the mold. This should result in a better surface figure than could otherwise be achieved in plastic. A positive element of the more strongly curved shape shown in view (c) would mold better than weaker (longer radius) types, since surface tension is then more effective.

The negative element shown in view (d) would mold poorly, since the injected material would fill the thicker region at the edge more easily than the thin center region. Furthermore, gases would tend to be trapped at the center in this design. A preferred configuration would have greater axial thickness so that the edge-to-center thickness ratio does not exceed 3:1.

The configuration of view (e) is reasonably easy to mold if care is taken to inject material into the lens region (outside the clear aperture) and not into the flange. Flanges of this type are useful in creating multiple-element subassemblies, as shown in view (f). This is essentially an edge-contact design. Cemented interfaces, as illustrated by view (g), should be avoided because the cemented interface can develop considerable stress owing to CTE differences. View (h) shows a thick meniscus lens that would tend to mold well if properly proportioned and carefully gated for material injection.

SPDT is feasible with some plastics such as acrylic and produces optical quality surfaces suitable for many visible light and near-IR applications. Nonspherical surfaces can be made by this process on a "one-off" basis. They can be molded on plastic optics in quantity nearly as easily as spherical ones. Molds are simply made to the negative contour of the desired surface. Plummer (1994) described the high-order, non-rotationally symmetric polynomial aspherics built into the refracting corrector plate, concave mirror, and eye lens of the viewfinder for the unique, single-lens,

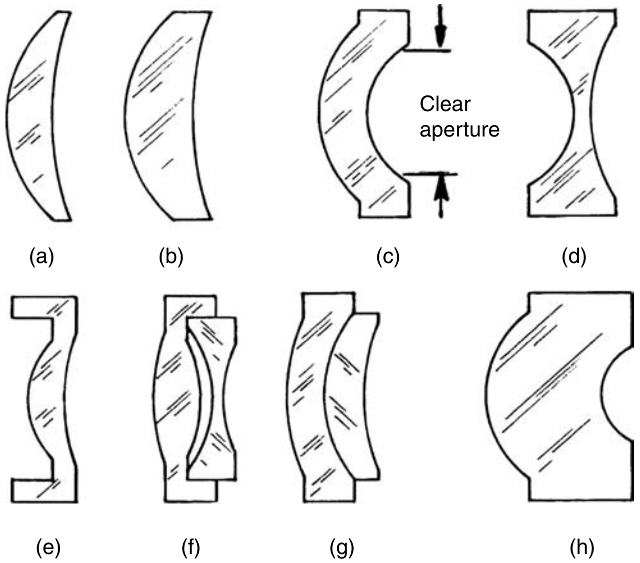

FIGURE 4.77 Different mechanical configurations of molded plastic lens elements that have distinct advantages and disadvantages as discussed in the text. (Adapted from Altman R.M. and Lytle, J.D., *Proc. SPIE*, 237, 380, 1980.)

reflex Polaroid SX-70 camera. Each element was made by injection molding. The molds were made by hand correcting steel surfaces shaped initially by SPDT. A customized coordinate measuring machine capable of at least 0.1 μm precision while sliding a 0.8-mm-diameter sapphire ball lightly over the surface to be measured provided error maps that defined where correction was required and how large the correction should be. This same technique can be applied to make molds for nearly any aspheric surface to be used in other applications.

Bäumer et al. (2003) described the design of a CMOS[‡] imaging sensor using an injection-molded plastic singlet. Intended for large-scale production, this sensor is shown conceptually in Figure 4.78. The lens is biconvex and has a circular recess in its entrance face to accommodate a filter. The lens fits into a barrel that, in turn, fits into a mount holding the focal plane assembly. The *f*/2.2 system is compatible with a 352 × 288 pixel format with 5.6 × 5.6 μm pixels. Table 4.4 lists the design specifications and the predicted performance of the nominal system. Comparison of the values indicates that some performance degradation from the effects of manufacturing tolerancing, stray light, and focus errors at assembly can be tolerated. The authors point out that careful consideration of these effects as well as the details of the manufacturing processes and material characteristics are vital to the ultimate success of the opto-mechanical design.

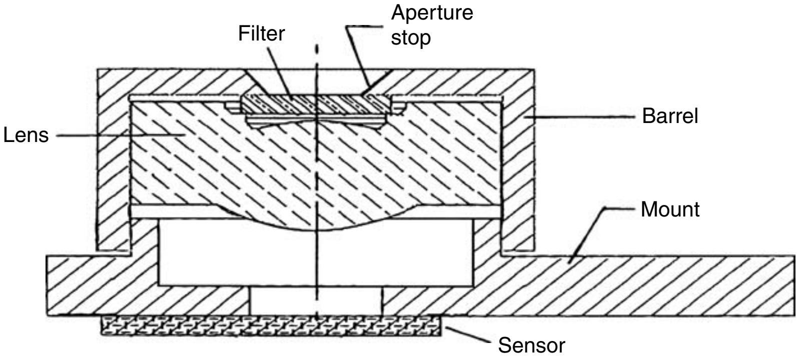

FIGURE 4.78 A small image forming system featuring injection-molded, plastic opto-mechanical components. (Adapted from Bäumer, S. et al., *Proc. SPIE*, 5173, 38, 2003.)

TABLE 4.4
Comparison of Specification Requirements and Nominal Design Performance of the CMOS Camera System Illustrated in Figure 4.78

	Specification	Design Capability
Horizontal field of view (HFOV)	54°	54°
MTF at on-axis at 50 lp/mm	> 50%	70%
HFOV at 25 lp/mm	> 35%	41%
Distortion	< 5%	4.5%
Relative illumination	> 50%	70%
Length	< 4mm	3.4 mm

Source: From Baumer, S. et al., *Proc. SPIE,* 5173, 38, 2003.

[‡] CMOS is a low-power consumption complementary metal oxide semiconductor used in sensor chips.

REFERENCES

Adams, G., Selection of tolerances, *Proc. SPIE*, 892, 173, 1988.

Ahmad, A. and Huse, R.L., Mounting for High Resolution Projection Lenses, U.S. Patent 4,929,054, 1990.

Altman, R.M. and Lytle, J.D., Optical design techniques for polymer optics, *Proc. SPIE*, 237, 380, 1980.

ANSI Y14.5M, *Dimensioning and Tolerancing*, ANSI, New York, (1982).

Arriola, E. W., Diamond turning assisted fabrication of a high numerical aperture lens assembly for 157 nm microlithography, *Proc. SPIE*, 5176, 36, 2003.

ASME B1.1, *Unified Inch Screw Threads (UN and UNR) Thread Form*, ASME International, New York, 2001.

Bacich, J.J., Precision Lens Mounting, U.S. Patent 4,733,945, 1988.

Baldo, A.F., Machine elements, in *Marks' Standard Handbook for Mechanical Engineers*, Avallone, E.A. and Baumeister, T., III, Eds., McGraw-Hill, New York, 1987, chap. 8.2, p. 8.

Bäumer, S., Shulepova, L., Willemse, J., and Renkema, K., Integral optical system design of injection molded optics, *Proc. SPIE*, 5173, 38, 2003.

Bayar, M., Lens barrel optomechanical design principles, *Opt. Eng*., 20, 181, 1981.

Bruning, J.H., DeWitt, F.A., and Hanford, K.E., Decoupled Mount for Optical Element and Stacked Annuli Assembly, U.S. Patent 5,428,482, 1995.

Carnell, K.H., Kidger, M.J., Overill, A.J., Reader, R.W., Reavell, F.C., Welford, W.T., and Wynne, C.G., Some experiments on precision lens centering and mounting, *Opt. Acta*, 21, 615, 1974.

Delgado, R.F. and Hallinan, M., Mounting of lens elements, *Opt. Eng*., 14, S-11, 1975; Reprinted in *SPIE Milestone Series*, Vol. 770, 1988, p. 173.

Erickson, D.J., Johnston, R.A., and Hull, A.B., Optimization of the optomechanical interface employing diamond machining in a concurrent engineering environment, *Proc. SPIE*, CR43, 329, 1992.

Fischer, R.E., Optimization of lens designer to manufacturer communications, *Proc. SPIE*, 1354, 506, 1990.

Guyer, R.C., Evans, C.E., and Ross, B.D., Diamond-turned optics aid alignment and assembly of a dual field infrared imaging sensor, *Proc. SPIE*, 3430, 109, 1998.

Hopkins, R.E., Some thoughts on lens mounting, *Opt. Eng*., 15, 428, 1976.

Hopkins, R.E., Lens mounting and centering, in *Applied Optics and Optical Engineering*, Vol. VIII, Shannon, R.R. and Wyant, J.C., Eds., Academic Press, New York, 1980, chap. 2.

Jacobs, D.H., *Fundamentals of Optical Engineering*, McGraw-Hill, New York, 1943.

Karow, *H.H., Fabrication Methods for Precision Optics*, Wiley, New York, 1993.

Kojima, T., Yield estimation for mass produced lenses based on computer simulation of the centering tolerance, *Proc. SPIE*, 193, 141, 1979.

Kowalskie, B.J., A user's guide to designing and mounting lenses and mirrors, in *Digest of Papers, OSA Workshop on Optical Fabrication and Testing*, North Falmouth, MA, 98, 1980.

Lytle, J.D., Specifying glass and plastic optics – what's the difference?, *Proc. SPIE*, 181, 93, 1979.

Lytle, J.D., The influence of physical configuration on the quality of injection molded lenses, in: *Digest of Papers, OSA Workshop on Optical Fabrication and Testing*, Mills College, Oakland, CA, 54, 1980.

Lytle, J.D., Polymeric Optics, in *OSA Handbook of Optics*, 2nd ed., Vol. II, Bass, M., Van Stryland, E., Williams, D.R., and Wolfe, W.L., Eds., McGraw-Hill, New York, 1995, chap. 34.

Miller, K.A., Nonathermal potting of optics, *Proc. SPIE*, 3786, 506, 1999.

MIL-O-13830A, *Optical Components for Fire Control Instruments; General Specification Governing the Manufacture, Assembly, and Inspection of*, U.S. Department of Defense, Washington, DC, (1975).

Parks, R.E., Optical component specifications, *Proc. SPIE*, 237, 455, 1980.

Parks, R.E., Optical specifications and tolerances for large optics, *Proc. SPIE*, 406, 98, 1983.

Plummer, J.L., Tolerancing for economies in mass production of optics, *Proc. SPIE*, 181, 90, 1979.

Plummer, W.T., Precision: How to Achieve a Little More of It, Even After Assembly, *Proceedings of the First World Automation Congress (WAC '94)*, Maui, 193, 1994.

Reavell, F.C. and Welford, W.T., Precision construction of optical systems, *Proc. SPIE*, 251, 2, 1980.

Rhorer, R.L. and Evans, C.J., Fabrication of optics by diamond turning, in *OSA Handbook of Optics*, 2nd ed. Vol.I, Bass, M., Van Stryland, E., Williams, D.R., and Wolfe, W.L., Eds., McGraw-Hill, New York, 1995, chap. 41.

Richey, C.A., Aerospace mounts for down-to-earth optics, *Mach. Des*. 46, 121, 1974.

Roark, R.J., *Formulas for Stress and Strain*, 3rd ed., McGraw-Hill, New York, 1954; see also Young, W.C. *Roark's Formulas for Stress & Strain,* 6th ed., McGraw-Hill, New York, 1989.

Shannon, R., How to design a lens for manufacturing, in *Digest of Papers, OSA 'How-To' Program*, Boston, MA, 1990.

Shigley, J.E. and Mischke, C.R., The design of screws, fasteners, and connections, *Mechanical Engineering Design*, 5th ed., McGraw-Hill, New York, 1989, chap. 8.

Smith, W.J., Fundamentals of establishing an optical tolerance budget, *Proc. SPIE*, 531, 196, 1985.

Smith, W.J., Optics in practice, *Modern Optical Engineering*, 3rd ed., McGraw-Hill, New York, 2000, chap. 15.

Steele, J.M., Vallimont, J.F., Rice, B.S., and Gonska, G.J., A compliant optical mount design, *Proc. SPIE*, 1690, 387, 1992.

Valente, T. and Richard, R., Interference fit equations for lens cell design using elastomeric lens mountings, *Opt. Eng.*, 33, 1223, 1994.

Vukobratovich, D., Flexure mounts for high-resolution optical elements, *Proc. SPIE*, 959, 18, 1988.

Vukobratovich, D., Optomechanical Systems Design, *The Infrared & Electro-Optical Systems Handbook,* Vol. 4, ERIM, Ann Arbor, and SPIE, Bellingham, 1993, chap. 3.

Vukobratovich, D., Bonded mounts for small cryogenic optics, *Proc. SPIE*, 4131, 228, 2000.

Vukobratovich, D., Introduction to Optomechanical Design, *SPIE Short Course SC014*, 2003.

Welham, W., Plastic optical components, in *Applied Optics and Optical Engineering*, Vol. VII, Shannon, R.R. and Wyatt, J.C., Eds. Academic Press, New York, 1979, chap. 3. p. 79.

Willey, R.R., Economics in optical design, analysis, and production, *Proc. SPIE*, 399, 371, 1983.

Willey, R.R., The impact of tight tolerances and other factors on the cost of optical components, *Proc. SPIE*, 518, 106, 1984.

Willey, R.R., Optical design for manufacture, *Proc. SPIE*, 1049, 96, 1989.

Willey, R.R. and Durham, M.E., Ways that designers and fabricators can help each other, *Proc. SPIE*, 1354, 501, 1990.

Willey, R.R. and Durham, M.E., Maximizing production yield and performance in optical instruments through effective design and tolerancing, *Proc. SPIE*, CR43, 76, 1992.

Willey, R.R., George, R., Odell, J., and Nelson, W., Minimized cost through optimized tolerance distribution in optical assemblies, *Proc. SPIE*, 389, 12, 1982.

Willey, R.R. and Parks, R.E., Optical fundamentals, in *Handbook of Optomechanical Engineering*, Ahmad, A., Ed., CRC Press, Boca Raton, FL, 1997, chap. 1.

Yoder, P.R., Jr., Lens mounting techniques, *Proc. SPIE*, 389, 2, 1983.

Yoder, P.R., Jr., Optomechanical designs of two special-purpose objective lens assemblies, *Proc. SPIE*, 656, 225, 1986.

Yoder, P.R., Jr., Axial stresses with toroidal lens-to-mount interfaces, *Proc. SPIE*, 1533, 2, 1991.

Yoder, P.R., Jr., *Mounting Optics in Optical Instruments*, SPIE Press, Bellingham, 2002.

Zaltz, A. and Christo, D., Methods for the control of centering error in the fabrication and assembly of optical elements, *Proc. SPIE*, 330, 39, 1982.

5 Mounting Multiple Lenses

5.1 INTRODUCTION

In this chapter, we consider examples of various ways in which two or more lenses or image-forming mirrors may be mounted together to form opto-mechanical subassemblies or assemblies. The treatment is by no means all-inclusive. The examples were chosen to illustrate multiple uses of the design features described in Chapter 4 as techniques for mounting individual elements and components. Included are discussions of means for establishing the proper spacing between elements, of lens assemblies with and without moving parts, of the *lathe assembly* technique, of typical refracting and reflecting microscope objectives, of assemblies involving plastic optical and mechanical parts, of techniques for coupling elements with liquids instead of cement, of a variety of catadioptric optical instrument configurations, and of some proven techniques for aligning lenses in assemblies.

5.2 MULTIELEMENT SPACING CONSIDERATIONS

In multielement lens assembly designs, elements frequently rest against shoulders or spacers whose axial lengths are carefully machined to obtain the required axial air spaces between surface vertices. A typical example is illustrated in Figure 5.1. The parameters indicated are those needed to find the length $L_{j,k}$ of the shoulder between the contact points P_j and P_k at heights y_j and y_k on the spherical surfaces with absolute radii $|R_j|$ and $|R_k|$ to produce the separation $t_{j,k}$ between the adjacent vertices. The sagittal depths of the surfaces measured from planes through P_j and P_k are S_j and S_k, respectively. They are assigned positive signs if contact occurs to the right of the vertex and negative signs if contact occurs to the left of the vertex. In the figure, S_j is negative while S_k, $t_{j,k}$, and $L_{j,k}$ are positive. The surface depths and the shoulder length are calculated by the following equations:

$$S_j = R_j^2 - (R_j^2 - y_j^2)^{1\backslash 2} \tag{5.1}$$

$$S_k = R_k^2 - (R_k^2 - y_k^2)^{1\backslash 2} \tag{5.2}$$

$$L_{j,k} = t_{j,k} - S_j + S_k \tag{5.3}$$

In many assemblies, the lenses are inserted into the cell or lens barrel in sequence with spacer rings to separate them by proper air spaces. A single retainer then holds all these parts in place. The axial lengths of the spacer rings may be calculated as described above for machined shoulders. Figure 5.2 shows an exploded view of a lens assembly comprising a cell, three lens components, two spacers, and a threaded retaining ring. The spacers are thin annular rings with rectangular cross sections. The surface contact interfaces between the ends of the spacers and the lens surfaces are shaped as appropriate for the nature of the lens surface, i.e., tangential (conical) metal surfaces for convex lens surfaces, toroidal (donut) metal surfaces for concave lens surfaces, and precision flat metal surfaces for flat or step bevels. Each of these interface types is discussed in Section 4.7.5. The setscrews indicated in the figure are used to clamp the retaining ring in place after it is tightened. As shown, they press against the thread on the ring. This use of setscrews is not advisable in that the force exerted by the screws will distort the threads, making that ring hard to remove for servicing the assembly. The use of a

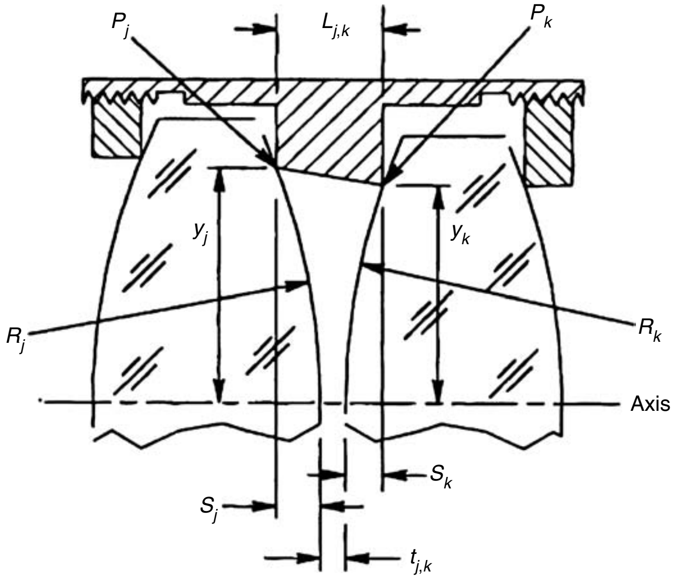

FIGURE 5.1 Parameters of importance when computing shoulder or spacer length to provide a given axial air space between two lenses.

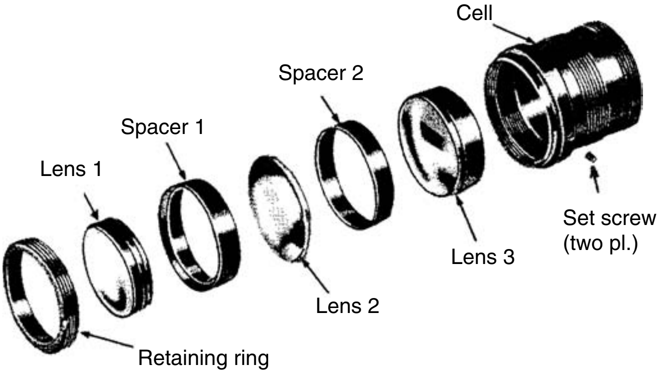

FIGURE 5.2 Exploded view of a lens subassembly with three elements and two spacers held in place with a threaded retainer.

thread-locking compound is preferable because it does not affect the shapes of the threads. In extreme vibration environments, a second retaining ring might be added to lock the first ring in place.

Westort (1984) described one technique used for machining precision lens spacers. His example involved parts for use in high-performance (i.e., $< 0.1\lambda$ maximum wavefront error in single-pass transmission at $\lambda = 0.63$ μm), 100 mm (3.94 in.) aperture, *f*/12 triplet relay lens assemblies used in submarine periscopes. This technique ensures the spacer's correct inside and outside diameters (ID and OD), roundness, parallelism of faces, and squareness of those faces to the axis. Figure 5.3 shows a spacer used in this assembly. Figure 5.4(a) shows the lens cell while Figure 5.4(b) shows the complete assembly. The spacer of Figure 5.3 is located between the first and second lenses in the assembly.

Since the above-listed attributes are desirable in spacers used in a variety of lens assemblies, Westort's procedure is summarized here. Figure 5.5 illustrates the major steps in the process. The material used is 400 series CRES. The spacer is first rough-machined to near-finish dimensions

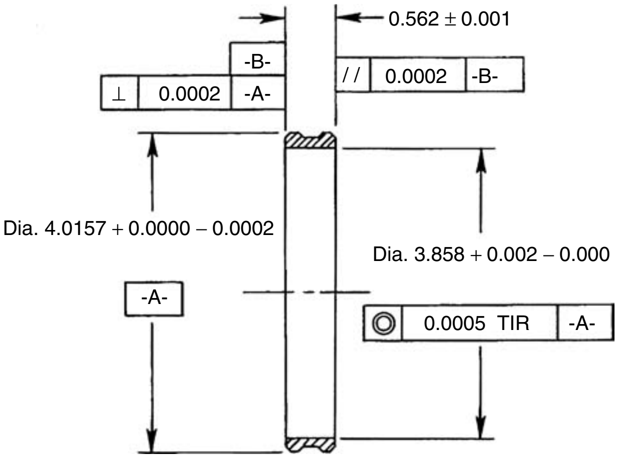
0.562 ± 0.001
-B-
⊥ 0.0002 -A-
// 0.0002 -B-
Dia. 4.0157 + 0.0000 – 0.0002
Dia. 3.858 + 0.002 – 0.000
-A-
◎ 0.0005 TIR -A-

FIGURE 5.3 A typical precision lens spacer. Dimensions are in inches. (From Westort, K., *Proc. SPIE*, 518, 40, 1984. With permission.

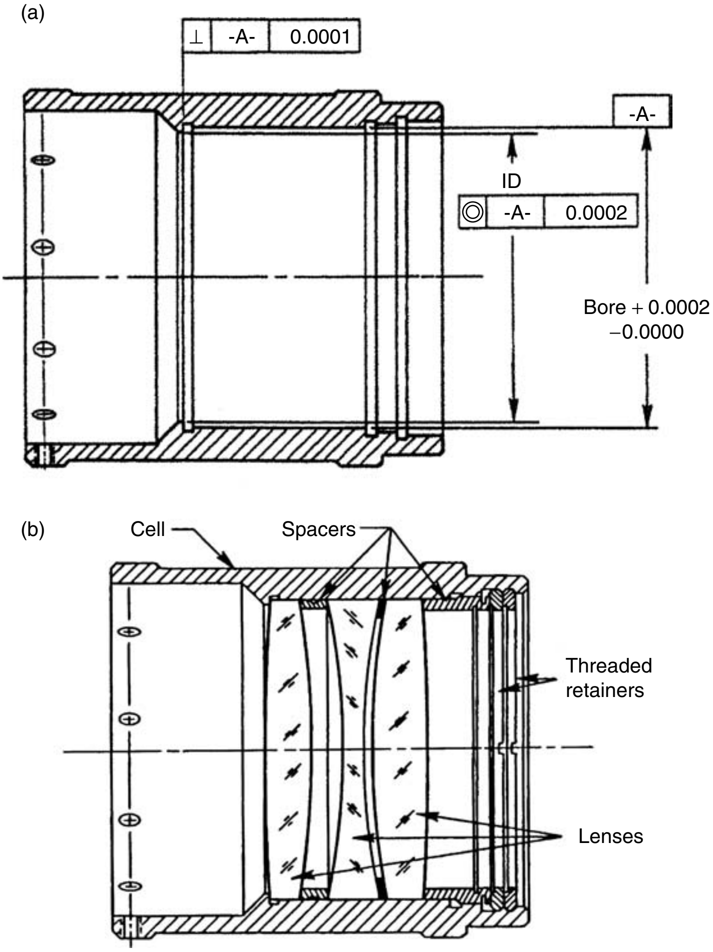
(a)
⊥ -A- 0.0001
-A-
ID
◎ -A- 0.0002
Bore + 0.0002
−0.0000
(b)
Cell
Spacers
Threaded
retainers
Lenses

FIGURE 5.4 (a) Cell designed to accept the spacer of Figure 5.3. (b) High-performance submarine periscope relay lens assembly. (From Westort, K., *Proc. SPIE*, 518, 40, 1984. With permission.)

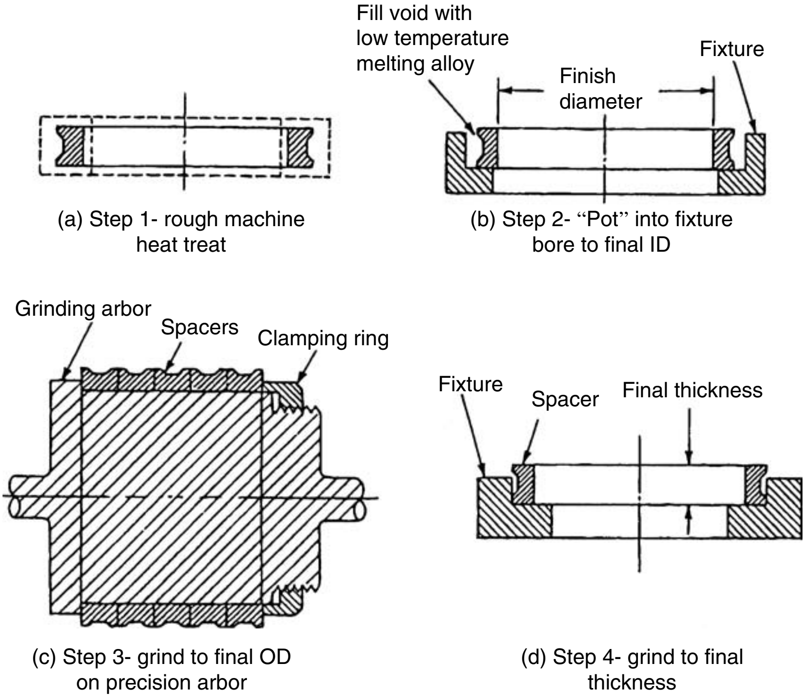
Fill void with
low temperature
melting alloy
Finish
diameter
Fixture
(a) Step 1- rough machine
heat treat
(b) Step 2- "Pot" into fixture
bore to final ID
Grinding arbor
Spacers
Clamping ring
Fixture
Spacer
Final thickness
(c) Step 3- grind to final OD
on precision arbor
(d) Step 4- grind to final
thickness

FIGURE 5.5 Sequence of major steps in one technique for machining precision lens spacers. (Adapted from Westort, K., *Proc. SPIE*, 518, 40, 1984.)

(view [a]) and heat-treated. It is then "potted" into a fixture with a low-melting-temperature alloy (view [b]), which ensures that the part is held in a stress-free condition as it is bored to its final ID. The alloy is then melted to release the part. A series of these spacers are slipped over a precision arbor, clamped axially, and ground to final OD (view [c]). Each spacer is then transferred to another fixture (view [d]) whose ID closely matches the OD of the spacer. The top surface is ground flat; then the spacer is turned over and the bottom side ground flat, parallel to the top, and to finished thickness. Finally, it is given a black finish. Spacers with conical surfaces intended for tangential contact on lens surfaces can be manufactured by an adaptation of this basic process. It should be noted that this method could also be used to advantage in the fabrication of retaining rings since they are typically quite thin and need to be round. Threads would be cut in step 3.

Another spacer is shown between the second and third lenses in the relay assembly of Figure 5.5. This is a very thin annular ring of stainless-steel sheet. It is thin enough that the metal deforms to match the spherical shape of the adjacent lens surfaces when preloaded with the retainer. The third spacer of Figure 5.5 serves two purposes. It acts as a slip ring so rotation of the retaining ring does not drag the lens with it and disturb the rotational alignment around the axis of the last lens. In precision assemblies, lenses are frequently manually rotated ("clocked" or "phased") during installation so that their residual optical wedges tend to cancel each other out and produce the best possible image. This spacer is also long enough to bring the retainer to a conveniently accessible location. Note that two retaining rings are used. The second locks the first to help prevent loosening under vibration. In addition, the threads of both rings are treated with locking compound.

Figure 5.6 shows a portion of an engineering drawing for a spacer used in a space application.

The die-cut plastic spacer shown in Figure 5.7(a) has three tabs that are inserted between two lenses that need a small axial air space in the manner just described with regard to the middle spacer of Figure 5.4. Addis (1983) described such spacers, made of polyester film, as a viable and inexpensive means for separating air-spaced doublets. The outer ring supports the tabs and lies outside

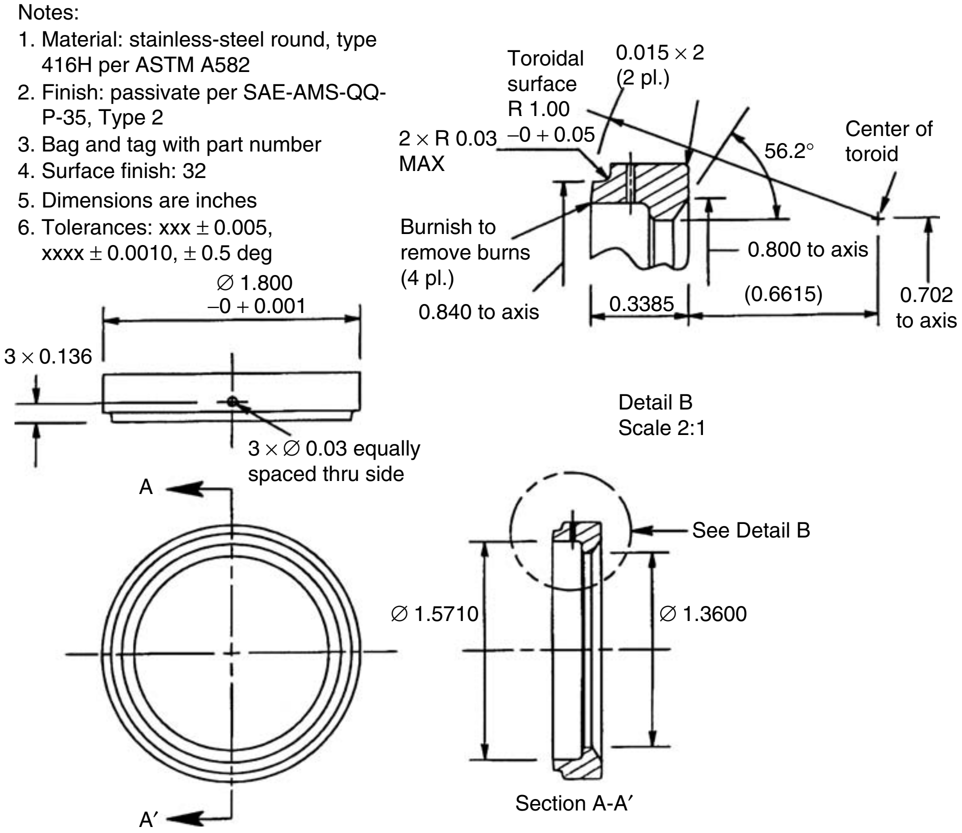
Notes:
1. Material: stainless-steel round, type 416H per ASTM A582
2. Finish: passivate per SAE-AMS-QQ-P-35, Type 2
3. Bag and tag with part number
4. Surface finish: 32
5. Dimensions are inches
6. Tolerances: xxx ± 0.005, xxxx ± 0.0010, ± 0.5 deg
∅ 1.800 −0 + 0.001
3 × 0.136
3 × ∅ 0.03 equally spaced thru side
A
A′
Toroidal surface R 1.00 −0 + 0.05
0.015 × 2 (2 pl.)
2 × R 0.03 MAX
56.2°
Center of toroid
Burnish to remove burns (4 pl.)
0.840 to axis
0.3385
0.800 to axis
(0.6615)
0.702 to axis
Detail B Scale 2:1
See Detail B
∅ 1.5710
∅ 1.3600
Section A-A′

FIGURE 5.6 Representation of a typical spacer as shown in an engineering drawing. The left end of this part has a toroidal surface for contacting a concave lens while the right end has a conical surface for contacting a convex lens surface.

the lens ODs. The tabs protrude between the lens surfaces to the clear apertures of the elements. An advantage pointed out by Addis is that gases can easily flow into the space between the lens surfaces when the assembly is purged to remove moisture. A continuous shim would not allow this to happen unless grooves were cut into the spacer or the lens rims.

Figure 5.7(b) shows a typical molded plastic spacer with grooves (vents) for air circulation. Contact with the lens occurs most of the way around the assembly to distribute preload. Molded spacers are advantageous from the cost viewpoint in quantity production; they can be made accurately enough for applications in which extreme accuracy is not required. If the spacers are made of black plastic and textured internally, as indicated schematically in the figure, stray light can be attenuated.

The need for a spacer to set the axial spacing between two lenses can, in certain designs, be eliminated by contacting the adjacent glass surfaces. Figure 5.8 shows an example. From the lens designer's viewpoint, this is a simple and space-saving way to control the usually critical small air spaces between strongly curved surfaces of the same algebraic sign. The design must be such that the two surfaces intersect at a reasonable diameter. The concave surface is beveled to the contact diameter and the tight tolerance on axial spacing is converted into the equivalent tolerance on the bevel ID. This diameter is easier to measure accurately than the spacing.

The self-aligning action of sharply curved convex and concave surfaces in contact under axial preload is, in some cases, an attractive feature of the edge-contacted configuration. In a typical mounting, the glass-to-metal and glass-to-glass interfaces are all on optically active, spherical

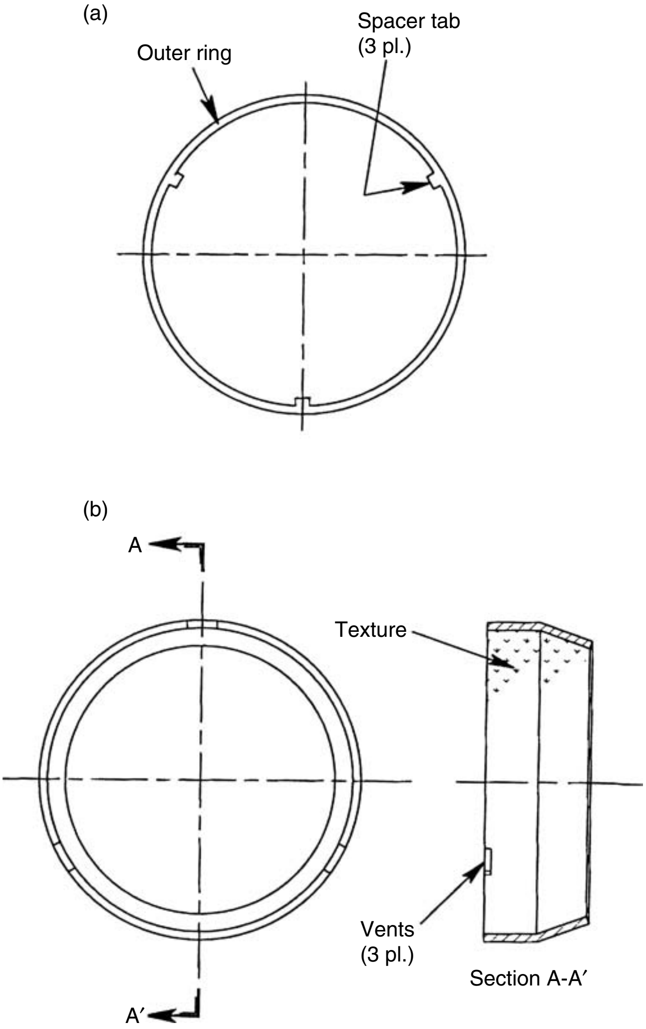

FIGURE 5.7 (a) A thin plastic spacer with tabs to separate the lens surfaces. (b) A molded plastic spacer with ventilation grooves. (Adapted from Addis, E. C., *Proc. SPIE,* 389, 36, 1983.)

surfaces. The success of such a design depends on many factors. Price (1980) listed the following as considerations before edge contacts are adopted (Polster, 1964):

- the relative radii of the two adjacent surfaces
- the ability to establish the contact at a reasonable diameter
- the brittleness and hardness of the glasses (especially of flint elements that are prone to chip)
- the surface radius-to-diameter ratio of the contact diameter
- the sensitivity of the design to air-space variations and lens tilts
- the sizes of the optics and their resulting masses

In some optical instruments, cylindrical lenses are employed to provide anamorphic magnification. The lenses may be rectangular instead of circular. Rotational alignment (clocking) of the cylindrical surfaces about the axis is usually critical in these applications. Since conventional annular spacers are not usable in such designs, we outline here a straightforward technique that has been

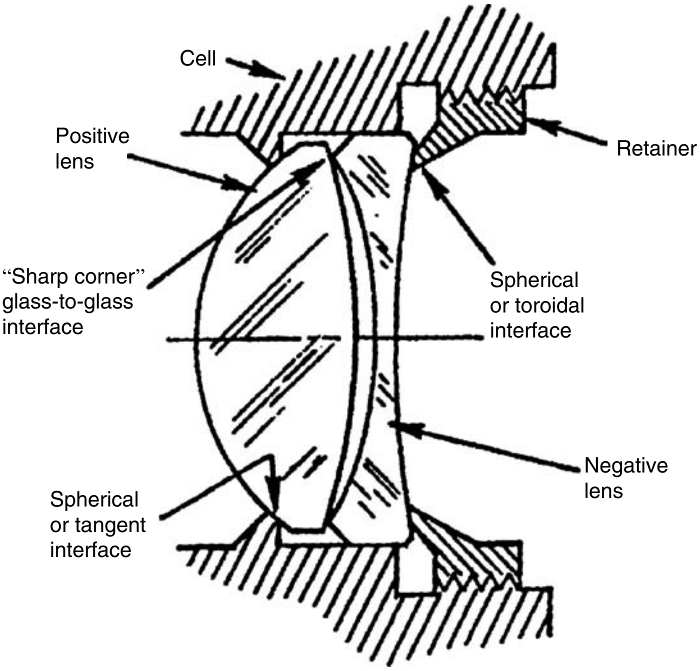
Cell
Positive lens
"Sharp corner" glass-to-glass interface
Spherical or tangent interface
Retainer
Spherical or toroidal interface
Negative lens

FIGURE 5.8 Mounting lenses with edge-contacted adjacent surfaces. (Adapted from Price, W. H., *Proc. SPIE*, 237, 466, 1980.)

found useful for ensuring that the correct axial separation and relative alignment of adjacent convex cylinders is achieved (Polster, 1964).

Figure 5.9(a) illustrates the concept while Figure 5.9(b) shows pertinent dimensions. Here, the lenses are installed into a cell with a rectangular aperture. The smaller dimension of the aperture is D_M. Two rods of the same radius r are inserted between the lenses near the edges of their apertures. These rods contact the inside surface of the cell and the cylindrical surfaces of absolute radii R_1 and R_2. The axial separation of the cylinder centers of curvature is A. The following equation defines the unique rod radius that gives the desired axial separation t_A:

$$r = \frac{R_1 + R_2}{2}(K_{\mathrm{CYL}}^2 - 1) + \frac{D_M K_{\mathrm{CYL}}^2}{2} - \frac{A}{R_2 - R_1}\left[\left(\frac{D_M}{2} + R_1\right)\left(\frac{D_M}{2} + R_2\right)(K_{\mathrm{CYL}}^2 - 1)\right]^{1\backslash 2} \tag{5.4}$$

where $K_{\mathrm{CYL}} = A/(R_2 - R_1)$. Note that preload is required to hold the lenses and spacers in place.

If the cylindrical surfaces have the same radii, then r is determined from the following equation:

$$r = \frac{D_M}{4} - \frac{R_1}{2} + \frac{\mathrm{A}^2}{4(\mathrm{D}_M + 2R_1)} \tag{5.5}$$

5.3 EXAMPLES OF LENS ASSEMBLIES WITH NO MOVING PARTS

5.3.1 MILITARY TELESCOPE EYEPIECE

Figure 5.10 shows a fixed-focus eyepiece subassembly for a military telescope. Here, two identical achromatic doublets back-to-back form a symmetrical eyepiece of the Ploessl type (Rosin, 1965).

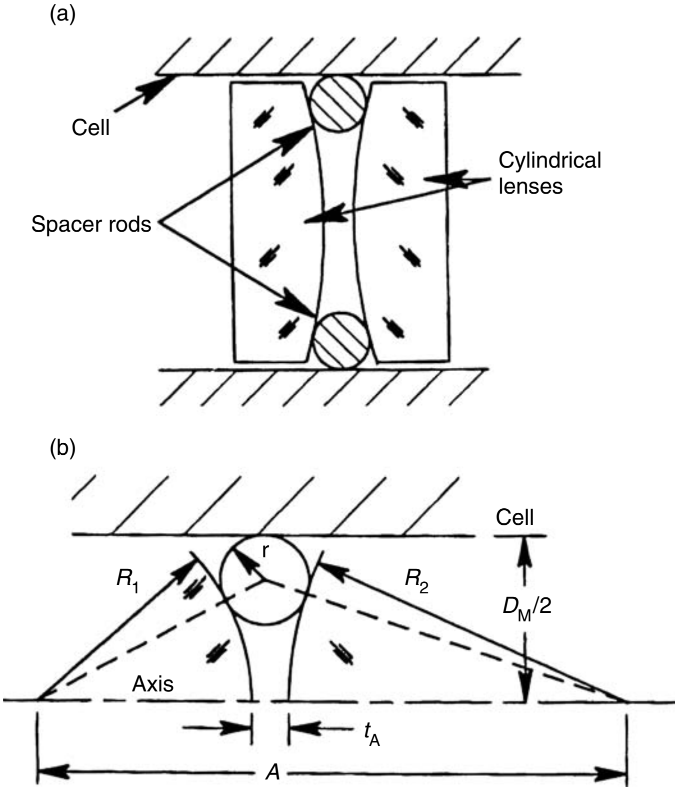
(a)
Cell
Spacer rods
Cylindrical lenses
(b)
Cell
r
R_1
R_2
$D_M/2$
Axis
t_A
A

FIGURE 5.9 Spacing cylindrical lenses in a cylindrical-aperture cell with parallel spacer rods. (Adapted from Polster, H. D., *Perkin-Elmer Internal Technical Memorandum HDP-105*, 1964.)

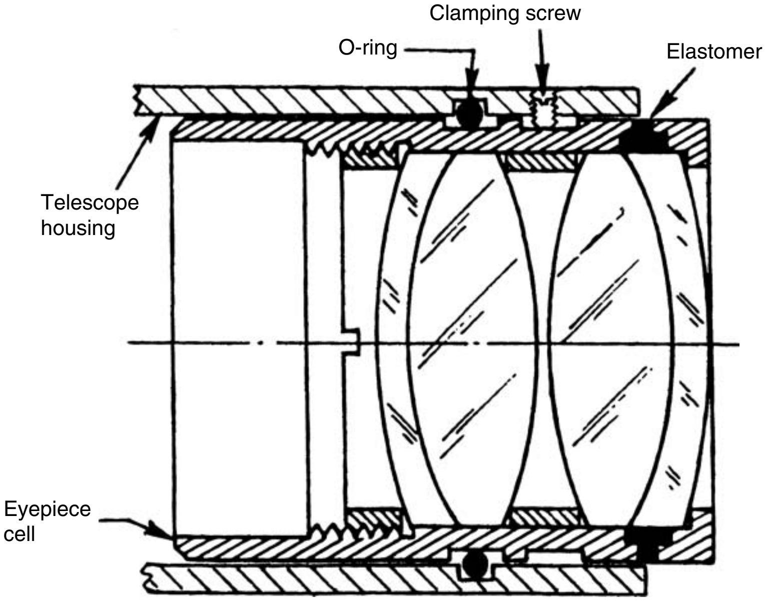
Clamping screw
O-ring
Elastomer
Telescope housing
Eyepiece cell

FIGURE 5.10 Example of a fixed-focus eyepiece subassembly for a military telescope. The interface with the telescope housing is shown. (From Yoder, P. R., Jr., *Proc. SPIE*, 389, 2, 1983.)

Both lenses and the spacer fit into an internal bore in an aluminum cell with typically 0.003 in. (0.075 mm) diametric clearance. These lenses are generally edged after cementing so that both elements have the same OD. The first inserted lens registers against the cell's shoulder shown at the right in the figure. The interface with the spacer is of the sharp-corner configuration, as is that at the threaded retainer, which holds both lenses in place. Because of the rather strong curvatures of the spherical surfaces, the lenses will tend to center themselves as they are squeezed together.

The right-hand lens is sealed against the environment by injecting sealing compound into three or more radially directed holes through the cell wall. These holes penetrate into an annular groove around the inside of the cell adjacent to the rim of the lens. Injection continues until sealant emerges from all holes and a continuous seal can be observed through the ground rim of the lens. After curing, this seal is usually quite effective in all the common military environments.

The two rectangular grooves on the outside of the cell are worth mentioning. This subassembly is designed to be inserted into a cylindrical hole in a telescope housing. Two setscrews project through the housing to the bottom of the right-hand groove and clamp the eyepiece after it has been focused. It is important to note that the setscrews do not bear against the OD of the eyepiece. Disruption of the groove surface by the setscrew ends will not prevent the eyepiece from being moved on the bearing interface with the housing ID. An O-ring located in the left-hand groove seals the eyepiece subassembly to the housing. Note that the O-ring is inside the clamping feature to avoid leakage at the screw holes.

5.3.2 MILITARY TELESCOPE OBJECTIVE

Figure 5.11 shows the opto-mechanical configuration of an air-spaced objective for a relatively high-performance military telescope intended to withstand a severe shock and vibration environment. The three singlets are edged to the same OD and fit into a type 316 stainless-steel cell with nominally 0.005-mm (0.0002-in.) radial clearance. All lenses are inserted from the right side. The first is Schott SF4 glass; it has a plano entrance face that registers against a flat shoulder on the cell. The first spacer is 0.066 ± 0.005 mm (0.0026 ± 0.0002 in.) thick and is made of stainless-steel sheet. The second lens is Schott SK16 glass and the third Schott SSK4 glass. The second spacer is made of the same steel as the cell and is shaped for tangential contact on the adjacent convex surfaces. The retainer is also made of the same steel as the cell and is machined square to interface with a precision annular flat on the third lens. The threads on the retainer have a Class 2 fit into the cell threads as recommended in Chapter 4. All metal parts are black-passivated.

The wedge tolerances on the lenses and spacers are 10 arcsec, whereas the maximum edge thickness variation from the annular flat to the first surface on the third element is toleranced at 10 μm (0.0004 in.). During assembly, the lens elements are phased by rotation about their axis for maximum symmetry of the on-axis aerial image.

5.3.3 FIXED-FOCUS RELAY LENS

A traditional technique for mounting several singlet elements and cemented components in series in an aluminum housing (or lens barrel) for use as a relay lens is illustrated in Figure 5.12. This is a fixed-aperture lens of the double-Gauss type comprising two cemented doublets and two singlets surrounding an aperture stop. The dashed lines indicate the apertures of the lenses to be used by the transmitted rays. The two front lenses are mounted directly into the aluminum lens barrel and held by threaded retaining rings. The two rear lenses are similarly mounted into a separate aluminum cell that screws into a mating thread on the barrel.

Each retaining ring is designed for sharp-corner line contact on the lens's spherical surface approximately 0.01–0.02 in. (0.25–0.50 mm) outside the specified clear aperture of the element. Toleranced dimensions X and Y on the barrel and Z on the cell control the central air space between surfaces 5 and 6, so their worst-case total error equals the allowable tolerance on the air space.

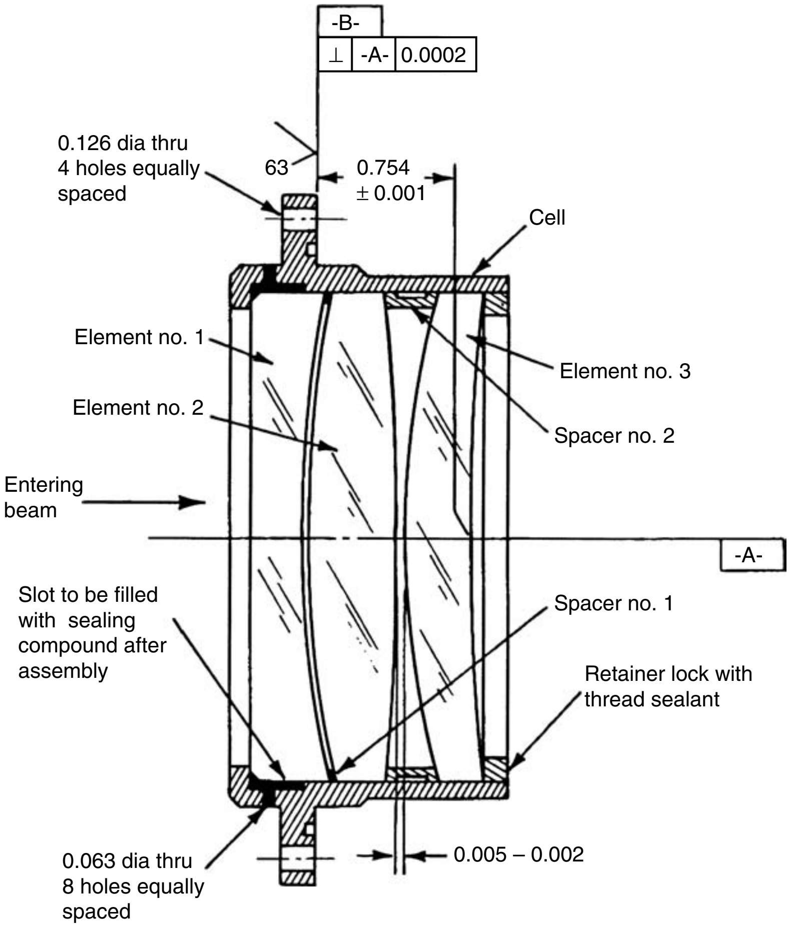
-B-
⊥ -A- 0.0002
0.126 dia thru
4 holes equally
spaced
63
0.754
± 0.001
Cell
Element no. 1
Element no. 3
Element no. 2
Spacer no. 2
Entering
beam
-A-
Slot to be filled
with sealing
compound after
assembly
Spacer no. 1
Retainer lock with
thread sealant
0.063 dia thru
8 holes equally
spaced
0.005 – 0.002

FIGURE 5.11 Example of a high-performance military telescope objective subassembly. Dimensions are in inches. (From Yoder, P. R., Jr., *Proc. SPIE*, 389, 2, 1983.)

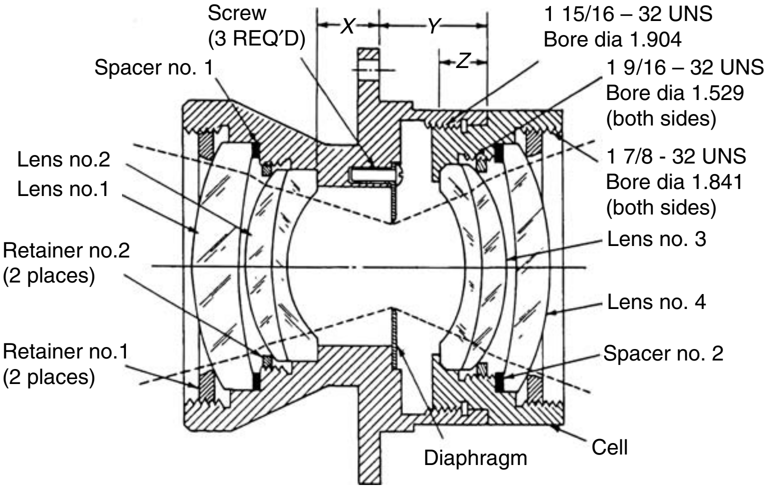
Screw
(3 REQ'D)
X
Y
Z
1 15/16 – 32 UNS
Bore dia 1.904
Spacer no. 1
1 9/16 – 32 UNS
Bore dia 1.529
(both sides)
Lens no.2
Lens no.1
1 7/8 - 32 UNS
Bore dia 1.841
(both sides)
Lens no. 3
Retainer no.2
(2 places)
Lens no. 4
Retainer no.1
(2 places)
Spacer no. 2
Diaphragm
Cell

FIGURE 5.12 Configuration of a fixed-focus relay lens subassembly. Dimensions are in inches.

Alternatively, this air space could be adjusted at assembly by machining the right end of the barrel to a computed value of *Y* that accounts for the measured actual values of *X* and *Z*. The latter approach adds an extra machining operation but allows three dimensions to be toleranced more loosely. Grinding the spacers located between the singlets and their seats to suit actual dimensions measured at assembly easily controls the small air spaces between the singlets and doublets. In production, a stock of spacers of slightly differing thicknesses could be provided and the appropriate spacers chosen for use in each individual assembly.

It should be noted that the ODs of the doublets are the same as the ODs of the singlets. The corresponding retaining rings can then be identical. These retaining rings would not be interchangeable if they were designed for tangential contact since the lens surfaces have different radii of curvature.

There are no moveable parts in this lens as it is intended to be focused by moving the entire assembly axially by external means and has a fixed ID aperture stop instead of an iris.

5.3.4 AERIAL PHOTOGRAPHIC OBJECTIVE LENS

Figure 5.13 shows an aerial photographic lens design. This is a 66 in. (1.67 m) focal length, *f*/8 assembly in which the six lenses are constrained by elastomeric seals as well as retaining rings (Bayar, 1981). In this design, sufficient clearances are provided between the OD of each element and the ID of the lens barrel so that the element can be adjusted radially on its seat until it is centered with respect to a reference piloting shoulder on the lens barrel. To do this, the lens barrel is mounted on a rotary table and adjusted laterally until the piloting shoulder is concentric with and perpendicular to the axis of rotation of the rotary table. To check the centering of the elements, either optical or mechanical measuring techniques (or both) may be employed; ways to do this were discussed in Chapter 4. After each element is centered within the required tolerances, the element is carefully constrained axially and laterally by means of a retaining ring. The gap between the element OD and the barrel ID is then filled with a room-temperature vulcanizing (RTV) compound, thereby encapsulating the edge of the element. Equation (4.25) or (4.26) is used to compute the required radial thickness of the resilient layer to make the assembly radially athermal. This determines the clearance required between lens OD and barrel ID.

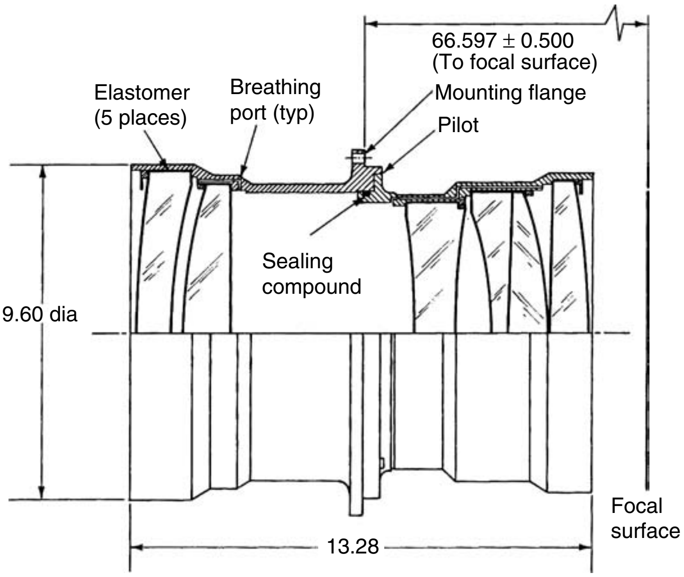

FIGURE 5.13 Aerial photographic objective assembly with lenses constrained elastomerically as well as with retaining rings. Dimensions are in inches. (Adapted from Bayar, M., *Opt. Eng.*, 20, 181, 1981.)

An important feature of this design is the presence of small passages or ports within the barrel walls to interconnect the air spaces, so they can be purged to remove moisture and then pressurized with dry nitrogen. These breathing ports can be seen at the top of lenses 2, 3, 4, and 5 in Figure 5.13. At least one valve (not shown) would be needed on the barrel to admit and vent the gas. Typically, this valve would resemble that used on an automobile tire. It could be located conveniently in the housing wall at the largest air space.

Important advantages of the elastomeric mounting technique are that the lenses can be accurately aligned and clamped in place during assembly, sealing against the environment is provided, and the tolerances on lens edging and the metal IDs are relatively loose. The disadvantages are that the sealing compound must be carefully selected to eliminate outgassing (especially if used in a space application), and disassembly for maintenance is more difficult.

5.3.5 LOW-DISTORTION PROJECTION LENS

A lens assembly with demanding optical performance requirements was described by Fischer (1991). This is a telecentric projection lens designed to provide near-diffraction-limited modulation transfer function (MTF) and distortion of less than 0.05% over its field of view. Figure 5.14 shows the opto-mechanical design schematically. The lens was intended to be used at finite conjugates in the visible spectral range with a lateral magnification of 4.23 times. The high level of distortion correction was achieved by including a single-point, diamond-turned, aspheric surface on the thin Cleartran™ zinc sulfide plate (lens 1 in the figure) located in front of the first doublet.

The mounting of the lens elements so as to achieve the required alignment and preserve that alignment over an operational temperature range of 0 to 60°C (32 to 140°F) posed a major design problem. Tolerances for some elements were as small as ± 0.0005 in. (±12.7 μm) decentration, 0.0001 in. (0.25 μm) edge thickness runout due to wedge angle, and 0.0003 in. (0.75 μm) surface edge runout due to tilt. The mechanical solution, attributed to Daniel Vukobratovich, was to center each element or group of elements in stainless steel cells while rotating the cells on a rotary table, and to inject a 0.015 in. (0.381 mm) thick annular ring of 3M 2216 epoxy to bond the lenses to their cells. After curing, the individual cell-lens subassemblies (sometimes called "pokerchips") were

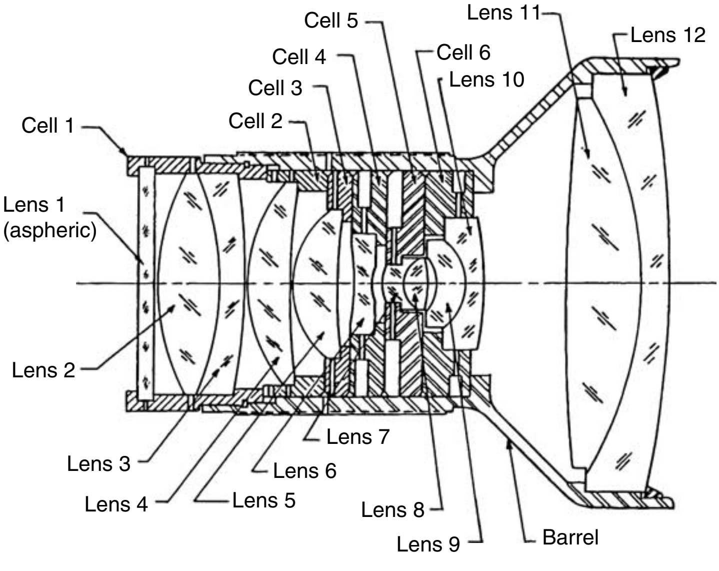

FIGURE 5.14 Opto-mechanical layout of a low-distortion, telecentric projection lens assembly with the lenses elastomerically supported in individual cells. (Adapted from Fischer, R. E., *Proc. SPIE,* 1533, 27, 1991.)

inserted into a CRES housing and held securely by retaining rings. Performance evaluation tests revealed that this lens assembly achieved the MTF and distortion requirements.

5.3.6 MOTION PICTURE PROJECTION LENS

Figure 5.15 is a sectional view through a 90-mm (3.54-in.) focal length, *f*/2 objective assembly designed for wide-screen motion picture projection. Only single-element lenses are used here, because the assembly is subjected to very high temperatures from the nearby high-intensity xenon lamp during operation and cemented components might be damaged. Large physical apertures are used in the lenses so that geometric vignetting is minimized and relative illumination remains high at the corners of the format. The MTF at 50 lp/mm is specified as over 70% on-axis, with the average radial and tangential MTF falling only to about 30% at the extreme corners of the image. The field curvature of the design is compatible with the natural cylindrical curvature of the film as it passes through the film gate, and helps to maintain image sharpness at the horizontal edges of that image. For the intended application of this lens, an iris is not needed; the lens operates at a fixed relative aperture.

As may be seen from the figure, mechanical construction of the assembly is conventional. All metal parts are anodized aluminum alloy. The barrel is made in two parts joined at the center by a piloted and threaded interface. Starting at the larger diameter end, a flat bevel on the concave surface of the first lens is seated against a shoulder in the larger barrel and held by a threaded retainer. The second and third lenses are inserted from the right side of this barrel and clamped together without a spacer and against a shoulder in the barrel by a second threaded retainer. In this case, the retainer bears against a flat bevel formed at the base of a deep step ground into the lens rim. The concave surface of the second lens contacts the convex surface of the third lens. The fourth and fifth lenses are held against a shoulder in series with an intermediate spacer of conventional design by a third retainer that fits into another deep step on the rim of the fourth lens. The sixth (outermost) lens in the smaller end of the assembly is held against a shoulder by a fourth threaded retainer. The assembly is not sealed.

5.3.7 COLLIMATOR DESIGNED FOR HIGH-SHOCK LOADING

Figure 5.16 is a sectional view of a collimating lens assembly designed as part of a military flight motion simulator. This assembly was developed by Janos Technology, Inc., Keene, NH to project an infrared target into a forward-looking infrared system during vibration testing of that device. The collimator has two air-spaced lens groups: the front group is a doublet with a diameter of approximately 9 in. (23 cm), while the rear group is a triplet with an average diameter of about 1.5 in. (3.8 cm). The lenses are made from silicon and germanium, so the optical system can operate in the 3 to 5 μm spectral band. Overall, the assembly is 24.179 in. (61.41 cm) long

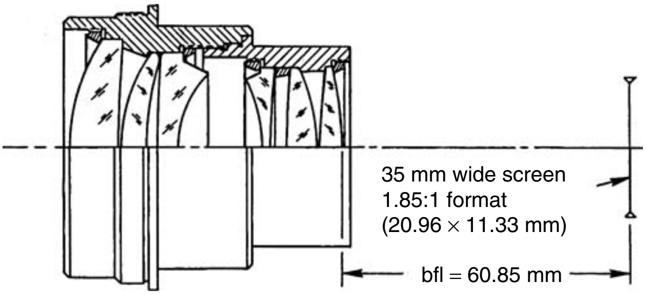

FIGURE 5.15 A 90-mm focal length, *f*/2 lens assembly for wide-screen motion picture projection. (Courtesy of Schneider Optics, Inc., Hauppauge, NY.)

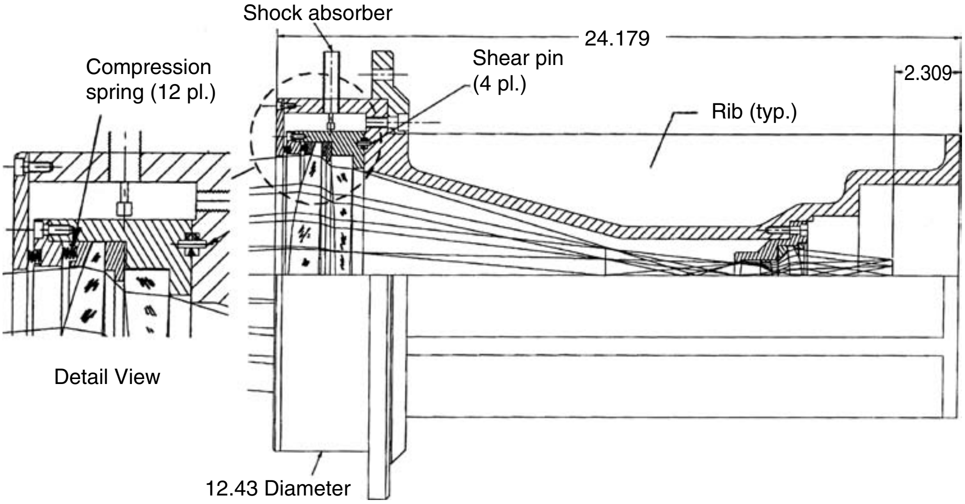

FIGURE 5.16 Sectional view of a collimating lens assembly designed to withstand high shock loading. Dimensions are in inches. (Courtesy of Janos Technology, Inc., Keene, NH.)

and 12.43 in. (31.57 cm) in diameter at the largest end (neglecting the larger mounting flange). It weighs approximately 80 lb (356 kg).

Palmer and Murray (2001) indicated that because of the high cost of the larger lenses, the end user of the assembly specified that those optics should survive, without damage, a failure on the part of the simulator system that caused severe impact. Rather than designing the entire assembly to withstand the shock, it was designed so that the mechanical supports for those costly lenses would fail at a load of $a_G = 30$, and that those components would be constrained in a safe manner so that they could be salvaged and reused.

The designers determined that the severe impact would occur only in a direction transverse to the axis of the assembly. To make the assembly mechanically stiff under bending forces, the main housing was made of 6061-T6 aluminum and configured with a unique cross section over most of its length. This construction may be seen in Figure 5.17, a photograph showing the exterior of the assembly. The lens groups occupy the cylindrical portions of the housing while the structure between the cylinders is that of a “paddle wheel” with six ribs of full external diameter supporting conformal wall portions that enclose the internal light beam emerging from the smaller lenses and expanding to fill the apertures of the larger lenses. These ribs enhance assembly stiffness while minimizing weight. Grooves machined into the internal surfaces of the walls reduce stray light reflections that could degrade image contrast.

The cell for the larger lenses was designed with a retaining flange that presses multiple, axially oriented compression springs against an annular pressure ring contacting the first lens. The preload so introduced presses a spacer against the second lens, which, in turn, registers against a shoulder. The cell is constrained radially in the housing by three axially oriented aluminum shear pins that engage-stainless steel inserts pressed into the lens cell and the housing. Without these pins, the cell would be able to slide laterally within clearances provided all around the rim of the cell. At assembly, the pins locate the cell and its lenses radially. The cell is pressed firmly against a shoulder in the housing by additional axially oriented compression springs that bear against the outermost flange.

The three pins are designed to shear under the prescribed shock load, allowing the cell to move. This cell motion is dampened by shock absorbers oriented radially at four points around the periphery of the assembly. Three of these are shown in the photograph and one is indicated in the section view. The shock absorbers are nonlinear; they become stiffer under higher accelerations.

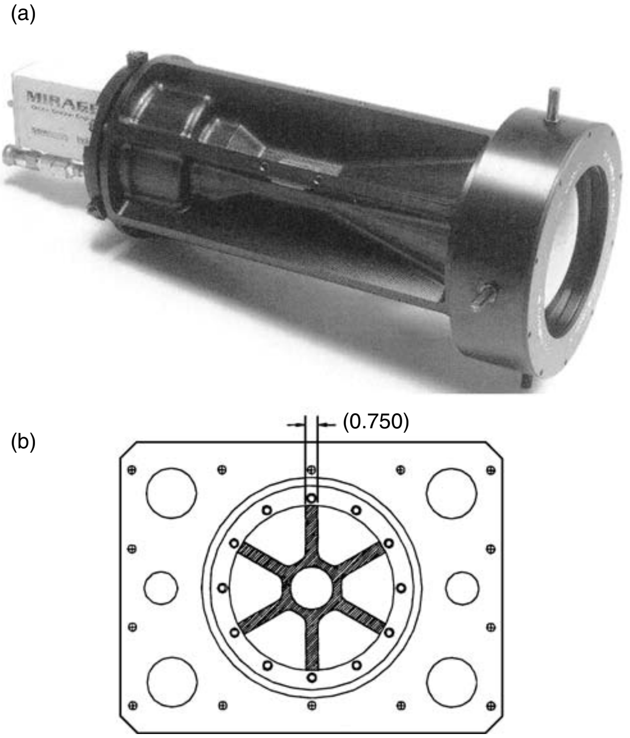

FIGURE 5.17 (a) Photograph of the collimator assembly of Figure 5.16 without the mounting flange. (b) Section view through the midpoint of the assembly. (Courtesy of Janos Technology, Inc., Keene, NH.)

5.3.8 LARGE ASTROGRAPHIC OBJECTIVE

A large high-performance lens assembly that illustrates elastomeric lens mounting was developed at the Optical Sciences Center, University of Arizona for the U.S. Naval Observatory. The optical system of the 81.102 in. (206 cm) focal length, *f*/10, ± 4.8° field-of-view lens, designed by Robert R. Shannon, is shown schematically in Figure 5.18. Its intended application is as an astrographic telescope objective.

Vukobratovich (1992) described the mechanical design and performance of the lens assembly. The housing of the assembly (see Figure 5.19 and Figure 5.20[a]) was machined from a billet of 6Al4V titanium. The technique used to mount the lens elements (diameters typically about 10.4 in. [26.4 cm]) was to bond them individually into 6Al-4V titanium cells (to approximate the CTEs of the glasses) of typically 0.25 in. (6.35 mm) annular thickness with an elastomeric ring approximately 0.20 in. (5.08 mm) thick (see Figure 5.21[a]). The elastomer used was Dow Corning 93-500 material.

The cells were assembled into the titanium housing by pressing them in place with slight interference fits. They were further constrained with two spacers and retaining rings. The photograph in Figure 5.20(b) shows the mechanical components of the lens assembly. The overall weight of the assembly was about 44.6 kg (98.3 lb), 21.9 kg (48.4 lb) of which was in the glass.

Valente and Richard (1994) described an analytical means for computing stresses introduced into the cells, elastomer layers, and lenses by this assembly technique. The closed-form equations given by those authors were verified to be accurate within about 8% by finite-element analysis. Their model is shown in Figure 5.21(b). Once the radial stress in each lens was known, the resulting birefringence was estimated from the stress optic coefficients of the glasses and the optical path lengths in the materials.

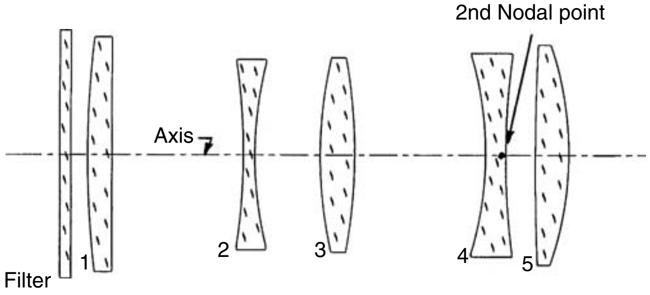
2nd Nodal point
Axis
Filter
1
2
3
4
5

FIGURE 5.18 Optical schematic of a high-performance astrographic telescope objective lens developed for the U.S. Naval Observatory. (From Vukobratovich, D., *Proc. SPIE*, 1752, 254, 1992. With permission.)

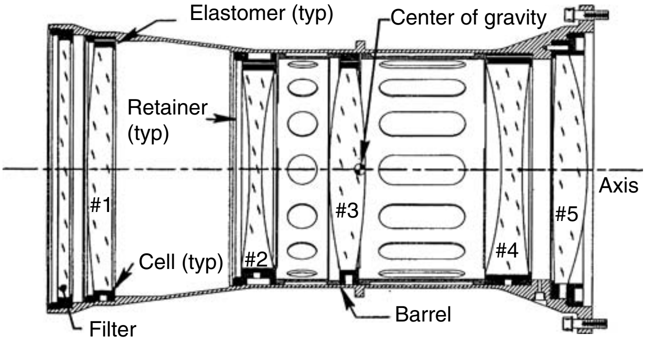
Elastomer (typ)
Center of gravity
Retainer (typ)
Axis
#1
#2
#3
#4
#5
Cell (typ)
Barrel
Filter

FIGURE 5.19 Sectional view of the astrographic telescope objective. The lenses are constrained elastomerically in their cells that are then interference-fit into the barrel. (From Vukobratovich, D., *Proc. SPIE*, 1752, 245, 1992, With permission.)

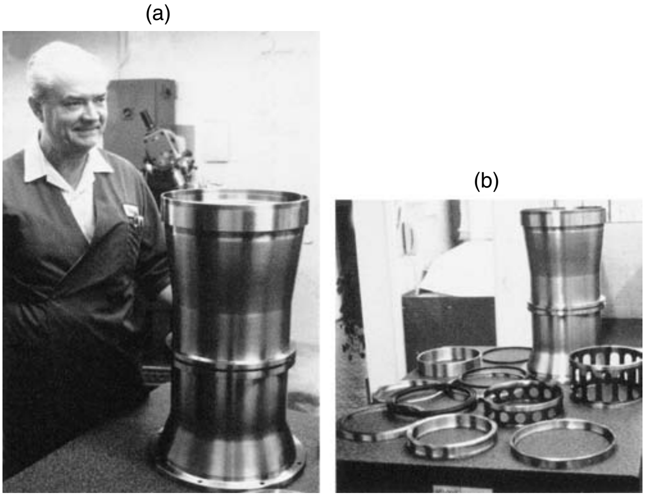

FIGURE 5.20 Components of the astrographic telescope objective. (a) Main titanium barrel, (b) barrel, cells for six lenses (solid rings), and two spacers (slotted rings). (Courtesy of D. Vukobratovich, Optical Sciences Center, University of Arizona.)

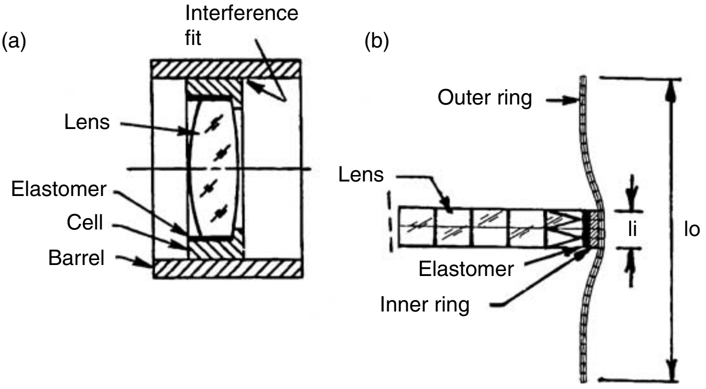

FIGURE 5.21 (a) Design concept for elastomeric lens mounting. (b) FEA model used to confirm radial stress calculations. (Adapted from Valente, T. M. and Richard, R. M., *Opt. Eng*., 33, 1223, 1994.)

These authors also derived an equation for computing the lateral deflections of the lens elements due to self-weight when the axis of the assembly is horizontal. That equation [see Eq. [4.27]] showed that the deflections of the lenses in this assembly would be extremely small (worst case, 0.0002 in. [5.1 μm]) and well within the allowable decentrations (0.001 in. [25.4 μm]) as determined from the lens performance requirements. Valente and Richard reported agreement within 6% between the analytical equation deflection and that determined by finite-element methods.

5.3.9 Infrared Sensor Lens

The opto-mechanical configuration of a 69 mm (2.71 in.) focal length, *f*/0.87 objective assembly designed for use in an infrared radiation sensor is illustrated in Figure 5.22. The singlet lens was silicon, while the first element of the cemented doublet was silicon and the second sapphire. The doublet was cemented with AO-805 adhesive (which is no longer available). Wedge angles of the flat bevels on the concave faces of the lenses were held to 10 arcsec for the singlet and 30 arcsec for the doublet to ensure good centration to the axis.

The cell was made of Invar 36 and was stabilized after rough machining by repeated cycling between 320°F and room temperature. The registering OD (datum -A-) and flange ear mounting interface surfaces (-B-) were closely toleranced for diameter and perpendicularity to the optical axis, respectively, to ensure precise alignment with related components of the sensor system.

The lenses were lathe-assembled with maximum 0.0002 in. clearances into the cell and constrained axially by threaded 303 CRES retainers. Prior to tightening the retainers, the lenses were differentially rotated about the axis to maximize symmetry of the axial image and to minimize decentration of the image relative to the OD (datum -A-).

5.4 EXAMPLES OF LENS ASSEMBLIES CONTAINING MOVING PARTS

5.4.1 Objectives Designed for Mid-IR Applications

The photograph in Figure 5.23 shows four *f*/2.3 lens assemblies produced by Janos Technologies, Inc., Keene, NH for use with standard commercial IR cameras in a variety of applications. They are designed to operate near the diffraction limit in the 3 to 5 μm spectral region and have optical and mechanical characteristics as shown in Table 5.1. Typical construction is indicated by the sectional view through one of the assemblies shown in Figure 5.24. The following description is adapted from information provided by Palmer and Murray (2001).

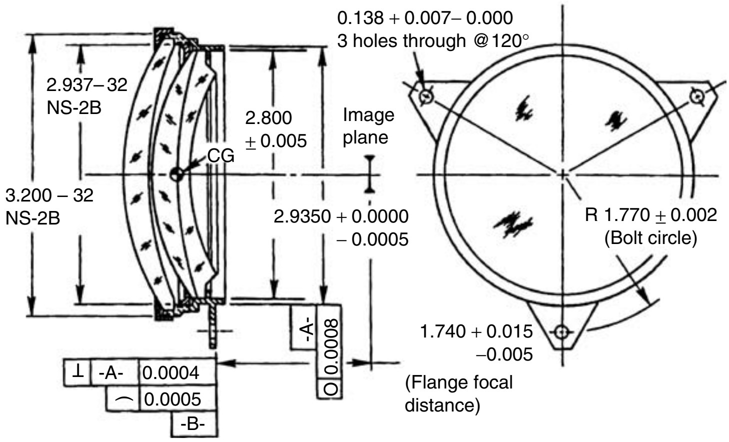
0.138 + 0.007– 0.000
3 holes through @120°
2.937–32
NS-2B
2.800
± 0.005
Image
plane
CG
3.200 – 32
NS-2B
2.9350 + 0.0000
– 0.0005
R 1.770 ± 0.002
(Bolt circle)
-A-
0.0008
1.740 + 0.015
–0.005
⊥ -A- 0.0004
⌒ 0.0005
-B-
(Flange focal
distance)

FIGURE 5.22 Sectional and frontal views of a triplet infrared sensor assembly. Dimensions are given in inches. (Courtesy of Goodrich Corporation, Danbury, CT.)

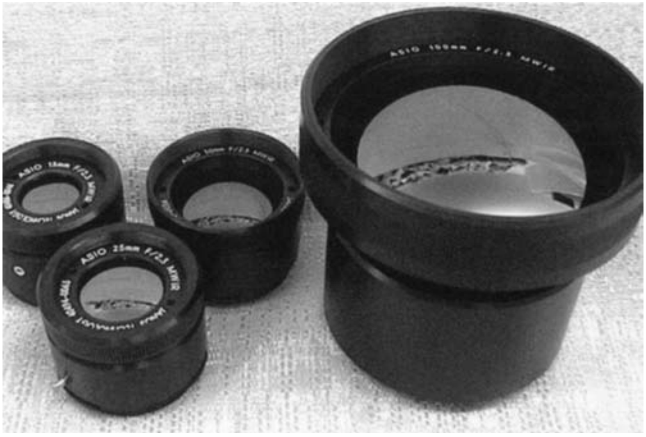

FIGURE 5.23 Photograph of four *f*/2.3 lens assemblies with focal lengths ranging from 13 to 100 mm (0.51 to 3.94 in.) operating in the 3- to 5-μm wavelength region. (Courtesy of Janos Technology, Inc., Keene, NH.)

TABLE 5.1
Characteristics of *f*/2.3 Commercial Mid-IR Lenses

Focal Length (mm)	Field of View (deg)	Length (mm)	Diameter (mm)	Weight (oz)
13	38.9	46.8	57.1	< 8
25	22.8	46.8	27.1	< 8
50	11.8	46.8	61.9	< 7.5
100	6.0	107.6	117.3	< 31

The mechanical parts are 6061-T6 aluminum and the lenses are silicon and germanium. The filter, cold stop, window, and detector array are contained in a separate dewar that is furnished by the user. During assembly, the applicable areas of the cell and the rims of each lens are primed with GE primer SS4155 to facilitate adhesion. Extreme care is exercised in applying the primer to the lenses since it can damage the polished surfaces if they are accidentally contacted. The lenses are then

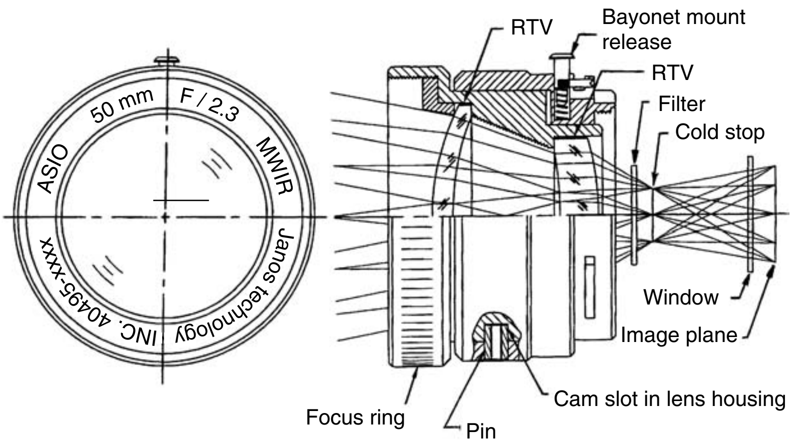

FIGURE 5.24 Sectional view of one of the lenses shown in Figure 5.23. All these lenses have essentially the same construction. (Courtesy of Janos Technology, Inc., Keene, NH.)

installed with their flat bevels contacting the shoulders provided in the cell and shimmed to center them within 30 μm relative to the mount axis. Each lens is then held in place with GE RTV Type 655 sealant. Once aligned, the RTV is applied with a fluid-dispensing system and cured according to the manufacturer's directions. A retaining ring is then installed. It does not apply significant preload to the lens, but serves as a convenient location for lens identification information.

Rotating the knurled ring at the front focuses each lens. This rotates the lens housing within the fixed mount body and drives the lenses axially as a group by virtue of a helical cam slot in the lens cell that engages a brass pin fixed in the body. The object space range is from infinity to 50, 150, 425, and 1750 mm, respectively, for the 13, 25, 50, and 100 mm EFL types. Focus is clamped with a soft-tip setscrew (not shown). Each lens attaches to the camera through a bayonet mechanism. The spring-loaded pin shown at top is used to unlock that mechanism.

5.4.2 INTERNALLY FOCUSING PHOTOGRAPHIC LENSES

A simplified illustration of a photographic lens depicting one way in which focusing can be accomplished by varying an internal air space is shown in Figure 5.25 from Jacobs (1943). Lenses 1 and 2 are mounted in cell A while lenses 3 and 4 are mounted in cell C. With this type of lens (Tessar) the spacing between elements 1 and 2 is very critical, so accurately machined shoulders maintain this spacing. Lens 1 is held in place by a threaded retaining ring, while the other elements are burnished into their cells. The air space between lenses 2 and 3 can be varied to focus the assembly by the rotation of ring B. The lenses do not rotate about the axis, so the image will not shift laterally while focusing. This requires cell A to be keyed to cell C by means not shown.

The configuration of this lens employs differential threads to achieve a fine-focusing adjustment with comparatively coarse threads. The threads connecting A and B might be 32 threads per inch tpi, while those connecting B and C might be 54 tpi. If the threads were made subtractive with rotation of ring B, the motion would be equivalent to a single thread of $1/[(1/32) - (1/54)] = 78.5$ tpi. If rapid focusing were to be desired, the threads could be made additive, giving the effect of a single thread of $1/[(1/32) + (1/54)] = 20.1$ tpi.

An example of a modern high-performance photographic lens assembly using the differential thread principle is the Carl Zeiss 85-mm *f*/1.4 *Planar* shown in Figure 5.26. Rotation of the knurled ring (outermost dark-colored part of the barrel) turns an inner threaded ring on fine and coarse threads to slide the entire inner subassembly carrying the lenses in the axial direction without rotating.

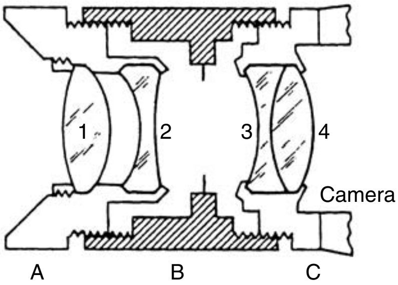

FIGURE 5.25 Illustration of a simple internally focusing lens mount. (Adapted from Jacobs, D. H., *Fundamentals of Optical Engineering*, McGraw-Hill, New York, 1943.)

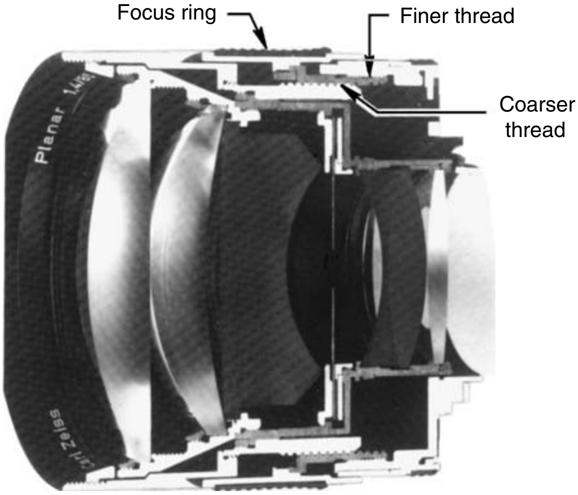

FIGURE 5.26 A modern, high-performance photographic objective with a differential thread internal focusing mechanism. (Courtesy of Carl Zeiss, Inc., Oberkochen, Germany.)

5.4.3 BINOCULAR FOCUS MECHANISMS

Since they are customarily used to observe objects at long distances, the objectives of most military telescopes, binoculars, and periscopes are not designed to be refocused for nearby objects. The angular calibration of reticle patterns used for controlling the fire of weapons then remains constant. If the magnification of such an instrument is greater than three power, its eyepiece(s) should be individually focusable to suit the user's eye accommodation. Refocusing the eyepiece(s) will have no effect on reticle calibration since the image of the target and the pattern are axially coincident at the objective's focal plane.

To accommodate variations in the focusing capability of the eyes of the user, a focus adjustment (called the "diopter adjustment" of at least ± 4 diopters (D) is usually provided for military instruments, while a range of + 2 to −3 D is common on consumer equipment. A scale calibrated in 1/4 or 1/2 D increments is usually placed on the eyepiece focus ring for ease of setting. Assuming that the entire eyepiece with an EFL of f_E (in mm or in.) is moved axially to make this adjustment, the displacement Δ_E for a 1 D change in collimation of the beam entering the eye is approximated by

$$\Delta_E = f_E^2/1000 \quad \text{for } \Delta_E \text{ (in mm)} \tag{5.6a}$$

$$\Delta_E = f_E^2/39.37 \quad \text{for } \Delta_E \text{ (in in.)} \tag{5.6b}$$

To illustrate the use of this equation in the design of an eyepiece-focusing mechanism, let us consider this example. Assume that the focus of an eyepiece with f_E = 1.110 in. (28.194 mm) is to be changed by ± 4 D. What axial motion is required? From Eq. 5.6(a), $\Delta_E = 1.110^2/39.37 = 0.031$ in. (0.795 mm) for a 1 D change, so ±4 D change would require a motion of ± 0.250 in. (± 6.350 mm). If this motion were to be produced by rotating the focusing ring 240° to prevent ambiguity in reading the focus scale, what should be the pitch of the thread? Then a thread pitch of (360/240)(0.250) = 0.375 in./thread or 2.667 tpi would be needed. The corresponding metric thread would be 9.54 mm/thread or 0.105 threads per millimeter.

The thread defined in this example is extremely coarse. Additive differential threads or, preferably, a multiple-lead thread (such as a set of 4–8 individual coarse threads in parallel) can be used to advantage here. Cams with cam followers also can be used in such cases.

Figure 5.27 shows the mating threaded parts for a 6-lead, 16-tpi eyepiece-focusing mechanism. The lenses move 6/16 = 0.375 in. per turn or (240/360)(0.375) = 0.250 in. (6.350 mm) in 240° rotation. This multiple-lead thread thus has precisely the characteristics required for the eyepiece focus mechanism described in the last example. The pitch diameter of each thread in this mechanism is approximately 1.18 in. (29.97 mm), while the axial length of the thread engagement is about 0.28 in. (7.11 mm). With six threads engaged, much averaging of minor manufacturing errors takes place so that the motion feels smooth to the user.

The focusing eyepiece assembly for a low-cost commercial binocular shown in Figure 5.28 is from Horne (1972). It has glass lenses in the Kellner form (Rosin, 1965) with the doublet eye lens burnished into a brass cell and the plano-convex field lens retained against a shoulder by a brass cell designed to hold a burnished-in glass reticle. The inner rotatable subassembly containing the lenses is molded of plastic and has an external multiple-start thread that mates with a similar internal thread on the fixed outer member. A knurled ring (also made of plastic) is locked to the inner subassembly with cone-point setscrews so that, as the ring is rotated, the lens assembly moves axially for focus adjustment. Since the lenses rotate to focus, the image may tend to move angularly because of wedge errors. This affects the collimation (i.e., parallelism of the lines of sight) of the binocular and may cause eyestrain during use.

The eyecup on this eyepiece is also molded of plastic and threaded onto the back of the knurled ring. It should be noted that the knurled ring retains the eye lens cell. This design is considered a good example of material choice and simple design to minimize costs while meeting the relatively low technical needs in the end product.

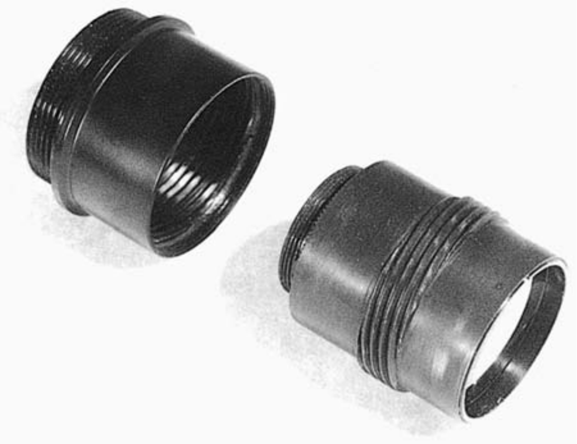

FIGURE 5.27 Mating threaded parts for a multiple-lead eyepiece focusing mechanism with six parallel grooves spaced at 0.0625 in. (1.587 mm) intervals. The axial motion is 0.375 in. (9.525 mm) per turn. (From Yoder, P. R., Jr., *Mounting Optics in Optical Instruments*, SPIE Press, Bellingham, WA, 2002.)

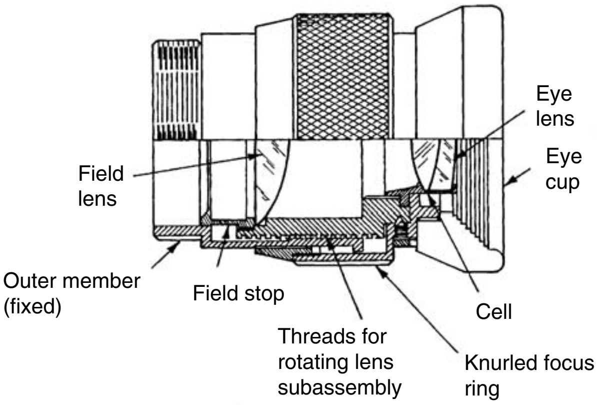
Eye lens
Eye cup
Field lens
Outer member (fixed)
Field stop
Cell
Threads for rotating lens subassembly
Knurled focus ring

FIGURE 5.28 A commercial telescope eyepiece with lenses that rotate to focus. It uses plastic mechanical parts to advantage. (Adapted from Horne, D. F., *Optical Production Technology*, Adam Hilger Ltd., Bristol, England, 1972.)

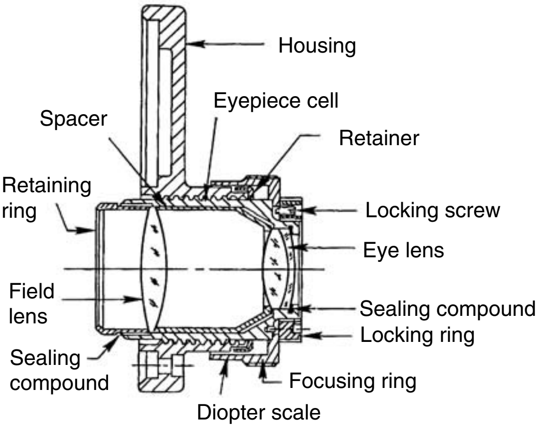
Housing
Eyepiece cell
Spacer
Retainer
Retaining ring
Locking screw
Eye lens
Field lens
Sealing compound
Locking ring
Sealing compound
Focusing ring
Diopter scale

FIGURE 5.29 Another focusing eyepiece with lenses that rotate to focus. This is for a military binocular application.

Another simple eyepiece with lenses that rotate to focus is shown in Figure 5.29. This is used in a military binocular. It is sealed reasonably well with sealant at the lens-to-metal interfaces and with heavy grease on the threads. The latter means for sealing the dynamic motion works fairly well except at very low temperatures, at which the mechanism can become quite stiff.

A more complex eyepiece configuration typical of those used in military applications is shown in Figure 5.30. Here the lenses are mounted in a cell (11) that slides axially to focus when the knurled ring (28) is turned on the thread (29). The stop pin (34) slides in a slot in the housing (13) to prevent rotation of this cell as the knurled ring is turned. The housing typically interfaces with the optical instrument by means of a threaded clamping ring (not shown) that is slipped over the eyepiece housing (13) before the ring (28) is installed. When engaged with a corresponding thread on the instrument housing, this ring presses against the right side of the flange on the housing (13) to hold the eyepiece in place. Since no mechanical indexing means is provided, care must be exercised with this design to ensure that the eyepiece is rotated about its axis so that the reference mark on the housing (13) for the diopter adjustment scale is visible in the normal using position of the instrument before clamping in place. An O-ring in the groove adjacent to the flange seals the eyepiece to the housing.

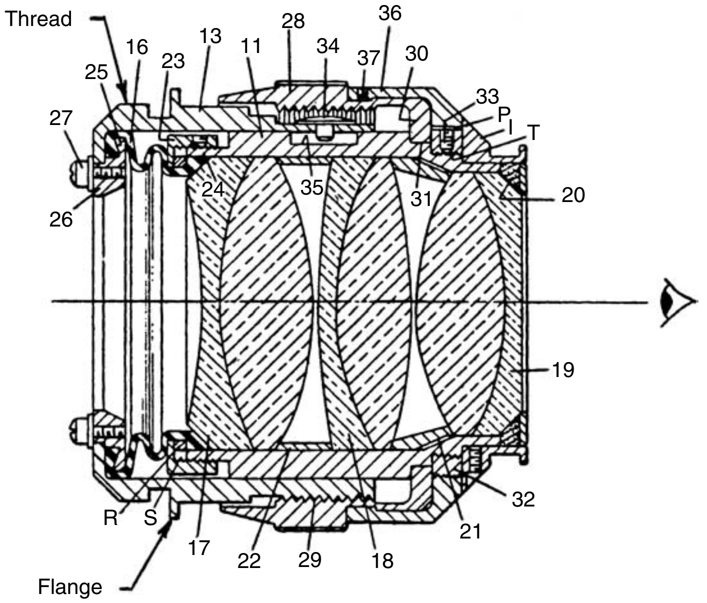

FIGURE 5.30 Typical construction of a more complex eyepiece for a military telescope. This design features a combined static/dynamic (rubber bellows) seal. The lenses do not rotate to focus. (From Quammen, M. L. et al., U. S. Patent 3,246,563,1966.)

A unique feature of this design is the combination static and dynamic seal accomplished with the rubber bellows (16). A static seal between the bellows and lens (17) is created by the clamping ring (23) threaded onto one end of the cell (11) and held in its tightened position by a setscrew (24). The bellows is similarly clamped at its other end to the eyepiece housing by a retaining ring (26). A flexible dynamic seal is thus established between the fixed and movable parts of the eyepiece. Sealing compound (20) is used to seal the eye lens (19) to its cell to prevent moisture from entering the air spaces between the lenses. A lubricant that retains its flexibility over a wide temperature range is typically applied to the threads.

Tests of military instruments such as binoculars using the last-described sealing techniques showed that pressure differentials of 5 lb/in.^{2} caused a pressure drop owing to leakage of no more than 0.05 lb/in.^{2} per h. This degree of sealing approaches that attained in instruments having only static seals, and exceeds the level attained with more conventional dynamic seals, such as lubricated packings and O-rings (Quammen et al., 1966).

Most nonmilitary telescopes and binoculars utilize different means for focusing on objects at different distances. Since there is usually no reticle pattern to keep in focus, either the eyepiece(s) or the objective(s) can be moved for this purpose. The classic design for focusable binoculars, as exemplified by Figure 5.31, moves both eyepieces simultaneously along their axes as the knurled focus ring located on the central hinge is rotated. One eyepiece has individual focus capability to allow accommodation errors between right and left eyes to be balanced. The eyepieces in this design slide in and out of holes in the cover plates on the prism housings. It is very difficult to seal the gaps between the eyepieces and these plates adequately. Most commercial instrument designs make no attempt to do so.

Figure 5.32 shows, in partial internal view fashion, one approach for providing focus in a commercial binocular without involving dynamic seals of the moving parts. Here, rotation of the focusing ring on the hinge moves an internal lens (arrow) to refocus the system. All externally exposed lenses are statically sealed. The rotary motion of the shaft carrying the focusing ring is sealed easily and adequately with a compressed O-ring.

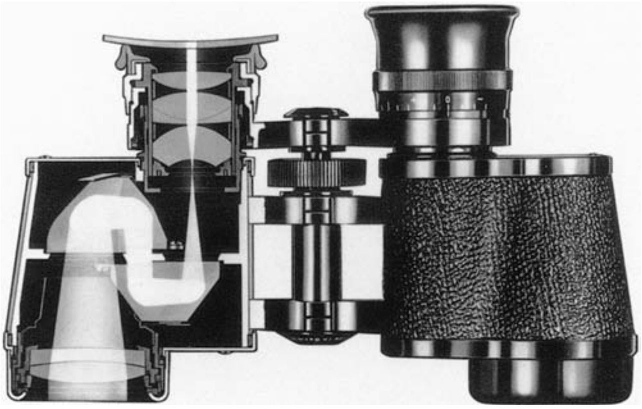

FIGURE 5.31 A commercial binocular of traditional design with focusable eyepieces. (Courtesy of Carl Zeiss, Inc., Oberkochen, Germany.)

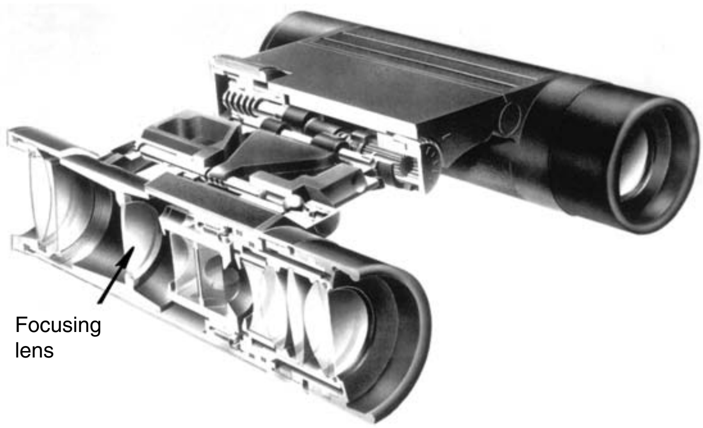

FIGURE 5.32 Partial internal view of a commercial binocular with internal focusing mechanism that allows the instrument to be statically sealed. The lens marked with an arrow moves axially to focus. (Courtesy of Swarovski Optik KG, Hall in Tyrol/Absam, Austria.)

5.4.4 ZOOM LENSES

Photographic and video camera zoom lenses for consumer, professional motion picture and television, and military applications owe their success in large part to the ability of mechanical engineers and designers to design mechanisms capable of moving lens groups smoothly, accurately, and quickly along the axis to change the focal length and field of view of the lens from wide-angle to telephoto positions, while maintaining sharp focus. Lens designers have succeeded in achieving fine image quality at reasonable relative apertures over large zoom ranges. Although most of these lenses work in the visible spectral region, infrared zoom telescopes suitable for incorporation into forward-looking infrared (FLIR) systems have also been developed for military and security use. In the following paragraphs, we summarize some key mechanical design features of several zoom systems.

Ashton (1979) described a classic design for a zoom lens intended for use with 35-mm cine cameras. This 25 to 250 mm-EFL, *f*/3.6, 10:1 range lens is illustrated by the mechanical sectional view of Figure 5.33. It covers a maximum of 45° horizontal field and can be focused down to about 1.2 m (4 ft) object distance. Approximate dimensions of the assembly are 300 mm (11.8 in.) barrel length and 150 mm (5.99 in.) diameter. The outermost doublet (left) is fixed; the next air-spaced

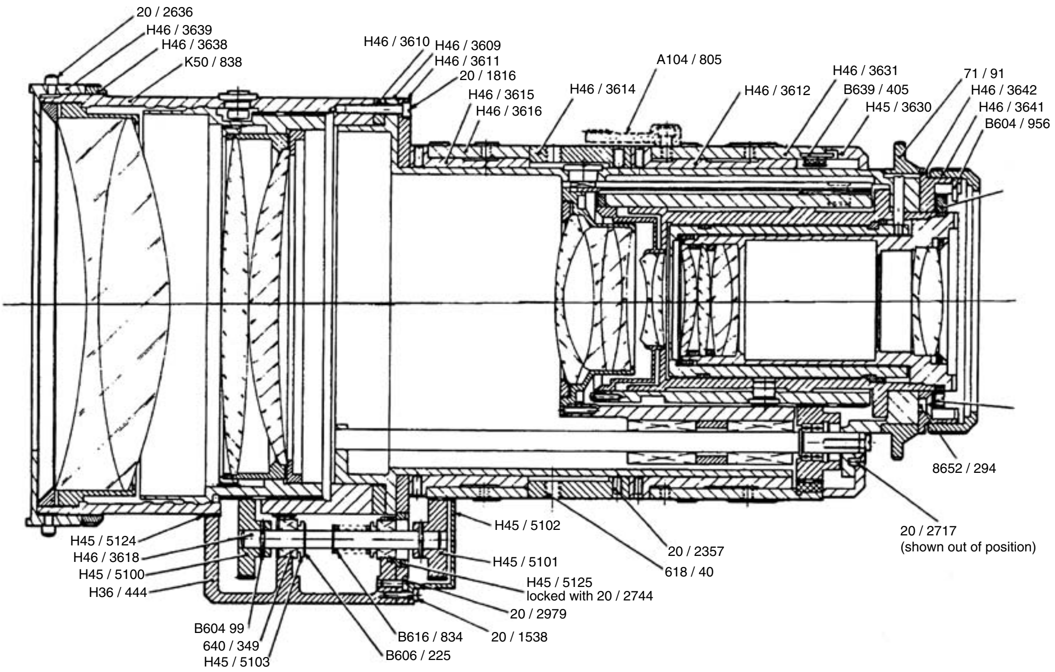
20 / 2636
H46 / 3639
H46 / 3638
K50 / 838
H46 / 3610
H46 / 3609
H46 / 3611
20 / 1816
H46 / 3615
H46 / 3616
H46 / 3614
A104 / 805
H46 / 3612
H46 / 3631
B639 / 405
H45 / 3630
71 / 91
H46 / 3642
H46 / 3641
B604 / 956
8652 / 294
20 / 2717
(shown out of position)
H45 / 5124
H46 / 3618
H45 / 5100
H36 / 444
B604 99
640 / 349
H45 / 5103
B606 / 225
B616 / 834
20 / 1538
20 / 2979
H45 / 5125
locked with 20 / 2744
H45 / 5101
H45 / 5102
20 / 2357
618 / 40

FIGURE 5.33 Sectional view of a 25–250-mm EFL, *f*/3.6, 10:1 range photographic zoom lens assembly. (Adapted from Ashton, A., *Proc. SPIE*, 163, 92, 1979.)

doublet is movable by an external motor (not shown) to change focus. As in most zoom lenses, the zoom functions are accomplished by moving two groups of lenses. The first group, consisting of a singlet and triplet, moves over a relatively long distance from the position shown in the figure at telephoto position to a forward position for wide-angle use. The second group is a doublet that moves forward from the telephoto position shown to a location where it reverses direction and then moves back to the wide-angle position. The remaining components in the lens train are fixed and serve to bring the image to focus at the image plane.

Figure 5.34 is an exploded view of the zoom mechanism. There are three main components: two sleeves (A and B) and a carriage (C). The front zoom group is attached to the front of the carriage. This carriage moves in ball bushings along a rod fitted into the lens housing parallel to the axis. The bushings are spring-loaded laterally to reduce image wander during zooming. A key fixed to the housing rides in a slot in the carriage to prevent rotation of the carriage. The second lens group (doublet) is attached to the front of sleeve B. This sleeve has an external ring gear and a helical cam machined into its outer surface. A cam follower (not shown) attached to the carriage rides in this cam to impart controlled motion to the doublet as the sleeve is rotated by an external motor (not shown). Sleeve A is fixed to the lens housing and carries another cam slot. A cam follower attached to sleeve B engages this slot and moves sleeve B as it rotates. The ring gear on sleeve B is long enough to maintain engagement with the drive gear throughout this axial motion. The movement of the carriage may be seen as the sum of the two cam forms.

Sleeves A and B are a matched subassembly. Raised rings on the outside of sleeve A serve as bearing surfaces against the ID of sleeve B during zoom motion. Both mating surfaces are hard-anodized for good wear characteristics; the rings on sleeve A are diamond-turned to fit closely and smoothly within the honed inside surface of sleeve B. Permissible clearance between these bearing surfaces is 7 to 10 μm (0.0003 to 0.0004 in.). Smaller clearance causes too much torque resistance and poor wear. Larger clearance causes the image to jump and go out of focus when the zoom motion reverses. Cam slots are diamond-turned to reproduce a master contour form. Cam followers

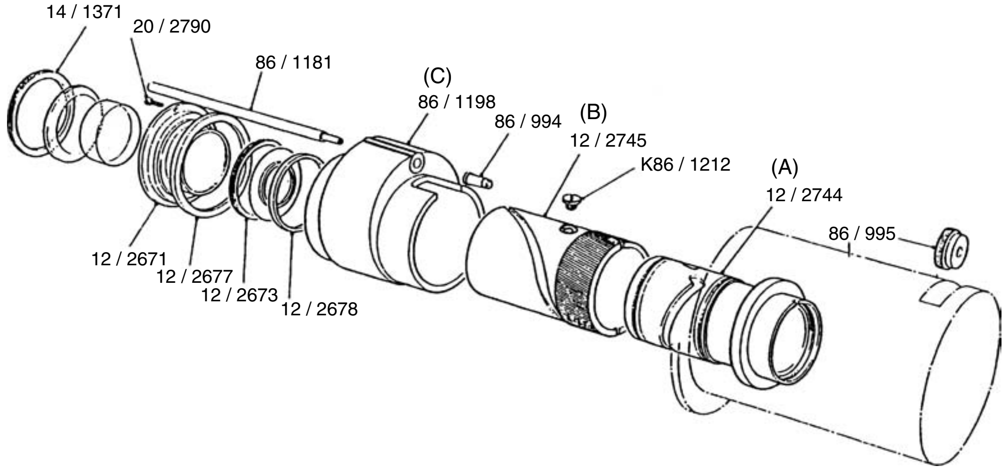

FIGURE 5.34 Exploded view of the zoom mechanism in the lens of Figure 5.33. (Adapted from Ashton, A., *Proc. SPIE*, 163, 92, 1979.)

are polyurethane and fit the slots without clearance to eliminate backlash. The lenses are mounted into aluminum cells and held by threaded retaining rings. The cells are, in turn, attached to the aluminum sleeves and carriage.

Figure 5.35 shows another lens assembly described by Ashton. This is a 20 to 100 mm EFL, *f*/2.8, 5:1 zoom lens with about the same physical dimensions as the example just discussed. It has a larger (58°) horizontal field at wide angle and focuses to within 0.35 m (13.8 in.). The front air-spaced doublet is fixed while the second group of elements is moved to focus. Two zoom groups (Z1 and Z3 in the figure) are attached to the same outer carriage so they move together. An inner zoom carriage with lens group Z2 moves in the opposite direction. The carriages are machined as skeletons to reduce weight. Both carriages have spring-loaded rollers that ride on diamond-turned inner bores of adjacent parts. Two spiral cam slots are machined into the inside surface of a sleeve that fits over the outside of the housing and runs in ball bearings. Cam followers attached to the carriages pass through axial slots in the housing to engage the cam slots. When the cam is rotated, both carriages move as required.

In this design, the lenses are mounted into closely machined stainless steel cells and held by threaded retaining rings. The cells are mounted onto the carriages by an adhesive. The cells are aligned to the carriages and rollers in jigs and then cemented in place. Rollers are made of Tufnol, which offers all-important smoothness and quietness of motion while retaining adequate alignment.

The following description of another zoom lens, the Bistovar 15 to 150 mm (0.59 to 5.90 in.) focal length, *f*/2.8 zoom lens assembly shown in Figure 5.36, is adapted from Yoder (2002). This assembly measures about 172 mm (6.77 in.) in length and 155 mm (4.53 in.) in diameter. At the camera end of the housing (item 26) is a standard C-mount interface for a video camera with an 11.0 mm (0.433 in.) format diagonal. The lens has fixed (infinity) focus; its focal length is variable over a 10:1 range. The field of view varies from 40.3 to 4.2° while the relative aperture varies from *f*/2.8 to *f*/16. In prototype form, the lens assembly weighs approximately 1600 g (3.57 lb).

The optical system contains, in sequence, a four-element passive stabilization system with 5° dynamic range at the entrance aperture; a seven-element, 5:1 zoom system; a five-element, dual-position 2:1 zoom subsystem; and a Schott GG475 (minus-blue) filter. The average polychromatic MTF performance over the zoom range at 20 lp/mm on-axis and at 0.9 field is 69 and 25%, respectively, including diffraction effects.

Movements of the two zoom lens groups (items 109 and 100, and item 101) in the 5:1 system are synchronized by a motor-driven cylindrical cam (item 44) carrying slots custom-machined for the specific set of lenses used in that assembly. A third, moving-lens group (items 102, 110, and

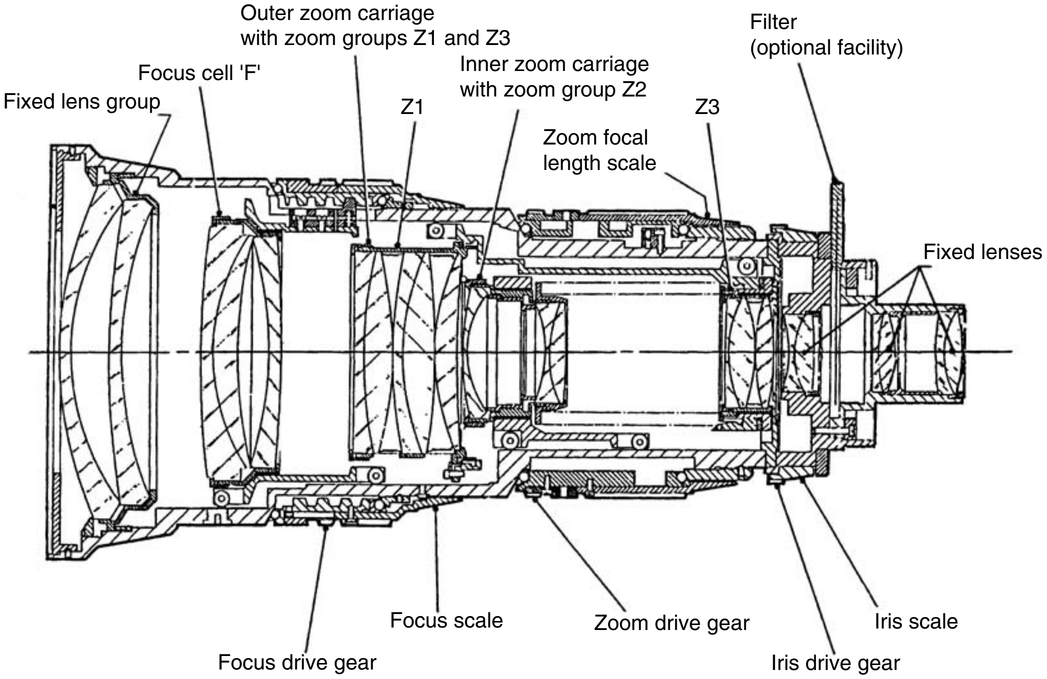
Outer zoom carriage
with zoom groups Z1 and Z3
Filter
(optional facility)
Focus cell 'F'
Inner zoom carriage
with zoom group Z2
Fixed lens group
Z1
Z3
Zoom focal
length scale
Fixed lenses
Focus scale
Zoom drive gear
Iris scale
Focus drive gear
Iris drive gear

FIGURE 5.35 Sectional view of a 20–100-mm EFL *f*/2.8, 5:1 zoom lens. (Adapted from Ashton, A., *Proc. SPIE*, 163, 92, 1979.)

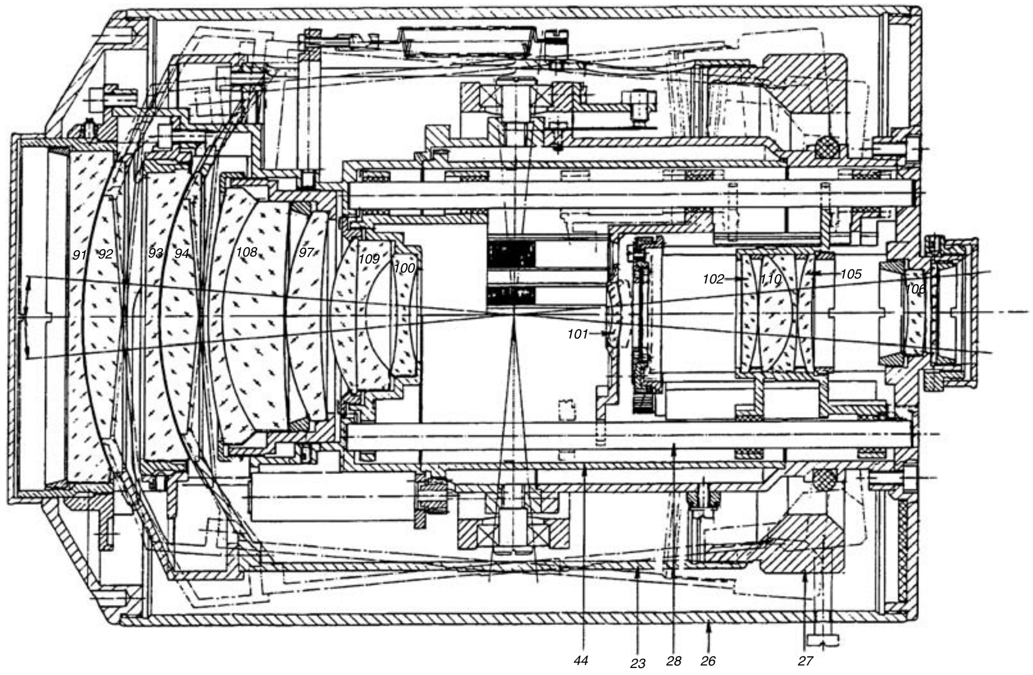
91
92
93
94
108
97
109
100
101
102
110
105
106
44
23
28
26
27

FIGURE 5.36 Opto-mechanical configuration of a 15 to 150 mm (0.59 to 5.90 in.) focal length, 10:1 zoom lens assembly designed with a passive image stabilization feature for use with a video sensor having an 11 mm (0.433 in.) diagonal. (Courtesy of Bystricky, K.M., Bista Research, Inc., Tragoss, Austria.)

105) moves axially under the control of a separate slot in the same cam so as to switch the 2:1 system whenever the main zoom system reaches its limits. Lenses 108, 97, and 106 remain stationary.

Two air-spaced doublets, each consisting of a plano-concave and a plano-convex element made of the same glass (Schott K10), make up the image stabilization subsystem. The curved surfaces of each doublet have the same absolute radius and are air-spaced by 0.25 mm. The positive singlets (items 92 and 94) are attached to a lightweight tubular structure (item 23) that pivots on ball bearings about either of two orthogonal gimbal axes. A counterweight (item 27) at the camera end of this tube statically balances the moveable lenses. These lenses are lightly spring-loaded toward the centered location. When centered, they act with their corresponding negative lenses as two plane-parallel plates in series that do not deviate the line of sight. When the assembly experiences rapid lateral acceleration due to vibration or shock, the inertias of the positive elements and associated mechanical parts tend to hold them stationary, thereby forming optical wedges that deviate the line of sight to hold the image centered on the focal plane array. Slow rotations of the lens assembly do not produce relative displacements of the moveable lenses, so the line of sight tracks the assembly axis.

Most of the lenses used in this assembly are mounted conventionally in aluminum cells and held in place by threaded retainers. A few glass-to-metal interfaces are spherical, but most are of the sharp-corner type. The beveled edge of one lens (item 100) directly contacts a flat bevel on the adjacent doublet (item 109). The pivoted lenses (items 92 and 94) and one fixed lens (item 101) are secured in place with adhesive (Ciba-Geigy Araldite 1118 epoxy), since there is no room for retainers.

Gardam (1984) described two infrared zoom lenses with essentially the same mechanical design, but somewhat different optical characteristics. One system has a zoom range of 6:1, an overall length of 380 cm (15 in.), and a front aperture of 266 mm (10.5 in.). The other lens has a zoom range of 3:1, a length of 200 mm (7.9 in.), and an aperture of 110 mm (4.3 in.). A prototype of one of these is shown in the sectional view of Figure 5.37. Four cylinders are machined as matched concentric sets. The inner two cylinders carry the zoom lens elements, and the outermost cylinder carries the front-focusing lens. Motion of this lens is also used to reduce the sensitivity of the design to temperature changes by adding differential motions controlled by temperature sensors. The fourth cylinder is fixed to a back plate of the lens. All four cylinders are keyed together to prevent relative rotation. The first lens is potted into its cell with a polyurethane adhesive. Cam followers riding in a double-cam cylinder located just inside the outermost cylinder drive the motions of the zoom lens groups. This cam cylinder turns in preloaded ball bearings.

The mechanical design of this zoom lens relies on the accuracy of machining for smoothness of motion and image stability during zooming. Tolerances on the centration of lens elements are on

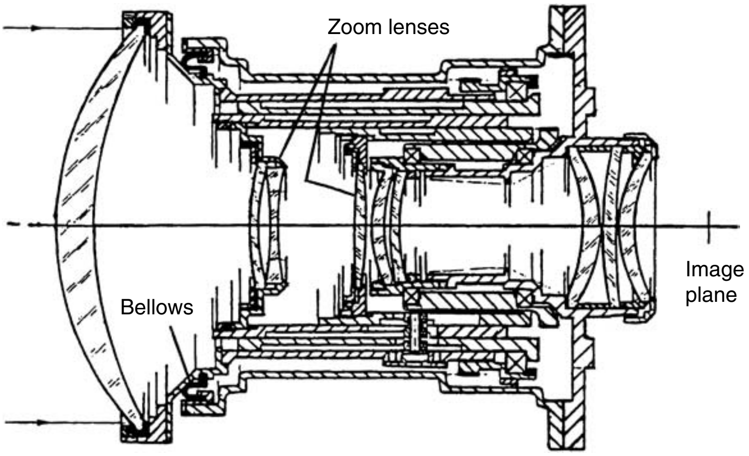

FIGURE 5.37 Sectional view of an infrared zoom lens prototype design. (Adapted from Gardam, A., *Proc. SPIE*, 518, 66, 1984.)

the order of 7.5 μm (3×10^{-5} in.). They would need to be considerably smaller if unmatched cylinders were used. Tolerances are also tight on backlash between the cam followers and the cam slots since spring-loading mechanisms could not be fitted into the very compact package. In these prototype lenses, the accuracy of fit was held to about 5 μm (0.0002 in.).

A refined version of the above mechanical design was described by Parr-Burman and Gardam (1985). Figure 5.38 shows a sectional view of this lens. The outermost cylinder holding the focusing front lens group now is shorter and the housing extends over the two DC servo focus and zoom drive motors and gearheads.

The closely toleranced fits between the cam followers and cam slots are more relaxed in this newer design because of the use of a dual roller cam follower, as shown in Figure 5.39. The left view shows the conventional approach in which a finite amount (typically, 5 μm) of lateral clearance must be allowed in order to prevent excessive friction. This expresses itself as lateral jitter of the image as the cam moves. The right view shows the new roller configuration. A rubber roller on the same shaft as the actual cam follower is slightly compressed against one side of the slot. This holds the cam follower securely against the opposite side of the slot. Only the latter side of the slot needs to be machined with high precision, and backlash is prevented.

The paper by Parr-Burman and Gardam (1985) provides an informative discussion of probability theory as applied to the production of zoom lenses.

The zoom lenses considered here so far are all continuous zoom designs in which good imagery is provided at all zoom settings. Some lenses are required to give good images only at two focal lengths. The opto-mechanical layout of such a dual focal length assembly is shown in Figure 5.40, an *f*/2.3 lens developed for use with a 3–5–μm infrared camera and described by Palmer and Murray (2001) and Palmer (2001). The lens system has focal lengths of 50 and 250 mm and is nearly diffraction-limited at each setting. Switching from one setting to the other is accomplished by sliding

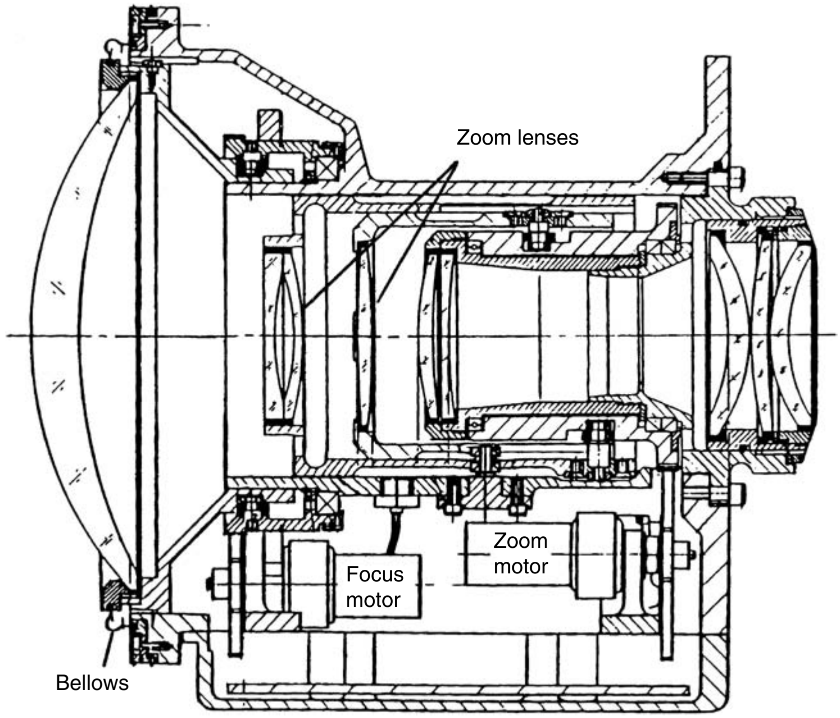

FIGURE 5.38 Sectional view of an improved version of the zoom lens mechanical design of Figure 5.37. (Adapted from Parr-Burman, P. and Gardam, A., *Proc. SPIE*, 590, 11, 1985.)

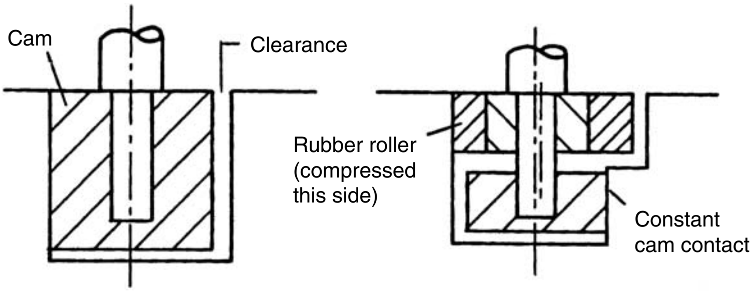

FIGURE 5.39 Comparison of conventional (left) and improved, dual-roller (right) versions of cam followers for zoom lenses. The improved version has a rubber roller and a stepped cam slot to spring- load the cam against one wall of the slot. (Adapted from Parr-Burman, P. and Gardam, A., *Proc. SPIE*, 590, 11, 1985.)

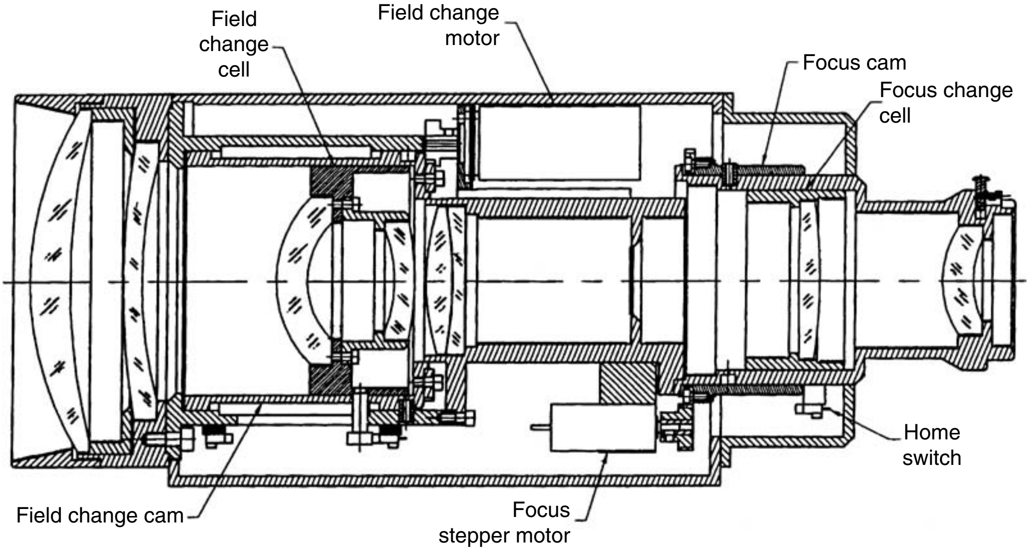

FIGURE 5.40 Section view of a dual field-of-view mid-IR objective lens. (Courtesy of Janos Technology, Inc., Keene, NH.)

a cell containing two lenses axially inside the assembly through a distance of about 1.5 in. (38.1 mm). Focus is established at either setting by a concurrent axial movement of another cell containing one lens. A DC motor drives the focal length-switching mechanism, while a stepper motor is used to drive the focus adjustment. Each mechanism contains a spur gear, which rotates a ring gear on a cylindrical cam. Helical slots in the cams engage pins affixed to the zoom lens cell and the focus lens cell and drive those cells axially as the cams rotate. The pins also engage slots in the fixed portion of the housing to prevent rotation of the lenses, thereby maintaining constant boresight alignment. Sliding surfaces are hard anodized and have 16 μin. surfaces, but are not lubricated. The radial clearance is typically 12 μm.

Figure 5.41 is a photograph of the exterior of the assembly. It is 321.3 mm (12.65 in.) long and generally cylindrical in configuration. The maximum lateral dimensions are 126.8 mm (4.99 in.) high and 133.0 mm (5.24 in.) wide. The assembly weighs 3.75 kg. The interface with the camera is a bayonet mount. A spring-loaded pin allows that mechanism to be released.

The main housing of the assembly is 6061-T6 aluminum; the lenses are silicon and germanium. The larger lenses are constrained by a threaded retaining ring and located by seating them against

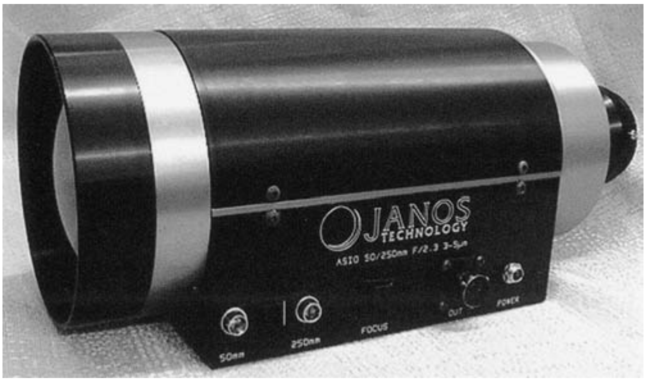

FIGURE 5.41 Photograph of the dual focal length lens assembly shown in Figure 5.40. (Courtesy of Janos Technology, Inc., Townshend, VT.)

shoulders. The spacer between these lenses also provides the seat for the outermost lens. The remaining lenses are held in place by GE RTV-655 seals around their rims.

In describing this design, Palmer (2001) indicated that a critical design requirement was that switching had to occur in less than 1 sec. This demanded high torque and high speed, plus smooth, low-friction, mechanical motion of the nested cylindrical parts, minimum mass of the moving subassemblies, and choice of an appropriate drive gear ratio. All these attributes were successfully achieved with commercially available motors. Limit switches and hard stops were incorporated into the design to enhance accuracy of the end positions of the motions.

Parr-Burman and Madwick (1988) described a high-performance, two-position zoom lens designed for airborne use that was athermalized by servo controlling the positions of the movable lenses in accordance with a polynomial algorithm based on temperatures sensed at three locations within the assembly. Each movable lens group was mounted on linear bearings and driven to position by a motor-actuated, recirculating ball screw. The authors of this paper cited ease of revision of the software (algorithms) and the use of the microprocessor to control multiple functions of the assembly as well as to monitor the assembly's behavior as desirable attributes of the design.

5.5 LATHE ASSEMBLY TECHNIQUES

In some lens mountings, elements are radially positioned by close fits to the ID of the mating cell or housing. The OD of each element must be precision ground to a high degree of roundness and measured. The ID of the mating part is then finish-machined to fit that specific element. In multielement designs, the axial positions of the various elements are established by properly locating the machined seats while cutting the IDs. Since this machining process is traditionally done on a lathe or similar machine tool spindle, it has come to be known as "lathe assembly."

In a high-performance lens assembled in this manner, nominal diametric clearance between the OD of the element and the ID of the metal part may be as small as 0.0002 in. (0.005 mm). This is sufficient for the lens to slide in place. The adequacy of a design in regard to radial loading of the lens due to differential shrinkage of the cell at low temperature may be evaluated by calculating the "hoop stress" using theory provided in Section 15.6.2.

To illustrate the actual lathe assembly process, let us consider the design of Figure 5.42. Here, the seat D for the convex surface of lens No. 1 is to be cut tangent to the surface and to the proper depth to position the vertex of that optical surface at 57.150 ± 0.010 mm from the flange-mounting surface B. The air space F is to be controlled to within ± 0. 015 mm of the nominal value from the lens design. Both lenses are to be constrained by a single threaded retaining ring acting through a pressure ring.

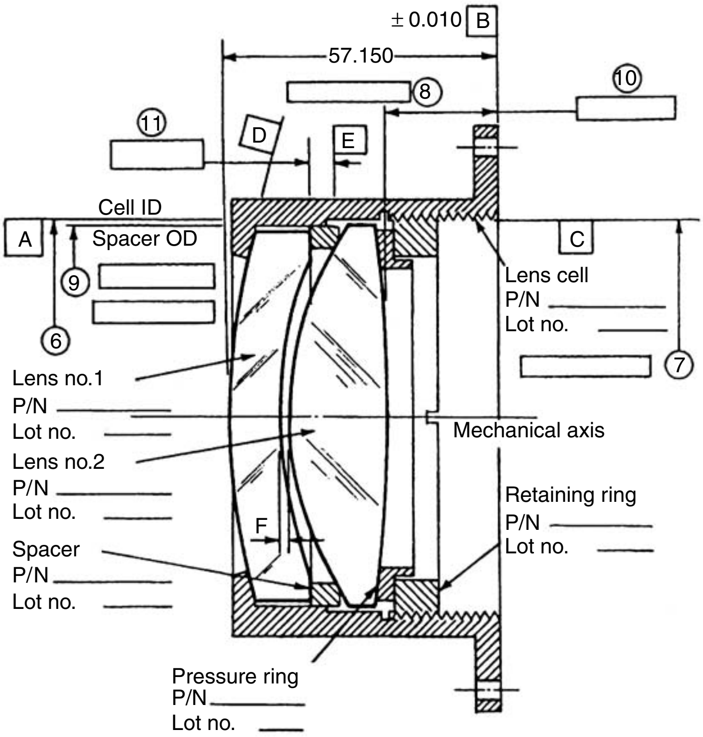

FIGURE 5.42 Illustration of an opto-mechanical lens assembled by the "lathe assembly" process. (From Yoder, P. R., Jr., *Proc. SPIE*, 389, 2, 1983.)

The first step is to measure the actual lenses to be assembled. The five boxes in Figure 5.43 indicate the five data items to be recorded, including air spaces from the system lens design. After the measurements are made, the lens surfaces might well be protected temporarily with peelable lacquer, except for areas to be mounted or measured subsequently.

The lens cell flange is mounted via an adapter plate (not shown in Figure 5.42) to a precision lathe spindle. The cell ID (surface A) is machined perpendicular within 15 arcmin to surface B and to obtain 0.007 to 0.012-mm diametric clearance over the actual OD of lens No. 1. The cell ID is measured and recorded as dimension 6. The second cell ID (surface C) is then machined concentric within 0.008 mm to surface A and to obtain 0.007 to 0.012-mm diametric clearance over the actual OD of lens No. 2. This ID is measured and recorded as dimension 7.

The angle for the conical surface D is then calculated from Eq. (4.24) and machined. In this case, the angle is ~75° from the mechanical axis. A tolerance of ± 0.5° applies in this case. The axial location of surface D is determined by iterating the facing operation with trial installations of the lens and measuring the convex vertex location relative to the required axial location from the flange. When within tolerance, the actual value of dimension 8 is recorded.

The spacer is separately machined on a lathe-mounted mandrel so that its interface with lens No. 2 is a sharp corner, its OD is perpendicular within 15 arcmin to its surface E, and the diametric clearance with respect to the ID of the cell (dimension 6) is 0.007 to 0.012 mm. This OD is measured and recorded as dimension 7. The spacer is inserted into the assembly so as to contact lens No. 1 and lens No. 2 is inserted. The actual axial location of the exposed surface of lens No. 2 relative to surface B is measured and recorded as dimension 10. The required thickness reduction of the spacer is computed as (dim. 8 – dim. 3 – dim. 4 – dim. 5 – dim. 10). Slightly less than this amount of material is removed from the spacer and the measurement repeated. When the error in thickness falls within the ±0.015 mm (±0.0006 in.) axial air-space tolerance (from the lens design), the

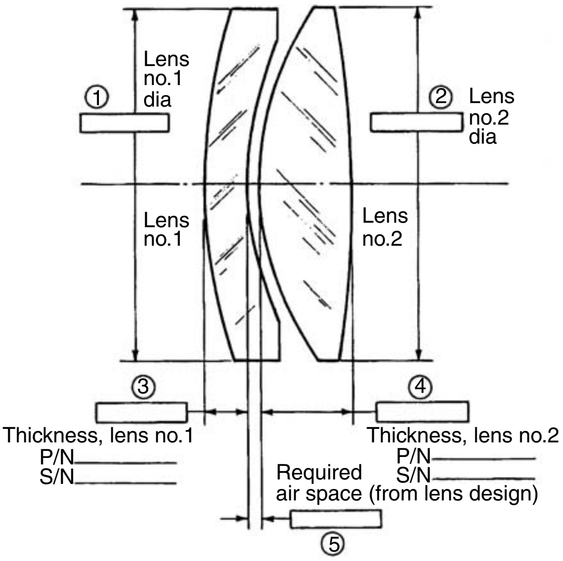

FIGURE 5.43 Data to be recorded for lathe assembly according to Figure 5.42. (From Yoder, P. R. Jr., *Proc. SPIE*, 389, 2, 1983.)

spacer dimension is recorded as dimension 11. The lenses and metal parts are then cleaned and reinstalled and the pressure ring and retaining ring installed to complete the assembly.

Figure 5.44 shows a cross section of a 24-in. (61-cm) focal length, *f*/3.5 aerial camera objective assembly designed for lathe assembly (Bayar, 1981). The titanium lens barrel is constructed in two parts so that a shutter and iris can be inserted between lenses 5 and 6 following optical assembly. The machining of the lens seats to fit the measured individual lenses begins with the components of smaller OD and proceeds toward the larger ones. Each lens is held with its own retaining ring so no separators are required. The front and back barrels are mechanically piloted together so that their mechanical and optical centerlines coincide after machining. The metal-to-glass interfaces on convex surfaces are tangential. Concave surfaces are precision-beveled flat during centering to minimize tilt. Elements 3 and 4 are deeply recessed to provide clearances for the retainers.

Another example of a high-performance lens designed for lathe assembly is shown in Figure 5.45. The optical characteristics and performance of this 9 in. (22.9 cm) focal length, *f*/l.5 objective were discussed by Yoder and Friedman (1972). The mechanical aspects of the design were described by Yoder (1986). Developed for use with an electro-optical image intensifier tube in a military aircraft periscope that provides nighttime vision, the lens also has an integral coaxial beam expander that projects a 1.06-μm-wavelength laser beam into object space for target designation and ranging purposes.

The paths of a main image-forming beam and laser beam through the optical system are illustrated in the optical schematic of Figure 5.46. The lens form was derived from the double-Gauss photographic objective but offers improved imagery over conventional designs in the 0.50–0.90 μm spectral region used by the image tube. The prism serves the triple purposes of folding the light path by 90°, allowing the laser beam to be injected through a central "piggyback" prism, and serving as a thick, meniscus-shaped lens near the focal plane to reduce field curvature.

The opto-mechanical assembly, shown in partial section view in Figure 5.47, is approximately 11.4 in. (29.0 cm) long and 6.7 in. (17.0 cm) in diameter at its largest point. The infinity focal plane is located 0.55 in. (14.0 mm) beyond the exit aperture to prevent high-voltage arc-over from the image intensifier to the metallic lens housing. The assembly is mounted on three ears protruding from the housing near the center of gravity. Custom-ground spacers attached to these ears parfocalize the assembly so that it is interchangeable with similar units.

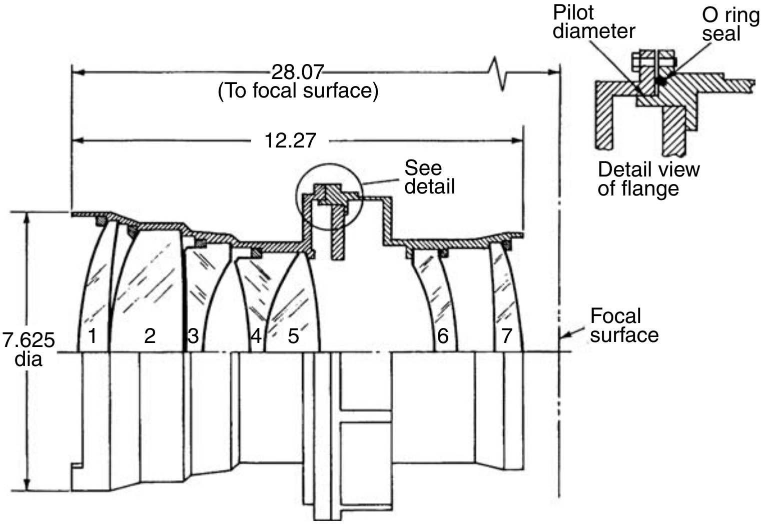

FIGURE 5.44 An aerial camera lens assembled by the lathe assembly process. Dimensions are in inches. (Adapted from Bayar, M., *Opt. Eng.*, 20, 181, 1981.)

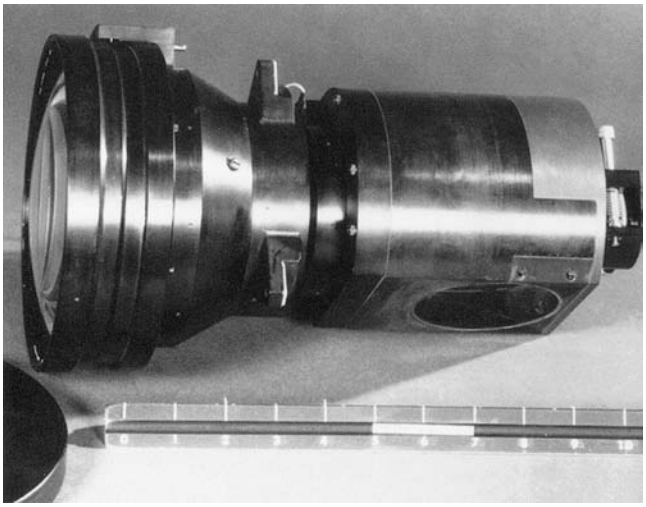

FIGURE 5.45 Objective lens with a coaxial laser channel used in a military night vision periscope. (From Yoder, P. R. Jr., *Proc. SPIE*, 656, 225, 1986.)

The front cell, containing a single meniscus-shaped lens element, is threaded onto the lens cone and can be rotated through ring and pinion gears by a reversible external motor (not shown) to focus the lens on objects as close as 45 m (~148 ft). The interface between this lens and its cell was shown schematically in Figure 4.32 and described in the accompanying text as an example of a lens with a spherical rim to facilitate insertion into the cell with minimal (a few micrometers) radial clearance. This design is practical only if the cell is finish-machined at the time of assembly to accommodate the lens.

Two individually rotatable optical wedges in the 7 mm (0.28 in.) diameter collimated input laser beam are used manually to boresight that beam to a reticle pattern in the visual periscope prior to a mission. The worm gear and control knob of one wedge may be seen on the right in Figure 5.45.

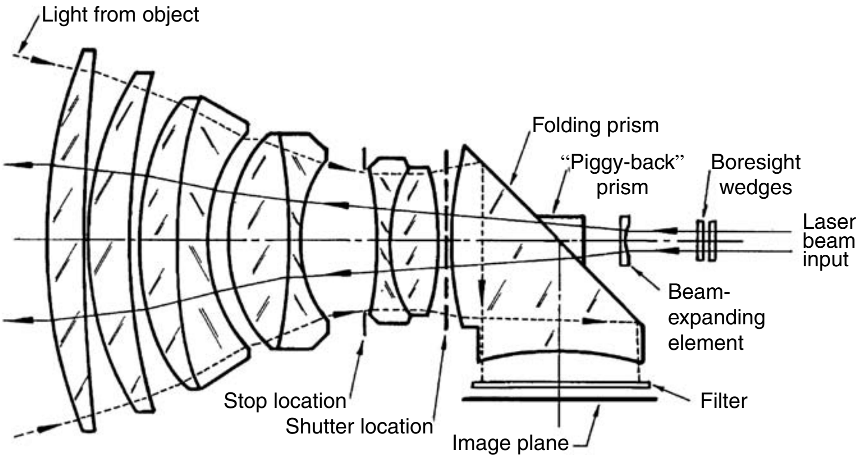
Light from object
Folding prism
"Piggy-back" prism
Boresight wedges
Laser beam input
Beam-expanding element
Filter
Stop location
Shutter location
Image plane

FIGURE 5.46 Optical schematic of the lens shown in Figure 5.45. (From Yoder, P. R., Jr. and Friedman, I., *Opt. Eng.*, 11, 127, 1972.)

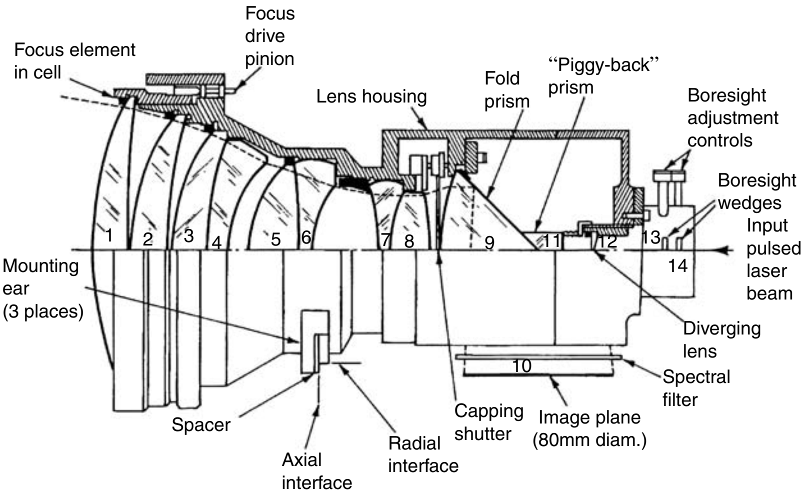
Focus element in cell
Focus drive pinion
Lens housing
Fold prism
"Piggy-back" prism
Boresight adjustment controls
Boresight wedges
Input pulsed laser beam
1
2
3
4
5
6
7
8
9
11
12
13
14
Mounting ear (3 places)
Diverging lens
10
Spectral filter
Spacer
Axial interface
Radial interface
Capping shutter
Image plane (80mm diam.)

FIGURE 5.47 Opto-mechanical design for the lens shown in Figure 5.45. (From Yoder, P. R., Jr. *Proc. SPIE*, 656, 225, 1986.)

As shown in Figure 5.47, a single-element negative lens diverges the beam as it enters the small "piggyback" prism cemented to an unaluminized central area on the fold prism hypotenuse. This beam refracts through the various lens elements of the assembly and emerges from the entrance aperture of the objective as a nominally collimated laser beam of 70 mm (2.8 in.) diameter.

The portions of the prism and lens apertures intercepted by the laser beam were antireflection-coated for the laser wavelength (1.06 μm) to minimize back reflections and light loss. Particular care was exercised during the optical design of this lens to place all focused, reflected, laser beam images in air spaces to protect the coatings. The design shown here has consistently withstood, for extended periods of time, input laser beam energy of typically 100 to 150 mJ/pulse at 10 pulses/per sec. A design feature contributing significantly to this operational capability was to enclose the beam path between the prism and the diverging lens (i.e., between elements 11 and 12 of Figure 5.47) with a stainless-steel bellows to prevent reflected and scattered light from reaching the inner surfaces of the metal housing and evaporating materials that would condense onto the optical surfaces, where they could be burned by the laser energy. It was found by experiment that impregnated castings and many types of finishes normally applied to metal parts must not be used in critical regions of this assembly. For this reason, the entire lens housing was machined from a forged billet of aluminum. To prevent problems with moisture trapped inside the lens assembly, it was sealed and evacuated, then backfilled, purged, and pressurized with dry nitrogen to an absolute pressure of about 19 lb/in.^{2} (i.e., ~4 lb/in.^{2} above ambient atmospheric pressure) through a valve (not shown).

As detailed in Section 15.8, conventional optical cements would not be satisfactory to make the doublets used in this system because of large differences in CTE of the adjacent glasses. Tests indicated that the lenses would fracture at the low temperatures of the application. A two-component silicone elastomer, Sylgard XR-63-489, formerly manufactured by Dow Corning Corporation, was successfully used. For flexibility, the cement layer used was approximately 0.050 mm (0.002 in.) thick. With cement joints this thick, it was necessary to exercise extreme care during the cementing operation to prevent excess optical wedge from being introduced.

5.6 MICROSCOPE OBJECTIVES

Precise mounting of microscope objective lens/mirror elements is essential to achieving the fine performance that can be designed into those optics. This is due largely to the extreme sensitivity to decentration and tilt of the small-diameter elements, many of which have very short radii. Some air spaces are critical in such designs, and accurate parfocalization is essential to their use.

As pointed out by Benford (1965), most microscope objectives require several adjustments before an acceptable image is attained. Since detailed descriptions of the methods used in assembling such objectives are rare in the literature, we paraphrase here the explanation given by Benford for assembly and adjustment of the typical 43-power refracting objective of 0.65 numerical aperture (N.A.) shown in Figure 5.48.

The steps involved in assembling this objective start with the mounting of the two doublets and the front hemispherical singlet into their separate cells. As described in Section 4.5.2, this is done by seating each lens against an internal shoulder and, with the cell rotating slowly in a precision lathe chuck, spinning or "burnishing" a thin rim of metal down onto the lens to lock it in place. After

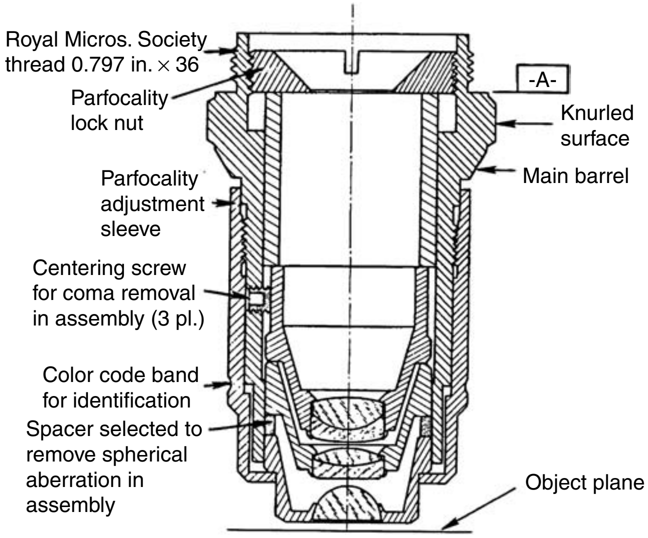
Royal Micros. Society thread 0.797 in. × 36
Parfocality lock nut
Parfocality adjustment sleeve
Centering screw for coma removal in assembly (3 pl.)
Color code band for identification
Spacer selected to remove spherical aberration in assembly
-A-
Knurled surface
Main barrel
Object plane

FIGURE 5.48 Typical mount design for a 43 power, 0.65 N.A. refracting microscope objective. (Adapted from Benford, J. R., Microscope objectives, in *Applied Optics and Optical Engineering*, Academic Press, New York, 1965.)

burnishing, the subassemblies are carefully cleaned and then inserted into their common mounting sleeve, with a nominal spacer between the lower lens mounts.

A simple means for testing the microscope objective is the *star test*. Malacara (1978) described the method in considerable detail. In this test, a back-illuminated pinhole forming an artificial star object is located on-axis at the objective's object plane. A standard microscope slide cover glass of the type to be used with this objective is placed between the pinhole and the objective to simulate the normal manner of use. The aerial image formed by the objective is observed through an auxiliary microscope. Adjustments are made to the objective until an image of acceptable quality is observed and the image is located at the appropriate distance from the flange on the objective housing.

The first adjustment is to correct spherical aberration, which is done by selecting the optimum spacer to go between the lower two lens mounts. Figure 5.49 shows the appearance of the images for typical correct and incorrect lens spacings. The operator tries different spacers until the correct image appearance for minimum spherical is achieved.

The second adjustment is to parfocalize the objective. Note from Figure 5.48 that the lens cells are supported in the main barrel by the "parfocality adjustment sleeve" and held in place by a threaded "parfocality lock nut." Loosening the latter and adjusting the former provides a precise means of moving the optics of the objective assembly axially to make the image lie at the standard distance from the mounting flange shoulder (datum –A–). This ensures that objectives on a multiple nosepiece can be interchanged without drastically losing focus.

The third adjustment is for coma. Three centering screws are used to move the upper doublet laterally in two orthogonal directions until coma is removed, again using the pinhole as the object and the auxiliary microscope to judge the image. At this point, the parfocality adjustment sleeve is a temporary sleeve with clearance holes to allow access to these screws. After the image is corrected, the screws are securely tightened. The temporary sleeve is removed and the final sleeve is installed. The objective is then given a final inspection and packaged for sale.

Microscope objectives are normally designed for use with a cover glass of 0.17 mm thickness and index of refraction 1.515 over the sample. Since not all cover glasses are exactly that thickness and the thickness of the embedding medium between the sample and the cover glass may vary, some high-power objectives may have externally accessible "correction collars" that are graduated in terms of cover glass thickness in millimeters. To achieve optimum performance of the microscope, this collar is adjusted manually for the particular situation of use. A Zeiss objective with this feature is shown in Figure 5.50. It has an adjustment range of 0.14 to 0.18 mm. Turning the correction collar typically moves an internal lens element axially to accomplish this adjustment.

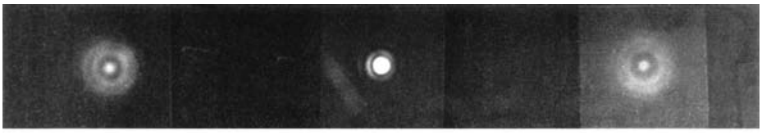

Below focus In focus Above focus

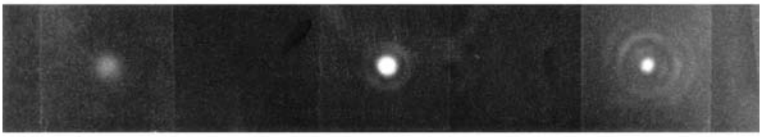

Below focus In focus Above focus

FIGURE 5.49 Appearances of artificial star images observed below, at, and above focus while adjusting spacing of a typical microscope objective. (a) Components correctly adjusted, out-of-focus ring details nearly identical; (b) components incorrectly spaced, ring structure visible above focus, but not below. (Adapted from Benford, J. R., Microscope objectives, in *Applied Optics and Optical Engineering*, Academic Press, New York, 1965.)

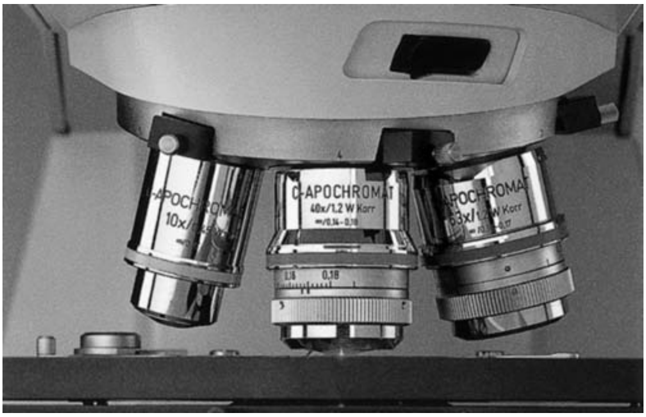

FIGURE 5.50 A microscope objective with a correction collar used to adjust internal lens spacing for different cover glass thicknesses. (Courtesy of Carl Zess MicroImaging, Inc., Thornwood, NY.)

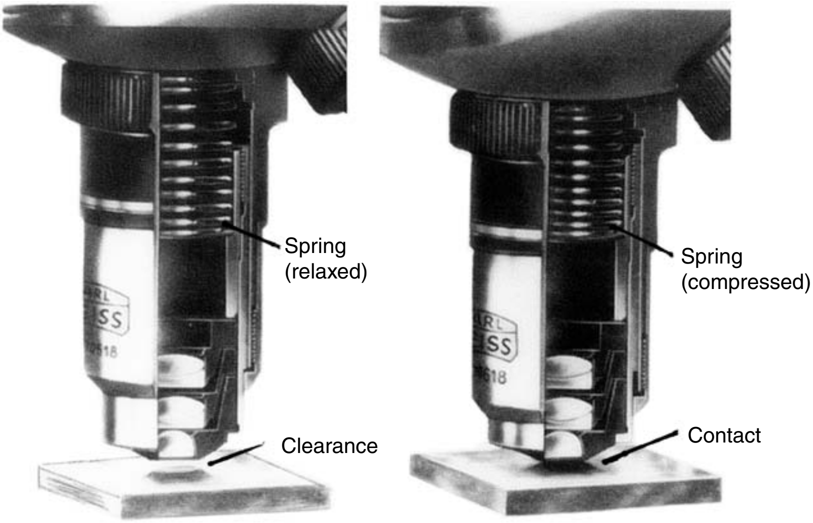

FIGURE 5.51 Resilient mount used to protect the specimen and the front of microscope objective if accidentally contacted during focusing. (Adapted from Benford, J. R., Microscope objectives, in *Applied Optics and Optical Engineering*, Academic Press, New York, 1965.)

Some objectives have resilient mounts to protect both the specimen and front of the objective from damage if they are accidentally brought into contact during focusing. Figure 5.51 shows an example with an internal coil spring to allow the inner subassembly to retract. Benford (1965) pointed out that such mechanisms must be designed and built to provide a very fine sliding fit so that the objective can retract without undue frictional resistance and yet hold its centration well on returning to the position of use. Some objectives, particularly those intended for oil immersion use, can be locked in the retracted position. This helps prevent contamination of the specimen with oil when the microscope objective turret nosepiece is turned.

Reflecting objectives for microscopes are generally simpler than their refractive counterparts since they consist only of two mirrors in the Schwarzschild configuration. Figure 5.52 illustrates a typical (generic) opto-mechanical design. The set-screws pressing against the conical surface of the

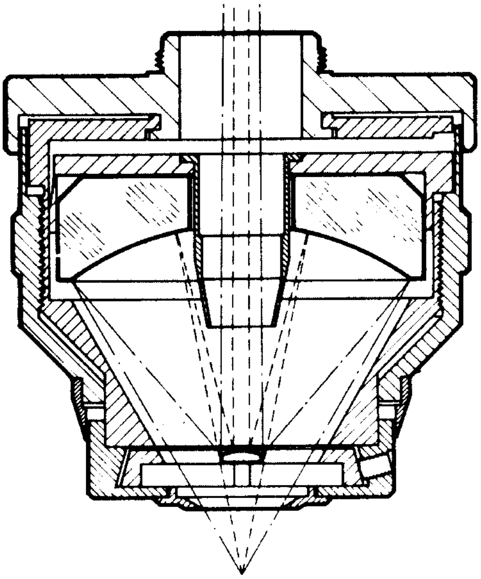

FIGURE 5.52 Opto-mechanical construction of a reflecting microscope objective.

secondary mirror cell are used to adjust the centration of that short-focal-length element to optimize performance. Although normally designed for use without cover glasses over the sample, more complex mechanical designs feature a graduated external (knurled ring) adjustment of axial spacing of the mirrors to compensate (within limits) for cover plate thickness.

5.7 ASSEMBLIES USING PLASTIC PARTS

Opto-mechanical assemblies using plastic lenses, cells, retaining means, and structures have become important parts of a large variety of the world's consumer products, as well as a smaller number of military and space applications. A few examples are camera viewfinders and objectives, magnifiers, television projection systems, compact disc readers, and helmet-mounted night-vision goggles. In this section, we outline some of the principles of design for such opto-mechanical assemblies and provide examples taken from the literature.

As mentioned in Section 4.11, mounting features can be easily incorporated into the optics themselves. Cells and housings can also be configured to minimize the number of parts as well as assembly labor, and to allow the use of mechanical fasteners, adhesives, or heat sealing. As an example, Figure 5.53 shows an air-spaced triplet objective of about 9 cm (3.5 in.) focal length designed and manufactured by U.S. Precision Lens, Inc. (Cincinnati, OH*) for use in a projection television system. It is labeled as a *Delta 20* design and is used to operate at a fixed relative aperture of *f*/1.2 with a nominal magnification of 9.3 ×. Dimensions of the assembly are 104.5 mm (4.11 in.) length, including the focus motion, and 117 mm (4.61 in.) diameter, not including the mounting flanges.

The three lenses are mounted in a longitudinally split (i.e., separately molded), two-part plastic mount that has integral axial locating tabs (acting as shoulders) and radial locating tabs. These tabs are sufficiently flexible to allow for slight variations in lens ODs and mount IDs occurring during the molding process. This type of mounting, sometimes called a "clamshell" mounting, is shown schematically in Figure 5.54 (Betinsky and Welham, 1979). The mount material is thermally similar to the lens

---

*Now 3M Precision Optics, Inc.

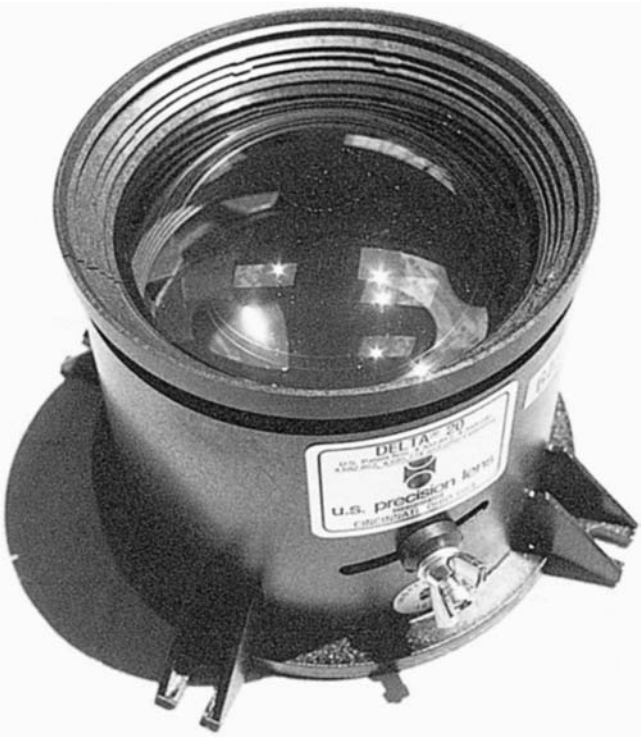
DELTA 20
u.s. precision lens

FIGURE 5.53 Photograph of an all-plastic television projection lens assembly manufactured by U.S. Precision Lens, Inc. (now 3M Precision Optics, Inc., Cincinnati, OH) (From Yoder, P. R., Jr., *Mounting Optics in Optical Instruments*, SPIE Press, Bellingham, WA, 2002.)

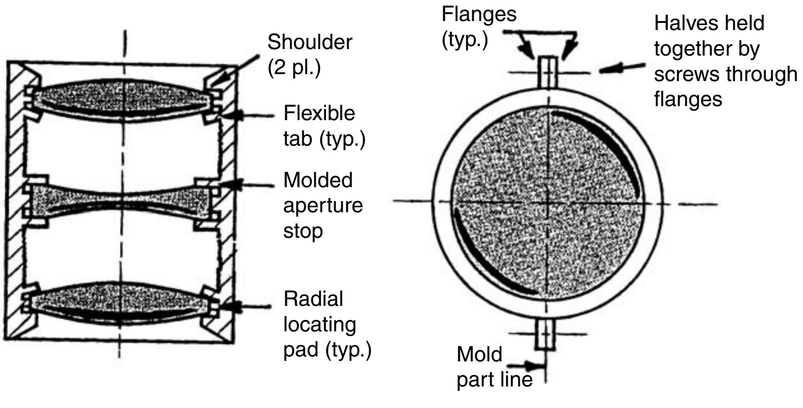
Shoulder (2 pl.)
Flexible tab (typ.)
Molded aperture stop
Radial locating pad (typ.)
Flanges (typ.)
Halves held together by screws through flanges
Mold part line

FIGURE 5.54 Schematic side and end views of the clamshell all-plastic lens mounting. (Adapted from a *The Handbook of Plastic Optics*, U.S. Precision Lens, Inc., Cincinnati, OH, 1983.)

material. The two halves of the mount are symmetrical, allowing them to be cemented or taped together after the lenses are installed. Other mounts of this type are manufactured so that the two halves can be fastened together with self-tapping screws, by sliding an outer sleeve over the assembly with slight interference fit (see Figure 5.55), or by heat sealing. Adhesives are not always suitable because their solvents can attack the plastic lens surfaces.

Figure 5.56 shows photographs of the interior of the assembly of Figure 5.53. View (a) has one half of the mount removed while view (b) has two of the lenses removed. Molded-in lens locating

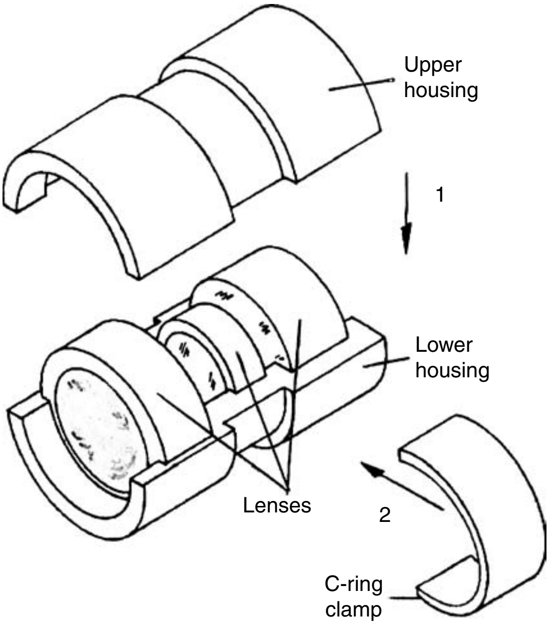

FIGURE 5.55 A technique for clamping housings of an all-plastic clamshell lens assembly using a slip-on C-ring. (From Lytle, J. D. Polymeric Optics, in *OSA Handbook of Optics*, McGraw-Hill, New York, 1995.)

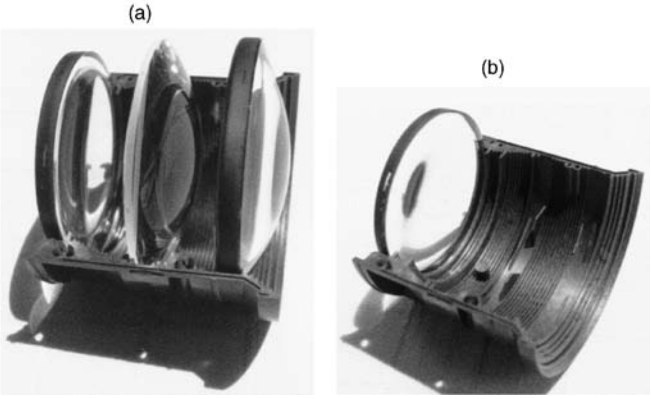

FIGURE 5.56 Photographs of the interior of the lens assembly shown in Figure 5.53. View (a) has half the cell removed and view (b) has two lenses removed. Details of lens locating features and some stray light reducing grooves are shown. (From Yoder, P. R., Jr., *Mounting Optics in Optical Instruments*, SPIE Press, Bellingham, WA, 2002.)

features and stray light reducing grooves can be seen here. The mount halves are assembled with self-tapping screws; holes for two such screws are visible in the figure (in the shadows). The assembled lens cell fits snugly into the ID of an outer housing and is focused by sliding axially when rotated about the axis. Two screws passing through a helical cam slot molded into the housing wall at diametrically opposite locations translate the rotary motion into the axial motion. Wing nuts on one or both of these screws allow the adjustment to be clamped after focusing has been accomplished. The housing is designed to be attached to the structure of the television set by screws passing through three mounting ears, two of which are visible in Figure 5.53.

Some projection lens assemblies of opto-mechanical design similar to the ones just described have an additional cam and cam-follower mechanism in the lens cell to allow the internal spacing of the lenses to be modified so as to change the system's focal length and, hence, the magnification.

Horne (1972) described the 35-mm slide projector objective lens assembly shown in Figure 5.57 as one designed to minimize cost. The housing is molded of plastic and has coarse integral threads for focusing. The lenses are separated by plastic spacers and held in place by a plastic retaining ring. Lens spacings and centering to high accuracy are not essential to the function of this assembly. The illumination system, shown schematically on the left in the figure comprises optics molded from heat-resistant glass (such as pyrex). These optics are constrained with spring clips to allow for dimensional changes with temperature.

Estelle (1979) compared a variety of all-glass, all-plastic, and hybrid (i.e., glass and plastic) designs for the 26-mm (1.02-in.) focal length *f*/1.9 objective for the Kodak EKTRAMAX camera. He indicated that the combination of a glass element with acrylic lenses could, in combination with plastic housing, produce a lens with zero shift in back focal length with temperature. With the glass lens located in front, the internal plastic elements are protected from some adverse environmental conditions.

5.8 LIQUID COUPLING OF LENSES

As pointed out at the end of Section 5.5, cementing of lenses made of glasses with widely differing CTEs using conventional optical cements in the usual very thin layers can cause problems at low temperatures. In the design of the lens assembly described in Section 5.5, a relatively thick layer of a transparent elastomer was employed to obtain greater joint flexibility, thereby avoiding the problem. Another approach to this problem is to couple lenses with thin layers of fluids. This technique is worthy of special consideration here.

Mast et al. (1999) described a camera objective lens assembly for the Deep Imaging Multi-Object Spectrograph (DEIMOS) used in the Keck II Telescope on Mauna Kea in Hawaii. As shown in Figure 5.58, this lens has nine elements made of six different materials. Three elements are CaF_2 with a CTE much larger than those of the other glasses. These elements also are more fragile than the glasses. The largest lens has a diameter of about 13 in. (330 mm) so temperature-induced dimensional changes are significant.

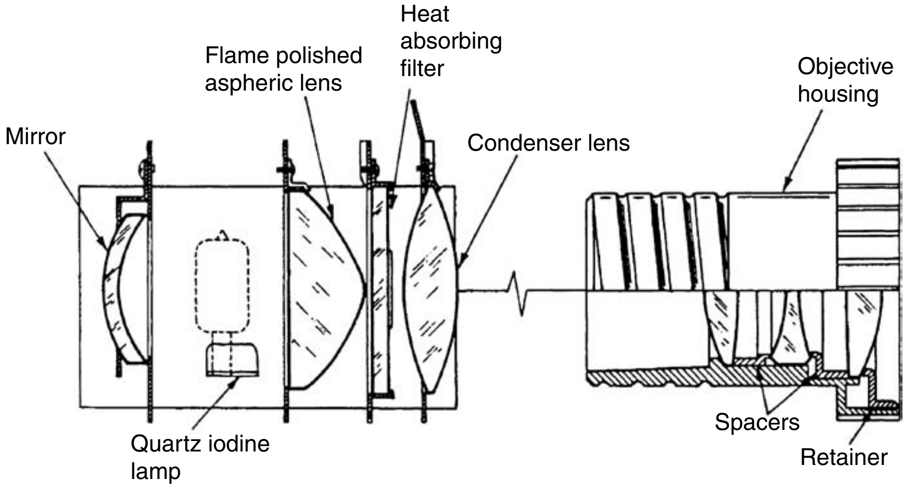

FIGURE 5.57 Schematic diagram of a 35-mm slide projector optical system featuring an objective with lenses, housing, spacers, and retaining ring made of plastic. The illuminating system also is shown. (Adapted from Horne, D. F., *Optical Production Technology*, Adam Hilger Ltd., Bristol, England, 1972.)

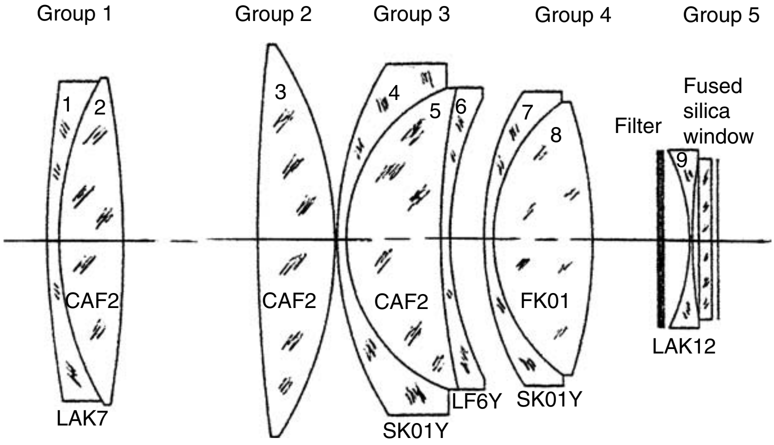

FIGURE 5.58 Optical system for the DEIMOS spectrograph camera lens. (Adapted from Mast, T. et al., *Proc. SPIE*, 3786, 499, 1999.)

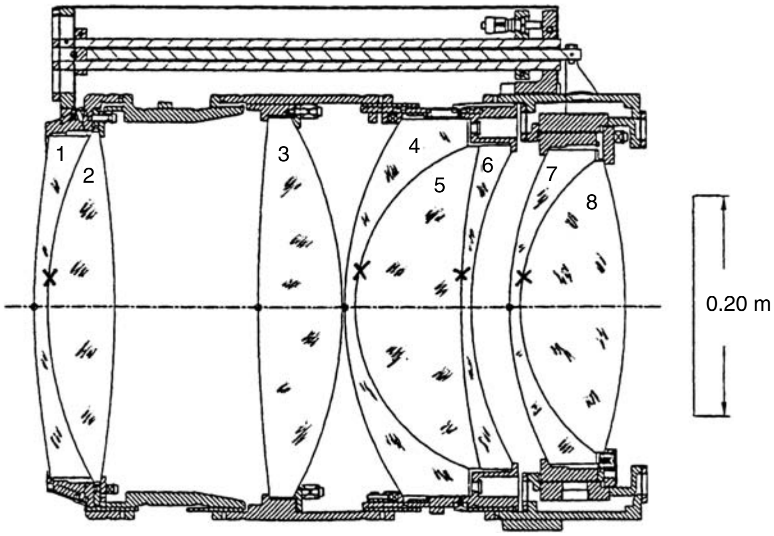

FIGURE 5.59 Opto-mechanical design layout for the DEIMOS camera assembly. (Adapted from Mast, T. et al., *Proc. SPIE*, 3786, 499, 1999.)

Figure 5.59 shows the opto-mechanical design for the DEIMOS lens. The barrel contains several 303 CRES segments with spacers to establish the required axial separations of the lenses. All lenses are mounted in ring-shaped CRES cells. The field flattener (lens 9) and the fused silica window are part of a separate detector assembly. The filter is also separately mounted. The elements within each multiple-element subassembly are held axially between a Mylar shim on a shoulder in a barrel segment and a spring-loaded Delrin retaining ring. Separation of the closely adjacent elements is by means of an annular shim at the periphery. The cavities thus formed between elements 1 and 2, 4 and 5, 5 and 6, and 7 and 8 are filled with an appropriate fluid. Each of these interfaces is identified with an "x" in the figure. The cavities are 0.077 to 0.152 mm (0.003 to 0.006 in.) thick on axis. The first and last elements in each multiple-element subassembly are bonded into their cell with GE-560 elastomer. These bonds support those elements and provide dams to contain the coupling fluid.

According to Hilyard et al. (1999), the required characteristics of the fluid for this application are: high light transmission from 0.38 to 1.10 μm; minimal Fresnel losses at the fluid–glass interfaces; and low reactivity with the glasses, CaF_2, the RTV sealant, and the O-ring seals. In addition, the following characteristics are desirable: low viscosity (to allow wicking into cracks that might develop in the CaF_2 material after assembly), low density (to minimize hydrostatic distortion of the lens elements, especially element 6, which is thin), and low CTE.

It was necessary in this design to provide fluid flow in and out of the cavities in Groups 1, 3, and 4 so they are vented to bladders to accommodate the specified survival temperature excursion (−20 to 30°C). Experiments reported by Hilyard et al. (1999) formed the basis for choice of Cargille LL1074 fluid,[†] 0.25 mm (0.010 in.) thick ether-based polyethylene film for the bladders, Viton VO763-60 or VO834-70 for O-ring fluid constraints, and Mylar for the shims. The bladders are heat sealed to avoid the use of adhesives.

5.9 CATADIOPTRIC ASSEMBLIES

A *catadioptric* optical system is one in which both refracting and reflecting components contribute to the optical power of the assembly. Usually, these are configured as variations of classical reflecting (i.e., catoptric) systems such as the Newtonian or Cassegrainian telescope, with refractive (i.e., dioptric) optics added to improve performance. The combined systems generally work at significantly faster relative apertures, are shorter, and cover larger fields of view than their corresponding reflecting versions. In this section, we consider opto-mechanical design aspects of several, widely different types of catadioptric systems ranging in physical size from a handheld camera objective to telecameras with long focal lengths used for missile tracking.

A "solid" catadioptric lens designed as a compact, durable, environmentally stable, telephoto objective for 35 mm single-lens reflex cameras is shown in Figure 5.60(a). As indicated in Rayces et al. (1970), the principle behind this design was, in effect, to fill the space between the primary and secondary mirrors of a Cassegrain system with useful glass. Image quality was maximized while the optical elements were closely coupled mechanically; their wide rims had large area contact with the internal bore of the lens housing to help maintain alignment in spite of vibration or shock. The assembly's total length was kept short to alleviate the need for critical parts to be supported over the long tube lengths that typically occur in lenses with a long focal length.

Several versions of this lens were manufactured, some by Perkin-Elmer Corporation and others by Vivitar. The one shown in the optical schematic diagram of Figure 5.60(b) had a focal length of 1200 mm (47.244 in.), a relative aperture of *f*/11.8 at infinity focus, and covered a 24 × 36 mm film format (semifield = 1.03°). The fifth through tenth elements served as field lenses for aberration correction and lengthened the back focal length and equivalent focal length in the manner of a Barlow lens.[‡] The system did not have an iris, so variations in lighting conditions were compensated for by exposure variations or by filtering. The filter located following the last lens was easily interchanged for this purpose.

Figure 5.61 shows an exploded view of the optical and mechanical parts of a typical solid catadioptric lens. The focusing mechanism causes the large elements to move axially with respect to the smaller elements and mounting flange. Travel of the moving elements is about 0.75 in. (19 mm) to change the focus from infinity to a 23 ft (7 m) object distance. A precision 14-lead Acme thread is used on the mating parts to provide this motion with a convenient rotation of the focusing sleeve of about one-third turn.

Tolerances on the mechanical dimensions of all components were controlled so that the optics could be inserted into the cells without resorting to lathe assembly techniques. Although not

---

[†] A Siloxane product of R.P. Cargille Laboraories, Cedar Grove, NJ.

[‡] The Barlow lens is defined by Morris (1992) as a "lens system used in telescopes, in which one or more strongly negatively powered lens elements are used to increase the effective focal length and thereby increase the magnification"

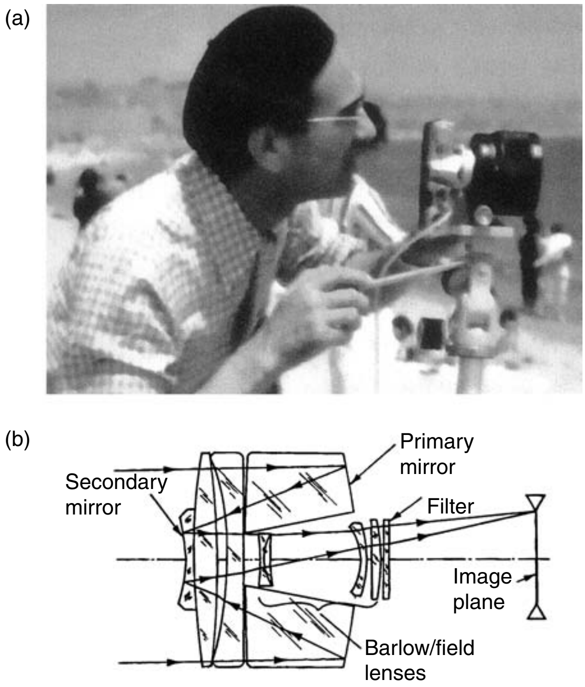
(a)
(b)
Primary mirror
Secondary mirror
Filter
Image plane
Barlow/field lenses

FIGURE 5.60 Photograph of an early model of a Solid Catadioptric Lens being tested on a 35-mm camera by its inventor in 1975. (Courtesy of Juan L. Rayces.) (b) Optical schematic of a solid catadioptric lens. (Courtesy of Goodrich Corp., Danbury, CT.)

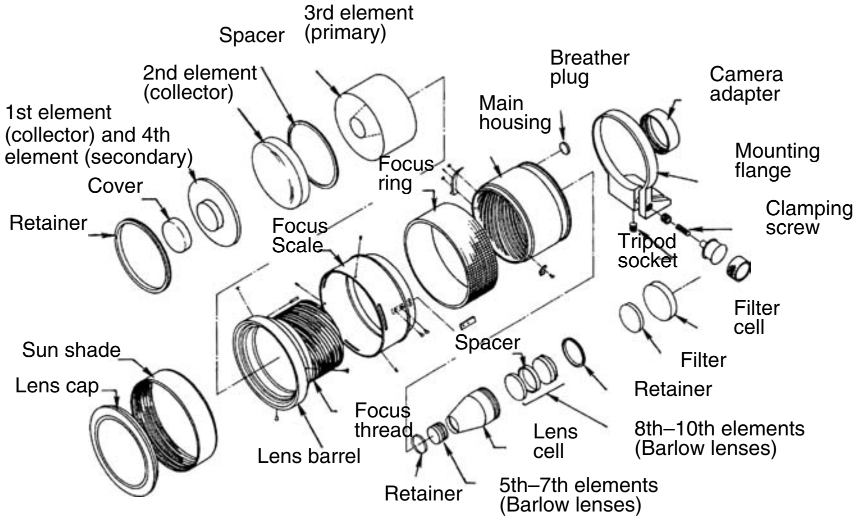
3rd element (primary)
Spacer
2nd element (collector)
1st element (collector) and 4th element (secondary)
Cover
Retainer
Breather plug
Camera adapter
Main housing
Mounting flange
Focus ring
Clamping screw
Focus Scale
Tripod socket
Filter cell
Filter
Sun shade
Spacer
Lens cap
Retainer
Focus thread
Lens cell
8th–10th elements (Barlow lenses)
Lens barrel
Retainer
5th–7th elements (Barlow lenses)

FIGURE 5.61 Exploded view of the solid catadioptric lens shown in Figure 5.60. (Courtesy of Goodrich Corp., Danbury, CT.)

specifically illustrated, light baffles were built into the lens to minimize stray light at the film plane.

A catadioptric lens developed for use as a space-borne star sensor in a spacecraft attitude-monitoring role (see Cassidy, 1982) is shown in Figure 5.62. This was a prototype design having a

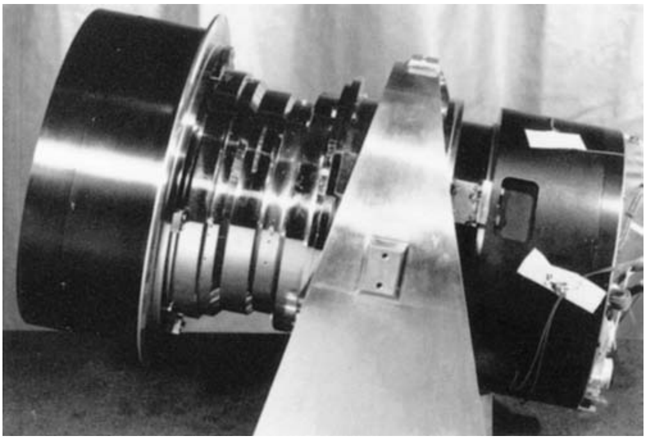

FIGURE 5.62 Prototype of a spacecraft attitude star sensor combining a fast catadioptric lens with a multi-detector focal plane array. (From Cassidy, L. W., *Digest of Papers, AIAA/SPIE/OSA Symposium, Technology for Space Astrophysics Conference: The Next 30 Years*, Danbury, CT, 1982. With permission.)

focal length of 10 in. (254 mm), a relative aperture of *f*/1.5, a field of view of ±2.8°, and a multi-element charge-transfer device as a detector. The aspheric design of this lens was discussed by Bystricky and Yoder (1985). Yoder (1986) discussed the mechanical details of the assembly.

From the opto-mechanical schematic of this assembly (Figure 5.63), it can be recognized as a derivative of the Cassegrain form with the secondary mirror coated directly on the inner surface of the second large-aperture refracting element. The infinity focal plane is located approximately 1.4 in. (36 mm) beyond the last vertex of the second field lens. This is a convenient distance for interfacing with the thermoelectrically cooled detector array.

The two larger lenses in this assembly are provided with precision annular flats that interface with shoulders in their Invar housing. They are preloaded axially with springs. The centering of these elements is adjusted at assembly by means of radially directed setscrews (not shown) threaded through the housing wall and bearing against the rims of the lenses. An elastomer (RTV-60) is then injected through 12 access holes into the annular space between the lenses and the housing. After curing, the setscrews are removed and the vacant holes sealed.

The convex back surface of the meniscus-shaped, front-surfaced, spherical primary mirror is referenced against concave, spherically ground seats in the rear cell. A retaining flange constrains the mirror by pressing against a flat annulus outside its clear aperture (see Figure 5.64). The mirror is also secured with RTV-60. The dimensions given in the figure indicate that the preload from the flange is applied at a different height from the constraint at the spherical seat centered at the arrow. In Section 15.5, we show how such an interface might bend the optic thereby introducing tensile stress and distorting the optical surface. In this case, the mirror is sufficiently stiff so that the stress and distortion resulting from this height mismatch neither threaten the survivability of the mirror nor degrade the performance of the system.

The field lenses (shown in Figure 5.43) are lathe-assembled into a cell (shown in Figure 5.42) and secured with a threaded retaining ring. The subassembly is centered to the optical axis at assembly. A custom-ground spacer between the cell flange and rear housing determines the axial spacing. Once aligned, the subassembly is pinned in place.

The detector subassembly, including the focal plane array, heat sink, thermoelectric cooler, and electronics, is supported from the main lens assembly by flexure blades, as indicated in Figure 5.63. Custom-ground spacers at each flexure attachment point fix the axial location of the array.

Figure 5.65 is a photograph of a 557-mm (21.9-in.) focal length, *f*/2.3 catadioptric lens designed to operate in the 8 to 12 μm spectral region. It is shown mounted on a tripod. The

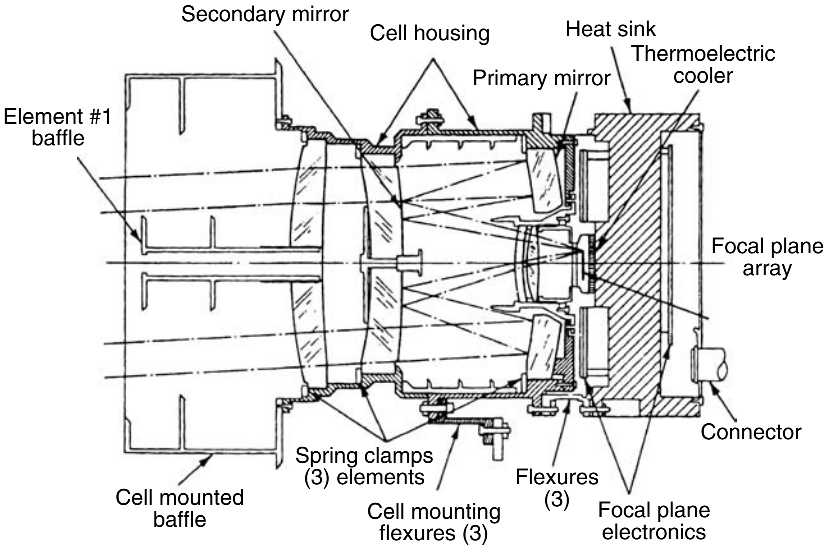
Secondary mirror
Cell housing
Heat sink
Thermoelectric cooler
Primary mirror
Element #1 baffle
Focal plane array
Connector
Spring clamps (3) elements
Flexures (3)
Cell mounted baffle
Cell mounting flexures (3)
Focal plane electronics

FIGURE 5.63 Opto-mechanical schematic of the star sensor shown in Figure 5.62. (Adapted from Cassidy, L. W., *Digest of Papers, AIAA/SPIE/OSA Symposium, Technology for Space Conference The Next 30 Years*, Danbury, CT, 1982.)

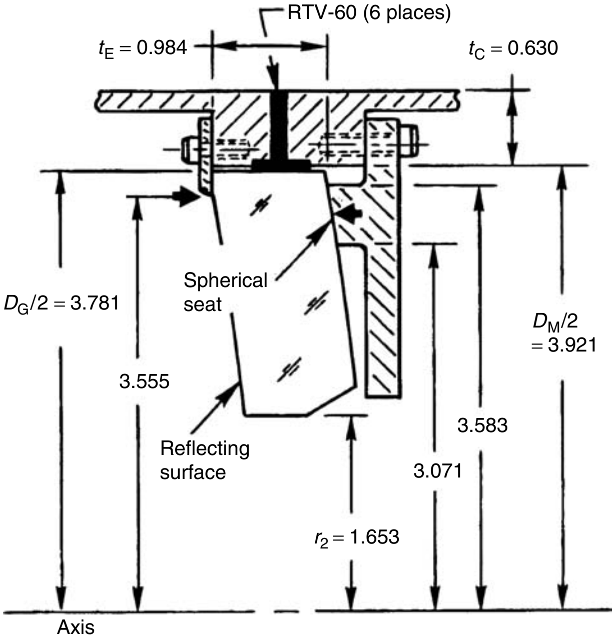
RTV-60 (6 places)
$t_E = 0.984$
$t_C = 0.630$
$D_G/2 = 3.781$
Spherical seat
3.555
Reflecting surface
$D_M/2 = 3.921$
3.583
3.071
$r_2 = 1.653$
Axis

FIGURE 5.64 Schematic diagram of the mounting for the spherical meniscus primary mirror used in the star-mapper lens assembly. Dimensions are given in inches. (From Yoder, P. R., Jr., *Mounting Optics in Optical Instruments*, SPIE Press, Bellingham, WA, 2002.)

rectangular object at the rear of the assembly is an infrared camera. The following description is from Yoder (2002).

Figure 5.66 shows the front and sectional side views of the lens. The mirrors and mechanical parts are made of 6061-T6 aluminum, while the field lenses are germanium. All optical surfaces and the

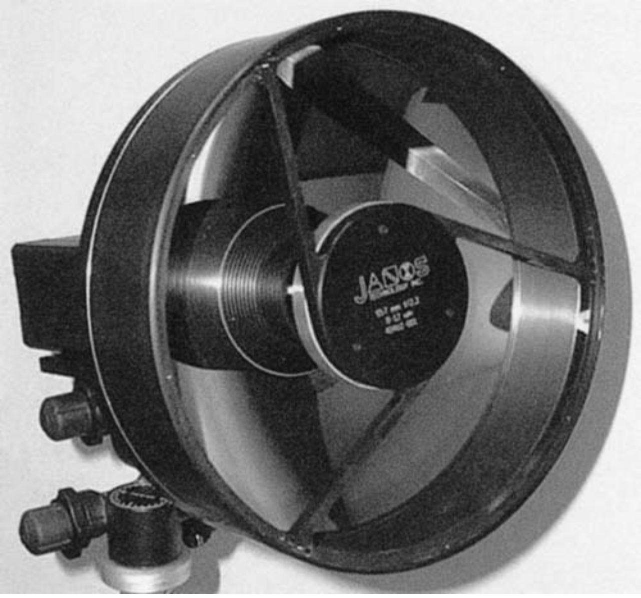

FIGURE 5.65 Photograph of a 557 mm (21.93 in.) focal length, *f*/2.3 catadioptric lens assembly with aluminum mirrors and structure. (Courtesy of Janos Technology, Inc., Keene, NH.)

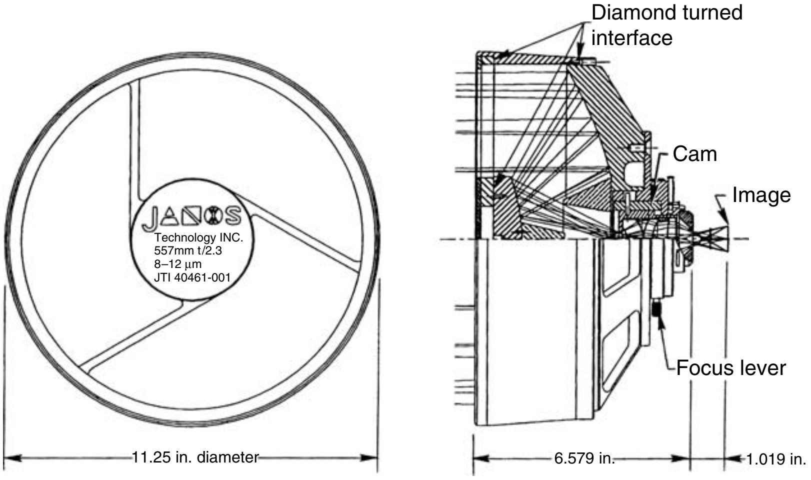

FIGURE 5.66 Front and side sectional views of the catadioptric lens assembly from the preceding figure. (Courtesy of Janos Technology, Inc., Keene, NH.)

opto-mechanical interfaces of this assembly are single-point diamond turned for highest alignment accuracy. Pockets are milled into the back of the primary mirror to reduce weight. The reflecting surfaces are coated with silicon monoxide to protect them during cleaning. Their reflectivities are greater than 98% in the 8 to 14 μm spectral range and the surfaces are adequately smooth for the application.

No adjustments for axial locations or optical component tilts are needed. Centering of the secondary mirror is accomplished in an interferometer (before installing the refractive components). Wavefront error is measured in the same test setup to ensure that the mirrors are not distorted. The lenses are held in place with RTV655. Internal baffles suppress stray light. The lens assembly is focused for various object distances by manual actuation of a helical cam that drives the lenses axially.

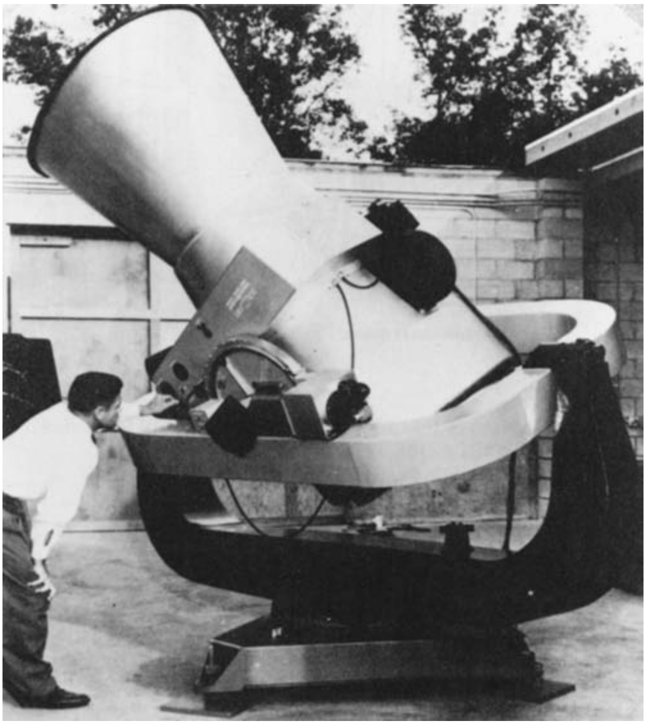

FIGURE 5.67 One of the first Satrack cameras shown at the Boller and Chivens plant in Pasadena, CA, during final checkout. (Courtesy of Goodrich Corp., Danbury CT.)

A classic example of a large-aperture, wide field of view, catadioptric objective is the Baker–Nunn "Satrack" camera shown in Figure 5.67. Developed in the mid-1950s to photograph orbiting satellites, the optical design is an enhancement of the Schmidt system. Both the aperture and focal length of the objective are 20 in. (50.8 cm), so it operates at *f*/l. To prevent vignetting at the edges of the field, the spherical primary mirror is about 31 in. (79 cm) in diameter.

A half-section plan view and a half-section elevation view of the camera are shown in Figure 5.68(a) and (b). The aperture stop of the system is very close to the center of curvature of the primary mirror, but the single correcting plate, which is normally located there in a Schmidt telescope, is split into a triplet for the purpose of eliminating the small amount of residual axial color in the single Schmidt plate. The four inner surfaces of this triplet are aspheric. The glass used in the central plate of the triplet is different from that used in the outer plates. This feature, and the distribution of Schmidt curvature among the four surfaces, tend to optimize performance.

The film is transported over a cylindrically curved platen that matches the curved focal plane of the image. The curvature in the plane at right angles to film motion must necessarily be zero because of the mechanical impossibility of bending the moving film into a compound curve. Consequently, the field coverage in this direction is limited to only 5°. In the direction of film travel, it reaches the amazing value of 31°. At the edges of this extreme field, the focal surface departs slightly from a spherical shape, and the film platen is slightly aspherical. The combination of careful design (optics by James G. Baker and mechanics by Joseph Nunn) and excellent execution during manufacture (optics by Perkin-Elmer Corp. and mechanics and assembly by Boller and Chivens Co.) resulted in a system wherein 80% of the energy from a point object anywhere in the field is concentrated within a circle 0.25 mm (0.001 in.) in diameter.

The Satrack cameras were conceived for the purpose of tracking the U.S. Vanguard satellites and later U.S. space missions. The first operational instrument was available just in time to take the

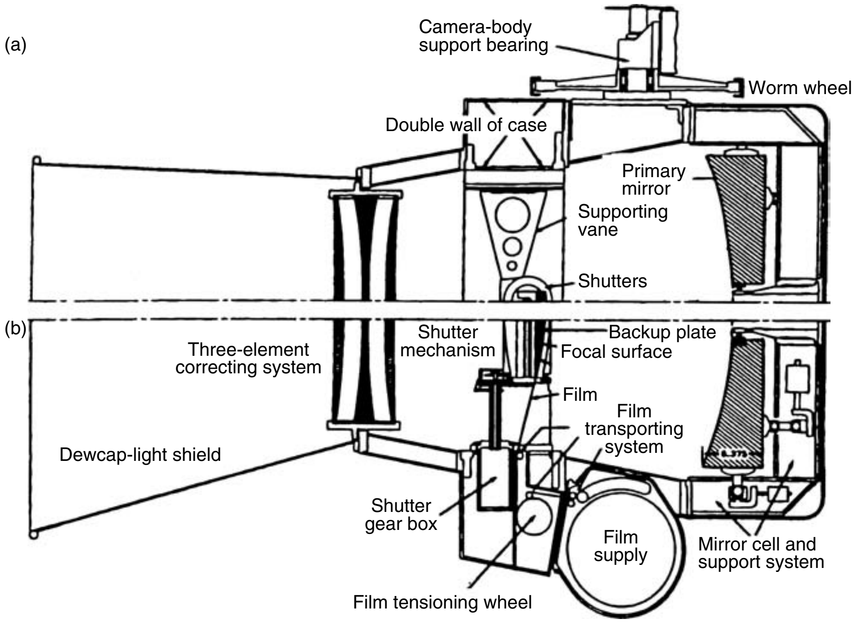
(a)
Camera-body support bearing
Worm wheel
Double wall of case
Primary mirror
Supporting vane
Shutters
(b)
Shutter mechanism
Backup plate
Focal surface
Three-element correcting system
Film
Film transporting system
Dewcap-light shield
Shutter gear box
Film supply
Mirror cell and support system
Film tensioning wheel

FIGURE 5.68 Half-section views of the Satrack camera assembly. (a) plan view; (b) elevation view. (Adapted from MIL-HDBK-141, *Optical Design*, Defense Supply Agency, Washington, DC, 1962.)

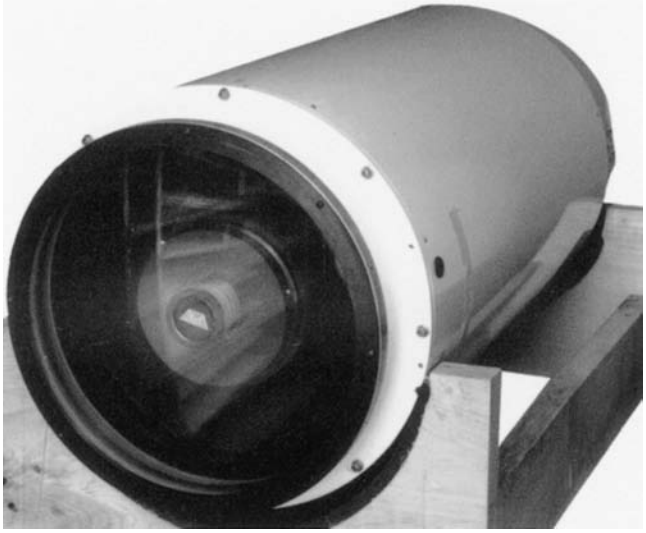

FIGURE 5.69 Photograph of a 150 in. (3.8 m) focal length, *f*/10 catadioptric missile-tracking camera objective. (Courtesy of Goodrich Corp., Danbury, CT.)

first photographs of the U.S.S.R.'s Sputnik I just 23 d after it was launched (Fahy, 1987). Many of these instruments were located at strategically selected points around the Earth and served for many years to photograph a variety of orbiting satellites.

A simpler catadioptric photographic objective is shown in Figure 5.69. This had a focal length of 150 in. (3.8 m), an aperture of 15 in. (38.1 cm), and operated at *f*/10. It was developed for use with a 70-mm Mitchell motion picture camera to photograph military missiles during launch at the

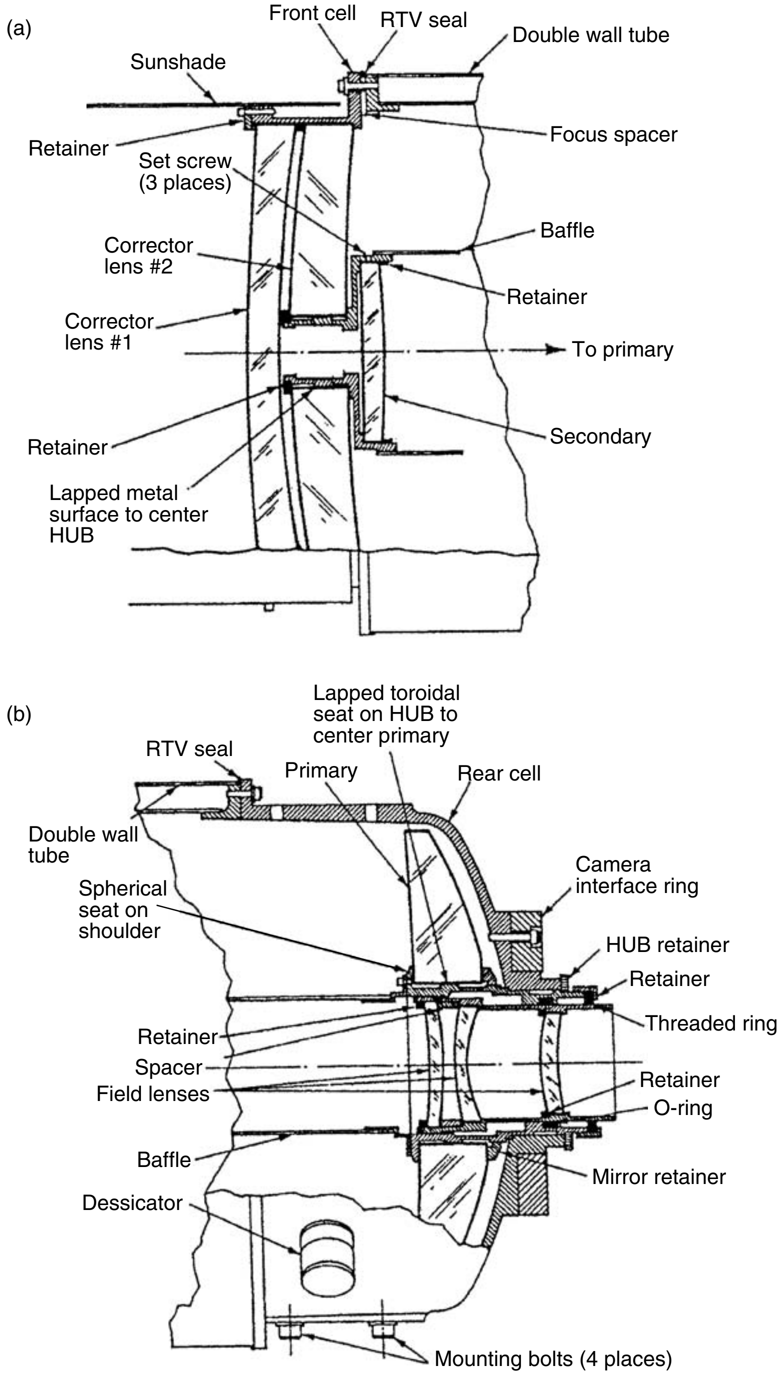
(a)
Front cell
RTV seal
Double wall tube
Sunshade
Retainer
Focus spacer
Set screw (3 places)
Baffle
Corrector lens #2
Retainer
Corrector lens #1
To primary
Retainer
Secondary
Lapped metal surface to center HUB
(b)
Lapped toroidal seat on HUB to center primary
RTV seal
Primary
Rear cell
Double wall tube
Camera interface ring
Spherical seat on shoulder
HUB retainer
Retainer
Retainer
Threaded ring
Spacer
Field lenses
Retainer
O-ring
Baffle
Mirror retainer
Dessicator
Mounting bolts (4 places)

FIGURE 5.70 Sectional views of (a) the front cell portion and (b) the rear cell portion of the catadioptric lens shown in Figure 5.69. (Courtesy of Goodrich Corp., Danbury, CT.)

U.S. Army's White Sands Proving Ground in New Mexico. The lens was mounted on a mount capable of scanning rapidly in azimuth and elevation through large angles.

Figures 5.70(a) and (b) show sectional views of the front and rear portions of the assembly. Basically, a Cassegrainian objective with two large refracting elements near the primary mirror's center of curvature and an air-spaced triplet field lens group, this assembly provided a flat field image over a ± 0.6° field of view. Mechanically, the assembly consisted of front and rear cells (castings) holding the corrector lenses/secondary mirror and the primary mirror/field lenses, respectively. The mounting interface for the assembly was at the rear cell, as were the camera optical and mechanical interfaces. The front cell was supported from the rear cell by a dual-wall aluminum tube with internal thermal insulation. A tubular lens shade was provided at the entrance aperture. The assembly was painted white to reflect solar energy.

Figure 5.71(a) shows how the two larger lenses are separated by a spacer ring and clamped against a shoulder by a bolt-on flange ring. The glass-to-metal axial interfaces were padded locally with single or multiple layers of 0.001 in. (0.025 mm) thick Mylar tape. The required thickness of the layer at each point is determined at assembly by supporting the cell with its axis vertical on a precision spindle and measuring the runout of each lens near its rim as it was slowly rotated. Once centered and squared-on to the axis to the accuracy limit of this mechanical method and blocked with radial shims (not shown), the retainer was installed to hold the alignment. Because of the long radii on the spherical surfaces, the radial components of the axial clamping forces were very small. Hence, there was essentially no possibility for the lenses to self-center.

As shown in Figure 5.71(b), the secondary mirror cell was attached to the second corrector lens and the mirror was aligned in its cell to eliminate wobble of the mirror surface as the lens assembly

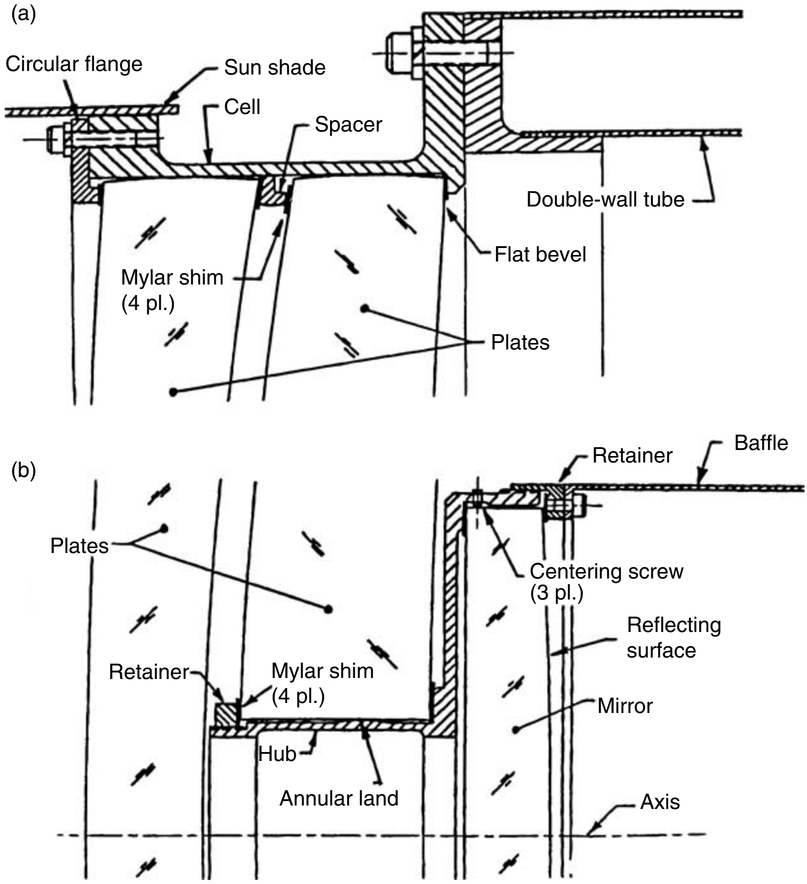

FIGURE 5.71 Schematics showing the use of multiple Mylar shims to pad the glass-to-metal interfaces in the front portion of the lens from Figure 5.70(a). (From Yoder, P. R., Jr., *Mounting Optics in Optical Instruments*, SPIE Press, Bellingham, WA, 2002. With permission.)

rotated on the spindle. Radial adjustment was by means of three setscrews pressing against the mirror's rim. Once properly centered, the mirror was blocked radially by Mylar shims (not shown) and clamped with the retainer.

In the rear cell, the primary mirror was center-mounted on a hub (see Figure 5.72[a]). The first (reflecting) surface of the mirror was seated against a convex, spherical seat of radius approximately matching the curved glass surface. A toroidal seat on the cylindrical hub was lapped to match the measured ID of the mirror perforation. A threaded retaining ring bearing against a precision flat on the back of the mirror held it in place axially with respect to the hub. The hub, in turn, was clamped in the central hole in the rear cell casting by a retaining ring. Mylar shims were used at all glass-to-metal interfaces.

Focus of the front and rear cells was accomplished as the tube subassembly was installed by inserting temporary shims of progressive thickness between the front cell and tube flange until the proper axial air space called for in the melt/axial-thickness recomputed optical design was established. The two cells were then aligned angularly by differentially varying the shim thicknesses to tilt the front cell slightly as required. No direct lateral adjustment means was provided, but the bolt clearance holes at the tube-to-cell interfaces were oversized so that centration could be achieved through successive approximations. Measurement of alignment error was by visual inspection of the image of an artificial star from a collimator using a microscope. Once adjustment was complete, permanent spacers of appropriate thicknesses were substituted for these shims.

The field lens assembly was lathe-assembled and then inserted into the hub in the rear cell. Axial location was measured mechanically and adjusted by rotating the threaded ring at the rear of the hub. When correct, the retainer was tightened. The assembly was then ready for a final photographic test.

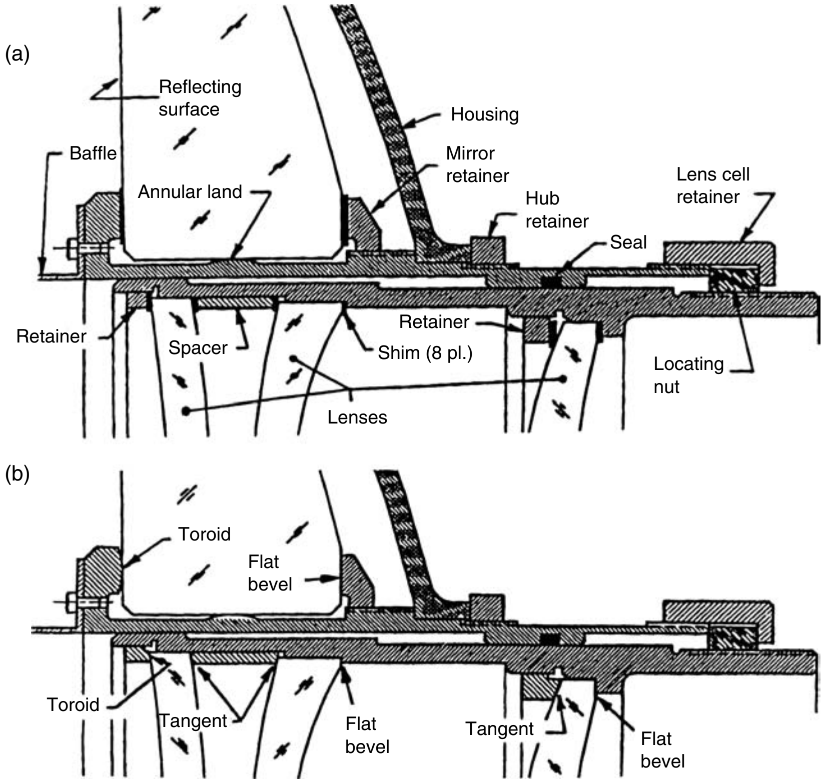

FIGURE 5.72 Schematics showing (a) the use of Mylar shims to pad the interfaces and (b) suggested alternative interfaces using techniques from Chapter 4 in the rear portion of the lens from Figure 5.70(b). (From Yoder, P. R., Jr., *Mounting Optics in Optical Instruments*, SPIE Press, Bellingham, 2002.)

A suggested alternative design for the primary mirror and field lens glass-to-metal interfaces is shown in Figure 5.72(b). No Mylar shims are used here; the interfaces are configured with tangential, toroidal, or flat surfaces, as discussed in Chapter 4. Similar direct interfaces without shims might be substituted in the mountings for the large corrector lenses and the secondary mirror.

5.10 ALIGNMENT OF MULTI-LENS ASSEMBLIES

In Section 4.10, we discussed four basic techniques for aligning single lens elements to their mounts, and some techniques for measuring the centration errors corrected during the alignment process. The same principles apply in the alignment of multiple lenses to a common axis in more complex designs. In most precision assemblies, the glass-to-metal interfaces are on the polished optical surfaces rather than on secondary (ground) surfaces. Figure 5.73, from Hopkins (1976), illustrates an extreme case of a triplet in which all lenses and spacers have wedge, the lens rims are not cylindrical, the spacers contact spherical surfaces, and those contacts are cut spherical to match the lenses or conical to ensure tangent contact. In spite of these errors, the lenses are aligned to a common optical axis. All that is needed to make this happen is a mount that provides the axial interfaces at the exposed surfaces of lens A and lens C, means to move the lenses laterally in the mount, and means for measuring errors. Hopkins also pointed out that although it is preferable that the spacers be round, this is not essential if the air spaces are measured and properly adjusted at assembly. This is not always convenient; in such cases we should strive for circularity of the spacers.

Figure 5.74 illustrates schematically a technique that has been used successfully in aligning multiple lenses to a common axis. The alignment telescope shown there is a commercially available device featuring a moveable relay lens with unusually large dynamic range so that the telescope can focus on targets at distances ranging from infinity to a location behind (i.e., to the left) of the objective lens. The focus mechanism is very accurately made so that the line of sight does not wander significantly as the focus distance varies. A typical alignment telescope is shown in Figure 5.75(a).

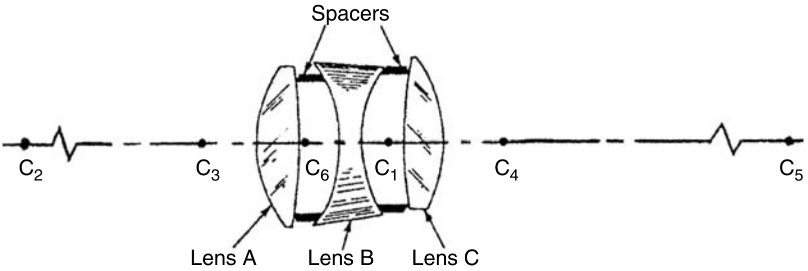

FIGURE 5.73 A triplet lens that is perfectly centered in spite of mechanical errors. (Adapted from Hopkins, R. E., *Opt. Eng.*, 15, 428, 1976.)

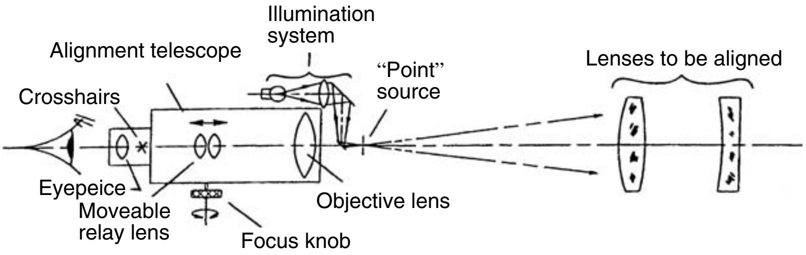

FIGURE 5.74 Schematic arrangement of an alignment telescope as it can be used to detect alignment errors of an air-spaced doublet.

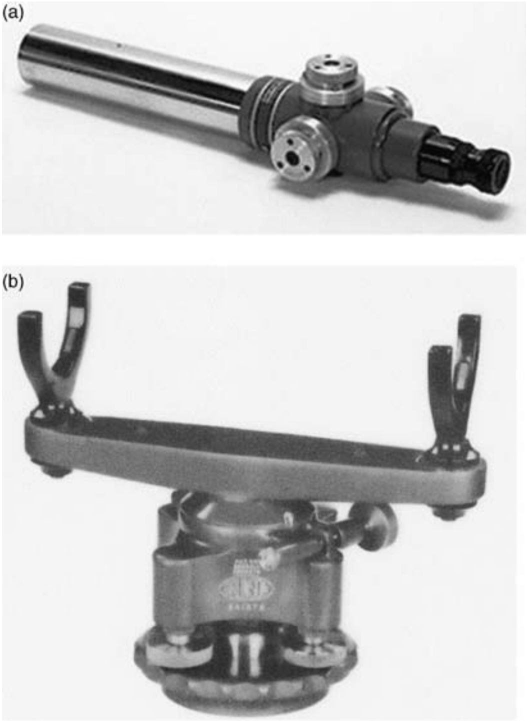

FIGURE 5.75 Photographs of (a) an alignment telescope and (b) an adjustable mount for the telescope. (Courtesy of Brunson Instrument Company, Kansas City, MO.)

It is mounted in an adjustable mount such as that shown in Figure 5.75(b). This mount provides orthogonal tilts in three axes to facilitate pointing of the telescope line of sight. Vertical and horizontal translations of the telescope also are provided by means not shown. For this instrument, image wander is smaller than 0.5 arcsec throughout the focus range. For the present application, the device is modified by adding an illumination system that creates a "point" source on the axis at the objective. This source illuminates the lenses to be aligned.

Figure 5.76 shows schematically (and not to scale) how the apparatus is used. In view (a), one ray from the beam incident upon the first lens is shown reflecting from R_1. The reflected ray appears to come from image 1 as it enters the alignment telescope. The telescope is focused on that image and tilted/translated so that the image is centered on the telescopes crosshairs. The lens system (lens 1 and lens 2 in the diagram) is then tilted so the image from R_2 seen when the telescope is refocused is also centered to the crosshairs (see view [b]). The telescope axis is then coincident with the axis of lens 1.

The focus of the telescope is then adjusted to image 3 from R_3, and the tilt and lateral location of lens 2 is adjusted independently from lens 1 so that image 3 is also on the crosshairs. This situation is shown in view (c). Finally, the focus is adjusted to image 4 and the orientation of lens 4 is refined so that the image appears centered to the crosshairs, as shown in view (d). If the focus is now changed to observe each image in turn, all should appear to be centered, indicating that the axis of lens 1 coincides with that of lens 2.

The simplest way to know which image comes from which surface is to raytrace the nominal (i.e., centered) system of lenses to be aligned, treating each surface in turn as a mirror and noting the sequence in which the images appear as the telescope focus is changed from infinity inward. In Figure 5.76, the right to left reflected image sequence is 1–4–2–3. Much more complex systems than that shown here can be aligned by this method. The use of a laser as the source may be necessary

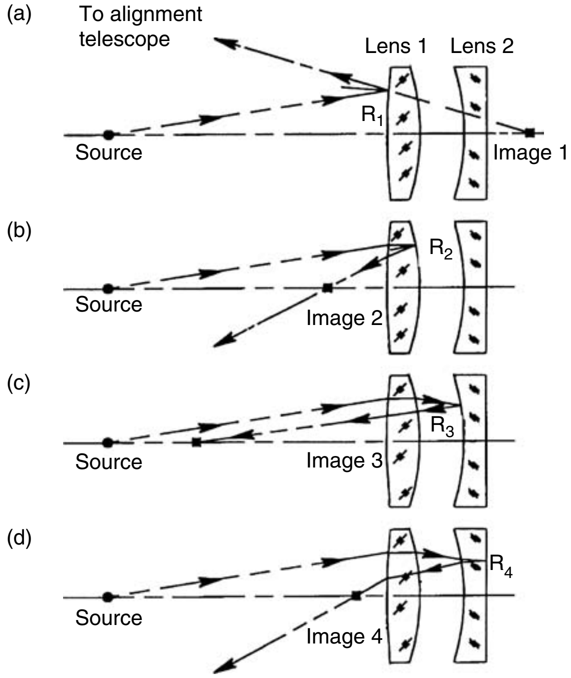

FIGURE 5.76 Schematic illustrations of the source and reflected images from lens surfaces during alignment using the apparatus of Figures 5.74 and 5.75.

if the Fresnel reflections from the various surfaces are dim because of the high efficiency of the antireflection coatings on those surfaces. Caution must be exercised to not exceed safety limits for laser beam intensity at the eye if that type of source is employed.

A higher precision technique for assembling a series of lens elements with nearly perfect centration was described by Carnell et al. (1974). Figure 5.77 is a simplified sectional view of the assembly, which was to be used as a wide-field (110°) objective lens for bubble-chamber photography. A large amount of optical distortion of a particular form was designed into the lens and was expected to appear very precisely (i.e., within a few micrometers of the design values) in the completed lens over the entire image.

The technique was to mount each lens individually in a brass cell that had been machined true by diamond turning on a precision air bearing. A rounded (0.25 mm, 0.010 in. radius) "knife-edge" seat (actually a toroidal interface) was turned inside each cell to contact the lens's spherical surface. All machining and lens assembly were completed before removing the cell from the spindle. As shown in Figure 5.78, centering was monitored by observing Fresnel interference fringes between the lens surfaces and a spherical test plate held close to the exposed surface of the lens. This test technique is the same as discussed in Section 4.10. Centration was judged to be correct when the fringe pattern appeared to remain stationary as the spindle was rotated slowly. This indicated that the rotating surface ran true to a centered sphere within a fraction of a wavelength of the laser beam used (typically, $\lambda = 0.63$ μm). The lens was then bonded to the cell with a room-temperature curing epoxy that remains slightly flexible when cured. An epoxy layer thickness of about 0.1 mm (0.004 in.) was reported to be satisfactory for the intended application. The individual cemented subassemblies were assembled into a precisely bored barrel. Upon evaluation, the authors reported that the system's centration errors did not exceed 1 μm (4×10^{-5} in.).

Variations of the last described technique for mounting lenses within subcells include designs in which each lens is burnished or epoxied in place. In some cases, the lenses are aligned to

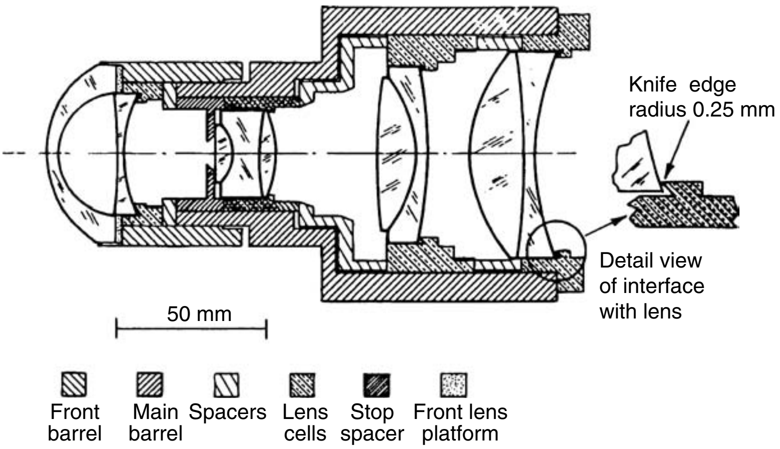
Knife edge
radius 0.25 mm
Detail view
of interface
with lens
50 mm
Front barrel
Main barrel
Spacers
Lens cells
Stop spacer
Front lens platform

FIGURE 5.77 Opto-mechanical configuration (simplified) of a lens assembly requiring very precise centration of several components. (Adapted from Carnell K. H. et al., *Opt. Acta,* 21, 615, 1974.)

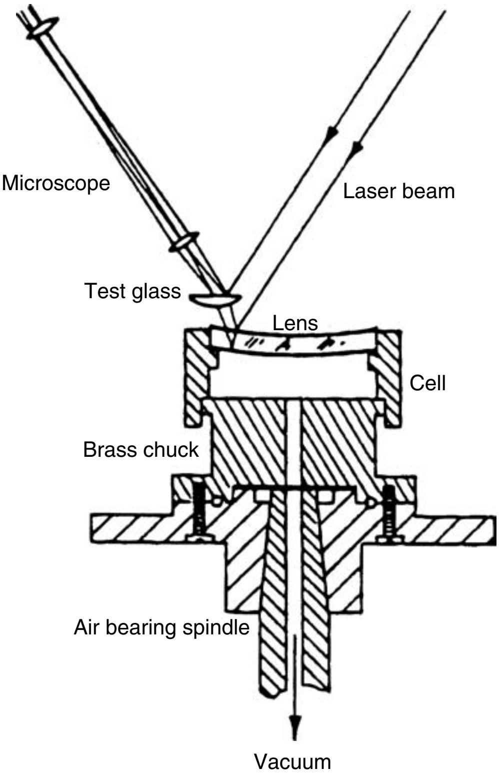
Microscope
Laser beam
Test glass
Lens
Cell
Brass chuck
Air bearing spindle
Vacuum

FIGURE 5.78 Instrumentation used to monitor centration of each optical surface in the assembly of Figure 5.77. (Adapted from Carnell K. H. et al., *Opt. Acta,* 21, 615, 1974.)

premachined cells; in other cases, the cylindrical outer surface of each cell is machined on a spindle to be concentric with and parallel to the optical axis of the lens after the lens is installed. The cell ODs are machined to the proper OD for insertion along with similarly machined subcells into a common barrel. Fabrication of lens/cell subassemblies using single point diamond turning

(SPDT) methods is described in Section 4.10. In a design by Daniel Vukobratovich (see Figure 5.19), subcells with prealigned and elastomerically supported lens components were press-fitted into a barrel with slight radial mechanical interference fits.

The assembly of lenses into individual cells facilitates performance optimization of the assembled product by fine transverse or axial adjustment of one or more lenses during the final stage of assembly. Figure. 5.79 shows an example of such an assembly in which the third element can be transversely adjusted with three screws to allow modification of its aberration contributions to compensate for residual aberrations of the optical system. When this technique is employed, the moveable lens must have sufficient sensitivity to the specific aberration to be compensated for so that reasonable movement produces the desired effect. On the other hand, it must not be too sensitive to this and other aberrations, for that would make the adjustment too critical. The choice of which element or elements to move is made by the lens designer during the tolerance analysis. In some lens assemblies, multiple components are chosen as "compensators," with each affecting one specific aberration more than others.

Williamson (1989) described one technique for selecting the appropriate compensator(s) and applied it to a typical high-performance, microlithographic projection lens. (see Figure 5.80). This

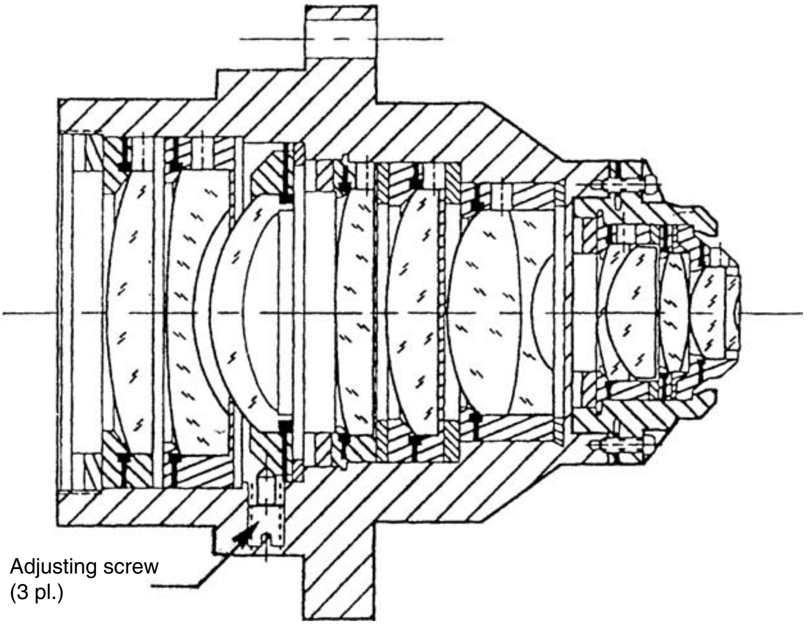

FIGURE 5.79 Sectional view of a lens assembly with one lens element acting as an aberration compensator for performance optimization by transverse adjustment during final assembly. (From Vukobratovich, D., Optomechanical systems design, in The Infrared & Electro-Optical Systems Handbook, Vol.4, ERIM, Ann Arbor and SPIE Press, Bellingham, 1993a.)

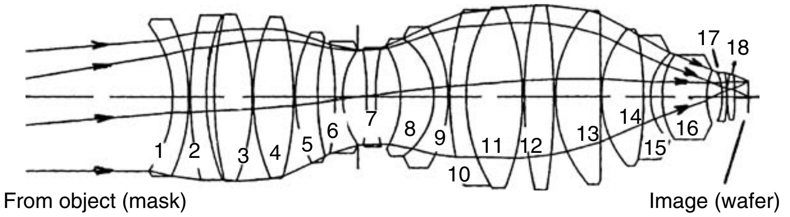

FIGURE 5.80 Optical schematic of a 5× reduction lens for a microlithography application. (From Williamson, D. M., *Proc. SPIE*, 1049, 178, 1989.)

lens, designed to be used at 5 × reduction, comprises 18 elements, has an image space numerical aperture of 0.42, and covers a 24 mm (0.944 in.) image field diameter. Compensation occurs in two stages: (1) recomputation of air spaces, radii, and clocking of elements before assembly to reduce the effects of minute measured residual errors on surface radii, element thicknesses, refractive indices, surface figure error, and surface irregularity; and (2) postassembly alignment optimization of the selected compensating element adjustments.

Williamson (1989) indicated that the fifth- and higher-order aberrations that are so carefully minimized during the design process are not strongly affected by small perturbations of lens element alignments. On the other hand, the third-order aberrations are significantly affected by these adjustments. Hence, the compensator selection process involves determination of sensitivities of each element for third-order spherical aberration, coma, astigmatism, and distortion as functions of axial, lateral, and clocking motions. These aberrations are expressed in terms of Zernike polynomial coefficients. The following are typical constraints applied in the selection process. Each compensator is limited to either an axial or a lateral displacement to reduce mechanical complexity. Preferably, the elements with largest diameters should not be selected as compensators, as the mechanism to affect the adjustments would tend to increase overall diameter. This parameter must usually be minimized in any practical assembly. To third-order, tilts and decentrations produce equivalent results, so only decentrations are considered. Finally, compensation must be accomplished without disassembly of the lens.

Figure 5.81(a) shows the results of the sensitivity analysis for individual element axial shifts of 25 μm. Elements 4, 7, 16, and 17 appear to be the best to correct coma, spherical aberration, astigmatism, and distortion respectively. Figure 5.81(b) shows similar results for element decentrations of 5 μm. If elements 5 and 6 are moved as a pair, then the coma changes of each add while the astigmatism contributions cancel and the distortion changes are opposite. Doublet 8–9 shows good orthogonality in that only astigmatism changes significantly when that lens subassembly is decentered. Doublet 14–15 would serve well to compensate distortion because it causes relatively little coma or astigmatism when decentered. From these results, the appropriate aberration compensators would be axial adjustment of element 7 for spherical and transverse motion of elements 5 and 6 moving together for coma, doublet 8–9 for astigmatism, and doublet 14–15 for distortion.

Successive iterations of the above axial and transverse adjustments except for the distortion compensator typically result in significant improvement of system performance as compared to that measured before alignment. Figure 5.82 shows the wavefront error results over the ±12 mm field in orthogonal directions for the lens system of Figure 5.80 expressed in terms of the rss of all Zernike coefficients, in waves at 633 nm wavelength, after tilt and defocus were removed. The design values are indicated as well as the measured values.

Williamson (1989) further indicated that after completion of the wavefront compensation, the distortion was measured by lithographic tests, the system was put back in the interferometer, and the distortion compensator was utilized to minimize that aberration. Finally, all compensators were used to reoptimize the wavefront errors. The measured residual distortion (shown by the lengths of the vectors at various points within the field) was then as indicated in Figure 5.83(a). The improvement over measured distortion performance before compensation (Figure 5.83[b]) is quite apparent.

A vital aspect of the aberration compensation technique is the availability of a suitable real-time means for measuring aberrations during the adjustment process. Figure 5.84 shows a generic test setup involving a lens barrel containing many lenses, three of which act as aberration compensators. These lenses are located at the axial locations indicated by "access holes." Orthogonal push rods driven by two micrometers penetrate such holes at each location to move each lens laterally by sliding its moveable lens/cell subassembly relative to all the others. A restoring force is exerted by a spring (not shown) acting through a third hole symmetrically located with respect to the movement of the micrometers in their plane of action. This allows the micrometers to operate essentially in a simple "push–pull" mode. Note that in some other alignment fixtures, piezoelectric actuators are used to provide the adjustment motions.

In the setup of Figure 5.84, the lens barrel is clamped to a “vee” block fixture that is in turn installed in an interferometer (not shown). Phase measuring interferometry is usually employed. The interferometer allows the effects of the movement of each lens on overall performance to be assessed. As mentioned earlier, optimization is accomplished by successive approximations. When the system’s performance is maximized, the moveable lenses are locked in place by some internal mechanisms (not shown) to preserve the alignment. The access holes are then sealed to keep moisture and dirt out.

To optimize the performance of some high-performance lens assemblies, including that of Figure 5.79, small movements of one or more lens/cell subassemblies in the axial direction are necessary in addition to lateral adjustments of other compensators. The use of threaded cells turning in mating threads in the barrel (similar to some objective or eyepiece focus adjustments) for axial positioning of the lens is not practical here because the threads are too coarse, even if they are designed to act differentially, and they may not be concentric with the axis. Furthermore, the cells must not be turned about their axes

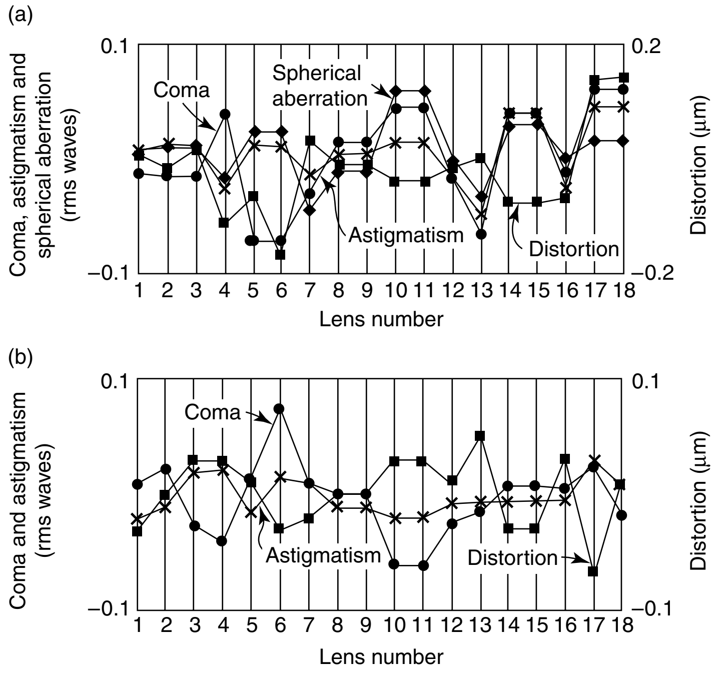

FIGURE 5.81 Effects on rms wavefront aberrations caused by (a) individual axial shifts of 25 μm magnitudes and (b) transverse shifts of 5 μm magnitudes for each element of the system of Figure 5.80. (Adapted from Williamson, D. M., *Proc. SPIE*, 1049, 178, 1989. With permission.)

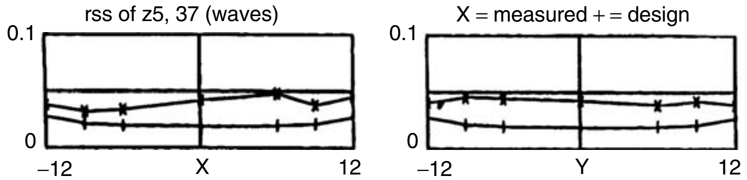

FIGURE 5.82 Design and measured rss values of all Zernike coefficients for the lens of Figure 5.80 over the ± 12 mm field in orthogonal meridians after compensation for wavefront aberrations. Tilt and focus errors have been removed. (From Williamson, D. M., *Proc. SPIE*, 1049, 178, 1989. With permission.)

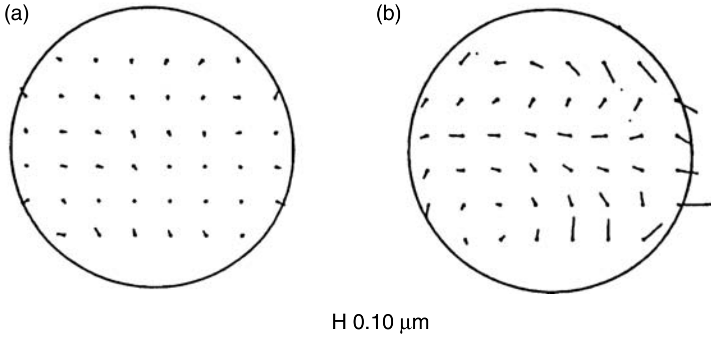

FIGURE 5.83 Measured residual distortion of the system of Figure 5.80 (a) after compensation and (b) before compensation. The lengths of the vectors indicate magnitudes of the localized aberrations. (From Williamson, D. M., *Proc. SPIE*, 1049, 178, 1989. With permission.)

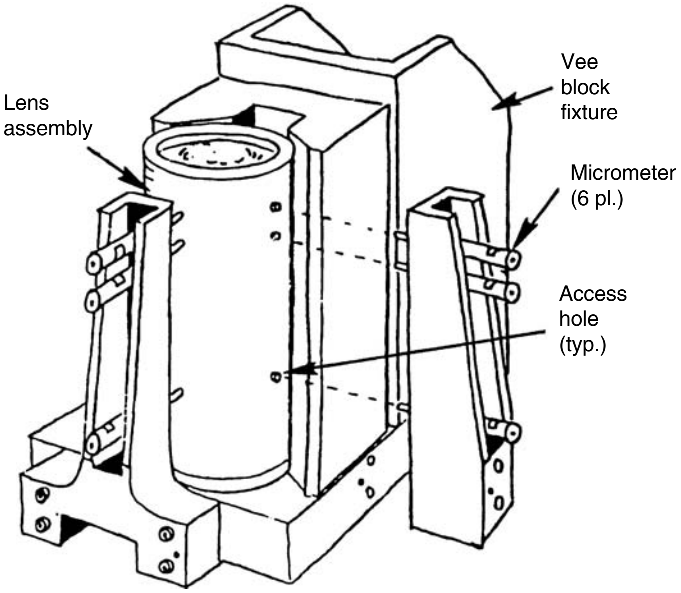

FIGURE 5.84 Schematic of a test fixture with a lens assembly in which three lenses are transversely adjustable for performance optimization. (From Yoder, P. R., Jr., *Mounting Optics in Optical Instruments*, SPIE Press, Bellingham, WA, 2002. With permission.)

during axial adjustment because residual wedge defects in the optical and mechanical components can then affect centration of the optics and increase aberrations.

Bacich (1988) described some mechanisms for making fine axial adjustments that are easily accessed from the outside of the lens barrel. Figure 5.85 shows two such mechanisms. In view (a), three balls distributed at 120° intervals slide in vertical holes in the lens cell and rest on cone-point setscrews penetrating the wall of the cell. Another lens cell (not shown) rests on top of the three balls. By accessing the screws through holes in the barrel wall and turning them by equal amounts, one can increase or decrease the air space between adjacent lenses by small amounts. In view (b), the same effect is obtained by setscrews driving into three wedged slots in the cell wall. Half-balls attached to the tops of the cantilevered wedges touch the next cell (not shown). In either case, when the cells are locked together axially, the adjustments are secured. The use of these adjustment means

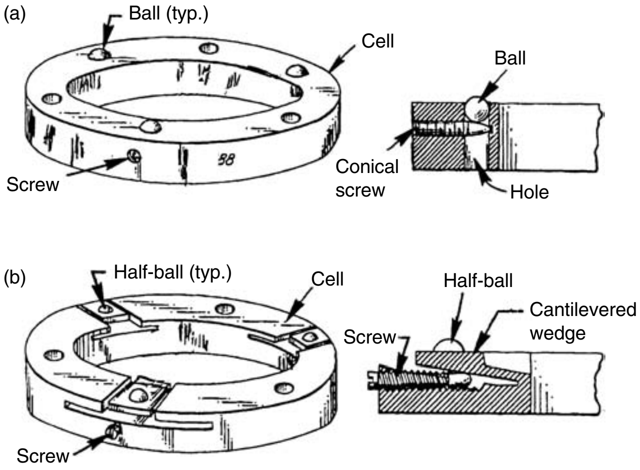

FIGURE 5.85 Typical mechanisms that can be used to adjust air spaces between adjacent lens/cell subassemblies. (Adapted from Bacich, J. J., U.S. Patent 4, 733, 945, 1988.)

to differentially tilt a lens is recommended only if the design does not require the cell rims to be aligned with each other.

Figure 5.86 shows another high-precision lens assembly. It is assembled and aligned in accordance with the fourth alignment technique described in Section 4.7. On the right side, one can clearly see the lenses. As shown on the left side of the figure, they are each attached to flexures machined integrally with their cells. The cells and the lens barrel are made of stainless steel, so there is a significant CTE mismatch between the lenses and the mechanical parts. Hence, the flexures are used to keep the lenses centered over a significant temperature range.

The lens elements are attached to the flexures with epoxy as shown in Figures 4.54(a) and (b). The cells are then diamond turned *in situ* as illustrated in Figure 4.65(b). The ODs of all but two cells are a few micrometers smaller than the ID of the barrel into which they are to be inserted. The two special cases are those for the third and fifth lenses from the top, which are transversely adjustable with radially directed screws, micrometers, or piezoelectric actuators to optimize performance at the final stage of alignment. The cell ODs are sufficiently undersized to allow the adjustments to be made. The adjustment mechanism is conceptually similar to that shown in Figure 4.60(b). A thick annular spacer is provided between the third and fourth lenses to determine the corresponding air space. Thin annular spacers (shims) of appropriate thicknesses (shown exaggerated in the figure) are located between the cells to allow those air spaces to be set within tolerances. These are made of the same material as the cells and barrel for thermal expansion compatibility.

Figure 5.87 illustrates an interferometric setup that might be used to monitor alignment of the lens assembly during adjustment of the two sliding lenses of Figure 5.86. Fringes formed in double-pass through the lens assembly between a reference flat surface and the retrodirective mirror are observed using a video camera located above the beamsplitter cube. The quality of the image is recorded after each iterative adjustment of the moveable lenses.

After the lens assembly's performance has been maximized, it can be clamped together using the means shown in Figure 5.88. Here, three rods pass through clearance holes in each cell and shim and thread into holes in the barrel's lower endplate. Nuts are attached to the upper threaded ends of the rods. By tightening the nuts, the rods are put in tension and clamp the cells together axially without disturbing centration because all interfacing pads on the cells are flat and perpendicular to the axis of the system.

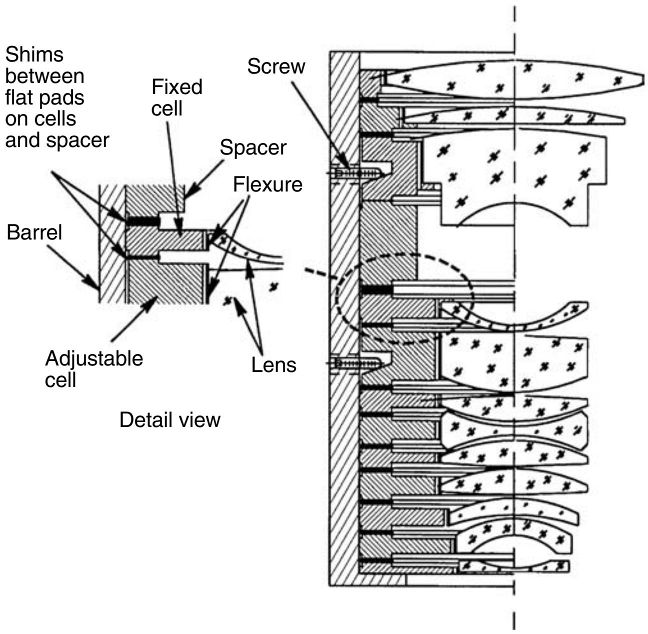

FIGURE 5.86 Schematic partial section view of a lens assembly with two laterally adjustable cells. The lenses are assembled and aligned in their cells and the cells machined precisely to fit the barrel ID. (From Yoder, P. R., Jr., *Mounting Optics in Optical Instruments*, SPIE Press, Bellingham, WA, 2002. With permission.)

Another concept for alignment and clamping together of lens/cell subassemblies is shown in Figure 5.89. Here, three cells with their lenses installed (but not depicted in the figure) are shown in exploded view. These cells are part of a stack of similar subassemblies that make up a complex lens assembly. Each cell has flat pads on its top and bottom faces. These pads are coplanar and parallel. Shims or spacers are used between the cell pads to establish axial spacings. Alternatively, the pads may contact each other to provide the proper air spaces between lens vertices when the cells are assembled into a stack. In the latter case, the heights of the pads would be carefully controlled. The lenses are flexure-mounted and aligned in the cells so that their optic axes are at the geometric centers of the cell ODs and perpendicular to the pad's faces.

The lower cell in Figure 5.89 has three rods pressed into or threaded into holes in the cell so as to be perpendicular to the plane defined by the pads on the cell's top surface. These rods protrude through clearance holes in the middle and top cells when they are brought together. During assembly, the lower cell acts as the reference and the middle cell is aligned by sliding it laterally until the optic axis of that second cell is collinear with that of the lower cell. This adjustment would be made on an air-bearing spindle using interferometric sensing of errors. When the adjustment is completed, the spaces between the rods and the holes in the upper cell are filled with epoxy and cured. The third cell is then placed on top and aligned in the same manner as the second. It too is epoxied in place. The same process could be followed to build a stack of all the lens cells in the assembly.

Figure 5.90 shows a schematic sectional view through a stack of 12 cells, each containing a lens or acting as a major spacer. Once precisely aligned to each other, they form a complete optical assembly. Two cells (5 and 10) are to be adjusted axially and radially to optimize the performance of the whole optical system. A test setup of the type shown in Figure 5.87 might be used. A fixture of the type shown in Figure 5.84 could provide a means for making the lateral adjustments. Custom-ground shims located between precision pads on the faces of the cells would be one means for adjusting the air spaces. These shims and pads are not shown in Figure 5.90.

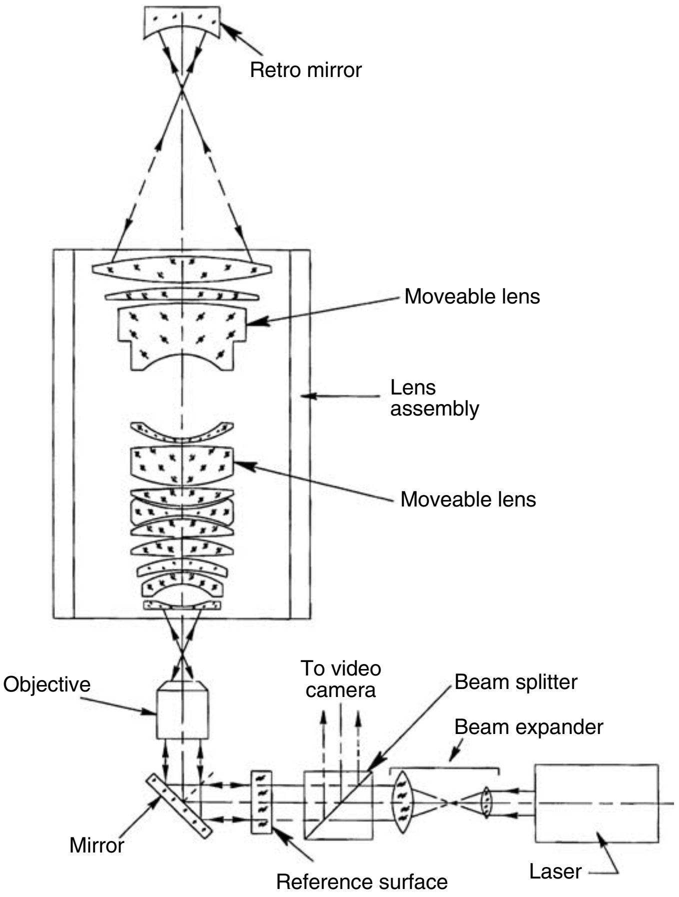

FIGURE 5.87 A test setup that might be used to evaluate the performance of an optical assembly during adjustment of laterally moveable aberration compensating lenses. (From Yoder, P. R., Jr., *Mounting Optics in Optical Instruments*, SPIE Press, Bellingham, WA, 2002. With permission.)

Mechanisms of the types shown in Figure 5.85 could be used in some other assemblies to provide the axial adjustment.

As may be noted from Figure 5.90, all cells except those to be adjusted are shown epoxied to the dowel rods that are firmly attached to cells 1, 2, 6, 7, and 11. At this stage during assembly, the non-adjustable components have already been aligned to a common axis and the adjacent air spaces corrected before the epoxy was inserted around the rods and cured. As shown, the assembly is ready for final positioning of the moveable cells and epoxying them to the rods. Once this is accomplished, the entire stack would be clamped together axially with tension rods as in Figure 5.74 or by some equivalent technique. A housing would then be added to enclose the assembly.

Sure et al. (2003) described some of the problems associated with assembly and alignment of high-power, high numerical aperture microscope objectives to be used in the UV at and below 248 nm wavelength in systems for inspection of state-of-the-art semiconductor chips and in other applications involving measurement at nanometer scale. Not the least of these problems are achieving the proper air spaces between lenses and assessing the performance of the system while adjusting positions of laterally adjustable elements. Because of the short wavelength and high photon energy of the transmitted beam, cemented lenses cannot be used in these objectives. Figure 5.91 shows a sectional view through a typical objective, the Leitz 150× DUV-AT with N.A. of 0.9. This objective has 17 air-spaced singlet lenses made of fused silica and calcium fluorite and is capable of resolving details

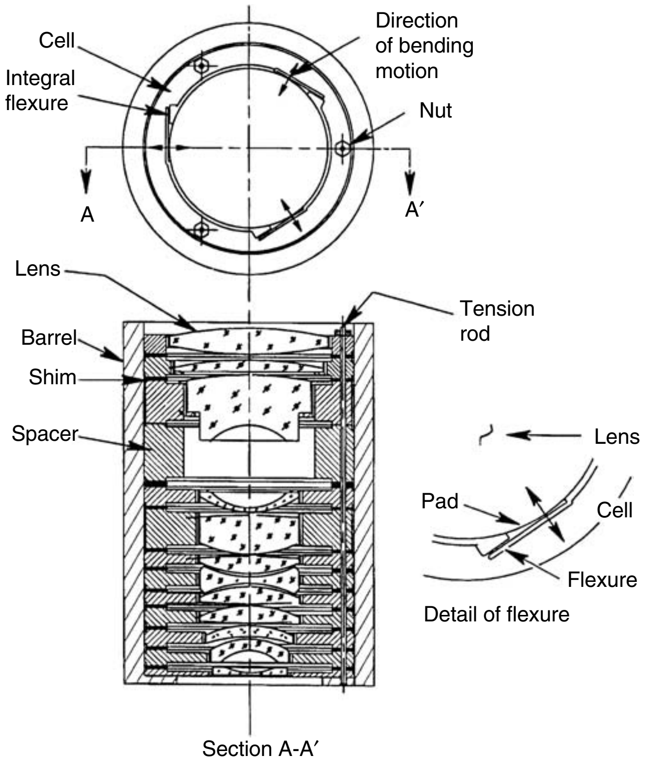
Cell
Integral flexure
Direction of bending motion
Nut
A
A′
Lens
Barrel
Shim
Spacer
Tension rod
Lens
Pad
Cell
Flexure
Detail of flexure
Section A-A′

FIGURE 5.88 Schematic of a means for axially clamping the lens cells in the assembly of Figure 5.86 after alignment is completed using tension rods at 120° intervals. Some details of the flexures are also shown. (From Yoder, P. R., Jr., *Mounting Optics in Optical Instruments*, SPIE Press, Bellingham, WA, 2002. With permission.)

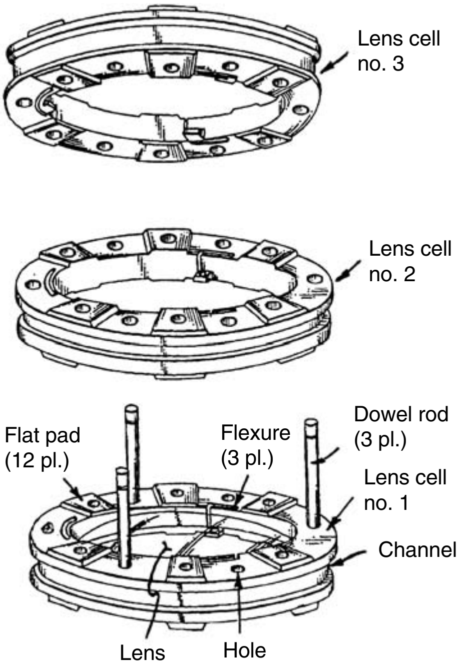
Lens cell no. 3
Lens cell no. 2
Flat pad (12 pl.)
Flexure (3 pl.)
Dowel rod (3 pl.)
Lens cell no. 1
Channel
Lens
Hole

FIGURE 5.89 Exploded view of three lens cells that illustrate a technique for affixing one cell to another by liquid pinning rods in clearance holes after alignment. (Adapted from Bacich, J. J., U.S. Patent 4,733,945,1988.)

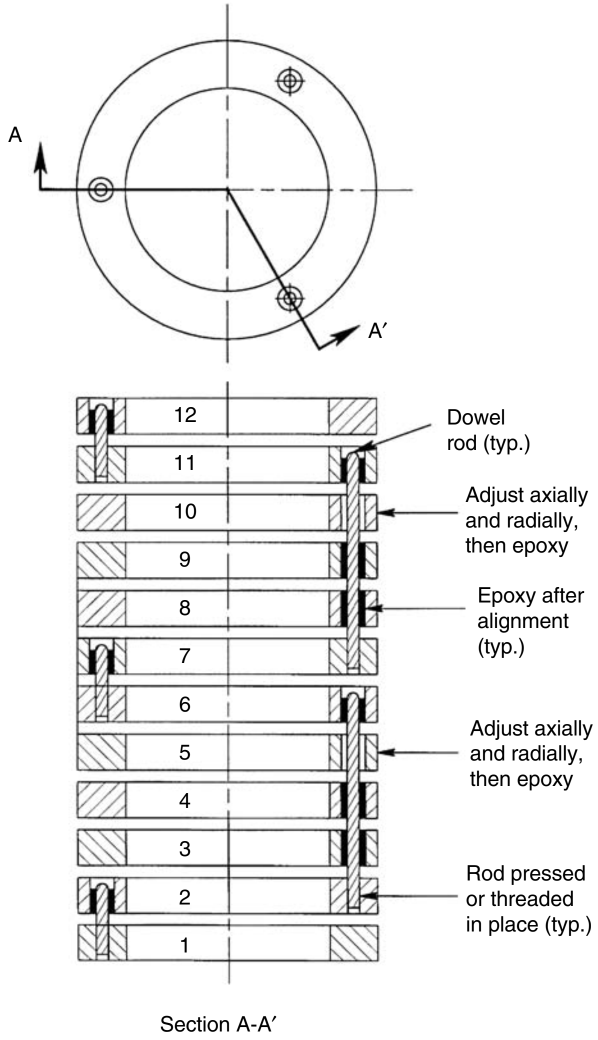
A
A′
12
11
10
9
8
7
6
5
4
3
2
1
Dowel rod (typ.)
Adjust axially and radially, then epoxy
Epoxy after alignment (typ.)
Adjust axially and radially, then epoxy
Rod pressed or threaded in place (typ.)
Section A-A′

FIGURE 5.90 Schematic of 12 lens cells stacked, aligned, and epoxied to dowel rods in preparation for final alignment of two adjustable cells. After alignment, those cells are epoxied in place on the rods. (Adapted from Bacich, J. J., U.S. Patent 4,733,945,1988.)

measuring 80–90 nm in an object. System Strehl ratios of > 0.95 and approaching 0.99 are needed. Obtaining this performance in production of this objective requires the application of special in-process inspection and alignment techniques. These are summarized in the following paragraphs.

The tolerances assigned to the design represented in Figure 5.91 are as indicated in the right-hand column of Table 5.2. Meeting the "limiting" tolerances entails great expense compared with the "typical" values applied to more common assemblies. In order to achieve $\pm\ 2\,\mu\text{m}$ maximum air-space thickness errors between elements, the location of each lens must be controlled with respect to its associated mechanical mount to $\pm\ 1\,\mu\text{m}$. Alignment of subassemblies is performed for the objective of Figure 5.91 using a Mirau interferometer as indicated in Figure 5.92. The location of the flat surface of the mount is determined by placing an optical flat on the annular knife edge and moving the interferometer so that its focus is on the flat surface. The flat is then removed and the lens subassembly to be measured is placed on the knife edge. The interferometer focus is readjusted to the vertex of the lens. Note that the interferometer can be tilted in two directions to ensure beam propagation along the lens' surface normal. The distance labeled "Δh" in the figure is then measured

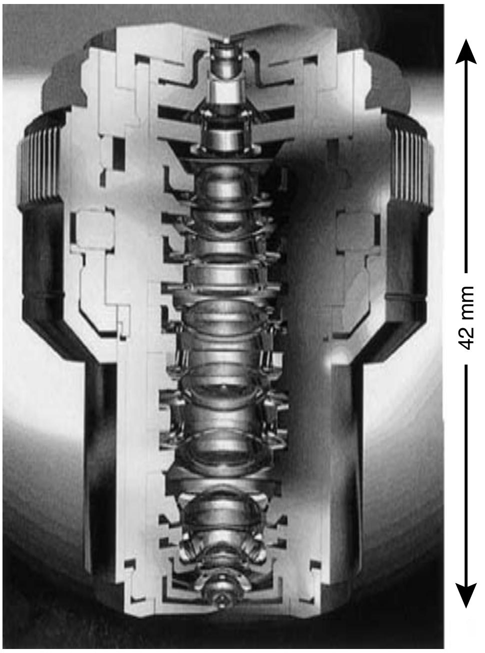

FIGURE 5.91 Cutaway sectional view of the Leitz 15 × DUV-AT microscope objective with N.A. of 0.9. (From Sure, T. et al., *Proc. SPIE*, 5180, 283, 2003. With permission.)

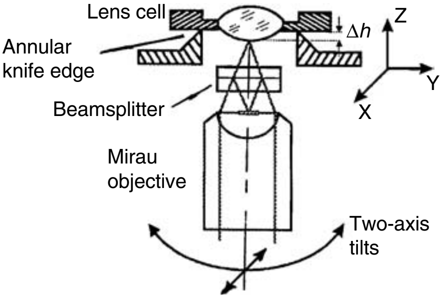

FIGURE 5.92 Schematic of a Mirau interferometer as used to determine the lens vertex-to-mount offset Δh to high precision. (From Sure, T. et al., *Proc. SPIE*, 5180, 283, 2003. With permission)

to an accuracy of ± 200 nm and compared to the design requirement. Subassemblies within tolerance are accepted for use in production of the objectives.

Wavefront error is monitored during adjustment of one or more laterally adjustable elements in a lens, such as that in Figure 5.91, using a more elegant version of the visual star test described in conjunction with the lens in Figure 5.48. Figure 5.93 shows this instrument schematically. With the reflection from the flat reference mirror obscured, the image formed by the imaging optics in a CCD camera can be observed directly and in real time on a video monitor at about 20 frames per second by the optician while the lens adjustment is accomplished. Wavefront errors such as coma, caused by the objective under test, result in asymmetry of the image. Once the image appears to be good visually, the reference beam can be allowed to interfere with the beam from the spherical reference mirror, and the point spread function (PSF) of the wavefront can be determined by Fast Fourier Transform methods from the fringe pattern. The technique

TABLE 5.2
Production Tolerances for High Performance UV Microscope Objective

For Each Lens	Typical	Limiting
Radius error	5λ[a]	0.5λ
Surface error	0.2λ	0.05λ
Surface roughness (rms) (nm)	5	0.5
Center thickness error (μm)	20	2
Refractive index error	2×10^{-4}	5×10^{-6}
Abbe number (%)	0.8	0.2
For the Assembly		
Decentration (μm)	5	2
Run-out (μm)	5	2
Fit of cell into housing (μm)[b]	10	2
Air space error (μm)	5	2

[a] All λ at 633 nm.

[b] Across diameter.

Source: Adapted from Sure, T. et al., *Proc. SPIE*, 5180, 283, 2003.

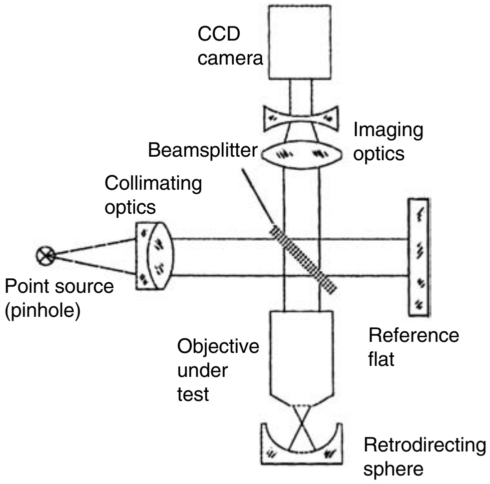

FIGURE 5.93 Sketch illustrating the principle of a Twyman–Green interferometer as used to measure performance of a microscope objective. (From Sure, T. et al., *Proc. SPIE*, 5180, 283, 2003. With permission.)

for doing this was summarized by Sure et al. (2003) and is discussed in more detail by Heil et al. (2005). In brief, a set of interferograms and the corresponding PSFs such as those shown in Figure 5.94 are interpreted as follows. The sequence of interferograms is recorded while the compensating element of the objective is moved to reduce coma. The initially observed ~2 fringes of coma (view [b]) are reduced to zero in view (j). Some residual higher order comatic wavefront error (trefoil) can be seen in view (j) because the lens under test is not perfect. The authors of this paper indicated that they chose this example because it demonstrates how the use of both fringe patterns and PSFs provide insight into the behavior of the test sample that is hard to gain from interferograms alone.

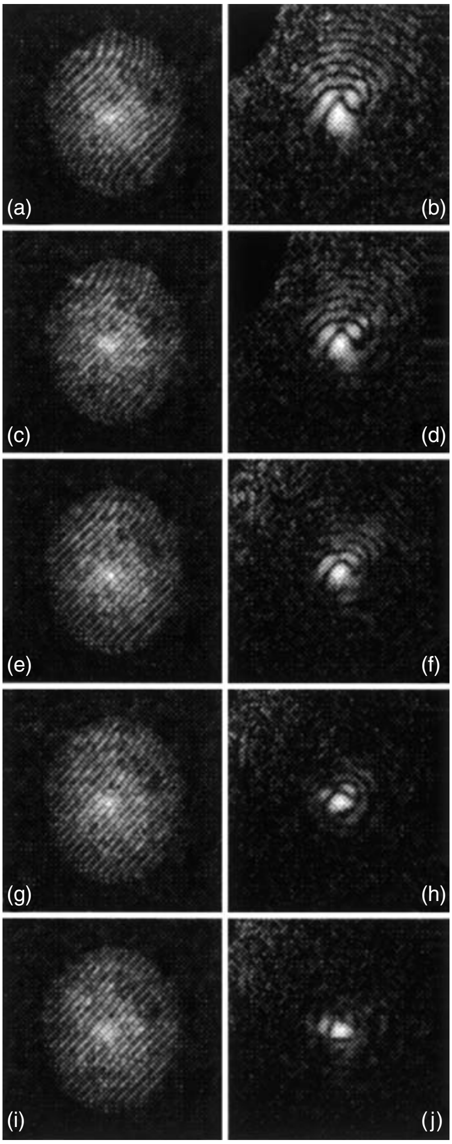

FIGURE 5.94 Interferograms (a), (c), (e), (g), and (i) and corresponding PSFs (b), (d), (f), and (j) for a Leitz 150 × DUV-AT microscope objective at $\lambda = 266$ nm recorded as the compensating element of the objective was adjusted. (From Sure, T. et al., *Proc. SPIE*, 5180, 283, 2003. With permission.)

5.11 ALIGNMENT OF REFLECTING TELESCOPE SYSTEMS

Much of what has just been presented with regard to techniques for aligning lens systems applies, in principle, to reflecting telescope systems as well. The need for centration of mirror surfaces to a common optical axis usually applies, especially if aspheric surfaces are included in the system. Space limitations prevent detailed discussion here of the techniques for measuring and correcting alignment errors in such systems. The interested reader would find useful information on this subject in Chapter 2 of Wilson (1999), where detailed instructions for aligning and testing Cassegrainian type telescopes are given. Much of that treatment can be extended to telescopes of Gregorian form. Also included in the same reference are guidelines for aligning Schmidt telescopes and field corrector lenses, and summaries of techniques for testing telescope systems and analyzing the images formed thereby. Another good source of information regarding alignment of optical systems in general and reflecting telescopes in particular may be found in Ruda (2004).

REFERENCES

Addis, E. C., Value engineering additives in optical sighting devices, *Proc. SPIE*, 389, 36, 1983.

Ashton, A., Zoom lens systems, *Proc. SPIE*, 163, 92, 1979.

Bacich, J. J., Precision Lens Mounting, U.S. Patent 4,733,945, 1988.

Bayar, M., Lens barrel optomechanical design principles, *Opt. Eng*., 20, 181, 1981.

Benford, J.R., Microscope objectives, in *Applied Optics and Optical Engineering*, Vol. III, Kingslake, R., Ed., Academic Press, New York, 1965, chap. 4.

Betensky, E. I. and Welham, B. H., Optical design and evaluation of large aspherical-surface plastic lenses, *Proc. SPIE*, 193, 78, 1979.

Bystricky, K. M. and Yoder, P. R., Jr., Catadioptric lens with aberrations balanced with an aspheric surface, *Appl. Opt*., 24, 1206, 1985.

Carnell, K. H., Kidger, M. J., Overill, A. J., Reader, R. W., Reavell, F. C., Welford, W. T., and Wynne, C. G., Some experiments on precision lens centering and mounting, *Opt. Acta* 21, 615, 1974.

Cassidy, L. W., Advanced stellar sensors — A new generation, in *Digest of Papers, AIAA/SPIE/OSA Symposium, Technology for Space Astrophysics Conference: The Next 30 Years*, Danbury, CT, 164, 1982.

Estelle, L. R., Design, performance and selection of Kodak's "EKTRAMAX" lens, *Proc. SPIE*, 193, 2, 1979.

Fahy, T. P., *Richard S. Perkin and The Perkin-Elmer Corporation*, The Perkin-Elmer Corp., Norwalk, CT, 1987.

Fischer, R. E., Case study of elastomeric lens mounts, *Proc. SPIE,* 1533, 27, 1991.

Gardam, A., The development of a compact far infra-red zoom telescope, *Proc. SPIE*, 518, 66, 1984.

Heil, J., Wesner, J., Mueller, W., and Sure, T., *Appl. Opt. Optical Technol. Biomed. Opt*., Vol.42, 5073, 2005.

Hilyard, D. F., Laopodis, G. K., and Faber, S. M., Chemical reactivity testing of optical fluids and materials in the DEIMOS spectrographic camera for the Keck II telescope, *Proc. SPIE*, 3786, 482, 1999.

Hopkins, R. E., Some thoughts on lens mounting, *Opt. Eng*., 15, 428, 1976.

Horne, D. F., *Optical Production Technology*, Adam Hilger Ltd., Bristol, England, 1972.

Jacobs, D. H., *Fundamentals of Optical Engineering*, McGraw-Hill, New York, 1943.

Lytle, J. D., Polymeric optics, in *OSA Handbook Of Optics*, 2nd ed., Bass M., Van Stryland, E., Williams, D.R., and Wolfe, W.L., Eds., McGraw-Hill, New York, 1995, chap. 34.

Malacara, D., *Optical Shop Testing*, Wiley, New York, 1978.

Mast, T., Faber, S.M., Wallace, V., Lewis, J., and Hilyard, D., DEIMOS camera assembly, *Proc. SPIE*, 3786, 499, 1999.

MIL-HDBK-141, *Optical Design*, Defense Supply Agency, Washington, DC, 1962.

Morris, C., *Dictionary of Science and Technology*, Academic Press, San Diego, 1992.

Palmer, T. A., Mechanical aspects of a dual field of view infrared lens, *Proc. SPIE*, 4444, 315, 2001.

Palmer, T. A. and Murray, D. A., personal communication, 2001.

Parr-Burman, P. and Gardam, A., The development of a compact IR zoom telescope, *Proc. SPIE*, 590, 11, 1985.

Parr-Burman, P. and Madwick, P., A high performance athermalized dual field of view I.R. telescope, *Proc. SPIE*, 1013, 92, 1988.

Polster, H. D., Spacing cylindrical optical elements, *Perkin-Elmer Internal Technical Memorandum HDP-105*, 1964.

Price, W. H., Resolving optical design/manufacturing hangups, *Proc. SPIE*, 237, 466, 1980.

Quammen, M. L., Cassidy, P. J., Jordan, F. J., and Yoder, P. R., Jr., Telescope Eyepiece Assembly with Static and Dynamic Bellows-Type Seal, U.S. Patent 3,246,563, 1966.

Rayces, J. L., Foster, F., and Casas, R. E., Catadioptric System, U.S. Patent 3,547,525, 1970.

Rosin, S., Eyepieces and magnifiers, in *Applied Optics and Optical Engineering*, Vol. III, Kingslake, R., Ed., Academic Press, New York, 1965, chap. 9.

Ruda, M., Introduction to Optical Alignment Techniques, *SPIE Short Course SC010*, 2004.

Sure, T., Heil, J., and Wesner, J., Microscope objective production: On the way from the micrometer scale to the nanometer scale, *Proc. SPIE*, 5180, 283, 2003.

U.S. Precision Lens, Inc., *The Handbook of Plastic Optics*, 2nd ed., Cincinnati, OH, 1983.

Valente, T. M. and Richard, R. M., Interference fit equations for lens cell design using elastomeric lens mountings, *Opt. Eng*., 33, 1223, 1994.

Vukobratovich, D., Design and construction of an astrometric astrograph, *Proc. SPIE*, 1752, 245, 1992.

Vukobratovich, D., Optomechanical systems design, in *The Infrared & Electro-Optical Systems Handbook*, Vol. 4, ERIM, Ann Arbor and SPIE Press, Bellingham, 1993a, chap. 3.

Vukobratovich, D., Introduction to Optomechanical Design, SPIE, *Short Course SC014*, 1993b.

Westort, K., Design and fabrication of high performance relay lenses, *Proc. SPIE*, 518, 40, 1984.

Williamson, D. M., Compensator selection in the tolerancing of a microlithography lens, *Proc. SPIE*, 1049, 178, 1989.

Wilson, R. N., *Reflecting Telescope Optics II*, Springer, Berlin, 1999.

Yoder, P. R., Jr., Lens mounting techniques, *Proc. SPIE*, 389, 2, 1983.

Yoder, P. R., Jr., Opto-mechanical designs of two special purpose objective lens assemblies, *Proc. SPIE*, 656, 225, 1986.

Yoder, P. R., Jr., *Mounting Optics in Optical Instruments*, SPIE Press, Bellingham, 2002.

Yoder, P. R., Jr. and Friedman, I., A low-light-level objective lens with integral laser channel, *Opt. Eng*., 11, 127, 1972.

6 Mounting Windows and Filters

6.1 INTRODUCTION

A window is used in an optical instrument primarily as a transparent interface between the internal components and the outside environment. Usually, it is a plane-parallel plate of optical glass, fused silica, plastic, or crystalline material that allows the desired radiation to pass through with minimal effect on intensity and image quality, but excludes dirt, moisture, and other contaminants and, in some cases, maintains a positive or negative pressure differential between the internal and external atmospheres. For IR applications, the window must not radiate due to its temperature in a manner that interferes with its function. The front apertures of some telescopes, such as Schmidt systems, are closed with windows that have one or both surfaces contoured so as to correct aberrations. These contours are generally aspheric and do not depart drastically from a nominal flat or gentle spherically curved shape. Meniscus-shaped windows, such as are used on a Maksutov system, are called shells. A deep shell is called a dome.

Critical aspects of window-mounting design may include freedom from mechanically and thermally induced distortions, sealing provisions, and location in the optical system. If at or near the aperture stop or a pupil, a prime consideration is deformation introduced into the transmitted wavefront. Cosmetic defects such as scratches, digs, and dirt are less significant. If the window is near an image, it can have little effect on the wavefront, but defects or dirt on the window's surfaces may appear superimposed on that image.

Since plane-parallel plates have essentially no effect on collimated light beams or ones with very slight convergence or divergence, they may be considered relatively benign elements of the optical system from an alignment viewpoint. If thick plane-parallel windows are located in beams with significant convergence or divergence, they will contribute aberrations in the same manner as prisms and are alignment sensitive. Usually, windows located inside the optical system are thin enough for this not to be a serious problem.

Typical specifications for allowable geometric wedge angle between faces of plane-parallel plate windows for high-performance systems such as a camera or an electro-optical sensor range from several arcminutes for monochromatic applications in which a fixed angular bias can be tolerated (or compensated) to less than 1 arcsec for polychromatic systems. Wedge angles from element to element are especially critical in segmented windows since image doubling and line-of-sight pointing errors due to aperture sharing across the interfaces must be controlled to preserve system performance. Windows that are wedged to control spurious Fresnel reflections may require special mounting arrangements to ensure proper orientation of the wedge apex. Spectral dispersion may be introduced if the wedge angle is appreciable. Index of refraction and thickness matching is also critical in segmented windows.

The optical performance of each of the window types discussed in this chapter is usually specified in terms of the maximum allowable deterioration of a transmitted plane wavefront over the full window aperture or selected subapertures. The requirements depend, of course, on the specific application and the wavelength used. For example, a visual viewing system may allow a wavefront error as large as one wave peak to valley (p-v) at 0.63 μm. A window for a conventional forward looking infrared (FLIR) sensor operating at 10.6 μm may tolerate 0.1 wave p-v wavefront error at that wavelength (equivalent to 1.7 waves p-v at 0.63 μm). A conformal window[*] for a missile might need less than 0.1 wave rms for any subaperture defined by the line-of-sight direction and sensor aperture. A high-performance photographic camera application may require the p-v error of a protective window in front of its aperture to contribute less than 0.05 wave error at 0.63 μm.

It should be noted that transmitted wavefront errors include contributions resulting from material inhomogeneity, as well as those resulting from residual surface figure errors from fabrication and from mechanical deformations due to mounting or environmental influences. Interferometric tests under ambient environmental conditions after assembly can reveal all these defects except those environmentally caused. Simulated environmental tests or rigorous analysis may be required in critical applications. Some success with correcting index inhomogeneities by localized computer-controlled polishing has been reported (Askinazi et al., 2003).

The design and development of conformal windows has received increasing attention in recent years because of significant advantages to be derived therefrom in military applications. This interesting topic is considered in this chapter.

One environmental exposure that is especially hazardous to windows is abrasion and erosion due to high-velocity impact of particulate matter, bugs, rain, or ice. This subject was discussed and several references for additional information cited in Section 2.2.10 and hence will not be considered here. The design of many windows, shells, and domes is predicated on analysis of pressure differentials imposed statically or dynamically by aerodynamic or hydrodynamic forces. This subject is considered in the final section of this chapter.

An optical filter is a special kind of window that is made of material with selective transmission characteristics as a function of wavelength or made of conventional refractive material that is coated appropriately to produce a desired transmissive effect. Mountings for filters are generally no different from those for windows. Special consideration must be given to mechanical design aspects if the material is especially fragile, energy absorbed from the beam causes temperatures to rise significantly, the filter is exposed to a high-velocity air stream, or the filter is segmented rather than of single-element construction.

Design and mounting configurations for typical types of window, shell, dome, and filter components are considered in the following sections. Guidelines for minimizing the effects of pressure differentials and temperature changes are also considered.

6.2 CONVENTIONAL WINDOW MOUNTS

Figure 6.1 shows a typical mounting design for small round aperture windows used to seal the interior of an optical system from the outside world. This window is a 20 mm (0.79 in.) diameter by 4 mm (0.16 in.) thick disk of BK7 glass. It is to be used in the *f*/10 beam of the illumination path in a military telescope reticle projection subsystem. The surfaces need be flat only to ±10 waves p-v of visible light and parallel to 30 arcmin. The window is bonded into a stainless-steel (CRES type 303) cell with a polysulfide base sealing compound according to military specification MIL-S-11031. A RTV-type elastomer would serve as well. This secures the window and forms an effective seal. Note that the glass is positioned axially against a flat annular shoulder inside the cell and that the adhesive fills the annular space created by undercutting that shoulder. The uniformity of the encapsulating adhesive layer's radial thickness can easily be achieved by inserting shims or gauge wires between the glass and metal before the adhesive is injected. These items can be removed after the sealant has cured. For best sealing, the spaces left after removing the shims or wires should be filled with sealant and cured.

Slightly simpler construction is provided with a little less reliability if the cell of Figure 6.1 does not have sealant injection holes and the sealant is carefully applied to the window rim and cell inside

---

[*] Trotta (2001) defined conformal optics as ones that "deviate from conventional form to best satisfy the contour and shape needs of system platforms." Examples would be a segmented window that blends into the profile of an aircraft or a hyperbolic dome for an advanced missile.

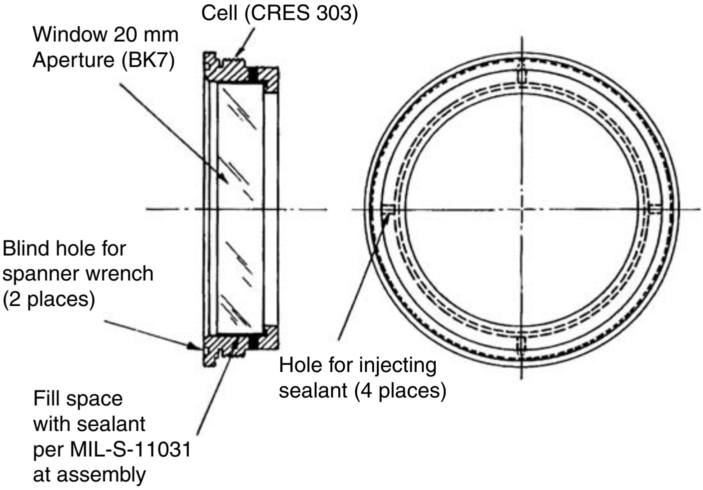

FIGURE 6.1 Instrument window subassembly featuring a bonded-in-place glass element. (Adapted from a U.S. Army drawing.)

diameter before inserting the window into the cell. In either case, excess sealant should be cleaned away before it sets. Suitability of the seal may be inferred from observation of sealant bead continuity around the window rim or, preferably, checked by pressure testing. An external thread on the cell mates with a threaded hole in the instrument housing. A flat gasket or O-ring would typically be used between the cell's flange and the housing to seal the interface.

The subassembly shown in Figure 6.2 has a BK7 window of 50.80 mm (2.0 in.) diameter and 8.8 mm (0.346 in.) thickness sealed with military specification sealant into a stainless-steel (CRES 416) cell and secured with a threaded retainer that also is made of stainless steel. This window is intended to be used as an environmental seal in front of the objective of a 10 power telescope. Since the light beam transmitted through this window is collimated and nearly fills the clear aperture at all times, the critical optical specifications are transmitted wavefront error (±5 waves of spherical power and 0.05 wave p-v of irregularity for green light) and wedge angle (30 arcsec maximum).

The maximum and minimum diametric clearances between glass and metal at ambient temperature are 0.53 mm (0.020 in.) and 0.22 mm (0.009 in.), respectively. The cell is provided with an annular groove for an O-ring that is used to seal the cell to the instrument housing at the next level of assembly. Dimensions of the groove are shown in the detail view. Note that the mounting holes are outside this seal. Screws used to attach the subassembly should thread into blind holes in the instrument housing. The seals are designed to hold 5 lb/in.^{2} (3.45×10^4 Pa) positive pressure inside the telescope for an extended period of time.

6.3 SPECIAL WINDOW MOUNTS

In this "special" category, we include windows for aerial reconnaissance cameras and electro-optical sensors such as FLIR systems, low-light-level television (LLLTV) systems, laser range finder/target designator systems, and windows for high-vacuum applications. We intentionally omit consideration of the windows used in high-energy laser systems because space limitations do not permit adequate explanation of their complex design. Readers interested in this type of window are referred to the voluminous literature on laser-induced effects on optical materials, including those referenced in Section 2.2.12.

Modern aerial reconnaissance cameras and electro-optical sensors are usually located within an environmentally controlled equipment bay in the aircraft fuselage or in an externally mounted pod. In most cases, an optical window is provided to seal the bay or pod and to provide aerodynamic

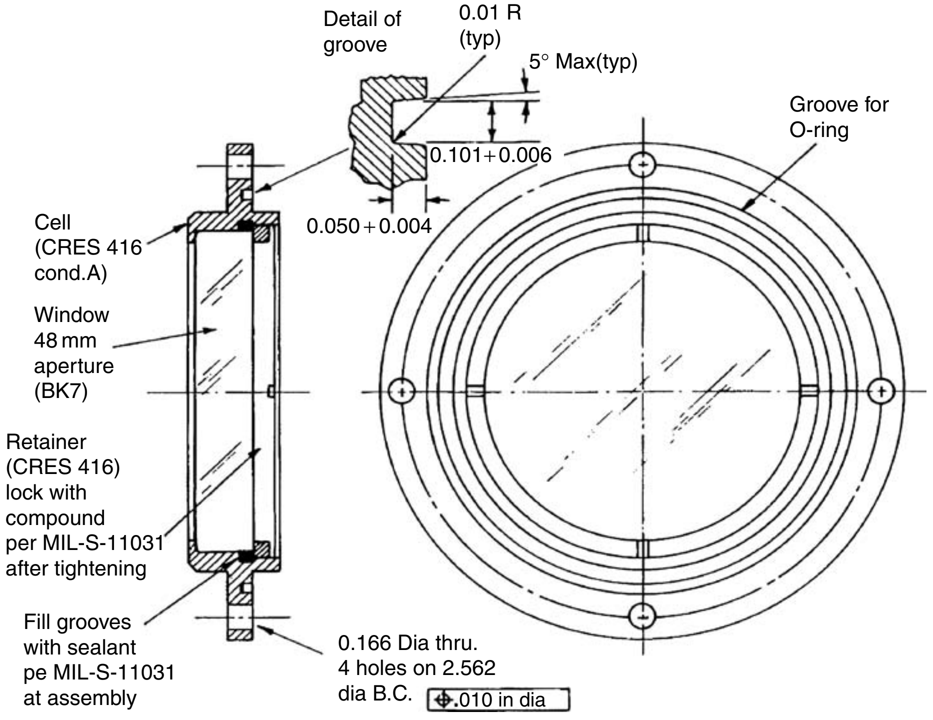
Detail of groove
0.01 R (typ)
5° Max(typ)
0.101+0.006
0.050+0.004
Groove for O-ring
Cell (CRES 416 cond.A)
Window 48 mm aperture (BK7)
Retainer (CRES 416) lock with compound per MIL-S-11031 after tightening
Fill grooves with sealant pe MIL-S-11031 at assembly
0.166 Dia thru. 4 holes on 2.562 dia B.C.
⌖.010 in dia

FIGURE 6.2 Instrument window subassembly with window held in place by a retaining ring. Dimensions are in inches. (Adapted from a U.S. Army drawing.)

continuity of the enclosure. Its quality must be high and long lasting in spite of exposure to adverse environments. Single- and double-glazing configurations are used as dictated by thermal considerations. Examples of both types are discussed below. Some windows for high-velocity aircraft or missiles may require cooling to counteract skin-heating effects of the airflow.

Figure 6.3 shows a window for a LLLTV system utilizing light in the spectral region 0.45 to 0.9 μm and mounted on a pod under the wing of an aircraft. Two plane-parallel plates of crown glass are laminated together to form the single 19 mm (0.75 in.) thick glazing of elliptical aperture approximately 25 cm × 38 cm (9.8 in. × 15.0 in.). It is mounted into a cast aluminum frame. The frame interfaces with the curved surface of the camera pod and is held in place by several screws through the recessed holes visible in the figure. The internal construction of this subassembly is shown schematically in the exploded view of Figure 6.4. The wires connect to an electrically conductive coating applied to one glass plate. The second plate is optically cemented over this coating to protect it. This coating provides heat for anti-icing and defogging purposes during a military mission. It also attenuates electromagnetic radiation. The design is such that the optic may be replaced if damaged. It is sealed in place with a RTV-type sealant. The assembled window is capable of withstanding, without damage, a proof pressure differential of 11 lb/in^2 (7.6×10^4 Pa) in either direction. Both exposed surfaces of the window are broadband antireflection-coated. The frame exterior is painted white.

The multiaperture window assembly shown in Figure 6.5 is designed for use in another military application involving an FLIR sensor operating in the spectral region of 8 to 12 μm and a laser range finder/target designator system operating at 1.06 μm. The larger window is used by the FLIR system and is made of a single plate of chemical vapor-deposited (CVD) zinc sulfide (ZnS), approximately 1.6 cm (0.63 in.) thick. Its aperture is 30 cm × 43 cm (11.8 in. × 16.9 in.). The smaller windows are similar and have elliptical apertures of 9 cm × 17 cm (3.5 in. × 6.7 in.). They are used

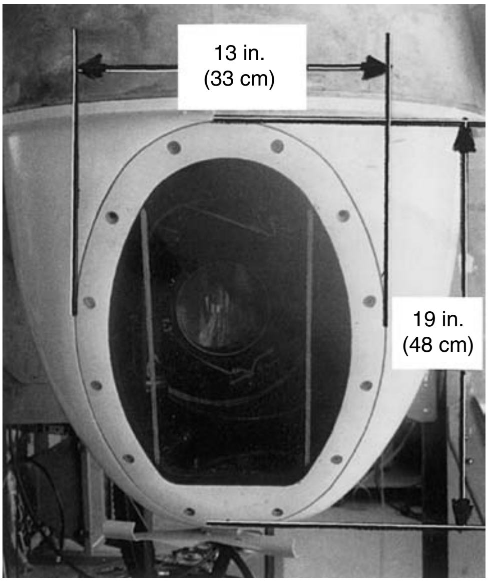
13 in.
(33 cm)
19 in.
(48 cm)

FIGURE 6.3 An elliptically shaped laminated glass window used in a low-light-level television system mounted on an aircraft pod. (Courtesy of Goodrich Corporation, Danbury, CT.)

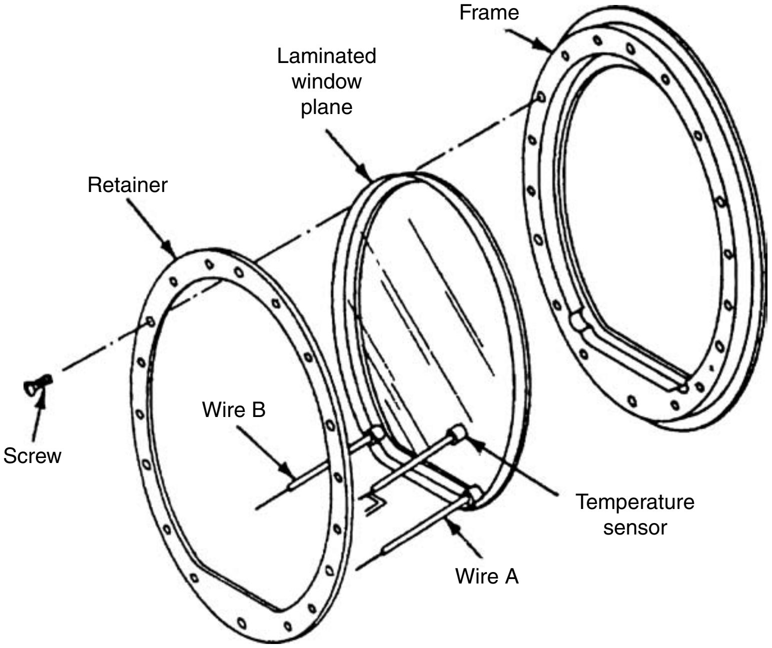
Frame
Laminated window plane
Retainer
Screw
Wire B
Temperature sensor
Wire A

FIGURE 6.4 Exploded view of the window subassembly shown in Figure 6.3. (Courtesy of Goodrich Corporation, Danbury, CT.)

by the laser system and are made of BK7 glass, 1.6 cm (0.63 in.) thick. All surfaces are appropriately antireflection-coated for maximum transmission at the specified wavelengths and a 47 ± 5° angle of incidence. The coatings also resist erosion due to rain at a rate of 1 in. (2.5 cm) per h, with an impact velocity approaching 500 mi/h (224 m/sec) for at least 20 min (Robinson et al., 1983).

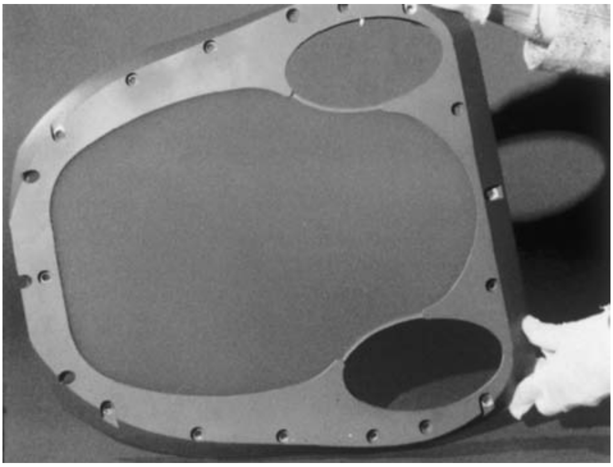

FIGURE 6.5 A multiaperture window subassembly. The larger element is IR-transmitting ZnS while the smaller ones are BK7 glass. (From Yoder, P.R., Jr., *Proc. SPIE*, 531, 1985.)

The specifications for transmitted wavefront quality are 0.1 wave p-v at 10.6 μm over any 2.5 cm (1 in.) diameter instantaneous aperture for the FLIR window and 0.2 wave p-v power, plus 0.1 wave irregularity at 0.63 μm over the full aperture for the laser transmitter and receiver windows.

The CVD ZnS used in this design is not the easiest material with which to work. Fortunately, it transmits in the visible adequately enough for the optician to identify the volume, within an oversized raw material blank, where the element should be located in order to avoid the worst inclusions and bubbles.

As is the case for many windows, the mechanical strength of each glazing is maximized by controlled material removal with progressively finer abrasive during grinding to ensure that all subsurface damage caused by previous operations have been removed (Stoll et al., 1961)[†]. The wedge is also brought within specified limits (66 arcsec maximum for the ZnS element and 30 arcsec maximum for the BK7 elements) during the grinding process. The edges of these windows also are controlled-ground and polished primarily for reasons of strength.

All three glazings are bonded with adhesive into a lightweight frame made of 606l-T651 aluminum plate anodized after machining to the complex contours shown in Figure 6.5. The bonded assembly attaches to the aircraft pod by screws through the several recessed holes around the edge of the frame. The mating surfaces of the frame and pod must match closely in contour in order not to deform the optics or disturb the seals because of distortions caused by attaching the frame to the stiffer pod structure.

Figure 6.6 illustrates a segmented window subassembly typical of those used with panoramic aerial cameras designed to photograph from horizon to horizon transverse to the flight path of a military aircraft. The size of the window required for use with such a camera is determined by the location and size of the lens's entrance pupil and the camera field of view. This window is of dual-element construction with fused silica glazings outside and BK7 glass glazings inside. Since the aircraft flies at high speed, a critical design problem here is a thermal one. Boundary-layer effects heat the outer window glazing, and since the material is a blackbody with an emissivity of about 0.9, it radiates heat towards the camera and its surrounding equipment. To combat this deleterious effect, the inside surfaces of the outer glazings are coated with a low-emissivity (gold) coating. This coating affects the window's visible light transmission minimally, but reflects IR out of the camera enclosure. All other window surfaces are conventionally antireflection-coated to maximize transmission in the film sensitivity spectral region.

[†] Controlled grinding is discussion further in Section 15.2

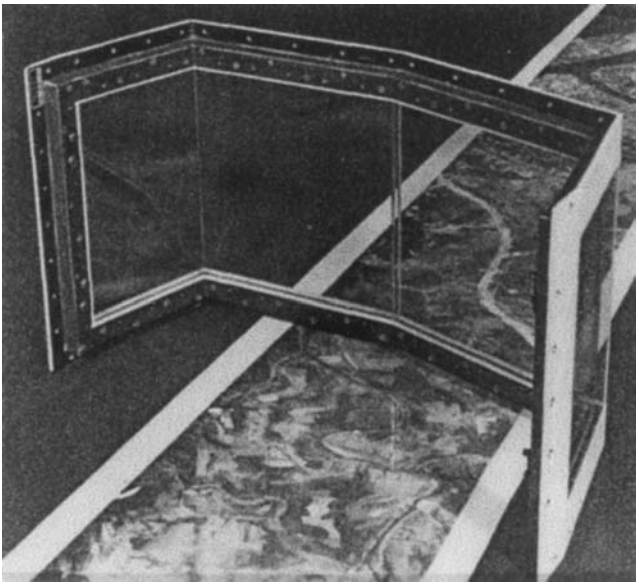

FIGURE 6.6 A segmented window subassembly used with a military panoramic aerial camera to photograph from horizon to horizon at high altitude. A simulated enlarged strip photograph of the type taken through this window is also shown. (Courtesy of Goodrich Corporation, Danbury, CT.)

The square elements in the center of the window subassembly have dimensions of approximately 12.6 in. × 13.0 in. (32 cm × 33 cm) and are 0.4 in. (1 cm) thick. The side glazings are somewhat smaller in one dimension. The glazings are separated by a few millimeters. Conditioned air is circulated through the space between glazings during flight. The adjacent edges of the individual elements in each of the inner and outer glazings of this segmented window are beveled and cloth-polished. These edges are cemented together with flexible adhesive. The paths of rays passing symmetrically through adjacent glazings at their interface are shown in Figure 6.7. The width of the beam obscuration due to such joints must be minimized in order not to degrade the optical performance of the system.

As indicated conceptually in Figure 6.7, the glass elements are sealed into recesses machined into the aluminum frame with an elastomeric-type adhesive and secured by a metal retainer. The contours of the subassembly and its mounting hole pattern are made to match those of the aircraft interface through use of special tooling and fixtures.

A window assembly developed for vacuum cryogenic applications on a double-walled dewar was described by Haycock et al. (1990). It is illustrated in Figure 6.8. The window was germanium and had a racetrack-shaped aperture of about 5.25 in. × 1.30 in. (133.3 mm × 33.0 mm). Since a vacuum-tight seal was required, a gasket of indium was compressed by a spring-loaded piston onto the heavily beveled rim of the window as shown in Figure 6.9. Deflection of the spring plate provided sufficient total preload (on the order of 530 lb [2350 N]) to hold the window in place at all temperatures between 77 and 373 K and to create a peak compressive stress in the indium of about 1200 lb/in.^{2} (8.27 MPa).

The spring plate was slit radially at its inner boundary to distribute the force evenly around the edge of the window. Titanium was used for the spring because of its low CTE, high Young's modulus, and high yield strength. The window frame was Nilo 42 ($Ni_{42}Fe_{58}$), which approximated the CTE of the germanium. The piston was aluminum for ease of fabrication to its unusual shape.

One important design parameter for this window was the width at the narrower end (bottom) of the triangular gap into which the indium was pressed. A small dimension was needed to maintain the

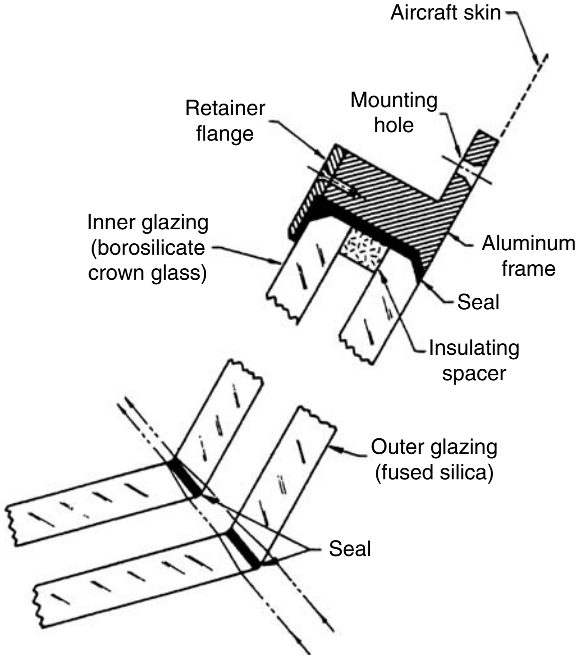

FIGURE 6.7 A partial schematic sectional view of the double-glazed, segmented aerial camera window shown in Figure 6.6. Note how refraction minimizes the beam obscuration at the joints. (Courtesy of Goodrich Corporation, Danbury, CT.)

required pressure within the seal, but if too small, it would be difficult to assemble the seal with complete packing of the indium into the available volume. It was found that a dimension of 0.010 in. (0.254 mm) was satisfactory for this application. Another critical dimension was the gap on either side of the piston under spring load. A value of 0.001 in. (25 μm) was appropriate to sufficiently minimize extrusion of the indium at higher temperatures so the seal would remain intact over time periods of the order of 1 week. Testing of the assembly at cryogenic temperature indicated that it was leak proof to the accuracy of the test apparatus (approximately 10^{-10} std atm cm^3/sec) during and after repeated cycling (>200 cycles) throughout the temperature range of 293 to 77 K.

Yoder (2002) indicated that a modification of the design described by Haycock et al. (1990) in which an elastomeric "gasket" formed in place at the bottom of a triangular gap between a beveled window and its mount, or an O-ring in that same location, might be spring-loaded with a piston in a manner similar to that described here. This would provide radially directed compression of the elastomer onto the rim of the window and seal it adequately for some noncryogenic applications such as those experienced in an aerospace-type apparatus. Because the rim of the window is heavily beveled, this design would also have the advantage of not requiring a separate means for providing preload normal to the window surface to press the window against its mounting interface.

Another design for a vacuum-tight window is illustrated by the section view in Figure 6.10. This window was a 7.6 cm (3 in.) diameter disk of sodium chloride (single crystal or polycrystalline) approximately 0.9 cm (0.35 in.) thick. The cell was made of CRES and no sealants were allowed because the assembly had to be chemically inert for an application involving multiple-photon laser-induced chemistry in a gaseous media. During long-term use, the window was specified to hold internal pressure of a few millitorr against normal ambient outside atmospheric pressure at temperatures of 200 to 275°C with helium leak rates of approximately 3×10^{-10} atm cm^3/sec while the sample (confined gas) was irradiated with pulsed laser radiation. Because the temperature fluctuated rapidly, the design had to resist thermal shock.

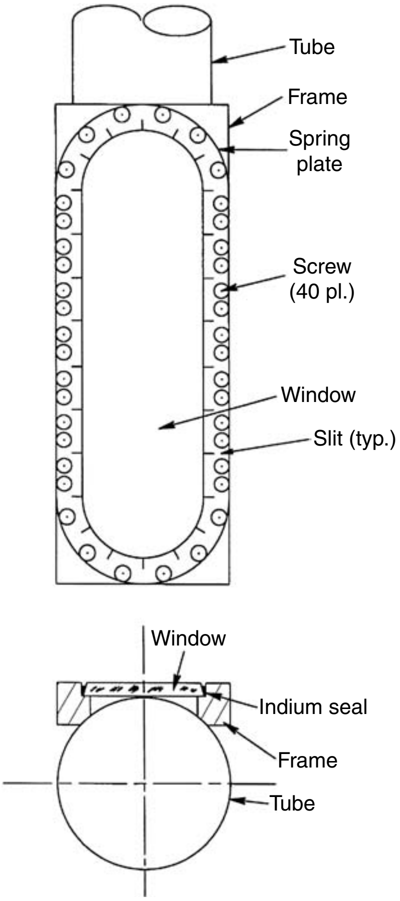
Tube
Frame
Spring plate
Screw (40 pl.)
Window
Slit (typ.)
Window
Indium seal
Frame
Tube

FIGURE 6.8 Plan and end views of a window subassembly with an indium seal to withstand vacuum cryogenic conditions. (Adapted from Haycock, R.H. et al., *Proc. SPIE*, 1340, 165, 1990.)

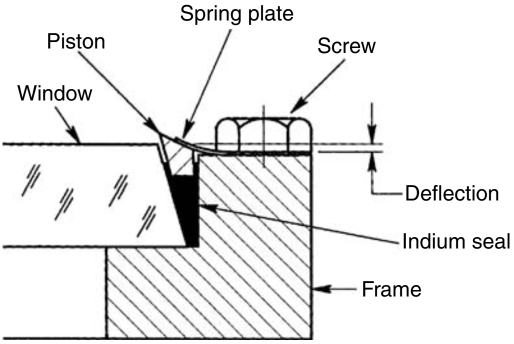
Spring plate
Piston
Screw
Window
Deflection
Indium seal
Frame

FIGURE 6.9 Detail view of the pressure-loaded indium seal for the window subassembly shown in Figure 6.8. (Adapted from Haycock, R.H. et al., *Proc. SPIE*, 1340, 165, 1990.)

The window surfaces were clamped between two thick CRES flanges by 12 equally spaced screws holding stacks of Belleville springs to provide uniform axial preloading with flexibility to withstand dimensional variations from temperature changes. Lateral motion was not constrained.

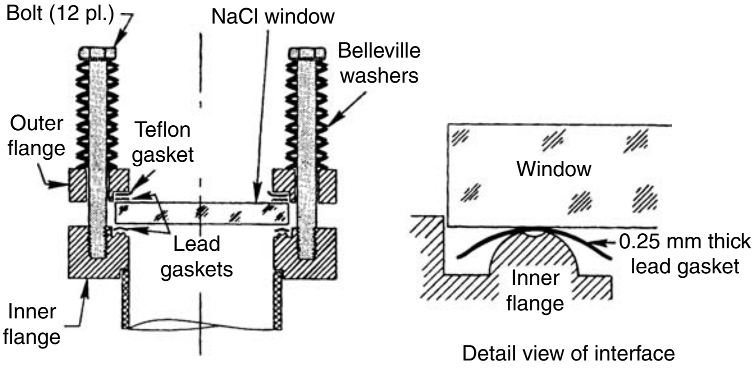

FIGURE 6.10 Illustrations of a high-temperature, vacuum-sealed NaCl window for an IR application. (Adapted from Manuccia, T.J. et al., Rev. Sci. *Instrum*., 52, 1857, 1981.)

The design relied upon friction to hold the window in place along two axes. The inner window surface was sealed to the flange through a 0.25-mm (0.010-in.)-thick lead gasket. The outer surface of the flange at this interface was shaped as shown in the detail view of the figure. A 1.9-mm (0.075-in)-wide convex toroidal projection from the flange surface had a central concave groove 0.19 mm (0.008 in.) wide cut into it. A 0.25-mm (0.010-in.)-thick lead gasket was placed between the window and the protrusion on the flange. When compressed by the springs, the sharp edges of the groove cut through the gasket trapping a ring of lead in the groove and forcing it to extrude into microscale irregularities of the metal and the crystal thereby forming a seal. At the outer surface of the window, gaskets of Teflon 0.125 mm (0.005 in.) thick and lead 0.25 mm (0.010 in.) thick formed an additional seal and cushioned the interface. The surfaces of this lead gasket were roughened so the high points would deform and distribute preload over a large area of the window.

6.4 MOUNTS FOR SHELLS AND DOMES

Meniscus-shaped shells are used as windows for applications such as electro-optical sensors requiring wide fields of view, such as Bouwers, Maksutov, or Gabor telescope objectives (Kingslake, 1978), ones requiring an ability to scan a line of sight over a large conical space, or protective windows for deep submergence vehicles. Domes are deep shells and hyperhemispheres are domes that extend beyond 180° angular extent.

A photograph of a mounted hyperhemisphere is shown in Figure 6.11. The outside diameter of this dome is 127 mm (5.0 in.), the dome thickness is 5 mm (0.2 in.), and the angular aperture is approximately 210°. The subassembly shown in this figure is made of crown glass, but many domes used for military applications are made of IR-transmitting materials. The resistances of most of the latter materials to corrosion, fungus, particulate abrasion, and rain erosion are lower than those needed for a long life in the intended environments. These problems as well as some attempts to improve the materials and protect them with coatings were discussed in Section 2.2.

Mountings for shells and domes usually involve (1) attaching them to a metallic ring-shaped flange or directly to an instrument housing by potting them in place with elastomers, (2) mechanically clamping them in place and sealing them with a gasket or elastomer, and (3) brazing the optic to the housing. Figure 6.12 illustrates three typical mounting configurations of types (1) and (2). View (a) shows a dome constrained by a ring-shaped flange that acts through a soft Neoprene gasket to seal the interface. View (b) shows a dome bonded to a flange or bezel using an epoxy and constrained axially by a retaining ring. The axial support was required in this case because the subassembly was attached to the front of an artillery projectile where it would experience high acceleration. The authors reported that the design was suitable for use on a mortar projectile where the stress due to about 11,000 times

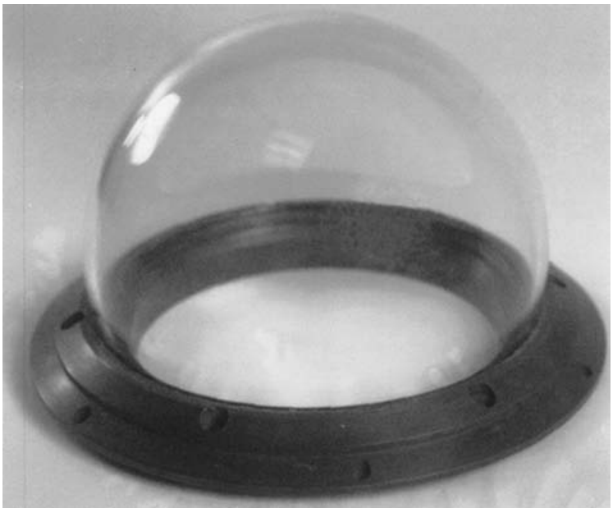

FIGURE 6.11 Photograph of a crown glass hyperhemispheric dome potted with elastomer into a metal flange.

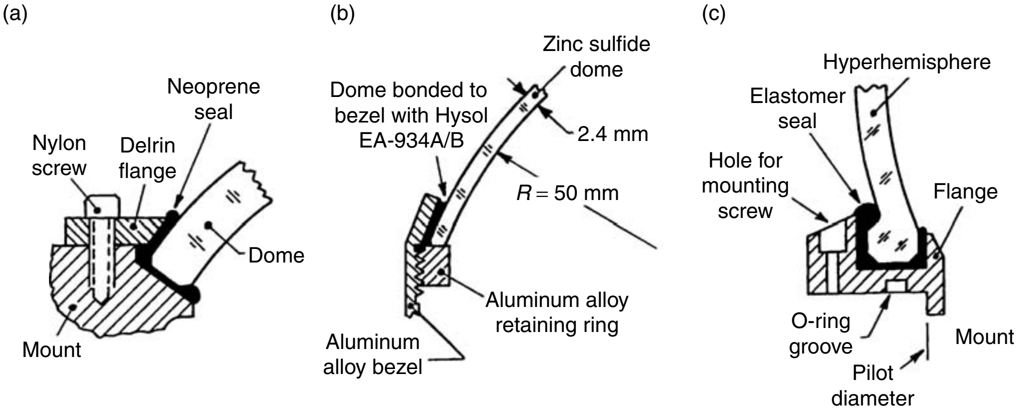
(a)
Neoprene seal
Nylon screw
Delrin flange
Dome
Mount
(b)
Zinc sulfide dome
Dome bonded to bezel with Hysol EA-934A/B
2.4 mm
R = 50 mm
Aluminum alloy retaining ring
Aluminum alloy bezel
(c)
Hyperhemisphere
Elastomer seal
Hole for mounting screw
Flange
O-ring groove
Mount
Pilot diameter

FIGURE 6.12 Three configurations for dome mountings: (a) dome clamped through a soft gasket with a flange. (Adapted from Vukobratovich, D., Introduction to Opto-Mechanical Design, *SPIE Short Course*, 2003.) (b) dome constrained by an internal retainer. (Adapted from Speare, J. and Belioli, A., *Proc. SPIE*, 450, 182, 1983.) (c) hyperhemisphere potted with elastomer.

gravity firing acceleration is approximately 26 MPa (3.8×10^5 lb/in.^{2}). View (c) shows a hyperhemisphere potted with elastomer into a ring-shaped mount in the manner illustrated by Figure 6.11.

Figure 6.13 shows schematically a military missile with a deep dome attached to the front end to protect a radar transceiver or an IR or visible light sensor used for target acquisition and homing. At the rear of the missile are fins to stabilize and guide the weapon and the rocket motor. The dome serves as a window transmitting the appropriate radiation to the sensor and as an aerodynamic structure while the missile is in flight. The missile body is essentially cylindrical. It contains the sensor and its electronics, a guidance controller, motors to drive the fins, a warhead, and fuel for the rocket motor. When the velocity of flight is subsonic, the dome may be made of optical plastic, glass, germanium, or some other crystals, depending on the wavelength used. For applications involving supersonic velocities, a material with low emittance is needed because air stream friction raises the dome's surface temperatures to very high values. The amount of IR radiation from this hot material

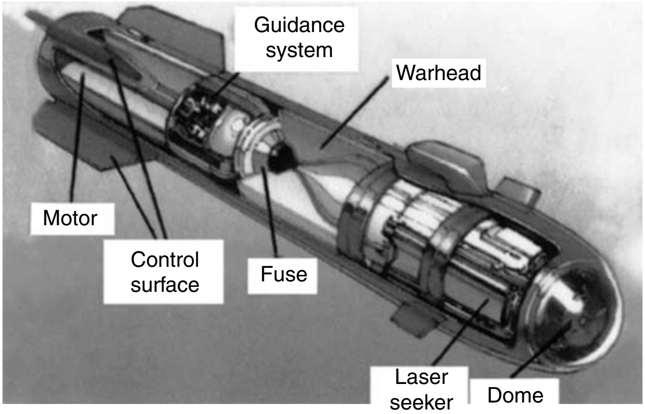

FIGURE 6.13 Schematic side view of a rocket-propelled missile with a dome-shaped window at the forward end to protect an internal sensor.

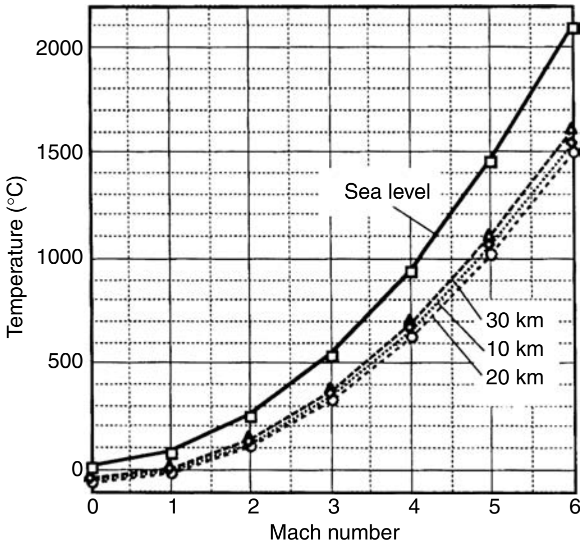

FIGURE 6.14 Variation of stagnation temperature at the apex of a dome as functions of velocity and altitude. (From Harris D.C., *Materials for infrared Windows and Domes, Properties and Performance*, SPIE Press, Bellingham, 1999.)

is determined, in part, by its emittance, which measures the fraction of the radiation that would radiate from a blackbody if it were at the dome's temperature. Figure 6.14 indicates the surface temperature at the apex of the dome as a function of Mach number and altitude. This temperature (called stagnation temperature) occurs at relatively low altitudes because the transfer of heat from the air to the dome material becomes smaller as the air density decreases with altitude. When the dome surface becomes hot in an IR sensor, the emission from that hot body will reduce the signal-to-noise ratio of the sensor or, in extreme cases, saturate the sensor so it becomes useless. Materials frequently used for such applications involving wavelengths of 3 to 5 μm are ALON, sapphire, and spinel. Figure 6.15 plots emittance (sometimes called emissivity) for these materials (and yttria) as functions of wavelength and temperature. In general, a low absorption coefficient means a low emissivity. Yttria is not frequently used for windows or domes because of its susceptibility to thermal shock.

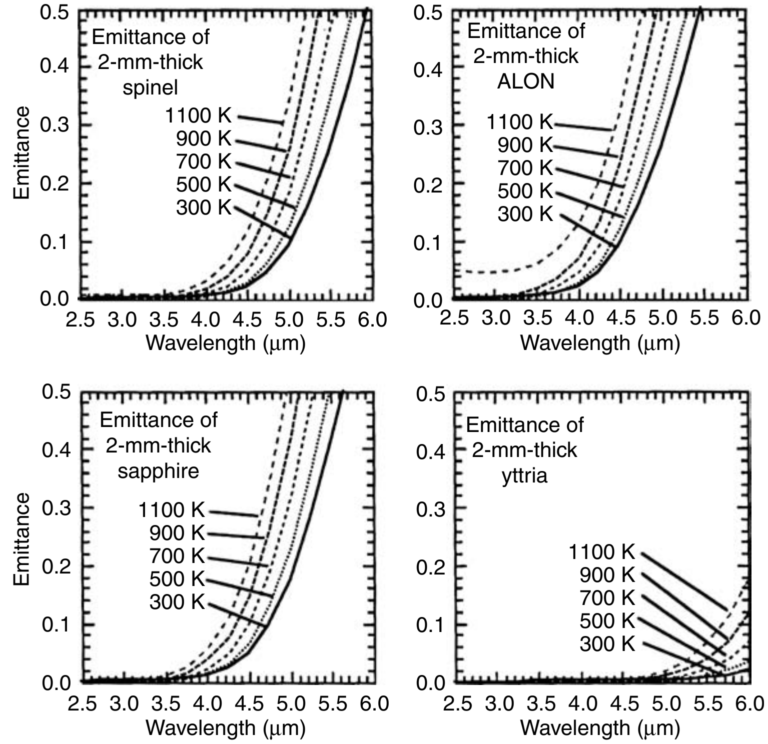

FIGURE 6.15 Temperature dependences of emittance for selected IR window materials as functions of wavelength. (From Harris D.C. *Material for Infrared Windows and Domes, Properties and Performance*, SPIE Press, Bellingham, 1999.)

Figure 6.16 shows two configurations for ceramic domes (typically sapphire), attached to the cylindrical titanium 6Al-4V housing of an air-to-air missile by brazing. In view (a), the base of the dome is butt-brazed with Incusil-ABA (an alloy of ~27.25% copper, ~12.5% indium, ~1.25% titanium, and the remainder silver that melts at ~700°C)[‡] to a flat surface on an intermediate transition cylindrical ring made of 99% niobium alloyed with 1% zirconium. This material has a CTE of 4 to 4.5×10^{-6} $°C^{-1}$, closely matching sapphire. The crystal's *c*-axis is approximately normal to the dome base. Four locating tabs are machined into the left end of the cylindrical ring to locate the dome during brazing. The right end of the cylindrical ring is inserted into the machined bore in the titanium missile nose with an interference fit accomplished by heating the titanium and cooling the niobium for assembly. Upon returning to ambient temperature the metals seize. The joint is then brazed with Gapasil-9 (an alloy of ~82% silver, ~9% palladium, and ~9% gallium that melts at ~930°C). Brazing the two joints is accomplished in a vacuum of $\leq 8 \times 10^{-5}$ torr and in two steps because the melting temperatures of the materials are so different. The metal-to-metal joint is brazed first and the metal-to-ceramic joint is brazed second. The missile housing extends axially beyond the second braze joint to provide aerodynamic continuity of the external surface of the missile. In Figure 6.16(a), a polysulfide seal is shown filling the gap between the dome and the nose. The transition ring in this design is thin enough to be slightly compliant radially. This allows differential expansion/contraction between the sapphire and titanium (which have significantly different CTEs of $\sim 5.3 \times 10^{-6}$ and 8.8×10^{-6} $°C^{-1}$, respectively) as the temperature changes and minimizes the chance for breakage of the dome.

[‡] Incusil and Gapasil are registered trademarks of WESGO, Inc., San Carlos, CA (www.wesgometals.com).

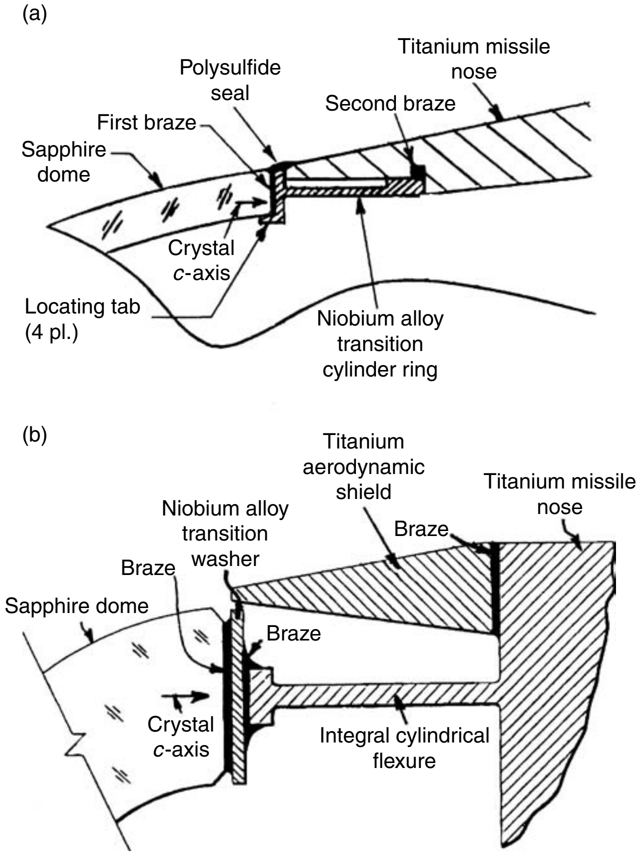
(a)
Titanium missile nose
Polysulfide seal
Second braze
First braze
Sapphire dome
Crystal c-axis
Locating tab (4 pl.)
Niobium alloy transition cylinder ring
(b)
Titanium aerodynamic shield
Titanium missile nose
Niobium alloy transition washer
Braze
Braze
Sapphire dome
Braze
Crystal c-axis
Integral cylindrical flexure

FIGURE 6.16 Sketches of mountings for domes in which the optic is brazed to the metal support: (a) design with a separate transition cylinder ring component and (b) design with an integral cylinder ring. (Adapted from Sunne, W.L. et al., U.S. Patent 5,884,864, 1999a and Sunne, W.L. et al., U.S. Patent, 5,941,479, 1999b.)

In Figure 6.16(b), an improved brazing method is depicted. Here, the cylindrical flexure ring is integral with the titanium missile housing thereby eliminating the need for the separate precisely machined transition cylinder and its interference fit into the bore ID of the missile nose. It is thin and radially compliant for the reason explained above. Two braze joints are used between the dome base and the flat end of the cylindrical ring. A flat washer of thickness 0.008 in. (0.20 mm) made of 99% niobium and 1% zirconium alloy is brazed to the dome base with Incusil-ABA alloy while the other side of the washer is brazed to the flat end of the transition ring with Incusil-15 alloy. This material has essentially the same composition as Incusil-ABA, but without titanium. The melting points of the two braze materials are practically the same at approximately 700°C. A titanium aerodynamic shield is brazed to a shoulder on the nose using the Incusil-15 alloy. All three joints are brazed in vacuum at the same time, thereby facilitating manufacture as compared to the design of view (a).

Both of the above-described designs with brazed domes have yielded durable dome-to-missile joints in production. They are proof-tested at a pressure differential of 90 lb/in^2. to verify strength and joint integrity. Further developments of the basic dome brazing technique were mentioned in Sunne (2003), but were not described in sufficient detail for inclusion here. That author also indicated that other ceramics, such as ALON, have been brazed successfully using the techniques described above. It is necessary that the dome material contain oxides that react somewhat with the brazing material in order for the joint to be successful.

6.5 CONFORMAL WINDOWS

A conformal window is one that blends in with the contours of the structure into which it is mounted so as to maximize aerodynamic performance. Typical applications are on optical instruments carried by high-speed aircraft, missiles, or projectiles where they replace prior configurations such as flat plates or spherical-surfaced shells and domes. By shaping the window to offer minimal disturbance of the adjacent air stream, its surface temperature at a given velocity and altitude can be reduced from that obtained with more conventional designs. This can significantly improve signal-to-noise and so enhance optical performance of the sensor. Conformal windows also can reduce aerodynamic drag (thereby increasing range of a weapon) and radar signature can be reduced. These advantages do not come without some drawbacks, however. Optical design is more difficult and fabrication and testing are more complex, i.e., more expensive and slower. Further, the achieved accuracies of the surfaces may be lower than with more conventional designs. Progress is being made toward reducing these disadvantages so the technology can be applied more freely in the future.

There are three basic configurations for conformal windows: (1) ones approximating the adjacent surface contour by multisegmented flat plates as shown in Figures 6.17(a) and (b), (2) single- and double-axis curved plates such as the cylindrical and toroidal windows shown in Figures 6.18(a) and (b), and (3) axisymmetric dome systems as illustrated in Figure 6.18(c).

The multifaceted configurations blend poorly with the surround, but are included here for completeness. The dual-glazing window represented in Figure 6.6 is of this general type. It was

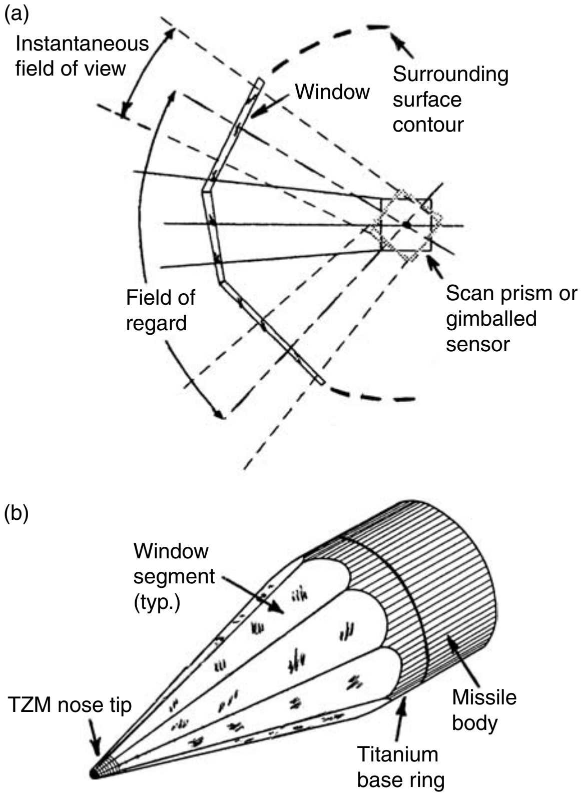

FIGURE 6.17 (a) Multisegmented flat-plate window providing a large field of regard but poor blending with surrounding surface contours (Adapted from Hartman, R., *Proc. SPIE*, 1760, 86, 1992). (b) Missile "dome" comprising eight flat-plate segments in conical configuration (Adapted from Fraser, B.J. and Hemingway, A., *Proc. SPIE*, 2286, 485, 1994.)

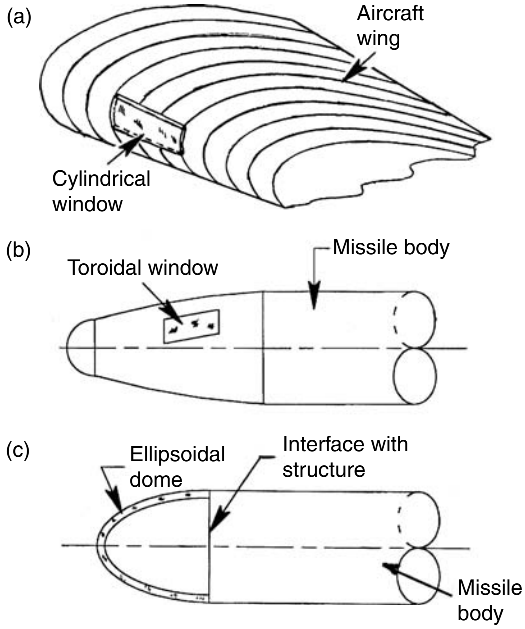

FIGURE 6.18 Conformal window configurations: (a) cylindrical plate, (b) toroidal plate, and (c) ellipsoidal dome.

designed to fit into the bottom of the fuselage of a reconnaissance aircraft. View (a) of Figure 6.17 defines the instantaneous field of view of the sensor as well as the field of regard swept out by the optical axis as a scan prism rotates about a transverse axis or the sensor scans about orthogonal gimbal axes. In view (b) the eight triangular flat plate segments form a "conical" surface that presents a more aerodynamically favorable shape than the conventional spherical dome. The apex of the window is capped with a tungsten/zirconium/molybdenum (TZM) tip that is resistant to the extreme temperature caused by friction at high velocity. The interface with the missile is by way of a titanium ring as indicated.

Figure 6.18 shows three different configurations of conformal windows. In view (a), a cylindrical meniscus window allows target radiation to reach an electro-optical sensor located within the wing of an aircraft. The window shape blends well with the leading edge of the airfoil. In view (b), a window is located in the conical surface of a missile. This window is toroidal meniscus in shape to conform to the differing radii of the cone in the axial and transverse directions. The missile dome of view (c) is ellipsoidal in shape and presents a more aerodynamically favorable blend into the missile skin than the conventional hemispherical dome represented in Figure 6.13. When mounted in a two-axis gimbal system, the sensor can scan in two directions relative to the missile axis.

The image quality of the sensor observing the outside world through a conformal dome will, in general, be increasingly degraded by aberrations as the line of sight departs from the axis of symmetry of the dome (see Figures 6.19[a] and [b]). Astigmatism is the most serious aberration thus introduced, while coma and spherical aberration are also somewhat increased (Shannon et al., 2001). Adding compensating elements to the optical system as in Figure 6.19(c) can reduce aberrations. The simplest systems would utilize fixed compensators (usually with strong asphericities) while more complex systems could have compensators that move in proportion to scan angle. Figure 6.20 shows the basic system of Figure 6.19(c) with two fixed aspheric elements added to improve imagery through the ellipsoidal MgF_2 dome. The main imaging system here is a solid catadioptric system made of CaF_2 since it must transmit IR in the 3 to 5 μm spectral region. The first compensator is ZnS while the second is made of TI-1173 material. The sensor optics are mounted

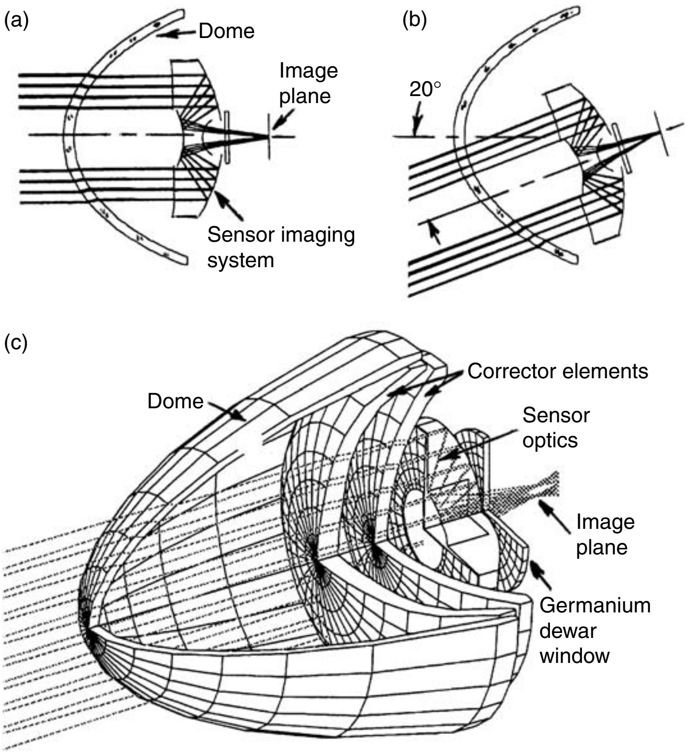

FIGURE 6.19 Sensor configuration using an ellipsoidal conformal dome: (a) line of sight at 0° scan angle, (b) line of sight at −20° scan angle, and (c) view of system with aberration compensating plates. (Adapted from Knapp, D.J. et al., *Proc. SPIE*, 4375, 146, 2001 and Trotta, P.A., *Proc. SPIE*, 4375, 96, 2001.)

in a two-axis gimbal system. The detector array located at the focal plane scans with the sensor optics. Its cryogenic dewar window (shown in Figure 6.19[c]) is germanium. According to Trotta (2001), this sensor provides imagery favorably comparable to that obtained with the corresponding spherical dome.

Figure 6.21 shows schematically how a single-axis horizontally scanning sensor looking through a tilted toroidal conformal window might be compensated with two cylindrical lens elements. In the side view of Figure 6.21(a), the window is seen to be tilted approximately 25° about a horizontal axis. In the top views of Figures 6.21(b) and (c), the sensor is oriented at 0 and + 15°, respectively. The axial spacing between the compensators is varied with scan angle to optimize the image quality. The magnitude of the spacing variation differs with range to the target observed (see Marushin et al., 2001; Mitchell and Sasian 1999).

Fabrication of any conformal window is more complex than the corresponding flat plate or hemispherical dome. One technique for making a doubly curved (toroidal) substrate is illustrated in Figure 6.22. Here, a blank is generated into a cylindrical meniscus shape and then cut into segments at angles as shown. The resulting so-called "barrel staves" are then edge-bonded together to form a rectangular-faceted substrate as shown in the bottom sketch. This substrate is then diamond-turned or ground to the near-net shape meniscus toroid and then polished by a computer-controlled polishing technique (see Gentilman et al., 2003; Marushin et al., 2001; Askinazi et al., 2003).

Creation of hemispherical domes by conventional generation, grinding, and polishing is shown in Figure 6.23(a). Here, three substrates are made from a crystal boule of given height and diameter. An advanced method is illustrated in Figure 6.23(b). Here, seven domes, each equivalent to one made by the conventional process are cut from the same sized boule as in view (a). Cutting is

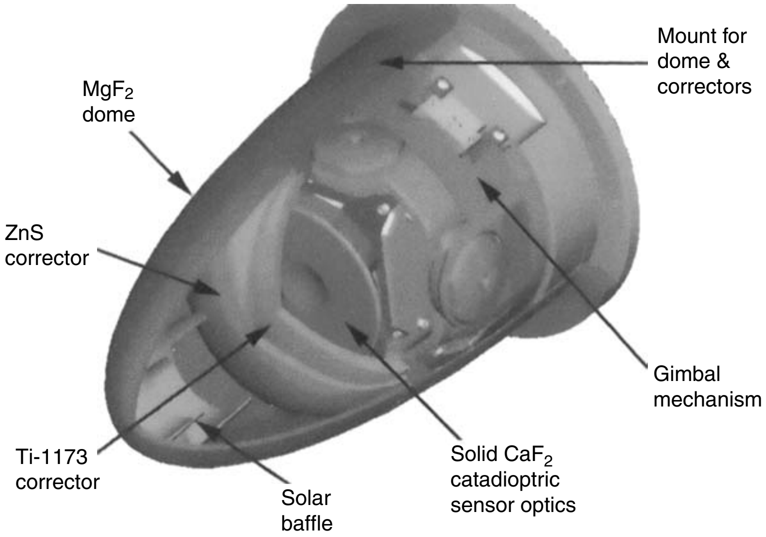
Mount for dome & correctors
MgF2 dome
ZnS corrector
Gimbal mechanism
Ti-1173 corrector
Solar baffle
Solid CaF2 catadioptric sensor optics

FIGURE 6.20 Cut-away view of the system shown in Figure 6.19. (Courtesy of Raytheon Missile Systems, Tucson, AZ.)

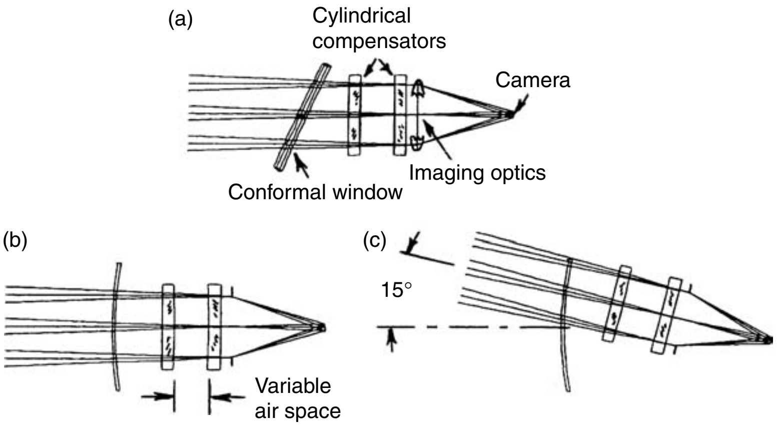
(a)
Cylindrical compensators
Camera
Imaging optics
Conformal window
(b)
Variable air space
(c)
15°

FIGURE 6.21 Schematic layout for horizontal-axis scanning sensor system with a tilted cylindrical conformal window and two cylindrical compensator elements: (a) side view, (b) top view at 0° scan angle, and (c) top view at 15° scan angle. (Adapted from Marushin, P.H. et al., *Proc. SPIE*, 4375, 154, 2001.)

accomplished with the diamond-impregnated edge of a shell-shaped tool using a "scooping" process. When scooping of a given blank is completed, it remains attached to the parent boule by a small central cylinder of material that is carefully broken to separate that blank. The surfaces are then finished to the required specification. Another successful process is to grow a crystal such as sapphire in a vertical-axis hemispherical molybdenum crucible in a vacuum chamber with a vertical temperature gradient by slowly lowering the crucible as the crystallization process builds up the required thickness of material (see Harris, 2003).

Techniques for making nonspherical domes include "hogging out" a blank as shown in Figure 6.23(a), shaping the optical and mechanical surfaces by single-point diamond turning or microgrinding on a computer numerically controlled grinding machine as described by Schaefer et al. (2001). The optical surfaces are then polished by computer-controlled polishing or magnetorheological

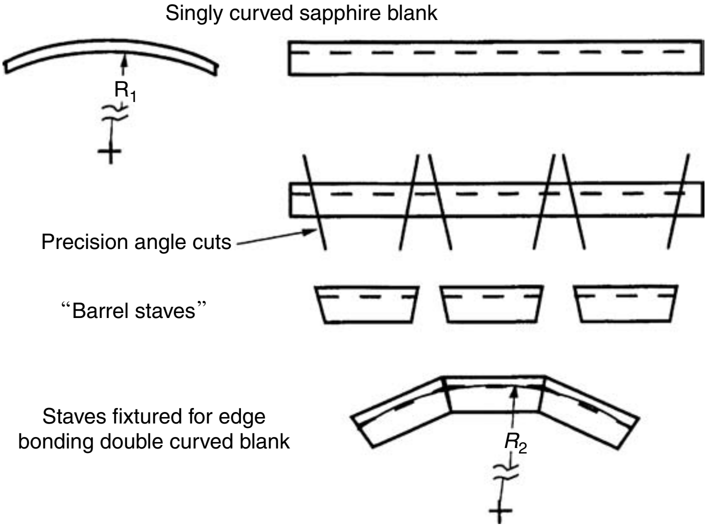
Singly curved sapphire blank
R_1
Precision angle cuts
"Barrel staves"
Staves fixtured for edge bonding double curved blank
R_2

FIGURE 6.22 Method for fabricating doubly curved sapphire "barrel staves" from a singly curved blank. The edges of the segments are then bonded together to form a toroidal window. (From Gentilman, R. et al., *Proc. SPIE*, 5078, 54, 2003.)

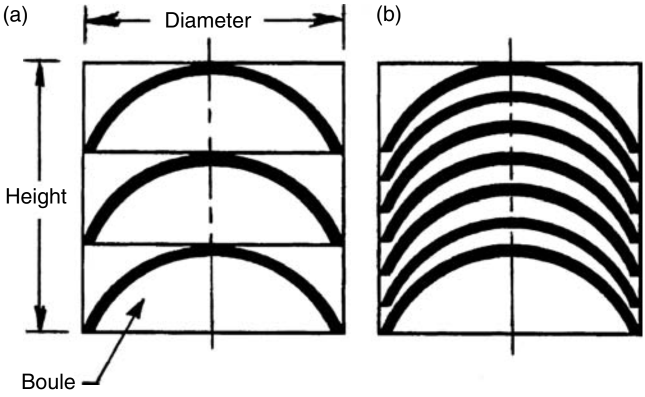

FIGURE 6.23 Fabricating hemispherical domes from cylindrical boules of sapphire: (a) by the conventional generating method and (b) by scooping with a spherical shell tool. (From Harris, D.C. *Proc. SPIE*, 5078, 1, 2003.)

finishing. Pollicove et al. (2003) described the latter technique, developed at the University of Rochester's Center for Optics Manufacturing in some detail. This process significantly reduces the time required to complete a window as compared to conventional means.

A simple test for a system containing a conformal window might be to assess the transmitted image in a simulated real-life setting using a target with known contrast and spatial characteristics. The system's limiting resolution as well as target detectability and identification capability can be measured in this manner. Testing of conformal windows at the component level can be more complex than testing more conventional windows. Hegg and Chen (2001) described a technique for interferometrically testing domes such as that used in the system of Figure. 6.19 and Figure 6.20 before assembly into the system. Their technique involved double-passing the dome as shown in Figure 6.24. An IR interferometer operating at 3.39 μm wavelength (not shown, but located on the far right of the figure) projects a collimated beam in sequence through an aberration compensating

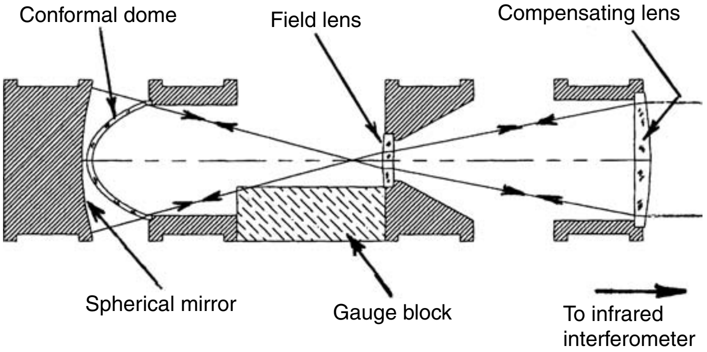

FIGURE 6.24 Schematic layout of setup for interferometrically testing a conformal dome using a null lens. (Adapted from Hegg, R.G. and Chen, C.B., *Proc. SPIE*, 4375, 138, 2001.)

lens, a field lens, and the dome. The transmitted beam retroreflects from a spherical mirror and returns by the same path. The compensating lens and the field lens combine to contribute aberrations equal to and opposite in sign to those introduced by the dome. This is a null test based on the principle of the Offner refractive null test (Offner, 1963). Typically, the compensating lens and the field lens will be plano-convex elements with aspheric curved surfaces. An alternative to aspheric lenses would be to use diffractive surfaces on spherical surfaces of those lenses. The optics shown in Figure 6.24 are mounted in cylindrical cells (shaded) of the same OD so they can be accurately centered to a common axis by simply supporting the cells on a mechanical vee-block. The separations between cells can be controlled accurately by the use of gauge blocks between adjacent surfaces as illustrated in the figure.

6.6 FILTER MOUNTS

Glass and better-quality plastic absorption filters are employed extensively in photography, photometers, automated chemical analysis equipment, and calorimeters. Glass interference filters used singly or in combination with conventional absorption filters are convenient means for isolating specific narrow transmission bands in systems such as those using lasers. Interference filters generally require temperature control.

Gelatin filters are noted for their low cost and wide variety. Inhomogeneities of optical quality, thickness, and surface figure, as well as low mechanical strength and poor durability, limit their use to rather low-performance applications. They are generally used in protected environments. If the gelatin is sandwiched between transparent plates of more durable material such as glass, its physical strength and durability can be greatly improved.

Many applications for optical filters require only that the component be supported approximately centered in and aligned to the light beam of interest. In fixed laboratory instruments, the filter can be simply dropped into a slot and held by gravity. Cell mountings such as the burnished, snap ring, elastomeric, and retaining ring designs described in Chapter 4 for lens elements are frequently employed in portable instruments. Clips that allow for thermal expansion may be used to restrain heat-absorbing filters for projectors and other high-temperature applications. The filter mount illustrated in Figure 4.25(b) is of this type. Interference filters generally require more precise angular orientation to the transmitted beam than ordinary filters, so more attention must be paid to that aspect of their mounting design.

Figure 6.25 shows a set of four glass filters mounted in a multiple-aperture filter wheel for use in a telescope. Each filter has a 25.4 mm (1.00 in.) clear aperture and 3 mm (0.12 in.) thickness. Because there is no need to seal the filters in place or to precisely control their locations and orientations

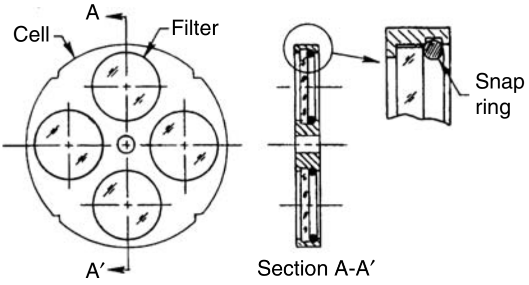

FIGURE 6.25 Schematic views of a simple filter wheel with four filters held in place with snap rings. The mount is provided with detents for indexing to a spring-loaded ball plunger. Reprinted with permission from Yoder, P.R., Jr., in *Handbook of Optomechanical Engineering*, 1997. Copyright CRC press, Bola Raton, FL.)

relative to the optical axis of the system, each disk is secured with a spring-type snap ring as described in Section 4.5.3 and Figure 4.29. The wheel is driven manually from one location to another with positioning at 90° intervals determined by a spring-loaded ball (not shown) dropping into the vee-shaped detents on the wheel's rim. If the application does not require the filters to be removed during the lifetime of the assembly, they could be held in place with an elastomer applied as a continuous ring or as discrete dabs of elastomer symmetrically applied around the edges of the disks. It should be noted that if the application requires one position of the wheel to provide maximum transmission without spectral filtering and the wheel is not in a collimated beam, that space in the wheel should be filled with a clear glass disk so the optical path length is maintained and the system remains in focus.

A filter in which the filter material is attached to a refracting substrate that provides mechanical rigidity or environmental protection to the subassembly is here defined as a *composite* filter. An example is shown in Figure 6.26. Here, a 1.2 mm (0.05 in.) thick sheet of red filter glass is cemented with conventional optical cement to a crown glass window of 7.5 mm (0.30 in.) axial thickness. The 88.9 mm (3.50 in.) diameter subassembly serves two purposes: it transmits into the spectral region characteristic of the filter and is sufficiently stiff to serve as a pressure window to seal an optical instrument against a 0.5 atm pressure differential. The composite construction was chosen to avoid the excessive light loss that would occur if the entire 8.7 mm (0.34 in.) thickness were made of filter glass. The maximum pressure-induced sag of the filter was specified to be ± 1 wave of red HeNe laser light. The pressure-induced bending of this composite filter was not sufficient to damage the cemented interface.

Another composite filter design, for a mosaic of narrow band-pass interference filters cemented between 290-mm (11.4-in.)-diameter crown glass windows, is shown in Figure 6.27. The windows and filter elements were all nominally 6 mm (0.24 in.) thick. The thicknesses of the latter elements were all the same within 0.1 mm (0.004 in.). Rather than control element wedge angle to an extremely tight tolerance, the square elements were made to a "reasonable" wedge tolerance and oriented at assembly to minimize the average beam deviation. This was permissible since the filter was intended for use in a nonimage forming application. The OD of the filter mosaic was made considerably smaller than the ODs of the windows so that an annular "guard ring" made up of crown glass segments could be cemented between the windows to protect the edges of the filters from the environment. The OD of the assembly was edged after cementing.

Because an interference filter is sensitive to temperature, an electrical heater strip was built into the mount so as to surround the cell containing the optical subassembly. A temperature sensor (mounted on one window surface outside the clear aperture) was used to drive a temperature control electrical circuit built into the instrument.

The cemented filter assembly described here was mounted in an aluminum cell and clamped around its edge with a retaining ring secured to the cell with several screws. An O-ring provided a seal. Figure 6.28 shows a sectional view through the mount. The assembly was not intended to be

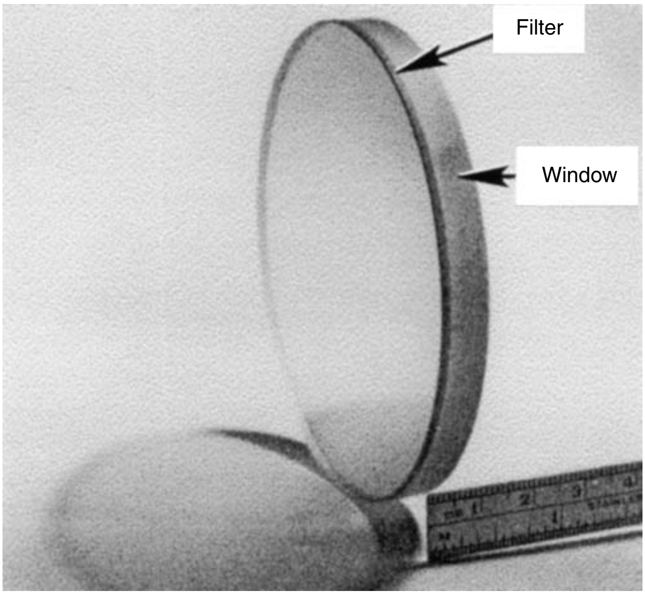
Filter
Window

FIGURE 6.26 A composite filter/window comprising a thin plate of filter glass cemented to a thicker pressure window.

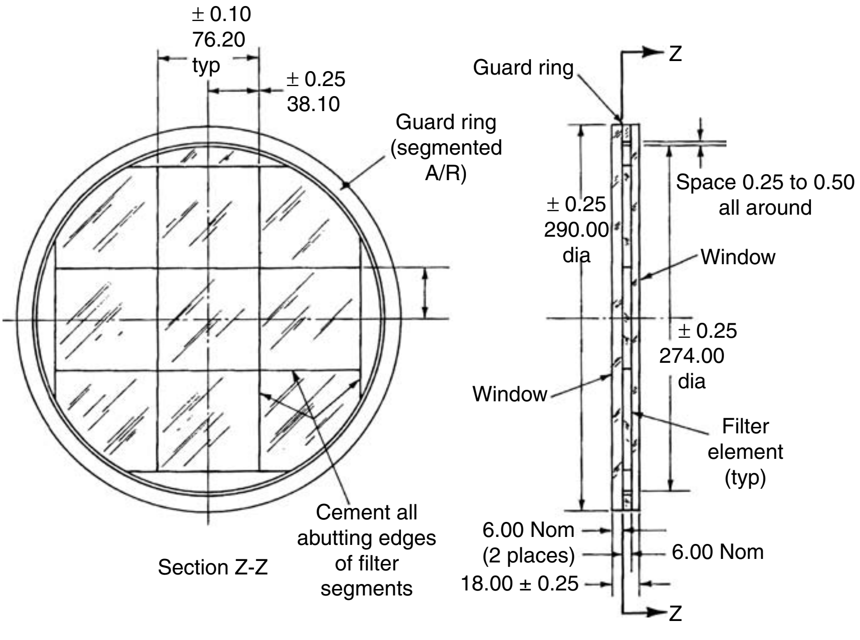
± 0.10
76.20
typ
± 0.25
38.10
Guard ring
(segmented
A/R)
Cement all
abutting edges
of filter
segments
Section Z-Z
Guard ring
Z
± 0.25
290.00
dia
Space 0.25 to 0.50
all around
Window
± 0.25
274.00
dia
Window
Filter
element
(typ)
6.00 Nom
(2 places)
18.00 ± 0.25
6.00 Nom
Z

FIGURE 6.27 Composite filter design consisting of a laminated and heated mosaic of interference filter elements. (Courtesy of Goodrich Corporation, Danbury, CT.)

exposed to a significant pressure differential. The cell was insulated thermally from the body of the optical instrument of which it was a part. The heater caused an acceptable temperature gradient across the aperture of the filter. The filter was designed for a nominal temperature of 45°C (113°F), and to have a spectral passband with nominal full-width-to-half-maximum of 30 Å centered at a

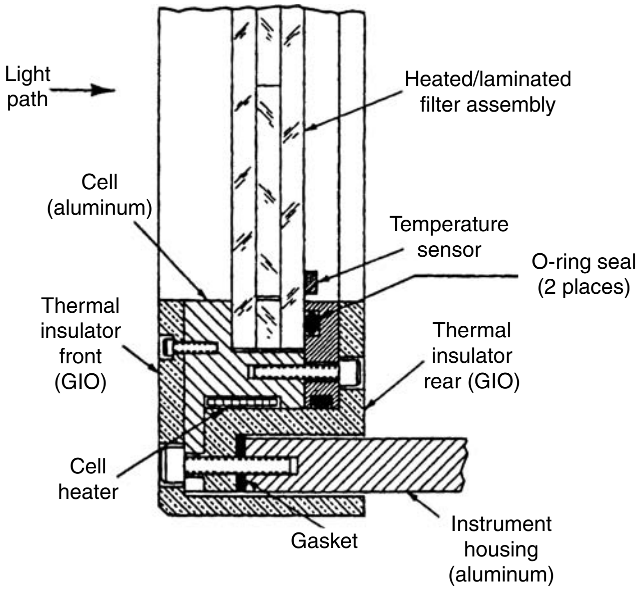
Light path
Heated/laminated filter assembly
Cell (aluminum)
Temperature sensor
O-ring seal (2 places)
Thermal insulator front (GIO)
Thermal insulator rear (GIO)
Cell heater
Gasket
Instrument housing (aluminum)

FIGURE 6.28 Schematic sectional view of the mounting for the filter shown in Figure 6.27. (Courtesy of Goodrich Corporation, Danbury, CT.)

specific near-IR laser wavelength. Radiation outside this passband was blocked with a separate absorption filter of conventional design (not shown).

6.7 WINDOWS SUBJECT TO A PRESSURE DIFFERENTIAL

There are two situations in which the thickness of a window or dome as compared to the diameter of that component becomes very important when the component is supporting a pressure differential. The first is survival and the second is effect upon optical performance. We will consider each of these in terms of their influence on component design.

6.7.1 SURVIVAL

Harris (1999) stated that a plane-parallel circular window subjected to a pressure differential ΔP_W applied uniformly over an unsupported aperture of diameter A_W should have a minimum thickness of t_W to provide a safety factor of f_S over the material's fracture strength S_F. Equation (6.1), adapted from Harris (1999), then applies:

$$t_W = 0.5A_W[K_W f_s \, \Delta P_W / S_F]^{1/2} \tag{6.1}$$

where K_W is a support condition constant, and is equal to 1.25 if the window is unclamped and equal to 0.75 if it is clamped. The customary value for f_S is 4. Typical minimum values for S_F at room temperature for some commonly used infrared window materials as given by Harris (1999) are listed in Table 6.1.

Figure 6.29 illustrates these two types of constraint at the window's edge. The unclamped condition applies approximately if an annular ring of elastomer as described in Section 4.5 supports the window. Maximum stress occurs at the center of this window. The clamped condition applies if a retainer or circular flange applies preload. Maximum stress then occurs at the edge of the clamped area.

TABLE 6.1
Typical Minimum Values for Fracture Strength S_F of Infrared Window Materials[a]

Material	S_F (MPa)	S_F(lb/in.^{2})
MgF_2 (single crystal)	142	2.05×10^4
MgF_2 (polycrystalline)	67	9.71×10^3
Sapphire (single crystal)	300	4.35×10^4
ZnS	100	1.45×10^4
Diamond (CVD)	100	1.45×10^4
ALON	300	4.35×10^4
Silicon	120	1.74×10^4
CaF_2	100	1.45×10^4
Germanium	90	1.30×10^4
Fused silica	60	8.70×10^3
ZnSe	50	7.25×10^3

[a] These values are approximate. They depend upon the quality of the surface finish, fabrication method, material purity, type of test, and size of the sample. *Source*: Adapted from. Harris, D.C., *Materials for Infrared Windows and Domes, Properties and Performance*, SPIE Press, Bellingham, 1999.

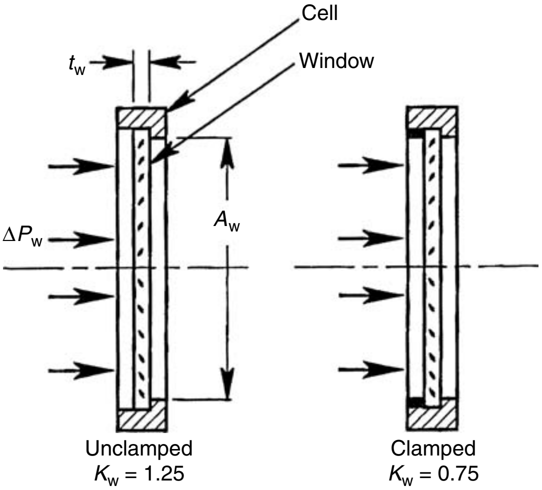

FIGURE 6.29 Schematic of (a) an unclamped circular window and (b) a clamped circular window. (Adapted from Harris, D.C., *Materials for Infrared Windows and Domes*, *Properties and Performance*, SPIE Press, Bellingham, 1999.)

To illustrate the use of Eq. (6.1) consider a sapphire window with an unsupported aperture of 14 cm (5.51 in.) subjected to a pressure differential of 10 atm (147 lb/in.^{2} or 1.01 MPa). Assuming a safety factor f_S of 4, what should its thickness be if it is potted into its mount with a ring of RTV elastomer (i.e., unclamped)? From Table 6.1, the minimum S_F for sapphire is approximately 300 MPa (43,511 lb/in^2.). By Eq. (6.1), $t_W = [(0.5)(14)]\{[1.25)(4)(1.01)]/300\}^{1/2} = 0.909$ cm (0.358 in.).

By examination of Eq. (6.1) written for the two constraint conditions, we see that $(t_{W\ CLAMPED}/t_{W\ UNCLAMPED}) = (0.75/1.25)^{1/2} = 0.775$, so if the same window is clamped, the required t_W can be reduced to (0.775)(0.909) = 0.704 cm (0.277 in.).

Dunn and Stachiw (1966) investigated the thickness-to-unsupported-diameter ratio t_W/A_W for relatively thick plane-parallel plate and conical-rim windows typically used in deep submergence vehicles (see Figure 6.30). The 90° conical window of view (a) is supported along its entire rim and its inner surface is flush with the smaller end of the conical mounting surface. The retaining ring compresses the neoprene gasket to constrain the window at low-pressure differentials. The flat window of view (b) is sealed with an O-ring midway along its rim and constrained to not fall out at zero pressure differential by a retaining ring. The rims of both windows were coated with vacuum grease prior to assembly. Dunn and Stachiw did not specify complete details for these operational designs, but one can infer that the tolerances reported for the experimental versions would also apply. Accordingly, the conical angles are held ±30 arcmin, minor diameters of conical windows are held to ±0.001 in. (25 μm), window rims and mating metal surfaces are finished to 32 rms finish. A radial clearance of 0.005 to 0.010 in. (0.13 to 0.25 mm) is typically provided around flat windows. The material considered was Rohm and Haas Grade B Plexiglas (polymethylmethacrylate).

The parameters varied by the authors included diameter, thickness, pressure differential, mounting flange configuration and, in the case of the conical windows, the included cone angle α (which was varied from 30 to 150°). During testing, the pressure was increased at a rate of 600 to 700 lb/in.^{2} (4.13 to 4.83 MPa) per min to failure. The cold-flow displacement (extrusion) of the window material into the lower-pressure space also was measured. The strength of conical windows was found to increase nonlinearly with the included cone angle, the greatest improvements coming at the lower end of the angular range. Flat windows and 90° conical rim windows of the same t/D_G ratio were found to fail at approximately the same critical loading. Typically, a 1.0 in. (2.5 cm) diameter 90° conical rim window of $t/D_G = 0.5$ failed at about 16,000 lb/in.^{2} (110 MPa). It was concluded that the failure pressure scales as the t/D_G ratio.

The results from Dunn and Stachiw's parametric study typically indicate that, for a 4.0 in. (10.2 cm) unsupported diameter, the windows should be 2.0 in. (5.1 cm) thick. Failure would be anticipated at about 4000 lb/in.^{2} (27 MPa). The window material would be expected to extrude through the cylindrical aperture of the mount by about 0.5 in. (1.3 cm) at the time of failure. The authors wisely recommended proof testing of windows for man-rated applications.

The ability of a thin shell or dome to withstand a pressure differential was discussed by Harris (1999). The pertinent geometry is as shown schematically in Figure 6.31. The optic has a uniform

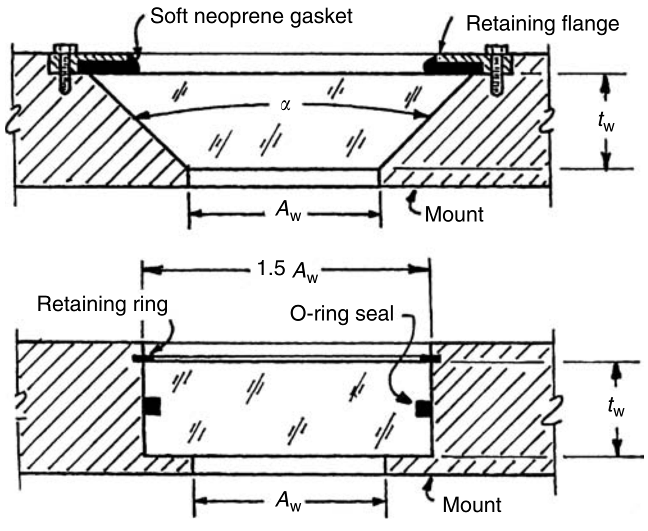

FIGURE 6.30 Typical configurations for high-pressure plane-parallel plate windows made of polymethylmethacrylate for deep submergence vehicles (a) with a 90° conical rim and (b) with a cylindrical rim. (Adapted from Dunn, G., and Stachiw, J., *Proc. SPIE*, 7, D-XX-1, 1966.)

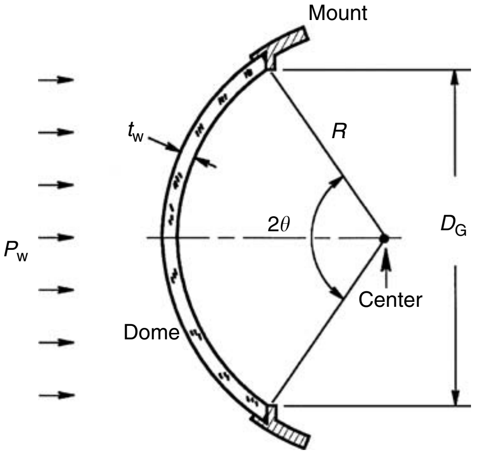

FIGURE 6.31 Geometry of a dome with simply supported base subjected to a pressure differential. (Adapted from Harris, D.C., *Materials for Infrared Windows and Domes, Properties and Performance*, SPIE Press, Bellingham, 1999.)

thickness t_W, a spherical radius R_W, a diameter D_G, an included angle 2θ, and is either simply supported or clamped around the circular rim. We assume that a uniform positive aerodynamic pressure is applied to the exterior surface of the optic. The stress generated in the glass by the pressure differential is compressive if the rim is clamped and tensile if the rim is simply supported. Since glass-like materials fail at lower stress levels in tension than in compression, we here limit our considerations to the latter condition.

Harris (1999) quoted the following equation attributed to Pickles and Field (1994) as applicable to this situation:

$$S_W = [R\Delta P_W/(2t_W)]\ \{\cos\theta[1.6 + 2.44\sin\theta(R/t_W)^{1/2}]-1\} \tag{6.2}$$

An example would be helpful here. Assume that a ZnS dome with $R = 50$ mm and $\theta = 30°$ is exposed to a pressure differential ΔP_W of 1.42 MPa. From Table 6.1, the fracture strength of ZnS is 100 MPa. If we allow a safety factor of $f_S = 4$, then S_W should not exceed 25 MPa. Equation (6.2) cannot be used directly to find the minimum value for thickness t_W that makes this happen, but it can be used for this purpose either by successive approximations or by plotting S_W as a function of t_W and choosing t_W that meets our requirement. Figure 6.32 is a plot of S_W vs. t_W for this example. We see that t_W should be at least 5.27 mm.

Harris (1999) discusses another interesting application involving a pressure differential across a dome. This is the case of a homing sensor at the front of a cannon-launched projectile. Since this is such a special and extreme application, the interested reader is referred to Harris' treatment.

The dual-pane panoramic camera window shown in Figure 6.6 and Figure 6.7 was intended for a military application and was designed, produced, and used in aerial reconnaissance during the Vietnam War. Although its design was critically analyzed from the thermal environment viewpoint, the analytical technology available at that time did not allow prediction of the probability of window failure due to surface defects from manufacture, handling, and environmental exposure (impact with airborne dust, rain, hail, stress corrosion, dynamic fatigue, etc.). Over the years, statistical methods based on fracture mechanics of brittle materials have been developed and applied to a variety of window applications. Fuller et al. (1994) presented a thorough discussion of current technology as applied to a dual-pane BK7 glass window intended for aircraft use with high-resolution photographic equipment aboard a commercial aircraft. In this case, U.S. Federal Air Regulations

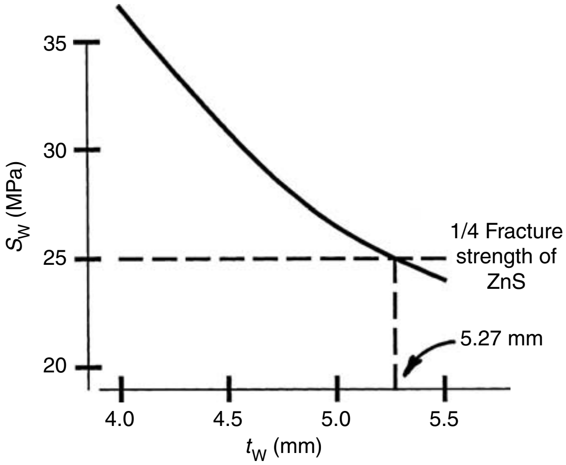

FIGURE 6.32 Plot of tensile stress vs. dome thickness for an example discussed in the text.

applied and posed strict criteria for design acceptance based on demonstrated 95% confidence of 99% survival probability for the window after at least 10,000 h under operating conditions plus fail-safe design.

Pepi (1994) described a window design that met these reliability requirements and provided high optical quality. The complex program of analyses and testing necessary before flights were permitted was also described. A dual-pane configuration was chosen and the window was designed so that the inner pane would remain intact and hold the applicable pressure differential in case of catastrophic failure of the outer pane. In addition, the outer pane was required to survive and maintain the same pressure differential for at least 8 h after failure of the inner pane. Figure 6.33 shows a cross-sectional view of the window mounting in its frame.

The theory underlying the papers by Fuller et al. (1994) and by Pepi (1994) is discussed in more detail in Section 15.2 in connection with the establishment of tolerances for stresses in optical components.

6.7.2 OPTICAL PERFORMANCE DEGRADATION

Vukobratovich (1992) gave the following approximate formula for the optical path difference (OPD) introduced into a transmitted beam by a simply supported, rim-mounted window when it is deformed by a uniform load ΔP_W on its face of unsupported diameter A_W:

$$\text{OPD} = 0.00889\ (n\text{-}1)\Delta P_W^2 A_W^6/(E_G^2 t_W^5) \tag{6.3}$$

where n is refractive index of the window and E_G is Young's modulus for the window material.

If the OPD is equated to the Rayleigh quarter-wave tolerance, the window thickness is given by

$$t_W = 0.5131[(n-1)\Delta P_W^2 A_W^6/(E_G^2 \lambda)]^{0.2} \tag{6.4}$$

Obviously, if the specification were to be a fraction of the Rayleigh tolerance, we would apply that fraction to Eq. (6.3) and derive a new version of Eq. (6.4).

Vukobratovich (1992) indicated that, if this window were to be loaded only by acceleration a_G, the magnitude of ΔP_W to substitute into Eq. (6.3) or (6.4) would be

$$\Delta P_W = a_G \rho_G t_W \tag{6.5}$$

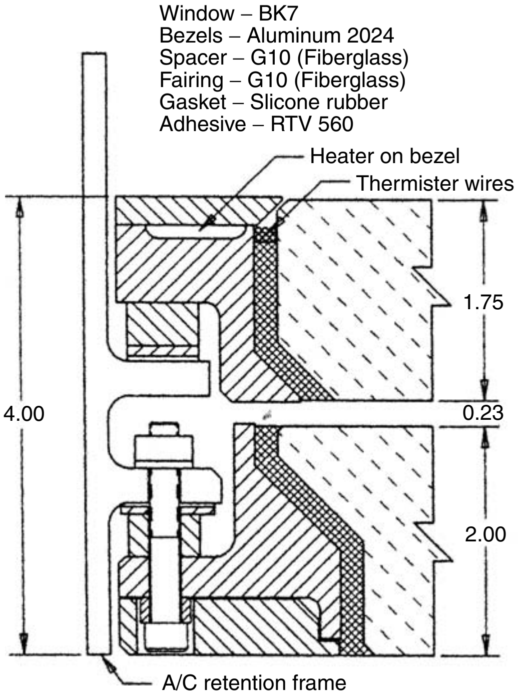

FIGURE 6.33 Cross-section view of the mounting for a dual-pane aircraft window designed for high optical performance in aerial photography as well as high reliability in operation and failsafe capability in case of failure of either pane. Dimensions are in inches. (From Pepi, J.W., *Proc. SPIE*, 2286, 431, 1994.)

where a_G is the acceleration expressed as "times gravity" and ρ_G is the window material's density.

Vukobratovich (1992) also advised that, if the window experiences only aerodynamic loading, then the following applies:

$$\Delta P_W = 0.7PM^2 \tag{6.6}$$

where P is the free stream air pressure and M is the Mach number.

Another way to determine the effect of pressure differential across a window on performance of an optical system containing that window is to set a tolerance on the deflection of the window from its nominal unstressed condition. The following equation from Roark (1954) can be applied:

$$\Delta_x = 3Wa^2(m^2-1)/(16\pi E_G m^2 t_W^3) \tag{6.7}$$

where Δ_x is the deflection of the window's center (in mm or in.), a the radius over which pressure is applied (in mm or in.), $W = w\pi a^2 =$ the total applied load (in N or lb), w the unit applied load (in Pa or lb/in.^{2}), m the reciprocal of Poisson's ratio for the glass, E_G the glass modulus of elasticity (in MPa or lb/in.^{2}), and t_W the window thickness (in mm or in.).

To apply Eq. (6.7) to a practical example, let us calculate the thickness required for the composite window/filter of Figure 6.26 if the maximum pressure-induced surface deflection is to be 1.0 wave of 0.63-μm light (or (1.0)(0.00063)/25.4 = 2.48×10^{-5} in.) when a pressure differential of 0.5 atm is applied uniformly over the central 3.0-in. diameter aperture ($a = 1.50$ in.). We will assume that the material is homogeneous and BK7 glass ($v_G = 0.208$, $E_G = 1.17 \times 10^7$ lb/in.^{2}). The window is clamped all around over an annular zone outside the aperture. Then, $W = (0.5)(14.7)(\pi)(1.50)^2 = 51.95$ lb. Rearranging Eq (6.7) to solve for t_W we get

$$
\begin{aligned}
t_w &= \{3Wa^2(m^2 - 1)/(16\pi E_G m^2 \, \Delta y)\}^{1/3} \\
&= \{(3)(51.95)(1.50^2)(23.114 - 1)/[(16\pi)(1.17 \times 10^7)(4.808^2)(2.48 \times 10^{-5})]\}^{1/3} \\
&= 0.284 \text{ in.}(7.214 \text{ mm})
\end{aligned}
$$

This is about 20% smaller than the actual thickness of the composite filter shown in Figure 6.26 so the deflection tolerance should easily be met.

REFERENCES

Askinazi, J., Estrin, A., Green, A., and Turner, A., Recent advances in the application of computer controlled optical finishing to produce very high quality, transmissive optical elements and windows, *Proc. SPIE*, 5078, 97, 2003.

Dunn, G. and Stachiw, J., Acrylic windows for underwater structures, *Proc. SPIE*, 7, D-XX-1, 1966.

Fraser, B.S. and Hemingway, A., High performance faceted domes for tactical and strategic missiles, *Proc. SPIE*, 2286, 485, 1994.

Fuller, E.R., Jr., Freiman, S.W., Quinn, J.B., Quinn, G.D., and Carter, W.C., Fracture mechanics approach to the design of glass aircraft windows: a case study, *Proc. SPIE*, 2286, 419, 1994.

Gentilman, R., McGuire, P., Fiore, D., Ostreicher, K., and Askinazi, J., Large-area sapphire windows, *Proc. SPIE*, 5078, 54, 2003.

Harris, D.C., *Materials for Infrared Windows and Domes, Properties and Performance*, SPIE Press, Bellingham, 1999.

Harris, D.C., A peek into the history of sapphire crystal growth, *Proc. SPIE*, 5078, 1, 2003.

Hartman, R., Airborne FLIR optical window examples, *Proc. SPIE*, 1760, 86, 1992.

Haycock, R.H., Tritchew, S., and Jennison, P., A compact indium seal for cryogenic optical windows, *Proc. SPIE*, 1340, 165, 1990.

Hegg, R.G. and Chen, C.B., Testing and analyzing conformal windows with null lenses, *Proc. SPIE*, 4375, 138, 2001.

Kingslake, R., *Lens Design Fundamentals*, Academic Press, New York, 311, 1978.

Knapp, D.J., Mills, J.P., Hegg, R.G., Trotta, P.A., and Smith, C.B., Conformal optics risk reduction demonstration, *Proc. SPIE*, 4375, 146, 2001.

Manuccia, T.J., Peele, J.R., and Geosling, C.E., High temperature ultrahigh vacuum infrared window seal, *Rev. Sci. Instrum.*, 52, 1857, 1981.

Marushin, P.H., Sasian, J.M., Lin, J.E., Greivenkamp, J.E., Lerner, S.A., Robinson, B., and Askinazi, J., Demonstration of a conformal window imaging system: design, fabrication, and testing, *Proc. SPIE*, 4375, 154, 2001.

MIL-S-11031B, *Sealing Compound, Adhesive: Curing (Polysulfide Base)*, U.S. Government Printing Office, Washington, DC, 1998.

Mitchell, T.A. and Sasian, J.M., Variable aberration correction using axially translating phase plates, *Proc. SPIE*, 3705, 209, 1999.

Offner, A., Null corrector for paraboloidal mirrors, *Appl. Opt.*, 2, 153, 1963.

Pepi, J.W., Failsafe design of an all BK-7 glass aircraft window. *Proc. SPIE*, 2286, 431, 1994.

Pickles, C.S.J. and Field, J.E., The dependence of the strength of zinc sulfide on temperature and environment, *J. Mater. Sci.*, 29, 1115, 1994.

Pollicove, H.M., Fess, E.M., and Schoen, J.M., Deterministic manufacturing processes for precision optical surfaces, *Proc. SPIE*, 5078, 90, 2003.

Roark, R.J., *Formulas for Stress and Strain*, 3rd ed., McGraw-Hill, New York, 1954.

Robinson, B., Eastman, D.R., Bacevic, J., Jr., and O'Neill, B.J., Infrared window manufacturing technology, *Proc. SPIE*, 430, 302, 1983.

Schaefer, J.P., Eicholtz, R.A., and Sulzbach, F., Fabrication challenges associated with conformal optics, *Proc. SPIE*, 4375, 128, 2001.

Shannon, R.R., Mills, J.P., Pollicove, H.M., Trotta, P.A., and Durvasula, L.N., Conformal optics technology enables window shapes that conform to an application, not to conventional optical limitations, *Photon. Spectra*, 35, 86, 2001.

Speare, J. and Belioli, A., Structural mechanics of a mortar launched IR dome, *Proc. SPIE*, 450, 182, 1983.

Stoll, R., Forman, P.F., and Edleman, J., The effect of different grinding procedures on the strength of scratched and unscratched fused silica, *Proceedings of Symposium on the Strength of Glass and Ways to Improve It*, Union Scientifique Continentale du Verre, Charleroi, Belgium; Vol. 1, 1961.

Sunne, W.L., Dome attachmant with brazing for increased aperture and strength, *Proc. SPIE*, 5078, 121, 2003.

Sunne, W.L., Ohanian, O., Liguori, E., Kevershan, M., Samonte, J., and Dolan, J., Vehicle Having a Ceramic Radome Affixed Thereto by a Compliant Metallic Transition Element, U.S. Patent 5,884,864, 1999a.

Sunne, W.L., Nagy, P.A., and Liguori, E. B., Vehicle Having a Ceramic Radome Affixed Thereto by a Compliant Metallic 'T'-Flexure element, U.S. Patent 5,941,479, 1999b.

Trotta, P. A., Precision conformal optics technology program, *Proc. SPIE*, 4375, 96, 2001.

Vukobratovich, D., Introduction to Opto-Mechanical Design, *SPIE Short Course* SC014, 2003.

Yoder, P. R., Jr., Non-image-forming optical components, *Proc. SPIE*, 531, 206, 1985.

Yoder, P. R., Jr., Optical mounts: lenses, windows, small mirrors, and prisms, in *Handbook of Optomechanical Engineering*, CRC Press, Boca Raton, FL, 1997, Chap. 6.

Yoder, P. R., Jr., *Mounting Optics in Optical Instruments*, SPIE Press, Bellingham, 2002.

7 Designing and Mounting Prisms

7.1 INTRODUCTION

In this chapter, we first address the geometric relationships that govern the function of prisms and then consider specific designs for prisms that serve useful purposes in optical instruments, but do not contribute optical power and, hence, cannot form images by themselves. Small motions or misalignments of some such components relative to other system components may not affect overall system performance. Good examples are a Porro prism that tilts about an axis perpendicular to the plane of reflection or a cube corner prism that tilts about any of three orthogonal axes. In both cases, for small tilts of the optic, the reflected beams are not disturbed. In spite of these and similar peculiarities of specific prism types, it is good engineering practice to carefully establish and maintain the locations and orientations of all prisms. Mountings for these components then become rigorous opto-mechanical design problems.

The principal uses of prisms in optical instruments are as follows:

- To bend (deviate) light around corners
- To fold an optical system into a given shape or package size
- To provide proper image orientation
- To displace the optical axis laterally
- To provide for optical path length adjustment
- To divide or combine beams by intensity or aperture sharing at a pupil
- To divide or combine images at an image plane
- To provide dynamic scanning of beams
- To disperse light spectrally
- To modify the aberration balance of the system of which they are a part

Designs for many types of prisms that accomplish most of these functions are considered in this chapter. We then discuss various ways in which selected standard forms of prisms are usually mounted.

7.2 GEOMETRIC RELATIONSHIPS

7.2.1 REFRACTION AND REFLECTION AT PRISM SURFACES

The behavior of light rays at an interface between two media such as air and glass is determined by the laws of refraction and reflection (see Figure 7.1). Refraction is expressed by Snell's law, which is written as follows:

$$n \sin I = n'_i \sin I'_i \tag{7.1}$$

where n_i and n'_i are the refractive indices before and after the ith interface and I_i and I'_i the angles of incidence and refraction of a given ray before and after that same interface, respectively.

Reflection at an optical surface follows the law of reflection, which is

$$I'_i = I_i \tag{7.2}$$

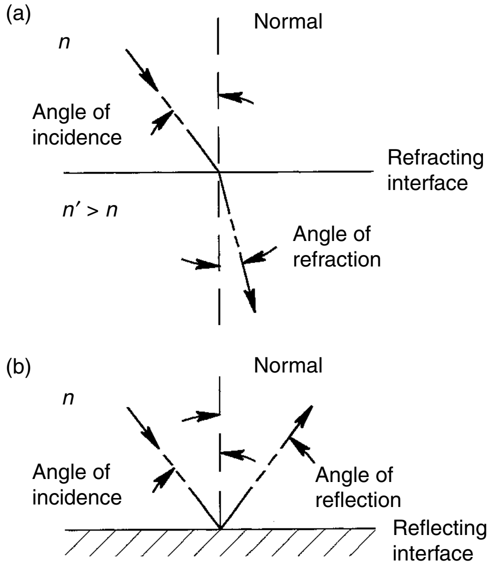

FIGURE 7.1 (a) Refraction and (b) reflection at a plane interface.

where the angles are those of incidence and reflection. A change of algebraic sign is understood to occur upon reflection because the incident and reflected rays lie on opposite sides of the surface normal at the point of incidence.

7.2.2 ABERRATIONS CAUSED BY PRISMS AND PLATES

Internally reflecting prisms are generally designed so that entrance and exit faces are both perpendicular to the optical axis of the transmitted beam. If the beam is collimated and passes through the prism normal to the entrance and exit faces, no aberrations are introduced. Aberrations are introduced if the beam is divergent or convergent; they become asymmetric if the beam enters the prism at an angle to the axis. In a converging beam, a prism overcorrects the three longitudinal aberrations (spherical, chromatic aberration, and astigmatism) while it undercorrects the transverse aberrations (coma, distortion, and lateral color). Smith (2000) provided, in his Section 4.8, convenient, exact, third-order equations for computing the aberration contributions of a prism of index of refraction *n* by defining it as a thick plane-parallel plate of thickness *t* oriented with the surfaces normal to the axis or tilted through some angle relative to the axis. These aberrations can also be determined by surface-by-surface ray tracing in a lens design code.

7.2.3 BEAM DISPLACEMENTS CAUSED BY PRISMS AND PLATES

The refraction-induced axial displacement Δ of an image formed through a plane-parallel plate of index *n* and thickness *t* oriented normal to the axis is shown in Figure 7.2, while the transverse displacement *D* of an axial ray passing through a plane-parallel plate tilted by an angle *I* is illustrated in Figure 7.3. The exact equations for these displacements are

$$\Delta = t\left(1 - \frac{\tan U'}{\tan U}\right) = t/n\left(n - \frac{\cos U}{\cos U'}\right) \tag{7.3}$$

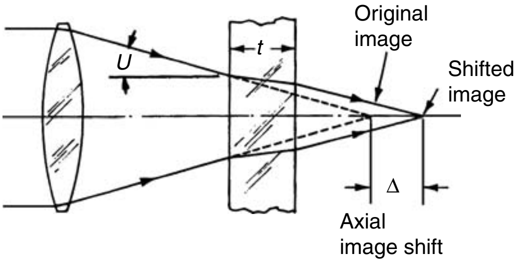

FIGURE 7.2 Axial shift of an image by a plane-parallel glass plate or prism with refracting surfaces oriented perpendicular to the axis of a convergent beam.

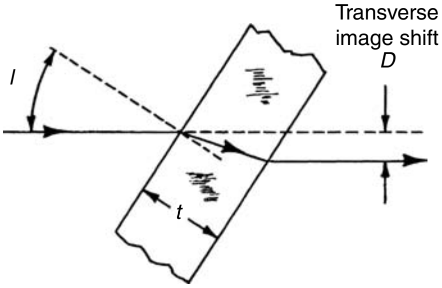

FIGURE 7.3 Lateral displacement of an axial ray by a tilted plane-parallel plate or prism.

$$D = t \sin I \left(1 - \frac{1 - \sin^2 I}{n^2 - \sin^2 I}\right)^{1/2} \tag{7.4}$$

For small angles, these reduce to the following paraxial versions:

$$\Delta = t(n - 1)/n \tag{7.5}$$

$$D = \Delta i \tag{7.6}$$

where i is the tilt angle in radians.

7.2.4 TUNNEL DIAGRAMS

Reflection at a mirror or within a prism constitutes a form of "folding" of the ray paths. In Figure 7.4, a lens images a distant vertical arrow (not shown) as the image AB. If a mirror is inserted as indicated by the dashed line MM′, the reflected image is formed at A′B′. Note that if the page were to be folded along the line MM′, the virtual image AB and the solid-line rays would exactly coincide with the real image A′B′ and the reflected (dashed-line) rays. It is frequently convenient to represent such a folded diagram by its simpler in-line or unfolded counterpart. With internally reflecting prisms, an unfolded diagram is called a *tunnel diagram*. Such diagrams are particularly helpful when designing an optical instrument using prisms, since they simplify the determination of required apertures and, hence, prism size. Figure 7.5 shows the tunnel diagram for a right-angle prism ABC. Rays a-a″ and a-a′ as well as b-b″ and b-b′ are symmetrical about the reflecting surface A-B.

To illustrate one use of a tunnel diagram, let us consider the telescope optical system shown in Figure 7.6. This might be a spotting telescope or one side of a binocular with a Porro prism-erecting

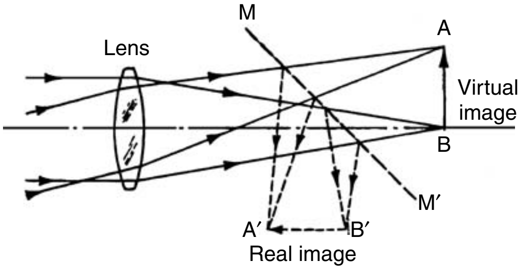

FIGURE 7.4 Folding an optical path with a mirror.

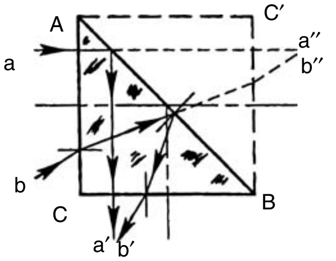

FIGURE 7.5 The tunnel diagram for a right-angle prism. (From Yoder, P.R., Jr., *Mounting Optics in Optical Instruments*, SPIE Press, Bellingham, 2002.)

system. The prisms erect the image as indicated by the "arrow crossed with a drumstick" symbols at various locations in the figure. Figure 7.7 shows the front portion of this optical system with the prisms represented by tunnel diagrams. The diagonal lines indicate folds in the light path. In view (a), the conventional refracted path through each Porro prism is indicated by unfolding the path at each reflecting surface. For prisms of square face width A to sharp corners, the axial length of each prism is $2A$. In view (b), the tunnel diagrams are represented with axial lengths $2A/n$; these are the thicknesses of air optically equivalent to the paths through the glass plates. In the latter diagram, the marginal rays converging to the axial image point are not refracted at the surfaces; they are drawn straight through the glass. To paraxial approximation, their intercepts on the prism surfaces are identical to the actual values.

Smith (2000) used such a diagram to illustrate the computation of the minimum size Porro system that can be used for a 7 × 50 binocular. He chose an objective focal length of 7 in. (177.8 mm) and an image diameter of 0.625 in. (15.88 mm). He noted from a figure similar to Figure 7.7(b) that the proportion of face width A_i to "equivalent air thickness" was A_i: $2A_i/n_i$ or $n_i/2$. For $n = 1.5$, this ratio reduces to 1:2/1.5 = 3:4. Smith then drew a diagram of the type shown in Figure 7.8 to illustrate the use of this ratio to define the minimum prism apertures A_1 and A_2. The dashed lines drawn from the top front corners of the prisms to the opposite vertices have slopes m of half the ratio just derived or $n_i/4$. These lines are the loci of the sharp corners of a family of prisms that have the proper proportions. The heights of the intersections of the dashed lines and the outermost full-field ray (called the upper rim ray [URR] directed to the top of the image) locate the corners of the prisms. It should be noted that the prism tunnel diagrams must be spaced along the optical axis with the proper air spaces of the system design.

We see from Figure 7.8 that the slope of the URR is

$$\tan U'_{\mathrm{URR}} = \frac{(D/2) - H'}{EFL_{\mathrm{OBJ}}} \tag{7.7}$$

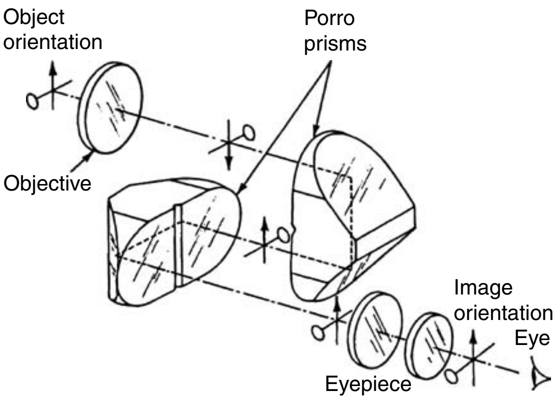
Object orientation
Porro prisms
Objective
Image orientation
Eye
Eyepiece

FIGURE 7.6 Optical system of a typical prism-erecting telescope.

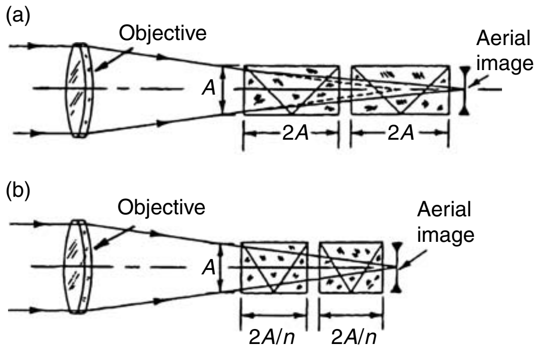
(a)
Objective
Aerial image
A
2A
2A
(b)
Objective
Aerial image
A
2A/n
2A/n

FIGURE 7.7 Objective from Figure 7.6 with two Porro prisms shown by (a) conventional tunnel diagrams with refraction occurring at the air–glass interfaces and (b) tunnel diagrams with equivalent air thickness allowing rays to pass straight through. (Adapted from Smith, W.J., *Modern Optical Engineering*, 3rd ed., McGraw-Hill, New York, 2000.)

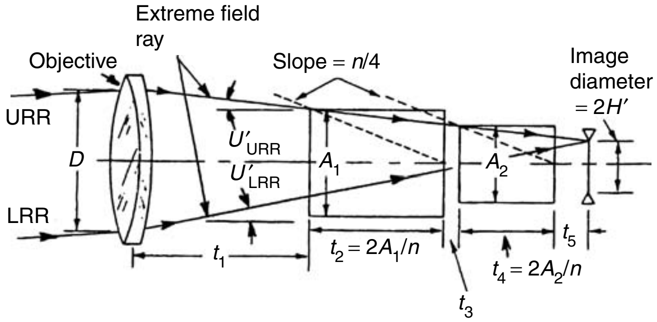
Extreme field ray
Objective
Slope = n/4
Image diameter = 2H′
URR
D
LRR
U′URR
U′LRR
A1
A2
t1
t2 = 2A1/n
t3
t4 = 2A2/n
t5

FIGURE 7.8 More detailed version of Figure 7.7(b) allowing the determination of minimum prism apertures from the geometric proportions of the prisms and extreme unvignetted rays for glass $n = 1.5$. (Adapted from Smith, W.J., *Modern Optical Engineering*, 3rd ed., McGraw-Hill, New York, 2000.)

and the semiaperture of the second prism is $A_2/2 = H' + (t_4 + t_5)(\tan U')$. This semiaperture is also $A_2/2 = (m)(t_4) = (n_i)(t_4)/4$. Equating these expressions, we obtain the thickness of the second prism as

$$t_4 = \frac{(t_5 \tan U'_{\mathrm{URR}}) + H'}{(n_i/4) - \tan U'_{\mathrm{URR}}} \tag{7.8}$$

and so

$$A_2 = n_i t_4/2 \tag{7.9}$$

Using similar logic, we derive the following expressions for the thickness and aperture of the first Porro prism as

$$t_2 = \frac{(t_3 + t_4 + t_5)\tan U'_{\mathrm{URR}}) + H'}{(n_i/4) - \tan U'_{\mathrm{URR}}} \tag{7.10}$$

and

$$A_1 = n_i t_2/2 \tag{7.11}$$

These approximations for the prism dimensions should be confirmed by ray tracing. The dimensions might well be increased by a few percent to allow for protective bevels and dimensional tolerances before the design is considered final.

Generally, in visual optical systems, optical surfaces such as the exit face of the second prism are kept at least 15 diopters away from the eyepiece infinity image plane so that dirt and surface imperfections are out of focus. In Smith's example, the eyepiece had a focal length of (objective EFL divided by the magnification) = 7 in./7 = 1 in. (25.4 mm). One diopter of focus error would then be approximately (eyepiece EFL)^2/39.37 = 0.025 in. (0.645 mm). Fifteen diopters would then be 0.375 in. (9.68 mm). He chose an air space of 0.5 in. (12.7 mm), so the prism surface was well out of focus to the observer's eye.

This same general geometric technique can be applied to other types of prisms used in converging or diverging light beams. The derivations of the appropriate analytic equations for computing apertures in such applications are left to the reader. Once the prism apertures have been defined, we can determine the beamprints of the refracted beam on the prism's reflecting surfaces by an adaptation of the technique discussed in Section 8.3 for finding beamprints on mirrors. The primary difference is the use of the refracted ray slope inside the glass. Geometric ray tracing and many CAD programs can also define these beamprints.

7.2.5 TOTAL INTERNAL REFLECTION

When a light ray is incident at an interface where $n>n'$ (as, e.g., at the hypotenuse surface [surface 2] inside a right-angle prism), total internal reflection (TIR) can occur. In our discussion of tunnel diagrams, we assumed that all rays would reflect, as they would if the surface had a reflective coating such as silver or aluminum. We call such a surface a silvered surface. If the prism's hypotenuse surface is bare, however, Snell's law says that for small angles of incidence and low values of prism index, a ray can refract through that surface into the surrounding air (see ray a-a′ in Figure 7.9). This ray does not contribute to the image formed below the prism. If the ray angle I_2 increases, the angle I'_2 also increases. For some value of I_2, I'_2 will reach 90°. Then sin I'_2 is unity. Since this function cannot exceed unity, we find that rays with $I_2 > I_C$ will reflect internally, as if the surface were silvered. The value of I_2 corresponding to $I'_2 = 90°$ is called the *critical angle*, abbreviated as I_C. This angle is calculated from

$$\sin I_C = n'_2/n_2 \quad \text{or} \quad \sin I_C = 1/n_2 \qquad \text{when } n'_2 \text{ is unity (air or vacuum)} \tag{7.12}$$

We can take advantage of TIR in prisms by choosing a refractive index high enough that the incidence angles for all rays that we want to reflect exceed I_C at the reflecting surface. Then, the

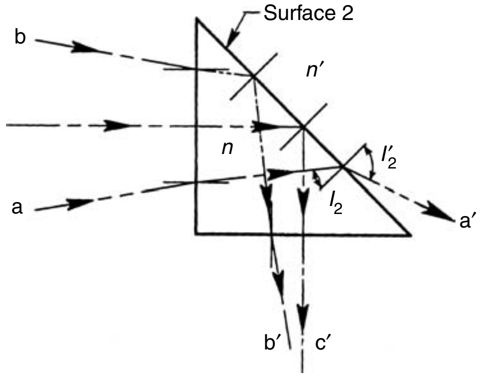

FIGURE 7.9 Ray paths through an unsilvered right-angle prism of low refractive index. Ray a-a is at an angle of incidence I_2 smaller than the critical angle I_C, so it "leaks" through the surface, while I_2 for each of rays b-b and c-c exceeds I_C so they totally reflect internally. (From Yoder, P.R., Jr., *Mounting Optics in Optical Instruments*, SPIE Press, Bellingham, 2002.)

reflections take place without photometric loss, and reflective coatings are not needed on that surface. Because TIR occurs only on clean surfaces, special care must be taken not to let the reflecting surface become contaminated with condensed moisture, fingerprints, or foreign matter that can increase the refractive index outside that surface and allow rays to escape from the prism.

To illustrate TIR, let us assume that the prisms shown in Figure 7.6 are not silvered, are in air, and have a refractive index of 1.620. What total field of view in object space will be seen through the telescope? The objective focal length is 7.0 in. (177.800 mm) and its aperture D is 1.968 in. (50.000 mm). From Eq. (7.12), $\sin I_C = 1/1.620 = 0.61728$, so $I_C = 38.1181°$. From Figure 7.9, the angle I' for ray a-a′ at the prism entrance face is $(45° - I_C) = 6.8819°$. From Snell's law, the ray angle in front of each prism is then $\sin I = (1.620)(\sin 6.8819°) = 0.19411$, so $I = 11.1930°$. This ray angle equals the slope of the lower rim ray (LRR) passing from the bottom of the lens aperture to the top of the image. Hence, $U'_{\mathrm{LRR}} = 11.1930°$ and $\tan U'_{\mathrm{LRR}} = 0.19788$.

Modifying Eq. (7.7) to apply to the LRR (by changing the minus sign to a plus sign in the numerator), we get $\tan U'_{\mathrm{LRR}} = [(D/2) + H']/EFL_{\mathrm{OBJ}} = [(50.000/2) + H']/177.800 = 0.19788$. Solving for the image height, we get $H' = 10.18277$ mm. Since $H' = (EFL_{\mathrm{OBJ}})(\tan U'_{\mathrm{PR}})$, we find that the unvignetted telescope field of view is $\pm \arctan(H'/EFL_{\mathrm{OBJ}}) = \pm 3.2778°$. This, then, is the total usable field of view of the telescope.

7.3 DESIGNS FOR TYPICAL PRISMS

A reference commonly used by optical designers and engineers as a guide in designing prisms is Chapter 13 in MIL_HDBK-141, *Optical Design*, published by the U.S. Department of Defense in 1962. This chapter gives generic equations for prism dimensions, axial path lengths, and tunnel diagrams for many common types of prisms. Most examples included there were similarly described in a now out-of-print book, *Design of Fire Control Optics, ORDM 2-1*, written by Otto K. Kaspereit of Frankford Arsenal and published by the U.S. Army in 1953. Excerpts from one or both of these references were published by Walles and Hopkins (1964), Hopkins (1965), De Vany (1981), Wolfe (1995), Smith (2000), and Yoder (2002). To make this important design information more readily available, we here summarize the designs for 33 types of prisms and prism subassemblies. All types are represented by geometric or functional diagrams. Dimensional equations based on a prism aperture of A are given for most types and, in some cases, isometric views and equations for approximate prism volume and minimum and maximum bonding areas are included. The latter information on area is needed to utilize the mounting techniques described in Section 7.6. Definitions of parameters used in these designs are listed in Table 7.1.

TABLE 7.1
Definitions of Parameters Used in Prism Designs

Parameter	Definition
A	Aperture for passage of a collimated beam
B, C, D, etc.	Other linear dimensions
a, b, c, d, etc.	Typical bevel dimensions
δ, θ, φ, etc.	Angles
t_A	Axial path length
V	Prism volume (neglecting bevels)
ρ	Glass density
a_G	Acceleration factor (times ambient gravity)
Q_{MIN}	Minimum bond area
Q_{MAX}	Maximum circular (C) or racetrack (RT) bond area achievable on prism bonding surface
C (as subscript)	Pertains to circular bond area
RT (as subscript)	Pertains to racetrack shaped bond area
J	Adhesive joint strength.
f_S	Factor of safety

Note: As discussed in Section 15.8, the stresses created by temperature changes may determine upper limits on bond sizes.

7.3.1 THE RIGHT-ANGLE PRISM

The right-angle prism serves several functions, one of which is to fold a light beam by 90°, as shown in the tunnel diagram of Figure 7.5. Figure 7.10 shows three views of the prism with a bonded interface indicated on one of its triangular sides. Table 7.2 provides design equations for this prism as well as nine other prisms derived from the right-angle prism. The numerical values given for the various parameters in each case apply to a particular design as defined in the footnote.

7.3.2 THE BEAM SPLITTER (OR BEAM COMBINER) CUBE PRISM

Two right-angle prisms cemented together at their hypotenuse surfaces with a partially reflective coating at the interface form a cube-shaped beam splitter or beam combiner. This type of prism is shown in Figure 7.11. Its design equations are given in Table 7.2.

If this prism (or any multiple-component prism) is to be bonded to a mechanical mounting, the adhesive joint should be limited to one component; the bond would then not bridge the cemented joint. This is because the two glass surfaces may not be accurately coplanar and the strength of the bond may be degraded by differences in adhesive thickness. If the adjacent surfaces are reground after cementing, bonding across the joint may be acceptable.

Most of the design equations for the beam splitter cube also apply to a monolithic cube such as might be used as a rotating prism in a high-speed camera. With a solid cube, the bond area can be as large as $Q_{MAX} = 0.785A^2$.

7.3.3 THE AMICI PRISM

The Amici prism (see Figure 7.12 and Table 7.2) is a right-angle prism with its hypotenuse shaped as a 90° "roof," so the reflected beam makes two reflections instead of just one. The transmitted image is inverted in the meridian normal to the roof edge. The prism can be used in such a manner that the transmitted beam is split by the dihedral edge between the roof surfaces, or with a larger prism for constant beam size, so the beam hits the roof surfaces separately and in sequence. These possibilities are illustrated in Figures 7.13(a) and (b), respectively. If the beam is split, the dihedral

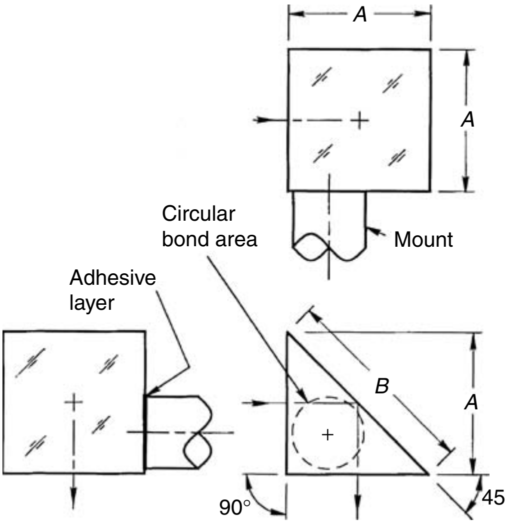

FIGURE 7.10 Design configuration of a right-angle prism. (From Yoder, P.R., Jr., *Mounting Optics in Optical Instruments*, SPIE Press, Bellingham, 2002.)

angle must be accurately 90° (i.e., within a few arcsec) in order not to produce a noticeable double image. This makes the smaller component's cost higher because of the added labor and fixturing required to perfect the roof angle. The prisms of Figure 7.13 are drawn as equal sizes, so the beam of view (b) cannot be larger than $A/2$. The beam axis is displaced laterally by $A/2$ in this case. In view (a), the beam can be almost as large as the prism edge A and is centered.

7.3.4 THE PORRO PRISM

A right-angle prism oriented so that the beam enters and exits the hypotenuse surface, as shown in Figure 7.6 and Figure 7.14(a), is called a "Porro prism." Ray a-a′ travels parallel to the axis, while rays b-b′ and c-c′ enter the prism at different field angles. Note that rays a-a′ and b-b′ turn around and exit parallel to the entering rays. This is true even if the prism is rotated about an axis normal to the 90° dihedral edge. Hence, the prism is retrodirective in the plane of reflection. Rotation about an axis parallel to the central ray connecting the reflecting surfaces results in deviation of the reflected beam by twice the prism rotation angle.

Path c-c′ represents a field ray entering near the edge of the prism. It intercepts the hypotenuse surface A-C at grazing incidence, has three reflections, and produces an inverted image. Such a ray is called a "ghost" ray since it does not contribute useful information to the main image. It does add stray light. This ray can be eliminated by the groove cut into the center of the hypotenuse surface. The tunnel diagram shown in Figure 7.14(b) shows all these rays and the groove.

Figure 7.15 defines the design parameters for this prism. Its design equations are included in Table 7.2.

7.3.5 THE ABBE VERSION OF THE PORRO PRISM

Ernst Abbe modified the design of the Porro prism by rotating one half of the prism about the optic axis by 90° with respect to the other half. Figure 7.16 illustrates this prism, while Table 7.2 provides its design equations. Note that the aperture A of this prism is shown at the same scale as in Figure 7.15. The Abbe version is slightly larger than the standard Porro version because it includes larger bevels. The presence of these bevels and their sizes are design options. This prism is sometimes referred to as a Type 2 Porro prism.

TABLE 7.2
Design Equations for the Right-Angle Prism and a Variety of Prism Types Derived therefrom[a]

Prism Type	Equations
Right-angle (Figure 7.10)	$t_A = A = 1.500$ in. (38.1 mm) $B = 1.414A = 2.121$ in. (53.881 mm) $V = 0.500A^3 = 1.688$ in.^{3} (27.653 cm^3) $Q_{MIN} = V\rho a_G f_S/J = 0.0046$ in.^{2} (2.972 mm^2) $Q_{MAX(C)} = 0.230A^2 = 0.517$ in.^{2} (333.870 mm^2)
Beam splitter/ beam combiner cube (Figure 7.11)	$t_A = A = 1.500$ in. (38.1 mm) $V = A^3 = 3.375$ in.^{3} (55.306 cm^3) $Q_{MIN} = V\rho a_G f_S/J = 0.0092$ in.^{2} (5.944 mm^2) $Q_{MAX(C)} = 0.230A^2 = 0.517$ in.^{2} (333.870 mm^2)
Amici (Figure 7.12)	$t_A = 2.707A = 4.061$ in. (103.140 mm) $a = 0.354A = 0.530$ in. (13.472 mm) $B = 1.414A = 2.121$ in. (53.881 mm) $C = 0.854A = 1.280$ in. (32.522 mm) $D = 1.354A = 2.031$ in. (51.587 mm) $E = 2.415A = 3.621$ in. (91.981 mm) $V = 0.888A^3 = 2.997$ in.^{3} (49.118 cm^3) $Q_{MIN} = V\rho a_G f_S/J = 0.008$ in.^{2} (5.278 mm^2) $Q_{MAX(C)} = 0.164A^2 = 0.369$ in.^{2} (238.064 mm^2) $Q_{MAX(RT)} = 0.306A^2 = 0.689$ in.^{2} (444.338 mm^2)
Porro (Figure 7.15)	$t_A = 2.3A = 3.450$ in. (87.630 mm) $a = 0.1A = 0.15$ in. (3.810 mm) $b = 0.293A = 0.439$ in. (11.163 mm) $B = 1.1A = 1.650$ in. (41.910 mm) $C = 1.414A = 2.121$ in. (53.881 mm) $V = 1.286A^3 = 4.340$ in.^{3} (71.124 cm^3) $Q_{MIN} = V\rho a_G f_S/J = 0.012$ in.^{2} (7.644 mm^2) $Q_{MAX(C)} = 0.608A^2 = 1.368$ in.^{2} (882.579 mm^2)
Abbe version of Porro (Figure 7.16)	$t_A = 2.400A = 3.600$ in. (91.440 mm) $a = 0.100A = 0.150$ in. (3.810 mm) $b = 0.414A = 0.606$ in (15.392 mm) $B = 1.200A = 1.800$ in. (45.720 mm) $C = 2.200A = 3.300$ in. (83.820 mm) $D = 1.556A = 2.334$ in. (59.284 mm) $V = 1.832A^3 = 6.183$ in.^{3} (101.321 cm^3) $Q_{MIN} = V\rho a_G f_S/J = 0.017$ in.^{2} (10.890 mm^2) $Q_{MAX(C)} = 0.388A^2 = 0.873$ in.^{2} (563.225 mm^2)
Porro erecting system (cemented) (Figure 7.17)	$t_A = 4.6A = 6.900$ in. (175.260 mm) $a = 0.1A = 0.150$ in. (3.810 mm) $B = 1.556A = 2.334$ in. (59.284 mm) $V = 2.572A^3 = 8.634$ in.^{3} (142.303 cm^3) $Q_{MIN} = V\rho a_G f_S/J = 0.024$ in.^{2} (15.295 mm^2) $Q_{MAX(C)} = 0.459A^2 = 1.033$ in.^{2} (666.289 mm^2)
Abbe erecting system (cemented) (Figure 7.18)	$t_A = 4.650A = 7.050$ in. (179.070 mm) $a = 0.1A = 0.150$ in. (3.810 mm) $S = 0.050A = 0.075$ in. (1.905 mm)

(*Continued*)

TABLE 7.2 (*Continued*)

Prism Type	**Equations**
	$B = 2.250A = 3.450$ in. (87.630 mm) $V = 3.815A^3 = 12.852$ in.^{3} = (210.606 cm^3) $Q_{\mathrm{MIN}} = V\rho a_G f_S/J = 0.035$ in.^{2} (22.636 mm^2)
Rhomboid (Figure 7.19)	$B =$ variable $t_A = 2A + B = 4.000$ in. (101.600 mm) [assuming $B = 1.000$ in. (25.400 mm)] $C = 1.414A = 2.121$ in. (53.881 mm) $D = 2A + B = 4.000$ in. (101.600 mm) $V = A^2(A + B) = 5.625$ in.^{3} (92.177 cm^3) $Q_{\mathrm{MIN}} = V\rho a_G f_S/J = 0.017$ in.^{2} (10.890 mm^2) $Q_{\mathrm{MAX(C)}} = 0.785A^2 = 1.767$ in.^{2} = (1140.094 mm^2) $Q_{\mathrm{MAX(RT)}} = 0.578A^2 + 0.500AB$ $= 2.051$ in.^{2} (1323.336 mm^2)
Dove (Figure 7.20)	$\theta = 45°, I = 90° - \theta = 45°$ $I' = \arcsin[(\sin I)/n] = 27.783°$ $\delta = I - I' = 17.217°$ $a = 0.050A = 0.075$ in. (1.905 mm) $t_A = (A + 2a)/\sin\delta = 5.574$ in. (14.580 mm) $B = (A + 2a)[(1/\tan\delta) + (1/\tan\theta)]$ $= 6.925$ in. (177.165 mm) $C = B - 2a = 6.875$ in. (173.355 mm) $D = B - 2(A + 2a) = 3.675$ in. (93.345 mm) $E = (A + 2a)/\cos\theta = 2.333$ in. (59.270 mm) $F = (A + 2a)/[2\tan(\theta/2)] = 1.992$ in. (50.590 mm) $V = (A)(B)(A + 2a) - A(A + 2a)^2 - Aa^2$ $= 13.170$ in.^{3} (215.819 mm^3) $Q_{\mathrm{MIN}} = V\rho a_G f_S/J = 0.036$ in.^{2} (23.196 mm^2) $Q_{\mathrm{MAX(C)}} = \pi[(A + 2a)/2]^2 = 2.138$ in.^{2} (1379.511 mm^2) $Q_{\mathrm{MAX(RT)}} = Q_{\mathrm{MAX(C)}} + (A + 2a)(B - 2F)$ $= 7.074$ in.^{2} (4563.678 mm^2)
Double-dove (Figure 7.21)	$\theta = 45°, I = 90° - \theta = 45°$ $I' = \arcsin[(\sin I)/n] = 27.783°$ $\delta = I - I' = 17.217°$ $a = 0.050A = 0.075$ in. (1.905 mm) $t_A = [(A/2) + a)/\sin\delta = 2.787$ in. (70.795 mm) $B = (A + 2a)[(1/\tan\delta) + (1/\tan\theta)]/2$ $= 3.487$ in. (88.578 mm) $C = [(A/2) + a]/\cos\theta = 1.167$ in. (29.635 mm) $D = B - (A + 2a) = 1.837$ in. (46.660 mm) $E = [(A/2) + a]/[2\tan(\theta/2)] = 0.996$ in. (25.295 mm) $V = AB(A + 2a) - 2A[(A/2) + a]^2$ $= 6.589$ in.^{3} (107.979 cm^3) $Q_{\mathrm{MIN}} = V\rho a_G f_S/J = 0.018$ in.^{2} (11.606 mm^2) $Q_{\mathrm{MAX(C)}} = \pi[(A/2) + a]^2/4 = 0.535$ in.^{2} (344.878 mm^2) $Q_{\mathrm{MAX(RT)}} = Q_{\mathrm{MAX(C)}} + [(A/2) + a](B - 2E)$ $= 1.768$ in.^{2} (1140.919 mm^2)

[a] Numerical values represent application of the equations to a typical design with $A = 1.500$ in. The glass type is BK7 ($\rho = 0.091$ lb/in.^{3}), $a_G = 15$, $J = 2000$ lb/in.^{2}, and $f_S = 4$, unless otherwise noted.

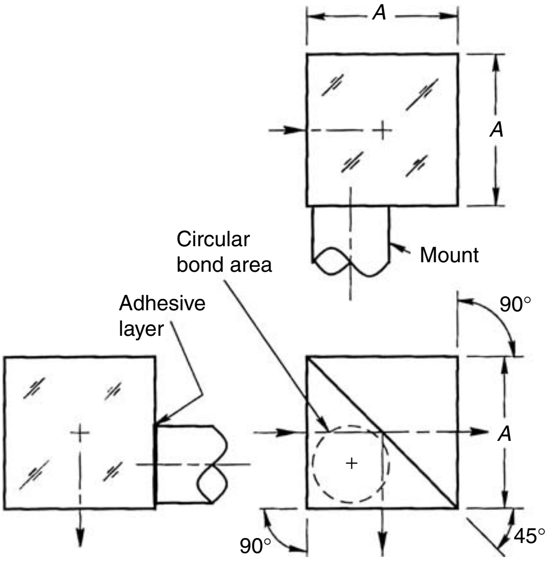
A
A
Circular
bond area
Mount
Adhesive
layer
90°
A
90°
45°

FIGURE 7.11 Design configuration of a beam splitter or beam combiner cube prism. (From Yoder, P.R., Jr., *Mounting Optics in Optical Instruments*, SPIE Press, Bellingham, 2002.)

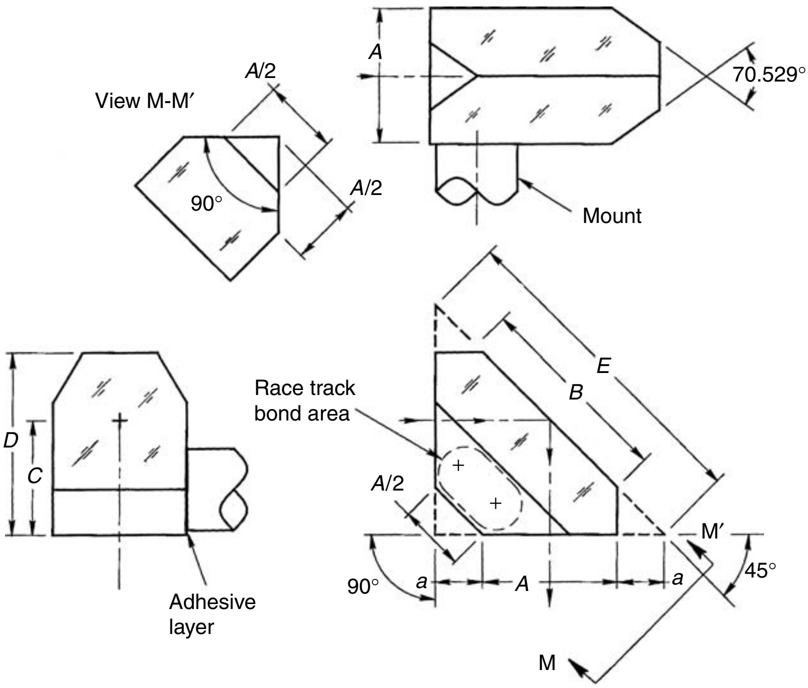
View M-M′
A/2
A/2
90°
A
70.529°
Mount
E
B
Race track
bond area
A/2
D
C
Adhesive
layer
90°
a
A
a
M′
45°
M

FIGURE 7.12 Design configuration of an Amici prism. (From Yoder, P.R., Jr., *Mounting Optics in Optical Instruments*, SPIE Press, Bellingham, 2002.)

7.3.6 THE PORRO ERECTING SYSTEM

Two Porro prisms oriented at a right angle to each other and air spaced as shown in Figure 7.6 or cemented together, as shown in Figure 7.17, constitute a Porro erecting system. The axis is displaced laterally in each direction by *A* plus the width *a* of the bevel on the apex of each prism. Table 7.2 gives

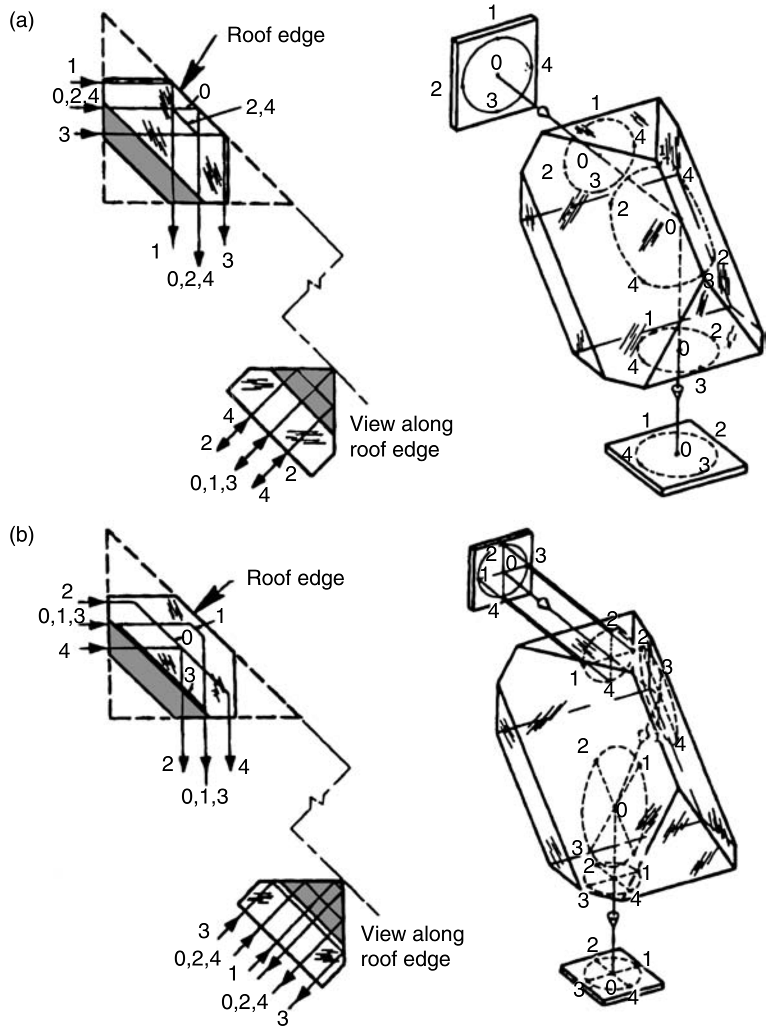
(a)
Roof edge
1
0,2,4
3
0
2,4
1
0,2,4
3
View along
roof edge
4
2
0,1,3
2
4
(b)
Roof edge
2
0,1,3
4
1
0
3
2
0,1,3
4
View along
roof edge
3
0,2,4
1
0,2,4
3

FIGURE 7.13 The Amici prism used (a) symmetrically as a split-beam reflector and (b) off-center as a full-beam reflector. (From MIL-HDBK-141, *Optical Design*, Defense Supply Agency, Washington, DC, 1962.)

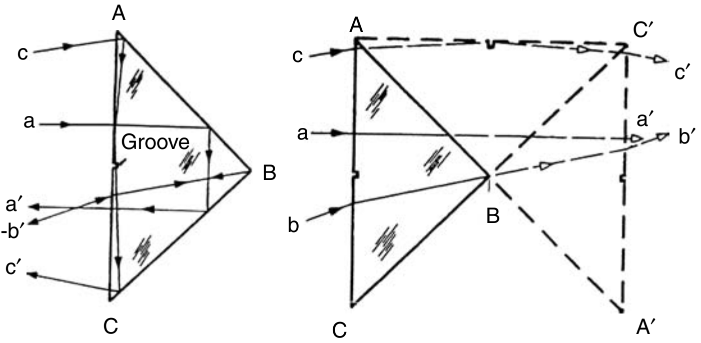
A
c
a
Groove
B
a′
b-b′
c′
C
A
C′
c
c′
a
a′
b′
B
b
C
A′

FIGURE 7.14 (a) Typical ray paths through a Porro prism. (b) The prism's tunnel diagram. (From Yoder, P.R., Jr., *Mounting Optics in Optical Instruments*, SPIE Press, Bellingham, 2002.)

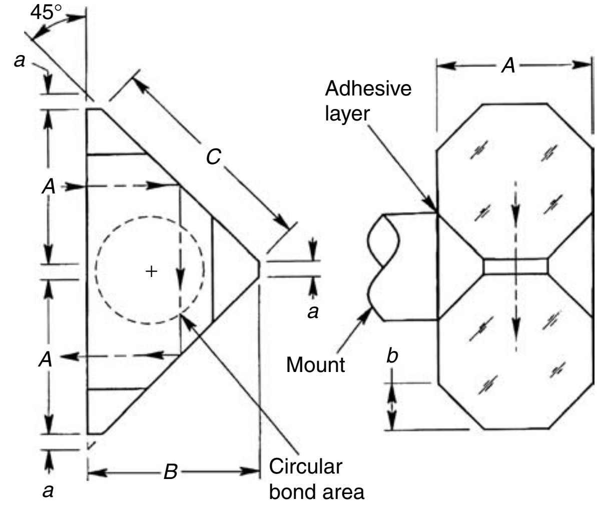

FIGURE 7.15 Design configuration of a Porro prism. (From Yoder, P.R., Jr., *Mounting Optics in Optical Instruments*, SPIE Press, Bellingham, 2002.)

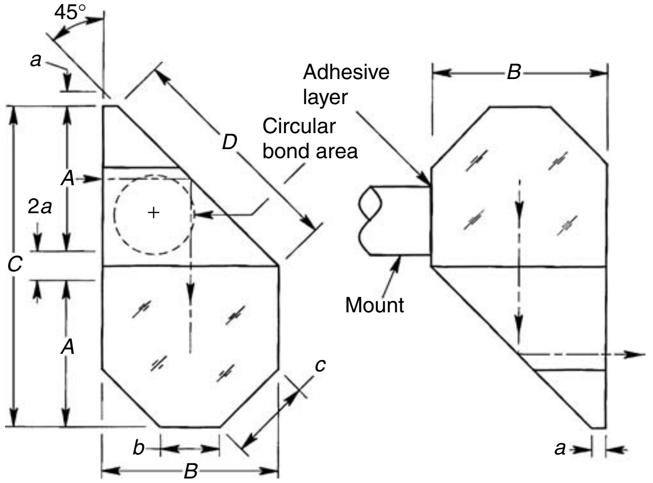

FIGURE 7.16 Design configuration of the Abbe version of a Porro prism. (From Yoder, P.R., Jr., *Mounting Optics in Optical Instruments*, SPIE Press, Bellingham, 2002.)

its design equations. This system is most frequently used in binoculars and telescopes to erect the image. It is not a constant-deviation prism subassembly.

7.3.7 THE ABBE ERECTING SYSTEM

The combination of two Abbe (or Type 2 Porro) prisms of the type described in Section 7.3.5 cemented together side by side with entrance and exit surfaces facing in opposite directions creates an erecting prism subassembly that functions in the same manner as a Porro erecting system. In the optically equivalent design shown in Figure 7.18 and Table 7.2, two right-angle prisms are cemented to a single Porro prism. This arrangement has the advantage that the side of the Porro prism can be bonded to a mount (as shown in the figure). For a given prism aperture, *A*, and with

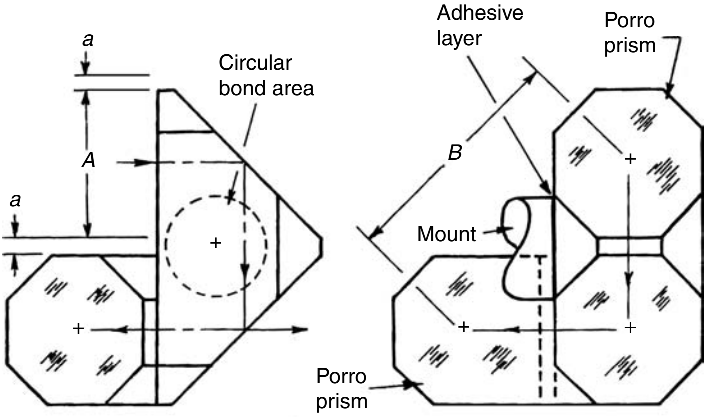

FIGURE 7.17 Design configuration of a Porro-erecting subassembly. (From Yoder, P.R., Jr., *Mounting Optics in Optical Instruments*, SPIE Press, Bellingham, 2002.)

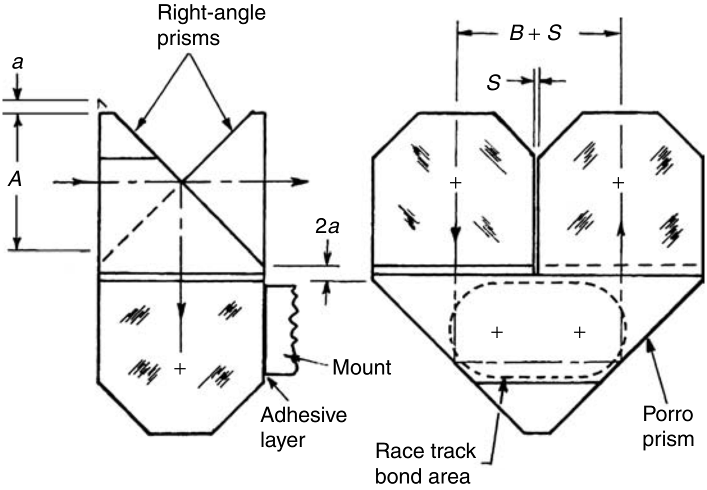

FIGURE 7.18 Design configuration of an Abbe-erecting subassembly. (From Yoder, P.R., Jr., *Mounting Optics in Optical Instruments*, SPIE Press, Bellingham, 2002.)

equal bevels, the lateral offset of this configuration is ~77% of that with the Porro arrangement. The Abbe erector is not a constant-deviation prism.

7.3.8 THE RHOMBOID PRISM

The rhomboid prism shown in Figure 7.19 and designed with the aid of equations from Table 7.2 is essentially a combination of two right-angle prisms with their reflecting surfaces parallel. It is used to displace the axis laterally without changing the axis direction. The image seen through such a device is erect in both meridians.

The prism is insensitive to tilt about an axis normal to the plane of reflection, so it provides constant deviation in that plane. Rotations about the long axis of the prism result in the usual relationship of 2:1 beam deviation vs. reflecting surface rotation. The length of the rectangular central portion of the prism (designated in the figure by the dimension *B*) is a design variable. The rhomboid prism is frequently used as a periscope in military applications to raise the line of vision in order that targets might be seen from entrenchments, from behind obstructions, or from within enclosed vehicles.

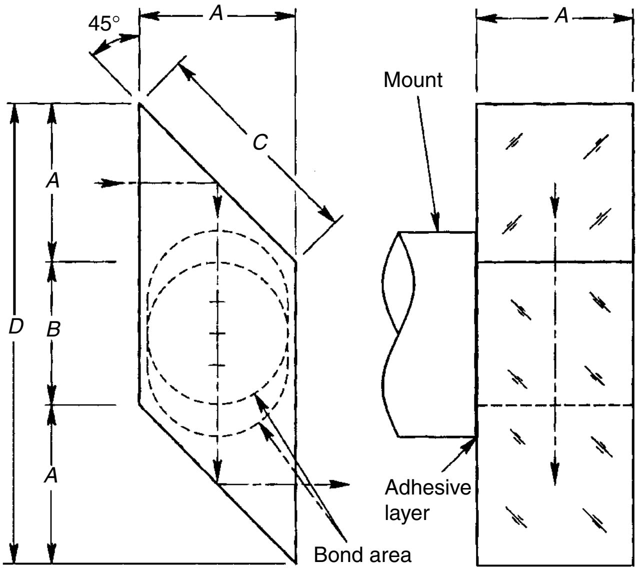

FIGURE 7.19 Design configuration of a rhomboid prism. (From Yoder, P.R., Jr., *Mounting Optics in Optical Instruments*, SPIE Press, Bellingham, 2002.)

7.3.9 THE DOVE PRISM

The Dove prism* is a right-angle prism with the apex section removed and the optical axis parallel to the hypotenuse face as shown in Figure 7.20 (see also Table 7.2). This single-reflection prism inverts the image only in the plane of refraction. If the prism is rotated about its optical axis, the image then rotates at twice the speed of the prism. It is most commonly used to counteract the rotation of an image caused by a line of sight scanning motion of other components in an optical system.

Because of the oblique incidence of the axis at the entrance and exit faces, the prism can be used only in a collimated beam. Alternative versions can have faces tilted at other angles (Sar-El, 1991). Here, we limit consideration to the 45°-incidence case because it is the most common.

The prism dimensions depend upon the prism's refractive index because of deviation of the optical axis at the tilted faces. Table 7.3 shows how the dimensions of a typical Dove prism vary with changes in refractive index. These values were all obtained with the equations given in Table 7.2.

7.3.10 DOUBLE-DOVE PRISM

The double-Dove prism comprises two Dove prisms, each of aperture $A/2$ by A, attached at their hypotenuse faces. Figure 7.21 shows the configuration while Table 7.2 relates its dimensions. It is commonly used as an image rotator or derotator in the manner described for the Dove prism.

The prisms of the double-Dove can be air spaced by a small distance with their hypotenuses parallel and held mechanically. Then, TIR will occur. They can also be cemented together. In that case, a reflective coating such as aluminum or silver is placed on one prism face before the prisms are cemented to keep the light from passing through the interface. For a given aperture, A, the double-Dove prism is one half the length of the corresponding standard Dove prism. To minimize light loss, the leading and trailing edges of both prisms are given only minimal protective bevels.

As shown in the end view of Figure 7.21, a circular beam entering a double-Dove prism is converted into a pair of "D-shaped" beams with curved edges. This tends to reduce the quality of the transmitted image slightly because of diffraction effects. The apertures of optics downstream from the

---

* Also known as the Harting-Dove prism.

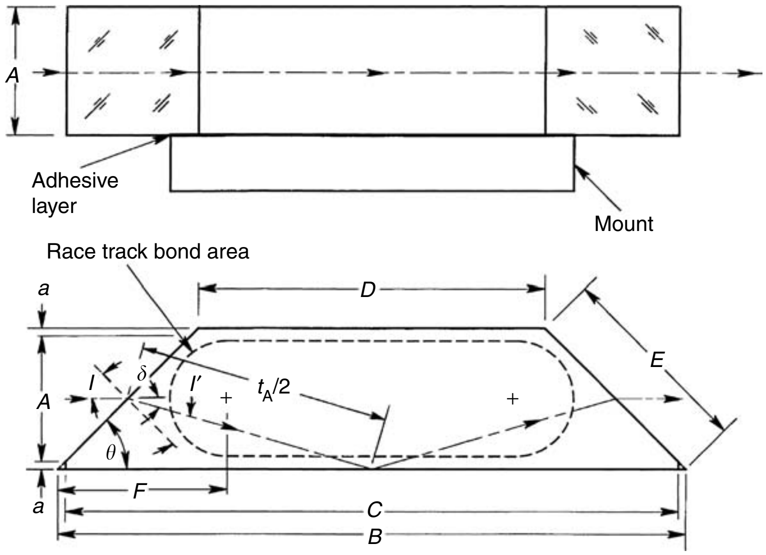

FIGURE 7.20 Design configuration of a Dove prism. (From Yoder, P.R., Jr., *Mounting Optics in Optical Instruments*, SPIE Press, Bellingham, 2002.)

TABLE 7.3
Variations in Dove Prism Dimensions with Refractive Index *n*. The Prism Aperture is Constant at 1.500 in.

n	1.5170	1.6170	1.7215	1.8052
B (in.)	6.975	6.423	6.006	5.746
C (in.)	6.825	6.273	5.856	5.596
D (in.)	3.675	3.123	2.706	2.446
E (in.)	2.333	2.333	2.333	2.333
t_A (in.)	5.574	5.050	4.658	4.416

double-Dove prism must be large enough to accept the overall square shape of the converted beam if vignetting is to be avoided. A double image can result if the reflecting surfaces of the prism are not accurately parallel and the 45° angles are not accurately made.

A cemented version of the double-Dove prism is sometimes used as a means for scanning the line of sight of an optical system in the plane of reflection. In such a prism, the faces with dimensions "C" shown in Figure 7.20 are extended such that the faces marked "D" are reduced almost to zero, thereby forming a prism subassembly that is essentially cube-shaped. To scan, the prism is rotated about an axis normal to the plane of reflection (i.e., parallel to the hypotenuse faces) passing through the prism's geometric center. When it is located in front of a camera, periscope, or other optical instrument with a collimated beam entering from the object, such a prism can scan the system line of sight over 180° in object space.

7.3.11 THE PENTA PRISM

The penta prism neither reverts nor inverts the image; it merely turns the axis by exactly 90°. Its design is defined in Figure 7.22 and in Table 7.4. A useful characteristic of this prism is that it provides constant deviation in the plane of reflection. For this reason, it is used in applications such as optical range finders and surveying equipment, where an exact right-angle deviation is needed.

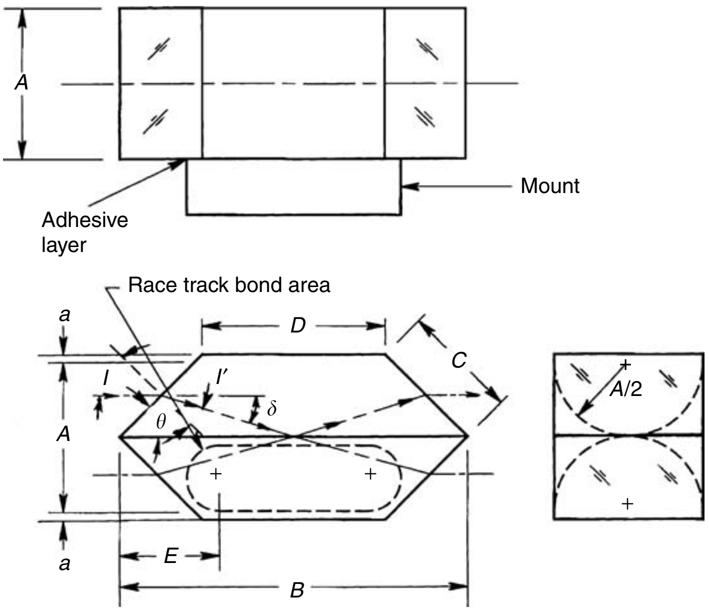
A
Mount
Adhesive layer
Race track bond area
a
D
C
I
I′
δ
θ
A
a
E
B
A/2

FIGURE 7.21 Design configuration of a double-Dove prism subassembly. (From Yoder, P.R., Jr., *Mounting Optics in Optical Instruments*, SPIE Press, Bellingham, 2002.)

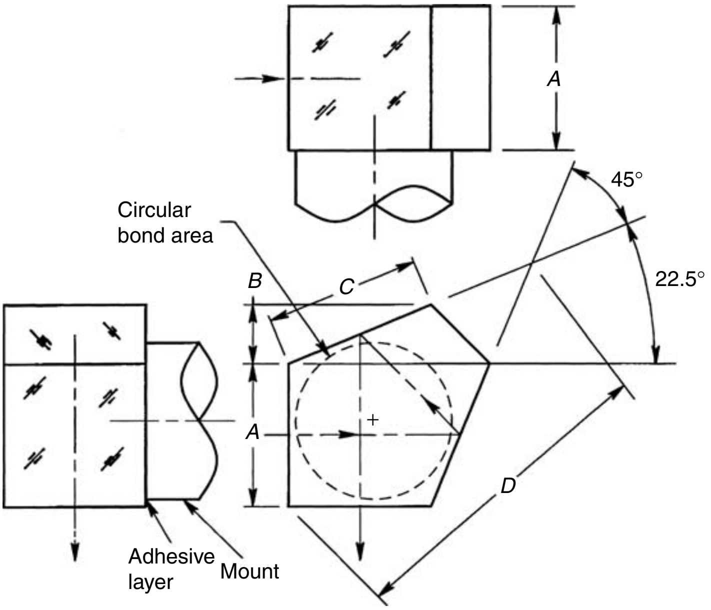
A
45°
22.5°
Circular bond area
B
C
A
D
Adhesive layer
Mount

FIGURE 7.22 Design configuration of a penta prism. (From Yoder, P.R., Jr., *Mounting Optics in Optical Instruments*, SPIE Press, Bellingham, 2002.)

7.3.12 THE ROOF PENTA PRISM

If we configure one reflecting surface of a penta prism as a 90° roof, the prism inverts the transmitted image in the direction normal to the plane of refraction. For a given aperture and material, the roof penta is about 17% larger and 20% heavier than the standard penta. Adding the roof does

TABLE 7.4
Design Equations for the Penta and Roof Penta Prisms[a]

Prism Type	Equations
Penta	$t_A = 3.414A = 5.121$ in. (130.073 mm)
(Figure 7.22)	$B = 0.414A = 0.621$ in. (15.773 mm)
	$C = 1.082A = 1.623$ in. (41.224 mm)
	$D = 2.414A = 3.621$ in. (91.973 mm)
	$V = 1.500A^3 = 5.062$ in.^{3} (82.959 cm^3)
	$Q_{MIN} = V\rho a_G f_S / J = 0.014$ in.^{2} (8.916 mm^2)
	$Q_{MAX(C)} = 1.129A^2 = 2.540$ in.^{2} (1638.868 mm^2)
Roof penta	$t_A = 4.223A = 6.334$ in. (160.896 mm)
(Figure 7.23)	$a = 0.237A = 0.355$ in. (9.030 mm)
	$b = 0.383A = 0.574$ in. (14.592 mm)
	$B = 0.414A = 0.621$ in. (15.773 mm)
	$C = 1.082A = 1.623$ in. (41.224 mm)
	$D = 1.651A = 2.476$ in. (62.903 mm)
	$E = 2.986A = 4.479$ in. (113.767 mm)
	$F = 1.874A = 2.811$ in. (71.399 mm)
	$G = 1.621A = 2.431$ in. (61.760 mm)
	$V = 1.795A^3 = 6.058$ in.^{3} (99.275 cm^3)
	$Q_{MIN} = V\rho a_G f_S / J = 0.016$ in.^{2} (10.670 mm^2)
	$Q_{MAX(C)} = 0.824A^2 = 1.854$ in.^{2} (1196.126 mm^2)

[a] Numerical values represent application of the equations to a typical design with $A = 1.500$ in. The glass type is BK7 ($\rho = 0.091$ lb/in.^{3}), $a_G = 15$, $J = 2000$ lb/in.^{2}, and $f_S = 4$, unless otherwise noted.

not change the penta prism's constant deviation characteristic. The roof penta is shown in Figure 7.23 and its design equations are given in Table 7.4.

7.3.13 The Amici/Penta and Right-Angle/Roof Penta Erecting Systems

A combination of an Amici prism with a penta prism provides two reflections in each direction perpendicular to the axis, so it can be used as an erecting system. Usually, the prisms are cemented together as illustrated in Figure 7.24(a). This design has been used in some binoculars. A functionally similar erecting system can be obtained by combining a right-angle prism with a roof penta prism (see Figure 7.24[b]). For a given aperture *A*, the indicated height dimensions for the two subassemblies differ by about 4%. The latter version is most commonly used in military periscopes. A more easily manufactured variation of this design, illustrated in Figure 7.25, was used in an experimental compact military binocular (Yoder, 1960). It was found to be heavier than other equivalent designs and its light transmission was lower than desired, so it was never produced.

7.3.14 The Reversion, Abbe Type A, and Abbe Type B Prisms

The reversion prism is a two-component cemented prism subassembly configured as shown in Figure 7.26. It has three reflections and functions as an image rotator/derotator that can be used in converging or diverging beams. To design such a prism, one uses the equations from Table 7.5. The central reflecting face, dimensioned "C" in the figure, must have a reflective coating to prevent refraction through it. A protective coating such as electroplated copper and paint usually covers this surface.

Two similar versions of this prism have the central reflecting surface C replaced by a 90° roof to invert the image in the direction perpendicular to the plane of reflection. These prisms are designated

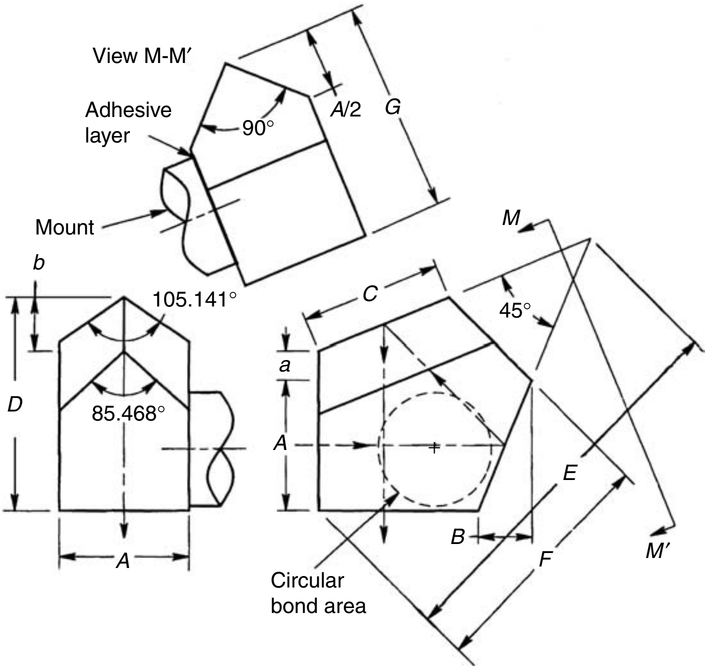

FIGURE 7.23 Design configuration of a roof penta prism. (From Yoder, P.R., Jr., *Mounting Optics in Optical Instruments*, SPIE Press, Bellingham, 2002.)

Abbe Type A and Type B and are shown in Figure 7.27 and Figure 7.28. Table 7.5 gives their design equations. With an even number of reflections in each meridian, these prisms can be used as erecting systems, but not as image rotator/derotator prisms. Functionally the same, they differ primarily in construction and the number of elements. Type A comprises two elements while Type B has three. The latter subassembly is symmetrical.

7.3.15 THE DELTA PRISM

The delta prism is shown in Figure 7.29 while its design equations are included in Table 7.5. The path of an axial ray is depicted in the figure. TIR must occur at both the entrance and exit faces. The intermediate (bottom) face is silvered to make it reflect. With the proper choice of index of refraction and apex half-angle the internal path can be made symmetrical about the vertical axis of the prism; the exiting axial ray is then collinear with the entering axial ray. With three reflections, the delta prism can be used as an image rotator/derotator. Because it has tilted entrance and exit faces, it can be used only in a collimated beam.

Design of this prism starts with choice of n, the index of refraction. A value for θ (one half of the apex angle) is then assumed. The angle of incidence, I_1, at the first surface equals θ. We vary n and θ until the same value for I'_1 is obtained by Eqs. (7.13) and (7.14) as follows:

$$I'_1 = \arcsin(\sin I_1/n) \tag{7.13}$$

$$I'_1 = 4\theta - 90^\circ \tag{7.14}$$

We then calculate I_2 from

$$I_2 = 2\theta - I'_1 \tag{7.15}$$

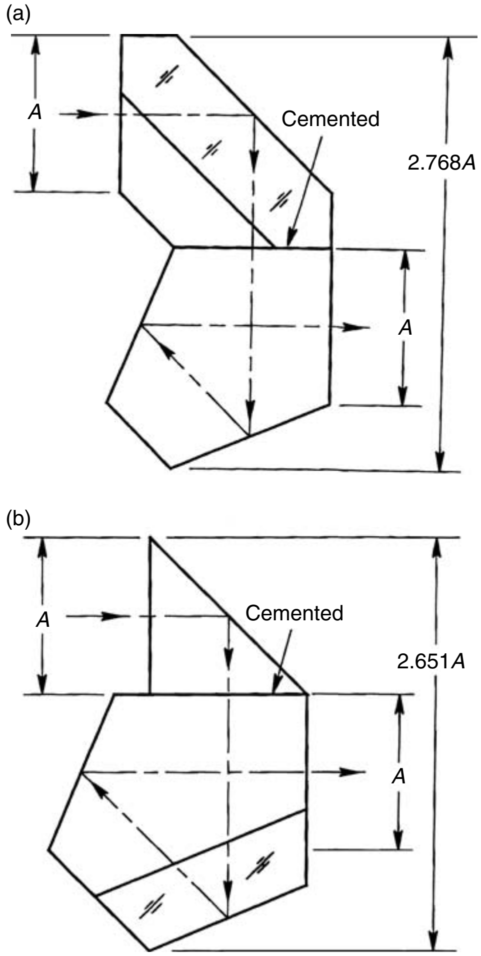
(a)
A
Cemented
2.768A
A
(b)
A
Cemented
2.651A
A

FIGURE 7.24 Other erecting prism subassemblies: (a) Amici/penta system (b) Right-angle/roof penta system. (From Yoder, P.R., Jr., *Mounting Optics in Optical Instruments*, SPIE Press, Bellingham, 2002.)

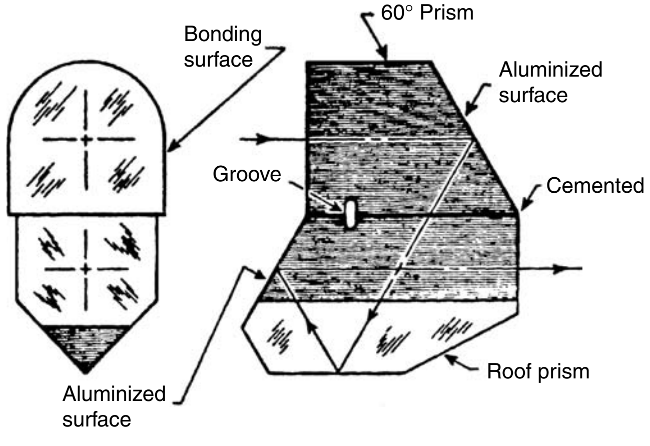
60° Prism
Bonding surface
Aluminized surface
Groove
Cemented
Roof prism
Aluminized surface

FIGURE 7.25 A compact erecting prism assembly used in an experimental military binocular. (From Yoder, P.R., Jr., *J. Opt. Soc. Am.*, 50, 491, 1960.)

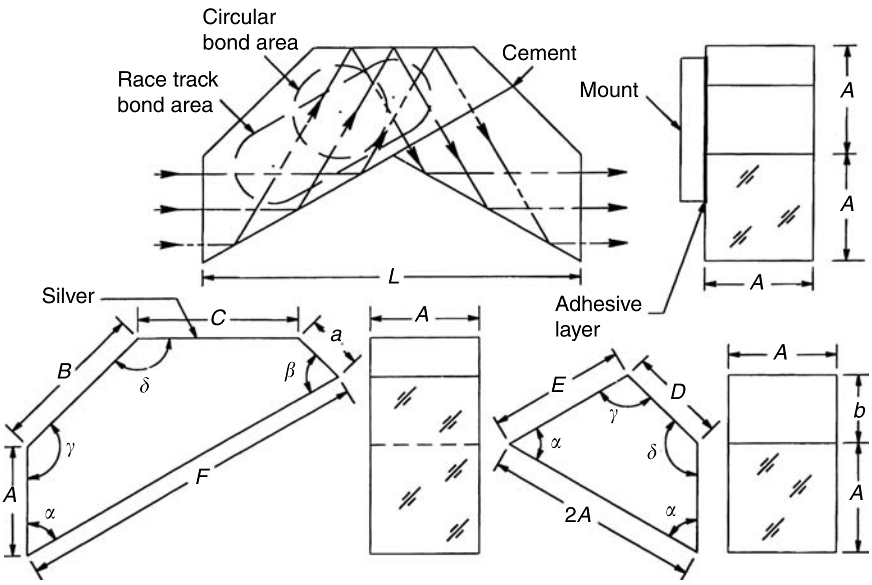

FIGURE 7.26 Design configuration of a reversion prism. (From Yoder, P.R., Jr., *Mounting Optics in Optical Instruments*, SPIE Press, Bellingham, 2002.)

This value for I_2 is compared with I_C from Eq. (7.13) to see if TIR occurs, i.e., $I_2 > I_C$, for the chosen glass. If so, we proceed to design the prism. If not, we choose a higher index and repeat the computations until TIR does occur.

For practical reasons, when choosing the index, we should select values that correspond to an available glass type. Typically, the index that allows TIR will exceed 1.700. Figure 7.30 shows the nearly linear variation of θ with n_d for five typical Schott glasses selected from Table 3.2. Note that the angular relationships for this prism in Table 7.5 apply to an axial ray. In order for all field rays to reflect internally, we can determine the extreme lower rim ray angle U_{LRR} by using the geometry shown in Figure 7.31 and the following equations:

$$I'_1 = 2\theta - I_c \qquad (7.16)$$

$$I_1 = \arcsin(n \sin I'_1) \qquad (7.17)$$

$$U_{URR} = I_1 - \theta \qquad (7.18)$$

For the delta prism example given in Table 7.5, $I_C = 32.715°$, $I'_1 = 19.116°$, $I_1 = 37.295°$, and $U_{LRR} = 11.379°$. Any ray entering the prism at a smaller positive angle of incidence than this ray, or any ray entering with a negative angle of incidence, will totally reflect internally.[†]

7.3.16 THE PECHAN PRISM

The Pechan prism has five reflections and is frequently used as a compact image rotator/derotator in place of the Dove, double-Dove, and delta prisms because it can be used in convergent or divergent beams. The design is shown in Figure 7.32. The design equations are given in Table 7.6. Because this prism uses TIR at the two internal reflections at the largest surface, these uncoated surfaces are air spaced by a small separation on the order of 0.1 mm (0.004 in.). Normally, the prisms

---

[†] Using the sign convention of Smith (2000), a ray with a positive angle of incidence turns clockwise to the normal.

TABLE 7.5
Design Equations for the Reversion, Abbe Type A, Abbe Type B, and Delta Prisms[a]

Prism Type	Equations
Reversion (Figure 7.26)	$\alpha = 30°$, $\beta = 60°$, $\gamma = 45°$, $\delta = 135°$ $a = 0.707A$ = 1.060 in. (26.937 mm) $b = 0.577A$ = 0.865 in. (21.984 mm) $c = 0.500A$ = 0.750 in. (19.050 mm) $t_A = 5.196A$ = 7.794 in. (197.968 mm) $B = 1.414A$ = 2.121 in. (53.873 mm) $C = 1.464A$ = 2.196 in. (55.778 mm) $D = 0.867A$ = 1.300 in. (33.020 mm) $E = 1.268A$ = 1.902 in. (48.311 mm) $L = 3.464A$ = 5.196 in. (131.978 mm) $V = 4.196A^3$ = 14.161 in.^{3} (232.065 cm^3) $Q_{MIN} = V\rho a_G f_S/J$ = 0.039 in.^{2} (24.942 mm^2) $Q_{MAX(C)} = 1.108A^2$ = 2.493 in.^{2} (1608.384 mm^2) $Q_{MAX(RT)} = 2.037A^2$ = 4.583 in.^{2} (2956.930 mm^2)
Abbe type A (Figure 7.27)	$\alpha = 30°$, $\beta = 60°$, $\gamma = 45°$, $\delta = 135°$ $a = 0.707A$ = 1.060 in. (26.937 mm) $b = 0.577A$ = 0.865 in. (21.984 mm) $c = 0.500A$ = 0.750 in. 19.050 mm) $t_A = 5.196A$ = 7.794 in. (197.968 mm) $B = 1.414A$ = 2.121 in. (53.873 mm) $C = 1.309A$ = 1.963 in. (49.860 mm) $L = 3.464A$ = 5.196 in. (131.978 mm) $V = 3.719A^3$ = 12.552 in.^{3} (205.684 cm^3) $Q_{MIN} = V\rho a_G f_S/J$ = 0.034 in.^{2} (21.935 mm^2) $Q_{MAX(C)} = 0.802A^2$ = 1.805 in.^{2} (1164.514 mm^2) $Q_{MAX((RT)} = 1.116A^2$ = 2.512 in.^{2} (1620.642 mm^2)
Abbe type B (Figure 7.28)	$\alpha = 30°$, $\beta = 60°$, $\gamma = 135°$ $a = 0.707A$ = 1.060 in. (26.937 mm) $b = 0.577A$ = 0.865 in. (21.984 mm) $c = 0.500A$ = 0.750 in. (19.050 mm) $t_A = 5.196A$ = 7.794 in. (197.968 mm) $B = 1.155A$ = 1.672 in. (42.469 mm) $L = 3.464A$ = 5.196 in. (131.978 mm) $V = 4.117A^3$ = 13.894 in.^{3} (227.696 cm^3) $Q_{MIN} = V\rho a_G f_S/J$ = 0.038 in.^{2} (24.471 mm^2) $Q_{MAX(C)} = 0.589A^2$ = 1.325 in.^{2} (854.998 mm^2) $Q_{MAX(RT)} = 1.039A^2$ = 2.338 in.^{2} (1508.223 mm^2)
Delta (Figure 7.29)	n, θ are variables. Per text, iterate until Eqs. (7.13) and (7.14) give the same value for I'_1 Assuming $n = 1.85025$ (Schott LaSFN9 glass) and $\theta = 25.916°$, then $\varphi = 90° - \theta = 64.084°$ $I_1 = \theta = 25.916°$ $I'_1 = \arcsin[(\sin I)/n] = 13.663°$ [by Eq. (7.13)] $I'_1 = 4\theta - 90° = 13.663°$ [by Eq. (7.14)] $\delta = I_1 - I'_1 = 12.253°$ (using average value for I'_1) I_C @ surface 2 = $\arcsin(1/n) = 32.715°$

(*Continued*)

TABLE 7.5 (*Continued*)

Prism Type	Equations
	$I_2 = \delta + \theta = 38.168°$ [this is $> I_C$ therefore TIR occurs) $a = 0.1A = 0.15$ in. (3.810 mm) $B = \{(A + 2a)(\sin(180° - 4\theta)/[(2\cos\theta)(\sin\theta)]\} - a$ $= 2.225$ in. (56.508 mm) $C = 2(B + A)\tan\theta = 3.620$ in. (91.958 mm) $t_1 = [(A/2) + a][\sin 2\theta]/\{[\cos\theta][\sin(90° - 2\theta + I')]\}$ $= 1.001$ in. (25.420 mm) $t_2 = [B - (A/2) - a - t_1 \sin\delta]/\cos\theta$ $= 1.237$ in. (31.413 mm) $t_A = 2(t_1 + t_2) = 4.475$ in. (113.658 mm) $V = A\,[(B + a)^2 - a^2]\tan\theta = 4.094$ in.^{3} (67.087 cm^3) $Q = V\rho a_G f_S/J = 0.011$ in.^{2} (7.208 mm^2) $Q_{MAX(C)} = \pi[(C^2/4)\tan 2(\varphi/2)]$ $= 1.438$ in.^{2} (927.510 mm^2)

[a] Numerical values represent application of the equations to a typical design with $A = 1.500$ in. The glass type is BK7 ($\rho = 0.091$ lb/in.^{3}), $a_G = 15$, $J = 2000$ lb/in.^{2}, and $f_S = 4$, unless otherwise noted.

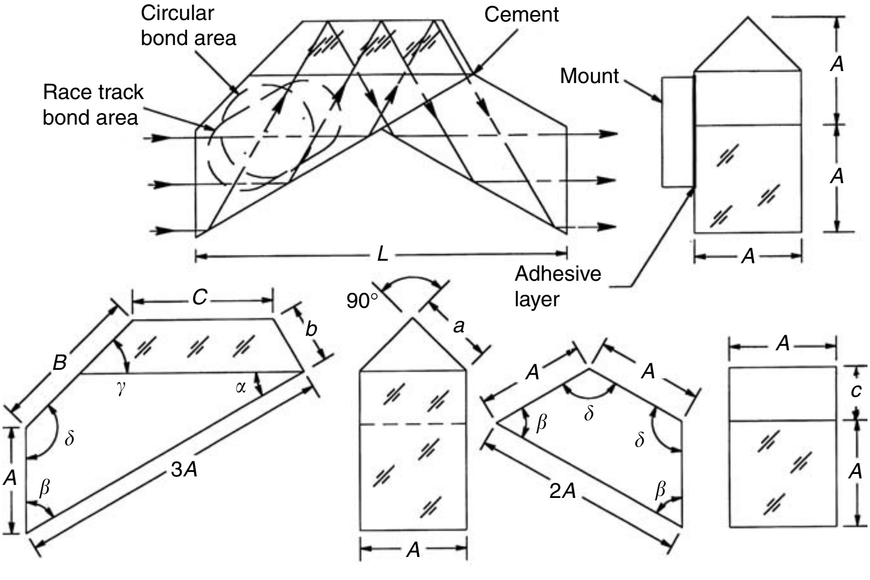

FIGURE 7.27 Design configuration of an Abbe Type A prism. (Adapted from Kaspereit, O.K., *Design of Fire Control Optics ORDM2-1*, Vol. I, U.S. Army, Washington, DC, 1952.)

are held mechanically to form a subassembly and then mounted by clamping or bonding one prism to a base plate. The optical axis of the nominal design is displaced very slightly owing to the small central air space, but it is not deviated. The two outer reflecting surfaces must have reflective coatings and protective overcoats or paint. Light transmission suffers relative to other types of rotation/derotation prisms because of these second-surface reflections and the two uncoated transmitting surfaces.

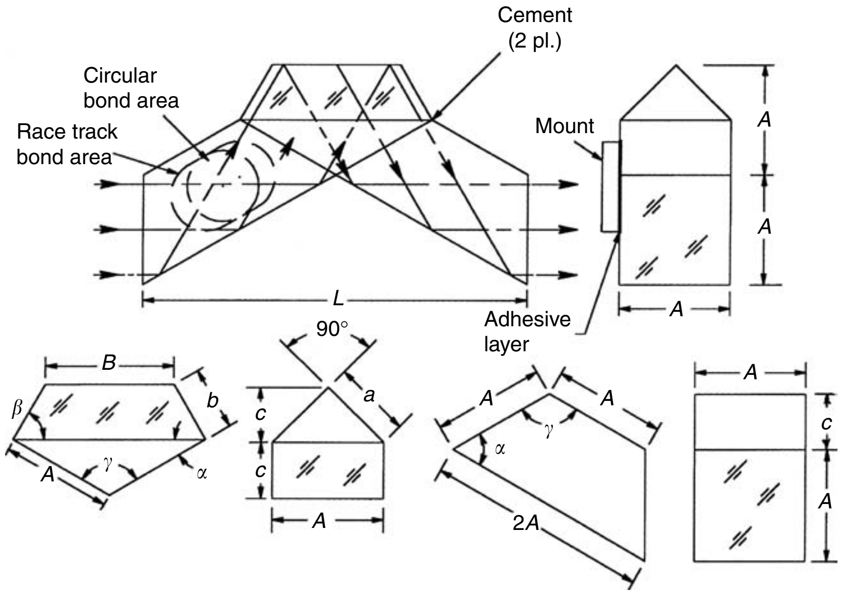
Cement
(2 pl.)
Circular
bond area
Race track
bond area
Mount
A
A
L
A
90°
Adhesive
layer
B
b
β
γ
α
A
a
c
c
A
A
A
γ
α
2A
A
c
A

FIGURE 7.28 Design configuration of an Abbe Type B prism. (Adapted from Kaspereit, O.K., *Design of Fire Control Optics ORDM2-1*, Vol. I, U.S. Army, Washington, DC, 1952.)

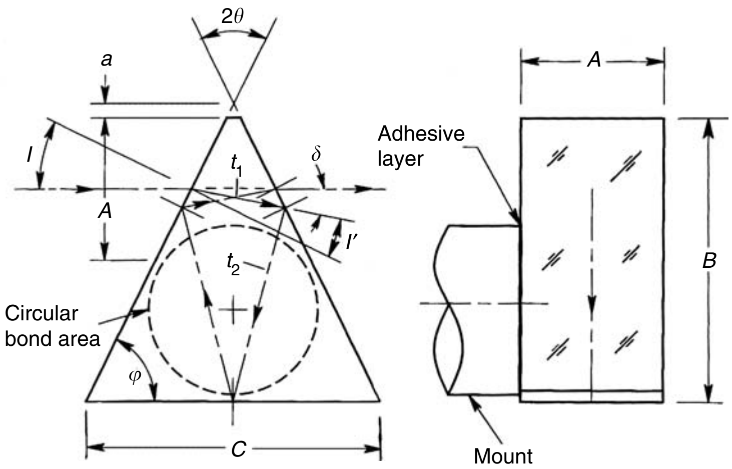
2θ
a
A
I
t_1
δ
Adhesive
layer
A
I′
t_2
B
Circular
bond area
φ
C
Mount

FIGURE 7.29 Design configuration of a delta prism. (From Yoder, P.R., Jr., *Mounting Optics in Optical Instruments*, SPIE Press, Bellingham, 2002.)

7.3.17 THE SCHMIDT PRISM

The Schmidt prism has a 90° roof, so it will invert an image in two meridians. It is usually used as an erecting system in telescopes. It also deviates the axis by 45°, which allows a convenient eyepiece axis orientation with respect to the objective axis for a horizontally viewing telescope. The entrance and exit faces are normal to the axis. The design is shown in Figure 7.33. Design equations for the prism are given in Table 7.6. The prism's refractive index must be high enough for TIR to occur at the entrance and exit faces. A variation of this design substitutes a flat surface for the roof. Such a prism would invert the image only in one meridian.

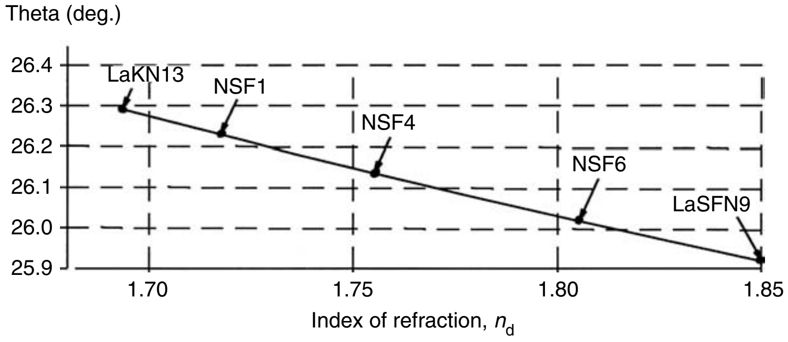

FIGURE 7.30 Variation of apex half-angle θ with refractive index for delta prisms.

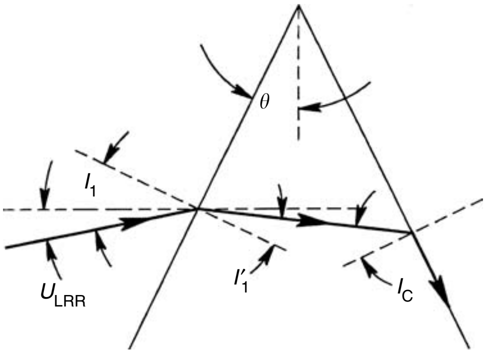

FIGURE 7.31 Geometry allowing determination of limiting field ray angle (U_{LRR}) for TIR in a delta prism.

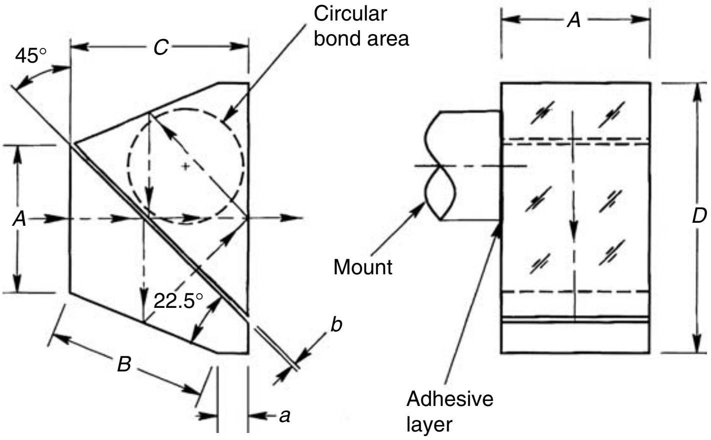

FIGURE 7.32 Design configuration of a Pechan prism subassembly. (From Yoder, P.R., Jr., *Mounting Optics in Optical Instruments*, SPIE Press, Bellingham, 2002.)

If a 90° roof is added to the delta prism described in Section 7.3.15, an image-erecting system with coaxial input and output optical axes will result. The modified prism would resemble the Schmidt prism, but the entrance and exit faces would be tilted with respect to the axis. This prism must be used in a collimated beam.

TABLE 7.6
Design Equations for the Pechan, Schmidt, 45° Bauernfeind, Frankford Arsenal Nos. 1 and 2, and Leman Prisms[a]

Prism Type	Equations
Pechan	$a = 0.207A = 0.310$ in. (7.887 mm)
(Figure 7.32)	$b = 0.004$ in. (0.102 mm)
	$B = 1.082A = 1.623$ in. (41.224 mm)
	$C = 1.207A = 1.810$ in. (45.987 mm)
	$D = 1.707A = 2.560$ in. (65.037 mm)
	$t_{\mathrm{A}} = 4.621A = 6.931$ in. (176.060 mm)
	$V = 1.801A^3 = 6.075$ in.^{3} (99.552 cm^3)
	$Q_{\mathrm{MIN}} = V\rho \mathrm{a}_{\mathrm{G}}\mathrm{f}_{\mathrm{S}}/J = 0.017$ in.^{2} (10.700 mm^2)
	$Q_{\mathrm{MAX(C)}} = 0.599A^2 = 1.348$ in.^{2} (869.514 mm^2)
Schmidt	$a = 0.1A = 0.150$ in. (3.810 mm)
(Figure 7.33)	$b = 0.185A = 0.277$ in. (7.041 mm)
	$c = 0.131A = 0.196$ in. (4.980 mm)
	$B = 1.468A = 2.202$ in. (55.942 mm)
	$C = 1.082A = 1.624$ in. (41.239 mm)
	$D = 1.527A = 2.291$ in. (58.194 mm)
	$t_{\mathrm{A}} = 3.045A = 4.568$ in. (116.022 mm)
	$V = 0.863A^3 = 2.913$ in.^{3} (47.729 cm^3)
	$Q_{\mathrm{MIN}} = V\rho \mathrm{a}_{\mathrm{G}}\mathrm{f}_{\mathrm{S}}/J = 0.008$ in.^{2} (5.130 mm^2)
	$Q_{\mathrm{MAX(C)}} = 0.318A^2 = 0.715$ in.^{2} (461.612 mm^2)
45° Bauernfeind	$a = 0.293A = 0.439$ in. (11.163 mm)
(Figure 7.34)	$B = 1.082A = 1.624$ in. (41.250 mm)
	$C = 1.707A = 2.561$ in. (65.040 mm)
	$D = 1.414A = 2.121$ in. (53.881 mm)
	$t_{\mathrm{A}} = 1.707A = 2.561$ in. (65.040 mm)
	$V = 0.750A^3 = 2.531$ in.^{3} (41.480 cm^3)
	$Q_{\mathrm{MIN}} = V\rho \mathrm{a}_{\mathrm{G}}\mathrm{f}_{\mathrm{S}}/J = 0.007$ in.^{2} (4.458 mm^2)
	$Q_{\mathrm{MAX(C)}} = 0.325A^2 = 0.730$ in.^{2} (471.289 mm^2)
Frankford Arsenal No.1	$\alpha = \delta = 115°$
(Figure 7.35[a])	$\beta = 32.5°$
	$a = 0.707A = 1.060$ in. (26.937 mm)
	$b = 0.732A = 1.098$ in. (27.889 mm)
	$B = 1.186A = 1.779$ in. (45.187 mm)
	$C = 0.931A = 1.396$ in. (35.471 mm)
	$D = 0.461A = 0.691$ in. (17.564 mm)
	$E = 1.723A = 2.584$ in. (65.646 mm)
	$t_{\mathrm{A}} = 1.570A = 2.355$ in. (59.817 mm)
	$Q_{\mathrm{MAX(C)}} = 0.119A^2 = 0.268$ in.^{2} (172.875 mm^2)
Frankford Arsenal No.2	$\alpha = \beta = \delta = 60°$
(Figure 7.35[b])	$a = 0.155A = 0.232$ in. (5.893 mm)
	$b = 0.268A = 0.402$ in. (10.211 mm)
	$c = 0.707A = 1.061$ in. (26.949 mm)
	$B = 1.464A = 2.196$ in. (55.778 mm)
	$C = 0.732A = 1.098$ in. (27.889 mm)
	$t_{\mathrm{A}} = 2.269A = 3.403$ in. (86.436 mm)
	$Q_{\mathrm{MAX(RT)}} = 0.776A^2 = 1.746$ in.^{2} (1126.449 mm^2)
Leman	$\alpha = 30°$
(Figure 7.36)	$\beta = 60°$
	$\gamma = 120°$

continued

TABLE 7.6 (*Continued*)

Prism Type	Equations
	$a = 0.707A = 1.061$ in. (26.949 mm)
	$b = 0.577A = 0.866$ in. (21.996 mm)
	$B = 1.310A = 1.965$ in. (49.911 mm)
	$C = 0.732A = 1.098$ in. (27.889 mm)
	$t_A = 5.196A = 7.794$ in. (197.968 mm)
	$Q_{MAX(C)} = 0.676A^2 = 1.522$ in.^{2} (981.829 mm^2)
	$Q_{MAX(RT)} = 1.727A^2 = 3.886$ in.^{2} (2506.925 mm^2)

[a] Numerical values represent application of the equations to a typical design with $A = 1.500$ in. The glass type is BK7 ($\rho = 0.091$ lb/in.^{3}), $a_G = 15$, $J = 2000$ lb/in.^{2}, and $f_S = 4$, unless otherwise noted.

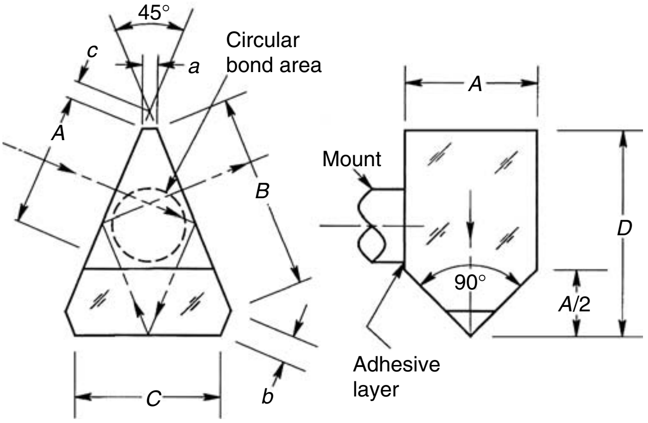

FIGURE 7.33 Design configuration of a Schmidt prism. (From Yoder, P.R., Jr., *Mounting Optics in Optical Instruments*, SPIE Press, Bellingham, 2002.)

7.3.18 THE 45° BAUERNFEIND PRISM

The Bauernfeind prism provides a 45° deviation of the axis using two internal reflections. The first reflection is by TIR, while the second takes place at a silvered reflecting surface. The smaller element of the Pechan prism is of the latter type. Figure 7.34 and Table 7.6 provide design information.

The combination of a modified Schmidt prism having no roof with a 45° Bauernfeind prism modified to add a roof forms a compact in-line erecting system for binoculars. Moving the roof from the Schmidt prism to the Bauernfeind prism produces a subassembly that lends itself nicely to packaging in a conveniently shaped housing configuration. This subassembly is sometimes called the Schmidt–Pechan roof prism (Seil, 1991). An example of a mounting for such a prism is described in Section 7.6.

7.3.19 THE FRANKFORD ARSENAL PRISMS NOS. 1 AND 2

These two prisms, shown in Figure 7.35, were included in a set of seven prisms described by Kaspereit (1952). They were designed at the U.S. Army's Frankford Arsenal for use in military telescopes with various requirements for beam deviation to suit specific hardware applications. Rather than being named for their inventors, the prisms in this set were designated as Frankford Arsenal Prisms Nos. 1 through 7.

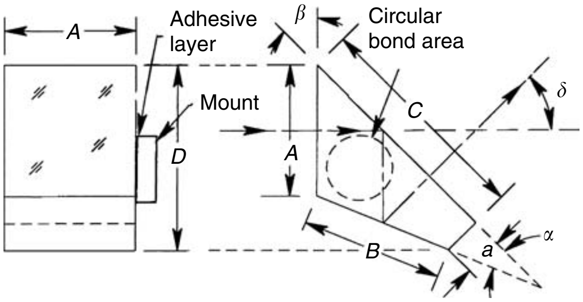

FIGURE 7.34 Design configuration of the 45° Bauernfeind prism. (From Yoder, P.R., Jr., *Mounting Optics in Optical Instruments*, SPIE Press, Bellingham, 2002.)

Prisms Nos. 1 and 2 invert the image in both meridians, and can hence be used to erect an image. As indicated in Table 7.6, these designs deviate the line of sight by 115° and 60°, respectively. Both may be thought of as variations of the Amici prism, which deviates the beam by 90°. The No. 1 design is similar to that of the 120°-deviation roof prism used in the Abbe Type B prism shown in Figure 7.28.

7.3.20 THE LEMAN PRISM

The Leman prism shown in Figure 7.36 is most commonly used in visual instruments. Table 7.6 gives the prism's design equations. It has been found to be particularly useful in binoculars that need wide separation of the objective axes to enhance stereoscopic observation, because the axis is offset by $3A$ in each prism for a maximum total objective separation of $6A+\text{IPD}$ (see Figure 7.37). The more traditional Porro prism erecting system offsets the axis by $1.56A$, so the objectives of a binocular with that type of erector (see Figure 5.31) are separated by a maximum of $3.12A+\text{IPD}$. In a binocular with in-line roof prism erectors, such as that shown in Figure 5.32, the objectives are separated by the observer's interpupillary distance (IPD), so no stereoscopic enhancement is provided.

7.3.21 AN INTERNALLY REFLECTING AXICON PRISM

Axicons have conical surfaces as their active optical surfaces. A typical application is to change a small circular laser beam into an annular beam with a larger OD. The version shown in Figure 7.38 has a single conical surface and a coated, flat, reflecting surface to return the beam to and through the conical surface. Its design equations are given in Table 7.7.

Because of its rotational symmetry, this axicon is made with a circular cross section, and is usually elastomerically secured in a tubular mount. The apex is either a sharp point or carries only an extremely small protective bevel. A centrally perforated flat mirror at 45° can provide a convenient way to separate the coaxial beams if it is located in front of this prism. An in-line refracting version of this axicon with identical conical surfaces at either end has been used to accomplish the same function, but without the reversal of beam direction. It is twice as long and is more expensive to fabricate because of the additional conical surface.

7.3.22 THE CUBE-CORNER PRISM

A corner cut symmetrically and diagonally from a solid glass cube creates a prism in the geometrical form of a tetrahedron (four-sided polyhedron). Such a prism has been referred to as a cube-corner, corner-cube, or tetrahedral prism. Light entering the diagonal face reflects internally from the other three faces and exits through the diagonal face. TIR usually occurs at each internal surface for commonly used refractive index values. The return beam contains six segments, one from each of the pie-shaped areas within the circular aperture shown in Figure 7.39. Table 7.7 shows its design equations.

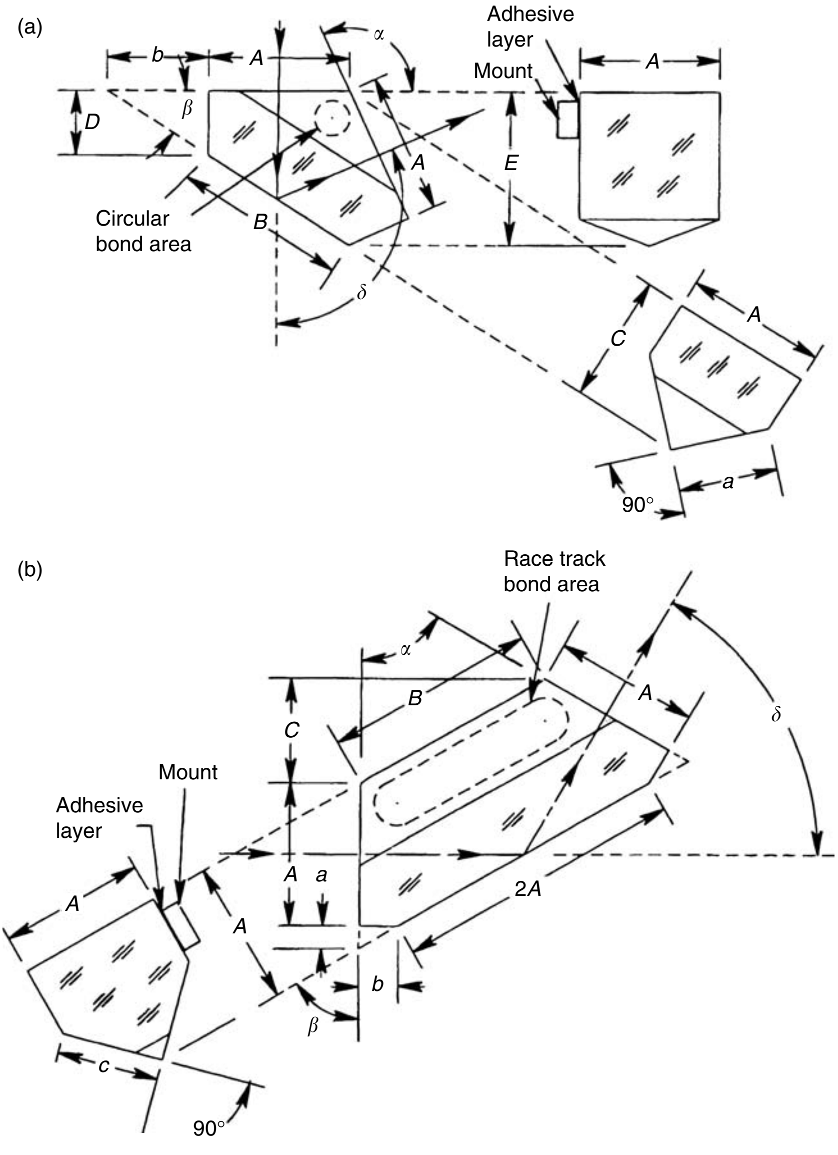

FIGURE 7.35 Design configurations for Frankford Arsenal Prisms: (a) No. 1 and (b) No. 2. (Adapted from Kaspereit, O.K., *Design of Fire Control Optics ORDM2-1*, Vol. I, U.S. Army, Washington, DC, 1952.)

If the three dihedral angles between the adjacent reflecting surfaces are exactly 90°, the prism is retrodirective, even if the prism is significantly tilted. If one or more of these dihedral angles differs from 90° by an error ε, the deviation differs from 180° by as much as 3.26ε and the reflected beams diverge (Yoder, 1958). This retrodirective feature is used to advantage in such applications as interferometry, laser tracking of cooperative targets, or those involving widely separated transmitter and receiver optical systems used for large-baseline ranging by triangulation.

The cube-corner prism shown in Figure 7.39 has a triangular form with sharp dihedral edges. A variation of this design has its rim ground to a circular shape circumscribing the aperture (the dashed line). Figure 7.40 shows an example. This is one of the 426 fused silica prisms used on the Laser Geodynamic Satellite (LAGEOS) launched by NASA in 1976 to provide scientists with extremely accurate

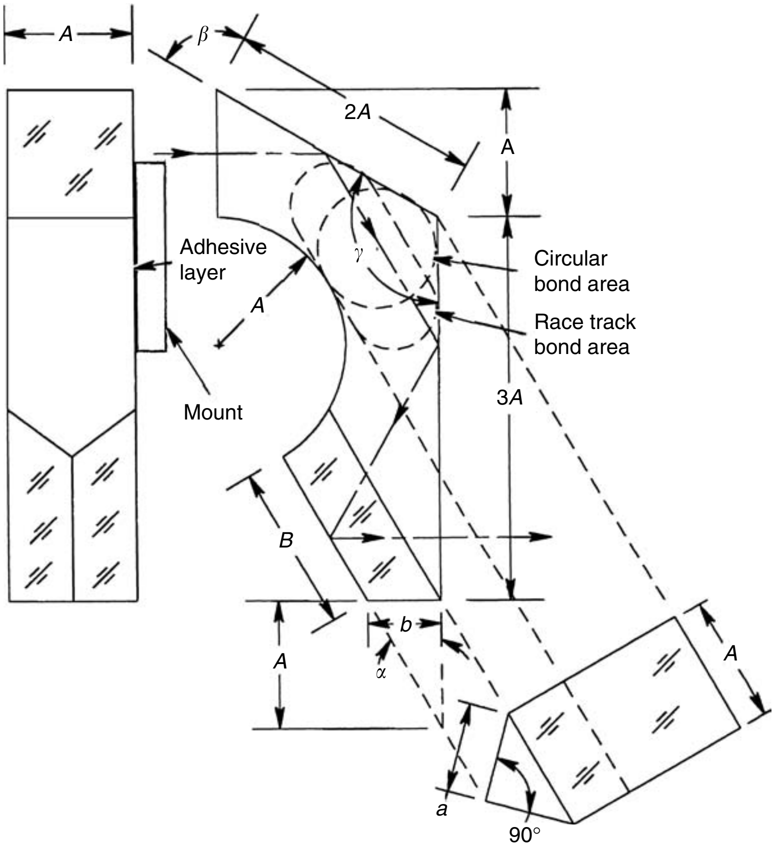

FIGURE 7.36 Design configuration for the Leman prism. (Adapted from Kaspereit, O.K., *Design of Fire Control Optics ORDM2-1*, Vol. I, U.S. Army, Washington, DC, 1952.)

measurements of movements of the Earth's crust as a possible aid to understanding earthquakes, continental movement, and polar motion. The dihedral angles of the prisms were each 1.25 arcsec greater than 90°. A laser beam transmitted to the satellite was returned with sufficient divergence to reach a receiver telescope even though the satellite moved significantly during the beam's round-trip transit time.

Another possible cube-corner prism configuration has the rim cut to a hexagonal shape circumscribing the prism's circular clear aperture. This allows several of the prisms to be tightly grouped together to form a mosaic of closely packed retrodirective prisms, thereby increasing the effective aperture of the group.

Mirror versions of the cube-corner prism are frequently used when operation outside the transmission range of normal refracting materials is needed (see Section 8.6). This so-called "hollow cube-corner" generally has reduced weight as compared with a solid prism version for a given aperture.

7.3.23 AN OCULAR PRISM FOR A COINCIDENCE RANGEFINDER

The prism subassembly shown in Figure 7.41 was designed and made by Zeiss for use in a split-field coincidence-type optical rangefinder. In order to facilitate explanation of its design, we first describe the function of this type of rangefinder.

As indicated schematically in Figure 7.42(a), light from a target enters the rangefinder through windows (not shown) at either end of the instrument and is folded toward the center of the device by penta prisms. Images formed by the two objective lenses are combined by the ocular prism and viewed through an eyepiece. Because the target is at a finite distance, the beams forming the images

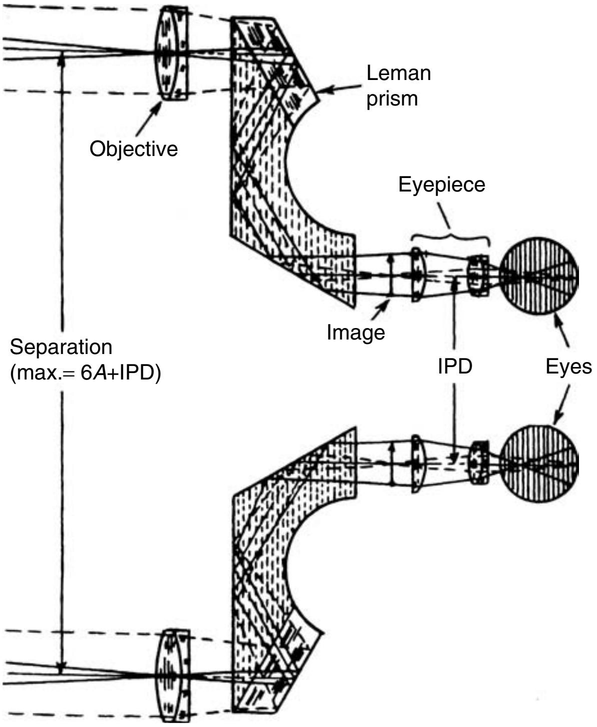

FIGURE 7.37 Application of Leman prisms in a binocular. (Adapted from Kaspereit, O.K., *Designing of Optical Systems for Telescopes*, U.S. Army, Washington, DC, 1933.)

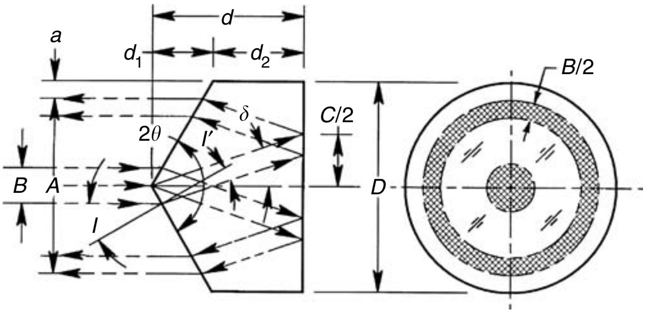

FIGURE 7.38 Design configuration of an internally reflecting axicon prism. (From Yoder, P.R., Jr., *Mounting Optics in Optical Instruments*, SPIE Press, Bellingham, 2002.)

are slightly inclined with respect to the axis and the images are not coincident. The operator deflects the image from one side of the instrument by moving an adjustable compensator (shown in view [a] as a longitudinally sliding wedge; see Section 7.3.26.3) so that it appears superimposed upon the image from the other side of the instrument. By reading a scale connected to the movable wedge, the angle θ is measured and range R to the target is calculated from the equation

$$R = B/\tan\theta \tag{7.19}$$

where B is the lateral separation of the beams entering the rangefinder and θ the small parallactic angle of divergence between the axes of the two input light beams from the target (see Patrick, 1969).

TABLE 7.7
Design Equations for an Internally Reflecting Axicon Prism and a Cube Corner Prism[a]

Prism Type	Equations
Internally reflecting axicon (Figure 7.38)	A = annulus OD = 1.500 in. (38.100 mm)
	B = input beam OD = 0.118 in. (3.000 mm)
	w = annulus width = $B/2$ = 0.059 in. (1.500 mm)
	$a = 0.1A$ = 0.150 in. (3.810 mm)
	$\theta = 60°$
	$I_1 = 90° - \theta = 30°$
	$I'_1 = \arcsin(\sin I_1/n) = 19.247°$
	$\delta = I_1 - I'_1 = 10.753°$
	$d = (A/4)[(1/\tan \theta) + (1/\tan \delta)]$ = 2.191 in. (55.642 mm)
	$d_1 = [(A/2) + a]/\tan \theta$ = 0.520 in. (13.198 mm)
	$d_2 = d - d_1$ = 1.671 in. (42.444 mm)
	$C = 2d \tan \delta$ = 0.832 in. (21.139 mm)
	$D = A + 2a$ = 1.800 in. (45.720 mm)
	$t_A = A/(2 \sin \delta)$ = 4.019 in. (102.079 mm)
	$V = (0.785d_2 + 0.262d_1)A^2$ = 3.258 in.^{3} (53.385 cm^3)
Cube-corner (Figure 7.39)	$\theta = 35.264°$
	$\varphi = 54.736°$
	A = aperture = 1.500 in. (38.100 mm)
	$B = [(A/2)/\sin 30°] + (A/2)$ = $1.500A$ = 2.250 in. (57.150 mm)
	$C = 2B \tan 30° = 1.732A$ = 2.598 in. (65.989 mm)
	$D = 0.707A$ = 1.060 in. (26.937 mm)
	$E = 1.225A$ = 1.837 in. (46.672 mm)
	$F = 0.866A$ = 1.299 in. (32.995 mm)
	$t_A = 2D = 1.414A$ = 2.121 in. (53.873 mm)

[a] Numerical values represent application of the equations to a typical design with A = 1.500 in. The glass type is NBK7 (n_d = 1.51680).

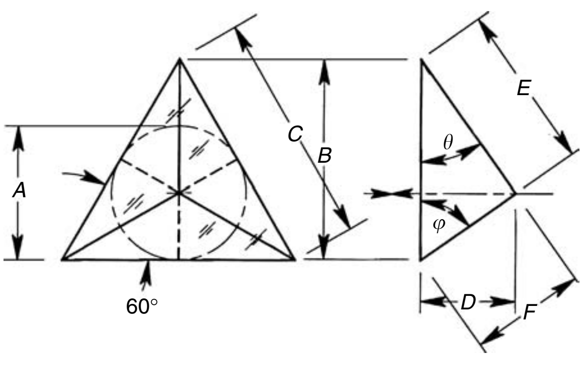

FIGURE 7.39 Design configuration of a cube-corner prism. (From Yoder, P.R., Jr., *Mounting Optics in Optical Instruments*, SPIE Press, Bellingham, 2002.)

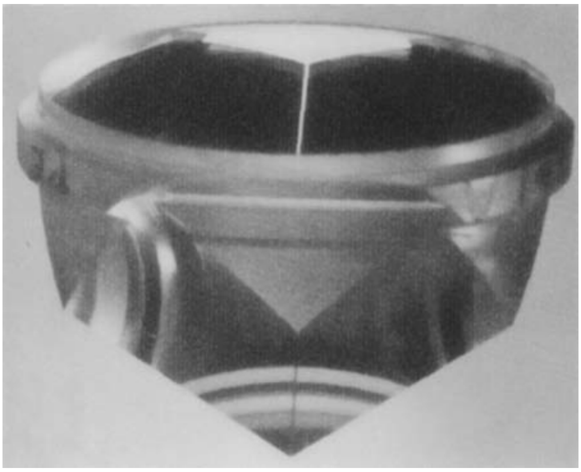

FIGURE 7.40 A precision-fused silica cube-corner prism with a 3.81 cm (1.50 in.) circular aperture. (Courtesy of Goodrich Corp., Danbury, CT.)

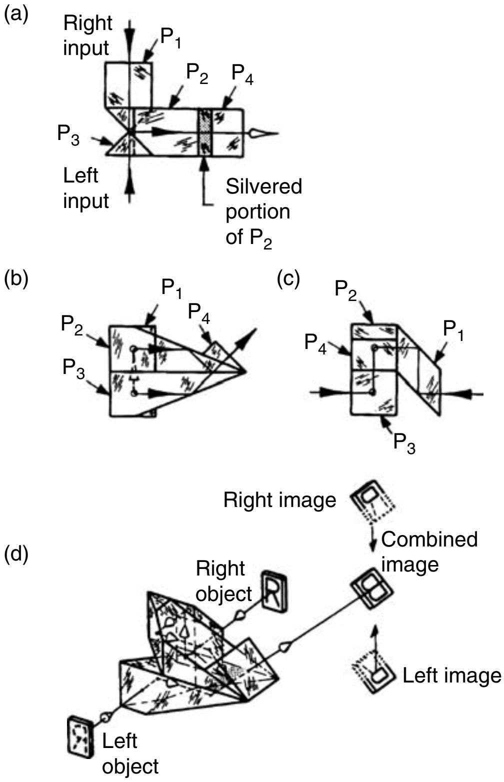
(a)
Right input
P1
P2
P4
P3
Left input
Silvered portion of P2
(b)
P1
P4
P2
P3
(c)
P2
P1
P4
P3
Right image
Combined image
(d)
Right object
Left image
Left object

FIGURE 7.41 An ocular prism designed by Zeiss for a coincidence-type optical rangefinder: (a) Top view, (b) side view, (c) end view, and (d) isometric view. (Adapted from MIL-HDBK-141, *Optical Design*, Defense Supply Agency, Washington, DC, 1962.)

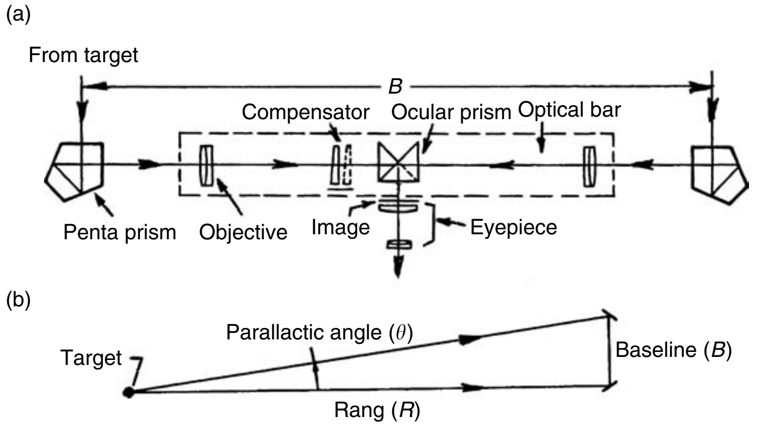

FIGURE 7.42 (a) Optical schematic of a typical coincidence-type optical rangefinder. (b) The range triangle showing parameters used to determine the range to a target.

The optics within the dashed rectangle of view (a) are all mounted together on a rigid structure called an optical bar in order to maintain precise alignment to each other. This structure is usually made of material with low CTE to maximize its thermal stability. Because of their inherent insensitivity to tilt in the plane of the figure, the penta prisms need not be attached to the bar.

The particular ocular prism design depicted in Figure 7.41 comprises four prism elements, designated P_1 through P_4, cemented together. The refracting angles of P_2, P_3, and P_4 are all 22.5° and the eyepiece axis is inclined upward at 45°. The beam from the right objective enters the rhomboid prism P_1 and, after five internal reflections in P_1 and P_2, passes through P_4 and focuses at the image plane. The last reflection in this path is at a silvered area on a portion of the bottom surface of P_2, so this beam forms the top half of the image. The beam from the left objective reflects twice inside P_3 and passes through P_4 to the image plane. This beam misses the silvered area on P_2 and forms the bottom half of the image. The fact that the observed image is divided vertically into parts coming through different optical systems leads to the designation of this rangefinder as a split-field, coincidence-type instrument. The operator sees the two half images misaligned laterally until he adjusts the compensator to bring one image directly over the other image, thereby establishing coincidence and allowing the range to be determined.

Several other versions of ocular prisms for rangefinders are described by Kaspereit (1952) and MIL-HDBK-141 (1962). All function in the same manner as just described, i.e., they combine the images produced by the left and right optical systems so that the angle θ can be measured.

7.3.24 A BIOCULAR PRISM SYSTEM

The prism system shown in Figure 7.43 can be used in telescopes and microscopes when both eyes are to observe the same image as presented by a single objective. It does not provide stereoscopic vision and is hence called “biocular” rather than “binocular.” From view (a), it can be seen to consist of four prisms: a right-angle prism, P_1, cemented to a rhomboid prism, P_2, with a partially reflective coating at the cemented interface; an optical path equalizing block, P_3; and a second rhomboid prism, P_4. The observer’s interpupillary distance is designated as “IPD”. By rotating the prisms symmetrically about the input axis, the IPD is changed to suit the individual using the instrument. Typically, the IPD is adjustable from at least 56 to 72 mm (2.20 to 2.83 in.). An external scale usually is provided on the optical instrument to allow easy reference for setting this distance.

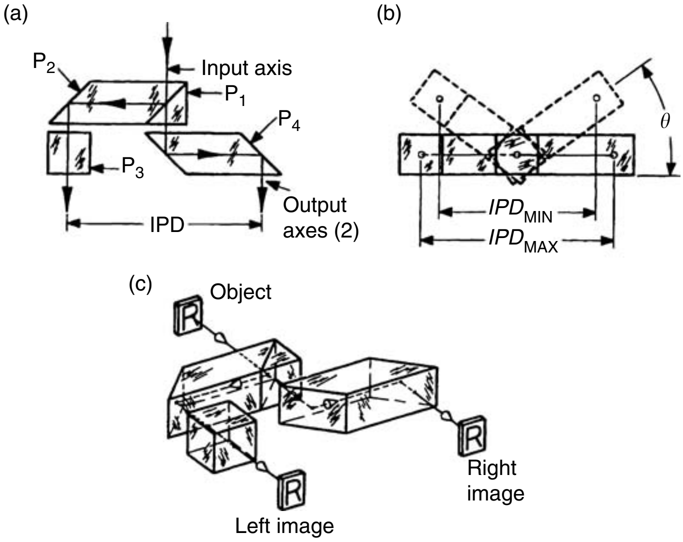

FIGURE 7.43 A beam splitting biocular prism system: (a) Top view, (b) end view, and (c) isometric view. IPD is the interpupillary distance. (From Yoder, P.R., Jr., *Mounting Optics in Optical Instruments*, SPIE Press, Bellingham, 2002.)

7.3.25 DISPERSING PRISMS

Prisms are frequentlyly used to disperse polychromatic light beams into their constituent colors in instruments such as spectrometers and monochromators. The index of refraction n of the optical material varies with wavelength, so the deviation (measured with respect to the initial incident ray direction) of any ray transmitted at other than normal incidence to the prism's entrance and exit surfaces will depend upon n, the angle of incidence at the entrance face, and the prism's apex angle, θ.

Figure 7.44 illustrates two typical dispersing prisms. In each case, a single ray of "white" light is incident at angle I_1. Inside each prism, this ray splits into a spectrum of variously colored rays. For clarity, the angles between rays are exaggerated in the figures. After refraction at the exit faces, rays of blue, yellow, and red wavelengths emerge with different deviation angles δ_λ. The blue ray is deviated the most because $n_{BLUE} > n_{RED}$. If the emerging rays are imaged onto film or a screen by a lens or mirror, a multiplicity of images of different colors will be formed at slightly different transverse locations. Although we refer to colors such as blue, yellow, and red here, it should be understood that the phenomenon of dispersion applies to all wavelengths, so we really mean the shorter, intermediate, and longer wavelength radiation under consideration in any given application.

In the simpler prism design shown in Figure 7.44(a), only refraction occurs. In Figure 7.44(b), the deviation is unchanged for small rotations of the prism about an axis perpendicular to the plane of refraction; hence, the prism is designated as "constant deviation." The refractive index in this case usually is chosen to be large enough to cause TIR to occur at the reflecting surface, because this enhances light transmission.

If a collimated beam of light of wavelength λ passes symmetrically through a prism so that $I_1 = -I'_2$ and $I'_1 = -I_2$, the deviation of the prism for that wavelength is a minimum and $\delta_{MIN} = 2I_1 - \theta$. This condition is the basis of one means for experimental measurement of the index of refraction of a transparent medium in which the minimum deviation angle, δ_{MIN}, of a prism made of that material is measured by successive approximations, and the following equation is applied:

$$n_{PRISM} = \sin[(\theta + \delta)/2]/\sin(\theta/2) \tag{7.20}$$

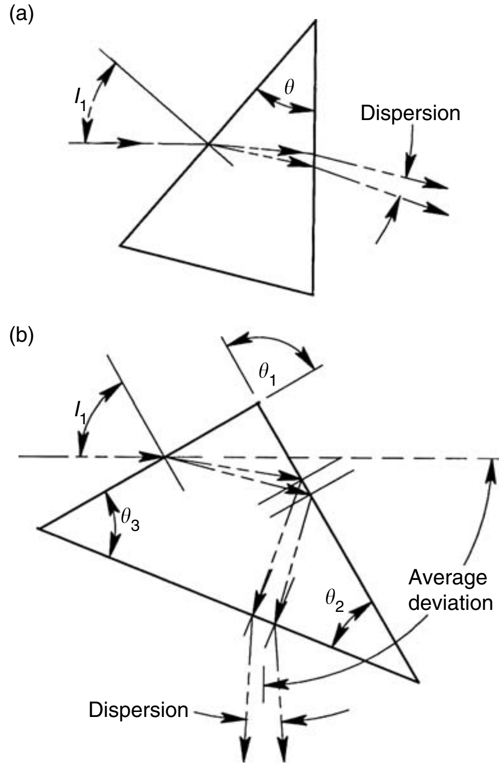

FIGURE 7.44 Dispersion of white light by (a) a simple prism and (b) a constant-deviation prism involving TIR. (From Yoder, P.R., Jr., *Mounting Optics in Optical Instruments*, SPIE Press, Bellingham, 2002.)

If we want any two of the various colored rays to emerge from the prism parallel to each other, we must use a combination of at least two prisms made of different glasses. Usually, these prisms are cemented together. Such a prism is called an "achromatic prism." Figure 7.45 shows one configuration for an achromatic prism. All such prisms can be designed by choosing refractive indices and the first prism's apex angle, and then repeatedly applying Snell's law to find the appropriate incident angle and second prism apex angle that gives the desired deviation for a chosen wavelength and the desired dispersion for two other wavelengths that bracket the chosen one. The angle between the exiting rays with the shortest and longest wavelengths is called the "primary chromatic aberration"; here, it should be essentially zero. The angle between either of these extreme wavelength rays and that with an intermediate wavelength is called "secondary chromatic aberration" of the prism.

The design of an achromatic prism of the type shown in Figure 7.45 might well proceed as follows. We first choose the glasses to try in the design. We then might assume that the yellow ray enters the first prism at minimum deviation in air. For any assumed value for θ, the angles $I_1' = I_2 = \theta/2$ for that ray. The red and blue rays would, of course, be dispersed. We use Snell's law (Eq. [7.1]) to find angle I_1 for the white ray. We then add the second prism and redetermine angle I_2'. Finally, we calculate the required angle θ_2 from

$$\operatorname{cotan} \theta_2 = -\left[\frac{\Delta n_2}{2\Delta n_1 \sin(\theta_1/2)\cos I_2'}\right] + \tan I_2' \tag{7.21}$$

where Δn_1 and Δn_2 are the index differences for the red and blue wavelengths in prisms 1 and 2.

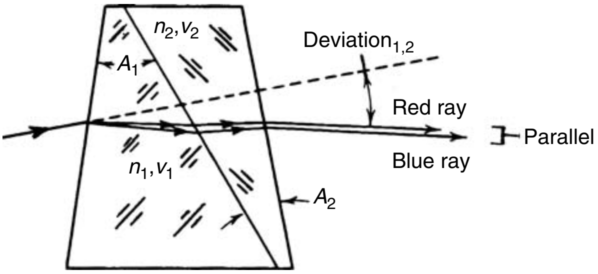

FIGURE 7.45 A typical achromatic dispersing prism. (From Smith, W.J., *Modern Optical Engineering,* 3rd ed., McGraw-Hill, New York, 2000.)

To complete the first-order design of a dispersing prism requires the calculation of only the required apertures. Usually, we assume a collimated input beam and make the apertures of the prism large enough to not vignette any of the dispersed beams.

7.3.26 THIN-WEDGE PRISM SYSTEMS

7.3.26.1 The Thin Wedge

Prisms with small geometric apex angles and axial thicknesses that are small compared with the component apertures are called "optical wedges." A typical example is shown in Figure 7.46. Since the apex angle is small, we can assume that the angle expressed in radians equals its sine, and, rewriting Eq. (7.20), we obtain the following simple equation for the wedge deviation in air:

$$\delta_\lambda = (n_\lambda - 1)\theta \tag{7.22}$$

Another important equation expresses the dispersion, i.e., the chromatic aberration, of the wedge as

$$d\delta_\lambda = dn_\lambda \theta \tag{7.23}$$

A wedge designed with these equations is one of minimum deviation. A common arrangement in optical instruments has the incident beam normal to the entrance face. Then $I_2 = \theta$, $I'_2 = \text{arc}\sin(n \sin I_2)$, and $\delta = I'_2 - \theta$. If not otherwise specified, we would assume n to apply to the center wavelength of the spectral bandwidth of interest. The deviation angle will differ only very slightly from that given by Eq. (7.22).

7.3.26.2 The Risley Wedge System

Two identical thin optical wedges mounted in series and rotated equally in opposite directions about the optical axis form an adjustable wedge. They are used in various applications, such as to provide variable pointing of laser beams, to angularly align the axis of one portion of an optical system to that of another portion of that system, to test ocular convergence in ophthalmology, or to measure distance in some optical range finders. They are referred to as Risley wedges or as a diasporometer, the latter term most frequently associated with their use in rangefinders.

The action of a Risley wedge system is shown Figure 7.47. Usually, the wedges are circular in shape; here, their apertures are shown (on left) as small and large rectangles for clarity. In views (a) and (c), the wedges are shown in their two positions for maximum deviation. The apexes are adjacent and the deviation $\delta_{\text{SYSTEM}} = 2\delta$, where δ is the deviation of one wedge. If the wedges are turned from either maximum deviation position in opposite directions by β (see Figure 7.47[d]), the deviation becomes

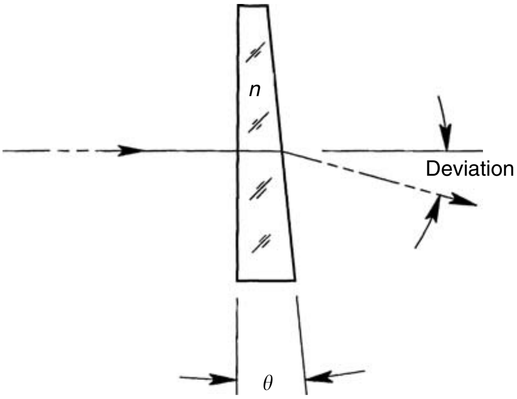

FIGURE 7.46 Deviation of a ray in a thin optical wedge. (From Yoder, P.R., Jr., *Mounting Optics in Optical Instruments*, SPIE Press, Bellingham, 2002.)

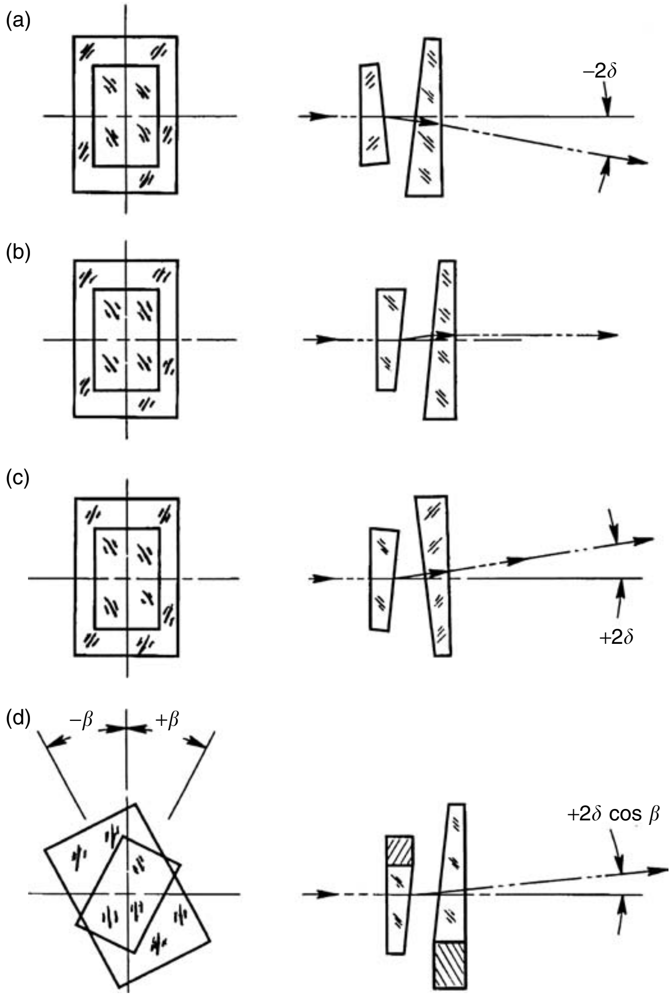

FIGURE 7.47 The function of a Risley wedge prism system: (a) bases together with deviation down, (b) bases opposed for zero deviation, (c) bases together for deviation up, general case with wedges counterrotated by ± *β*. (From Yoder, P.R., Jr., *Mounting Optics in Optical Instruments*, SPIE Press, Bellingham, 2002.)

$\delta_{\text{SYSTEM}} = 2\delta \cos \beta$ and the change in deviation from the maximum achievable value is $2\delta(1 - 2\cos\beta)$. If we continue to turn the wedges until $\beta = 90°$, we obtain the condition shown in Figure 7.47(b), where the apexes are opposite, the system acts as a plane-parallel plate, and the deviation is zero.

Since counter rotation of the wedges in a Risley wedge system provides variable deviation in one axis, a second such system, usually identical to the first, is sometimes added in series with the first to provide independent variation in the orthogonal axis. The deviations from the two systems add vectorially in a rectangular coordinate system. Another arrangement has a single Risley wedge system mounted such that both wedges can be rotated together about the optical axis as well as counter rotated with respect to each other. This provides variation of deviation in a polar coordinate system.

7.3.26.3 The Longitudinally Sliding Wedge

A wedge prism located in a converging beam will deviate the beam so that the image is displaced laterally by an amount proportional to both the wedge deviation (in radians) and the distance from the wedge to the image plane. See Figure 7.48 for a schematic of the device. If the prism is moved axially by $D_2 - D_1$, the image displacement varies from $D_1\delta$ to $D_2\delta$.

An important application for this device was in military optical range finders before the advent of the laser range finder. In the figure, a range scale shows the change in range to a target as a function of wedge movement for a typical rangefinder, such as that shown in Figure 7.42. Note that this is a nonlinear variation. This principle can be used in other more contemporary applications in which an image needs to be variably displaced laterally by a small distance. If used with a long focal-length lens, the wedge should be achromatic.

7.3.26.4 A Focus-Adjusting Wedge System

Two identical optical wedges arranged with their bases opposite and mounted in linear stages so that each can be translated laterally by equal amounts relative to the optical axis provide a variable optical path through glass. Figure 7.49 shows the principle of operation of the device. At all settings, the two wedges act as a plane-parallel plate. If located in a convergent beam, this system allows the image distance to be varied and can be used to bring images of objects at different distances into focus at a fixed image plane.

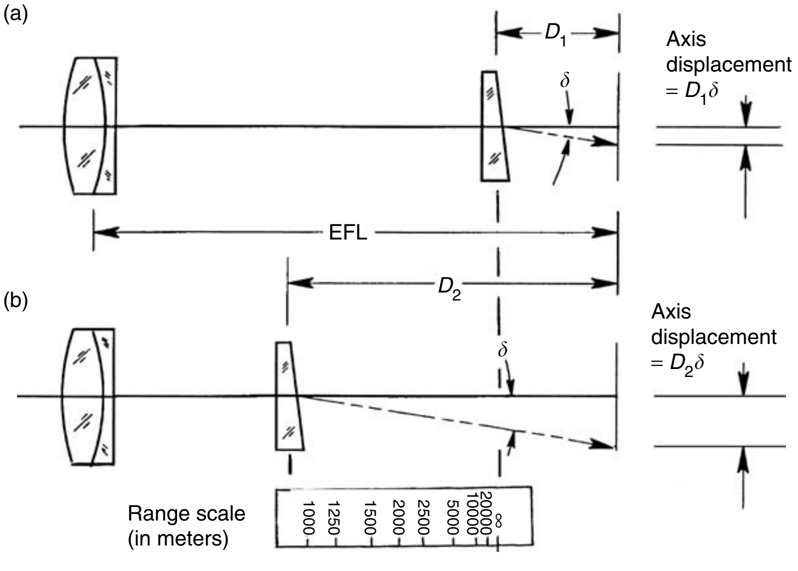

FIGURE 7.48 A longitudinally sliding wedge beam deviating system for an optical rangefinder. (Adapted from Kaspereit, O.K., *Design of Fire Control Optics ORDM2-1*, Vol. I, U.S. Army, Washington, DC, 1952.)

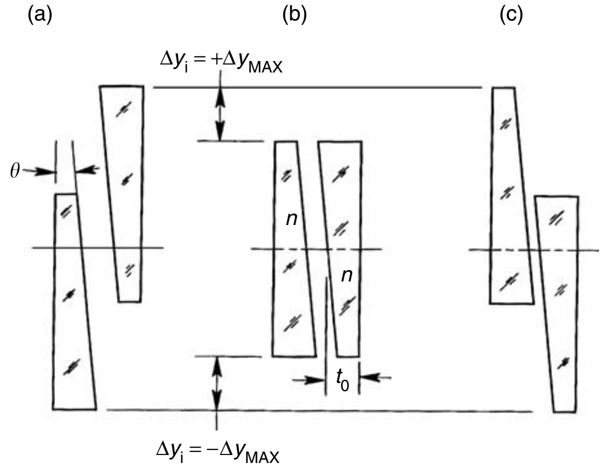
(a)
(b)
(c)
$\Delta y_i = +\Delta y_{MAX}$
θ
n
n
t_0
$\Delta y_i = -\Delta y_{MAX}$

FIGURE 7.49 A translating focus adjusting wedge system: (a) minimum optical path, (b) nominal optical path, and (c) maximum optical path. (From Yoder, P.R., Jr., *Mounting Optics in Optical Instruments*, SPIE Press, Bellingham, 2002.)

This type of focus-adjusting system has been used in large-aperture aerial cameras and telescopes such as those used for tracking missiles or spacecraft launch vehicles, where target range changes rapidly and the image-forming optics are large and heavy, and so cannot be moved rapidly and precisely to maintain focus. To a first-order approximation, $t_i = t_0 \pm \Delta y_i \tan\theta$ and the focus variation is $2t_i[(n - 1)/n]$. Here t_0 is the axial thickness of each wedge at its geometric center.

Figure 7.50 shows the optical schematic for a typical application featuring a focus-adjusting wedge system. The system is the Recording Optical Tracking Instrument (ROTI) used to track spacecraft launches at Cape Canaveral and other sites. As described in MIL-HDBK-141 (1962), it is basically an f/4.17 Newtonian telescope with a series of collimating doublet lenses and five Biotar-type photographic objectives forming a five-step selectable variable magnification lens subsystem following the tracking reticle located at primary mirror focus. The minimum EFL of the system is 100 in. (2.54 m). This is variable in equal steps to 500 in. (12.7 m).

The focus wedges immediately following the reticle in this telescope changed the glass path as the wedges were moved laterally so as to vary system focus in object space from infinity to 3000 yd. The wedge mechanism was linked to a radar system that measured range in real time to keep the photographic system in focus. Two operators controlled the line of sight of the system by observing the target through two auxiliary elbow telescopes, one for azimuth and the other for elevation.

7.3.27 ANAMORPHIC PRISM SYSTEMS

A refracting prism used at other than minimum deviation changes the width of a transmitted collimated beam in the plane of refraction (see Figure 7.51[a]). The beam width in the orthogonal plane (perpendicular to the plane of the figure) is unchanged, so anamorphic magnification results. The beam is deviated by the prism and chromatic aberration is introduced. Both of these defects can be eliminated if two identical prisms are arranged in opposition as shown in Figure 7.51(b). Lateral displacement of the axis then occurs, but the angular deviation and chromatic aberration are zero. The beam compression or expansion ratio depends upon the prism apex angles, the refractive indices, and the orientations of the two prisms relative to the input axis. The configuration shown in Figure 7.51(b) is a telescope in one meridian since the degree of collimation of the beam is unchanged while it is passing through the optics.

Two-prism anamorphic telescopes were first described by Brewster in about 1835 to replace the cylindrical lenses then used for the purpose (Kingslake, 1983). They are commonly used today to

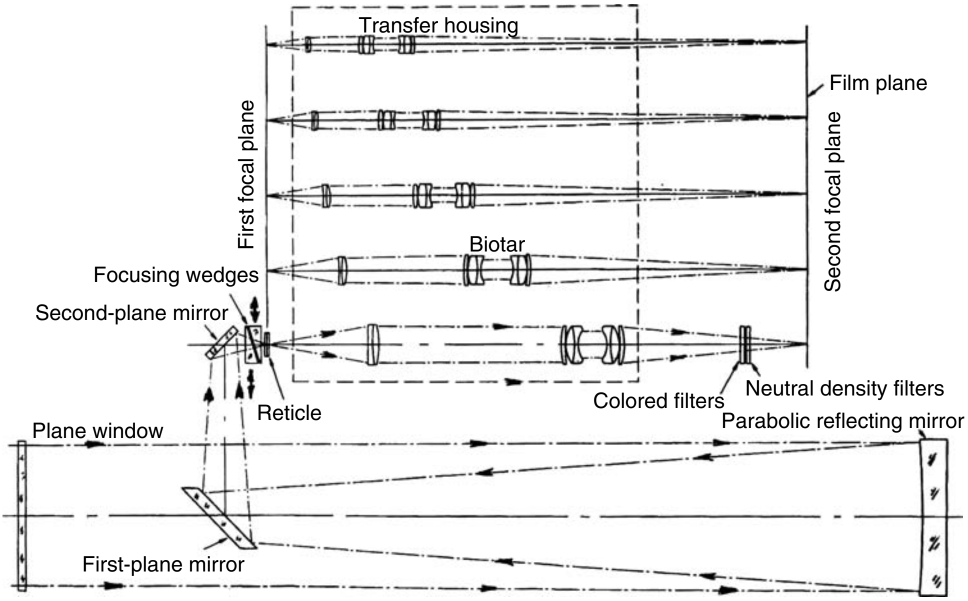
Transfer housing
Film plane
First focal plane
Second focal plane
Biotar
Focusing wedges
Second-plane mirror
Reticle
Colored filters
Neutral density filters
Parabolic reflecting mirror
Plane window
First-plane mirror

FIGURE 7.50 Optical schematic of the Recording Optical Tracking Instrument (ROTI) featuring an adjustable wedge focusing system. (From MIL-HDBK-141, *Optical Design*, Defense Supply Agency, Washington, DC, 1962.)

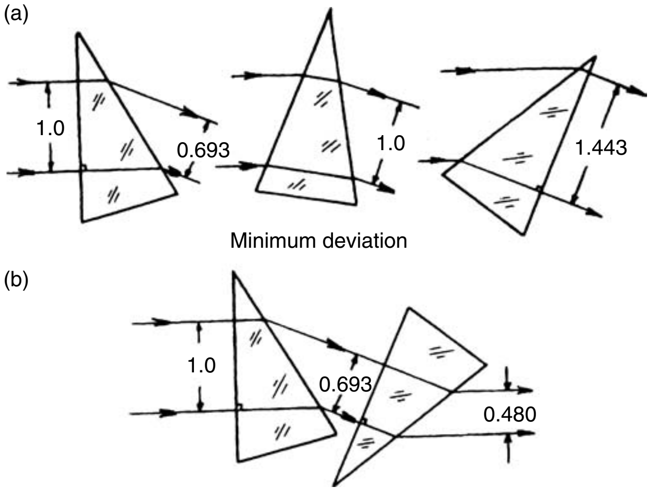
(a)
1.0
0.693
1.0
1.443
Minimum deviation
(b)
1.0
0.693
0.480

FIGURE 7.51 Functions of anamorphic prisms. (a) Individual prisms at various incident angles and (b) an anamorphic telescope. (Adapted from Kingslake, R., *Optical System Design*, Academic Press, Orlando, 1983.)

change diode laser beam size and angular divergence differentially in orthogonal directions, or to convert rectangular laser beams, such as those from Excimer lasers, into more suitably shaped ones for materials processing and surgical applications.

The telescope shown in Figure 7.52(a) has achromatic prisms to allow a broad spectral range to be covered (Lohmann and Stork, 1989). Anamorphic telescopes with many cascaded prisms to produce higher magnification have been described. An extreme example with ten prisms is shown in Figure 7.52(b). This configuration is reported to be optimal for single-material achromatic expanders of moderate to large magnifications (see Trebino, 1985; Trebino et al., 1985).

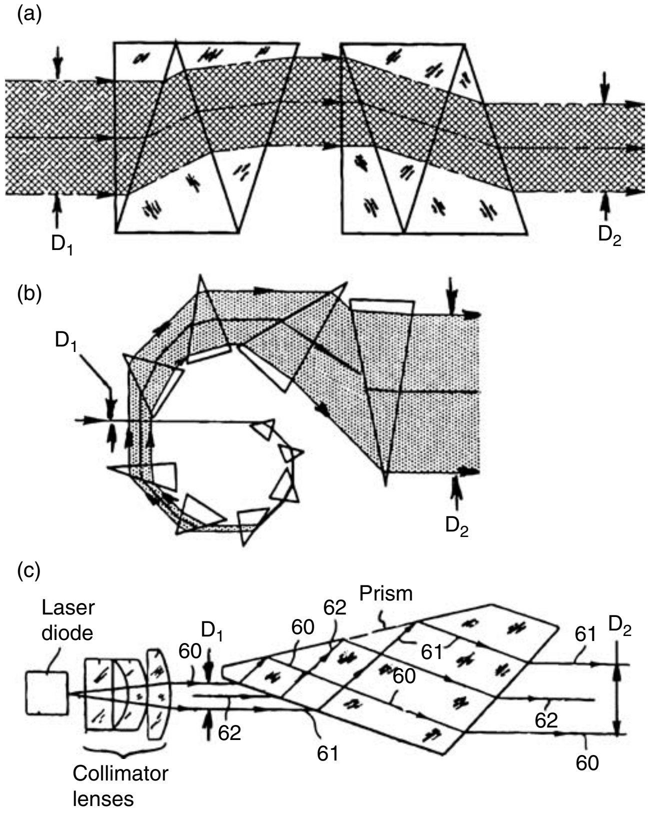

FIGURE 7.52 Three anamorphic prism telescope optical systems: (a) an achromatic prism assembly (adapted from Lohmann, A.W. and Stork, W., *Appl. Opt*., 28, 1318, 1989), (b) a cascaded assembly (adapted from Trebino, R., *Appl. Opt*., 24, 1130, 1985), and (c) a single-prism design (adapted from Forkner, J.F., U.S. Patent No. 4,623,225, 1986.)

An interesting anamorphic telescope consisting of only one prism from Forkner (1986) is shown in Figure 7.52(c). It has three active faces, one of which reflects by TIR. The entrance and exit faces can be oriented at Brewster's angle so the Fresnel reflection losses at those surfaces are eliminated for polarized beams.

7.4 KINEMATIC AND SEMIKINEMATIC PRISM MOUNTING PRINCIPLES

A body in space has six degrees of freedom (DOF), or ways in which it can move. These are translations along the three rectangular coordinate axes and rotations about those same axes. A body is constrained kinematically when each of these possible movements is singly prevented from occurring with point contacts with the mount. If any one movement is constrained in more than one way, then the body is overconstrained and may be deformed by the forces applied externally by the mount. Deformations of optical components are highly undesirable, so opto-mechanical engineers go to great lengths not to introduce overconstraints. Application of kinematic principles is appropriate in many prism-mounting designs because they tend to minimize problems.

Figure 7.53 indicates how the required six constraints might be applied to a body with the shape of a rectangular parallelepiped such as a simple cube prism. In the sketch on the left, we see a series of six balls attached to three mutually orthogonal flat surfaces. If the body is held in point contact with all six balls, it will be uniquely constrained. Three points in the *X*–*Z* plane define a plane on

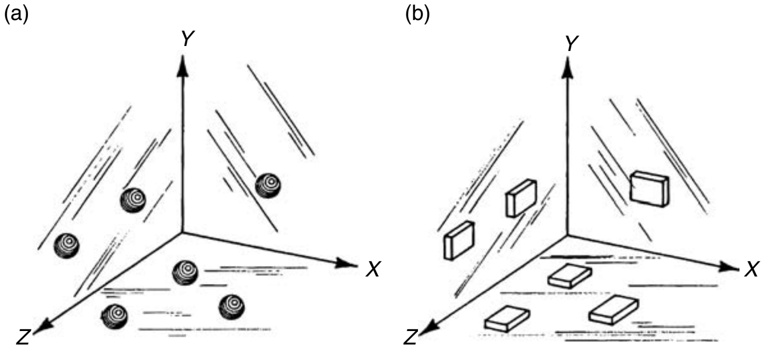

FIGURE 7.53 Position-defining reference surfaces for a rectangular parallelepiped optic such as a cube prism. (a) Kinematic mounting with point contacts on balls; (b) Semikinematic mounting with small area contacts. (Adapted from Smith, W.J., *Modern Optical Engineering*, 3rd ed., McGraw-Hill, New York, 2000.)

which the lower face of the body rests; these points prevent translation in the Y direction and rotation about the X- and Z-axis. Two points in the Y–Z plane prevent translation along the X-axis and rotation about the Y-axis. The single point in the X–Y plane controls the last DOF (translation along the Z-axis). A single force exerted against a near point on the body and directed toward the origin will hold the body against all six balls. Ideally, this force should pass through the center of gravity of the body. If the force is light and gravity is ignored, the contact surfaces are not deformed elastically and we have a kinematic design.

The sketch on the right in Figure 7.53 illustrates one way of reducing this mount concept to practice. The point contacts are replaced by small *area* contacts on pads. The multiple pads in the X–Z and Y–Z planes are machined carefully so that they are very accurately coplanar. The reference surfaces on all the pads must have the proper angular relationship (nominally at 90° to each other) so that the area contacts with the cube prism do not degenerate into lines.

The minimum preload force P_{MIN} (in lb) to be exerted against the body by the external load in order to prevent its lifting off the pads may be calculated using

$$P_{\mathrm{MIN}} = W f_{\mathrm{s}} \sum a_{\mathrm{G}} \tag{7.24}$$

where W is the weight of the body (in lb), f_{S} the assigned safety factor, and Σa_{G} the vector sum, in the direction of P_{MIN}, of all the externally applied static and dynamic forces such as constant acceleration, random vibration, resonant vibration, and shock. Each force is expressed as a multiple of ambient gravity (a_{G}). The direction of P_{MIN} should pass through the center of gravity of the body. Since all types of external forces do not generally occur simultaneously, the magnitude of Σa_{G} can be reduced to the most probable value or the worst-case value. This value must be determined for each particular situation. For simplicity, we assume that a single value for a_{G} prevails, and we ignore friction and moments at the small area contacts. Equation (7.24) then reduces to

$$P_{\mathrm{MIN}} = W f_{\mathrm{s}} a_{\mathrm{G}} \tag{7.24a}$$

Note that if the prism weight is expressed in kg, this equation must include an additional multiplicative factor of 4.448 to convert units. The force then is in newtons (N).

Many of the mountings for prisms considered in this chapter conform to varying degrees with the principles of kinematics. Although prisms can be treated more or less as rigid bodies, surface distortions due to mounting forces must be carefully controlled. Unfortunately, no simple equations can be given here for relating surface deformations to applied forces. The best way to determine deformations for a given prism mounting being created or evaluated is to apply FEA methods. The details of using FEA for this purpose are beyond the scope of this book.

7.5 MOUNTING PRISMS BY CLAMPING

The appropriateness of the design of a mechanical mounting for a prism depends on a variety of factors, such as the inherent rigidity of the optic; the tolerable movements and distortions of the surfaces (especially reflecting ones); the magnitudes, locations, and orientations of the steady-state forces holding the optic against its mounting surfaces during operation; the transient forces driving the optic against or away from those surfaces during exposure to extreme shock and vibration; thermal effects; the shape of the mounting surface on the optic; the sizes, shapes, and orientations of the mounting surfaces (pads) on the mount; and the rigidity and long-term stability of the mount. In addition, the design must be compatible with assembly, adjustment, maintenance, package size, weight, and configuration constraints. Further, it must also be affordable in the context of the cost of the entire instrument.

7.5.1 Prism Mounts: Semikinematic

Generally, prisms are solid polyhedrons with flat surfaces intersecting at various dihedral angles. Some prisms, such as axicons and cube-corner prisms, have surfaces with curved apertures that conform to rotationally symmetric beams. Others, such as the Porro prism, may have curved edges for weight reduction and packaging reasons.

An example of mounting a cube-shaped beam splitter prism in a semikinematic mount was described by Lipshutz (1968). It is shown in Figure 7.54. The prism (view [a]) is made of two similar right-angle prisms cemented together. It may be treated as a rigid body subject to six positional constraints. Surface distortions may result from improperly applied forces and size variations may occur when the temperature changes.

A prism of this type is frequently used to divide a beam converging toward an image plane into two parts, each forming its own image, as indicated in view (b). In order for these images to maintain a constant alignment relative to each other and the structural reference of the optical instrument, the prism must not translate in the plane of reflection (*X*–*Y*) nor rotate about any of the orthogonal axes. Pure translation along the *Z*-axis does not introduce any error.

Once the optical train is aligned, the beam splitter must always be pressed against its five mounting pads, indicated in the figure by the symbol K_∞ in view (a). These are raised areas on the instrument structure that are assumed to have spring rates approaching infinity. The pads constrain translations in two directions and rotations about the three axes. Five constraining forces (K_i in Figure 7.54[a]) have relatively low spring constants; they are illustrated as compression springs. These elements are located opposite the mounting pads to put the glass in pure compression, thereby minimizing surface distortion.

The dashed lines in Figure 7.54(b) show how increased temperature will expand the cube. The light path to each image (at the *X* and *Y* detectors) is not deviated, owing to such changes with this mounting configuration.

When the prism configuration is other than a cube, the mounting design is more complex since it is more difficult to apply restraining forces directly opposite support pads. Figure 7.55 illustrates this point. Figure 7.55(a) shows a right-angle prism semikinematically registered against its refracting faces and one edge. Three coplanar pads on the base plate provide constraints in the *Y* direction, while three locating posts pressed into the base plate add three more (*X*–*Y*) constraints. Note that a perforation is required in the base plate for light passage. This is not shown in the figure. Ideally, all pads and posts would contact the prism outside its optically active apertures (not shown).

In Figure 7.55(b), the same prism is shown in side view. The preload forces F_1 and F_2 are oriented perpendicular to the hypotenuse face and touch the prism near the longer edges of the hypotenuse. F_1 is aimed symmetrically between the nearest pad (b) and the nearest post (d), while

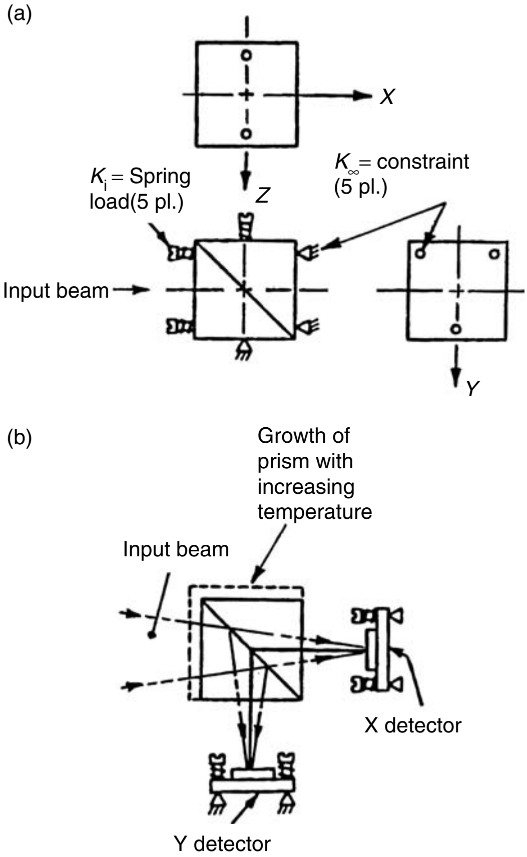
(a)
X
K_i = Spring load(5 pl.)
Z
K_∞ = constraint (5 pl.)
Input beam
Y
(b)
Growth of prism with increasing temperature
Input beam
X detector
Y detector

FIGURE 7.54 (a) Three views of a semikinematic mounting for a cube-shaped beam splitter prism. (b) Schematic of the typical optical function of the beamsplitter showing the effect of a temperature rise. (Adapted from Lipschutz, M.L., *Appl. Opt.*, 7, 2326, 1968.)

F_2 is aimed symmetrically between pads a and c and post e. Horizontal force F_X holds the prism against pin f, and horizontal and vertical components of F_1 and F_2 hold the prism against the three pads and remaining two locating posts. Although not optimum in terms of freedom from bending tendencies (i.e., moments) because the forces are not directed toward the pads, this arrangement is adequate since the prism is relatively stiff.

In Figure 7.55(c), the hypotenuse face of a Porro prism is positioned against three coplanar flat pads on a perforated plate (perforation again not shown), while one triangular face touches two posts and one beveled edge touches a third post. The posts must be perpendicular to the plate surface. Optical clear apertures are not shown. A force, F_Z, directed parallel to and slightly above the base plate holds the prism against two posts (d and e), while force F_X, also just above the plate, holds it against the third post (f). A third force, F_Y, holds the prism against the three pads (a, b, and c). This force acts against the dihedral edge of the prism at its center. Because the prism is stiff, surface distortion is minimal. Any distortion that does occur can be reduced by dividing F_Y into two parallel forces, one directed toward pad a and the other toward the midpoint of the line connecting the centers of pads b and c.

Figure 7.56 shows a right-angle prism referenced to one triangular ground face. The prism is pressed against three coplanar raised pads and three locating posts, all on the base plate. Three long screws threaded into the base plate pull the clamping plate through a resilient (elastomeric) pad to clamp the prism against the three pads. A leaf spring anchored at both ends (here, we define this as a “straddling” spring) presses the prism horizontally against two of the locating posts. An attractive

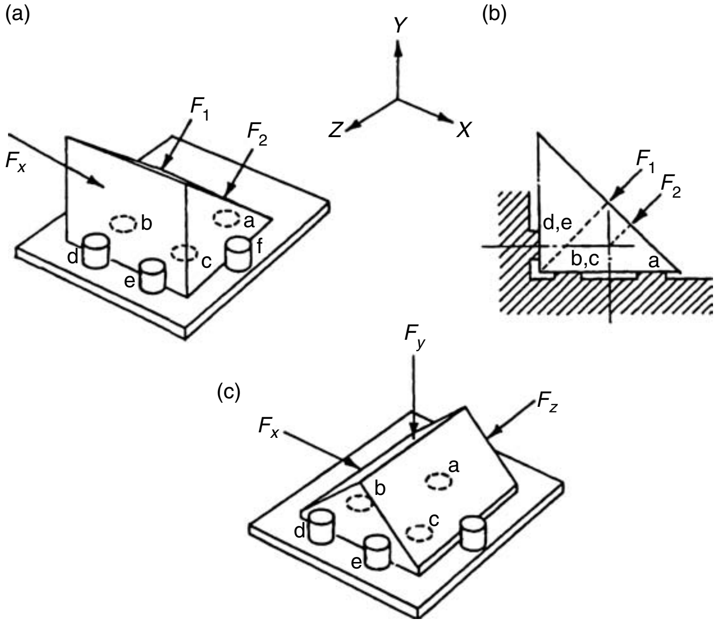

FIGURE 7.55 Schematics of semikinematic mountings for (a) and (b) a right-angle prism referenced to its refracting surfaces and one edge, and (c) a Porro prism referenced to its hypotenuse surface, one triangular surface and one edge. (Adapted from Durie, D.S.L., *Mach. Des.*, 40, 184, 1968.)

feature of this mounting is that it can be configured so that the circular clear apertures of optically active surfaces are not obscured and are not likely to be distorted by the imposed forces.

The resilient pad (in compression) and the three screws (in tension) provide the preload necessary to hold the prism in place under shock and vibration. We assume here that the spring constant of the pad is considerably smaller than that of the screws acting together, so the latter can be ignored. We can design the subassembly only if the elastic characteristic of the pad material is known. Its spring constant, C_P, is defined as the preload that must be applied normal to the pad surface to produce a unit deflection. This is expressed as follows:

$$C_P = P/\Delta y \tag{7.25}$$

Most resilient materials have a limited elastic range, tend to creep with time, and take a permanent set under sustained high compressive load, i.e., one greater than that for which the material acts elastically. For these reasons, these materials might be considered unreliable for use in the manner suggested here. However, if properly used, they provide a convenient way to mount some prisms.

A material called Sorbothane™, a viscoelastic, thermoset, polyether-base polyurethane, behaves as indicated in Figure 7.57 for different durometers and three deflections as percentages of the pad thickness. This material is commonly used in vibration isolators for machines and deflects elastically if the change in thickness is between 10 and 25% of the total thickness. A softer (i.e., lower durometer) material deflects more per unit load. It is appropriate to design the interface for the maximum applied force that occurs at maximum acceleration. If we choose the 20% deflection curve shown in Figure 7.57, the deflections under lesser accelerations would lie within the linear range of the material. The manufacturer's literature indicates that pad deflection, Δy, is related to load, P (in the USC system), as follows:

$$\Delta y = \frac{0.15 P t_P}{C_S A_P (1 + 2\gamma^2)} \tag{7.26}$$

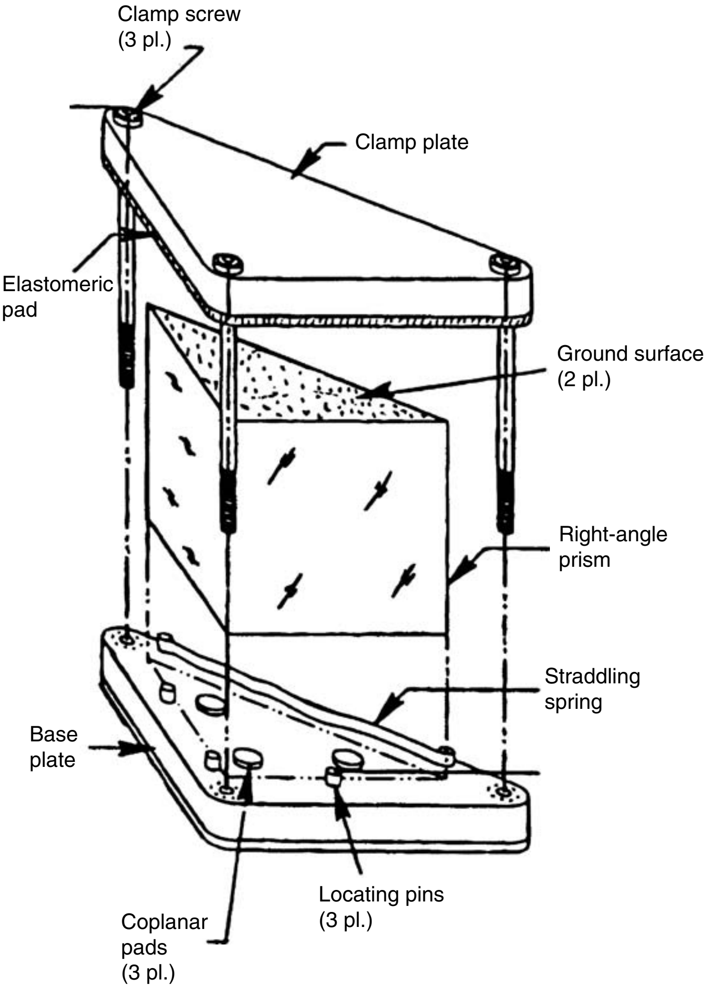

FIGURE 7.56 A semikinematic mounting for a right-angle prism preloaded by a compressed elastomeric pad. (Adapted from Vukobratovich, D., in *The Infrared & Electro-Optical Systems Handbook*, Vol. 4, ERIM, Ann Arbor and SPIE Press, Bellingham, 1993.)

where P is the required preload, t_P the uncompressed pad thickness, $\gamma = D_P/4t_P$ a "shape factor", in which D_P the pad width or diameter, $A_P = D_P^2$ for a square pad or $\pi D_P^2/4$ for a circular pad, and C_S the compressive stress in the pad per Figure 7.57.

We illustrate the design of such a mounting with an example adapted from Yoder (2002) as follows. Assume that a penta prism with $A = 2.000$ in. and weight 2.244 lb is clamped against three pads on a base plate in the manner shown in Figure 7.56. Constraint is to be provided for $a_G = 10$, so a preload of 22.44 lb is needed. A circular pad with thickness $t_P = 0.375$ in. made of 30 durometer material characterized by Figure 7.57 is placed between the clamping plate and the prism. We see from Figure 7.57 that if the pad is compressed 20%, C_S is ~3.7 lb/in.^{2}. Then, $\gamma = D_P/4t_P = D_P/[(4)(0.375)] = 0.6667D_P$. The area of the pad $A_P = \pi D_P^2/4 = 0.7854D_P^2$. From Eq. (7.26), $\Delta y = (0.15)(22.44)(0.375)/[(3.7)(0.7854D_P^2)][1 + (2)(0.6667D_P^2)]$. This deflection must equal 20% of 0.375 in. Equating and solving quadratically for D_P, we obtain $D_P = 1.431$ in. (36.347 mm). Note that a smaller pad could be used if a stiffer material were used or the pad thickness were to be reduced.

Another semikinematic mounting is illustrated schematically in Figure 7.58. Here, a penta prism is pressed against three circular coplanar pads on a base plate by three cantilevered springs.

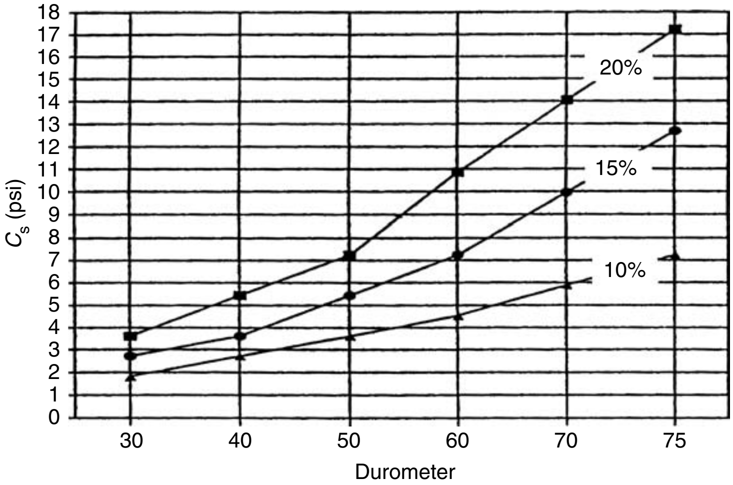

FIGURE 7.57 Plot of compressive stress (C_S) vs. durometer for a viscoelastic material with deflections of various percentages of the pad thickness. (Courtesy of Sorbothane, Inc., Kent, OH.)

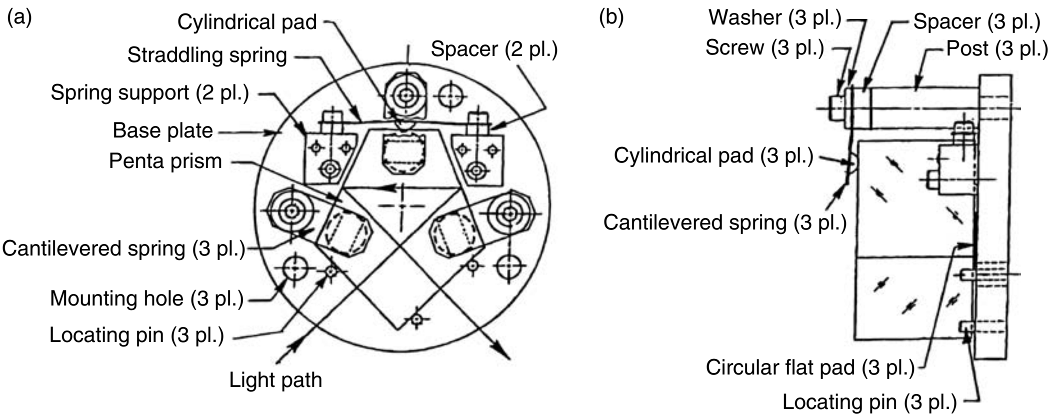
(a)
Cylindrical pad
Straddling spring
Spacer (2 pl.)
Spring support (2 pl.)
Base plate
Penta prism
Cantilevered spring (3 pl.)
Mounting hole (3 pl.)
Locating pin (3 pl.)
Light path
(b)
Washer (3 pl.)
Spacer (3 pl.)
Screw (3 pl.)
Post (3 pl.)
Cylindrical pad (3 pl.)
Cantilevered spring (3 pl.)
Circular flat pad (3 pl.)
Locating pin (3 pl.)

FIGURE 7.58 A semikinematic mounting for a penta prism with cantilevered and straddling spring constraints: (a) plan view, (b) elevation view. (From Yoder, P.R., Jr., *Mounting Optics in Optical Instruments*, SPIE Press, Bellingham, 2002.)

This constrains one translation and two tilts. The other translations and the third tilt are constrained by preloading the prism against the three locating pins with a straddling leaf spring.

Equations (4.22) and (4.23) are used to design the cantilevered springs for this application and to check the bending stress in each spring clip as they were used in Section 4.7.4 in designing similar constraints for lenses. For the convenience of the reader, they are repeated here:

$$\Delta = (1 - v_M^2)(4PL^3)/(E_M bt^3 N) \tag{4.22}$$

$$S_B = 6PL/(bt^2 N) \tag{4.23}$$

where v_M and E_M are Poisson's ratio and Young's modulus for the spring material, P the total preload, L the free (cantilevered) length of the spring, b and t the width and thickness of the spring, and N the number of springs employed. Once again, S_B should not exceed 50% of the yield stress of the material.

Another useful equation pertinent to cantilevered spring design is the angle at which the end of the cantilevered portion of the spring is bent relative to the fixed portion of the spring. This equation (adapted from Roark, 1954) is

$$\varphi = \frac{6PL^2(1 - v_M^2)}{E_M bt^3} \tag{7.27}$$

The use of cylindrical pads between the springs and the prism surfaces in the mounting design of Figure 7.58 ensures that line contact will occur in a reliable manner at each interface. In the absence of a pad, a deflected cantilevered spring could touch the prism at the edge of its protective bevel as shown in Figure 7.59(a). This is highly undesirable since the edge is sharp and, as will be shown in Chapter 15, the stresses at a sharp corner interface are large, so the prism is vulnerable to damage from the force exerted by the spring. An alternative interface, again without a pad, is illustrated in Figure 7.59(b). Here, the deflected spring nominally lies flat against the top prism surface by virtue of the wedge-shaped parts placed above and below the spring on the post. The angles of the wedges are set by Eq. (7.27). While this is good from the viewpoint of stress in the prism if the spring is in close contact with an appreciable area on the prism, a potential problem with this design is that the angle might be wrong because of a minor manufacturing error or unfavorable tolerance buildup that could cause the end of the spring to touch the prism surface (if the angle is too steep) or the spring to touch the bevel (if the angle is too shallow). Either of these conditions could damage the prism because of a concentration of stress.

Another version of the area interface illustrated in Figure 7.59(b) is shown in Figure 7.60(a). Here, a flat surface on a wedged pad attached to the end of the spring nominally brings the pad in close contact with the prism surface. This design is also susceptible to angular errors that could make it deteriorate into sharp corner contact at the inner or outer edge of the pad, resulting in undue stress.

Line contact at a rounded portion of the spring occurs if the end of the spring is bent to a convex cylindrical shape as indicated in Figure 7.60(b). Since it may be difficult to form the spring into a smooth cylinder of a particular radius, a better interface results if a pad is machined directly into the spring as indicated in Figure 7.60(c). Note that a separately machined cylindrical pad can also be

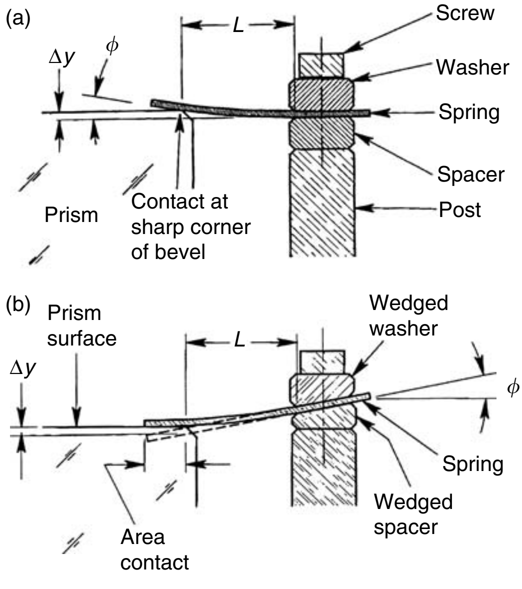

FIGURE 7.59 Two configurations of cantilevered spring interfaces with a prism. (a) Spring touching prism bevel, (b) spring lying flat on prism surface. (From Yoder, P.R., Jr., *Mounting Optics in Optical Instruments*, SPIE Press, Bellingham, 2002.)

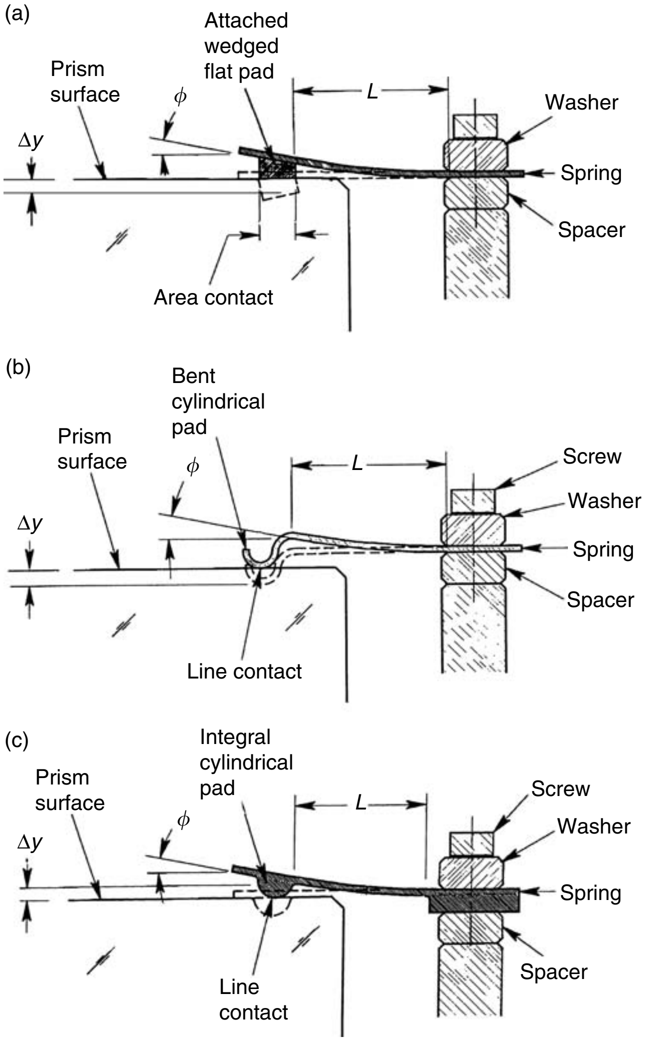
(a)
Attached
wedged
flat pad
Prism
surface
ϕ
Δy
L
Washer
Spring
Spacer
Area contact
(b)
Bent
cylindrical
pad
Prism
surface
ϕ
Δy
L
Screw
Washer
Spring
Spacer
Line contact
(c)
Integral
cylindrical
pad
Prism
surface
ϕ
Δy
L
Screw
Washer
Spring
Spacer
Line
contact

FIGURE 7.60 Configuration of a cantilevered spring interface with pads of various shapes pressing against a flat surface on the prism: (a) flat pad, (b) spring bent to convex cylindrical curve, (c) integrally machined cylindrical or spherical pad. (From Yoder, P.R., Jr., *Mounting Optics in Optical Instruments*, SPIE Press, Bellingham, 2002.)

attached to the spring by screws, welding, or adhesive and achieve the same function. In either case, stress introduced at the interface between the convex cylinder and the flat prism surface can be estimated and adjusted to an acceptable level by careful design. We explain how to do this in Chapter 15.

The designs of the cylindrical pads for use on cantilevered or straddling springs should include consideration of the angular extent of the curved surfaces. Figure 7.61 shows the pertinent geometrical relationships. R_{CYL} is the pad's radius, d_{P} the width of the pad, and α one half the angular extent of the cylindrical surface measured at its center of curvature. In Figure 7.61(a), the pad is tangent to the prism surface before the spring is bent. In Figure 7.61(b), the spring is bent to exert preload P, tilting the pad by the angle φ per Eq. (7.27). If the worst-case α is greater than φ, no sharp edge contact will occur. Once α is determined, we calculate the minimum value for d_{P} as $2R_{\text{CYL}} \sin \alpha$.

Figure 7.62 shows how a straddling spring can be used instead of cantilevered spring clips to hold a prism in place. A curved pad is shown at the center of the spring as a means for distributing the force over a specific small area on the prism. A flat pad could be used if we could be sure that

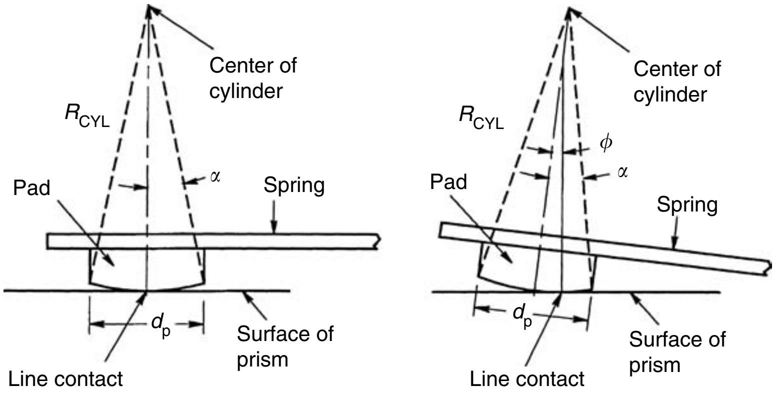
Center of cylinder
R_{CYL}
α
Pad
Spring
d_p
Surface of prism
Line contact
Center of cylinder
R_{CYL}
ϕ
α
Pad
Spring
d_p
Surface of prism
Line contact

FIGURE 7.61 Geometric relationships applied in the design of cylindrical pads for springs. The same geometry applies to spherical pads. (From Yoder, P.R., Jr., *Mounting Optics in Optical Instruments*, SPIE Press, Bellingham, 2002.)

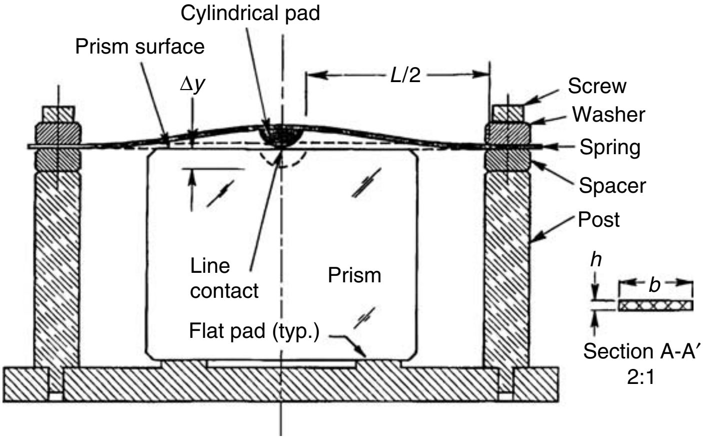
Cylindrical pad
Prism surface
Δy
$L/2$
Screw
Washer
Spring
Spacer
Post
Line contact
Prism
Flat pad (typ.)
h
b
Section A-A′ 2:1

FIGURE 7.62 A straddling spring constraint for a prism shown with a cylindrical or spherical pad. (From Yoder, P.R., Jr., *Mounting Optics in Optical Instruments*, SPIE Press, Bellingham, 2002.)

the spring action is symmetrical and that the pad lies flat on the prism. Dimensional errors or tolerance buildup could, however, tilt the pad at the wrong angle and cause stress concentration at a pad edge. Curving the pad into a cylindrical or spherical shape eliminates this possibility. Additional springs can be used if one is not sufficient to provide the required preload or to reduce stress at each interface.

The deflection Δy from the relaxed shape and the bending stress S_B in the straddling spring are given by the following equations adapted from Roark (1954):

$$\Delta y = 0.06251(1 - v_M^2)(P_i L^3)/(E_M b t^3) \tag{7.28}$$

$$S_B = 0.75 P_i L/(b t^2) \tag{7.29}$$

where P_i is the preload per spring (equal to total preload/N, where N is the number of springs), L the spring's total free length, b the spring width, t the spring thickness, and v_M and E_M the Poisson's ratio and Young's modulus, respectively, for the spring material.

To illustrate the use of these equations, consider the example of a single BeCu straddling spring used to constrain a prism weighing 0.267 lb (0.121 kg) under 12 times gravity acceleration. The preload P_i is then (0.267)(12) = 3.204 lb (1.452 N). The spring dimensions are $L = 1.040$ in. (26.416 mm), $b = 0.250$ in. (6.350 mm), and $t = 0.0115$ in. (0.292 mm), while $v_M = 0.35$ and $E_M = 18.5 \times 10^6$ lb/in.^{2} (1.27×10^5 Pa). We assume the yield strength of BeCu to be 155,000 lb/in.^{2} (1.069×10^3 MPa). From Eq. 7.25, $\Delta y = (0.0625)(1 - 0.35^2)(3.204)(1.040^3)/[(18.5 \times 10^6)(0.250)(0.0115^2)] = 0.0281$ in. (0.714 mm). From Eq. 7.26, $S_B = (0.75)(3.204)(1.040)/[(0.250)(0.0115^2)] = 75{,}590$ lb/in.^{2} (521.2 MPa). The spring's safety factor is then an acceptable 155,000/75,590 = 2.05.

An application of the straddling spring is illustrated in Figure 7.63. This is a drawing of a portion of the housings for a commercial binocular offered by Swarovski Optik in Austria. The centers of the springs press against the apexes of the prisms and hold them against shoulders provided inside the housings. One end of each spring is attached with a screw to the housing while the other end slips into a slot provided in the housing wall. This arrangement allows the springs to slide in the slots, as its chord length changes slightly when the spring is bent to apply preload. It also removes the necessity for four threaded holes and four screws. Note that in this design, no pads are used on the springs.

Another version of the straddling spring prism mounting is illustrated schematically in Figure 7.64. Here, the refracting surfaces of an Amici prism are held against flat pads inside a military elbow

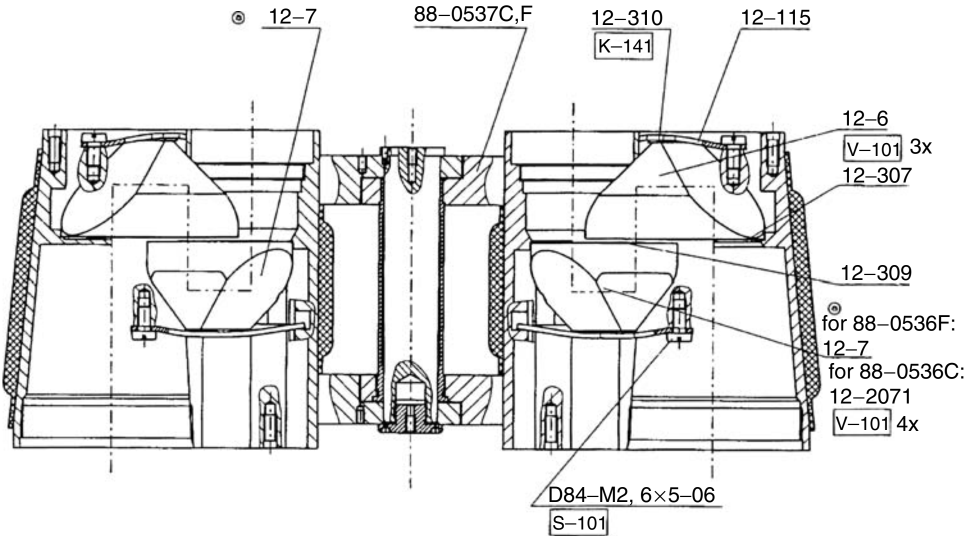

FIGURE 7.63 Porro prism constraints using straddling springs as found in a modern commercial binocular. (Courtesy of Swarovski Optik KG, Absam/Tyrol, Austria.)

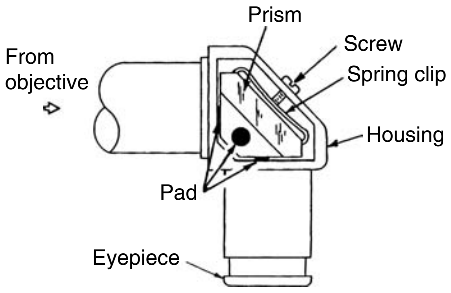

FIGURE 7.64 Schematic diagram of a small military elbow telescope with an Amici prism spring loaded against reference pads. (Reprinted with permission from Yoder, P.R., Jr., 1997. Copyright CRC Press, Boca Raton, FL.)

telescope housing by a flat spring with bent ends. The screw pressing against the center of the spring forces the spring's ends against ground surfaces on the prism. It is not apparent from the figure, but constraint perpendicular to the plane of the figure is provided by slightly resilient pads attached to the inside surfaces of triangular-shaped covers that are attached with screws to both sides of the cast housing.

This design has a deficiency in that sharp and perhaps irregular edges on the spring ends could touch the glass. Failure of the glass might be expected to occur under extreme accelerations because of concentrated contact stress. This author has examined a telescope of this design and observed a fracture in the glass at the spring interface. If the design had specified that special care be exercised to round both spring ends during manufacture, we would not expect such damage.

It is also very important in this design that the screw not protrude far enough into the housing for the spring to touch the roof edge of the prism under vibration or shock, especially at extreme temperatures. The design should specify the correct screw length and appropriate tolerances to give sufficient preload to the prism without the possibility of spring contact with the prism and provide explicit instructions in the manufacturing procedures to check the actual clearance at assembly.

7.5.2 PRISM MOUNTS: NONKINEMATIC

We next consider a series of mounts that utilize springs to clamp prisms against mounting surfaces in nonkinematic fashion. The first of these examples is the Porro prism-erecting system used widely in military and commercial binoculars and telescopes. Figure 7.65 illustrates the design used in many 7 × 50 military binoculars of World War II vintage. In this design, the prisms are light, barium, crown-type, 573574 optical glass, the shelf is aluminum, the straps are spring-temper phosphor bronze, the light shields are aluminum alloy painted matte black, and the pads are cork. Note that cork supports fungus growth, and is no longer used for this purpose.

The index of refraction of the prism glass is high enough for TIR to take place, so the prisms are not silvered. The light shields reduce the level of stray light entering the optical path through the reflecting surfaces. Tabs provided at the edges of the shields are bent inward, so the shields do not touch the glass within the reflecting apertures. The prisms fit into "flat-bottomed" recesses machined into both

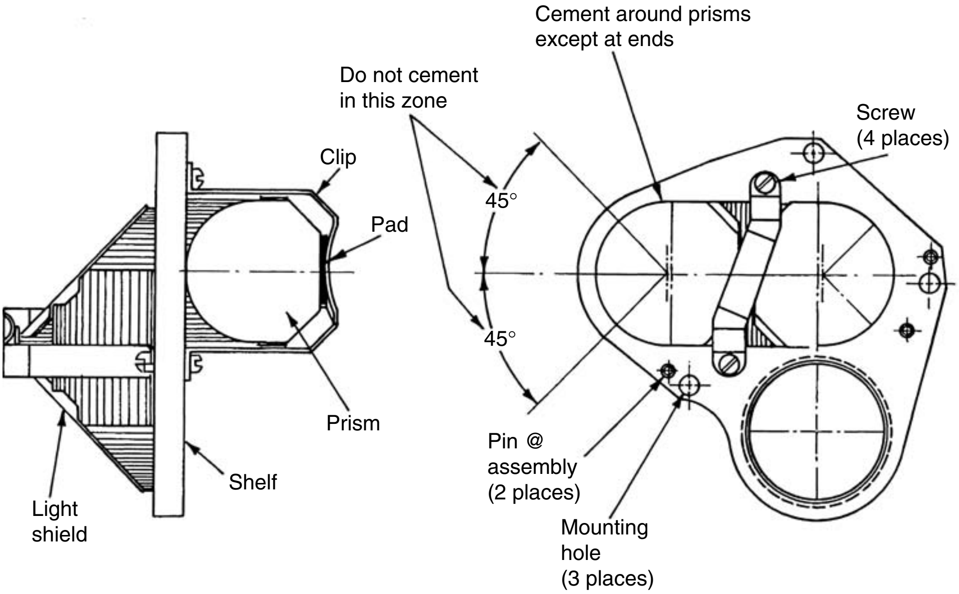

FIGURE 7.65 Schematic view of a typical strap mounting for a Porro prism erecting subassembly used in telescopes and binoculars. (Adapted from Yoder, P.R., Jr., 1985.)

sides of the shelf. These recesses are contoured as race track shapes to fit the prism hypotenuse faces, thereby constraining rotation and translation of the prisms under the straps. Extra restraint was afforded in this particular design by injecting rubber cement into the glass-to-metal gaps along the straight edges of the prisms. Today, one would probably use an elastomer such as an RTV elastomer for this purpose.

Another example of a clamped prism is the periscope head prism arrangement shown in Figure 7.66. This subassembly is also from a military optical instrument and uses a single Dove prism with face angles of 35°, 35°, and 110° that can be tilted about the horizontal transverse axis to scan the line of sight in elevation from the zenith down to about 20° below the horizon.

The prism is held in its cast aluminum mount by four spring clips screwed fast to the mount adjacent to the entrance and exit prism faces. The edges of the reflecting surface (hypotenuse) of the prism rest on narrow, nominally parallel lands machined into the casting. The prism faces protrude slightly ($<$ 0.5 mm [0.02 in.]) above the mount and the undersides of the springs are stepped back locally so that the approximately proper preload is obtained when the springs bottom against the mount. Once centered, the prism cannot slide parallel to its hypotenuse surface because of the convergence of the clamping forces. The vector sum of these forces is nominally normal to the mounting surface.

Figure 7.67(a) illustrates the scanning function of the prism in the instrument shown in Figure 7.66. Rotation occurs about a horizontal axis located, as shown, a short distance below the prism center and slightly behind the reflecting surface. This motion is usually limited optically by vignetting of the refracted beam at the extreme angles. Mechanical stops are built into the instrument to limit physical motion, so that the vignetting at the end points is acceptable for the application.

Figure 7.67(b) shows beam scanning using a double-Dove prism. The total scan angle can exceed 180°. The transmitted beam can here be twice as large as that scanned by the Dove-type prism of the same aperture. The rotation axis is now located at the prism center.

The most popular types of prisms used for image rotation or derotation about the axis are the Dove, double-Dove, Pechan, and delta. In order to function successfully, all these prisms must be mounted securely yet be capable of adjustment at the time of assembly to minimize image motion during operation. A mechanical design for one type of adjustable derotation prism mounting is discussed next.

In Figure 7.68, we see a sectional view of a representative Pechan prism mounting as described by Delgado (1983). If this type of prism is used in a collimated beam, it requires only angular adjustment

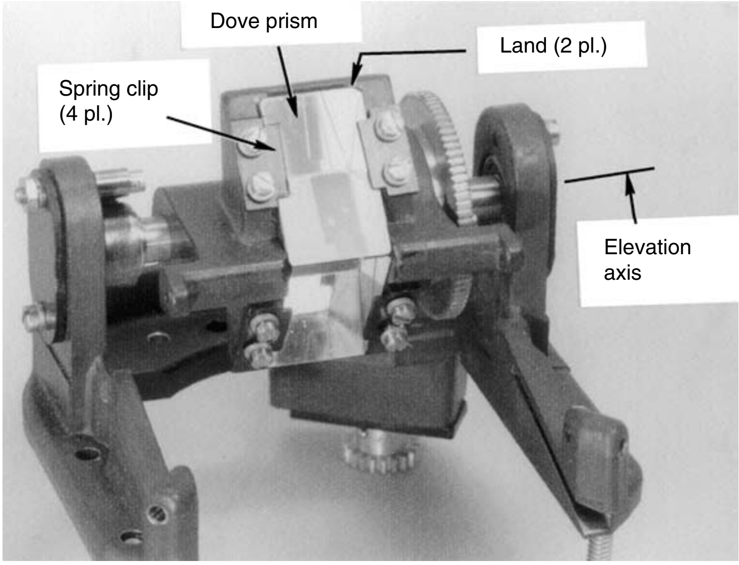

FIGURE 7.66 A clamped Dove-type prism used in the elevation scanning head subassembly of a military periscope.

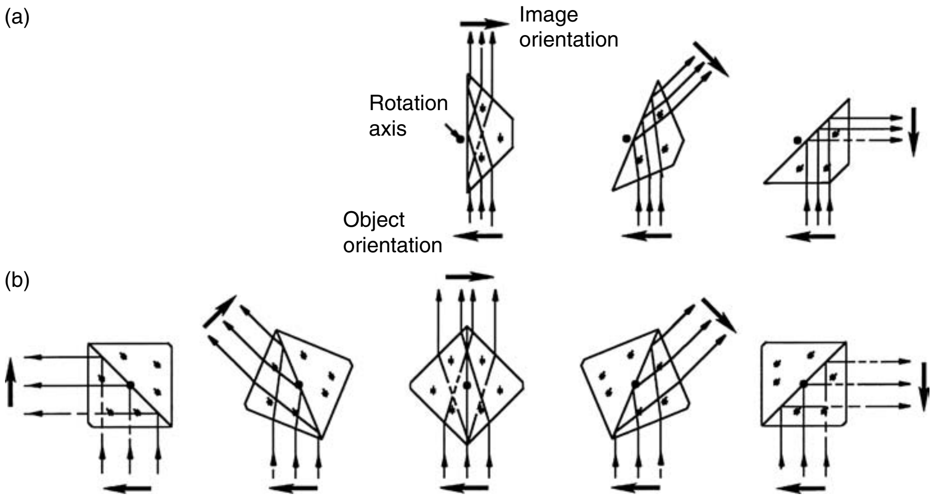
(a)
Image orientation
Rotation axis
Object orientation
(b)

FIGURE 7.67 (a) Beam scanning with a Dove-type prism. (b) Beam scanning with a double-Dove-type prism.

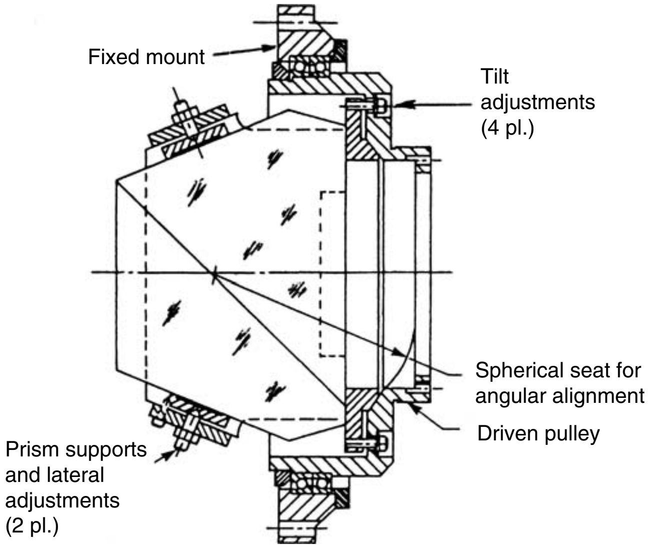
Fixed mount
Tilt adjustments (4 pl.)
Spherical seat for angular alignment
Driven pulley
Prism supports and lateral adjustments (2 pl.)

FIGURE 7.68 Opto-mechanical configuration of a Pechan prism image derotation subassembly. (Adapted from Delgado, R.F., *Proc. SPIE*, 389, 75, 1983.)

of the optical axis relative to the rotation axis. In this case, the prism was to be used in a converging beam, so both angular and lateral adjustments were needed. Bearing wobble would cause angular errors. To minimize this in the design considered here, class 5 angular contact bearings, mounted back to back, were oriented with factory-identified high spots matched and then preloaded. Runout over 180° rotation was measured as about 0.0003 in. (7.6 μm). The bearing axis was adjusted laterally by fine-thread screws (not shown) that permitted centration with respect to the optical system axis to better than 0.0005 in. (12.7 μm). The prism was adjusted laterally within the bearing housing in the plane of refraction by sliding it against a flat vertical reference surface with fine-thread screws pressing against the reflecting surfaces through pressure pads. A spherical seat with its center of rotation at the intersection of the hypotenuse face with the optic axis (to minimize axis cross-coupling) was provided for angular adjustment. The adjustment screws indicated controlled this movement.

In the mountings depicted in Figures 7.65, 7.66, and 7.68, the Porro, Dove, and Pechan prisms are pressed against machined surfaces on the mounts. Since it is virtually impossible for these surfaces to be as flat as the polished glass, contact will occur at the three highest points on the machined surfaces. Undoubtedly, these points are not directly in line with the clamping forces, so moments are applied to the glass, and surface distortions might occur. The designs work in their intended visual applications because the prisms are stiff enough not to bend significantly. In higher precision applications, it would be advisable to create highly precise lands on the metal surfaces to ensure that the clamping force vectors pass perpendicularly through these lands. Mountings should not depend on frictional forces between the glass and reference surfaces to constrain lateral motions. Independent positive lateral constraints should be provided if possible.

7.6 MOUNTING PRISMS BY BONDING

A technique that is highly favored by many opto-mechanical engineers for mounting prisms involves glass-to-metal bonds using adhesives. This design technique generally results in reduced interface complexity and compact packaging while providing mechanical strength adequate for withstanding the severe shock, vibration, and temperature changes characteristic of most military and aerospace applications. The technique is also frequently used in less rigorous applications because of its inherent simplicity and reliability.

The critical aspects of a glass-to-metal bond are the characteristics of the chosen adhesive, thickness of the adhesive layer, cleanliness of the surfaces to be bonded, dissimilarity of coefficients of thermal expansion for the materials bonded, dimensions of the bond, environment that the bonded assembly will experience, and care with which the bonding operation is performed. Several adhesives commonly used for this purpose are listed in Chapter 3, along with some of their major characteristics. The manufacturer's recommended procedures for applying and curing these adhesives should be followed unless special requirements of the application dictate otherwise. The manufacturer should be consulted if there is any question about process or material suitability for any particular application. Experimental verification of the choice of adhesive and methods is advisable in critical applications.

For maximum bond strength, the adhesive layer should have a specific thickness. In the case of epoxy EC2216-B/A, mentioned at various points in this book, experience has indicated a thickness of 0.075 to 0.125 mm (0.003 to 0.005 in.) to be appropriate. One method of ensuring the right layer thickness is to place spacers (wires, plastic fishing line, or flat shims) of the specified thickness at three places symmetrically located on one bonding surface before applying the adhesive. Care must be exercised to register the glass part against these spacers during assembly and curing. The adhesive should not extend between the spacers and either part to be bonded since this could affect the adhesive layer thickness. Another technique for obtaining a uniform thin layer of epoxy between the glass and metal surfaces is to mix small glass beads[‡] into the epoxy before applying it to the surfaces to be bonded. When the parts are clamped securely together, the largest beads contact both faces and hold those surfaces apart by the bead diameters. Since such beads can be procured with closely controlled diameters, the achievement of specific thickness joints is relatively simple. As one might expect, the addition of the beads may have a small beneficial effect on the coefficient of thermal expansion of the epoxy.

It has been clearly demonstrated by Hatheway (1993) and Miller (1999) that a thin adhesive bond is stiffer than a thick one. The variation in Young's modulus with thickness can be as large as a factor of 100. This variation can affect the ability of the bond to "give" under shock and vibration as well as when the temperature changes.

[‡] See, for example, certified sized products made by Duke Scientific Corp. (www.dukescientific.com).

Guidelines for determining the appropriate adhesive area for bonding prisms to mechanical mounts have appeared in the literature (Yoder, 1988, 2002). In general, the minimum area of the bond, Q_{MIN}, in the USC system of units, is determined by

$$Q_{\mathrm{MIN}} = W a_{\mathrm{G}} f_{\mathrm{s}} / J \tag{7.30}$$

where W is the weight of the optic, a_{G} the worst-case expected acceleration factor, f_{S} the safety factor, and J the shear or tensile strength of the adhesive joint (usually approximately equal). The safety factor should be at least 2 and possibly as large as four to allow for some unplanned, nonoptimum conditions, such as inadequate cleaning during processing.

Because the dimensional changes of the adhesive bond during curing (shrinkage) and during temperature changes (expansion or shrinkage depending upon the sign of the change) are proportional to the dimension of the bond, it is advisable not to make the bond area too large. If a large area is necessary to hold a heavy optic, the bond should be divided into a group of smaller areas, such as a triangular or ring pattern of circles or spots of any shape.

Figure 7.69 shows a simple mounting design for a large Porro prism used in a military telescope. In this application, the prism is cantilevered from a nominally vertical mounting surface. The prism is made of Schott SK16 glass and weighs 2.2 lb. It is bonded to a type 416 stainless-steel bracket with EC2216-B/A adhesive with $J = 2500$ lb/in.^{2} over the maximum available area. The thermal expansion coefficients of the glass, metal, and adhesive are $\alpha_{\mathrm{G}} = 3.9$ ppm/°F, $\alpha_{\mathrm{M}} = 5.5$ ppm/°F, and $\alpha_{\mathrm{e}} = 57$ ppm/°F. The bonding surface finishes are fine ground (KH grit) on the glass and 63 on the metal.

If we know the area of the bond interface on such a prism mounting, the maximum acceleration that the subassembly should withstand can be easily computed. Conversely, given the maximum acceleration specification, the minimum bond area can be computed. In the case of the prism shown in Figure 7.69, the adhesive is spread uniformly over an area of 5.6 in.^{2} Using Eq. (7.30), we estimate the acceleration factor that this subassembly should withstand with a safety factor of 4 as $a_{\mathrm{G}} = JQ/Wf_{\mathrm{S}} = (2500)(5.6)/[(2.2)(4)] = 1591$ times gravity. This particular prism subassembly is known to have survived > 1200 times gravity when shock tested as part of a military periscope in an armored vehicle. The design was therefore deemed to be successful.

Figure 7.70 shows photographs of a roof penta prism bonded to a cast and machined aluminum plate for use in another military periscope. In this case, the prism weight was ~0.26 lb and the circular bond had an area of 0.76 in.^{2} Assuming that EC2216B/A adhesive is used and that this prism assembly is expected to experience shocks of 1500 times gravity, we predict that the safety factor for this design $f_{\mathrm{S}} = JQ/Wa_{\mathrm{G}} = (2500)(0.76)/[(0.26)(1500)] = 4.9$. This should be more than adequate. Note that the bonding area is not centered on the plate. Rather, it is centered with respect to the prism's center of gravity.

Figure 7.71 shows a bond configuration appropriate to a two-part prism; in this case, a Pechan prism. The adhesive is applied only to one prism because the ground surfaces on the adjacent

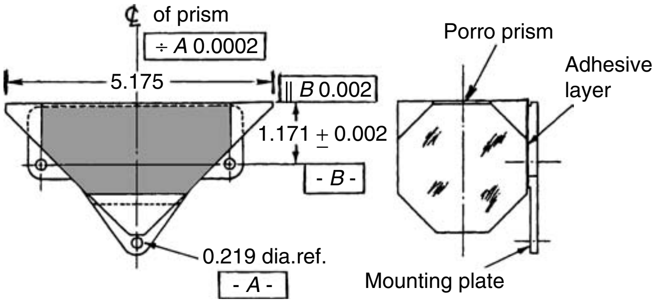

FIGURE 7.69 Mounting for a Porro prism bonded in cantilevered fashion to a bracket.

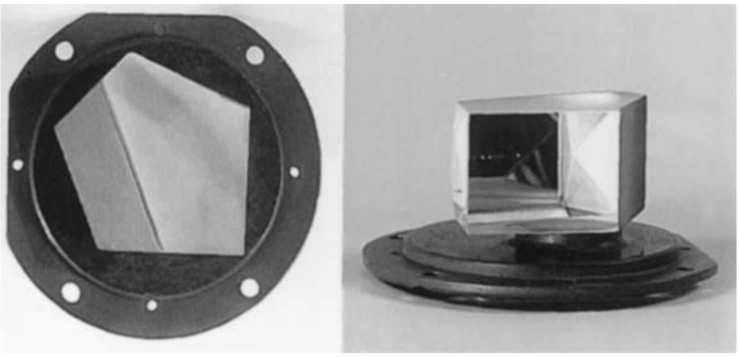

FIGURE 7.70 Photographs of a typical roof penta prism bonded to a flange.

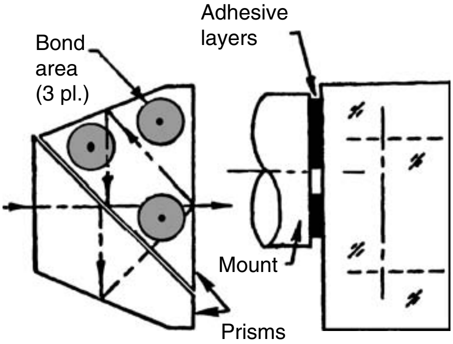

FIGURE 7.71 A triangular distribution of circular adhesive bonds on one prism of a multiple-component (Pechan) prism subassembly. (From Yoder, P.R., Jr., *Mounting Optics in Optical Instruments*, SPIE Press, Bellingham, 2002.)

components cannot be assumed to be coplanar. Therefore, the uniform thickness adhesive layer required for reliability cannot be guaranteed. The adhesive is applied as a triangular array as suggested earlier for a bonded mirror. If the prism surfaces to be bonded were to be fine-ground after cementing, it may be possible that a successful bond can be achieved with the adhesive applied to both prisms.

Conventionally, the main weapon of an armored vehicle (tank) is operated by a gunner who uses two optical instruments to acquire and fire at hostile targets. The primary fire control sight is usually a periscope protruding through the turret roof, while the secondary sight usually is a telescope protruding through the front of the turret alongside and attached by links to the weapon. The key design features of a typical embodiment of the latter type of instrument were discussed by Yoder (2002) and are summarized here.

The specific telescope considered is of the articulated form, i.e., it is hinged near its midsection so that the front end can swing in elevation with the gun, while the rear section is essentially fixed in place so that the gunner has access to the eyepiece without significantly moving his head. Figure 7.72 shows the optical system schematically. It has a fixed magnification of 8-power and a field of view of about 8°. The exit pupil diameter is about 5 mm, so the entrance pupil diameter is about 40 mm. The telescope housing diameter throughout its length is generally about 2.5 in.; naturally, the prism housings are larger. Widely separated relay lenses erect the image and transfer the image from the objective focus to the eyepiece focus.

Two prism assemblies are shown in Figure 7.72. The first contains three prisms, two 90° prisms and a Porro prism, that function within the mechanical hinge and keep the image erect at all gun-elevation

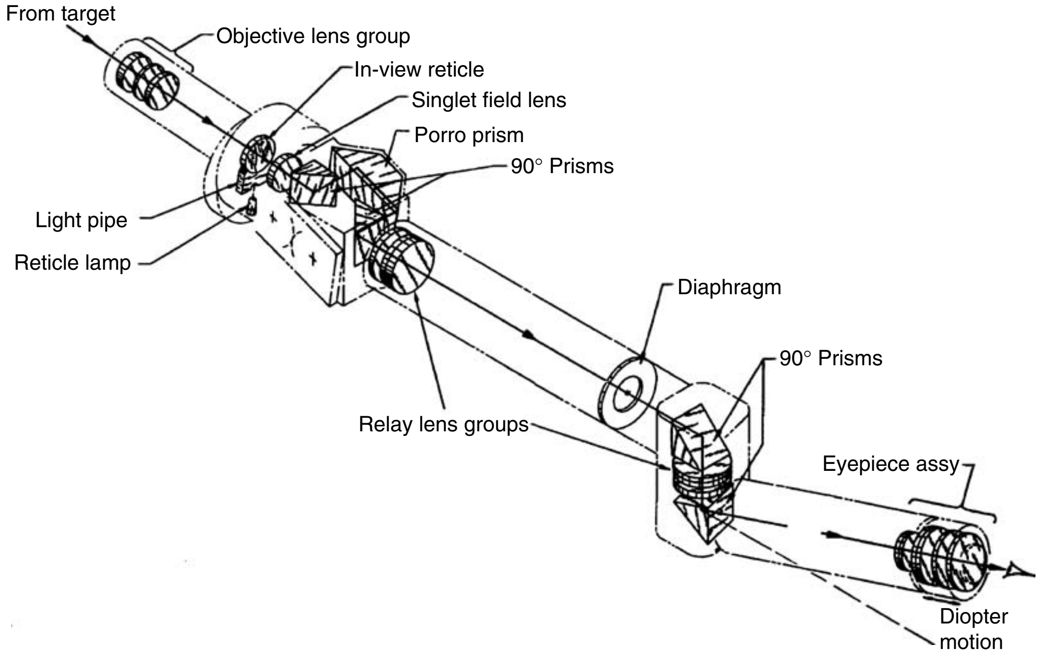
From target
Objective lens group
In-view reticle
Singlet field lens
Porro prism
90° Prisms
Light pipe
Reticle lamp
Diaphragm
90° Prisms
Relay lens groups
Eyepiece assy
Diopter motion

FIGURE 7.72 Optical schematic of an articulated telescope. (Courtesy of the U.S. Army.)

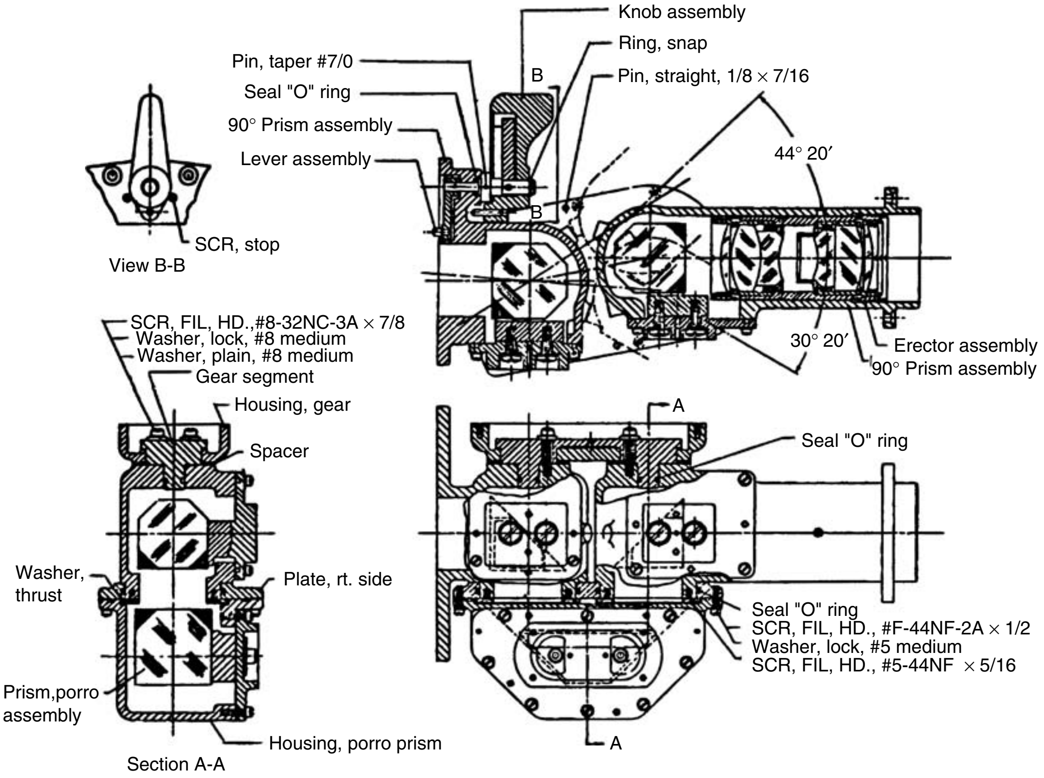
Knob assembly
Ring, snap
Pin, taper #7/0
B
Pin, straight, 1/8 × 7/16
Seal "O" ring
90° Prism assembly
44° 20′
Lever assembly
B
SCR, stop
View B-B
SCR, FIL, HD.,#8-32NC-3A × 7/8
Washer, lock, #8 medium
Washer, plain, #8 medium
Gear segment
30° 20′
Erector assembly
90° Prism assembly
Housing, gear
A
Spacer
Seal "O" ring
Washer, thrust
Plate, rt. side
Seal "O" ring
SCR, FIL, HD., #F-44NF-2A × 1/2
Washer, lock, #5 medium
SCR, FIL, HD., #5-44NF × 5/16
Prism,porro assembly
Housing, porro prism
A
Section A-A

FIGURE 7.73 The articulated joint mechanism for the telescope shown in Figure 7.72. (Courtesy of the U.S. Army.)

angles. The second prism assembly with two 90° prisms offsets the axis vertically and turns that axis 20° in a horizontal plane to bring the eyepiece to a convenient location near the gunner's eye. The balance of this discussion deals with the articulated joint and the mounting arrangement for the prisms therein.

The articulated joint mechanism is shown in Figure 7.73. The first right-angle prism of the articulated joint is mounted in "Housing, 90° Prism" (see Figure 7.74). The prism is bonded to a bracket that is attached with two screws and two metal pins to a plate that is in turn attached with four screws to the housing. After assembly and alignment, a cover is installed over the screws and sealed in place. Surface "W" of that housing attaches to the exit end of the reticle housing.

The second right-angle prism is mounted in "Housing, Erector" as indicated in Figure 7.75. It is also bonded to a bracket that is attached with two screws and two metal pins to a plate that is screwed fast to the housing. The note in this figure indicates the alignment requirements for the prism. Surface "W" mentioned there is shown in Figure 7.74. After alignment, a cover is sealed over the screws.

As shown in Figure 7.73, the Porro prism is contained within a separate housing and, together with a gear housing on the opposite side of the telescope, forms the mechanical link between the

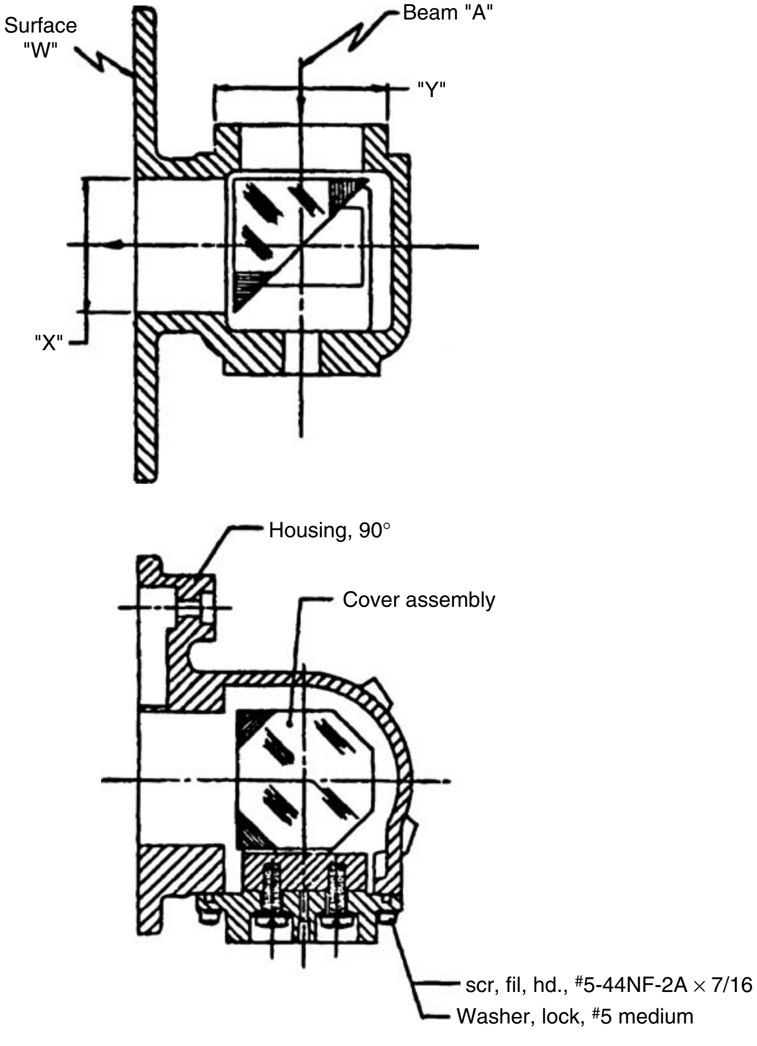

FIGURE 7.74 First right-angle prism assembly for the telescope shown in Figure 7.72. (Courtesy of the U.S. Army.)

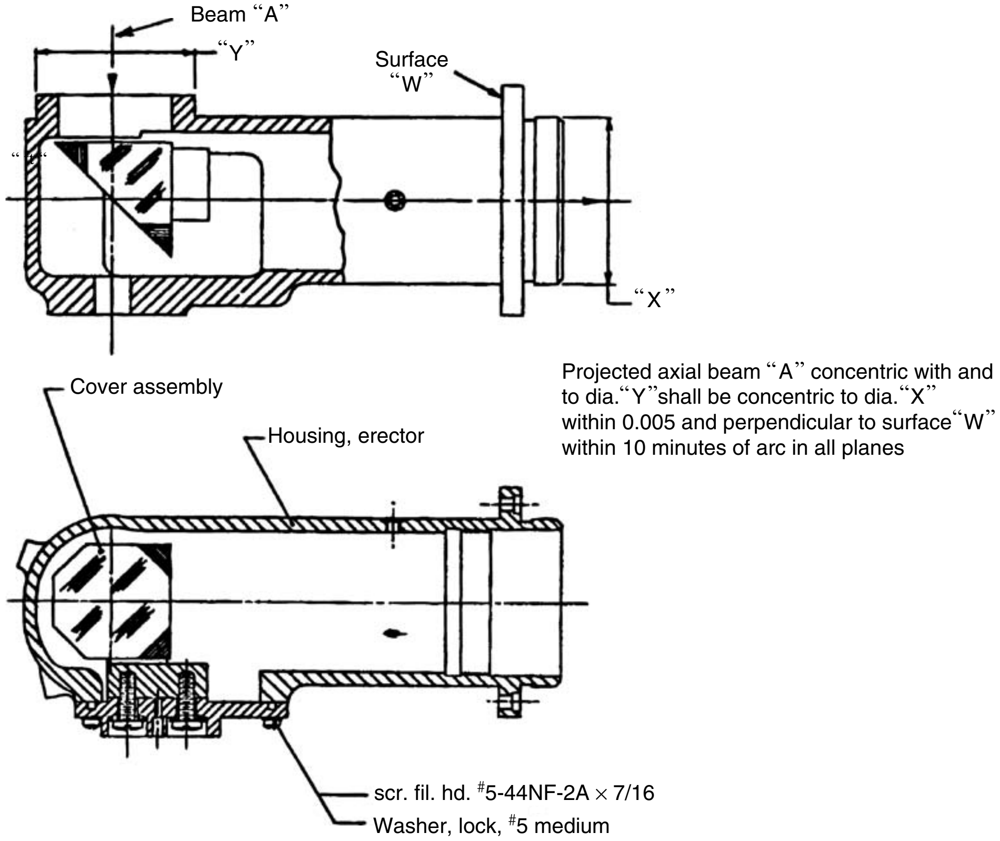
Beam "A"
"Y"
Surface "W"
"t"
"X"
Projected axial beam "A" concentric with and to dia."Y"shall be concentric to dia."X" within 0.005 and perpendicular to surface"W" within 10 minutes of arc in all planes
Cover assembly
Housing, erector
scr. fil. hd. #5-44NF-2A × 7/16
Washer, lock, #5 medium

FIGURE 7.75 Second right-angle prism assembly for the telescope shown in Figure 7.72. (Courtesy of the U.S. Army.)

telescope's front and rear portions. The action of the gear train keeps the prism oriented angularly midway between the front and rear portions of the telescope. This angular relationship maintains the erect image. The housing for the Porro prism is made of hardened stainless steel since it acts as a bearing for the angular motion. The rotary joints in the assembly are sealed with lubricated O-rings that seat in grooves in the mating parts. The prism is bonded to a bracket that is attached to a cover by two screws riding in two slots. After installation of the bonded prism assembly in the housing, the prism is slid in the slots to adjust the optical path through the assembly; the screws are then secured and the plate pinned in place. A protective cover is then installed.

An opto-mechanical design using double-sided support for a Schmidt prism was described by Willey (1991). Figure 7.76 illustrates the concept. The prism was supported between nominally parallel inside surfaces of a U-shaped aluminum bracket by 3M EC2216B/A epoxy injected through centrally located holes (marked "P") in the arms of the frame. Initially, tests of several subassemblies at low temperature caused fractures to occur in the prisms at the tops of the bonded areas. Analysis indicated that differential contraction of the metal with respect to the glass caused the stiff arms to rotate about the hardened epoxy at the bottom of the bond area and to exert large tension forces at the top of each bond. The design was improved by locally reducing the thickness of one arm (as indicated in the figure) below the bond. This allowed the arm to flex with temperature changes and sufficiently reduce the stress within the bond, thereby solving the problem.

Beckmann (1990) described yet another approach to double-sided mounting for prisms used successfully in The Netherlands. The prism was a crown glass beam splitter cube; it was to be bonded between the arms of a U-shaped frame. In this case, the frame was stainless steel so thermal mismatch

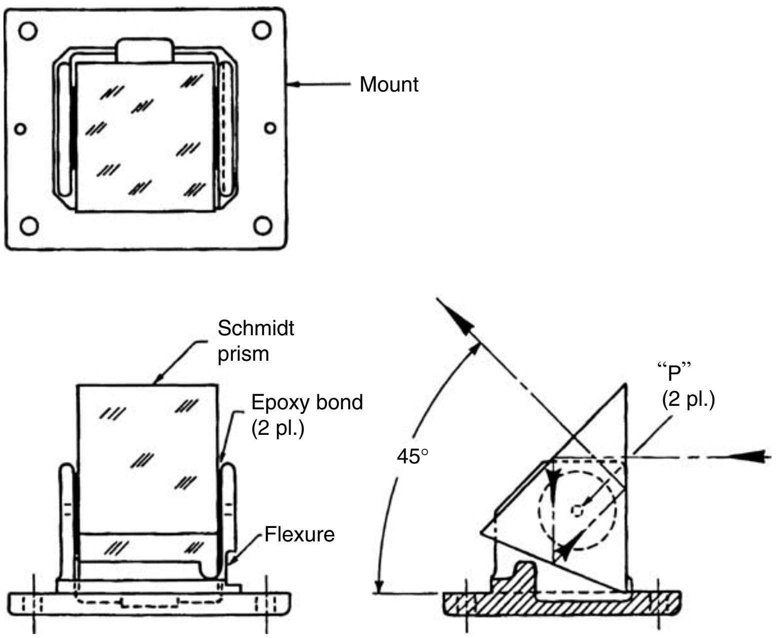

FIGURE 7.76 Schematic diagrams of a Schmidt prism bonded on both sides to a U-shaped mount. (From Wiley, R., private communication, 1991.)

was minimal. An alternate technique to injecting epoxy through holes in the side arms directly into the interface region was sought after low-temperature tests produced fractures of the glass centrally under the injection holes. This was attributed to localized contraction of the plug of epoxy filling the injection holes. In a later approach, shown in Figure 7.77(a) and (b), the prism was aligned (by fixturing) inside the frame, and two short stainless steel plugs were inserted through slightly oversized holes in the arms. The ends of these plugs were bonded in place to the sides of the prism with thin layers of epoxy (1st bond). A small quantity of glass beads of appropriate diameter mixed into the epoxy assured proper bond thickness. After the plug-to-prism bonds were cured, the plugs were epoxied to the frame arms (2nd bond). This design reduces the requirement for close control of prism thickness between the bonding faces, precise parallelism of those faces, or precise parallelism between the frame arms.

The diagrams shown in Figures 7.77(c) and (d) show a modification of the Beckmann design, in which only one plug is used, the prism being bonded directly to one arm of the mount during the initial bonding step. The end result is similar to that obtained with the approach shown in Figures 7.77(a) and (b). Note that it is necessary that the bonding surface of the arm to which the prism is bonded be accurately positioned relative to the desired prism location and orientation because the only adjustments available at the time of bonding are rotation about an axis perpendicular to that surface and two orthogonal translations parallel to that surface.

When using an epoxy bond between glass and a rigid material such as a metal, care should be exercised during application of the epoxy to ensure that fillets of excess adhesive are not formed around the glass-to-metal joint. Shrinkage during curing along the diagonal face of the fillet will tend to stress the glass. Shrinkage of the epoxy along this diagonal surface has been known to pull chunks of glass from the optic at a low temperature. Figure 7.78 diagrams an undesirable fillet in view (a). View (b) shows a preferred configuration of the adhesive joint. This configuration can be achieved by carefully controlling the volume of adhesive applied.

A different way for bonding of prisms, described by Seil (1991, 1997), is illustrated in Figure 7.79. Here, a cemented roof prism subassembly of the Schmidt–Pechan configuration is inserted

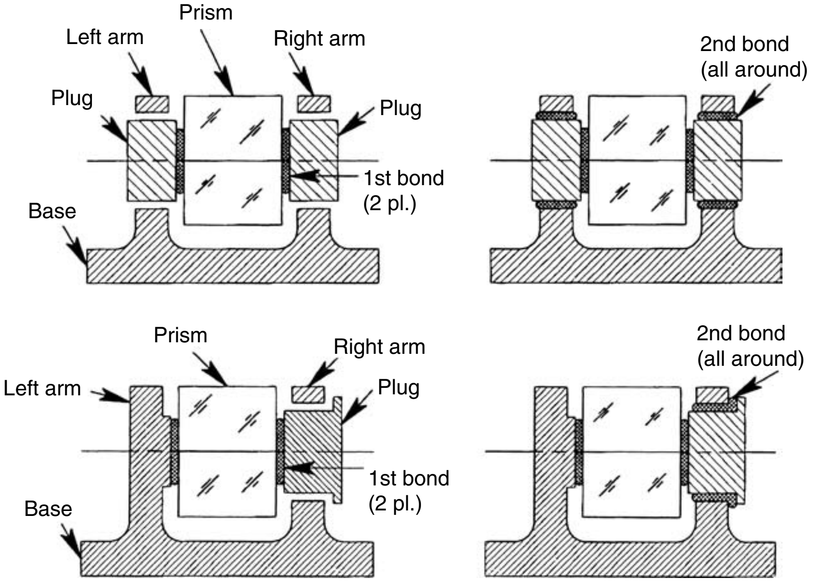

FIGURE 7.77 Two concepts for double-sided bonding of a prism to a U-shaped mount. (Adapted from Beckmann, L.H.J.F., private communication, 1990.)

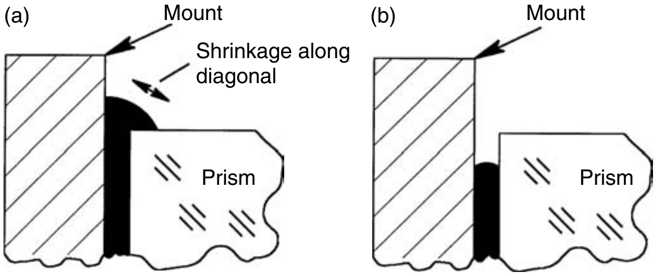

FIGURE 7.78 View (a) illustrates an undesirable adhesive joint configuration in which a fillet of excess epoxy is formed at the edge of the joint. Shrinkage of the epoxy along the diagonal face of the fillet during cure or at low temperature can distort or fracture the prism. View (b) shows a more desirable configuration without a fillet.

into a close-fitting seat molded in the filled-plastic housing of a commercial binocular. The prism subassembly is provisionally secured in place with several dabs of UV-curing adhesive applied through openings in the housing walls. After the temporary bond has cured and proper alignment is confirmed, the prisms are secured by adding several beads of urethane adhesive through the same wall openings. The slight resiliencies of the housing and the adhesive accommodate the differential thermal expansion characteristics of the adjacent materials, thereby minimizing the potential problem of diagonal shrinkage in the adhesive beads. With precision-molded structural members and built-in reference surfaces, adjustments are not required. Figure 7.80 shows some details of the internal configuration of such a prism mounting.

Figure 7.81 is a photograph from Seil (1997) of an assembly consisting of a Porro prism-erecting system and a rhomboid prism mounted by the same general two-step technique just described. In this design, one Porro prism is attached with adhesive to its plastic bracket. This bracket slides on two parallel metal rods attached to the main portion of the subassembly containing a second Porro prism to provide axial movement of the first prism relative to the second for adjusting the

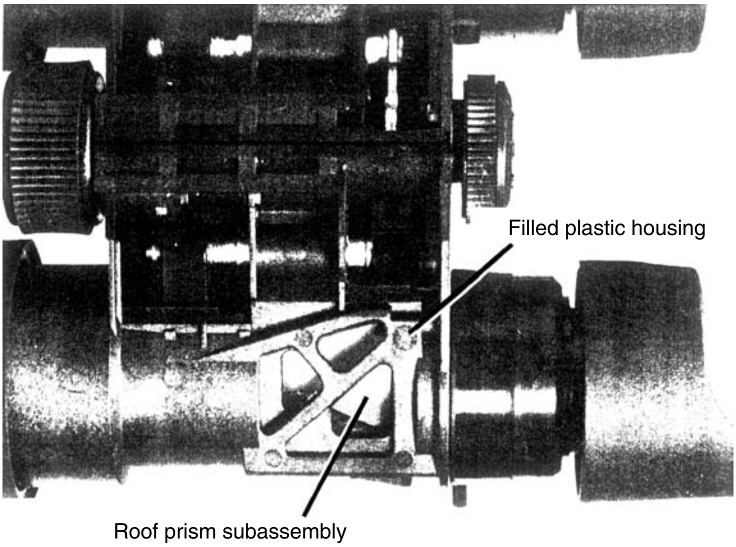
Filled plastic housing
Roof prism subassembly

FIGURE 7.79 A Schmidt–Pechan roof-erecting prism subassembly mounted in a plastic binocular housing by locally applied urethane adhesive in a two-step bonding process. (Adapted from Seil, K., *Proc. SPIE*, 1533, 48, 1991.)

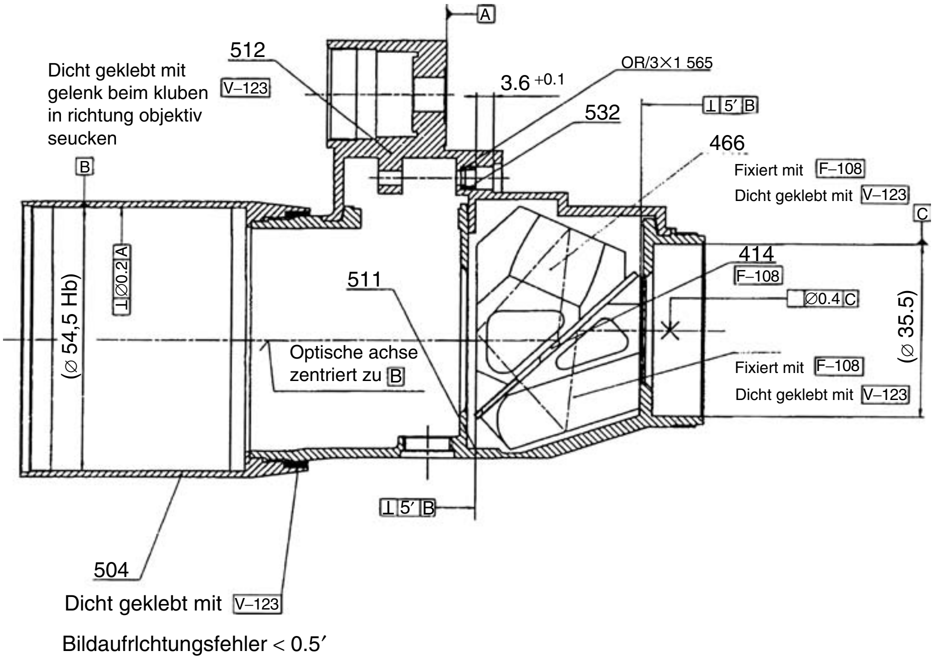
A
512
Dicht geklebt mit gelenk beim kluben in richtung objektiv seucken
V–123
B
3.6 +0.1
OR/3×1 565
532
⊥ 5′ B
466
Fixiert mit F–108
Dicht geklebt mit V–123
C
(⌀ 54,5 Hb)
⊥ ⌀0.2 A
511
Optische achse zentriert zu B
414
F–108
⌀0.4 C
(⌀ 35.5)
Fixiert mit F–108
Dicht geklebt mit V–123
⊥ 5′ B
504
Dicht geklebt mit V–123
Bildaufrlchtungsfehler < 0.5′

FIGURE 7.80 Drawing of a roof prism subassembly mounted in the manner shown in Figure 7.79. (Adapted from Seil, K., private communication, 1997.)

focus of an optical instrument. The adhesive beads securing the prisms are clearly shown in Figure 7.82. Minimization of the number of components and ease of assembly are prime features of this design. Customer acceptance of products made by this technique has demonstrated the durability and adequacy of the opto-mechanical performance achievable with this type of assembly.

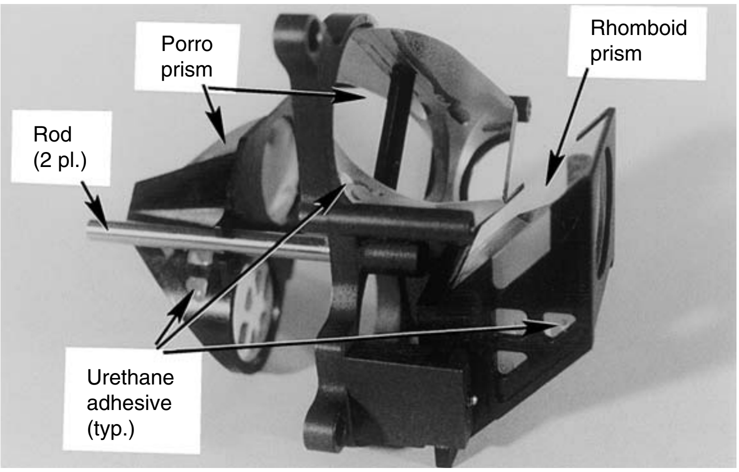
Porro prism
Rhomboid prism
Rod (2 pl.)
Urethane adhesive (typ.)

FIGURE 7.81 Photograph of a Porro prism image-erecting system with variable separation and a rhomboid prism mounted in plastic housings by adhesive bonding using the same two-step bonding process shown in Figure 7.79. (Adapted from Seil, K., private communication, 1997.)

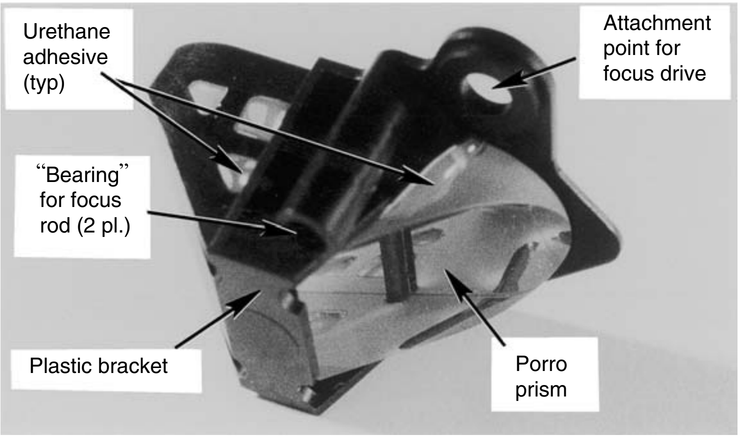
Urethane adhesive (typ)
Attachment point for focus drive
"Bearing" for focus rod (2 pl.)
Plastic bracket
Porro prism

FIGURE 7.82 Close-up photograph of the mounted moveable Porro prism from the subassembly of Fig. 7.81. (Adapted from Seil, K., private communication, 1997.)

7.7 FLEXURE MOUNTS FOR PRISMS

Large prisms frequently present difficult mounting problems because of their weight and physical size. They typically have significant separations between mounting points. Differential thermal expansion over these distances can introduce strains into the interfaces, and these strains may cause misalignment or distortion of the optical surfaces. The use of flexures in the mounting design will usually avoid these problems.

The prism-mounting concept shown in Figure 7.83 supports a prism on three compound flexures bonded directly to the prism base and attached mechanically to the structure. To reduce strain on the cemented joints, all three flexures are designed to have three directions of bending. Flexure No. 1 is used to locate the prism horizontally at a fixed point; the second flexure locates the prism in rotation about that fixed point, but allows relative expansion in a radial direction between the first and second flexures. The third flexure has the equivalent of a universal joint at both top and bottom.

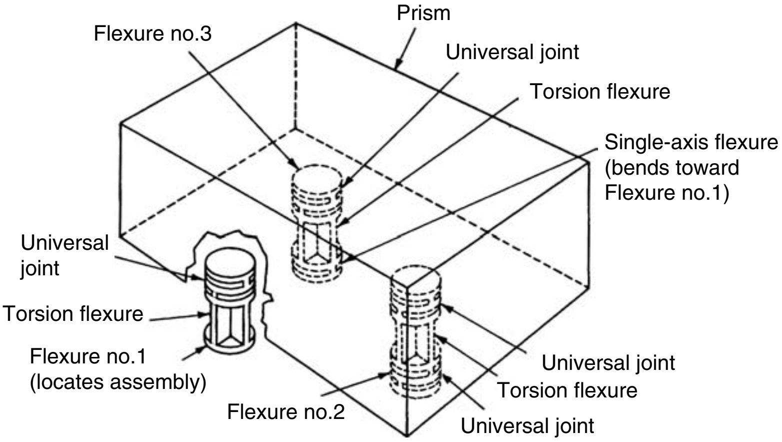

FIGURE 7.83 Conceptual sketch for a flexure mounting for a large prism.

Thus, it merely supports the prism vertically and prevents rotation about the line connecting the other two flexures. It does not constrain the prism radially.

Figure 7.84 is a schematic of a prism subassembly mounted as just described. This three-component compound prism functions as a series of first-surface mirrors fashioned as a right-angle reflector and a mirror version of an Amici prism. Its function in a microlithography mask projection system is illustrated in Figure 7.85. The composite prism is 6 in. (15.2 cm) wide, 7.3 in. (18.5 cm) long, and 6.3 in. (16.0 cm) high. The prisms are made of Zerodur (CTE essentially zero). The prism assembly is mounted at three points on a cast-aluminum structure (CTE 12 ppm/°F). The mounting points are separated by as much as 4 in. (10.2 cm). Over this distance, differential expansion for a temperature change of 40°F characteristic of shipping in a semicontrolled environment is about 2×10^{-3} in. (0.051 mm). With a rigid mounting, significant forces would be exerted on the prism and its mounting. To accommodate temperature changes with these different CTEs without damage, flexures were used to attach the prism to the structure. The mounting configuration is designed to prevent thermally induced translation along two axes (X and Y) in the coordinate system shown and rotation about all three axes. Small translations along the Z-axis due to temperature changes are of no concern. The operating environment is controlled to ± 2°C, and the entire instrument is externally isolated against severe shock and vibration.

Figure 7.86 is a photograph of the prism assembly. The wing prisms are optically contacted to one face of the right-angle base prism, which is in turn mounted on the system's structure by the three flexures attached to the hypotenuse of the base prism. The multiple flexure blades are 0.020 in. thick and 0.120 in. long; they are machined into 0.750-in.-diameter Invar posts. Post "B" has a torsion flexure and a universal joint; it is bonded with EC2216B/A epoxy into a hole in the base prism. The other two posts are bonded with the same adhesive to the lower surface of the base prism. One of these posts has one universal joint and a single flexure blade that is compliant in the direction toward post "B." The third post has two universal joints. The sectional view AA′ shown in Figure 7.84 shows the locations of the posts at the corners of a nearly equilateral triangle and the orientations of key flexures that minimize the effects of temperature changes on the prism. Each post has a threaded section at the bottom that passes through holes in the base plate and is secured with nuts acting through stacks of Belleville washers to preload the threads and provide the slight axial compliance required for the anticipated temperature changes.

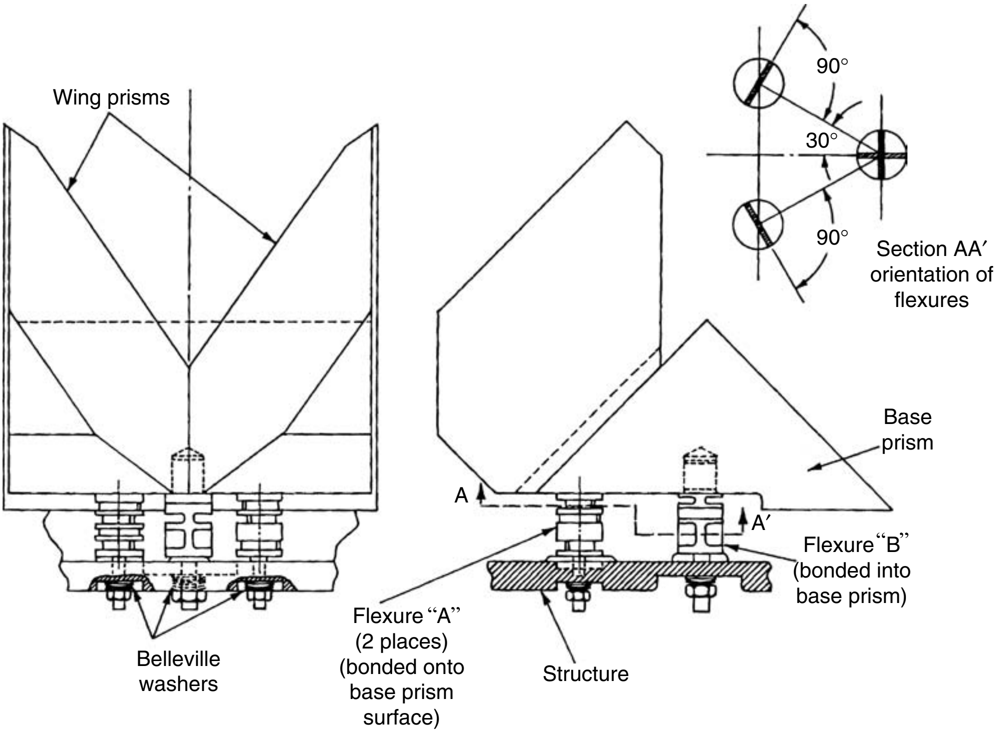
Wing prisms
90°
30°
90°
Section AA′ orientation of flexures
Base prism
A
A′
Flexure "B" (bonded into base prism)
Belleville washers
Flexure "A" (2 places) (bonded onto base prism surface)
Structure

FIGURE 7.84 Opto-mechanical configuration of a large prism assembly with three flexure mounting posts bonded in place. (Courtesy of ASML Lithography, Wilton, CT.)

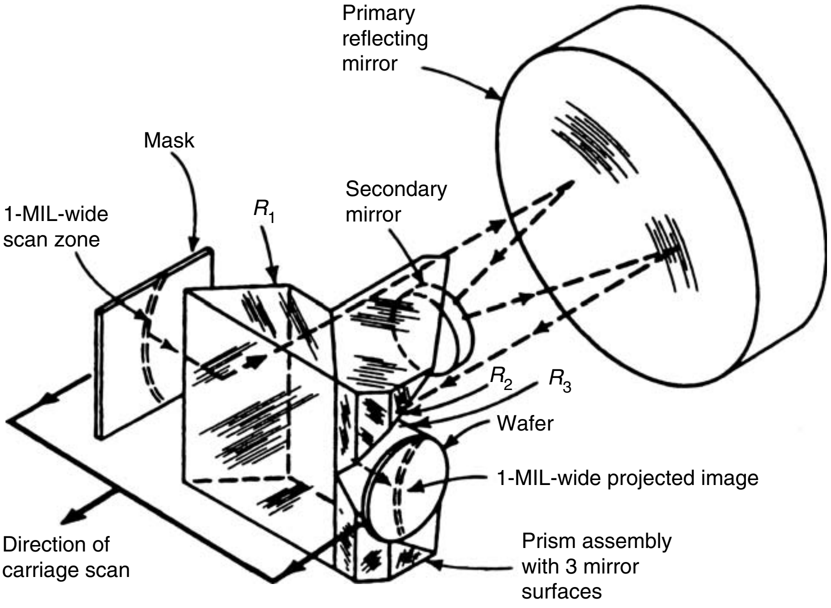
Primary reflecting mirror
Mask
1-MIL-wide scan zone
R_1
Secondary mirror
R_2
R_3
Wafer
1-MIL-wide projected image
Direction of carriage scan
Prism assembly with 3 mirror surfaces

FIGURE 7.85 Schematic diagram of a microlithography mask projection system using the prism subassembly shown in Figure 7.84. (Courtesy of ASML Lithography, Wilton, CT.)

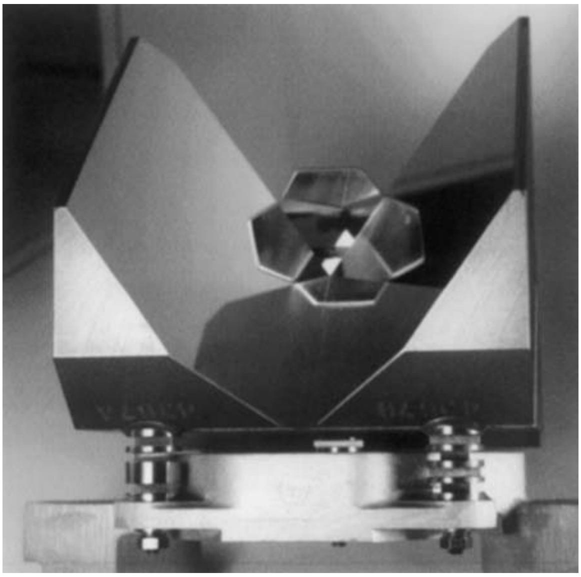

FIGURE 7.86 Photograph of the compound prism of Figure 7.80. (Courtesy of ASML Lithography, Wilton, CT.)

REFERENCES

Beckmann, L.H.J.F., private communication, 1990.

De Vany, A.S., *Master Optical Techniques*, Wiley, New York, 1981.

Delgado, R.F., The multidiscipline demands of a high performance dual channel projector, *Proc. SPIE*, 389, 75, 1983.

Durie, D.S.L., Stability of optical mounts, *Mach. Des.*, 40, 184, 1968.

Forkner, J.F., Anamorphic prism for beam shaping, U.S. Patent No. 4,623,225, 1986.

Hatheway, A.E., Analysis of adhesive bonds in optics, *Proc. SPIE*, 1998, 2, 1993.

Hopkins, R.E., Mirror and Prism Systems, in *Applied Optics and Optical Engineering*, Vol. III, Kingslake, R., Ed., Academic Press, New York, 1965, chap. 7.

Kaspereit, O.K., Ordnance Technical Notes No. 14, *Designing of Optical Systems for Telescopes*, U.S. Army, Washington, DC, 1933.

Kaspereit, O.K., *Design of Fire Control Optics ORDM2-1*, Vol. I, U.S. Army, Washington, DC, 1952.

Kingslake, R., *Optical System Design*, Academic Press, Orlando, 1983.

Lipshutz, M.L., Optomechanical considerations for optical beam splitters, *Appl. Opt.*, 7, 2326, 1968.

Lohmann, A.W. and Stork, W., Modified Brewster telescopes, *Appl. Opt.*, 28, 1318, 1989.

MIL-HDBK-141, *Optical Design*, Defense Supply Agency, Washington, DC, 1962.

Miller, K.A., Nonathermal potting of optics, *Proc. SPIE 3786*, 506, 1999.

Patrick, F.B., Military Optical Instruments, in *Applied Optics and Optical Engineering*, Vol. V, Kingslake, R., Ed., Academic Press, New York, 1969, chap. 7.

Roark, R.J., *Formulas for Stress and Strain*, 3rd ed., McGraw-Hill, New York, 1954.

Sar-El, H.Z., Revised Dove prism formulas, *Appl. Opt.*, 30, 30, 1991.

Schubert, F., Determining optical mirror size, *Mach. Des.*, 51, 128, 1979.

Seil, K., Progress in binocular design, *Proc. SPIE*, 1533, 48, 1991.

Seil, K., private communication, 1997.

Smith, W.J., *Modern Optical Engineering*, 3rd ed., McGraw-Hill, New York, 2000.

Trebino, R., Achromatic N-prism beam expanders: optimal configurations, *Appl. Opt.*, 24, 1130, 1985.

Trebino, R., Barker, C.E. and Siegman, A.E., Achromatic N-prism beam expanders: optimal configurations II, *Proc. SPIE*, 540, 104, 1985.

Vukobratovich, D., Optomechanical Systems Design, in *The Infrared & Electro-Optical Systems Handbook*, Vol. 4, Dudzik, M.C., Ed., ERIM, Ann Arbor and SPIE Press, Bellingham, 1993, chap. 3.

Walles, S. and Hopkins, R.E., The orientation of the image formed by a series of plane mirrors, *Appl. Opt.*, 3, 1447, 1964.

Willey, R., private communication, 1991.

Wolfe, W.L., Nondispersive Prisms, in *OSA Handbook of Optics*, 2nd. ed., Vol. II, Bass, M., Van Stryland, E., Williams, D.R., and Wolfe, W.L., Eds., McGraw-Hill, New York, 1995, chap. 4.

Yoder, P.R., Jr., Study of light deviation errors if triple mirrors and tetrahedral prisms, *J. Opt. Soc. Am.*, 48, 496, 1958.

Yoder, P.R., Jr., Two new lightweight military binoculars, *J. Opt. Soc. Am.*, 50, 491, 1960.

Yoder, P.R., Jr., Optical Mounts: Lenses, Windows, Small Mirrors, and Prisms, *Handbook of Optomechanical Engineering*, CRC Press, Boca Raton, FL, 1997, chap. 6.

Yoder, P.R., Jr., Design guidelines for bonding prisms to mounts, *Proc. SPIE*, 1013, 112, 1988.

Yoder, P.R., Jr., Non-image forming optical components, *Proc. SPIE*, 531, 206, 1985.

Yoder, P.R., Jr., *Mounting Optics in Optical Instruments*, SPIE Press, Bellingham, 2002.

8 Design and Mounting Small, Nonmetallic Mirrors, Gratings, and Pellicles

8.1 INTRODUCTION

According to U.S. MIL-STD-1472D, an average man using both hands can safely pick up an object from the floor, carry it, and place it on a horizontal surface 5 ft (1.52 m) high if it weighs no more than 56 lb (25.4 kg). If we assume a cylindrical plane-parallel mirror of 9:1 diameter-to-thickness ratio made of ULE, this weight would correspond to a diameter of $\sim$ 20.0 in. ($\sim$ 51 cm) and a thickness of $\sim$ 2.23 in. (5.66 cm). Although arbitrary, this calculation forms the basis for the size boundary used here to delineate between a "small" and a "large" mirror. Designs for single-substrate mirrors as large as $\sim$ 8 m ($\sim$ 26 ft) — for which the main considerations are ways to reduce weights and surface deflections to tolerable levels — are discussed in Chapter 9. Techniques for mounting large mirrors in different orientations relative to gravity are considered in Chapters 10–12. Chapter 12 also includes some considerations of segmented-aperture mirror arrays of large size. The design and mounting of metallic mirrors of various sizes are the subjects of Chapter 13.

We first address some general aspects of designing mirrors. Their common applications are listed to remind the reader how we use mirrors. They are then considered from the geometric, image orientation, and system function viewpoints. Methods to determine the required apertures of flat reflecting surfaces for diverging, converging, and collimated beams of given sizes are summarized. The formation of ghost images by second-surface mirrors and a method for estimating their intensities relative to those of the main images are explained. The influences of selected types of reflecting coatings on main image and ghost image intensities are summarized.

Flat mirrors and thin-membrane versions thereof (called *pellicles*) as well as curved mirrors must, of course, be mounted in order to incorporate them in an optical instrument. Reflecting optics are more sensitive to applied forces than refracting optics because the change in localized optical path in a reflected wavefront resulting from a given surface deformation is twice the magnitude of that deformation. The angular deflection of a reflected ray due to a surface deformation is twice the magnitude of the local surface tilt. On the other hand, small linear displacements or angular misalignments of such optics in particular ways relative to other system components may not affect overall system performance. Two good examples are a truly flat mirror or pellicle that moves in its own plane without changing orientation and a Porro mirror subassembly that tilts about an axis perpendicular to the plane of reflection.

Although they have many properties in common with mirrors, diffraction gratings do not enjoy quite as much freedom of motion as mirrors because they are sensitive to orientation of their grooves. Mirrors with curved optical surfaces are also sensitive to translations and tilts because of their image-forming properties. In general, the locations and orientations of all mirrors, pellicles, and gratings should be carefully maintained. Mountings for these components can then become rigorous opto-mechanical design problems. Typical examples of mountings for small mirrors, gratings, and pellicles are presented to illustrate a variety of techniques that have been used successfully.

8.2 GENERAL CONSIDERATIONS

8.2.1 MIRROR APPLICATIONS

Flat mirrors, used singly or as combinations of two or more, serve useful purposes in optical instruments, but do not contribute optical power and, hence, cannot form images by themselves. The principal uses of these mirrors in optical instruments are as follows:

- To bend (deviate) light around corners
- To fold an optical system into a given shape or package size
- To provide proper image orientation
- To displace the optical axis laterally
- To divide or combine beams by intensity or aperture sharing at a pupil
- To divide or combine images by reflection at an image plane
- To provide dynamic scanning of beams
- To disperse light spectrally (with gratings)

Most of these functions are the same as mentioned in Chapter 7 for prisms. Curved mirrors can do a few of these things, but their most common applications involve image formation, as is the case in reflecting telescopes.

8.2.2 GEOMETRIC CONFIGURATIONS

Most small mirrors have single solid substrates in the form of right circular cylinders or rectangular parallelepipeds. Some special-purpose mirrors have other face shapes. One example is the folding flat mirror in a Newtonian telescope that is elliptical in shape so as to minimize obscuration of the input beam when inclined at 45° to the axis. Mirrors can have flat, spherical, aspherical, cylindrical, or toroidal optical surfaces. Curved surfaces can be convex or concave. Usually, the second, or back, surface of a small mirror is flat, but some are shaped to make the overall profile into a meniscus. Most mirrors used in optical instruments are of the first-surface reflecting type and have thin, metallic film, reflecting coatings, such as aluminum, that are overcoated with protective dielectric coatings (typically magnesium fluoride or silicon monoxide). Nonmetallic substrates are typically borosilicate crown glass, fused silica, or one of the low-expansion materials (such as ULE or Zerodur). The thickness of the substrate is traditionally chosen as 1/5 to 1/6 the largest face dimension. Thinner or thicker substrates are used as the application allows or demands.

Second-surface mirrors have a reflecting coating on the mirror's back side; the first surface then acts as a refracting surface. An image-forming mirror of this type offers distinct advantages from an optical design viewpoint as compared with the corresponding first-surface version because it has more design variables (a glass thickness, a refractive index, and one more radius) to be used for aberration correction. The refracting surface typically receives an antireflection (A/R) coating such as magnesium fluoride to reduce the effects of ghost images from that surface.

8.2.3 REFLECTED IMAGE ORIENTATION

Reflection from a single mirror results in an image that is left-handed. By this we mean that the object appears reversed (or reverted) in the plane of reflection. Figure 8.1 shows this reversal for an arrow-shaped object A-B. If the observer at O looks directly at the object, the point (B) appears on the right. It appears on the left in the image A′-B′. Note that the entire image can be observed with one eye using the portion of the mirror extending from P to P′. If the object is a word, it can be easily read directly, but the left-handed image will appear backward and cannot be read easily without careful thought. Figure 8.2 shows, in view (a), the letter "P" as right-handed. It can be read, even if upside down. In view (b), it appears left-handed and is not as easy to read, regardless of how the page is turned.

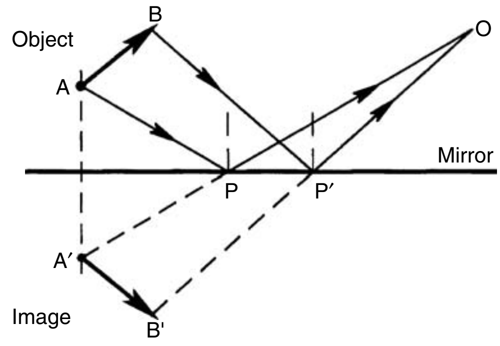

FIGURE 8.1 Reflection of an arrow-shaped object by a flat mirror as seen by an observer at the point O. Note the apparent inversion of the image relative to the object as seen directly and the limited portion of the mirror's surface used by the light rays.

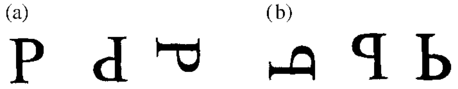

FIGURE 8.2 (a) Right- and (b) left-handed images. The images in (a) can be oriented for easy reading by rotating about the line of sight, but this is not true for the images in (b).

With systems of mirrors, the orientation of the image becomes a little more complex. Each reflection reverts the image. An odd number of reflections creates a left-handed image while an even number creates a right-handed image. In optical systems where an erect and unreverted image is needed, such as a terrestrial telescope, careful consideration must be given to the number of reflections occurring in each meridian. If the planes of reflection of multiple mirrors are not oriented orthogonally, the image may appear rotated about the axis. An image rotator/derotator (such as the delta prism discussed in Section 7.3.15) might be needed to correct this potential orientation problem.

Each reflection at oblique incidence deviates a ray by some angle, which we will call δ_i. With reflections in the same plane from multiple mirrors, deviations add algebraically. This is shown in Figure 8.3 for two mirrors. The total deviation is $\delta_1 + \delta_2$. This principle is applied in the layouts of two periscopes shown in Figure 8.4. In view (a), mirrors M_1 and M_2 are parallel and inclined to the X-axis by 45° angles. Since the mirror normals at the reflecting surfaces are opposed, we know that the deviations have opposite signs. Hence, $\delta = \delta_1 + \delta_2 = 0$, and the output ray is parallel to the input ray. The intermediate ray path is vertical, so the x separation of the points of incidence on the mirrors is zero.

In view (b) of Figure 8.4, we see the more general case of a periscope in which the intermediate ray between the two mirrors is traveling at an angle σ to the Y-axis and the output ray travels at an angle with respect to the input ray direction. Now we have both X and Y separations (Δx and Δy) of the points of incidence. Once again, the total deviation is the sum of the individual deviations of the two mirrors; the second deviation taken as negative for the reason stated above. Signs assigned to other angles are as noted in the figure. To design such a periscope, one typically would start with desired vertical and horizontal offsets Δx and Δy plus a desired deviation δ. Equations that can be used to determine the other parameters are as follows:

$$\tan \sigma = \Delta x / \Delta y \tag{8.1}$$

$$\theta_1 = (\sigma + 90°)/2 \tag{8.2}$$

$$\theta_2 = (\delta - \sigma - 90°)/2 \tag{8.3}$$

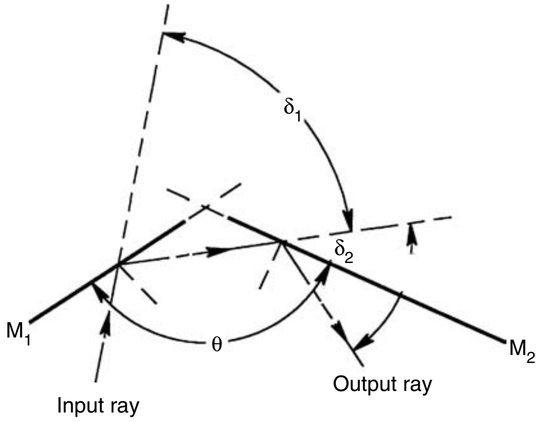

FIGURE 8.3 Deviations of a light ray upon intersecting two flat mirrors oriented at an angle δ to each other. The total deviation is the sum of δ_1 and δ_2.

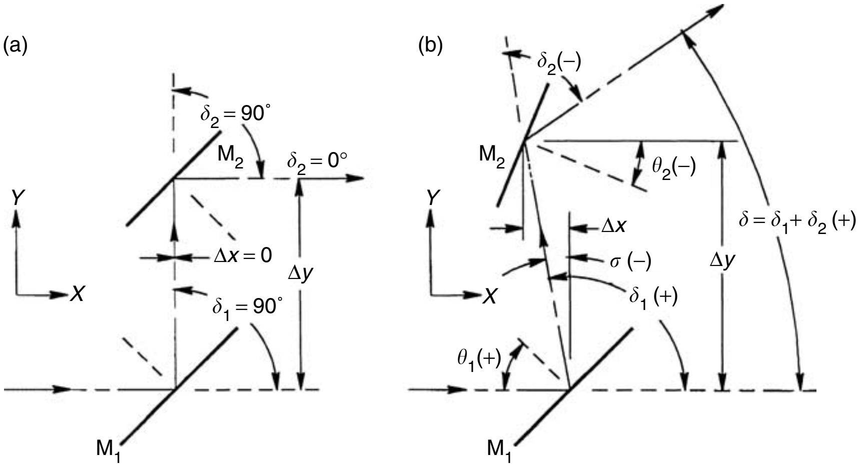

FIGURE 8.4 Deviation and lateral displacement of a ray by two mirrors arranged as a periscope. In view (a) the mirrors are parallel and oriented for 45° incidence. The general case is shown in view (b). The algebraic signs of the angles are indicated in parentheses in the latter view.

$$\delta_1 = 180° - 2\theta_1 \tag{8.4}$$

$$\delta_2 = \delta + \sigma - 90° \tag{8.5}$$

For example, let $\Delta x = -2.000$ in. (50.800 mm), $\Delta y = 24.000$ in. (609.600 mm), and $\delta = 30°$. Then, $\sigma = \arctan(-2.000/24.000) = -4.763°$, $\theta_1 = (-4.763° + 90°)/2 = 42.618°$, and $\theta_2 = (30° + 4.763° - 90°)/2 = -27.618°$. The individual deviations are $\delta_1 = 180° - (2)(42.618°) = 94.764°$ and $\delta_2 = 30° - 4.763° - 90° = -64.763°$. As expected, the sum of the last two angles is the desired deviation of 30°.

This rather simple design becomes much more complex if the light path through the periscope is to be three-dimensional, i.e., involving out-of-plane angles. Then, one might resort to surface-by-surface ray tracing in a lens design program or a vector analysis technique such as that described by Hopkins (1965). The packaging of systems with many reflections, such as that illustrated in Figure 8.5, yields well to such techniques. The process of laying out a convoluted optical path is sometimes called "optical plumbing."

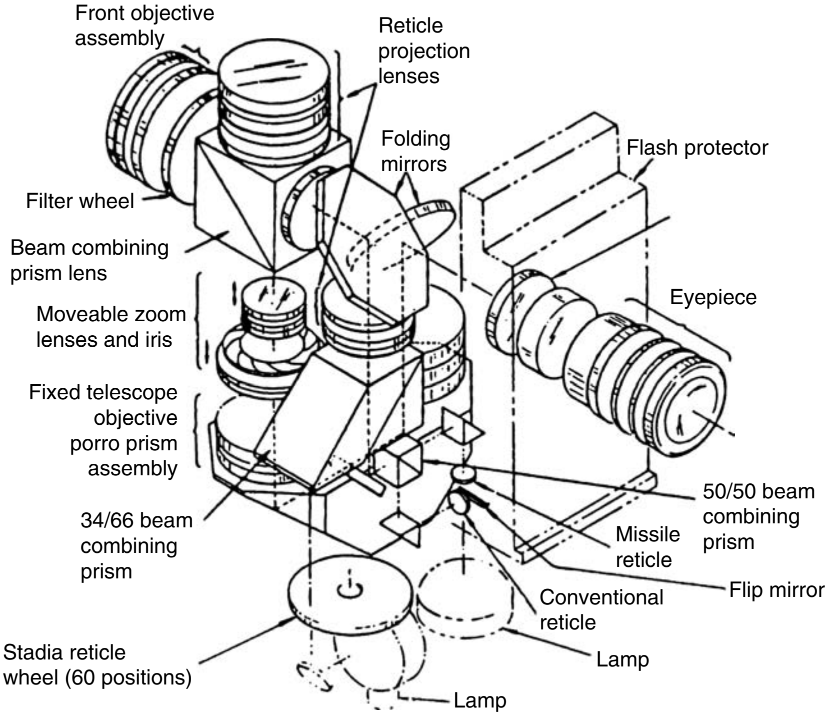
Front objective assembly
Reticle projection lenses
Folding mirrors
Flash protector
Filter wheel
Beam combining prism lens
Eyepiece
Moveable zoom lenses and iris
Fixed telescope objective porro prism assembly
50/50 beam combining prism
34/66 beam combining prism
Missile reticle
Flip mirror
Conventional reticle
Stadia reticle wheel (60 positions)
Lamp
Lamp

FIGURE 8.5 Optical system schematic of a zoom telescope intended for use in a gunner's periscope for an armored vehicle. Layout of a convoluted light path such as this is facilitated by use of vector representations of mirror normals. (Courtesy of the U.S. Army.)

Another important aspect of the use of multiple mirror systems is the orientation of the intermediate and final images. A simple technique used by many designers is to sketch the system in isometric form and visualize the changes that take place at each mirror when a "pencil crossed with a drumstick" is "bounced" from the reflecting surface. This is illustrated in Figure 8.6. View (a) applies in the plane of reflection while view (b) shows how the change occurs in both meridians. The inversion that naturally occurs at an objective lens or relay lens can be included (see Figure 8.7[a]). In this figure the object at A is projected by a lens B onto a screen at S. The center of the image is located at distances Δx and Δy from the lens. One of the many possible mirror systems that could be designed for this purpose using the logic described by Smith (2000) is shown in Figure 8.7(b). This discussion would make interesting reading for the engineer faced with a similar design problem.

8.2.4 BEAM PRINTS ON OPTICAL SURFACES

The physical size of the front surface mirror is determined primarily by the size and shape of the irradiated area (called the beam print) of the light beam on the reflecting surface plus any allowances considered appropriate for mounting provisions, misalignment, and beam motion during use. This beam print can be determined from a scaled layout of the optical system showing the extreme rays of the light beam in at least two meridians. This method is rather time-consuming to use and often inaccurate owing to compounded, minor, drafting errors. CAD programs that have the capability of representing light beams can be used with ease for this purpose. Another method is to have the lens designer ray trace the optical system and determine the extreme ray intercepts on mathematical representations of the reflecting surfaces. In cases where the beam has rotational symmetry, this may be an overkill of a simple optical engineering problem.

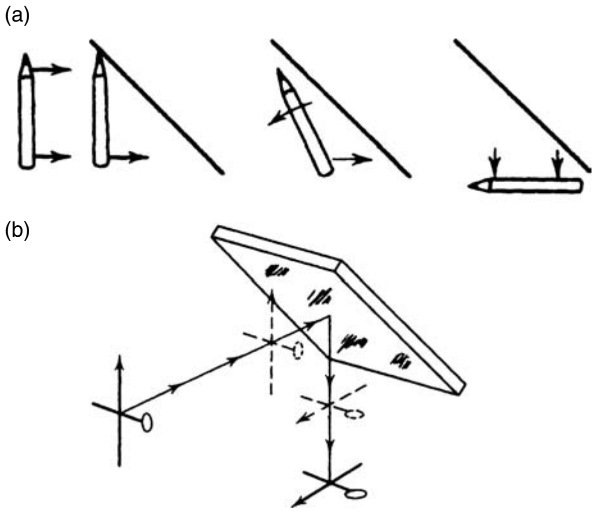

FIGURE 8.6 (a) Visualization of in-plane changes in image orientation upon reflection at a flat mirror through use of a "bouncing pencil." (b) Two-dimensional image orientation changes can be visualized with an object configured as an arrow crossed by a drumstick. (Adapted from Smith, 2000.)

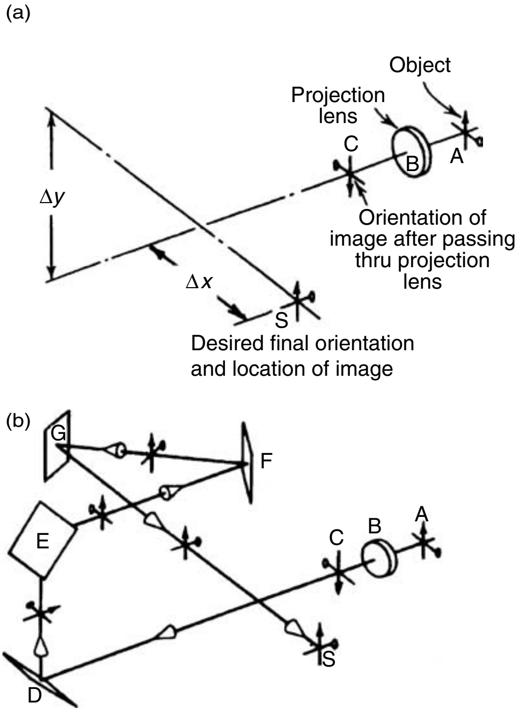
(a)
Object
Projection lens
C
B
A
Δy
Orientation of image after passing thru projection lens
Δx
S
Desired final orientation and location of image
(b)
G
F
E
C
B
A
D
S

FIGURE 8.7 (a) Representation of a typical mirror system design problem in which an object at A is to be imaged at a particular location on a screen S with a particular orientation. (b) One of many possible mirror arrangements that could be designed for this purpose. (Adapted from Smith, 2000.)

The use of geometric equations, such as those given by Schubert (1979), allows the beam intercept contour of a symmetrical beam on a tilted flat mirror to be expressed in terms of the major and minor axes of an ellipse oriented and located properly with respect to the intercept, on the surface, of the beam's optical axis. This is shown in Figure 8.8. Following are adaptations of Schubert's equations:

$$W = D + 2\,L \tan \alpha \tag{8.6}$$

$$E = \frac{W \cos \alpha}{2 \sin(\theta - \alpha)} \tag{8.7}$$

$$F = \frac{W \cos \alpha}{2 \sin(\theta + \alpha)} \tag{8.8}$$

$$A = E + F \tag{8.9}$$

$$G = (\mathrm{A}/2) - F \tag{8.10}$$

$$B = \frac{AW}{(A^2 - 4G^2)^{1/2}} \tag{8.11}$$

where W is the width of the beam print at the mirror/axis intercept, D the beam diameter at a reference plane perpendicular to the axis and located at an axial distance L from the mirror/axis intercept, α the beam divergence angle of the extreme off-axis reflected ray, E the distance from the top edge of the beam print to the mirror/axis intercept, θ the mirror surface tilt relative to the axis (or 90° minus the tilt of the mirror normal), F the distance from the bottom edge of the beam print to the mirror/axis intercept, A the major axis of the ellipse, G the offset of the beam print center from the mirror/axis intercept, and B the minor axis of the beam print.

These equations apply for either propagation direction of the beam as long as the reference plane is located where D is smaller than W. For a collimated beam propagating parallel to the axis, α and G are zero, and the above equations reduce to the symmetrical case where

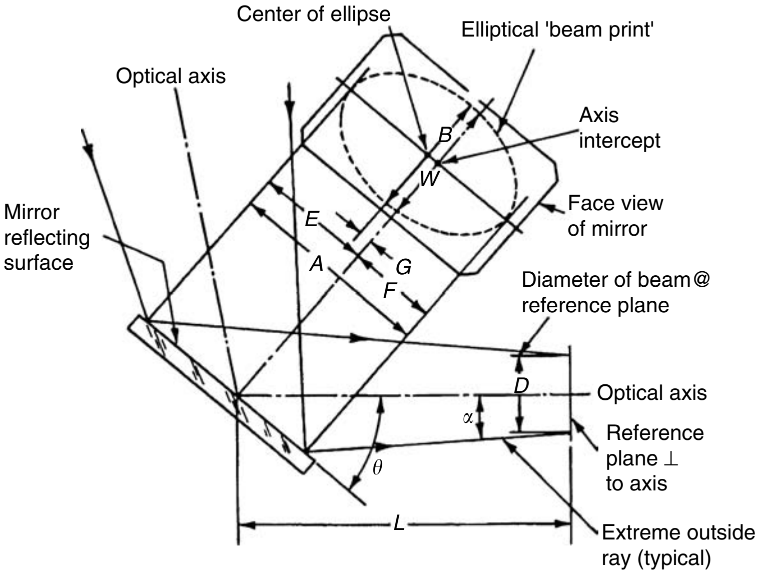
Center of ellipse
Elliptical 'beam print'
Optical axis
Axis intercept
B
W
Face view of mirror
Mirror reflecting surface
E
A
G
F
Diameter of beam@ reference plane
D
Optical axis
α
Reference plane ⊥ to axis
θ
L
Extreme outside ray (typical)

FIGURE 8.8 Geometric relationships used to define the beam print of a rotationally symmetric beam on an inclined mirror. (Adapted from Schubert, F., *Mach. Des.*, 51, 128, 1979.)

$$B = W = D \tag{8.12}$$

$$E = F = \frac{D}{2 \sin \theta} \tag{8.13}$$

$$A = D/\sin \theta \tag{8.14}$$

To illustrate such a calculation, let us determine the beam print dimensions on a flat mirror for a centered circular beam with diameter $D = 2.000$ in. on a reference plane located at $L = 2.000$ in. from the axis intercept with the mirror. The mirror surface is tilted at an angle of $\theta = 30°$ to the axis and the beam divergence α is $\pm 0.6°$. Applying the above equations, $W = 2.000 + (2)(2.000)(\tan 0.6°) = 2.042$ in., $E = (2.042)(\cos 0.6°)/[2 \sin(30° - 0.6°)] = 2.080$ in., $F = (2.042)(\cos 0.6°)/[2 \sin(30° + 0.6°)] = 2.006$ in., $A = 2.080 + 2.006 = 4.086$ in., $G = (4.086/2) - 2.006 = 0.037$ in., and $B = (4.086)(2.042)/[4.086^2 - (4)(0.037^2)]^{1/2} = 2.042$ in. Note that the elliptical beam print is slightly decentered upward with respect to the axis in the plane of reflection, but is symmetrical to the axis in the orthogonal plane.

If the beam in this example were to be collimated, α would be zero and so, from Eqs. (8.12)−(8.14), $B = W = D = 2.000$ in., $E = F = 2.000/((2)(\sin 30°)) = 2.000$ in., and $A = 2.000/\sin 30° = 4.000$ in. The beam print is now symmetrical in both directions. To create a conservative design, the overall reflecting-surface dimensions should be increased from these computed values to allow for the factors mentioned above (mounting, beam motion, etc.) and for tolerances on the geometric parameters used in the calculations.

8.2.5 MIRROR COATINGS

Most mirrors used in optical instruments have light-reflective coatings made of metallic or nonmetallic thin films. The metals commonly used as coatings are aluminum, silver, and gold because of their high reflectivities in the UV, visible, and IR spectral regions. Protective coatings such as silicon monoxide or magnesium fluoride may be placed over metallic coatings to increase their durability. Nonmetallic films consist of single layers or multilayer stacks of dielectric films. The stacks are combinations of materials with high and low indices of refraction. Dielectric reflecting films function over narrower spectral bands than the metals, but have very high reflectivities at specific wavelengths. They are especially useful in monochromatic systems such as those using laser radiation.

Figure 8.9 shows typical visible light reflectance vs. wavelength curves for (a) protected aluminum and (b) UV-enhanced aluminum first-surface reflective coatings at normal and 45° incidence. Figure 8.10(a) shows IR reflectance vs. wavelength for first-surface-protected gold, while Figure 8.10(b) shows the IR reflectance of first-surface-protected silver. The reflectance of a typical first-surface, multilayer dielectric film appears in Figure 8.11(a). That of a second-surface mirror coating of silver is shown in Figure 8.11(b). This location for the coating is advantageous from a durability viewpoint because the reflecting side of the film is then protected from the outside environment and physical damage due to handling or use. The exposed back of such a thin-film coating is typically given a protective coating such as electroplated copper plus enamel for this same purpose.

The reflectance of a surface varies as the angle of incidence and the state of polarization of the incident radiation change. These effects may be noted from the multiple curves in, for example, Figure 8.9(a). They are also shown quite clearly in Figure 8.12, which applies to an uncoated surface of glass with index 1.523 in air. The solid line represents the reflectance of unpolarized light, the line of short dashes is for p-polarized light with the electric vector parallel to the plane of incidence, and the line of long dashes is for the s-polarized beam with the E-vector perpendicular to the same plane*. At the polarizing angle, the p-polarized component disappears.

---

* To minimize confusion from the fact that both English words "parallel" and "perpendicular" begin with the same letter, the terminology used for the perpendicularly polarized beam comes from the German word "senkrecht" for normal.

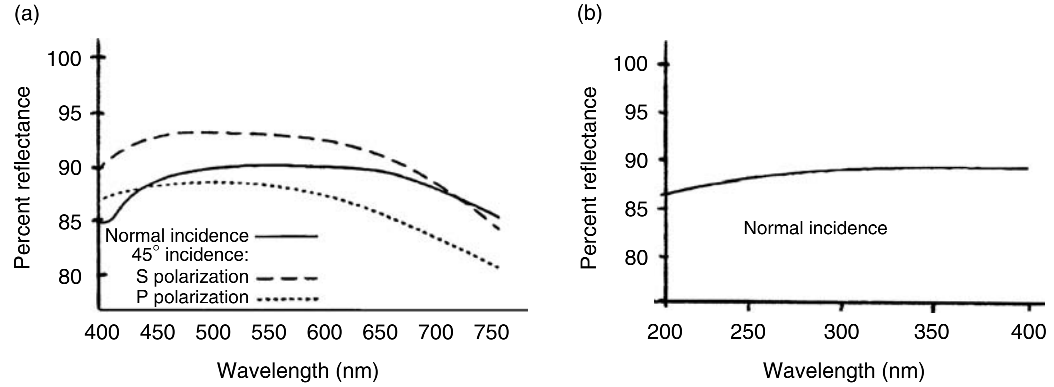

FIGURE 8.9 Reflectance vs. wavelength for first-surface metallic coatings of (a) protected aluminum and (b) UV-enhanced aluminum. (From Yoder, P.R., Jr., *Mounting Optics in Optical Instruments*, SPIE Press, Bellingham, 2002. With permission.)

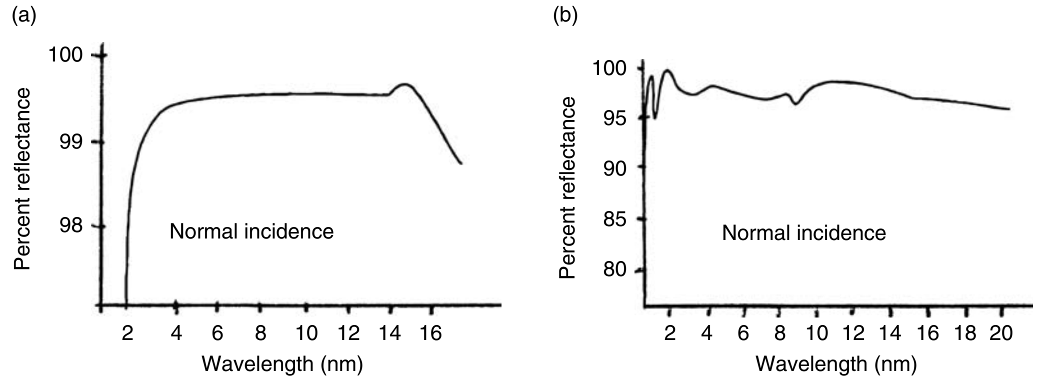

FIGURE 8.10 Reflectance vs. wavelength for first-surface thin films of (a) protected gold and (b) protected silver. (From Yoder, P.R., Jr., *Mounting Optics in Optical* Instruments, SPIE Press, Bellingham, 2002. With permission.)

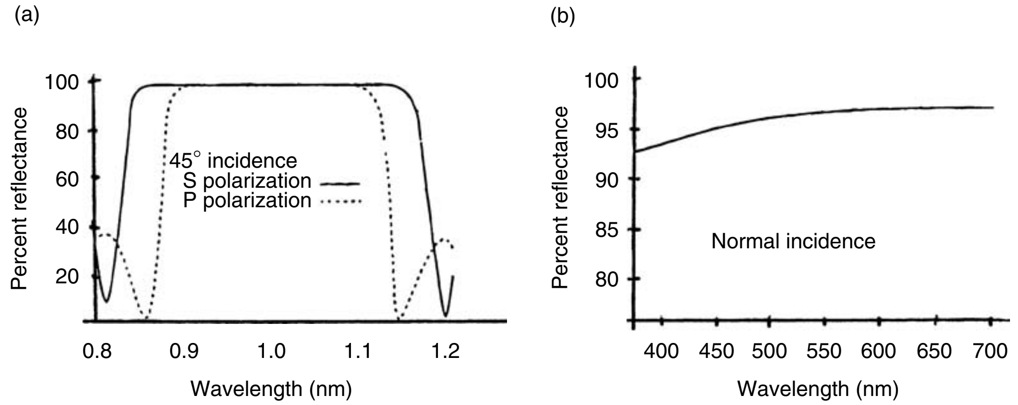

FIGURE 8.11 Reflectance vs. wavelength for (a) a first-surface multilayer dielectric thin film and (b) a second-surface thin film of silver. (From Yoder, P.R., Jr., *Mounting Optics in Optical Instruments*, SPIE Press, Bellingham, 2002. With permission.)

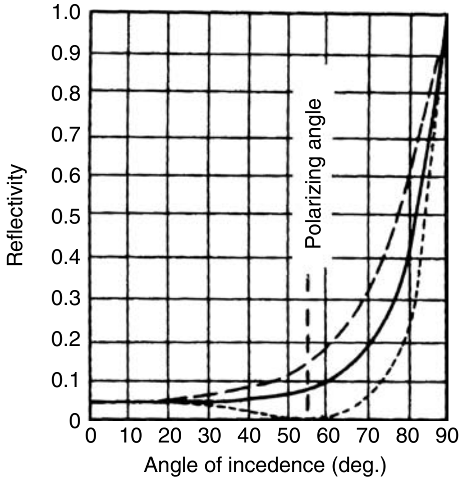

FIGURE 8.12 Reflectivity of a single air-to-glass interface at various angles of incidence. The glass refractive index is 1.523. The solid line represents unpolarized light while the fine and coarse dashed lines represent the p-polarized and s-polarized components, respectively. (Adapted from Jenkins, F.A. and White, H.E., *Fundamentals of Optics*, McGraw-Hill, New York, 1957.)

At normal incidence, the intensity $(I_R)_\lambda$ of the beam reflected from a surface relative to the incident intensity $(I_1)_\lambda$ can easily be estimated once its reflectance $(R_s)_\lambda$ is known. Equation (8.15) applies:

$$(I_R)_\lambda = (I_1)_\lambda(R)_\lambda \tag{8.15}$$

where the dependence of each term on wavelength of the radiation is indicated by the subscript λ.

The transmittance $(T_s)_\lambda$of a surface that does not have a fully reflective coating is given by

$$(T_s)_\lambda = 1 - (R_s)_\lambda - (A_s)_\lambda \tag{8.16}$$

where $(A_S)_\lambda$ is the absorptance of any coating on the surface. As the transmitted beam propagates through the substrate, its intensity is reduced by the absorptance of that material.

At normal incidence, the reflectance $(R_s)_\lambda$ of the interface between two materials with refractive indices n_1 and n_2 is obtained from Fresnel's equations (see Jenkins and White, 1957 or Smith, 2000) as follows:

$$(R_s)_\lambda = \frac{(n_2 - n_1)^2_\lambda}{(n_2 + n_1)^2_\lambda} \tag{8.17}$$

For example, the monochromatic reflectance of an uncoated surface on glass with index 1.523 in air at normal incidence is $R_s = (1.523 - 1.000)^2/(1.523 + 1.000)^2 = 0.043$. Note that this is the value plotted in Figure 8.12 at zero angle of incidence.

The monochromatic transmittance of the same surface at normal incidence is, by Eq. (8.16), equal to $1 - 0.043$ or 0.957 since there is no absorption until the radiation penetrates into the glass. The intensity of a monochromatic beam actually entering the glass is then $I_G = I_I T$ or $0.957 I_I$, in accordance with Eq. (8.15).

The Fresnel reflectance at a given wavelength of a dielectric surface such as glass at other than normal incidence is given by the following equation:

$$R_s = \frac{1}{2}\left[\frac{\sin^2(I - I')}{\sin^2(I + I')} + \frac{\tan^2(I - I')}{\tan^2(I + I')}\right] \tag{8.18}$$

where I and I' are the angles of incidence and refraction respectively, the first term inside the brackets refers to the s-polarized component of the radiation, and the second term inside the brackets refers to the p-polarized component. At normal incidence, this equation is replaced by Eq. (8.17).

Applying Eq. (8.18) to the surface of an optic with n of 1.523 and I of 70°, we find I' to be 38.097° and obtain $R_s = (1/2)[(\sin^2 31.902°/\sin^2 108.0975°) + (\tan^2 31.902°/\tan^2 108.0975°)] = 0.175$. This is approximately the value shown for that glass in Figure 8.12.

An A/R coating is usually applied to refracting optical surfaces to reduce the surface reflectance and, hence, the intensities of beams reflected from those surfaces. These coatings are single-layer thin-film coatings or a stack of thin-film coatings. The simplest case of a single-layer coating causes destructive interference between a first beam reflecting from the air/film interface and a second beam reflecting from the film/glass interface. Destructive interference occurs when these beams are exactly 180° (or one-half wavelength) out of phase. Since the second beam passes through the film twice, the desired $\lambda/2$ phase shift results if the optical thickness $(n)(\lambda)$ of the film is $\lambda/4$. The combined intensity of the two out-of-phase reflected beams is then zero, because their wave amplitudes subtract. The amplitude of a reflected beam is $(R_\lambda^{1/2})$.

Note that complete destructive interference occurs only at one specific wavelength and then only if the beam amplitudes are equal. The latter condition occurs if the following equation is satisfied:

$$n_2 = (n_1 n_3)^{1/2} \tag{8.19}$$

where n_2 is the index of refraction of the thin film, n_1 the index of refraction of the surrounding medium (typically air with $n = 1$), and n_3 the index of refraction of the glass. All indices are at a specific wavelength λ.

If a thin-film material with exactly the right index to A/R coat a given type of glass is not available, imperfect cancellation of the two reflected beams occurs. We can calculate the resultant surface reflectance R_s as

$$R_s = [(R_{1,2})^{1/2} - (R_{2,3})^{1/2}]^2 \tag{8.20}$$

where $R_{1,2}$ is the reflectance of the air/film interface and $R_{2,3}$ the reflectance of the film/glass interface.

To illustrate the use of the last equation, consider a glass substrate of index $n_3 = 1.523$ coated with a single-film A/R coating of MgF_2 with $n_2 = 1.380$. Assume normal incidence. The optical thickness of the film in green light ($\lambda = 0.5461$ µm) is $\lambda/4 = 1.5461/4 = 0.231$ µm. We would like to know the reflectivity of the coated surface and the intensity of the reflected beam. From Eq. (8.19), the film index n_2 should be $[(1.000)(1.523)]^{1/2} = 1.234$ to function perfectly as an A/R coating. This is not the case for MgF_2, so the A/R coating is imperfect on this glass. From Eq. (8.17), $R_{1,2} = (1.380 - 1.000)^2/(1.380 + 1.000)^2 = 0.0255$ and $R_{2,3} = (1.523 - 1.380)^2/(1.523 + 1.380)^2 = 0.0024$. From Eq. (8.20), the surface reflectance is $R_s = [(0.0255)^{1/2} - (0.0024)^{1/2}]^2 = 0.012$. Note that even though the thin-film index is not optimum for the given substrate material, it does reduce the relative intensity of the reflected beam to about one fourth that of the same surface if uncoated (as calculated above to be 0.043).

High-efficiency, multilayer, dielectric A/R coatings can be designed to have zero reflectivity at a specific wavelength or significantly reduced variations of reflectivity with wavelength. Figure 8.13 shows plots of reflectance vs. wavelength for a single-layer (MgF_2) coating, a "broadband" multilayer coating with low reflectivity over the entire visible spectrum, and two multilayer coatings with zero reflectivity at $\lambda = 550$ nm. All these coatings are applied to crown glass. Coatings V1 and V2 are called "V-coats" because of their characteristic downward-pointing triangular shapes.

8.2.6 GHOST IMAGE FORMATION BY SECOND-SURFACE MIRRORS

An obvious difference between first- and second-surface mirrors is that a transparent substrate is needed for the latter, but not for the former. Tables 3.13–3.16 list mechanical properties and "figures

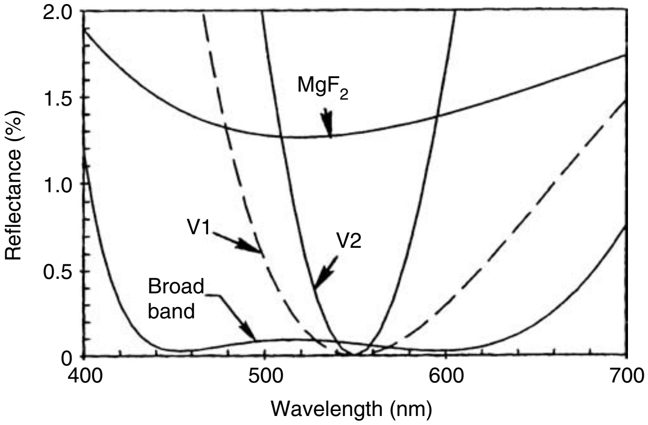

FIGURE 8.13 Variations of reflectance within the visible spectrum for several common antireflection coatings. (From Yoder, P.R., Jr., *Mounting Optics in Optical Instruments*, SPIE Press, Bellingham, 2002. With permission.)

of merit" for common nonmetallic and metallic mirror substrate materials. Of these, fused silica has the best refractive properties and most of the remaining candidates have very poor or no refractive characteristics. Second-surface mirrors are usually made of optical glasses (see Table 3.1) or crystal (see Tables 3.4–3.7). The plastic materials listed in Table 3.3 are not very good for mirror applications from a mechanical viewpoint. A distinct advantage of the second-surface mirror for image-forming mirrors is that an additional surface radius, asphericity, axial thickness, and index are available for controlling aberrations.

Figure 8.14 shows what happens when a converging beam reflects from a tilted plane-parallel second-surface mirror, such as a beam splitter plate, that is tilted at 45° to the axis. Two equal-sized images are formed. The main image comes from the silvered or beam splitting back surface, while a "ghost" image comes from the front surface. These images do not coincide; they are separated axially by d_A and laterally by d_L. At normal incidence, only axial separation would be observed.

The second-surface image-forming mirror configuration is most frequently used in primary or secondary mirrors in catadioptric systems for photographic and moderate-sized astronomical telescope applications. Second-surface designs obviously do not work in mirrors that do not have solid substrates or ones with tapered or arched back surfaces.

Figure 8.15 illustrates a concave second-surface mirror and its function in forming a normal or main image of a distant object. Since the light to be reflected by the second-surface mirror must pass through the front (refracting) mirror surface to get to the reflecting surface, a ghost image is formed by the front surface. This ghost image of the object is superposed upon the main image. If the depth of focus of the optical system includes both the normal and ghost images and the intensity of the ghost relative to that of the main image is great enough, a double image will be observed. The axial separation d_A of the two images is calculated paraxially from equations due to Kaspereit (1952) by finding the image distance for the second surface S_3' by Eq. (8.21) and the image distance for the first surface S_1' by Eq. (8.22) and taking the difference between these quantities:

$$S_3' = \frac{1}{2}\frac{[nR_1 - (n-1)t][2t + R_2] - (n-1)tR_2]}{[nR_1 - (n-1)t][nR_1 - (n-1)(t + R_2)]} \tag{8.21}$$

$$S_1' = R_1 \tag{8.22}$$

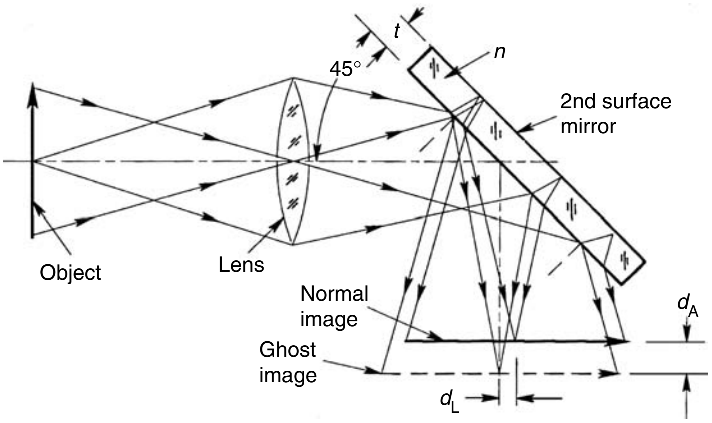
t
n
45°
2nd surface mirror
Object
Lens
Normal image
Ghost image
d_A
d_L

FIGURE 8.14 Ghost image formation from the first surface of a second-surface flat mirror inclined at 45° to the axis. (Adapted from Kaspereit, O.K., *Design of Fire Control Optics ORDM2-1*, Vol. I, U.S. Army, Washington, DC, 1952.)

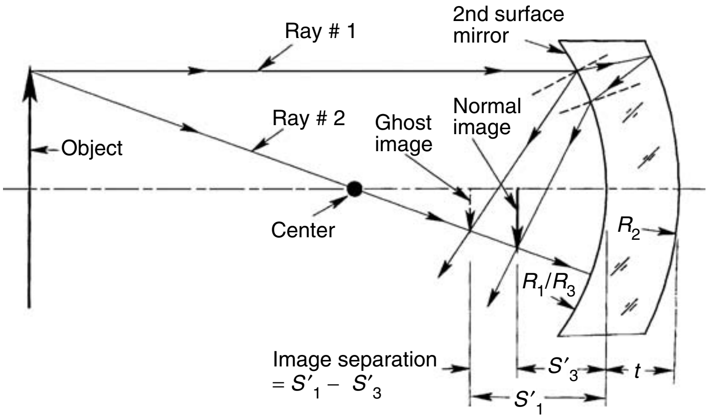
Ray # 1
2nd surface mirror
Ray # 2
Ghost image
Normal image
Object
Center
R_2
R_1/R_3
Image separation $= S'_1 - S'_3$
S'_3
t
S'_1

FIGURE 8.15 Ghost image formation from the first surface of a second-surface meniscus mirror with concentric spherical surfaces. (Adapted from Kaspereit, O.K., *Design of Fire Control Optics ORDM2-1*, Vol. I, U.S. Army, Washington, DC, 1952.)

$$d_A = S'_1 - S'_3 \tag{8.23}$$

For the special case where the mirror surfaces are concentric, $R_2 = R_1 - t$, and S'_3 is given by

$$S'_3 = \frac{(2t + nR_2)R_1}{2(t + nR_2)} \tag{8.24}$$

The paraxial image separation for a particular concentric second-surface mirror of aperture diameter 2.000 in. with $n = 1.542$, $R_1 = -25.000$ in., $t = 0.250$ in., and $R_2 = R_1 - t = -25.250$ in. is determined as follows: from Eq. (8.24), $S'_3 = [(2)(0.250) + (1.542)(-25.250)][-25.000]/[2(0.250 + (1.542)(-25.250)] = -12.419$ in. From Eq. (8.22), $S'_1 = -25.000/2 = -12.500$ in. Hence, $d_A = -12.500 - (-12.419) = -0.081$ in. by Eq. (8.23).

To judge whether this ghost image would be significantly displaced from the main image, we might apply Rayleigh's quarter-wave OPD criterion to this system as follows: first, we must determine the focal length of the mirror and then its relative aperture. Equations (8.25) and (8.26), also from Kaspereit (1952), apply to the general and concentric cases, respectively:

$$\text{EFL} = \frac{-R_1}{2}\left[\frac{nR_1R_2}{[nR_1-(n-1)t][nR_1-(n-1)(t+R_2)]}\right] \tag{8.25}$$

$$\text{EFL} = \frac{-nR_1R_2}{2[nR_1-(n-1)t]} \tag{8.26}$$

For the above concentric example, the EFL is (1.542)(−25.000)(−25.250)/{2[(1.542)(−25.000) − (1.542 − 1)(0.250)]} = 12.581 in. The mirror's relative aperture or *f*/# = EFL/aperture = 12.581/2.000 = 6.290. According to Smith (2000), the tolerable depth of focus in green light under Rayleigh's criterion is $\pm 2\lambda(f/\#)^2 = \pm\,(2)(0.000022)(6.290)^2 = 0.0017$ in. The maximum image separation for this mirror that meets this tolerance is then 0.0034 in., which is about 24 times smaller than the value of d_A just calculated. We conclude that the ghost would not be seen in the image. It would, of course, contribute stray light to the system.

It should be noted that the above equations for the image distances and focal lengths of second surface image forming mirrors apply equally well to convex and concave mirrors.

The main and ghost image separation d_A can be increased or decreased by choosing different mirror radii. A practical example is the Straubel mirror. It is designed so that the main image and the ghost image lie at the same paraxial axial distance from the mirror's first surface. Applying this design to a searchlight by placing a light source at this location (actually at the object distance for the mirror) causes the intensities of the two reflections to add without image doubling. In this case, the second radius of the mirror and its EFL are given by

$$R_2 = \frac{n^2(R_1-t)^2-t^2}{n^2R_1-(n^2-1)t} \tag{8.27}$$

$$\text{EFL} = \frac{-R_1[nR_1-(n+1)t]}{2[nR_1-(n-1)t]} \tag{8.28}$$

To reduce the spherical aberration in such a mirror and thereby improve the collimation of the projected beam, one could use a parabolic first surface and a deformed parabolic second surface on the mirror (Kaspereit, 1952).

A special second-surface mirror design is attributed to A. Mangin and bears his name. It is capable of producing a nearly spherical, aberration-free image of a distant target. The difference from the mirrors discussed above is that the Mangin mirror has R_2 larger than R_1 by an amount greater than t. The image of an object at infinite distance is formed at the center of curvature of R_1. Hence,

$$S_3' = R_1 \tag{8.29}$$

Figure 8.16 shows this type of mirror with a target at a long, but finite distance. The main image is formed just beyond the center of curvature of R_1. The radius of the second surface that makes this happen is given by Eq. (8.30). The focal length of the mirror is given by Eq. (8.31):

$$R_2 = \frac{2[nR_1^2-(2n-1)tR_1+(n-1)t^2]}{(2n-1)R_1-2(n-1)t} \tag{8.30}$$

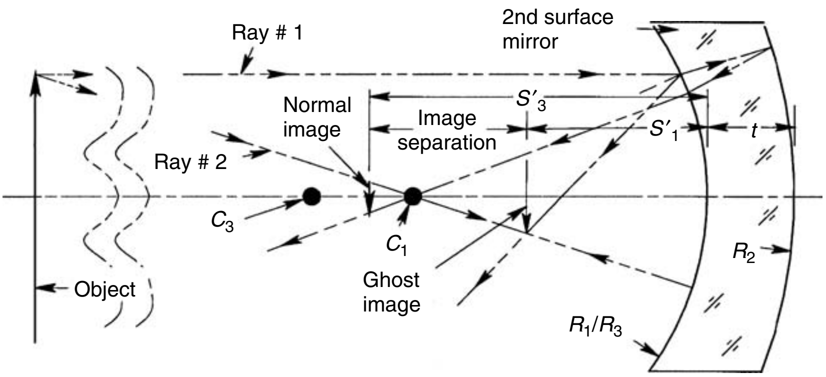

FIGURE 8.16 Ghost image formation from the first surface of a second-surface Mangin-type meniscus mirror. (Adapted from Kaspereit, O.K., *Design of Fire Control Optics ORDM2-1*, Vol. I, U.S. Army, Washington, 1952.)

$$\mathrm{EFL} = R_1 - \frac{tR_1}{nR_1 - (n-1)t} \tag{8.31}$$

These equations can be applied in the design of a typical Mangin mirror as follows: let $R = -2.000$ in., $t = 0.100$ in., and $n = 1.5165$. From Eq. (8.30), $R_2 = (1.542)^2\,(-25.000 - 0.250)^2 - 0.250^2/[(1.542)^2(-25.000)-(1.542^2 - 1)-(1.542^2 - 1)(0.250)] = -25.354$ in. The focal length of the mirror is, by Eq. (8.31), $\mathrm{EFL} = -(1.542)(-25.000)(-25.354)/\{2[(1.542)\,(-25.000) - (1.542 - 1)(0.250)]\} = 25.354$ in.

The intensity of the ghost reflection from the first surface of a second-surface mirror relative to that of the main image can be estimated from the Fresnel equation by following the steps in the following example: we assume a concentric second-surface silvered mirror made of BaK2 optical glass with $n = 1.542$ in green light ($\lambda = 0.5461$ µm). The following assumptions are made: the front surface is uncoated, the index of the surrounding air is 1.000, absorption can be neglected, and the incident beam has an intensity of unity. Applying Eq. (8.17) at the first surface, $(R_S)_1 = (1.542 - 1.000)^2/(1.542 + 1.000)^2 = 0.045$. Multiplying this factor by the intensity of the incident beam, we obtain the intensity of the ghost beam, which is 0.045. Applying Eq. (8.16), the transmission of the first surface is $T_1 = 1 - 0.045 = 0.955$. From Figure 8.4(b), the green-light reflectance R_2 of the silvered surface at 0.5461 µm is 0.970. The light beam reflected from the mirror's second surface passes twice through the front surface. Hence, its intensity upon exiting the mirror is $(0.955)^2\,(0.970) = 0.885$ times the intensity of the incident beam or 0.885. The intensity of the ghost image relative to that of the image reflected from the mirror's second surface is then $0.045/0.885 = 0.051$ or 5.1%.

8.3 SEMIKINEMATIC MOUNTINGS FOR SMALL MIRRORS

When choosing mounting configurations for small mirrors, it is best to observe the basic principles of kinematics, as outlined in Chapter 7. Although most prisms can be treated more or less as rigid bodies, mirrors must be considered flexible plates unless they are quite thick compared with their other dimensions. In Chapter 7, we listed the factors determining the appropriateness of a mounting for a prism. Because they apply just as well to mirrors, we repeat them here. Included are the inherent rigidity of the mirror; the tolerable movements and distortions of the reflecting surfaces; the magnitudes, locations, and orientations of the steady-state forces holding the mirror against its mounting surfaces during operation; the transient forces driving the mirror against or away from the mounting surfaces during exposure to extreme shock and vibration; thermal effects; the shape of the mounting surface on the mirror; the sizes, shapes, and orientations of the mounting surfaces (pads) on the mount; and the rigidity and long-term stability of the mount. Once again, the design must be compatible with assembly, adjustment, maintenance, package size, weight, and configuration constraints, and be affordable.

Figure 8.17 shows a relatively simple means for attaching a glass-type mirror configured as a plane-parallel plate to a metal surface. The reflecting surface is pressed against three flat, coplanar, machined (lapped) pads by three spring clips. The spring contacts are directly opposite the pads so as to minimize bending moments. This design constrains one translation and two tilts. The spacers that position the clips are machined to the proper thickness for the clips to exert clamping forces (preload) of controlled magnitude normal to the mirror.

The spring clips should be strong enough to restrain the mirror against the worst-case shock and vibration to which it may be subjected. They are usually designed as cantilevered beams of free length equal to the distance between the edge of the restraining means (the screw in Figure 8.17) and the nearest edge of the contact area on the mirror. A safety factor f_S of about two beyond the force needed to overcome imposed dynamic loads is frequently employed to place an upper limit on preload. Equation (7.24a) (repeated here) may be used to compute the total preload P required of all the clips:

$$P_{\mathrm{MIN}} = W f_s a_G \tag{7.24a}$$

where W, in this case, is the weight of the mirror. Each of N clips should then provide a force of P/N units. We can determine the deflection required of a spring clip to provide a particular preload using Eq. (4.22), which is repeated here for convenience:

$$\Delta = (1 - \nu_{\mathrm{M}}^2)(4PL^3)/(E_{\mathrm{M}} b t^3 N) \tag{4.22}$$

where ν_{M} is Poisson's ratio for the spring material, P the preload, L the free (cantilevered) length of the spring, E_{M} the Young's modulus for the spring material, b the width of the spring, t the thickness of the spring, and N the number of springs employed.

The stress S_{B} within the cantilevered spring created by the imposed bending may be calculated from Eq. (4.23), which is

$$S_{\mathrm{B}} = 6PL/(bt^2N) \tag{4.23}$$

where all parameters are as defined above. Note that if the spring were attached to the mount by some means that did not require it to be perforated, the bending stress would be reduced by a factor of about 3 from that given by Eq. (4.23).

Lateral motions of the mirror on the pads and rotation about its normal are not constrained other than by friction in the design represented in Figure 8.17. This may be allowable because performance

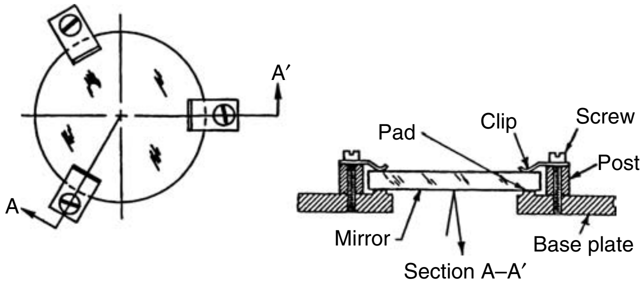

FIGURE 8.17 A concept for mounting a flat mirror to coplanar pads on a base plate with three spring clips. (Adapted from Durie, D.S.L., *Mach. Des.*, 40, 184, 1968.)

of a flat mirror is insensitive to these motions. Excessive lateral movement of the optic can be prevented by adding stops or, if the mirror is round, by sizing the supports to provide a minimal clearance to the mirror. Thermal expansion differences must be taken into consideration if the mirror touches the stops.

Figure 8.18 illustrates a less-desirable mounting design from Durie (1968) in which the mirror rim rests directly on a supporting surface machined into the plate. Spring clips provide the clamping forces, as in Figure 8.17, but unless the supporting surface is as flat as the mirror, minor irregularities can occur anywhere on that surface. Hence, bending moments can be introduced and the reflecting surface may be deformed. Similar irregularities could result from foreign matter (such as dust) trapped between the mirror and the mounting surface. The likelihood of this happening with localized small pads is significantly less than with a continuous optic-to-mount contact. With multiple irregularities in the supporting surface, there may also be uncertainty as to the orientation of the mirror — particularly if it shifts under vibration.

An arrangement sometimes used when mounting flat first-surface mirrors to an unperforated base plate is illustrated in Figure 8.19. Here, the clips are solid, so they do not bend. Resilience is built into the mount by inserting three small pads of soft material such as neoprene under the mirror at the clips. This gives a form of three-point suspension around the mirror periphery. Compression of the pads tends to accommodate thickness variations in the mirror. The soft pads can be located between the mirror surface and clips, but then the supporting surface on the plate must be very flat or have raised pads in order not to overly distort the mirror owing to misaligned contact areas. Thin strips of plastic such as Mylar tape may be used as these pads. Wedge in the mirror substrate must, in this case, be accounted for in the design. A disadvantage of this mounting is the fact that the resilient material may, over time, become either permanently deformed or so stiff that the preload is changed.

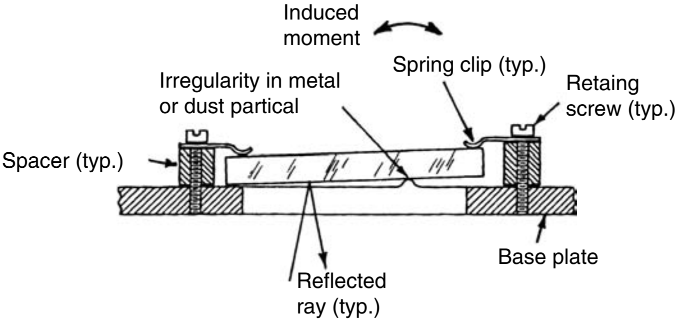

FIGURE 8.18 A less desirable design for mounting a flat mirror to a base plate without pads. The effect of a dirt particle in the interface is depicted. (Adapted from Durie, D.S.L., *Mach. Des.*, 40, 184, 1968.)

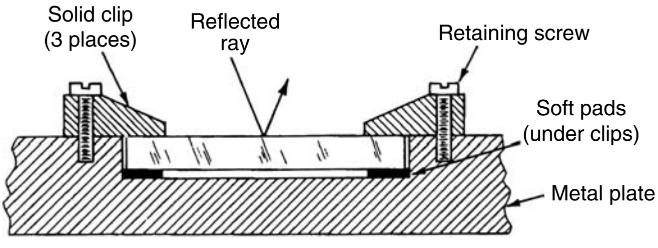

FIGURE 8.19 A common, but potentially unsatisfactory, technique for mounting a flat mirror to a base plate using resilient pads and solid clips.

Circular, rectangular, or nonsymmetrically shaped mirrors can often be mounted in the same manner as a lens. Circular mirrors up to perhaps 4 in. (10.2 cm) in diameter can be held with threaded retaining rings. The OD limit for a threaded mount is set primarily by the increasing difficulty of machining thin, circular, retaining rings with sufficient quality in larger diameters. Larger circular ones can be held with continuous (i.e., annular) flanges. Any can be held with three or more cantilevered spring clips. The number of clips obviously depends upon the size of the mirror because more required total preload demands more clips in order to keep the bending stress in each clip within reason.

Figure 8.20 shows the retaining ring concept as applied to a small, circular, image-forming mirror. The mirror is shown as a convex sphere, although a mirror with an aspheric, concave, or flat surface could be mounted similarly. The reflecting surface in this example is aligned against a shoulder in the mount by an axial preload exerted by tightening the retainer. The ring typically has a loose fit in the mount's internal thread, so it can align itself to the mirror. Contact occurs on the polished surface of the mirror to encourage precise centering of the curved-surfaced optic on the mechanical axis of the mount as a result of balancing of radial components of the axial force (see Figure 4.7). As in the case of lens surfaces, ones with long radii will not self-center. Radial locating pads such as the one shown in the figure are custom-fit to the existing spaces at various points around the periphery of the mirror once it is properly centered.

Precise edging or close tolerances on the OD of the mirror are not required if custom-fitted spacers are used as radial locating pads. As indicated in Figure 8.20, contact on the reflecting surface should occur at the same height from the axis as the center of the opposite contact area to minimize bending of the mirror. To minimize contact stress in the mirror, a tangential (conical) or toroidal (donut-shaped) interface should be used with a convex or concave mirror surface respectively. Section 4.7.5 gives details of various shapes of mechanical interfaces for lenses that are equally applicable to small mirrors. Note that temperature changes can create problems with regard to the fit of the radial locating pads and the constancy of axial preload in this and all the other mirror mounts discussed here because of differential expansion or contraction of the optical and mechanical parts. This topic is considered and corrective measures outlined in Chapter 15.

As in lens mounting, the magnitude of the nominal total preload (*P*) developed in a threaded retainer mirror mounting design with a specific torque (*Q*) applied to the ring at a fixed temperature can be estimated by Eq. (4.13b), which is

$$P = 5Q/D_T \tag{4.13b}$$

where D_T is the pitch diameter of the thread.

Another mounting for a small circular mirror, in this case a concave second-surface type, is shown in Figure 8.21. Here, the mirror surface registers against a tangential interface while the flat

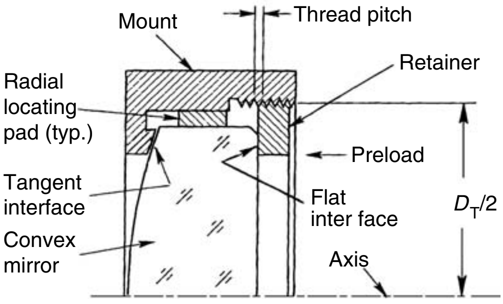

FIGURE 8.20 Conceptual configuration of a convex first-surface mirror secured in its mount with a threaded retaining ring. (Adapted from Yoder, P.R., Jr., *Mounting Optics in Optical Instruments*, SPIE Press, Bellingham, 2002. With permission.)

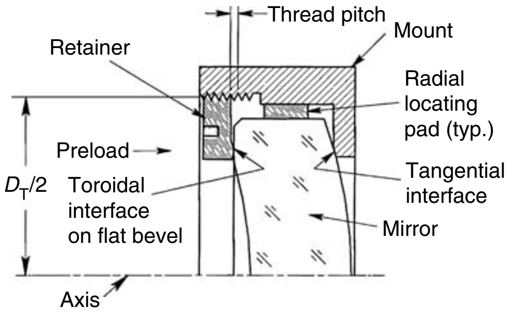

FIGURE 8.21 Conceptual configuration of a threaded retaining ring mounting for a second-surface meniscus-shaped mirror. (From Yoder, P.R., Jr., *Mounting Optics in Optical Instruments*, SPIE Press, Bellingham, 2002. With permission.)

bevel on the front of the mirror touches a toroidal interface on the retainer. Contacts occur at the same height on both sides. The choice of these interface shapes, the dimensions, and a "loose" fit in the retainer threads ensure minimal contact stress as well as minimal tendency to bend the mirror by mount-induced moments.

The function of the continuous flange in the design shown in Figure 8.22 is the same as that of the threaded retainer described earlier for a lens mounting. The magnitude of the total preload exerted for a given flange deflection Δ can be estimated using Eqs. (4.17)–(4.19), which, according to Roark (1954), apply to a perforated circular plate with the outer edge fixed and an axially directed load applied uniformly along the inner edge to deflect that edge. These equations are repeated here for convenience:

$$\Delta = (K_A - K_B)\,(P/t^3) \tag{4.18}$$

where

$$K_A = 3(m^2 - 1)\,[a^4 - b^4 - 4a^2b^2 ln(a/b)]/(4\pi m^2 E_M a^2) \tag{4.19a}$$

$$K_B = \frac{3(m^2 - 1)(m + 1)[2\,ln\,(a/b) + (b^2/a^2) - 1][b^4 + 2a^2b^2\ln(a/b) - a^2b^2]}{4\pi m^2 E_M[b^2(m + 1) + a^2(m - 1)]} \tag{4.19b}$$

and P is the total preload, t the thickness of the flange cantilevered section, a the outer radius of the cantilevered section, b the inner radius of the cantilevered section, m the reciprocal of Poisson's ratio (ν_M) of the flange material, and E_M the Young's modulus of the flange material.

The spacer between the mount and the flange can be ground at assembly to the particular thickness that produces the predetermined flange deflection when firm metal-to-metal contact is achieved by tightening the clamping screws. Customizing the spacer accommodates variations in as-manufactured lens thicknesses. The flange material and thickness are the prime design variables. The dimensions a and b, and hence the annular width (a - b), can also be varied, but these are usually set primarily by the mirror diameter, mount wall thickness, and overall dimensional requirements.

The stress, S_B, built up in the bent portion of the flange must not exceed the yield strength S_Y of the material. Equations (4.20) and (4.21) adapted from Roark (1954) apply here:

$$S_B = K_C P/t^2 = S_Y/f_s \tag{4.20}$$

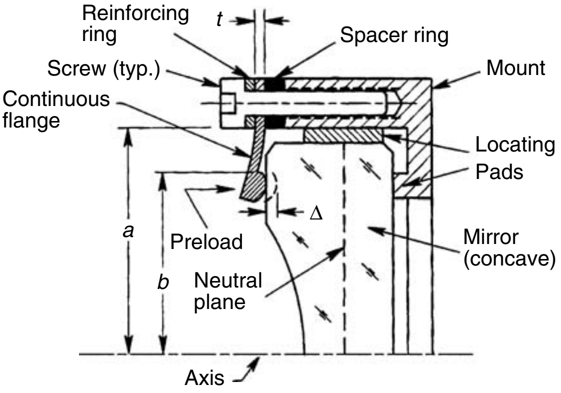

FIGURE 8.22 Conceptual configuration for a concave first-surface mirror preloaded with a continuous ring flange. (From Yoder, P.R., Jr., *Mounting Optics in Optical Instruments*, SPIE Press, Bellingham, 2002. With permission.)

where

$$K_C = \left[\frac{3}{2\pi}\right]\left[1 - \frac{2mb^2 - 2b^2(m+1)ln(a/b)}{a^2(m-1) + b^2(m+1)}\right] \tag{4.21}$$

and f_S is the safety factor. The reader is referred to Section 4.7.3 for discussions of the use of these equations and for worked-out numerical examples illustrating their application.

As in the case of lenses, the localized deflections Δ of the flange as measured between the attachment screws should be essentially the same as those existing at the screws. This ensures uniform preload around the mirror's edge. This can be accomplished by machining the flexing portion of the flange as a thinned, annular region in a thicker ring, thereby providing extra stiffness at the clamped annular zone of the flange. Stiffening the flange with a reinforcing ring as shown schematically in Figure 8.22 could also do this.

Increasing the number of screws also tends to reduce the possibility of nonuniform preload around the mirror's edge. Shigley and Mischke (1989) considered the spacing of screw constraints on a gasketed flange for a high-pressure chamber. If we apply this guidance to the mirror-mounting case, the number of screws, N, should be

$$3 \leq \pi D_B/(Nd) \leq 6 \tag{8.32}$$

where D_B is the diameter of the bolt circle passing through the centers of the screws and d the diameter of the screw head. This criterion is probably overly conservative in an optical instrument application, especially if a stiff backup ring is employed or if the flange is thickened in the region where it is clamped. The application of good engineering judgment and possibly experimentation is suggested. Alternatively, the use of a threaded cap as shown in Figure 4.25 to secure the flange may be successful if the mirror is not too large.

Figure 8.23 shows a semikinematic mounting for a partially reflecting mirror used as a plate-type beam splitter. The beam splitting coating is on the front face. That face of the plate registers against small-area-fixed pads and is spring loaded directly opposite these points. Here, and in any design with hard contacts against the reflecting side of the mirror, the location and orientation of that surface do not change with the temperature of the optic. Displacements of the constraints caused by temperature changes may, of course, affect the location and orientation of that surface.

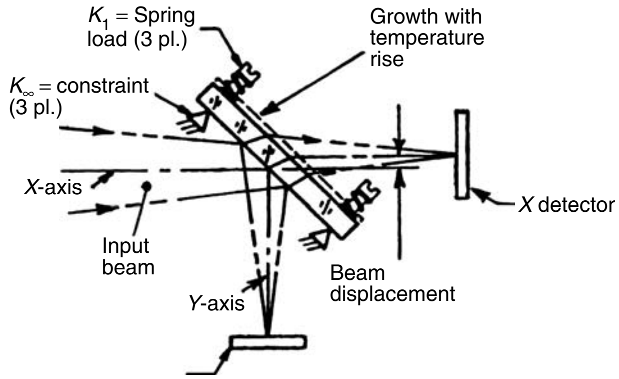
K_1 = Spring load (3 pl.)
K_∞ = constraint (3 pl.)
Growth with temperature rise
X-axis
Input beam
Y-axis
Beam displacement
X detector

FIGURE 8.23 A mounting for a front-surface beam splitter plate. (Adapted from Lipshutz, M.L., *Appl. Opt.*, 7, 2326, 1968.)

The optics are constrained laterally only by friction in the designs represented in Figures 8.17–8.19 and Figure 8.23. This may be acceptable because the performance of a flat mirror is generally insensitive to these motions. Excessive lateral movement of the optic can be prevented by spring loading it against fixed stops. CTE differences must be considered if the mirror touches hard stops without any resiliency.

A mirror-mounting concept from Yoder (1997) that utilizes one spring-loaded mechanism and two fixed constraints at 120° from each other in a plane parallel to the reflecting surface, and three spring-loaded mechanisms to preload the mirror against coplanar pads in the orthogonal direction, is illustrated in Figure 8.24. While compression coil springs are shown, cantilevered clips could be employed. This mount is semikinematic since all six DOF are constrained by the spring loads, and the contacts are small areas instead of points.

The interfaces between the mirror and the pads are self-aligning in this design because of the flexibility of the springs. Intimate contacts over the pad areas can safely be assumed. In a design without that flexibility, localized line contact between the glass and the edges of the pads could occur if the pads were not perfectly aligned to the mirror surface. The stress concentration that might then occur could be detrimental to the mirror's optical figure quality. This potential problem can be eliminated and the design made more deterministic from a stress-buildup viewpoint if the pads were to be provided with curved interfacing surfaces. Spherical pads on cantilevered springs are illustrated in Figure 8.25(a). The interfaces with the mirror are then small circles formed by localized elastic deformation of the metal and the glass under preload. The resulting stress can then be predicted using Hertzian theory or the technique described in Section 15.3.1 based on equations from Roark (1954). Spherical pads can be used to interface the springs with convex or concave optical surfaces as well as with flat surfaces. Then, the deformed regions would be circular.

A type of small mirror mount sold commercially by several suppliers has a cylindrical cavity slightly larger in ID than the OD of the cylindrical mirror to be mounted. Such a mount is illustrated schematically in Fig. 8.25. The mirror's rim rests on two Nylon rods embedded into the lower wall of the mount. The rods are nominally parallel to each other and to the cavity axis. The mirror is pressed against the rods by a light radial preload from a Nylon setscrew at the top of the mount. The back of the mirror should be spaced slightly away from the shoulder in the mount. The slight radial compliance of the Nylon components helps to prevent distortion or damage to the mirror when the temperature changes. Some designs use Delrin parts instead of Nylon.

The Nylon retaining ring shown in the figure is usually not used because axial preload would tend to distort the mirror if it is pressed against the undoubtedly imperfect shoulder. Note that the retainer could be used to advantage as a safety feature by screwing it into the mount far enough to

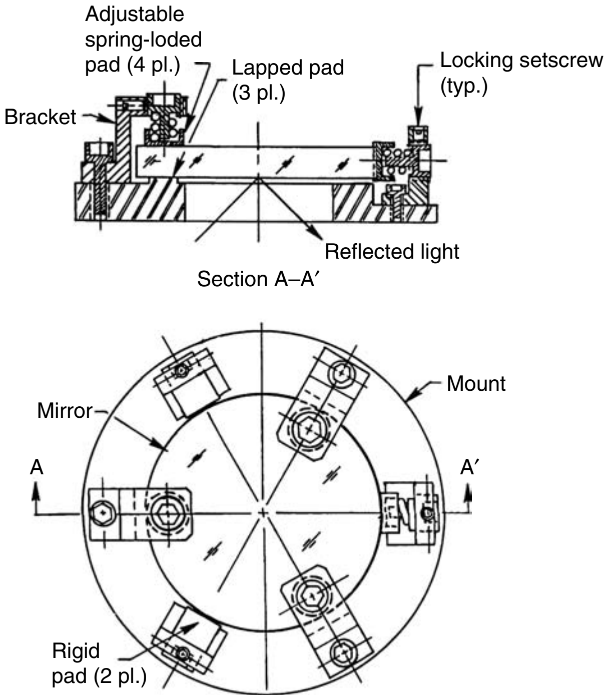
Adjustable spring-loded pad (4 pl.)
Lapped pad (3 pl.)
Locking setscrew (typ.)
Bracket
Reflected light
Section A–A′
Mount
Mirror
A
A′
Rigid pad (2 pl.)

FIGURE 8.24 Concept for a spring-loaded semikinematic mirror mounting. (Adapted from Yoder, P.R., Jr., in *Handbook of Optomechanical Engineering*, Ahmad, A., Ed., CRC Press, Boca Raton, FL, 1997.)

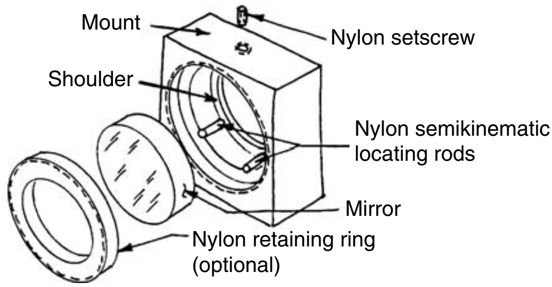
Mount
Nylon setscrew
Shoulder
Nylon semikinematic locating rods
Mirror
Nylon retaining ring (optional)

FIGURE 8.25 A typical commercially available mount for small mirrors featuring a resilient setscrew constraining the optic's rim against two parallel resilient locating rods in the manner of a V-mount. The retaining ring is best used as a safety restraint rather than to provide axial preload. (From Vukobratovich, D., *SPIE Short Course SC014*, 2003. With permission.)

act as a stop in case the mirror and its mount are tilted forward, but not far enough for the ring to touch the mirror during normal use.

Vukobratovich (2003) suggested the kinematic configuration shown in Figure 8.26 for mounting a rectangular mirror on edge. The mirror back is supported at three points located at the lower corners and at the midpoint of the top edge. In the vertical direction, the mirror is supported at two points located at distances of $0.22a$ from the ends, where a is the length of the longer (horizontal) edge of the mirror. These locations minimize the mirror's deflection due to gravity. Note that the mirror is not preloaded against the back supports and the only preload acting vertically is self-weight. If the bottom supports are located slightly in front of the plane containing the CG of the mirror, an overturning moment would be exerted. This moment would tend to press the mirror against

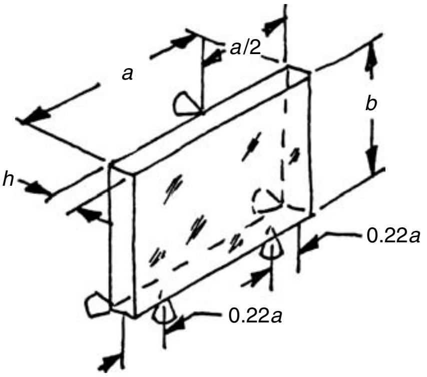

FIGURE 8.26 Sketch of a kinematic mounting configuration for a rectangular mirror supported on edge. (From Vukobratovich, D., *SPIE Short Course SC014*, 2003. With permission.)

the top back support. In the absence of friction, the mirror would also tend to slide on the lower edge point supports until it contacts the lower back supports. If the point contacts are changed to small area contacts to make the design semikinematic, friction would come into play and there would be no guarantee that the mirror would touch the lower back supports. If the mirror is intentionally moved by applying an external horizontal force, the desired contact with those supports could be established. Friction should then hold the mirror in place unless disturbed.

Whenever an optic (such as a mirror) is preloaded against an opposing reference surface or surfaces, it is advantageous for the preload force to be applied perpendicular to the optic's faces and to be arranged so the line of force passes directly through the optical material toward the centers of appropriately shaped pads touching the other side of that optic. Typical configurations of this type in which mirrors are constrained axially are illustrated in Figures 8.17 and 8.21–8.24. Figure 8.27 indicates what can happen if this is not the case. In view (a), the mirror interfaces are properly arranged and the mirror is not deformed by the applied forces. In view (b), the pads are not aligned with the forces and moments are applied to the mirror, tending to bend it as shown. In Figure 9.25, the radial force exerted by the screw is directed between the opposing Nylon rod supports. Small mirrors are stiff radially, so surface deformations from this force may be of small concern. A larger mirror clamped in this manner might distort significantly from the radial force of such a screw. The V-mount for large horizontal-axis mirrors, discussed in Section 10.3, is basically similar to the mount shown in Figure 8.25, but relies upon gravity to hold those mirrors in place radially.

The mounting for the secondary mirror of the Cassegrainian telescope used in NASA's Geostationary Operational Environmental Satellite (GOES) is shown in Figure 8.28 and Figure 8.29. The aperture of the primary mirror is 12.25 in. (31.1 cm), while that of the secondary mirror is 1.53 in. (3.9 cm). Structural aspects of the telescopes design are discussed in Section 14.5.3.2. That structure is illustrated schematically in Figure 14.51.

Hookman (1989) reported that the ULE secondary mirror is mounted in an Invar cell, is supported radially and axially by pads of RTV566, and is registered against three 0.002-in. (0.05-μm)-thick Mylar pads equally spaced around the periphery of the mirror's aperture. The pads are bonded in place with epoxy to ensure that they do not move. The radial RTV pads are 0.200 in. (5.1 mm) in diameter and 0.01 in. (0.25 mm) thick, while the axial pads have the same diameters and are 0.025 in. (0.64 mm) thick. The Invar retaining ring is held by three screws to the end of the cell as shown in the exploded view of Figure 8.28. When bottomed against the cell, the cured axial RTV pads are compressed 0.002 in. (0.05 mm) to preload the subassembly nominally by about 2.15 lb (9.6 N). The radial pads are centered axially at the neutral plane of the mirror.

To minimize temperature effects caused by a mismatch of CTEs of the Invar mirror cell and the aluminum mounting, the cell is supported on the ends of three flexure blades machined integrally

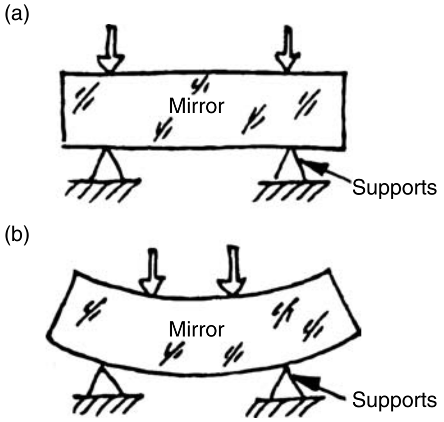
(a)
Mirror
Supports
(b)
Mirror
Supports

FIGURE 8.27 Schematic representations of (a) a mirror constrained by directly opposing forces and supports and (b) the same mirror subjected to a bending moment by forces directed between the supports. (From Vukobratovich, D., *SPIE Short Course SC014*, 2003. With permission.)

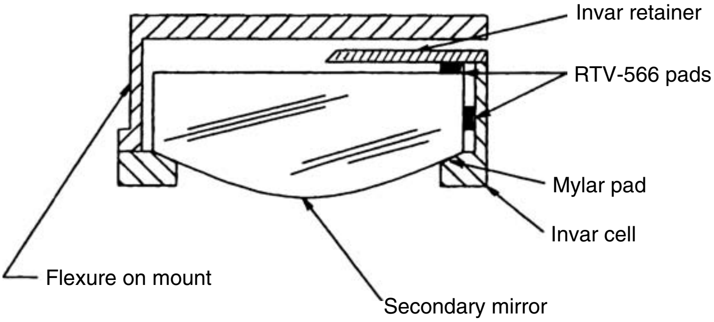
Invar retainer
RTV-566 pads
Mylar pad
Invar cell
Flexure on mount
Secondary mirror

FIGURE 8.28 Partial section view of the secondary mirror mount for the GOES satellite telescope. (Adapted from Hookman, R., *Proc. SPIE*, 1167, 368, 1989. With permission.)

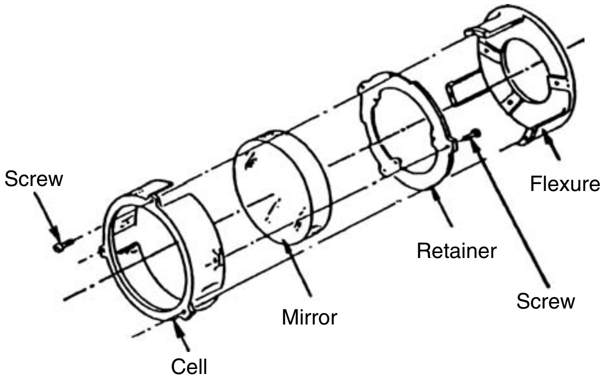
Screw
Flexure
Retainer
Screw
Mirror
Cell

FIGURE 8.29 Exploded view of the secondary mirror mount shown in Figure 8.27. (From Hookman, R., *Proc. SPIE*, 1167, 368, 1989. With permission.)

into the secondary mount. The mount is 6061-T6 aluminum. The flexure blades are 0.5 in (12.7 mm) long, 0.32 in. (8.1 mm) wide, and 0.020 in. (0.5 mm) thick. Temperature changes do not disturb the radial location or tilt of the mirror.

8.4 MOUNTING MIRRORS BY BONDING

Small mirrors can be mounted with glass-to-metal bonds using adhesives. This design technique is simple and compact while also providing mechanical strength adequate for withstanding the severe shock, vibration, and temperature changes characteristic of most military and aerospace applications. The technique is frequently used in less rigorous applications because it is easy to apply and is reliable when performed properly.

In Chapter 7 we listed the critical aspects of a glass-to-metal bond as the inherent characteristics of the adhesive, thickness of the adhesive layer, cleanliness of the surfaces to be bonded, dissimilarity of coefficients of thermal expansion for the materials bonded, dimensions of the bond, environment that the bonded assembly will experience, and care with which the bonding operation is performed. Several adhesives commonly used for this purpose are listed in Chapter 3, along with some of their major characteristics. The manufacturer's recommended procedures for applying and curing these adhesives should be followed unless special requirements of the application dictate otherwise. Experimental verification of the choice of adhesive and methods is advisable in critical applications.

For maximum bond strength, the adhesive layer should have a specific thickness. In the case of epoxy EC2216-B/A, mentioned at various points in this book, experience has indicated a thickness of 0.075 to 0.125 mm (0.003 to 0.005 in.) to be appropriate. One method of ensuring the right layer thickness is to place spacers (wires, plastic fishing line, or flat shims) of the specified thickness at three places symmetrically located on one bonding surface before applying the adhesive. Care must be exercised to register the glass part against these spacers during assembly and curing. The adhesive should not extend between the spacers and either part to be bonded since this could affect the adhesive layer thickness. Another technique for obtaining a uniformly thin layer of epoxy between the glass and metal surfaces is to mix small glass beads[†] into the epoxy before applying it to the surfaces to be bonded. When the parts are clamped securely together, the largest beads contact both faces and hold those surfaces apart by the bead diameters. Since such beads can be procured with closely controlled diameters, the achievement of specific thickness joints is relatively simple. As one might expect, the addition of the beads has a small beneficial effect on the coefficient of thermal expansion of the epoxy.

It has been clearly demonstrated by Hatheway (1993) and Miller (1999) that a thin adhesive bond is stiffer than a thick one. The variation in Young's modulus with thickness can be as large as a factor of 100. This variation can affect the ability of the bond to "give" under shock and vibration as well as when the temperature changes.

The backs of first-surface mirrors with dimensions up to about 6 in. (15 cm) can be bonded directly to a mechanical support. The ratio of largest face dimension to thickness of the mirror should be less than 6:1 so that adhesive shrinkage during curing or at extreme temperatures does not distort the optical surface. Figure 8.30 illustrates such a design. The mirror is made of Schott BK7 glass, and is 2 in. (5.1 cm) in diameter and 0.33 in. (0.84 cm) thick (6:1 ratio). It weighs about 0.09 lb. The mounting base is stainless-steel type 416 and has a circular raised surface (or land) to which the mirror is to be bonded. The design task is to determine how big this bond should be.

Guidelines for determining the appropriate adhesive area for bonding prisms to mechanical mounts were provided in Section 7.6. These guidelines apply to mirrors as well. In general, the minimum area of the bond, Q_{MIN}, is determined by

$$Q_{\mathrm{MIN}} = W a_{\mathrm{G}} f_{\mathrm{s}} / J \tag{7.30}$$

where W is the weight of the optic, a_{G} the worst-case expected acceleration factor, f_{S} a safety factor, and J the shear or tensile strength of the adhesive joint (usually approximately equal). The safety factor should be at least two and possibly as large as four to allow for some unplanned, nonoptimum conditions, such as inadequate cleaning during processing.

[†] See, for example, certified sized products made by Duke Scientific Corp. (www.dukescientific.com).

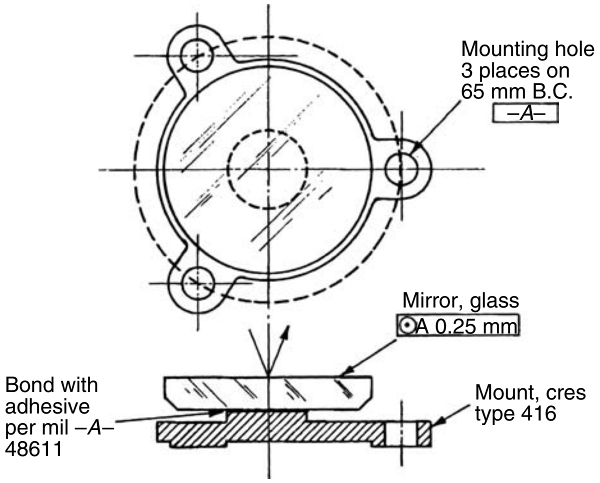

FIGURE 8.30 A first-surface flat mirror subassembly with the optic bonded on its back to a flat pad on the mounting flange. (From Yoder, 1985. With permission.)

Because the dimensional changes of the adhesive bond during curing (shrinkage) and during temperature changes (expansion or shrinkage depending upon the sign of the change) are proportional to the dimension of the bond, the bond area should not be too large. If a large total area is necessary to hold a heavy mirror, the bond should be divided into a group of smaller areas such as a triangular or ring pattern of circles or spots of any shape.

To illustrate, consider a circular Zerodur mirror with a diameter D_G of 4.250 in. (107.950 mm), thickness 0.708 in. (17.983 mm), and weight 0.914 lb (0.414 kg) that is to withstand 200 times gravity accelerations with a safety factor of 4 when bonded with epoxy of strength 2500 lb/in.^{2} (17.24 MPa). From Eq. (7.30), the minimum total bond area Q_{MIN} required is $(0.914)(200)(4)/2500 = 0.292$ in.^{2} (1.884 cm^2). With the adhesive in a single circular area, the diameter is $2(Q_{MIN}/\pi)^{1/2} = (2)(0.292/\pi)^{1/2} = 0.610$ in. (15.494 mm). If a triangular pattern of three equal circular areas is used, their diameters are $2(Q_{MIN}/3\pi)^{1/2} = (2)[0.292/(3\pi)]^{1/2} = 0.352$ in. (8.941 mm). If the bonds are 6 equal circular areas arranged in a ring at the 0.7 zone on the mirror's back, their diameters are $2(Q_{MIN}/6\pi)^{1/2} = (2)[0.292/(6\pi)]^{1/2} = 0.249$ in. (6.333 mm). The single and multiple bond areas would appear on the back of the mirror as shown in Figure 8.31 where they are drawn to the same scale.

In Section 4.8, we described the use of annular rings of elastomeric material to pot the rims of lenses into cylindrical mounts. This technique might be considered a variation of bonding; it can be applied to small and moderate-sized mirrors just as well as lenses. Figure 8.32 illustrates such a mounting. The elastomer fills the entire gap of thickness t_e between the mirror and cell ID. The similarity to Figure 4.51 is apparent. Equation (4.25) or (4.26) can be used to determine t_e to make the design approximately athermal in the radial direction. Equations (4.27) and (4.28) can then be used to estimate how much the mirror would decenter radially due to its self-weight or radially directed acceleration. Rectangular mirrors can also be secured using this technique.

Figure 8.33(a) shows another technique for elastomerically potting a mirror into a mount. Here, the mirror has the dimensions indicated in the figure. It is attached to its mount with 12 discrete segments or pads of elastomer applied in the gap between the mirror OD and the cell ID. In this case, the mirror is fused silica ($\alpha_G = 0.5 \times 10^{-6}$), the cell is Kovar ($\alpha_M = 5.5 \times 10^{-6}$), and the elastomer is Dow Corning 6-1104 silicone ($\alpha_e = 261 \times 10^{-6}$). The nominal "athermal" thickness of the elastomer pads according to Eq. (4.25) is 0.914 mm (0.036 in.). The pad edge dimension (if square) or diameter (if circular) is d_e. This dimension is a design parameter.

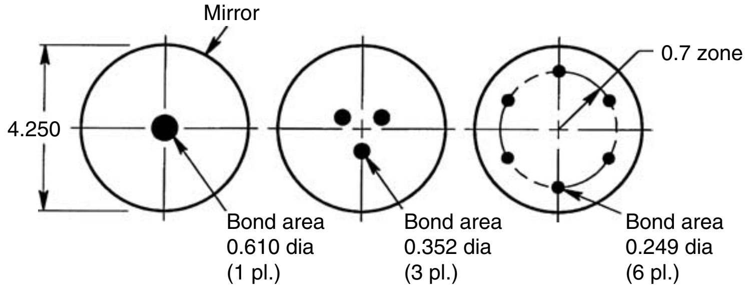

FIGURE 8.31 Schematic diagrams of equal total area bonds on the back of a first-surface mirror. (a) Single bond, (b) three bonds in a triangular pattern, (c) six bonds approximately at the 0.7 radius zone. Dimensions are in inches.

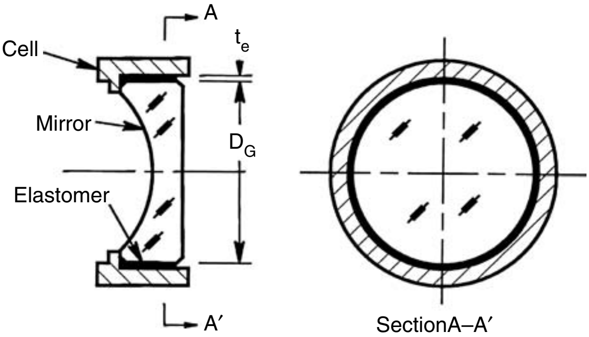

FIGURE 8.32 Schematic configuration of a concave first-surface mirror potted with an elastomeric ring into a cell in the same manner as shown for a lens mounting in Figure 4.51.

A finite element analysis of vibrational modes for this design reported by Mammini et al. (2003) indicated that the fundamental frequencies of the piston and tip/tilt modes varied with t_e. Figure 8.33(b) shows these variations as spline fits through the data points listed in the referenced paper. The application required that these frequencies be at least 300 Hz. The long vertical line shows that d_e should then be at least 0.28 in. (7.11 mm). The actual dimension used was 0.289 in. (7.34 mm). Thermal analysis showed that a 10°C temperature change would cause an out-of-plane surface distortion of less than 1/300 wavelength at 633 nm over the entire mirror surface.

Vukobratovich (2003) described a technique for radially constraining a circular lens or mirror with a shim strip of Mylar located between the OD of the optic and the ID of the cell (see Figure 8.34). The shim is perforated at three places such that the holes line up with radially directed holes through the cell wall. RTV compound is injected through the holes to reach the rim of the mirror. Pads of RTV formed after curing hold the mirror from rotating about its axis (clocking), and constrain the optic radially.

If we know the area of the bond interface on any bonded mirror mounting, the maximum acceleration that the subassembly should withstand can easily be computed. Conversely, given the maximum acceleration specification, the minimum bond area can be computed. An example of such a calculation for a prism mounting was given in Section 7.6.

When an epoxy bond is placed between a mirror and a metal mounting surface, care should be exercised during application of the epoxy to ensure that fillets of excess adhesive are not formed around the glass-to-metal joint. Shrinkage during curing along the diagonal face of the fillet will tend to stress the glass. Shrinkage of the epoxy along this diagonal surface has been known to pull chunks of glass from the optic at a low temperature. Figure 7.78 shows an undesirable fillet in view (a). View (b) shows the preferred configuration of the adhesive joint.

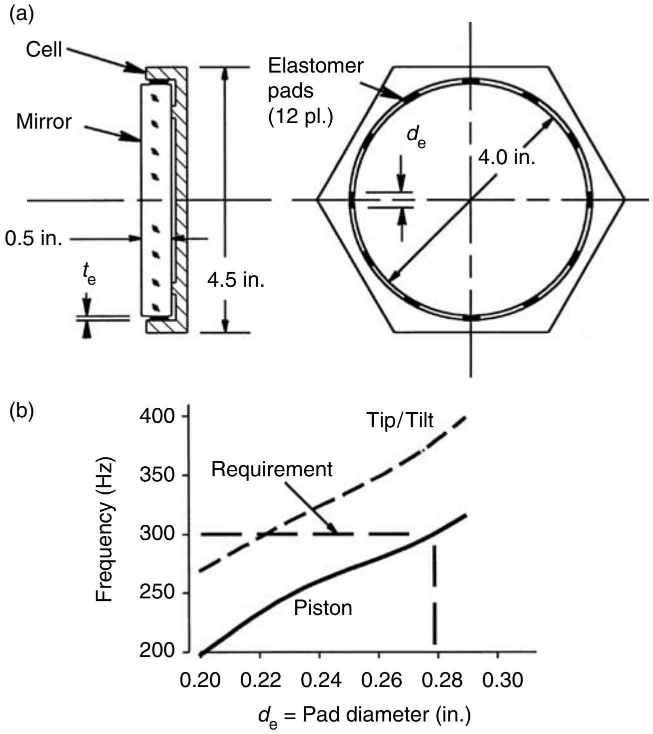

FIGURE 8.33 (a) A flat mirror rim-mounted on multiple (12) discrete elastomer pads of dimension d_e and thickness t_e. (b) Plots of fundamental frequency for piston and tip/tilt vibrational modes for this mirror mounting. (Adapted from Mammini, P., Holmes, B., Nordt, A., and Stubbs, D., *Proc SPIE*, 5176, 26, 2003.)

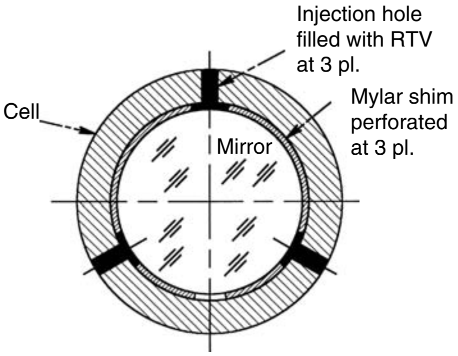
Injection hole filled with RTV at 3 pl.
Cell
Mirror
Mylar shim perforated at 3 pl.

FIGURE 8.34 A mirror-mounting concept in which three pads of an elastomer (RTV) are injected through three holes in the cell wall and through three corresponding holes in a Mylar radial shim. (Adapted from Vukobratovich, D., *SPIE Short Course SC014*, 2003. With permission.)

8.5 FLEXURE MOUNTS FOR MIRRORS

In this section, we consider a few typical examples of ways in which mirrors can be mounted on flexures. Figure 8.35 illustrates the principle of one type of in-plane flexure mounting for a circular mirror in a cell. The cell is suspended from three flexure blades. The curved arrows indicate the directions of free motion for each flexure acting alone. Ideally, these lines of freedom should intersect at a point, the flexure lengths should be equal, and the grounded ends of the three flexures

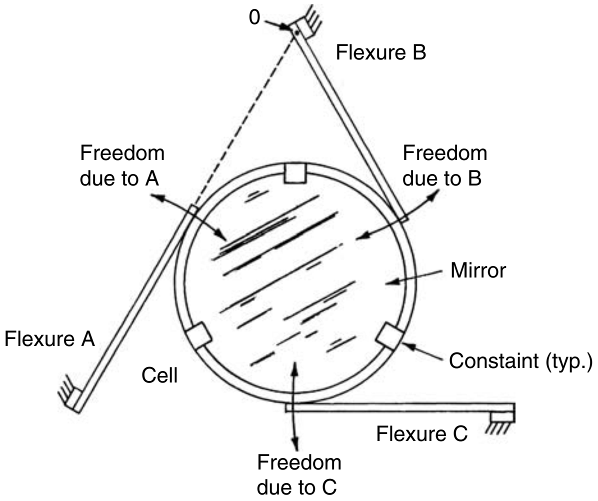

FIGURE 8.35 Conceptual sketch for an in-plane flexure mounting for a circular mirror.

should form an equilateral triangle. The function of this system of flexures may be explained as follows. In the absence of C, the combination of flexures A and B will only permit rotation about point O, which is the intersection of flexure B with a line extending flexure A. With C in place, rotation about O is prevented since flexure C is stiff in that direction.

Although not apparent in the frontal view of the figure, the flexure blades have sufficient depth perpendicular to the page to provide beam strength to prevent the mirror from translating along its normal. Even if temperature changes cause thermal expansion, the radial motion of the optic will be impeded without stressing the mirror. The only permitted motion due to expansion or contraction is a small rotation about the mirror normal through the intersection of the lines of freedom. This occurs because of slight changes in the lengths of the flexures. The magnitude Θ of this rotation in radians may be approximated by the expression $\theta = 3\alpha\,\Delta T$ where α is the CTE of the flexure material (typically in ppm/°F) and ΔT the temperature change. If the flexure is beryllium copper with a CTE of 8.0 ppm/°F and ΔT is 20°F, θ is only about 1.6 arcmin.

A quite different technique for bonding a mirror to a mechanical support is sketched in Figure 8.36. Here, a circular mirror is bonded to three flat flexure blades that are, in turn, attached mechanically by screws, rivets, or adhesive to a circular post or tube of essentially the same diameter as the mirror. The flexures are flat, so they can bend radially to accommodate differences in thermal expansion. They are of the same free length and material so that thermally induced tilts are minimized. The local areas on both the mirror and mount where the springs are attached are flattened in order to obtain adequate contact area for bonding and to prevent cupping of the springs. The flexures should be as light and flexible as is consistent with vibration and shock requirements. Høg (1975) discussed a design of this general type. This mounting arrangement can be used to support image-forming mirrors as well as flat ones. The design tends to keep the optic centered in spite of temperature changes.

Figure 8.37 illustrates a mounting for a so-called *mushroom mirror*. The mirror has a cylindrical protrusion or stalk centrally located on its back face. This stalk is an integral part of the mirror or bonded in place with adhesive. The intersection of the integral stalk and the mirror's back face should have a fillet for ease of fabrication and to minimize residual stress rather than the sharp corner indicated in the figure. The stalk is inserted into and bonded to the IDs of a series of N flexure blades machined into a cylindrical portion of the mounting flange. The flexures are radially compliant and act in the same manner as the flexures of Fig. 8.36 to keep the mirror centered when the temperature changes. Mirror deformations are thus minimized.

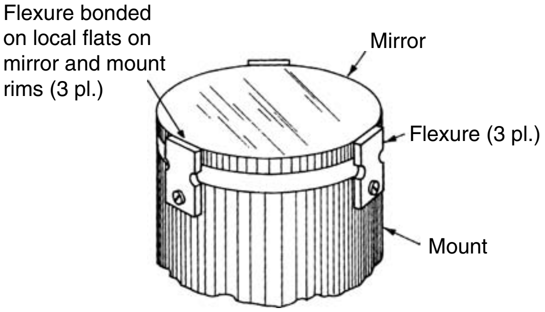
Flexure bonded on local flats on mirror and mount rims (3 pl.)
Mirror
Flexure (3 pl.)
Mount

FIGURE 8.36 Conceptual sketch of an "end-on" mounting for a circular mirror employing radially compliant flexures. (Adapted from Høg, E., *Astron. Astrophys.*, 4, 107, 1975.)

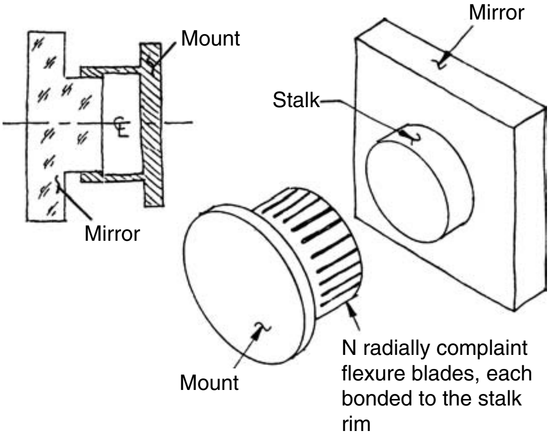
Mount
Mirror
Mirror
Stalk
Mount
N radially complaint flexure blades, each bonded to the stalk rim

FIGURE 8.37 Concept for a radially compliant mounting for a square mirror featuring an integral central stalk. The flexure blades machined into the mount are bonded to the stalk. (Adapted from Vukobratovich, D., *SPIE Short Course SC014*, 2003. With permission.)

Figure 8.38(a) shows a flexure-mounting concept in which the cylindrical rim of a circular mirror is bonded to the centers of three flexures oriented tangentially to that rim and attached to the structure at both ends (see Fig. 8.38[b]). Some tangential compliance should be provided in the interface to the mount at one end of each flexure to allow for temperature changes if the flexure is not made of the same material as the mount. Special fixtures are needed to align the mirror to the flexures at the time of bonding.

Figure 8.39 shows a concept for the interface between a cantilevered flexure arm and the rim of a circular mirror. A square boss is bonded to the rim of the mirror. The free end of the flexure is bonded to this boss while the fixed end is attached to the structure. In order to accommodate small misalignments between the bosses and the seats caused by manufacturing or assembly errors, subflexures are provided at four places in each flexure as indicated. The bonded interfaces to the bosses are shown at the squared-off ends of the subflexures. Alternate designs might have bent or machined tabs oriented at right angles to the main flexure to provide more bonding area for strength in the joints. In either case, the fit between the sub-flexures and the boss must allow the correct spacings for the adhesive layers. Other boss and flexure designs intended for use with larger mirrors are shown and discussed in Chapter 9.

A small mirror of square or rectangular shape might be supported in a cell attached to three cantilevered flexure blades as shown in Figure 8.40. The dashed lines indicate the directions of freedom

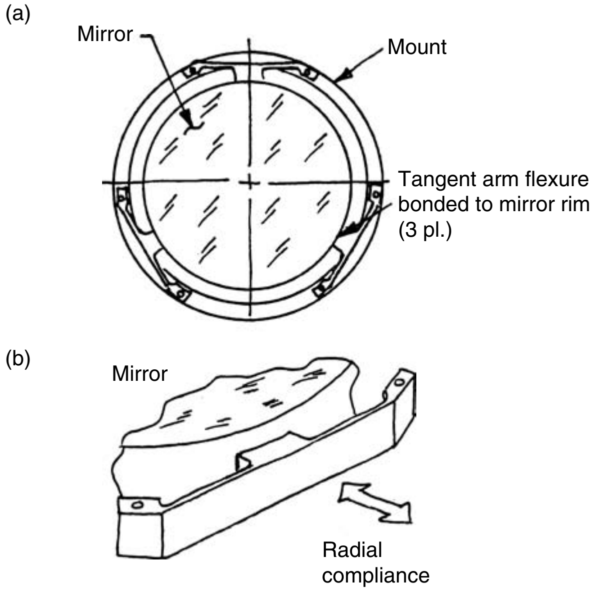

FIGURE 8.38 (a) Conceptual sketch of a mounting for a circular mirror using three tangentially oriented flexures supported at both ends as shown in View (b). (Adapted from Vukobratovich, D. and Richard, R., 1988.)

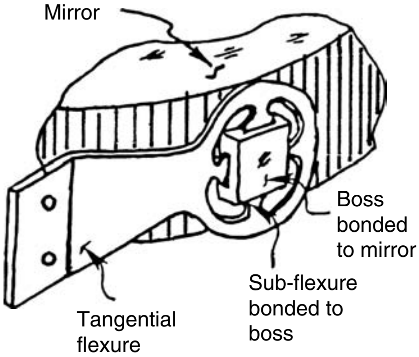

FIGURE 8.39 A possible interface between the free end of a cantilevered flexure and a boss bonded to the rim of a circular mirror. (Adapted from Vukobratovich, D. and Richard, R., 1988.)

(approximated as straight lines). In this case, the intersection of these lines, which is stationary, does not coincide with the geometric center of the mirror or the center of gravity of this particular mirror and cell combination. By changing the angles of the corner bevels and relocating the flexures, the intersection point could be centralized at the CG and the design improved from a dynamic viewpoint. Differential thermal expansion across the mount-to-structure interface can occur without excessively stressing the mirror. Axial movement of the mirror is prevented by the high stiffness of the blades in that direction resulting from depth of the blade.

Another concept for mounting a circular mirror with cantilevered tangential flexures is depicted in Figure 8.41. Here, the flexures are integral with the body of the ring-shaped mount. Machining narrow slots using an EDM process would create the flexures. This mirror mounting is similar to a design concept discussed as a means for lens mounting in Section 4.9. Once again, the blades are

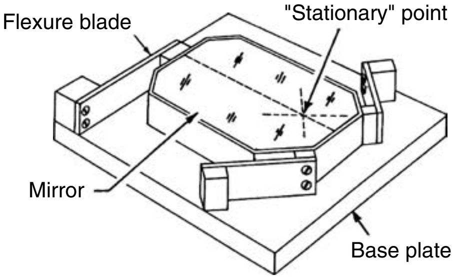

FIGURE 8.40 Concept for a flexure mounting for a cell-mounted rectangular mirror. (From Yoder, P.R., Jr., *Mounting Optics in Optical Instruments*, SPIE Press, Bellingham, 2002. With permission.)

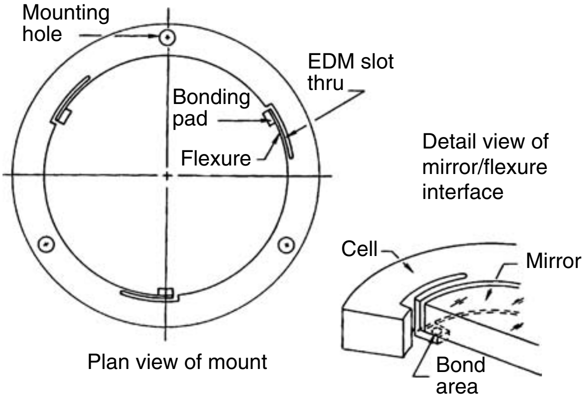

FIGURE 8.41 Concept for mounting a circular mirror on three flexures machined integrally into the inner wall of the cell. This mounting is similar to that shown for a lens in Figure 4.54(a) and (b).

stiff in the tangential and axial directions and compliant radially to minimize decentrations that are due to temperature changes.

Small mirrors used in very high-performance applications may benefit from being mounted in the manner shown in Figure 8.42. Here, a circular mirror with three bonded-on bosses is attached to tangentially oriented arms containing dual sets of universal joint-type flexures. Three axial-metering rod-type supports that include flexures are also attached to the bosses. Such a mounting is essentially insensitive radially to temperature changes because of the action of the tangent arm flexures. The thermal compensation units shown in the axial supports are intended to make the design less sensitive in that direction to temperature changes. The latter mechanism consists of selected lengths of dissimilar metals arranged in a reentrant manner. Differential screws might be employed as the means for attaching the fixed ends of the tangent arms to the brackets in some applications. This would provide fine adjustment of the lengths of the tangent flexures. The "turnbuckle" mechanisms shown in the metering rods would facilitate axial adjustment. These could also be differential screws. Two-axis tilts of the mirror can be adjusted with these axial mechanisms.

Figure 8.43 is a photograph of a 4-in.-diameter, 0.5-in.-thick fused silica mirror to which three pads are bonded with epoxy. These pads are attached to a set of three radially compliant bipod flexures machined integrally into an Invar 36 mounting plate. The bipods isolate the mirror and minimize surface distortions from temperature changes acting differentially on the materials with different CTEs (Mammini et al., 2003).

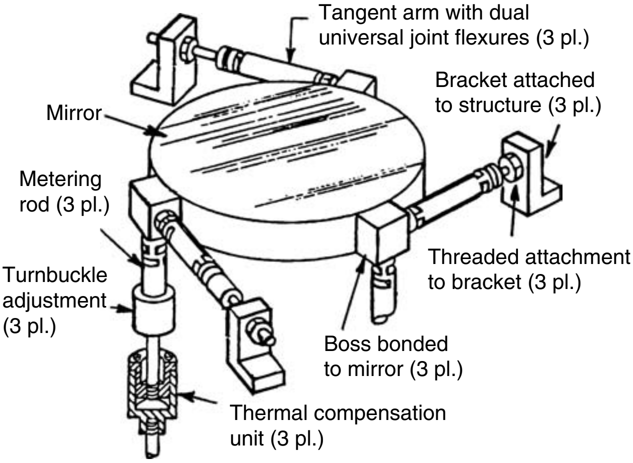
Tangent arm with dual universal joint flexures (3 pl.)
Bracket attached to structure (3 pl.)
Mirror
Metering rod (3 pl.)
Turnbuckle adjustment (3 pl.)
Threaded attachment to bracket (3 pl.)
Boss bonded to mirror (3 pl.)
Thermal compensation unit (3 pl.)

FIGURE 8.42 A system of flexures configured to minimize displacement, tilt, and/or distortion of the optical surface of a mirror caused by temperature changes or mounting forces. The mount also provides adjustments for all six degrees of freedom. (From Yoder, P.R., Jr., *Mounting Optics in Optical Instruments*, SPIE Press, Bellingham, 2002. With permission.)

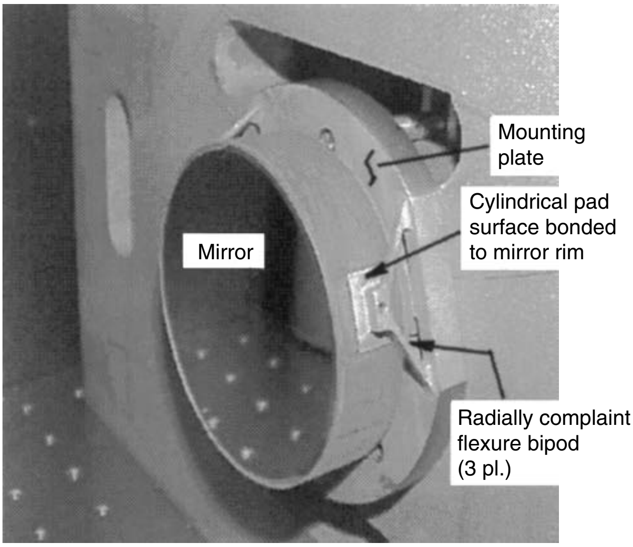
Mounting plate
Cylindrical pad surface bonded to mirror rim
Mirror
Radially complaint flexure bipod (3 pl.)

FIGURE 8.43 A 4-in.-diameter fused-silica mirror attached via pads to three radially compliant bipods machined integrally into an Invar 36 mounting plate. The pads are bonded to the mirror's rim with 3M 2216A/B epoxy. (From Mammini, P., Holmes, B., Nordt, A., and Stubbs, D., *Proc. SPIE*, 5176, 26, 2003. With permission.).

8.6 MULTIPLE-MIRROR MOUNTS

It is sometimes advantageous to use two or more mirrors in opto-mechanical subassemblies in order to serve some particular function. For example, two flat mirrors oriented at 45° to each other can be used to deviate a light beam by 90°. If rigidly attached together, this penta mirror will serve the same function as a penta prism but not require transmission of the beam through glass. This allows the penta mirror device to be used in the UV through IR spectral regions. Also, the weight of the penta mirror is generally lower than that of a penta prism of equivalent aperture.

A significant problem in the design and fabrication of multiple-mirror subassemblies is how to establish and hold the mirrors in the proper relative orientation so as to maintain long-term alignment stability and not distort the optical surfaces. One approach that has been used is to mechanically clamp the mirrors individually to a precision-machined metal block or to a built-up structure providing the appropriate angular and positional relationships between surfaces. Other approaches include bonding glass-to-glass or glass-to-metal parts and optical contacting glass parts. We next describe examples of these techniques.

Figure 8.44 shows a penta mirror constructed by mechanical clamping. Here, two rounded-end, rectangular, gold-coated mirrors were each held by three screws to three coplanar lapped pads on either side of an aluminum casting that accurately provided the 45° dihedral angle. The screws passed through clearance holes in the mirrors; each compressed two Belleville washers to preload the mirror against a pad. This hardware was used as part of an automatic theodolite system for prelaunch azimuth alignment of the Saturn space vehicles, so it was used in a generally stable environment inside a concrete bunker at Cape Canaveral (Mrus et al., 1971).

The bonded approach used successfully to make many stable penta mirror subassemblies for application in military optical rangefinders (see Patrick, 1969) had glass mirrors optically cemented on edge to a glass base plate as shown schematically in Figure 8.45. This subassembly was attached to the optical bar of the rangefinder. Figure 8.46 shows an actual penta reflector of this general type. The base plate in this example is metal. The useful aperture exceeds 50 mm (1.97 in.).

Figure 8.47 shows a penta mirror subassembly described by Yoder (1971) in which the polished faces of two flat Cer-Vit mirrors were optically contacted to a Cer-Vit angle block that had been ground and polished to within one arcsec of the nominal 45°. The angle block was hollowed out to reduce weight without reducing strength. Triangular Cer-Vit cover plates were then attached with optical cement to both the top and bottom of the assembly and a rectangular cover plate was cemented across its back. These three plates served not only as mechanical braces but also sealed the exposed edges of the contacted joints. An Invar plate was bonded to one of the cover plates to serve as a mounting interface. With mirror plates measuring approximately 11 × 16 × 1.3 cm (4.33

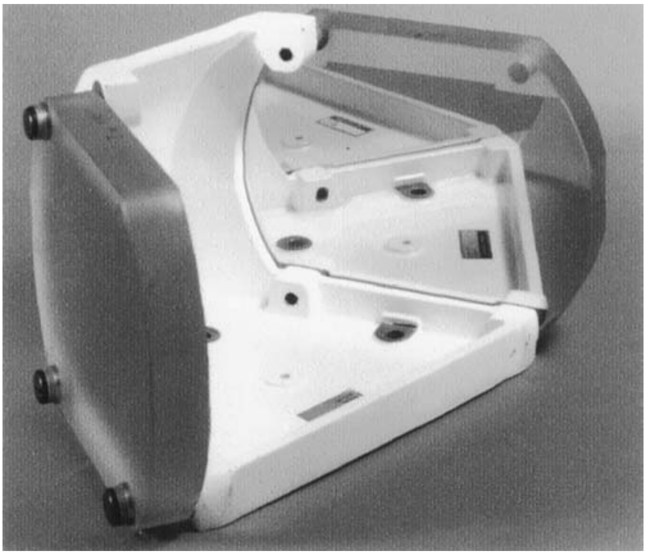

FIGURE 8.44 A penta mirror subassembly made by clamping mirrors directly to a precision metal casting. (Courtesy of Goodrich Corporation, Danbury, CT.)

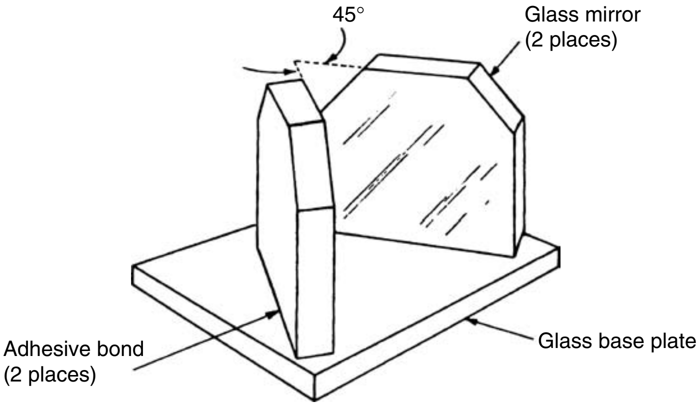

FIGURE 8.45 Penta mirror subassembly made by cementing mirrors on edge to a glass base plate.

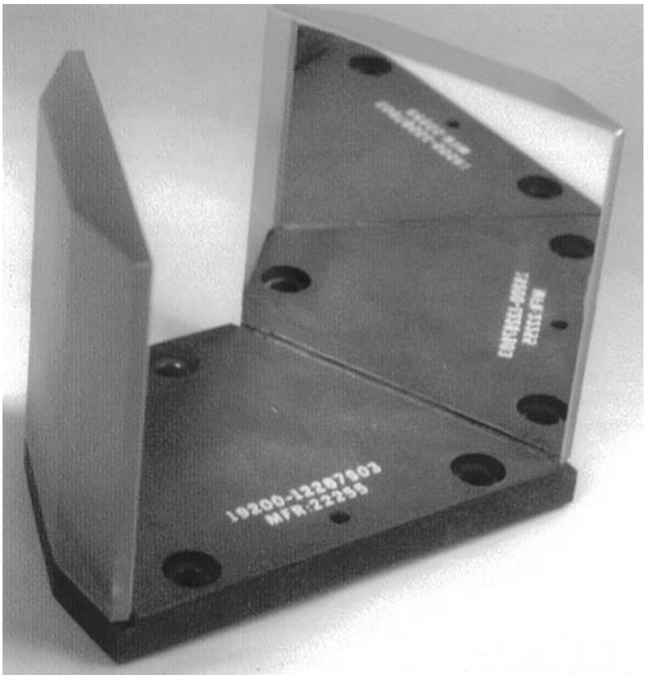

FIGURE 8.46 A penta mirror subassembly made by bonding mirrors on edge to a metal bracket. (Courtesy of PLX, Inc., Deer Park, NY.)

× 6.30 × 0.51 in.), the assembly had a clear aperture of 10 cm (3.94 in.). A roof penta mirror assembly of similar construction and size (see Figure 8.48) was also described in Yoder's paper.

To verify these optically contacted designs, a prototype of the penta mirror assembly was subjected to adverse thermal, vibration, and shock environments. First, it was temperature-cycled several times from −2 to +68°C (28 to 154° F) while monitoring the reflected wavefront interferometrically. The test setup was capable of detecting changes of $\lambda/30$ and had an inherent error of less than $\lambda/15$ for $\lambda = 0.63$ μm. The maximum thermally induced distortion in the penta mirror was $\lambda/4$ peak to valley. The assembly was then vibrated without failure at loadings up to

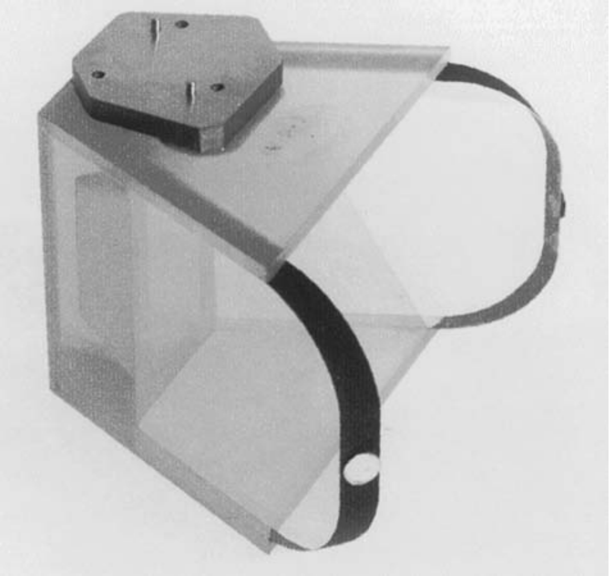

FIGURE 8.47 A penta mirror subassembly with an aperture of 10 cm (3.94 in.) made by optically contacting Cer-Vit components. (From Yoder, P.R., Jr., *Appl Opt.*, 10, 2231, 1971. With permission.)

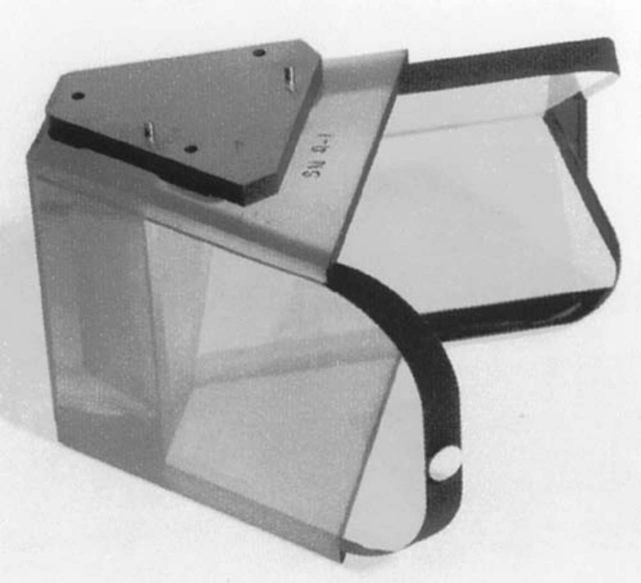

FIGURE 8.48 A roof penta mirror subassembly with an aperture of 10 cm (3.94 in.) made by optically contacting Cer-Vit components. (From Yoder, P.R., Jr., *Appl Opt.*, 10, 2231, 1971. With permission.)

5 g and frequencies of 5 to 500 Hz along each of three orthogonal axes. Resonances were noted at the higher frequencies in two axes. Shock testing at up to 28 g peak loading in 8 msec pulses in two directions also produced no permanent degradation of the prototype.

A roof mirror functionally equivalent to a Porro prism is shown in Figure 8.49. This assembly, made by PLX, Inc., Deer Park, NY, has an aperture of slightly over 1.75 in. (44.4 mm) × 4.0 in.

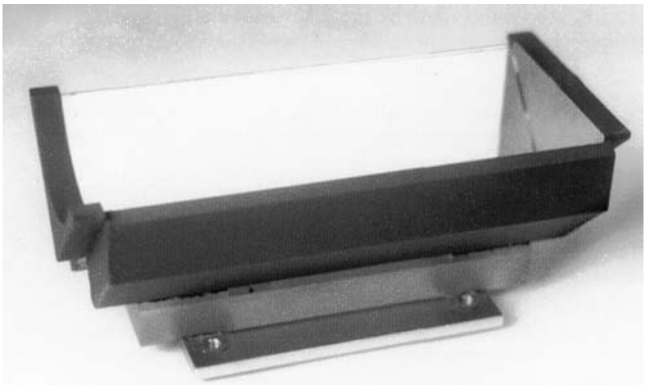

FIGURE 8.49 A Porro-type roof mirror assembly with an aperture approximately 1.75 in. (44.4 mm) by 4.0 in. (102 mm). (Courtesy of PLX, Inc., Deer Park, NY.)

(102 mm). Its mirrors are 0.5-in. (12.7-mm)-thick Pyrex. These mirrors are epoxied on one long edge to a Pyrex keel that is, in turn, bonded to a 0.125-in. (3.2-mm)-thick stainless steel mounting plate. The end plates are made with nominal 90° angles. Each plate is bonded to the top of one mirror and to the end of the other mirror. The mirrors are aligned to 90° within tolerances as small as 0.5 arcsec. The tolerance on mirror figure is as small as 0.1 wave at $\lambda = 0.63$ μm.

Figure 8.50 shows front and back views of a hollow corner retroreflector (HCR), which is the mirror version of a cube-corner prism. This unit, also made by PLX, Inc., comprises three, nominally square-faced Pyrex mirrors. The aperture of this unit is approximately 45 mm (1.77 in.). The mirrors are edge-bonded to each other and supported as a subassembly in an aluminum housing configured for ease of mounting using an elastomeric material (white) surrounding three rubbery inserts (gray). The accuracy of the 180° light deviation for such units typically lies between 0.25 and 5 arcsec. Reflected wavefront error can be as small as 0.08 wave of visible light, with the actual value depending upon aperture size. Apertures exceeding 5 in. (12.7 cm) are available.

Figure 8.51 depicts another commercially available HCR. According to Lyons and Lyons (2004), each of the three mirrors in this unit, made by PROSystems, Inc., Kearneysville, WV, is fashioned with a groove along one edge. Adjacent mirror edges are bonded together in these grooves. This design provides very small seam widths of 0.001 in. (25 μm) at the mirror interfaces. The dimensions relate the clear aperture to the outside frontal diameter of the device.

In the HCR shown in Figure 8.52, a glass plate is cemented at one end to the back of one mirror while, at the other end, it is bonded to a notch machined into a metal mounting base. The base has a threaded hole for attachment to the structure of the particular hardware application. Units with apertures of 2.50 in. (6.35 cm) and 4.00 in. (10.16 cm) have dimensions as indicated in the diagram. Pyrex or Zerodur mirrors and aluminum or Invar bases are used depending upon the temperature range of the application and cost constraints. Testing has indicated some models to be stable with regard to optical and mechanical performance over temperature ranges as large as ~ 200°C (~ 360°F). Some have operated well at 170 K.

Figure 8.53 illustrates a special kind of HCR in which the virtual apex of the 3-mirror array is located at the center of a metal sphere within 0.0001 to 0.0005 in. (2.54 to 12.70 μm). This type of device is commonly referred to as a spherically mounted retroreflector (SMR). Sphere diameters typically range from 0.5000 to 1.5000 in. (12.700 to 38.100 mm). SMRs are used in the manufacturing and metrology industries as targets for tracking and measuring distances with electro-optical coordinate measuring machine (CMM) or target trackers employing laser beams. One such tracker was described by Bridges and Hagan (2001). See Figure 8.54 for a schematic diagram of the function of

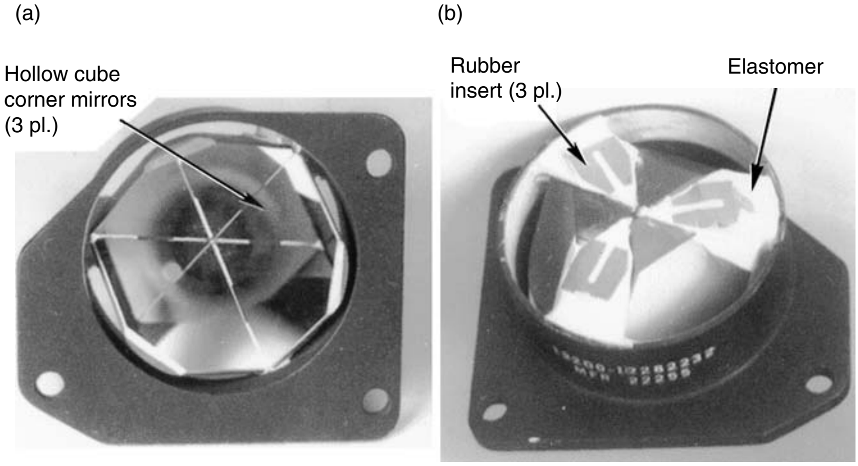

FIGURE 8.50 Front and back views of a hollow cube-corner retroreflector (HCR) of aperture ~ 45 mm (1.77 in.) mounted in a flange-type cell. (Courtesy of PLX, Inc., Deer Park, NY.)

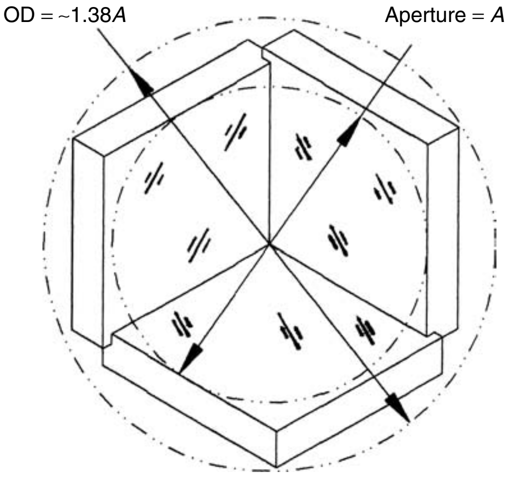

FIGURE 8.51 Frontal view schematic diagram of a hollow cube-corner retroreflector (HCR) as manufactured by PROSystems, Inc. (Courtesy of PROSystems, Inc., Kearneysville, WV.)

such a system. Those authors reported that the device measures feature locations on objects as far away as ~ 35 m (~ 115 ft) with an accuracy of ± 25 μm (± 0.001 in.) at 5 m (16.4 ft) range. Key to the success of such a device is absolute distance measurement in which round-trip time of flight of a modulated IR beam is transmitted coaxially with the tracker beam to the SMR. This allows measurements to be resumed without recalibration if the beam is temporarily obscured during operation. It also allows the system to monitor slow alignment drifts.

The bodies of the spherical targets are typically made of Type 420 CRES for corrosion resistance and magnetic characteristics. Target surfaces are CNC machined, hand ground, and polished to a high degree of sphericity (typically true spheres within ±0.000025 in. [0.64 μm]). They can be held magnetically in three-faced (kinematic) pockets on the tracker for system calibration. During operation, the target is attached to or held by hand in contact with the surface or feature to be measured. As the target is moved over the surface, the tracker determines the surface coordinates at

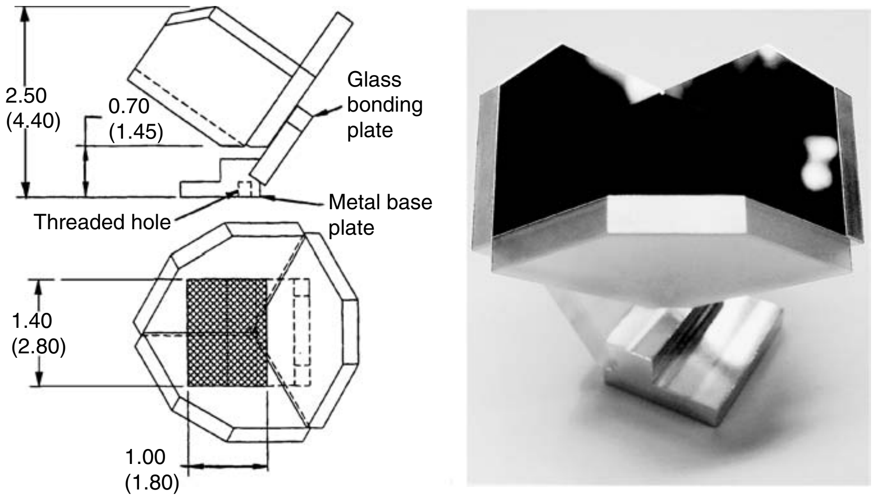
2.50
(4.40)
0.70
(1.45)
Glass bonding plate
Threaded hole
Metal base plate
1.40
(2.80)
1.00
(1.80)

FIGURE 8.52 Schematic diagram and photograph of a HCR bonded to a metal base. Dimensions pertain to models with ODs of 2.50 in. and (4.00 in.). (Courtesy of PROSystems, Inc., Kearneysville, WV.)

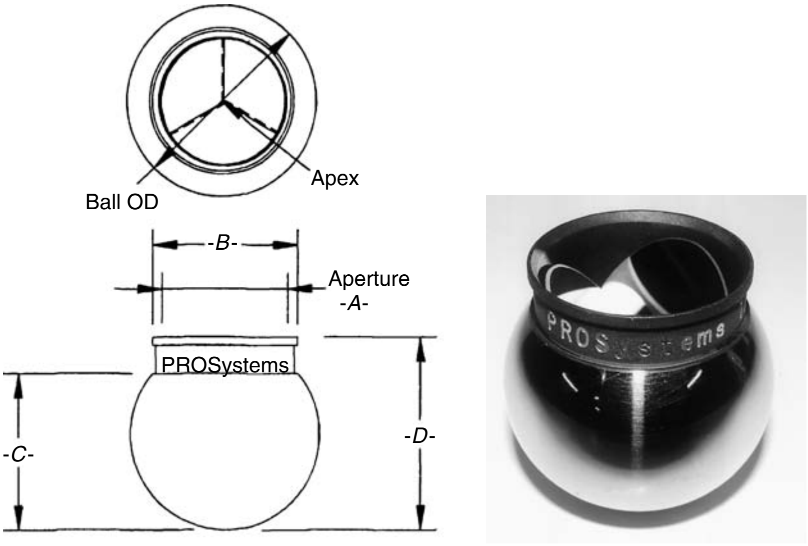
Apex
Ball OD
-B-
Aperture
-A-
PROSystems
-C-
-D-
PROSystems

FIGURE 8.53 Schematic diagram and photograph of a spherically mounted hollow retroreflector (SMR). Dimensions (in in.) are A = 0.30, 0.50, and 1.00; B = 0.37, 0.60, and 1.15; C = 0.42, 0.73, and 1.23; and D = 0.52, 0.92, and 1.51 for sphere diameters of 0.500, 0.875, and 1.500 in., respectively. (Courtesy of PROSystems, Inc., Kearneysville, WV.)

selected points and, hence, its contour and the relative locations of features on the surface. The system's software automatically compensates for the radius of the sphere.

It is important in this application that errors in the dihedral angles and the maximum differences between those angles for a given target unit are small. As pointed out by Yoder (1958), angle errors from exactly 90° in a cube-corner prism or in an HCR determine the absolute accuracy of 180° beam deviation. The return beam actually comprises six beams. Two come from each mirror. For an HCR, the worst-case deviation error δ is given by

$$\delta = 3.26\varepsilon \tag{8.33}$$

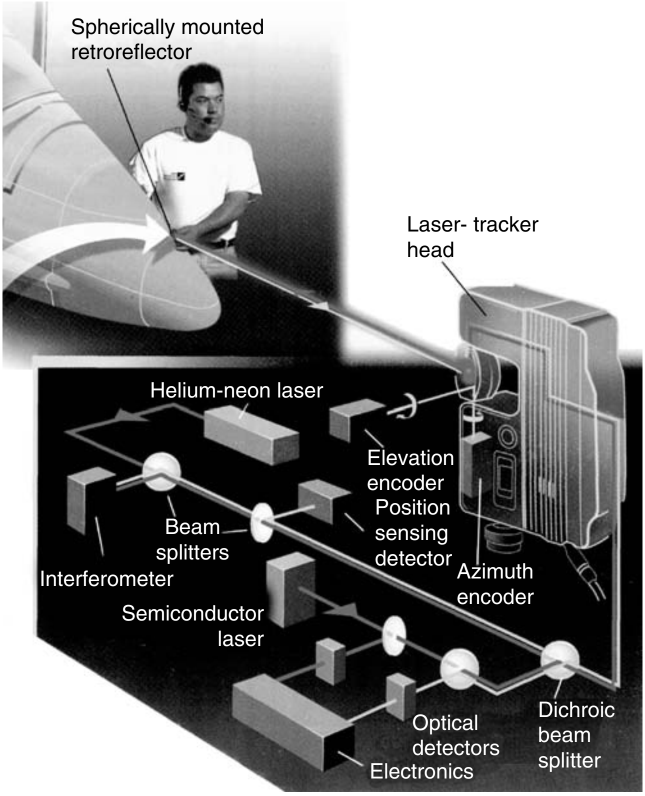
Spherically mounted retroreflector
Laser- tracker head
Helium-neon laser
Elevation encoder
Position sensing detector
Beam splitters
Interferometer
Azimuth encoder
Semiconductor laser
Optical detectors
Electronics
Dichroic beam splitter

FIGURE 8.54 Function of a laser tracker using a SMR to remotely measure locations of selected points on a distant object. (From Bridges, R. and Hagan, K., *The Industrial Physicist,* 28, 200, 2001, Copyright 2001, American Institute of Physics.)

where ε is the error in dihedral angle and all such errors are equal and have the same sign. In a laser tracker application, if deviation errors are too large, the tracker will “jump” from one return beam to another at long target ranges. The angle errors and the differences between angles determine the value for the constant in Eq. (8.33). SMRs offered by PROSystems, Inc. typically have angle errors ranging from 3 to 10 arcsec and angle differences of 2 to 10 arcsec. Apex centration error is as small as 0.0002 in. (5.1 μm).

An important characteristic of an HCR is the coating applied to the mirrors. Ordinary first-surface mirror coatings could introduce a phase shift into the polarized light beam from the tracker. This would degrade the system’s performance. Special coatings can be applied to the mirrors to minimize this problem. One type of coating that reduces this phase shift is the “Zero Phase Silver” coating offered by Denton Vacuum Company, Moorestown, NJ. Bridges and Hagan (2001) indicated that the actual residual phase shifts introduced by the coatings on a batch of mirrors should be measured and sets of mirrors with similar phase shifts selected for use in a given SMR unit. This tends to maximize the range at which the tracker can acquire and track that particular target.

An interesting adaptation of the design of a hollow corner retroreflector is the lateral transfer retroreflector (LTR). An example of a device of this type, commercially available from PLX, Inc., Deer Park, NY, is shown in Figure 8.55. It comprises a single mirror at one end of an elongated box and a roof mirror at the other end of that box. All three mirrors are mutually perpendicular, so the device acts as a “slice” through an HCR of very large aperture. Lateral offsets of the beam up to 30 in. (76 cm) and apertures up to 2 in. (5 cm) are available.

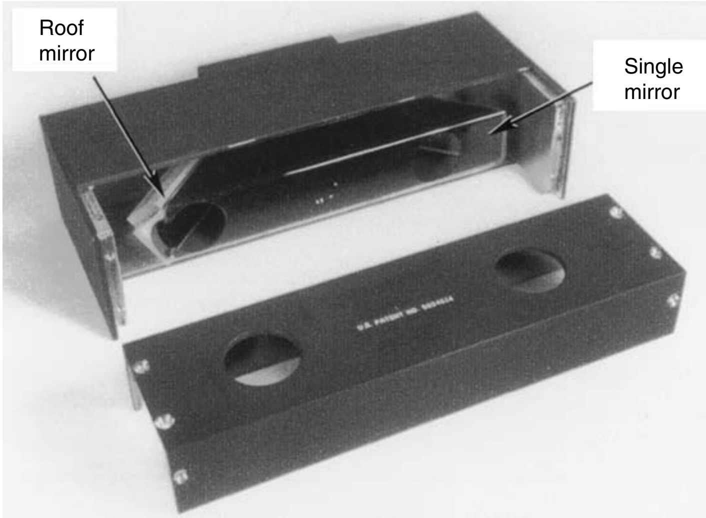

FIGURE 8.55 A commercially available lateral transfer hollow retroreflector of aperture ~ 1.0 in. (2.5 cm) and offset approximately 5 in. (13 cm) with cover removed to show the mirrors. (Courtesy of PLX, Inc., Deer Park, NY.)

8.7 MOUNTINGS FOR GRATINGS

The substrates for gratings are similar to those for mirrors. The grating surface is typically contoured with shallow parallel grooves or saw-tooth steps that diffract the incident radiation and split it spectrally into its constituent "colors." A typical grating is created by ruling with a diamond point into an evaporated metallic film such as aluminum on a glass substrate. The grooves so produced are extremely parallel and uniform in depth and contour. Typically, a grating for visible light spectroscopy has about 15,000 grooves. Finer patterns can be created; the limit is established by the capability of the machine doing the ruling.

Gratings are frequently used in laboratory environments with the temperature carefully controlled and the related optical components mounted for extreme long-term stability. Portable instruments and those destined for aerial or space missions are designed to minimize the effects of vibration and maximize stability under changing temperature. One particular space borne spectrograph is described below as an example of careful design.

The Far Ultraviolet Spectroscopic Explorer (FUSE) is a NASA-sponsored, low earth-orbiting astrophysical observatory that was designed to provide high spectral resolution observations across a 905 to 1195 Å spectral band. Figure 8.56 shows the optical arrangement of the spectrograph schematically. Light is collected by four off-axis parabolic telescope mirrors (not shown) and focused onto four slit mirrors that act both as movable entrance slits for the spectrometer and as mirrors that direct the visible star field to fine error sensors (also not shown). The diverging light passing through the slits is diffracted and reimaged by four holographic grating mount assemblies. The spectra are collected on two microchannel plate detectors. The orbital temperature operating range is 15 to 25°C while the survival range is 10 to 40°C. During an observation, the temperature is stabilized within 1°C.

According to Shipley et al. (1995, 1997), the four gratings are identical in size at 266 × 275 × 68.1 mm (10.422 × 10.827 × 2.681 in.). They are made of Corning 7940 fused silica, class 0, grade F. This material was chosen for its low CTE and ability to accommodate the process of adding holographic gratings. The weight of each blank is reduced by machining the rib pattern shown in Figure 8.57 in its back surface. Two corners were removed to accommodate an anticipated envelope interference.

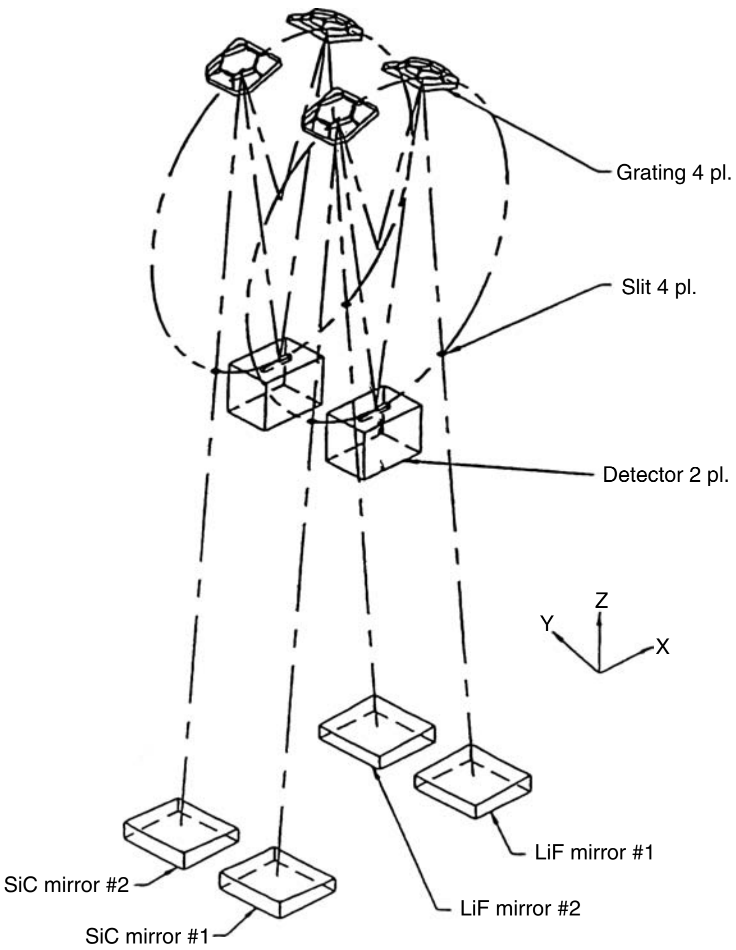

FIGURE 8.56 Optical configuration of the FUSE spectrograph. (From Shipley, A., Green, J.C., and Andrews, J., *Proc. SPIE,* 2542, 185, 1995. With permission)

Strength and fracture control requirements dictated that the blank be acid etched after ruled surfaces were coated with LiF or SiC to optimize performance in the desired spectral bands.

The mounting brackets, made of Invar, were constructed with rectangular pockets that were bonded with Hysol EA9396 epoxy to the ribs machined into the back of the substrates. Tests of bonded samples showed that the bond strength consistently was $>$ 4000 lb/in.^{2}, with some samples exceeding 5000 lb/in.^{2}. This bond strength was considered more than adequate for the application.

Calculations of fracture probability using Gaussian and Weibull statistical methods were inconclusive. The fact that the nonoptical surfaces of the gratings were not polished contributes significantly to this problem. In order to ensure success, a conservative mechanical interface design was employed. This design was thoroughly evaluated by finite-element means throughout the design evolution. One major improvement was to add the flexure pivots shown in Figure 8.58 to allow compliance in the directions perpendicular to the radial flexures. The radial flexure blades were reduced in length to accommodate this addition while maintaining the height of the mechanism.

Figure 8.59 shows details of the flexure pivot installations. Each pivot comprises outer and inner pivot housings, two 0.625-in. (15.88-mm)-diameter welded cantilevered units, and eight cone-point setscrews. The location of each pivot is maintained by the setscrews, which are driven into shallow conical divots machined at two places at each cantilevered end of the flexure. Rigorous vibration testing of prototype and flight model grating mounts confirmed the success of the design.

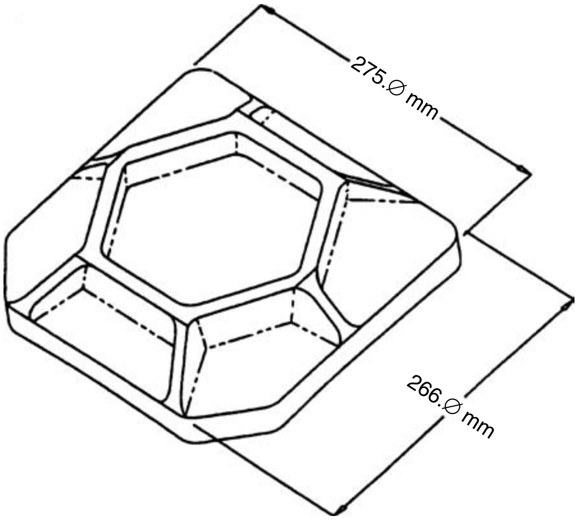
275.∅ mm
266.∅ mm

FIGURE 8.57 View of the back side of the FUSE grating showing its machined rib structure. (From Shipley, A., Green, J.C., and Andrews, J., *Proc. SPIE,* 2542, 185, 1995. With permission.)

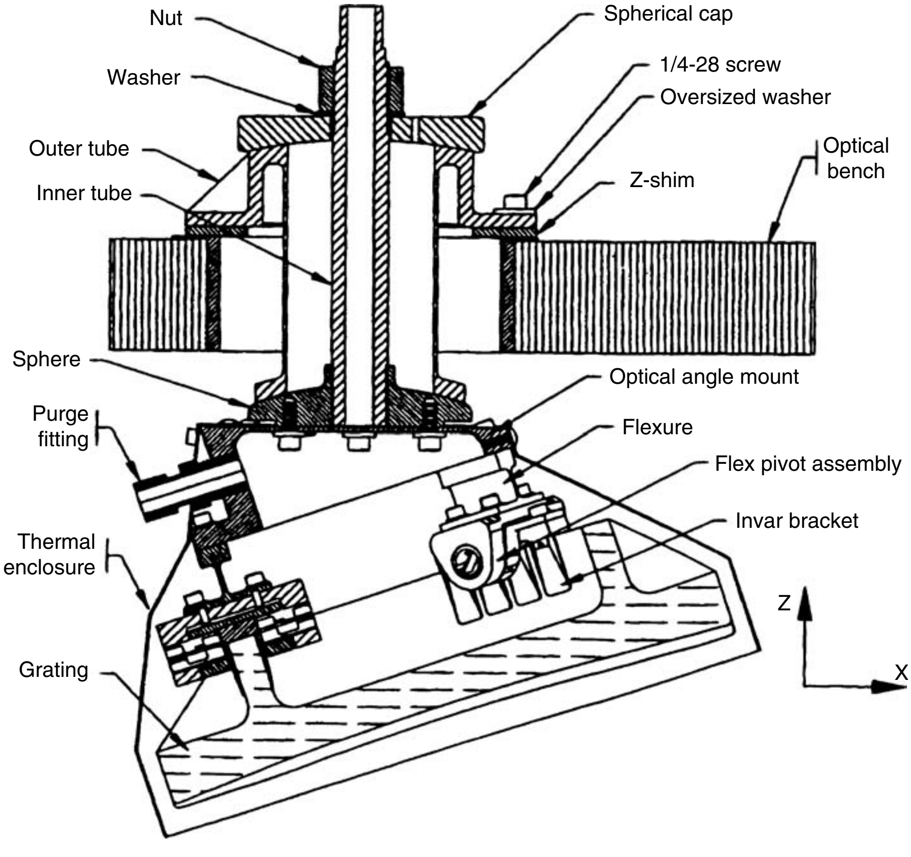
Nut
Washer
Outer tube
Inner tube
Sphere
Purge fitting
Thermal enclosure
Grating
Spherical cap
1/4-28 screw
Oversized washer
Z-shim
Optical bench
Optical angle mount
Flexure
Flex pivot assembly
Invar bracket
Z
X

FIGURE 8.58 Sectional view of the grating mount showing its adjustment provisions. (From Shipley, A., Green, J.C., Andrews, J., Wilkinson, E., and Osterman, S., *Proc. SPIE*, 3132, 98, 1997. With permission.)

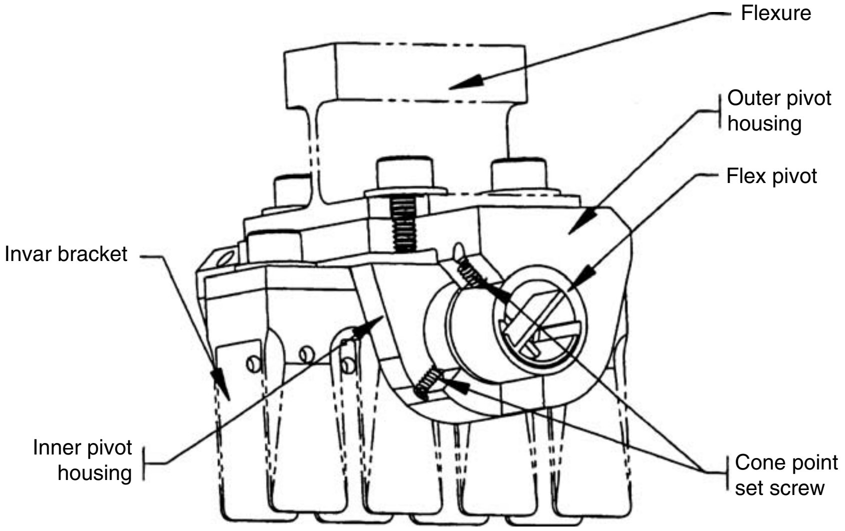

FIGURE 8.59 Detail view of the flex pivot feature in the grating mount. (From Shipley, A., Green, J.C., Andrews, J., Wilkinson, E., and Osterman, S., *Proc. SPIE*, 3132, 98, 1997. With permission.)

The wedge-shaped optical angle mounting seen in Figure 8.59 between the radial flexures and the bottom of the outer tubular central structure orients the grating at the proper angle relative to the coordinate system of the device. A custom spacer was used between the outer tube and the optical bench for axial adjustment. The outer tube interfaces with spherical seats at top and bottom. This allows fine adjustment of the angular orientation by external motorized screws in an alignment fixture. This adjustment is clamped by torquing the nut at the top of the assembly. Optical cubes attached to the gratings are used with theodolites as the metrology means during alignment.

Titanium was used extensively in the grating mount because of its high strength and relatively low CTE. All titanium parts except the flexures were Tiodized* to reduce friction between mating surfaces during alignment and to facilitate cleaning at assembly. The convex sphere and the spherical washer of Figure 8.59 were made of type 17-4-PH CRES, the nut was type 303 stainless steel, and the Z-shim was a type 400 stainless steel.

8.8 PELLICLE DESIGN AND MOUNTING

Very thin films of material such as nitrocellulose, polyester, or polyethylene can be used as substrates for mirror, and beam splitter or beam combiner coatings. Their thicknesses are typically 5 μm (0.0002 in.) ±10%, although 2-μm (0.00008-in.)-±10%-thick films are available commercially. Special pellicles as thick as 20 μm (0.0008 in.) can also be made. The surface quality of standard varieties is typically better than 40/20 scratch and dig while visible light figure typically is 0.5λ to 2λ per inch. The base material transmits well (> 90%) from 0.35 to 2.4 μm, but has numerous, deep, absorbing regions beyond 2.4 μm. Figure 8.60 provides a simplified representation of the transmission characteristics of a typical standard type pellicle. Pellicles can be coated to reflect, split, or combine light beams in the visible to near-IR region with conventional or custom-designed coatings. Standard A/R coatings can be applied to the back side of the films.

---

*Tiodize® is a proprietary metal treating process from Tiodize, Co., Huntington Beach, CA.

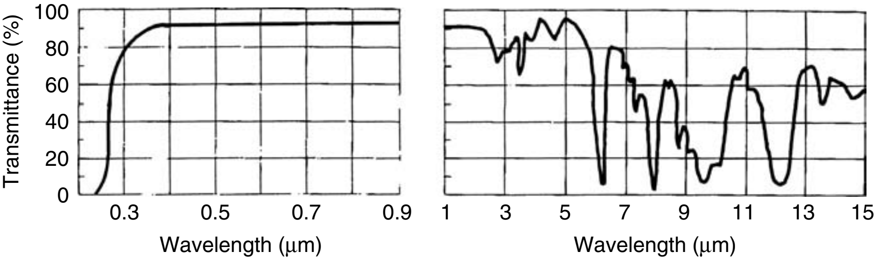

FIGURE 8.60 Simplified transmission characteristics of a standard nitrocellulose pellicle in the visible and infrared regions. (Courtesy of National Photocolor Corp., Mamaroneck, NY.)

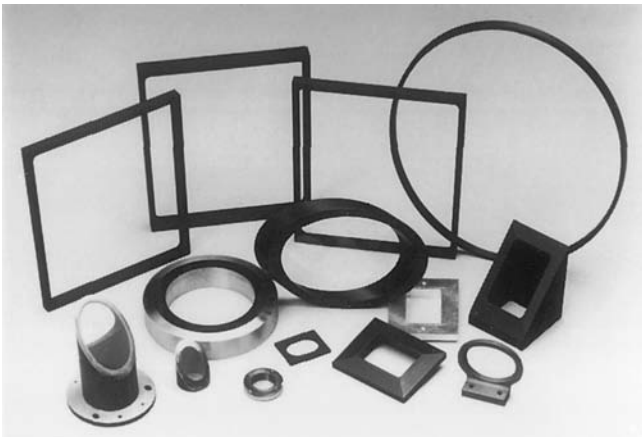

FIGURE 8.61 A variety of nonstandard pellicle mounts (frames) as supplied by one manufacturer. (Courtesy of National Photocolor Corp., Mamaroneck, NY.)

A prime advantage of a pellicle over thicker conventional glass components is the absence of ghost imaging since the first- and second-surface reflections at normal or oblique incidence are so close together they appear superimposed. Interference effects may, however, be seen. A pellicle with uncoated front and A/R-coated back surfaces at 45° incidence can serve as a 4% visible light beam sampler. If both surfaces are uncoated, it would have about 8% total reflectance and transmittance of about (0.92)(0.90) = 83% in the visible spectral passband.

Pellicles are supported by circular, square, or rectangular frames with beveled and lapped front surfaces to which the stretched film is attached. Frames typically are black anodized aluminum and have holes for mounting. Special units can be made of stainless steel or ceramic. Figure 8.61 shows some nonstandard pellicle frames as supplied by one manufacturer. The configurations and dimensions of a few standard pellicle frames are shown in Figure 8.62.

Since pellicles are so thin, they are much more fragile than conventional plane-parallel glass plates. They are susceptible to acoustic vibration of adjacent air volumes, but work well in a vacuum. Some thicker varieties made of polyester films can be used under water. The temperature range of pellicle usefulness is about +40 to +90°C. They can tolerate relative humidity to about 95%. The frames supporting pellicles must be mounted so that they are not deformed, because that would distort the optical surfaces. Semikinematic interfaces would be desirable. These can be achieved with localized flat and coplanar pads on both mating parts and screws passing through those pads. Custom frames can be designed to have stiffer configurations than the standard versions. These thicker frames will withstand more significant mounting forces.

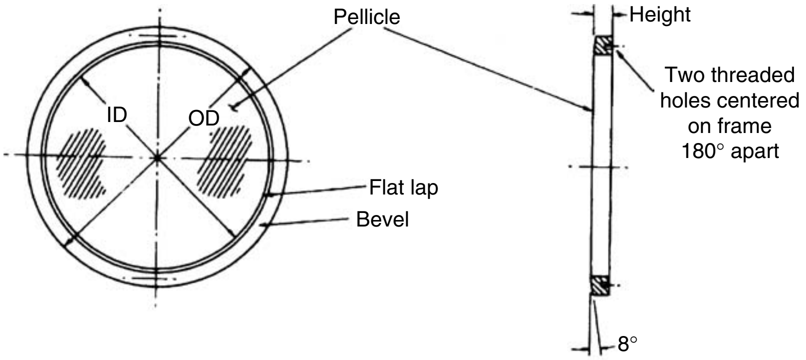
Pellicle
Height
Two threaded holes centered on frame 180° apart
ID
OD
Flat lap
Bevel
8°

Size	ID	OD	Height	Mounting holes
1″	1″(25.4 mm)	$1^{3}/_{8}$″(34.9 mm)	$^{3}/_{16}$″(4.8 mm)	#2-56 thd. × $^{1}/_{8}$″ dp.
2″	2″(50.8 mm)	$2^{3}/_{8}$″(60.3 mm)	$^{3}/_{16}$″(4.8 mm)	#2-56 thd. × $^{1}/_{8}$″ dp.
3″	3″(76.2 mm)	$3^{1}/_{2}$″(88.9 mm)	$^{1}/_{4}$″(6.4 mm)	#6-32 thd. × $^{1}/_{8}$″ dp.
4″	4″(101.6 mm)	$4^{1}/_{2}$″(114.3 mm)	$^{1}/_{4}$″(6.4 mm)	#6-32 thd. × $^{1}/_{8}$″ dp.
5″	5″(127.0 mm)	$5^{1}/_{2}$″(139.7 mm)	$^{5}/_{16}$″(7.9 mm)	#6-32 thd. × $^{1}/_{8}$″ dp.
6″	6″(152.4 mm)	$6^{1}/_{2}$″(165.1 mm)	$^{3}/_{8}$″(9.5 mm)	#6-32 thd. × $^{3}/_{16}$″ dp.

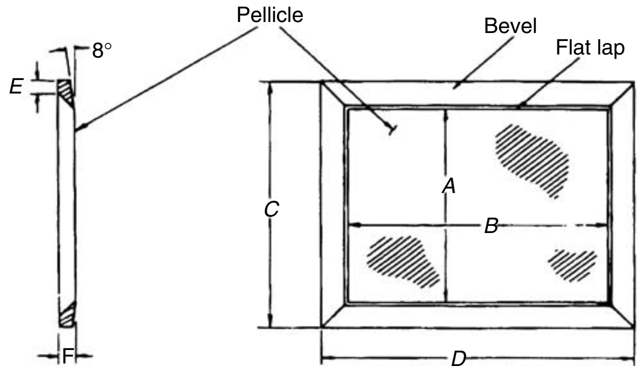
Pellicle
Bevel
Flat lap
8°
E
F
A
B
C
D

Nominal dimensions

	Inches	Millimeters
A	5	127.0
B	7	177.8
C	$6^{5}/_{8}$	168.3
D	$6^{3}/_{8}$	212.7
E	$^{5}/_{16}$	7.9
F	$^{5}/_{16}$	11.1

FIGURE 8.62 Some standard pellicle frame designs and dimensions. (Courtesy of National Photocolor Corp., Mamaroneck, NY.)

REFERENCES

Bridges, R. and Hagan, K., Laser tracker maps three-dimensional features, *The Industrial Physicist*, 28, 200, 2001.

Durie, D.S.L., Stability of optical mounts, *Mach. Des.*, 40, 184, 1968.

Hatheway, A.E., Analysis of adhesive bonds in optics, *Proc. SPIE*, 1998, 2, 1993.

Høg, E., A kinematic mounting, *Astron. Astrophys.*, 4, 107, 1975.

Hookman, R., Design of the GOES telescope secondary mirror mounting, *Proc. SPIE*, 1167, 368, 1989.

Hopkins, R.E., Mirror and prism systems, in *Applied Optics and Optical Engineering*, Vol. III, Kingslake, R.., Ed, Academic Press, New York, 1965, chap. 7.

Jenkins, F.A. and White, H. E., *Fundamentals of Optics*, McGraw-Hill, New York, 1957.

Kaspereit, O.K., *Design of Fire Control Optics ORDM2-1*, Vol. I, U.S. Army, Washington, DC, 1952.

Lipshutz, M.L., Optomechanical considerations for optical beam splitters, *Appl. Opt*., 7, 2326, 1968.

Lyons, P.A. and Lyons, J.J., private communication, 2004.

Mammini, P., Holmes, B., Nordt, A., and Stubbs, D., Sensitivity evaluation of mounting optics using elastomer and bipod flexures, *Proc. SPIE*, 5176, 26, 2003.

MIL-STD-1472D, *Human Engineering Design Criteria for Military Systems, Equipment, and Facilities,* U.S. Department of Defense, Washington, DC, 1989.

Miller, K.A., Nonathermal potting of optics, *Proc. SPIE*, 3786, 506, 1999.

Mrus, G.J., Zukowsky, W.S., Kokot, W., Yoder, P.R., Jr., and Wood, J.T., An automatic theodolite for pre-launch azimuth alignment of the Saturn Space Vehicles, *Appl. Opt.*, 10, 504, 1971.

Patrick, F.B., Military optical instruments, in *Applied Optics and Optical Engineering*, Vol. V Kingslake, R., Ed, Academic Press, New York, 1969, chap. 7.

Roark, R.J., *Formulas for Stress and Strain*, 3rd ed., McGraw-Hill, New York, 1954.

Schubert, F., Determining optical mirror size, *Mach. Des.*, 51, 128, 1979.

Shigley, J.E. and Mischke, C.R., *The design of screws, fasteners, and connections*, in *Mechanical Engineering Design*, 5th ed., McGraw-Hill, New York, 1989, chap. 8.

Shipley, A., Green, J.C., and Andrews, J., The design and mounting of the gratings for the Far Ultraviolet Spectroscopic Explorer, *Proc. SPIE*, 2542, 185, 1995.

Shipley, A., Green, J.C., Andrews, J., Wilkinson, E., and Osterman, S., Final flight grating mount for the Far Ultraviolet Spectroscopic Explorer, *Proc. SPIE*, 3132, 98, 1997.

Smith, W.J., *Modern Optical Engineering*, 3rd ed., McGraw-Hill, New York, 2000.

Tiodize Process Literature, Tiodize Co., Huntington Beach, CA.

Vukobratovich, D. and Richard, R., Flexure mounts for high-resolution optical elements, *Proc. SPIE*, 959, 18, 1988.

Vukobratovich, D., Introduction to optomechanical design, *SPIE Short Course SC014*, 2003.

Yoder, P.R., Jr., Study of light deviation errors in triple mirrors and tetrahedral prisms, *J. Opt. Soc. Am.*, 48, 496, 1958.

Yoder, P.R., Jr., Non-image-forming optical components, *Proc. SPIE*, 531, 206, 1985.

Yoder, P.R., Jr., Design guidelines for bonding prisms to mounts, *Proc. SPIE*, 1013, 112, 1988.

Yoder, P.R., Jr., High precision 10-cm aperture penta and roof-penta mirror assemblies, *Appl. Opt*., 10, 2231, 1971.

Yoder, P.R., Jr., Optical mounts: lenses, windows, small mirrors, and prisms, in *Handbook of Optomechanical Engineering*, Ahmad, A., Ed., CRC Press, Boca Raton, FL, 1997, chap. 6.

Yoder, P.R., Jr., *Mounting Optics in Optical Instruments*, SPIE Press, Bellingham, 2002.

9 Lightweight Nonmetallic Mirror Design

9.1 INTRODUCTION

Various configurations for lightweight substrates for larger mirrors are considered from the mechanical design viewpoint in this chapter. It is important to study this subject before examining mounting arrangements for such mirrors, since the performance of the assembly depends significantly on the design compatibility of the substrate and the mount. Here, we deal primarily with the mirror's geometric configuration. Because mirror size is a prime driver of design and of material choice, we consider sizes ranging from about 51 cm (~ 20 in.) (the upper limit considered in Chapter 8) to large, astronomical telescope-sized ones with diameters up to 8.4 m (27.6 ft). As diameters increase, minimizing weight is increasingly important from the total system weight viewpoint and to minimize self-weight deflection effects. We therefore consider various ways of reducing mirror weight by removing unnecessary material from a solid piece or combining separate pieces to create a built-up structure. Mounting methods for larger nonmetallic mirrors are discussed in Chapters 10–12. Metal mirrors and their mounts are also not included here; those are the subjects of Chapter 13.

No matter what technique is used to minimize mirror weight, the end product must be of high quality and capable of economical fabrication and testing. Rodkevich and Robachevskaya (1977) correctly stated the fundamental requirements for precision mirrors and lightweight versions of them. These statements may be paraphrased as follows:

1. The mirror material must be highly immune to outside influences such as mechanical forces and temperature changes; it must be isotropic and possess stable properties and dimensions.
2. The mirror material must accept a high-quality polished surface and a coating having the required reflection characterisics.
3. The mirror construction must be capable of being shaped to a specified optical surface contour, must retain this shape under operating conditions, and return to this contour after exposure to extreme conditions.
4. Lightweight mirrors must have a lower mass than those of equivalent size made to traditional designs — while maintaining adequate stiffness and homogeneity of properties.
5. Similar techniques should be used for fabricating conventional and lightweight mirrors.
6. If possible, mounting and load relief during both testing and use should employ conventional techniques and should not excessively increase the mass of the mirror and the complexity of the mechanisms involved.

These principles would serve as useful guidelines for the design of any mirror. Material availability and selection, fabrication methods, dimensional stability, and configuration design are key elements in meeting these demanding guidelines.

Designs for lightweight mirrors have developed over many years — primarily for astronomical purposes. The same basic design principles apply to mirrors for space science and communications systems, for large laser beam directors, or for a host of other military and aerospace applications.

Many of the design principles discussed here apply to smaller mirrors as well, since excess weight is detrimental to many common optical instruments using mirrors.

Seibert (1990) provided a “menu” for selecting a mirror/mount design from the variety of candidate structural constructions, surface contours, materials, and mount configurations. This menu is shown in Figure 9.1. The path indicated by arrows is one possible combination of an unsymmetrical, sandwich structure in a meniscus shape made of ULE and supported on a whiffletree mount. The number of possible combinations that can be made from the items listed here is obviously quite large. In order to select the “optimum” combination, one must consider many performance-related requirements, such as the magnitude and distribution of allowable surface figure errors at various possible orientations under self-weight, gravity-free or acceleration conditions; thermal inputs and losses, including gradients; coating spectral reflectance and durability; microroughness contributions to scatter; radiation hardening requirements; overall and local size and weight constraints; material availability; production feasibility and lead time; cost; etc. Although only a few of these requirements can be treated in any detail here, this chapter is intended to help the reader understand the advantages and disadvantages of various types of lightweight mirror designs.

9.2 MATERIAL CONSIDERATIONS

Table 3.13 lists material properties, such as coefficient of thermal expansion, thermal conductivity, Poisson’s ratio, Young’s modulus, and density, that relate to a mirror’s inherent behavior under static and dynamic environmental conditions. Dimensional stability and homogeneity of properties differ from one material type to another. Further information on these topics may be found in other publications, such as those by Englehaupt (1997) and Paquin (1997).

If minimizing weight is not a driving requirement, solid pieces of glass or metal may be used for mirrors of modest size. Once the material has been chosen, the major concerns during mirror design are to provide the necessary size (diameter and thickness); the mounting interface; and optical parameters such as curvature, asphericity, and central perforations. Thickness-to-diameter ratios of 1:5 to 1:10 are common with solid substrates. Thin substrates pose severe problems in mounting, as will be considered in depth in the next three chapters.

An important design consideration in choosing the thickness-to-diameter relationship is the ratio of material Young’s modulus of elasticity E to density ρ because this ratio enters into calculations of the self-weight deformations of the finished product. Table 3.15 lists this so-called “specific stiffness” for a variety of materials of interest. A large number is favorable. Table 3.16 gives a variety of

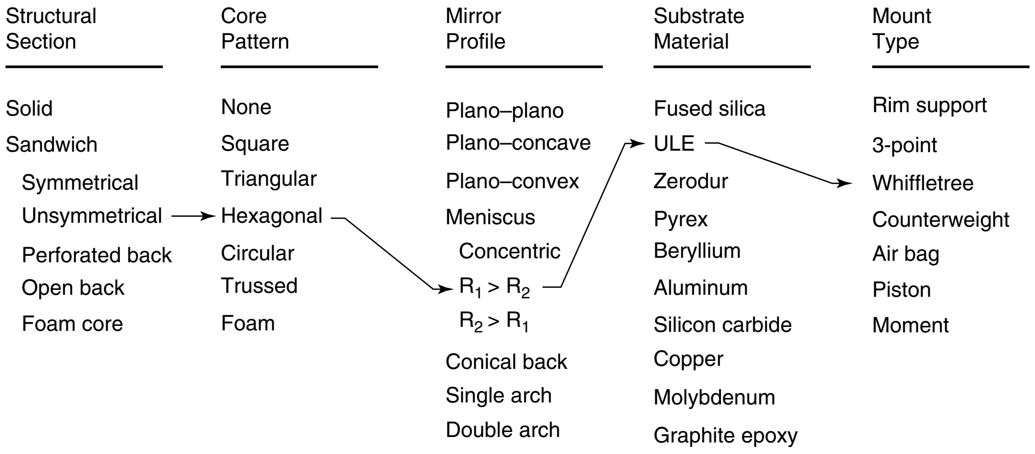
Structural Section
Core Pattern
Mirror Profile
Substrate Material
Mount Type
Solid
Sandwich
Symmetrical
Unsymmetrical
Perforated back
Open back
Foam core
None
Square
Triangular
Hexagonal
Circular
Trussed
Foam
Plano–plano
Plano–concave
Plano–convex
Meniscus
Concentric
$R_1 > R_2$
$R_2 > R_1$
Conical back
Single arch
Double arch
Fused silica
ULE
Zerodur
Pyrex
Beryllium
Aluminum
Silicon carbide
Copper
Molybdenum
Graphite epoxy
Rim support
3-point
Whiffletree
Counterweight
Air bag
Piston
Moment

FIGURE 9.1 “Menu” of possible structural and shape configurations, materials, and mounting arrangements for lightweighted mirrors. One possible combination is indicated by arrows. (Adapted from Seibert, G.E., *SPIE Short Course SC18*, 1990.)

other criteria for choosing the mirror material as given by Paquin (1997). It includes proportionality factors for weight, resonant frequency, and self-weight deflections as well as two types of thermal distortion coefficients under slow or rapid temperature changes. For a successful mirror, these factors should, of course, be small.

It should be noted that no material listed in Table 3.16 is optimum for all criteria. If the weight of a mirror of given aperture is to be reduced from that of the equivalent solid disk, techniques other than reducing axial thickness must be employed. Generally, the approach to passive weight reduction is either to create cavities within the substrates (as discussed in Sections 9.3–9.8) or to contour the rear surface into spherical, conical, or arch shapes. The latter approach to lightweighting is discussed in Section 9.9. Mirrors with thin face sheets are discussed in Section 9.10. General scaling relationships for lightweight mirrors are considered in Section 9.11.

One technique for lightweighting utilizes a sandwich structure with a fine cellular or porous foam core possessing physical properties significantly different from those of the base material used. Foam pyroceram, foam silica, foam Zerodur, foam metal, and metal matrix materials are typical of this case. Some mirrors with thin front and back plates attached to a nonmetallic foam core have been built (see Vukobratovich, 1989). Metal foam core mirrors are considered in Section 13.6.

Mirror structures with large substrate cells are practical and have been utilized successfully in many large, operational, ground-based and spaceborne optical systems. In these cellular structures, the materials retain the characteristics of the base materials, thereby facilitating the optomechanical design process.

Although the choice of proper material for a given application is very important to the success of a mirror design, the processes used in its fabrication are also major considerations. Typical fabrication methods, surface finishes, and coatings for mirrors made of various materials are listed in Table 3.28.

9.3 CORE CELL CONFIGURATIONS

A mirror lightweighted with a cellular or a cored cross section is structurally more efficient than its equivalent-sized solid version. Mirrors of this type are frequently called *honeycomb* structures. Provision of axial supports (parallel to the axis), radial supports (normal to the axis), and "defining supports" (typically three axially adjustable hard points locating and orienting the mirror) pose major design issues. Some designs have the supporting forces applied within the interior of the substrate at or near the neutral surface where gravitational moments of the localized volumes are balanced. Gross material density near the neutral surface of the mirror that contributes little to bending stiffness is usually reduced by lightweighting. Shear deflections are, however, increased so they may partially offset the bending stiffness improvement. Since mirror weight is reduced, the net stiffness-to-weight ratio generally improves.

Figure 9.2 shows five basic built-up structures used for lightweight cellular mirrors. In some designs, the core is integral, and the front and back face sheets (or face plates) and unwanted material are machined away. In others, the core is made as a separate part and completely or partially attached to those sheets. Attachment means for the latter types of construction include fusion bonding, "frit" bonding, adhesive bonding, and (for metal mirrors) brazing and welding. The geometric parameters available to the designer for lightweighting a mirror are material characteristics; face sheet thickness; strut* height, spacing, and thickness; and cell size and pattern. Figure 9.3 shows in views (b)–(d), the three commonly used cell patterns for cellular mirrors. View (a) of that figure shows the key cross-sectional dimensions of any cell in the models. These dimensions are as follows: t_F is the front face sheet thickness, t_B is the back face sheet thickness, t_C is the core wall thickness, h_C is the core height, and N_A is the distance from the front of the mirror to the neutral surface.

As a first approximation of the mirror design, designers frequently develop a two-dimensional (2D) FEA model. In essence, the mirror is a membrane with stiffness equivalent to the actual mirror.

---

*Struts in the core are referred to as *webs* by some authors.

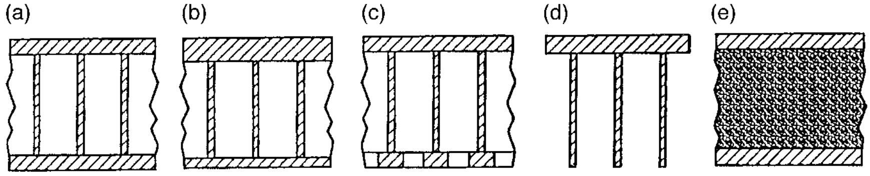

FIGURE 9.2 Representative cross sections for machined or built-up cellular mirror substrates. (a) symmetrical sandwich, (b) unsymmetrical sandwich, (c) partially open back, (d) open back ("waffle"), and (e) foam sandwich. (Adapted from Seibert, G.E., *SPIE Short Course SC18*, 1990.)

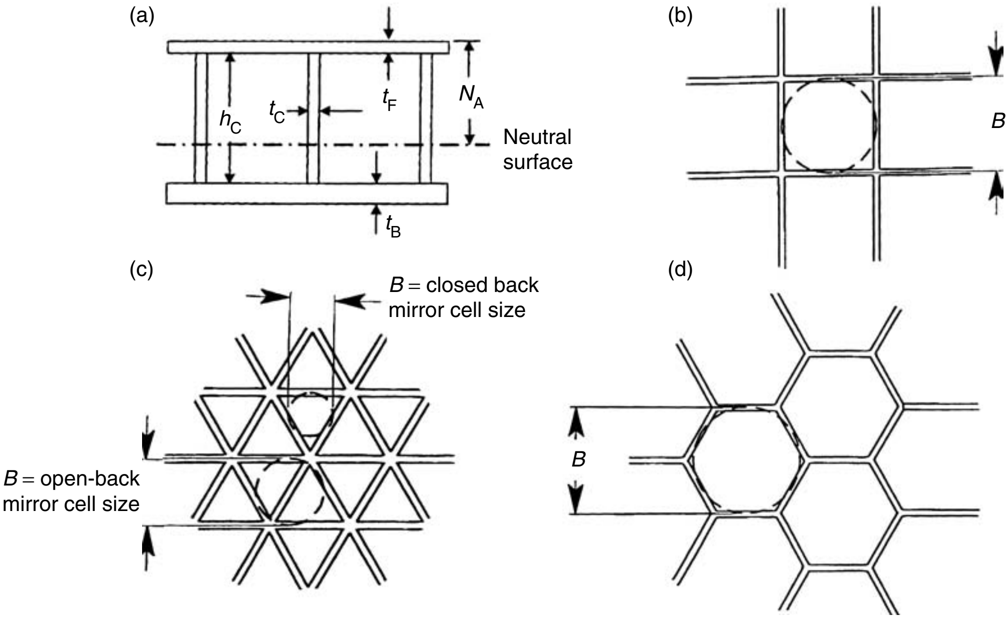
(a)
h_C
t_C
t_F
N_A
Neutral surface
t_B
(b)
B
(c)
B = closed back mirror cell size
B = open-back mirror cell size
(d)
B

FIGURE 9.3 (a) Variables for two-dimensional models of cellular substrates. Views (b)–(d): regular polygon patterns for square, triangular, and hexagonal cells. Scale is graphic. (Adapted from Doyle et al., *Integrated Optomechanical Analysis*, SPIE Press, Bellingham, 2002.)

If this model proves favorable, a more accurate 3D FEA model is created and thoroughly analyzed. For any cell shape, the mirror's rib solidity ratio α and the effective thickness T_M of the equivalent-stiffness membrane are defined as

$$\alpha = t_C/B \tag{9.1}$$

$$T_M = t_F = t_B + \alpha h_C \quad \text{for } t_F \neq t_B \tag{9.2a}$$

$$T_M = 2t + \alpha h_C \qquad \text{for } t_F = t_B = t \tag{9.2b}$$

Given these parameters, the location of the neutral surface can be estimated as

$$N_A = \left[\frac{t_F^2}{2} + t_B\left(\frac{t_B}{2} + h_c + t_F\right) + \alpha h_C\left(\frac{h_C}{2} + t_F\right)\right]/T_M \text{for } t_F \neq t_B \tag{9.3a}$$

$$N_A = (h_c/2) + t_F \qquad \text{for } t_F = t_B \tag{9.3b}$$

Doyle et al. (2002) defined other parameters needed for the 2D FEA of mirror surface deflections. Both bending and shear effects were considered. Because the magnitudes and distributions of the localized deflections depend significantly on how the mirror is supported and on the mirror axis orientation with respect to gravity, it is not possible to generalize such calculations here. Details of the 2D modeling technique and of the more realistic 3D modeling technique also described briefly by Doyle et al. (2002) are beyond the scope of this book.

A common deficiency of any cellular mirror substrate is local deflection of the surface between the core struts due to pressure of the lap during polishing. This so-called *quilting* results in inaccuracies in the final surface figure. The p-v value for this effect can be estimated and combined with the surface rms surface deflections calculated by the FEA model to determine the mirror's predicted error. This combination is done on a root-sum-square (rss) basis after scaling the quilting p-v value by 0.3 to derive an approximate rms value. The following equation (from Vukobratovich, 1997 or Doyle et al., 2002) gives the p-v quilting deformation

$$\delta_{\mathrm{QUILTING}} = \frac{12\psi PB^4\,(1+\nu^2)}{Et_{\mathrm{F}}^3} \tag{9.4}$$

where ψ is a shape-dependent factor equal to 0.00151, 0.00126, or 0.00111 for triangular, square, or hexagonal cell shapes, respectively, B as defined in Figure 9.3, and P the applied pressure.

9.4 CAST RIBBED SUBSTRATES

The 200 in. (5.1 m) Hale Telescope completed in 1950 has as its primary mirror the first successful large mirror of "lightweight" construction. In that 24-in. (61-cm)-thick mirror, a rib structure was cast directly into the back of the Pyrex disk (see Figure 9.4). The ribs and face plate are 3 to 5 in. (7.6 to 12.7 cm) thick. The mirror's ability to maintain thermal equilibrium with its environment is enhanced over that of prior solid disks, since no point within this mirror is more than about 2 in.

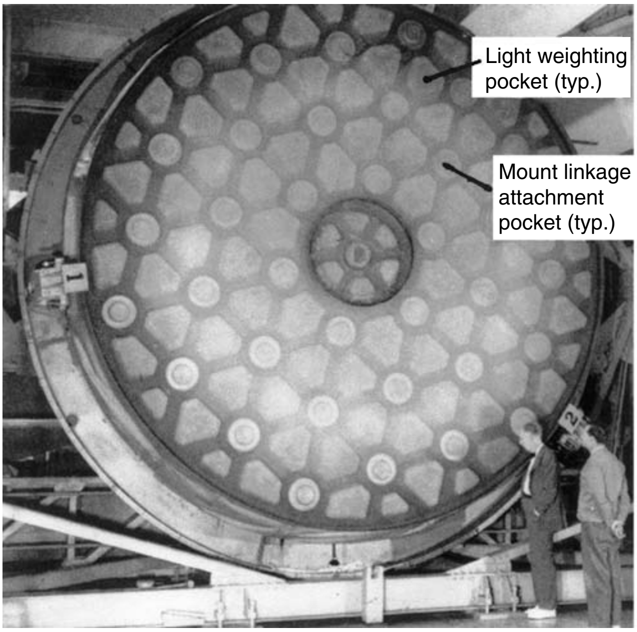
Light weighting pocket (typ.)
Mount linkage attachment pocket (typ.)
1
2

FIGURE 9.4 Photograph showing the cast ribbed structure of the 200-in. (5.08-m)-diameter Hale Telescope primary mirror. (Adapted from Bowen, I.S., in *Telescopes*, Kuiper, G. and Middlehurst, B., Eds., University. of Chicago Press, 1960.)

(5 cm) from a surface exposed to the surrounding air. The ribbed design also permitted a significant weight reduction. For equal self-weight deflection, a solid disk would have weighed 40 tons (3.6×10^4 kg). The existing ribbed mirror weighs 20 tons (1.8×10^4 kg), so a weight saving of 50% was achieved (Loytty, 1969; Loytty and DeVoe, 1969).

Although this mirror has a desirably short thermal relaxation time, it is by itself relatively flexible. This is due to the absence of a back sheet and the presence of circular mounting holes that interrupt the rib structure. To support the mirror adequately against gravitational forces at various elevations required the application of variable compensating forces axially and radially. Bowen (1960) explained how this was achieved with 36 sets of mechanical counterweights acting through levers to apply their radial and axial thrusts in the plane of the mirror's CG and to the back of the mirror, respectively. This type of mechanical mount is discussed in Section 12.2.

In the expectation that many lightweight mirrors for new telescopes in the aperture range 6 to 10 m (240 to 400 in.) would be needed by the world's major observatories, advanced techniques for the manufacture of large cellular blanks by casting glass have been developed. According to Angel and Hill (1982), there are two ways to cast a large mirror: face-up or face-down. Four possible methods are represented in Figure 9.5. If the mirror is face up, the complex parts of the mold must rest on or be fastened to the base. If the upper surface is left free, it will be flat as in view (a) and the reflecting surface will have to be excavated to make it concave. Relatively large amounts of glass would have to be removed. This would not be necessary if a convex dome were pressed into the molten glass, as sketched in view (b). Similar contours could be realized by slowly spinning the entire furnace as in view (c) so that centrifugal force creates a concave (nominally parabolic) surface as the glass solidifies. If the mirror is cast face-down, the base of the mold should be a convex dome and the core inserts that create the honeycomb must be suspended from above as in view (d).

Casting techniques based on configuration (c) of Figure 9.5 were developed by the Steward Observatory and University of Arizona and by Schott Glaswerke in Germany for making spin-cast lightweight substrates up to at least 8.4 m (27.6 ft) diameter from borosilicate crown glass and Zerodur, respectively. Techniques and facilities for doing so were described by Angel and Hill (1982), Angel (1983), Angel et al. (1983, 1990), Marker et al. (1985), Goble et al. (1988a, 1998b), Olbert et al. (1994), Anderson et al. (1994), and Martin et al. (1996).

In the Steward Observatory's approach, the raw material (typically Ohara E6 borosilicate crown) is placed directly into a flat-bottomed mold containing an array of void formers (core inserts) and heated to about 1200°C (2192°F) in an electric furnace that can rotate about a vertical axis on a large (12-m [39.4-ft]-diameter) turntable. Figure 9.6 shows a partial sectional drawing of the furnace with a set of void formers (cores) for an 8.4 m (27.6 ft) blank in place. Piles of glass chunks are spread over the cores and melted at about 1180°C. The mold walls are typically SiC-based ceramic lined with aluminosilicate refractory fiberboard to prevent chemical reactions between the SiC and the molten glass. The cores are typically vacuum-formed ceramic fiber boxes

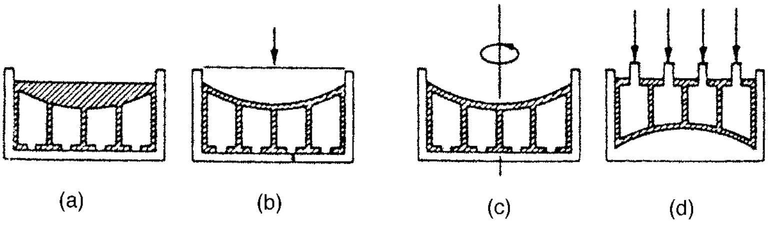

FIGURE 9.5 Possible configurations of honeycomb sandwich mirror structures (sectioned) cast as monolithic substrates around expendable cores (shown in white). Gravity is vertical. (From Angel, J.R.P. and Hill, J.M., *Proc. SPIE*, 332, 298, 1982.)

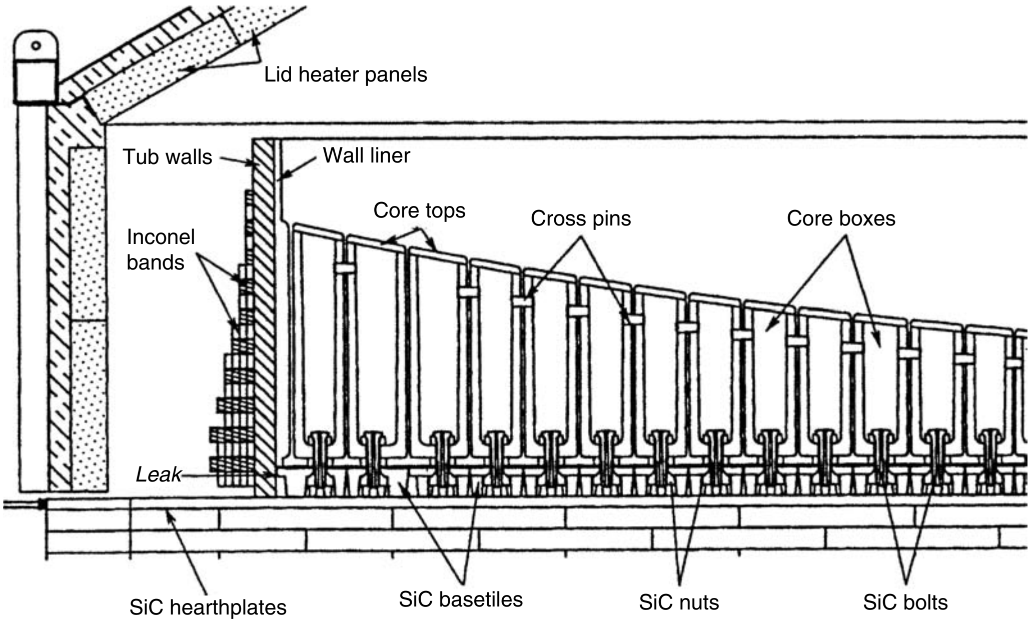

FIGURE 9.6 Cross-sectional drawing of the furnace and mold for a 8.4 m (27.6 ft) diameter mirror blank for the Large Binocular Telescope (LBT). (From Hill, J.M. et al., *Proc. SPIE*, 3352, 172, 1998.)

(Goble et al., 1988a; Hill et al., 1998). The thermal control system for this furnace was described by Cheng and Angel (1986).

At Schott Glaswerke in Mainz, Germany, a casting facility with a concave bottom has been built and used successfully to make several meniscus-shaped mirror blanks of diameters as large as 8.2 m (26.9 ft) with thicknesses of about 17.8 cm (7.00 in.) (Müller et al., 1990, 1994; Morian et al., 1996). The Schott approach involves pouring molten Zerodur into the rotating mold from a separate melter. The cast blank is first cooled into the glassy state and coarse-machined. It is then transformed thermally into the partially crystallized state and further machined to nearly final size and shape. A third heat treatment places the surfaces under compression and the blank is ready for final machining. Experience has indicated that the finished products are remarkably free of stress. Since they are made of low-CTE material, thermal stability of a finished mirror is excellent.

Although borosilicate crown glass materials used at the Steward Observatory have significantly higher coefficients of thermal expansion (~ 2.4 ppm/°C) than the glass ceramics used in the Schott mirror blanks and in some other mirrors described in this book near room temperature, they are considered suitable for some very large ground-based telescopes or long-wavelength spaceborne systems. Ribbed or honeycomb mirrors have low thermal inertia, so they can be stabilized by ventilating with conditioned air in ground installations or by radiant heat transport means in space. Borosilicate crown also has a lower CTE at 30 to 50 K than glass ceramics or fused silica, so it may be more suitable for cryogenic applications than the latter materials (Voevodsky and Wortley, 2003).

The largest monolithic mirror substrates made as of this writing are two that have diameters of 8.42 m (27.62 ft), central holes of 0.889 m (2.92 ft) diameter, edge thicknesses of 0.894 m (2.93 ft), and weights of 16,000 kg (35,274 lb). These blanks, used in the Large Binocular Telescope (LBT) on Mt. Graham in Arizona, were cast at the Steward Observatory Mirror Laboratory in 1997 and 2000 using the furnace configuration of Figure 9.6. Figure 9.7 shows the first mirror blank along with many of the individuals who contributed to its successful manufacture (Hill et al., 1998).

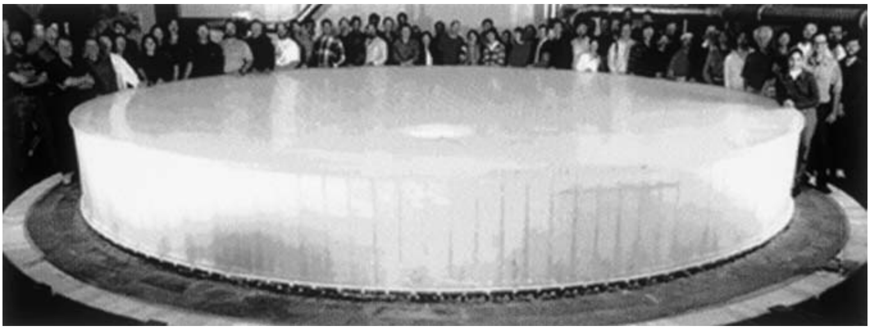

FIGURE 9.7 Photograph of the first 8.4-m (27.6-ft)-diameter spin-cast mirror blank for the Large Binocular Telescope. (From Hill J.M. et al., *Proc. SPIE*, 3352, 172, 1998.)

9.5 SLOTTED-STRUT AND FUSED MONOLITHIC SUBSTRATES

Modern techniques for making dimensionally stable, lightweight, built-up mirror blanks from low-expansion materials have evolved from a slotted-strut (egg crate) configuration developed by Corning Glass Works in the late 1950s. The edges of the struts in those blanks were fused to the front and back face sheets, but the struts were not fused together, so the structures were not very stiff against shear. Figure 9.8 is a diagram of a 32-in. (81-cm)-diameter fused silica mirror of this type. The actual mirror is shown in Figure 9.9. It was used in the Orbiting Astronomical Laboratory (OAO-C) launched in 1972 by NASA. It weighed approximately 105 lb (48 kg). The equivalent solid-disk mirror would have weighed 360 lb (164 kg).

In the 1960s, Corning Glass Works developed a technique for making monolithic mirror structures with improved shear resistance by fusing or welding together many "ell"-shaped parts to create an egg crate core and then fusing on the front and back plates. Figure 9.10 shows schematically how two joints of premachined parts are simultaneously torch-welded. Figure 9.11 shows a portion of a typical triangular cell core made in this same manner. According to Hamill (1979), the core stiffness of a totally fused design is typically twice that of the equivalent partially fused (slotted-strut) design.

The fused monolithic construction is feasible only with materials of essentially zero CTE because they do not fracture from temperature-gradient-induced stresses when rapidly heated or cooled during the fusion process. Corning Glass Works Code 7971 ULE ceramic glass composed of about 92.5% SiO_2 and 7.5% TiO_2 is well suited for this type of construction. Its CTE is predictably near zero in the temperature range 5 to 35°C. Furthermore, its actual CTE can be measured precisely

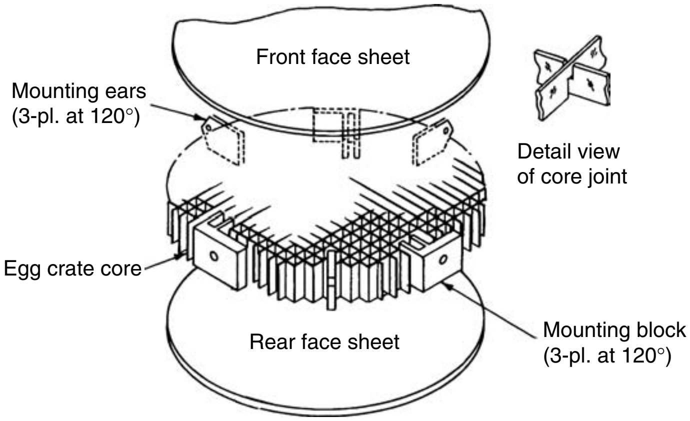

FIGURE 9.8 Constructional details of the 32-in. (81-cm) diameter, slotted-strut egg-crate mirror used in OAO-C. (Courtesy of Goodrich Corporation, Danbury, CT.)

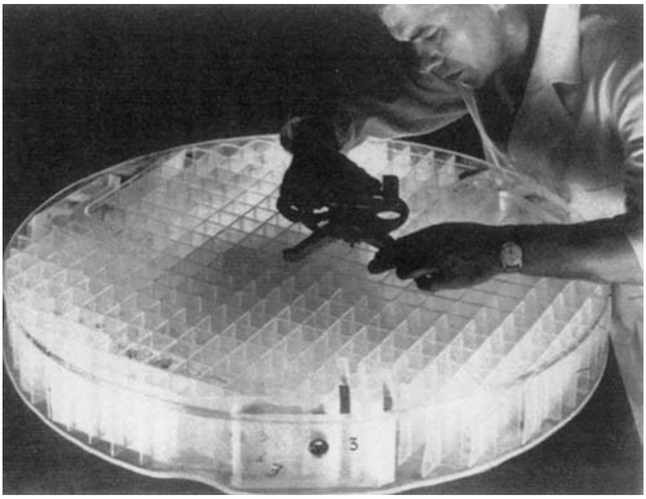

FIGURE 9.9 Photograph of the OAO-C lightweight primary mirror prior to coating. (Courtesy of Goodrich Corporation, Danbury, CT.)

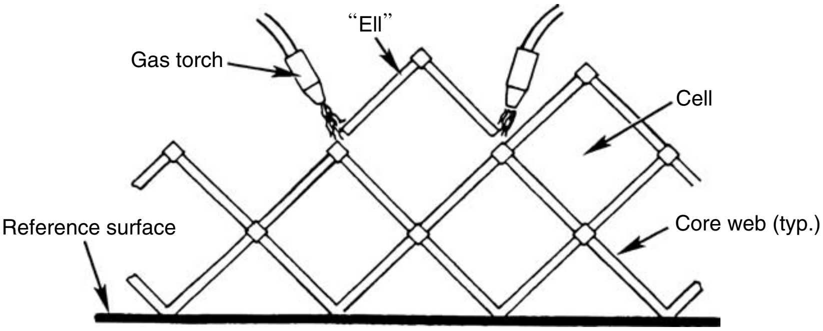
"Ell"
Gas torch
Cell
Reference surface
Core web (typ.)

FIGURE 9.10 Attaching 90° "ells" by torch welding to form a monolithic mirror core. (Adapted from Lewis, W.C., in *OSA Optical Fabrication and Testing Workshop*, Tucson, AZ, 1979, chap. 5.)

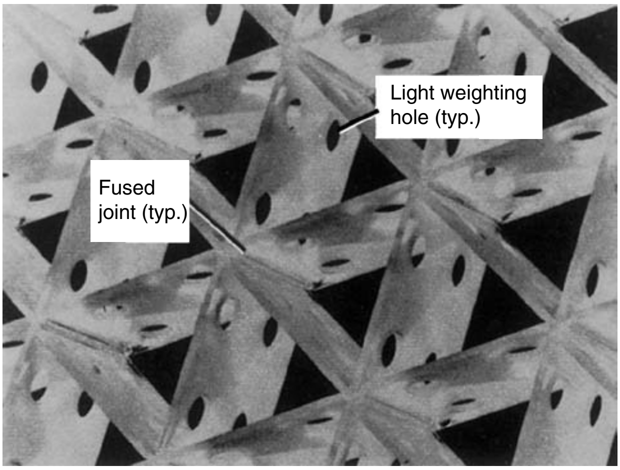
Light weighting hole (typ.)
Fused joint (typ.)

FIGURE 9.11 Close-up photograph of a typical triangular-cell fused monolithic core structure for a lightweight mirror. (Adapted from Loytty, E.Y., *Optical Telescope Technology, MSFC Workshop*, *April 1969*, NASA Rept. SP-233, 241, 1969.)

by nondestructive testing using ultrasonic velocity measurement techniques (Hagy and Shirkey, 1975). The characteristics of this material are listed in Table 3.13. Hobbs et al. (2003) reported that fused silica can also be fusion-welded, but that the process requires higher temperatures and is therefore more difficult.

Numerous ULE mirrors of the fused monolithic type have been constructed and used successfully in aerospace systems. A mirror substrate typically comprises two thin perforated plates, a built-up core, and inner and outer rings, as illustrated in Figure 9.12. The materials for the two plates are closely matched to within 0.01 ppm/°C for coefficient of thermal expansion. The front plate is the one that is accurately polished and figured. The glass for this is selected for freedom from inclusions in order to minimize defects in the surface. Plates as large as ~ 2.8 m (~ 110 in.) can be made by heating a stack of raw material boules so they flow to the required diameter. Plates as large as ~ 8.4 m (~ 331 in.) can be made by fusing hexagonal segments edge to edge (Hobbs et al., 2003). The segments are created from slices of the required thickness cut from a raw material boule.

Manufacture of the core is more complex. If, for example, a 25.4-cm (10-in.)-thick core with 5.08-mm (0.2-in.)-thick struts is required, the necessary number of boule slices to create the required volume of material are stacked vertically, placed in a furnace, and heated to about 1600°C. At this temperature the slices fuse together to form a single monolithic plate. The individual cell strut sections are cut and ground to the proper thickness. These components are then flame-welded together to form "ells" and then cells as shown in Figure 9.10. This procedure is continued row by row until the overall core size is adequate, at which point the core is cut into a circular shape and ground to the proper height. Inner and outer rings are made by sagging flat strips to the proper cylindrical radius by heating them on a mold. The individual sections are then flame-welded together to form complete rings.

The plates, core, and rings are next placed in a furnace in their proper positions to make a complete plano–plano assembly. The rings are positioned to be concentric with the core and spaced a short distance away from the core rim. Gas burners then heat this assembly from above, and a fusion seal is achieved, which bonds the uppermost plate to the core and rings. The assembly is then cooled slowly, inverted, and placed back in the furnace, but this time resting on a convex mandrel of appropriate radius to approximate the desired mirror radius of curvature. It is then heated from above a second time, this time not only to seal the other plate to the core and rings, but also to allow the structure to slump to conform to the domed hearth and achieve the meniscus-shaped, monolithic, mirror substrate configuration. The substrate is annealed and is then ready for inspection and subsequent shipment to the finisher. Figure 9.13 shows the flow of this manufacturing process.

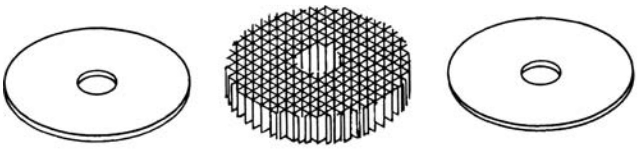

Front plate Fused core Rear plate

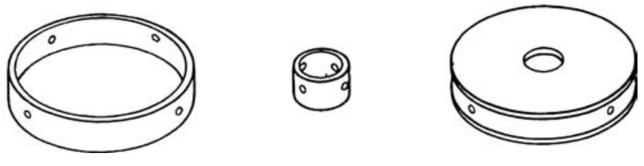

Outer ring Inner ring Fused substrate

FIGURE 9.12 Basic parts of a typical perforated fused monolithic mirror substrate. (Adapted from Lewis, W.C., in *OSA Optical Fabrication and Testing Workshop*, Tucson, A2, 1979, chap. 5.)

Three advantages of the built-up type of construction in making monolithic lightweight mirror blanks are (1) tight dimensional control (because they are made of precision premachined parts), (2) repairability (within limits), and (3) simplicity of incorporating provisions for mounting. If a core is damaged while in process, it can be reworked. In certain instances, repairs can also be made to mirrors damaged in optical finishing or even during their end use.

Figure 9.14 shows a mounting block fused into the rim of a typical lightweight monolithic mirror structure. These blocks provide "strong points" for attaching the mirror with flexures to the mirror cell or instrument structure. The mirror shown here is a typical 1.52-m (60-in.)-diameter, fused monolithic ULE mirror substrate with 7.6 cm (3 in.) square cells. The front and back face sheets are

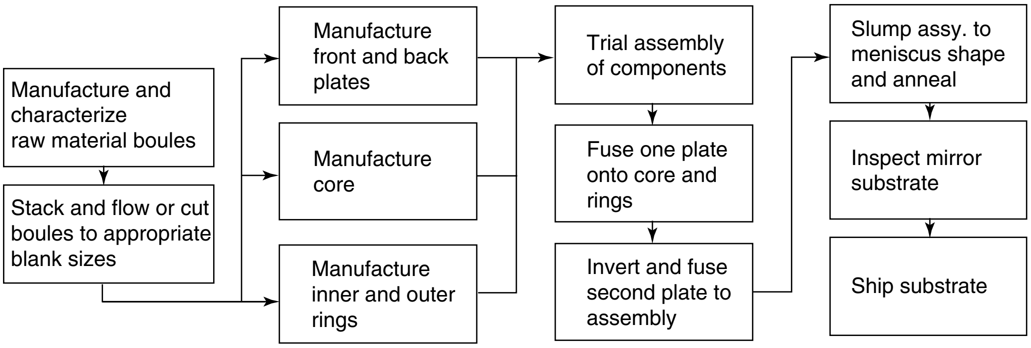
Manufacture and characterize raw material boules
Stack and flow or cut boules to appropriate blank sizes
Manufacture front and back plates
Manufacture core
Manufacture inner and outer rings
Trial assembly of components
Fuse one plate onto core and rings
Invert and fuse second plate to assembly
Slump assy. to meniscus shape and anneal
Inspect mirror substrate
Ship substrate

FIGURE 9.13 Flow chart for the Corning manufacturing process used to create large monolithic meniscus-shaped mirror substrates from ULE. (Based on Hobbs T.W. et al., 2003.)

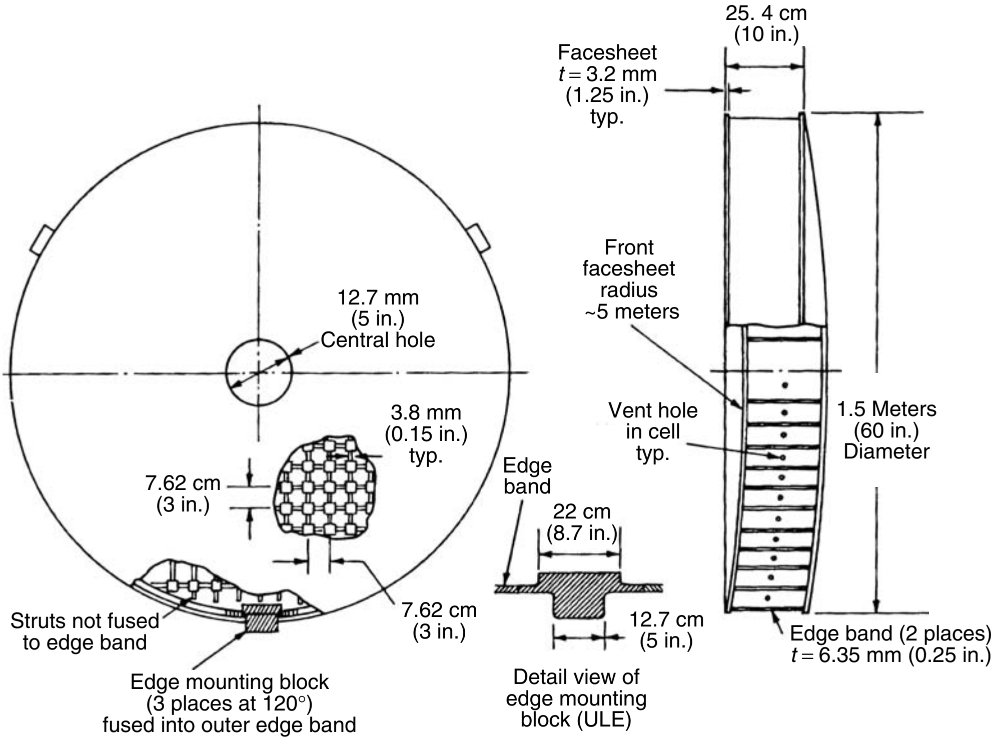
25. 4 cm
(10 in.)
Facesheet
t = 3.2 mm
(1.25 in.)
typ.
Front
facesheet
radius
~5 meters
12.7 mm
(5 in.)
Central hole
3.8 mm
(0.15 in.)
typ.
7.62 cm
(3 in.)
Vent hole
in cell
typ.
1.5 Meters
(60 in.)
Diameter
Edge
band
22 cm
(8.7 in.)
Struts not fused
to edge band
7.62 cm
(3 in.)
12.7 cm
(5 in.)
Edge band (2 places)
t = 6.35 mm (0.25 in.)
Edge mounting block
(3 places at 120°)
fused into outer edge band
Detail view of
edge mounting
block (ULE)

FIGURE 9.14 Conceptual layout of a typical 1.52 m (60 in.) diameter fused and slumped monolithic ULE mirror blank.

nominally 3.2 cm (1.25 in.) thick and the overall blank thickness is 25 cm (10 in.). The finished face sheet thicknesses are 1.5 cm (0.60 in.), so the finished mirror thickness is 22 cm (8.8 in.). The basic core struts are 3.8 mm (0.15 in.) thick, except in the vicinity of the nine mounting points, where the struts are thickened to 9.5 mm (0.38 in.) as shown.

Since fusing and slumping of this type of mirror structure entails softening of the material, the raw blank typically suffers many types of undesirable deformations. Figure 9.15(a) illustrates some of the more common defects. In general, changes in dimensions are nonlinear and hard to predict accurately. Since the face sheets may depart significantly from the best-fit sphere, it is necessary to allow extra glass thickness so that the desired surface can be located below the deepest valley. Radial clearance is normally provided between the core and inner- and outer-edge rings to prevent localized contacts that could modify the stiffness of the structure in those areas and affect polishing. Nonuniformities of mass distribution properties may also result from shape and dimensional changes during fusion.

Another type of common defect in fused mirror blanks is incomplete fusion of the core struts to each other, to the face sheets, or to the mounting blocks. Usually, defects such as large bubbles within the fused area and gaps between parts are obvious during visual inspection. A good seal shows up as a clear or, at worst, a medium-gray area. Dark-gray areas indicate poor fusion.

Inclusions such as seeds and bubbles within the front face sheet of a mirror may create problems if they occur too frequently in the region where the final optical surface is to be created. Specifications for mirror blanks generally subdivide this sheet into zones with different requirements for freedom from inclusions. Figure 9.15(b) illustrates a typical zone distribution. Starting from the outermost surface, we first find the zone from which material must be removed to eliminate contour deformations such as shown in Figure 9.15(a) and to bring the face sheet to near-final thickness. Next, we encounter the critical zone that is to contain the finished optical surface. Below the critical zone is the noncritical zone, where larger inclusions may occur. In most applications, freedom from bubbles and seeds in or near the final surface is especially important. The specifications should call for a thin "supercritical" zone with extremely tight inclusion limitations. Table 9.1 lists typical specifications in the various zones for such a mirror.

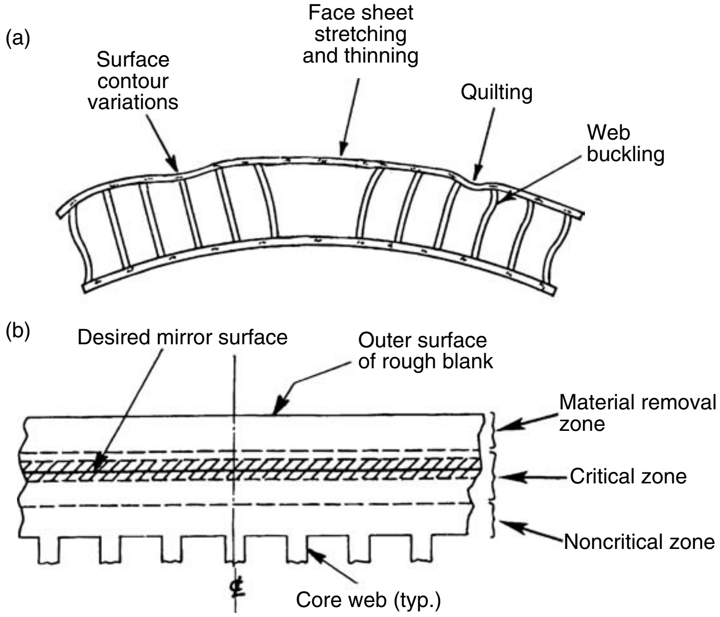

FIGURE 9.15 Details of the monolithic fused mirror blank. (a) Typical defects caused by heating ULE above the annealing temperature, (b) location of the mirror surface within the best region of the front sheet.

TABLE 9.1
Zonal Inclusion Specifications for a Typical 32-mm (~ 1.25-in.)-Thick Large Mirror Front Face sheet

Supercritical Zone: A selected 1.5-mm (0.06-in.)-thick region within the critical zone crossing the entire face sheet aperture with
No visible opaque inclusions
Maximum number of visible seeds/bubbles = 100
Maximum diameter of seeds/bubbles = 2 mm (0.08 in.)
Maximum inclusion distribution density = 1/10 cm^2 (~ 10/ft^2)

Critical Zone: The 10-mm (0.4-in.)-thick region lying between the material removal zone and noncritical zone and including the supercritical zone crossing the entire facesheet aperture. Allowable average diameter of seeds/bubbles = 0.33 mm (0.013 in.)

Noncritical Zone: The 8.0-mm (0.32-in.)-thick innermost zone crossing the entire face sheet aperture with
Maximum mean diameter of seeds/bubbles = 6.5 mm (0.26 in.)
Maximum average diameter of seeds/bubbles = 0.33 mm (0.013 in.)
Maximum inclusion distribution density = 1/10 cm^2 (~ 10/ft^2)

Material Removal Zone: The 14.0-mm (0.55-in.)-thick outermost zone crossing the entire face sheet aperture and having no limitations on inclusions

In another fusion technique developed at the University of Arizona (Angel and Wangsness, 1986) and now used at Hextek Corporation, also of Tucson, AZ, similar lengths of circular glass tubing are placed on end between drawn-glass face sheets to form a sandwich configuration as shown in Figure 9.16. The rear sheet is perforated with small holes, one for each tube. The assembly is placed over a manifold in an oven. The top sheet is weighted down and gas is admitted to the tubes under sufficient pressure to just balance the weighted top sheet. The oven temperature is raised until the tubes are fully fused to both sheets. Then the pressure is increased to press the softened tubes outward until they contact and fuse to the adjacent tubes. Depending on the initial tube layout, the structure becomes monolithic with either a square (see Figure 9.16[a]) or hexagonal (see Figure 9.16[b]) core pattern. An integral sidewall is also formed on the core as the tubes expand. After annealing and cooling, finished substrates appear as shown in Figure 9.17. The larger blank is 1 m (40 in.) in diameter × 17 cm (6.7 in.) thick and has been slumped to a *f*/0.5 sphere in a second firing over a convex refractory mold.

The unique aspect of this process is the pneumatic support of the structure during the firing. This permits use of substantially higher temperatures during firing than would be possible without pressurization. Superior bonding of the tubes results without excessive quilting of the face sheets between the ribs formed by the tube walls. Typical cell size in a Hextek blank is 6.4 cm (2.5 in.); face sheet thickness is of the order of 1 cm (0.4 in.) (Parks et al., 1990). Use of thin-wall tubing, wide separations, and very thin face sheets are all possible and result in ultralight construction with reasonably uniform rib geometry. For example, the smaller blank shown in Figure 9.17 is 0.45 m (17.7 in.) in diameter and 10 cm (3.9 in.) thick. Its areal density is 31.8 kg/m^2. Ongoing efforts by Hextek and NASA MSFC toward reducing areal density to 15 kg/m^2 were reported by Voevodsky et al. (2003).

The gas fusion process is reported to be rapid and relatively inexpensive, to make efficient use of materials, and to produce 100% fusion bonds between components. Borosilicate glass, such as Corning Pyrex 7740, Schott Tempax (with a CTE of 3.2 ppm/°C), and Schott Borofloat™ glass, is generally used, although Vycor and fused silica have also been employed. Acid etching of cut glass parts to remove surface impurities introduced during raw material production was found to be desirable for aesthetic reasons, but not essential to the technical quality of the blank (Cannon and Wortley, 1988). Blanks with central perforations and internal mounting bosses at the neutral surface

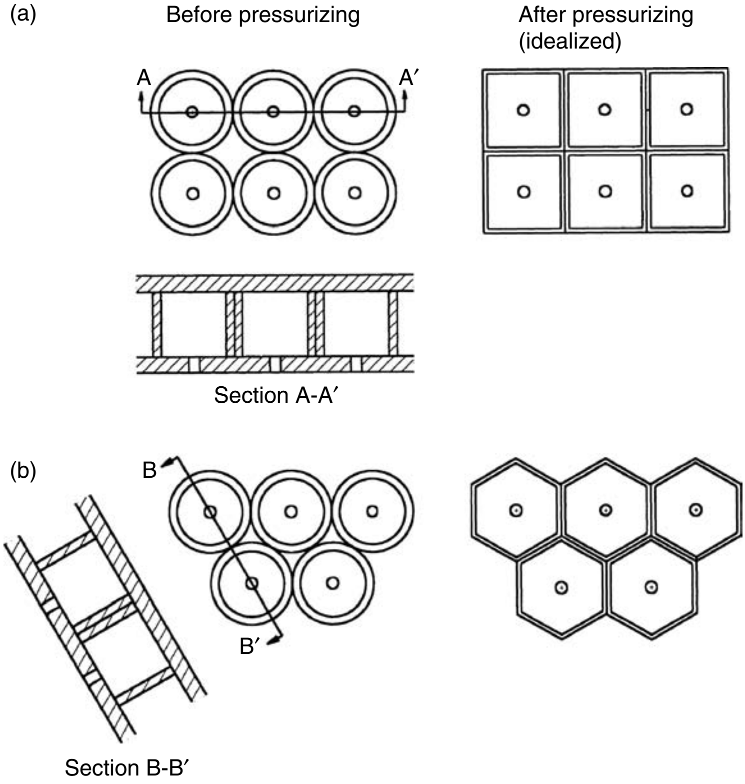
(a)
Before pressurizing
After pressurizing
(idealized)
A
A′
Section A-A′
(b)
B
B′
Section B-B′

FIGURE 9.16 Tube placement pattern prior to heating and pneumatic expansion in the Hextek mirror manufacturing process: (a) square cells, (b) hexagonal cells. (Adapted from Parks R.E. et al., *Proc. SPIE*, 1236, 735, 1990.)

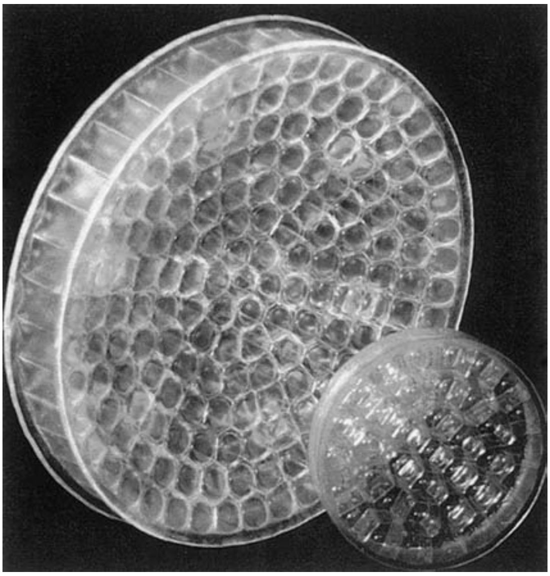

FIGURE 9.17 Photographs of two fused monolithic mirror blanks made by the Hextek process. (Courtesy of Hextek Corporation, Tucson, AZ.)

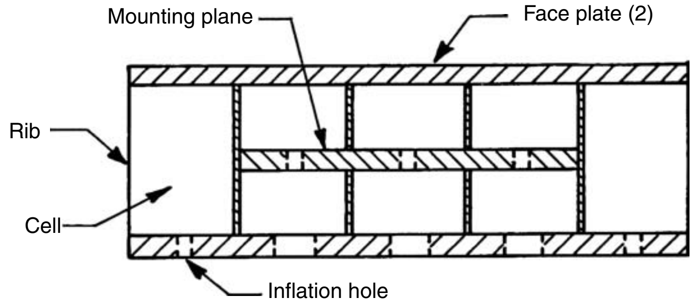

FIGURE 9.18 Cross-sectional view of a Hextek mirror blank with integral centralized mounting boss. (From Cannon, J.E. and Wortley, R.W., *Proc. SPIE*, 966, 309, 1988.)

of the blank (see Figure 9.18) can be made, and either concave or convex face sheet contours can be created.

Voevodsky et al. (2003) indicated that this technology is capable of creating convex, concave, or flat substrates as fast as *f*/0.5 and apertures as large as 2.0 m (78.7 in.). Further, it is reported by those authors to be capable of achieving areal densities as low as 15 kg/m^2, which is similar to the requirement for the mirrors of the James Webb Space Telescope.

9.6 FRIT-BONDED SUBSTRATES

Except for the Hextek gas fusion process, the high-temperature processes used to fuse the substrates discussed in Sections 9.4 and 9.5 tend to buckle or collapse the struts, especially if they are too thin to support the weight of the upper sheet. In order to allow reductions in strut thickness, Corning Glass Works developed an adhesive material (frit) containing an organic vehicle and a powdered glass material that melts at a lower temperature than ULE, but has essentially the same low coefficient of thermal expansion as that material. Prior frits, used typically to bond the face plate to a television tube funnel, had much larger expansion properties.

According to Spangenberg-Jolley and Hobbs (1988), firing of the fritted core/face sheet assembly bakes off the organic vehicle and devitrifies the powdered glass into a glass ceramic that closely (within ±100 ppm/°C) matches the thermal expansion coefficient of the mirror components. Reliable seals with localized fillets to blend the adjacent parts together geometrically are produced. This and the thermal expansion match are important because they minimize stress and risk of fracture during firing and increase the strength of the joints. These attributes of the process also enhance the long-term stability of the mirror by reducing residual stress after returning to room temperature.

Frit bonding also offers a distinct advantage to the FEA analyst since mirror analytical models do not have to accommodate mirror blank distortion. The resulting bonds are typically two to three times stronger than fusion-welded joints. Well-filleted frit bonds have a break strength of the order of $>$ 5000 lb/in.^{2}, as opposed to 3000 lb/in.^{2} for fused joints (Hobbs et al., 2003).

Corning's proprietary vehicle for frit application has the interesting property that it is amenable to a dipping application. A layer of the viscous frit vehicle is spread to uniform thickness onto a mold whose curvature matches that of the mirror sheet to be bonded. Actually, this might be the mold used to slump the face sheet to the appropriate curvature. The contoured core is dipped into the compound and lifted clear. The adhesive sticks to the core webs so that, when placed against the face sheet, the appropriate thickness of adhesive exists throughout the interface. The assembly is then vibrated to facilitate the flowing and wetting action of the vehicle and fired to create a permanent bond (Hamill, 1979). Frit-bonded mirror blanks come to the optical processor within a few millimeters of finished dimension, thereby eliminating the removal of large amounts of glass in preparation for polishing.

Table 9.2 compares a frit-bonded design with a fused monolithic technology example. The diameters of the two mirrors are the same, and the rigidities (or deflections when simply supported) are about the same as well; both represent very rigid mirrors. The blank weight has been significantly reduced from 33 lb (15 kg) to 9 lb (4.1 kg) by using frit as the bonding medium for thinner struts.

The frit-bonded mirror described in the table is sketched in Figure 9.19. Although not shown, mounting blocks can be fused into the core as required. Optical figure quality of 0.024 wave rms at 0.63 μm wavelength was reportedly achieved by conventional polishing methods. A series of tests of this mirror before and after a series of temperature cycles from −100 to 200°F (−73 to 93°C)

TABLE 9.2
Comparison of Classical vs. Frit-bonded Mirror Blanks

Measurement	Classical	Frit-bonded
Diameter (in.)	20	20
Thickness (in.)	5	3
Self-weight deflection (simply supported) (in.)	3.9×10^{-6} in.	6.4×10^{-6} in.
Weight (lb)	33	9
Core density (%)	12.5	7.0
Joint strength (lb/in.^{2})	2800	> 5000

Source: Adapted from Fitzsimmons, T.C. and Crowe, D.A., *RADC-TR-81-226*, Rome Air Development Ctr., Rome, NY, 1981.

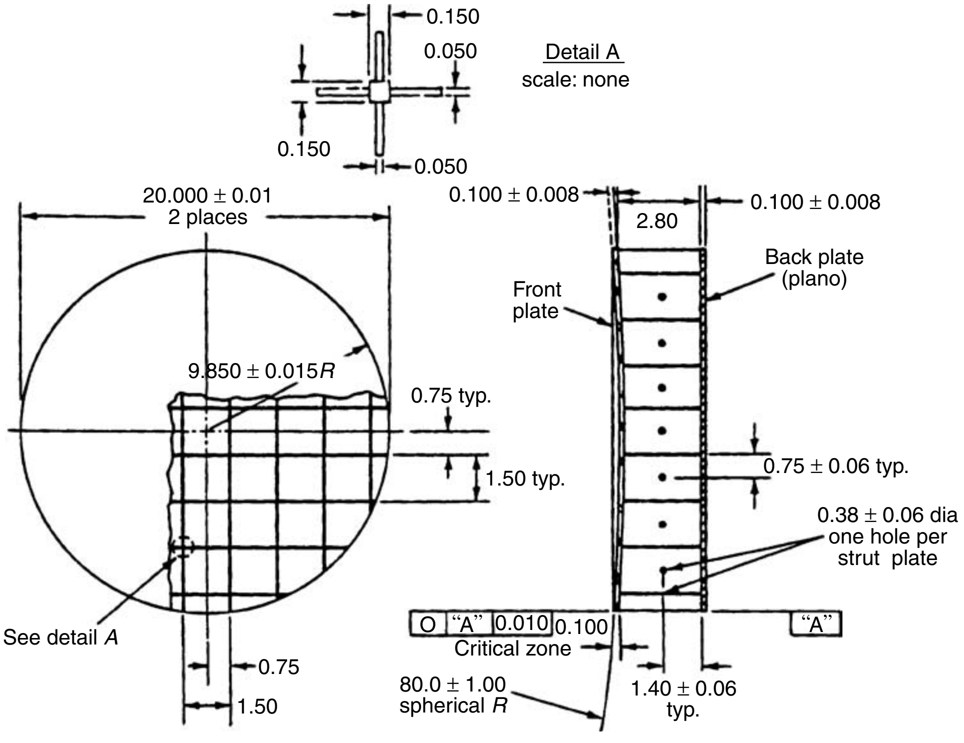
0.150
0.050
Detail A
scale: none
0.150
0.050
20.000 ± 0.01
2 places
0.100 ± 0.008
2.80
0.100 ± 0.008
Back plate
(plano)
Front
plate
9.850 ± 0.015R
0.75 typ.
1.50 typ.
0.75 ± 0.06 typ.
0.38 ± 0.06 dia
one hole per
strut plate
See detail A
O "A" 0.010 0.100
Critical zone
"A"
0.75
1.50
80.0 ± 1.00
spherical R
1.40 ± 0.06
typ.

FIGURE 9.19 A generic mirror design suitable for frit bonding. Dimensions are inches. (Adapted from Fitzsimmons, T.C. and Crowe, D.A., RADC-TR-81-226, Rome Air Development Ctr., Rome, NY, 1981.)

disclosed no measurable figure change. The purpose of this thermal cycle test was to induce elastic deformation in the joints to emphasize any instability that might exist. The mirror was also tested isothermally at 100, 70, and 0°F (38, 21, and -18°C). The purpose of this test was to detect and measure any surface quilting due to the strain mismatch between the frit and the glass. Analysis had predicted that, for these temperature changes, no quilting would be observed in the surface. This proved to be true. No measurable quilting was observed. A mechanical deflection test was run to flex the joints in order to disclose any instabilities that might be in the blank. The mirror was simply supported and a uniform 4 g load was applied ten times. The pre- and postoptical tests measured no optical figure change. The mirror was then introduced into a hard-vacuum chamber at approximately 10^{-6} torr, with no noticeable change. The success of these tests seems to indicate the technical advantages of frit-bonded ULE mirrors. Several mirrors of various sizes have been made and successfully applied to aerospace applications.

Anthony et al. (2003) reported early progress in frit bonding silicon mirror substrates for cryogenic applications. A 44 kg (96.9 lb) assembly of silicon plates with overall dimensions of 113 × 400 × 400 mm (4.45 × 15.7 × 15.7 in.) has been bonded with frit as a cost-effective alternative to the equivalent boule of the material. Other samples fabricated and tested indicated that the process would be economical, that the bond strengths were $> 80\%$ those of homogeneous silicon, and that the substrates could be polished to excellent optical figure. Cryogenic tests indicated that the optical figure would be reasonably well preserved at low temperatures.

One silicon mirror of 600 mm (23.6 in.) diameter and 600 mm (23.6 in.) spherical radius fabricated by this frit bonding process was constructed and evaluated. This mirror had a square-cell machined core. The test results were as follows: overall figure error was 0.074λ rms relative to a specification of 0.1λ rms, and surface roughness was 0.52 nm rms relative to a specification of 1.0 nm rms. The mirror's cryogenic surface deformation, warm to cold was $< 0.06\lambda$ rms. All wavelengths here were 0.633 nm.

Koch et al. (2004) mentioned that an 85% lightweighted, 1.4-m (55.1-in.)-diameter ULE primary was being developed for the Schmidt telescope to be used in the photometer for NASA's Kepler Mission to search for habitable planets orbiting distant solar-like stars. Although no details of the mirror or its mounting have as yet appeared in the open literature, it was stated by those authors that the mirror would be frit-bonded by Corning. Completion of this mirror is expected late in 2005. It is hoped that further information about its opto-mechanical design will be available soon thereafter.

9.7 LOW-TEMPERATURE BONDED SUBSTRATES

In an attempt to reduce the significant cost and time required to fabricate large lightweight mirror structures by fusion or frit-bonding techniques, Schott Glass Technologies of Duryea, PA and Goodrich Corporation of Danbury, CT have reported progress of cooperative efforts to bond Zerodur by a low-temperature bonding technique. Plano–plano mirror substrates as large as 292 mm (11.5 in.) diameter and 50.8 mm (2.0 in.) overall thickness with a 2.9-mm (0.11-in.)-thick front and a 2.0-mm (0.08-in.)-thick back face plate have been fabricated (Strzelecki et al., 2003).

In the basic bonding process, one side of each slightly oversized face plate is polished to ~ 200 nm p-v flatness, as are the top and bottom of a core that has previously been lightweighted by an abrasive water jet (AWJ) process (see Section 9.8). The second side of each face plate is polished to ~ 630 nm p-v figure. The core and one plate, which have previously been chemically prepared to provide hydrophilic surfaces, are placed in a Class 100 clean box, where a robot applies a thin layer of aqueous inorganic bonding agent between the prepared surfaces. Bonding occurs under self-weight of the plate over a period of the order of 1 d duration at room temperature or slightly elevated temperature. The subassembly is then turned over and the second plate is bonded in place by the same process. After curing and inspection, the subassembly is ready for final sizing and figuring. Experimentation and process development is continuing on this process.

9.8 MACHINED-CORE SUBSTRATES

Another fundamental method of lightweighting mirrors is to machine depressions into the back of a solid disk. A mirror made by this approach resembles that of the Hale Telescope primary, which has cavities obtained by casting the glass around strategically placed cores. Similar recesses can be sandblasted or waterblasted† into the disk, or ground by a CNC milling machine using diamond-impregnated tools to form the chosen web structure configuration. Generally, mirrors with this type of construction have lower rigidity than designs with a back face sheet.

Stiffer mirrors are obtained if the cavities are created by a milling tool entering a solid plate through small blind access holes drilled into the back surface. The access holes have only a small effect on the blank stiffness. This technique is not new. A mirror design described by Simmons (1970) and illustrated by Figure 9.20 and Figure 9.21 had triangular internal cavities obtained by undercutting with a grinding tool through a series of blind access holes 2.5 in. (6.4 cm) in diameter drilled into the back of a 64-in. (1.62-m)-diameter × 12-in. (30.5-cm)-thick solid disk. The ribs between cavities were 0.20 in. (5.1 mm) thick. All fillets at the intersection of ribs with one another and with the front and back plates had 0.75 in. (19 mm) radii. This left a large post of material at the intersection of each set of six triangles. Weight was reduced at some expense in stiffness by removing material from the centers of these posts by machining a 1.5-in. (3.8-cm)-diameter cylindrical cavity into them. The center-to-center distance of these holes was 7.30 in. (18.5 cm). The height of each equilateral triangle was 5.25 in. (13.3 cm).

This blank contained 138 large, shaped cavities and 55 small, cylindrical cavities. It weighed 1035 lb (~ 470 kg). If solid, it would weigh 3475 lb (~ 1580 kg); this represented a weight reduction of 70%. Dimensional control of the internal surfaces created by this technique was comparable with that achieved with normal metalworking. After removal of the desired mass of material from the cavities, the mirror was machined to its final external dimensions. It was then acid-etched to remove surface imperfections and local stresses in the surfaces.

A mirror design described by Pepi and Wollensak (1979) and Pepi et al. (1980) had a separate core lightweighted by machining numerous through holes of specific shapes and locations (see Figure 9.22) into a solid disk of fused silica. Fused to that core were preformed, fused silica front and back face sheets. This design had a biconcave, symmetrical cross section, flat neutral surface,

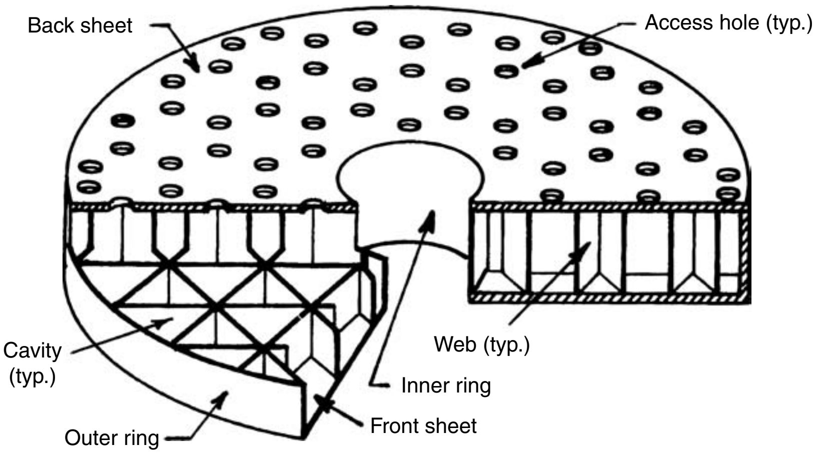

FIGURE 9.20 Cutaway view of the back of a lightweight mirror blank containing triangular internal cavities undercut through multiple access holes (circles). (Adapted from Simmons, G.A., *Optical Telescope Technology, MSFC Workshop, April 1969*, NASA Rept. SP-233, 219, 1970.)

---

† Waterblasting is similar to sandblasting except that the medium propelling the abrasive is a highly pressurized water jet.

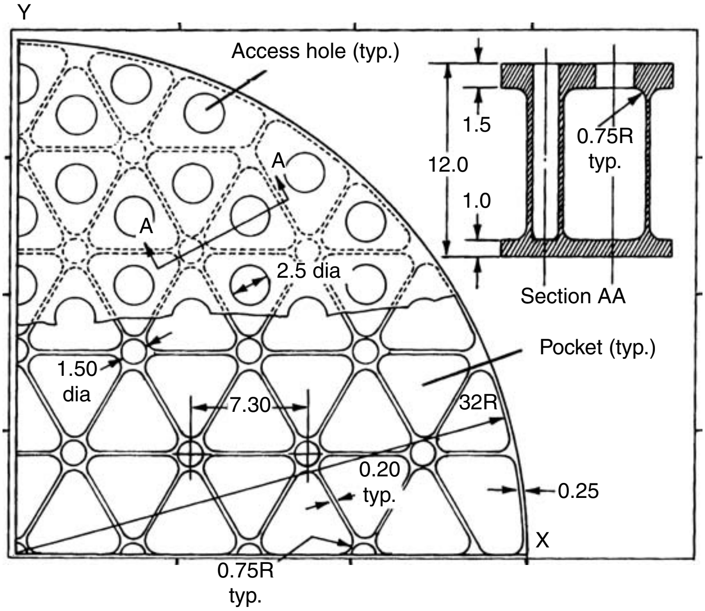
Y
Access hole (typ.)
A
A
2.5 dia
1.5
12.0
1.0
0.75R
typ.
Section AA
Pocket (typ.)
1.50
dia
7.30
32R
0.20
typ.
0.25
X
0.75R
typ.

FIGURE 9.21 Configuration of a 64 in.(1.62 m) diameter Cer-Vit mirror of the type shown in Fig. 9.20. All dimensions are inches. (Adapted from Simmons, G.A., *Optical Telescope Technology, MSFC Workshop, April 1969*, NASA Rept. SP-233, 219, 1970.)

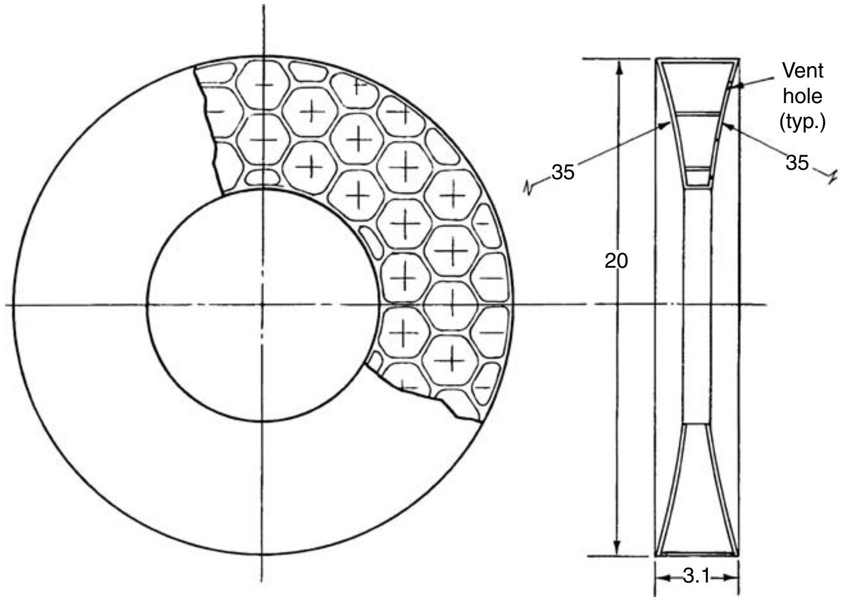
Vent
hole
(typ.)
35
35
20
3.1

FIGURE 9.22 Configuration of a symmetrical concave mirror blank with its core machined from a solid disk. The front and back plates were heated and sagged over a convex mandrel to meniscus shape and then fused to the core. Dimensions are inches. (From Pepi, J.W. and Wollensak, R.J., *Proc. SPIE*, 183, 131, 1979.)

and CG located in that surface. The 20-in. (50.8-cm)-diameter mirror weighed about 16 lb (7.3 kg). Gravity sag when the mirror was oriented with axis horizontal had a minimal value.

The core fabrication process was generally as follows. The core blank was first diamond-generated to the double-concave configuration. Drilling and cavity grinding utilized bonded diamond annular (core) drills and end mills to produce rib thicknesses of approximately 3 mm. Factors considered to minimize the risk associated with these operations beyond the obvious use of high-quality diamond tooling were to properly support the blank from the back and careful removal of the plugs that remained after core drilling. Figure 9.23 shows a typical coring pattern. The cusps remaining after coring were removed by milling with a diamond cutter.

The preparation of the face sheets for this mirror required no new technology. The plates were fabricated as meniscus blanks approximately 0.75 in. (19 mm) thick on conventional optical sphere generating equipment. Extra face plate thickness was provided for sufficient stiffness to minimize quilting effects during the subsequent fusing operation. The face plates were thinned to their final thicknesses of 0.21 in. (5.3 mm) by diamond generating after the blank was fused. The reflecting surface was then aspherized into an *f*/1.7 ellipse for a particular application in a cryogenic orbital environment.

A modern example of mirror fabrication by this technique is shown in Figure 9.24. This is a diagram of the back side of the 2.7-m (106-in.)-diameter primary mirror for the Stratospheric Observatory for Infrared Astronomy (SOFIA) telescope. The mirror design is a plano-concave structure with a heavily beveled rim formed into "flying buttress" lateral supports and a circular central hole. Hexagonal internal cells with thin webs were machined into the Zerodur blank using diamond tools to undercut material through blind access holes drilled into the back surface. A nearly complete back plate remained. After machining, the substrate was acid etched to further reduce weight and to remove microscopic cracks created during the grinding operation. The weight of the resulting structure was about 880 kg (1940 lb). This is about 20% of the weight of a corresponding solid mirror. The supports for this mirror are described in Chapter 12.

Another machining technique for making a lightweight core from a solid blank uses the AWJ cutting process perfected by Corning Glass Works. Edwards (1998) described the technique and apparatus used (see Figure 9.25) as follows:

> The system is powered by two 250 horsepower motors driving hydraulic pumps, which in turn feed intensifiers that output over 60,000 psi water pressure. Passing through a 0.040 in. (1.02 mm) diameter sapphire jewel orifice, the water jet creates a vacuum, pulling abrasive garnet into the stream. After fully

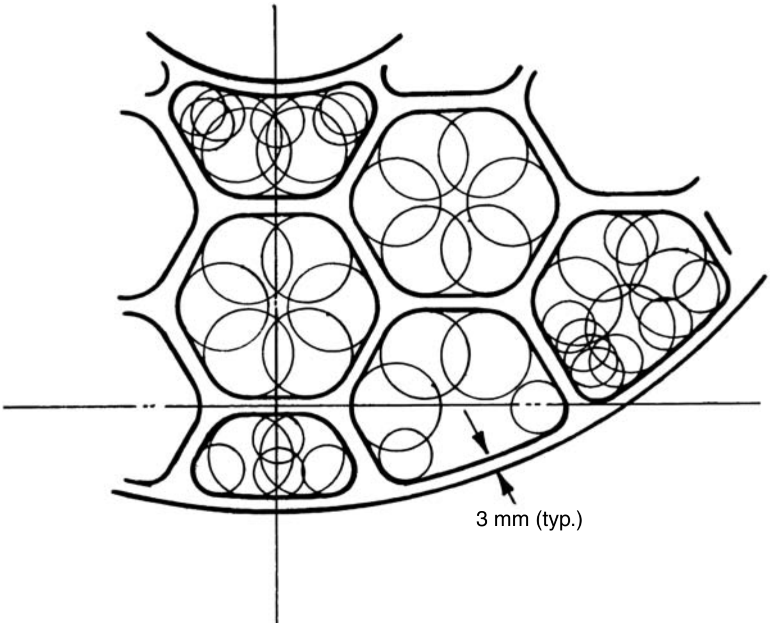

FIGURE 9.23 Typical core machining pattern for a mirror such as that shown in Figure 9.22. (From Pepi, J.W. and Wollensak, R.J., *Proc. SPIE*, 183, 131, 1979.)

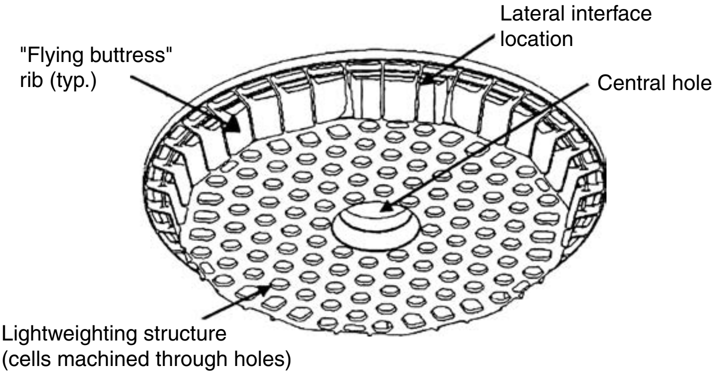
"Flying buttress" rib (typ.)
Lateral interface location
Central hole
Lightweighting structure (cells machined through holes)

FIGURE 9.24 Diagram of the back side of the SOFIA primary mirror lightweighted by machining pockets through holes in the back surface. (Adapted from Erdman, M. et al., *Proc. SPIE*, 4014, 309, 2000.)

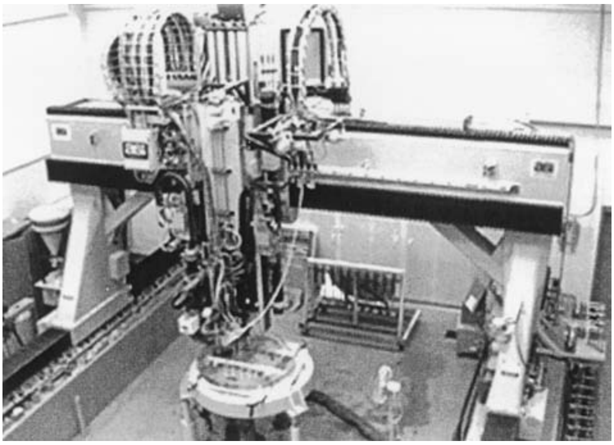

FIGURE 9.25 Photograph of the Corning abrasive water jet (AWJ) machine used to make lightweight mirror cores. (From Edwards, M.J., *Proc. SPIE*, 3356, 702, 1998.)

> entraining the abrasive in a mixing tube, the water exits the nozzle at over Mach 2, capable of cutting through 30 cm thick glass. A tool check station provides alignment and process parameter calibration. The five-axis head can compensate for slight changes in the shape of the cut due to wear of the jewel and mixing tube during jet-on time as well as any slight part movement. The system manipulator positions the nozzle in the 150 in. × 250 in. × 48 in. workspace to an accuracy of better than ± 0.0025 in., repeatable to within ± 0.001 in. Each day the operator makes test cuts that are measured to determine the health and contour of the jet. Ongoing verification throughout the waterjet process ensures tight dimensional tolerances are maintained in the resultant lightweight cores.

Hobbs et al. (2003) further described the AWJ process and indicated that substrates up to ~ 3 m (~ 118 in.) can be processed, that cores can be customized to accommodate special mirror mounts, and that spatial nonuniformities and variable stiffness distributions can be produced if desired.

Figure 9.26 shows a typical mirror core made by the Corning AWJ process. This is a 1.1-m (43.3-in.)-diameter core to be incorporated into one of the tertiary mirrors for the 6.5 m (255.9 in.) aperture Magellan Telescopes. This particular design incorporated thicker webs at the outer edge and central mounting hub, a hexagonal pattern superimposed on an elliptically shaped blank, and a circular central through-hole (Edwards, 1998).

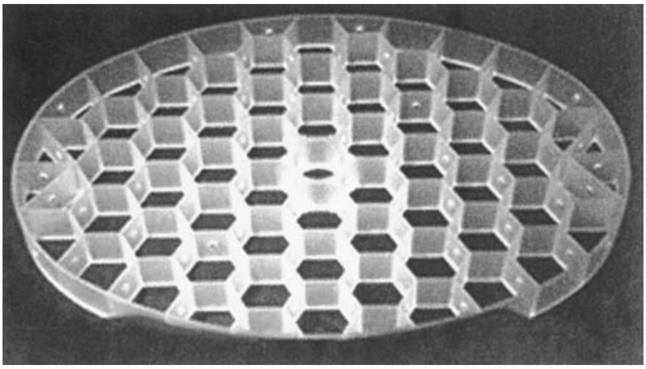

FIGURE 9.26 Typical example of a 1.1-m (43.3-in.)-diameter mirror core lightweighted by the Corning AWJ process. (From Edwards, M.J., *Proc. SPIE*, 3356, 702, 1998.)

9.9 CONTOURED-BACK SOLID MIRROR CONFIGURATIONS

The baseline configuration for mirrors with flat, concave, and convex first (reflecting) surfaces is the regular solid having a flat second surface. Reduction of weight by thinning the baseline substrate reduces stiffness, increases self-weight deflection, and increases susceptibility to acceleration forces. Hence, this technique can only be used within limits. A better way to reduce the weight of front-surface mirrors is to contour the second (back) surface. Figure 9.27 illustrates this approach for a series of 6 concave mirrors with the same diameter $D_G = 2r_2$ and radius of curvature of the reflecting surface (R_1). Fabrication complexity increases from left to right in views (a)–(f). Figure 9.27(g) shows, for comparison, a double-concave version that is not lightweighted.

Yoder (2002) discussed each variation of contoured back mirrors in turn and showed how to calculate mirror volume, which, when multiplied by the appropriate density, gives the mirror weight. In that reference, typical examples were given in which the mirror diameters, axial thicknesses, radii of curvature of the reflecting surfaces, and material types were all the same, but their R_2 surfaces were variously contoured. Included were mirrors with the baseline flat back, a tapered back, a concentric meniscus, a meniscus with $R_2 < R_1$, a single arch with a Y-axis parabolic back, a single arch with an X-axis parabolic back, a double-arch back, and a double concave with $R_2 = -R_1$. Note that the latter configuration was not lightweighted; it was included for comparison only. The two types of parabolic single-arch contours are shown in Figure 9.28. They differ with regard to the location of the vertex of the parabola.

The calculations in Yoder (2002) allow direct comparisons of relative weights for the different designs for one particular set of opto-mechanical parameters. Table 9.3 summarizes the results of this analysis by showing the volumes, weights, and weights relative to the baseline configuration for these optically equivalent mirrors. The data indicate that a single-arch mirror with an X-axis parabolic back surface (vertex at the mirror's rim) is lighter in weight than all other configurations listed. Its weight advantage over the Y-axis single-arch version is, however, minimal.

The reader is referred to the detailed treatment by Cho and Richard (1990) for information about the effect of changing rear surface contours on the mirror's opto-mechanical performance, including variations of axis orientation with respect to the gravity vector. One relationship of particular interest given by Cho and Richard (1990) allows the self-weight axial deflection of a contoured back mirror to be scaled as the mirror size (but not configuration) is varied. This is:

$$\delta = \left(\frac{\rho}{\rho_{\mathrm{REF}}}\right)\left(\frac{E_{\mathrm{REF}}}{E}\right)\left(\frac{A}{A_{\mathrm{REF}}}\right)\delta_{\mathrm{REF}} \tag{9.5}$$

where δ_{REF}, E_{REF}, A_{REF}, and ρ_{REF} are the rms deflection, Young's modulus, cross-sectional area, and density of the initial (reference) mirror, respectively. The same parameters without subscripts pertain to the new mirror.

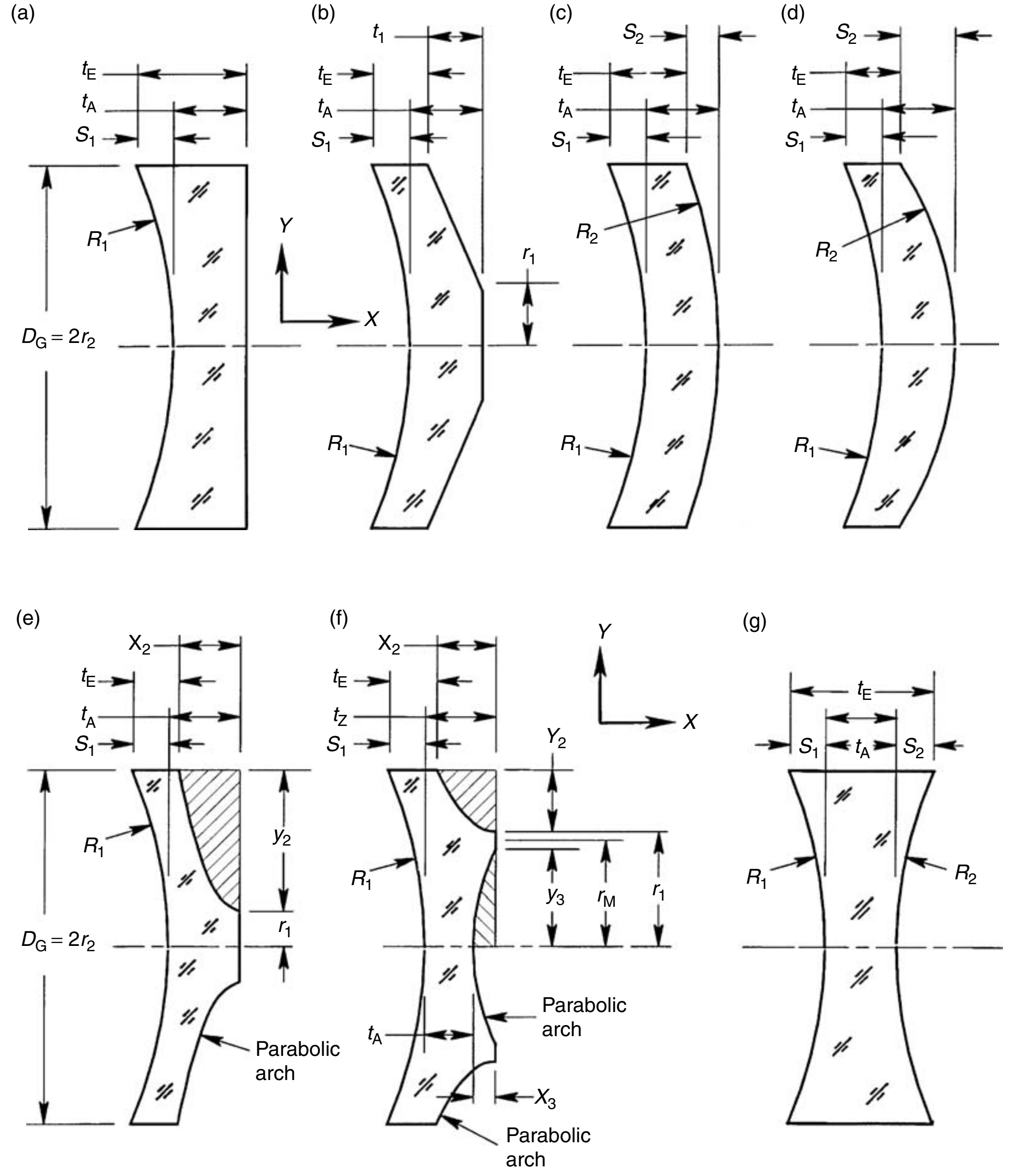
(a)
t_E
t_A
S_1
R_1
$D_G = 2r_2$
(b)
t_1
t_E
t_A
S_1
Y
X
r_1
R_1
(c)
S_2
t_E
t_A
S_1
R_2
R_1
(d)
S_2
t_E
t_A
S_1
R_2
R_1
(e)
X_2
t_E
t_A
S_1
R_1
y_2
r_1
$D_G = 2r_2$
Parabolic arch
(f)
X_2
t_E
t_Z
S_1
R_1
Y
X
Y_2
y_3
r_M
r_1
Parabolic arch
t_A
X_3
Parabolic arch
(g)
t_E
S_1
t_A
S_2
R_1
R_2

FIGURE 9.27 Examples of concave mirrors with weight reduced by contouring the rear surface. (a) baseline with flat rear surface, (b) tapered (conical) rear surface, (c) concentric spherical front and rear surfaces with $R_2 = R_1 + t_A$, (d) spherical rear surface with $R_2 < R_1$, (e) single-arch configuration, (f) double-arch configuration. (g) double-concave configuration (not lightweighted) for comparison. (From Yoder, P.R., Jr., *Mouting Optics in Optical Instruments*, SPIE Press, Bellingham, 2002.)

Vukobratovich (1997) also discussed these mirror forms and their relative merits. He pointed out that the variation in axial thickness of contoured mirrors causes different parts of the mirror to react differently to changes in temperature. This would tend to introduce temporally variable optical surface distortion. Further, he indicated that, in the single-arch mirror, the CG tends to be near or in front of the reflecting surface vertex, so it is difficult to support the mirror radially in the plane

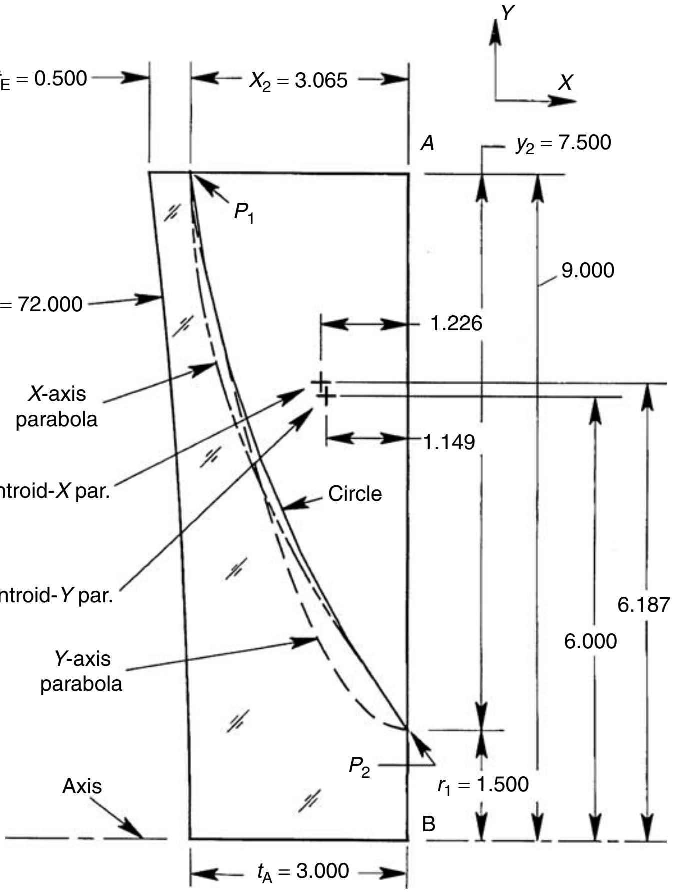

FIGURE 9.28 Three possible contours (*X*-axis parabola, *Y*-axis parabola, and circle) for the single-arch mirror plotted to the same scale. Dimensions are inches and apply to the designs summarized in Table 9.3. (From Yoder, P.R., Jr., *Mounting Optics in Optical Instruments*, SPIE Press, Bellingham, 2002.)

through the CG. When the axis of such a mirror is horizontal, the optical surface tends to become astigmatic. The double-arch mirror configuration is less susceptible to this problem because the CG is usually inside the mirror, so radial support can be at a more favorable location.

9.10 THIN FACE SHEET MIRROR CONFIGURATIONS

Interest in the design of large-diameter mirrors with abnormally thin face sheets is growing throughout the world as a means for reducing the weight of mirror substrates. Designs with diameter-to-thickness ratios of 100:1 or even 200:1 are being considered, as are diameters of 30 m (~ 98 ft) and larger. The weight savings in telescope designs using such mirrors as compared with more conventional configurations could be large since the overall system weight escalates rapidly with the weight of the primary owing to the massive structure and complex mechanisms required to support the mirror.

A particularly attractive concept is to support a relatively thin mirror face sheet from a "rigid" backing structure by means of a multiplicity of actuators that function in closed loop servo fashion to maintain, or adapt, the figure of the optical surface under the real-time control of a system performance measurement system. Active compensation for atmospheric effects has also been demonstrated with some existing large astronomical telescopes having active or adaptive mirror systems.

TABLE 9.3
Comparison of Volumes and Weights of Contoured-Back Mirrors of Equal Overall Dimensions and Concave Radius[a], but with Back Surfaces Contoured as Depicted in Figure 9.27

Configuration	Figure View	Volume (in.^{3})	Weight (lb)	Relative Weight(%)	Pearson's Ratio[b]
Flat back (baseline)	(a)	835.2	66.6	100	4.9
Tapered back	(b)	456.0	36.3	55	8.9
Concentric meniscus	(c)	766.3	61.1	92	5.3
Meniscus ($R_2 < R_1$)	(d)	460.3	36.7	55	8.8
Single-arch (Y-axis parabolic)	(e)	257.4	20.5	31	15.8
Single-arch (X-axis parabolic)	(e)	239.4	19.1	29	16.9
Double-arch	(f)	389.2	31.0	47	10.4
Double-concave (not lightweighted)	(g)	906.9	72.3	109	4.5

[a] $D_G = 18.0$ in., $t_A = 3.0$ in., $R_1 = 72.0$ in., Corning ULE.

[b] Defined in Section 9.11.

Note: Volume and weight data from Yoder (2002).

The theoretical and experimental work along these lines that currently appears in the literature indicates rewarding applications to space- and ground-based telescopes.

Further considerations of thin face sheet mirrors may be found in Section 12.7.

9.11 SCALING RELATIONSHIPS FOR LIGHTWEIGHT MIRRORS

Pearson (1980) defined lightweight monolithic mirrors as those with diameter-to-thickness ratios greater than 8. He also suggested that the ratio (surface area)$^{1.5}$/(mirror volume) > 7 could be used to define a lightweight mirror. The latter ratio applies equally to substrates with uniform thickness and to those with variable thickness. As an example of the use of this criterion, let us consider the series of contoured-back mirrors listed in Table 9.3. In each case, the surface area is $\pi(D_G/2)^2 = \pi(18/2)^2 = 254.5$ in.^{2} Dividing by the mirror volumes from the third column of the table, we obtain the Pearson ratios listed in the last column of that table. The configurations that meet Pearson's criterion are the tapered back, the meniscus with $R_2 < R_1$, both single- and the double-arch mirrors. The mirror with a flat back, the concentric-meniscus mirror, and the double-concave mirror would not be considered lightweight. Parametric analysis of Pearson's ratio shows that for constant *f* number and D_G/t_A, the ratio is independent of mirror diameter. Further, it varies slowly with *f* number.

A direct comparison of open-back, symmetrical sandwich, and single- and double-arch contoured-back mirrors (see Figure 9.29) was reported by Valente and Vukobratovich (1989). Mirror diameter of 40 in. (1 m) and material type (fused silica) were held constant. Self-weight deflection, overall thickness, weight, and efficiency (defined as the ratio of surface deflection to thickness) for each mirror type oriented with gravity parallel to the mirror axis were computed. Certain reasonable assumptions were made by the authors with regard to various mirror parameters such as sandwich mirror core solidity,[‡] face sheet thickness, rib thickness, etc. The results of this parametric analysis were plotted in various ways, so the mirror designer can easily visualize the consequences of parameter variations. One figure from this study especially pertinent to the present topic is shown in Figure 9.30.

[‡] Mehta (1987) defined core solidity η as $(2B + t_W)(t_W)/(B + t_W)^2$, where B the diameter of the circle inscribed in the cell and t_W the web thickness.

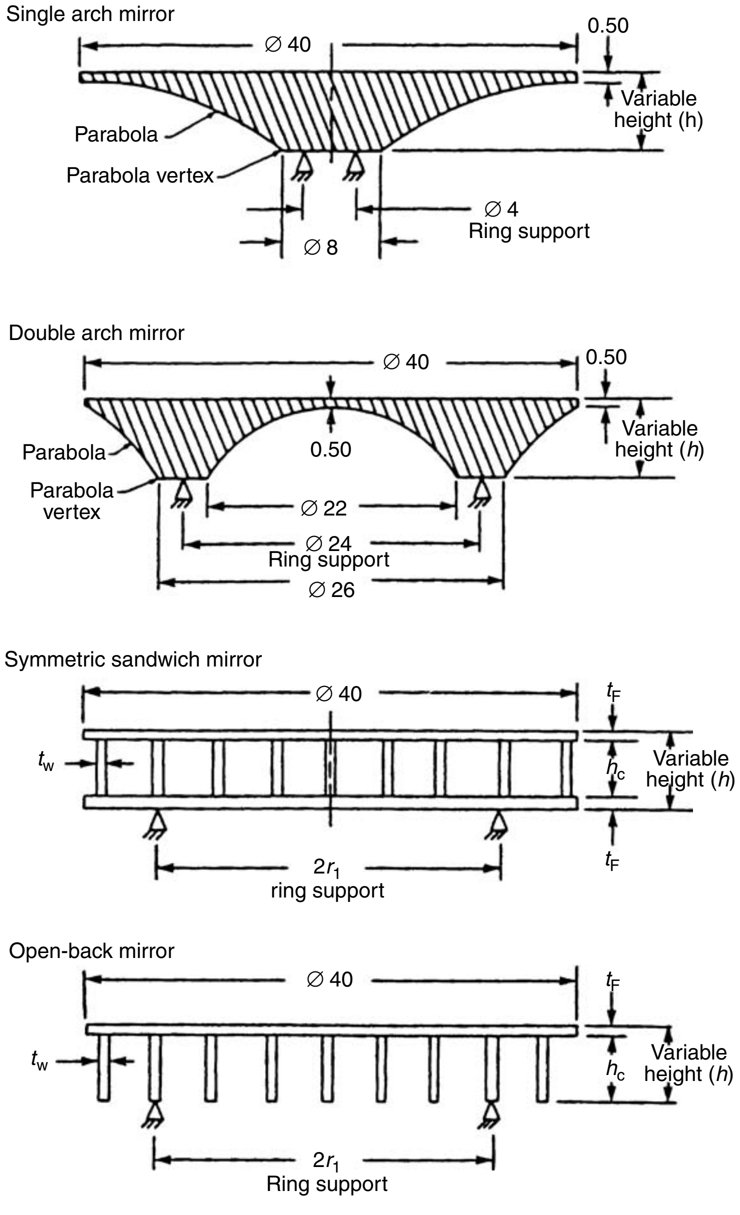
Single arch mirror
Ø 40
0.50
Variable height (h)
Parabola
Parabola vertex
Ø 4
Ring support
Ø 8
Double arch mirror
Ø 40
0.50
Variable height (h)
Parabola
0.50
Parabola vertex
Ø 22
Ø 24
Ring support
Ø 26
Symmetric sandwich mirror
Ø 40
tF
tW
hC
Variable height (h)
tF
2r1
ring support
Open-back mirror
Ø 40
tF
tW
hC
Variable height (h)
2r1
Ring support

FIGURE 9.29 Mirror geometry for single-arch, double-arch, symmetric sandwich, and open-back mirrors studied by Valente and Vukobratovich. All dimensions are inches. (From Valente, T.M. and Vukobratovich, D., *Proc. SPIE*, 1167, 20, 1989.)

In the same study, fabrication issues and case of mounting were considered. The qualitative comparisons made there provide meaningful guidance to the mirror designer and user alike. The cost impact of critical decisions can be recognized even though specific numerical relationships are not included.

Cho et al. (1989) presented a comparative analysis of the surface deformations under self-weight conditions at zenith and horizon orientations for various mirror types (contoured back and foam core) with various support types. The results were presented graphically. A few general conclusions were drawn: (1) optical performance depends on material characteristics, contoured-back

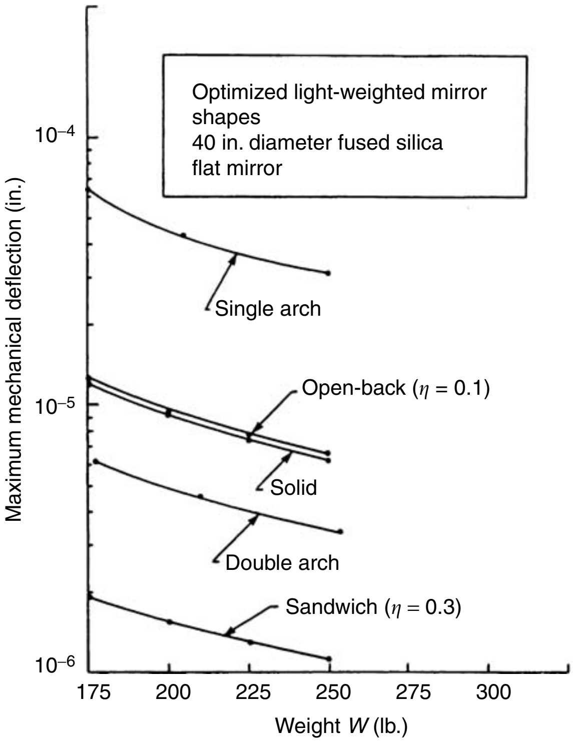

FIGURE 9.30 Graphs of maximum self-weight mechanical deflections with axis vertical vs. mirror weight for various mirror configuations. (From Valente, T.M. and Vukobratovich, D., *Proc. SPIE*, 1167, 20, 1989.)

mirror shape, and support location, (2) structural deflection over the optical surface does not always indicate optical performance, (3) optimum shape of a double-arch metal foam core (SXA material) mirror is a ring support at the 50% radial zone, and (4) the optimum support location for three equally spaced support points is inside the 50% radial zone regardless of contoured back shape.

A cubic relationship between diameter and weight was applied to conventional (nonlightweighted) mirrors for many years. Vukobratovich (1993) refined this expression to

$$W = 246D_G^{2.92} \tag{9.6}$$

where W is mirror's weight in kg, D_G the mirror's diameter in m, and D_G/t_A the aspect ratio 6:1. He also stated that the mount for such a mirror probably weighs about as much as the mirror itself. That same publication gave two approximate expressions for weight vs. diameter as

$$W = 120D_G^{2.82} \tag{9.7}$$

for conventional lightweighted mirrors (weight approximately 30 to 40% of that of a conventional solid mirror) and

$$W = 53D_G^{2.67} \tag{9.8}$$

for state-of-the-art lightweighted designs (weight approximately 20% of that of a conventional mirror). These relationships were based on the analysis of several existing mirror designs. Since those designs were almost all different, no single relationship was felt to apply adequately to all.

On the other hand, Hamill (1979) suggested the following single equation for all lightweighted mirrors:

$$W = \frac{kD_G^{2.6}}{(D_G/t_A)} \tag{9.9}$$

where k is a constant and the other parameters are as defined previously.

Valente (1990) reported an extensive analysis of weight and diameter data for both solid mirrors (13 examples) and various types of lightweighted mirrors (48 examples). Solid mirrors with an aspect ratio < 0.1 were considered in the lightweight class. A series of 19 different curve-fitting expressions were tried in order to obtain a best fit to the data in various groupings. In each case, the goodness of fit was calculated to determine the optimum expression. The following expressions were found to apply to the indicated groups:

$$w = 246\,D_G^{2.92} \quad \text{for all solid mirrors} \tag{9.10}$$

$$w = 82D_G^{2.95} \quad \text{for all lightweight mirrors} \tag{9.11}$$

$$w = 68D_G^{2.90} \quad \text{for all structured mirrors} \tag{9.12}$$

$$w = 106D_G^{2.71} \quad \text{for all contoured mirrors} \tag{9.13}$$

$$w = 26D_G^{2.31} \quad \text{for beryllium mirrors} \tag{9.14}$$

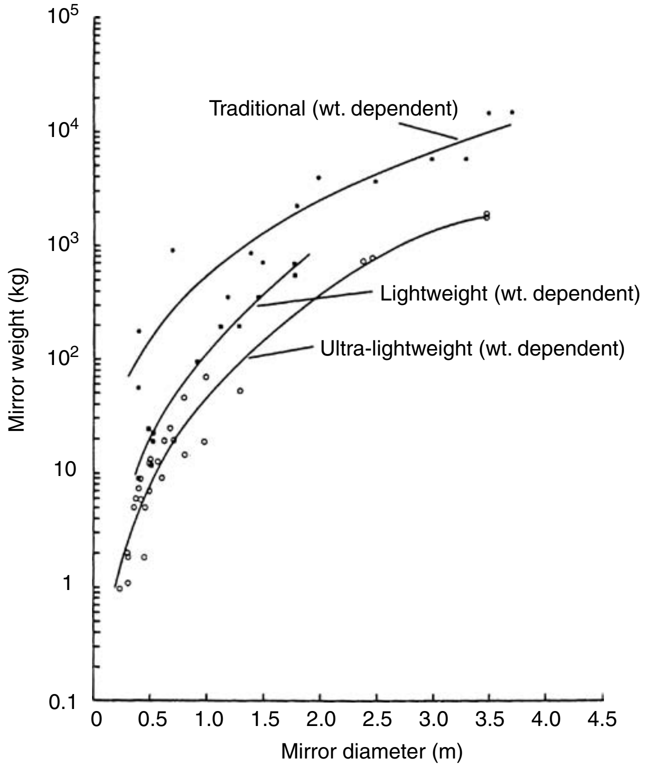

FIGURE 9.31 Weight vs. diameter for traditional (solid), lightweight, and ultra-lightweight mirrors fitting Eqs. (9.15)–(9.17). (From Valente, T.M., *Proc. SPIE*, 1167, 20, 1989.)

Hamill's relationship (Eq. [9.9]) also was used by Valente to analyze these data. She grouped all the solid mirrors and the heavier lightweights together, called them "traditional" mirrors, and calculated the value of k for this group. The average k was then substituted into the power function equation to determine the applicable "average" exponent. The same was done for groups of lightweight mirrors and ultra-lightweight mirrors. The results were as follows:

$$w = 192D_G^{2.76} \quad \text{for traditional mirrors } (k_{\text{AVG}} = 2560) \tag{9.15}$$

$$w = 120D_G^{2.82} \quad \text{for lightweight mirrors } (k_{\text{AVG}} = 802) \tag{9.16}$$

$$w = 53D_G^{2.67} \quad \text{for ultra-lightweight mirrors } (k_{\text{AVG}} = 387) \tag{9.17}$$

Note that the results for "all solid mirrors" and for "ultra-lightweight mirrors" are the same as reported by Vukobratovich (1993).

Valente plotted graphical representations of the various relationships along with the data from which the curves were derived. For example, Figure 9.31 represents the relationships of Eqs. (9.15)–(9.17). To the eye, the curves fit the data remarkably well; the goodness-of-fit calculations reported by Valente verify this visual conclusion.

REFERENCES

Anderson, D.S., Martin, H.M., Burge, J.H., Ketelsen, D.A., and West, S.C., Rapid fabrication strategies for primary and secondary mirrors at Steward Observatory Mirror Laboratory, *Proc. SPIE*, 2199, 199, 1994.

Angel, J.R.P., New techniques for fusion bonding and replication for large glass reflectors, *Proc. SPIE*, 383, 52, 1983.

Angel, J.R.P. and Hill, J. M., Manufacture of large glass honeycomb mirrors, *Proc. SPIE*, 332, 298, 1982.

Angel, J.R.P. and Wangsness, P.A.A., U.S. Patent 4,606,960, 1986.

Angel, J.R.P., Davison, W.B., Hill, J.M., Mannery, E. J., and Martin, H.M., Progress toward making lightweight 8 m mirrors of short focal length, *Proc. SPIE*, 1236, 636, 1990.

Angel, J.R.P., Woolf, N.J., Hill, J.M., and Gable, L., Steps toward 8 m honeycomb mirror blanks: IV: some aspects of design and fabrication, *Proc. SPIE*, 444, 194, 1983.

Anthony, F.M., McCarter, D.R., Tangedahl, M., and Wright, M., Frit bonding: A way to larger and more complex silicon components, *Proc. SPIE*, 5179, 194, 2003.

Bowen, I.S., The 200-inch Hale telescope, in *Telescopes*, Kuiper, G. and Middlehurst, B., Eds., Univ. of Chicago Press, Chicago, IL, 1960, p. 1.

Cannon, J.E. and Wortley, R.W., Gas fusion center-plane-mounted secondary mirror, *Proc. SPIE*, 966, 309, 1988.

Cheng, A.Y.S. and Angel, J.R.P., Steps toward 8 m honeycomb mirrors VIII: Design and demonstration of a system of thermal control, *Proc. SPIE*, 628, 536, 1986.

Cho, M.K. and Richard, R.M., Structural and optical properties for typical solid mirror shapes, *Proc. SPIE*, 1303, 78, 1990.

Cho, M.K., Richard, R.M., and Vukobratovich, D., Optimum mirror shapes and supports for light weight mirrors subjected to self-weight, *Proc. SPIE*, 1167, 2, 1989.

Doyle, K.B., Genberg, V.L., and Michels, G.J., *Integrated Optomechanical Analysis*, SPIE Press, Bellingham, 2002.

Edwards, M. J., Current fabrication techniques for ULE™ and fused silica lightweight mirrors, *Proc. SPIE*, 3356, 702, 1998.

Englehaupt, D., Fabrication methods, in *Handbook of Optomechanical Engineering*, Ahmad, A., Ed., CRC Press, Boca Raton, FL, 1997, chap. 10.

Erdmann, M., Bittner, H., and Haberler, P., Development and construction of the optical system for the airborne observatory SOFIA, *Proc. SPIE*, 4014, 309, 2000.

Fitzsimmons, T.C. and Crowe, D.A., Ultra-Lightweight Mirror Manufacturing and Radiation Response Study, *RADC-TR-81-226*, Rome Air Development Ctr., Rome, NY, 1981.

Goble, L., Ford, R., and Kenagy, K., Large honeycomb mirror molding methods, *Proc. SPIE*, 966, 291, 1988a.

Goble, L.W., Angel, J.R.P., and Hill, J.M. Spincasting of a 3.5-m diameter *f*/1.75 mirror blank in borosilicate glass, *Proc. SPIE*, 966, 300, 1988b.

Hagy, H.E. and Shirkey, W.D., Determining absolute thermal expansion of titania-silica glasses: a refined ultrasonic method, *Appl. Opt.*, 14, 2099, 1975.

Hamill, D., Fabrication technology for advanced space optics, *OSA Workhop on Optical Fabrication and Testing*, Tucson, AZ, 1979, chap. 24.

Hill, J.M., Angel, J.R.P., Lutz, R.D., Olbert, B.H., and Strittmatter, P.A., Casting the first 8.4-m borosilicate honeycomb mirror for the large binocular telescope, *Proc. SPIE*, 3352, 172, 1998.

Hobbs, T.W., Edwards, M., and VanBrocklin, R., Current fabrication techniques for ULE® and fused silica lightweight mirrors, *Proc. SPIE*, 5179, 1, 2003.

Koch, D., Borucki, W., Dunham, E., Geary, J., Gilliland, R., Jenkins, J., Latham, D., Bachtell, E., Berry, D., Deininger, W., Duren, R., Gautier, N., Gillis, L., Mayer, D., Miller, C., Shafer, D., Sobeck, C., and Weiss, M., Overview and status of the Kepler mission, *Proc. SPIE*, 5487, 1491, 2004.

Lewis, W.C., Space telescope mirror substrate, *OSA Optical Fabrication and Testing Workshop*, Tucson, AZ, 1979, chap. 5.

Loytty, E.Y., Lightweight Mirror Structures, *Optical Telescope Technology, MSFC Workshop, April 1969,* NASA Rept. SP-233, 241, 1969.

Loytty, E.Y. and DeVoe, C.F., Ultralightweight mirror blanks, *IEEE Trans. Aerospace Electron. Syst. AES-5*, 300, 1969.

Marker, A.J., Fuhrmann, H., Tietze, H., and Froelich, W., Lightweight large mirror blanks of Zerodur, *Proc. SPIE*, 571, 5, 1985.

Martin, H.M., Burge, J.H., Ketelsen, D.A., and West, S.C., Fabrication of the 6.5-m primary mirror for the multiple mirror telescope conversion, *Proc. SPIE*, 2871, 399, 1996.

Mehta, P., Flexural rigidity characteristics of lightweighted mirrors, *Proc. SPIE*, 748, 158, 1987.

Morian, H.F., Mackh, R., Müller, R.W., Höness, H.F., Performance of the four 8.2-m zerodur mirror blanks for the ESO/VLT, *Proc. SPIE*, 2871, 405, 1996.

Müller, R.W., Höness, H.W., and Marx, T.A., Spin-cast Zerodur® mirror substrates of the 8 m class and lightweighted substrates for secondary mirrors, *Proc. SPIE*, 1236, 723, 1990.

Müller, R.W., Höness, H.F., Morian, H.F., and Loch, H., Manufacture of the first primary mirror blank for the very large telescope (VLT), *Proc. SPIE*, 2199, 164, 1994.

Olbert, R.D., Angel, J.R.P., Hill, J.M., and Hinman, S.F., Casting 6.5-meter mirrors for the MMT conversion and Magellan, *Proc. SPIE*, 2199, 144, 1994.

Paquin, R.A., Materials for optical systems, in *Handbook of Optomechanical Engineering*, Ahmad, A., Ed., CRC Press, Boca Raton, FL, 1997, chap. 3.

Parks, R.E., Wortley, R.W., and Cannon, J.E., Engineering with lightweight mirrors, *Proc. SPIE*, 1236, 735, 1990.

Pearson, E.T., Thin mirror support systems, in *Proceedings of Conference on Optical and Infrared Telescopes for the 1990's*, Vol. 1, Hewett A., Ed., Kitt Peak Nat. Observ., Tucson, AZ, 1980, p. 555.

Pepi, J.W. and Wollensak, R.J., Ultra-lightweight fused silica mirrors for a cryogenic space optical system, *Proc. SPIE*, 183, 131, 1979.

Pepi, J.W., Kahan, M.A., Barnes, W.H., and Zielinski, R.J., Teal Ruby-design, manufacture and test, *Proc. SPIE*, 216, 160, 1980.

Rodkevich, G.V. and Robachevskaya, V.I., Possibilities of reducing the mass of large, precision mirrors, *Sov. J. Opt. Technol.*, 44, 515, 1977.

Seibert, G.E., Design of Lightweight Mirrors, *SPIE Short Course SC18*, 1990.

Simmons, G.A., The design of lightweight Cer-Vit mirror blanks, *Optical Telescope Technology, MSFC Workshop, April 1969,* NASA Rept. SP-233, 219, 1970.

Spangenberg-Jolley, J. and Hobbs, T., Mirror substrate fabrication techniques of low expansion glasses, *Proc. SPIE*, 1013, 198, 1988.

Strzelecki, M.T., Magida, M., O'Malley, R., Steir, M., Trefny, K., and Wykoff, N.P., Low temperature bonding of light-weighted mirrors, *Proc. SPIE*, 5179, 50, 2003.

Valente, T.M., Scaling laws for light-weight optics, *Proc. SPIE*, 1340, 47, 1990.

Valente, T.M. and Vukobratovich, D., A comparison of the merits of open-back, symmetric sandwich and contoured back mirrors as light-weighted optics, *Proc. SPIE*, 1167, 20, 1989.

Voevodsky, M. and Wortley, R.W., Ultra-lightweight borosilicate gas-fusion™ mirror for cryogenic testing, *Proc. SPIE*, 5179, 12, 2003.

Vukobratovich, D., Lightweight laser communications mirrors made with metal foam cores, *Proc. SPIE*, 1044, 216, 1989.

Vukobratovich, D., Introduction to Optomechanical Design, SPIE Short Course SC014, 2003.

Vukobratovich, D., Lightweight mirror design, in *Handbook of Optomechanical Engineering*, Ahmad, A., Ed., CRC Press, Boca Raton, FL, 1997, chap. 5.

Yoder, P.R., Jr., *Mounting Optics in Optical Instruments*, SPIE Press, Bellingham, 2002.

10 Mounting Large, Horizontal-Axis Mirrors

10.1 INTRODUCTION

In Chapter 8, we considered a variety of ways in which to mount mirrors in the size range up to about 20 in. (51 cm). A few of those techniques are applicable, within limits, to larger elements, but totally inadequate for really large mirrors. The important criteria for mounting suitability are allowable deflection due to gravity, thermal effects, and performance level required. When the aperture is modest, the thickness and material choice conducive to high stiffness, and the performance requirements low, the optic can be considered a "rigid" body and mounted semikinematically or with a multiple point mount, such as the Hindle mount. Larger mirrors are more flexible so require more careful consideration. In any practical application, large mirrors are susceptible to deformations due to temperature gradients, thermal property inhomogeneities, internal stresses, and imposed forces such as acceleration and gravity. Changes in orientation of the optic during use within the Earth's gravitational field are also of significance, as are variations in thermal loading. Release of gravitational effects must be considered in the case of mirrors fabricated, tested, and mounted on Earth and then launched into space. The largest gravitationally caused deformations of the mounted mirror occur when gravity acts along the optic axis. Back supports are used in astronomical and similar instruments that point upward or downward from the horizontal to counter these effects. That situation is the subject of Chapter 11. The more general case of mounting mirrors for variable axis orientation is discussed in Chapter 12. Constructional details for metallic mirrors and the unique aspects of mountings for those mirrors are discussed separately in Chapter 13.

The fixed, horizontal-axis mirror is also deformed by gravity. The deformations that occur in this case are not rotationally symmetrical about the mirror axis. In this chapter, we examine a variety of radial support mount designs for horizontal-axis mirrors. Some designs are included primarily for their historical value. We start with simple designs and progress to more complex configurations. The first mounts considered are V-mounts built to interface with conventional, solid, nonmetallic mirror substrates of circular or rectangular shape and various dimensions. Typical strap mounts, multipoint mounts, mercury tube supports, and push–pull mounts are then considered. All these mounts are intended for fixed-orientation applications (such as in a laboratory). It should be noted that if the mirror is tested in the same orientation relative to gravity as it will always be used, the errors due to gravitational forces can, for the most part, be compensated for during the polishing operation.

Radial forces should always be applied to the horizontal-axis mirror in its neutral surface (defined in Section 9.3) to minimize astigmatic distortion of the optical surface. Vukobratovich (2004) indicated that violation of this rule by only 0.1 mm (0.004 in.) in mounting a 1.8-m (70.9-in.)-diameter, lightweighted, fused silica sandwich mirror caused as much as $\lambda/4$ astigmatism at $\lambda = 633$ nm.

10.2 GENERAL CONSIDERATIONS OF GRAVITY EFFECTS

In a classical paper on mirror flexure due to gravity, Schwesinger (1954) explained the two types of forces exerted on the edge of a mirror supported with its optic axis horizontal. Radially directed forces, tensile or compressive, that vary in magnitude around the periphery of the mirror form the first type. These are generally distributed uniformly as indicated in Figure 10.1(a) and are transmitted through the mirror so as to support the weight of each volume element. Potential deformations at a point on the surface of the mirror are V_R radially, V_φ tangentially, and V_Z axially. The mirror diameter is D_G, its axial thickness t_A, and its weight W.

If the cross section of the mirror is not of uniform thickness, that is, concave (as indicated in Figure 10.1[b]) or convex, the transmitted forces also produce moments that tend to bend the mirror. These are illustrated schematically in view (c), which shows an element of average thickness $t + (dt/2)$ with the transmitted radial forces applied to the opposite faces. The upward and downward resultants of these forces are axially displaced by $dt/2$, thereby producing an elemental moment. When integrated over the entire mirror, these elements have a resultant force equal to $W\xi$, where ξ is the distance from the center of mass to the midplane (dashed vertical line in Figure 10.1[b]). This resultant is balanced by a distribution of bending moments m_R, at the mirror edge as indicated at the bottom of view (b). These moments form the second type of boundary forces due to gravity. They tend to bend the mirror surface.

Schwesinger also gave a theory for calculating the surface deformations and the resulting reflected wavefront errors caused by these two types of forces. Shear stresses and the effects of central perforations in the mirrors were not considered. Subject to these limitations, we will apply that theory to explain the advantages and disadvantages of a variety of mechanical mounts for horizontal-axis mirrors of various configurations and sizes.

10.3 V-TYPE MOUNTS

Figures 10.2–10.5 illustrate four versions of a mount type in which the weight of a horizontal-axis mirror is supported radially by line contact of the rim against two parallel horizontal, cylindrical posts located symmetrically with respect to the vertical centerline. In the mount shown in Figure 10.2, a third post is provided at top center of the mirror. It normally does not contact the mirror but supports a clip extending in front of the mirror's rim to prevent the mirror from falling forward if bumped. It is advantageous to use a sleeve of plastic material such as Kevlar as the contacting surface on the posts to provide a slightly resilient interface and some thermal insulation, and to reduce friction. Rollers are also used sometimes to minimize friction. The contacts between the posts and

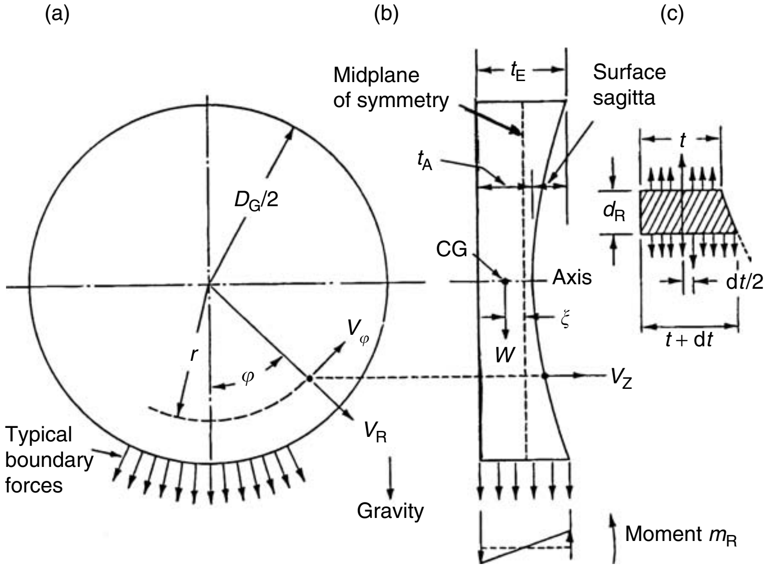

FIGURE 10.1 Quantities entering the gravity-induced deflection problem for a horizontal-axis solid mirror. (Adapted from Schwesinger, G., *J. Opt. Soc. Am.*, 44, 417, 1954.)

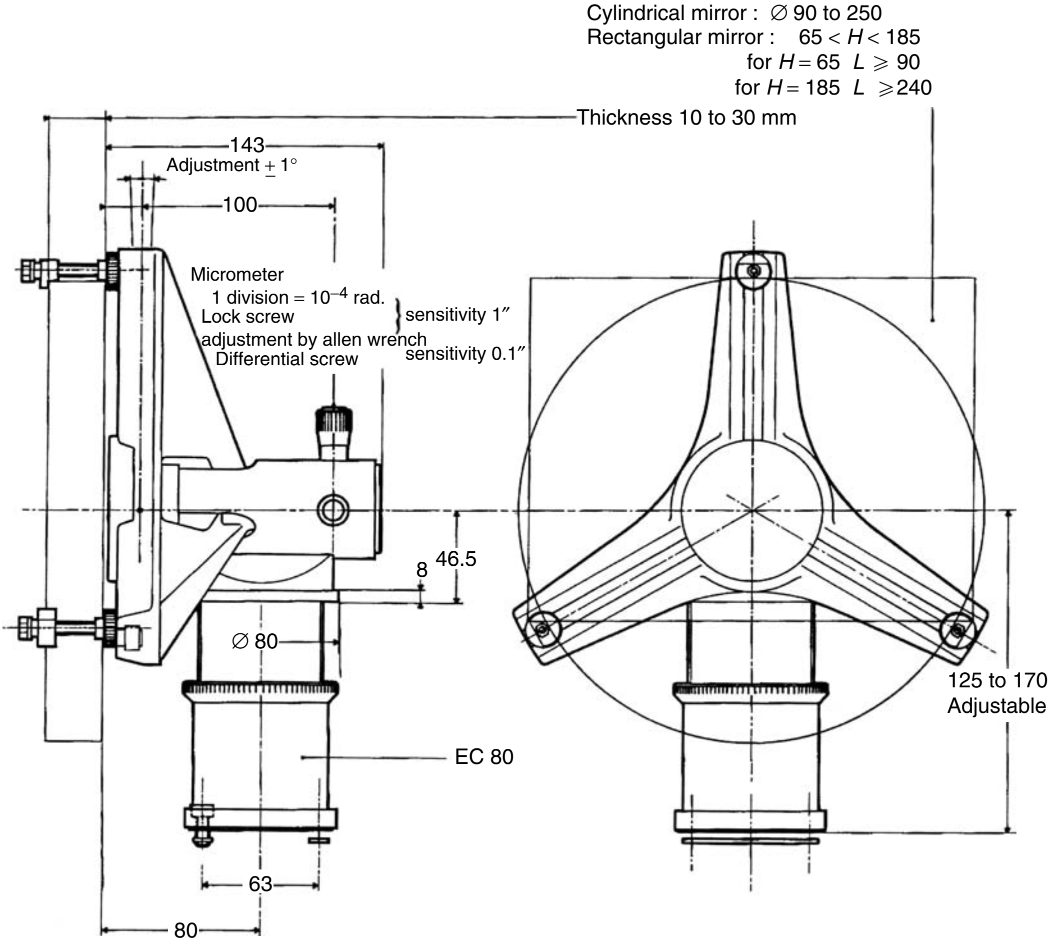
Cylindrical mirror : ∅ 90 to 250
Rectangular mirror : 65 < H < 185
for H = 65 L ⩾ 90
for H = 185 L ⩾240
Thickness 10 to 30 mm
143
Adjustment ± 1°
100
Micrometer
1 division = 10^{-4} rad.
Lock screw
sensitivity 1″
adjustment by allen wrench
Differential screw
sensitivity 0.1″
8
46.5
∅ 80
125 to 170
Adjustable
EC 80
63
80

FIGURE 10.2 A commercial V-mount that supports the rim of solid mirrors of various diameters or rectangular dimensions on two horizontal posts equally spaced on either side of the vertical centerline. Tilt and translational adjustments are provided. Dimensions are mm. (Courtesy of Newport Corp., Irvine, CA.)

the mirror rim are between different diameter parallel-axis cylinders if the mirror is circular. This type of mount is called a *V-mount* since it functions as if the circular mirror rim sits in a V-block. A rectangular mirror can also be supported in such a mount. The contacts at the posts are then between cylinders and a flat surface. In each case, the axial position of the mirror is maintained by clamping its rim lightly with clips on each of the lower posts. Each clip and the corresponding pad immediately behind it on the back plate of the mount contact only small areas on the mirror so as to minimize local bending moments should the interfacing surfaces not be exactly parallel. Springs may be used to provide the clamping forces.

Support against gravity is at ±60° to the vertical centerline of the mirror in the design shown in Figure 10.2. In the design of Figure 10.3, the corresponding radial support is at ±45°. These designs are sometimes referred to as 120° and 90° V-mounts, respectively. Commercial mounts of the type shown in Figure 10.2 accommodate mirrors in the 3.5-in. (9-cm) to 9.8-in. (25-cm)-diameter range while those of the type shown in Figure 10.3 have been made to accommodate mirrors in sizes ranging from 4 in. (10 cm) to 30 in. (76 cm) diameter. In the larger sizes, the mirror is sometimes constrained by five posts. All these designs provide a means for adjusting the tilt of the mirror axis. Translational adjustments are also provided in the designs shown in Figure 10.3.

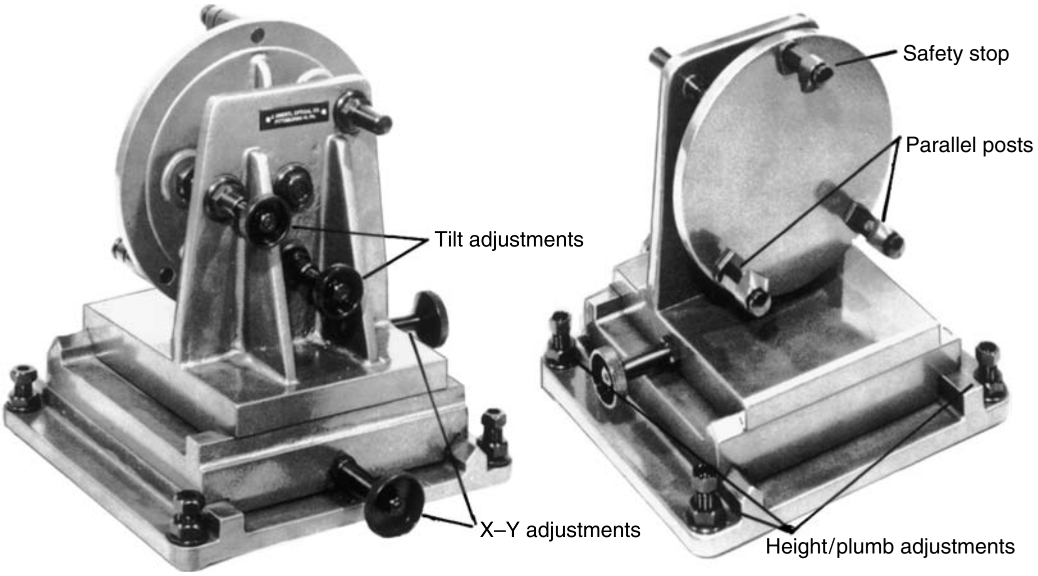
Safety stop
Parallel posts
Tilt adjustments
X–Y adjustments
Height/plumb adjustments

FIGURE 10.3 An open-type mount that supports the lower rim of a mirror on two parallel horizontal posts. A clip on a third post at top center prevents the mirror from falling forward if bumped. Tilt and translational adjustments are provided. (Adapted from a brochure from John Unertl Optical Company, Pittsburgh, PA.)

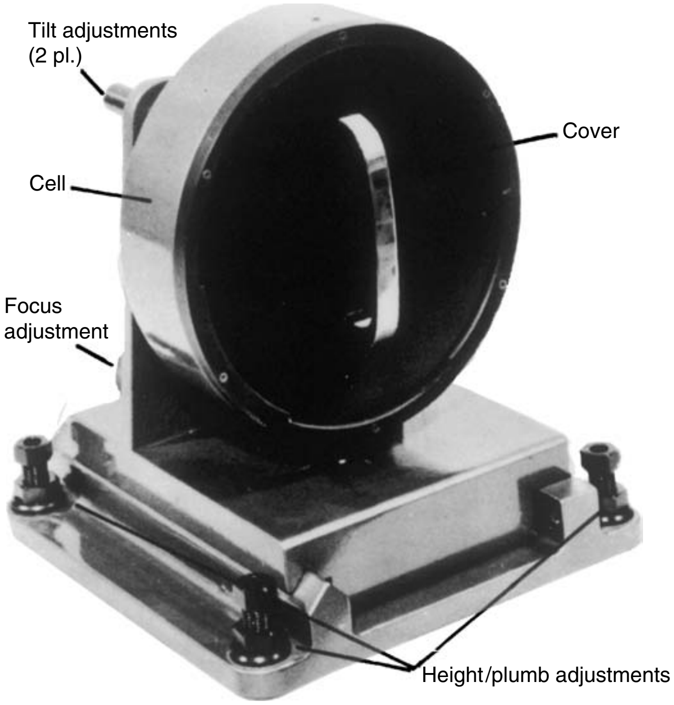
Tilt adjustments
(2 pl.)
Cover
Cell
Focus
adjustment
Height/plumb adjustments

FIGURE 10.4 A cell-type mount that encloses the mirror. Small pads on the cell ID support the mirror radially. An annular front flange ring provides axial constraint. Tilt and translational adjustments are provided. (Adapted from a brochure from John Unertl Optical Company, Pittsburgh, PA.)

The cell-type mirror mount shown in Figure 10.4 supports the horizontal-axis mirror against gravity by small-area radial contact against pads at two places on the lower portion of the inner wall of the cell. A third radial constraint is provided at top center. Axial constraint is provided by lightly clamping the mirror continuously about its rim. An annular flange attached with screws to the front of the cell presses the mirror rim lightly through a resilient pad against the back wall of the cell. This flange is relieved at three places to allow a protective cover to be inserted when the mirror is not in use.

The commercial mirror mount shown in Figure 10.5 (and sketched in Figure 8.25) is much smaller than those described above, but is still a V-type mount. Here, mirrors with diameters of about 1 in. (25.4 mm) can be supported on two parallel, horizontally oriented, plastic rods (typically made of Nylon or Delrin) inserted into recesses in the ID of a hole bored into a mounting plate. The mirror is secured in place by a Nylon setscrew pressing gently against the top center of the mirror. Usually, the mirror is located axially in such a mount by manually registering it very lightly against a shoulder or pads machined into the plate as the setscrew is tightened. Friction then constrains the mirror against axial motion.

A horizontal-axis mirror mounted in any of the above-described V-mounts will exhibit surface deformations due to gravitational effects. These effects are usually found to be significant only if the mirrors are large. Axial constraints can also deform the mirror, but if they are carefully located and the axis is truly horizontal, the forces imposed in a benign environment such as a laboratory need not be large since it is necessary only to prevent the mirror from tipping over if disturbed.

According to Schwesinger (1954), the rms departure δ_{RMS} from perfection (in waves) of the surface of a gravitationally deformed horizontal-axis mirror can be computed from

$$\delta_{\mathrm{RMS}} = C_{\kappa} \rho D_{\mathrm{G}}^{2} / (2 E_{\mathrm{G}} \lambda) \tag{10.1}$$

where C_{κ} is a computed factor given by Schwesinger for each of six specific types of mounts used to support a mirror, ρ and E_{G} the density and Young's modulus, respectively, of the mirror material, D_{G} the mirror diameter, and λ the wavelength of light reflected from the mirror. The rms error of the reflected wavefront would be $2\delta_{\mathrm{RMS}}$. Table 10.1 gives Schwesinger's values for C_{κ} for four of the six mount configurations that are of greatest interest here and for specific values of a factor κ defined (after minor adaptation of nomenclature from Schwesinger's definition) as

$$\kappa = D_{\mathrm{G}}^{2} / (8 t_{\mathrm{A}} R) \tag{10.2}$$

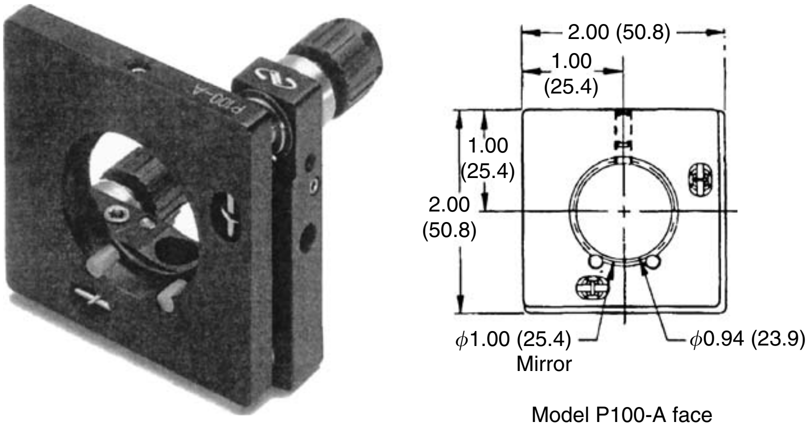

Model P100-A face

FIGURE 10.5 A typical commercially available V-type mount providing parallel plastic rods for rim support of small mirrors. Dimensions are in. (mm). (Courtesy of Newport Corp., Irvine, CA.)

where R is the optical surface radius of curvature and the other terms are as previously defined. Schwesinger limited his numerical considerations (and hence the data in Table 10.1) to the common case where $D_G = 8t_A$. Then, $\kappa = 0.5/(\text{mirror } f\text{-number})$.

Vukobratovich (1993) gave a series expansion derived as an approximation for Schwesinger's factor C_κ to allow Eq. (10.1) to be applied to mirrors with any D_G/t_A ratio and to any value of κ in any of four types of mount.

$$C_\kappa = a_0 + a_1\gamma + a_2\gamma^2 \tag{10.3}$$

where the constants a_i are as listed in Table 10.2 and $\gamma = \kappa$. Vukobratovich (2004) indicated that his constants for the strap mount (single asterisk) were derived by fitting to experimental data. The other constants for that mount (double asterisk) were derived by fitting to Schwesinger's value C_κ. The last two columns of the table compare values of C_κ for $\kappa = 0.2$ as computed with Vukobratovich's equation with those from Schwesinger's paper (see Table 10.1).

Schwesinger (1954) analyzed a variety of mountings involving radially directed forces applied to the lower rim of a mirror disk. The simplest case evaluated had the mirror standing on one point on its rim, whereas in another more practical case, the mirror was supported in a V-mount of variable dihedral angle. The mounts of Figures 10.2–10.5 generally correspond to the latter case. We will now use Schwesinger's method to analyze one such configuration.

For a ±45° V-mount of the type shown in Figure 10.3, a mirror with $D_G/t_A = 8$ and Poisson's ratio equal to 0.21, Schwesinger's values of C_κ as functions of assumed values for κ from Table 10.1 and Eq. (10.1) can be used to find δ_{RMS} or, conversely, the size of the mirror that causes a given rms wavefront error. Figure 10.6 shows graphically the variation of $2\delta_{RMS}$ in waves of green light vs.

TABLE 10.1

Values for Schwesinger's Factor C_κ to be Used in Eq. (10.1) for Circular Mirrors with Axis Horizontal in Three Types of Mounts and for Particular Values of the Factor κ

	k =	**0 (flat)**	**0.1**	**0.2**	**0.3**
	Relative aperture =	**—**	**f/5**	**f/2.5**	**f/1.67**
±45° V-mount	C_κ	0.0548	0.0832	0.1152	0.1480
Ideal support	C_κ	0	0.0018	0.0036	0.0055
Strap mount	C_κ	0.00743	0.0182	0.0301	0.0421

TABLE 10.2

Values for Vukobratovich's Constants to be Used in Eq. (10.2) for Circular Mirrors with Axis Horizontal in Four Types of Mirror Mounts

		Constant		**C_κ for $\kappa = 0.2$ per**	
Mount Type	**a_0**	**a_1**	**a_2**	**Vukobratovich**	**Schwesinger**
One point at $\varphi = 0°$	0.06654	0.7894	0.4825	0.2440	0.246
±45° V-mount	0.05466	0.2786	0.1100	0.1148	0.1152
±30° V-mount	0.09342	0.7992	0.6875	0.6348	—
Strap mount*	0.00074	0.1067	0.0308	0.0340	0.0301
Strap mount**	0.00743	0.1042	0.0383	0.0421	0.0421

*Based on experiments at Optical Sciences Center, University of Arizona per Vukobratovich (2004).

**Based on theory presented by Schwesinger (1954).

Source: From Vukobratovich (1993).

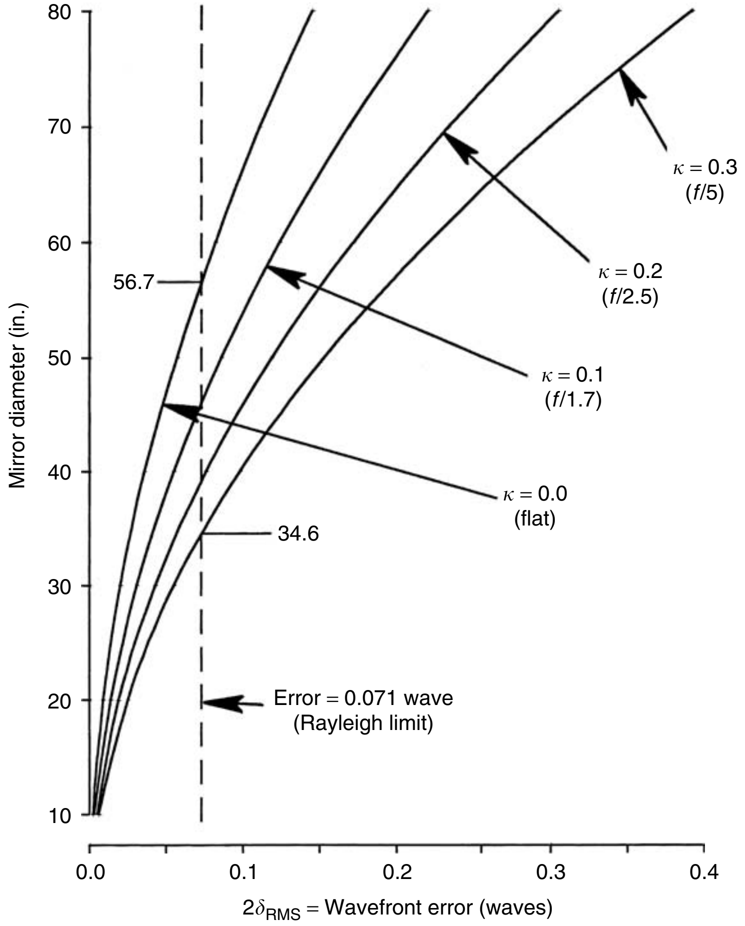

FIGURE 10.6 Variation of gravitationally induced rms wavefront error in green light for axis-horizontal circular solid Pyrex substrate mirrors in ±90° V-mounts as a function of mirror diameter for different κ values. Mirror thicknesses are diameter/8. (Computed according to Schwesinger, G., *J. Opt. Soc. Am.*, 44, 417, 1954.)

mirror diameter for each of the given values of κ. The material here is Pyrex, its Poisson's ratio is 0.2, which is essentially the same as that assumed by Schwesinger. The vertical dashed line corresponds to $2\delta_{\text{RMS}} = \lambda/14 = 0.071\lambda$, which, according to Maréchal (1947) as explained by Born and Wolf (1964), is the Rayleigh diffraction limit. We observe that a perfect flat mirror made of Pyrex mounted in a ±45° V-mount may be as large as 56.7 in. (144 cm) in diameter for diffraction-limited performance if gravitational deformation is the only error source. The diameter of a concave Pyrex mirror with $\kappa = 0.3$ (corresponding to *f*/1.7 for the 8:1 diameter-to-thickness ratio considered here) should be no larger than 34.6 in. (87.9 cm) for this same performance level.

The calculations leading to the graphs in Figure 10.6 were repeated for ULE and Zerodur materials to show the variations due to the different Young's modulus and density values of those materials as compared to Pyrex. All other parameters were unchanged. Figure 10.7 shows the diameter vs. rms wavefront error relationships. Zerodur appears to be the best material. This is attributed primarily to the higher Young's modulus for that material (13.6×10^6 lb/in.^{2}) as compared with (9.1×10^6 lb/in.^{2}) for Pyrex.

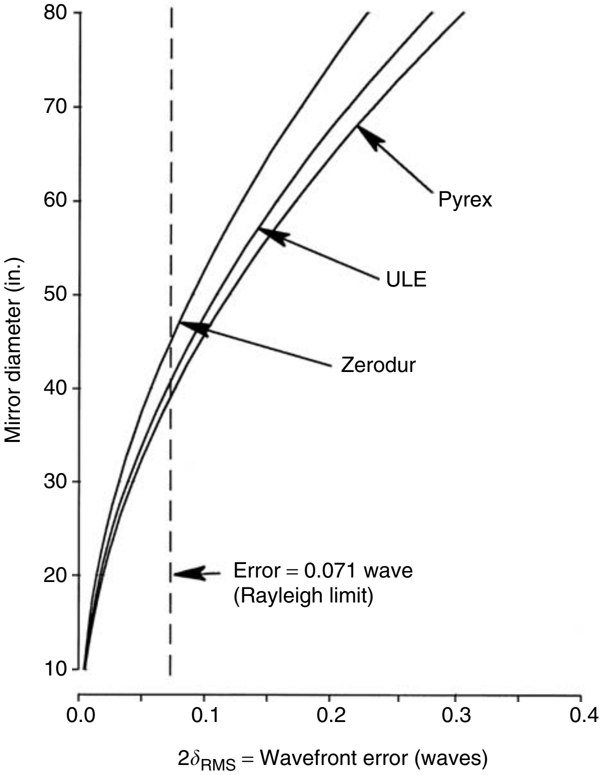

FIGURE 10.7 Variation of gravitationally induced rms wavefront error in green light for axis-horizontal circular solid Zerodur, ULE and Pyrex mirrors in ±90° V-mounts as a function of mirror diameter for $\kappa = 0.2$ (*f*/2.5 surface). Mirror thicknesses are diameter/8. (Computed according to Schwesinger, G., *J. Opt. Soc. Am.*, 44, 417, 1954.)

Malvick (1972) studied the theoretical elastic deformations of two solid centrally perforated mirrors, one a 230-cm (90.6-in.)-diameter primary mirror of a stellar telescope at Steward Observatory and a 154-cm (60.6-in.)-diameter biconcave mirror used at the University of Arizona's Optical Sciences Center for experimental purposes. One of the cases he considered was the larger mirror supported on edge by two pads located at ±30° from the vertical centerline. If the pads were located axially in the plane containing the mirror's center of curvature, the gravitationally induced surface deflections would be as shown in Figure 10.8(a). Opening the support angle to ±45° would change the surface contours to appear as shown in Figure 10.8(b). The inherent astigmatism of the surface is reduced by a factor of the order of 3 in the latter case, but the contours are more complex.

In actual use, the pads supporting the above-described mirror were at ±30° from the vertical and located about 5 cm (2 in.) in front of the center of gravity (i.e., toward the mirror face), presumably to ensure against the mirror's accidentally falling forward out of the mount. Malvick analyzed the effect of this shift and found that gravity and the reactions of the mirror's back supports to the moment introduced by the offset radial supports produced the surface contours illustrated in Figure 10.9. The deformations are about six times larger than those shown in Figures 10.8(a) or (b).

From these theoretical evaluations, we gather insight into why the simple V-mounts described above work reasonably well for modest-sized solid mirrors. Of course, these performance predictions assume that the mirror axis remains exactly horizontal. Tipping the mirror in the terrestrial gravity field changes the supporting force conditions, and more sophisticated radial mounting arrangements may then be necessary since the influences of axial forces must be considered.

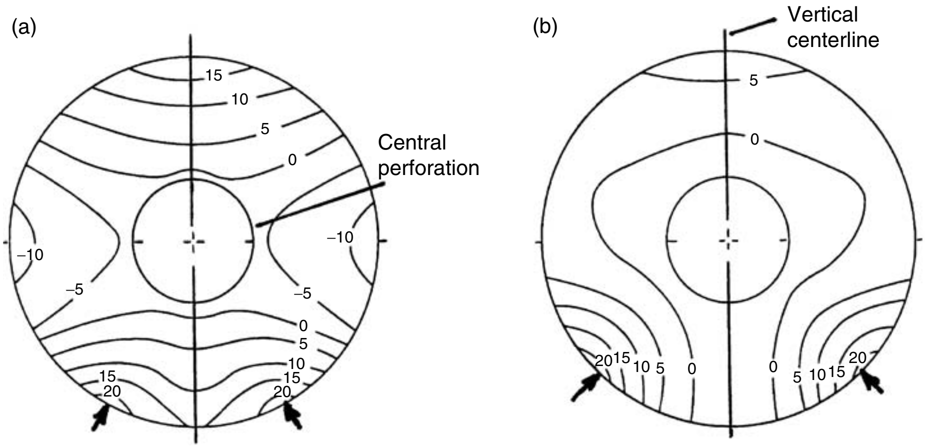

FIGURE 10.8 Surface deformation contours of a 91 in. (230 cm) diameter solid mirror due to gravity in a horizontal-axis orientation when supported on a V-mount with two pads at (a) ± 30° and (b) ± 45°. Radial support is in the plane of the mirror CG. The contour interval is 10^{-6} cm. (Adapted from Malvick, A.J., *Appl. Opt.*, 11, 575, 1972.)

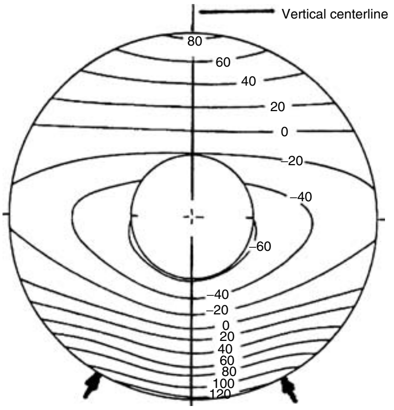

FIGURE 10.9 Surface deformation contours for the same mirror as shown in Figure 10.7(a), but with the ±30° radial pads located 5 cm (2 in.) in front of the plane of the CG. Contour interval = 10^{-6} cm. The surface deformation is increased by a factor of about six from the prior case. (Adapted from Malvick, A.J., *Appl. Opt.*, 11, 575, 1972.)

10.4 MULTIPOINT EDGE SUPPORTS

As pointed out by Vukobratovich (1997, 2003), mechanical support to a horizontal-axis mirror can be obtained through a system of lever mechanisms applying forces normal to the lower portion of the mirror's rim. A circular mirror with such a support is shown schematically in Figure 10.10. Each mechanism is a whiffletree* arrangement. Constraints are evenly distributed spatially at eight points located at 180°/7 = 25.7° intervals in the configuration depicted in the figure. Support at fewer points could be obtained with a simpler design while support at additional points could be obtained by adding more whiffletrees.

If the mirror is rectangular and its axis is always horizontal, vertical support can also be furnished at several points as illustrated schematically in Figure 10.11 for two- through five-point cas-

---

*A whiffletree is a lever or rocker mechanism, hinged at the center and supporting loads at each end in the manner of a two-horse harness for a wagon. See Section 11.4.2 for more details.

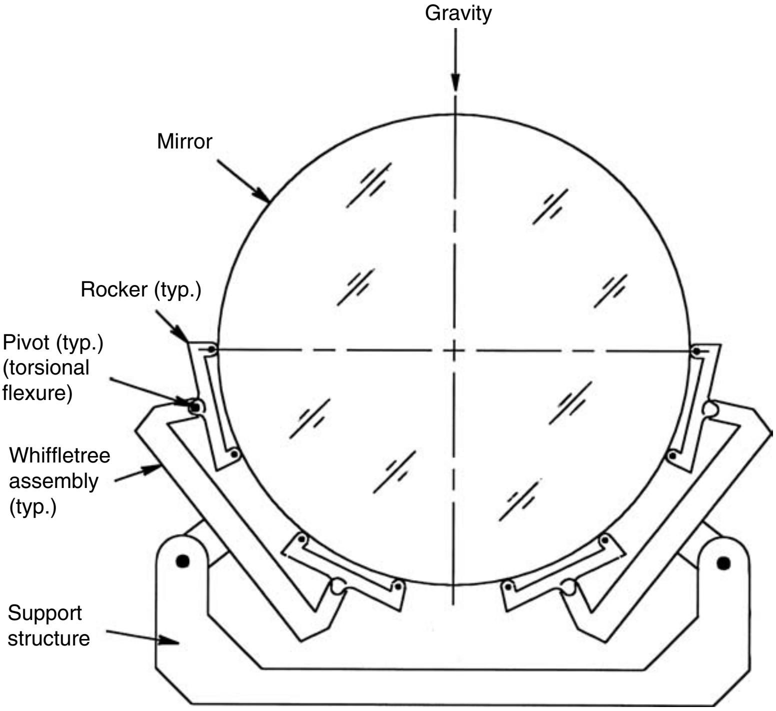
Gravity
Mirror
Rocker (typ.)
Pivot (typ.) (torsional flexure)
Whiffletree assembly (typ.)
Support structure

FIGURE 10.10 Multipoint (whiffletree) edge support for a horizontal-axis circular mirror.

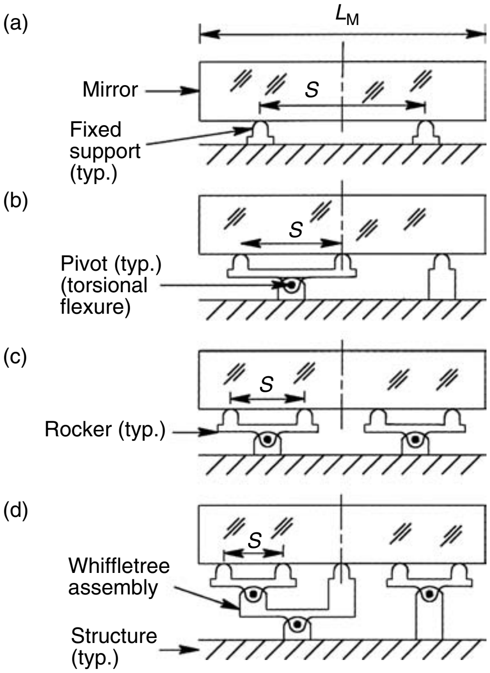
(a)
L_M
Mirror
S
Fixed support (typ.)
(b)
S
Pivot (typ.) (torsional flexure)
(c)
S
Rocker (typ.)
(d)
S
Whiffletree assembly
Structure (typ.)

FIGURE 10.11 Family of cascaded multipoint lever mechanism supports for a rectangular mirror: (a) two-point support, (b) three-point support, (c) four-point support, and (d) five-point support. (Adapted from Vukobratovich, D., Introduction to Optomechanical Design, *SC014 Short Course*, 2003.)

TABLE 10.3
Values per Eq. (10.4) for Support Point Separation *S* for Rectangular Mirrors with Axis Horizontal Supported on One Long Edge by *N* Supports in a Multipoint Mount as Shown in Figure 10.11. L_M is Constant at 3.674 in. (93.32 mm)

N	2	3	4	5
S	2.121 in. (53.873 mm)	1.299 in. (32.995 mm)	0.949 in. (24.105 mm)	0.750 in. (19.050 mm)

caded supports. Once again, increasing the complexity of the design could provide additional supports. According to Vukobratovich (2003), for a given mirror length L_M, the optimum separation S of the support points is given by

$$S = L_M/(N^2 - 1)^{1/2} \tag{10.4}$$

where N is the number of supports. Table 10.3 applies this equation to the case of Figure 10.11. In the absence of friction, each of the lever mechanisms can deliver force uniformly at the discrete contacts. If the areas of contact are small, the configuration can be considered semikinematic. Friction causes the mirror to become astigmatic. Rollers at the contacts can reduce frictional distortion of the optical surface.

It should be noted that edge support of a rectangular mirror could, in principle, be provided by a long, narrow, air bag support of the type described in Section 11.3. This author is not aware of any application of this type of support.

10.5 THE IDEAL RADIAL MOUNT

An "ideal" mount for horizontal-axis circular mirrors of larger size was defined by Schwesinger (1954) as one in which the disk is balanced by radially directed forces around its periphery. The magnitudes of these forces vary as the cosine of the polar angle φ measured from the downward-pointing radius of the disk. The radial forces are maximum compressive at the bottom of the vertical centerline, decrease to zero at both sides on the horizontal centerline, and then change sign to tensile forces of increasing magnitude, reaching a common maximum at the top of the disk. Figure 10.12 illustrates this condition for a large 4-m (157-in.)-diameter perforated mirror analyzed by Malvick and Pearson (1968). The contour lines represent mirror surface displacements and indicate that the surface becomes astigmatic owing to edge moments generated by gravity. Similar deformations, of lesser magnitude of course, occur in smaller solid mirrors when similarly mounted.

The analytical method used by Malvick and Pearson (1968) included shear effects as well as those of a large, central hole in a solid disk mirror. Using an analytical method called *dynamic relaxation* as developed by Day (1965), Otter et al. (1996), and Malvick (1968) and a tensor formulation, Malvick and Pearson expressed the three-dimensional (3D) equations of elasticity as three equilibrium equations and six stress displacement equations. The body of the mirror was divided into a "reasonable" number of nonorthogonal curvilinear elements. Normal stresses were defined at the centers of the elements, shear stresses were defined at the centers of the element edges, and displacements were defined at the centers of the element faces. The equilibrium equations were set equal to the sum of acceleration and viscous damping terms. Initial stress, displacement, and velocity distributions at a time t_0 were assumed. All three distributions at a later time t_1 were predicted mathematically. The process was iterated until the element velocities damped out to negligible values, leaving the static surface displacements corresponding to equilibrium in the 3D body.

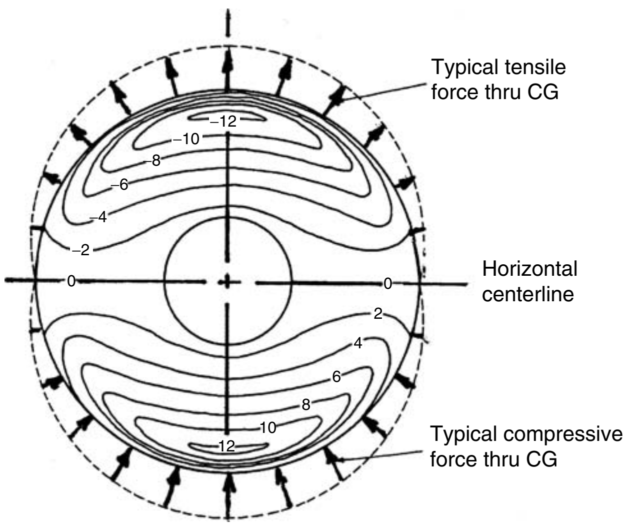
Typical tensile force thru CG
−12
−10
−8
−6
−4
−2
0
Horizontal centerline
0
2
4
6
8
10
12
Typical compressive force thru CG

FIGURE 10.12 Surface deformation contours due to gravity for a large solid mirror when mounted with axis horizontal in an approximately "ideal" edge support with tensile and compressive radial forces. Contour interval = 10^{-6} cm. (Adapted from Malvick, A.J. and Pearson, E.T., *Appl. Opt.*, 7, 1207, 1968.)

The analytical method given by Schwesinger (1954) and applied earlier to the V-mount is also applicable, within limits, to the ideal mount design having a cosine distribution of radial forces. Equation (10.1) and data from Table 10.1 are used.

Note that, since C_κ is zero for a flat mirror, there would theoretically be no limitation on the diameter of such a mirror mounted in this manner. A *f*/1.67 ($\kappa = 0.3$) solid Zerodur mirror of 78.74 in. (2.00 m) diameter and 8:1 D_G/t_A ratio would theoretically produce an rms wavefront error of 0.011λ (approximately 1/6th the diffraction limit) when mounted in this manner. As noted earlier, Schwesinger's method did not include shear stresses, so this conclusion is overly optimistic. It is apparent, however, that perfect flat- and curved-surface mirrors could be quite large while providing subdiffraction-limited performance *if* we could provide an "ideal" mount. Unfortunately, the physical realization of the ideal mount is much more difficult than its conception, and compromises must be made.

10.6 MERCURY TUBE MOUNTS

An approximation to the "ideal" mount is to support the mirror's edge by radially directed compressive forces of variable magnitude proportional to $(1 + \cos \varphi)$, where φ is the polar angle measured from the downward-pointing radius. Figure 10.13 illustrates the forces applied and the resultant surface contour deformations for the same 4-m (157-in.)-diameter mirror as formed the basis for the "ideal" mount analysis depicted in Figure 10.12. This type of force field results approximately when the mirror is "floated" within an annular mercury-filled tube located between the mirror rim and a rigid cylindrical cell wall. The width of the tube is chosen so that when it is nearly full of mercury, the mirror will be floated. Typical designs call for flattened, neoprene-coated, Dacron tubes to hold the mercury. The axial location of the tube center should coincide with the plane through the center of gravity of the mirror so that overturning moments are avoided.

According to Chivens (1968), mirrors as large as 60 in. (1.5 in.) in diameter have been held centered within 0.0005 in. (0.012 mm) in astronomical telescopes with mercury tube radial supports. Vukobratovich and Richard (1991) indicated some practical difficulties encountered with this type of mount. The mirror contour is somewhat affected by irregularities in the tube such as seams, fill ports, and wrinkles. The fluid also tends to slosh from side to side under vibration so is usable only

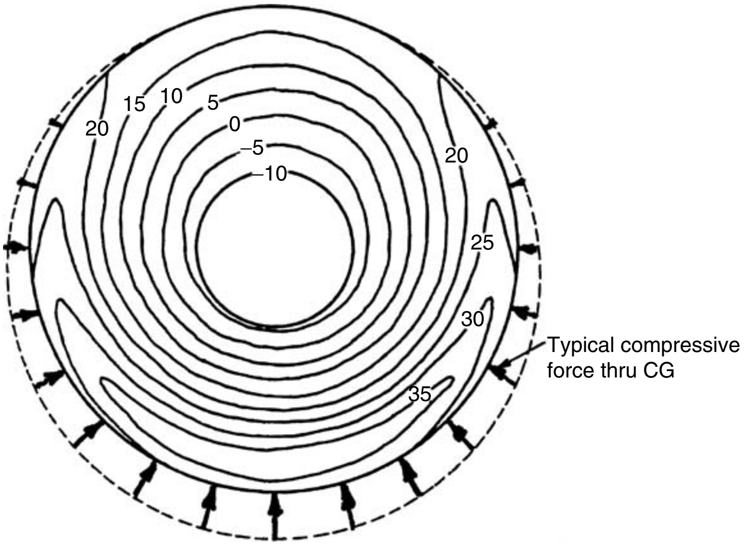

FIGURE 10.13 Surface deformation contours due to gravity for a large solid mirror when mounted with axis horizontal in a mercury-filled tube edge support. Contour interval = 10^{-6} cm. (Adapted from Malvick, A.J. and Pearson, E.T., *Appl. Opt.*, 7, 1207, 1968.)

in relatively benign environments. To these we must add the potential for a human health hazard owing to the mercury itself.

10.7 STRAP AND ROLLER-CHAIN MOUNTS

Figure 10.14 shows two distributions of forces around the rim of a mirror as defined by Schwesinger (1954) and extending from $-\pi/2 < \varphi < +\pi/2$. The angle φ was defined earlier in this chapter as the azimuthal angle around the mirror axis. The curve labeled “optimum distribution” in this figure represents an optimum force distribution for a mount supporting only the lower half of the mirror’s rim. The straight horizontal curve represents the force distribution for a strap mount. It approximates the optimum distribution.

A typical strap mount is illustrated by Figure 10.15. This is a commercial mount in which the mirror’s rim rests in a sling supported at both upper ends from a vertical plate. The strap mount was first described by Draper (1864) as a means of reducing the astigmatism of a mirror supported on edge (i.e., axis horizontal). This type of mount was first used to support mirrors used to test other optical components and is still used for that purpose. It has never been very successfully applied to telescopes because it is not suited for systems involving changes in elevation of the mirror axis.

Schwesinger (1954) gave values for C_κ as shown in Table 10.1 for various values of κ for this type of mount. With Eq. (10.1) and these data, one can find the diameter of mirror corresponding to a specific rms wavefront error. Figure 10.16, from Malvick and Pearson (1968), shows the surface deformations typical of a large solid mirror in a simple strap mount with axis fixed horizontal. Vukobratovich (2004) reported that observed deflections for mirrors larger than about 1.5 m (59.0 in.) mounted in this manner were somewhat larger than those predicted by Schwesinger’s 1954 equations. At least some of the discrepancy could be attributed to friction between the strap and the mirror’s rim.

Malvick (1972) analyzed the performance of the basic strap mount supplemented by a variety of judiciously positioned point supports to off-load some of the mirror’s weight. The advantages of adding the point supports were judged not to be worth the additional complexity of mounting. Since the strap mount design offers the dual advantages of high performance and simplicity, it is quite popular for commercial and custom, fixed, horizontal-axis applications.

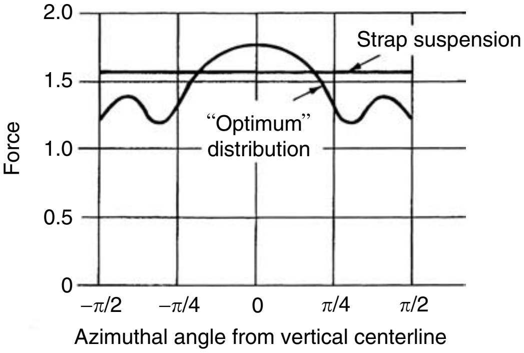

FIGURE 10.14 Plots of the uniform compressive force distribution provided by a strap mount (horizontal straight line) and the "optimum" force distribution for a large horizontal-axis solid mirror in that type mount. (Adapted from Schwesinger, G., *J. Opt. Soc. Am.*, 44, 417, 1954.)

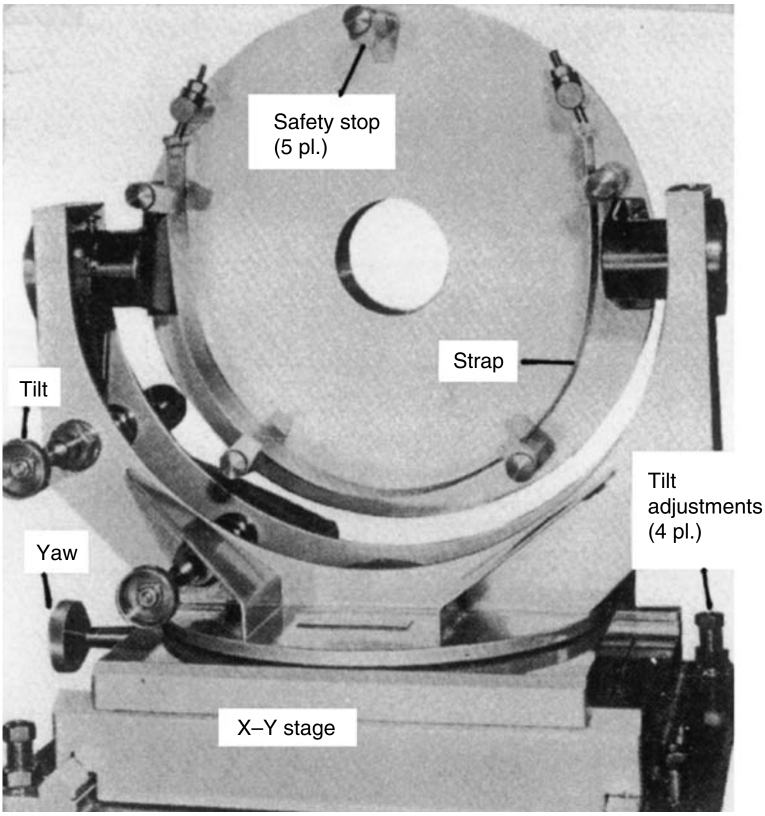

FIGURE 10.15 Typical commercial strap, or belt, mount for horizontal-axis mirrors. (Adapted from a brochure from John Unertl Optical Company, Pittsburgh, PA.)

Dual steel cables have been used successfully as a strap for larger mirrors. Malvick (1972) investigated the advantages of this splitting of the strap support into two narrower and separated straps to give more localized support to the mirror's rim. He showed that, by carefully adjusting the locations of these two supports in the axial direction, surface roll-off effects at the mirror's edge could be minimized.

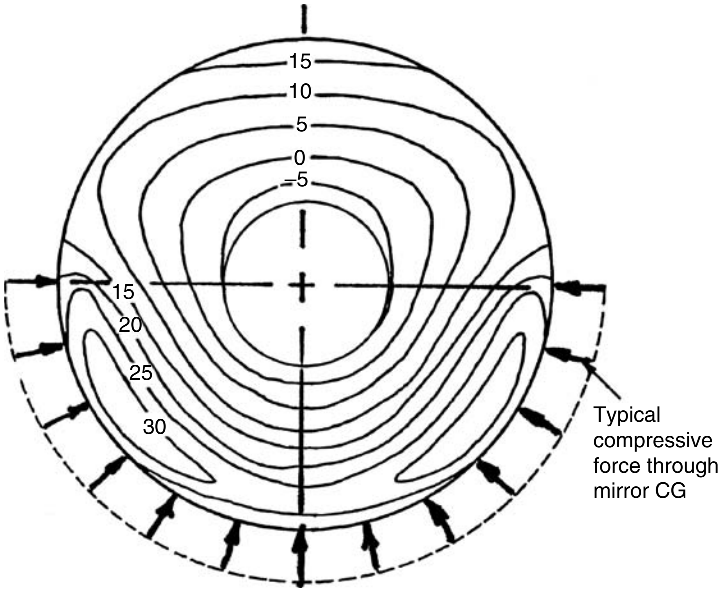

FIGURE 10.16 Surface deformation contours due to gravity for a large solid mirror when mounted with axis horizontal in a strap mount with radial support over the lower 180° of the mirror. Contour interval = 10^{-6} cm. (Adapted from Malvick, A. J. and Pearson, E.T., *Appl. Opt.*, 7, 1207, 1968.)

Dual commercial roller chains have been used successfully instead of continuous straps to support several large, horizontal-axis mirrors. This type of support offers the advantages of reduced friction, ability to rotate the mirror about its axis, and stability without the need for axial support. Vukobratovich and Richard (1991) described the technique, in part, as follows:

> Roller chains are preferred over conventional bands primarily due to reduction in friction between the edge of the mirror and the chain. It is a mistake to use either plastic rollers or an insulating elastic layer between the rollers and the mirror edge. Plastic rollers will take a permanent deformation or set with the passage of time, increasing friction. Friction is also increased with the use of an elastic layer between the mirror edge and roller chain. Conventional roller chain, sold as conveyor chain with oversize rollers, employing steel rollers, is preferred.
>
> An important advantage of the roller chain is the commercial availability of roller chain. A wide variety of chain sizes and load capacities are available, and are relatively low in cost. Special chain links are available to permit the attachment of spacers and safeties to the roller chain. Roller chain supports are very compact, taking space around the mirror edge equal to the chain thickness. For optical shop testing, a roller chain permits ease of rotation of the mirror in its support to test for astigmatism.
>
> Point contact between rollers and the mirror edge, with resulting high stress and possible local fracture, is a drawback of the roller chain support. Careful installation and adjustment of the roller chain minimizes potential fracture at the mirror edge…
>
> Whenever possible, a standard chain size should be selected. Two roller chains, symmetrical about the center of gravity of the mirror, are normally used. A two chain support is stable without the use of a back support, an important safety consideration. A safety factor of at least four with respect to the strength of the chain is suggested. For example, a 1 in. pitch chain with 0.625 diameter rollers, and a average tensile strength of 3700 lbs, is suitable for a 56 in. [1.42 m] diameter solid fused silica mirror 9 in. [22.9 cm] thick, assuming a safety factor of four.
>
> A chain hanger provides termination of the chains, permits adjustment of the chain with respect to the mirror, and connects the support to the rest of the mirror mount. The chain hanger provides three adjustments: location of the centroid of the two chains along the axis of the mirror, axial spacing between the two chains, and a vertical adjustment for mirror wedge. A standard hanger design for a 1.5 m [59.05 in.] mirror incorporating the above adjustments is shown in figure 5 (here Figure 10.17). A universal joint is

provided at the top of the chain hanger to insure static determinacy of the support. Two chain hangers, one on each side of the mirror are provided. The chain hangers are attached to the mirror mount; for shop testing this is a large steel weldment called an easel, as shown in figure 6 (here Figure 10.18).

The surface distortion of a 1.54-m (60.63-in.)-diameter solid CerVit mirror when mounted with axis horizontal in a dual roller-chain mount were analyzed by Malvick (1972). Figure 10.19 shows the results graphically. Vukobratovich and Richard (1991) reported that a mirror of this design was tested and found to have an rms figure error of 0.078 waves.

Figure 10.20 compares deflections for horizontal-axis mirrors having different surface sag-to-thickness ratios. The 90° V-mount is better than the 120° version thereof. The strap mount works best of all types considered.

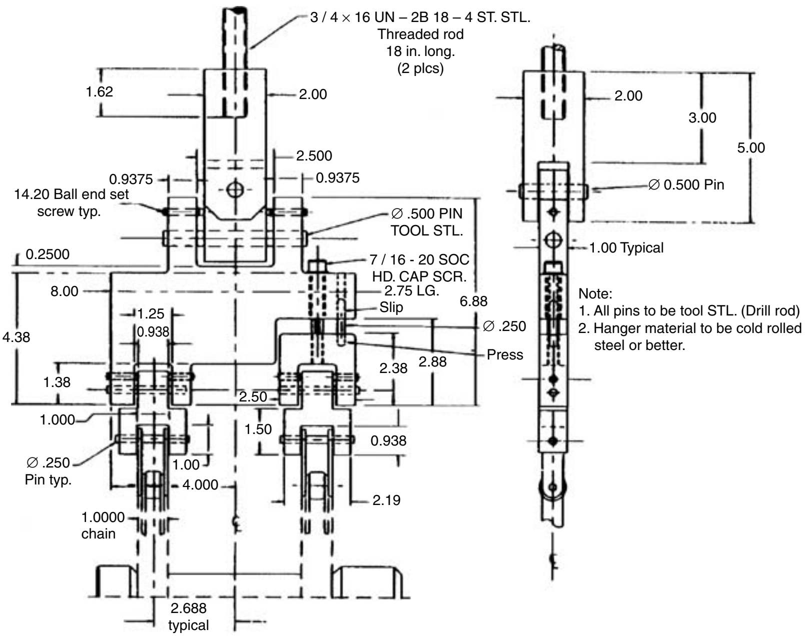
3 / 4 × 16 UN – 2B 18 – 4 ST. STL.
Threaded rod
18 in. long.
(2 plcs)
1.62
2.00
2.500
0.9375
0.9375
14.20 Ball end set
screw typ.
∅ .500 PIN
TOOL STL.
0.2500
7 / 16 - 20 SOC
HD. CAP SCR.
2.75 LG.
Slip
6.88
8.00
1.25
0.938
4.38
∅ .250
Press
2.38
2.88
1.38
2.50
1.000
1.50
0.938
∅ .250
Pin typ.
1.00
4.000
2.19
1.0000
chain
2.688
typical
2.00
3.00
5.00
∅ 0.500 Pin
1.00 Typical
Note:
1. All pins to be tool STL. (Drill rod)
2. Hanger material to be cold rolled
steel or better.

FIGURE 10.17 A typical adjustable support mechanism for a dual roller-chain support as used in a horizontal-axis mirror mount. Dimensions are in inches. (Adapted from Vukobratovich, D. and Richard, R.M., *Proc. SPIE*, 1396, 522, 1991.)

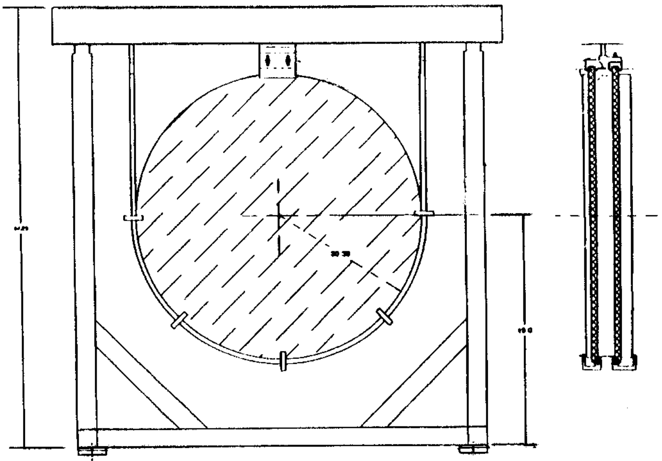

FIGURE 10.18 Diagram of a typical dual roller-chain mirror mount. (Adapted from Vukobratovich, D. and Richard, R.M., *Proc. SPIE*, 1396, 522, 1991.)

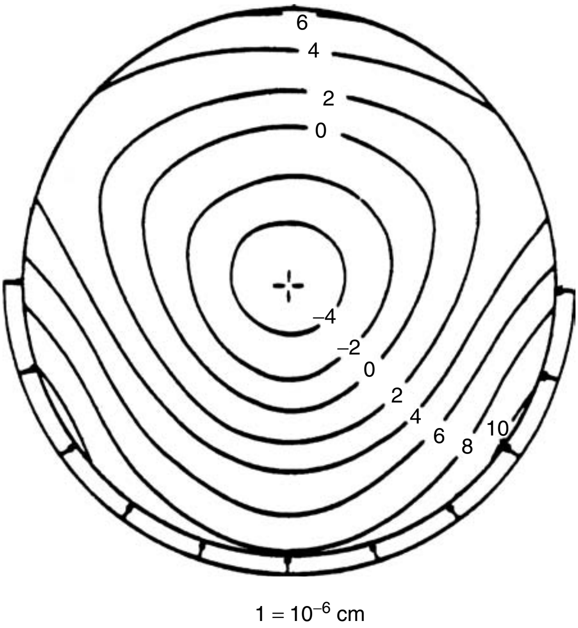

FIGURE 10.19 Predicted surface contours of a 1.54-m (60.63-in.)-diameter solid CerVit mirror in a dual roller-chain support. (From Vukobratovich, D. and Richard, R.M., *Proc. SPIE*, 1396, 522, 1991.)

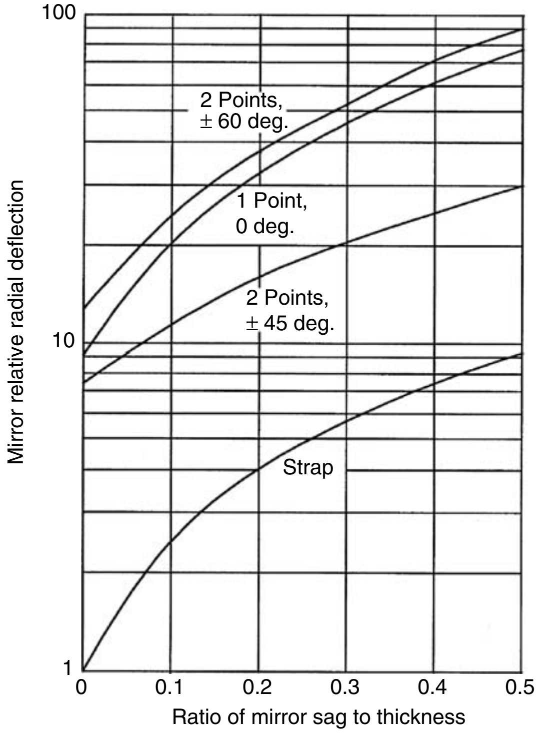

FIGURE 10.20 Variations of predicted relative surface deflections for horizontal-axis mirrors mounted in four ways as functions of surface sag-to-thickness ratios. (Adapted from Vukobratovich, D., personal communication, 2004.)

10.8 PUSH–PULL MOUNTS

A more complex, custom-designed mount that provides both push and pull radial forces is illustrated in Figure 10.21. Here, six metal flexures are bonded to the rim of the mirror at polar angles of $\varphi = 0°$ and $\pm 45°$ from the vertical centerline in both upper and lower semiapertures. All the flexures lie in the neutral plane of the mirror. These flexures are flexible in all directions perpendicular to the radial direction and attach to a "rigid" cell. The mirror is shown mounted for interferometric testing, i.e., not in its final system installation, but those configurations are functionally equivalent. Tensile forces are applied to the three upper supports, whereas compressive forces act on the three lower supports. The mirror shown here is 18.1 in. (46 cm) in diameter, is meniscus in cross section with a uniform thickness of 3.10 in. (7.87 cm), and has a spherical, reflecting, surface radius of curvature of about 24 in. (61.0 cm). The mirror is made of Schott Zerodur and nominally weighs 37.45 kg (82.6 lb).

Figure 10.22(a) shows the distribution of radial forces required to support this mirror with nearly minimum surface deformation. Forces are proportional to the cosine of the angle off vertical. Tangential supports attached to three of the six Invar blocks bonded to the mirror rim as attachment points for the radial flexure system nominally carry essentially zero force.

The computed deformations of the reflecting surface from the best-fitting reference sphere are shown by the contour lines in Figure 10.22(b). The wavelength interval is 0.005λ for $\lambda = 633$ nm. It may be noted that the surface is essentially undistorted over most of the aperture. By careful fine adjustment of the radial forces applied, this level of performance can be and has been achieved in

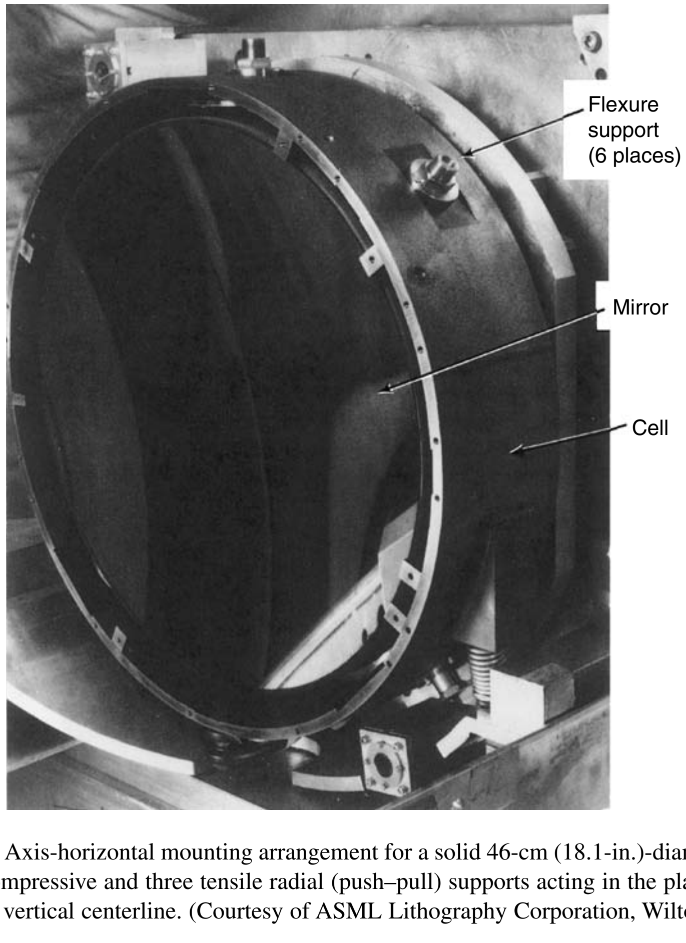

FIGURE 10.21 Axis-horizontal mounting arrangement for a solid 46-cm (18.1-in.)-diameter Zerodur mirror featuring three compressive and three tensile radial (push–pull) supports acting in the plane of the mirror CG at ±45° from the vertical centerline. (Courtesy of ASML Lithography Corporation, Wilton, CT.)

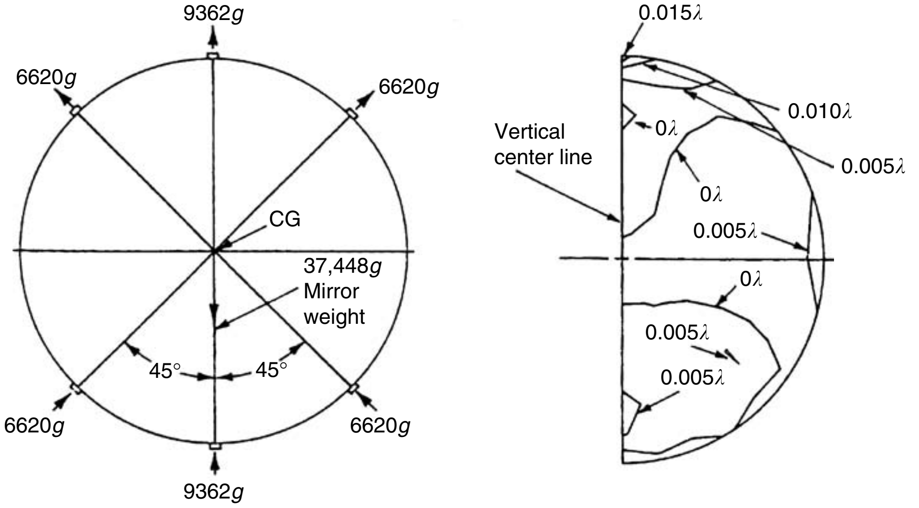

FIGURE 10.22 (a) Distribution of radial forces used to support the mirror of Figure 10.21 for minimal surface deformation due to gravity. (b) Contours of surface deformation relative to the best-fit sphere computed by FEA for this mirror under the forces of view (a). (Courtesy of ASML Lithography Corporation, Wilton, CT.)

practice for large production quantities of mirrors. Typically, this mirror and mount combination reliably displays no more than 0.004 wave rms figure error at $\lambda = 633$ nm including all manufacturing errors, mounting deformations, and gravity effects.

10.9 COMPARISON OF DYNAMIC RELAXATION AND FINITE-ELEMENT ANALYSIS TECHNIQUES

The above-mentioned dynamic relaxation (DR) analytical method used by Malvick and Pearson (1968) to determine the surface deformations of large mirrors due to terrestrial gravity effects was for many years the only available method to evaluate proposed or actual mirror and mount designs. The results of their analyses using this method have proved extremely useful to engineers and astronomers in evaluating mirror and mount designs in the 2 to 4 m (79 to 157 in.) class. Indeed, the surface deformation results provided in this chapter and in the two chapters that follow to show the nature of and, in some cases, the magnitudes of the surface gravitational deformations under certain common mounting arrangements are nearly all derived through use of the DR method. This information is believed to be useful to opto-mechanical designers and engineers engaged in evaluations of smaller or larger mirrors mounted in the same types of mounts since, in general, the contours remain the same as magnitudes scale approximately with size.

In order to determine whether the same technical results would be obtained through application of more modern FEA methods to these design problems, Hatheway et al. (1990) recomputed the deflections of a mirror that was analyzed by Malvick and Pearson (1968) when supported in a strap mount. Figure 10.23 shows the mirror model analyzed. It has 20 equal 18° angular sectors, 10 annular rings, and 5 nearly flat layers (front to back). The entire model has 1000 structural elements, each with eight nodes and six sides. Dihedral symmetry was assumed to apply in both cases. The FEA model was processed using the MSC/O-POLY preprocessor and MSC/NASTRAN software. This allowed up to 100 Zernike polynomials of the surface to be evaluated.

The results of this FEA are shown in Figure 10.24(b). The shapes and magnitudes of the surface deflections should be compared with those shown in view (a) of Figure 10.24, which represents Malvick and Pearson's results for the same mirror/mount combination. Note that Figure 10.24(a)

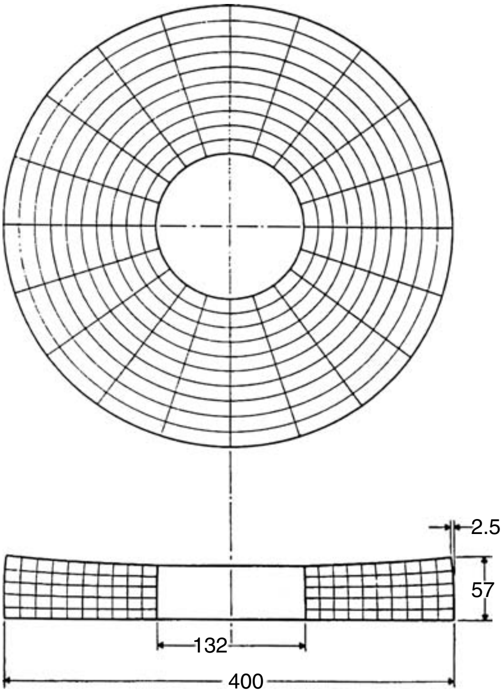

FIGURE 10.23 Model used by Malvick and Pearson (1968) and by Hatheway et al. (1990) to evaluate surface deformations of a large solid glass mirror when supported by a strap mount using dynamic relaxation and FEA methods, respectively. Units are in cm. (From Hatheway, A.E. et al., *Proc. SPIE*, 1303, 142, 1990.)

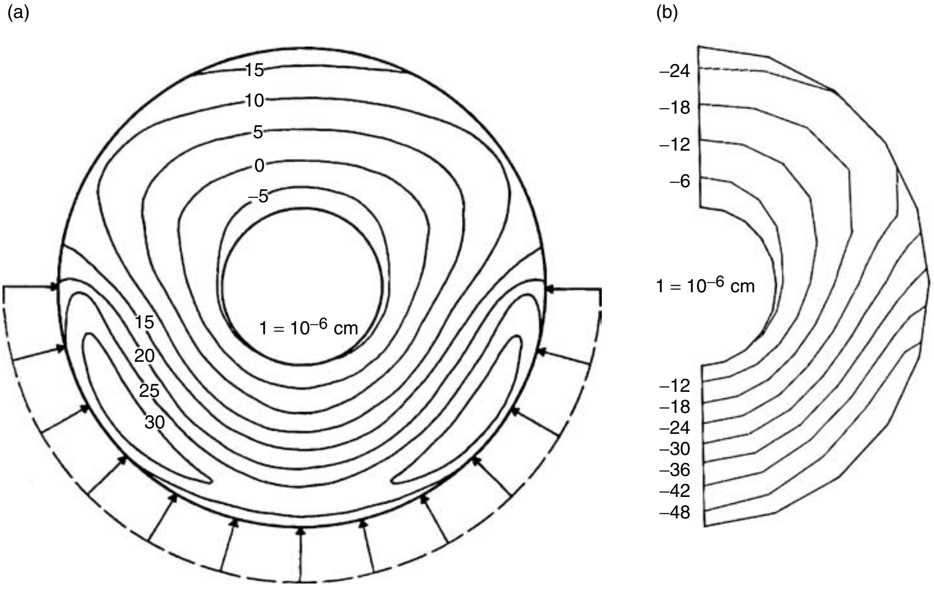

FIGURE 10.24 Applied loads and resulting surface contours of the 4-m (157-in.)-diameter centrally perforated solid glass mirror when supported in a strap mount as evaluated (a) by Malvick and Pearson (1968) using the dynamic relaxation method and (b) by Hatheway et al. (1990) using a FEA method. Contour intervals are 10^{-6} cm. (From Hatheway, A.E. et al., *Proc. SPIE*, 1303, 142, 1990.)

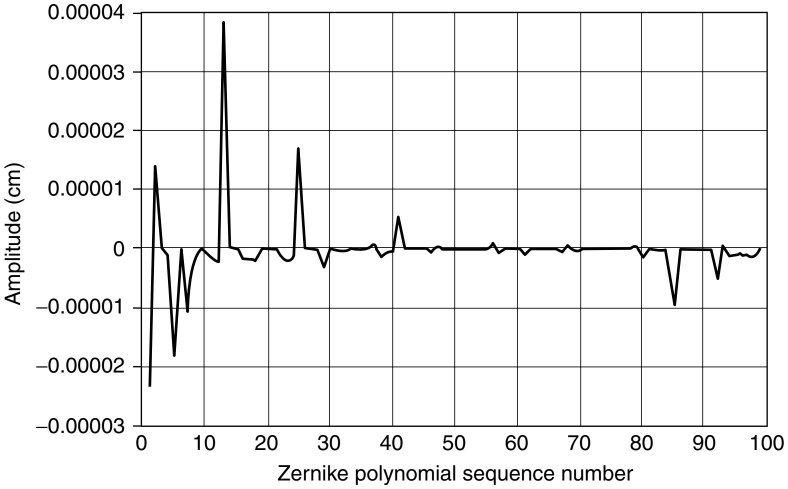

FIGURE 10.25 Amplitudes of the first 100 Zernike polynomials representing the surface deformation of the mirror modeled as shown in Figure 10.24. (From Hatheway, A.E. et al., *Proc. SPIE*, 1303, 142, 1990.)

is the same as Figure 10.16. Hatheway and his coworkers compared the two analyses as follows: (1) The algebraic signs of the results are reversed. This resulted from coordinate system redefinition. (2) The locations of the zero contours are slightly different. This was attributed to differences in the support points used to control rigid-body motions. (3) In general, the shapes of the contours are similar. The "lobing" (hexifoil deviation from circular contours) is reduced in the FEA results as compared with the DR results. This was attributed to elimination in the FEA model of a slight conical shape (drift angle) for the mirror's rim in the DR model owing to the necessity in the FEA case to balance axial forces resulting from uniform pressure over the rim. (4) The peak-to-valley ranges of the displacement fields for the two cases are very close (50×10^{-6} cm for DR and 54×10^{-6} cm for FEA).

With the small differences accounted for, Hatheway and his coauthors concluded that the two methods give essentially the same results. This is reassuring since any other conclusion would cast doubts on the many design decisions made in the past based on Malvick and Pearson's outstanding work, and greatly reduce the willingness of designers to use that work as the basis for future designs.

A significant benefit of the newer FEA technique in analyzing opto-mechanical structures such as mirrors and their mounts is the ability to present the results in Zernike coefficient form. Figure 10.25 shows the magnitudes of the first 100 coefficients for Malvick and Pearson's mirror. The expected concentration of errors in the first 20 terms is seen, but 2 spikes at terms 85 and 92 are noticeable. The significance of these two spikes might be evaluated approximately by considering the ratio of the areas under those spikes to the total area under the spikes for the first 20 terms. On this basis, the higher order terms do not have much impact.

REFERENCES

Born, M. and Wolf, E., *Principles of Optics*, 2nd ed., Macmillan, New York, 1964. p. 468.

Chivens, C.C., Air bags, in *A Symposium on Support and Testing of Large Astronomical Mirrors*, Crawford, D. L., Meinel, A. B., and Stockton, M. W., Eds., Kitt Peak Nat. Lab. and the University of Arizona, Tucson, 105, 1968.

Day, A.S., An introduction to dynamic relaxation, *The Engineer*, 219, 218, 1965.

Draper, H., On the construction of a silvered glass telescope, fifteen and a half inches in aperture, and its use in celestial photography, *Smithsonian Contributions to Knowledge*, 14, 1864.

Hatheway, A.E., Ghazarian, V., and Bella, D., Mountings for a four meter glass mirror, *Proc. SPIE*, 1303, 142, 1990.

Malvick, A.J., Dynamic relaxation: a general method for determination of elastic deformation of mirrors, *Appl. Opt.*, 7, 2117, 1968.

Malvick, A.J., Theoretical elastic deformations of the Steward Observatory 230-cm and the Optical Sciences Center 154-cm mirrors, *Appl. Opt.*, 11, 575, 1972.

Malvick, A.J. and Pearson, E.T., Theoretical elastic deformations of a 4-m diameter optical mirror using dynamic relaxation, *Appl. Opt.*, 7, 1207, 1968.

Maréchal, A., Etude des effets combinés de la diffraction et des aberrations géométriques sur l'image d'un point lumineux, *Rev. Opt.*, 26, 257, 1947.

Otter, J.R.H., Cassell, A.C., and Hobbs, R.E., Dynamic relaxation, *Proc. Inst. Civil Eng.*, 35, 633, 1966.

Schwesinger, G., Optical effect of flexure in vertically mounted precision mirrors, *J. Opt. Soc. Am.*, 44, 417, 1954.

Vukobratovich, D., Optomechanical System Design, *The Infrared and Electro-Optical Systems Handbook*, ERIM, Ann Arbor, MI and SPIE Press, Bellingham, WA, Dudzik, M., Ed., 1993, chap. 3.

Vukobratovich, D., Optomechanical design principles, in *Handbook of Optomechanical Engineering*, Ahmad, A., Ed., CRC Press, Boca Raton, FL, 1997, chap. 2.

Vukobratovich, D., Introduction to Optomechanical Design, *SC014 Short Course,* 2003.

Vukobratovich, D., personal communication, 2004.

Vukobratovich, D. and Richard, R. M., Roller chain supports for large optics, *Proc. SPIE*, 1396, 522, 1991.

11 Mounting Large Vertical-Axis Mirrors

11.1 INTRODUCTION

The mounts considered in this chapter all provide axial support for fixed vertical-axis mirrors. Included are single- and multiple-ring mounts; air bag (bladder) mounts supplying continuous (large area) or independent annular or pie-shaped zone support; multiple-point mounts, Hindle (whiffletree) mechanisms, counterweighted mechanisms, pneumatic or hydraulic supports; and metrology mounts that are used to support a mirror while it is being polished or tested. The latter mounts are used when a gravity-free (space) environment must be simulated in the laboratory. Examples involving 36- and 52-point supports are discussed. Lateral constraints for the vertical axis mirror in its mount are also considered.

11.2 RING MOUNTS

Continuous-ring mounts and closely spaced discrete point approximations thereof are acceptable supports for fixed, vertical-axis mirrors if the deflections of unsupported regions of the surface due to gravity are within tolerance for the specific application. Another necessary condition for acceptability is that the resulting radius (i.e., optical power) change can be tolerated or compensated for by refocusing. Nonsymmetrical mirrors, such as those with elliptical or rectangular apertures, do not possess this symmetry and sag more along the longer dimension, thereby becoming astigmatic as well as changing in power.

The simplest type of ring support obtains when a solid mirror is supported on a continuous line contact near the mirror's edge, as illustrated in Figure 11.1. If the mirror is very stiff and the mount surface contacting the mirror is not as true as the glass surface (undoubtedly the case), the actual contact will be at the three highest points along the line. The mirror would then bridge over those points. Generally, it is assumed that the mount is stiffer than the mirror and that it does not deform because of the mirror's weight. In real life, all mirrors and most mounts are somewhat flexible, so they do deform, and contact occurs more or less continuously along the ring. Since both the mirror and the mount are elastic, the contact is not a line, but actually a narrow localized zone as discussed in our considerations of contact stress in Chapter 15.

Here, we are primarily concerned with the gross deformation of the mirror's surface under the influence of gravity. Using the theory of simple, unclamped plate flexure under uniform load from Roark (1954), we can estimate the central deflections ΔY_C for circular mirrors, ΔY_R for rectangular mirrors, and ΔY_E for elliptical mirrors from

$$\Delta Y_C = \frac{0.0149W(m-1)(5m+1)D_G^2}{E_G m^2 t_A^3} \quad \text{(round)} \tag{11.1}$$

$$\Delta Y_R = \frac{0.1422wb^4}{E_G t_A^3 (1 + 2.21\alpha^3)} \quad \text{(rectangular)} \tag{11.2}$$

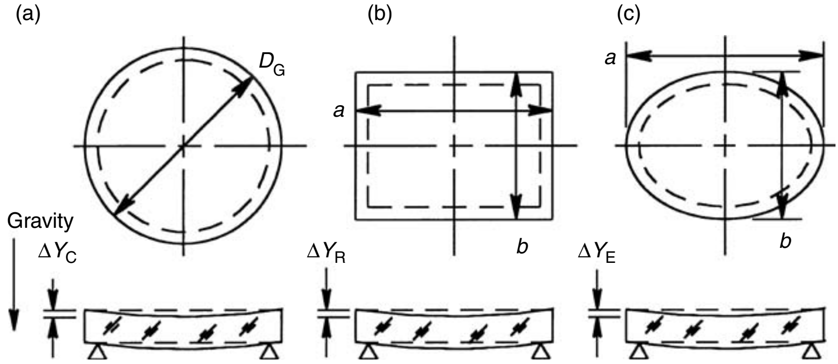

FIGURE 11.1 Schematics of (a) circular, (b) rectangular, and (c) elliptical solid fixed vertical-axis mirrors simply supported continuously around their edges.

$$\Delta Y_E = \frac{(0.146 - 0.1\alpha)wb^4}{E_G t_A^3} \quad \text{(elliptical)} \tag{11.3}$$

where W is the mirror's weight; w its weight per unit area; m is 1/Poisson's ratio v_G for the glass; D_G, a, and b are dimensions as depicted in Figure 11.1; $\alpha = b/a$; E_G the Young's modulus for the glass; and t_A the mirror's thickness. As would be expected, making the mirror thicker or using a material with greater Young's modulus reduces the magnitude of the gravitational deflection.

Assuming typical mirrors for each case to be made of fused silica with parameters as listed in Table 11.1, we can compare the self-weight sagittal depths at the geometric centers for the three types of mirrors with the same overall size. Substituting into Eqs. (11.1)–(11.3), we compute ΔY_C as $(0.0149)(83.767)(4.882)(30.410)(20^2)/[(10.6 \times 10^6)(5.882^2)(3.333^3)] = 5.466 \times 10^{-6}$ in. (0.139 μm), $\Delta Y_R = (0.1422)(0.267)(12.5^4)/\{(10.6 \times 10^6)(3.333^3)[(1 + (2.21)(0.625^3)]\} = 1.534 \times 10^6$ in. (0.039 μm), and ΔY_E as $\{[0.146 - (0.1)(0.625)][0.267][12.5]^4\}/[(10.6 \times 10^6)(3.333)^3] = 1.387 \times 10^{-6}$ in. (0.035 μm). These values are equivalent to 0.25, 0.07, and 0.06 wavelengths in green light, respectively. The self-weight deflections of these mirrors are significantly different, as might be expected because the supports along the long edges of the rectangular and elliptical mirrors are closer together than those for the circular mirror and so allow smaller deflections in one meridian.

If the lines of support in these two cases are moved inward from the edges of the mirrors, the regions outside and inside the contacts sag owing to gravity. For a circular mirror, the following general equation attributed to Williams and Brinson (1974) by Vukobratovich (1993) gives the deflection ΔY_C at the center of the mirror:

$$\Delta Y_C = \frac{C_s \rho_G r_Z^4 (1 - v_G^2)}{E_G t_A^2} \tag{11.4}$$

where C_S is a constant determined by the conditions of support; ρ_G, v_G, and E_G are the mirror material's density, Poisson's ratio, and Young's modulus, respectively; r_Z the radius of zonal support; and t_A the mirror's thickness. Vukobratovich (1993) gave values for C_S for three support conditions as listed in Table 11.2. Here, the supports are in one ring, but at discrete points rather than along a continuous line. The zonal radii represent the locations giving minimum deflections. Nelson et al. (1982) showed that increasing the number of points in a single ring beyond six and approaching infinity (i.e., a continuous ring) has only a very small effect on the mirror's gravitational surface deflection and the zonal radius for minimum deflection. This is shown graphically in Figure 11.2, which depicts mirror deflections for various numbers of support points. The best locations for the zonal radii of support can be approximated from the curve minimums.

TABLE 11.1
Mirror Parameters for Self-Weight Deflection Examples

Parameter	Circular Mirror	Rectangular Mirror	Elliptical Mirror
Mirror diameter D_G	20.0 in. (50.8 cm)		
Mirror longest dimension a		20.0 in. (50.80 cm)	20.0 in. (50.80 cm)
Mirror shortest dimension b		12.5 in. (31.75 cm)	12.5 in. (31.75 cm)
$\alpha = b/a$		0.625	0.625
Mirror thickness t_A	3.333 in. (8.466 cm)	3.333 in. (8.466 cm)	3.333 in. (8.466 cm)
Density ρ_G	0.080 lb/in.^{3} (2.205 g/cm^3)	0.080 lb/in.^{3} (2.205 g/cm^3)	0.080 lb/in.^{3} (2.205 g/cm^3)
Total weight W	83.767 lb (37.997 kg)	66.660 lb (30.237 kg)	52.3546 lb (23.748 kg)
Unit load (weight/area) w		0.267 lb/in.^{2} (1.875 × 10^2 kg/cm^2)	0.267 lb/in.^{2} (1.875 × 10^2 kg/cm^2)
Reciprocal of Poisson's ratio m	5.882	5.882	5.882
Young's modulus E_G	10.6 × 10^6 lb/in.^{2} (7.3 × 10^4 MPa)	10.6 × 10^6 lb/in.^{2} (7.3 × 10^4 MPa)	10.6 × 10^6 lb/in.^{2} (7.3 × 10^4 MPa)

TABLE 11.2
Values of C_s in Eq. (11.4) for Selected Single-Ring Support Conditions for Circular Mirrors with Axis Vertical

Condition	C_s
Three-point support equally spaced at edge of mirror	0.412
Three-point support equally spaced at radius of $0.645r_{MAX}$ (minimum)	0.318
Six-point support equally spaced at radius of $0.681r_{MAX}$ (minimum)	0.0414

Applying Eq. (11.4) to the circular, fused silica mirror defined in Table 11.1 under each of the conditions defined in Table 11.2, we determine first that all the self-weight deflections would equal $(0.080)(10.000^4)(1 - 0.170^2)C_S/[(10.6 \times 10^6)(3.333^2)] = 6.597 \times 10^{-5}C_S$. Then, for the first condition in the table (support at three points equally spaced around the edge of the mirror), $\Delta Y_C = 2.72 \times 10^{-6}$ in. (0.069 μm). For the second condition (support at three points equally spaced at a zone of radius $0.645R_{MAX}$), $\Delta Y_C = 2.098 \times 10^{-6}$ in. (0.053 μm). For the third condition (support at six equally spaced points at a zone of radius $0.681R_{MAX}$), $\Delta Y_C = 2.73 \times 10^{-7}$ in. (0.007 μm). These deflections equal 0.13, 0.10, and 0.01 wavelengths, respectively, in green light. The advantage of supporting the mirror with at least six supports at the appropriate zonal radius is obvious.

Vukobratovich (2004) indicated that his polynomial representations of surface deflections on rings of points are valid for mirror diameters up to about 1.5 m (59.0 in.). This limitation is caused by the increasing importance of shear effects that are not included in the analysis.

Larger mirrors or ones with lower stiffness because their thickness-to-diameter ratio is smaller or because the material has a lower Young's modulus will need more support points. In general, these can be arrayed in a variety of patterns such as in additional rings or, for large numbers of points, as any of a variety of patterns such as triangular, square, or hexagonal grids. Hall (1970) gave an equation for the number of support points N needed to limit the mirror surface deflection between discrete supports to some tolerable value δ. Slightly simplified, this equation is

$$N = \left(\frac{0.375D_G^2}{t_A}\right)\left(\frac{\rho_G}{E_G\delta}\right)^{1/2} \tag{11.5}$$

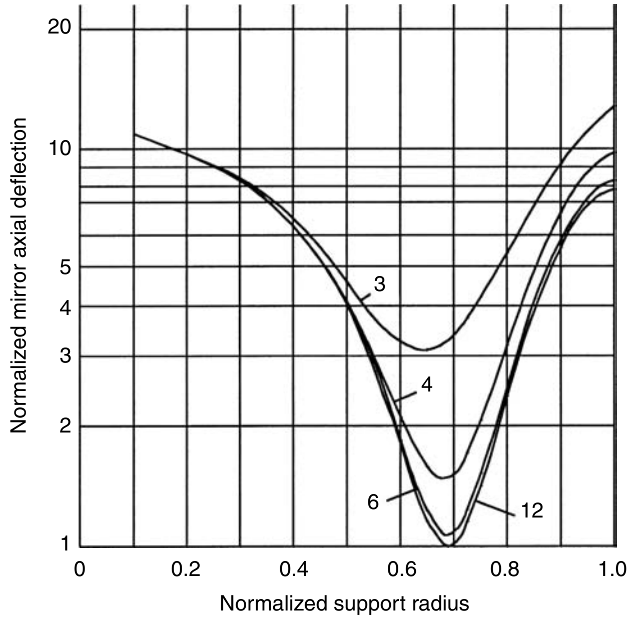

FIGURE 11.2 Normalized deflections of vertical-axis mirrors with multiple supports arranged in rings as functions of normalized ring radius. The number of supports is indicated for each case. (Adapted from Vukobratovich, D., private communication, 2004.)

All parameters are as previously defined. As an example of the use of Hall's equation, consider a 39.37-in. (100.000-cm)-diameter, 5.625-in. (14.288-cm)-thick, fused silica mirror that is to deflect by no more than 0.01 wave at 0.633 μm wavelength. By Eq. (11.5), its axial support would need at least $[(0.375)(39.370^2)/5.625]\{0.080/[(10.6 \times 10^6)(2.492 \times 10^{-7})]\}^{1/2} = 17.98$ or 18 supports. (See considerations of multiple-support systems in Sections 11.4 and 12.7.)

Because the mirror must be relatively stiff and approximate a plane-parallel plate for these equations to apply, they should be used only for mirrors having uniform or nearly uniform thickness and thickness-to-diameter ratios of 6:1 or less. Surface deflections under gravity and mount-induced forces for mirrors meeting these criteria (but having curved optical surfaces and flat backs), meniscus mirrors (which behave as shells), and all larger mirrors would best be analyzed by FEA techniques. Many of these mirror configurations can also be evaluated by closed-form methods described by Mehta (1984).

11.3 AIR BAG (BLADDER) MOUNTS

Pneumatic (air bag or bladder) supports have been used in many astronomical telescope primary mirror mounts as a means of distributing axial forces over the back surface of the mirror. They are of three general types: those with large area contact provided by flat, air-filled bladders, those with annular area contacts at two or more selected radial zones, and those with multiple, pie-shaped segments. Each of these types is considered here.

Single bladder supports typically are made of two sheets of nonporous material such as neoprene or neoprene-coated fabric such as Dacron, joined and sealed together at the edges as shown in Figure 11.3. Vukobratovich (1992) indicated that a special variety of ozone-resistant neoprene is needed if the air bag is to be used at a high altitude, such as in mountaintop observatories.

The mirror's axial location and orientation are usually referenced to three, small-area, pad-type, adjustable supports (called hard or defining points) projecting from the cell back structure through sealed holes (not shown) in the bladder. The bladder supports 90 to 95% of the mirror's weight, and

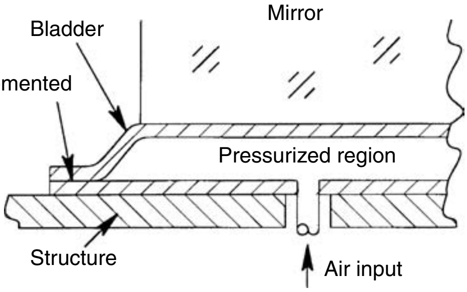

FIGURE 11.3 Schematic diagram of a bladder-type air bag axial support for a vertical-axis mirror. (Adapted from Chivens, C. C., *A Symposium on Support and Testing of Large Astronomical Mirrors*, Crawford, D. L., Meinel, A. B., and Stockton, M. W., Eds., Kitt Peak Nat. Lab. and The University of Ariz., Tucson, 1968, p. 105.)

the remaining weight is supported by the hard points. A low-pressure pump supplies air to the bladder through a pressure regulator. In some cases, a spare pump that is automatically switched into operation if the main pump fails provides redundancy. The pumps are operated considerably below maximum rated pressure and at lower than full speed. This increases useful life.

Doyle et al. (2002) indicated that an FEA model created during design of an air bag support must take into consideration the shape of the interface between the bag and the mirror at the mirror's rim. If the mirror is rotationally symmetric, the pressure should be adjusted so that the bag is tangent to the mirror at the rim as shown in Figure 11.4(a). The authors showed how corrections are applied if this is not the case, i.e., the bag is over inflated or under inflated as shown in Figure 11.4(b) and (c) respectively. They also showed how to adjust the FEA model if the mirror is not symmetrical. One case of such a mirror configuration is the off-axis paraboloid illustrated in Figure 11.4(d).

Crawford and Anderson (1988) described the manufacture of a 1.8-m (70.9-in.)-diameter, f/2.7 paraboloid that was to be used as a spare mirror for the original multiple mirror telescope (MMT) located on Mt. Hopkins. During polishing, this 1200 lb (544 kg) slumped, fused silica, egg crate mirror was supported on its back with approximately 93% of its weight on a full-diameter. Neoprene air bladder and the remaining 7% supported by three swivel defining pads (see Figure 11.5). The mirror was first ground and polished to a sphere. This allowed the choice of weight distribution between bladder and pad support to be based on measurements of the effects of varying pressure vs. the observed 3θ Zernike polynomial coefficient. The pad "print through" was adequately minimized at that weight distribution.

An air bladder in direct large area contact with the back of a mirror thermally insulates the mirror from its surround (Sisson, 1958). This might be undesirable for stability and fast accommodation of temperature changes and must be taken into consideration during the design of the mirror's temperature control system.

It is difficult to design a single air bladder that will produce the required force distribution for uniform support of mirrors with thickness varying significantly in the radial direction. Multiple annular air bags can have different pressures, thereby accommodating this variation. Control of pressure to the required degree of precision is no small task in any air bag system; the problem is compounded if multiple bags are involved.

Baustian (1968a) described a double annular air bag support used with a 150–in. (3.8–m)–diameter mirror. The design radii for the zonal contacts were $0.48R_{\mathrm{MAX}}$ and $0.85R_{\mathrm{MAX}}$, respectively, where R_{MAX} is one half the disk diameter. During operation, the axial location of the mirror was fixed by three "defining units" (hard points) at the $0.722R_{\mathrm{MAX}}$ zone. Figure 11.6 shows a sectional view sketch of one ring support, while Figure 11.7 shows the layout of the mirror in its cell. The annular widths of the inner and outer air bags were 4.8 and 5.1 in. (12.2 cm and 13.0 cm), respectively. As may be seen in the front view, the annular bags were made in sections. This was done for reasons of cost and ease of installation.

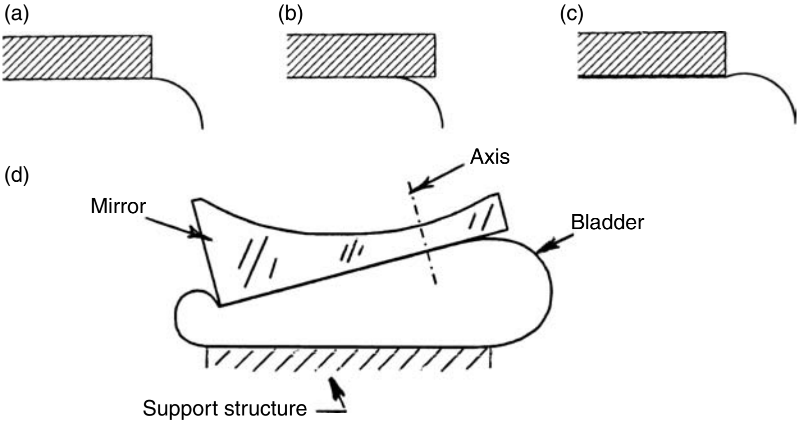

FIGURE 11.4 Four possible edge conditions for air bladder axial support of a mirror: (a) tangent, (b) overinflated, (c) underinflated and (d) exaggerated diagram of a nonsymmetrical (off-axis paraboloid) mirror supported by an air bladder. (Adapted from Doyle, K. B. and Forman, S. E., *Proc. SPIE*, 3132, 2, 1970.)

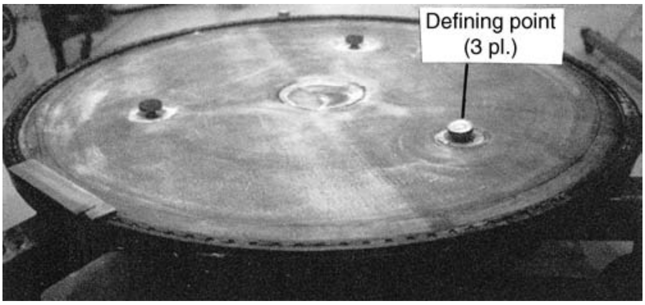

FIGURE 11.5 Photograph of the full-diameter air bladder support used during polishing of the 1.8-m (70.9-in.) diameter, *f*/2.7 paraboloidal spare mirror for the original MMT. (Adapted from Crawford, R. and Anderson, D., *Proc. SPIE*, 966, 322, 1988.)

Figure 11.8, shows the computed symmetrical surface deformation typical of a 4-m (158-in.)-diameter mirror when supported with axis vertical by two concentric rings as with the double annular air bag support. The ring radii in this example were nearly the same ($0.51R_{\text{MAX}}$ and $0.85R_{\text{MAX}}$) as those provided by the design shown in Figure 11.7. The p-v surface deformation indicated in Figure 11.8 was 3×10^{-6} cm (0.06 wave in green light) over most of the aperture.

The bladder supporting a mirror over its full back surface area may be constructed in the form of three or more pie-shaped sectors connected in parallel to an air manifold (Chivens, 1968). Figure 11.9 shows a diagram of the back of a mirror supported by three such segmented bladders. In such designs, the hard points can be located at the radial intersections of the sectors. The lack of support at the narrow regions between the sectors can usually be tolerated.

A variation on the concept of the air bag uses the mirror disk itself as a piston with one or more flexible gaskets or an O ring to seal it at or near its rim to a closed cell (see Figure 11.10). Pulling a partial vacuum with a pump reduces the air pressure within the sealed region. The atmospheric pressure difference between the front and back of the mirror then supports the weight of the mirror and holds it against three defining pads (one shown in the figure). Chivens (1968) mentioned this approach. Several telescopes have been built with this type of support. One such design is used to support the primary mirrors in the Gemini telescopes. Multiple axial actuators provide partial support for this mirror. It is used in a variable orientation telescope and so is described in Chapter 12.

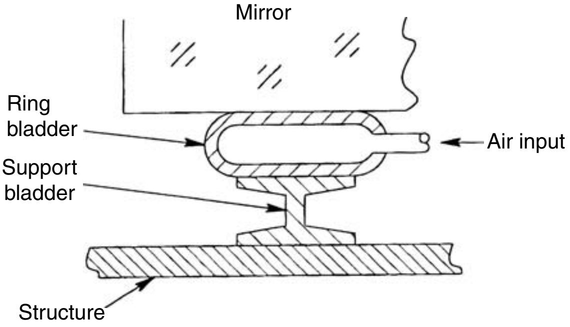
Mirror
Ring bladder
Air input
Support bladder
Structure

FIGURE 11.6 Sketch of a ring-type air bag axial support for a large mirror. (Adapted from Baustian, W. W., *A Symposium on Support and Testing of Large Astronomical Mirrors*, Crawford, D. L., Meinel, A. B., and Stockton, M. W., Eds., Kitt Peak Nat. Lab. and The University of Ariz., Tucson, 1968a, p. 109.)

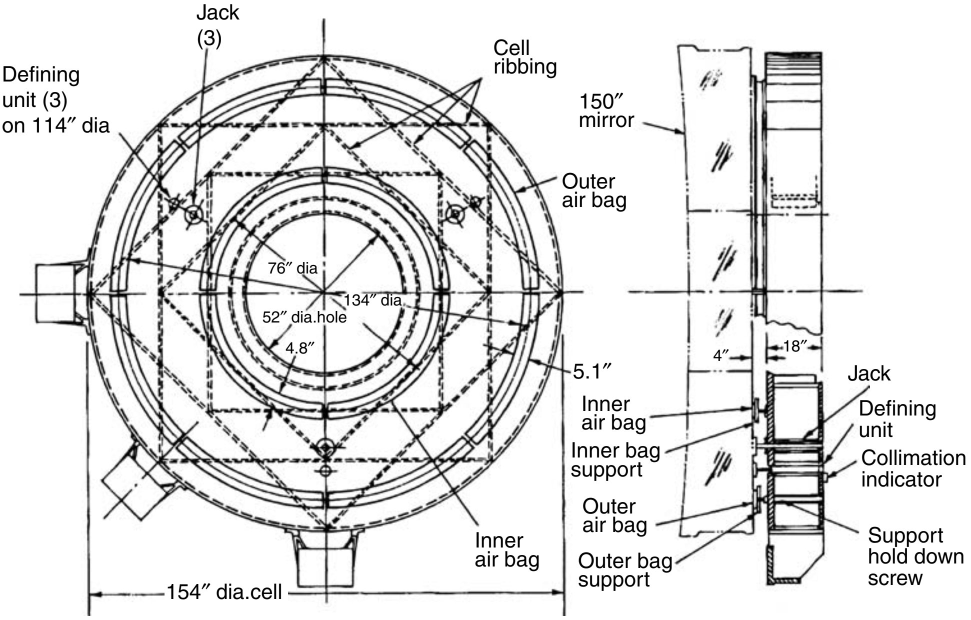
Jack (3)
Defining unit (3) on 114″ dia
Cell ribbing
150″ mirror
Outer air bag
76″ dia
134″ dia
52″ dia.hole
4.8″
5.1″
Inner air bag
154″ dia.cell
4″
18″
Jack
Defining unit
Collimation indicator
Inner air bag
Inner bag support
Outer air bag
Outer bag support
Support hold down screw

FIGURE 11.7 Layout of a double annular air bag support for a 150-in. (3.8-m) diameter telescope primary mirror. Dimensions are inches. (Adapted from Baustian, W.W., *A Symposium on Support and Testing of Large Astronomical Mirrors*, Crawford, D. L., Meinel, A. B., and Stockton, M. W., Eds., Kitt Peak Nat. Lab. and The University of Ariz., Tucson, 1968b, p. 150.)

11.4 MULTIPLE-POINT SUPPORTS

11.4.1 THREE-POINT MOUNTS

The simplest mount for a vertical-axis mirror of symmetrical configuration provides support at three localized points on the mirror's back as sketched in Figure 11.11. If symmetry is to be preserved, the three points should lie on a circle centered about the mirror's axis and at equal (120°) angular intervals around the circle.

The deformation distribution on the mirror surface due to gravity differs in magnitude and configuration with the radius of the support circle. Figure 11.12(a) shows the typical warped surface

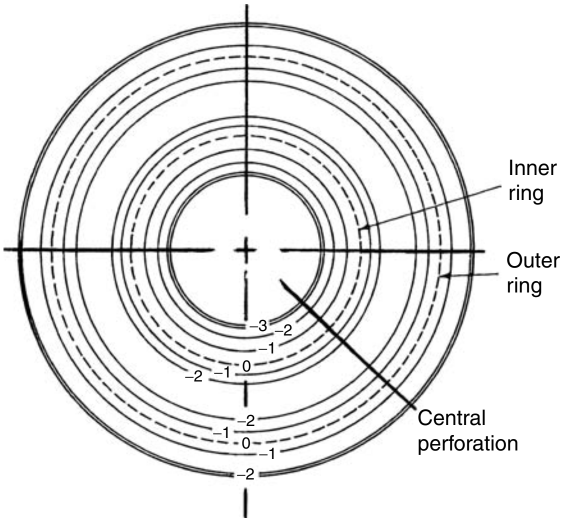

FIGURE 11.8 Computed surface deformation for a 4-m (158-in.) diameter vertical-axis mirror supported on two annular rings located at the dashed lines. Contour interval = 10^{-6} cm. (Adapted from Malvick, A. J. and Pearson, E. T., *Appl. Opt.*, 7, 1207, 1968.)

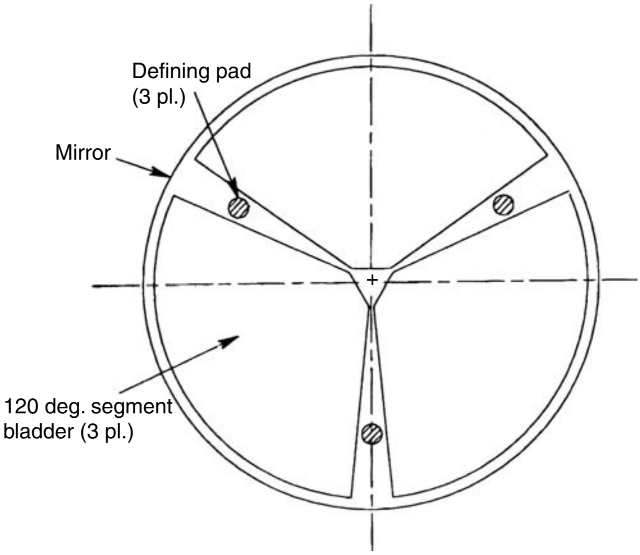

FIGURE 11.9 Schematic rear view of a large mirror supported axially by three 120° segmented air bladders. Defining point supports are also indicated.

obtained from a three-point support with those points at the 96% zone of a 4-m (158-in.)-diameter solid disk mirror with a 1.32-m (52-in.)-diameter central hole. The diameter-to-thickness ratio was approximately 7:1. Malvick and Pearson (1968) stated that the example was intended to illustrate the effect of using three fixed, i.e., hard, points to define the location of a mirror otherwise uniformly supported. If these points are used to support a small fraction (say, 1%) of the weight of this mirror, the p-v deflection of the surface would be determined approximately from the contour line count and scale factor as $[14 - (-8)](10^{-4}\ \text{cm})(10^{-2}) = 0.22\ \mu\text{m} = 0.41$ wave for green light.

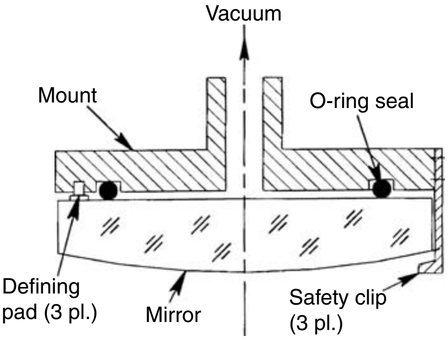

FIGURE 11.10 Conceptual schematic sketch of a plano convex mirror axially supported facing downward by atmospheric pressure in the manner of a negative air bladder support. (Adapted from Vukobratovich, D., in *SPIE*, *Short Course SC014*, 2003.)

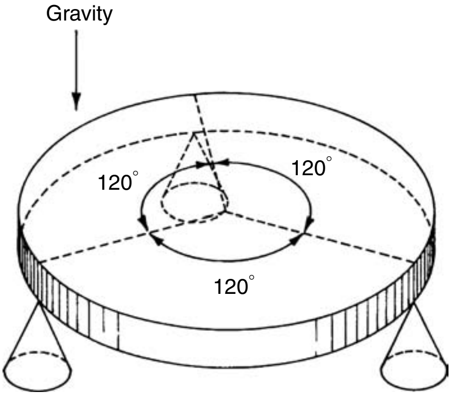

FIGURE 11.11 Sketch of a simple three-point support for a vertical-axis mirror with point contacts at the edge of the mirror's back.

Figure 11.12(b) shows the deflections produced by mounting the same mirror on three hard points located at the 72.5% zone. The p-v deflection range is now only $[4 - (-2)](10^{-4}\,\text{cm})(10^{-2}) = 0.06\ \mu\text{m} = 0.11$ wave. If mounted near the center hole (see Fig. 11.12[c]), the deflection of the mirror edge would be 0.22 μm, i.e., the same as the center deflection with support at the edge. In all these cases, the location of the "zero" contour was arbitrary. The deflection contour patterns of a mirror lightly clamped to the support points would appear the same as for the unclamped mirror if the clamping forces are normal to the contacted surfaces and pass directly through the centers of the contacting areas. Otherwise, localized moments would be exerted that tend to distort the mirror.

As may be inferred from examination of Figure 11.12, there is an optimum radius for a three-point support that gives minimum p-v surface deflection. For a uniform-thickness unperforated plate of diameter $2R_{\text{MAX}}$, this radius is $0.645R_{\text{MAX}}$ as indicated for the second case in Table 11.2. Three equally spaced point supports on a circle of this radius will produce a "central hole and a downward rolled edge" contour in a vertical-axis, upward-facing mirror under the influence of gravity.

Because most large-mirror mount designs use three hard point supports only to define the axial location and angular orientation of the reflecting surface and not to support a significant fraction of the mirror's weight, we next consider mechanical means for off-loading the bulk of that weight.

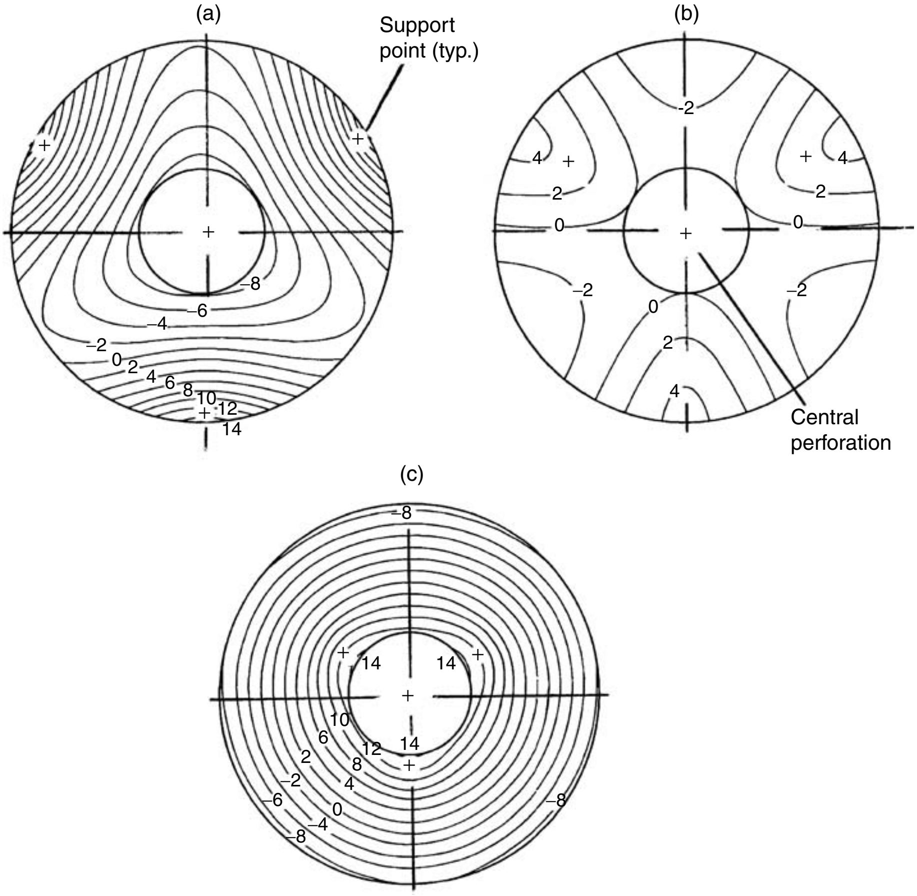

FIGURE 11.12 Contour plots of computed surface deflections of a 4-m (158-in.)-diameter solid mirror when supported on three points at (a) 96%, (b) 73%, and (c) 38% zones. Contour interval = 10^{-4} cm. (Adapted from Malvick, A. J. and Pearson, E. T., *Appl. Opt.*, 7, 1207, 1968.)

11.4.2 HINDLE MOUNTS

In a classical paper on mirror flotation systems, Hindle (1945) described a mounting technique that now bears his name. Starting with three support points angularly equidistant on a circle just outside the radius of equilibrium R_E that divides the constant-thickness mirror into a central disk of one third the total weight and an annulus of two thirds that weight, he explained how a three-point support could be provided around each of the first three points to form a nine-point, two-ring mount. The geometry is shown in Figure 11.13(a). Three and six support points lie on inner and outer circles of radius R_I and R_O respectively. Equations (11.6)–(11.9) relate the various radii to the disk diameter D_G.

$$R_E = \left(\sqrt{3}/6\right)D_G = 0.289D_G \tag{11.6}$$

$$R_I = \left(\sqrt{3}/12\right)D_G = 0.144D_G \tag{11.6}$$

$$R_O = \left(\sqrt{6}/6\right)D_G = 0.408D_G \tag{11.6}$$

$$R_S = 0.304D_G \tag{11.6}$$

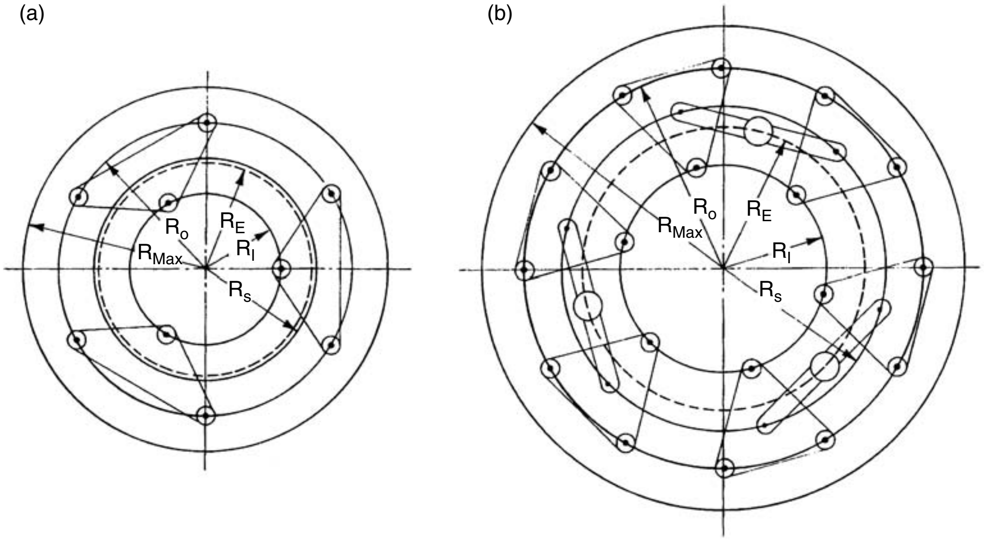

FIGURE 11.13 Multipoint (Hindle) mechanical floatation configurations for mirrors: (a) nine-point and (b) 18-point versions.

In the nine-point Hindle mount, sets of three adjacent support points are connected by plates that are usually triangular in shape pivoted at a point one third of the way up the triangle's altitude from its base. Each contact point carries essentially equal weight. Hindle pointed out that in practice, each of these plates must be individually balanced and restrained from rotation in its plane if it is to function properly. Arms (or bars) connect the plates. They have swivel joints at their centers and ends. Each of these subassemblies is called a *whiffletree.*

Hindle went on to describe an 18-point mirror support. Two triangular plates are supported from each of three bars that are, in turn, centrally supported from three points equally spaced on a circle of radius R_E. As in the nine-point mount, R_E divides the surface area into central and annular areas in a 1:2 ratio (see Fig. 11.13[b]).

Figure 11.14 illustrates details of a typical whiffletree subassembly for an 18-point mount design. The two squares on the plan view of the triangular plate are protrusions or lugs that straddle the pivoted bar to keep the plates from rotating. Hindle suggested that the arm-to-plate joint be made by means of spherical balls and sockets, and that the spherical seats in the plates be closed slightly over the balls at assembly to constrain them axially. Universal joint-type flexures such as that shown in Figure 11.15 are commonly used today for this purpose. A flexure bearing of the type shown in Figure 11.16 is typically used at the center of the arm. These bearings have crossed flat flexure blades supporting inner and outer sleeves. The fixed sleeves are attached to the structure; the rotating sleeves carry the load. Deflection ranges are typically ± 7.5, ± 15, and ± 30°. Cantilevered (single ended) and double-ended versions of these bearings are commercially available in diameters ranging from 0.125 in. (3.175 mm) to 1.000 in. (25.4 mm). They are typically made of 400 series CRES and are used at 30% of maximum load and deflection ranges. They show very small amounts of hysteresis and transverse shift of the axis with small angular deflections. These devices can be used in a hard vacuum.

Under normal operating conditions, flexure bearings have essentially infinite life. Doyle and Forman (1997) reported the use of FEA to explain failures of some flexure bearings when randomly vibrated. Defective welds or brazed joints within the pivots were found to crack owing to high stress concentrations. These authors indicated that the problems could be solved by manufacturing the flexures without joints by using an electrical discharge milling (EDM) process or by using shunts to limit radial movement.

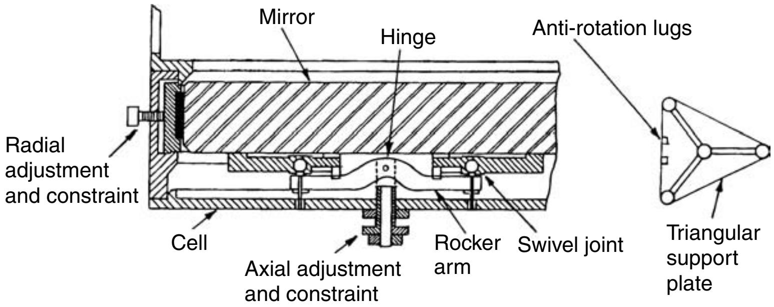
Mirror
Hinge
Anti-rotation lugs
Radial adjustment and constraint
Cell
Axial adjustment and constraint
Rocker arm
Swivel joint
Triangular support plate

FIGURE 11.14 Sketches of one mirror support subassembly for an 18-point Hindle mount. (Adapted from Hindle, J. H., in *Amateur Telescope Making, Advanced*, Ingalls, A. G., Ed., Scientific American, New York, 229, 1945.)

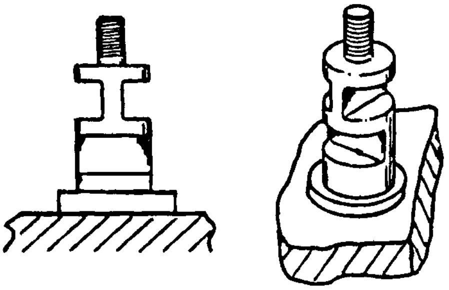

FIGURE 11.15 Concept for a universal joint-type flexure such as is frequently used in place of ball joints in Hindle mirror mounts.

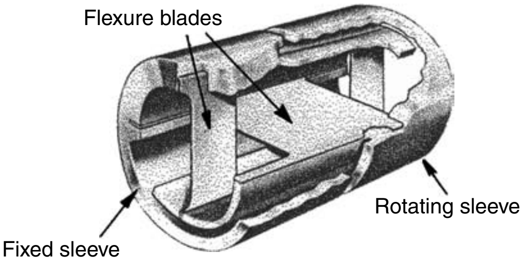
Flexure blades
Rotating sleeve
Fixed sleeve

FIGURE 11.16 Schematic of a single-ended flexure bearing of a type frequently used to eliminate friction in the hinges of counterweight type support mechanisms for mirrors. (Adapted from a figure provided by Riverhawk company, New Hartford, NY.)

The above design considerations for Hindle mounts apply strictly only to plates of uniform thickness and do not take into account shear effects. The calculations are more complex for curved-surface mirrors since the weight distribution is nonlinear with radius. An FEA analysis is frequently used for such cases.

Mehta (1983) described, in detail, a method for analyzing the gravity-induced surface deflections of a thin, uniform-thickness circular plate of diameter $2a$ supported by a multilevel mechanical mount. Both unperforated plates and those with central holes of radius b were considered. He applied his method to the nine-point Hindle mount with symmetrical and unsymmetrical triangular plates, but indicated that it was applicable to Hindle mounts with 18, 27, 36, 81, and larger numbers of support points. An unsymmetrical triangular plate case allows alternate floating support points of the outer ring to be located on circles of slightly different radii and facilitates determination of the sensitivity of a given design to dimensional perturbations. Examples of such computations were included in Mehta's paper. The equations derived there are nonlinear and transcendental. He demonstrated that they could be used to compute the surface deflections as a function of normalized radius *R/a* in any meridian and find the mount design that provided the minimum rms surface deformation (i.e., figure error) given the substrate's dimensions, Poisson's ratio, and modulus of rigidity.

Figure 11.17 compares Mehta's closed-form solution with an FEA computation of the deflections of a thin (D_G/t_A = 40/1) unperforated plate of 100 in. (~2.5 m) diameter and 2.5 in. (6.4 cm) thickness supported at the 50 and 90% zones on a nine-point Hindle mount with symmetrical triangular plates. The two curves represent the deflections along the meridian through the inner support point ($\theta = 0$) and along the meridian at $\theta = 60°$ to the first. Both methods obviously give the same results. Mehta indicated that the closed-form solution was computed much more quickly and more economically than the FEA solution and would be preferred for trade-off studies or preliminary design work.

There is no fundamental reason why Hindle mounts cannot be used to suspend mirrors looking vertically downward. Indeed, such mounts are frequently used to support large mirrors that must be mounted at the top of optical test chambers. For equivalent designs, the mirror surface deflections are the same for face-up and face-down cases.

11.4.3 COUNTERWEIGHTED MOUNTS

A series of mechanisms with weighted levers can be used to apply force at many discrete points on the back of a vertical-axis mirror to support it more or less uniformly in the axial direction. Figure 11.18 shows schematically one typical kind of lever back support; it is very similar to the one described by Couder (1932). This particular mechanism was designed to support the McDonald Observatory 107-in. (2.7-m)-diameter telescope primary mirror. It was described by Smith (1968). The design provided pointed thrust rods seated at each end in conical cups. The "points" at the ends of the rods were actually polished to a 0.014 in. (0.356 mm) spherical radius; the rods were made of tool steel, case hardened

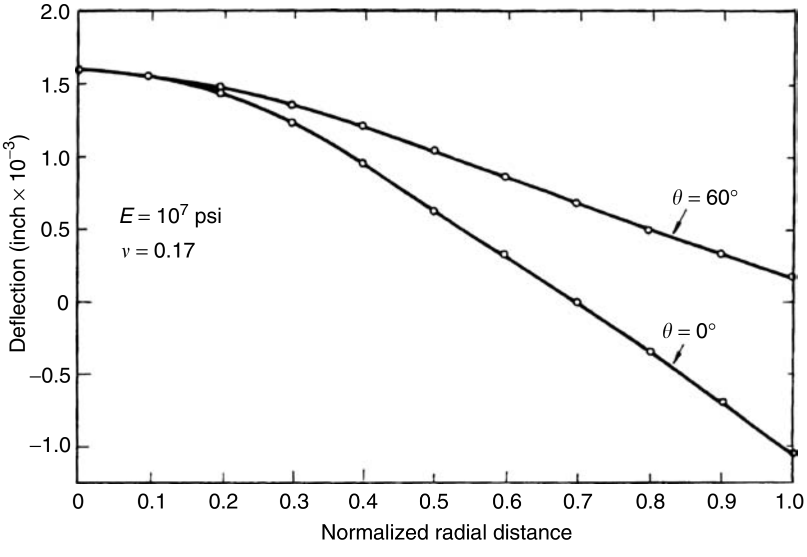

FIGURE 11.17 Comparison between closed-form (lines) and FEA (circles) computations for the self-weight surface deflections of an unperforated circular plane parallel mirror supported by a nine-point Hindle mount. Characteristics of the plate and geometry are indicated in the text. (From Mehta, P.K., *Proc. SPIE*, 518, 155, 1984.)

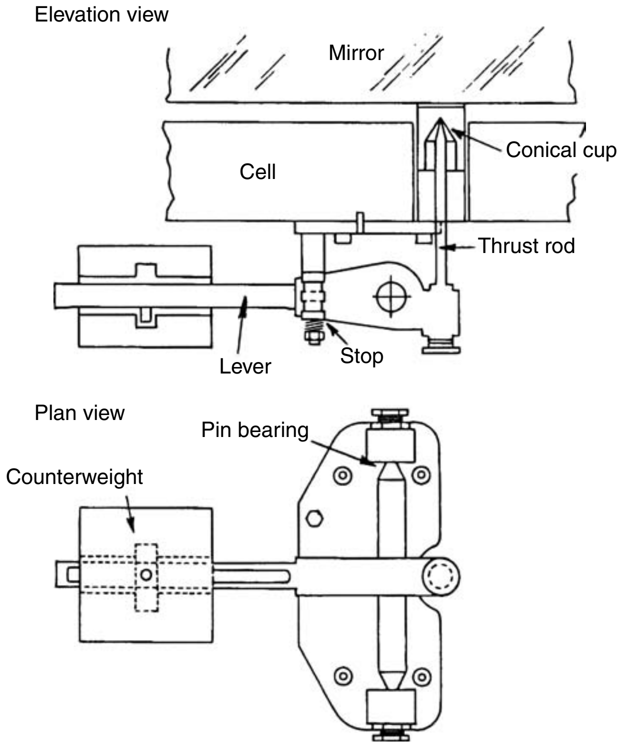

FIGURE 11.18 Schematic of a lever-type counterweighted support mechanism typically used for axial support of a mirror. (Adapted from Smith, H.J., *A Symposium on Support and Testing of Large Astronomical Mirrors*, Crawford, D. L., Meinel, A. B., and Stockton, M. W., Eds., Kitt Peak Nat. Lab. and The University of Ariz., Tucson, 169, 1968.)

to a 65 Rockwell hardness. The design pressures on the rod ends were about 200,000 lb/in.^{2} (1.38×10^3 MPa). The cups were packed with silicone grease to prevent contamination.

A major deficiency of counterweight-type mounts is the friction inherent in the bearings. The lateral axis of the mechanism shown in Figure 11.18 was originally designed with pin-type bearings. In order to enhance long-term reliability and eliminate friction, these were replaced by single-axis flexure bearings of the general type illustrated in Figure 11.16.

More complex types of lever counterweight mechanisms are described in Chapter 12 in the context of variable-orientation mirror support systems. Simple lever-type designs using flexure bearings are described in Section 11.5.3 as elements of a typical metrology mount.

11.4.4 PNEUMATIC/HYDRAULIC MOUNTS

Multipoint mounts using gas- or liquid-filled actuators are frequently used to provide the force field required to support vertical-axis mirrors. The actuators are usually arranged in rings of radii R_I and R_O and spaced approximately at equal intervals in each ring. Figure 11.19 shows a typical arrangement for eighteen points in two rings.

A frontal view of a typical mount of this type as described by Barnes (1974) is shown in Figure 11.20. The mirror supported by this mount was a 1.25-m (49.2-in.)-diameter, 0.2-m (7.9-in.) thick Cer-Vit disk with an *f*/2.5 parabolic reflecting surface. The mount has 27 pneumatic actuators. Figure 11.21, shows schematically a cross section of a generic rolling diaphragm actuator. The interface to the mirror is through the upper pad that rests on a spherical bearing or is attached through a universal joint flexure. The angle of the interface can be made to match that of the curved

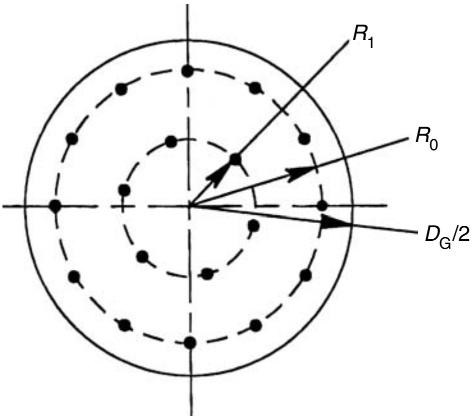

FIGURE 11.19 An arrangement of 18 points on two rings to axially support a circular mirror.

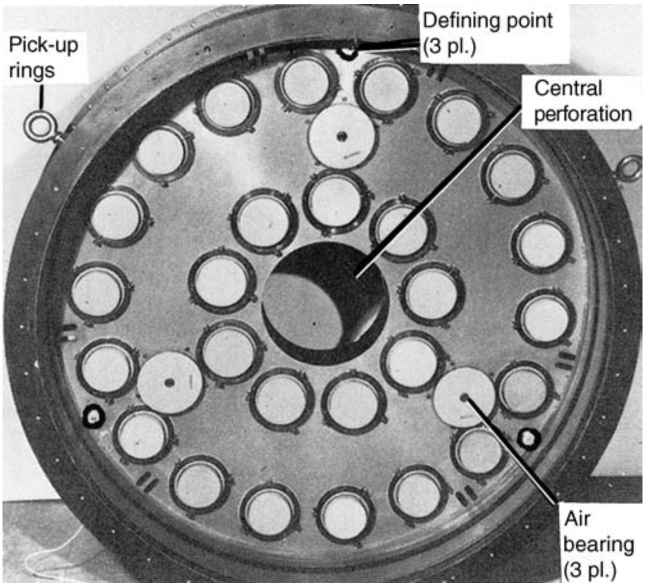

FIGURE 11.20 A multiple-point axial mirror mount comprising 27 pneumatic actuators arranged as two concentric rings. The mount is sized for a 1.2-m (47-in.)-diameter mirror. (Adapted from Barnes, W. P., Jr., *Proceedings of 9th Congress of The International Commission for Optics*, Thompson, B. J. and Shannon, R. R. Eds., Nat. Acad. Sci., Santa Monica, CA, 1974, p. 171.)

back surface of a mirror. Nonuniform weight distribution in the mirror disk can be accommodated with a single actuator design by varying the pressure exerted against the piston to meet the force requirements for units located at different locations. This type of actuator can function with either gas or liquid as the active medium.

In the design of Figure 11.20, the actuators are arranged in rings of nine and eighteen points near the inner and outer edges of the annular mirror disk, provide essentially equal force at each reaction point, and off-load most of the mirror's weight. Three adjustable defining point pads located at 120° intervals support the remaining portion of that weight. Displacement transducers attached to the pads provide axial positioning (piston) and tilt correction motions as directed by the telescope focus and pointing control system.

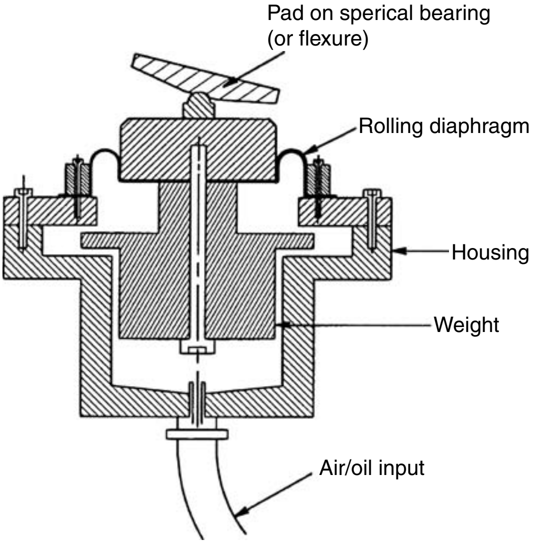

FIGURE 11.21 Configuration of a rolling-diaphragm-type pneumatic/hydraulic actuator suitable for supporting the back surface of a large, upward-looking mirror. (From Yoder, P. R., Jr., *Mounting Optics in Optical Instruments*, SPIE Press, Bellingham, 2002.)

11.5 METROLOGY MOUNTS

Optical metrology is the subdiscipline of optical engineering in which performance-related characteristics such as surface figure, radius of curvature, focal length, reflected wavefront quality, and modulation transfer function of optical components and systems are measured to a high degree of accuracy. These measurements are typically made at various in-process stages during manufacture and upon completion of the optics; the measured values are compared with previously established standards to determine acceptability.

It is frequently not practical to perform these evaluations under the exact conditions of final use. A prime example is a large mirror manufactured for eventual use in the gravity-free environment of space. Even if the mirror is always to remain on Earth, conditions such as the direction of the gravity vector during use may be different from those occurring during grinding and polishing. The forces normal and tangential to the surface imposed during optical finishing must also be taken into consideration since they might be quite significant — especially when large-diameter or very thin mirrors are polished by conventional techniques.

The mount used to support a mirror during testing in the final stages of manufacture is frequently referred to as a metrology mount. Generally, the mirror's axis is vertical and its mount must accurately locate the mirror surface relative to the optical test equipment and provide a stable, predictable, and repeatable support for the mirror. The metrology mount most frequently employed simulates a zero-gravity environment. Typically, such a mount supports the mirror at many points so that self-weight deflections from three strategically located position/orientation defining points and interspan self-weight deflections are within specification. As mentioned earlier, Hall (1970) gave a "rule-of-thumb" criterion for the minimum number N of support points needed to prevent self-weight deflections larger than specific p-v values during testing. Although not rigorously derived, Hall indicated that this criterion, expressed by Eq. (11.5), has proved satisfactory for mirrors ranging from 40 in. (1 m) diameter × 4 in. (10 cm) thick to 103 in. (2.6 m) diameter × 12 in. (30 cm) thick. If the same mount is to be used to support a mirror during polishing as well as during testing, the additional loading due to polishing tools and auxiliary weights must be considered when computing the number of support points.

The most common types of metrology mounts are those using pneumatic or hydraulic actuators and those using mechanical levers with counterweights or springs. A 36-point pneumatic mount suitable for supporting a 150-in. (3.8-m)-diameter mirror was described by Cole (1970). A 27-point hydraulic metrology mount for a 70-in. (1.8-m)-diameter mirror was described by Wollensak and Rose (1975). A 64-point hydraulic mount for a nearly rectangular lightweighted mirror of dimensions 71 × 193 cm (28 × 76 in.) was described by Barlow (1975).

A 52-point spring-loaded lever mount used with a 60-in. (1.5-m)-diameter mirror in an advanced demonstration of the fabrication and testing techniques to be applied to NASA's 98-in. (2.49-m)-diameter Hubble Space Telescope (HST) primary mirror was described by Montagnino et al. (1979). Krim (1982) outlined the design, modeling, and testing of the metrology mount actually used later with the HST primary. The latter mount was determined to simulate a zero-G environment within $\lambda/438$ rms at $\lambda = 0.633$ μm, even though the characteristic gravity deflection of the mirror if simply supported with axis vertical in the Earth's nominal gravitational field would be approximately 12 λ.

Space constraints permit only three of the above-referenced mount designs to be considered here. Cole's description of the 150 in. (3.8 m) mirror mount, Wollensak and Rose's report on the 70 in. (1.8 m) mirror mount, and Perkin-Elmer's design for the 60 in. (1.5 m) mirror mount are summarized in the following sections.

11.5.1 A 36-POINT PNEUMATIC METROLOGY MOUNT

Figure 11.22 shows an integrated fabrication/test facility used to manufacture a 150-in. (3.8-m)-diameter plano-concave mirror. The metrology mount was located between the back surface of the mirror and the table of a grinding/polishing machine. This mount provided mirror support both during fabrication and during tests. Figure 11.23 shows the upper surface of the mount, which was fitted with arrays of 36 circular actuator pads, 36 rectangular rubber cushion blocks, and three race-track-shaped air bearings. Figure 11.24 shows a close-up view of the pneumatic supports.

During optical tests, the mirror rested on the 36 pads. Three pads from the outer ring were deflated and thin spacers inserted between their pistons and the mirror to serve as hard, location-defining points. The maximum air pressure was about 8 lb/in.^2, slightly different in the two rings, and adjusted so that all 36 pads supported essentially equal parts of the mirror weight.

For polishing, the spacers were removed and the mirror floated on all 36 pads. The weight of the polishing tool (9000 lb or ~4100 kg) pressed the mirror's back against the 36 rubber cushion blocks. Cole pointed out that special precautions were necessary in order for the tool weight to be supported equally by the blocks. The rear surface of the mirror and top surface of the table were lapped to match and the blocks ground to the same height. To distribute the effects of residual height discrepancies, the mirror was periodically rotated on the mount. To do this, the mirror was lifted by the three air bearings so that it could be moved on a thin layer of air. After rotating, it was lowered back onto the blocks and polishing resumed.

11.5.2 A 27-POINT HYDRAULIC METROLOGY MOUNT

An experimental optical fabrication program was conducted by Itek Corporation to demonstrate techniques for producing high-quality (~$\lambda/60$ rms at $\lambda = 0.633$ μm) optical surfaces on large-diameter, lightweight mirrors (see Wollensak and Rose, 1975). The mirror used was a 70 in. (1.8 m), monolithic (fused), ULE substrate with thickness of ~12 in. (30.48 cm) having 25-mm (~1.0-in.)-thick front and back face sheets. This mirror had been slumped to meniscus shape representing a *f*/2.2 concave sphere. Its weight was ~1200 lb (544.3 kg).

The metrology mount utilized was as shown in Figure 11.25. It had 27 hydraulic axial actuator supports arranged in two rings and three defining pad supports. The actuators were connected to a common manifold, so the pressures were equal (see Figure 11.26). Fluid was allowed to flow freely between actuators. No compensation for spatial nonuniformity of weight distribution in the mirror was possible with this arrangement.

As shown in Figure 11.25 and Figure 11.26, there were 18 separately adjustable mechanisms to constrain the mirror laterally during polishing. They were adjusted to contact the substrate firmly at

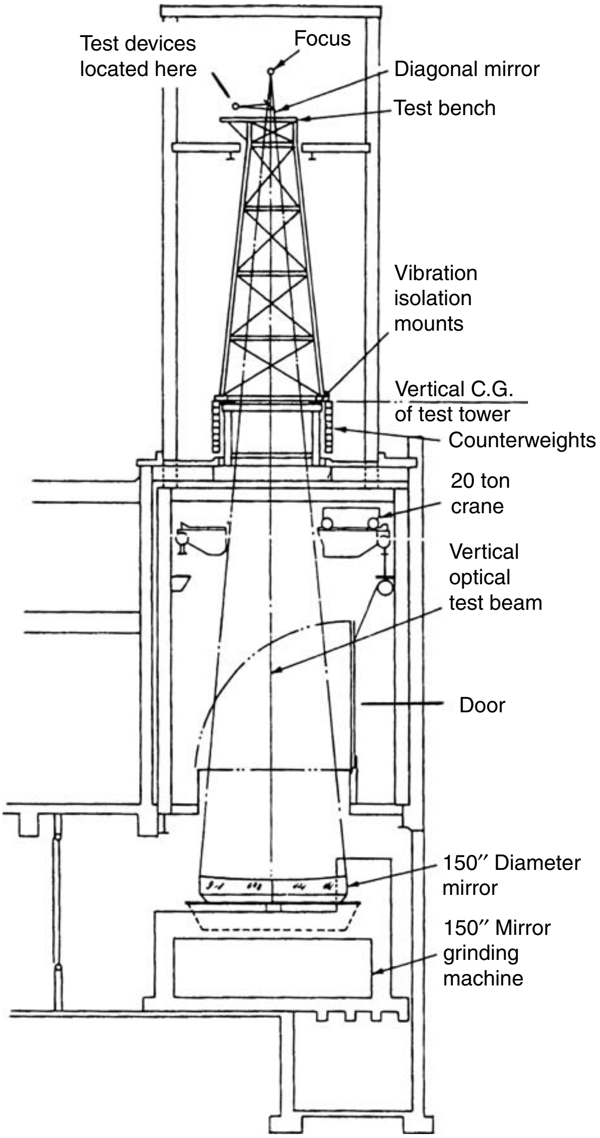
Test devices located here
Focus
Diagonal mirror
Test bench
Vibration isolation mounts
Vertical C.G. of test tower
Counterweights
20 ton crane
Vertical optical test beam
Door
150″ Diameter mirror
150″ Mirror grinding machine

FIGURE 11.22 Schematic of an integrated polishing/metrology vertical test chamber facility designed for in-situ finishing and testing large mirrors. (Adapted from Cole, N., *Optical Telescope Technology Workshop, April 1969*, *NASA Rept.*, SP-233, 307, 1970.)

the rims of both the front and back face sheets during polishing. Interferometric testing was accomplished in a separate test facility with the mirror/mount assembly transported carefully from one station to another between fabrication and test cycles. During testing, the lateral constraints were backed-off so as not to influence the results.

11.5.3 A 52-Point Spring Matrix Metrology Mount

In preparation for building the HST primary mirror, NASA authorized Perkin-Elmer Corporation to demonstrate their proposed metrology mount design. A solid ULE mirror of 60 in. (1.5 m) diameter having a 10 in. (25 cm) central hole was prepared as a meniscus with a thickness of 3.82 in.

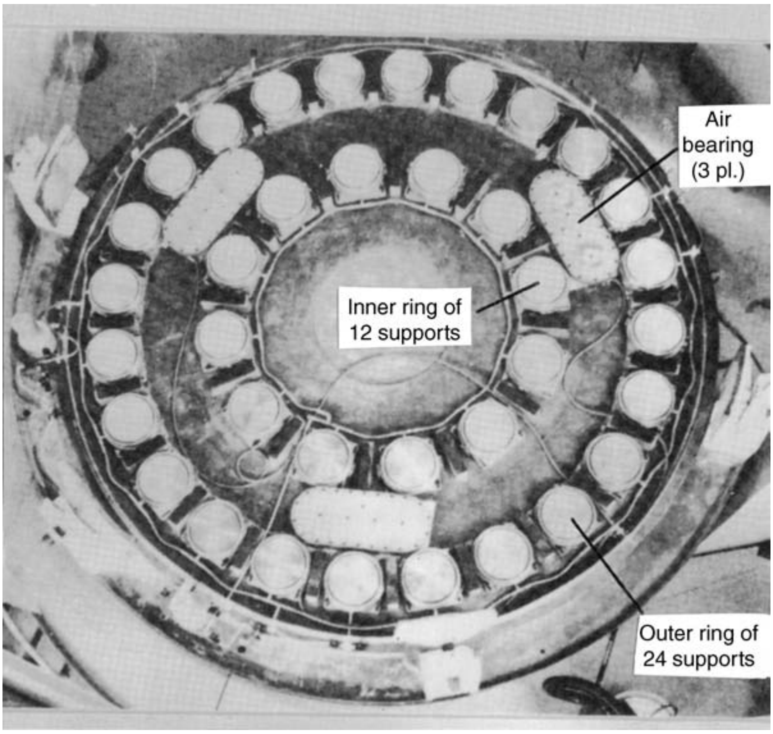
Air bearing (3 pl.)
Inner ring of 12 supports
Outer ring of 24 supports

FIGURE 11.23 Photograph of a pneumatic multipoint fabrication/metrology mount for a 150 in. (3.8 m) diameter mirror. (Adapted from Cole, N., *Optical Telescope Technology Workshop*, *April 1969*, *NASA Rept.*, SP-233, 307, 1970.)

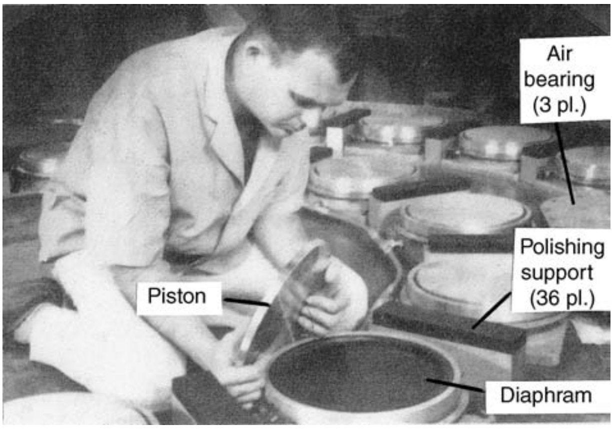
Air bearing (3 pl.)
Polishing support (36 pl.)
Piston
Diaphram

FIGURE 11.24 Close-up photograph of a piston and roll diaphragm support mechanism used in the mount of Fig. 11.23. (Adapted from Cole, N., *Optical Telescope Technology Workshop*, *April 1969*, *NASA Rept.*, SP-233, 307, 1970.)

(9.70 cm) so that it simulated the speed (*f*/2.3) and structural flexibility of the full-sized, lightweighted HST primary. The surface figure goal for the demonstration was $\lambda/60$ rms at $\lambda = 0.633$ μm. Following is a description derived from Montagnino et al. (1979) of the experimental mount (see Figure 11.27) designed to meet this specification. Figure 1.18 showed this mirror on its

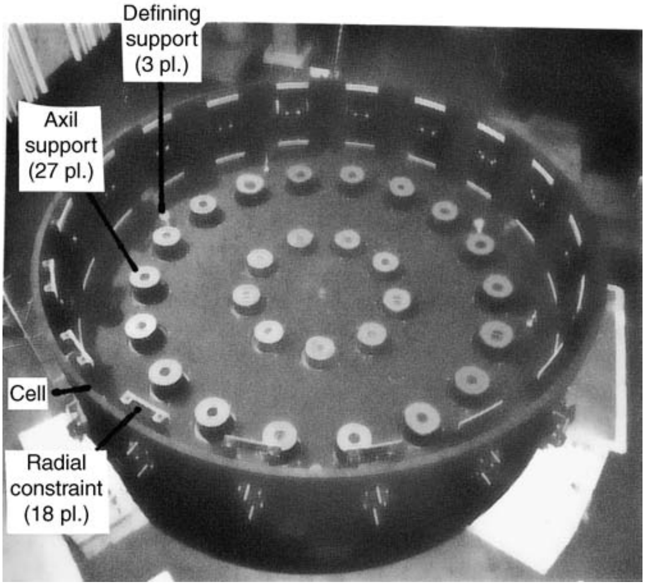
Defining support (3 pl.)
Axil support (27 pl.)
Cell
Radial constraint (18 pl.)

FIGURE 11.25 Photograph of a 27-point mirror metrology mount with hydraulic actuators and edge constraint mechanisms. (Adapted from Wollensak, R. J. and Rose, C. A., *Opt. Eng.*, 14, 539, 1975.)

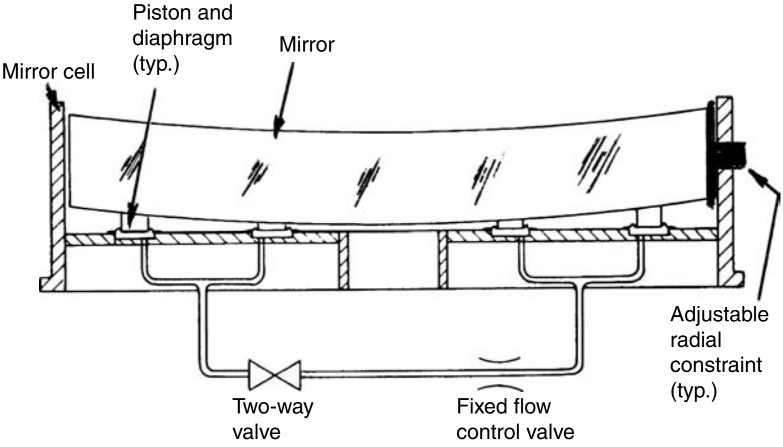
Piston and diaphragm (typ.)
Mirror
Mirror cell
Adjustable radial constraint (typ.)
Two-way valve
Fixed flow control valve

FIGURE 11.26 Schematic of the metrology mount of Figure 11.25 showing the hydraulic system connections. (Adapted from Wollensak, R.J. and Rose, C.A., *Opt. Eng.*, 14, 539, 1975.)

mount as it was positioned in the test tower for in-process interferometric evaluation. The mount was attached to rails that allowed the mirror and mount to be transported from the test station to the fabrication station without disturbing the relative alignment of those components.

The base of the mount was a 60-in. (152-cm) square by 1-in. (2.5-cm)-thick cast and annealed aluminum jig plate. Aluminum was selected for dimensional stability, low cost, and lightness of weight. Parallel ribs, 4 in. (10.2 cm) high on 8 in. (20.4 cm) centers, were mounted to the upper surface of the baseplate. These provided mounting surfaces for the axial force mechanisms and stiffened the baseplate. Four additional ribs were bolted to the bottom surface of the plate perpendicular to the upper ribs to increase the cross axis stiffness.

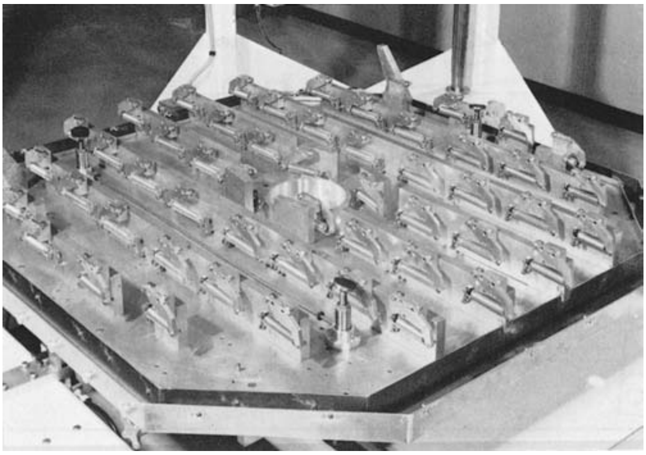

FIGURE 11.27 Configuration of the 52-point metrology mount used to support a 60-in. (1.5-m) diameter mirror during fabrication and testing in a simulated gravity-free environment. This mount is also shown in Figure 1.18. (From Montagnino, L., Arnold, R., Chadwick, D., Grey, L., and Rogers, G., *Proc. SPIE*, 183, 109, 1979.)

The force mechanisms, one of which is shown in Figure 11.28, were designed to provide a very low spring rate. This low spring rate assured that after each mechanism was adjusted to a precise force, the force would not be altered by a minor change in mirror position or baseplate deflection. The low spring rate was achieved by use of a nonlinear linkage loaded by a conventional extension spring. The negative force gradient of the linkage was designed to nearly cancel the positive force gradient of the spring. This mechanism could have been designed to have a positive, negative, or zero net spring rate over the normal travel range. In practice, it was determined that a positive spring rate of 2 to 3 lb/in. provided best performance. This made it possible to control precisely the net force reaction at three position control (hard) points by a slight adjustment in vertical position of the mirror. Each linkage was mounted on a flexure pivot of the general type shown in Figure 11.16 for minimum friction and low hysteresis. The vertical force developed by each force mechanism was transmitted to the mirror by a ball bearing mounted at the end of each lever. Horizontal force components and moments transmitted to the mirror were minimized by this design.

The bottom surface of the mirror was spherical. Cer-Vit buttons 1.25 in. (32 mm) in. diameter were bonded to the spherical surface at each support point to provide a horizontal interface surface for the bearing. This was required to avoid lateral force components that would result if the bearing contacted a sloped surface. Cer-Vit was selected to minimize thermal stress at the ULE mirror interface. Since the bond was compression-loaded, a soft material (RTV silicone rubber) was used as the adhesive to minimize stress in the mirror from bond curing and to provide for easy removal of the buttons at the completion of the fabrication cycle. A screw adjustment was provided in each mechanism for precise adjustment of spring force. The adjusting screws were located to be accessible for adjustment with the mirror installed on the mount.

The high compliance of the force mechanisms did not ensure stability of mirror position. Vertical displacement of the mirror would also affect the calibration precision of the support force mechanisms. Thus, a second condition, stable mirror position, was required for precise metrology operations. This was achieved with three hard points equispaced around the outer edge of the mirror. It was necessary to monitor vertical force as well as position at these points. With mirror position restrained at the three locating points, the algebraic sum of the force errors at each of the support force points reacted at the position control points. This required precise calibration of the support forces. The position-monitoring points were instrumented to measure the force reaction. This made it possible to

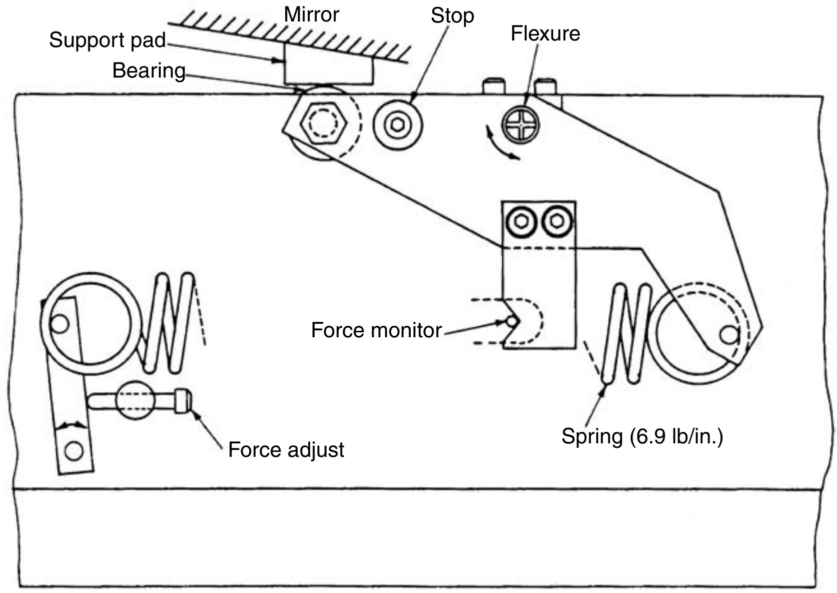

FIGURE 11.28 Schematic of one of the force mechanisms used in the metrology mount shown in Figure 11.27. (Courtesy of Goodrich Corporation, Danbury, CT.)

trim local support forces with the mirror in place in order to meet the force limits specified at the position control points to limit figure errors due to local bending of the mirror.

A mirror deflection sensitivity analysis indicated that a maximum force reaction on the mirror of ± 0.25 lb (0.11 kg) at each of the three position control points was required to limit local mirror deflection. Conformity to this specification required precise calibration of the support force mechanisms and precise initial centering of the mirror on the mount. Final force balance was achieved by mirror position bias and slight trimming adjustments of support forces near the position control mechanisms. These operations required the position/force monitors to have high force gradients to restrain position and to be capable of measuring force over the range of 0 to 6 lb (2.7 kg).

The matrix of forces applicable over the surface of the mirror was computed from the measured weight of the mirror by a 3D FEA. A series of error analyses defined the tolerable errors in support force calibration, geometric parameters, thermal distortion, and bearing friction. It was concluded that, with reasonable tolerances on all these variables, the mount would be capable of supporting the mirror adequately for figure measurement to $< \lambda/60$ rms as specified. Figure 11.29 shows an interferogram of the full aperture of the completed mirror. The used clear aperture was 57 in. (145 cm) and the linear central obscuration 30%. Computer analysis of this interferogram indicated that the specified quality had been attained over this prescribed annular aperture.

11.5.4 LATERAL CONSTRAINTS DURING POLISHING

In order to minimize lateral shifts of a large vertical-axis mirror due to horizontal forces exerted during polishing on a metrology mount, constraints must be built into the mirror support mechanism. Hall (1970) described success with a polishing mount having an array of calibrated compression springs, some or all of which had been damped by submersion in very soft pitch. Figure 11.30 shows one such pitch-spring support.

As mentioned in Section 11.5.2, lateral constraint during polishing was provided to the 70 in. (1.8 m) mirror described by Wollensack and Rose (1975) by multiple constraint mechanisms adjusted to touch the mirror rim.

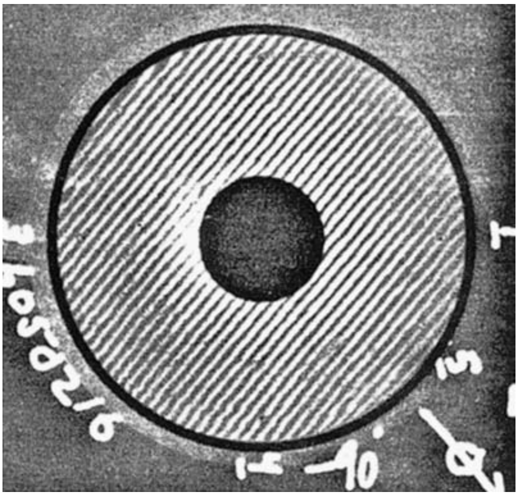

FIGURE 11.29 Interferogram of the 60-in. (1.5-m) diameter, $\lambda/61$ wave rms aspheric mirror fabricated as a subscale demonstration model of the primary for the HST. The metrology mount shown in Figure 11.27 supported this mirror during polishing and testing. (From Montagnino, L., Arnold, R., Chadwick, D., Grey, L., and Rogers, G., *Proc. SPIE*, 183, 109, 1979.)

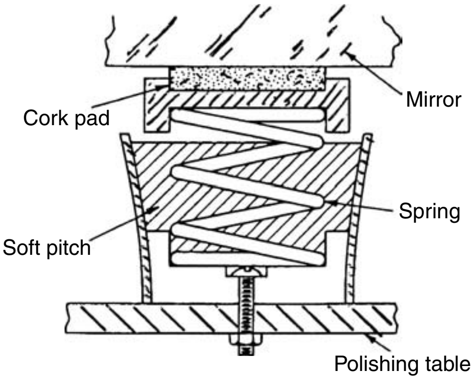

FIGURE 11.30 Schematic of a spring mechanism with soft pitch viscous damping used provide both axial and radial support of a large mirror during polishing and testing. (Adapted from Hall, H.D., *Optical Telescope Technology Workshop*, *April 1969*, *NASA Rept.*, SP-233, 149, 1970.)

Precise control of the lateral position of the 60 in. (1.5 m) mirror discussed in Section 11.5.3 during polishing and testing was provided by three tangent bars attaching the mirror to mount structure at symmetrically located position control points. The tangent bars had universal flexures at each end to minimize vertical or lateral force reactions that would affect mirror figure. Both the axial and lateral forces imposed by the computer-controlled polishing technique (see Babish and Rigby, 1979) used to figure both the simulated and actual Hubble Telescope primaries were inherently much lower than with conventional polishing techniques (see Jones, 1980, 1982).

REFERENCES

Babish, R. C. and Rigby, R. R., Optical fabrication of a 60-inch mirror, *Proc. SPIE*, 183, 105, 1979.
Barlow, B. L., Optical fabrication of a large lightweight mirror of unusual shape, *Opt. Eng.*, 14, 514, 1975.

Barnes, W. P., Jr., Terrestrial engineering of space-optical elements, *Proceedings of 9th Congress of the International Commission for Optics*, Thompson, B. J., and Shannon, R. R. Eds., Nat. Acad. Sci., Santa Monica, CA, 1974, p. 171.

Baustian, W. W., Annular air bag back supports, *A Symposium on Support and Testing of Large Astronomical Mirrors*, Crawford, D. L., Meinel, A. B., and Stockton, M. W., Eds., Kitt Peak Nat. Lab. and The University of Ariz., Tucson, 1968a, p. 109.

Baustian, W. W., Mirror cell design, *A Symposium on Support and Testing of Large Astronomical Mirrors*, Crawford, D. L., Meinel, A. B., and Stockton, M. W., Eds., Kitt Peak Nat. Lab. and The University of Ariz., Tucson, 1968b, p. 150.

Chivens, C. C., Air bags, *A Symposium on Support and Testing of Large Astronomical Mirrors*, Crawford, D. L., Meinel, A. B., and Stockton, M. W., Eds., Kitt Peak Nat. Lab. and The University of Ariz., Tucson, 1968, p. 105.

Cole, N., Shop supports for the 150-Inch Kitt Peak and Cerro Tololo primary mirrors, *Optical Telescope Technology Workshop*, *April 1969*, *NASA Rept.* SP-233, 307, 1970.

Couder, M. A., Researches sur les déformations des grands miroirs employés aux observations astronomiques, *Bull. Astron. Obs. Paris*, 7, 201, 283, 1932.

Crawford, R. and Anderson, D., Polishing and aspherizing a 1.8-m, *f*/2.7 paraboloid, *Proc. SPIE*, 966, 322, 1988.

Doyle, K. B. and Forman, S. E., Using finite element analysis and fractography to resolve a flex pivot failure problem, *Proc. SPIE*, 3132, 2, 1997.

Doyle, K. B., Genberg, V. L., and Michels, G. J., *Integrated Optomechanical Analysis*, SPIE Press, Bellingham, 2002.

Hall, H. D., Problems in adapting small mirror fabrication techniques to large mirrors, *Optical Telescope Technology Workshop*, *April 1969*, *NASA Rept.*, SP-233, 149, 1970.

Hindle, J. H., Mechanical flotation of mirrors, in *Amateur Telescope Making*, *Advanced*, Ingalls, A. G., Ed., Scientific American, New York, 229, 1945. (Reprinted 1996 as Chapter B.8 in *Amateur Telescope Making*, *2*, Willman-Bell, Inc., Richmond.)

Jones, R. A., Computer controlled polisher demonstration, *Appl. Opt.*, 19, 2072, 1980.

Jones, R. A., Computer-controlled grinding of optical surfaces, *Appl. Opt.*, 21, 874, 1982.

Krim, M. H., Metrology mount development and verification for a large spaceborne mirror, *Proc. SPIE*, 332, 440, 1982.

Malvick, A. J. and Pearson, E. T., Theoretical elastic deformations of a 4-m diameter optical mirror using dynamic relaxation, *Appl. Opt.*, 7, 1207, 1968.

Mehta, P. K., Flat circular optical elements on a 9-point Hindle mount in a 1-g force field, *Proc. SPIE*, 450, 118, 1983.

Mehta, P. K., Non-symmetric thermal bowing of flat circular mirrors, *Proc. SPIE*, 518, 155, 1984.

Montagnino, L., Arnold, R., Chadwick, D., Grey, L., and Rogers, G., Test and evaluation of a 60-inch test mirror, *Proc. SPIE*, 183, 109, 1979.

Nelson, J. E., Lubliner, J., and Mast, T. S., Telescope mirror supports: plate deflections on point supports, *Proc. SPIE*, 332, 212, 1982.

Roark, R. J., *Formulas for Stress and Strain*, 3rd ed., McGraw-Hill, New York, 1954.

Sisson, G. M., On the design of large telescopes, *Vistas Astron.*, 3, 92, 1958.

Smith, H. J., McDonald 107-inch telescope, *A Symposium on Support and Testing of Large Astronomical Mirrors*, Crawford, D. L., Meinel, A. B., and Stockton, M. W., Eds., Kitt Peak Nat. Lab. and University of Ariz., Tucson, 1968, p. 169.

Vukobratovich, D., private communication, 1992.

Vukobratovich, D., Optomechanical system design, in *The Infrared and Electro-Optical Systems Handbook*, Vol. 4, ERIM, Ann Arbor and SPIE Press, Bellingham, 1993, chap. 3.

Vukobratovich, D., Introduction to Optomechanical Design, in *SPIE Short Course SC014*, 2003.

Vukobratovich, D., private communication, 2004.

Williams, R. and Brinson, H. F., Circular plate on multipoint supports, *Journal of the Franklin Institute* 297, 429, 1974.

Wollensak, R. J. and Rose, C. A., Fabrication and test of 1.8-meter-diameter high quality ULE mirror, *Opt. Eng.*, 14, 539, 1975.

Yoder, P. R., Jr., *Mounting Optics in Optical Instruments*, SPIE Press, Bellingham, 2002.

12 Mounting Large, Variable-Orientation Mirrors

12.1 INTRODUCTION

Although mechanical mounts for large, horizontal- and vertical-axis mirrors are important for fixed installations such as in test equipment associated with mirror fabrication, the variable-orientation case presents many more mount design challenges. Optical instruments for astronomical, military, aerospace, and industrial applications that involve large mirrors generally require those mirrors to be moved about with respect to the Earth's gravitational field. Much of what was said in Chapters 10 and 11 regarding various radial and axial supports in the contexts of horizontal- and vertical-axis mirror applications applies to the variable-orientation mirror as well. Means for controlling the distribution of forces acting on the mirror to minimize optical surface deflection as a function of the changing direction of gravity are needed.

To illustrate the changes that occur in the surface contour of a large mirror as its orientation relative to the local gravity vector changes, let us consider the combination of a two-ring axial support of the general type shown in Figure 11.7 with an "ideal" push-pull radial support applying forces directed through the mirror center of gravity. The radial force application shown in Figure 10.12 applies. With the mirror axis vertical, only the axial forces would act and the optical surface deformation contours would resemble those shown in Figure 11.8. With the mirror axis horizontal, only the radial forces would act, so the surface deformations would then resemble the example shown in Figure 10.12. At an inclination of 45°, both sets of supports would be active and a pattern similar to that shown in Figure 12.1 would be observed. These three surface contour patterns were all computed by Malvick and Pearson (1968) using the dynamic relaxation technique. As might be expected, the maximum deflections and asymmetry of this pattern are intermediate between the horizontal- and vertical-axis cases.

As the elevation angle θ of the mirror's axis changes, the rms surface deformation δ_θ varies continuously in general accordance with

$$\delta_\theta = [(\delta_A \sin \theta)^2 + (\delta_R \cos \theta)^2]^{1/2} \tag{12.1}$$

where δ_A is the surface error with axis vertical, δ_R the surface error with axis horizontal, and θ is measured from the horizontal axis. Let us assume that the rms self-weight deflections of a certain mirror with its axis horizontal and vertical are 0.08 wave ($\lambda/12.5$) and 0.20 wave ($\lambda/5$), respectively. The typical variation of its deflection with θ is then as shown in Figure 12.2.

In this chapter, we consider a variety of mounting arrangements for large, variable-orientation mirrors selected from the literature.

12.2 MECHANICAL FLOTATION MOUNTS

Figure 12.3 illustrates the geometry of a counterweighted lever mirror flotation mechanism. One axial and one radial support mechanism are shown. Counterweights W_1 and W_2 act through levers hinged to the support structure at H_1 and H_2, respectively. Arrays of these mechanisms located

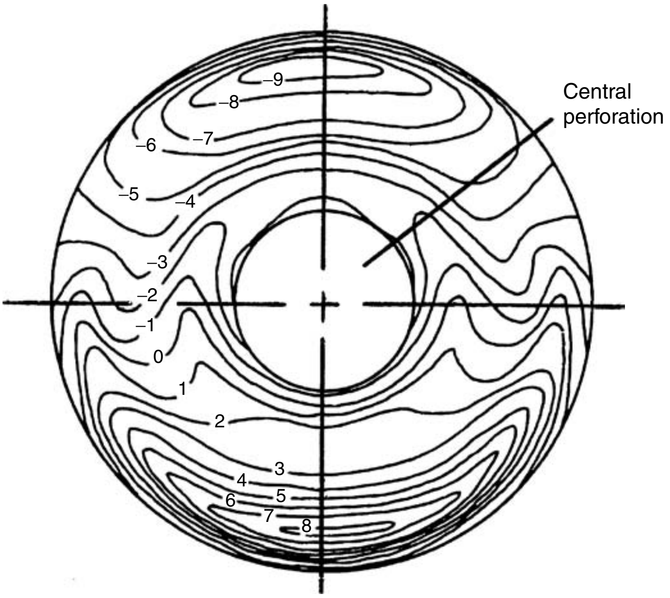

FIGURE 12.1 Computed contours of surface deformation for a 4-m (157-in.)-diameter solid mirror supported by a two-ring axial support and a cosine-variable push-pull “ideal” radial support when oriented at 45° to gravity. Contour interval = 1 × 10^{-6} cm. (Adapted from Malvick, A.J. and Pearson, E.T., *Appl. Opt.*, 7, 1207, 1968.)

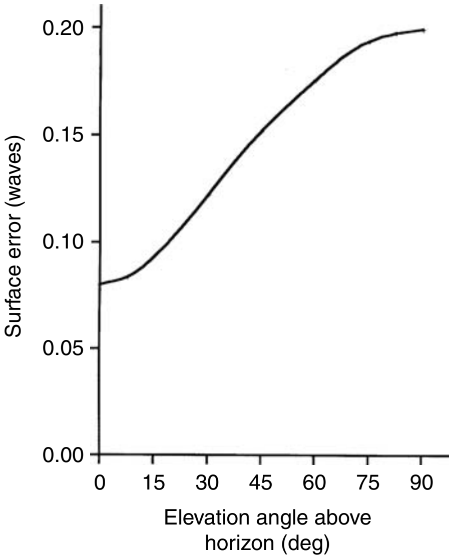

FIGURE 12.2 Variation of rms surface deflection of a mirror as a function of axis elevation angle as calculated from Eq. (12.1).

strategically (usually symmetrically) about the back and edge of the mirror automatically provide forces determined by the inclination angle. Each axial force delivered is proportional to sin θ while each radial force is proportional to cos θ. Each of N mechanisms supports approximately $1/N$ times the mirror’s total weight component for the applicable value of θ. The mechanical advantages of the levers are x_1/x_2 and y_1/y_2 for the axial and radial supports, respectively.

Franza and Wilson (1982) pointed out the importance of the levers in these mechanisms functioning astatically. By this they meant that the force exerted would be essentially constant in the presence of small changes in the location of the lever fulcrum due to structural or thermal shifts. If the fulcrum of a typical axial support moves by an amount δy as indicated in Figure 12.4, the angular motion of the lever will be $\delta\theta = \arcsin(\delta y/x_1)$. The corresponding force change δF in force F is $F(1 - \cos\theta)$. For $\delta y = 1.000$ mm (0.0394 in.) and $x_1 = 100.0$ mm (3.937 in.), δF would be only 0.005% of F. Such a large value of the error δy would not be expected in any good mirror mount

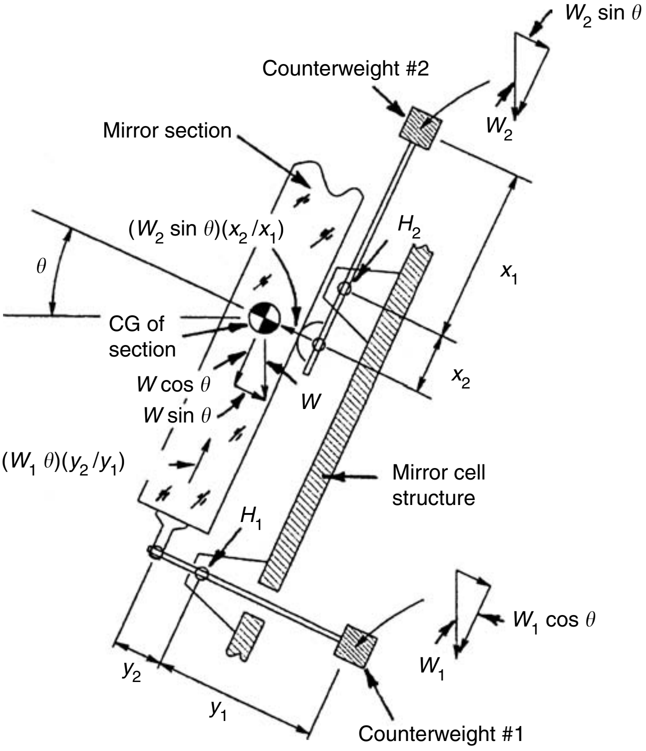
$W_2 \sin\theta$
Counterweight #2
Mirror section
W_2
$(W_2 \sin\theta)(x_2/x_1)$
H_2
θ
x_1
CG of section
x_2
$W\cos\theta$
$W\sin\theta$
W
$(W_1\,\theta)(y_2/y_1)$
Mirror cell structure
H_1
$W_1\cos\theta$
W_1
y_2
y_1
Counterweight #1

FIGURE 12.3 Geometry of a typical lever/counterweight axial and radial mirror floatation system. The force vectors are not to scale. (From Yoder, 2002.)

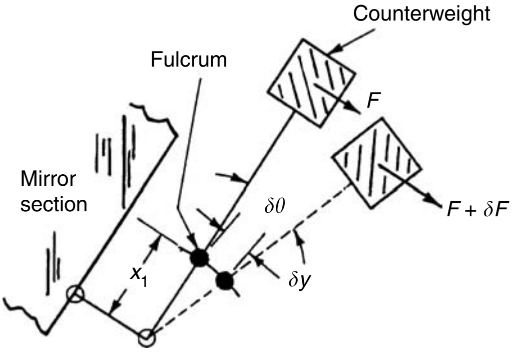
Counterweight
Fulcrum
F
Mirror section
$\delta\theta$
$F + \delta F$
x_1
δy

FIGURE 12.4 Geometry of the creation of a force error δF when the fulcrum of a lever/counterweight mechanism is dislocated by δy. (Adapted from Franza, F. and Wilson, R.N., *Proc. SPIE*, 332, 90, 1982.)

design, so the force exerted by this mechanism will be essentially constant. Similar calculations made for the radial support would result in the same general conclusion.

A simple axial support involving a lever/counterweight mechanism was shown in Figure 11.13. Meinel (1960) described a typical early embodiment of a lever/counterweight-type support mechanism of more complex design. It is shown in Figure 12.5. Multiple sets of this hardware were used to support the 2.08-m (82 in.)-diameter primary mirror of a telescope used at McDonald Observatory. In this design, the back pad A transfers its share of the mirror's weight to a rolling ball that contacts a flat surface attached to a rod that carries sockets for rollers attached to the short ends of two levers. At the long ends of the levers are two counterweights W_A. The ball-on-flat interface allows lateral motion of the mirror and pad A when the temperature changes. The radial support involved edge pad (B) that was tied to the rim of the mirror with two strong Nylon cords (to keep the pads from falling off during assembly). This pad was also attached through a rod to a ball-on-flat interface with levers and counterweights W_R functioning in the same manner as the axial counterparts to provide the needed radial force. Meinel indicated that the function of the ball/flat joint proved not to be very satisfactory because of friction and small alignment errors in the radial mechanism that caused binding in the axial interface.

Ribbed-back mirrors usually have lever-type mounting mechanisms providing both the axial and radial support functions. Figure 12.6 schematically shows such a device as used in the 84 in. (2.13 m) telescope at the Kitt Peak National Observatory. The dimensions are in inches. Similar dual-purpose mechanisms were used in the Hale Telescope and the 120 in. (3 m) Lick Observatory Telescope. A photograph of a typical mechanism in a test stand is shown in Figure 12.7. The operation of this device as described by Baustian (1960, 1970) is summarized as follows: the radial forces are transmitted through the lateral support assembly located at the upper end of the unit, and are carried by a central lever arm whose disc-shaped counterweight is visible at the bottom of the unit. The axial component of the mirror weight is supported on a flange located at the central section, with the load

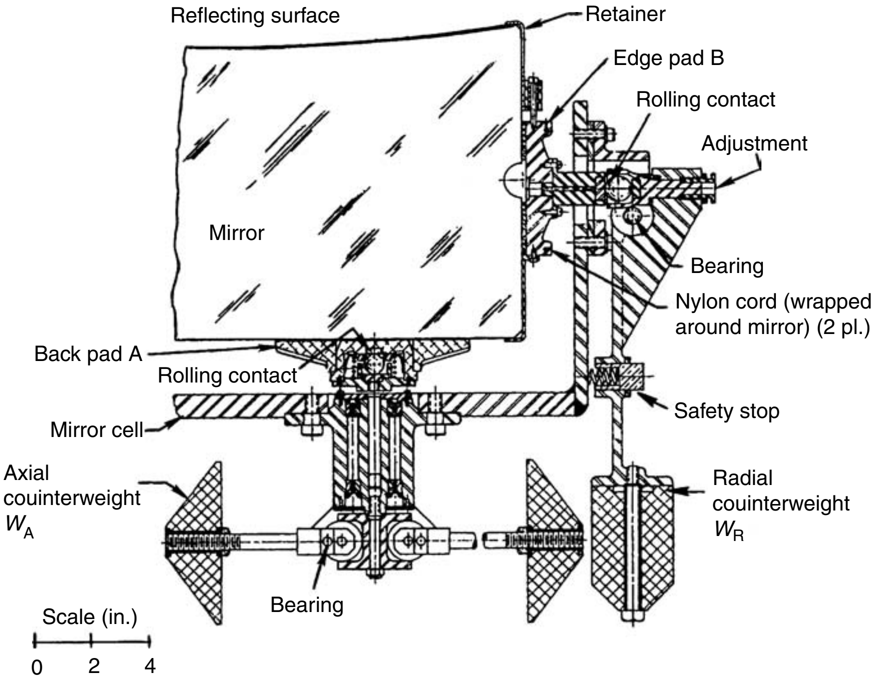

FIGURE 12.5 Cross section of a lever/counterweight mirror support mechanism for a large solid mirror such as one used in the 82 in. (2.08 m) McDonald Telescope. (Adapted from Meinel, A.B., in *Telescopes*, Kuiper, G.P. and Middlehurst, B.M., Eds., University of Chicago Press, Chicago, 1960, p. 25.)

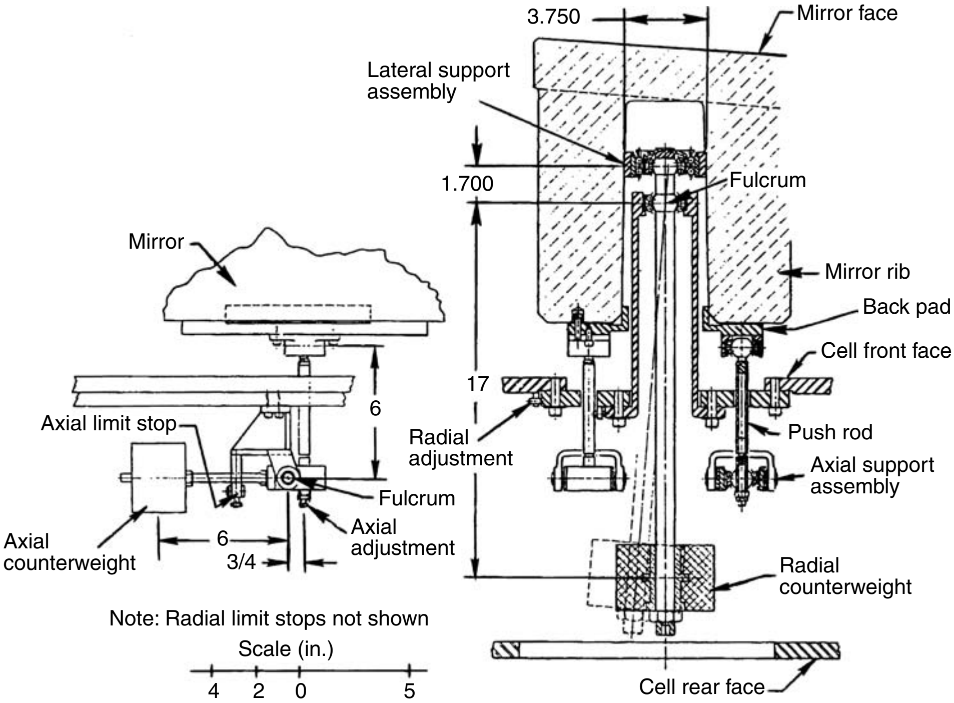
3.750
Mirror face
Lateral support assembly
1.700
Fulcrum
Mirror
Mirror rib
Back pad
Cell front face
17
6
Axial limit stop
Radial adjustment
Push rod
Axial support assembly
Fulcrum
Axial counterweight
6
3/4
Axial adjustment
Radial counterweight
Note: Radial limit stops not shown
Scale (in.)
4 2 0 5
Cell rear face

FIGURE 12.6 Cross section of typical axial (left) and radial (right) support mechanisms for a large ribbed mirror such as one used in an 84 in. (2.13 m) telescope at Kitt Peak Observatory. (Adapted from Meinel, A.B., in *Telescopes*, Kuiper, G.P. and Middlehurst, B.M., Eds., University of Chicago Press, Chicago, 1960, p. 25.)

being transmitted through three push rods to their individual levers and counterweight located below the mounting flange. The cylindrical counterweight of one of these levers is visible in the left foreground. The rectangular counterweights are auxiliary balance weights used to neutralize the shift of the CG of the mirror.

The primary mirror of the Hale Telescope was shown in Figure 9.4. There are 36 pockets cast into the back surface of the mirror as locations for the support mechanisms. Both axial and radial forces were provided by the same mechanism. One of the original mechanisms is sketched in Figure 12.8. The mirror here is looking at the zenith. The function of this mechanism, as described by Bowen (1960), is as follows.

The support ring B contacts the mirror in a plane normal to the optic axis through the CG of the mirror. As the telescope turns from the zenith, the lower end of the support system, including the weights W, attempts to swing about the gimbals G_1, and exerts a radial force on ring B through the gimbals G_2. The weights and lever arms are adjusted so that the force exerted balances the component in the opposite direction of gravity acting on the section of the mirror assigned to this support. Similarly, the weights W pivot about bearings P in such a way as to exert axial force along the rod R that is transmitted to the ring S by the gimbals G_2. These weights and lever arms are adjusted so that the force exerted balances the component parallel to the optic axis of the pull of gravity on this same section of the mirror. The mirror floats on these supports and no forces or moments are transmitted across the mirror.

Because the range of motion of lever/counterweight mirror support mechanisms is limited, substituting flexure bearings of the general type shown in Figure 11.16 can eliminate the friction inherent in the ball or roller bearings used in many hardware designs. The optical performances of some telescopes originally provided with mirror support mechanisms using ball or roller bearings have been substantially improved by the change to flexure bearings.

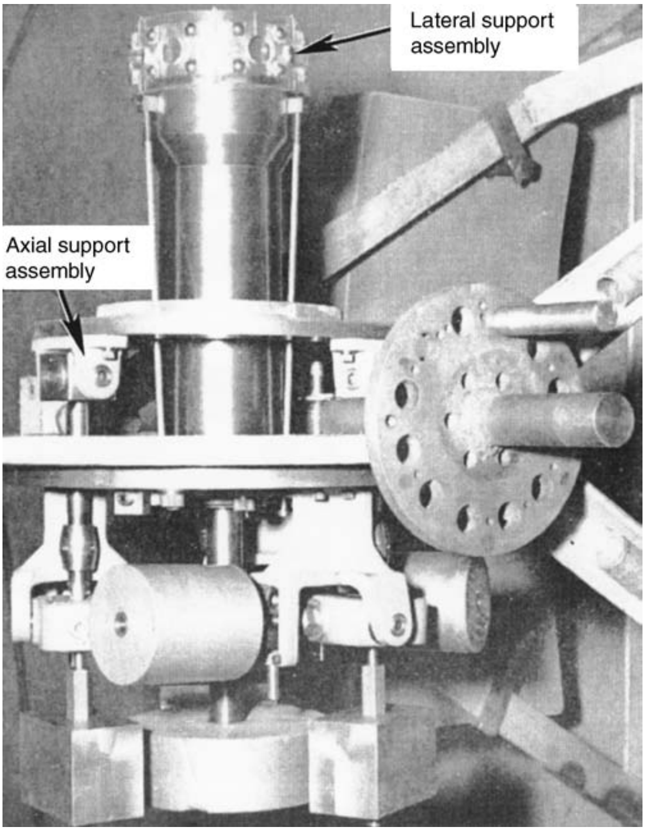

FIGURE 12.7 Photograph of axial and radial support hardware functioning in the manner of the mechanisms shown in Figure 12.6. (Adapted from Baustian, W.W., in *Telescopes*, Kuiper, G.P. and Middlehurst, B.M., Eds., University of Chicago Press, Chicago, 1960, p. 16.)

To define the orientation of the optic axis of the mirror and the position of the mirror for axial translation, three of the weights located at 120° intervals in the outer ring of supports are locked in a fixed position. For radial translation, the mirror is defined by four pins mounted on the tube that extends through the central hole in the mirror to support the Coudé flat. These pins bear on the inside of the 40-in. (101.6-cm)-diameter central hole in the mirror. They are constructed of materials to compensate for differences in the thermal expansion of Pyrex and steel and operate through ball bearings to eliminate the transmission of forces parallel to the axis.

A different approach that was used for radial constraint of the 36-in. (19-cm)-diameter primary mirror in the balloon-borne Stratoscope II telescope is shown in Figure 12.9. Each support interface with the mirror was epoxied to the rim of the fused silica disk through an Invar button. Either compression or tension forces could be applied with this design depending upon whether the interface with the mirror was on the bottom or top edge, respectively.

A variation of this design, illustrated in Figure 12.10, was used as axial support for a 37-in. (94-cm)-diameter flat with its reflecting face downward in the test tunnel used for testing the Stratoscope II primary mirror. Since this flat mirror was used in a fixed axis vertical orientation, no radial support mechanisms were required. Scott (1962) reported "no errors produced by the support are detectable."

The use of buttons or bosses made of low-expansion metal such as Invar 36 bonded with adhesive to the backs or rims of mirrors made of fused silica, ULE, or Zerodur is common practice as a means for attaching mechanical supports. Figure 12.11 shows several types of such bosses. Some are bonded into holes ground into the mirror substrates while others are bonded externally to mirror

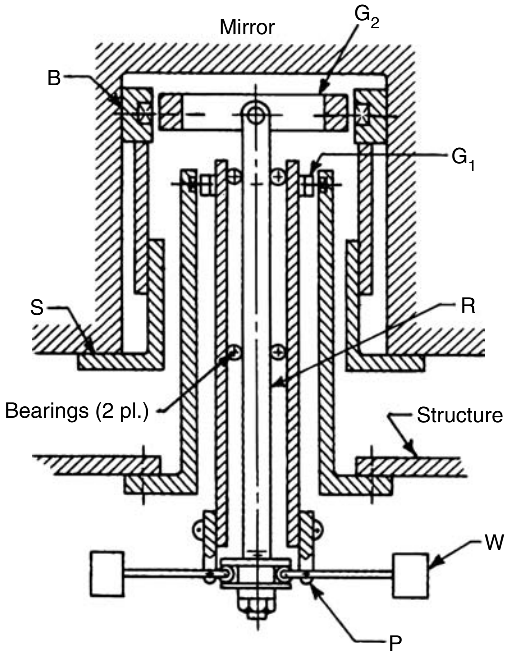

FIGURE 12.8 One of the 36 combined axial/radial mechanisms used to support the ribbed primary of the 200 in. (5.08 m) Hale Telescope. (Adapted from Baustian, W.W., in *Telescopes*, Kuiper, G.P. and Middlehurst, B.M., Eds., University of Chicago Press, Chicago, 1960, p. 16.)

surfaces. The bosses shown in Figure 12.11(b) have flexures to minimize transfer of moments into the mirror because such moments could distort the optical surface.

Many mirrors use bosses attached to their rims as attachment points for flexures. Typical concepts for mountings needing this feature were shown in Figure 8.39 and Figure 8.42. Circular mirrors might have bonded-on bosses of the type shown in Figure 12.12. The mirror for which this particular boss was designed was 15.0 in. (38.1 cm) in diameter, so the bonding surface of the boss was shaped cylindrically with a nominal radius the same as that of the mirror rim. The flexure designed to mate with this boss is shown in Figure 12.13. It was angled so that it could be attached to a flat pad on the ID of a cylindrical structure. Note the square hole at the interface between the two components. It was intended to maintain angular alignment between the mating parts.

Rectangular mirrors, with or without cells, may also be attached to structures with flexures as in Figure 8.40. Possible designs for the bosses and flexures for such mounts are shown in Figure 12.14 and Figure 12.15. The flexures in this case are straight because the mirror edges are nominally parallel to the structure surfaces to which those flexures are attached.

An example of a large mirror supported through different types of bonded-on bosses is shown in Figure 12.16. The monolithic ULE substrate is shown in Figure 9.14. It has a diameter of 60 in. (1.52 m) and a thickness of 25.4 cm (10 in.). The core struts in this substrate are nominally 3.8 mm (0.15 in.) thick except in the nine regions where it is attached to a nine-point Hindle-type axial support mechanism. In these regions, the thicknesses are increased to 9.5 mm (0.38 in.) to increase strength. Attachments to the triangular Hindle mount plates are through rods with necked-down regions that serve as dual-axis flexures. Radial support to the mirror is provided by three links oriented tangentially to the rim of the mirror as shown in Figure 12.16. These links are attached to edge-mounting blocks fused into the outer ring as indicated in Figure 9.14. These links also have flexures to minimize transfer of moments.

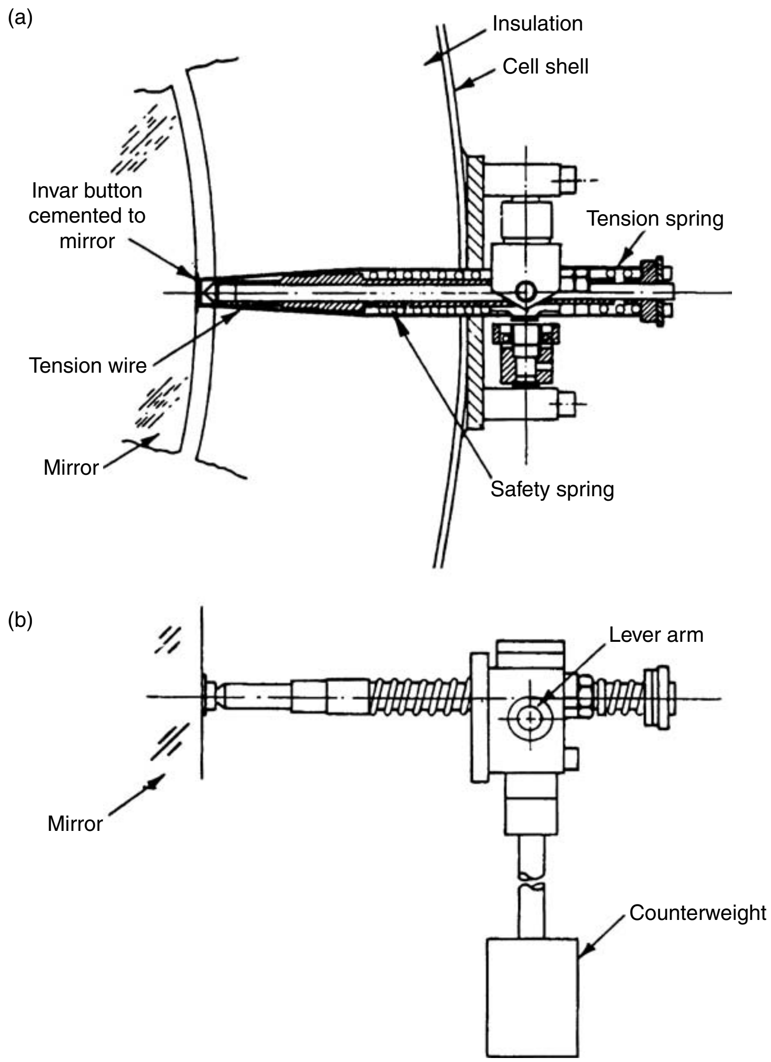
(a)
Insulation
Cell shell
Invar button cemented to mirror
Tension spring
Tension wire
Mirror
Safety spring
(b)
Lever arm
Mirror
Counterweight

FIGURE 12.9 Front and side views of a spring-loaded lever radial support of the type used in the mirror mount for Stratoscope II. (Adapted from Scott, R.M., *Appl. Opt.*, 1, 387, 1962.)

12.3 HYDRAULIC/PNEUMATIC MOUNTS

12.3.1 Historical Background

A radial support mechanism that avoided some problems of friction was designed by W.W. Baustian and described by Meinel (1960). It is shown in Figure 12.17. This mechanism used a closed hydraulic system to transmit the forces. A bellows coupled the pad A to the counterweight. This system had an advantage over an all-mechanical system in that the counterweight W and the control bellows could, if more convenient, be located at a distance from the load bellows and connected to that bellows by a hose.

The multiple-point pneumatic mirror mount from Barnes (1974) shown in Figure 11.20 is an example of a design that can be used in any orientation. The 27 pneumatic pistons were of the rolling-diaphragm type and were servo-controlled to provide equal force at each reaction point. Axial position and tilt correction signals were fed to the servo system by three displacement transducers

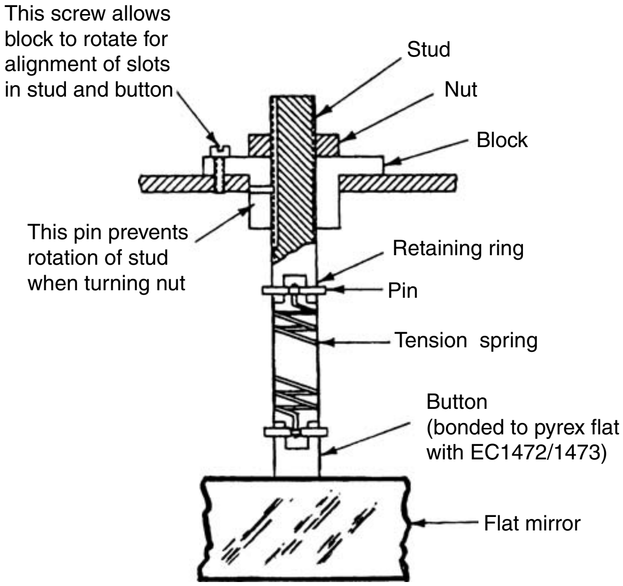
This screw allows block to rotate for alignment of slots in stud and button
Stud
Nut
Block
This pin prevents rotation of stud when turning nut
Retaining ring
Pin
Tension spring
Button (bonded to pyrex flat with EC1472/1473)
Flat mirror

FIGURE 12.10 Cross section of a spring-loaded axial support for a downward-facing flat mirror of 94 cm (37 in.) diameter. (Adapted from Scott, R.M., *Appl. Opt.*, 1, 387, 1962.)

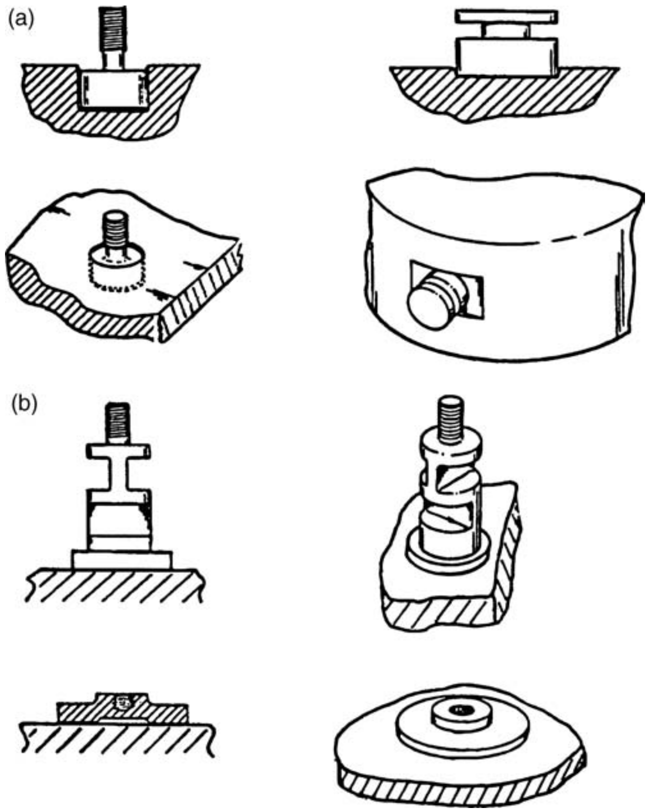

FIGURE 12.11 Configurations of some different types of bosses, threaded studs, and flexures that can be bonded to mirrors (or prisms) for attachment to structure. (From Yoder, 2002.)

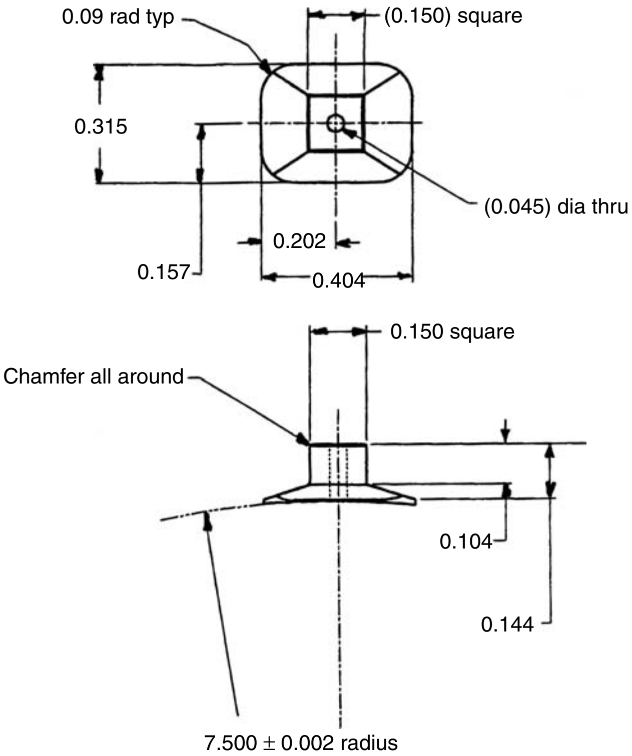

FIGURE 12.12 Design of a boss suitable for bonding to the rim of a 15.0-in. (38.1-cm)-diameter mirror. (From Yoder, 2002.)

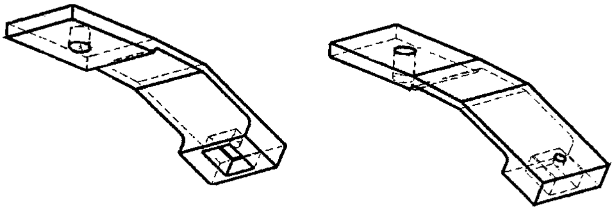

FIGURE 12.13 Schematic top and bottom views of cantilevered flexures shaped to interface with the boss of Figure 12.12 and the cylindrical rim of a mirror. (From Yoder, 2002.)

touching the rear surface of the mirror. For stable operation of the servo system, it was necessary to continuously bleed gas through each actuator. Although not shown in the figure, radial support was provided by a pair of mercury-filled elastomer tubes of the type discussed in Section 10.6. The mount was designed to operate at elevations of −5° to 95° and at "moderate" tracking rates in a ground-based installation.

A 4.2-m (165-in.)-diameter telescope of 8:1 diameter-to-thickness ratio described by Mack (1980) used a three-ring array of 60 pneumatic actuators as the axial support and a series of counterweighted radial levers arranged so as to exert parallel push-and-pull forces on the mirror's edge at 24 places as indicated in Figure 12.18. The radial forces were equal in magnitude, supported equal weight vertical slices of the disk, and acted in a plane through the mirror's CG. FEA of the mirror in the axis-horizontal orientation indicated that the gravity-induced positive deformations of the lower half of the disk (one quadrant is shown in Figure 12.19) were matched by equal negative

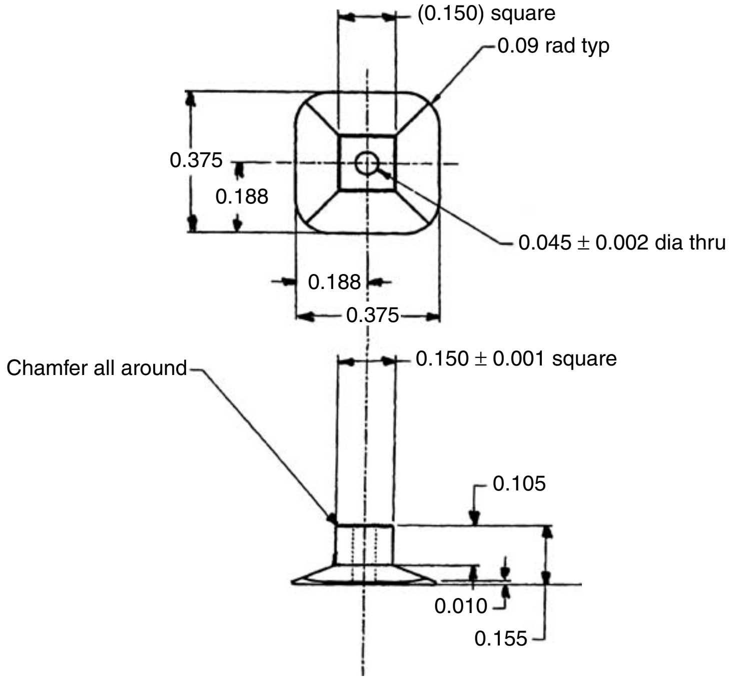

FIGURE 12.14 Configuration of a boss suitable for bonding directly to the rim of a rectangular mirror or to its cell for mounting as shown in Figure 8.40. (From Yoder, 2002.)

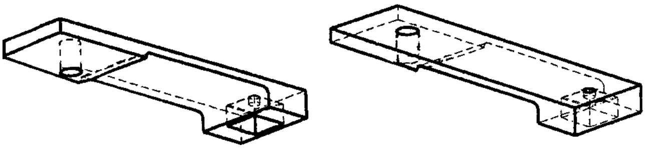

FIGURE 12.15 A cantilevered flexure shaped to interface with the boss of Figure 12.14. (From Yoder, 2002.)

deformations in the upper half. The reflected wavefront would then be tilted slightly about the horizontal centerline, but the peak deformations from a true parabola would not exceed 0.03 μm or $\lambda/21$ wave at $\lambda = 0.63$ μm.

There were 12, 21, and 27 axial pad supports in the three rings of this axial support. These rings were located optimally at radii of 0.798, 1.355, and 1.880 m (31.42, 53.35, and 74.00 in.), respectively. The pads were 0.30 m (11.75 in.) in diameter. The analysis indicated that the surface deflections at various zones outside the 0.5 m radius zone would be as depicted in Figure 12.20. All pads were operated at the same pressure and were servo-controlled using load cells in contact with the rear surface of the mirror to provide closed-loop control of rigid-body tilt. Analysis further predicted that the stress distribution within the mirror when its axis was vertical and the three rings of pads supported its weight would be as shown in Figure 12.21. The units here are kPa. Note that the region near the optical surface is relatively stress free.

12.3.2 GEMINI TELESCOPES

A different type of pneumatic mounting from those previously discussed was developed for each of the two 8.1-m (318.9-in.)-diameter ULE meniscus primary mirrors installed in the Gemini telescopes located on Mauna Kea and Cerro Pachon.

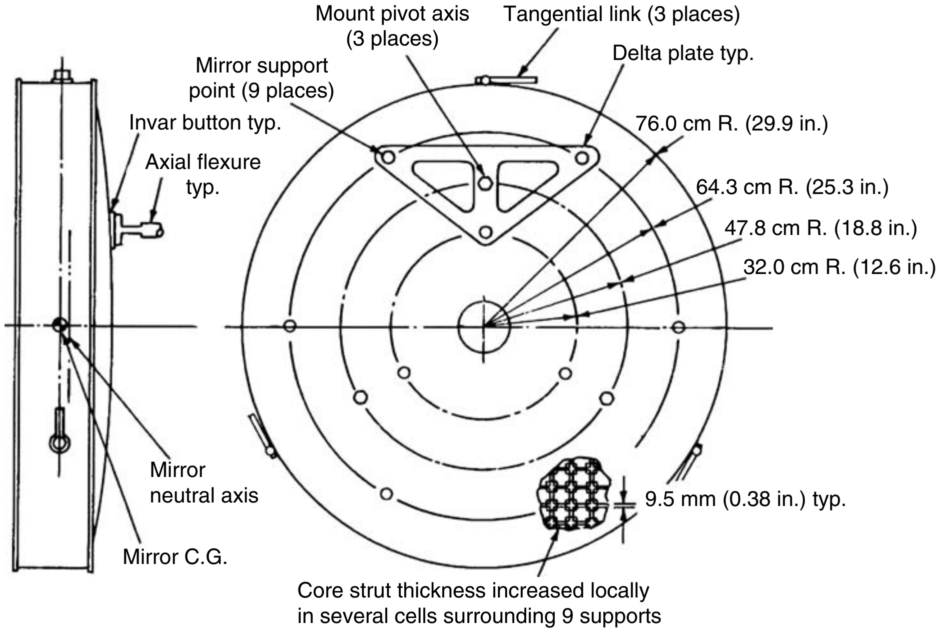
Mount pivot axis (3 places)
Tangential link (3 places)
Delta plate typ.
Mirror support point (9 places)
Invar button typ.
Axial flexure typ.
76.0 cm R. (29.9 in.)
64.3 cm R. (25.3 in.)
47.8 cm R. (18.8 in.)
32.0 cm R. (12.6 in.)
Mirror neutral axis
Mirror C.G.
9.5 mm (0.38 in.) typ.
Core strut thickness increased locally in several cells surrounding 9 supports

FIGURE 12.16 Conceptual layout for supporting the mirror of Figure 9.14 from a nine-point Hindle mount (for axial support) and from three tangential links (for radial support). (From Yoder, P.R., Jr., *Mounting Optics in Optical Instruments*, SPIE Press, Bellingham, 2002.)

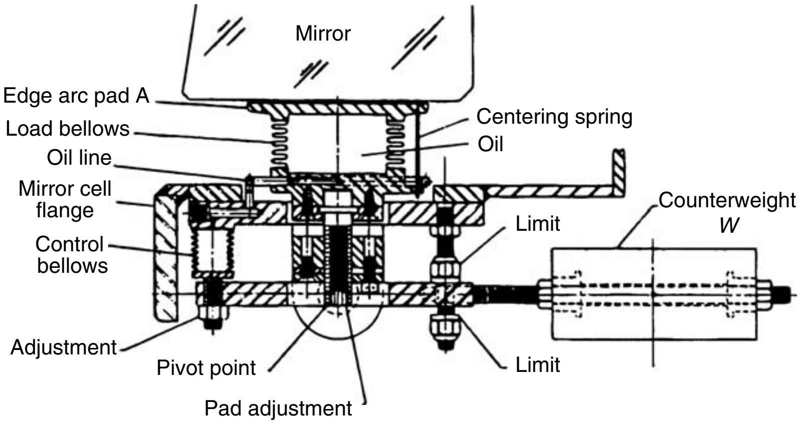
Mirror
Edge arc pad A
Load bellows
Oil line
Mirror cell flange
Control bellows
Adjustment
Pivot point
Pad adjustment
Centering spring
Oil
Limit
Counterweight W
Limit

FIGURE 12.17 Cross section of a hydraulic edge support such as was used with the 36 in. (0.91 m) solid mirror for a Kitt Peak Observatory telescope. (Adapted from Meinel, A.B., in *Telescopes*, Kuiper, G.P. and Middlehurst, B.M., Eds., University of Chicago Press, Chicago, 1960, p. 25.)

The axial support consists of uniform air pressure behind the 220-mm (7.87-in.)-thick mirror (which acts as a piston and is enclosed by seals at the outer and inner edges of the mirror) plus 120 mechanisms, each of which includes a passive hydraulic cylinder and an active pneumatic actuator (Stepp et al., 1994). The radial support system has 72 hydraulic mechanisms located around the rim of the mirror. Both axial and radial supports use hydraulic whiffletree systems to define the position of the mirror. These are adjusted as the telescope changes orientation, introducing small, controlled mirror translations and tilts to maintain alignment with the rest of the telescope optics. The mounting system also compensates for thermally induced surface deformations; errors in force

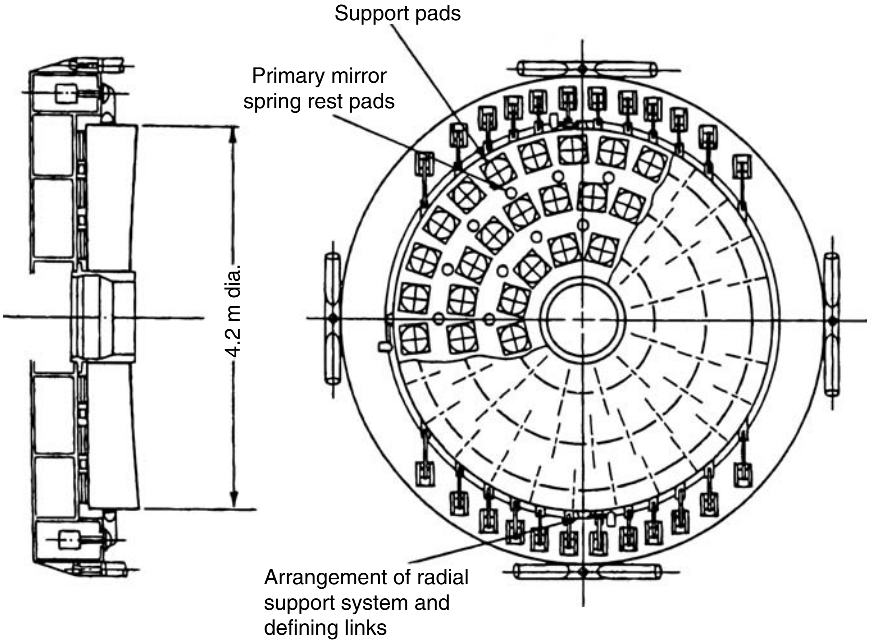
Support pads
Primary mirror spring rest pads
4.2 m dia.
Arrangement of radial support system and defining links

FIGURE 12.18 Schematic showing axial and vertical supports of a U.K. 4.2 m (165 in.) telescope primary mirror in its mount. (Adapted from Mack, B., *Appl. Opt.*, 19, 100, 1980.)

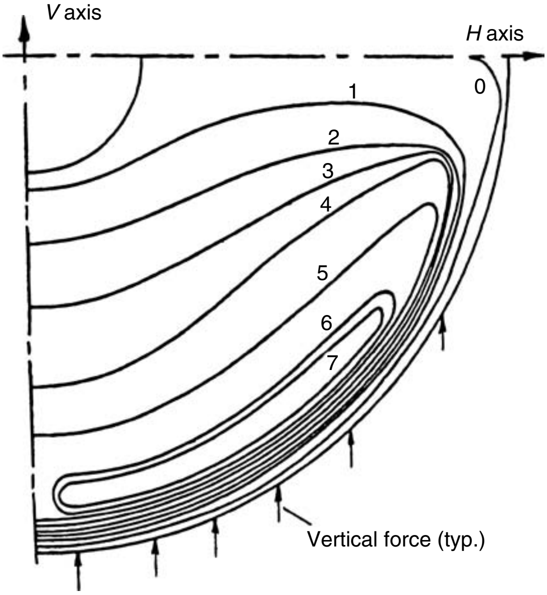

FIGURE 12.19 Estimated stress distribution in the mirror of Figure 12.18 that is due to its ring supports with axis horizontal. (Adapted from Mack, B., *Appl. Opt.*, 19, 100, 1980.)

magnitude, angle, and position; radial support errors; and air pressure errors. In addition, the system can compensate for gravity sag of the secondary mirror and, if needed, change the primary figure from a parabola for use in a Cassegrain system configuration to a hyperbola for use in a Ritchey–Chretien system configuration (Cho, 1994).

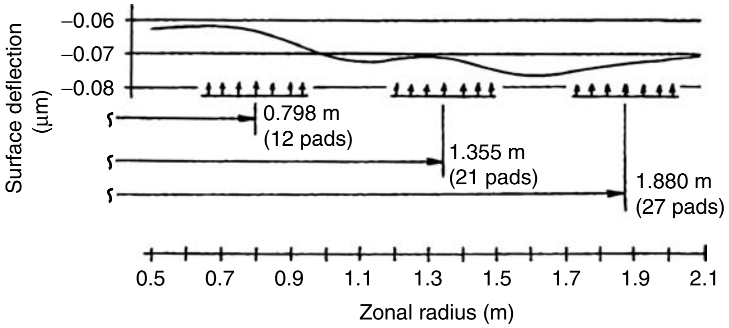

FIGURE 12.20 Estimated surface deflection vs. zonal radius for the mirror of Figure 12.18 with axis vertical. (Adapted from Mack, B., *Appl. Opt.*, 19, 100, 1980.)

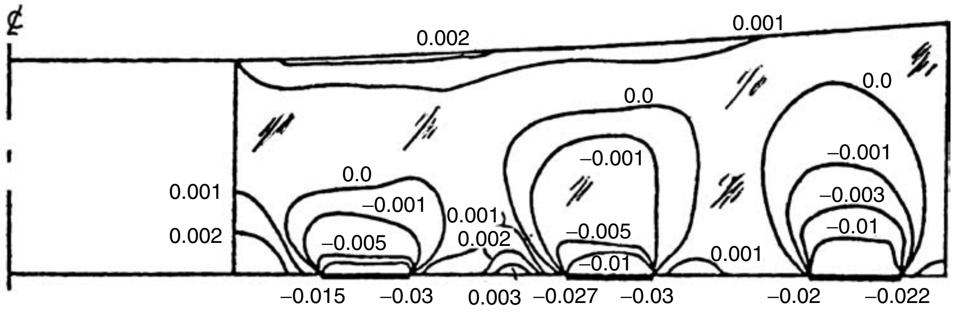
℄
0.002
0.001
0.0
0.0
0.0
−0.001
−0.001
−0.001
−0.003
−0.01
0.001
0.002
−0.005
0.001
0.002
−0.005
−0.01
0.001
−0.015
−0.03
0.003
−0.027
−0.03
−0.02
−0.022

FIGURE 12.21 Estimated stress distribution within the mirror of Figure 12.18. The axis is vertical. Note the low stress values near the optical surface. (Adapted from Mack, B., *Appl. Opt.*, 19, 100, 1980.)

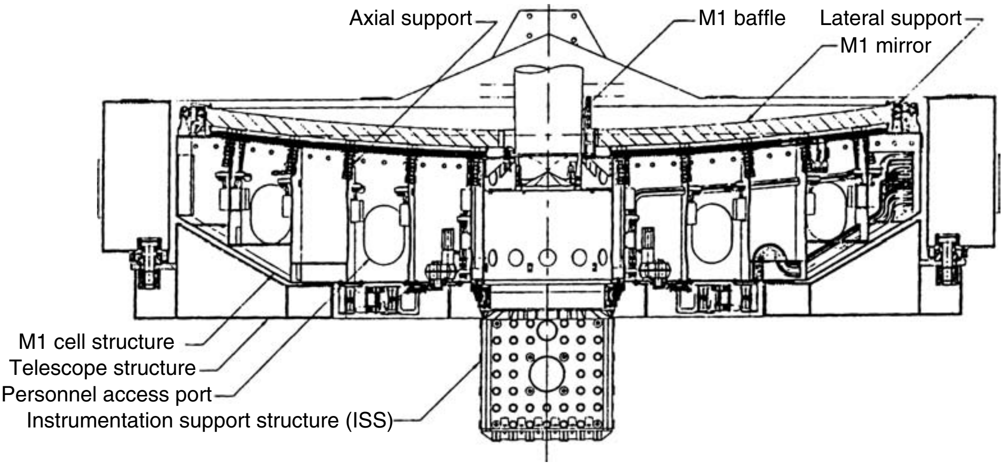
Axial support
M1 baffle
Lateral support
M1 mirror
M1 cell structure
Telescope structure
Personnel access port
Instrumentation support structure (ISS)

FIGURE 12.22 Schematic diagram of the Gemini primary mirror in its cell. The axial supports are indicated. (From Huang, E.W., *Proc. SPIE*, 2871, 291, 1996.)

The primary mirror assembly consisting of the cell, mirror, and axial and radial actuators is shown in Figure 12.22. The welded steel mirror cell was designed as a honeycomb structure to ensure stiffness without adding excessive weight (see Figure 12.23). It is supported from the telescope structure on four bipods oriented at 45° to the elevation axis at a radius of about 60% of the

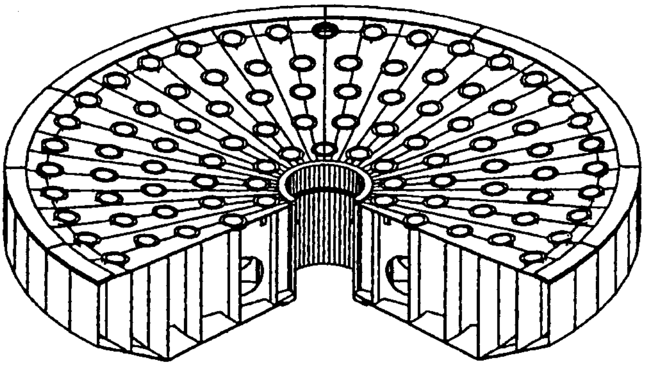

FIGURE 12.23 Cut-away sketch of the honeycomb structure of the Gemini primary mirror cell. (From Stepp, L., Huang, E., and Cho, M., *Proc. SPIE*, 2199, 223, 1994.)

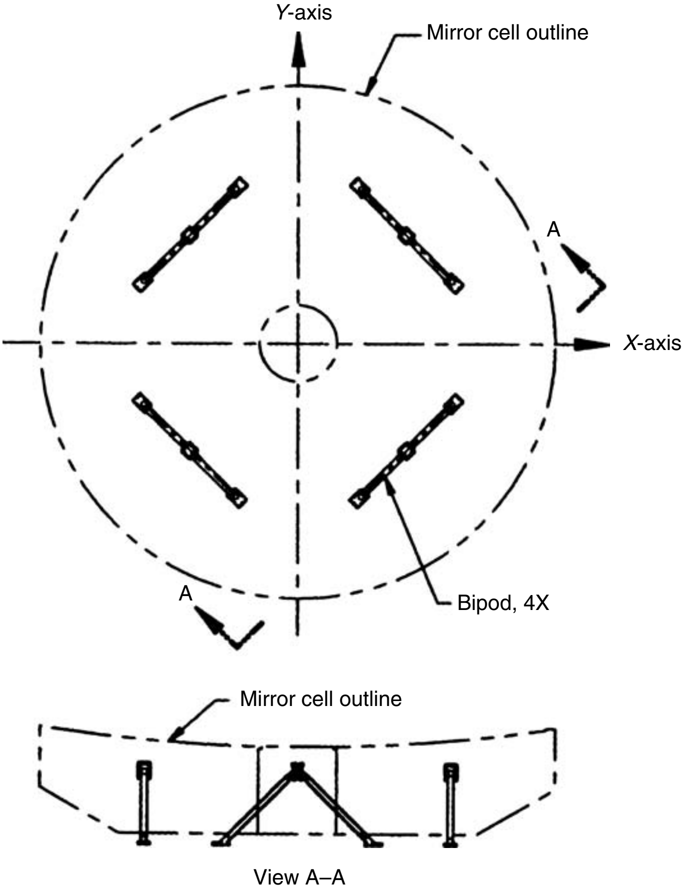
Y-axis
Mirror cell outline
A
X-axis
Bipod, 4X
A
Mirror cell outline
View A–A

FIGURE 12.24 Schematic of the bipod support for the Gemini primary mirror cell. (From Stepp, L., Huang, E., and Cho, M., *Proc. SPIE*, 2199, 223, 1994.)

cell radius as illustrated in Figure 12.24. This bipod orientation was chosen because any distortion of the cell from horizon-pointing loading is symmetrical about the Y-axis and antisymmetrical about the X-axis. This minimizes flexure of the mirror. Under normal conditions, flexure of the telescope

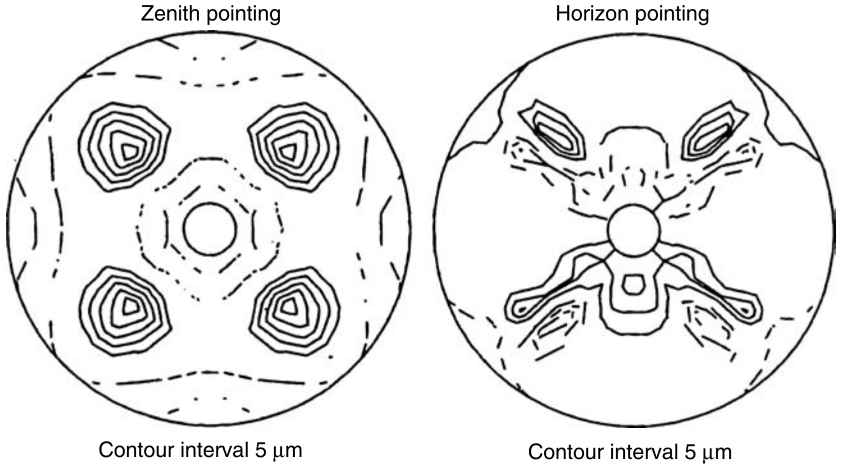

FIGURE 12.25 Anticipated extreme gravitational deflections of the top surface of the Gemini mirror cell on its four-bipod mounting. (From Stepp, L., Huang, E., and Cho, M., *Proc. SPIE*, 2199, 223, 1994.)

will not bend the mirror. Typical worst-case distortion contours of the cell's top surface (to which the mirror is attached) at the zenith and horizon are shown in Figure 12.25. FEA indicated that the expected cell distortions would be within the allowable error budget for that portion of the system (Stepp et al., 1994; Cho, 1994).

About 80% of the weight of the mirror is supported axially by the air pressure of ~ 3460 Pa (0.5 lb/in^2.) applied to its back surface. This pressure, combined with the forces exerted by the seals, produces a small amount (~ 100 nm rms) of spherical aberration in the mirror's surface. The active support system can easily compensate for this error. The remaining 20% of the mirror's weight is carried by the 120 support and defining mechanisms. The actuators operate in push mode only and do not need to be connected (as by bonding) to the mirror. Removal of the mirror from its cell for recoating is significantly simplified by this design choice.

Figure 12.26 shows the mirror surface contours at the 120 discrete support points that are arranged in five rings of 12, 18, 24, 30, and 36 contacts. The localized forces of magnitudes between 285 N (64 lb) and 386 N (86.7 lb) produce bumps on the surface as indicated by the contour maps. The maximum heights of these bumps are only about 10 nm rms. Since these errors are fixed on the surface, they can be compensated for by localized polishing in the axis vertical orientation during manufacture so the "print-through" pattern disappears. The air pressure is controlled throughout the operational inclination range of 0.5° to 75° so the errors are tolerable (Cho, 1994).

The axial actuators are hydraulic cylinders connected as indicated in Figure 12.27. They are operated under computer control in either of two modes: three-zone semikinematic support and six-zone overconstrained (nonkinematic) support. Opening or closing valves in the pipelines chooses the mode. Figure 12.28 illustrates the advantage of the overconstrained mode in controlling surface deformation when the telescope is undergoing uneven wind loading. Surface errors under typical adverse wind conditions can be reduced by a factor of six by changing the mode (Stepp et al., 1994).

The mirror is supported laterally by 72 actuators applying forces at the locations indicated in Figure 12.29. Because of the meniscus shape of the mirror, the radial forces have three-dimensional components. The resultant force components are indicated by the directions of the vectors in the figure (shown as two-dimensional projections). Figure 12.30, shows typical mirror deformations from optimized lateral forces and corrective active forces. The contour interval is 5 nm. The p-v surface error is 38 nm while its rms error is 5 nm.

Because all large telescopes are more or less exposed to wind loading, numerous studies and experiments have been conducted during the past 20 years to find ways to alleviate seeing problems

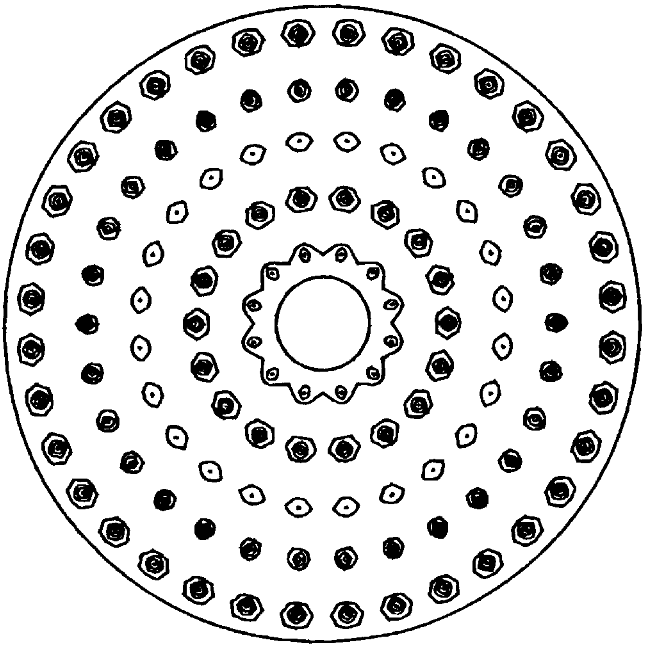

FIGURE 12.26 Computed spatially fixed-surface contours expected for the Gemini primary mirror with axis vertical when supported on its 120-point mount without localized correction during polishing. Bump heights are about 10 nm rms. The effects of air pressure seals are included. (From Cho, M.K., *Proc. SPIE*, 2199, 841, 1994.)

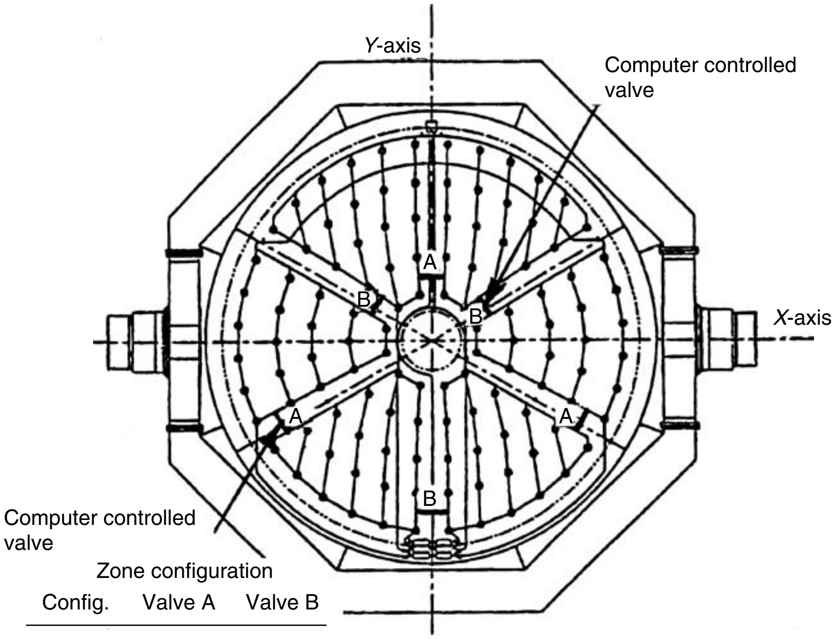
Y-axis
Computer controlled valve
A
B
B
X-axis
A
A
B
Computer controlled valve

Zone configuration

Config.	Valve A	Valve B
3 Zone A	Open	Closed
3 Zone B	Closed	Open
6 Zone	Closed	Closed

FIGURE 12.27 Schematic of the three- and six-zone hydraulic system connection modes in the Gemini primary mirror mount. (From Huang, E.W., *Proc. SPIE*, 2871, 291, 1996.)

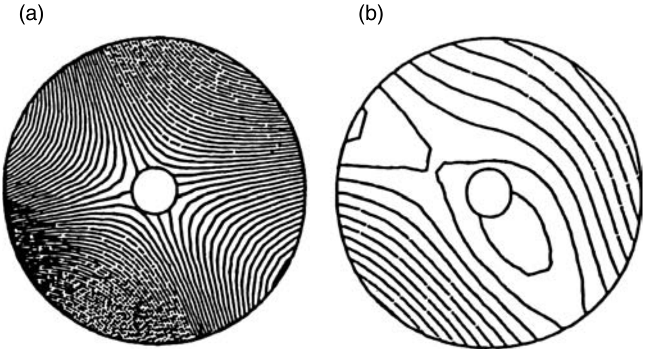

FIGURE 12.28 Predicted surface deformations of a Gemini primary mirror under typical uneven wind loads with axial support operating in (a) three-zone (semikinematic) and (b) six-zone (overconstrained) modes. (From Huang, E.W., *Proc. SPIE*, 2871, 291, 1996.)

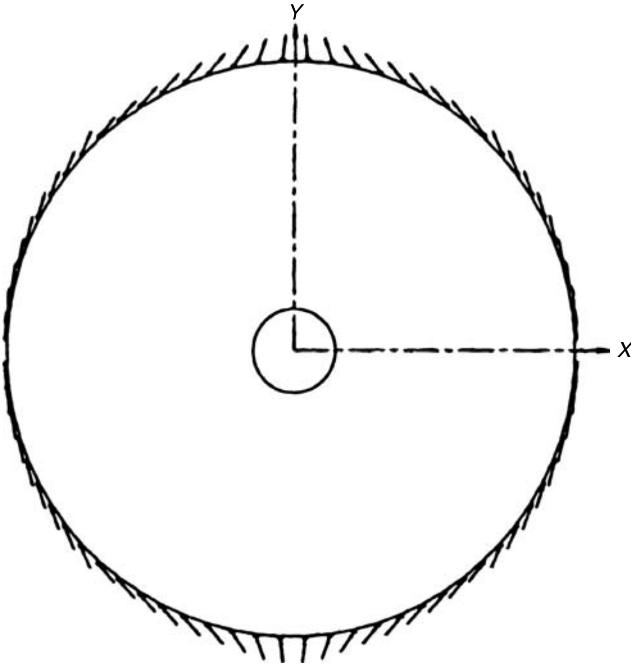

FIGURE 12.29 Distribution and resultant directions of radial support forces applied to the rim of the Gemini primary mirror. (From Cho, M.K., *Proc. SPIE*, 2199, 841, 1994.)

during operation. Tests with scaled models in water tunnels and wind tunnels were helpful in that they allowed visualization of air flow (Hertig et al., 1988; Wong and Forbes, 1991; Pottebaum et al., 2004). The wind patterns at observatory sites have been characterized by several investigators, including Forbes (1984) and Hiriart et al. (2001). Computational fluid dynamics techniques have also been applied to this problem. Cho et al. (2003) indicated that modeling limitations of such techniques limit results to average pressure patterns.

A definitive investigation of wind effects used the Gemini South Telescope on Cerro Pachon as a test vehicle, (Cho et al., 2003). The intent was threefold: (1) to verify prior investigations, (2) to establish operational optimization procedures, and (3) to guide the design of future extremely large

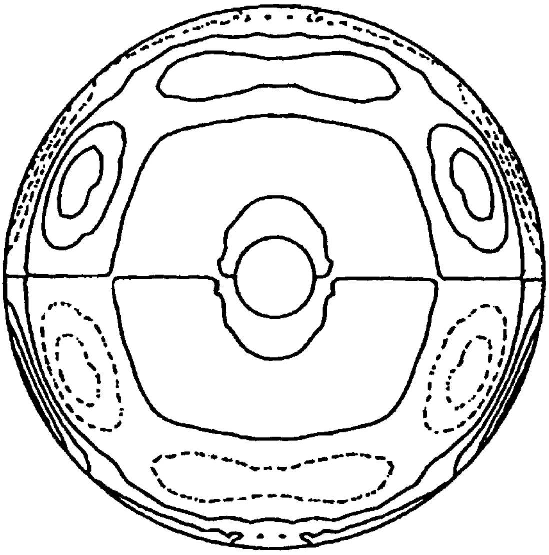

FIGURE 12.30 Computed surface contours for the Gemini primary mirror with axis horizontal and typical radial support optimization. Surface errors are 38 nm p-v and 5 nm rms. (From Cho, M.K., *Proc. SPIE*, 2199, 841, 1994.)

systems. The telescope (with a dummy primary mirror) was instrumented with 32 pressure sensors. Measurements were taken in a series of 116 test runs of 5 min duration with 300 time steps per test. Modal tests were also conducted. The data provided insights as to best location for side vents in the enclosure, showed that elevation angle was not a strong driver for performance, and provided a basis for FEA determination of mirror deformations, including piston, tip, tilt, focus, and astigmatism terms. Because the telescopes' secondary mirrors have fast tip-tilt-focus mechanisms, only the astigmatism is really significant. The allowable wind velocity at which the Gemini telescope would meet its error budget was determined. In addition, the data revealed that the correlation length of the wind pressure is typically 1 to 2 m. This has significance with regard to the performance of segmented mirrors with segments of similar dimensions. All this information is expected to facilitate successful operation of the Gemini Telescopes and to provide useful guidance for future monolithic and segmented telescope developments.

12.3.3 NEW MULTIPLE MIRROR TELESCOPE

The multiple mirror telescope (MMT) installed on Mt. Hopkins in 1979 originally had six 1.8 m (70.9 in.) *f*/2.7 primary mirrors as parts of an array of six Cassegrainian telescopes arranged in a ring. It contributed much knowledge to telescope design and to astronomical science because of its large effective aperture of 4.5 m (177.2 in.). The combined image was optimized through active control of the secondary mirrors. According to Antebi et al. (1990), other advantages of this telescope over smaller, ground-based telescopes included the use of an elevation-over-azimuth mount, in which gravity affects the optical structure in only one plane as the telescope changes elevation angle, thereby allowing the mirror mounts to be simplified; and the use of a building that rotates with the telescope rather than a stationary dome. This feature allowed the enclosure's size to be minimized and reduced convective air currents in the enclosure.

When the technology for making large mirrors by spin casting had sufficiently matured, it was decided to redesign the telescope to utilize the largest single mirror that would fit inside the existing elevation yoke and a slightly modified observatory building (Antebi et al., 1990). A 6.5-m (256.5-in.)-diameter borosilicate honeycomb mirror with a relative aperture of *f*/1.25 was cast for this purpose. The opto-mechanical design for this telescope has several interesting features that warrant description here.

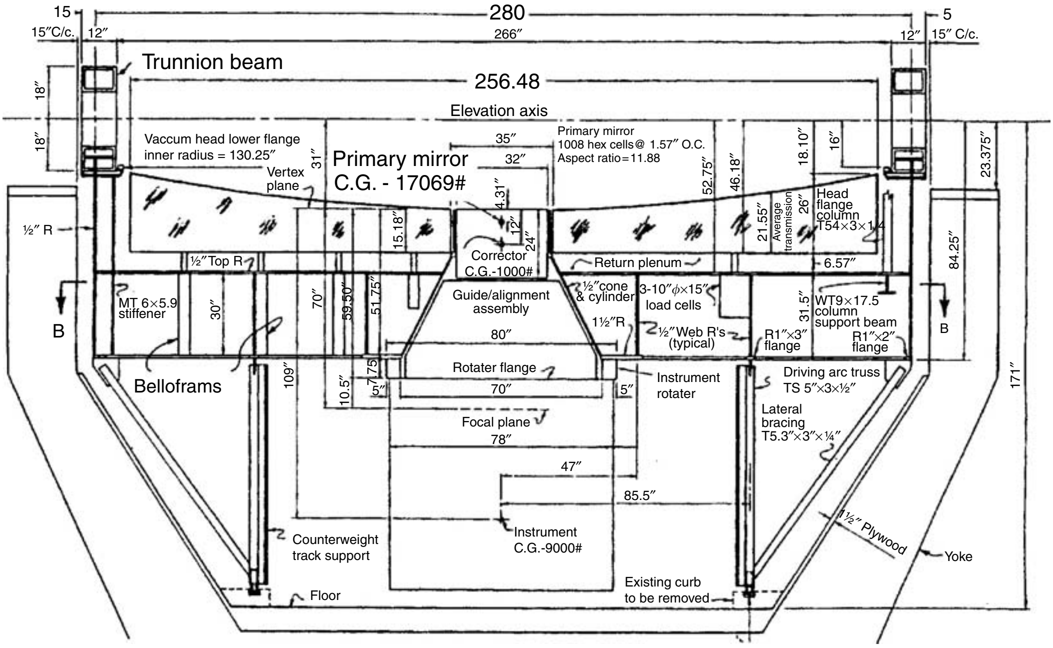
15
15″C/c.
12″
280
266″
5
12″
15″ C/c.
Trunnion beam
256.48
Elevation axis
18″
18″
Vaccum head lower flange
inner radius = 130.25″
Vertex plane
31″
Primary mirror
C.G. - 17069#
35″
32″
Primary mirror
1008 hex cells@ 1.57″ O.C.
Aspect ratio=11.88
4.31″
12″
24″
15.18″
52.75″
46.18″
18.10″
16″
23.375″
21.55″
Average transmission
26″
Head flange column T54×3×1/4
½″ R
½″Top R
Corrector C.G.-1000#
Return plenum
6.57″
84.25″
MT 6×5.9 stiffener
30″
70″
59.50″
51.75″
Guide/alignment assembly
80″
½″cone & cylinder
1½″R
3-10″ϕ×15″ load cells
½″Web R's (typical)
31.5″
R1″×3″ flange
WT9×17.5 column support beam
R1″×2″ flange
B
B
Bellofram
109″
10.5″
7.75
5″
Rotater flange
70″
5″
Instrument rotater
Driving arc truss TS 5″×3×½″
Lateral bracing T5.3″×3″×¼″
171″
Focal plane
78″
47″
85.5″
Counterweight track support
Instrument C.G.-9000#
½″ Plywood
Yoke
Existing curb to be removed
Floor

FIGURE 12.31 Diagram of the new 6.5 m (256.5 in.) diameter MMT primary mirror in its cell. Dimensions are in inches. (Adapted from Antebi, J., Dusenberry, D.D., and Liepins, A.A., *Proc. SPIE*, 1303, 148, 1990.)

The primary mirror for the new MMT is mounted in a cell that serves multiple structural purposes as well as holding the mirror. Figure 12.31 shows the new plano-concave mirror in its cell with the associated components aft of the elevation axis. The mirror is supported axially and radially by 104 pneumatic actuators (called "belloframs" in the figure). Figure 12.32(a) shows part of the honeycomb structure with actuators acting independently and through double and triple whiffletree load spreaders at the points indicated (Gray et al., 1994). Figure 12.32(b) shows (as rectangles) typical locations of the supports for the actuators on the octagonally shaped mirror cell. This cell consists of a top plate reinforced by a grid of webs, 30 in. (762 mm) high, that forms compartments (West et al., 1996).

These compartments contain the actuators and other mechanisms and are closed by removable covers, but are interconnected by holes through the webs to form part of the thermal control system. A return plenum for this system is formed by the space between the back of the mirror and the top plate of the cell as shown in Figure 12.33. Pressurized air from an off-board chiller and blower is forced through each of many ejector nozzles and passes through jet ejectors drawing air from the mirror cells and into the input plenum. The mixture of new air and the air from the mirror cells exhausts from that plenum back into the mirror cells via a series of ventilation nozzles, and the cycle repeats. About 10% of the air volume escapes from the cell to allow space for the pressurized air input. This forced-air ventilation through the honeycomb cells of the mirror keeps that optic within 0.15°C of ambient and isothermal to 0.1°C (see Siegmund et al., 1990; Cheng and Angell, 1986; Lloyd-Hart, 1990). This is consistent with the findings of Pearson and Stepp (1987) and Stepp (1989) regarding thermal gradient effects on telescope image quality. Details of the design of the thermal control system and of the temperature-sensing system for the new MMT mirror may be found in Lloyd-Hart (1990) and in Dryden and Pearson (1990).

As indicated earlier, most of the actuators contact the mirror through load spreaders that function exactly as their name suggests. Diagrams of these mechanisms are shown in Figure 12.34. The actuator attachment is at the center of each device. The frames for these load spreaders are made of Invar and steel with dimensions to match thermal deformations of the Ohara E6 glass in the mirror.

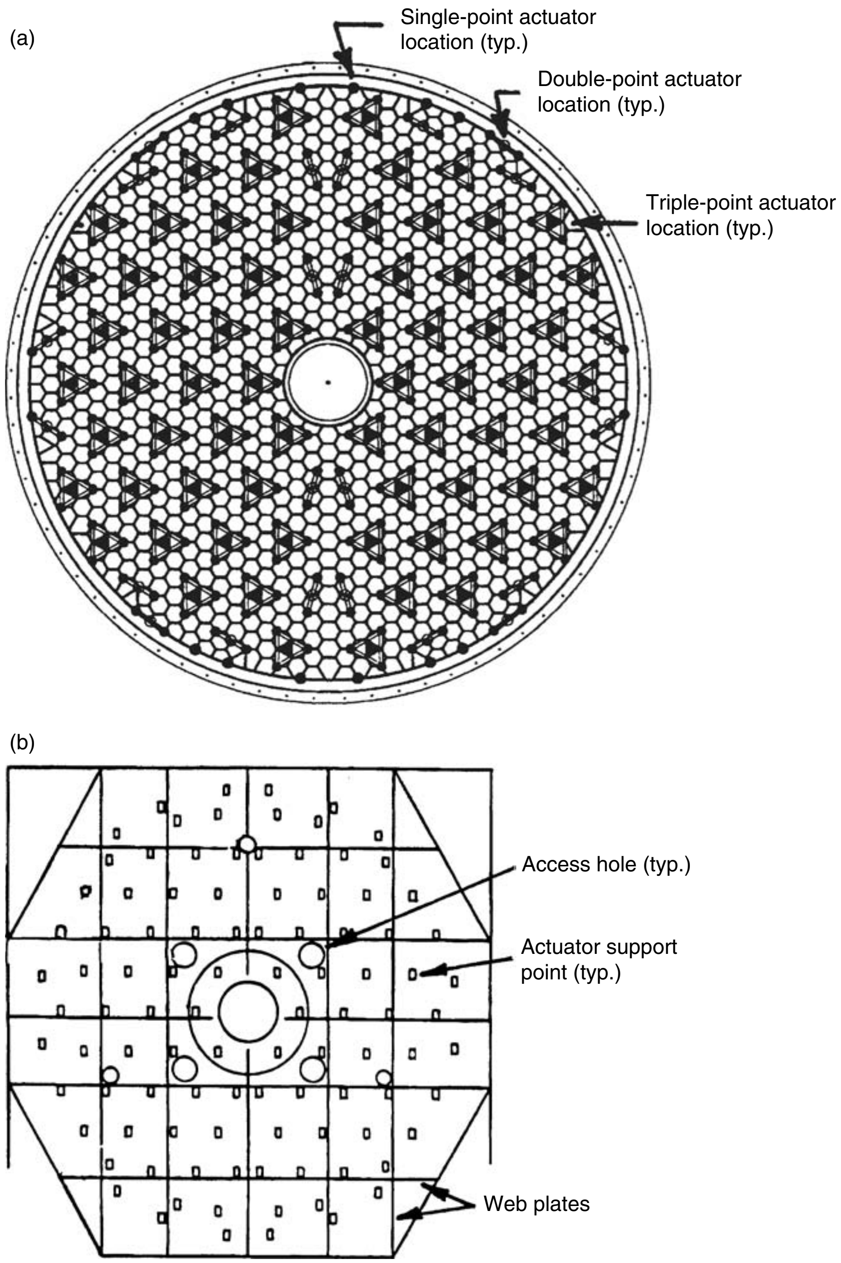
(a)
Single-point actuator location (typ.)
Double-point actuator location (typ.)
Triple-point actuator location (typ.)
(b)
Access hole (typ.)
Actuator support point (typ.)
Web plates

FIGURE 12.32 (a) Layout of support points (some single and others acting through double- and triple-load spreaders) on a portion of the MMT mirror. (Adapted from Gray, P.M., Hill, J.M., Davison, W.B., Callahan, S.P., and Williams, J.T., *Proc. SPIE*, 2199, 69, 1994.) (b) Section view B-B′ from Figure 12.31 passing through the support mechanisms. (Adapted from Antebi, J., Dussenberry, D.D., and Liepins, A.A., *Proc. SPIE*, 1303, 148, 1990.)

Contact is through 100-mm (3.94-in.)-diameter pucks made in two parts from the same batch of steel so the CTEs are the same. The lower part is a conical annulus to minimize weight and optimize load-induced distortions. The upper part has a necked rod flexure to decouple the puck from twisting of the load spreader frame. Each puck is attached to the mirror with a 2-mm (0.078-in.)-thick layer of

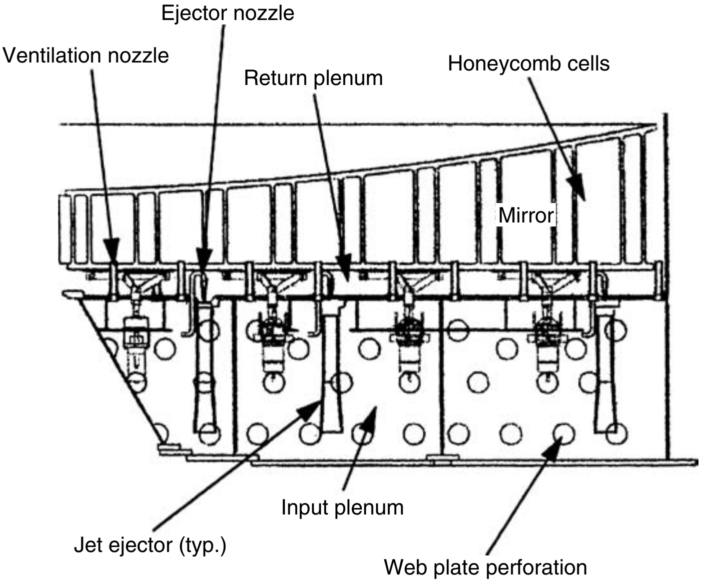

FIGURE12.33 Layout of thermal control system components in the MMT mirror cell. (From West, S.C., Callahan, S., Chaffee, F.H., Davison, W., DeRigne, S., Fabricant, D., Foltz, C.B., Hill, J.M., Nagel, R.H., Poyner, A., and Williams, J.T., *Proc. SPIE*, 2871, 38, 1996.)

silicone rubber adhesive (Dow Corning type 93-076-2) whose compliance absorbs thermally induced stresses and cushions the load.

Also shown in Figure 12.34 are rubber static supports that are spaced at short distances from the corners of the load spreaders to serve as mirror constraints if the air pressure to the actuators were to fail during operation or when the system is inactive. These are commercial engine mounts; they consist of rubber “donuts” bonded to steel shafts. Shoulder bolts connected to the corners of the load spreaders limit shear and axial tension forces when the stops are in use.

The actuators themselves consist of pneumatic cylinders with pressure regulators, a load cell for force feedback, and a ball decoupler to eliminate transverse forces and moments. Figure 12.35 shows the two basic configurations. At left is a single-axis actuator with a double load spreader. It provides axial force only. The arrangement at right has two actuators, one working axially and the other working at 45° to the mirror’s back surface. There are 58 of the latter type of devices. They apply radial forces near the back plate of the mirror and therefore produce net moments as well as deflections. These are cancelled by axial correction forces. An enlarged view of the two-actuator device is shown in Figure 12.36.

The MMT mirror is constrained in its cell as a rigid body by an astatic flotation support with forces independent of small displacements and automatically distributed in fixed proportions among the actuators. Six hard point supports are provided, as indicated in Figure 12.37. Each of these supports is adjustable, but when clamped, it becomes a very stiff strut that connects the back plate of the cell to the back plate of the mirror. These struts are arranged as three bipods, so orientation and location of the mirror are completely determined. Each strut includes a load cell that provides information that is fed back to the actuators. Adjustments are made so that near-zero force is exerted at each hard point (Martin et al. 1998.)

12.4 CENTER-MOUNTED MIRRORS

In Section 5.9, we discussed a hub mounting for a perforated meniscus-shaped, first surface mirror of about 15 in. (381 cm) diameter as used in a catadioptric objective. As shown in Figure 5.72, this

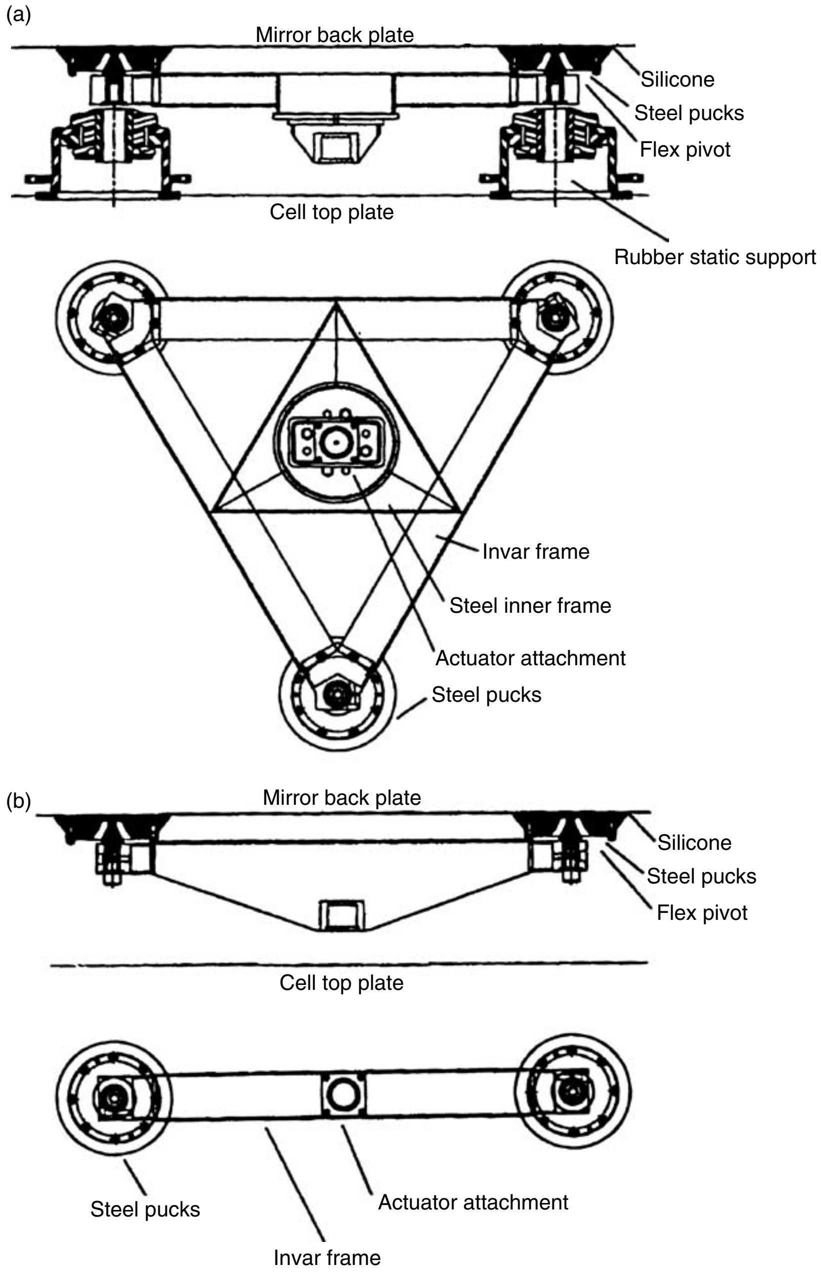
(a)
Mirror back plate
Silicone
Steel pucks
Flex pivot
Cell top plate
Rubber static support
Invar frame
Steel inner frame
Actuator attachment
Steel pucks
(b)
Mirror back plate
Silicone
Steel pucks
Flex pivot
Cell top plate
Steel pucks
Actuator attachment
Invar frame

FIGURE 12.34 (a) Triple- and (b) double-load spreaders for the new MMT primary mirror. (Adapted from Gray, P.M., Hill, J.M., Davison, W.B., Callahan, S.P., and Williams, J.T., *Proc. SPIE*, 2199, 691, 1994.)

mirror was clamped axially between a shoulder and a retaining ring and constrained radially by a close (near interference) fit between a toroidal surface on the hub and the ID of the hole in the mirror. The tapered edge of the mirror substrate was not constrained. The opto-mechanical interfaces at the mirror's thickest zone provided adequate support for the intended application as a camera objective for a missile-tracking application. Many Cassegrain and Gregorian astronomical telescope primary mirrors are supported in a similar manner.

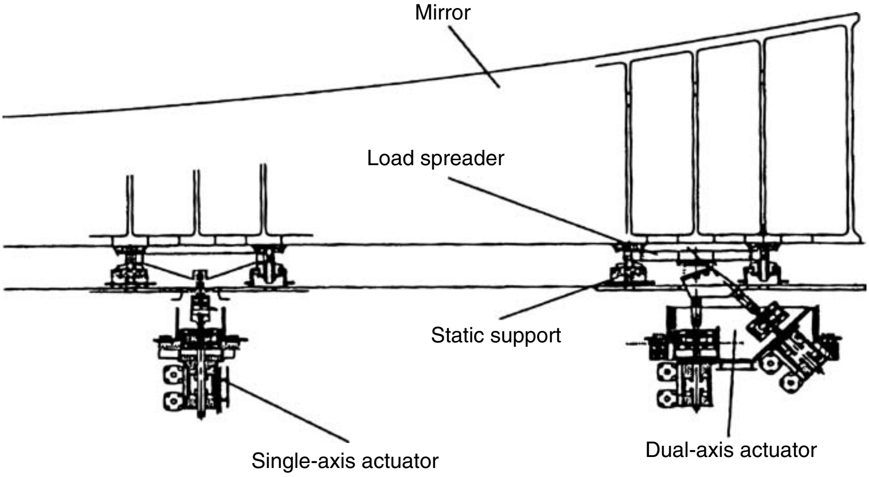

FIGURE 12.35 Schematic showing a single- and a dual-axis actuator as used to support the new MMT mirror. (From West, S.C., Callahan, S., Chaffee, F.H., Davison, W., DeRigne, S., Fabricant, D., Foltz, C.B., Hill, J.M., Nagel, R.H., Poyner, A., and Williams, J.T., *Proc. SPIE*, 2871, 38, 1996.)

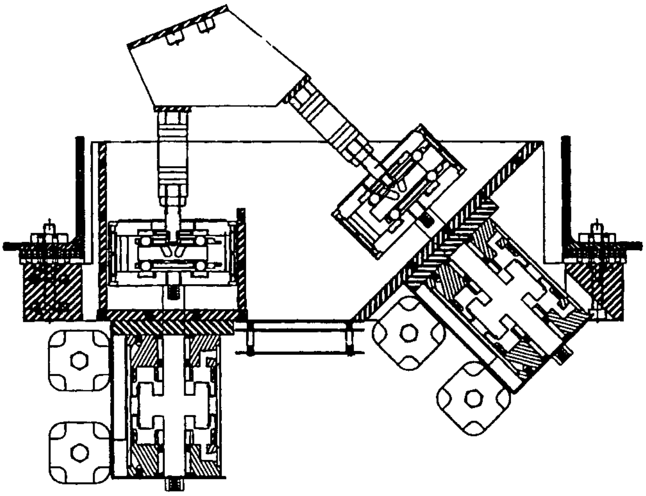

FIGURE 12.36 Dual-action actuator used at 58 locations on the new MMT primary mirror. (From Martin, H.M., Callihan, S.P., Cuerden, B., Davison, W.B., DeRigne, S.T., Dettmann, L.R., Parodi, G., Trebisky, T.J., West, S.C., and Williams, J.T., *Proc. SPIE*, 3352, 412, 1998.)

Single-arch mirrors of the type shown in Figure 9.27(e) are also hub-mounted through a central perforation. One design of this type, due to Carter (1972), is illustrated in Figure 12.38. Here, we see a 152-cm (59.8-in.)-diameter mirror made of Cer-Vit. Its edge thickness was chosen to be 2.5 cm (1.0 in.), and the sectional thickness was computed at each 0.25 mm increment of radius so as to maintain a uniform stress on the mirror surface when oriented with axis vertical. For convenience, an available 16.5-cm (6.5-in.)-thick blank was used, so the curve on the back surface ended at a radius of ~39 cm (15.4 in.). The flat portion of the back surface was ground and polished and contacted a 79-cm (31.1-in.)-diameter stainless steel mounting plate. The mounting plate was 5 cm (1.96 in.) thick over the central 38.1 cm (1.50 in.) diameter and tapered to an edge thickness of 0.64 cm (0.25 in.). A 30-cm (11.8-in.)-diameter stainless-steel tube with 0.50 cm (0.21 in.) wall thickness was

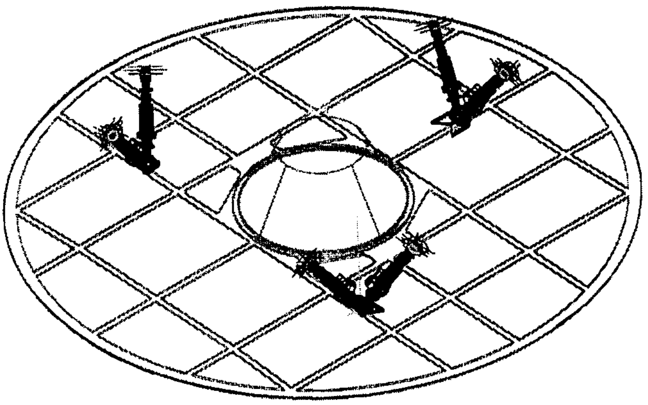

FIGURE 12.37 Configuration of six struts in bipod arrangements to provide adjustable hard point supports for determination of location and orientation of the new MMT mirror. (From West, S.C., Callahan, S., Chaffee, F.H., Davison, W., DeRigne, S., Fabricant, D., Foltz, C.B., Hill, J.M., Nagel, R.H., Poyner, A., and Williams, J.T., *Proc. SPIE*, 2871, 38, 1996.)

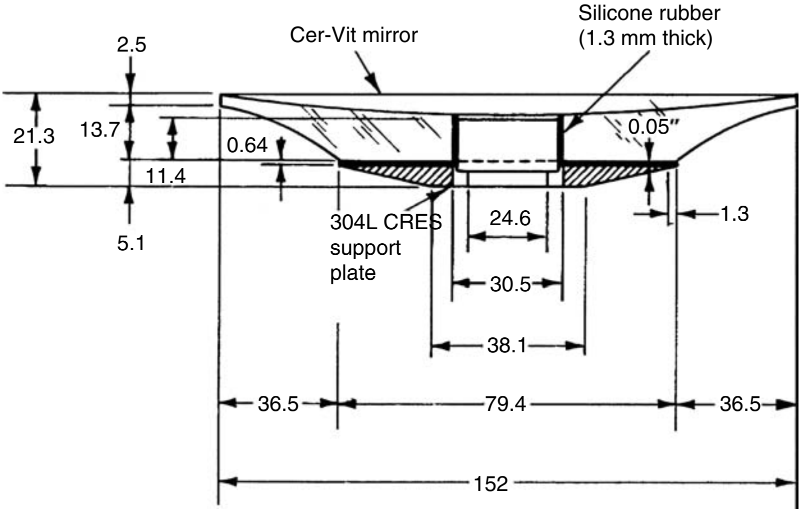

FIGURE 12.38 Schematic of an elastomer-secured center mount for a 152 cm (59.8 in.) diameter mirror. Dimensions are cm. (Adapted from Carter, W.E., *Appl. Opt.*, 11, 467, 1972.)

shrunk fit into a central hole in the mounting plate. The ID of the mirror was bonded to the OD of this tube with RTV silicone rubber (Dow Corning type 93-046, catalyst cured). The elastomer was 0.05 cm (0.02 in.) thick and was injected between the support tube and the glass through a series of grease fittings. Tapped holes in the back of the mounting plate allowed the mirror assembly to be bolted directly to a back plate that formed part of the telescope structure.

Buchroeder et al. (1972) described an interesting modification of the above design in which six screws were added to the telescope back plate. These were intended to allow axial pressure to be exerted differentially on the mounting plate around its circumference in the event that excessive warpage or figure errors of the mirror surface were found after assembly. The mirror maintained excellent figure when mounted and tested at variable orientations. However, a double image was observed in the first photographs made with the system. During troubleshooting, the adjusting screws were turned so as to just contact the mounting plate. The second image then disappeared.

Apparently, resonant vibration from the telescope drive motor operating at 25 steps per second needed to be damped.

A concept for mounting a single-arch glass mirror to a hub with a single clamp incorporating a conical interface was advanced by Sarver et al. (1990) as one of several concepts for possible use in mounting the 85-cm (33.5-in.)-diameter primary mirror of the Space Infrared Telescope Facility (SIRTF) (now known as the Spitzer Space Telescope). It is shown in Figure 12.39. The clamp would constrain the mirror in all six DOF near its CG at its thickest and strongest section with large area contact, thereby reducing stresses that could disturb the optical surface. A flat surface was provided on the back of the mirror; the axis of the cone would be perpendicular to this surface and the apex of the cone would coincide with it. Slight slippage could occur between the conical surfaces, but expansion or contraction of the mount materials would not alter the apex coincidence with the plane, so the mount would be athermal as long as all materials used in the metal parts of the mount were the same. A spherical bearing was incorporated into the design to ensure contact of the conical surfaces.

Vukobratovich (2004) reported that a significant drawback in hub mounting a single-arch mirror may arise if the CG is in front of the vertex of the optical surface. In such a situation, the hub mount cannot provide support in the plane containing that important point, and astigmatism is introduced at and near the axis-horizontal position. This limits the single-arch mirror configuration to cases where the diameter is smaller than about 1 m (39.4 in.) For such diameters, adequate stiffness is obtained and the astigmatic deformation is tolerable. They also would be usable in space applications where gravity is absent.

Anderson et al. (1982) described the fabrication and interferometric testing of a lightweighted mirror with a single-arch cross section. It was made from a blank of Heraeus TO-8 commercial type E composite material made by fusion of natural quartz. It was 20 in. (50.8 cm) in diameter × 4 in. (10.2 cm) thick with a 5-in. (12.7-cm)-diameter central hole. A spherical surface of radius 80 in. (2.03 m) was generated into the front surface of the blank before the arch contour was generated into the rear surface. This ensured firm support of the blank during surfacing. The arch-contouring operation was done with a cam-controlled diamond wheel. The axial thickness of the ground substrate

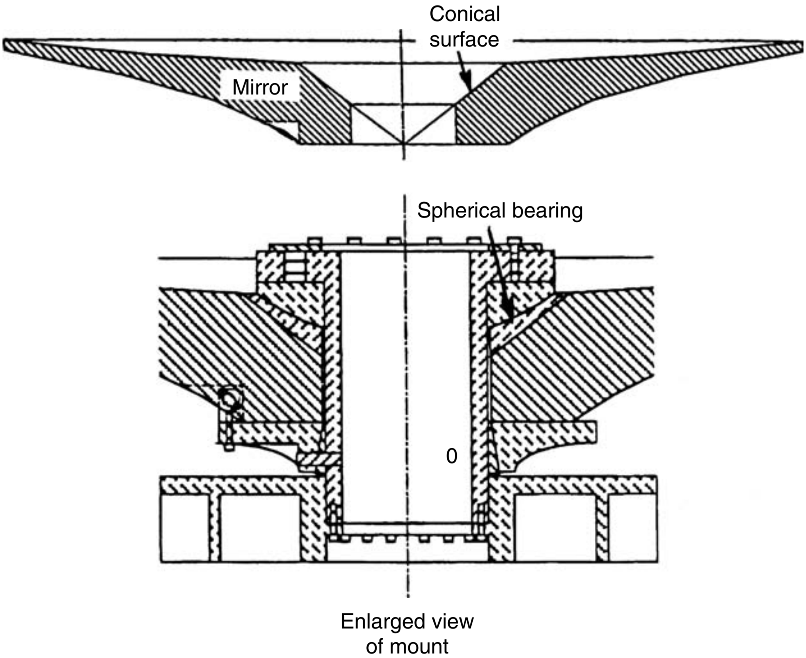

FIGURE 12.39 Concept of a conical-clamping center mount for a single-arch mirror. (Adapted from Sarver, G., Maa, G., and Chang, L., *Appl. Opt.*, 1, 387, 1990.)

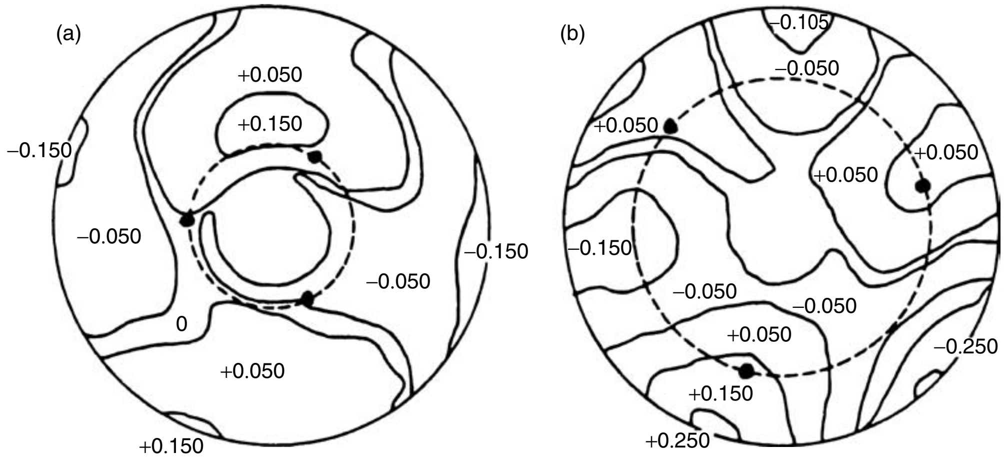

FIGURE 12.40 Computed twice self-weight surface deflection contour plots of (a) a single-arch mirror and (b) a double-arch mirror of similar materials, sizes, and configurations supported with axis vertical at the three points indicated by the black spots on the dashed circle. Contour intervals are waves at $\lambda = 0.63$ μm. (Adapted from Anderson, D., Parks, R.E., Hansen, Q.M., and Melugin, R., *Proc. SPIE*, 1531, 195, 1982.)

was 3.5 in. (8.9 cm). Three holes were core-drilled into the back of the mirror hub at 120° azimuthal intervals to interface with ball bearings that served as a three-point mount during testing.

After polishing, the mirror was tested interferometrically with its axis-vertical looking up. Testing was then repeated with the axis looking down. The intent was to estimate the mount-induced surface deformation that might be expected when the mirror was transferred from a 1 g load to a weightless environment. This was determined by taking the difference between the surface error interferograms in the +1 g and −1 g orientations on a point-for-point basis and dividing by 2. Residual figure errors in the reflecting surface were considered to be constant, so they would cancel in the subtraction.

Figure 12.40(a) from Anderson's paper shows the 2 g deflections due to three-point support near the center of the mirror. Considering a matrix of 672 test points, the surface deformations from the best-fit sphere at $\lambda = 0.633$ μm were computed to be 0.054 wave rms, 0.138 wave maximum, −0.148 wave minimum, and 0.286 wave p-v.

12.5 MOUNTS FOR DOUBLE-ARCH MIRRORS

A double-arch mirror of 20 in. (50.8 cm) diameter and 3.0 in. (7.6 cm) thickness was made at the Optical Sciences Center, University of Arizona, at the same time as the single-arch mirror just described. The material for this mirror was Corning code 7940 fused silica made by the flame hydrolysis method. It was similar to, but not identical with the fused natural quartz material used in the single-arch mirror.

This mirror was tested face up and face down in the same manner as the single-arch mirror to facilitate comparative evaluation of gravitational flexure effects. The 2 g deflections due to the three-point support were as depicted in Figure 12.40(b). Again considering a matrix of 672 test points, the surface deformations from the best-fit sphere at $\lambda = 0.633$ μm were computed as 0.094 wave rms, 0.243 wave maximum, −0.356 wave minimum, and 0.599 wave p-v. These data may be compared directly with those given earlier for the similar-sized single-arch mirror.

To understand better the deformations characteristic of the double-arch mirror in comparison to the equivalent single-arch version, Anderson and his co-authors computed a set of 36 Zernike polynomials from the interferograms, then resolved the data into successive angular components of the azimuthal angle θ. This separated radial (0θ), comatic (1θ), astigmatic (2θ), and "three-cornered hat" (3θ) errors for the two designs. Table 12.1 summarizes the results. The double-arch mirror had the largest 3θ deflection, so the single arch was judged to be stiffer in azimuth. Radially, the double-arch mirror was about four times stiffer than the single-arch mirror. Both suffered from coma and astigmatism. Changes in surface radius were not measured by this analysis, but were known to be appreciable. It was concluded that the double-arch design would be superior to a single-arch design, especially if supported at more than three points.

Vukobratovich et al. (1982) carried the study of the double-arch mirror further with FEA using a model with 60 quadrilateral elements and 61 nodes to optimize and then evaluate the design. To simplify the problem, the mirror model had a flat optical surface and no central perforation. During optimization, the radial location of the support ring was varied, new contours computed, and the gravitational deflections of the optical surface recomputed until a design with minimum deflection with axis vertical and horizontal was found. A three-point support interfacing with the mirror in the plane through the CG was assumed since it represented a worst-case condition. In the final design, the support ring radius was 0.65 times the mirror diameter and the CG plane was 1.008 in. (25.60 mm) behind the optical surface (see Figure 12.41). Mirror weight was calculated to be ~ 42 lb (19.0 kg).

Figure 12.42 shows the computed deformation of the nominally flat mirror surface in (a) the vertical-axis position and (b) the horizontal-axis position. The rms deformations were 2.016×10^{-6}

TABLE 12.1
Self-Weight Deflections of Single- and Double-arch Mirrors of Equivalent Size with Axis Vertical

	Single-arch		Double-arch	
	p-v	rms	p-v	rms
	(waves at 0.63 μm)		(waves at 0.63 μm)	
Total deflection	0.143	0.027	0.300	0.047
1θ terms	0.073	0.013	0.068	0.012
2θ terms	0.105	0.021	0.096	0.021
3θ terms	0.009	0.001	0.197	0.039
Radial terms	0.041	0.010	0.011	0.002

Source: Adapted from Anderson, D., Parks, R.E., Hansen, Q.M., and Melugin, R., *Proc. SPIE*, 332, 424, 1982.

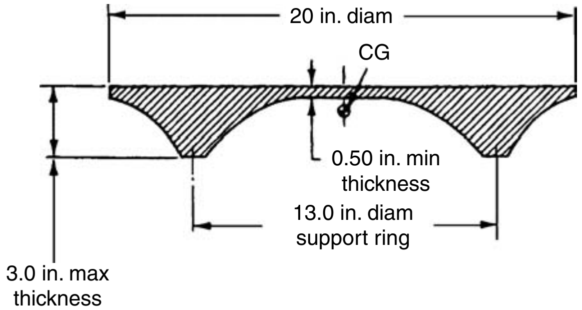

FIGURE 12.41 Cross section of a typical double-arch mirror example analyzed by Vukobratovich et al. (From Vukobratovich, D., Iraninejad, B., Richard, R.M., Hansen, Q.M., and Melugin, R., *Proc. SPIE*, 332, 419, 1982.)

in. (0.08λ) and 0.116×10^{-6} in. (0.005λ), respectively, at $\lambda = 0.633$ μm. The support points were at the locations indicated. The limiting defect in surface contour was found to be azimuthal deformation between the support points with axis vertical. With axis horizontal, the deflections might well be considered negligible.

A double-arch mirror might be mounted on a combined ring/point support system such as that shown schematically in Figure 12.43. In the vertical-axis position, it rests on an interrupted air bag support ring contacting the mirror back surface at the base of the double-cantilevered contour. As the mirror axis depresses toward the horizon, the weight is progressively picked up by three or more radial supports inserted into sockets in the mirror base. At the horizontal-axis position, the mirror

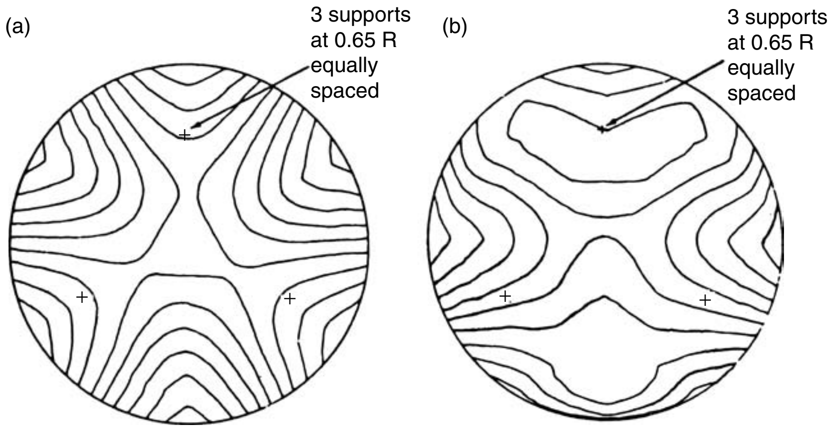

FIGURE 12.42 Surface deformation contour patterns computed for a 20-in. (50.8-cm)-diameter double-arch mirror on three-point supports with (a) axis vertical and (b) axis horizontal. Contour intervals are 0.432×10^{-6} in. in view (a) and 0.482×10^{-7} in. in view (b). (From Vukobratovich, D., Iraninejad, B., Richard, R.M., Hansen, Q.M., and Melugin, R., *Proc. SPIE*, 332, 419, 1982.)

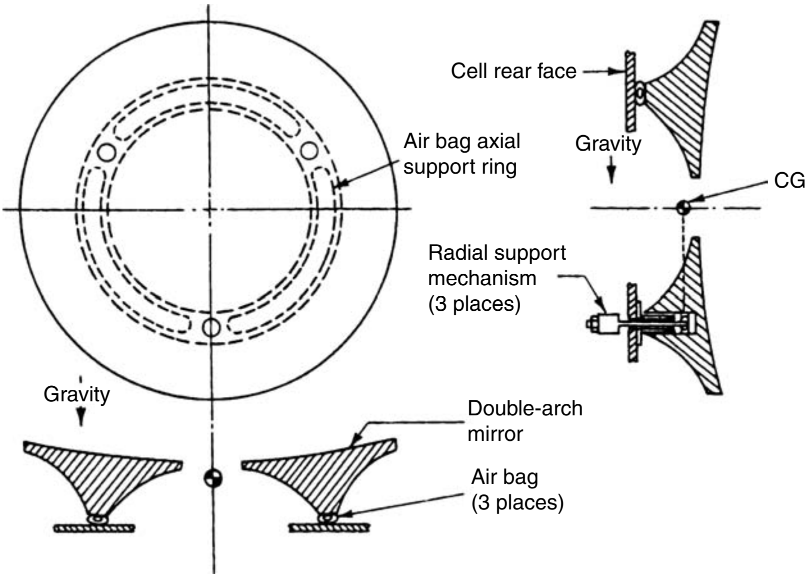

FIGURE 12.43 Schematic of a combined air bag ring axial and three-point radial support system for a double-arch mirror.

weight is supported entirely by the radial supports. They act in the plane through the mirror center of gravity to minimize optical surface deformation. The radial support shown in Figure 12.43 is of the general type shown in more detail on the right in Figure 12.6. The air bag ring support is similar to that sketched in Figure 11.6.

Another mount design for a 20-in. (50.8-cm)-diameter experimental double-arch fused-silica primary mirror was described by Iraninejad et al. (1983). As shown in Figure 12.44, the mirror was to be supported by three equally spaced clamp and flexure assemblies oriented so the flexures were compliant in the radial direction, but stiff in all other directions. This allowed the aluminum mounting plate to contract differentially with respect to the mirror as the temperature was reduced to operate at about 10 K. Each mirror clamp was a "T-shaped" piece made of Invar 36 that engaged a conical hole machined inside the thickest portion of the mirror's back. The twin flexures were 91-mm (3.6-in.)-long × 15-mm (0.6-in.)-wide parallel blades with high fundamental frequency. They were to be made of 0.04-in. (1.0-mm)-thick 6Al-4V-ELI titanium. The blades would be separated by 25 mm (1.0 in.).

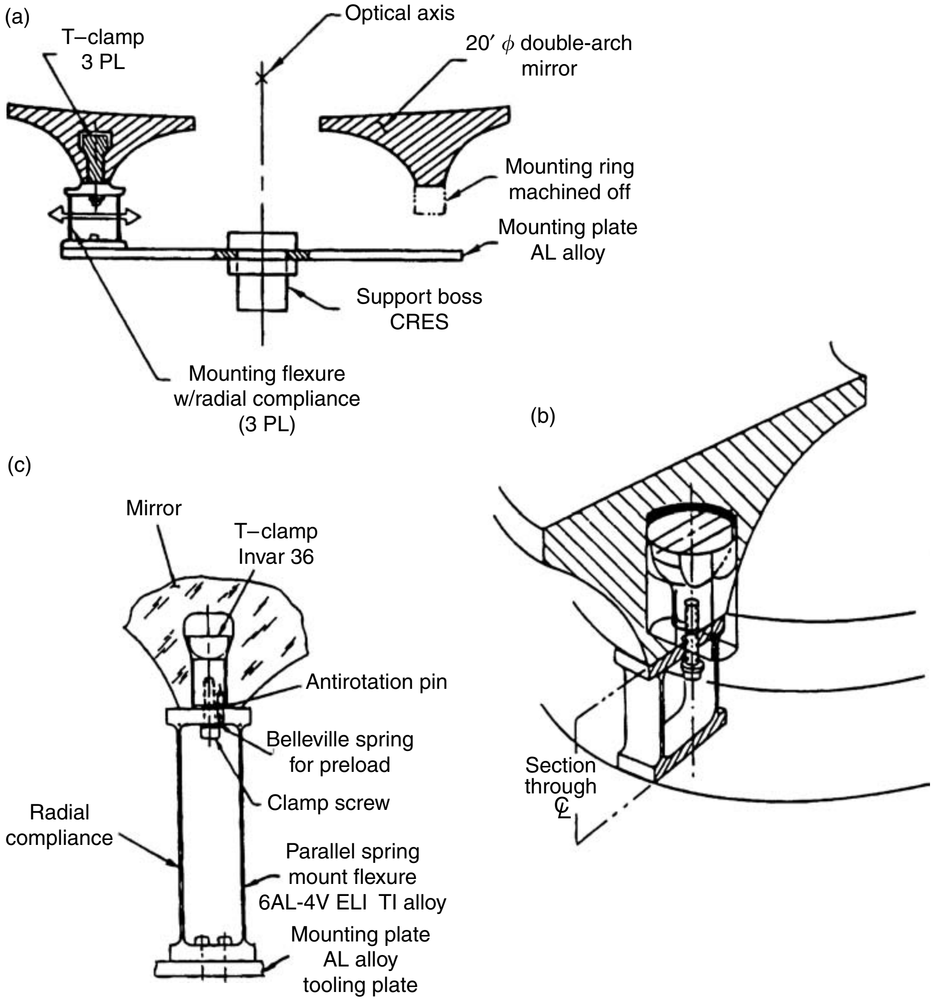
(a)
T–clamp
3 PL
Optical axis
20′ ϕ double-arch
mirror
Mounting ring
machined off
Mounting plate
AL alloy
Support boss
CRES
Mounting flexure
w/radial compliance
(3 PL)
(b)
(c)
Mirror
T–clamp
Invar 36
Antirotation pin
Belleville spring
for preload
Clamp screw
Radial
compliance
Parallel spring
mount flexure
6AL-4V ELI TI alloy
Mounting plate
AL alloy
tooling plate
Section
through
℄

FIGURE 12.44 An early design for mounting the SIRTF (now Spitzer) primary mirror: (a) sectional view of the assembly, (b) isometric view of one clamp/flexure mechanism, and (c) sectional view through the latter mechanism. (From Iraninejad, B., Vukobratovich, D., Richard, R., and Melugin, R., *Proc. SPIE*, 450, 34, 1983.)

A FEA study of this mounting arrangement indicated that the design was capable of surviving (with some damage) a crash landing of the Space Shuttle, as well as retaining full mirror performance after exposure to Shuttle launch loads.

12.6 BIPOD MIRROR MOUNTS

Bipod flexures are used in many high-precision mirror mount applications. In such a mount, three bipod subassemblies comprising six adjustable-length legs are attached to the back or edge of the mirror. A typical concept is shown in Figure 12.45. Each of the flexures is equivalent to a two-strip hinge or cross-strip flexure and provides rotational compliance. An advantage is its virtual pivot location. By adjusting the angles of the two legs in each bipod, the instantaneous pivot point can be located in the mirror's neutral plane at its CG even though the bipods are not actually attached to the mirror at that point. A two-axis flexure feature is usually built into each end of each strut or leg to prevent moments from being coupled into the mirror (Vukobratovich, 1988). Use of the bipod configuration with flexure legs allows temperature-change-induced variations in the dimensions of the adjacent structure to occur with reduced effect on the mirror.

Ulmes (1989) described a bipod mounting for a lightweight flat mirror intended for object-space scanning of the line of sight of a 110 in. (2.79 m) EFL, *f*/5.6 aerial reconnaissance camera. This elliptical mirror, illustrated in Figure 12.46, was made of fused ULE in a 4.55-in. (11.56-cm)-thick unsymmetrical closed sandwich configuration with 1.50-in. (3.81-cm)-square cells and 0.08-in. (2.03-mm)-thick webs. The front face sheet thickness was 0.20 in. (0.51 cm), whereas that of the rear face sheet was 0.15 in. (0.38 cm). An elongated perforation at the center of the mirror allowed the converging beam from the catadioptric optics to pass to the image behind the scan mirror (see Figure 12.47).

The bipod mounting for the mirror is shown in Figure 12.48. Each leg was attached to the back plate of the mirror with a ball joint. Intersections of the axes of the legs were located at the mirror's neutral plane generally in the manner shown in Figure 12.45. Vukobratovich et al. (1990) provided a detailed description of this mounting. The foot of each leg was attached to a concave spherical socket that clamped over a glass ball bonded to the mirror. These balls were equispaced on a common diameter. The bipod legs had "necked down" sections at each end that acted as flexures to minimize transfer of moments into the mirror.

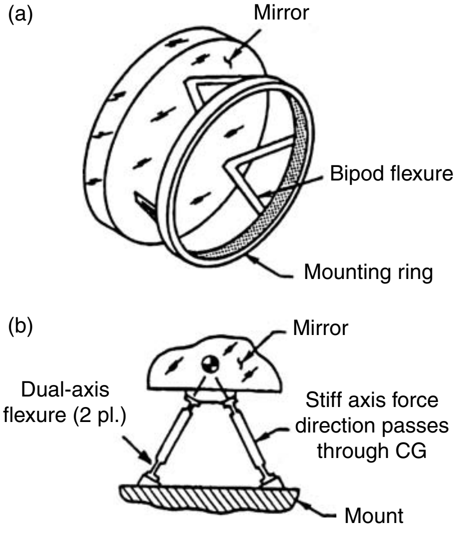
(a)
Mirror
Bipod flexure
Mounting ring
(b)
Mirror
Dual-axis flexure (2 pl.)
Stiff axis force direction passes through CG
Mount

FIGURE 12.45 Concept for a bipod-type flexure mirror mount: (a) isometric view, (b) side view. (From Vukobratovich and Richard, 1988.)

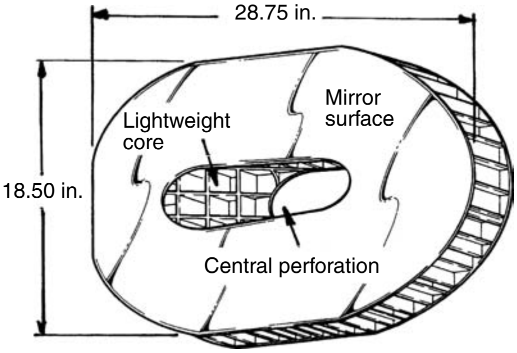

FIGURE 12.46 Schematic illustration of a lightweighted scan mirror used in a catadioptric camera system. (Adapted from Ulmes, J.J., *Proc. SPIE*, 113, 116, 1989.)

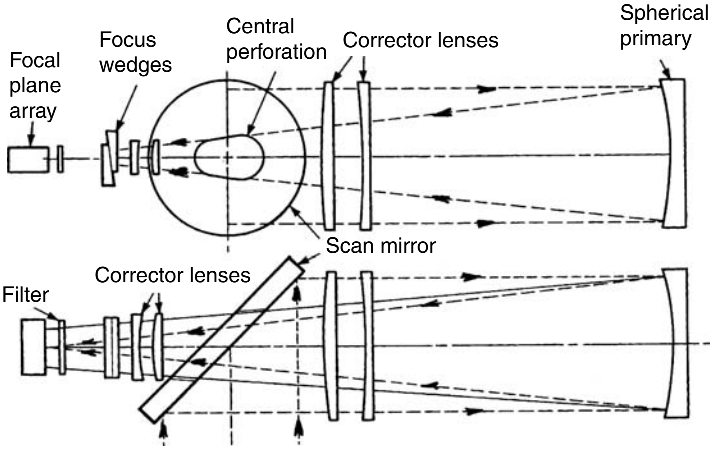

FIGURE 12.47 Optical schematic of the 110 in. (2.79 m) EFL, *f*/5.6 catadioptric lens featuring the scan mirror of Figure 12.46. (Adapted from Ulmes, J.J., *Proc. SPIE*, 113, 116, 1989.)

Sawyer et al. (1999) described another bipod mirror mounting that was developed for a space application. This mount provided three-axis linear motions of at least 3 mm (0.118 in.) plus three tilts and hence allowed adjustment of all six DOF. The mount was designed for easy access to the adjustments from behind the mirror and had positive locking means for long-term microradian-level stability. The same mount design accommodated multiple different types of reflective optical components of 12.7 to 25.4 cm (5 to 10 in.) dimensions and weights of 0.3 to 1.75 kg (0.66 to 3.8 lb) used at different locations in the optical system. The bipod arrangement allowed angular motions of off-axis mirrors to be centered at remote points on a common optical axis. A motion algorithm based on the hexapod control laws used for flight motion simulators was implemented to facilitate adjustment of each component under closed-loop computer control.

Figure 12.49 shows front and rear views of the mount as used with an off-axis mirror, while Figure 15.20 shows details of one bipod subassembly with its basic components identified. The retainer ring, seat, and retainer nuts provide the spherical bearing at each end of each leg that is required to preserve the kinematic motion.

For applications involving an off-axis mirror, a removable reflective vertex ball fixture (not shown) is attached to the bracket by way of a ball-vee-flat kinematic interface to locate the virtual vertex of the parent surface. This vertex ball would not be needed for simple flat- or spherical-mirror applications.

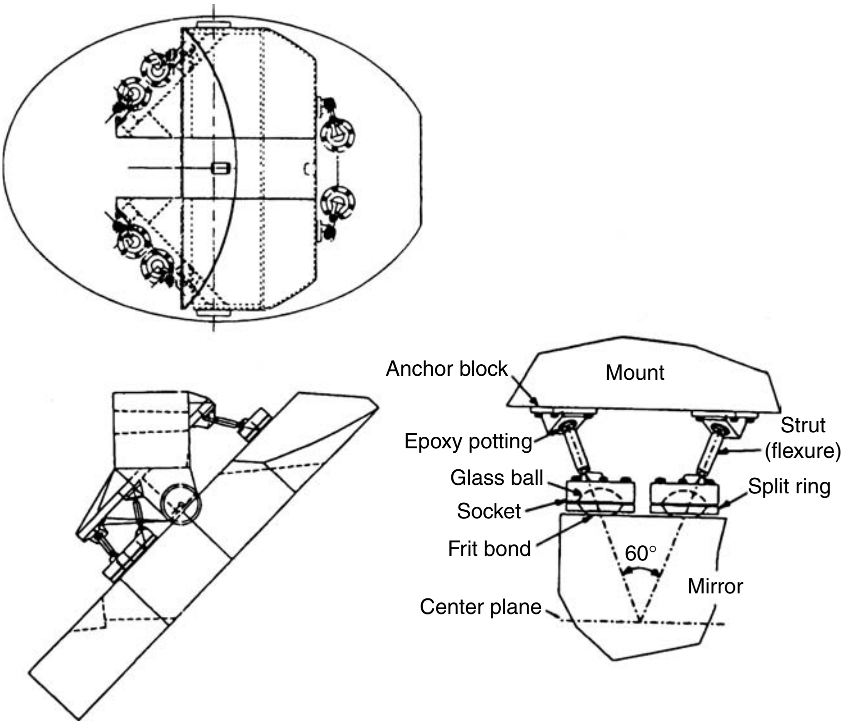
Anchor block
Mount
Strut
(flexure)
Epoxy potting
Glass ball
Split ring
Socket
Frit bond
60°
Mirror
Center plane

FIGURE 12.48 Bipod mounting arrangement for the scan mirror of Figure 12.46. (Adapted from Ulmes, J.J., *Proc. SPIE*, 113, 116, 1989.)

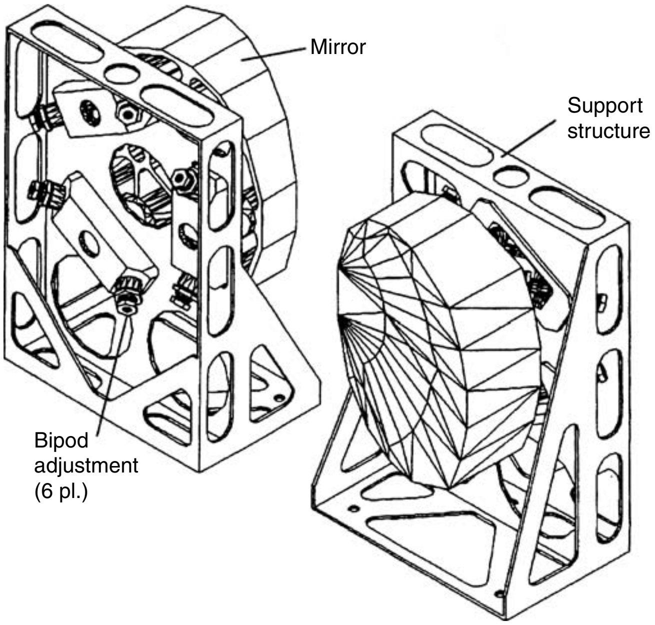
Mirror
Support
structure
Bipod
adjustment
(6 pl.)

FIGURE 12.49 Front and rear views of a typical mirror mounting with six DOF adjustable bipod supports. (Adapted from Sawyer, K.A., Hurley, B.N., Brindos, R.R., and Wong, J., *Proc. SPIE*, 3786, 281, 1999.)

Sawyer et al. (1999) described use of the locking mechanism at the outer end of a leg as follows: the lock seat is held from rotating while the adjustment nut is backed out. This action seats the retainer ring on the slack side of the leg ball. The adjuster nut stops when all clearance between the retainer nut and the lock seat is removed. The split nut immediately jams and locks the adjustment firmly. With practice, the authors were able to successfully lock all motions after fine alignment without degradation of that alignment.

Another example of the use of a bipod mounting is the radial support for the 2.705-m (106.50-in.)-diameter lightweighted monolithic Zerodur primary mirror of the Stratospheric Observatory for Infrared Astronomy (SOFIA) telescope. (For summaries of the development of this telescope, see Kaercher [2003] and Krabbe [2003]). According to Bittner et al. (2003), the mirror weighs 885 kg (1951 lb). This represents a weight reduction of ~ 80% from that of a plano-concave solid mirror fitting into the same envelope. The mass density of the mirror is 154 kg/m^3.

A back view of this mirror in its complex mount is shown in Figure 12.51. The mirror is attached to the ends of three bipods that are located at the ends of the three lateral support arms shown in the exploded view of Figure 12.52. Two of the bipods (see one labeled "A-frame" in Figure 12.52) may be seen in Figure 12.53(a). They are oriented tangentially to the mirror rim. Each bipod is a curved stainless steel bar as shown by the FEA model in view (b) of Figure 12.53. Flexures are built into each bipod to provide universal joint bending at four places. The ends of the bipods are attached with screws to Invar pads that are bonded to the mirror rim. Each bipod is stiff in the direction tangential to the mirror rim.

The axial support for the SOFIA mirror is an 18-point Hindle mount with three whiffletrees configured as shown in Figure 12.54. These whiffletrees are attached to the mirror support beams identified in Figure 12.52.

Because the normal mode of operation of the SOFIA telescope is in a Boeing 747SP aircraft with no window, air stream turbulence will cause extreme vibrational disturbance at frequencies up to 100 Hz. The telescope and all its parts must therefore be of high stiffness. This is the reason for the complex designs of both the axial and radial supports for the primary mirror. Bittner et al. (2003) indicated the first eigenfrequency (free–free) of the mirror to be 240 Hz. These results are due to a large degree

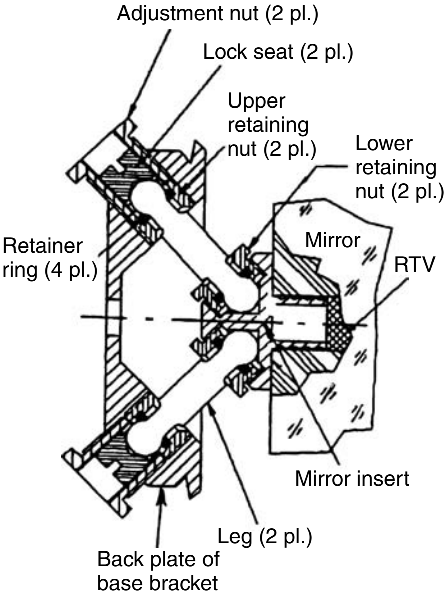

FIGURE 12.50 Details of one bipod subassembly for the mount shown in Figure 12.49. (Adapted from Sawyer, K.A., Hurley, B.N., Brindos, R.R., and Wong, J., *Proc. SPIE*, 3786, 281, 1999.)

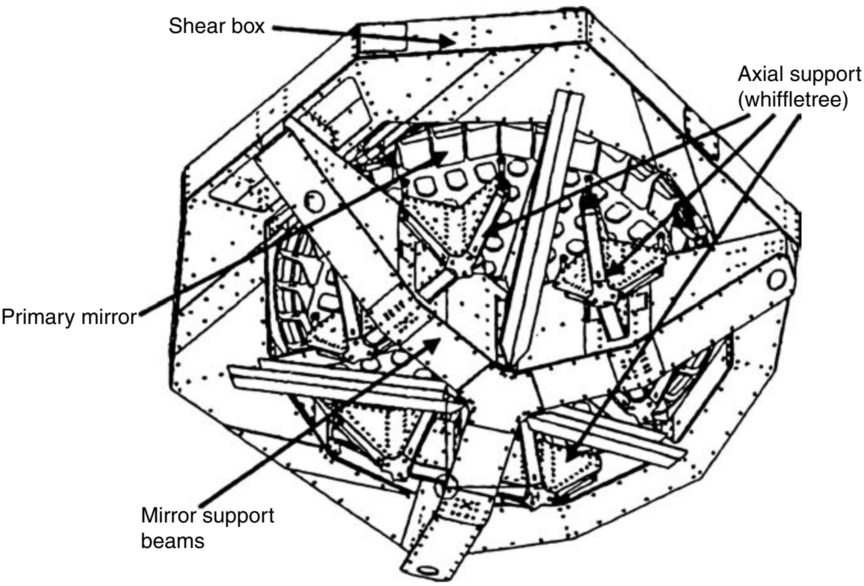

FIGURE 12.51 Back view diagram of the SOFIA primary mirror in its 18-point Hindle-type axial mounting. (From Erdmann, M., Bittner, H., and Haberler, P., *Proc. SPIE*, 4014, 309, 2000.)

to the use of a high-stiffness, low-density, low-CTE, carbon-fiber-reinforced plastic material in the mounting. Joints are bonded and riveted. Other materials used are steel and titanium. The optomechanical design is athermalized by judicious choice of materials, component dimensions, and intercomponent interfaces. Only low-outgassing materials are used in the mirror mounting so the mirror can be cleaned and recoated without removing it from the cell. To provide greater performance margin within the tight image-quality budget, the final figuring of the mirror surface compensates for the predicted surface deformation at the 45° mean elevation of the telescope during operation.

12.7 THIN FACE SHEET MIRROR MOUNTS

12.7.1 General Considerations

The inherent flexibility of thin monolithic face sheets used as mirror substrates leads to the use of axial support systems that apply forces at many points on the back of the mirror or in or near the plane of the mirror's CG. Optimization of the distribution of N axial support points for thin face sheet mirrors was the subject of a detailed paper by Nelson et al. (1982). To find the gravitationally induced deflections of a circular plate supported by a series of points, they divided the ensemble into groups of k points uniformly distributed around circles of fixed radius as shown in Figure 12.55. By superposition of the effects due to the individual groups, the total deflections of the surface were determined. Optimization involved variation of the forces, radii, and azimuthal orientations of the groups to minimize the rms deflection. Reflection symmetry was taken advantage of in order to reduce the mathematical complexity of finding a minimum in a ($3N$ - 4)-dimensional space, where N is the total number of support points.

Nelson and his coworkers found that the smallest rms deflections resulted from points arrayed in triangular patterns and that an infinite-sized triangular grid gave the best possible solution owing to its freedom from edge effects. They expressed the plate deflection $W_{(\rho,\Theta)}$ by the expression

$$W_{(\rho,\,\theta)} = \sum\nolimits_{1}^{n} \varepsilon_i w_i(n_i,\, \beta_i,\, \rho,\, \theta - \varphi_i) \tag{12.2}$$

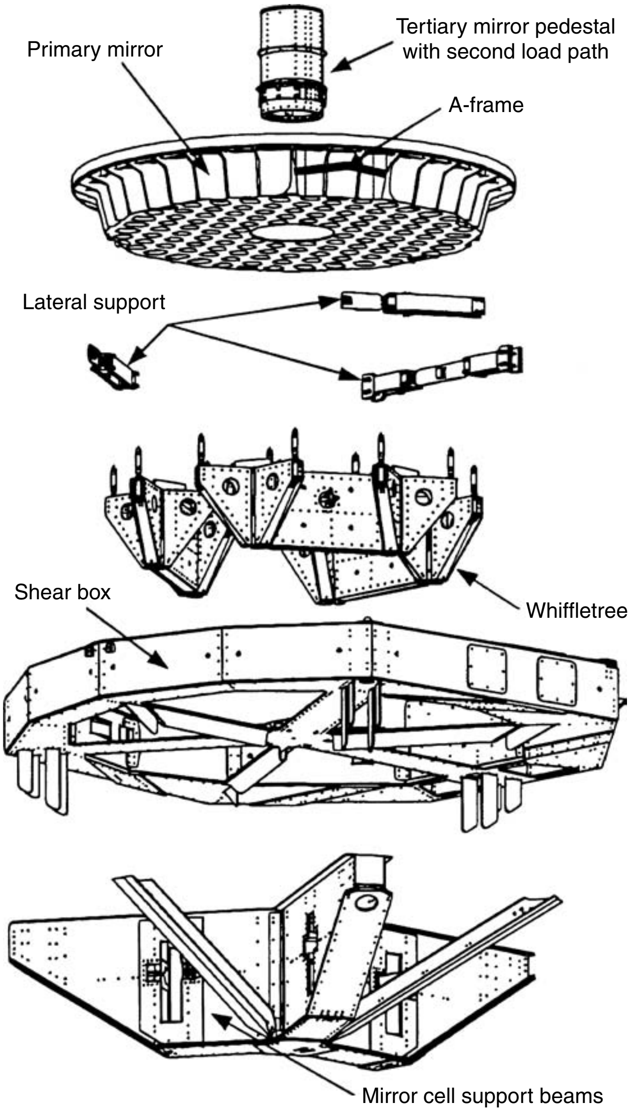
Primary mirror
Tertiary mirror pedestal with second load path
A-frame
Lateral support
Shear box
Whiffletree
Mirror cell support beams

FIGURE 12.52 Exploded view of the SOFIA primary mirror mount assembly. (From Bittner, H., Erdmann, M., Haberler, P., and Zuknik, K.-H., *Proc. SPIE*, 4857, 266, 2003.)

where n is the number of rings in the pattern, ε_i the fractional load carried by the ith ring, w_i the plate deflection with a single ring, n_i the number of points on the ith ring, β_i the radius of the ith ring, ρ the ring radius, and φ_i the azimuthal angular offset of points on the ith ring. This deflection was optimized for a variety of support configurations including as many as 36 support points. Table 12.2 lists parameters of interest for each of the 11 configurations. Shear effects are ignored in this table. In addition to the parameters identified above, we find the number of variables used in the optimization process, the applicable γ_N and the characteristic ratio of p-v to rms surface deflections. The parameter γ_N becomes a fixed constant for an optimized support configuration, at least in the limit of large N. For small values of N, there will be noticeable edge effects that will make γ_N a function of the number of support points. As the number of support points increases, γ_N will decrease to an asymptotic limit γ_∞. Improperly optimized support systems will, of course, have a larger γ than

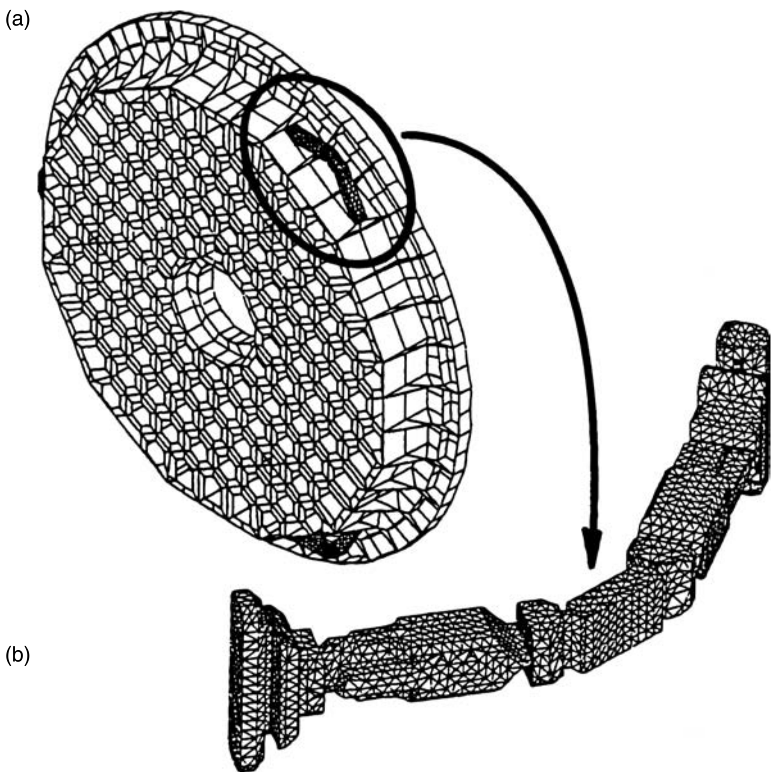

FIGURE 12.53 FEA models of the SOFIA primary mirror with three bipods attached for radial and azimuthal support. Note the multiple flexures in the bipod. (Adapted from Geyl, R., Tarreau, P., and Plainchamp, P., *Proc. SPIE*, 4451, 126, 2001.)

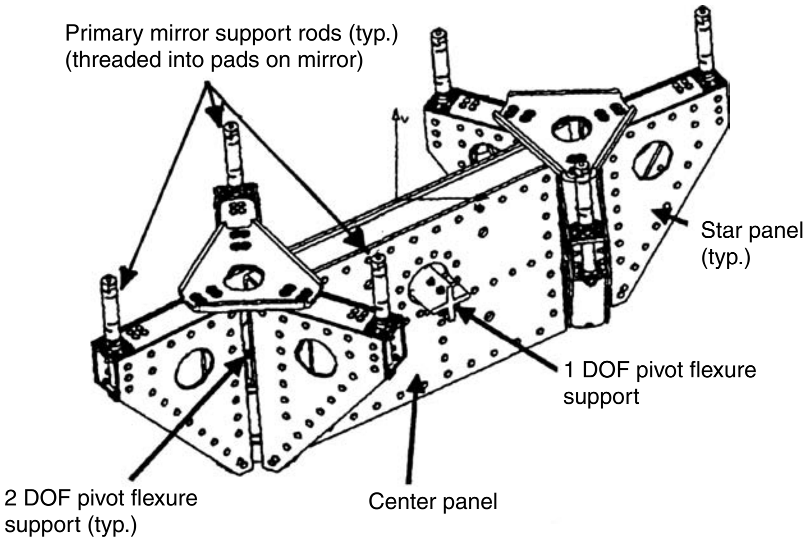
Primary mirror support rods (typ.)
(threaded into pads on mirror)
Star panel
(typ.)
1 DOF pivot flexure
support
2 DOF pivot flexure
support (typ.)
Center panel

FIGURE 12.54 One whiffletree from the SOFIA mirror mounting of Figure 12.52. (From Erdmann, M., Bittner, H., and Haberler, P., *Proc. SPIE*, 4014, 309, 2000.)

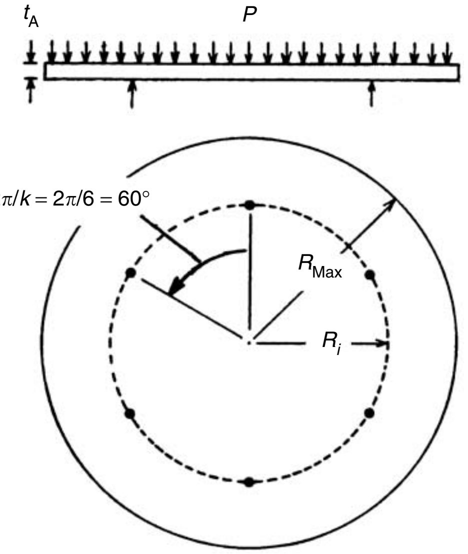

FIGURE 12.55 Typical geometry and notation for axially supporting an axis-vertical circular mirror on one ring with $k = 6$ points. P is the applied force distributed uniformly as in self-weight deflection. (From Nelson, J.E., Lubliner, J., and Mast, T.S., *Proc. SPIE*, 332, 212, 1982.)

otherwise. Recognizing that it is a measure of the efficiency of a given support configuration, Nelson et al. (1982) named γ_N the "support point efficiency."

The rms deflection due to gravitational bending may be computed from the support point efficiency γ_N by using the following equation:

$$\delta_{\text{rms}} = \gamma_N (q/F)(A/N)^2 \tag{12.3}$$

where q is the applied force per unit area, A the mirror area, N the number of support points, and F the flexural rigidity computed from

$$F = \frac{E_G t_A^3}{12(1-\nu_G^2)} \tag{12.4}$$

Here E_G and ν_G are the mirror material's Young's modulus and Poisson's ratio, respectively, and t_A the mirror thickness. Thickness variation as a function of zonal radius is neglected, and ν_G is assumed to be 0.25.

The effects of shear within the mirror are ignored in Eq. (12.3). An estimate of the deflection with shear effects can be made by multiplying the rms deflection by a factor $[1 + (2t_A^2/u^2)]$, where μ is the effective distance between support points. This distance is $\sim D_G/(2N^{1/2})$, where N is the total number of supports and D_G the mirror diameter.

To illustrate the findings reported in Nelson et al. (1982), consider Figure 12.56. Here we see the possible support topologies for an 18-point system. Threefold reflection symmetry reduces the complexity to 60° sectors. The nomenclature gives, in the superscript, the number of points on one axis of symmetry and, in the subscript, the number of points on the other axis. The optimal locations of the 18 points are indicated in Figure 12.57(a), while the resulting computed deflection contour maps are shown in Figure 12.57(b). The contour interval for each plot is one half the rms deflection of the surface from its mean deflection. The heavy lines represent the mean deflections. Arrangements18_0^0, 18_1^1, and 18_2^2 are equally efficient.

TABLE 12.2
Numerical Values for Geometric Parameters in N-Point Mirror Support Systems

N	No. of variables	γ_N ($\times 10^{-3}$)	p-v/rms	$n_i, \beta_i, \varepsilon_i, \varphi_i$								
1	0	2.60	3.8									
2	1	8.56	3.9	$\beta = 0.354$								
3	1	5.76	4.2	$\beta = 0.645$								
6_1^1	1	2.93	4.3	$\beta = 0.681$								
7_1^1	2	2.36	4.9	$n = 1$	6							
				$\beta = 0$	0.737							
				$\varepsilon = 0.118$	0.882							
				$\varphi = 0$	0							
9_1^1	5	3.76	5.0	$n = 3$	3	3						
				$\beta = 0.282$	0.794	0.770						
				$\varepsilon = 0.231$	0.364	0.405						
				$\varphi = 0$	0	1.047						
12_1^1	6	1.94	5.1	$n = 3$	3	3	3					
				$\beta = 0.315$	0.766	0.826	0.826					
				$\varepsilon = 0.278$	0.284	0.219	0.219					
				$\varphi = 0$	1.047	0.350	−0.350					
15_1^1	7	2.32	5.4	$n = 3$	3	3	3	3				
				$\beta = 0.319$	0.776	0.841	0.776	0.841				
				$\varepsilon = 0.283$	0.205	0.154	0.205	0.154				
				$\varphi = 0$	0.783	0.261	-0.783	-0.261				
18_1^1	9	1.89	5.5	$n = 3$	3	3	3	3	3			
				$\beta = 0.474$	0.319	0.817	0.854	0.817	0.854			
				$\varepsilon = 0.162$	0.207	0.173	0.142	0.173	0.142			
				$\varphi = O$	1.047	0.782	0.266	-0.782	0.266			
27_1^1	14	1.65	5.7	$n = 3$	3	3	3	3	3	3	3	3
				$\beta = 0.204$	0.874	0.478	0.555	0.879	0.857	0.555	0.879	0.857
				$\varepsilon = 0.115$	0.105	0.135	0.116	0.095	0.111	0.116	0.095	0.111
				$\varphi = 0$	0	1.047	0.340	0.428	0.838	−0.340	−0428	−0.838
36_1^1	9	1.63	6	$n = 6$	6	6	6	6	6			
				$\beta = 0.257$	0.577	0.577	0.883	0.883	0.883			
				$\varepsilon = 0.1671$	0.181	0.181	0.155	0.161	0.155			
				$\varphi = 0$	0.265	0,782	0.170	0.524	0.877			

Source: Adapted from Nelson, J.E., Lubliner, J., and Mast, T.C., *Proc. SPIE*, 332, 212, 1982.

To quantify these results, let us consider a thin Zerodur face sheet supported by 18 points arranged in an 18_1^1 pattern. Assumed dimensions of this mirror and various derived parameters are as listed in Table 12.3. From Table 12.2, the mirror's support point efficiency γ_N is 1.89×10^{-3}. From Eq. (12.4), its flexural rigidity $F = (13.6 \times 10^6)(2.667)^3/[(12)(1 - 0.240^2)] = 2.281 \times 10^7$ lb-in. The rms deflection of the mirror is then $\delta_{\text{rms}} = (1.89 \times 10^3)(0.243/2.281 \times 10^7)(1256.637)/18)^2 = 9.81 \times 10^8$

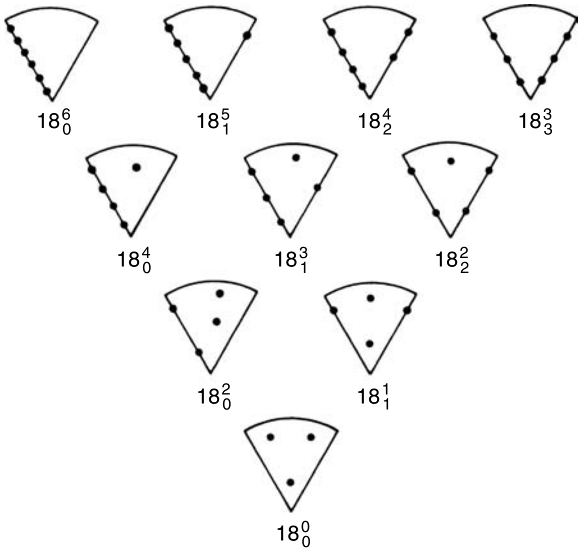

FIGURE 12.56 The possible support topologies for an 18-point axial support for a large thin mirror. The nomenclature gives, in the superscript, the number of points on one axis of symmetry and, in the subscript, the number of points on the other axis. (From Nelson, J.E., Lubliner, J., and Mast, T.S., *Proc. SPIE*, 332, 212, 1982.)

in. (2.489×10^6 mm). At $\lambda = 0.633$ μm, this equals 0.004 wave. Since for this mounting configuration the value of $\delta_{\text{p-v}}/\delta_{\text{rms}}$ is (from Table 12.2) equal to 5.5, we easily compute $S_{\text{p-v}}$ as 0.022 wave. Shear effects in the mirror would increase this deflection by 157% to 0.034 wave. For some applications, this would be considered a reasonable self-weight surface deflection. If the estimated deflection is too large, the number of mirror supports could be increased at the cost of increased mount complexity.

In some very-large-telescope mirror designs, the substrate is not monolithic, but divided into segments. This is desirable for fabrication reasons as ground-based mirror diameters grow in size or to accommodate launch vehicle size restrictions for space-borne telescopes. Substrates with pie-shaped or hexagonal segmentation receive consideration for both types of applications. Figure 12.58 shows a seven-segment, thin face sheet ULE mirror of 4.0 m (13.1 ft) overall diameter. The outer segments were ~ 1.7 cm (0.67 in.) thick and made from 2-m (80-in.)-diameter blanks. Obviously, the segments were extremely flexible and fragile. They required the utmost care at all stages of fabrication and handling. The segments were figured using computer-controlled techniques to <0.04 μm surface error from the required aspheric contour. Support was provided by a multipoint active control system.

12.7.2 THE KECK TELESCOPES

Nelson et al. (1982) described a design using 36 actively controlled hexagonal segments to form the 10 m (394 in.) mosaic primary mirrors of the Keck telescopes. Active control of intersegment alignment is an essential feature of the system design. The control system for such a mirror treats each segment as a rigid body with three DOF (two tilts and one axial position). Actuators placed at three points on the back of each segment as indicated in Figure 12.59 provide active support relative to a common support structure. The sensors that provide signals to the actuators through a computer monitor displacements between adjacent segments by measuring changes in electrical capacitance.

The interface to each segment actually consists of 36 point supports. Twelve are associated with each actuator (see Figure 12.60). By using this large number of support points, the 7.5-cm (2.95-in.)-thick hexagonal segments of 1.8 m (70.9 in.) circumscribed diameter are adequately supported. If we consider these as a 36^1_1 distribution in the manner of our last example, we can predict that the mirror's p-v self-weight deflection would be 4.31×10^{-6} mm or 0.041λ at 0.633 μm wavelength.

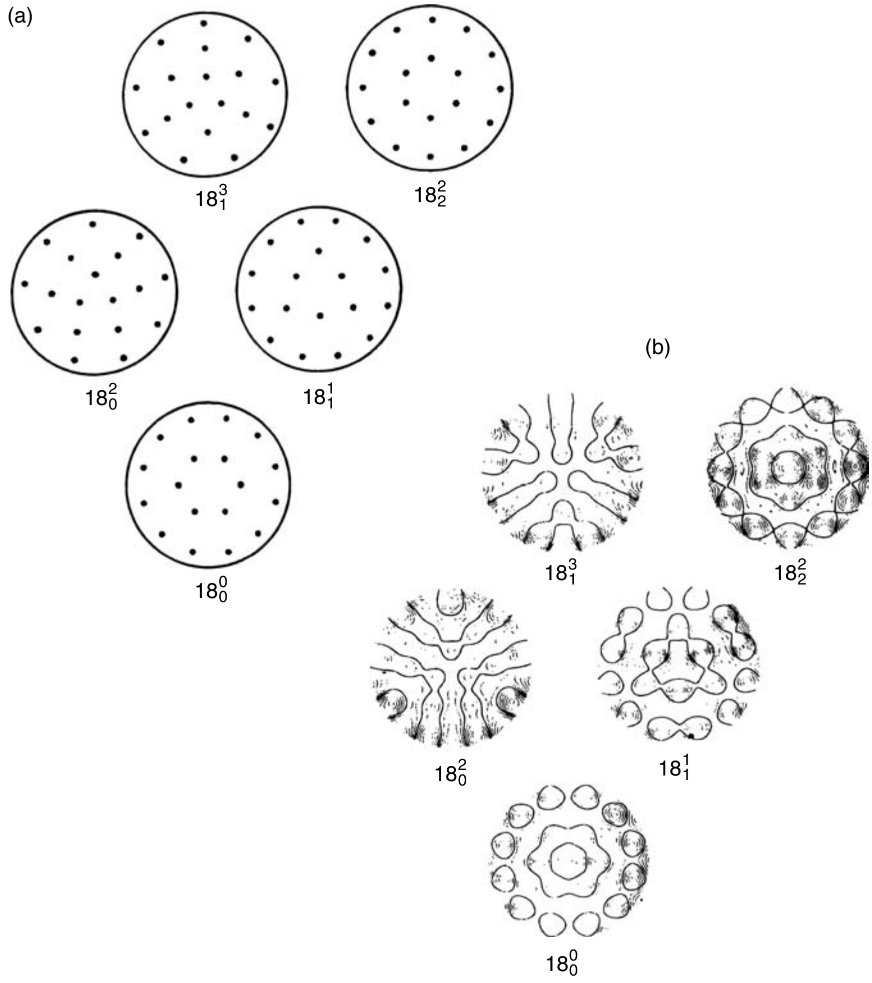

FIGURE 12.57 Results of optimization of 18-point mirror support systems: (a) Locations of points, (b) deflection contours for the same support configurations. (From Nelson, J.E., Lubliner, J., and Mast, T.S., *Proc. SPIE*, 332, 212, 1982.)

In this calculation, the effects of cutting to the hexagonal shape and of the mounting features (holes) described below are ignored. Adding the effects of internal shear, the p-v deflection of this mirror would be ~ 0.059 wave.

Each meniscus-shaped mirror segment has a diameter-to-thickness ratio of 24:1, a radius of curvature of ~ 35 m (114.8 ft), and is supported axially by a set of three whiffletrees, each interfacing with the structure at 3 points and with the mirror at 12 points as indicated in Figure 12.60. The latter interfaces are by means of flexure rods that penetrate into blind holes bored into the back of the mirror to the neutral plane. That plane is 9.99 mm (0.39 in.) in front of the midplane of the shell. The locations of the attachment points and the geometry of the whiffletrees were optimized for minimum rms mirror deflection under gravity loading in the axial direction. At the bottom of each axial support hole, the flexure rods are attached to Invar plugs that, in turn, are epoxied to the Zerodur mirror (see Figure 12.61). Iranineiad et al. (1987) showed that the thickness of the epoxy layer was critical in terms of mirror surface deformation and would be optimum at 0.25 mm (0.010 in.) thickness.

The last referenced publication defined the concept for the radial supports to the Keck segments also. A conceptual section view of one of these supports is shown in Figure 12.62. With the telescope

TABLE 12.3
Parameters for a Thin Facesheet Deflection Example in the Text

Parameter	Value
Diameter, D_G	40,000 in. (1016.000 mm)
Thickness, t_A	2.667 in. (67.742 mm)
D/t	15
Material	Zerodur
Poisson's ratio, v_G	0.240
Young's modulus, E_G	13.6×10^6 Ib/in,^{2} or in.^{3} (9.060×10^4 Mpa)
Density, ρ	0.091 lb/in,^{2} or in.^{3} (253 g/cm^3)
Area, $A = \pi(D_G/2)^2$	1256.637 in,^{2} or in.^{3} (8.107×10^5 mm^2)
Volume, $V = t_A A$	3351.451 in,^{2} or in.^{3} (5.492×10^7 mm^2)
Weight, $W = \rho V$	304.982 lb (138.340 kg)
Force/area, q	0.243 lb/in,^{2} or in.^{3} (1.673×10^3 Pa)
Number of points, N	18
Arrangement	1 1

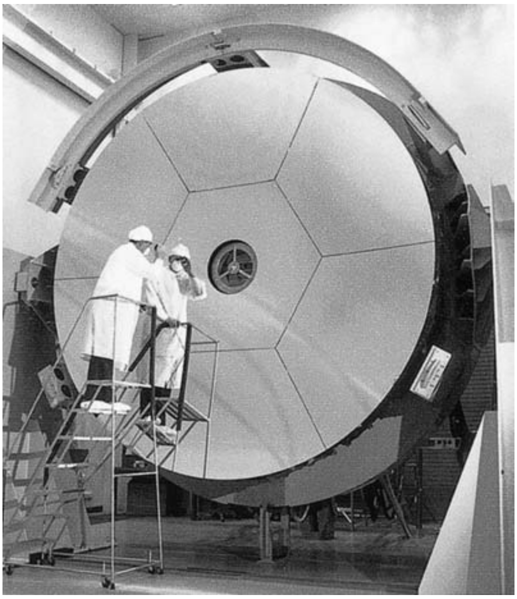

FIGURE 12.58 Photograph of a 4-m (13.1-ft) aperture, seven-segment, actively supported mirror with a thin face sheet. (Courtesy of Goodrich Corporation, Danbury, CT.)

axis horizontal, the weight of the segment is supported by a thin (0.25 mm [0.010 in.] thick) flexible stainless steel diaphragm attached at the center to a rigid post extending from the structure and at the edge to a 1-cm (0.4-in.)-thick Invar ring that is bonded into a circular blind hole of 25.4 cm (10 in.) diameter recessed into the center of the segment. Each interface between the cylindrical wall of this recess and the ring is through six flexure blades, as indicated in Figure 12.63. The Invar pads are epoxied to the wall with joints ~ 1.0 mm (0.04 in.) thick. The latter thickness is not critical.

The use of the diaphragm to support the segment radially allows it to move axially or tilt in any direction by small amounts as required to align it with respect to its neighbors. The orientation and

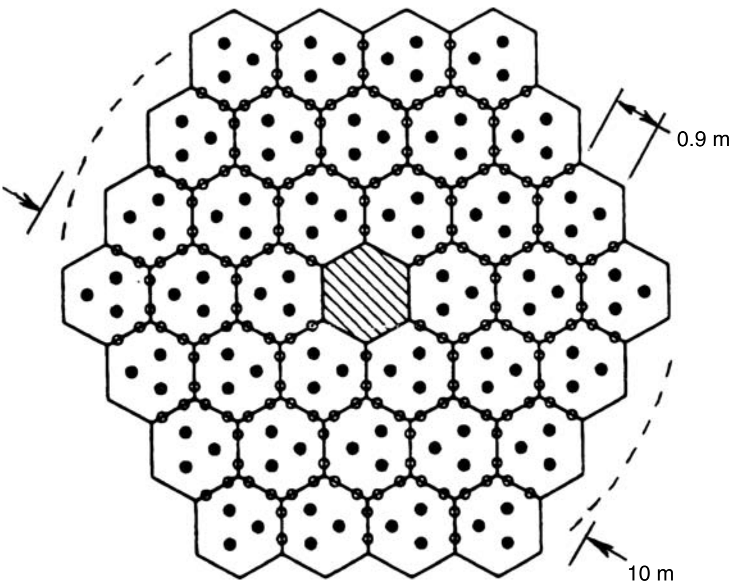

FIGURE 12.59 The locations of actuators (solid circles) and edge sensors (open circles) on the 10 m (400 in.) Keck telescope primary as seen from the concave side. (Adapted from Jared, R., Arthur, A., Andreae, S., Biocca, A., Cohen, R., Fuertes, J., Franck, J., Gabor, G., Llacer, J., Mast, T., Meng, J., Merrick, T., Minor, R., Nelson, J., Orayani, M., Saiz, P., Schaefer, B., and Witebsky, C., *Proc. SPIE*, 1236, 996, 1990.)

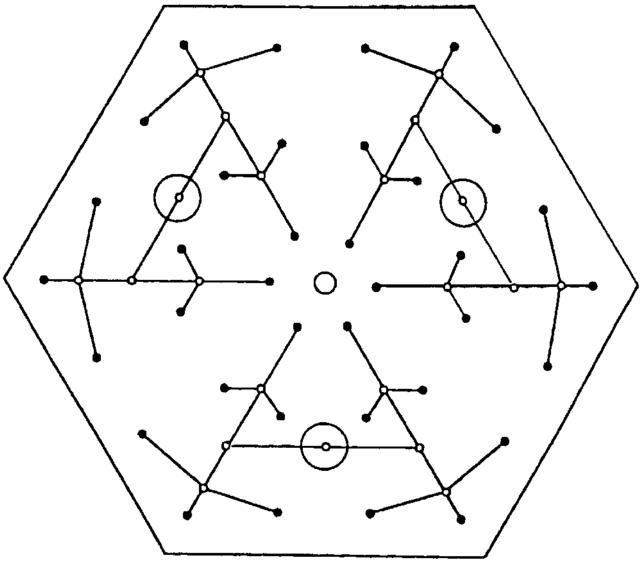

FIGURE 12.60 Schematic diagram showing locations of the three actuators (large open circles), 42 flexure pivots (small open circles), and 36 axial supports (solid circles) on one hexagonal segment of the Keck primary. (From Mast, T. and Nelson, J., *Proc. SPIE*, 1236, 670, 1990.)

axial position of each segment are measured with 12 edge sensors operating on the principle illustrated in Figure 12.64 and located as indicated in Figure 12.59. One half of each sensor is attached to one mirror and the other half to the adjacent mirror. Motions between the drive paddle and sensor body are sensed by the change in capacitance. A preamplifier/analog-to-digital converter measures

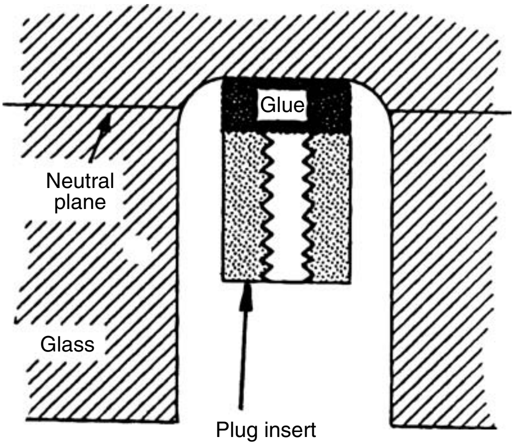

FIGURE 12.61 Schematic diagram of the axial support holes and Invar inserts bonded with epoxy into the back of a Keck primary segment. (From Iraninejad, B., Lubliner, J., Mast, T., and Nelson, J., *Proc. SPIE*, 748, 206, 1987.)

the change and produces an output proportional to the displacement. Errors in relative location of the adjacent mirrors are used to drive the three actuators on each mirror to optimize its location and orientation. The actuators (see concept in Figure 12.65) are motor-driven lead screws with encoders for feedback.

The three actuators associated with each segment are located within the cylindrical housings shown in Figure 12.66(a) at the center of each whiffletree. Some of the axial support flexures can be seen in this photo. The optical figures of the segments resulting directly from the polishing operation within the time frame of the program schedule were not adequate for the intended purpose. Mast and Nelson (1990) reported that the addition of leaf springs across the pivots of the whiffletrees as shown in Figure 12.67(b) and manual adjustment of the forces exerted by these springs would allow the mirror figure to be "tweaked" at the time of installation into the telescope to meet specifications. The set of springs attached to each whiffletree is called a "warping harness." Each spring is an aluminum bar measuring about 4 × 10 × 100 mm with an adjustment screw. Tightening the screw applies a moment to the whiffletree member. The force is measured with a strain gauge bonded to the bar. The design was intended to create moments that were stable to better than ± 5% for over a year throughout the normal operating temperature range of 2 ± 8°C and under gravity orientation changes from zenith to horizon.

Computations with an FEA model based on interferometric test results showed the moments required to correct any mirror. The strain gauges indicated when these moments had been achieved. Interferometric tests then confirmed the adjustments. Figure 12.67 shows a typical contour plot of measured minus predicted error for one segment after adjustment of the warping harness. The rms surface error of this segment is about 0.032 μm, whereas before applying the warping harness, the error was 0.21 μm. The expedient of using multiple warping harnesses proved to be faster and less costly than figuring the mirror surfaces completely using the best available techniques.

Phasing of the individual segments of the primary array of the Keck telescope to make it function as if it were a monolithic mirror is accomplished with a modified Shack-Hartman test setup as described by Chanan (1988). The apparatus can be used with faint stars as the source. By reimaging the primary at an array of microprisms, the test is conducted without the need for a full-aperture Hartman mask.

Ion figuring has been shown to be an efficient and deterministic optical fabrication method that imparts virtually no force upon an optical surface during material removal. The absence of lap/work piece edge effects and tool wear, as well as the ability to vary the removal rate locally in real time as the ion beam passes over the surface, makes this process attractive for high-aspect-ratio (thin)

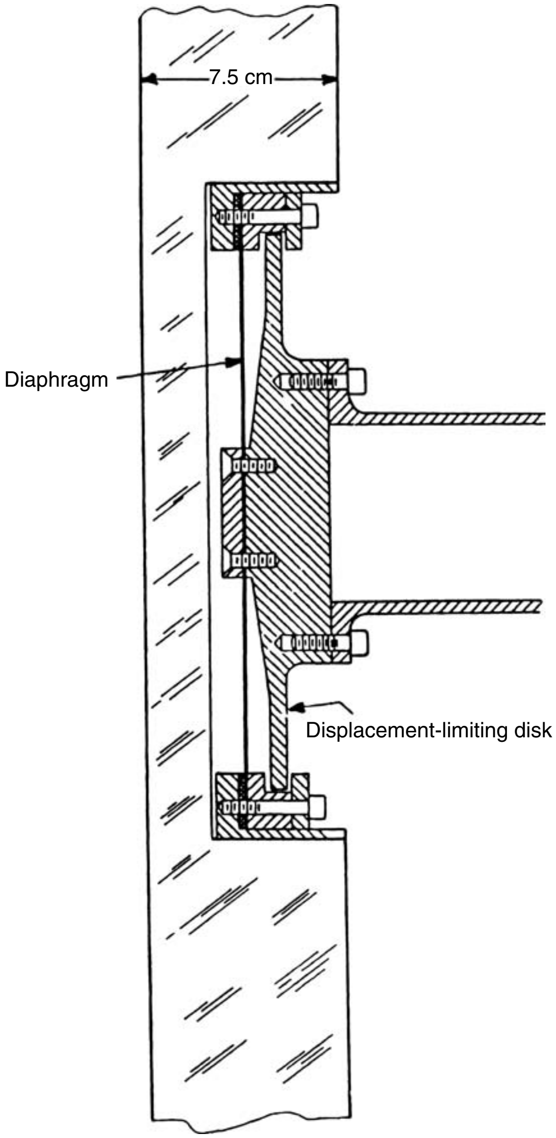

FIGURE 12.62 Radial support concept for a Keck primary mirror segment. (From Iraninejad, B., Lubliner, J., Mast, T., and Nelson, J., *Proc. SPIE*, 748, 206, 1987.)

mirrors (see Meinel et al., 1965; Wilson et al., 1988; Allen and Keim, 1989; Allen and Romig, 1990; Allen et al., 1991a; Allen, 1995). A facility capable of ion figuring large optics has been developed and applied at Eastman Kodak Company in Rochester, NY. Computer models of the ion beam-to-material interaction and of the material removal rate have been developed and confirmed experimentally. According to Allen et al. (1991b), the process was successfully applied to final figuring of several mirror segments for the Keck Telescopes.

12.7.3 ADAPTIVE MIRROR SYSTEMS

A very successful technique for optimizing optical system performance measures actual optical performance of the total optical system from object to image using natural or high-altitude artificial

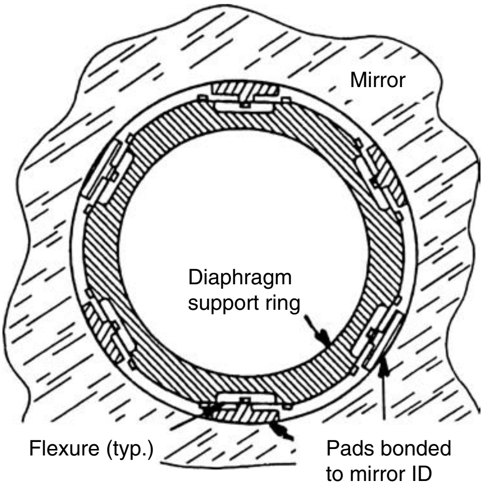
Mirror
Diaphragm support ring
Flexure (typ.)
Pads bonded to mirror ID

FIGURE 12.63 Frontal view of the radial support shown in Figure 12.62 showing tangential flexures bridging the interface between the Invar ring and the Zerodur mirror. (From Iraninejad, B., Lubliner, J., Mast, T., and Nelson, J., *Proc. SPIE*, 748, 206, 1987.)

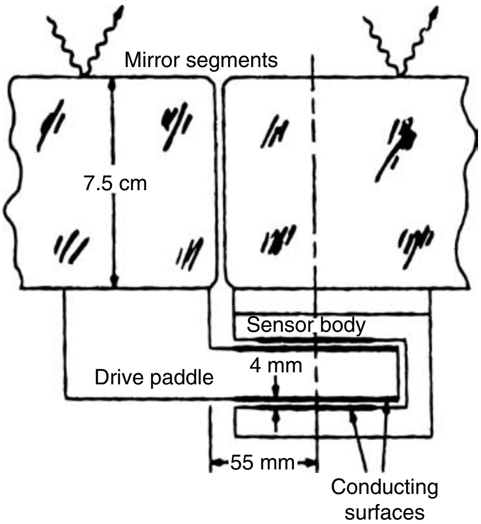
Mirror segments
7.5 cm
Sensor body
4 mm
Drive paddle
55 mm
Conducting surfaces

FIGURE 12.64 Schematic diagram of one edge sensor used to sense alignment errors between adjacent Keck mirror segments. (From Minor, R., Arthur, A., Gabor, G., Jackson, H., Jared, R., Mast, T., and Schaefer, B., *Proc. SPIE*, 1236, 1009, 1990.)

stars[*] as “point” sources and driving (or adapting) one or more mirror(s) in real time to compensate for all system errors, including the atmosphere. The system then produces a high-quality image of that source. So doing will optimize the imagery of other objects observed through that same system along the same optical path.

Coffey (2003) reported that the U.S. Air Force Research Laboratory has achieved 20 W of CW laser power in a diffraction-limited, single-frequency, projected yellow beam at 589.159 nm wavelength with which the mesospheric sodium layer at 90 km altitude above a ground-based telescope

---

[*] Sometimes called *laser beacons*.

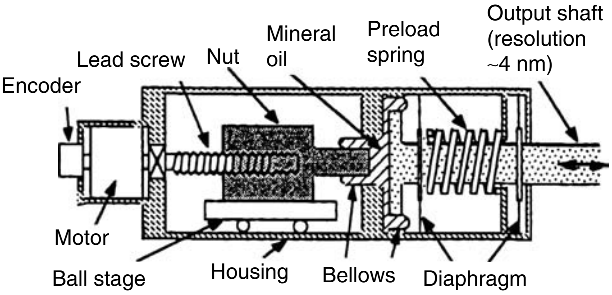
Output shaft
(resolution
~4 nm)
Preload
spring
Mineral
oil
Nut
Lead screw
Encoder
Motor
Ball stage
Housing
Bellows
Diaphragm

FIGURE 12.65 Schematic diagram showing the internal parts of one electro-mechanical/hydraulic actuator used to correct alignment errors of the Keck mirror segments. (Adapted from Meng, J., Franck, J., Gabor, G., Jared, R., Minor, R., and Schaefer, B., *Proc. SPIE*, 1236, 1018, 1990.)

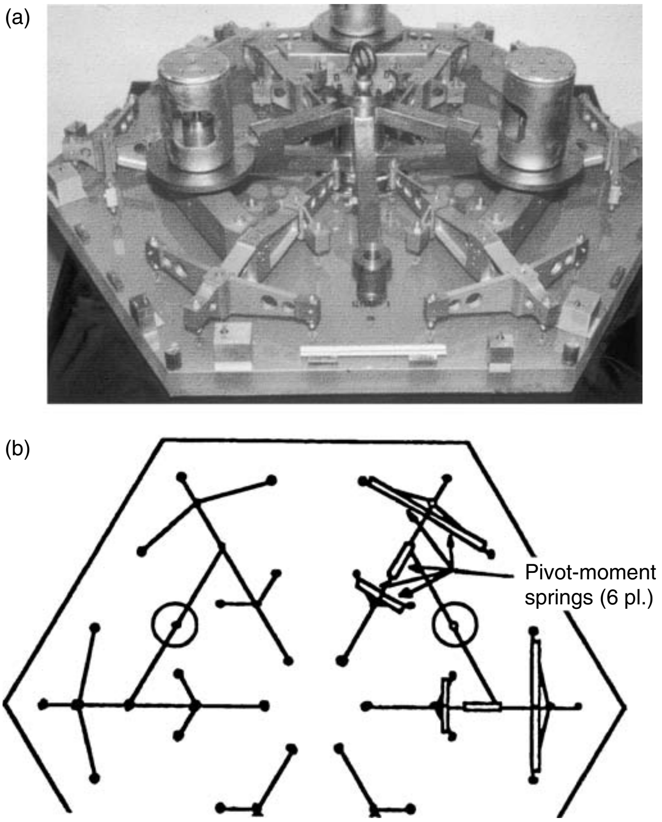
(a)
(b)
Pivot-moment
springs (6 pl.)

FIGURE 12.66 (a) Photograph of the 36-point whiffletree-type axial support system attached to a segment of the Keck primary mirror. (From Pepi, J.W., *Proc. SPIE*, CR43, 207, 1992.) (b) Diagram showing the locations of springs added to the whiffletree system in view (a) to create a warping harness used to manually adjust the shape of the polished mirror segments to final figure. (From Mast, T. and Nelson, J., *Proc. SPIE*, 1236, 670, 1990.)

could be excited to resonate and form an artificial star suitable for optical system and atmospheric effects compensation during astronomical observation. Availability of a natural star suitable for use as a guide star within the field of view of the telescope would not be necessary whenever a laser guide star can be produced.

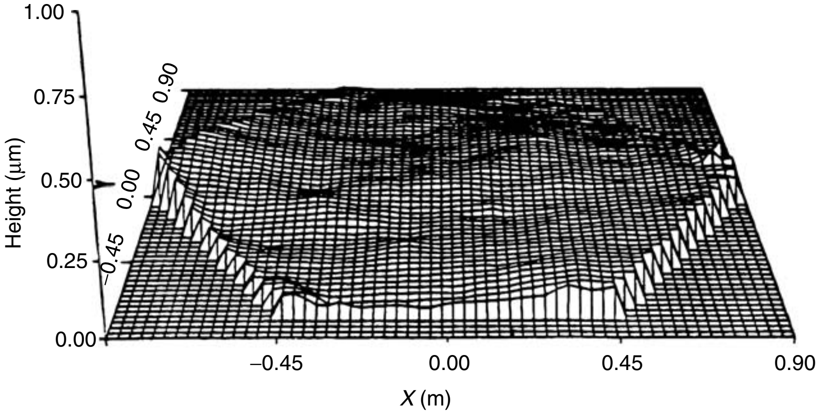

FIGURE 12.67 Interferometric test results showing the effectiveness of the warping harness on one of the Keck mirror segments. The difference between the measured and predicted error is plotted. (From Mast, T. and Nelson, J., *Proc. SPIE*, 1236, 670, 1990.)

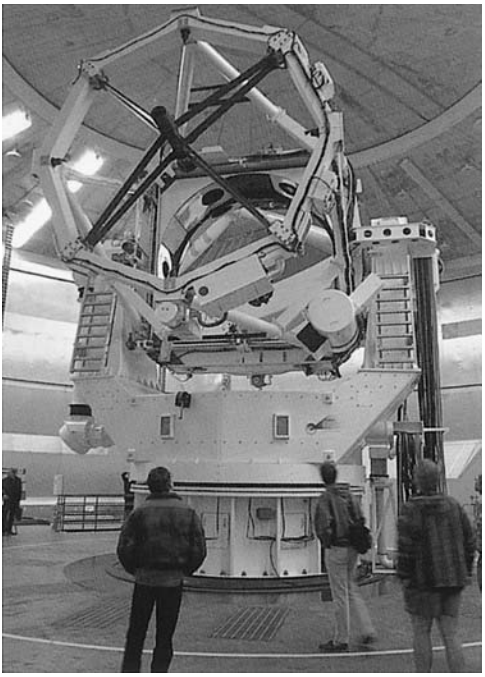

FIGURE 12.68 Photograph of the 363-cm (142.9-in.) aperture AEOS Telescope installed at the U.S. Air Force Maui Optical Station. (Courtesy of the U.S. Air Force.)

12.7.3.1 The Advanced Electro-Optical System Telescope

An example of a telescope system using adaptive optics is the Advanced Electro-Optical System (AEOS) Telescope installed at the U.S. Air Force's Maui Optical Station on Mount Haleakala to track, observe, and identify low-Earth orbit satellites, missiles, and aircraft as well as man-made objects in deep space. This *f*/200 Cassegrain telescope, shown in Figure 12.68, has a 3.67-m (144.5-in.)-diameter, *f*/1.5 primary mirror fashioned as a solid meniscus face sheet of $D_G/t_A = 22.3$. The 84 axial and 48 radial hydraulic actuators that support this mirror can correct the system's wavefront quality to provide near diffraction-limited system imaging of deep-space objects. Each actuator has two chambers, one for force generation and the other for pressure variation correction. Tangent arms stabilize the mirror radially and azimuthally. A 22 by 22 element Shack-Hartman wavefront sensor provides error signals to the control system for the telescope. The latter system was described by Kimbrell and Greenwald (1998).

The adaptive optics system has two control loops: a tip-tilt loop and a high-order wavefront correction loop. The former corrects for atmospheric effects and tracking errors while the latter corrects optical aberrations. The fine tracking function is provided by a 5.3-cm (2.09-in.)-diameter mirror that stabilizes the system line of sight at the target to <42 nrad over a dynamic range of ± 220 μrad. A 28.8-cm (11.34-in.)-diameter deformable mirror driven by 941 actuators is located at an image of the system entrance pupil to correct the wavefront reaching the cooled Si CCD array visible light image sensor. The system can be operated in either a 2 to 5.5 μm or 8 to 14 μm spectral range using cryogenically cooled Si and InSb detectors, respectively.

The AEOS telescope is mounted on a stiff concrete or steel pier that has a lowest natural frequency >20 Hz. This is inside a first building. A second building surrounds the first. The building-within-a-building design helps to isolate the optics from mechanical and acoustical vibrations. The observatory dome retracts downward during operation, so the AEOS telescope is in the open and unprotected from the wind. It experiences a wide variation of temperature. During the daytime, four air-conditioning units chill the telescope and the air within the dome to the predicted temperature of the nighttime observation period. A mirror purge system prevents moisture from condensing on the optical surface by blowing desiccated air into the mirror cell. Laminar airflow counteracts degradation effects of a warm mirror by directing conditioned air across the primary's surface (see Figure 12.69). Shortly before sunset, the dome is partially opened and outside air is pulled through the telescope truss structure to further reduce temperature differences. When the dome is retracted, the telescope is well prepared for observation.

12.7.3.2 The MMT Adaptive Secondary Mirror

Figure 12.70 depicts schematically the adaptive optics system for the new MMT telescope. The adaptive component here is the secondary mirror of the Cassegrain system. IR light from the telescope

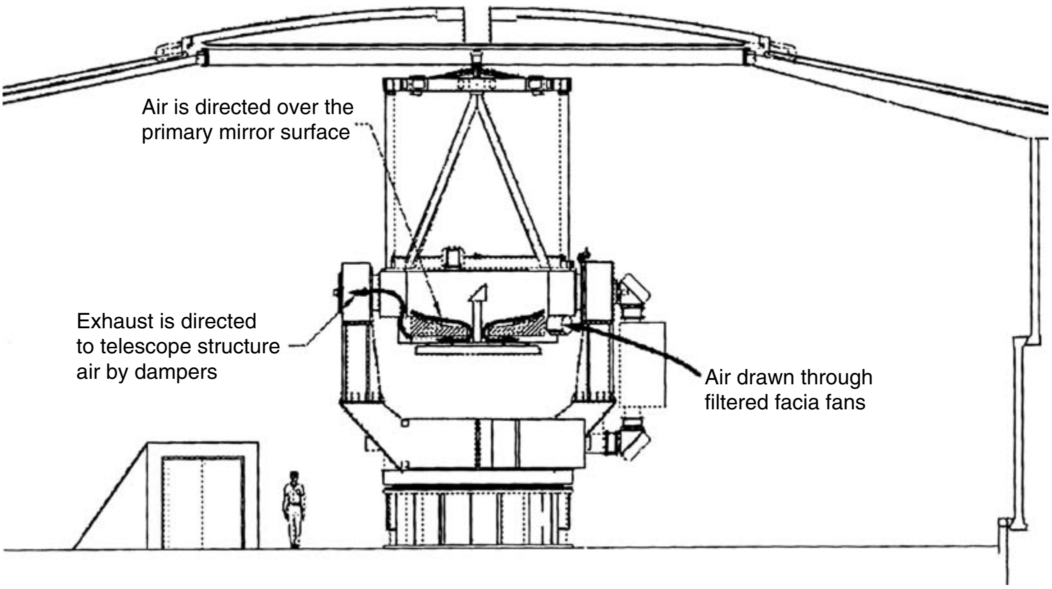
Air is directed over the primary mirror surface
Exhaust is directed to telescope structure air by dampers
Air drawn through filtered facia fans

FIGURE 12.69 Diagram showing the air path of the AEOS primary mirror temperature control system. (Adapted from Roberts, L.C. and Figgis, P.D., *Proc. SPIE*, 4837, 264, 2003.)

passes directly through the dichroic beam splitter into the science imaging array, while the laser light returning from the guide star is reflected from that beam splitter into the wavefront sensor. A portion of the IR light from a star within the field of view of the telescope also passes through the beam splitter to a tilt sensor that controls a steerable mirror located at a pupil of the telescope system to stabilize the image. Signals from the wavefront sensor control the adaptive secondary mirror.

The secondary mirror configuration is illustrated schematically in Figure 12.71. The lowest layer in the diagram is a 2-mm-thick deformable BK7 shell-shaped face sheet. It is supported at its center on a hub. The front (convex) surface of the shell is coated to serve as the secondary mirror of the

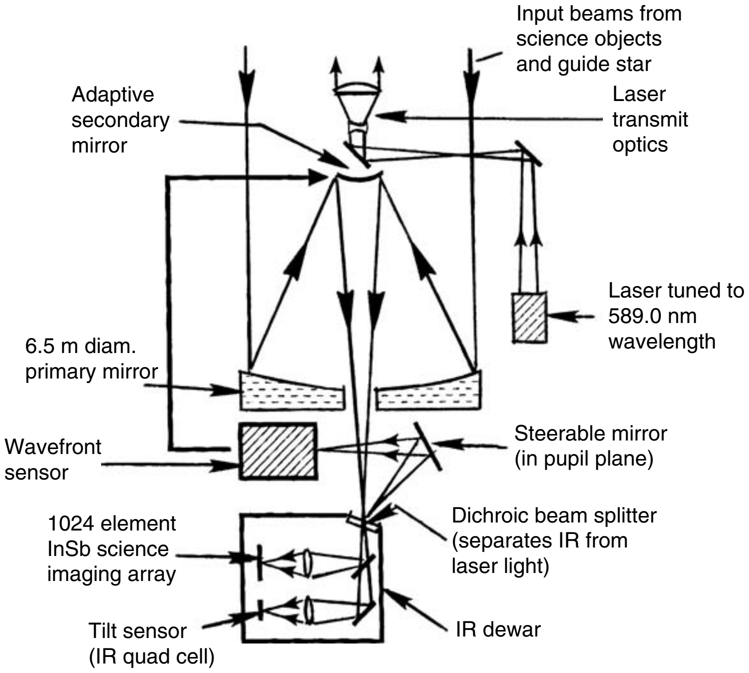
Input beams from science objects and guide star
Adaptive secondary mirror
Laser transmit optics
Laser tuned to 589.0 nm wavelength
6.5 m diam. primary mirror
Wavefront sensor
Steerable mirror (in pupil plane)
1024 element InSb science imaging array
Dichroic beam splitter (separates IR from laser light)
Tilt sensor (IR quad cell)
IR dewar

FIGURE 12.70 Schematic diagram of the adaptive optics system for the new MMT Telescope. (From Lloyd-Hart, M., Angel, J.R.P., Sandler, D.G., Groesbeck, T.D., Martinez, T., and Jacobsen, B.P., *Proc. SPIE*, 2871, M880, 1996.)

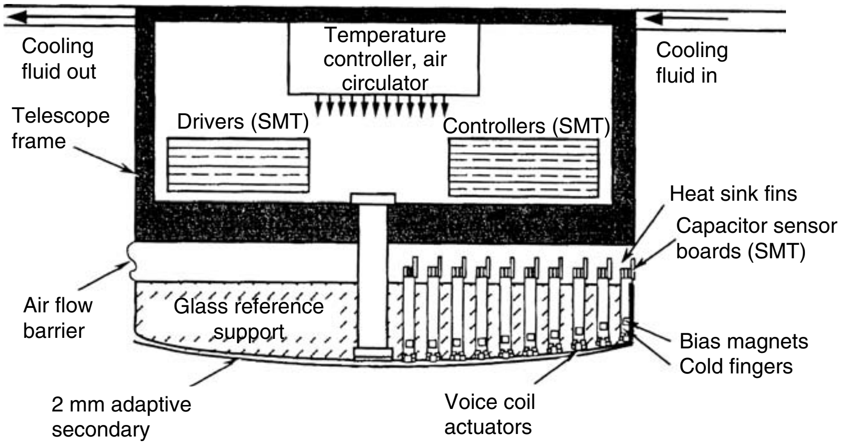
Cooling fluid out
Temperature controller, air circulator
Cooling fluid in
Telescope frame
Drivers (SMT)
Controllers (SMT)
Heat sink fins
Capacitor sensor boards (SMT)
Air flow barrier
Glass reference support
Bias magnets
Cold fingers
2 mm adaptive secondary
Voice coil actuators

FIGURE 12.71 Schematic diagram of the adaptive secondary for the new MMT Telescope. (From Bruns, D.G., Barrett, T.K., and Sandler, D.G., *Proc. SPIE*, 2871, 890, 1996.)

telescope. Its back (concave) surface is aluminized to serve as a reference surface for capacitive sensors associated with the actuators and to reflect heat from the actuators away from the shell. Above the shell is a 75-mm-thick plano-convex Zerodur reference support with a polished spherical front surface. It is separated from the back surface of the shell by nominally 0.100 mm, and is perforated by 324 holes through which pass fingers that support voice coils near small rare-earth magnets bonded to the back of the shell. The magnetic fields from the coils interact with the magnets to locally deflect the shell, thereby changing its optical figure. Around each hole through the reference support is a metalized ring that acts as the second plate for the capacitive displacement sensors that measure shell displacement (i.e., shell surface position) directly. The fingers supporting the actuator coils serve as cold fingers to transfer heat to the structure behind the secondary assembly.

12.8 MOUNTS FOR LARGE SPACE-BORNE MIRRORS

The major differences in large mirror mounting design for a space application are the need for manufacture in the normal gravity environment, but with simulated gravity-free conditions; the high accelerations experienced during launch; and the release of gravity effects in orbit. The first of these was considered in Chapter 11 in conjunction with a discussion of metrology mounts for the axis-vertical mirror. The second generally requires a means for locking or “caging” the mirror mount so that shock and vibrations do not damage the mechanisms or optics. The third requires that the optics be supported in a different manner during operation from those used during manufacture, testing, and handling on Earth. Some opto-mechanical aspects of design for accommodating these differences are discussed in the context of the following two hardware examples.

12.8.1 THE HUBBLE SPACE TELESCOPE

The primary mirror for the HST is a 2.49-m (98-in.)-diameter × 30.5-cm (12-in.)-thick fused monolithic egg-crate structure similar in construction to the mirror shown in Figure 9.13. It is made of Corning 7941 ULE. The clear aperture of the mirror is 2.4 m (94.5 in.). The central hole is 71.1 cm (28 in.) in diameter. The front and back face sheets are nominally 2.54 cm (1.0 in.) thick, and are separated by 25.4-cm (10.0-in.) × 0.64-cm (0.25-in.)-thick ribs on 10.2 cm (4.0 in.) centers. Inner and outer edge bands that are also 0.64 cm (0.25 in.) thick and equal in depth to the ribs form circumferential reinforcements. Three localized areas within the core where the flight supports (discussed below) are attached have comparatively thicker ribs for added strength. The mirror weighs 4078 kg (1850 lb); this is ~ 25% of the equivalent solid structure.

The concept for the multipoint mounting arrangement used to support the primary mirror during manufacture and testing with the axis vertical was described in Section 11.5 with regard to the preparation and testing of a scaled-down version of the flight mirror. Krim (1982) gave details pertaining to the 134-point metrology mounting. His analysis indicated that this number of support points was sufficient to simulate the gravity-free condition of operation. The actual thicknesses of the mirror’s components were mapped ultrasonically to an accuracy of ±0.05 mm (±0.002 in.) as required inputs to a detailed FEA model of the substrate that was used to determine the distribution of forces required to support the mirror.

After polishing was completed, the mirror was transferred from the metrology mounting to its flight mounting. There, the mirror is supported axially by three stainless steel links that penetrate the substrate at the three locations indicated in Figure 12.72. The cell structure of the mirror can also be seen in this photograph. It is supported radially by three tangent arms attached to Invar saddles bonded to the back of the mirror.

Figure 12.73 shows the rear surface of the mirror schematically. The detail view shows one tangent arm saddle and the clevis that connects it to a bracket, which is in turn attached to a main box ring outside the mirror. This ring is attached with tangent arms and axial links to the spacecraft structure. Figure 12.74 shows a schematic, partial, section view through one of the mirror axial supports.

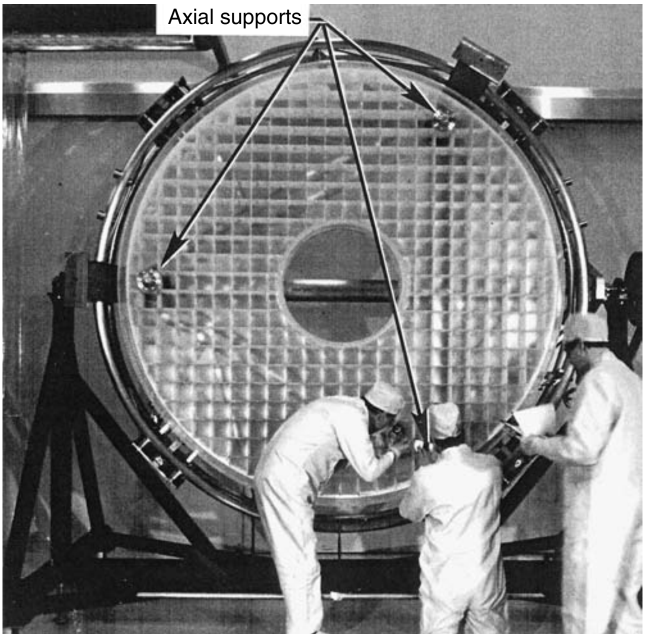

FIGURE 12.72 Frontal view of the primary mirror for the Hubble space telescope during preparation for coating. The internal cell structure and the forward ends of the flight axial supports can be seen. (Courtesy of Goodrich Corp., Danbury, CT.)

The relationship between the mirror and the main ring is more apparent in this view. The radial supports (tangent arms) for the main ring are not shown.

Also shown in Figure 12.73 are the locations of 24 bosses bonded to the back of the mirror to act as interfaces to actuators provided for limited on-orbit reshaping of the optical surface. These actuator mechanisms used stepper motors to drive precision ball-screws to apply localized forces to the mirror. They were not intended for real-time control of the mirror's figure, but were provided as a means to correct minor astigmatism anticipated as a result of gravity release in space. Unfortunately, owing to the square core configuration used in the substrate and the limited range of the actuators, it was not possible to correct curvature or spherical aberration with this figure-adjustment system. Had means for the adjustment of those parameters and sufficient dynamic range been provided, on-orbit correction of the asphericity error problem built into the mirror during manufacture might have been possible.

A brief explanation of the concept for attaching the axial supports to the mirror is as follows. Referring again to Figure 12.74, we see that a flexure link with a cruciform section lies between two spherical bearings. One bearing is attached to the bracket on the main ring and the other to the back of the mirror's rear face sheet. That face sheet is clamped between outer and inner plates that span a cell in the mirror core. Preload is applied by a threaded nut acting through a spring. This mechanism, repeated three places at ~ 120° intervals on the mirror's surface, is all that holds the mirror axially. The design provided sufficient rigidity to hold the mirror during coating, installation in the telescope, shipping, integration into the spacecraft, and launch. It still functions well in space where the gravitational environment is quite benign.

This design is also capable of supporting and protecting the mirror during the rigors of Space Shuttle landing in case the return of the telescope to Earth is attempted. The safety plate and nut shown in Figure 12.74 outside the front face sheet of the mirror serve as a stop to hold the mirror axially during the rapid axial deceleration accompanying such a landing. Note the small clearance between the safety plate and the mirror surface and the soft ring pad provided to soften the interface. Forward motion of the mirror would be constrained safely — the tension links transferring force to the bracket and thence to the main ring and structure.

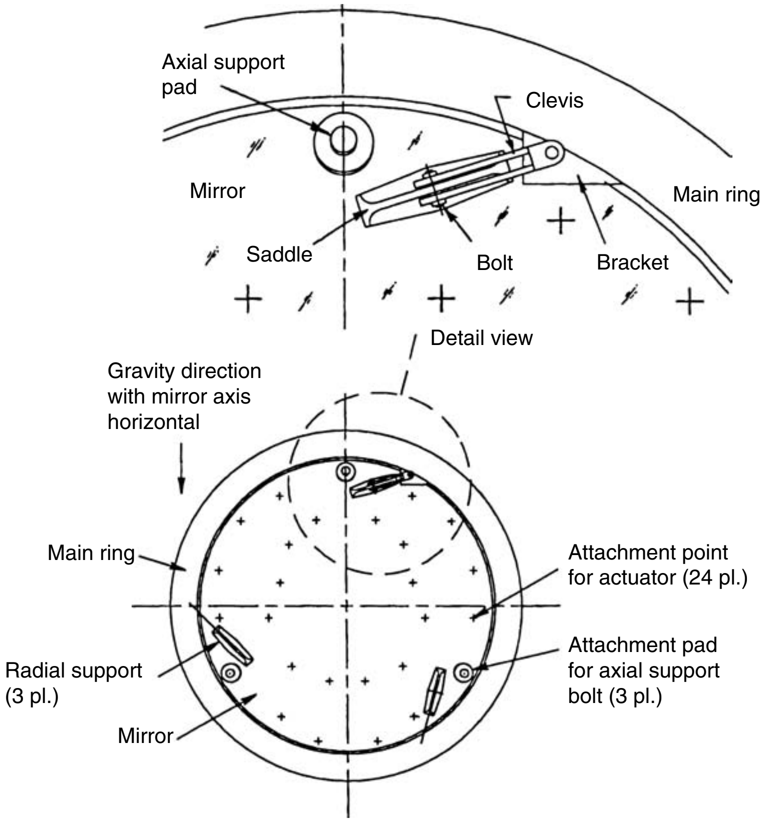
Axial support pad
Clevis
Mirror
Main ring
Saddle
Bolt
Bracket
Detail view
Gravity direction with mirror axis horizontal
Main ring
Attachment point for actuator (24 pl.)
Attachment pad for axial support bolt (3 pl.)
Radial support (3 pl.)
Mirror

FIGURE 12.73 Schematic diagram of the rear surface of the Hubble telescope primary mirror showing the axial and radial (tangent arm) supports as well as attachment points for actuators. (Adapted from drawings provided by Goodrich Corp., Danbury, CT.)

12.8.2 THE CHANDRA X-RAY TELESCOPE

The Chandra Telescope (formerly called the *Advanced X-ray Astrophysics Facility* [*AXAF*]), launched by NASA in July 1999, has two major modular assemblies: the optical bench assembly (OBA) and the high-resolution mirror assembly (HRMA). The OBA contains the main conical structural component supporting the 1588 kg (3500 lb) HRMA at the forward end and the 476 kg (1050 lb) integrated science instrument module (ISIM) at the aft end. The OBA also contains light baffles, strong magnets that deflect electrons away from the x-ray sensors in the ISIM, electronics, heaters, and wiring (Wynn et al., 1998; Olds and Reese, 1998).

The optical system, depicted in Figure 12.75, has 4 concentric cylindrical mirror pairs (paraboloids followed by hyperboloids) that intercept incoming x-rays at grazing incidence (between 0.5° and 1.5°) and focus them at the focal surface 10 m (394 in.) away. The configuration is known as Wolter I geometry (Wolter, 1952). The diameter of the largest mirror is 1.2 m (47.24 in.) while that of the smallest mirror is 0.68 m (26.77 in.). The mirrors are 0.84 m (33.1 in.) long. All mirrors were made of Zerodur, chosen for its low CTE (0.07×10^{-6} °C^{-1}), high polishability (better than 7 Å rms surface roughness), and compatibility with fabrication in the required cylindrical configuration. The mirrors were coated with iridium to enhance the reflectance of x-rays.

Each mirror is supported at the plane of its axial centroid by twelve titanium flexures oriented as indicated in Figure 12.76 and attached to Invar pads bonded to the mirrors with epoxy (Cohen et al., 1990). It should be noted that this figure shows 6 nested pairs of mirrors for a total of 12. The number of mirrors was reduced to four pairs subsequent to publication of the figure. The flexures

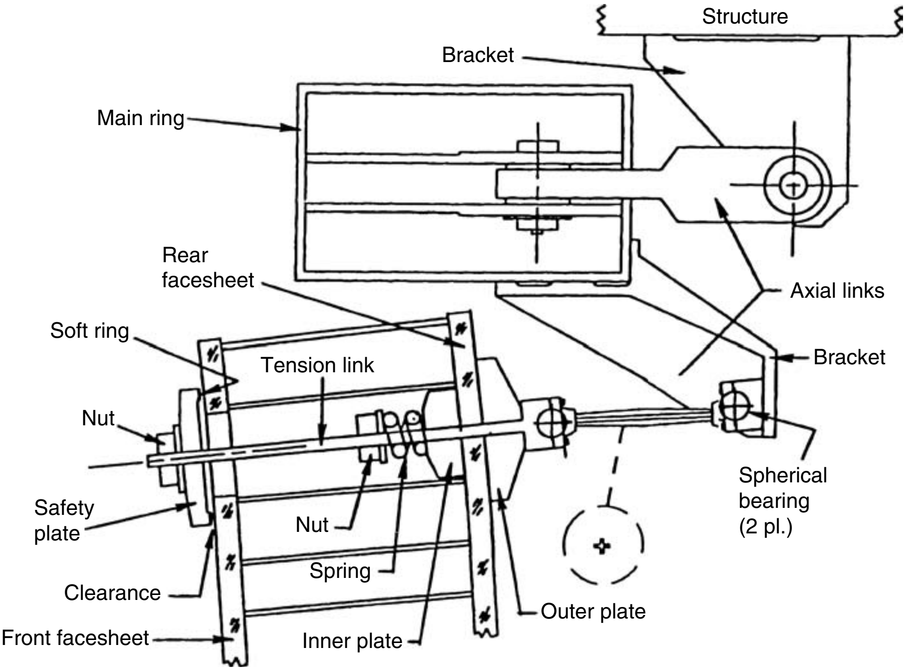
Structure
Bracket
Main ring
Rear facesheet
Soft ring
Tension link
Nut
Axial links
Bracket
Spherical bearing (2 pl.)
Safety plate
Nut
Spring
Clearance
Front facesheet
Inner plate
Outer plate

FIGURE 12.74 Schematic diagram of one axial support for the Hubble primary mirror. (Adapted from drawings provided by Goodrich Corp., Danbury, CT.)

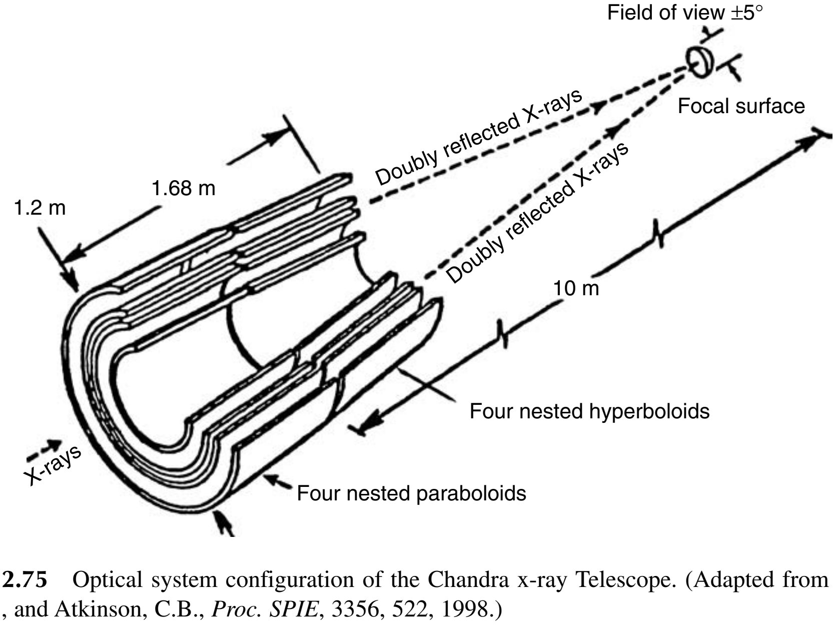
Field of view ±5°
Focal surface
Doubly reflected X-rays
Doubly reflected X-rays
1.68 m
1.2 m
10 m
Four nested hyperboloids
X-rays
Four nested paraboloids

FIGURE 12.75 Optical system configuration of the Chandra x-ray Telescope. (Adapted from Wynn, J.A., Spina, J.A., and Atkinson, C.B., *Proc. SPIE*, 3356, 522, 1998.)

are epoxy bonded to the ends of mirror support sleeves made of graphite epoxy. These sleeves are in turn attached to an aluminum central aperture plate. This plate has multiple rings of annular slots for passage of the x-rays. Aluminum inner and outer cylinders enclose the mirrors after installation. The outer cylinder interfaces with three sets of bipods (not shown) that link the optical assembly to the optical bench.

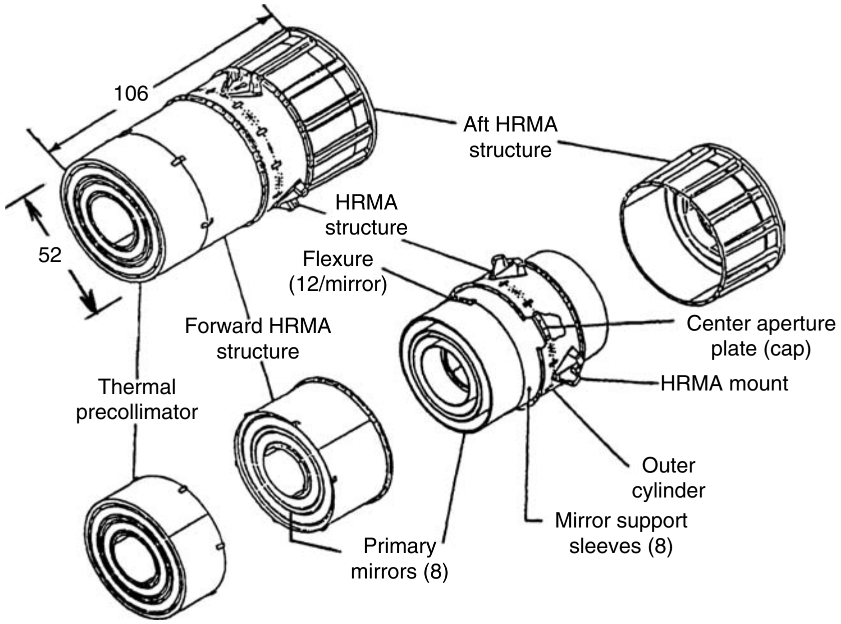

FIGURE 12.76 Opto-mechanical configuration of the Chandra Telescope's high-resolution mirror assembly (HRMA). Dimensions are in inches. (Adapted from Olds, C.R. and Reese, R.P., *Proc. SPIE*, 3356, 910, 1998.)

The assembled telescope was required to image collected x-rays from all four pairs of mirrors at an axial point, with 90% of the energy falling into a circle smaller than 0.05 mm (0.002 in.) diameter. This demanded that the mirrors be aligned within 0.1 arcsec in tilt and centered to a common axis within 7 μm. To mount the mirrors to the flexures without residual gravity-induced strain, each was first attached to a system of gravity off loaders. These off-loaders were attached to a cradle equipped with precision stepper motor-driven actuators capable of moving the mirror in all six DOF in 0.1 μm increments. When aligned, the mirrors were tack bonded in place with epoxy to prevent motion caused by hydrostatic pressure from the bonding gun, followed by full bonding and curing. The instrumentation used to sense alignment errors was capable of measuring tilt errors smaller than 0.01 arcsec and lateral displacements of 1 μm (Olds and Reese, 1998; Glenn, 1995).

The temperature control system for the telescope was designed to actively maintain the internal optical cavity at a constant temperature of 69.8°F (21.0°C), which duplicates the temperature at assembly. The rest of the telescope is maintained at 50°F (10°C) during observations. Temperature is adjusted by on-board computer controls using radiative heater plates at either end of the optical assembly, and temperature-controlled light baffles. Thermal isolation is provided by an external covering for the HRMA with multilayer insulation (MLI) and the OBA with MLI plus an external layer of silver-coated Teflon film (both for solar radiation rejection). A full-aperture door at the forward end of the HRMA serves as a contamination shield during launch and, once opened on orbit, shields the optics from direct sunlight beyond 45° to the line of sight. The ISIM is insulated and precisely temperature-controlled (Havey et al., 1998).

The entire telescope was designed to withstand the rigors of Space Shuttle launch, during which vibrational reaction loads as great as 30,000 lb (133,450 N) can be encountered. Static and dynamic FEA analyses were conducted throughout the design process to ensure stability of the structure. Measurements of the modal dynamic response of simulated critical components of the telescope to external driving forces verified the models for these analyses.

Weisskopf (2003) provides a good summary of the first 3 years' performance of the Chandra Telescope.

REFERENCES

Allen, L.N., Progress in ion figuring of large optics, *Proc. SPIE*, 2428, 237, 1995.

Allen, L.N. and Keim, R.E., An ion figuring system for large optic fabrication, *Proc. SPIE*, 1168, 35, 1989.

Allen, L.N. and Romig, H.W., Demonstration of an ion figuring process, *Proc. SPIE*, 1333, 22, 1990.

Allen, L.N., Hannon, J.J., and Wambach, R.W., Jr., Final surface correction of an off-axis aspheric petal by ion figuring, *Proc. SPIE*, 1543, 190, 1991a.

Allen, L.N., Keim, R.E., Lewis, T.S., and Ullom, J.R., Surface error correction of a Keck 10 m Telescope primary mirror segment by ion figuring, *Proc. SPIE*, 1531, 195, 1991b.

Anderson, D., Parks, R.E., Hansen, Q.M., and Melugin, R., Gravity deflections of lightweighted mirrors, *Proc. SPIE*, 332, 424, 1982.

Antebi, J., Dusenberry, D.O., and Liepins, A.A., Conversion of the MMT to a 6.5-m telescope, *Proc. SPIE*, 1303, 148, 1990.

Barnes, W.P., Jr., Terrestrial engineering of space-optical elements, *Proceedings of 9th International Congress of the International Commission for Optics*, Thompson, B.J. and Shannon, R.R., Eds., Nat. Acad. of Sci., Santa Monica, CA, p. 171, 1974.

Baustian, W.W., The Lick Observatory 120-inch Telescope, in *Telescopes*, Kuiper, G.P. and Middlehurst, B.M., Eds., University of Chicago Press, Chicago, 1960, p. 16.

Baustian, W.W., General philosophy of mirror support systems, *Optical Telescope Technology Workshop, April 1969, NASA Rept. SP-233*, 381, 1970, p. 381.

Bittner, H., Erdmann, M., Haberler, P., and Zuknik, K.-H., SOFIA primary mirror assembly: Structural properties and optical performance, *Proc. SPIE*, 4857, 266, 2003.

Bowen, I.S., The 200-inch Hale Telescope, in *Telescopes*, Kuiper, G.P. and Middlehurst, B.M., Eds., University of Chicago Press, Chicago, 1960, p. 1.

Bruns, D.G., Barrett, T.K., and Sandler, D.G., MMT adaptive secondary mirror prototype performance, *Proc. SPIE*, 2871, 890, 1996.

Buchroeder, R.A., Elmore, L.H., Shack, R.V., and Slater, P.N., The Design, Construction and Testing of the Optics for a 147-cm Aperture Telescope, Opt. Sci. Ctr. Tech. Rept. 79, University of Arizona, Tucson, 1972.

Carter, W.E., Lightweight center-mounted 152 cm, f/2.5 Cer-Vit mirror, *Appl. Opt.*, 11, 467, Tucson, 1972.

Chanan, G.A., Design of the Keck Observatory alignment camera, *Proc. SPIE*, 1036, 59, 1988.

Cheng, A.Y.S. and Angel, J.R.P., Steps towards 8 m honeycomb mirrors VIII: Design and demonstration of a system of thermal control, *Proc. SPIE*, 628, 536, 1986.

Cho, M.K., Optimization strategy of axial and lateral supports for large primary mirrors, *Proc. SPIE*, 2199, 841, 1994.

Cho, M.K., Stepp, L.M., Angeli, G.Z., and Smith, D.R., Wind loading of large telescopes, *Proc. SPIE*, 4837, 352, 2003.

Coffey, V.C., Powerful CW laser produces bright guidestar, *Laser Focus World*, p. 11, March 1, 2003.

Cohen, L.M., Cernock, L., Mathews, G., and Stallcup, M., Structural considerations for fabrication and mounting of the AXAF HRMA optics, *Proc. SPIE*, 1303, 162, 1990.

Dryden, D.M. and Pearson, E.T., Multiplexed precision thermal measurement system for large structured mirrors, *Proc. SPIE*, 1236, 825, 1990.

Erdmann, M., Bittner, H., and Haberler, P., Development and construction of the optical system for the airborne observatory SOFIA, *Proc. SPIE*, 4014, 309, 2000.

Franza, F. and Wilson, R.N., Status of the European Southern Observatory New Technology Telescope Project, *Proc. SPIE*, 332, 90, 1982.

Geyl, R., Tarreau, P., and Plainchamp, P., SOFIA primary mirror fabrication and testing, *Proc. SPIE*, 4451, 126, 2001.

Glenn, P., Centroid detector system for AXAF-I alignment test system, *Proc. SPIE*, 2515, 352, 1995.

Golini, D., Jacobs, S., Kordonski, W., and Dumas, P., Precision optics fabrication using magnetorheological finishing, *Proc. SPIE*, CR67, 251, 1997.

Gray, P.M., Hill, J.M., Davison, W.B., Callahan, S.P., and Williams, J.T., Support of large borosilicate honeycomb mirrors, *Proc. SPIE*, 2199, 691, 1994.

Havey, K., Sweitzer, M., and Lynch, N., Precision thermal control trades for telescope systems, *Proc. SPIE*, 3356, 10, 1998.

Hertig, J.-A., Alexandrou, C., and Zago, L., Wind Tunnel Tests for the ESO VLT, *Very Large Telescopes and their Instrumentation, Proc. ESO 30*, Ulrich, M.-H., Ed., 1988, European Space Organization, Garching, p. 855.

Hiriart, D., Ochoa, J.L., and Garcia, B., Wind power spectrum measured at the San Pedro Mártir Sierra, *Revista Mexicana de Astronomia y Astrofisica*, 37, 213, 2001.

Huang, E.W., Gemini primary mirror cell design, *Proc. SPIE*, 2871, 291, 1996.

Iraninejad, B., Lubliner, J., Mast, T., and Nelson, J., Mirror deformations due to thermal expansion of inserts bonded to glass, *Proc. SPIE*, 748, 206, 1987.

Iraninejad, B., Vukobratovich, D., Richard, R., and Melugin, R., A mirror mount for cryogenic environments, *Proc. SPIE*, 450, 34, 1983.

Jacobs, S.D., Yang, E., Fess, J.B., Feingold, J.B., and Gillman, B.E., Magnetorheological finishing of IR materials, *Proc. SPIE*, 3134, 258, 1997.

Jared, R., Arthur, A., Andreae, S., Biocca, A., Cohen, R., Fuertes, J., Franck, J., Gabor, G., Llacer, J., Mast, T., Meng, J., Merrick, T., Minor, R., Nelson, J., Orayani, M., Saiz, P., Schaefer, B., and Witebsky, C., The W.M. Keck Telescope segmented primary mirror active control system, *Proc. SPIE*, 1236, 996, 1990.

Johnson, K.W., Stress polishing applications, *Proc. SPIE*, 1618, 41, 1991.

Kaercher, H.J., The evolution of the SOFIA telescope system design — lessons learned during design and fabrication, *Proc. SPIE*, 4857, 257, 2003.

Kimbrell, J.E. and Greenwald, D., AEOS 3.67 m telescope primary mirror active control system, *Proc. SPIE*, 3352, 400, 1998.

Krabbe, A., Becoming reality: the SOFIA telescope, *Proc. SPIE*, 4857, 251, 2003.

Krim, M.H., Metrology mount development and verification for a large spaceborne mirror, *Proc. SPIE*, 332, 440, 1982.

Lambropoulos, J.C., Gillman, B.E., Zhou, Y., and Jacobs, S.D., Glass-ceramics: Deterministic microgrinding, lapping, and polishing, *Proc. SPIE*, 3134, 178, 1997.

Lloyd-Hart, M., System for precise thermal control of borosilicate honeycomb mirrors, *Proc. SPIE*, 1236, 844, 1990.

Lloyd-Hart, M., Angel, J.R.P., Sandler, D.G., Groesbeck, T.D., Martinez, T., and Jacobsen, B.P., Design of the 6.5 m MMT adaptive optics system and results from its prototype system FASTTRACK II, *Proc. SPIE*, 2871, 880, 1996.

Mack, B., Deflection and stress analysis of a 4.2-m diam. primary mirror of an altazimuth-mounted telescope, *Appl. Opt.*, 19, 1000, 1980.

Malvick, A.J. and Pearson, E.T., Theoretical elastic deformations of a 4-m diameter optical mirror using dynamic relaxation, *Appl. Opt.*, 7, 1207, 1968.

Martin, H.M., Callihan, S.P., Cuerden, B., Davison, W.B., DeRigne, S.T., Dettmann, L.R., Parodi, G., Trebisky, T.J., West, S.C., and Williams, J.T., Active supports and force optimization for the MMT primary mirror, *Proc. SPIE*, 3352, 412, 1998.

Mast, T. and Nelson, J., The fabrication of large optical surfaces using a combination of polishing and mirror bending, *Proc. SPIE*, 1236, 670, 1990.

Meinel, A.B., Design of reflecting telescopes, in *Telescopes*, Kuiper, G.P. and Middlehurst, B.M., Eds., University of Chicago Press, Chicago, 1960, p. 25.

Meinel, A.B., Bushkin, S., and Loomis, D.A., Controlled figuring of optical surfaces by energetic ionic beams, *Appl. Opt.*, 4, 1674, 1965.

Meng, J., Franck, J., Gabor, G., Jared, R., Minor, R., and Schaefer, B., Position actuators for the primary mirror of the W.M. Keck Telescope, *Proc. SPIE*, 1236, 1018, 1990.

Minor, R., Arthur, A., Gabor, G., Jackson, H., Jared, R., Mast, T., and Schaefer, B., Displacement sensors for the primary mirror of the W.M. Keck Telescope, *Proc. SPIE*, 1236, 1009, 1990.

Nelson, J.E., Lubliner, J., and Mast, T.S., Telescope mirror supports-plate deflections on point supports, *Proc. SPIE*, 332, 212, 1982.

Olds, C.R. and Reese, R.P., Composite structures for the advanced x-ray astrophysics facility (AXAF), *Proc. SPIE*, 3356, 910, 1998.

Pearson, E. and Stepp, L., Response of large optical mirrors to thermal distributions, *Proc. SPIE*, 748, 215, 1987.

Pepi, J.W., Test and theoretical comparisons for bending and springing of the Keck segmented ten meter telescope, *Proc. SPIE*, 1271, 275, 1990.

Pepi, J.W., Design considerations for mirrors with large diameter to thickness ratios, *Proc. SPIE*, CR43, 207, 1992.

Pottebaum, T.S. and MacMartin, D.G. Wind tunnel testing of a generic telescope enclosure, *Proc. SPIE*, 5495, 270, (2004).

Roberts, L.C. and Figgis, P.D., Thermal conditioning of the AEOS Telescope, *Proc. SPIE*, 4837, 264, 2003.

Sarver, G., Maa, G., and Chang, L., SIRTF primary mirror design, analysis and testing, *Proc. SPIE*, 1340, 35, 1990.

Scott, R.M., Optical Engineering, *Appl. Opt*., 1, 387, 1962.

Sawyer, K.A., Hurley, B.N., Brindos, R.R., and Wong, J., Launch rated kinematic mirror mount design with six degrees of freedom adjustments, *Proc. SPIE*, 3786, 281, 1999.

Siegmund, W.A., Stepp, L., and Lauroesch, J., Temperature control of large honeycomb mirrors, *Proc. SPIE*, 1236, 834, 1990.

Stepp, L., Thermo-elastic analysis of an 8-meter diameter structured borosilicate mirror, NOAO 8-meter Telescopes Engineering Design Study Report No. 1, National Optical Astronomy Observatories, Tucson, 1989.

Stepp, L., Huang, E., and Cho, M., Gemini primary mirror support system, *Proc. SPIE*, 2199, 223, 1994.

Turner, A.N., Rapid convergence on high frequency errors in computer-controlled optical fabrication, *Proc. SPIE*, 3134, 231, 1997.

Ulmes, J.J., Design of a catadioptric lens for long-range oblique aerial reconnaissance, *Proc. SPIE*, 1113, 116, 1989.

Vukobratovich, D., Flexure mounts for high-resolution optical elements, *Proc. SPIE*, 959, 18, 1988.

Vukobratovich, D., private communication, 2004.

Vukobratovich, D., Iraninejad, B., Richard, R.M., Hansen, Q.M., and Melugin, R., Optimum shapes for lightweighted mirrors, *Proc. SPIE*, 332, 419, 1982.

Vukobratovich, D., Richard, R., Valente, T., and Cho, M., *Final Design Rept. for NASA Ames/Univ. of Arizona Cooperative Agreement No. NCC2- 426 for period April 1*, *1989–April 30*, *1990*, Opt. Sci. Ctr., University of Arizona, Tucson, AZ, 1990.

Weisskopf, M.C., Three years of operation of the Chandra X-ray Observatory, *Proc. SPIE*, 4851, 1, 2003.

West, S.C., Callahan, S., Chaffee, F.H., Davison, W., DeRigne, S., Fabricant, D., Foltz, C.B., Hill, J.M., Nagel, R.H., Poyner, A., and Williams, J.T., Toward first light for the 6.5-m MMT telescope, *Proc. SPIE*, 2871, 38, 1996.

Wilson, S.R., Reicher, D.W., and McNeil, R.R., Surface figuring using neutral ion beams, *Proc. SPIE*, 966, 74, 1988.

Wolter, H., *Ann. Phys.*, 10, 94, 1952.

Wong, W.-Y., and Forbes, F., Water tunnel tests on enclosure concepts, *Gemini 8m Telescope Technical Report No. 1*, 1991.

Wynn, J.A., Spina, J.A., and Atkinson, C.B., Configuration, assembly, and test of the x-ray telescope for NASA's advanced x-ray astrophysics facility, *Proc. SPIE*, 3356, 522, 1998.

Yoder, P.R., Jr., *Mounting Optics in Optical Instruments*, SPIE Press, Bellingham, 2002.

13 Design and Mounting of Metallic Mirrors

13.1 INTRODUCTION

The mirror designer has at his disposal a number of metallic materials from which to choose. Table 13.1 lists key candidates. Table 13.2 lists properties generally considered in a materials trade-off analysis for a state-of-the-art mirror application. From the fabrication viewpoint, the metal-mirror designer should consider the available process options for each step and select those apparently best suited for the particular application. The typical fabrication cycle includes most, if not all, of the following steps: formation of the substrate, geometric shaping, stress relieving, plating (typically with electroless nickel [ELN]), optical finishing, testing, and coating. The stress-relieving step is especially important as a means for minimizing internal stress within the substrate that will tend to relieve itself with time or with changes in temperature, thereby causing the mirror surface to distort.

This chapter begins in Section 13.2 with some general considerations of metal mirrors as distinguished from nonmetallic ones. A variety of examples of metal mirror design and fabrication techniques are then discussed. Mirrors made of various materials are considered in Sections 13.3–13.5. Ones with metallic and composite foam cores are considered in Section 13.6. Because of the inherent porosity of some metal surfaces it is advantageous to plate them with an amorphous material. Electrolytic nickel (EN) and ELN are very common types of plating for such mirrors. In Section 13.7, we summarize some salient characteristics of these types of platings and describe their application.

Some, but not all, of the metals discussed here are compatible with material removal and final contouring to optical-quality surfaces by precision turning with single-point, gem-quality natural diamond tools. This process, commonly called single-point diamond turning (SPDT), is discussed in Section 13.8.

In Sections 13.9 and 13.10, we explain some of the techniques most commonly used to mount metal mirrors in optical instruments. It is quite feasible to interface many smaller metallic substrates with the various conventional mounts discussed earlier in this book for nonmetallic mirrors. We point out some design differences that accrue in such mountings because the mechanical properties of metals differ from those of nonmetals. Highly successful methods for supporting small- to moderate-sized metal mirrors involve mounting provisions built into the mirrors themselves. Integral mounting techniques are reviewed and some precautions to be observed in such designs are summarized.

Flexure mountings that provide the highest performance levels for larger metal mirrors are discussed in Section 13.11. The chapter closes in Section 13.12 with brief considerations of multiple metallic optical and mechanical component interfaces using SPDT techniques to facilitate assembly and optical alignment.

13.2 GENERAL CONSIDERATIONS OF METAL MIRRORS

Quantitative data on the physical characteristics of most of the material types listed in Table 13.2 are provided in Chapter 3 and the references cited therein. Because there is keen interest in athermalized opto-mechanical designs for various applications, many published evaluations have

TABLE 13.1
Typical Metallic and Metal Matrix Mirror Material Types

Aluminum	Beryllium	Copper	Molybdenum	Stainless Steel
356	I-70-H	101 (OFHC)	Low Carbon	304
2024	220-H	Glidcop™	TZM	316
5083 & 5086	I-250			416
6061	I-400			17-4PH
Tenzalloy	S-200-FH			
SXA	O-50 and O-30			

Source: Adapted from Paquin, R.A., Proc. SPIE 65, 12, 1975; Paquin, R.A., in *Handbook of Optomechanical Engineering*, CRC Press, Boca Rafon, FL, 1997, chap. 4; Howels, M.R. and Paquin, R.A., *Proc. SPIE*, CR67, 339, 1997.

TABLE 13.2
Key Material Properties Influencing the Behavior of Mirrors[a]

Mechanical	Physical	Optical	Metallurgical	Fabrication	Other
Young's modulus Yield strength Microyield strength Fracture toughness Modulus of rupture	Coefficient of thermal expansion Density Thermal conductivity Thermal diffusivity Specific heat Radiation resistance Vapor pressure Electrical conductivity Corrosion potential	Reflectivity Absorption Complex refractive index	Crystal structure Phases present Voids and inclusions Grain size Recrystallization temperature Stress relief temperature Annealing temperature Dimensional stability	Machinability Polishability Plateability Forgability Weldability Brazeability Solderability Heat treatability	Temperature sensitivity of the listed parameters Availability (including size and cost)

[a] Entries not necessarily in order of significance.

Source: Adapted from Paquin, R.A., *Proc. SPIE*, 65, 12, 1975; Howels, M.R. and Paquin, R.A., *Proc. SPIE*, CR67, 339, 1997.

been comparisons of key material properties as functions of temperature. For example, Figure 13.1 shows variations of the coefficient of thermal expansion (CTE) for two metals, aluminum and beryllium, compared with some glass and ceramic-type mirror materials. Obviously, these two metals are much more sensitive to temperature change than the nonmetals — except at very low temperatures. Table 13.3 lists measured values for the CTEs of a series of metals as functions of temperature over an extended range. High conductivities enhance performance at cryogenic temperatures.

In general, all materials approach "zero expansion" properties at cryogenic temperatures. ULE has a very small CTE at or near 300 K. Fused silica has a zero CTE near 190 K; beryllium and aluminum reach this condition at ~40 and ~15 K, respectively. Although a low value of CTE in the temperature region of interest is important in mirror design, it is also important for that property to be uniform throughout the substrate. Nonuniformities in CTE cause bumps, holes, or more complex changes in surface geometries to appear at temperatures other than that at which the mirror was fabricated. Materials that have low cryogenic CTEs generally have much higher CTEs at the temperature of the location where final polishing and figuring take place. This makes achievement of a specific surface

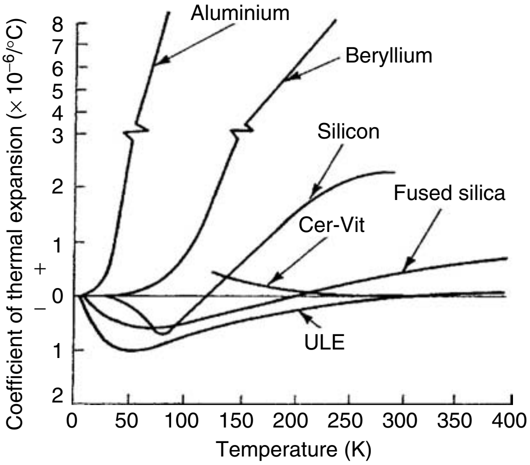

FIGURE 13.1 Thermal expansion coefficient variations with temperature for some mirror materials. (From Paquin, R.A. and Goggin, W., Perkin-Elmer Rept. IS11393, Norwalk, CT, 1972.)

figure and high smoothness difficult. Common practice is to iteratively test at low temperature and correct the surface at room temperature until the desired result is obtained or the process ceases to improve the low-temperature performance.

Minimizing spatial temperature gradients requires a high thermal conductivity k to dissipate the effects of surface thermal loads on the mirror. This is especially true for mirrors exposed to high thermal irradiation. Similarly, specific heat c_p is of importance. These properties and their general temperature dependences for temperatures below 300 K are shown graphically in Figure 13.2. Glasses have low values of k and c_p from 300 K to absolute zero. Metals have considerably higher values for these parameters at these temperatures. Room temperature values for these parameters may be found in Table 3.13 (for nonmetallic materials) and Table 3.14 (for metallic materials). Their significant variations with temperature are reported by Paquin (1994).

Aluminum, copper, and molybdenum have cubic crystal structures that serve best as mirror substrates in wrought forms. Castings of these materials tend to be more porous, but are less expensive than forgings. Very large metal mirrors used in less critical applications, such as solar simulators and solar energy collectors, are typically made of welded aluminum panels. Cast beryllium is thermally anisotropic owing to its hexagonal crystal structure. If pulverized and processed by powder-metallurgy techniques, it forms highly successful mirror substrates. Molybdenum and copper are frequently used in water-cooled mirrors for high-energy applications. Thoriated tungsten alloy and stainless steel have also been employed in mirrors.

It is well known that appreciable levels of residual internal stress can develop in metal substrates as a result of casting, forging, machining, and some heat-treating processes. Such stresses cause dimensional instabilities and usually reach maximum levels near the surfaces. Each metal substrate must therefore undergo stress relieving during manufacture. The nature of this operation required for a given optic is dictated by the application and the fabrication stage at which the stress relieving is performed. Chemical etching, heat treating, or a combination of these processes are usually used for this purpose.

13.3 ALUMINUM MIRRORS

Aluminum and its alloys are lightweight, strong, relatively inexpensive, and readily machinable materials widely used in optical instrument components and structures. Table 13.4(a) gives typical thermal cycling treatments for selected forms of aluminum alloys. Methods for stress relieving aluminum by heat treating for cryogenic mirror applications have been provided by many authors such as Fuller et al. (1981), Vukobratovich, et al. (1998), Ohl et al. (2002), and Toland, et al. (2003). Ohl

TABLE 13.3

Temperature Dependence of the Coefficient of Thermal Expansion ($\times 10^{-6}$ K^{-1}) for Selected Materials

Temperature (K)	6061 Al	Be	Cu	Au	Fe	304 CRES	416 CRES	Mo	Ni	Ag	Si	α-SiC	β-SiC
5		0.0003	0.005	0.03	0.01				0.02	0.015		0.01	
10		0.001										0.02	
20		0.005				9.8	4.3	0.3			0		
25		0.009	0.63	2.8	0.2			0.4	0.25	1.9	0	0.03	
50		0.096	3.87	7.7	1.3	10.5	4.9	1	1.5	8.2	−0.2	0.06	
75		0.47							4.3		−0.5	0.09	
100	12.2	1.32	10.3	11.8	5.6	11.4	6	2.8	6.6	14.2	−0.4	0.14	
125	18.7	2.55											
150	19.3	4.01				12.4	7				0.5	0.4	
175	20.3	5.54											
200	20.9	7.00	15.2	13.7	10.1	13.2	7.9	4.6	11.3	17.8	1.5	1.5	
225	21.5	8.32											
250	21.5	9.50				14.1	8.8				2.2	2.8	
293	22.5	11.3	16.5	14.2	11.8	14.7	9.5	4.8	13.4	18.9	2.6	3.3	3.26
300		11.5										3.4	3.29
350	23.8												3.46
400	25.0	13.6	17.6	14.8	13.4	16.3	10.9	4.9	14.5	19.7	3.2	4	3.62
450	26.3												3.77
500	27.5	15.1	18.3	15.4	14.4	17.5	12.1	5.1	15.3	20.6	3.5	4.2	3.92
600	30.1	16.6	18.9	15.9	15.1	18.6	12.9	5.3	15.9	21.5	3.7	4.5	4.19
700		17.8	19.5	16.4	15.7	19.5	13.5	5.5	16.4	22.6	3.9	4.7	4.42

Source: Adapted from Paquin, R.A., in *Handbook of Optics*, 2nd Ed., Optical Society of America, Washington, DC, 1994, chap. 35.

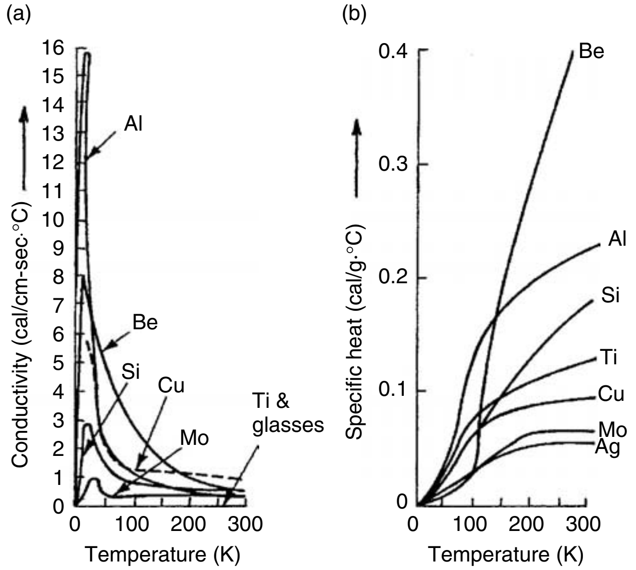

FIGURE 13.2 Low-temperature properties of selected candidate mirror materials. (a) Thermal conductivity; (b) specific heat. (From Paquin, R.A. and Goggin, W., Perkin-Elmer Rept. IS 11393, Norwalk, CT, 1972.)

et al. (2003) and Connelly et al. (2003) discussed the hardware applications that led to the research reported by Ohl et al. (2002).

Of the referenced papers on material processing, the most detail may be found in Ohl et al. (2002) where the authors reported on an investigation of five different heat-treatment methods (see Table 13.4[b]) conducted to empirically determine the best method for use in fabricating a series of mirrors from Al 6061-T651 plate stock. These mirrors had aspect ratios of 6:1, included curved surfaces and flats, and had dimensions ranging from 100 mm (3.94 in.) square to 269×286 mm (10.59×11.26 in.). The optical and mounting surfaces of the mirrors were created by SPDT machining. Fabrication specifications and tolerances were ±1% for radius, ±0.3 to 0.8% for conic constant, figure error $< 0.1\lambda$ rms (at 0.633 mm and 293 K), and microroughness of <10 nm rms. The authors stated that these requirements represented the "best achievable surface error for state-of-the-art single-point diamond machining" of mirrors from this material. A further requirement inherent in the intended application was that the change in optical figure when the temperature dropped to 80 K was to be minimized and that any measured change was to be repeatable over multiple temperature cycles. Included in the test program was measurement of optical performance, tensile strength, microstrain, and metallographic grain structure. The reported experimental results indicated that method SR 5 of Table 13.4(b) gave the best overall performance for the application.

Toland et al. (2003) reported experiments with forged Al 6061-T651 and compared those results with those for plate stock of the same material as reported by Ohl et al. (2003) and summarized briefly here. It was concluded that similar heat-treating processes would produce mirrors with similar optical performance for different types of stock materials.

Because of the inherent porosity and poor polishing characteristics of aluminum, achievement of a smooth reflecting surface requires that surface to be plated. ELN plating (see Section 13.7) is the most commonly used process. A proprietary aluminum plating* of $> 99.9\%$ pure amorphous aluminum on aluminum alloy substrates is also available (Vukobratovich et al., 1998). ELN and pure aluminum platings can be diamond-turned to achieve high-quality optical surface figure with good smoothness characteristics. Thin film coats of aluminum or gold provide good reflectivity for visible and IR applications, respectively.

---

*AlumiPlate™ plating process developed by AlumiPlate Corporation, Minneapolis, MN.

TABLE 13.4(a)
Thermal Cycling Treatments for Stabilizing Various Aluminum Mirror Substrates

Material	Treatment	Cycle Duration at High Temp.	Cycle Duration at Low Temp.	Total No. of Cycles	Temperature Change Rate
6061	Solution treat at 530°C, quench in PG[a], age at 175°C in stages	30 min at 150°C	30 min at <40°C	>3	<3°C/min or <1°C/min during polishing
SXA (after finish machining)	Solution treat at 495°C, quench in PG[a], age at 190°C for 12 h	30 min	Quench to −195°C	until no dimension change	
SXA (after ELN plating)	Solution treat at 495°C, quench in PG[a], age at 190°C for 12 h	4 h at 170°C	30 min at −75°C	>5 or until no dimension change	<5°C/min
5000 series alloys	Anneal at 350°C, slow cool	60 min at 150°C	30 min at <−40°C	>3	<3°C/min or <1°C/min during polishing

[a] PG is 20% polyalkylene glycol solution in water.

Source: From Howells, M.R. and Paquin, R.A., *Proc. SPIE*, CR67, 339, 1997.

TABLE 13.4(b)
Candidate Stress Relief Methods for Mirrors Made from Al 6061-T651 Plate Stock

Step	SR 1 Control–No Heat Treatment	SR 2 Simple Heat Treatment	SR 3 SR 2 + Up-hill Quench	SR 4 Solution Treat w/28% Glycol Quench	SR 5 SR 4 w/Up-hill Quench	SR 6 Solution Treat w/H_2O Quench & Up-hill Quench
1	Rough machine	Rough machine	Rough machine	Rough machine	Rough machine	Rough machine
2		Heat treat at 260°C for 2 h	Heat treat at 260°C for 2 h			
3				Solution treat at 530°C	Solution treat at 530°C	Solution treat at 530°C
4				Quench within 15 sec in UCON Quenchant A at 29–35°C	Quench within 15 sec in UCON Quenchant A at 29–35°C	Quench within 15 sec in H_2O at 18–24°C
5			Up-hill quench: Allow to reach 23°C, slowly place in LN_2, dunk in boiling H_2O		Up-hill quench: Allow to reach 23°C, slowly place in LN_2, dunk in boiling H_2O	Up-hill quench: Allow to reach 23°C, slowly place in LN_2, dunk in boiling H_2O
6				Age at 175°C, 8 h	Age at 175°C, 8 h	Age at 175°C, 8 h

Continued

TABLE 13.4(b) (*continued*)
Candidate Stress Relief Methods for Mirrors made from Al 6061-T651 Plate Stock

Step	SR 1 Control– No Heat Treatment	SR 2 Simple Heat Treatment	SR 3 SR 2 + Up-hill Quench	SR 4 Solution Treat w/28% Glycol Quench	SR 5 SR 4 w/Up-hill Quench	SR 6 Solution Treat w/H_2O Quench & Up-hill Quench
7	Finish machine	Finish machine	Finish machine	Finish machine	Finish machine	Finish machine
8				Age at 175°C, 8 h	Age at 175°C, 8 h	Age at 175°C, 8 h
9				Thermal cycle 3× at rate <1.7° C/min, cool to 83 K, hold 30 min, heat to 23°C, hold 15 min, heat to 150°C, hold 30 min, cool to 23°C	Thermal cycle 3× at rate <1.7°C/min, cool to 83 K, hold 30 min, heat to 23°C, hold 15 min, heat to 150°C, hold 30 min, cool to 23°C	Thermal cycle 3× at rate <1.7°C/min, cool to 83 K, hold 30 min, heat to 23°C, hold 15 min, heat to 150°C, hold 30 min, cool to 23°C
10	Figure test at 293 and 80 K 3×	Figure test at 293 and 80 K 3×	Figure test at 293 and 80 K 3×	Figure test at 293 and 80 K 3×	Figure test at 293 and 80 K 3×	Figure test at 293 and 80 K 3×

Source: From Ohl, R. et al., *Proc. SPIE*, 4822, 51, 2002.

We next consider experiences reported in the literature with making cast and wrought aluminum mirror substrates. This is followed by discussions of typical machined and welded mirror configurations. Some referenced experiences and investigations indicate significant potential advantages of aluminum mirrors over nonmetallic ones for astronomical applications involving large (i.e., >4-m [~13-ft])-diameter mirrors (Leblank and Rozelot, 1991; Rozelot, 1992; Dierickx, 1992; Barr and Livingston, 1992). In the minds of some interested parties, the basic reason why such mirrors have not actually been developed to date is reluctance on the parts of financial sponsors to fund metallic mirror developments, deemed more risky than more conventional approaches using nonmetallic mirror substrates (Bingham, 1992). This observation seems especially appropriate in the light of recent demonstrated successes of thin, large-diameter, spin-cast nonmetallic mirror substrates reported in Chapter 12.

13.3.1 CAST ALUMINUM MIRRORS

Forbes (1968) described two historically significant 60-in. (153-cm)-diameter mirrors built at the University of Arizona for use in photometric astronomical telescopes. Both were made of Tenzalloy aluminum. This is an age-hardening alloy containing about 7.5% zinc, 0.6% copper, 0.4% magnesium, and 91.5% pure aluminum. The mirrors were cast in a tapered cross-section form (the type shown in Figure 9.27[b]) very close to the desired configuration. By cooling the blanks quickly, porosity was reduced. They were machined to within 0.001 in. (0.025 mm) of final optical figure and central through holes were bored. The blanks were then annealed at 420°C for 2 h and cycled four times between −18°C and ambient temperature. This temperature cycling was repeated at weekly intervals for four weeks. The blanks were then ground spherical within 0.0005 in. (0.013 mm), ELN-plated, ground and polished to within about one wave (visible light) of spherical shape, and aluminized. Forbes (1968) indicated from operational use of the mirrors that this manufacturing process resulted in metal mirrors of high stability. Forbes (1992) reported that further testing of these mirrors showed long-term stability of the order of 0.25 to 1.0 wave (visible light) per year.

Aluminum alloy 356-T6 (composition about 7% silicon, 0.4% magnesium, and the balance pure aluminum) has been used in other cast mirrors of various sizes. This material is easily cast, experiences few cracks, and has good homogeneity throughout. It accepts nickel plating well. However, the superiority of Tenzalloy as compared with 356-T6 with regard to temporal stability when used as mirror substrates was indicated by a direct comparison reported by Forbes and Johnson (1971). The mirrors evaluated were 38×56 cm (15.0×22.0 in.) elliptical flats. Two were made of each material type. All were initially figured to within about two waves of plane (at $\lambda = 0.5$ µm). Subsequent optical tests indicated that both the 356-T6 flats warped by many waves in a short time. One of the Tenzalloy flats retained its figure quite well for at least 1 year. The other Tenzalloy flat warped by less than two waves in that time period.

13.3.2 MACHINED ALUMINUM MIRRORS

Aluminum alloy 6061 (composition about 1.0% magnesium, 0.7% iron, 0.6% silicon, 0.3% copper, and the balance aluminum) has predominated in metal mirror applications because of its superior long-term stability. Typical manufacturing processes start with a forged blank tempered to T6 condition (solution heat-treated and artificially aged) and machined by normal methods to within 0.05 in. (1.3 mm) of the nominal configuration. Manufacture then proceeds through various cycles of precision machining, heat treating, plating, and optical finishing.

Fuller et al. (1981) listed the sequence of steps used for fabrication of two 27-in. (68.6-cm) diameter flat mirrors and a 25-in. (63.5-cm)-aperture off-axis aspheric mirror from 6061-T6 aluminum. These were intended for a vacuum cryogenic application at 20 K. The design called for coolant to be circulated through coils attached to the back of the substrate. See Figure 13.3 for a diagram of one mirror. The process steps for fabricating the aspheric mirror were as follows: (1) receive raw stock 6061-T6 aluminum, (2) rough machine to approximate shape including a centered spherical radius,

(3) fabricate cooling coils and braze to mirror back surface, (4) solution heat treat at 950°F, quench in glycol/water solution, and cycle between liquid nitrogen and boiling water, (5) final machine mounting surfaces and prepare optical surface, (6) polish to hyperbolic optical surface, (7) subject to preplate heat treatment (450°F liquid nitrogen to boiling water cycling), (8) plate all surfaces with an equal thickness of ELN, (9) postplate heat treat as in step 7, (10) finish optical surface to required accuracy and smoothness, (11) test to determine surface figure, (12) temperature cycle from ambient temperature to 77 K as many times as necessary until there is no surface figure change between two succeeding cycles and (13) if step 12 results in out-of-tolerance optical figure, restore figure by repolishing. Repeat steps 11, 12, and 13 until the figure is within tolerance, (14) apply reflecting coating (electrolytic gold), and (15) perform final optical tests. It should be noted that each major manufacturer of metal mirrors has its own proprietary process for thermal cycling and machining substrates. The above sequence is not necessarily optimal.

As may be noted from Figure 13.3, the general configuration of the mirror was a solid disk with a tapered rear surface and an integral mounting base. The diameter of the "necked down" region between the mirror and mounting base was about 40% of the mirror diameter. The configuration is sometimes called a "mushroom" shape. It tends to isolate the optical surface from mounting stresses, yet provides good heat transfer. The authors reported that analysis of the design indicated a maximum temperature difference between a node adjacent to the cooling coil and the extreme edge of the mirror surface of 0.016°C after stabilizing. This gradient was claimed to be insufficient to cause measurable deformation of the optical surface.

An aluminum mirror designed for use in NASA's Kuiper Airborne Observatory (KAO) was described by Downey et al. (1989). This Cassegrain-type IR telescope used a 7.3-in. (18.5-cm)-diameter oscillating secondary mirror to rapidly switch the field of view from the target of interest to the nearby sky background for calibration purposes. Minimization of mass to be moved was vital to proper performance of the system. After a trade-off comparison of light-weighted glass, beryllium, silicon carbide, solid aluminum, and foam-structured aluminum substrate designs, an aluminum substrate lightweighted by machining pockets into the back surface of a 0.7-in. (1.78-cm)-thick solid 5083-O alloy blank as illustrated in Figure 13.4 was selected. The mirror's total weight was 1.1 lb (0.5 kg), representing a 70% weight reduction from a solid 7:1 diameter-to-thickness ratio substrate. The central hub had three holes for screws interfacing to the drive mechanism of the telescope.

The mirror was machined to final shape and mounting surfaces created by diamond turning. The first step was to diamond-turn a 1.490-in. (3.785-cm)-diameter central counterbore on the front (convex) side. This surface was then used as the mounting reference for machining the back surface. The mirror was turned around and the hyperboloidal optical surface of the mirror was

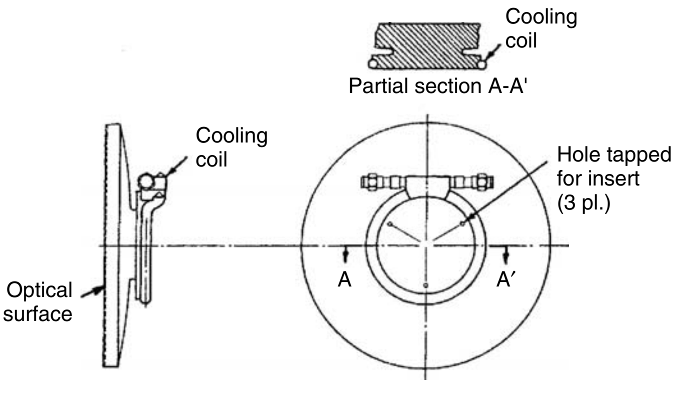

FIGURE 13.3 Schematics of a 25-in. (63.5-cm)-diameter 6061-T6 aluminum off-axis aspheric mirror used in a vacuum cryogenic application. (Adapted from Fuller, J.B.C., Jr., et al., *Proc. SPIE*, 288, 104, 1981.)

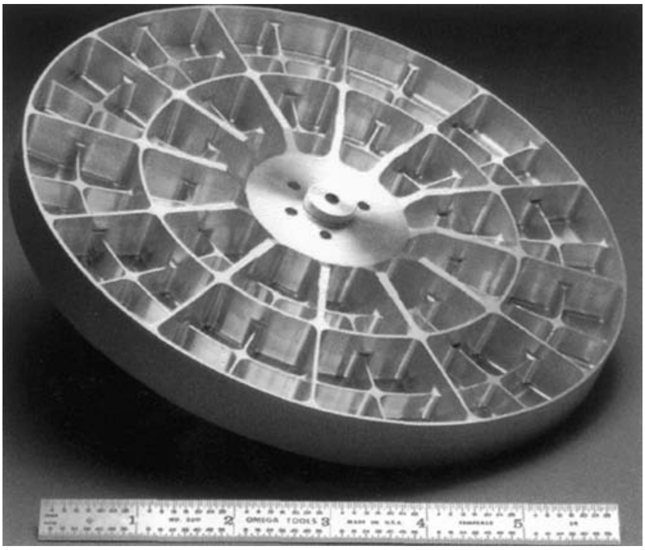

FIGURE 13.4 Photograph of the machined back surface of the lightweighted aluminum secondary mirror developed for the Kuiper Airborne Observatory (KAO). (From Downey, C.H. et al., *Proc. SPIE*, 1167, 329, 1989.)

diamond-turned to final figure. It was then coated with aluminum and silicon monoxide thin films. Interferometric tests indicated the quality of the surface to be ~0.65 wave p-v at 0.633 μm wavelength over 90% of the aperture. Surface roughness was estimated to be ~80 Å rms. Mechanical aspects of mounting this mirror to the telescope are discussed in Section 13.10.

13.3.3 WELDED ALUMINUM MIRRORS

A 40-cm (15.75-in.)-diameter *f*/2 spherical aluminum alloy mirror made by welding together six individually cast Tenzalloy segments was described by Forbes (1969, 1992). The configuration was as shown in Figure 13.5. The substrate was machined, annealed, and lapped prior to electrolytic deposition of a 0.0003-in. (0.0075-mm)-thick coating of nickel. The mirror was then figured. It was temperature-cycled from +30 to −17°C three times during grinding and polishing. After figuring, it was cycled twice from 30 to −35°C, holding at the lower temperature for more than 4 h. Thermally induced warpage due to inhomogeneity in the weldment was minimized by matching the coefficient of expansion of the welding materials to the Tenzalloy. The stress-relieving temperature cycling after welding tended to reduce distortions due to that step in the fabrication process.

The mirror's surface was judged from Ronchi tests to deform by no more than one wave of visible light when the temperature was changed from 25 to −35°C. Interferometric tests reported by Forbes (1992) showed print-through of the pie-shaped segments.

Taylor (1975) described a series of aluminum mirrors in the size range of 4.6 m (180 in.) to 7 m (276 in.) in diameter made of welded aluminum plates for use in solar simulators. Figure 13.6(a) shows the basic equilateral, triangular, rib pattern chosen for those mirrors. Figure 13.6(b) shows a typical mirror with heating and cooling coils added. Taylor indicated that 24 cavities gave adequate structural rigidity to a 5.5 m (216 in.) mirror. Table 13.5 summarizes the specifications for this mirror. Aluminum alloy 5086 H112 or H116 (composition 0.4% silicon, 0.5% iron, 0.2 to 0.7% manganese, 3.5 to 4.5% magnesium) was used. The finished mirror achieved the required optical and thermal performance for the intended application. Taylor attributed the good thermal behavior and stability of the mirror at least in part to the choice of a non-heat-treatable alloy. As long as the material never reaches an operational temperature higher than that used in stress relieving, the material remains in an annealed condition with enhanced dimensional stability. Taylor's paper provided surprisingly detailed descriptions of the design

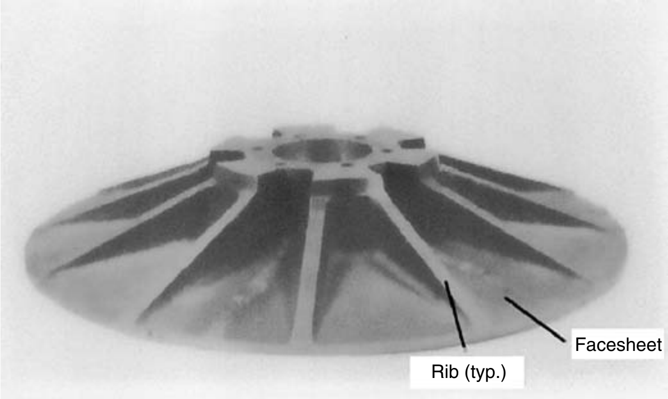
Facesheet
Rib (typ.)

FIGURE 13.5 Photograph of a welded-segment Tenzalloy mirror of 40 cm (15.75 in.) diameter. (Adapted from Forbes, F.F., *Appl. Opt.*, 8, 1361, 1969.)

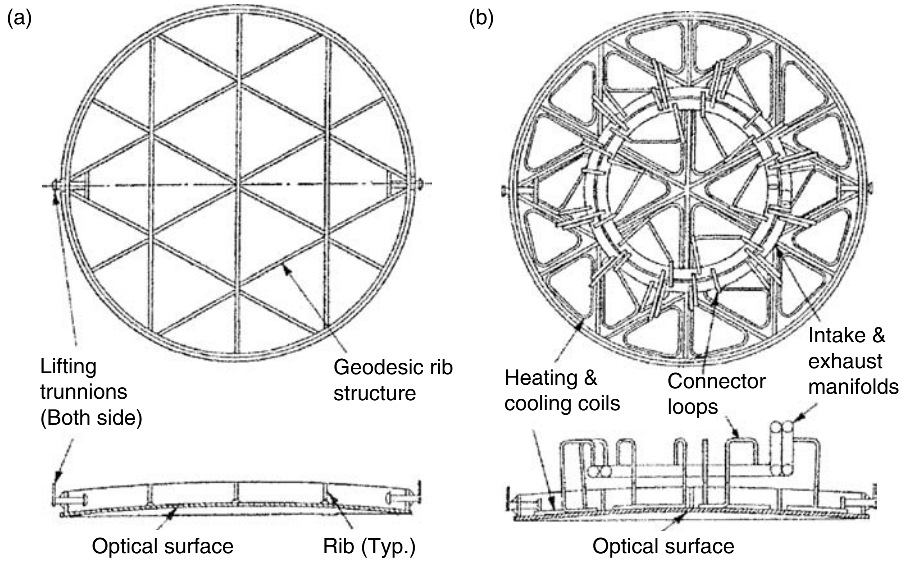
(a)
Lifting trunnions (Both side)
Geodesic rib structure
Optical surface
Rib (Typ.)
(b)
Heating & cooling coils
Connector loops
Intake & exhaust manifolds
Optical surface

FIGURE 13.6 Schematics of (a) a large-diameter welded aluminum mirror for a solar simulator application and (b) the same mirror with added temperature control system. (Adapted from Taylor, D., *Opt. Eng.*, 14, 559, 1975.)

and fabrication processes used to make the solar simulator mirrors. It also considered at length the unique problems associated with handling and transporting large metal mirrors.

Leblank and Rozelot (1991) reported interest on the part of European researchers in large aluminum mirrors as a potentially lower cost alternative to glass mirrors. Active control of the thin meniscus mirror was recognized as necessary. Under a preliminary phase of the Large Active Mirror in Aluminum (LAMA) Project, an investigation of the feasibility of an aluminum version of the ESO Very Large Telescope (VLT) primary was initiated. Although an 8.3-m (26.9-ft)-diameter spin-cast Zerodur mirror design was actually adopted for use in this telescope (see Dierickx et al., 1996), the metal mirror investigation is summarized here for its general informative value in terms of other applications, potentially including large space borne optics.

The metal mirror and its mount were to have the following general characteristics: 8.2 m (26.9 ft) OD, 1 m (40 in.) diameter perforation, 18 cm (7.1 in.) thickness, meniscus shape, 28.8 m (94.5 ft) concave radius, 150 axial supports, and 60 radial supports. Figure 13.7 shows the basic configuration

TABLE 13.5
Design Specifications for a Large Aluminum Mirror

Optical Requirements	
Diameter	5.5 m + 6.4 mm
Radius of curvature	30.7 m ± 100 mm
Slope error tolerance	<30 arcsec
Reflectivity as aluminized	>82%
Reflectivity uniformity	±2% over aperture
Clear aperture (minimum)	5.3 m
Substrate material	Aluminum alloy 5086-H112 or -H116
Optical surface	Aluminized electroless nickel
The mirror shall meet the specifications for the radius of curvature, slope error tolerance, reflectivity uniformity, and reflectivity after installation in the dome of the space chamber.	
Structural Requirements	
Temperature control	Coils welded to rear of dish, manifolds, and interconnected loops
Support system	12-point Hindle mount mechanism
Mirror structure	One-piece construction
The mirror and suspension mechanism shall be designed to meet an earthquake coefficient of 0.3g.	
Thermal Requirements	
Cooling	+20 to −73°C in 2.5 h at an approximately linear rate of cooling
Heating	−73 to +20°C in 4 h at an approximately linear rate of heating
Range of mirror operating temperature	−100 to +100°C
Temperature control medium	Nitrogen gas, 115 psig maximum
The mirror shall meet the temperature control specifications in a vacuum.	

Source: Adapted from Taylor, D., *Opt. Eng.*, 14, 559, 1975.

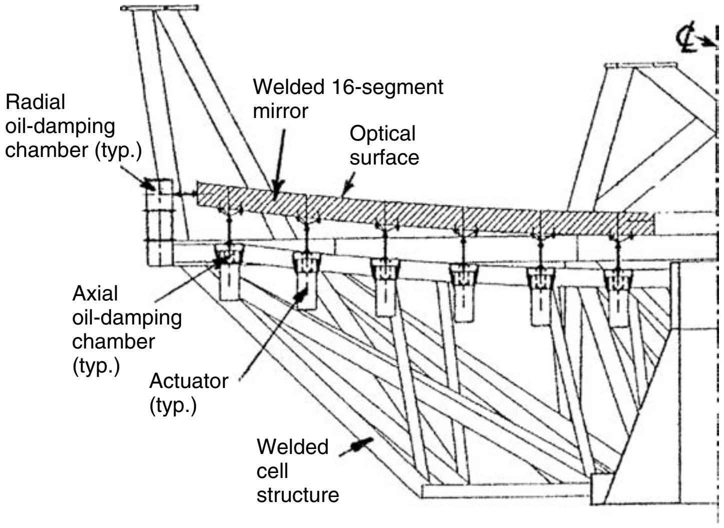

FIGURE 13.7 Schematic diagram of the aluminum mirror and axial support structure investigated for the ESO Very Large Telescope (VLT) Project. (Adapted from Leblank, J-M. and Rozelot, J-P., *Proc. SPIE*, 1535, 122, 1991.)

of the mirror and its support mechanisms. Passive oil motion-damping chambers and parallel-mounted actuators were planned for axial support.

A Series 5000 aluminum/magnesium alloy was chosen as a good compromise between mechanical characteristics and welding capabilities. The blank was to be formed by electron beam welding 16 hot-forged segments and stabilized by heating and cryogenic cooling in liquid nitrogen at various stages of rough machining to within 50 μm (0.002 in.) of nominal figure. The surface was to be chemically nickel-coated to a 300 μm (0.012 in.) ±10% thickness and then ground to within 35 μm (0.0012 in.) of desired shape. Polishing would then follow. Initial experiments showed that the welded joints would not show through the nickel coating. Similar results have been reported by Enard (1990) with regard to other aluminum mirror technology developments by ESO.

13.4 BERYLLIUM MIRRORS

Beryllium has several unique properties: low density (two thirds that of aluminum), high stiffness-to-weight ratio, high specific heat, and high conductivity. Owing to its hexagonal crystalline structure, beryllium is highly anisotropic. Its thermal expansion coefficient is typically 7.7×10^{-6} $°C^{-1}$ along the axis perpendicular to the hexagonal-face axis and 10.6×10^{-6} $°C^{-1}$ along the orthogonal axes.

In order to develop an isotropic structure and increase strength, beryllium parts are usually fabricated by powder metallurgical methods. Isotropy of macro particles is approached statistically with a large number of very small particle grains having random relative orientations. Figure 13.8 illustrates schematically the vacuum hot-pressing (VHP) method for making a blank such as might be used as a mirror substrate. The powder is fed into a cylindrical graphite or steel die and, with mechanical vibration, is compacted to approximately 50% of bulk density. The two end rams are then driven together to consolidate the material to better than 99% of bulk density. The process takes place under vacuum and at an elevated temperature to promote sintering.

Highly stable blanks for mirrors have also been made by cold compacting beryllium powder and then vacuum sintering it at an elevated temperature. Densities in excess of 98% of bulk density have been achieved by this process. Moberly and Brown (1970) explained how, by recycling the material several times through the cold compacting step in this process, the randomness of the aggregate can be improved.

Although materials manufactured by both of these methods have been used to make beryllium mirrors, a preferred material comes from a process involving hot sintering followed by hot isostatic pressing (HIP) (Shemenski and Maringer, 1969) (see Figure 13.9). The HIP process is more expensive, but it yields blanks with low porosity and few inclusions. Some grain boundary concentrations of metallic impurities and beryllium oxide are characteristically observed. According to Lindsey and Franks (1979), these concentrations do not affect microyield strength, machinability,

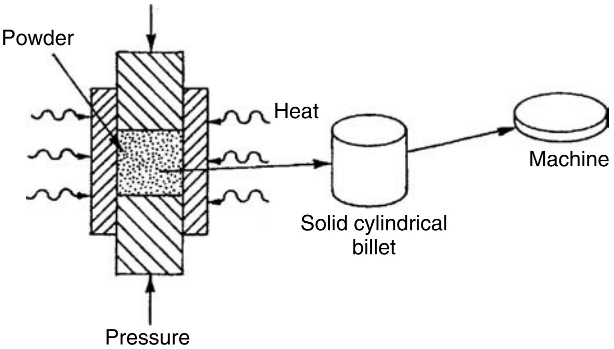

FIGURE 13.8 Schematic of the vacuum hot pressing (VHP) process for making a blank substrate for a mirror. (From Paquin, R.A. and Goggin, W., Perkin-Elmer Rept. IS11393, Norwalk, CT, 1972.)

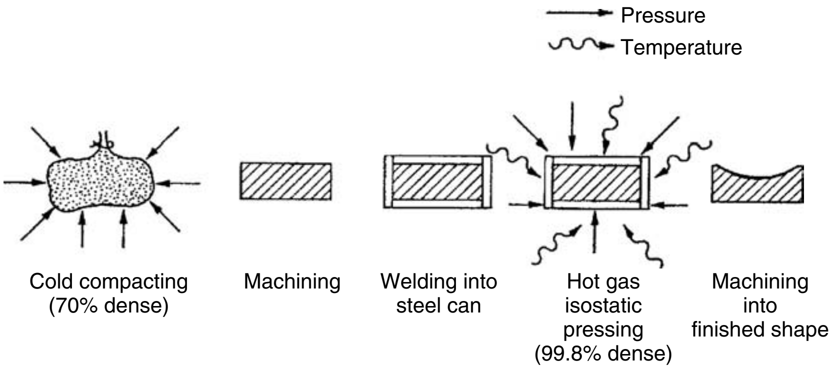
Pressure
Temperature
Cold compacting (70% dense)
Machining
Welding into steel can
Hot gas isostatic pressing (99.8% dense)
Machining into finished shape

FIGURE 13.9 Beryllium mirror blank preparation by the cold compacting plus hot isostatic pressing (HIP) process. (From Paquin, R.A. and Goggin, W., Perkin-Elmer Rept. IS11393, Norwalk, CT, 1972.)

or growth structure (rib print-through) in the polished overcoating. A comparison of the VHP and HIP processes was reported by Gossett et al. (1989).

The fastening of separate pieces of beryllium (such as plates made by VHP) by welding, brazing, diffusion bonding, or adhesive bonding to make a mirror substrate is quite difficult and generally gives poor results. Early experiments with brazing beryllium mirrors used silver lithium and aluminum silicon alloys as brazing materials. A 20-in. (50.8-cm)-diameter spherical mirror 1.0 in. (2.54 cm) thick with a brazed eggcrate core and brazed-on front and back face sheets weighing less than 6 Ib (2.7 kg) was fabricated and tested by Paquin and Goggin (1972). Sensitivity to changes in ambient temperature of about $\lambda/25$ per °F for visible light was measured. Open-back machining, chemical milling, or advanced powder metallurgy methods are preferable techniques for achieving weight reduction.

Altenhof (1976) described a manufacturing process for two mirrors made of HIPed beryllium cylinders and lightweighted by an open-back machining process. One of these mirrors is shown in Figure 13.10. This mirror posed some significant design and fabrication challenges owing to its complex "kidney" shape, its large face dimensions of 65×40 in. (165 cm×102 cm), maximum weight constraint of 118 Ib (54 kg), optical figure requirements of $\lambda/12$ rms at $\lambda=0.63$ μm, operational temperature exposure range of 300 to 150 K, and mechanical requirements, including 15 g vibration exposure and >50 Hz natural frequency. The square lightweighting pocket pattern was chosen after a trade-off analysis to provide the minimum weight consistent with stiffness requirements to prevent deformation during fabrication and under the gravity loading of ground testing. The design of the mounting points and the interfaces with the system structure was considered an integral part of the mirror design. The opto-mechanical aspects of the mounting design are discussed in Section 13.11.

The manufacturing process for both mirrors was generally as follows. Upon completion of rough contouring at the machining facility, an initial heat treatment removed the high residual stresses buildup from that operation. The lightweighting machining operations removed about 90% of the excess material from the raw blank. Altenhof indicated that either blind-hole boring or tracer milling could be used for this operation. Studies of dynamic strain from these techniques during machining indicated that tracer milling would be less severe by a factor of 5 to 10. This would provide added safety margin at the expense of schedule.

Since the lightweighting operations produced subsurface damage layers as deep as 0.010 in. (0.25 mm), a second heat treatment was performed prior to the finish-machining operation. Subsurface damage resulting from lightweighting was then removed by chemical etching that typically removed 0.021 in. (0.53 mm) per surface with typical uniformity of 0.005 in. (0.13 mm). Critical surfaces were then finish-machined, followed by a light chemical etch of 0.005 in. (0.13 mm) to remove residual subsurface damage. Thermal stabilization by repeated high- and low-temperature cycling completed the blank processing.

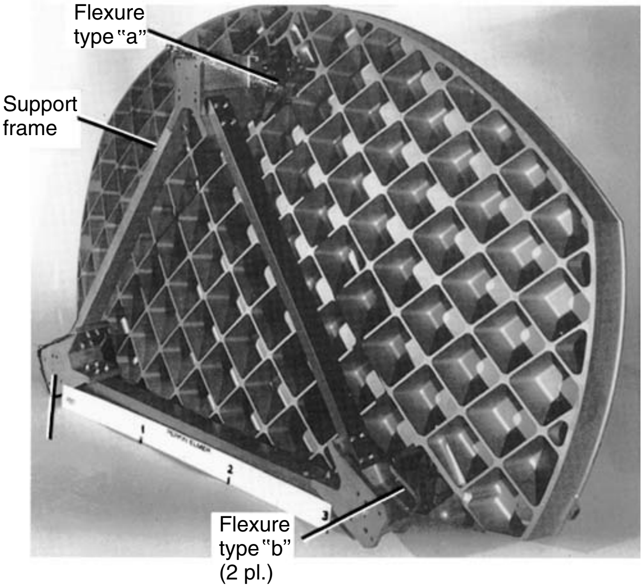

FIGURE 13.10 Photograph of the machined back side of a lightweight mirror made of hot isostatically pressed beryllium. (Adapted from Altenhof, R.R., *Opt. Eng.*, 15, 265, 1976.)

The grinding and polishing of this mirror were also described by Altenhof (1976). The first operation was grinding against a cast iron lap for about 20 h with progressively finer loose abrasive. This brought the surface errors to within about 1 μm (4×10^{-5} in.) of the desired contour. Polishing of the bare optical surface was accomplished under strict environmental control on the special three-axis computer-controlled polishing machine depicted in Figure 13.11. Jones (1975) described the use of this polishing machine in detail.

Paquin et al. (1984) and Paquin (1997) described how successful Be mirrors have been made to near-net-shape configuration by a process wherein the powdered Be is constrained within precision-manufactured metal (typically, low-carbon steel) containers of the desired dimensions, and shape, outgassed at $>670°C$, sealed, and autoclaved at a pressure of <103 MPa (15×10^3 lb/in.^{2}) and temperature of 825 to 1000°C. Upon removal of the container and annealing, the substrate requires minimal final shaping to achieve the desired end product.

Geyl and Cayrel (1997) reported that the blanks for each of the four secondary mirrors for ESO's VLT were manufactured by the HIP process from I-220-H Be powder as plano-convex solids. They were rough-machined into open-back lightweight form with triangular cells having 70 mm (2.76 in.) inscribed diameters, ribs of 3 mm (0.12 in.) thicknesses, and front face sheet thickness of 7 mm (0.28 in.). The mirror specifications called for overall diameters of 1.12 m (44.09 in.), center thicknesses of 130 mm (5.12 in.), radii of curvature of 4553.57 ± 10 mm 179.274 ± 0.394 in.), weights <42 kg (92.5 lb) with ELN coating, and hyperbolic figures. The machined blanks were heat-treated and acid-etched to remove surface stresses at appropriate times during fabrication, fine-ground, ELN plated, and polished. A typical mirror exhibited a wavefront error of 349 nm rms, 1770 nm p-v, 0.22 arcsec surface slope error, and ≤15 Å microroughness.

Figure 13.12 shows the back side of one mirror with its titanium support frame. A bayonet-type interface is provided at the mirror's center for temporary alignment, calibration, and observation devices. Six mount interfaces are machined into the mirror's core. Bipods at three of these interfaces are used to support the mirror at its neutral surface. The remaining three mount interfaces are for safety devices that prevent the mirror from falling in case of mount breakage.

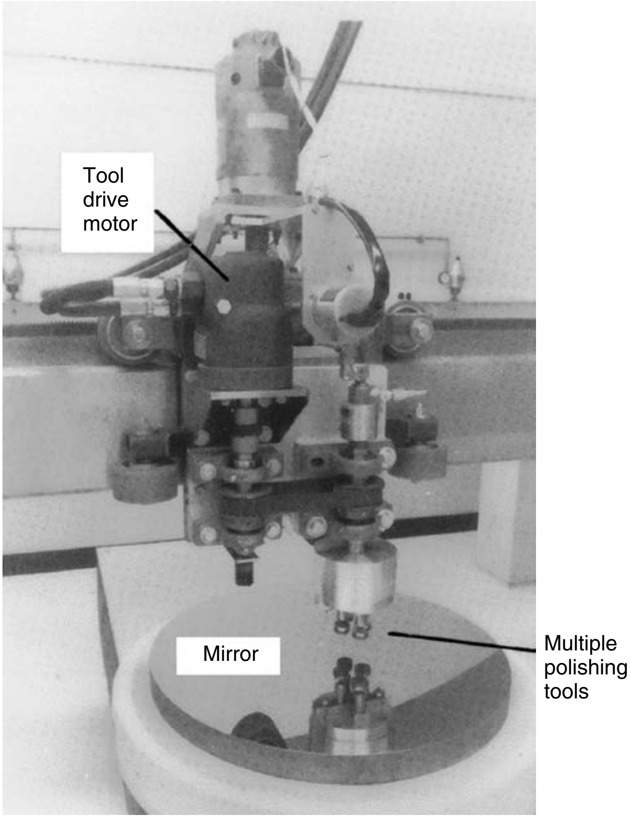

FIGURE 13.11 Photograph of the head assembly of a computer-controlled grinding and polishing machine developed for manufacture of Be mirrors. (Adapted from Altenhof, R.R., *Opt. Eng.*, 15, 265, 1976.)

The mirror support frame is attached to a multipurpose drive unit as shown in Figure 13.13. This unit provides five degrees of freedom adjustment including focus along the telescope axis, centering during observation to compensate for varying gravity influences, tilt to stabilize the field of view, and chopping (oscillatory) motion to calibrate the system against the background sky. Details regarding the drive unit are given by Stanghellini et al. (1996).

Voids can be built into open- and closed-back Be mirror substrates during the HIP process using monel or copper void formers as described by Gould (1985). These void formers are easily removed by acid leaching. Figure 13.14 illustrates the basic steps of the process.

Two 9.5-in. (24.1-cm)-diameter × 1.2-in. (2.8-cm)-thick I-70A optical grade beryllium mirrors of monolithic closed sandwich form, weighing only 2.16 lb (0.98 kg) and made by the Gould process, are shown in Figure 13.15 (Paquin et al., 1984; Paquin, 1985). They had monolithic configurations with 1 in. (2.5 cm) hexagonal core cells, 0.05-in. (1.3-mm)-thick webs, and thin, uniform-thickness front and back face sheets. Core density was about 12.5%. Optical figure of $\lambda/25$ p-v at $\lambda = 0.63\ \mu m$ was achieved. The substrate material was determined to have homogeneity and isotropy essentially the same as those of low-expansion glasses and ceramics.

These experimental flat mirrors were described as extremely stiff structures with first resonances at about 8700 Hz. Scaling this design with demonstrated unit area density of 0.030 lb/in.^{2} (21.1 kg/m^2) to 36 in. (91.4 cm) diameter would result in a mirror weighing 31 lb (14.1 kg). Its axis-vertical self-weight deflection would be 7.5×10^{-7} in. (0.019 μm). A three-point back support would be adequate during polishing, testing, and operation. Manufacture of mirrors with even lower unit area density is quite feasible. Substrate diameter is limited primarily by capability of available HIP tooling.

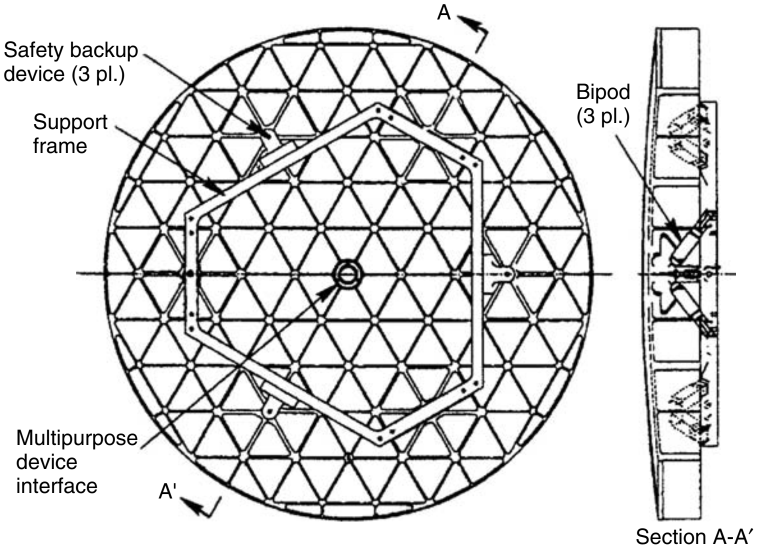
A
Safety backup device (3 pl.)
Support frame
Bipod (3 pl.)
Multipurpose device interface
A'
Section A-A′

FIGURE 13.12 Schematic of the back side of the VLT secondary mirror showing its support frame. (Adapted from Cayrel, M., *Proc. SPIE*, 3352, 721, 1998.)

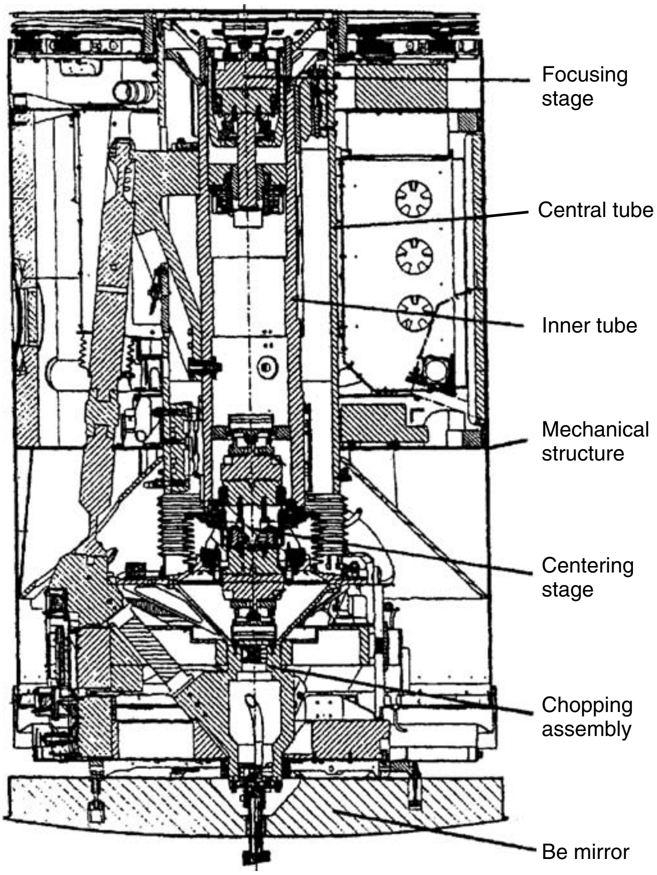
Focusing stage
Central tube
Inner tube
Mechanical structure
Centering stage
Chopping assembly
Be mirror

FIGURE 13.13 Section view through the 5-DOF drive mechanism for the VLT secondary mirror. (Adapted from Barho, R. et al., *Proc. SPIE*, 3352, 675, 1998.)

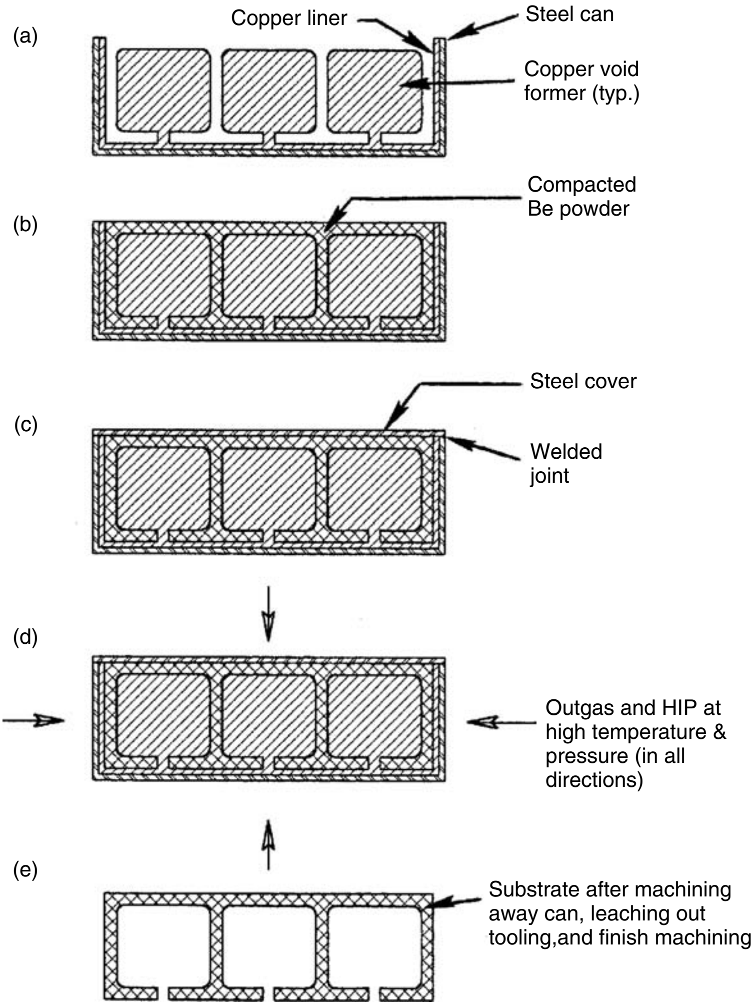
(a)
Copper liner
Steel can
Copper void former (typ.)
(b)
Compacted Be powder
(c)
Steel cover
Welded joint
(d)
Outgas and HIP at high temperature & pressure (in all directions)
(e)
Substrate after machining away can, leaching out tooling,and finish machining

FIGURE 13.14 Sequence of steps in fabricating a lightweighted Be mirror substrate by near-net-shape HIPing around leachable void formers. (Adapted from Paquin, R.A. and Gardopee, G.J., *Proc. SPIE*, 1618, 61, 1991.)

Paquin and Gardopee (1991) described the fabrication and testing of a 1.0-m (39.4-in.)-diameter, *f*/0.58, elliptically figured, lightweight Be mirror made by the same near-net-shape HIP process as just described. Void formers created a closed-back honeycomb core. The mirror's final weight was less than 18 kg (39.7 lb). Procedures for achieving the optical surface by full-aperture plunge grinding and flexible polishing laps were described by the authors.

Since the rough and finish machining, fine grinding and polishing steps in fabricating beryllium mirrors each introduce some amounts of residual stress, appropriate annealing and thermal cycling treatments of the mirror substrate are needed to relieve these stresses. Paquin (1997) indicated that the stabilization sequence given in Table 13.6 has been used successfully. Dimensional stability of beryllium was addressed by Paquin (1990, 1991).

The very smooth, low-scatter surface quality of some large glass mirrors — typically measured as low as 5 Å rms at very high spatial frequencies — has yet to be achieved with polished bare beryllium mirrors. This characteristic of the surface is frequently called microroughness. Current polishing techniques typically achieve 15 to 25 Å microroughness on bare beryllium surfaces of moderate aperture (Parsonage, 2004). Experiments have indicated that a thin film of beryllium sputtered onto a beryllium substrate can be polished to optical surfaces with ~5 Å microroughness (Murray et al., 1991).

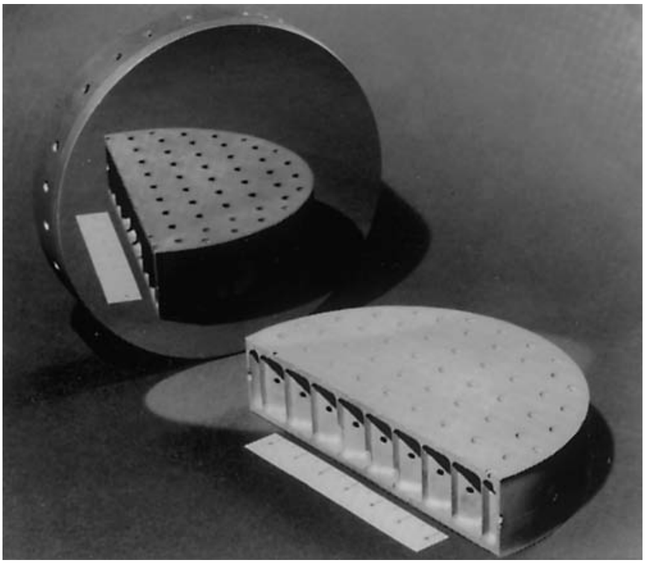

FIGURE 13.15 Photograph of two 9.5-in. (24.1-cm)-diameter lightweighted monolithic closed-back Be mirrors fabricated by near-net-shape HIPing around leachable void formers. The unit area density is 0.030 lb/in.^{2} (From Paquin, R.A., *Opt. Eng.*, 25, 2003, 1986.)

For long-wavelength IR applications, it is unnecessary to coat beryllium; its reflectivity at various wavelengths is typically as shown in Figure 13.16. At shorter wavelengths, applying a thin film of Be or a thicker (sputtered) layer of that material to the Be substrate improves the reflectance. All-beryllium mirrors have the following three advantages over those with ELN-plated surfaces: they are not susceptible to bimetallic effects when the temperature changes, they are slightly lighter, and they are less vulnerable to radiation damage due to natural or nuclear radiation such as might be encountered in some types of space missions (Sweeney, 1991).

Mirrors intended for use at cryogenic temperatures should be temperature-cycled and tested at or near the operating temperature (e.g., see Mikk, 1975). Compensation for changes at low temperature with or without plating can then be built into the mirror figure. Figure 13.17 shows a computer plot of in-process surface errors for the bare beryllium primary mirror for the Infrared Astronomical Satellite (IRAS) Telescope showing the required room-temperature correction needed on the reflecting surface to compensate for changes anticipated at 2 K based on in-process interferometric tests at the latter temperature as well as known instrumental errors.

Parsonage (2004) described the advantages of a new formulation of beryllium called O-30 that is created by a gas atomization process (Parsonage, 1998). This process involves vacuum melting of solid high purity beryllium and pouring it through a small orifice where it encounters a stream of high velocity gas that breaks the stream into small spherical droplets as it cools under ambient atmospheric pressure. The resulting material has the lowest beryllium oxide content ever produced by powder metallurgy technology, is highly isotropic, and behaves well during HIPing. Mechanical characteristics of HIPed O-30 are compared to other forms of this material in Table 3.20.

According to Parsonage (2005), the low scatter and isotropy of HIPed O-30 beryllium makes it ideal for making optical mirrors; especially ones intended for cryogenic applications. Tests conducted under the Sub-scale Beryllium Mirror Demonstrator (SBMD) and Advanced Mirror Systems Demonstrator (AMSD) programs on 0.5 m diameter and 1.4 m hexagonal mirrors, respectively, demonstrated that O-30 Be would be better than ULE or SiC for making the primary, secondary, and tertiary mirrors of the James Webb Space Telescope (JWST) (Parsonage, 2004). Figure 13.18 shows results of the interferometric cryogenic testing of the AMSD mirror. Reproducibility from one 300 to 30 K cryo cycle to the

TABLE 13.6
Typical Sequence of In-Process Fabrication, Annealing, and Thermal Cycling Stress Relieving Steps for Be Mirrors to be Used in Cryogenic Applications[a]

Rough machine
Acid etch
Anneal at 790°C
Finish machine
Acid etch
Thermal cycle three to five times (limits determined by application, but at least −40 to +100°C)
Grind, etch, and thermal cycle
Figure and thermal cycle
Final polish and thermal cycle

[a] When ELN or Be coatings are used, they should be applied after the grind/etch/thermal cycle steps. For thin Be coatings, deposition should be after the figure/thermal cycle step.

Source: From Paquin, R.A., in *Handbook of Optomechanical Engineering*, CRC Press, Boca Raton, FL, 1997, chap. 4.

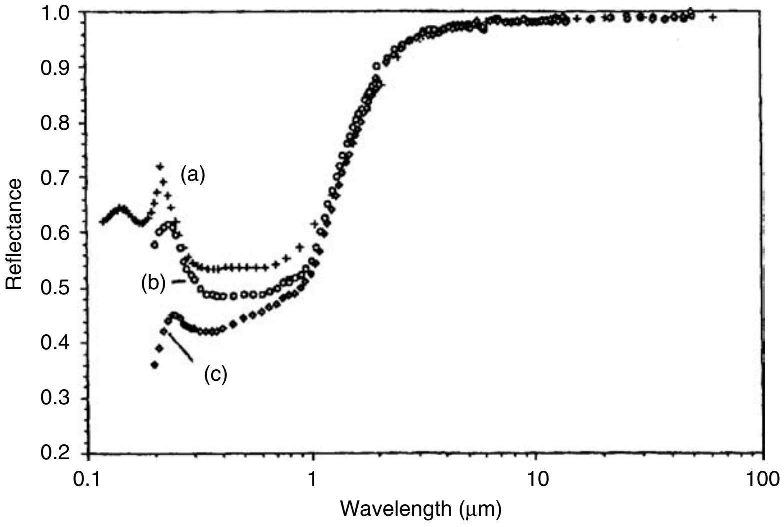

FIGURE 13.16 Reflectance vs. wavelength of polished surfaces of (a) evaporated high-purity thin film Be, (b) high-purity thick Be cladding, and (c) bulk HIPed Be (2% BeO). (From Paquin, R.A., in *Handbook of Optics*, 2nd Ed., Vol. II, Bass, M., Van Stryland, E.W., Williams, D.R., and Wolfe, W.L., Eds., Optical Society of America, Washington, 1994, chap. 35.)

next was 0.0110 μm rms. Aerial density of the mirror was <15 kg/m^2 and its first mode frequency was at least 220 Hz. These results support expectations that the JWST mirrors will meet all specifications.

Beryllium has earned an unfortunate reputation as a hazardous material. Piccolo (1980) and Sawyer (1980) discussed contamination control for Be. Paquin (1997) indicated that studies concluding that it is a potential human carcinogen have been shown to be flawed. Nevertheless, the U.S. Environmental Protection Agency continues to claim that this is probably the case. Medical data (Hoover et al., 1992) have shown that only about 3% of workers who work with Be appear to be susceptible to disease. These individuals typically have a genetic tendency toward allergy and must inhale Be dust to be affected. With proper precautions used in proper manufacturing facilities, the health risk from machining bare Be is minimal. Simple exhaust systems at the source of dust creation with

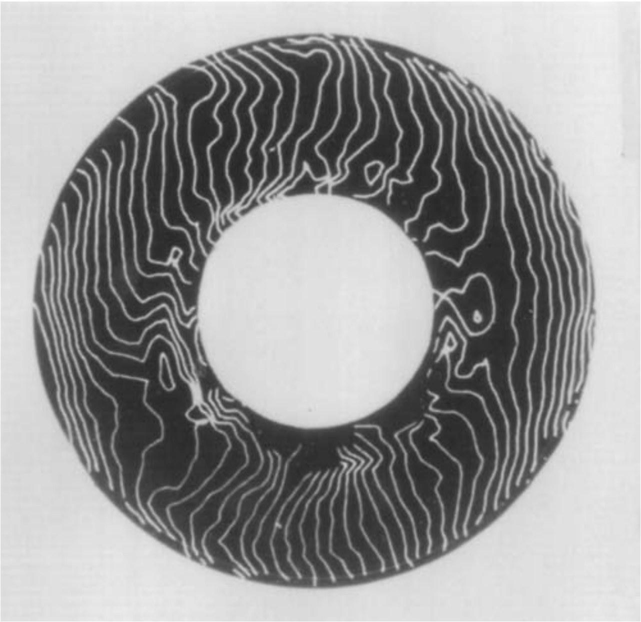

FIGURE 13.17 In-process computer plot of equivalent double-pass surface error contours needed in the Be primary mirror for the Infrared Astronomical Satellite (IRAS) Telescope at room temperature to compensate for instrumental errors and changes anticipated for operation at 2 K. (From Harned, N. et al., *Opt. Eng.*, 20, 195, 1981.)

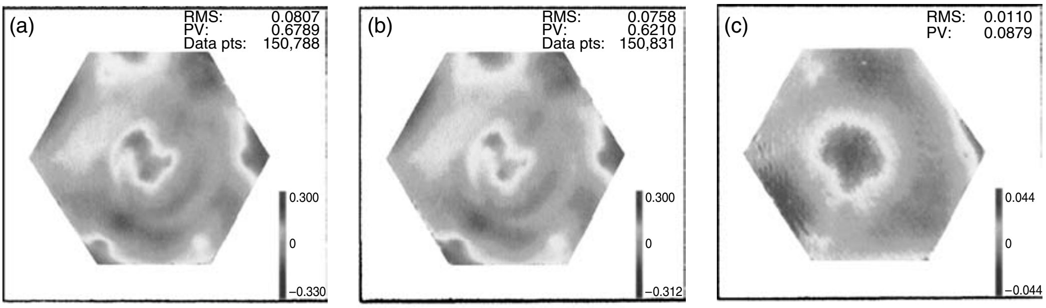

Cycle #1 [30G−295G] Cycle #2 [29a−294A] Reproductibility of cryogenic deformation

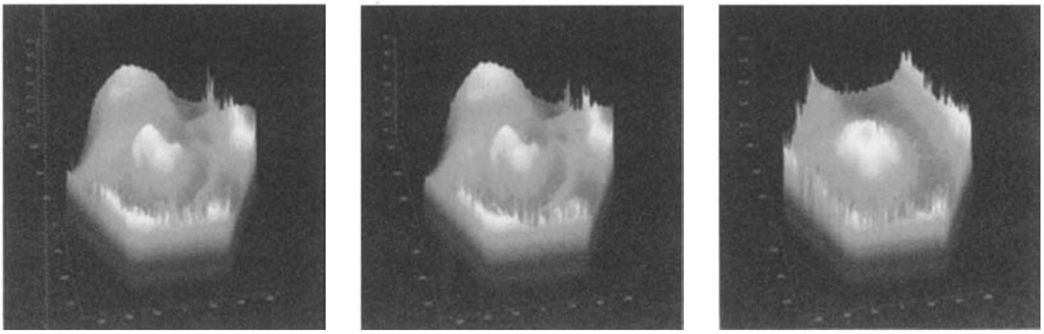

FIGURE 13.18 Interferometric test results for the AMSD beryllium mirror: (a) Cycle #1, (b) Cycle # 2, (c) reproducibility (difference) for two cycles. Figure errors are μm. (From Parsonage, T., *Proc. SPIE*, 5494, 39, 2004.)

efficient filters are very effective. In loose abrasive grinding of optical surfaces, there is no hazard if the slurry is captured and not allowed to dry on exposed surfaces. The contaminated waste is not considered hazardous under U.S. law and can be disposed of by a licensed disposal firm without problems. Paquin (1997) pointed out that fine dust of other optical materials such as SiO_2 and SiC could also cause respiratory disease if inhaled, so they should be handled and machined very carefully.

13.5 MIRRORS MADE FROM OTHER METALS

Metal mirrors are frequently used in applications involving high-energy electromagnetic beam irradiance of the reflecting surface and requiring active cooling by flowing pressurized fluid through channels machined into the substrate or indirect cooling by way of contact with cooled pressure plates. Aluminum, copper, molybdenum, tungsten, and silicon carbide are popular materials for such mirrors (Klein, 1981; Oettinger and McClellan, 1976; Howells and Paquin, 1997). Stainless steel has also been employed in some instances, particularly for synchrotron beam line mirrors (Parks, 1974; Howells and Paquin, 1997). We consider copper, molybdenum, silicon carbide, and some metal matrix mirrors in this section.

13.5.1 COPPER MIRRORS

Bare copper mirrors perform well at IR wavelengths because they are highly reflective. Reflectance of 98.6% is typical at 10.6 μm wavelength. At visible wavelengths, they are much less efficient; ~60% reflectance at 0.5 μm is typical (Paquin, 1994). These mirrors have good thermal properties and are economical to produce. Experiments reported by Lester and Saito (1977) indicated that a visible oxide layer forms on a freshly polished bare copper surface within 120 h, but the reflectivity at 10.6 μm does not degrade by more than ~0.5%, nor does the reflectivity at 0.633 μm degrade by more than ~2% in that time period. The scattering effect of the polished surface was found to increase with age.

Copper mirrors are usually made of oxygen-free, high-conductivity (OFHC) base material with characteristics as listed in Tables 3.14–3.16. A lower cost mirror material with slightly reduced performance characteristics has been called "laboratory copper" by Spawr and Pierce (1976). Mirrors made from either material are typically configured as solid disks or rectangular plates with thicknesses of about one-sixth the diameter or diagonal of the face. Denny et al. (1979) indicated that OFHC copper mirrors as large as 30 in. (76 cm) in major face dimension had been made to a surface figure accuracy of $\lambda/20$ for visible light. Hoffman et al. (1975) reported success in ion-polishing copper mirrors to increase smoothness and decrease absorptivity.

A form of copper called Glidcop™ AL-15, UNS C15715 having 0.3 wt% Al_2O_3 has been used successfully for cooled beam folding and focusing mirrors in synchrotron beam lines (Howells and Paquin, 1997). The material can be ELN plated, ruled to make gratings, and brazed if special precautions are followed. Its characteristics are given in Tables 3.14–3.16.

13.5.2 MOLYBDENUM MIRRORS

Molybdenum mirrors have favorable thermal properties for use in high-thermal-irradiance applications and are generally cooled. Reflectivity of bare, polished Mo is typically greater than 90% for wavelengths longer than 1.8 μm. Low-carbon, vacuum-arc-cast plate is the preferred material for polished Mo mirrors. This is produced by vacuum-arc melting of powdered Mo in a water-cooled copper mold. It is generally of high purity and has a minimum of second-phase particles. Other forms used with varying degrees of success are powder metallurgy Mo produced from compacted and sintered Mo powder and TZM alloy[†] produced by vacuum-arc melting of carbon-deoxidized Mo with titanium and zirconium in a water-cooled mold. Powder-metallurgy Mo typically has voids and oxide particles as impurities. The additives in TZM promote a dispersion of fine carbon particles that improve the strength and high-temperature stability of that material (Bennett et al., 1980).

[†] TZM is an alloy of molybdenum, titanium, zirconium and carbon. It has a higher recrystallization temperature, higher creep strength, and higher tensile strength than pure molybdenum

Kurdock et al. (1975) described techniques for superpolishing Mo, TZM, and beryllium–copper mirrors to microroughness less than 20 Å rms. Important features of the recommended process were the use of controlled grinding, i.e., the use of progressively finer abrasives, with total material removal equal to at least three times the size of the previously used (coarser) grit, to minimize subsurface damage and acid etching to eliminate work-hardened layers. Table 13.7 defines the etching treatments found to be successful.

Bennett et al. (1980) detailed fabrication process data and physical and chemical analysis results for several Mo samples evaluated. The major conclusions of that study were as follows: (1) poor or imperfect polishing of Mo produces a surface finish that has no relation to the microstructure of the bulk materials; (2) polishing of any Mo material produces a thin adherent oxide layer that can be removed by sputter etching; (3) the reflectance of all well-polished types of Mo appears to be independent of processing and microstructure; (4) well-polished Mo surfaces have surface topographies directly related to the microstructure and hence the processing of the material; (5) in high-purity Mo such as vacuum-arc-cast material, the grain and subgrain structure are revealed on the optically polished surface; (6) particles such as alloy carbides harder than the Mo matrix polish more slowly, protrude from polished surfaces, and dominate the surface finish, so TZM is not a good optical mirror material; (7) in Mo prepared by powder-metallurgical techniques, porosity may adversely affect the surface finish, but extensive working to sheet dimensions reduces or eliminates this porosity; (8) in sheet material, a well-developed crystallographic texture is developed in powder-metallurgy material, but is absent in vacuum-arc-cast material; (9) polishability appears to be independent of texture; (10) the optimum type of Mo to use for smooth, low-scatter mirrors is low-carbon, vacuum-arc-cast plate or sheet material. Later experiments reported by Bennett et al. (1983) confirmed the final conclusion of the earlier work and provided details of advanced polishing techniques that tend to improve the smoothness of the mirror surface. Figure 13.19 shows Nomarski photomicrographs (a) of conventionally polished Mo, (b) of dual-abrasive polished Mo, and (c) of a polished, thick layer of sputtered Mo on a Mo substrate. The grain size in the sputtered layer is typically <0.5 μm. The structure of that layer is lightly textured and has oriented grains. The polished Mo appears nearly featureless.

13.5.3 SILICON CARBIDE MIRRORS

Silicon carbide mirror blanks are made primarily by either of two processes: chemical vapor deposition (CVD) or reaction bonding (RB). Physical characteristics of both types of SiC are summarized in Tables 3.14–3.16 and Table 3.21. The CVD process involves pyrolysis of vapor

TABLE 13.7
A Recommended Etching Process for Some Metals

Substrate	Etchant Acid	Temperature (°C)	Material Removed (mm)	Process Time (min)
Be–Cu	50% acetic 30% nitric 10% hydrochloric 10% orthophosphoric	70	0.008	~15
Mo and TZM	50% sulfuric 50% nitric	78	0.003	~10

Source: Adapted from Kurdock, J. et al., *Appl. Opt*., 14, 1808, 1975.

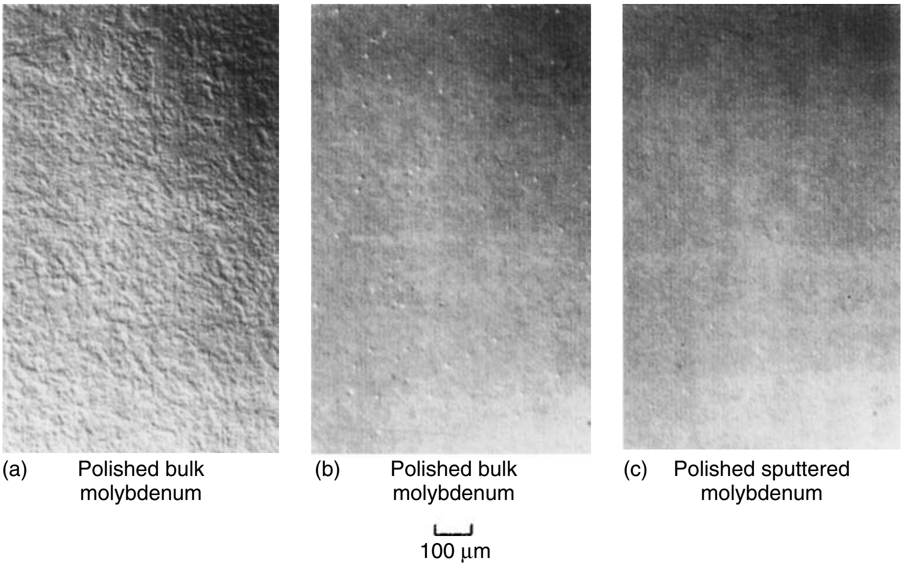
(a) Polished bulk molybdenum
(b) Polished bulk molybdenum
(c) Polished sputtered molybdenum
100 μm

FIGURE 13.19 Nomarski photomicrographs of three types of molybdenum surfaces: (a) conventionally polished bulk material, (b) dual-abrasive polished bulk material, and (c) polished sputtered material. (From Bennett, J.M. et al., *Appl. Opt.*, 22, 4048, 1983.)

methyltrichlorsilane in excess hydrogen within a subatmospheric-pressure CVD reactor. The process and the reactor have been described by Goela et al. (1991) and by Goela and Pickering (1997), as well as in references cited by those authors. The resulting SiC is a theoretically dense, polycrystalline material, free of voids and microcracks. The CVD process is also compatible with replication of high-precision optical surfaces onto substrates (Goela and Taylor [1989a, 1989b]). RB SiC is made by casting a slurry of α SiC[‡] into a mold, drying, prefiring, firing, and "siliconizing" to fill pores (Ealey et al., 1997). A cladding of silicon may then be added to facilitate polishing. Both materials are generated or ground with high-speed diamond wheels or diamond grit on hard laps (Paquin et al., 1991).

Goela et al. (1991) claimed that their subscale process experimentation results with CVD SiC were scalable to 1.0 m (40 in.) diameters. Measurements by those authors supported the following conclusions: (1) elastic modulus degrades by only 10% when the temperature of the SiC is raised from room temperature to 1350°C (2462°F); (2) SiC can be polished to a surface roughness of less than 0.1 nm rms; (3) BRDF of a highly polished SiC sample is 1×10^{-5} at 10.6 and 0.633 μm wavelengths for angles of 3 to 18° from specular; (4) minimal figure change ($\lambda/125=0.005$ μm rms) occurs when a SiC sample is cooled from room temperature to −190°C (−310°F); (5) no appreciable surface degradation occurs when thermal atomic oxygen flux of 2×10^{18} atom/cm^2-sec is directed onto the sample for 6 h; (6) small changes in surface reflectivity in the wavelength range $200 < \lambda < 600$ nm occur when an atomic-oxygen beam of broad energy spectrum (0 to 10 eV) with a peak at 5 eV is directed onto CVD SiC; (7) electron-beam irradiation of SiC yields a surface damage threshold of 0.5 cal/cm^2.

Reaction-bonded SiC is a two-phase material manufactured (cast) by well-established techniques developed for nonoptical applications. Paquin et al. (1991) indicated this to be a desirable material for mirrors because of the flexibility of the fabrication process (allowing adjustment in physical, thermal, and mechanical properties), low cost relative to other forms of SiC, compatibility with ion beam sputtering to obtain a smooth polishable surface, and scalability to large sizes. Those authors reported achievement of areal densities as low as 10 kg/m^2 and microroughness of 8 to 15 Å on small flat and spherical SiC mirrors. Then current technology allowed production of mirrors with diameters about 0.5 m (19.7 in.); however, future achievement of diameters of 2.5 m (98 in.) with moderate investment in facilities was predicted.

[‡] α-SiC is the hexagonal form while β-SiC is the cubic isotropic form of single-crystal material.

Ealey et al. (1997) described a process used to produce RB SiC mirrors under the proprietary CERAFORM process developed by United Technologies Corporation. Included in their publication were plots of CTE (or α) and κ for the material in comparison with the same parameters for 6061 Al, I-70A Be, and ULE as functions of temperature. These are reproduced as Figure 13.20 and Figure 13.21. Additionally, they plotted a factor called thermal stability figure of merit (FOM) vs. temperature for those same materials (see Figure 13.22). This figure of merit was defined as κ/α. It should be noted that using room-temperature data from Table 3.14, this FOM would be essentially identical for RB SiC (30% Si) and CVD SiC.

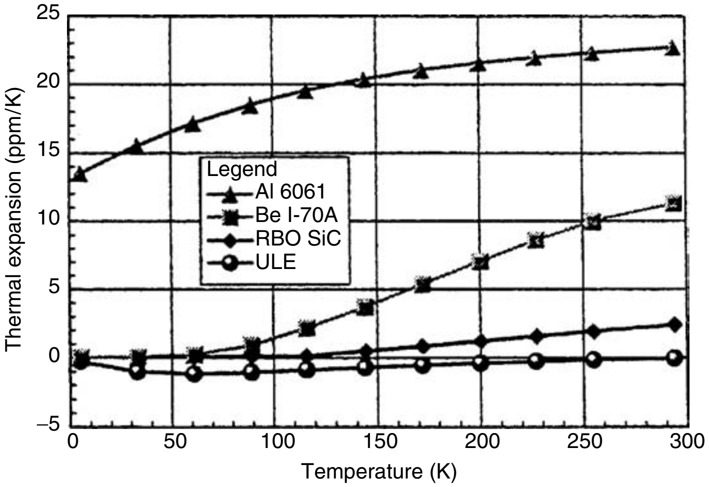

FIGURE 13.20 Plots of thermal expansion coefficient α vs. temperature for four types of mirror materials. (From Ealey, M.A. et al., *Proc. SPIE*, CR67, 53, 1997.)

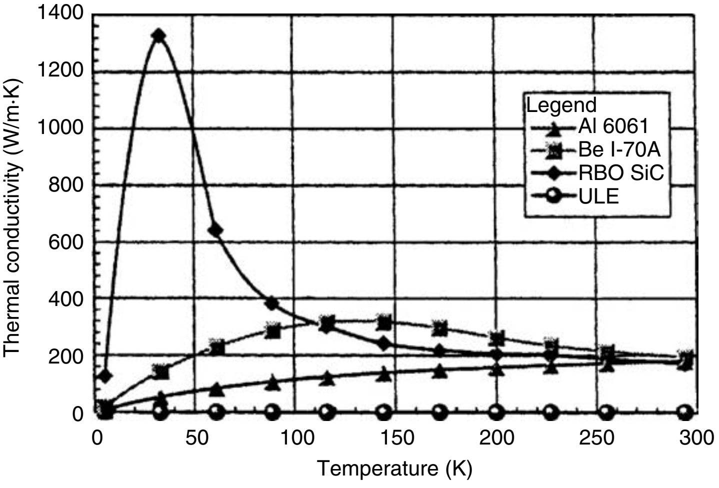

FIGURE 13.21 Plots of thermal conductivity κ vs. temperature for four types of mirror materials. (From Ealey, M.A. et al., *Proc. SPIE*, CR67, 53, 1997.)

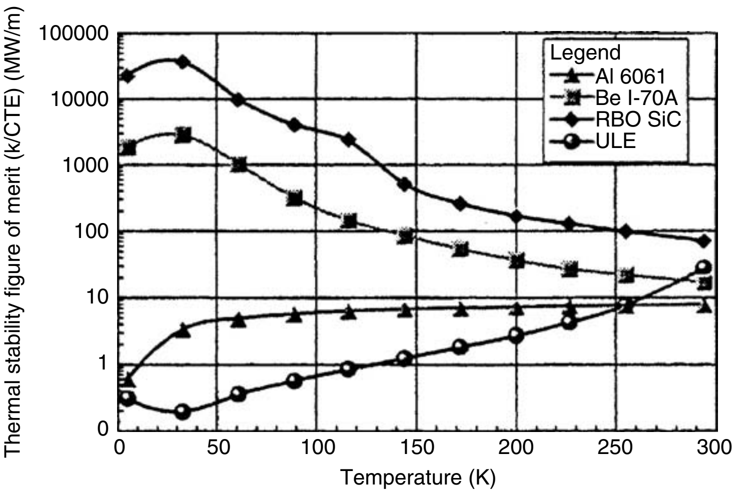

FIGURE 13.22 Plots of thermal stability figure of merit (κ/α) vs. temperature for four types of mirror materials. (From Ealey, M.A. et al., *Proc. SPIE*, CR67, 53, 1997.)

13.6 MIRRORS WITH FOAM AND METAL MATRIX CORES

Conventional lightweight mirrors as discussed in Chapter 9 face fundamental limitations on minimizing web thicknesses because of the resulting flexibility and susceptibility to distortion at high temperatures typically used for fusing these structural members to the other components of the mirror. The webs must be separated by distances large relative to their thickness, thereby allowing the mirror face sheet to sag between the webs under gravitational load or during polishing forces (creating "print-through" surface distortions). Mirrors with foam cores significantly reduce these problems because the face sheets are essentially uniformly supported on a micrometer level rather than on a millimeter level. By shaping the core to near-net-shape prior to adding the face sheets, some problems of thermal distortion during manufacture are eliminated. Weight reduction results primarily from the large percentage of open space (typically >90%) within that structure. Goodman and Jacoby (2001) compared these and some other characteristics of conventional web and foam cores for mirrors, as indicated in Table 13.8.

Although foamed fused silica was a fairly widely known material in the U.S. optical industry during the 1960s, attempts to build lightweight mirrors using this material as a structural core between face sheets were unsuccessful because the core was hard to shape, fuse to the sheets, and attach to a mount (Noble, 1966; Angele, 1969). The use of cellular metals such as aluminum for this purpose was investigated during the early 1980s (Catura and Vieira, 1985) with greater success. The latter approach did not really get started until development of foamed aluminum as a material for heat exchangers resulted in the availability of material with density as low as 4% of the parent material that was low in cost, easily fabricated, and easily brazed with minimum distortion to aluminum sheets. These favorable attributes led Pollard and coworkers to design and analyze a lightweight mirror made from this material (Pollard et al., 1987). Their model was a 12.0-in. (30.5-cm)-diameter mirror comprising 0.12-in. (3.05-mm)-thick concave face sheets and a core of nominal density 10% that of base material. Finite element analysis (FEA) and experiments did not have the expected correlation; this was attributed, in part, to differences between the actual and purported density of the foam and to variations in other mechanical properties of that material.

Stone et al. (1989) gave results of an investigation of the shear modulus of foam materials. New techniques were found to be needed since the ASTM standard for such measurements was not adequate. Ceramic (Amporox T and Amporox P), nickel, and aluminum/silicon carbide foams were tested. For materials of differing cell density, the measurements included mass density, density

TABLE 13.8
Advantages of Foam Core Mirrors Relative to Conventional Web Core Mirrors

Roles/Requirements	Foam	Webs
Support against polishing pressure	Distributed load paths under mirror surface, easier to support axially	Concentrated load paths leading to print-through of web outlines, more difficult to support axially
Dynamics/stability/stiffness/vibrational mode frequency	Higher stiffness, higher resonance frequency	More mass for the same stiffness and resonant frequency
Self-weight deflection (varies with pocket width)	Pockets typically ~10 μm	Pockets typically ~10 to 100 mm
Micrometeoroid susceptibility	Natural bumper material and ripstop	Little or no protection
Reliability/redundancy	Many alternate load paths, more graceful failure	Structural failure effect greater, catastrophic failure

Source: From Goodman, W.A. and Jacoby, M.T., *Proc. SPIE*, 4198, 260, 2001.

relative to that of the base material, shear modulus, and shear modulus relative to that of the base material. FEA of a 1.0-m (40-in.)-diameter mirror substrate design utilizing foam material indicated the sensitivity of the design to variations of the various material properties. In the analysis, Poisson's ratio was assumed to be zero. Vukobratovich (1989) pointed out that the so-called *Ashby's relationship* (Gibson and Ashby, 1988) for cellular solids did not agree with the results of experiments at the University of Arizona.

A design for an aluminum foam core/aluminum face sheet mirror described by Vukobratovich (1989) is shown in Figure 13.23. The use of aluminum/silicon carbide metal matrix composite (MMC) face sheets with an nickel foam core and MMC face sheets with an MMC foam core were suggested as possible improvements over the aluminum version.

Mohn and Vukobratovich (1988) described a design for an all-MMC telescope of 0.3 m (12 in.) aperture. Figure 13.24 shows this design schematically. The truss that supports the primary and secondary mirrors was made from 25-mm (1.0-in.)-diameter extruded structural-grade MMC tubing with 1.25 mm (0.05 in.) wall thickness. The secondary support was made from structural-grade MMC extruded bar stock. The secondary mirror was machined from optical-grade MMC, ELN plated, and polished. The double-concave-shaped primary was fashioned from MMC core with MMC face sheets. It was ELN plated on both sides, thermally cycled for stability, and polished to an optical figure of about 1 visible-light fringe. The entire telescope weighed 4.5 kg (10 Ib).

A lightweight, open-back, flat scanning mirror to be used atop a military periscope was described by Ulph (1988). To minimize weight as well as cost in quantity production, the mirror was constructed of SXA,[§] which is an aluminum/silicon carbide MMC comprising 2024 aluminum and 30%, by volume of SiC particulate. The mirror was generally trapezoidal in shape with the top and bottom edges rounded to conform to the beam footprint at various elevation angles. Its overall face dimensions were such as to fit within a 25 cm (9.8 in.) circumscribed circle. Thickness of the mirror was not stated. Finished weight of the mirror was 806 g (28.4 oz).

A total of 56 pockets were machined into the back surface leaving ribs of thickness 2 mm and a front face sheet of 3 mm thickness. Polycrystalline diamond cutters were used to CNC mill the pockets in the

---

[§] SXA is made by Advanced Composite Materials Corporation, Greer, SC.

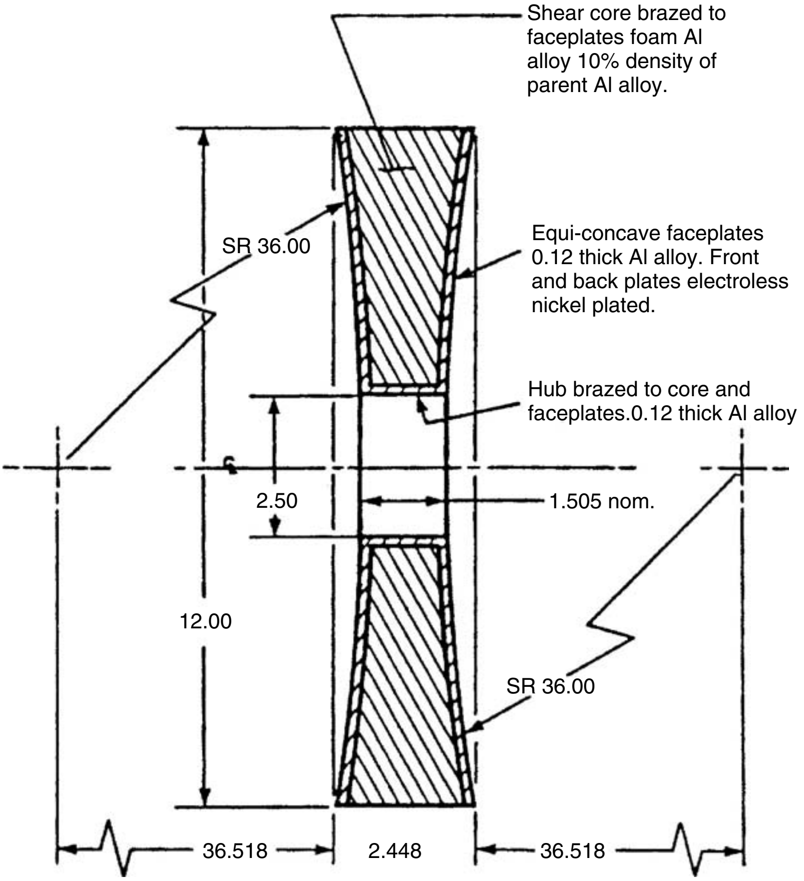
Shear core brazed to faceplates foam Al alloy 10% density of parent Al alloy.
SR 36.00
Equi-concave faceplates 0.12 thick Al alloy. Front and back plates electroless nickel plated.
Hub brazed to core and faceplates.0.12 thick Al alloy
℄
2.50
1.505 nom.
12.00
SR 36.00
36.518
2.448
36.518

1. Est. weight: 4.3 pounds
2. One side finished as *f*/1.5 parabola, second side finished as *f*/1.5 sphere.

FIGURE 13.23 Design for a lightweight mirror with aluminum facesheets and an aluminum foam core. Dimensions are inches. (From Vukobratovich, D., *Proc. SPIE*, 1044, 216, 1989.)

substrate. After thermal stress relieving the substrate at low and high temperatures, the optical surface was loose-abrasive ground approximately flat prior to plating. All surfaces except the mounting hub were ELN plated to a thickness of about 0.003 in. (0.076 mm). The plated optical surface was pitch-polished using coarse (1 μm) and fine (0.1 μm) alumina powder. Measurements after coating indicated warpage of the mirror, so it was again stress relieved, repolished, and recoated. The surface figure was then flat within ~$\lambda/8$ power and ~$\lambda/6$ irregularity at a visible wavelength over any 120 mm diameter area. The mirror withstood, without change, exposure to 160°C temperatures.

Jacobs (1992) reported that tests of the long-term dimensional stability of carefully heat-treated SXA averaged 5.7 ± 1.0 ppm per year. A typical stabilization treatment is described in Table 13.4(a).

McClelland and Content (2001) as well as Hadjimichael et al. (2002) described ways for optimizing the design of aluminum foam core/aluminum face sheet mirrors for cryogenic applications. They cited the advantages of newly developed techniques for super-polishing bare aluminum surfaces to ~0.6 nm rms microroughness to eliminate the need for applying a polishable plating such as ELN (see Lyons and Zaniewski, 2001) and athermal construction to allow manufacture and testing at room temperature and operation at cold temperatures with minimal mirror deformation. Sample concave,

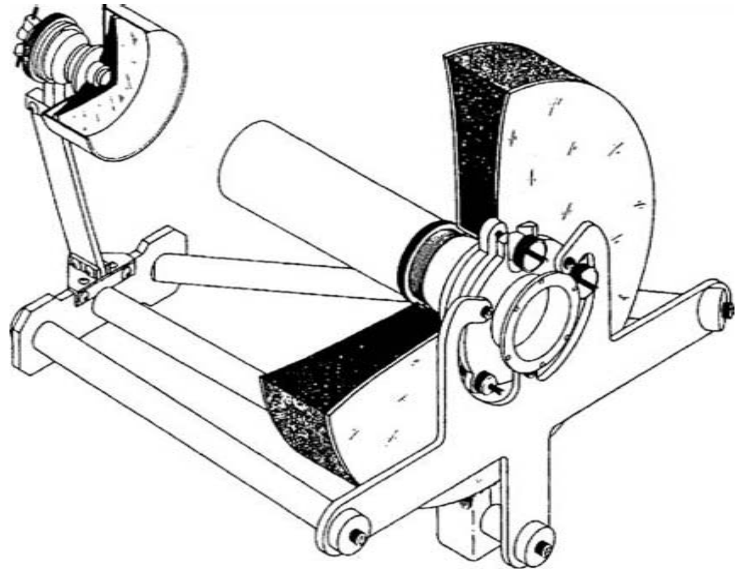

FIGURE 13.24 Schematic isometric view of an *f*/5 telescope using the mirror shown in Figure 13.23. (From Vukobratovich, D., *Proc. SPIE*, 1044, 216, 1989.)

spherical mirrors having diameters of 5 in. (127 mm) and clear apertures of 4 in. (101.6 mm) with high stiffness, low weight, and minimal print-through from the internal structure have been made and tested. The cores were fabricated from 40 pore per inch (ppi) open-cell aluminum foam with ~8% density of solid aluminum. Figure 13.25 shows a cross-sectional view of one of these mirrors. An outer ring was provided to stiffen the mirror laterally. The mount was integrated into the back face sheet to simplify mounting of the mirror. The cores were brazed to the face sheets and outer ring by a proprietary process. The brazed assembly was slowly annealed to relieve stress. Areal density of the mirror was <20 kg/m^2. The optical surface was diamond-turned to required contour after annealing.

Fortini (1999) described research into the use of open-cell silicon foam as a core material for ultralight mirrors with single-crystal silicon face sheets (see Figure 13.26[a]). Silicon typically has a density of 2.3 g/cm^3, a CTE of 2.6×10^{-6} K^{-1}, and a thermal conductivity of 150 W/m-K at room temperature. Figures 13.27(a) and (b) show the variations with temperature of α and k for silicon as compared with the same parameters for Be. The data plotted in view (a) are given in Table 13.3. For cryogenic applications, the very low CTE and high k of Si would be favorable for mirror applications. The single-crystal reflecting surface of a silicon mirror can be polished to an optical figure of typically $<\lambda/10$ p-v at $\lambda = 0.633$ μm wavelength and microroughness <5 Å rms. Figure 13.28 shows a scanning electron micrograph of the typical open-cell microstructure. Key mechanical properties, such as density and stiffness, can be adjusted during the manufacturing process.

The effort reported by Fortini (1999) involved small substrates with diameters of 9.45 cm (3.72 in.) and foam cells of 65 ppi. It had as its goal the determination of the optimal face sheet thickness, foam density relative to bulk silicon, effects of bonding the face sheets to the core, and effects of edge-bonding single-crystal silicon plates to obtain larger face sheets. An areal density of 15 kg/m^2 was targeted. The results reported indicated 5% dense foam combined with two 0.889-mm (0.035-in.)-thick face sheets to be optimal for this areal density. The resulting substrate would have stiffness equivalent to a 3.81-cm (1.50-in.)-thick single-crystal silicon monolith (diameter/thickness = 2.48). The latter substrate would, however, have an areal density six times greater than the foam structure. Modeling indicated that mirrors with even greater stiffness and lower densities could be produced.

Bonding experiments reported by Fortini (1999) indicated no significant effects on optical figure due to cycling between room and liquid-nitrogen temperatures with face sheet-to-core bonds.

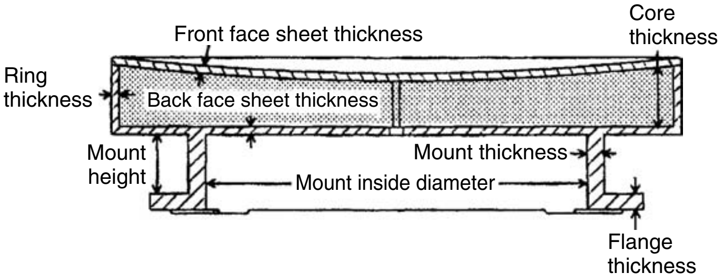
Front face sheet thickness
Core thickness
Ring thickness
Back face sheet thickness
Mount height
Mount thickness
Mount inside diameter
Flange thickness

FIGURE 13.25 Schematic sectional view of an aluminum foam core/aluminum facesheet mirror with integral mount. (From McClelland, R.S. and Content, D.A., *Proc. SPIE*, 4451, 77, 2001.)

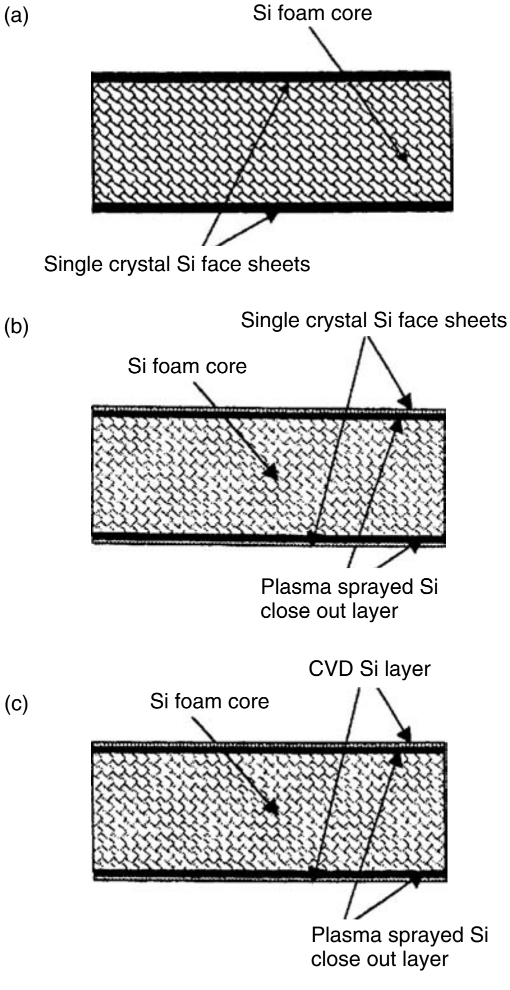
(a)
Si foam core
Single crystal Si face sheets
(b)
Single crystal Si face sheets
Si foam core
Plasma sprayed Si close out layer
(c)
CVD Si layer
Si foam core
Plasma sprayed Si close out layer

FIGURE 13.26 Schematic sectional views of mirrors with Si facesheets and foam cores: (a) basic design (adapted from Fortini, A.J., *Proc. SPIE*, 3786, 440, 1999.), (b) design with plasma sprayed layers (adapted from Jacoby, M.T. et al., *Proc. SPIE*, 3786, 460, 1999.), and (c) design with external CVD Si layers (adapted from Jacoby, M.T. et al., *Proc. SPIE*, 4451, 67, 2001.)

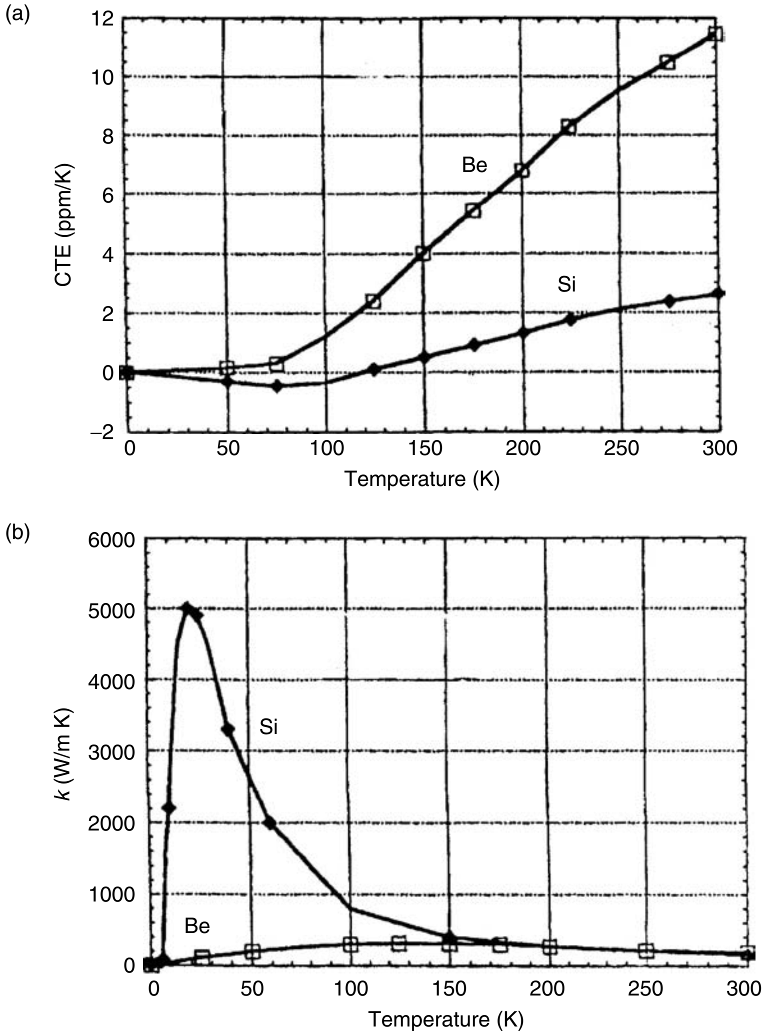

FIGURE 13.27 Comparisons of variations with temperature of (a) thermal expansion coefficients and (b) thermal conductivities for Be and Si. (From Fortini, A.J., Proc. SPIE 3786, 440, 1999.)

Similarly, face sheet edge bonds did not seem to affect figure under the same temperature changes. These results were considered encouraging in terms of future developments of mirrors with significantly larger diameters.

Jacoby et al. (1999) reported further experiments with silicon-foam core mirrors at temperatures to −183°C. These mirrors had cores with 65 ppi cells and the architecture illustrated by Figure 13.26(b). They differed slightly from the construction shown in Figure 13.26(a) in that the cores were contoured to near-net-shape by controlled crushing between precision mandrels prior to silicon infiltration. Also, the faces of the silicon cores were plasma sprayed with layers of polycrystalline silicon typically 0.025 to 0.030 in. (0.635 to 0.762 mm) thick to close out the open structure locally, then annealed and polished flat before bonding to the face sheets. The polishing process smoothed the plasma sprayed surfaces to ensure a good bond.

A further development of mirrors with silicon foam cores having the architecture shown in Figure 13.26(c) was reported by Jacoby et al. (2001). The process comprises the following steps: (1) bring open-cell or reticulated vitreous carbon (RVC) foam to near-net-shape by CNC machining, (2) plasma

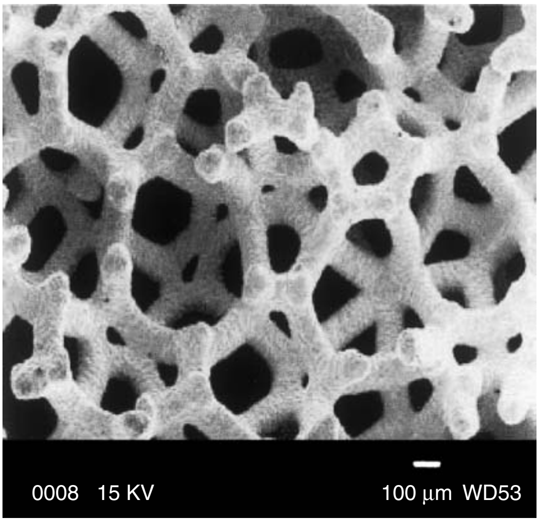

FIGURE 13.28 Scanning electron micrograph of a typical Si open-cell foam structure. (From Fortini, A.J., Proc. SPIE 3786, 440, 1999.)

spray with polycrystalline silicon to build a layer 0.025 to 0.030 in. (0.635 0.762 mm) thick through inter-particle bonding and a sintering reaction, (3) lap surface to flatness and test interferometrically, (4) apply layer of highly densified polycrystalline silicon by a CVD process to form face sheets on the core totaling 1.0 mm (0.039 in.) thick (sprayed layer plus CVD layer), (5) superpolish one face to $\leq$3.0 nm rms and figure quality $<$70 nm p-v, and (6) apply coating as appropriate. Inspection naturally takes place upon completion of each step. The authors indicated that this manufacturing process avoids the significant cost and technical problems of producing large, single-crystal face sheets as well as potential problems with bonding subdiameter crystals to form large face sheets. Analyses reported by Goodman and Jacoby (2001) based on both classical and FEA techniques predicted that mirrors with diameters of at least 0.5 m (19.7 in.) and areal densities of 7.0 kg/m^2 could be made in the manner just described. Further, these mirrors should have high first-mode frequencies of about 447 Hz and be relatively insensitive to the dynamics of space applications. Developments of silicon foam core mirrors for specific space-application experiments were described by Jacoby et al. (2001) and by Goodman et al. (2001). Cryogenic (177 K) and vacuum (10^{-5} torr) test results of a 6.0-in. (152.4-mm)-diameter mirror were also reported. Optical figure stability going from 300 to 177 K and back was said to be excellent.

The evolution of foam core lightweight mirrors has continued in recent years, largely through the efforts of Schafer Corporation (Albuquerque, NM), NASA/MSFC (Huntsville, AL), and NASA/GSFC (Greenbelt, MD). Goodman et al. (2002) discussed the design, manufacture, and testing of three demonstration mirrors using an improved (simplified) manufacturing process. The process has fewer steps and improves the resulting mirrors over prior types. These steps are: (1) CNC machine silicon or silicon carbide foam core to approximate size and shape, (2) encapsulate with a continuous polycrystalline silicon or beta silicon carbide skin by a CVD process, (3) grind to finished dimensions and shape, (4) polish the optical surface, (5) coat as appropriate. Once again, inspections occur at strategic points during manufacture.

Table 13.9 identifies these experimental mirrors and summarizes their characteristics. The so-called “Offner” mirrors were intended for use in a unity-power relay optical system based on the configuration invented for use in one of Perkin-Elmer Corporation’s early optical microlithography projector systems (see Offner, 1981). Significant improvements in performance relative to that of the mirror described by Goodman and Jacoby (2001) are apparent.

TABLE 13.9
Characteristics of Three 13 cm (5.1 in.) Diameter Concave Spherical Silicon Foam Core Mirrors Manufactured by an Improved Process

Characteristic	Offner Mirror 1	Offner Mirror 2	UV Demonstrator	Predicted Achievable
Areal density (kg/m^2)	15	15	9.8	6 to 7
Surface figure (waves rms at 633 nm)	0.084	0.033	0.021	0.005
Surface finish (Å rms)	10	5	4	1
Radius of curvature (mm)	600±12	600±12	598.5±9 +0.005	600±1
Surface quality (scratch and dig)	60/40	60/40	20/20	10/5

Source: From Goodman, W.A. et al., *Proc. SPIE*, 4822, 12, 2002.

Goodman et al. (2002) indicated that an important contributing factor in the performance improvement that they reported was that the foam core mirrors were mounted in a structure-made, carbon-fiber-reinforced silicon carbide (Cesic®). This material¶ has a low density (~2.65 g/cm^3); high stiffness (up to 269 GPa) and high bending strength (up to 210 MPa); low CTE ($\sim 2.5\times 10^{-6}$ K^{-1} at room temperature and near zero below 100 K) — nearly the same as that of silicon; high thermal conductivity k (up to 135 W/m-K); no porosity and no outgassing; isotropy in CTE, k, and other mechanical properties; low machining cost; and high chemical, corrosion, and abrasion resistance. (See Goodman et al. [2001], Devilliers and Krödel [2004], and Krödel [2004] for more details regarding this material.) The close match of CTEs for silicon and Cesic minimize variations of mounting forces applied to the mirror by the mount during temperature changes, thereby preserving optical figure of the mirror in cryogenic applications.

According to Müller et al. (2001), the process for manufacturing the raw Cesic carbon–carbon greenbody material follows these steps: (1) select standard, randomly oriented, short, carbon fiber felt and phenolic resin, mold resin, and felt to form a carbon fiber reinforced plastic (CFRP) blank; (2) pyrolize the CFRP in a vacuum at 1000°C; and (3) graphitize it in a vacuum at 2100°C. The easily machined greenbody is then reduced to near net shape of the desired optical or mechanical component and chemically processed by (1) conventional techniques such as milling, turning, drilling, and joining components as required, (2) infiltrating with molten silicon at >1400°C, (3) converting into silicon carbide at 1600°C, (4) annealing to room temperature, and (5) sandblasting or grinding with diamond-faced tools to desired dimensions. The material can also be shaped by the electric discharge milling (EDM) process because it has a high electrical conductivity.

If an optical component (mirror) is being made from Cesic, the next step is to completely encapsulate the part with a CVD layer of silicon carbide. This can be accomplished by applying a silicon carbide-based slurry and consolidating that material by firing. This creates a dense, homogeneous, two-phase ceramic cladding comprising silicon and silicon carbide. The thickness of this layer is usually between 0.25 and 1.27 mm (0.010 to 0.050 in.). Goodman (2005) indicated that overall diameter-to-thickness ratios of 25:1 and core thicknesses up to ~2 in. (~51 mm) are feasible. The optical surface can then be polished or superpolished into the clad mirror face to the required optical quality. The maximum sizes of components that can be processed by these techniques are currently limited by the capacity of facilities available for cladding to no larger than ~1.5 m (~59 in.).

¶Cesic® is a proprietary formulation produced by ECM Ingenieur-Unternehmen für Energie- und Umwelttechnik GmbH, of Munich, Germany. This company is referred to as ECM elsewhere in this section.

It should be noted that the physical characteristics of Cesic® to be used in mechanical parts such as mirror mounts are nearly the same as those of a silicon lightweighted mirror. For example, Figure 13.29 shows the variation of microstrain of silicon and two types of C/SiC with temperature. The composites are designated A-3 and D-4. The former is standard Cesic® as manufactured by ECM while the latter is a special formulation wherein the carbon fibers are treated to modify the reaction with liquid silicon during manufacture. The slope of any of the curves at a selected temperature is the CTE of the material at that temperature. From Figure 13.29, one can find the CTEs of both Cesic® types and of silicon at room temperature to be 2.09×10^{-6} and 2.56×10^{-6} K^{-1}, respectively. In the range of 90 to 25 K of great interest for many applications, the CTEs of A-3 Cesic® and silicon are essentially identical at -0.4×10^{-6} K^{-1}. That of D-4 Cesic® is nearly the same over that range. The similarity of CTEs for these materials tends to athermalize an opto-mechanical assembly made therefrom. Typical mechanical and thermal properties of silicon may be found in Table 3.14 while those of Cesic® are listed in both Table 3.14 and Table 3.18.

An example of a silicon foam core lightweight mirror of 5 in. (127 mm) diameter manufactured by the process corresponding to Figure 13.26(c) and of a mount made of Type A-3 Cesic® was described by Goodman et al. (2001) and Goodman et al. (2002). Figure 13.30(a) shows the mount. It is essentially a cylinder with a perforated wide flange at one end (bottom in the figure) for attaching it to a test fixture. The mirror is bonded to the other (top) end of the cylinder using a proprietary stress-free technique. As shown in Figure 13.30(b), a Cesic® cover protects the mirror from accidental damage. It is held in place by a series of radially directed screws. The cover does not contact the mirror. The opto-mechanical design of this assembly was checked by modal analysis to determine its frequency response under vibration. The lowest structural frequency was for cantilever modes at 1448 Hz. This was interpreted by the authors to indicate that no aberrations would be introduced into the mirror by the intended space application. An FEA using the model shown in Figure 13.31 showed that the optical figure should not change when cooled to 25 K.

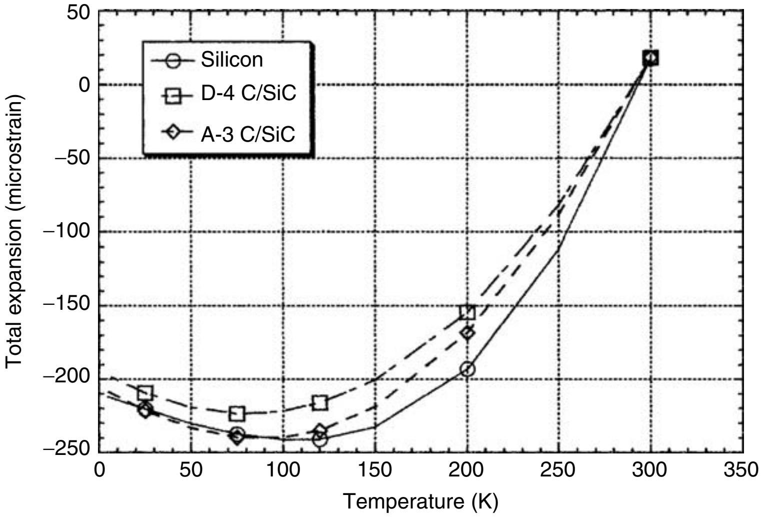

FIGURE 13.29 Variation of microstrain with temperature for C/SiC (Cesic®) Types A-3 and D-4 and for single-crystal silicon. The slope of each curve at any point gives the CTE of the material at the selected temperature. (From Goodman, W.A. et al., *Proc. SPIE*, 4822, 12, 2002.)

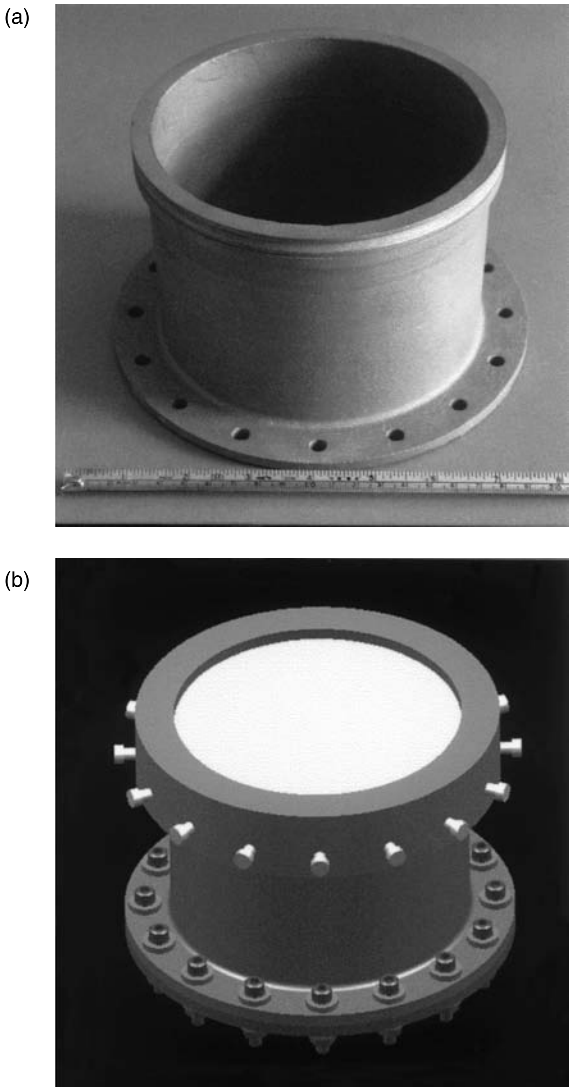

FIGURE 13.30 A mount made of Cesic® material. (a) Cylindrical housing with mounting flange. (b) Lightweight silicon foam mirror of 5 in. (127 mm) diameter installed in the mount and protected by a cover held in place with many Cesic® screws. (From Goodman, W.A. et al., *Proc. SPIE*, 4822, 12, 2002.)

Goodman et al. (2002) and Jacoby et al. (2003) reported the results of environmental testing of this assembly (see Figure 13.32). At ambient temperature, the uncoated mirror's figure was $\lambda/17$ rms with a slight amount of astigmatism attributed to the mechanical support. The figure degraded by $\lambda/22.6$ at 193 K, by $\lambda/14.7$ at 77 K, and by $\lambda/13.6$ at 27 K. All measurements were over 90% of the clear aperture. Retesting at ambient after low-temperature measurement indicated no hysteresis.

Goodman and Jacoby (2004) discussed the design, manufacture, and cryogenic testing of a 25 cm (9.80 in.) aperture, lightweighted Cassegrain telescope using a silicon open-cell foam primary mirror mounted in a structure made of carbon fiber-reinforced silicon carbide (A-3 Cesic®). Schafer Corporation's improved manufacturing process described above was used to make the primary mirror. It has a concave *f*/1.5 parabolic reflecting surface with figure error $\leq\lambda/4$ p-v at 633 nm, vertex radius of curvature of 762 mm (30.0 in.), diameter of 30 cm (11.81 in.), and a clear aperture of 254 mm (10.0 in.). The secondary mirror of the telescope is made of single-crystal silicon. It has a convex

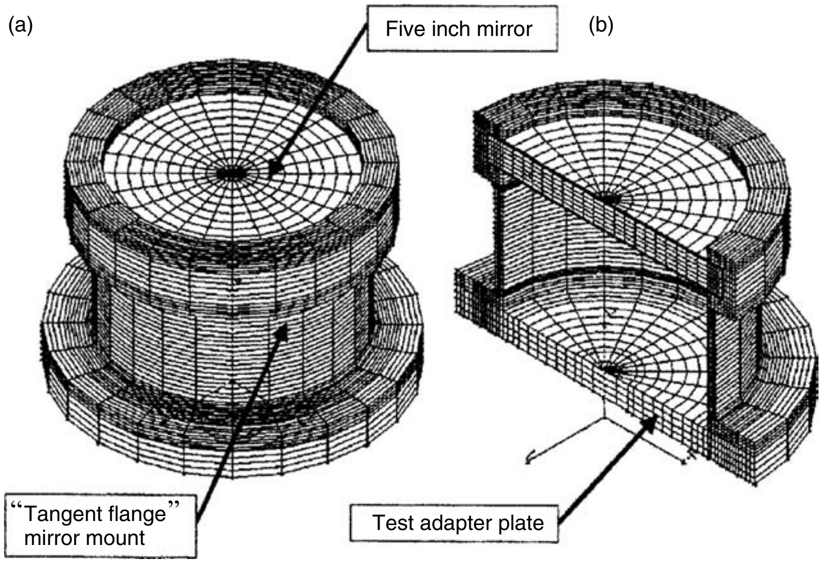

FIGURE 13.31 (a) Computer model of the mount from Figure 13.30(a) used to demonstrate its thermal behavior upon cooling from ambient to cryogenic temperature. (b) The mount is attached to an aluminum adapter plate. (From Goodman, W.A. et al., *Proc. SPIE*, 4451, 468, 2001.)

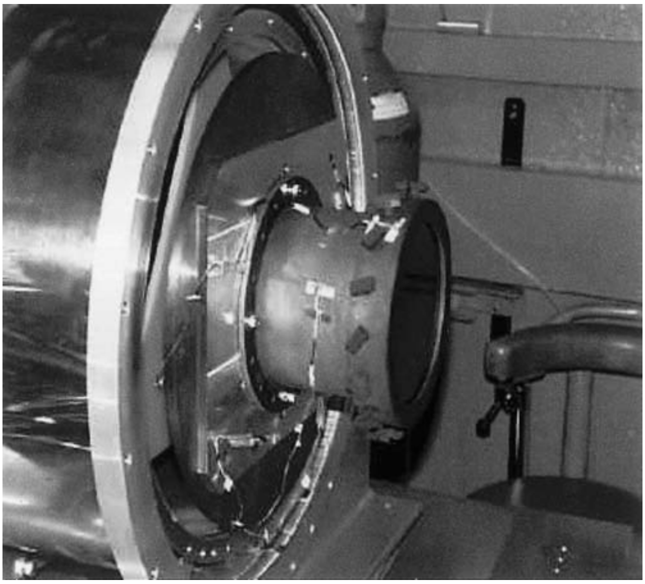

FIGURE 13.32 Silicon foam mirror in its Cesic® mirror mount and attached to the cold plate of a cryogenic test chamber for low temperature testing. (From Goodman, W.A. et al., *Proc. SPIE*, 4822, 12, 2002.)

hyperbolic reflecting surface, which is also figured to $\leq \lambda/4$ p-v at 633 nm. The vertex radius of curvature is 78.10 mm (3.075 in.), the diameter is 3 cm (1.18 in.), and the clear aperture is 27 mm (1.063 in.). Both mirrors are bonded to their respective structural supports. Figure 13.33(a) shows the Cesic components of the telescope while Figure 13.33(b) shows three views of the completed instrument. The weight of the telescope is 6.4 kg (14.1 Ib). Performance of the system has yet to be reported, but is expected to indicate that the assembly is athermal and performs well at cryogenic temperatures.

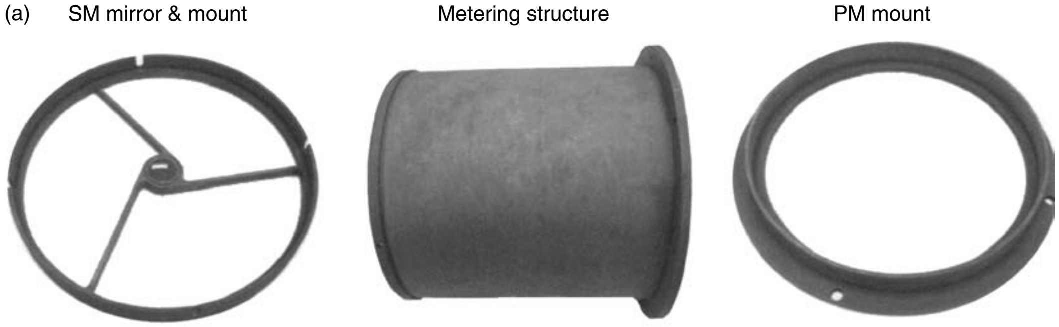
(a)
SM mirror & mount
Metering structure
PM mount

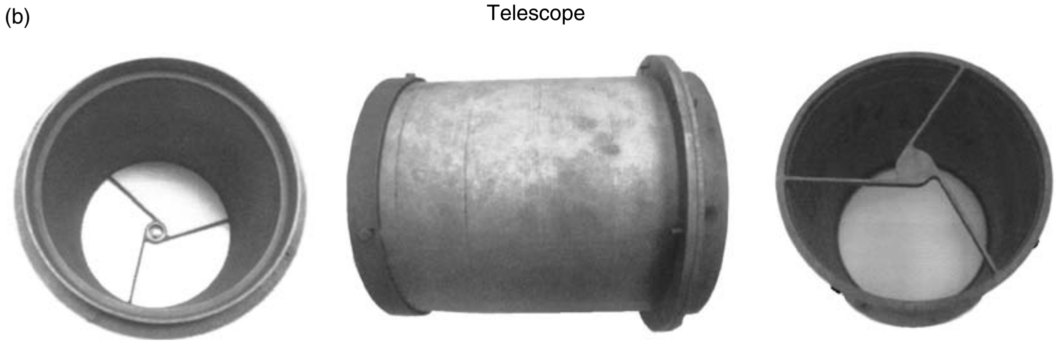
(b)
Telescope

FIGURE 13.33 (a) Cesic® structural components for the 25.4-cm (10-in.) aperture-Cassegrain telescope shown in view (b). (From Goodman, W.A. and Jacoby, M.T. *Proc. SPIE*, 5528, 72, 2004.)

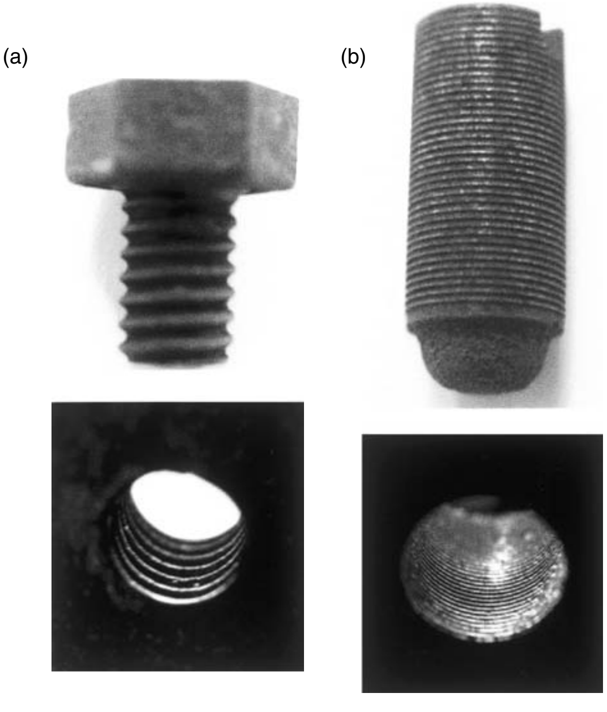

FIGURE 13.34 (a) High-strength 1/4-20 cap screw and (b) 1/4-80 alignment screw made from Cesic® material. The mating threaded holes in Cesic® structural components are shown for each case. Use of the same material in each part eliminates differential thermal expansion problems. (From Goodman, W.A. and Jacoby, M.T. *Proc. SPIE*, 5528, 72, 2004.)

One final note about Cesic is appropriate to mention here. This is its compatibility with manufacture of screws and machining of threaded holes into the material so that components of that material can be attached to each other. View (a) of Figure 13.34 shows a 1/4-20 threaded cap screw and view (b) of that figure shows a 1/4-80 alignment-adjusting screw. Each is shown with its mating threaded hole in a structural part. The material's inherent high fracture strength allows the attachment screws to be assembled with high tensile force approaching 50,000 N (11,240 Ib). Because the CTEs of the screws and of the parts held together are the same, no thermal effects will occur in the joint.

13.7 PLATING OF METAL MIRRORS

Because of the inherent crystalline structure, softness, and ductility of some metals, it is virtually impossible to achieve a high-quality optical finish directly on the base metal. Aluminum and beryllium benefit by having thin layers of a metal such as nickel plated onto the base metal and the optical surface single-point diamond-turned and polished into these layers to achieve a smooth finish. Smoothness of optical surfaces on substrates made of CVD or RB silicon carbide can be improved with a thin layer of vapor-deposited pure copper added. Gold can be plated onto various types of metal substrates to form good IR-reflecting mirrors.

Similar improvements in surface smoothness can be achieved in some cases with plated layers of the same material as the substrate. The proprietary AlumiPlate™ process for plating aluminum on aluminum is a prime example. As mentioned earlier, the smoothness and thermal damage threshold of copper and molybdenum mirrors can be improved if a thin amorphous layer of the base metal is deposited onto the substrates before polishing.

The most frequently used plating material is nickel. Two basic processes are available for plating nickel layers onto mirror substrates. These are electrolytic and electroless plating. EN can be plated to a thickness of 0.030 in. (0.76 mm) or more. It has a Rockwell hardness of 50 to 58. The process is simple but slow and does not require precise temperature control. Typically, 140 ± 15°F (60 ± 8°C) is adequate. Uniformity of coating thickness is not easily attained with this process. Electroless nickel (ELN) is an amorphous material with phosphorus content in the range of 11 to 13%. It can be plated more evenly, is more corrosion resistant, and its application process is less complex mechanically and electrically than EN. On the negative side, the maximum practical thickness of the ELN layer is about 0.008 in. (0.20 mm), so the substrate must have nearly the proper contour before plating. The process temperature of ~200°F (93°C) for ELN plating is higher than that for EN and must be controlled to ±5°F (±3°C). Rockwell hardness of ELN plating is typically 49 to 55, but it can be increased by heat treating. An excellent detailed discussion of ELN was given by Hibbard (1997).

Mismatch of thermal expansion characteristics of the plated layer and the base metal of the mirror substrate is a cause of dimensional instability in the completed optic. For nickel and beryllium, this mismatch is about 2 ppm/K, whereas that for nickel and aluminum is about five times larger. The resultant bimetallic effect may be quite significant in high-performance systems. Vukobratovich et al. (1997) investigated possible approaches to minimizing bimetallic effects for an ELN-plated 6061 Al concave mirror with diameter 180 mm (7.09 in.). The mirror configurations studied are shown in Figure 13.35. Design variations from the baseline plano-concave shape (view [a]) included (1) increasing the substrate thickness to resist bending (view [c]); (2) meniscus shape (view [d]); (3) designing the substrate with a symmetric cross section to produce equal and opposite bending effects (view [e]); and, (4) for all configurations, plating both sides of the substrate with equal and unequal thicknesses of nickel. The plano-plano configuration of view (b) was included for general information with regard to the effect of front-to-back surface-plating thickness differences.

Both closed-form analyses using a method from Barnes (1966) and the finite-element method were conducted. Vukobratovich et al. (1997) concluded that (1) the closed-form results did not correlate well with the FEA results, the FEA results being considered more accurate; (2) surface deformations comprising both correctable aberrations (piston and focus) and uncorrectable aberrations need to be determined rather than just surface departure from nominal; (3) because of mounting

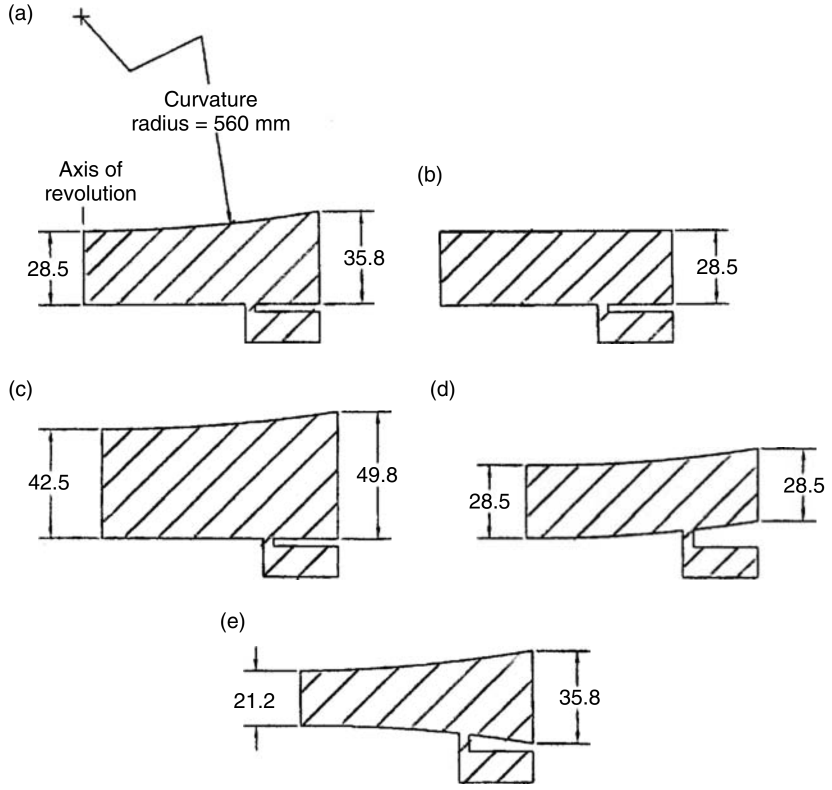

FIGURE 13.35 Mirror shapes investigated by Vukobratovich et al. (1997) to determine bimetallic bending effects of various ELN claddings.

constraints on the mirror's back, equal thickness platings front and back may increase rather than decrease bimetallic bending; (4) increasing mirror thickness does not help; and (5) symmetric shaping of the substrate significantly reduces bending even if the back surface is not plated. The mirror and mounting design adopted by Vukobratovich et al. (1997) upon completion of their investigation is discussed in Section 13.8.

Moon et al. (2001) extended the work of Vukobratovich et al. (1997) to include both aluminum and nickel plating on aluminum and beryllium substrates. The mirror configurations of Figure 13.35 were again investigated. The results of this later effort indicated that aluminum plating on aluminum surfaces works best with equal thicknesses applied to front and back surfaces, and that ELN plating on aluminum surfaces works best with only the front surface plated for the baseline and double-concave mirror configurations. The best plating arrangement for the thick and meniscus substrates were found to be equal thicknesses front and back. With ELN plating on beryllium substrates configurations, the best arrangement would be plating on the front surface only. This conclusion applied to all mirror configurations.

A factor contributing to the long-term stability of ELN-coated metallic mirrors is the stress inherent in the coating. Paquin (1997) discussed the dependence of this internal stress on the phosphorus content of the deposited nickel. In most cases, it is possible to specify a phosphorous content (typically <12%) for zero stress when annealed. Hibbard (1990, 1992, 1995, 1997) considered this factor, among others, in discussions of means for minimizing dimensional instability of ELN-plated mirrors. Varying the chemical composition and heat treatment applied allows the zero residual stress level to be located at the center of a given operational temperature range. Hibbard (1997) provided information with regard to the dependence of CTE, density, Young's modulus, and hardness of ELN coating with phosphorus content. These parameters are important in modeling mirror designs.

The stress in plated coatings is conveniently measured by plating one side of thin metal strips as witness samples of the base material to be coated. Hibbard (1997) described the technique. Generally, these strips measure 4 in. (102 mm) × 0.40 in. (10.2 mm) × ~0.03 in. (0.76 mm) with the latter dimension depending upon the particular material. The opposite faces of the strips are ground flat and parallel with inherent bending not exceeding 0.001 in. (25 μm). Release of residual stress due to the plating bends the strip. The magnitude of the bending, and hence the stress, is determined by placing the strips on edge under a microscope and measuring contour departure from a straight line along the long dimension. Typical bending magnitudes for ELN coatings on aluminum are in the 0.010 to 0.015 in. (0.25 to 0.38 mm) range, so are easily measured with reasonable accuracy.

13.8 SINGLE-POINT DIAMOND TURNING OF METAL MIRRORS

The use of single-crystal diamond cutting tools and specialized machinery to produce precision surfaces on selected materials by very accurately cutting away a thin portion of the surface is called "single-point diamond turning," "precision machining," and "precision diamond turning" by various people. We here adopt the first terminology and abbreviate it as SPDT hereafter in this chapter. The technique has developed from crude experiments to fully qualified production processes since the early 1960s (Saito and Simmons, 1974; Saito, 1978; Sanger, 1987; Rhorer and Evans, 1995).

The basic SPDT process generally involves the following steps: (1) preform or conventionally machine the part to rough shape with ~0.1 mm (0.004 in.) excess material left on all surfaces to be processed; (2) heat treat the part to relieve stress; (3) mount the part with minimal induced stress in an appropriate chuck or fixture on the SPTD machine; (4) select, mount, and align the diamond tool on the machine; (5) finish machine the part to final shape and surface quality with multiple light cuts under computer control; (6) inspect the part (*in situ*, if possible); and (7) clean the part to remove cutting oils and solvents. For some applications of the optic, plating the surfaces following step (2) is required to provide an amorphous layer to be diamond-turned. In some cases, step (7) is followed by polishing the optical surface or surfaces to smooth it or them and applying the appropriate optical coating.

The machine used for SPDT operations can legitimately be termed an "instrument" since it unquestionably meets the classical definition of Whitehead (1954), who states: "an instrument may be defined as any mechanism whose function is directly dependent on the accuracy with which the component parts achieve their required relationships." In this case, that accuracy is achieved, in part, from inherent mechanical rigidity and freedom from self-generated and external vibration and thermal influences. Predictability and high resolution of rotary and linear motions and low wear characteristics of its mechanisms are inherent attributes of a good SPDT design.

Inherent in the SPDT technique is the production of a periodic grooved surface that scatters and absorbs incident radiation. Figure 13.36(a) illustrates schematically a highly magnified view of the localized contour of the turned surface in a machine functioning in a facing operation as shown in Figure 13.37 and Figure 13.38. The inherent roughness of the surface is depicted on the left of Figure 13.36(a). The diamond tool has a small curved nose of radius R. The motion of the tool across the surface creates parallel grooves as indicated on the right. The theoretical p-v height h of the resulting cusps is given by the following simple equation involving the parameters designated in Figure 13.36(b):

$$h = \frac{f^2}{8R} \tag{13.1}$$

where f is the transverse linear feed of the tool per revolution of the surface. For example, if the spindle speed is 360 rpm, the feed rate is 8.0 mm/min, and the tool radius is 6 mm, the value for

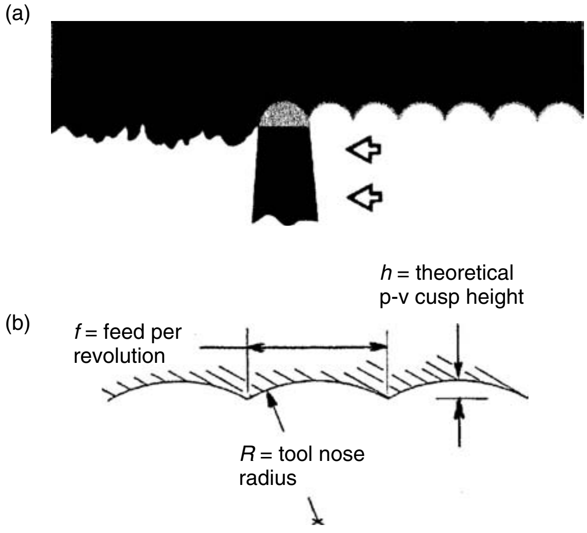
(a)
(b)
f = feed per revolution
h = theoretical p-v cusp height
R = tool nose radius

FIGURE 13.36 Schematic illustrations of (a) a single-point diamond tool advancing from right to left over the surface of a substrate and (b) the geometry of the cusped surface resulting from the SPDT process. (Adapted from Rhorer, R.L. and Evans, C.J., in *Handbook of Optics*, 2nd Ed., Vol. II, Bass, M., Van Stryland, E.W., Williams, D.R., and Wolfe, W.L., Eds., Optical Society of America, Washington, DC, 1995, chap. 41.)

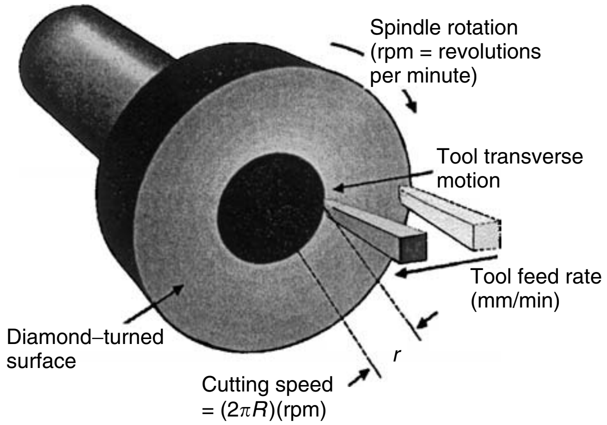
Spindle rotation (rpm = revolutions per minute)
Tool transverse motion
Tool feed rate (mm/min)
Diamond–turned surface
r
Cutting speed = $(2\pi R)$(rpm)

FIGURE 13.37 Schematic of a SPDT facing operation. (Adapted from Rhorer, R.L. and Evans, C.J., in *Handbook of Optics*, 2nd Ed., Vol. II, Bass, M., Van Stryland, E.W., Williams, D.R., and Wolfe, W.L., Eds., Optical Society of America, Washington, DC, 1995, chap. 41.)

$f = 8.0/360 = 0.0222$ mm per revolution. Hence, $h = (0.0222)^2/[(8)(6)] = 1.03 \times 10^{-5}$ mm or 1.03 Å. Note that the width of each cusp equals f.

The tool of an SPDT machine must follow an extremely accurate path relative to the surface being cut throughout the procedure. Rhorer and Evans (1995) listed several factors as sources of errors in the machined surface contour beyond the cusped structure just described. These may be paraphrased as: (1) waviness from inaccuracies of travel of slide mechanisms providing tool motions; (2) nonrepeatability of axial, radial, and tilt motions relative to the spindle rotation; (3) external and self-generated vibration; (4) effects within the turned material wherein differential elastic recovery of adjacent grains and impurities cause contour "steps" or "orange peel" appearance in the surface; and (5) repeated structure within the cusps because of irregularities in contour of the tool cutting edge.

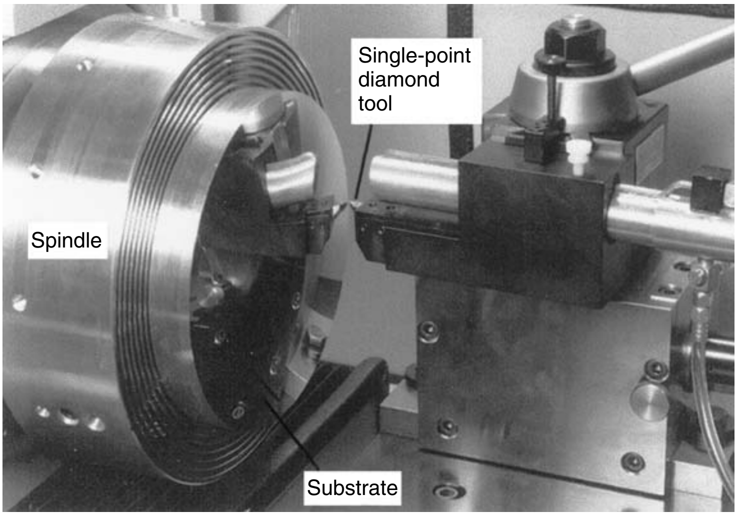

FIGURE 13.38 Photograph of a facing operation on a SPDT instrument. (Adapted from a photograph furnished by Rank, Taylor Hobson, Inc., Keene, NH.)

The earliest applications of SPDT were to windows, lenses, and mirrors for use in the IR region because such optics could have rougher and less accurate surfaces than ones for use with shorter wavelengths. With advances in SPDT technology, diamond-machined optics can today be made smooth enough to be used in visual and lower-performance UV instruments. Surface microroughness typically achieved in quantity production on bare 6061 aluminum mirror surfaces is 80 to 120 Å rms, while that achieved on plated surfaces is about 40 Å rms (Vukobratovich, 2003).

Materials that can be machined by SPDT techniques with more or less success are listed in Table 13.10. Compatibility with the process is not an intrinsic property of the material. Rather, it is an expression of practicality. Some materials, such as ferrous metals, ELN, and silicon *can* be diamond-turned but wear the cutting tools rapidly, so this technique is not generally considered economical for machining them. Some alloys of listed generic metals can be processed with great success while others are doomed to failure. For example, good surfaces can be cut on 6061 aluminum while 2024 aluminum typically ends up with poor surfaces. Rhorer and Evans (1995) indicated that, in general, ductile materials (those hard to polish by traditional methods) are compatible with SPDT, whereas hard, brittle materials polish easily, but are not suitable for SPDT. In some cases, brittle materials can be processed to high precision on an SPDT machine by substituting a grinding head for the diamond cutter.

Plate, rolled, extruded, or forged wrought forms of metals are most commonly used for SPDT, but considerable success has been achieved in the diamond turning of carefully prepared near-net-shape castings of types 201-T7, 713-T5, and 771-T52 aluminum alloys (Dahlgren and Gerchman, 1988). Those authors indicated that to present a homogeneous substrate to the diamond, a casting must be made of virgin, metallurgically pure raw material (<0.1% impurity), its hydrogen content must be <0.3 ppm, the material handling equipment and gating system must not increase the impurity level of the raw material, and the rate of casting solidification must be carefully controlled so that cooling occurs isotropically from the optical surface inward. Similar success with SPDT machining of aluminum castings was reported by Ogloza et al. (1988). Their paper included comparisons of different aluminum alloys and different operational setups of the SPDT instrument.

Polycrystalline materials may not machine very well because their grain boundaries may be emphasized by the cutting action of the tool. Gerchman and McLain (1988) described an investigation of SPDT results when diamond turning various forms of single-crystal and polycrystalline

TABLE 13.10
Materials that Usually can be Diamond-Turned

Aluminum	Calcium fluoride	Mercury cadmium telluride
Brass	Magnesium fluoride	Chalcogenide glasses
Copper	Cadmium fluoride	Silicon (?)
Beryllium copper	Zinc selenide	Polymethylmethacrylate
Bronze	Zinc sulfide	Polycarbonate
Gold	Gallium arsenide	Nylon
Silver	Sodium chloride	Polypropylene
Lead	Calcium chloride	Polystyrene
Platinum	Germanium	Polysulfone
Tin	Strontium fluoride	Polyamide
Zinc	Sodium fluoride	Ferrous metals (?)
ELN (K >10%)	KDP	
EN(?)	KTP	

Note: Materials with (?) cause rapid diamond wear.

Source: Adapted from Rhorer, R.L. and Evans, C.J., in *Handbook of Optics*, 2nd Ed., Vol. II, Bass, M., Van Stryland, E.W., Williams, D.R., and Wolfe, W.L., Eds., Optical Society of America, Washington, DC, 1995, chap. 41; Gerchman, M., *Proc. SPIE*, 607, 36, 1986.

germanium. For IR applications, the differences in results were found to be insignificant, and the presence of grain boundaries did not seem to cause brittle fracture to surfaces.

Gerchman (1986) gave a rather complete summary of specifications and manufacturing considerations for SPDT optics including guidelines for selecting and specifying material characteristics, translating optical surface descriptions from the lens designer's terminology into SPDT machine terminology, surface tolerancing, evaluation techniques (including the use of null compensators), controlling surface texture (tool marks) and lay orientations, minimizing and measuring surface errors and cosmetic defects, as well as clarifications as to which U.S. MIL specifications to apply to measuring such flaws.

Sanger (1987) provided a very thorough review of SPDT developmental history and technology including machine design features and capabilities, work piece support techniques, diamond tool characteristics, numerical (computer) control systems, environmental control, work piece preparation, machining operation guidelines (depth of cut, speeds and feeds, tool wear), and techniques for testing of finished surfaces.

There are two basic types of SPDT instruments: the *lathe* type, in which the work piece rotates and the diamond tool translates, and the *fly cutter* type, in which the tool rotates and the work piece translates. Parks (1982) described 14 different geometries of SPDT instruments designed to create cylinders, exterior and interior cones, flats, spheres, toroids, and aspheres. We will consider here only five of these configurations.

Figure 13.39 shows a lathe-type SPDT instrument with the linear tool axis parallel to the spindle axis. This resembles the conventional machinist's lathe. The work piece is mounted between live and dead centers (as shown) or cantilevered from a faceplate on the spindle. By appropriate fixturing, the diamond tool can also be positioned to turn the ID of a hollow cylinder. If the linear tool slide is rotated about a vertical axis so as to lie at a horizontal angle to the spindle axis, this instrument can be used to machine external or internal cones.

Figure 13.40 illustrates a fly-cutting SPDT instrument. Here the work piece is a flat generated by a single or double series of slightly displaced, parallel, arcuate tool cuts. If the spindle axis is not accurately perpendicular horizontally to the linear axis, the surface becomes cylindrical. Faceted scanner mirrors are machined by a variation of this geometry in which the work piece is indexed about an axis inclined with respect to both the spindle and linear axis. The design and manufacture,

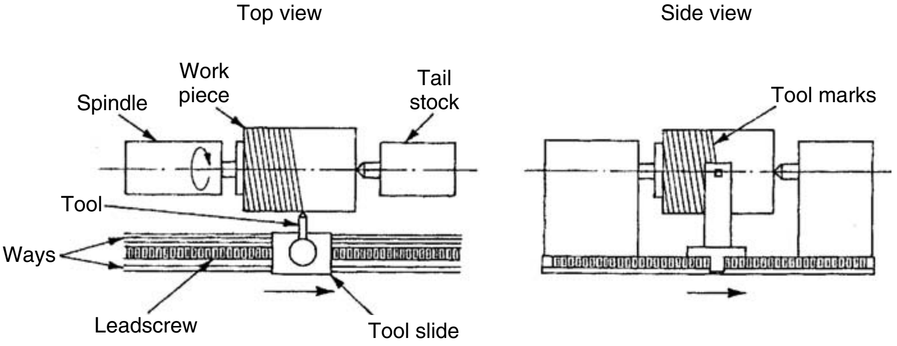

FIGURE 13.39 Schematic of a lathe-type SPDT instrument as used to create cylindrical surfaces. (From Parks, R.E., Introduction to Diamond-Turning, *SPIE Short Course*, 1982.)

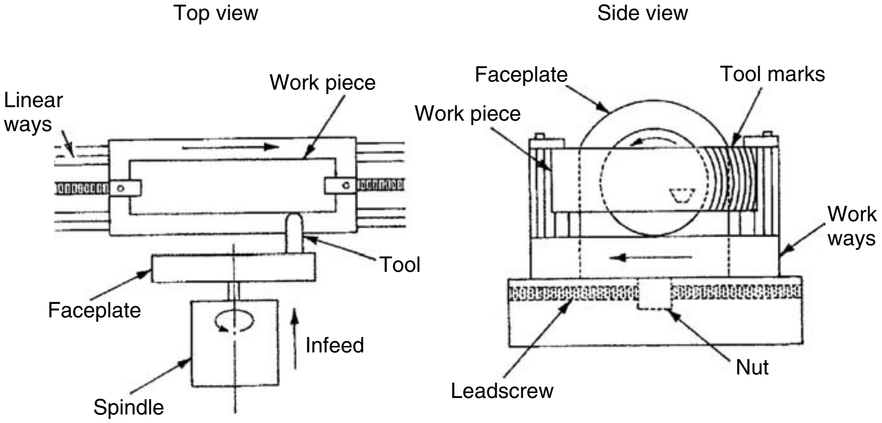

FIGURE 13.40 Schematic of a fly-cutter SPDT instrument as used to create flat surfaces. (From Parks, R.E., Introduction to Diamond-Turning, *SPIE Short Course*, 1982.)

by SPDT techniques, of precision polygon scanners were discussed in depth by Colquhoun et al. (1988). The only practical method of machining scanner mirrors directly into a substrate with closely spaced, flat, internal-reflecting facets is through SPDT techniques.

Another type of fly-cutting SPDT instrument designed to create spherical surfaces is illustrated in Figure 13.41. Here, two rotary motions about coplanar and intersecting axes carry both the work piece and the tool. The radius R created equals $r/\sin\,\theta$, where these parameters are as depicted in the figure. The function is similar to that of a diamond-cup surface-generating machine as used in mechanical and optical shops. As shown, a concave surface is machined; a convex one is created if the point C representing the intersection of the two axes is moved behind (i.e., to the left of) the work piece. This is generally accomplished by supporting the tool on a yoke with arms passing on both sides of the work piece spindle. If the tool is mounted on a linear feed rotating about the axis through point C of this figure, the configuration is called an "R–θ" instrument. It cuts aspherical as well as spherical surfaces.

Gerchman (1990) described the capability of a four-axis system involving three linear motions (X, Z, and Z') plus rotation of the work piece with encoder readout of rotational position. The Z-axis of this system is a limited, rapid linear motion of the diamond tool. By coordinating the motion of the tool with the work piece's rotational position, a nonaxisymmetric surface can be generated. Gerchman's paper described how such a machine might be used to create off-axis aspheric surfaces equivalent to the segments of the Keck telescope primary mirror described earlier.

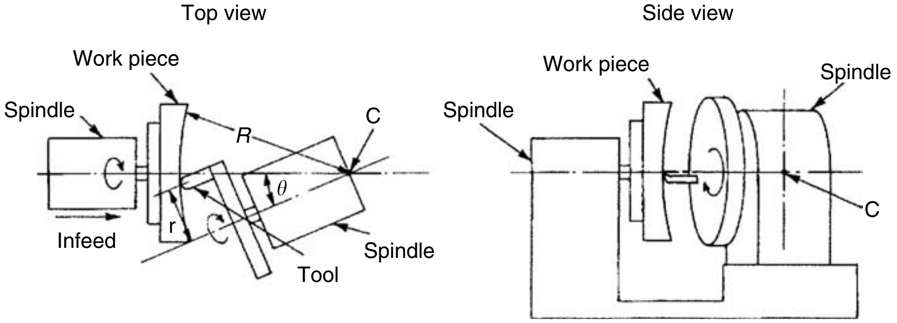

FIGURE 13.41 Schematic of a dual rotary axis fly-cutter SPDT instrument configured to machine concave spherical surfaces. Here, $R = r/\sin\theta$. (From Parks, R.E., Introduction to Diamond-Turning, *SPIE Short Course*, 1982.)

Figure 13.42 shows an instrument with four axes, two rotary and two linear, the latter being stacked vertically. Rotation of the tool occurs about the center of the circular cutting edge through action of a stepper motor. This motor is indexed after individual or every few rotations of the work piece spindle. This keeps the tool normal to the work piece and eliminates error due to variation of radius, hardness, and finish along the tool cutting edge. It also allows a shorter-radius tool to be used, thus allowing greater slope variation on the machined surface. With this number of motions, convex and concave aspheric surfaces can be easily machined. Figure 13.43 shows a way in which three rectangular-aperture, off-axis parabolas can be mounted for simultaneous precision diamond turning on such an instrument. Centering pins and reference flats on the mirrors control orientation.

A variety of single- and multiple-axis SPDT machines with different work piece size capacities and surface contour capabilities are available from various manufacturers worldwide. For example, Figure 13.44 shows a typical commercial five-axis SPDT instrument. Although inclusion here does not constitute endorsement of this product, it does represent the state of the art in commercially available production instruments at the time of this writing (late 2004). The specifications and capability of this instrument, the NANOTECH® 500FG Ultra-Precision Freeform Generator produced by Moore Nanotechnology Systems, LLC of Keene, NH, are summarized in Table 13.11. It can perform SPDT operations on axisymmetric work pieces to 500 mm (19.7 in.) diameter and on nonaxisymmetric work pieces to 250 mm × 250 mm × 150 mm (9.8 in. × 9.8 in. × 5.9 in.), or precision grinding of materials not compatible with SPDT. Typical optical figure accuracy and surface texture of the SPDT surfaces produced by these techniques are 0.2 μm and 6 nm, respectively, on materials such as single-crystal germanium, aluminum alloy, or OFHC copper. Typical optical figure accuracy and surface texture for ground surfaces on glasses such as SF12 are 0.3 μm and 10 nm, respectively. These surfaces are adequate for IR applications and some visible-light applications. With postprocess polishing, surfaces can be brought to visible-light quality standards.

Single-crystal diamond chips have unique characteristics that make them ideal for SPDT applications. They are very hard (when properly oriented), have low contact friction, are very stiff mechanically, have good thermal properties, and take an edge sharp to atomic dimensions. They can also be resharpened when wear becomes excessive. The cutting-edge radius may vary for the particular application from infinity to as small as 0.030 in. (0.76 mm). Typical maximum defect depths in properly sharpened diamond tools are $<0.3\times10^{-6}$ in. (8×10^{-3} μm) as indicated by scanning-electron-microscope measurements. The radius can be held constant to about 6×10^{-6} in. (1.5 μm) for typical (short) radii. The diamond chips may be brazed to standard lathe tool bits as shown in Figure 13.45 for physical support. When so mounted, they can be easily handled and attached to the SPDT instrument. Cubic boron nitride tools have proven effective for SPDT machining of bare beryllium substrates (Sweeney, 1991).

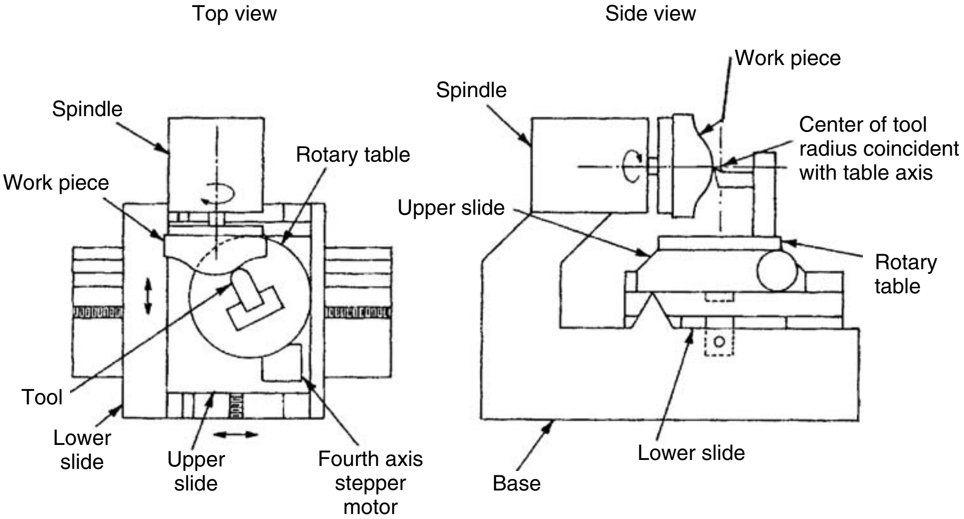
Top view
Side view
Spindle
Work piece
Rotary table
Tool
Lower slide
Upper slide
Fourth axis stepper motor
Spindle
Work piece
Center of tool radius coincident with table axis
Upper slide
Rotary table
Base
Lower slide

FIGURE 13.42 Schematic of a four-axis SPDT instrument with stacked linear slides and stepwise control of the diamond tool's orientation relative to the workpiece. (From Parks, R.E., Introduction to Diamond-Turning, *SPIE Short Course*, 1982.)

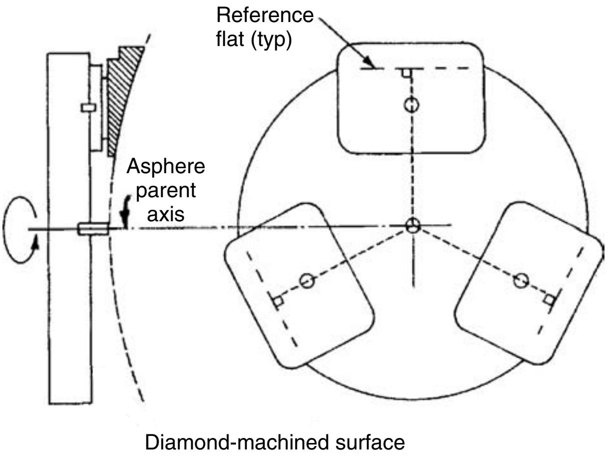
Reference flat (typ)
Asphere parent axis
Diamond-machined surface

FIGURE 13.43 Typical fixturing for SPDT of multiple off-axis aspheric mirrors. (Adapted from Curcio, M.E., *Proc. SPIE*, 226, 91, 1980.)

Figure 13.46 shows a multiple fly-cutter head with three diamond tools installed so that cuts can be made at different locations on the work piece, at different depths, or by different shaped tools during each pass so as to reduce the number of passes required to finish the surface.

Stress-free mounting of the work piece on the SPDT instrument is vital to achieving true surface contours and accuracy of machined dimensions. Techniques employed to ensure minimum stress include vacuum chucking (Hedges and Parker, 1988), potting (Sanger, 1987), and flexure mounts (Sanger, 1987). Figure 13.47 illustrates the vacuum technique as applied to a thin germanium lens element, whereas Figure 13.48 illustrates a potting technique as applied to a circular mirror substrate and Figure 13.49 shows a flexure technique as applied to an axicon element. The use of centering chucks to facilitate SPDT operations on crystalline lenses and on opto-mechanical subassemblies was discussed in Section 4.10, in Erickson et al. (1992), and in Arriola (2003).

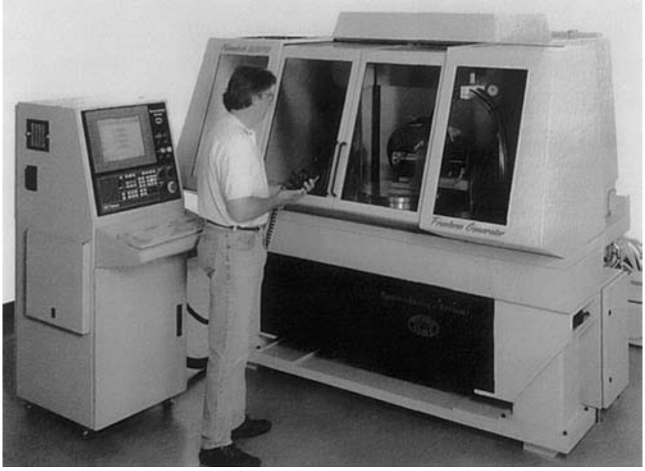

FIGURE 13.44 Photograph of an ultra-precision, free-form SPDT/Grinding machine, the Moore NANOTECH® Model 500FG. (Courtesy of Moore Nanotechnology Systems, Keene, NH.)

TABLE 13.11
Key Features and Capabilities of the NANOTECH® 500FG SPDT/Grinding Machine Shown in Figure 13.44

General Features

Natural granite structure. Dimensions: 1.42 m × 1.57 m × 0.46 m
3-point passive air vibration isolation system
Fanuc 15I control system, Windows NT operated
X, Z, and Y linear axes. Slide travels: X and $Z = 300$ mm; $Y = 200$ mm "T" orientation with Y axis mounted integral to Z axis. Slide straightness: 0.3 μm over full travel; 0.075 μm over any 25 mm travel
Flood coolant system temperature control within ±1°C

Performance

Linear axes position feedback resolution: 8.6 nm
Rotary axis encoder angular resolution: 0.25 arcsec

Source: From Moore Nanotechnology Systems, LLC, Keene, NH.

Diamond-turned surfaces may not have sufficient smoothness for some purposes, so postturning polishing may be needed. Brown et al. (1981), Sanger (1987), and Roybal et al. (1997) summarized techniques and materials for doing this operation by variations of conventional optical shop procedures. A computer-controlled belt-polishing technique for polishing SPDT annular surfaces was described by Bender et al. (1988).

Many studies of the quality of metallic optics surfaces achieved by SPDT techniques have appeared in the literature since the mid-1970s. Some of these are the works of Saito and Simmons (1974), Baker et al. (1975), Stover (1975), Sollid et al. (1976), Arnold et al. (1977), Church et al. (1977), Shagam et al. (1977), Saito (1978), Decker et al. (1978), Decker and Grandjean (1978), Lindsey and Franks (1979), Bennett and Decker (1981), Taylor et al. (1986), Sanger (1987), Lange (1988), Ogloza et al. (1988), Palum (1988), Song and Vorburger (1991), Hibbard (1992), Roybal et al. (1997), and Hibbard (1997). The various techniques discussed in these papers included full-aperture interferometry to measure surface figure as well as subaperture interferometry, white light

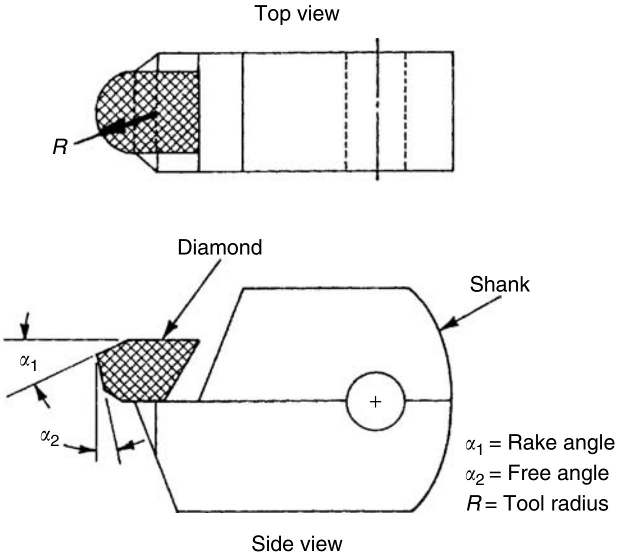
Top view
R
Diamond
Shank
α_1
α_2
α_1 = Rake angle
α_2 = Free angle
R = Tool radius
Side view

FIGURE 13.45 One type of diamond-tipped tool used for SPDT machining of optical surfaces.

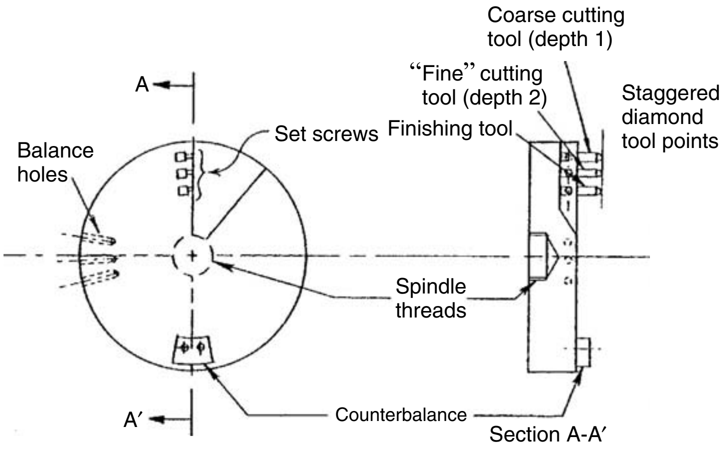
Coarse cutting tool (depth 1)
"Fine" cutting tool (depth 2)
Staggered diamond tool points
A
Set screws
Finishing tool
Balance holes
Spindle threads
A′
Counterbalance
Section A-A′

FIGURE 13.46 Schematic of a multiple-diamond fly-cutter head. (Adapted from Sanger, G.M., in Applied Optics and Optical Engineering, Vol. 10, Shannon, R.R. and Wyant, J.C., Eds., Academic Press, San Diego, 1987, chap. 6.)

scanning differential interference microscopy, and stylus profilometry to measure microroughness and other statistical properties of the surface. Direct measurements of the total integrated scatter (TIS) of light and of BRDF that discloses the angular dependence of light scattered from the surface were also considered.

Surface microroughness is especially important in the case of SPDT optics because of the cyclic nature of the process. The grooves scatter and diffract light more than a smooth surface. Figure 13.50 defines the useful ranges of some of the methods used to measure this parameter. Roybal et al. (1997) pointed out that simultaneous achievement of good optical figure and low microroughness on beryllium mirrors is very difficult.

In a discussion of surface characterization of SPDT metal optics, Bennett and Decker (1981) used the figure shown as Figure 13.51 to illustrate their observation that "the optical figure (shape)

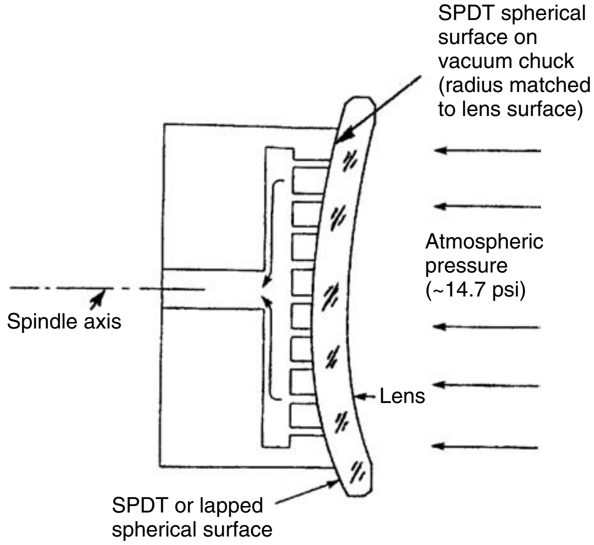
SPDT spherical surface on vacuum chuck (radius matched to lens surface)
Atmospheric pressure (~14.7 psi)
Spindle axis
Lens
SPDT or lapped spherical surface

FIGURE 13.47 Schematic diagram of a vacuum-chuck technique for supporting a thin germanium lens on the spindle of a SPDT instrument. (Adapted from Hedges, A.R. and Parker, R.A., *Proc. SPIE*, 966, 13, 1988.)

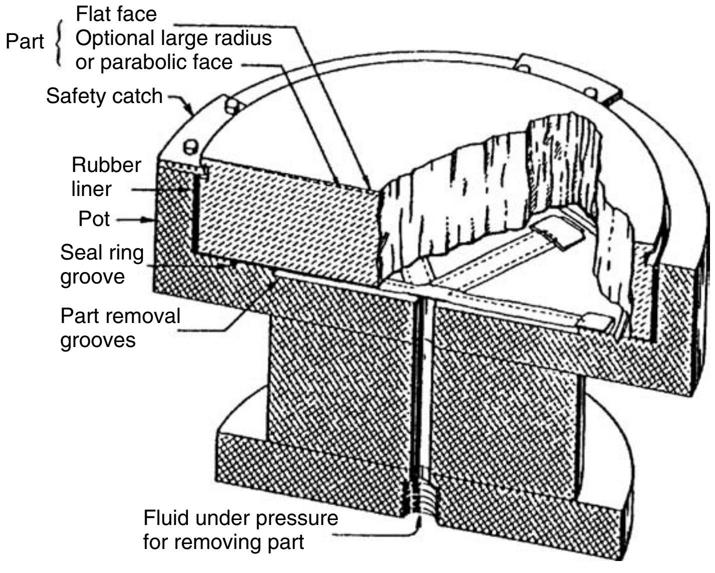
Part
Flat face
Optional large radius or parabolic face
Safety catch
Rubber liner
Pot
Seal ring groove
Part removal grooves
Fluid under pressure for removing part

FIGURE 13.48 Schematic diagram of a potting technique for supporting a circular mirror substrate on the spindle of a SPDT instrument. (From Sanger, G.M., in *Applied Optics and Optical Engineering*, Vol. 10, Shannon, R.R. and Wyant, J.C., Eds., Academic Press, San Diego, 1987, chap. 6.)

of the part has almost no relation to the quality of the surface finish. Parts have been made that are very flat but have a very rough, deeply grooved surface; other parts such as this one may have a rather poor optical figure but produce relatively small amounts of scattered light." They also pointed out how different measurement and analytical techniques lead to different values for microroughness. In the case of the surface represented by Figure 13.51, a 170 Å rms roughness value resulted from profilometry, whereas TIS measurements indicated a 28.5 Å rms value. Disagreements such as these may be attributed to the geometry of the scatterometer, which limits

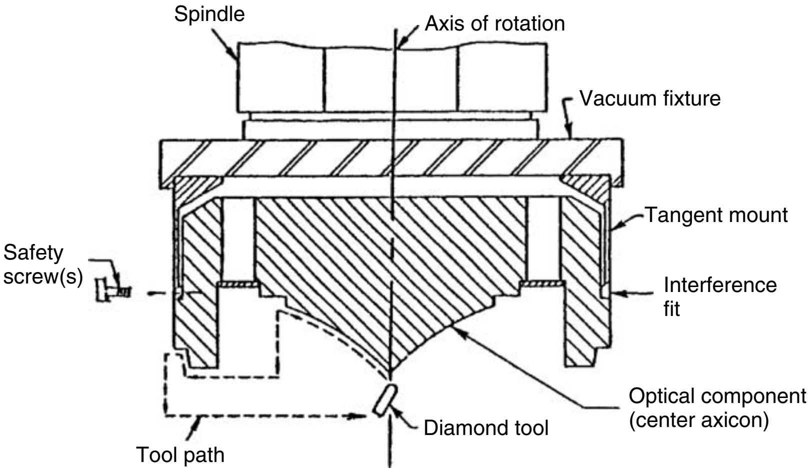
Spindle
Axis of rotation
Vacuum fixture
Tangent mount
Safety screw(s)
Interference fit
Optical component (center axicon)
Diamond tool
Tool path

FIGURE 13.49 Schematic diagram of a flexure technique for supporting an axicon substrate on the spindle of a SPDT instrument. (From Sanger, G.M., in *Applied Optics and Optical Engineering*, Vol. 10, Shannon, R.R. and Wyant, J.C., Eds., Academic Press, San Diego, 1987, chap. 6.)

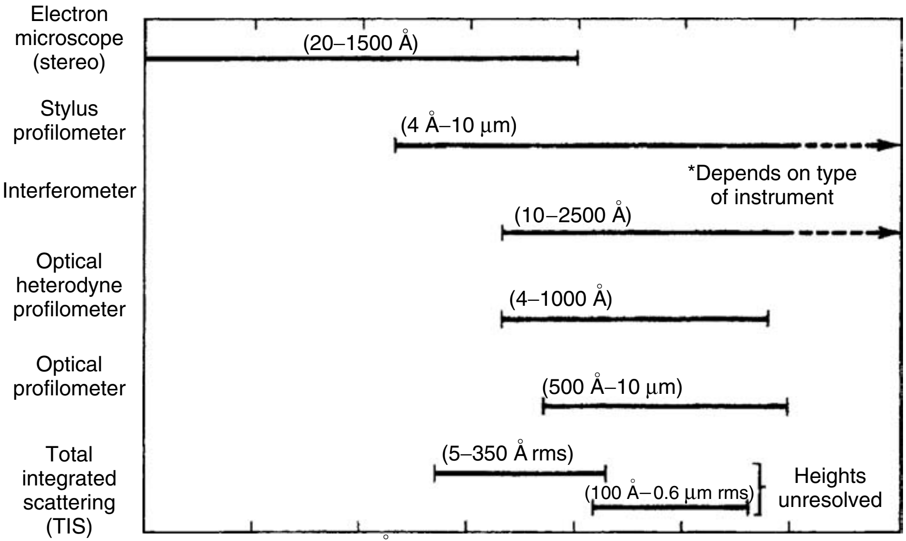

FIGURE 13.50 Capabilities of various techniques for assessing surface microroughness. The bars represent the applicable ranges of spatial wavelengths while the numbers in parentheses give the approximate limits of surface height measurements. (From Bennett, J.M. and Decker, D.L., *Proc. SPIE*, 288, 534, 1981.)

its measurement capability to a small spectrum of spatial frequencies, whereas profilometry measures practically all frequencies. Since the significance of scattered and diffracted light is geometry-dependent in most optical instruments, the designer may be able to choose the feed rate of the tool to be used in making SPDT optics for those instruments so that the unwanted light goes in harmless directions.

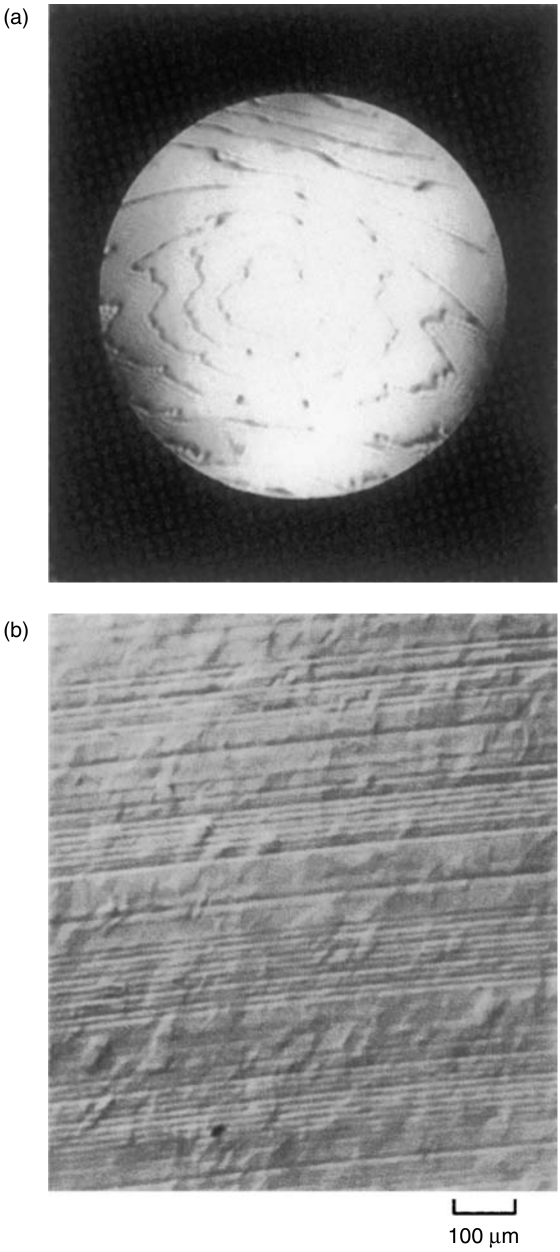

FIGURE 13.51 Interferogram (a) and Nomarski micrograph (b) of a copper mirror surfaced by SPDT. The microroughness from surface profile measurement is 170 Å rms while the effective roughness from a TIS measurement is 28.5 Å rms. (From Bennett, J.M. and Decker, D.L., *Proc. SPIE*, 288, 534, 1981.)

13.9 CONVENTIONAL MOUNTINGS FOR METAL MIRRORS

Small- and moderate-sized metal mirrors can be mounted in the same ways discussed in Chapter 7 for nonmetallic mirrors if there are no unusual requirements inherent in the application. Unusual requirements include extreme temperatures (e.g., cryogenic applications as illustrated by the actively cooled mirror of Figure 13.3), exposure to high-energy radiation (such as that from lasers or solar simulators), and extreme acceleration, shock, or vibration. Because metal mirrors can have optimally located attachment interfaces machined directly into the backs of the substrates, their mountings can be simpler, and the mirrors would experience smaller self-weight deflections than if mounted by clamping near their rims against annular or localized pads using retaining rings or multiple springs.

The primary differences between the designs of mountings for metal mirrors and those made of glass-type materials lie in the values for key mechanical parameters such as density, modulus of elasticity, Poisson's ratio, thermal conductivity, coefficient of thermal expansion, and specific heat. Table 3.13 and Table 3.14 listed these and some other parameters for several important metallic materials as well as nonmetallic ones. To illustrate these differences, let us use Eq. (11.1) to compute the sag at the center of a solid 20-in. (50.8-cm)-diameter I-70-A beryllium mirror with thickness-to-diameter ratio 1:6 and simply supported continuously about its edge. The equation and appropriate parameter values (from Table 3.14) are as follows:

$$\Delta Y_c = \frac{0.0149W(m-1)(5m+1)D_G^2}{E_G m^2 t_A^3} \tag{11.1}$$

where $m = 1$/Poisson's ratio ($=1/0.08 = 12.5$), E_G is Young's modulus of elasticity ($=42\times10^6$ lb/in^2), D_G mirror diameter ($=20.0$ in.), t_A mirror thickness ($=D_G/6 = 3.333$ in.), density of beryllium ($=0.067$ lb/in.3), and W the mirror's weight ($=\pi\ (D_G/2)^2 t_A\ \rho = 70.16$ lb). Substituting, we obtain $\Delta Y_C = 1.26\times10^{-6}$ in. (3.20×10^{-5} mm) or about 0.06 wave in green light. Comparing this with the 0.25 wave of green light for the solid fused silica mirror of the same dimensions computed in Chapter 11 as an example of the use of this equation, we find that the metal mirror deflects only about 25% as much as the nonmetallic one. This is because the beryllium is stiffer and somewhat less dense. For an application in which a 0.25 wave deflection is tolerable, the beryllium mirror thickness could be reduced by a factor of 0.49 to 1.63 in. (41.4 mm). This thinner mirror would weigh only about one-half as much as the equivalent fused silica version. Similar design adaptations would be appropriate with other types of conventional mountings.

The procedure for designing a multiple-point axial support mount such as the Hindle mount (see Section 11.4.2), the counterweighted mount (see Section 11.4.3), or the pneumatic/hydraulic mount (see Section 11.4.4) for a constant-thickness metal mirror is similar to that for a nonmetallic mirror. The number of support points required to limit p-v or rms surface deformation to less than some given value is, of course, dependent on the material's characteristics. For example, Eq. (11.4) representing

TABLE 13.12
Number *N* of Axial Support Points Required by Hall's Criterion (Eq. [11.4]) for 0.1 λ deflection at 0.633 μm for 39.37 in. (1 m) Diameter Mirrors of 1.734 in (4.404 cm) Thickness Made of Various Materials

Material	Young's Modulus (lb/in.^{2})	Density (lb/in.^{3})	N^a	Support Points in Hindle Mount
Be I-70	4.2×10^7	0.067	9	9
SiC-12%Si	5.4×10^7	0.112	10	18
SiC-30%Si	4.5×10^7	0.106	11	18
Zerodur	1.36×10^7	0.091	18	18
Fused silica	1.06×10^7	0.08	19	27
ULE	9.8×10^6	0.08	20	27
Ohara E6	8.5×10^6	0.079	21	27
6061-T6 Al	9.9×10^6	0.1	22	27
Pyrex	9.1×10^6	0.2	32	36

[a] Rounded up to next integer.

Hall's "rule-of-thumb" criterion for the number of support points required to achieve a given deflection between supports in a multiple-support mount indicates that a 39.37-in. (1-m)-diameter solid I-70 beryllium mirror of 1.734 in. (4.404 cm) thickness (22.7:1 diameter-to-thickness ratio) would need only a 9-point mount to have $<0.1\ \lambda$ p-v deformation at $\lambda = 0.633\ \mu$m wavelength, whereas a fused silica mirror of the same dimensions would need at least a 27-point support for that same deflection. Table 13.12 summarizes these calculations as well as similar ones for other commonly used mirror materials for the same mirror geometry. The materials are listed in order of increasing number of support points needed (rounded up to the next integer). If a Hindle-type mount were to be used, the number of supports would be as indicated in the last column.

13.10 INTEGRAL MOUNTINGS FOR METAL MIRRORS

An attribute of most types of metal mirrors that facilitates mounting is their compatibility with machining. This includes conventional and SPDT shaping and surfacing, and drilling and threading of holes to accept fasteners such as screws. If the latter operations take place in regions of the mirror sufficiently removed from the optical surface(s), little or no optical performance degradation results. Although attractive because of its simplicity, direct mounting by screwing a mirror to a structural interface can lead to problems if care is not exercised in the design and execution of both surfaces involved in the interface. As a rule-of-thumb, mounting surfaces must be flat to the same tolerances and coplanar (or, in some designs, simply parallel) as the related optical surface(s) if mirror distortion is not to be introduced when the screws are tightened. The use of kinematic mounting techniques or provision of rotational compliance at the interfaces tends to reduce distortion, but may result in complex designs. Thermal properties of mirror and mount should match as nearly as possible in order not to introduce distortions when the temperature changes.

A simple approach unique to metal mirrors uses SPDT processes to establish mounting surfaces integral to the mirror in the same machine setup as used to create the optical surface. Zimmerman (1981) described several designs featuring "strain-free" mirror mounts. Figure 13.52(a) illustrates schematically a design that uses slots to create mounting ears that isolate the optical surface from the bending stresses that might be introduced as the mirror is attached to its interface. The multiple mounting surfaces are, in this case, diamond-turned on the back of the same piece of material that has the reflecting surface diamond-turned into its front surface. Figure 13.52(b) is a photograph of ears on such a mirror. In this design, the mirrors edges are heavily beveled all around. The slots are cut with a cylindrical "core cutter" whose axis is parallel to the mounting surface. Threaded holes for attachment screws can be seen.

Figure 13.53 shows a flat mirror, also described by Zimmerman (1981), that has its mounting pads on the front side of the mounting flange to facilitate machining them parallel to the reflecting surface in the same SPDT instrument setup. This simplifies alignment of the mirror at the time of installation by essentially eliminating the angle error (wedge) between these critical surfaces.

Sweeney (1991) described the integral flexure-arm mount sketched in Figure 13.54 as a stress-free design that has been successfully applied to several beryllium mirrors. The mating surfaces of both the arms and the surface to which they were attached were precision-lapped to minimize distortion of the mirror surface when clamped in place. The mirror supports were not sufficiently stiff to hold the mirror during rough machining or grinding. The substrate was held by the cylindrical ring on the back of the mirror during these operations. It was later transferred to the flexure arms for final figuring when the forces exerted would be smaller.

Figures 13.55(a) and (b) show mounting flexure tab features machined into the rear surfaces of two metal mirrors intended for use in the Infrared Multi-Object Spectrograph (IRMOS) developed as a facility for the Kitt Peak National Observatory's 3.8 m Mayall Telescope, and as a pathfinder for the planned multiobject spectrograph in the JWST (see Ohl et al., 2003). The mirror in view (a) is an off-axis section of a concave prolate ellipsoid measuring 264×284 mm (10.39×11.18 in.). Pockets

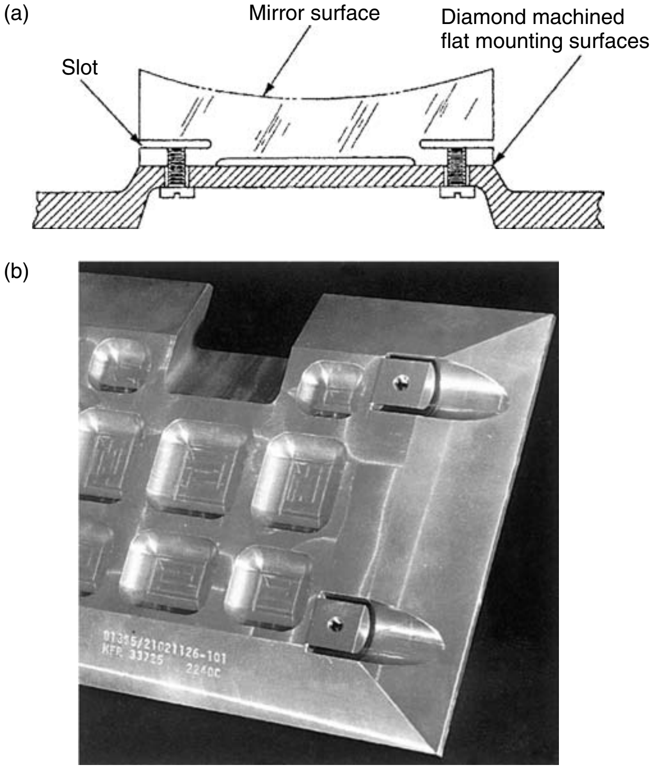
(a)
Mirror surface
Diamond machined flat mounting surfaces
Slot
(b)
01355/21021126-101
KFR 33725
2240C

FIGURE 13.52 (a) Schematic diagram of one type of strain-free mounting for a metal mirror. (b) Photograph of mounting ears (flexures) formed by a diamond-tipped core cutter moving parallel to the reflecting surface of a metal mirror and cutting into the heavily beveled edges. Also shown are machined recesses that reduce mirror weight. (From Zimmerman, J., *Opt. Eng*., 20, 187, 1981.)

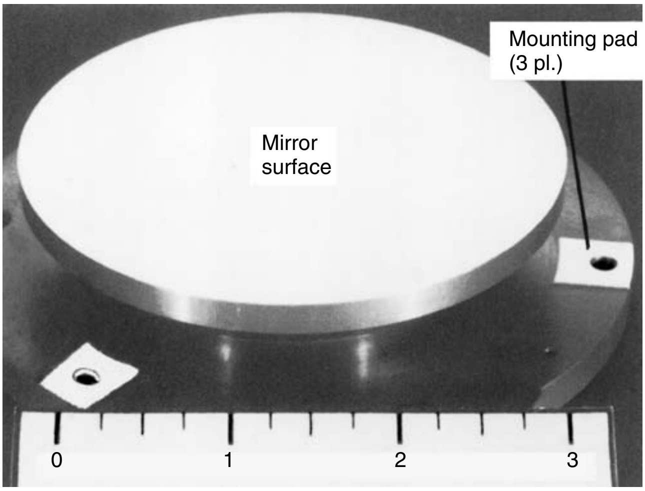
Mounting pad (3 pl.)
Mirror surface
0
1
2
3

FIGURE 13.53 Example of a metal mirror with front mounting pads created in the same SPDT setup as the reflecting surface. (From Zimmerman, J., *Opt. Eng*., 20, 187, 1981.)

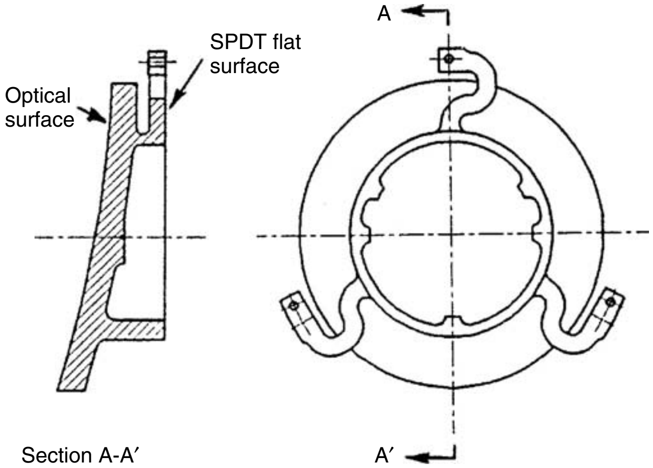

FIGURE 13.54 Be mirror with integral flexure-arm supports. (Adapted from Sweeney, M.M., *Proc. SPIE*, 1485, 116, 1991.)

are machined into the rear surface of this mirror to reduce its weight. The mirror in view (b) is an off-axis section of a convex oblate ellipsoid measuring 90×104 mm (3.54×4.09 in.). It is not lightweighted. Both mirrors are made with a 6:1 diameter-to-thickness ratio of 6061-T651 aluminum and stress relieved by a preferred heat-treating method as indicated in the column headed SR 5 in Table 13.4(b). All mounting and optical surfaces of both mirrors are finish machined by SPDT processing.

To facilitate assembly and alignment, the flexure tabs are cut into the mounting surfaces by a plunge EDM process to form the shapes indicated schematically in Figure 13.55(c). The flexures minimize optical surface deformation due to mounting forces by bending to translate as much as ±0.025 mm (0.001 in.) and tilt by ±0.1° . A threaded hole for attaching screws is provided in each tab.

The spectrograph is to operate at 80 K. Its structure is fabricated from the same type of material (Al 6061-T651) as the mirrors so as to form an athermal assembly. Alignment of the system is facilitated by several cross-hair fiducial marks scribed into the mirror rear and side surfaces during SPDT machining. One of these is pointed out in Figure 13.55(b). The slot and pinhole indicated in that same view serve as alignment references when the substrate is attached to the SPDT machine.

The general design principles underlying all these mirror examples are the following. (1) Mounting stresses are isolated from the mirror surface by incorporating flexure arms, geometric undercuts, or slots that create a form of flexure mounting. (2) The mirror should be designed to be a stiffer spring than the interfacing mounting structure. Deformations then occur in the mount rather than in the mirror substrate. (3) The mirror should, if possible, be held during machining in precisely the same manner as it will be held during operation. Then, mounting strains will be the same in both conditions. (4) The mounting surfaces should be machined flat and parallel to the same degree of precision as the optical surface(s).

It should be noted that compliance with the second of these principles might result in a design in which rigid-body displacement or tilt of the optical surface can occur during mounting. Provision should, in this case, be made for alignment adjustment subsequent to installation. A further possible consequence of adhering to this principle is elimination of the need for adherence to the final principle.

In Section 13.3, the 7.3-in. (18.5-cm)-diameter aluminum secondary mirror developed for NASA's Kuiper Airborne Observatory (see Figure 13.4) was described briefly. This mirror and its oscillating (or chopping) drive mechanism were mounted on a four-legged spider to the telescope structure. Figure 13.56 shows how the mirror was screwed directly to the mounting hub. The mirror's back surface had three coplanar pads (not shown) that interfaced with the hub. These pads

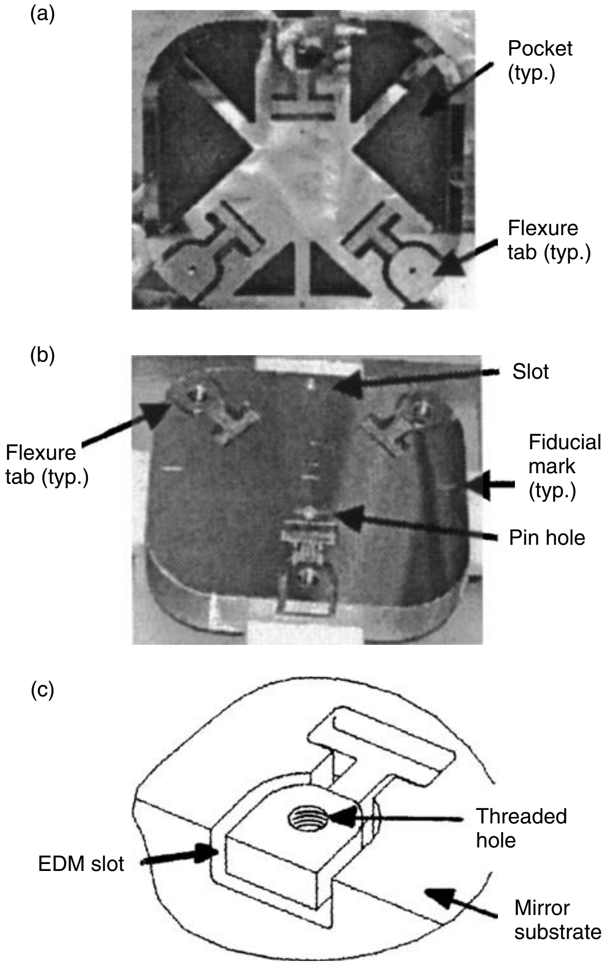

FIGURE 13.55 (a) and (b) Rear mounting and alignment surfaces of two aspheric aluminum mirrors featuring flexure tabs to minimize mounting-induced optical surface distortions. The fiducial markings, pin hole, and slot shown in view (b) facilitate alignment during machining and assembly. (c) Schematic diagram of one flexure tab with a threaded screw hole. (From Ohl, R. et al., *Proc. SPIE*, 4841, 677, 2003.)

were SPDT-machined, as was the optical surface. Belleville spring washers were used to provide preload and accommodate differential expansion between the stainless-steel screws and the aluminum mirror. The mechanical interface was within the central obscuration of the system to minimize distortion effects upon the surface figure.

Four electromagnetic actuators provided the required high frequency (up to 40 Hz), ±23 arcmin scanning motion of this mirror relative to a fixed baseplate. The actuator coils were fixed to the baseplate, whereas the magnetic armatures were attached to the moving assembly. This removed any necessity for wires to cross the gimbal axes and disturb the mirror motion. To prevent unwanted structural vibrations from being transmitted to the mirror and to minimize force reactions, it was pivoted about the center of mass of the entire moving assembly on a two-axis flex pivot gimbal. The mass moved was approximately 2 lb (0.91 kg). The entire baseplate with all its associated parts were moved axially by ±1.3 cm (±0.51 in.) relative to the spider with a DC motor and ball screw for open-loop adjustment of focus. This assembly proved to be quite successful in flight, with no resonances within the operational frequency spectrum or evidence of vibration due to wind turbulence at high altitude.

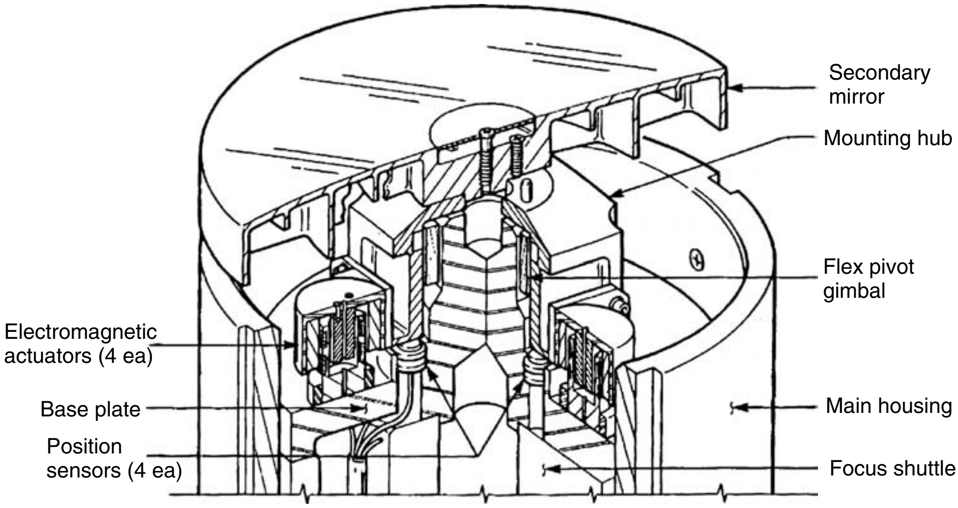

FIGURE 13.56 Schematic diagram of the aluminum secondary mirror and scanning drive mechanism developed for the Kuiper Airborne Observatory. (From Downey, C.H. et al., *Proc. SPIE*, 1167, 329, 1989.)

In Section 13.7, we summarized an investigation by Vukobratovich et al. (1997) dealing with the bimetallic effect of plating metal mirrors with dissimilar material. Their finite element study indicated the best configuration for a 180-mm (7.09-in.)-diameter beryllium mirror to be a plano-concave one in which only the front (optical) surface was ELN plated. Figure 13.57 shows the opto-mechanical design for that mirror. View (a) is a section through the mirror showing the axial interface pads at three places and a pilot diameter that engaged the ID of a hole in the telescope back plate for centering purposes. The pilot diameter is shown in view (b) and its interface with the back plate is shown in view (c). The mirror is attached with three screws as shown. By SPDT machining the axial pads perpendicular to the axis of the optical surface, tilt alignment of the mirror and the mirror's axial location were automatically established.

Additional examples of SPDT-machined optics that were designed to establish a high degree of accuracy between the optical surface and mechanical interface by using the latter as the datum for machining are shown in Figures 13.58(a)–(c) from Addis (1983). These designs were intended for military applications, so they were ruggedized for high shock and vibration levels.

In view (a), a 6061-T6 aluminum mirror is clamped to a closely toleranced centerless-ground stainless-steel shaft. The bearing surfaces (shown shaded) ground on the shaft were used as the part orientation reference during SPDT machining of the mirror face. When pivoted in high-class bearings, the subassembly provided a precision optical tracking mechanism. Another aluminum scan mirror is shown in view (b). Here, the cylindrical surface -A- provides the machining datum. The mirror normal is perpendicular to -A-. The mirror shown in view (c) is a static component with its optical face and its mounting interfaces at -A- accessible for machining parallel to each other in the same SPDT setup. The pilot diameter indicated in view (c) interfaces with a corresponding ID in the optical device. An O-ring seal is accommodated in the groove adjacent to the pilot diameter. This aluminum component resembles that shown in Figure 13.53 and features a necked-down region to serve as a flexure to isolate the optical surface from mounting stresses.

13.11 FLEXURE MOUNTINGS FOR LARGER METAL MIRRORS

When mirrors are to undergo large temperature changes or significant accelerations (such as might be exerted during spacecraft launch), or when small angular and translational motions are needed without friction, the use of flexure mountings should be considered. Two flexure support designs

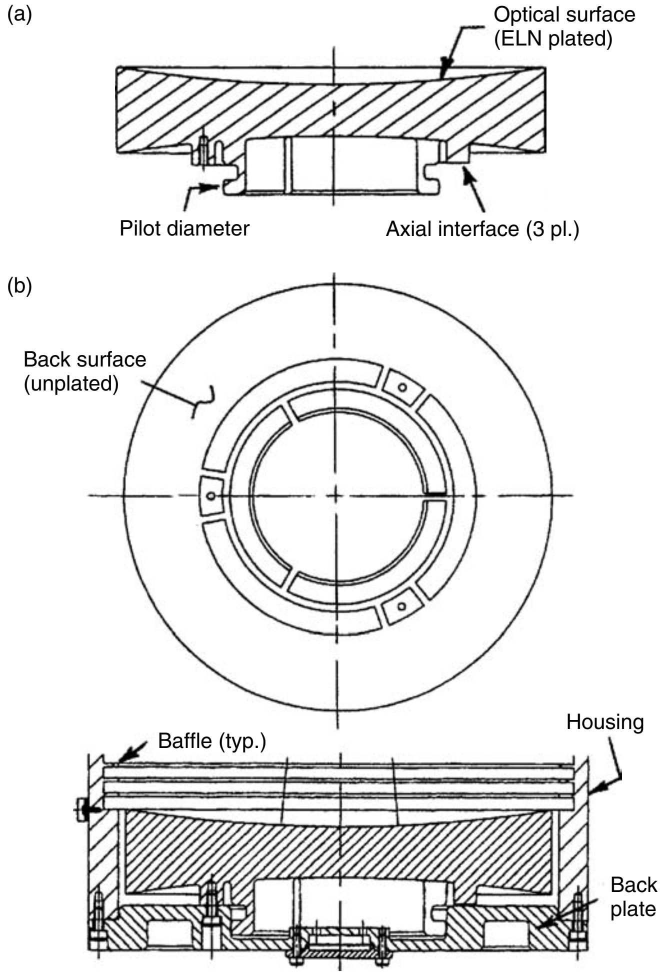

FIGURE 13.57 Opto-mechanical design (view [b]) for mounting a biconcave beryllium mirror (view [a]) incorporating the results from an investigation of bimetallic effects of ELN plating. (Adapted from Vukobratovich, et al. 1997.)

for metal mirrors typical of such applications will now be described. The 65×40 in. (165×102 cm) kidney-shaped beryllium mirror shown in Figure 13.10 was designed to be mounted on a kinematic mount with the DOF indicated in Figure 13.59(a). The support attached at point 1 reacted only axial ($\pm Z$) loads while that attached at point 2 reacted axial and vertical ($\pm Z$, $\pm Y$) loads. The support at point 3 reacted loads in all three axes ($\pm X$, $\pm Y$, $\pm Z$). This arrangement ensured that no pair of supports could restrain the mirror on a line connecting their centers and (theoretically) could not induce strain in the mirror. This required frictionless connections at the interfaces with the external supporting structure and infinitely compliant links to the structure.

The support concept developed and proven for this application utilized flexures with a cruciform cross section, as shown in Figure 13.60. This design was based on a series of criteria including the following: (1) ability to withstand combined launch loads of 10 to 15 times gravity in all three axes, (2) ability to withstand operation at 300 to 150 K, (3) ability to maintain optical figure quality of the reflecting surface $\lambda/12$ rms at $\lambda = 0.633$ μm wavelength, (4) compatibility with supporting the mirror at its neutral surface, (5) natural frequency >50 Hz, (6) flexure link to fit within a 4×4×3.5 in. (10×10×8.9 cm) pocket envelope, and (7) ability to accommodate local thermally induced deflections between the beryllium and dissimilar support materials such as stainless steel or titanium.

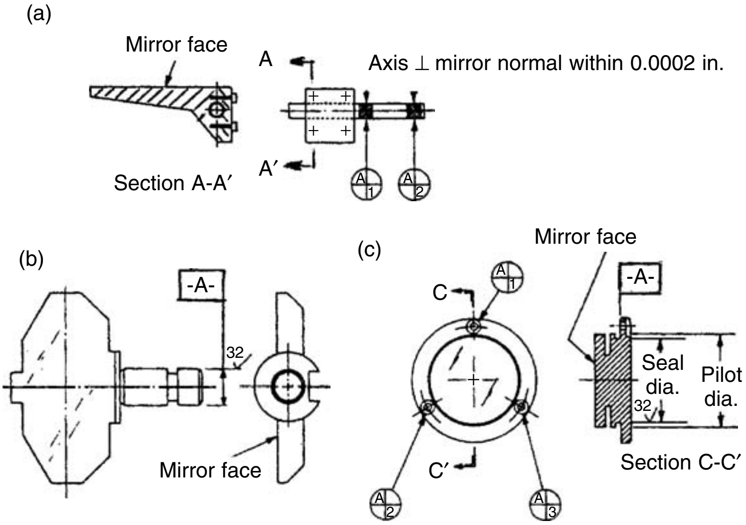
(a)
Mirror face
A
A′
Axis ⊥ mirror normal within 0.0002 in.
Section A-A′
A1
A2
(b)
-A-
32
Mirror face
(c)
Mirror face
C
C′
A1
-A-
Seal dia.
Pilot dia.
32
Section C-C′
A2
A3

FIGURE 13.58 Three configurations of mirrors fabricated by SPDT techniques to accurately orient the optical surfaces to mechanical mounting interfaces. Dimensions are in inches. (Adapted from Addis, E.C., *Proc. SPIE*, 389, 36, 1983.)

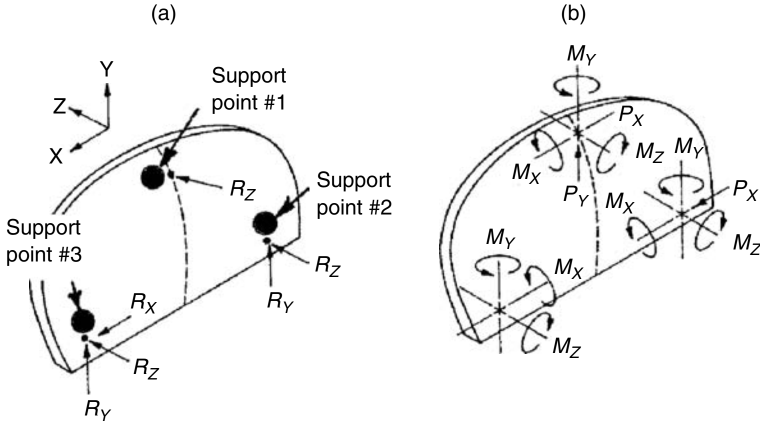
(a)
(b)
Y
Z
X
Support point #1
Support point #2
Support point #3
R_Z
R_Z
R_Z
R_X
R_Y
R_Y
M_Y
P_X
M_X
M_Z
M_Y
P_Y
M_X
P_X
M_Y
M_X
M_Z
M_Z

FIGURE 13.59 Analytical considerations of the support for the Be mirror of Figure 13.10. (a) Reaction forces applied at three semikinematic support locations and (b) unit moments applied to the mirror at its support points. (Adapted from Altenhof, R.R., *Opt. Eng.*, 15, 265, 1976.)

FEA of proposed flexure configurations and materials indicated the suitability of 6Al-4V titanium because of its high spring merit factor (yield stress/elastic modulus), good thermal match to the beryllium mirror, and low density. Other materials considered and rejected were stainless steel, beryllium, aluminum, and beryllium–copper. Figure 13.61 is a photograph of one of the three flexures used in this application.

To determine whether the redundant forces and moments that would result from use of these flexures as mirror supports would be acceptable, the finite element model was used as follows: (1) Unit forces (*P*) and moments (*M*) were applied singly at each support point of Figure 13.59(a) in the directions indicated in Figure 13.59(b). These loads represented inputs to the mirror due to uncorrected errors in spring rates and positioning of the flexures. (2) The worst-case total deflections resulting

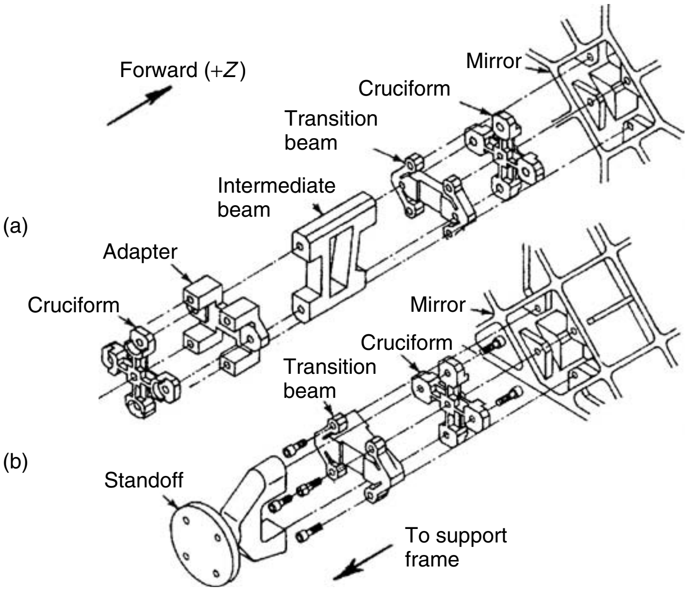
Forward (+Z)
Mirror
Cruciform
Transition beam
Intermediate beam
(a)
Adapter
Cruciform
Mirror
Cruciform
Transition beam
(b)
Standoff
To support frame

FIGURE 13.60 Exploded views of the flexure links used to support the Be mirror shown in Figure 13.10: (a) as used at point 1, (b) as used at points 2 and 3. (Adapted from Altenhof, R.R., *Opt. Eng*., 15, 265, 1976.)

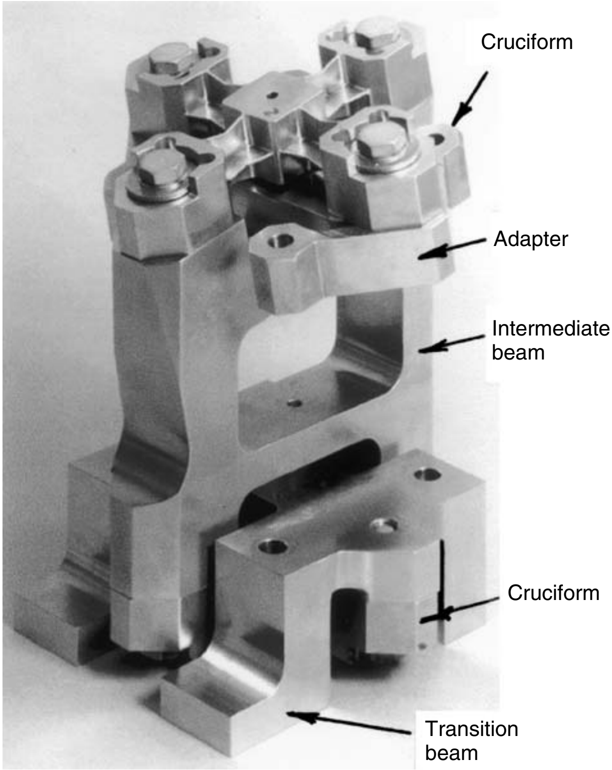
Cruciform
Adapter
Intermediate beam
Cruciform
Transition beam

FIGURE 13.61 Photograph of the flexure link sketched in Figure 13.60(a). (Adapted from Altenhof, R.R., *Opt. Eng*., 15, 265, 1976.)

from moment, force, and gravity terms in the above analysis were obtained. These are given in Table 13.13 for the apparent worst nodes. A deflection tolerance of 13 μin. (0.33 μm) over any instantaneous subaperture during self-weight testing was applied to this design. The right-hand column of the table indicates the corresponding computed values. All are well within the tolerable value. Moment and force values corresponding to this tolerable deflection were determined to be 0.5 Ib-in. and 0.5 Ib (0.2 kg), respectively. These inputs were assumed to exist at each support point simultaneously.

Another flexure-mounted metal mirror of classic design was the 27.8 lb (12.6 kg), 24.4-in. (62.0-cm)-diameter, *f*/2 beryllium primary of the highly successful Infrared Astronomical Satellite (IRAS) orbited by NASA in 1983 (see Figure 13.62). The following description of the mirror and its mount is based on papers by Schreibman and Young (1980) and Young and Schreibman (1980).

The mirror was made of Kawecki-Berylco HP-81 beryllium with inhomogeneity specified to be no greater than 76×10^{-6} K^{-1}. It was lightweighted by machining pockets into the back surface. The design was optimized by FEA for minimum susceptibility to mount-induced and gravity-released distortions. A constraint on the design was that cryogenic testing (at 40 K) was to be conducted in an available chamber that accommodated the mirror only in the axis-horizontal orientation. Asymmetric distortion due to gravity was therefore of great significance. The analytical model consisted of 336 nodes and 252 plate elements representing the mirror's front face supported by 276 beam elements for the radial and circumferential ribs. The computed rms surface deformation due to gravity effects after removal of defocus, decentration, and tilt was 0.020λ at $\lambda=0.633$ μm. The system error budget allowed $\lambda/10$ wave for this deformation. Figuring at room temperature progressively reduced the errors revealed during cryogenic testing. The cryogenic test/figure cycle was repeated until the mirror was deemed acceptable.

The mirror was cantilevered from a large beryllium baseplate in the telescope structure by three flexure links of the "T-shaped" configuration shown in view (a) of Figure 13.63. These were located at 120° intervals on a 9.2 in. (23.4 cm) radius as shown in view (b). The flexure design provided stiff axes as indicated in the latter view. The points of attachment of the flexures were in the neutral planes of the baseplate and the mirror. In the case of the mirror, this plane was 1.74 in. (4.42 cm) from the back surface. The flexures were 5Al-2.5Sn ELI titanium alloy [**] with a CTE closely matching that of beryllium. Vukobratovich et al. (1990) indicated that Ti-6Al-4V ELI is a better material for such flexures because of the low values of fracture toughness of the former material as reported by Carman and Katlin (1968) and other researchers.

TABLE 13.13

Worst-Case Summations of Mirror Deflections with Unit Loads Applied at Support Points of the Mirror Modeled in Figure 13.59

Node Number	Deflections Due to Moments (μin.)	Deflections Due to Forces (μin.)	Deflections Due to Gravity (μin.)
9[a]	7.24	14.2	4.8
56[a]	−1.71	−7.0	4.6
31	1.33	3.9	1.9
1	1.89	6.3	−2.3
60	0.56	1.3	2.0
4	4.88	15.7	2.0
66	0.73	−0.5	2.9

[a] These nodes represent peak deflection points.

Source: Adapted from Altenhof, R.R., *Opt. Eng.*, 15, 265, 1976.

[**] ELI means "extra-low interstitial."

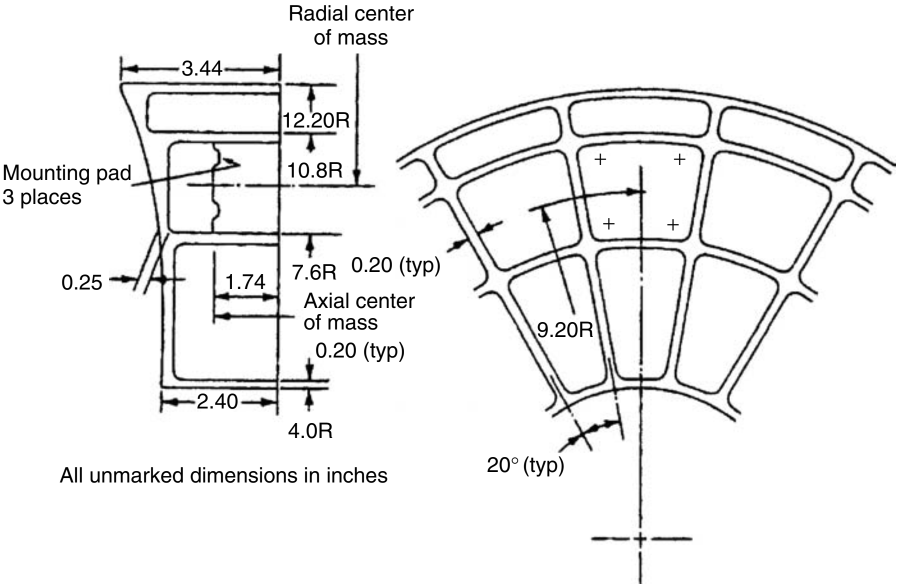
Radial center of mass
3.44
12.20R
10.8R
Mounting pad 3 places
7.6R
0.20 (typ)
0.25
1.74
Axial center of mass
0.20 (typ)
2.40
4.0R
9.20R
20° (typ)
All unmarked dimensions in inches

FIGURE 13.62 Detail views of the IRAS primary mirror. (Adapted from Young, P. and Schreibman, M., *Proc. SPIE*, 251, 171, 1980.)

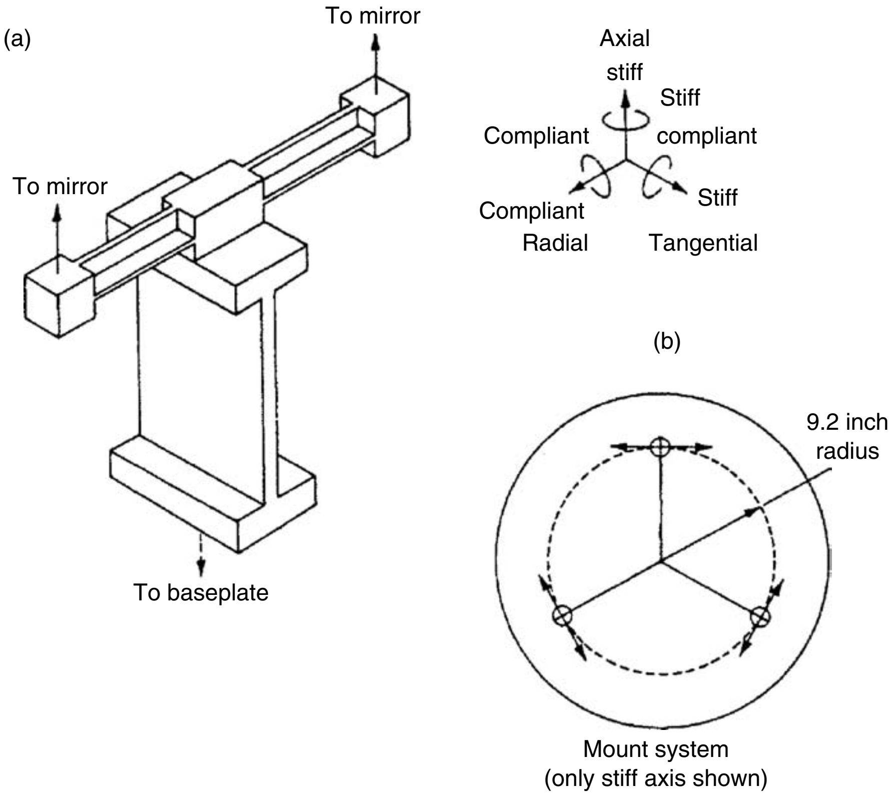
(a)
To mirror
To mirror
To baseplate
Axial
stiff
Stiff
compliant
Compliant
Compliant
Stiff
Radial
Tangential
(b)
9.2 inch radius
Mount system
(only stiff axis shown)

FIGURE 13.63 (a) Schematic of one flexure link used to support the IRAS primary mirror from the telescope baseplate. (b) Frontal view of the mirror showing the orientation of the three flexure links. The tangential axis is indicated for each flexure. (Adapted from Schreibman, M. and Young, P., *Proc. SPIE*, 250, 50, 1980.)

13.12 INTERFACING MULTIPLE SPDT COMPONENTS TO FACILITATE ASSEMBLY AND ALIGNMENT

A major advantage of SPDT as a means for manufacturing precision optical components is the ability to integrate locating and optical surfaces directly into each work piece of multiple-component systems during fabrication, frequently without removing the work piece from the SPDT instrument. This ensures maximum alignment accuracy of the optical surfaces to other portions of the overall system.

Figure 13.64 schematically shows six types of optical assemblies featuring this type of construction. Each system shown has at least one SPDT mechanical interface between separate opto-mechanical components. Each of the latter components is SPDT machined to accurately align its optical surface(s) to the mechanical interfaces. The axis of symmetry of each system is indicated by a curved arrow. All but one system (e) has a mirror machined integrally with a spider support. The system in view (a) involves two centered conical (axicon) reflecting optical surfaces; hence the name *reflaxicon*. The fast Cassegrain telescope shown in view (b) requires only two components because it is so short, while the longer, slow Cassegrain telescope of view (c) is most conveniently made with three components. The central component is essentially a spacer. The reflecting microscope objective system of view (d) also has a spacer that allows focus to be established. It is assembled with two

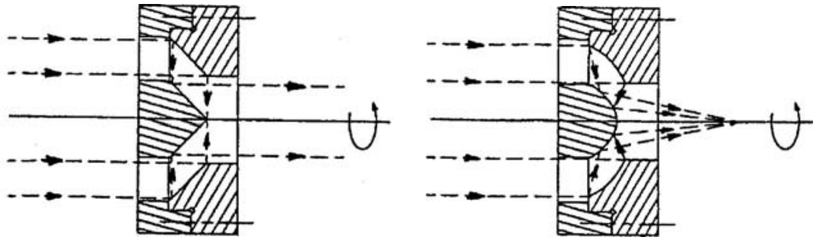

(a) Reflaxicon beam expander (b) Fast Cassegrain telescope

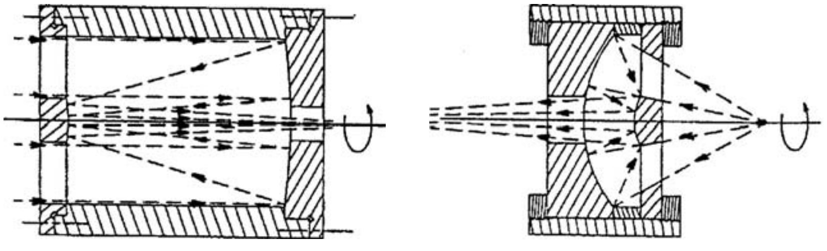

(c) Slow Cassegrain telescope (d) Schwarzschild microscope objective

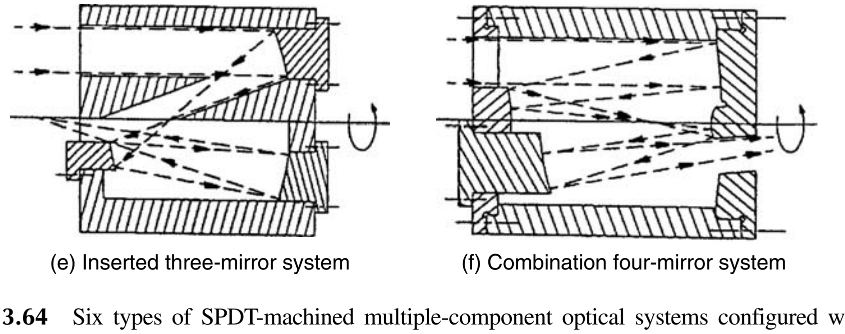

(e) Inserted three-mirror system (f) Combination four-mirror system

FIGURE 13.64 Six types of SPDT-machined multiple-component optical systems configured with integral locating surfaces to facilitate alignment and simplify assembly. The axis of symmetry is indicated for each system. (Adapted from Gerchman, M., *Proc. SPIE*, 751, 113, 1987.)

threaded retaining rings. Note that the light path is from right to left in this view. The three-mirror system of view (e) has separate, off-axis optical components that need to be machined with reference mechanical surfaces or locating pins to facilitate rotational alignment. It also has integral stray light baffling provisions. The relatively complex four-mirror system of view (f) embodies features of all the other systems.

The mechanical interfaces in systems such as are shown in Figure 13.64 might well be configured generally as shown in Figure 13.65 in order to provide centering and axial positioning. Minimal stress is introduced into the components if the radial interface involves close sliding contact, all surfaces providing the axial interface are coplanar flats and accurately normal to the component axes or a toroidal surface contacting a flat, and the bolt constraints are centralized in the contacting pads.

Morrison (1988) provided a detailed description of the design, fabrication, assembly, and testing of an unobscured aperture, 10-power, afocal telescope assembly comprising two parabolic mirrors (one of which is off-axis) and a housing with two integral stray light baffles. Figure 13.66 shows a sectional view of the system. Figure 13.67 is a drawing of the primary mirror while Figure 13.68 is a drawing of the secondary mirror.

Each mirror has a flat flange on the reflecting surface side of the substrate that interfaces with the parallel ends of the housing. The interfacing surfaces and the optical surfaces are SPDT machined to high accuracy with regard to location and minimal tilt with respect to the optical axes. The flat surfaces also serve as alignment references during setup for testing. The length of the housing controls the vertex-to-vertex separation of the mirrors. The end surfaces are flat to $\lambda/2$ at 0.633 μm, parallel to 0.5 arcsec, and separated by the nominal length ±0.005 in. (0.127 mm). The actual length is measured to $\pm 10 \times 10^{-6}$ in. (0.25 μm) and the part serialized for identification.

The primary mirror is attached to a sub plate (fixture) for diamond turning. This sub plate is vacuum-chucked to the SPDT instrument and diamond-turned flat to $<\lambda/2$ at 0.633 μm. The rim of the sub plate is then turned to $\pm 5 \times 10^{-6}$ in. (0.13 μm) roundness to provide an accurate reference for centering six precision, jig-bored, dowel holes in pairs 2.906 in. (51.692 mm) apart on a 2.000 in. (50.800 mm) bolt circle to match the dowel pin holes on the primary mirror. A central dowel hole

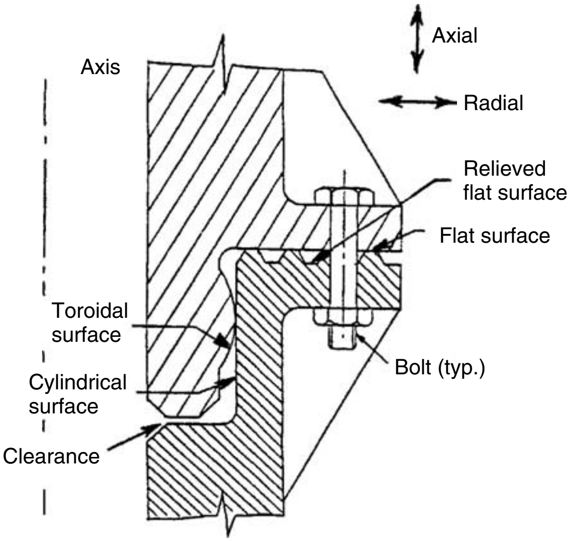

FIGURE 13.65 Typical interface between SPDT optical components to ensure axial and radial alignment and to minimize stress buildup due to mounting forces. (Adapted from Sanger, G.M., in *Applied Optics and Optical Engineering*, Vol. 10, Shannon, R.R. and Wyant, J.C., Eds., Academic Press, San Diego, 1987, chap. 6.)

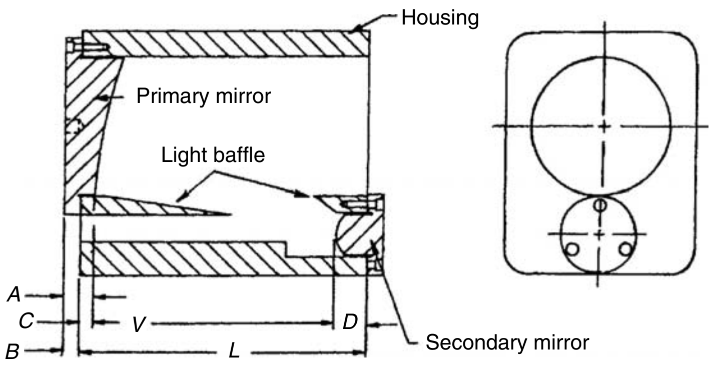
Housing
Primary mirror
Light baffle
A
C
B
V
D
L
Secondary mirror

FIGURE 13.66 Example of a 10 power, afocal telescope comprising primary and secondary mirrors and a telescope housing with two light baffles. The mechanical interfaces are SPDT machined for accurate alignment at assembly. (Adapted from Morrison, D., *Proc. SPIE*, 966, 219, 1988.)

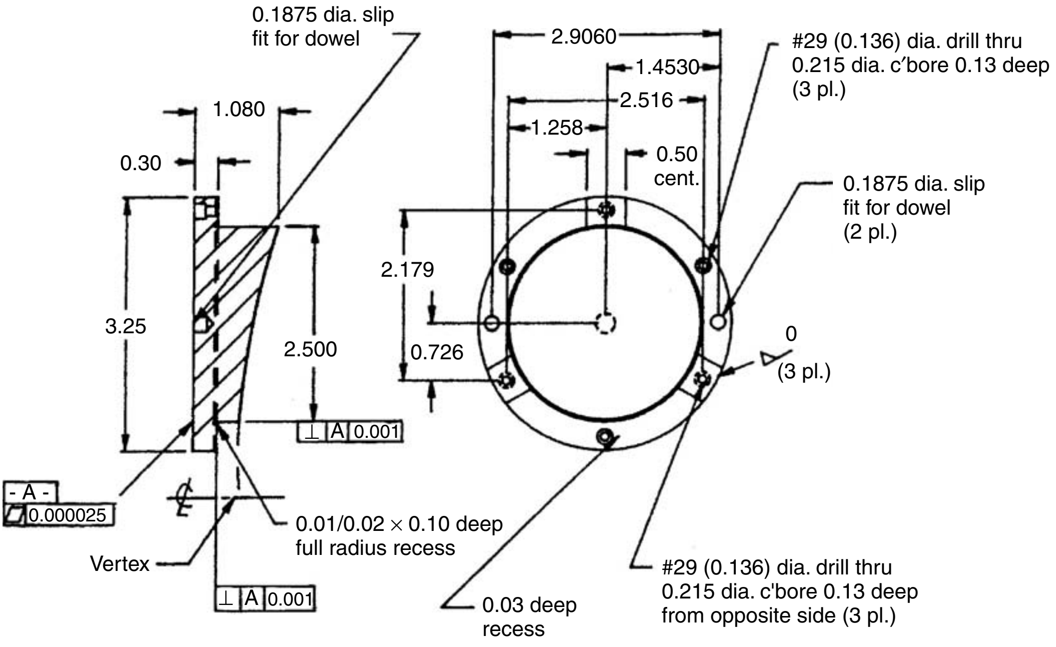
0.1875 dia. slip fit for dowel
1.080
0.30
3.25
2.500
⊥ A 0.001
- A -
0.000025
Vertex
0.01/0.02 × 0.10 deep full radius recess
⊥ A 0.001
2.9060
1.4530
2.516
1.258
0.50 cent.
2.179
0.726
#29 (0.136) dia. drill thru 0.215 dia. c′bore 0.13 deep (3 pl.)
0.1875 dia. slip fit for dowel (2 pl.)
0
(3 pl.)
0.03 deep recess
#29 (0.136) dia. drill thru 0.215 dia. c'bore 0.13 deep from opposite side (3 pl.)

FIGURE 13.67 Drawings of the primary mirror for the telescope shown in Figure 13.66. (Adapted from Morrison, D., *Proc. SPIE*, 966, 219, 1988.)

also is bored at this time. Three mirror blanks are mounted on the subplate as shown in Figure 13.69 for simultaneous machining.

After the optical surface of a set of primary mirrors are completed, their actual axial thicknesses are measured to 1×10^{-6} in. (0.025 μm) and recorded as dimension A of Figure 13.66. Nominally, this dimension is 0.550 in. (13.970 mm). The mirrors are then individually mounted on a vacuum chuck using a central dowel for centering. The mounting flange is turned until $A - B = 0.250 \pm 0.002$ in. (6.350 ± 0.051 mm). The actual dimension C, to the nearest microinch, is then recorded. The length L of the housing is also measured to the nearest microinch.

The secondary mirror is mounted individually on a vacuum chuck using a central dowel for centering, and the optical surface is diamond-turned. Its flange is then machined in the same setup so

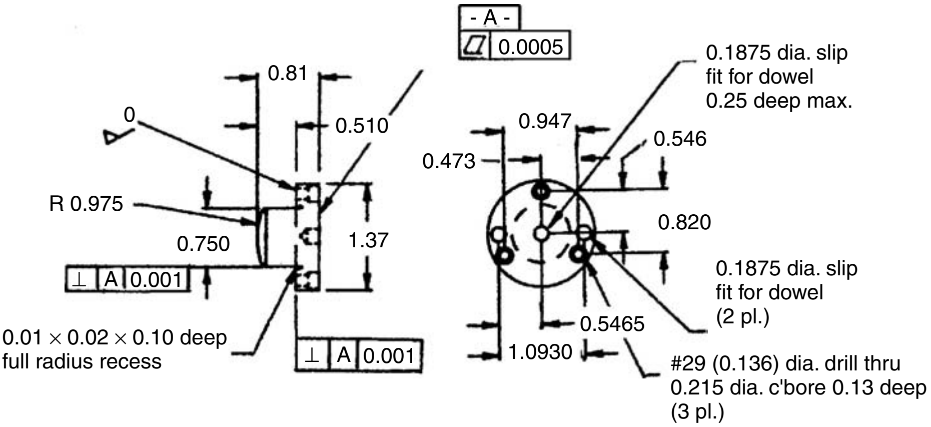
-A-
0.0005
0.81
0
0.510
R 0.975
0.750
⊥ A 0.001
1.37
0.01 × 0.02 × 0.10 deep
full radius recess
⊥ A 0.001
0.947
0.473
0.1875 dia. slip
fit for dowel
0.25 deep max.
0.546
0.820
0.1875 dia. slip
fit for dowel
(2 pl.)
0.5465
1.0930
#29 (0.136) dia. drill thru
0.215 dia. c'bore 0.13 deep
(3 pl.)

FIGURE 13.68 Drawings of the secondary mirror for the telescope shown in Figure 13.66. (Adapted from Morrison, D., *Proc. SPIE*, 966, 219, 1988.)

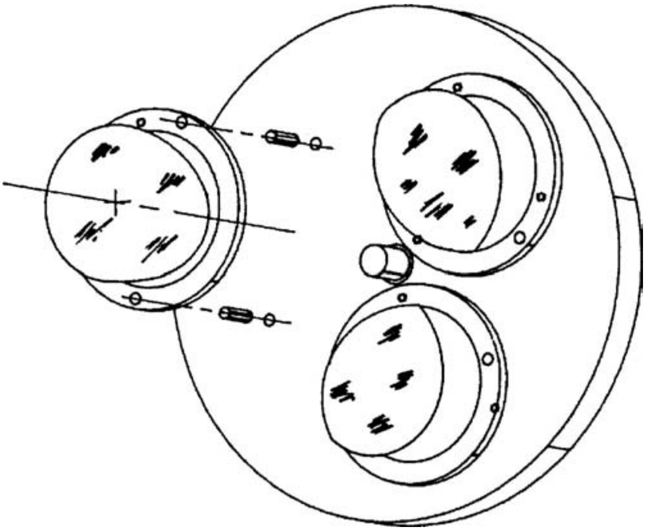

FIGURE 13.69 Schematic fixturing arrangement for simultaneous SPDT machining of three off-axis secondary mirrors. This is functionally similar to that shown in Figure 13.43. (Adapted from Morrison, D., *Proc. SPIE*, 966, 219, 1988.)

that its dimension D (see Figure 13.66) equals $L - V - C$. All mirrors are machined in the same manner so that they are automatically positioned correctly upon installation.

Because all critical dimensions have been machined to close tolerances, no adjustments are needed during assembly. The fabrication process has, in each system, determined the optical alignment. Morrison (1988) indicated that a telescope could be completely assembled within 30 min.

Another telescope featuring similar diamond-turned features to facilitate alignment was described by Erickson et al. (1992). Figure 13.70 shows the telescope schematically. All components were made of 6061 aluminum for thermal stability. All surfaces marked SPDT were diamond-turned as described below. The 8-in. (203.2-mm)-diameter primary mirror had an integral mounting flange isolated from the optical surface by a necked-down flexure region similar in principle to that of Figure 13.58(c). The primary and secondary mirrors had integral spherical reference surfaces diamond-turned concentric with the nominal telescope focal point as indicated in Figure 13.70. We here summarize major details

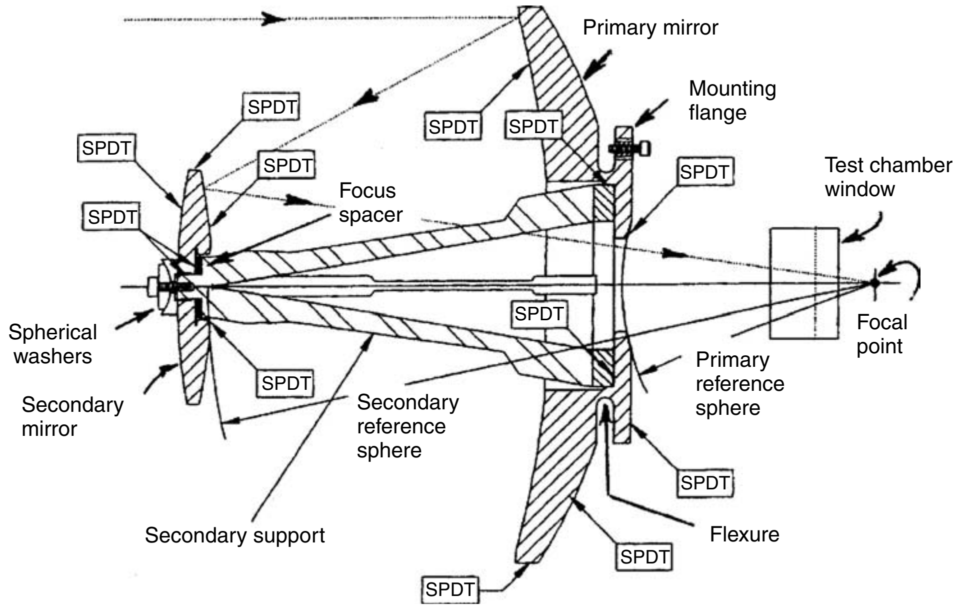

FIGURE 13.70 Schematic diagram of an all-aluminum telescope with optical surfaces, mechanical interfaces, and alignment reference surfaces SPDT machined for ease of assembly. (Adapted from Erickson, D.J. et al., *Proc. SPIE*, CR43, 329, 1992.)

of the component manufacturing process to show how these surfaces were used to facilitate accurate machining and assembly.

After conventional machining to near net shape and size, the secondary mirror was mounted on an SPDT instrument for diamond turning the back (nonoptical) surface. The substrate was then turned over and attached to a vacuum chuck for diamond turning the mirror's OD and ID, the convex aspheric optical surface, the concave spherical reference surface, and the interface for the focus spacer.

The following surfaces on the primary mirror were diamond-turned in a single machine setup: the flat mounting flange surface, the concave spherical reference surface, the convex spherical mirror back surface, and the mirror's OD and ID. It was then turned over and mounted by its flange to the SPDT faceplate. The substrate was centered to the spindle axis by minimizing runout of the precision OD. The concave aspheric optical surface and the axial interface for the secondary support were then turned, and the mirror's ID was matched to the conventionally machined OD of the secondary support. Without removing the primary mirror from the spindle, the secondary support was attached with screws (not shown in Figure 13.70) and the OD and axial interface for the secondary mirror turned. This ensured accurate alignment of the mirror axes.

After removal of the primary/secondary support subassembly from the spindle, the focus spacer was ground to thickness and parallelism and the secondary mirror installed. When the axial separation of the optical surfaces was correct, fringes could be observed between an auxiliary reference surface concentric with the focal point and both diamond-turned reference surfaces on the mirrors. The authors indicated that no subsequent alignment was needed to achieve $<\lambda/4$ reflected wavefront accuracy at $\lambda = 0.633$ μm from production telescopes.

REFERENCES

Addis, E.C., Value engineering additives in optical sighting devices, *Proc. SPIE*, 389, 36, 1983.
Altenhof, R.R., Design and manufacture of large beryllium optics, *Opt. Eng.*, 15, 265, 1976.

Angele, W., Main Mirror for a 3-Meter Spaceborne Optical Telescope, *Optical Telescope Technology*, NASA SP-233, 281, 1969.

Arnold, J.B., Morris, T.O., Sladky, R.E., and Steger, P.J., Machinability studies of infrared window materials and metals, *Opt. Eng.*, 16, 324, 1977.

Arriola, E.W., Diamond turning assisted fabrication of a high numerical aperture lens assembly for 157 nm microlithography, *Proc. SPIE*, 5176, 36, 2003.

Baker, P.C., Sonderman, J.B., and Saito, T.T., Finishing of precision generated metal optical components, *Proc. SPIE*, 65, 42, 1975.

Barho, R., Stanghellini, S., and Jander, G., VLT secondary mirror unit performance and test results, *Proc. SPIE*, 3352, 675, 1998.

Barnes, W.P., Some effects of the aerospace thermal environment on high-acuity optical systems, *Appl. Opt.*, 5, 701, 1966.

Barr, L.D., Livingston, W.C., Mirror seeing control in thick, solid mirrors and the planned upgrade of the McMath-Pierce Solar Telescope, *Proc. SPIE*, 1931, 53, 1992.

Bender, J., Tuenge, S., and Bartley, J., Computer-controlled belt polishing of diamond-turned annular mirrors, *Proc. SPIE*, 966, 29, 1988.

Bennett, J.M., Archibald, P.C., Rahn, J.P., and Klugman, A., Low-scatter molybdenum surfaces, *Appl. Opt.*, 22, 4048, 1983.

Bennett, J.M. and Decker, D.L., Surface characterization of diamond-turned metal optics, *Proc. SPIE*, 288, 534, 1981.

Bennett, J.M., Wong, S.M., and Krauss, G., Relation between the optical and metallurgical properties of polished molybdenum mirrors, *Appl. Opt.*, 19, 3562, 1980.

Bingham, R.G., The next steps, (panel discussion), *Proc. SPIE*, 1931, 150, 1992.

Brown, N., Baker, P., and Parks, R., Polishing to figuring transition in turned optics, Proc. SPIE, 306, 58, 1981.

Carman, C.M. and Katlin, J.M., Plane strain fracture toughness and mechanical properties of 5Al-2.5Sn ELI and commercial titanium alloys at room and cryogenic temperature, *Applications-Related Phenomena in Titanium Alloys, ASTM STP432*, American Society for Testing and Materials, 1968, pp. 124–144.

Catura, R. and Vieira, J., Lightweight aluminum optics, *Proc. ESA Workshop: Cosmic X-Ray Spectroscopy Mission, Lyngby, Denmark, 24-26 June, 1985, ESA SP-2*, 173, 1985.

Cayrel, M., VLT beryllium secondary mirror No. 1 - performance review, *Proc. SPIE*, 3352, 721, 1998.

Church, E.L., Jenkinson, H.A., and Zavada, J.M., Measurement of the finish of diamond-turned metal surfaces by differential light scattering, *Appl. Opt.*, 360, 1977.

Colquhoun, A., Gordon, C., and Shepherd, J., Polygon scanners – an integrated design package, *Proc. SPIE*, 966, 184, 1988.

Connelly, J.A., Ohl, R.G., Mentzell, J.E., Madison, T.J., Hylan, J.E., Mink, R.G., Saha, T.T., Tveekrem, J.L., Sparr, L.M., Chambers, V.J., Fitzgerald, D.L., Greenhouse, M.A., and MacKenty, J.W., Alignment and performance of the Infrared Multi-Object Spectrometer, *Proc. SPIE*, 5172, 1, 2003.

Curcio, M.E., Precision-machined optics for reducing system complexity, *Proc. SPIE*, 226, 91, 1980.

Dahlgren, R. and Gerchman, M., The use of aluminum alloy castings as diamond machining substrates for optical surfaces, *Proc. SPIE*, 890, 68, 1988.

Decker, D.L., Bennett, J.M., Soileau, M.J., Porteus, J.O., and Bennett, H.E., Surface and optical studies of diamond-turned and other metal mirrors, *Opt. Eng.*, 17, 160, 1978.

Decker, D.L. and Grandjean, D.J., Physical and optical properties of surfaces generated by diamond-turning on an advanced machine, in *Laser Induced Damage in Optical Materials*: 1978, NBS *Spec. Publ. 541*, Nat'l. Bureau of Standards, Washington, DC, 1978, p. 122.

Denny, C., Spawr, W.J., and Pierce, R.L., Metal mirror selection guide update, *Proc. SPIE*, 181, 84, 1979.

Devilliers, C. and Krödel, M., CESIC® A new technology for lightweighted and cost-effective space instrument structures and mirrors, *Proc. SPIE*, 5494, 285, 2004.

Dierickx, P., Optical quality and stability of 1.8-m aluminum mirrors, *Proc. SPIE*, 1931, 78, 1992.

Dierickx, P., Enard, D., Geyl, R., Paseri, J., Cayrel, M., and Béraud, P., The VLT primary mirrors: mirror production and measured performance, *Proc. SPIE*, 2871, 385, 1996.

Downey, C.H., Abbott, R.S., Arter, P.I., Hope, D.A., Payne, D.A., Roybal, E.A., Lester, D.F., and McClenahan, J.O., The chopping secondary mirror for the Kuiper Airborne Observatory, *Proc. SPIE*, 1167, 329, 1989.

Ealey, M.A., Wellman, J.A., and Weaver, G., CERAFORM SiC: roadmap to 2 meters and 2 kg/m^2 areal density, *Proc. SPIE*, CR67, 53, 1997.

Enard, D., E.S.O. VLT Project I: a status report, *Proc. SPIE*, 1236, 63, 1990.

Erickson, D.J., Johnston, R.A., and Hull, A.B., Optimization of the optomechanical interface employing diamond machining in a concurrent engineering environment, *Proc. SPIE*, CR43, 329, 1992.

Forbes, F.F., Large aperture aluminum alloy telescope mirrors, *Appl. Opt.*, 7, 1407, 1968.

Forbes, F.F., A 40-cm welded-segment lightweight aluminum alloy telescope mirror, Appl. Opt., 8, 1361, 1969.

Forbes, F.F., Cast Tenzalloy aluminum optics, *Proc. SPIE, 1931*, 2, 1992.

Forbes, F.F. and Johnson, H.L., Stability of Tenzalloy aluminum mirrors, *Appl. Opt.*, 10, 1412, 1971.

Fortini, A.J., Open-cell silicon foam for ultralight mirrors, *Proc. SPIE*, 3786, 440, 1999.

Fuller, J.B.C., Jr., Forney, P., and Klug, C.M., Design and fabrication of aluminum mirrors for a large aperture precision collimator operating at cryogenic temperatures, *Proc. SPIE* 288, 104, 1981.

Gerchman, M., Specifications and manufacturing considerations of diamond-machined optical components, *Proc. SPIE*, 607, 36, 1986.

Gerchman, M., Diamond-turning applications to multimirror systems, *Proc. SPIE*, 751, 113, 1987.

Gerchman, M., A description of off-axis conic surfaces for non-axisymmetric surface generation, *Proc. SPIE*, 1266, 262, 1990.

Gerchman, M. and McLain, B., An investigation of the effects of diamond machining on germanium for optical applications, *Proc. SPIE*, 929, 94, 1988.

Geyl, R. and Cayrel, M., The VLT secondary mirror — a report, *Proc. SPIE*, CR67, 327, 1997.

Gibson, L.J. and Ashby, M.F., *Cellular Solids*, Pergamon Press, Oxford, England, 1988.

Goela, J.S., and Pickering, M.A., Optics applications of chemical vapor deposited β-SiC, *Proc. SPIE*, CR67, 71, 1997.

Goela, J., Pickering, M., Taylor, R., Murray, B., and Lompado, A., Properties of chemical-vapor-deposited silicon carbide for optics applications in severe environments, *Appl. Opt.*, 30, 3166, 1991.

Goela, J. and Taylor, R., Large scale fabrication of lightweight Si/SiC LIDAR mirrors, *Proc. SPIE*, 1118, 14, 1989a.

Goela, J. and Taylor, R., CVD replication for optical applications, *Proc. SPIE*, 1047, 198, 1989b.

Goodman, W.A., Private communication, 2005.

Goodman, W.A. and Jacoby, M.T., Dimensionally stable ultra-lightweight silicon optics for both cryogenic and high-energy laser applications, *Proc. SPIE*, 4198, 260, 2001.

Goodman, W.A. and Jacoby, M.T., Lightweight athermal SLMS^{TM} innovative telescope, *Proc. SPIE*, 5528, 72, 2004.

Goodman, W.A., Jacoby, M.T., Krödel, M., and Content, D.A., Lightweight athermal optical system using silicon lightweight mirrors (SLMS) and carbon fiber reinforced silicon carbide (Cesic$^{®}$) mounts, *Proc. SPIE*, 4822, 12, 2002.

Goodman, W.A., Müller, C.E., Jacoby, M.T., and Wells, J.D., Thermo-mechanical performance of precision C/SiC mounts, *Proc. SPIE*, 4451, 468, 2001.

Gossett, E., Marder, J., Kendrick, R., and Cross, O., Evaluation of hot isostatic pressed beryllium for low scatter cryogenic optics, *Proc. SPIE*, 1118, 50, 1989.

Gould, G., Method and Means for Making a Beryllium Mirror, U.S. Patent 4,492,669, 1985.

Hadjimichael, T., Content, D., and Frohlich, C., Athermal lightweight aluminum mirrors and structures, *Proc. SPIE*, 4849, 396, 2002.

Harned, N., Harned, R., and Melugin, R., Alignment and evaluation of the cryogenic corrected Infrared Astronomical Satellite (IRAS) telescope, *Opt. Eng.*, 20, 195, 1981.

Hedges, A.R. and Parker, R.A., Low stress, vacuum-chuck mounting techniques for the diamond machining of thin substrates, *Proc. SPIE*, 966, 13, 1988.

Hibbard, D., Dimensional stability of electroless nickel coatings, *Proc. SPIE*, 1335, 180, 1990.

Hibbard, D., Critical parameters for the preparation of low scatter electroless nickel coatings, *Proc. SPIE*, 1753, 10, 1992.

Hibbard, D., Electrochemically deposited nickel alloys with controlled thermal expansion for optical applications, *Proc. SPIE*, 2542, 236, 1995.

Hibbard, D.L., Electroless nickel for optical applications, *Proc. SPIE*, CR67, 179, 1997.

Hoffman, R.A., Lange, W.J., and Choyke, W.J., Ion polishing of copper: some observations, *Appl. Opt.*, 14, 1803, 1975.

Hoover, M.D., Seiler, F.A., Finch, G.L., Haley, P.J., Eiddson, A.F., Mewhinney, J.A., Bice, D.E., Brooks, A.L., and Jones, R.K., *Space Nuclear Power Systems*, Orbit Book Co., Malabar, FL, 1992, p. 285.

Howells, M.R. and Paquin, R.A., Optical substrate materials for synchrotron radiation beam lines, *Proc. SPIE*, CR67, 339, 1997.

Jacobs, S.F., Variable invariables: dimensional instability with time and temperature, *Proc. SPIE*, CR43, 181, 1992.

Jacoby, M.T., Goodman, W.A., and Content, D.A., Results for silicon lightweight mirrors (SLMS), *Proc. SPIE*, 4451, 67, 2001.

Jacoby, M.T., Goodman, W.A., Stahl, H.P., Keys, A.S., Reily, J.C., Eng, R., Hadaway, J.B., Hogue, W.D., Kegley, J.R., Siler, R.D., Haight, H.J., Tucker, J., Wright, E.R., Carpenter, J.R., and McCracken, J.E., Helium cryo testing of a SLMS™ (silicon lightweight mirrors) athermal optical assembly, *Proc. SPIE*, 5180, 199, 2003.

Jacoby, M.T., Montgomery, E.E., Fortini, A.J., and Goodman, W.A., Design, fabrication, and testing of lightweight silicon mirrors, *Proc. SPIE*, 3786, 460, 1999.

Jones, R.A., Final figuring of a lightweighted beryllium mirror, *Proc. SPIE*, 65, 48, 1975.

Klein, C.A., Mirror figure-of-merit and material index-of-goodness for high power laser beam reflectors, *Proc. SPIE*, 288, 69, 1981.

Krödel, M., Cesic® — Engineering material for optics and structures, *Proc. SPIE*, 5494, 297, 2004.

Kurdock, J., Saito, T., Buckmelter, J., and Austin, R., Polishing of super-smooth metal mirrors, *Appl. Opt.*, 14, 1808, 1975.

Lange, S., Very high resolution profiler for diamond turning groove analysis, *Proc. SPIE*, 966, 157, 1988.

Leblank, J-M. and Rozelot, J-P., Large active mirror in aluminium (LAMA), *Proc. SPIE*, 1535, 122, 1991.

Lester, R.S. and Saito, T.T., Aging of optical properties of polished copper mirrors, *Appl. Opt.*, 16, 2035, 1977.

Lindsey, K. and Franks, A., Metal optics versus glass optics, *Proc. SPIE*, 163, 46, 1979.

Lyons, J.J., III and Zaniewski, J.J., High Quality Optically Polished Aluminum Mirror and Process for Producing, *U.S. Patent 6,350,176 B1*, 2002.

McClelland, R.S. and Content, D.A., Design, manufacture, and test of a cryo-stable Offner relay using aluminum foam core optics, *Proc. SPIE*, 4451, 77, 2001.

Mikk, G., Cryogenic testing of a beryllium mirror, *Proc. SPIE*, 65, 89, 1975.

Moberly, J.W. and Brown, H.M., Technical note on fabricating isotropic beryllium, *Int. J. Powder Metall.*, Vol. 6, 1970.

Mohn, W.R. and Vukobratovich, D., Recent applications of metal matrix composites in precision instruments and optical systems, *Opt. Eng.*, 27, 90, 1988.

Moon, I.K., Cho, M.K., and Richard, R.M., Optical performance of bimetallic mirrors under thermal environment, *Proc. SPIE*, 4444, 29, 2001.

Morrison, D., Design and manufacturing considerations for the integration of mounting and alignment surfaces with diamond turned optics, *Proc. SPIE*, 966, 219, 1988.

Müller, C., Papenburg, U., Goodman, W.A., and Jacoby, M., C/SiC high precision lightweight components for optomechanical applications, *Proc. SPIE*, 4198, 249, 2001.

Murray, B.W., Ulph, E., and Richard, P., Thick fine-grained beryllium optical coatings, *Proc. SPIE*, 1485, 106, 1991.

Noble, R.H., Lightweight Mirrors for Secondaries, *Proceedings of Symposium on Support and Testing of Large Astronomical Mirrors, Tucson, AZ 4–6 Dec. 1966*, Kitt Peak National Observatory and University of Arizona, Tucson, 1966, 186.

Oettinger, P.E. and McClellan, R.P., High power laser refractory metal mirrors made of thoriated tungsten, *Appl. Opt.*, 15, 16, 1976.

Offner, A., Restricted Off-Axis Field Optical System, U.S. Patent 4,293,186, 1981.

Ogloza, A., Decker, D., Archibald, P., O'Connor, D., and Bueltmann, E., Optical properties and thermal stability of single-point diamond-machined aluminum alloys, *Proc. SPIE*, 966, 228, 1988.

Ohl, R., Barthemy, M., Zewari, S., Toland, R., McMann, J., Puckett, D., Hagopian, J., Hylan, J., Mentzell, J., Mink, L., Sparr, L., Greenhouse, M., and MacKenty, J., Comparison of stress relief procedures for cryogenic aluminum mirrors, *Proc. SPIE*, 4822, 51, 2002.

Ohl, R., Preuss, W., Sohn, A., Conkey, S., Garrard, K.P., Hagopian, J., Howard, J.M., Hylan, J., Irish, S.M., Mentzell, J.E., Schroeder, M., Sparr, L.M., Winsor, R.S., Zewari, S.W., Greenhouse, M.A., and MacKenty, J.W., Design and fabrication of diamond machined aspheric mirrors for ground-based, near-IR astronomy, *Proc. SPIE*, 4841, 677, 2003.

Palum, R., Surface profile error measurement for small rotationally symmetric surfaces, *Proc. SPIE*, 966, 138, 1988.

Paquin, R.A., Selection of materials and processes for metal optics, *Proc. SPIE*, 65, 12, 1975.

Paquin, R.A., Advanced lightweight beryllium optics, *Proc. SPIE*, 513, 355, 1985.

Paquin, R.A., Hot isostatic pressed beryllium for large optics, *Opt. Eng.*, 25, 2003, 1986.

Paquin, R., Dimensional stability: an overview, *Proc. SPIE*, 1335, 2, 1990.

Paquin, R., Materials Properties and Fabrication for Stable Optical Systems, *SPIE Short Course* SC 219, 1991.

Paquin, R.A., Properties of metals, in *Handbook of Optics*, 2nd. Ed., Vol. II, Bass, M., Van Stryland, E.W., Williams, D.M., and Wolfe, W.L., Eds., Optical Society of America, Washington, DC, 1994, chap. 35.

Paquin, R.A., Metal mirrors, in *Handbook of Optomechanical Engineering*, CRC Press, A. Ahmad, Ed., Boca Raton, FL, 1997, chap. 4.

Paquin, R.A. and Gardopee, G.J., Fabrication of a lightweight beryllium one-meter f/0.58 ellipsoidal mirror, *Proc. SPIE*, 1618, 61, 1991.

Paquin, R.A. and Goggin, W., Beryllium Mirror Technology, State-of-the-art Report, Perkin-Elmer Rept. IS 11393, Norwalk, CT, 1972.

Paquin, R.A., Levenstein, H., Altadonna, L., and Gould, G., Advanced lightweight beryllium optics, *Opt. Eng.*, 23, 157, 1984.

Paquin, R.A., Magida, M.B., and Vernold, C.L., Large optics from silicon carbide, *Proc. SPIE*, 1618, 53, 1991.

Parks, R.E., Making and testing an f/0.15 parabola, *Appl. Opt.*, 13, 1987, 1974.

Parks, R.E., Introduction to Diamond Turning, *SPIE Short Course*, 1982.

Parsonage, T., Advances in beryllium optical technology utilizing spherical powder, *Proc. SPIE*, 3352, 130, 1998.

Parsonage, T., JWST beryllium telescope: material and substrate fabrication, *Proc. SPIE*, 5494, 39, 2004.

Parsonage, T., Personal communication, 2005.

Piccolo, S.K., Working with beryllium, *OSA Optical Fabrication and Testing Workshop,* North Falmouth, MA, 1980.

Pollard, W., Vukobratovich, D., and Richard, R., The structural analysis of a light-weight aluminum foam core mirror, *Proc. SPIE,* 748, 180, 1987.

Rhorer, R.L. and Evans, C.J., Fabrication of optics by diamond turning, in *Handbook of Optics*, 2nd. Ed., Vol. II, Bass, M., Van Stryland, E.W., Williams, D.R., and Wolfe, W.L., Eds., Optical Society of America, Washington, DC, 1995, chap. 41.

Roybal, E.A., McIntosh, M.B., and Hull, H.K., Current status of optical grade sputtered, bare beryllium, and nickel-plated beryllium, *Proc. SPIE*, CR67, 206, 1997.

Rozelot, J-P., The 'L.A.M.A' (Large Active Mirrors in Aluminium) programme, *Proc. SPIE*, 1931, 33, 1992.

Saito, T.T., Diamond turning of optics: the past, the present, and the exciting future, *Opt. Eng*., 17, 570, 1978.

Saito, T.T. and Simmons, L.B., Performance characteristics of single point diamond machined metal mirrors for infrared laser applications, *Appl. Opt.*, 13, 2647, 1974.

Sanger, G.M., The precision machining of optics, in *Applied Optics and Optical Engineering*, Vol. 10, Shannon, R.R. and Wyant, J.C., Eds., Academic Press, San Diego, 1987, chap. 6.

Sawyer, R.N., Contamination control in aspheric element fabrication, OSA *Optical Fabrication and Testing Workshop, North Falmouth*, MA, 1980.

Schreibman, M. and Young, P., Design of Infrared Astronomical Satellite (IRAS) primary mirror mounts, *Proc. SPIE,* 250, 50, 1980.

Shagam, R.N., Sladkey, R.E., and Wyant, J.C., Optical figure inspection of diamond-turned metal mirrors, *Opt. Eng.,* 16, 375, 1977.

Shemenski, R.M. and Maringer, R.E., Microstrain characteristics of isostatically hot-pressed beryllium, *J. Less-Common Metals*, 17, 15, 1969.

Sollid, J.E., Sladky, R.E., Reichelt, W.H., and Singer, S., Single-point diamond-turned copper mirrors: figure evaluation, *Appl. Opt.*, 15, 1656, 1976.

Song, J.F. and Vorburger, T.V., Stylus profiling at high resolution and low force, *Appl. Opt.*, 30, 42, 1991.

Spawr, W.J. and Pierce, R.L., *Metal Mirror Selection Guide, Doc. SOR-74- 004*, Spawr Optical Research, Corona, CA, 1976.

Stanghellini, S., Manil, E., Schmid, M., and Dost, K., Design and preliminary tests of the VLT secondary mirror unit, *Proc. SPIE*, 2871, 105, 1996.

Stone, R., Vukobratovich, D., and Richard, R., Shear moduli for cellular foam materials and its influence on the design of light-weight mirrors, *Proc. SPIE*, 1167, 37, 1989.

Stover, J.C., Roughness characterization of smooth machined surfaces by light scattering, *Appl. Opt.*, 14, 1796, 1975.

Sweeney, M.M., Manufacture of fast, aspheric, bare beryllium optics for radiation hard, space borne systems, *Proc. SPIE*, 1485, 116, 1991.

Taylor, D., Metal mirrors in the large, *Opt. Eng.*, 14, 559, 1975.

Taylor, J.S., Syn, C.K., Saito, T.T., and Donaldson, R.R., Surface finish measurements of diamond-turned electroless nickel-plated mirrors, *Opt. Eng.*, 25, 1013, 1986.

Toland, R.W., Ohl, R.G., Barthelmy, M.P., Zewari, S.W., Greenhouse, M.A., and MacKenty, J.W., Effects of forged stock on cryogenic performance of heat treated aluminum mirrors, *Proc. SPIE*, 5172, 21, 2003.

Ulph, E., Fabrication of a metal-matrix composite mirror, *Proc. SPIE*, 966, 116, 1988.

Vukobratovich, D., Lightweight laser communications mirrors made with metal foam cores, *Proc. SPIE*, 1044, 216, 1989.

Vukobratovich, D., Personal communication, 2003.

Vukobratovich, D., Don, K., and Sumner, R.E., Improved cryogenic aluminum mirrors, *Proc. SPIE*, 3435, 9, 1998.

Vukobratovich, D., Gerzoff, A., and Cho, M.K., Therm-optic analysis of bi-metallic mirrors, *Proc. SPIE*, 3132, 12, 1997.

Vukobratovich, D., Richard, R., Valente, T., and Cho, M., Final design report for NASA Ames/Univ. of Arizona Cooperative Agreement No. NCC2-426 for period April 1, 1989–April 30, 1990, Optical Sci. Ctr., University of Arizona, Tucson, 1990.

Whitehead, T.N., The *Design and Use of Instruments and Accurate Mechanism, Underlying Principles*, Dover, New York, 1954.

Young, P. and Schreibman, M., Alignment design for a cryogenic telescope, *Proc. SPIE*, 251, 171, 1980.

Zimmerman, J., Strain-free mounting techniques for metal mirrors, *Opt. Eng*., 20, 187, 1981.

14 Optical Instrument Structural Design

14.1 INTRODUCTION

Most of the topics considered so far in this book have dealt with the individual components and subassemblies of an opto-mechanical instrument. We have discussed component interrelations and interfaces with regard to certain types of devices, but have touched only lightly on how these parts are held together to form a complete optical instrument. This chapter addresses some important structural aspects of instrument design and discusses selected examples illustrating typical kinds of constructions. We begin with the consideration of designs with rigid housings made of materials such as cast aluminum. This structural configuration serves as a baseline for the design of most optical instruments. Each subsequent example involves some unique structural feature that distinguishes it from the baseline construction. Our discussion of basic structural configurations of optical instruments continues with descriptions of several instruments with modular construction and one with a structure designed to fail gracefully under high shock. A major portion of this chapter is devoted to discussions of athermalization of instruments, including reflecting systems featuring uniform thermal expansion characteristics and ones with metering rods or trusses to compensate for temperature effects on axial spacings between mirrors. Key principles for athermalizing refracting optical systems are also outlined. We close with considerations of various types and geometries of truss structures for ground-based and spaceborne telescope applications.

14.2 RIGID HOUSING CONFIGURATIONS

The traditional configuration for optical instruments has the various optics mounted individually and directly into a rigid (usually metal) housing. Required adjustments for alignment and focus of the optics are usually incorporated into the component interfaces. Intermediate cells may be used to facilitate adjustments or form subassemblies. Several examples of this type of construction were discussed in Chapter 5. In this section, we consider additional examples of instruments with rigid housing construction. Although the optical instruments discussed in this section have been classified as ones with "rigid structures," it must be recognized that there is no such structure in the real world. Deformations of walls, housings, and other structural members do occur in the presence of thermal, acceleration, mounting, or other externally applied loads. We should therefore consider our structural designs to be adequately rigid only if the physical displacements of the interrelated components and the mechanical stresses imposed thereon are smaller than the tolerable limits under all anticipated operational, storage, and transport storage conditions. Finite-element analyses (FEA) and tests of models or preproduction prototypes are appropriate means for demonstrating adequacy of designs, as discussed in Chapter 1.

14.2.1 MILITARY BINOCULARS

A 7 × 50 military binocular of World War II vintage is illustrated in Figure 14.1. The basic construction of this instrument has two monocular telescopes hinged together in such a way as to provide variable separation of the eyepieces to match a 58 to 72 mm (2.28 to 2.83 in.) interocular separation of an observer's eyes. The cemented doublet objective lens of each telescope is mounted into a cast aluminum body housing (typically 6061-T6 alloy) through an eccentrically bored cell and an eccentric ring (see Figure 14.2). These eccentric parts are rotated with respect to the instrument and relative to each other at assembly to align both optical lines of sight to the hinge axis and, hence, to each other. This ensures that the parallelism of the lines of sight entering the eyes from a common target is sufficient to minimize eyestrain. The Porro prism assemblies (of the type shown

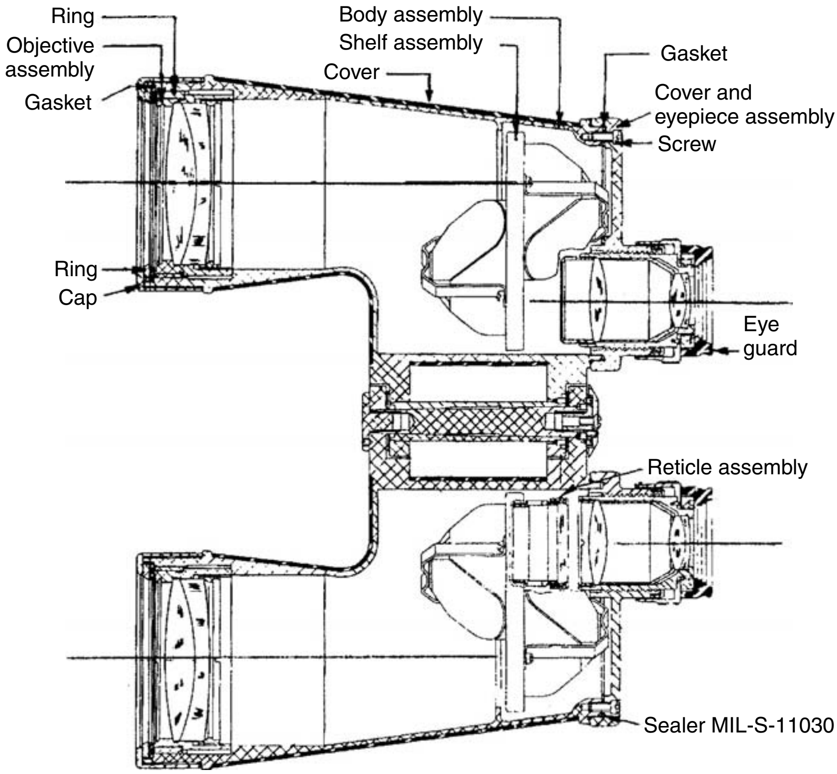
Ring
Objective assembly
Gasket
Ring
Cap
Body assembly
Shelf assembly
Cover
Gasket
Cover and eyepiece assembly
Screw
Eye guard
Reticle assembly
Sealer MIL-S-11030

FIGURE 14.1 Sectional view of the 7 × 50 M17 Binocular of World War II vintage. (Courtesy of the U.S. Army.)

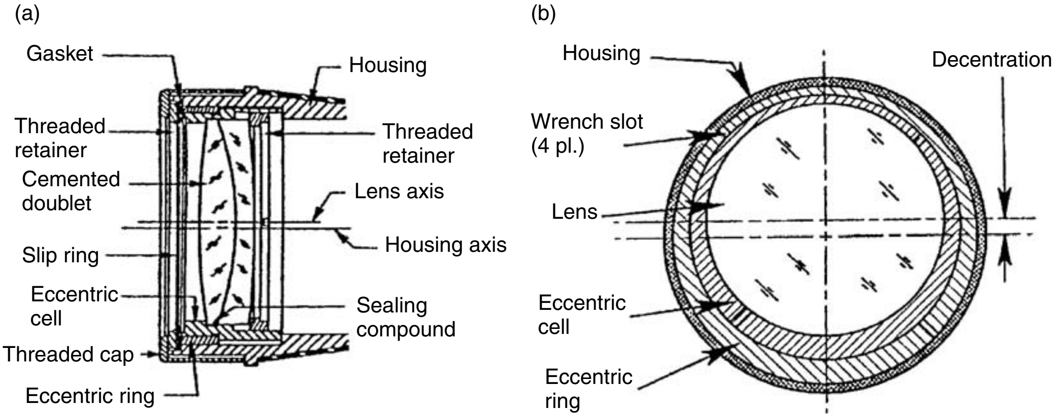
(a)
Gasket
Threaded retainer
Cemented doublet
Slip ring
Eccentric cell
Threaded cap
Eccentric ring
Housing
Threaded retainer
Lens axis
Housing axis
Sealing compound
(b)
Housing
Wrench slot (4 pl.)
Lens
Eccentric cell
Eccentric ring
Decentration

FIGURE 14.2 (a) Classical binocular objective mounting with a cemented doublet seated in an eccentric ring and eccentric cell. View (b) shows the design principle (eccentricity exaggerated) in Figure 7.17) are attached to a plate as shown in Figure 7.65 that, in turn, is attached with screws and mechanically pinned to lugs cast into the housing walls.

The eyepiece subassemblies are threaded into aluminum cover plates (see Figure 5.29) that are screwed fast to the rear openings in the body housings. Gaskets are used to seal these joints. Adjustment of eyepiece focus for the user's visual accommodation is achieved by rotating each eyepiece as a unit to translate the lenses axially. Since the military binocular is intended to view distant targets, it is focused at infinity. A calibrated reticle is placed at the left eyepiece focal plane for making angular measurements related to directing weapons fire.

The threaded joints between the coaxial tubes comprising the eyepiece-to-housing interface are "sealed" by applying a heavy grease. The externally exposed lenses are sealed into their mechanical mounts with a viscous compound such as 3M EC801 polysulfide sealant. The central hinge features a tapered axle inside an internally tapered tube. Axial loading of this tapered bearing introduces static friction (stiction) to hold the two telescopes at the proper separation during use. The tapered surfaces must be lapped to provide smooth motion and lubricated.

Figure 14.3 shows a partially cut-away view of a more recent military binocular with Porro prisms. This is an adaptation of a 7 × 50 commercial design by Steiner of Bayreuth, Germany. Its housings are constructed of glass-fiber-filled polycarbonate Makrolon 8035 per (Vukobratovich, 2004) covered with a thick, protective layer of green rubber. The binocular has an air-spaced doublet objective held in place with a threaded retaining ring. A molded plastic carriage supports the prisms. BaK4 glass is used in the

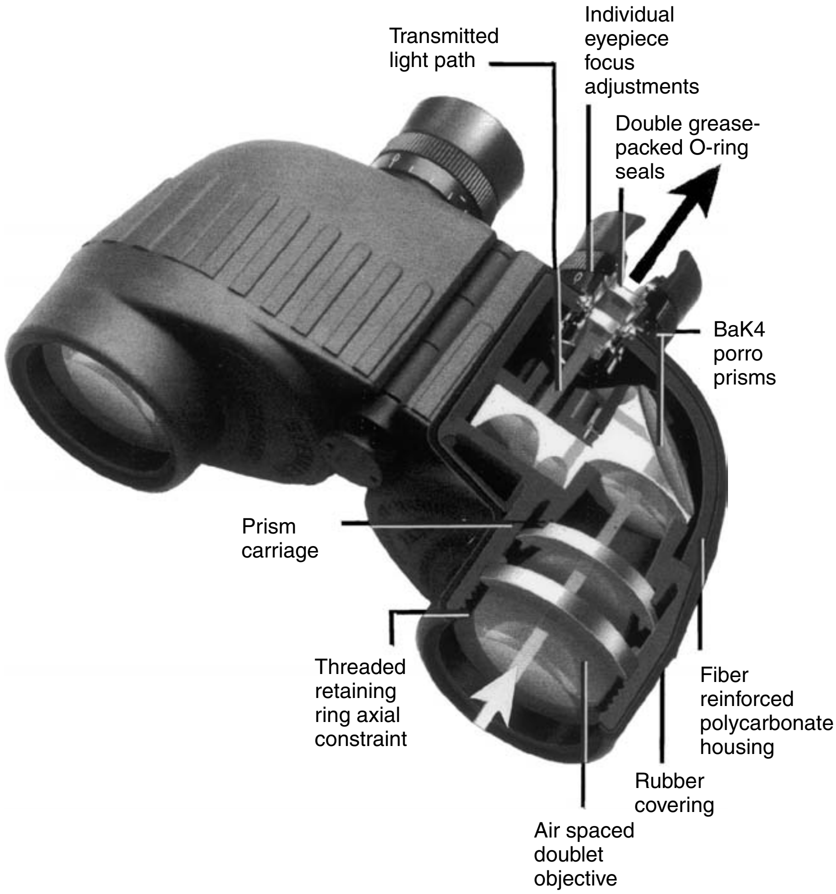
Transmitted light path
Individual eyepiece focus adjustments
Double grease-packed O-ring seals
BaK4 porro prisms
Prism carriage
Threaded retaining ring axial constraint
Fiber reinforced polycarbonate housing
Rubber covering
Air spaced doublet objective

FIGURE 14.3 Partial cut-away view of the Steiner 7 × 50 Binocular used as a U.S. military instrument under the designation M22. (Adapted from a diagram provided by Steiner, Pioneer Research, Moorestown, NJ.)

prisms. A reticle is provided for angular measurements in target space. The eyepieces are individually focusable Kellner types. The focus motion is sealed by double, grease-packed O rings. This binocular, known as the M22, is used by the U.S. Army. The German Army has used a similar binocular.

Wear of the hinge mechanism, small movements of the internal optical components resulting from mishandling or environmental extremes, and failure of seals are common maintenance problems with all military binoculars. The first two of these problems cause changes in parallelism of the telescope lines of sight (commonly called collimation errors) and may produce user eyestrain under extended use. Periodic servicing to realign and clean the optics is necessary for continued operation in the military environment. The modular military Binocular M19, designed to alleviate some of these problems, is described in Section 14.3.

Many other examples of military binoculars are described by Seeger (1996). Some of these are very large instruments that have been used by combat personnel worldwide as high-magnification observation devices on land and aboard ships. Because of their sizes and weights, these instruments pose significant structural design problems and are generally complex to manufacture and align. An extreme example is a WWII vintage Zeiss 25 × 200 binocular that weighed about 1000 lb (454 kg) with its mount. The eyepieces were inclined for convenient observation by the seated observer and the instrument was articulated so the eyepieces remained stationary when the line of sight was elevated for antiaircraft use. Complex internal mechanical mechanisms were required to provide interpupillary adjustment and to maintain an erect image at all elevation angles.

The main housings for this binocular were constructed of welded steel. This was cited by Seeger (1996) as an engineering feat, considering the tight tolerances that would be needed to achieve correct system alignment. Only a few of these binoculars were completed before the end of WWII hostilities. Tests showed that the large aperture, wide apparent field optics provided significant improvement over smaller units, but this superiority did not warrant the expenditures in time and money required to produce them.

14.2.2 COMMERCIAL BINOCULARS

Binoculars intended for nonmilitary (i.e., consumer) applications differ from their military counterparts mainly with regard to mechanical construction and materials used. With the exception of the so-called "opera glass," which is a coupled pair of simple, low-magnification, narrow field-of-view Galilean telescopes, the same basic types of objective and eyepiece lenses and erecting prisms are used in many military and commercial binoculars. Most commercial binoculars have adjustable focus for targets at different ranges. The optical alignment requirements are also similar no matter what the application. The degree with which these requirements are met may, however, vary with cost. A binocular intended for repeated use by a commercial fisherman whose business success depends in no small manner on his ability to detect visual evidence of concentrations of fish requires higher performance than the one used by a spectator casually watching a sports event. Consequently, the fisherman may be willing to pay a premium price for higher quality and long-term reliability.

Both cost and weight are key factors in the design of all commercial binoculars. Metal housings generally have thin walls to reduce weight. Plastic materials (such as glass-filled polycarbonate or dense polystyrene) may be used instead of metals (aluminum or magnesium) for the housing materials (Vukobratovich, 1989; Seil, 1991, 1997). Plastic lenses and prisms have been tried as means to reduce both cost and weight, but have not proven acceptable for any but the very lowest performance applications. Lower-cost binoculars with glass components generally use Porro prisms, whereas roof prisms may be used in other units to reduce overall instrument width and to provide "in-line" optical paths. The sizes of the optics themselves are sometimes reduced to cut costs. Excessive reductions in prism apertures and refractive index may reduce illumination due to vignetting, especially at the corners of the field of view. Square exit pupils indicate this condition (Vukobratovich, 1989).

Figure 5.31 and Figure 14.4 illustrate fairly traditional opto-mechanical designs for high-quality commercial binoculars. In both instruments, the Porro prisms are held against opposite sides of

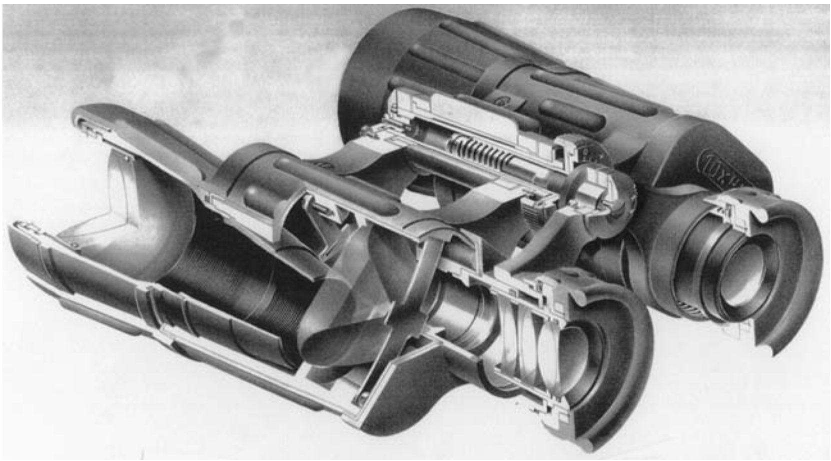

FIGURE 14.4 Partial cut-away drawing of a high quality commercial binocular with Porro prism erecting system. (Courtesy of Swarovski Optik, Hall in Tyrol/Absam, Austria.)

an internal shelf by straddling springs.* The objectives are cemented doublets. The eyepiece of the unit shown in Figure 14.4 is a relatively complex design offering a wide field of view. The general mechanical construction of the commercial binocular has significant differences from that of the military unit shown in Figure 14.1.

In order for the user to focus this instrument conveniently on objects at near or far distances, a central focus mechanism is provided to slide both eyepieces simultaneously in the axial direction by rotating a knurled knob on the hinge. One eyepiece has an individual focus adjustment with which to tune the focus for differences in accommodation of the user's eyes. Rubber quad-ring gaskets are used to seal the sliding eyepiece tubes into the main housing. Some other binoculars have internal focus-adjustment mechanisms that move one or more lenses axially inside both housings. The latter design produces an improved seal against moisture and dust. An example was shown in Figure 5.32. More expensive commercial binoculars are sealed and flushed with dry nitrogen at assembly to remove excess moisture and resist immersion in water.

Another significant difference between military and commercial binoculars is that a reticle is not needed in the commercial unit. This not only eliminates that component (and frequently, a similar optical component without the pattern in the other side of the instrument), but also eliminates the need for mounting provisions within the housings and for the step during alignment wherein the reticle is brought into sharp focus simultaneously with the image of the target.

Figure 14.5 illustrates another modern high-quality binocular. This one has in-line configuration and uses using Pechan prisms with roofs to erect the image and minimize total length by folding the light path. This instrument also features internal focus and diopter movement mechanisms controlled by knurled knobs on the hinge. The multiple-element objectives are not radially adjustable, so the roof prisms are mounted in angularly adjustable mounts to facilitate alignment. The housings are sealed with gaskets or O rings and flushed with dry nitrogen.

14.2.3 TANK PERISCOPES

Figure 14.6 shows a prototype of a telescope designed for use with an external, vertically offset rhomboid arrangement of mirrors (not shown) as a visual periscope mounted in the turret roof of a

---

[*] Straddling springs are generally flat metal strips attached to structure at both ends. In prism mountings, they usually press against the prisms at the spring's center. The design of such springs is described in Chapter 7.5.1.

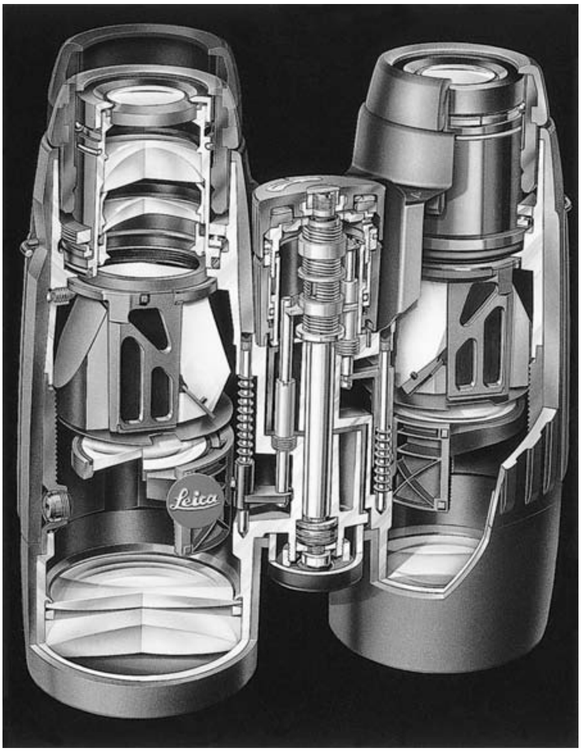

FIGURE 14.5 Partial cutaway view of a modern high-quality commercial binocular with roof-Pechan prism erecting system. (Courtesy of Leica Camera Group, Solms, Germany.)

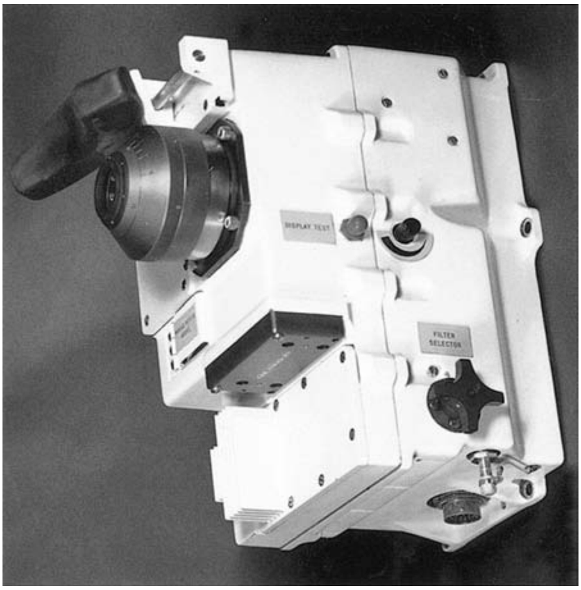

FIGURE 14.6 External photograph of a prototype zoom telescope developed for use in a tank commander's periscope. (Courtesy of Goodrich Corporation, Danbury, CT.)

military armored vehicle (tank). Its optical configuration (see Figure 14.7) features an afocal zoom telescope followed by a fixed-focus telescope. The image is erected by the two 90° fold mirrors and a Porro prism, which together form an Abbe erecting system. These optics and those of a triple-channel reticle projection system are mounted inside a two-part housing attached to the periscope assembly at the flange shown at the right in Figure 14.6. The front and rear housings of this periscope are aluminum castings machined locally to minimum wall thicknesses of approximately 0.1 in. (2.5 mm). Bosses, ribs, and flanges are cast into these walls at interfaces and other appropriate places to provide sufficient strength to withstand anticipated loads.

Of prime importance in the design of this telescope were requirements for compact packaging into a small allotted space within the tank turret and for rugged construction to withstand ballistic impact on the turret that could result in shock loads of >1000 times ambient gravity at the telescope. Electronics associated with servo drives for the zoom mechanism and for remotely projecting any of a series of reticle patterns into the periscope's field of view were designed to conform to multiple available spaces within the housing. Space was provided as shown in front of the eyepiece for insertion of a flash protector device to prevent eye injury from the intense flashes of nuclear weapons on the battlefield.

Figure 14.8 shows the telescope with the rear housing (carrying the eyepiece and flash protector) removed. All the optics except the objective subassembly (shown in Figure 5.11) and the eyepiece are mounted together as a removable main optical assembly. This assembly, shown in frontal view in Figure 14.9, consists of various subassemblies designed and fabricated as replaceable units (modules) for ease of maintenance. Many of the opto-mechanical subassemblies making up the viewing and reticle projection systems are visible in this figure.

A typical module is the cam-driven, mechanically compensated zoom mechanism shown in Figure 14.10. The two axially movable lenses slide on ball bushings on diametrically opposite, parallel rods under control of a nonlinear cylindrical cam located immediately below the lenses.

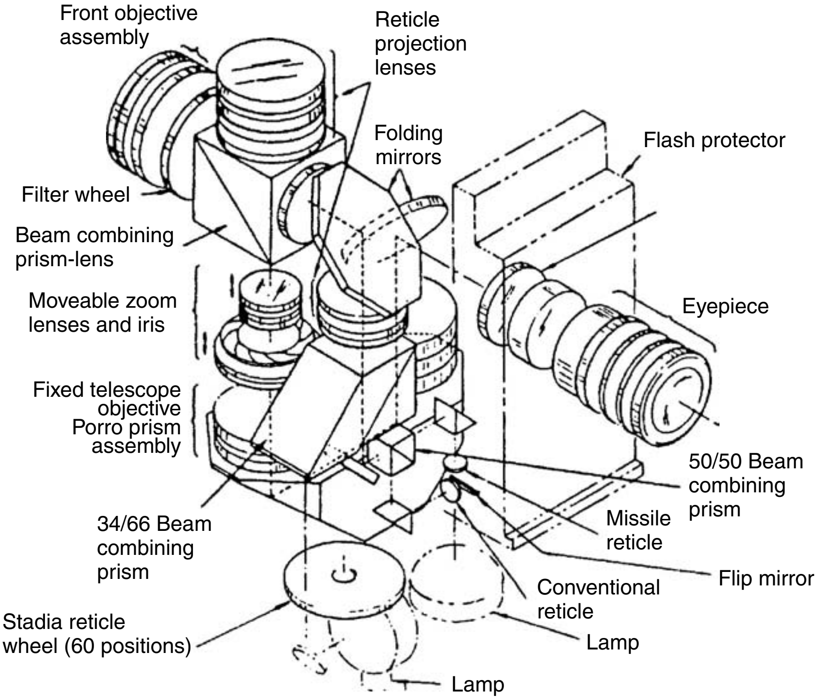
Front objective assembly
Reticle projection lenses
Folding mirrors
Flash protector
Filter wheel
Beam combining prism-lens
Moveable zoom lenses and iris
Eyepiece
Fixed telescope objective
Porro prism assembly
50/50 Beam combining prism
34/66 Beam combining prism
Missile reticle
Flip mirror
Conventional reticle
Stadia reticle wheel (60 positions)
Lamp
Lamp

FIGURE 14.7 Optical system configuration of the telescope in Figure 14.6. (Courtesy of Goodrich Corporation, Danbury, CT.)

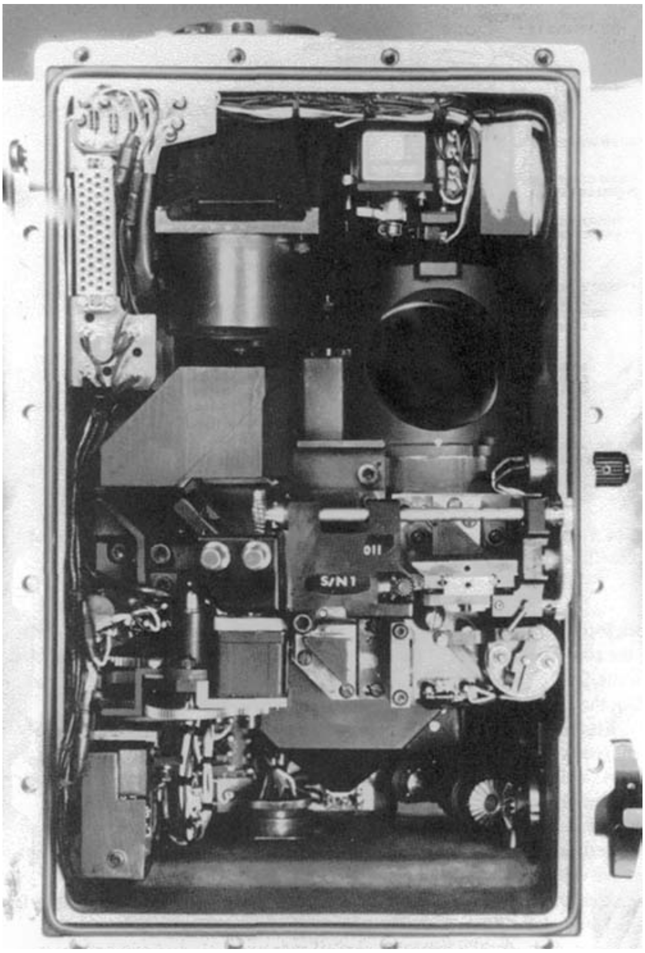

FIGURE 14.8 The interior of the front housing of the telescope of Figure 14.6 with the rear housing removed. (Courtesy of Goodrich Corporation, Danbury, CT.)

Cam-driven micro switches that limit the travel of the moveable lenses at their extreme positions can be seen at the lower left of the figure.

14.2.4 SPACE-BORNE SPECTRO-RADIOMETER CAMERAS

The Multiangle Imaging Spectro-Radiometer (MISR) is a NASA space payload orbiting aboard the EOS-TERRA spacecraft since December 1999. The science goals are to monitor global atmospheric particulates, cloud movements, surface BRDF, and vegetative changes on the day-lit side of Earth during a nominal 6-year mission in polar orbit. Ford et al. (1999) indicated that it employs nine cameras to collect data in four spectral bands within the 0.440 to 0.880 μm spectral region at nine different angles ranging from 0 to 70.5° along the flight path. Data from each observed point on Earth is compared for similarities and differences. Key design requirements included an operational temperature range of 0 to 10°C, survival of -40 to $+80$°C temperature extremes, ability to withstand launch accelerations, and minimizing long-term light transmission losses in the Earth's polar radiation environment.

To minimize costs, four lens designs were employed in the nine cameras. Three systems (designated type A) are identical and observe at and near nadir. The remaining designs (designated types

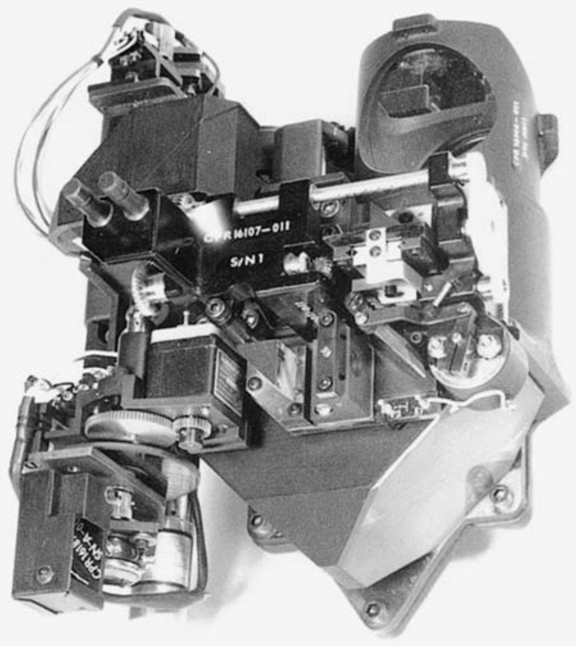

FIGURE 14.9 Front view of the main optical assembly of the telescope in Figure 14.6. (Courtesy of Goodrich Corporation, Danbury, CT.)

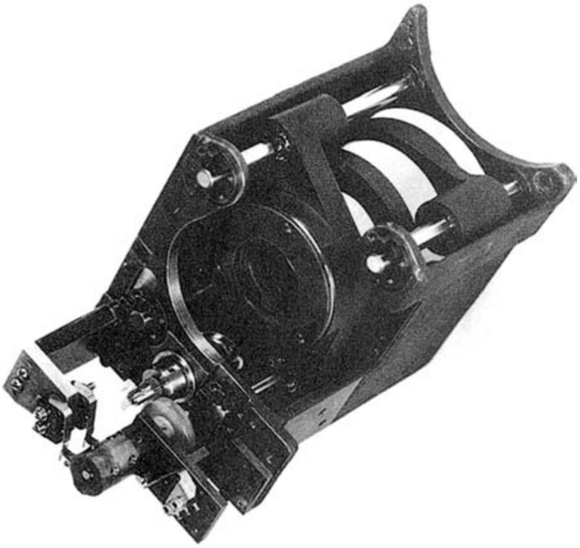

FIGURE 14.10 The zoom module used in the telescope in Figure 14.6. (Courtesy of Goodrich Corporation, Danbury, CT.)

B, C, and D) are located in pairs symmetrically disposed at larger angles relative to the nadir. Focal lengths increase in sequence from the nadir outward. Figure 14.11 shows the four lens designs. Their characteristics are listed in the figure caption. Glass types for all the designs are as indicated in the figure for design type D. Unmarked elements are filters. The detectors are at right in each design.

Note that the image sizes are essentially constant. The detectors are charge-coupled devices with four independent line arrays and 1504 active pixels per line.

Figure 14.12 shows a sectional view through lens design D. This is representative of all four designs. The main housing is aluminum, with walls about 6.3 mm (0.25 in.) thick to minimize radiation penetration in orbit, so is quite rigid. To control clamping force changes with temperature,

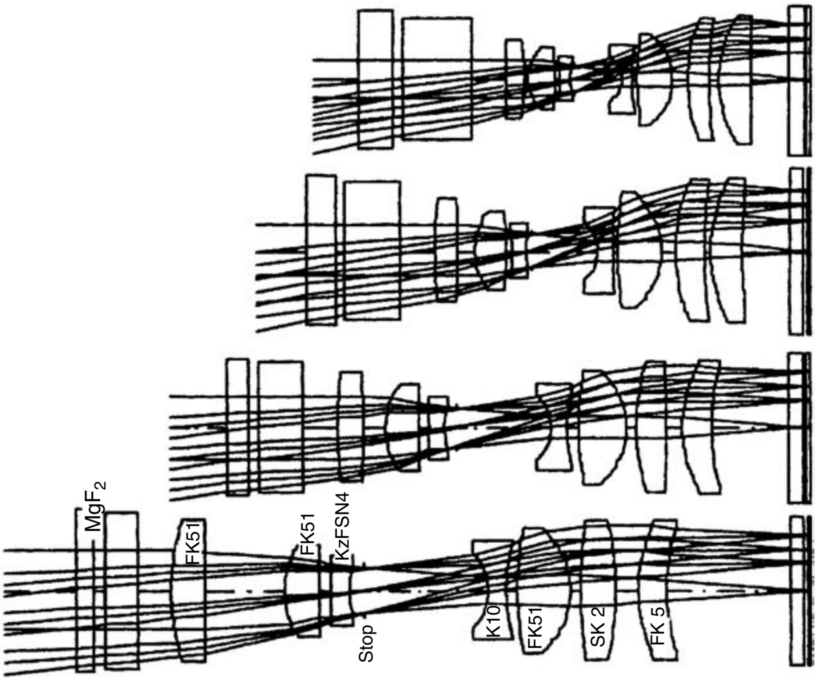

FIGURE 14.11 Optical schematics for the four MISR lens designs. Characteristics are, from top to bottom, Type A, EFL = 59.3 mm, field = 14.9°, length = 111 mm; Type B, EFL = 73.4 mm, field = 12.1°, length = 124 mm; Type C, EFL = 95.3 mm, field = 9.4°, length = 144 mm; and Type D, EFL = 123.8 mm, field = 7.3°, length = 181 mm. (From Ford, V.G., White, M.L., Hochberg, E., and McGown, J., *Proc. SPIE*, 3786, 264, 1999.)

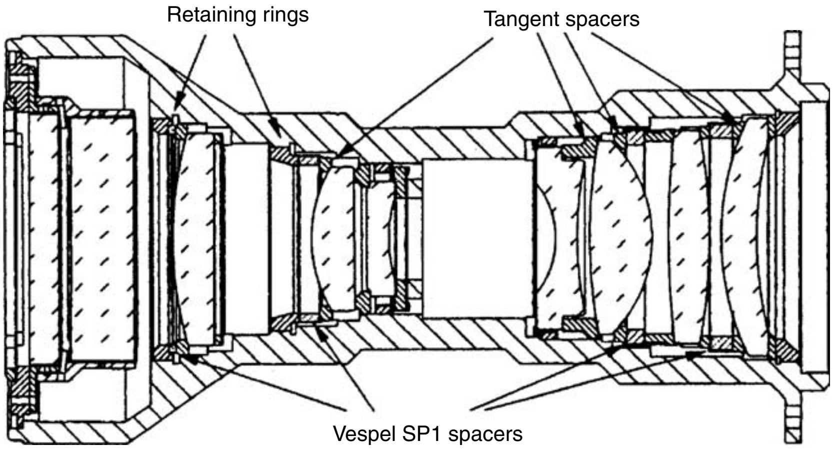

FIGURE 14.12 Sectional view through MISR lens Type D. (From Ford, V.G., White, M.L., Hochberg, E., and McGown, J., *Proc. SPIE*, 3786, 264, 1999.)

spacers made of Vespel SP1 were used under each retaining ring. The CTE of this material is larger than that of aluminum. The thickness of each spacer was chosen to compensate for the difference in CTEs for the housing, the spacer, and the lens or lenses clamped. This rendered the optical train length essentially constant with temperature at the force achieved with about 5 oz-in. (0.035 N-m) of torque on each threaded retainer. Experiments showed this preload to be adequate under the specified vibration/shock loading, including launch in an Atlas rocket. The assemblies were vibrated gently after the retainers were tightened to help seat the lenses with minimal axial separations. This condition corresponds to the maximum possible degree of centration with the existing frictional conditions. The retainers were then retorqued to the specified value.

Tangential opto-mechanical interfaces were used between the spacers and all lenses with convex surfaces to minimize contact stress. Initially, the radial force from the axial preload acting at each tangent interface with a convex surface was expected to be adequate to center those lenses. This was not confirmed during assembly, so aluminum centering rings with rectangular cross sections were fabricated to nearly fill the radial gaps around the convex lenses, thereby limiting decentrations of the lenses.

Lenses with concave surfaces had flat or step bevel interfaces. They were centered mechanically to the local IDs of the housing at each lens location using annular spacers made of Vespel SP1 and shaped as indicated in Figure 14.13. The IDs and ODs of the spacers were machined for close sliding fits to the housing IDs and to the lens ODs, then milled locally to create flexures. This created rim contact-type interfaces without the radial stress problems that could otherwise occur with hard mounting under the expected temperature changes.

What might be termed an "elegant" method for athermalization of back focal length (i.e., focus) of the MISR lens assemblies during operation is discussed in Section 14.5.3.3.

14.2.5 LARGE AERIAL CAMERA LENS

The straight or folded tubular rigid aluminum or titanium housing construction shown at several places in Chapter 5 for objective lenses to be used in aerial photographic or astrographic applications is adequate for apertures to perhaps 10 in. (25.4 cm). The weights of rigid housings might well be excessive in larger systems.

To illustrate how this potential weight problem was circumvented in one instance, we consider next a refracting camera lens system of 72 in. (1.8 m) focal length and *f*/4 relative aperture. Figure 14.14 shows the in-line optical schematic of the Petzval-type lens designed for this application.

The lens system consisted of eleven elements. The clear aperture and diameter of the first element were 18.0 in. (45.7 cm) and 18.75 in. (47.6 cm), respectively. As indicated in the figure, we refer to the elements as numbers 1, 2, 3, etc. The mechanical design concept called for these elements to be mounted in four different lens cells, which we refer to as numbers 1–4. Cells 1, 2, and

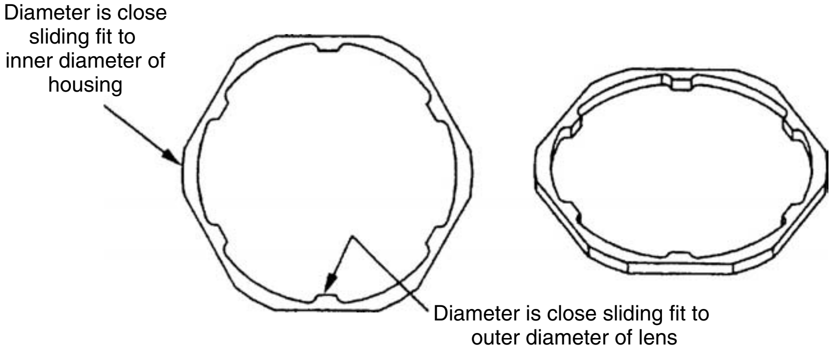
Diameter is close sliding fit to inner diameter of housing
Diameter is close sliding fit to outer diameter of lens

FIGURE 14.13 Vespel SP1 centering spacer ring design for MISR lenses with concave surfaces and flat bevels. (From Ford, V.J., White, M.L., Hochberg, E., and McGown, J., *Proc. SPIE*, 3786, 264, 1999.)

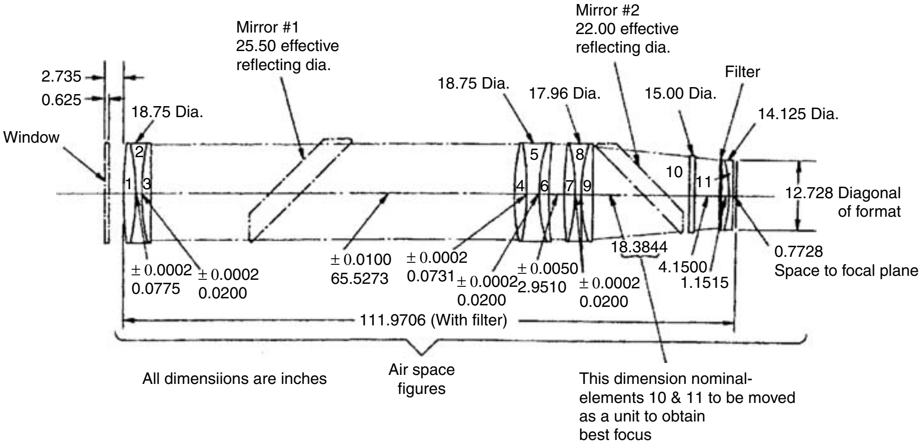
Mirror #1
25.50 effective
reflecting dia.
Mirror #2
22.00 effective
reflecting dia.
2.735
0.625
18.75 Dia.
Window
18.75 Dia.
17.96 Dia.
15.00 Dia.
Filter
14.125 Dia.
1
2
3
4
5
6
7
8
9
10
11
12.728 Diagonal of format
± 0.0002
0.0775
± 0.0002
0.0200
± 0.0100
65.5273
± 0.0002
0.0731
± 0.0002
0.0200
± 0.0050
2.9510
± 0.0002
0.0200
18.3844
4.1500
1.1515
0.7728
Space to focal plane
111.9706 (With filter)
All dimensiions are inches
Air space figures
This dimension nominal-
elements 10 & 11 to be moved
as a unit to obtain
best focus

FIGURE 14.14 Optical schematic of a 72 in. (1.83 m) EFL, 18 in. (45.7 cm) aperture, f/4 high-acuity aerial reconnaissance camera lens. (Courtesy of Goodrich Corporation, Danbury, CT.)

3 housed three lenses each. Cell 4 housed the two field correctors as well as a filter, which need not enter into this particular discussion.

The three elements mounted in cell number 1 were chosen to be moved (as a unit) along the optical axis for focusing. Analysis showed that the alignment of elements 4–9 would be the most critical within the assembly. Hence, it was decided that the optical axis formed by these six elements would be used to define the overall optical axis and that the other elements would be given the proper adjustment mechanisms to allow them to be aligned to this axis. The positioning accuracies of the various optical elements are shown in Figure 14.15 along with their required DOF.

The facts that (1) the CG of the lens assembly had to be accessible so that a rigid mechanical structure and stabilized mount could be designed around it, and (2) the overall system had to be as compact as possible, made it mandatory to fold the lens. The configuration finally decided on had the form of an inverted "U," with the focusing triplet objective at one end of the U and the camera at the other end. This necessitated the inclusion of two flat folding mirrors into the lens design. The lens cone structure chosen for this instrument was of the semimonocoque type. This is a design type in which lateral frames (or bulkheads), spaced at various intervals (depending on the critical loading points), are tied together by longitudinal stringers. A skin is attached to isolate the system from its environment and to provide a significant structural rigidity to the assembly. In this case, the skin was internal to the frames and stringers, thereby providing an insulating air space between this wall and an external layer of insulating material. This design also removed the metal structure as far as possible from external thermal inputs, which could introduce gradients and affect lens performance. Figure 14.16 shows the lens cone at a late stage of system assembly before adding the insulating layer. The black assembly just below the lady's right hand is the camera.

Aluminum was chosen as the structural material for this lens assembly for two reasons. First, a study was made of the effects of temperature changes on the image position assuming three lens cone materials: aluminum, titanium, and stainless steel. The results of this study (see Figure 14.17) showed aluminum to be the most desirable since focus was held more constant over the temperature range of interest. This study considered the effects of temperature change on the lens cone, lens material (including index changes), and optical path. Second, material and fabrication labor estimates based on preliminary designs with each material made it clear that aluminum would be by far the cheapest and easiest material to use.

The most important feature of the lens cone design was the requirement that it be extremely rigid yet lightweight. The rigidity specification called for the axis to deflect by a maximum of 0.001 in. (0.025 mm) when subjected to a self-weight static load in any of three mutually perpendicular planes.

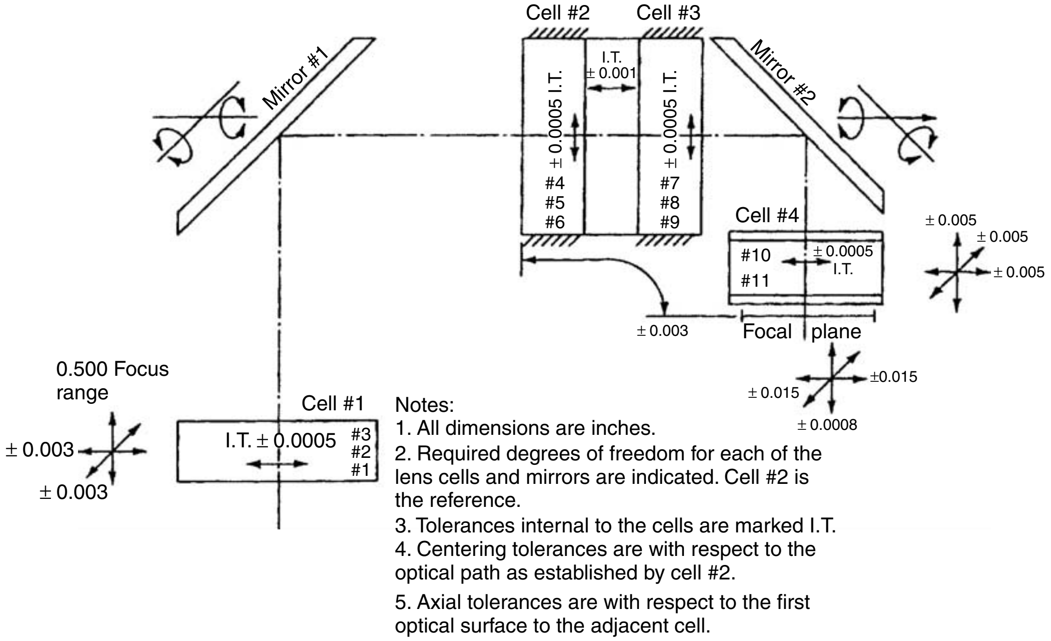
Cell #2
Cell #3
Mirror #1
Mirror #2
I.T.
± 0.001
± 0.0005 I.T.
± 0.0005 I.T.
#4
#5
#6
#7
#8
#9
Cell #4
#10
#11
± 0.0005
I.T.
± 0.005
± 0.005
± 0.005
± 0.003
Focal plane
±0.015
± 0.015
± 0.0008
0.500 Focus range
± 0.003
± 0.003
Cell #1
I.T. ± 0.0005
#3
#2
#1

Notes:
1. All dimensions are inches.
2. Required degrees of freedom for each of the lens cells and mirrors are indicated. Cell #2 is the reference.
3. Tolerances internal to the cells are marked I.T.
4. Centering tolerances are with respect to the optical path as established by cell #2.
5. Axial tolerances are with respect to the first optical surface to the adjacent cell.

FIGURE 14.15 Tolerances on locations and alignment of the lenses, lens cells, mirrors, and image plane for the lens system shown in Figure 14.14. (Courtesy of Goodrich Corporation, Danbury, CT.)

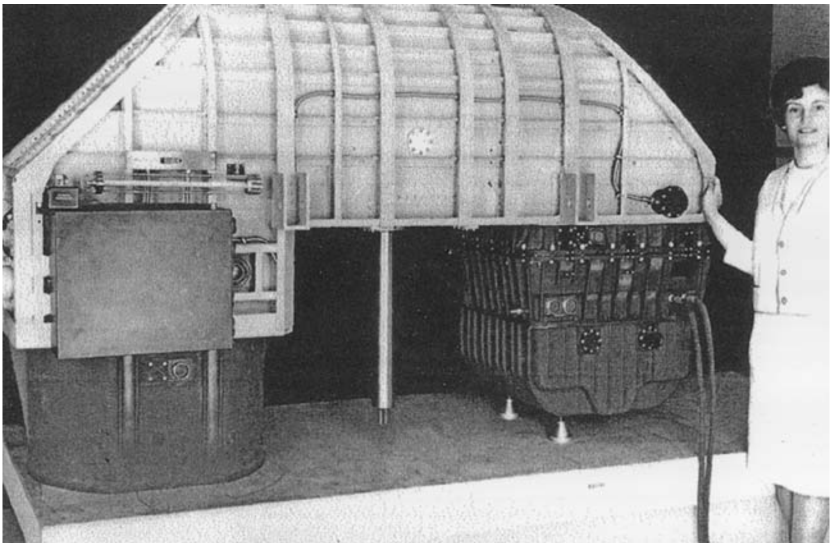

FIGURE 14.16 Photograph of the large aperture high-acuity camera system represented in Figure 14.14. (Courtesy of Goodrich Corporation, Danbury, CT.)

Analysis indicated that aluminum would meet these requirements. Tests of the completed assembly confirmed this prediction.

The first and last of the four lens cells were made of 43% nickel–steel alloy, whereas the central two cells were made of titanium A-70. Both these metals had thermal expansion properties closely matching those of at least one type of glass used in the supported lenses throughout the −65

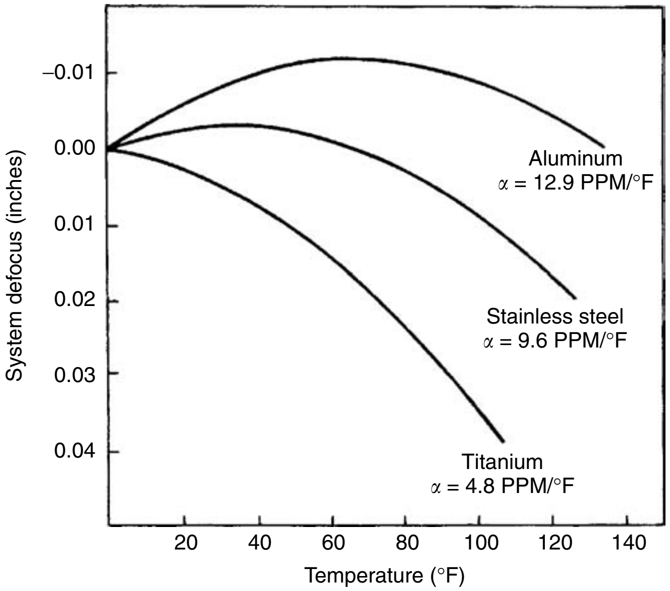

FIGURE 14.17 Plots of defocus vs. temperature for the optical system of Figure 14.14 computed for three different lens cone structural materials. Effects on index of refraction and expansion of the glass and metal parts were considered. (Courtesy of Goodrich Corporation, Danbury, CT.)

to 130°F (−54 to 54°C) temperature environment. Titanium was used instead of the less expensive steel in cells 2 and 3 to lower the system's CG to coincide with the gimbal axes of the stabilized mount located inside the U-shaped lens housing.

The differential radial expansion between the elements of each large triplet and its mounting would produce unacceptable stress at low temperature if the radial clearances around the elements were sufficiently small to position the elements properly at high temperature. In this design, dissimilar materials were used to provide temperature compensation and maintain lens centering over a wide range of temperature. Figure 14.18 shows the opto-mechanical design of the mounting for one triplet. The positive elements were Schott BaLF6, whereas the central negative element was Schott KzFS4. The thermal expansion coefficients of these materials were 6.7×10^{-6} °C^{-1} (3.7×10^{-6} °F^{-1}) and 4.5×10^{-6} °C^{-1} (1.8×10^{-6} °F^{-1}), respectively. The system was designed to operate in the environment of flight at 100,000 ft (91 km) altitude. The corresponding temperature range was specified as −65 to 130°F (−54 to 54°C).

For the design of this lens cell, material with CTE nearly matching that of the BaLF6 glass was chosen. This was titanium A-70 (CTE = 8.1×10^{-6} °C^{-1} [4.5×10^{-6} °F^{-1}]) machined from a forged cylinder. Radially oriented aluminum plugs nominally 1 in. (2.5° cm) long, but slightly oversized, were inserted at 120° intervals to support the negative lens in the cell. Iterative lapping reduced the lengths of the plugs until the lens was centered and the caps could be bottomed against the cell. This combination of metals and lengths made the design nominally insensitive radially to temperature changes. The seats for the two outer lenses were line-bored concentric to a tight tolerance. Mechanical contacts with the positive lens surfaces were on the spherical surfaces rather than their rims. Mylar spacers were inserted between the rims of these lenses and the cell ID once the lenses were centered.

The triplet was retained axially by assembling the lenses against retainers attached to each end of the cell. Lead spacers were located between adjacent lens surfaces to maintain the axial spacing. These spacers were hand-scraped at assembly to minimize optical wedge due to the tilt of the lenses. One retainer had three aluminum plugs that athermalized the assembly in the axial direction.

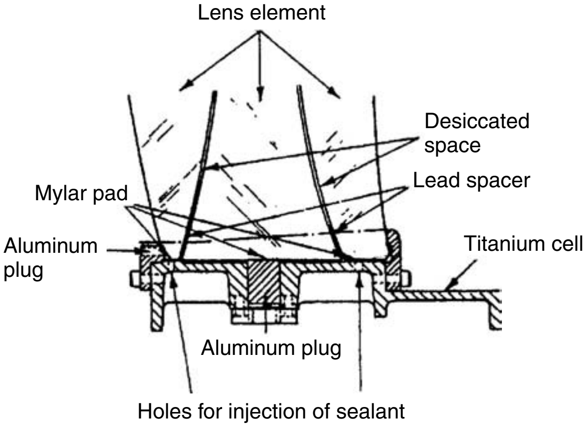

FIGURE 14.18 Technique for athermalizing the mounting for the lens elements in one large-diameter triplet of the system shown in Figure 14.14. The elements' thermal expansion characteristics differ significantly. (Adapted from Scott, R.M., *Appl. Opt.*, 1, 387, 1962.)

A further complication caused by the environment was that the central (KzFS4) elements of the triplets had to be kept dry. In this case, a seal was provided by the injection of polysulfide sealant (3M EC801) around the edges of the outer elements after assembly. This material never cures hard and therefore provides no mechanical support. In this design, it simply insures that the flow of air in and out of the separation space is through a desiccator.

The method of mounting the lens cells to the lens cone structure had to satisfy the requirements that the mounting method be rigid, compact, lightweight, temperature-stable, and in the case of the front and rear lens cells, adjustable. In the final design, each large cell was mounted by means of three tangential arms, each of which was approximately 0.13 in. (3.3 mm) thick × 3.0 in. (76.2 mm) wide. In the case of the smaller rear cell, the width was only 1.5 in. (38.1 mm). One end of each arm was bolted and pinned to its respective cell. In the case of cells 2 and 3, the other end of each arm went to a fixed fitting on the lens cone structure. In the case of cells 1 and 4, they went to adjustable eccentric bolts on the structure. The tangential mounting arms proved to be relatively lightweight. They did occupy slightly more space than would some other types of mountings since the arms effectively increased the OD of the lens cells. It should be noted that temperature changes resulted in a lengthening or shortening of the arms in this design. This tended to rotate the cells very slightly about the optical axis, but this had essentially no effect on the image. The attachments of the arms to the cell and the lens cone structure had to be very rigid since any looseness at these points would result in tilts of the cells with respect to the optical axis. The arms supporting cell 1 (the focusing triplet) were attached to three axially oriented ball screws by means of three eccentric nuts. The eccentric nuts provided a means of adjusting the optical center of this cell with respect to the ball screws so that the focus movement would not disturb the lateral alignment of the system.

To establish proper focus of the film to the image produced by this lens, four adjustable hardened buttons were provided on the surface of cell 4 facing the image plane. These buttons mated with four similar fixed buttons on the camera assembly. The buttons on cell 4 were adjusted individually at final assembly to align the film platen to the aerial image.

The development of this large camera system was, of course, not accomplished without encountering problems. Although the aluminum lens cone structure was rigid, it was hard to hold during machining operations. Problems were also encountered in sealing the riveted sheet metal structure. Alternative materials (such as graphite-epoxy composites) would probably be considered seriously if such a lens system were to be developed today.

14.2.6 A THERMALLY STABLE OPTICAL STRUCTURE

DeAngelis (1999) described the use of state-of-the-art strain gage technology to improve the design of the rigid housing for a precision portable coordinate measurement instrument. This instrument employs a two-axis gimbaled laser tracking system that must retain 1 arcsec repeatability throughout a 10 to 40°C (50 to 104°F) temperature range over an extended time period in an industrial environment without recalibration. The application of this tracking system is in a coordinate measuring machine (CCM) that measures feature locations of objects as far away as 35 m (~115 ft). Measurement accuracy of this CCM was reported by Bridges and Hagan (2001) to be 25 μm (0.001 in.) at 5 m (16.4 ft) range. See Figure 8.54 and the accompanying description.

The prior welded multicomponent housing design for this laser tracker that suffered from minute thermally-induced distortions was replaced by a single part machined from a cast aluminum ingot. The general configuration of the baseline housing is indicated in Figure 14.19. The elongated shape allowed mounting of a HeNe laser tube inside the curved back cover. The housing was made of the following aluminum materials: 4.5 in. OD × 0.15 in. wall 6061-T6 pipe stock; 0.375 × 0.750 in. 6061-T6 extruded bar stock; 4 × 5 in. 6061-T651 extruded bar stock; and 0.375 in. thick 6061-T6 plate stock. The rough-machined parts were screwed together with 6061 aluminum screws using 1100 aluminum shims in the joints and dip brazed in an 1100°F salt bath. After mechanical straightening and heat-treating to restore the T6 temper, the housing was finish machined to specified dimensions and black anodized. Careful measurements with strain gages indicated thermal distortions as large as 8 μm/m over the above-specified temperature range. These distortions were attributed to slight CTE variations in the different aluminum parts and residual stresses resulting from the fabrication process. An additional source of error not included in these test results would be thermal gradients introduced by the laser during operation.

The improved housing design shown in Figure 14.20 is machined (hogged-out) from a single ingot of aluminum, heat treated, and final machined. This provides uniform CTE throughout and

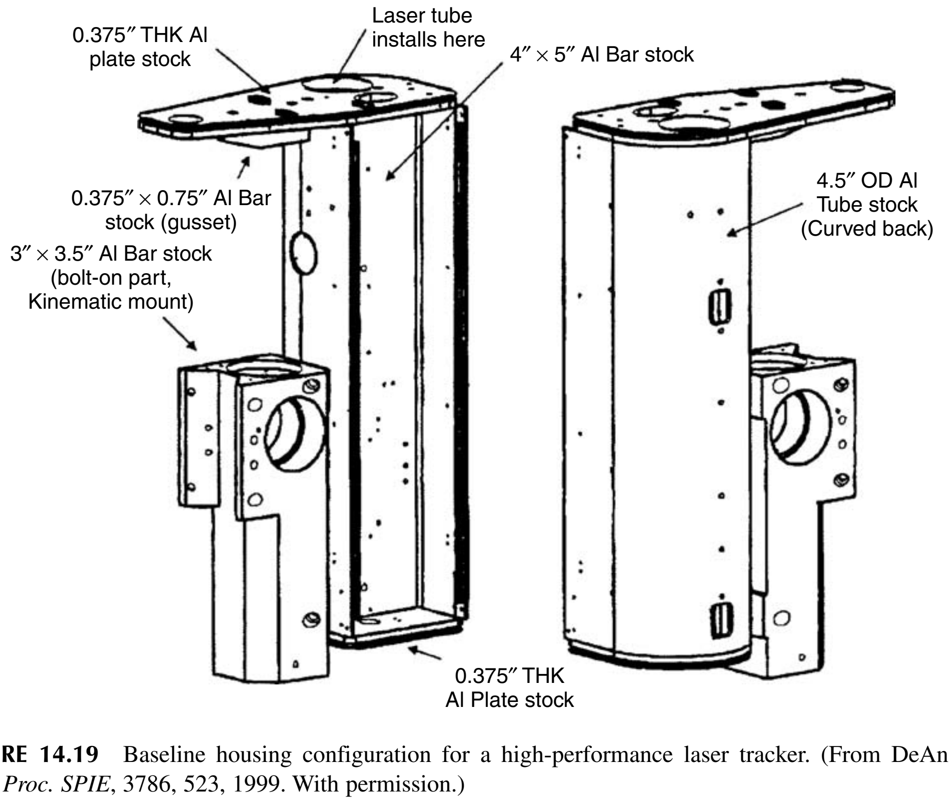
0.375″ THK Al plate stock
Laser tube installs here
4″ × 5″ Al Bar stock
0.375″ × 0.75″ Al Bar stock (gusset)
3″ × 3.5″ Al Bar stock (bolt-on part, Kinematic mount)
4.5″ OD Al Tube stock (Curved back)
0.375″ THK Al Plate stock

FIGURE 14.19 Baseline housing configuration for a high-performance laser tracker. (From DeAngelis, D.A., *Proc. SPIE*, 3786, 523, 1999. With permission.)

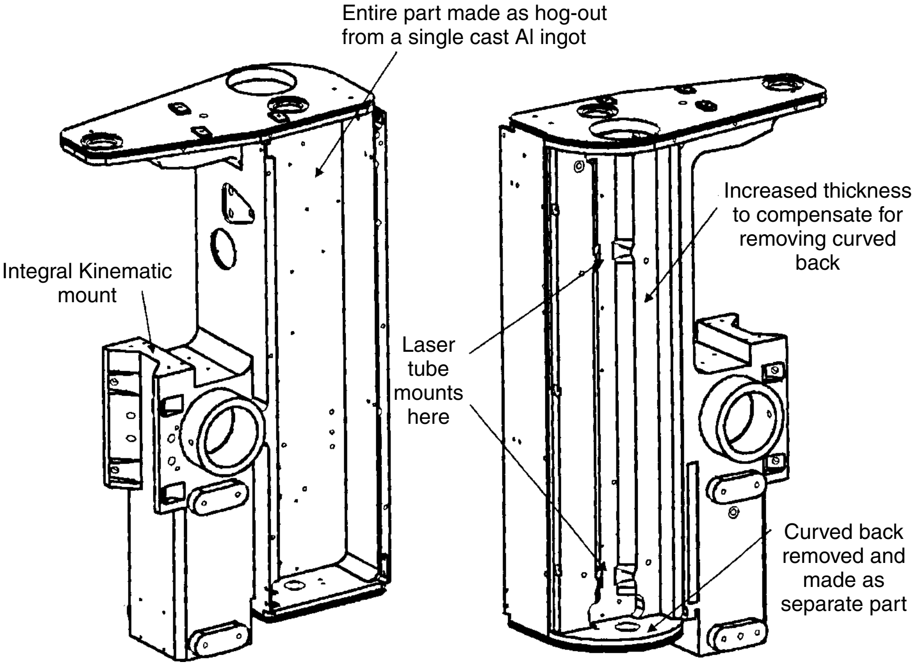
Entire part made as hog-out from a single cast Al ingot
Integral Kinematic mount
Laser tube mounts here
Increased thickness to compensate for removing curved back
Curved back removed and made as separate part

FIGURE 14.20 Improved housing design that replaced the one shown in Figure 14.19 and provided a thermally stable platform for the laser tracker. (From DeAngelis, D.A., *Proc. SPIE*, 3786, 523, 1999.)

minimal residual stress. The design also replaced the brazed-on curved back with a separate curved cover attached to a stiffened structure. Heat from the laser would then produce smaller bending effects on material located away from the housing's neutral axis. Temperature tests of the new housing showed essentially zero micro strain over the specified temperature range.

DeAngelis (1999) provided detailed descriptions of the strain gages used for the housing tests and ways of using these devices to maximize sensitivity and minimize instrumental errors. The verified accuracy of the gages described here significantly exceeds that published by the manufacturer for their standard products. A comparison of strain gage considerations such as foil alloy, gage resistance, bonding adhesives, lead wires, curing, stabilizing, soldering, and installation techniques is included in that paper.

This hardware development is considered a prime example of the truth of advice offered by Vukobratovich (2003) regarding the relative stiffness of structures constructed by different possible means. He indicated the order of decreasing structural stiffness to be as follows: (1) hog-out from solid, (2) cast, (3) welded [or brazed], (4) over bolted [with many bolts], (5) riveted, (6) bolted per normal practice, and (7) cemented [or bonded].[†]

14.3 MODULAR DESIGN PRINCIPLES AND EXAMPLES

The assembly, alignment, and maintenance of optical instruments are simplified if groups of related opto-mechanical components are constructed as prealigned and interchangeable modules. In some cases, the individual modules are considered to be nonmaintainable, and the instrument is repaired by replacing defective modules, usually without requiring system realignment.

Vukobratovich (1999) discussed the alignment accuracy and structural stiffness resulting from modular design and fabrication methods. He gave the following as the basic principles for this type of design: (1) the optical system is assembled as a series of mechanical modules; (2) each module is designed to exploit the inherent precision of the tool used to produce it. Specifically, the critical surfaces of a module should be flat or round. Key surfaces are concentric, parallel, or perpendicular to datum surfaces used as references during assembly; (3) each module is provided with datum surfaces for assembly into the system; (4) the optics in each module are aligned relative to datum surfaces; (5) the datum surfaces ensure that the positions of the modules are repeatable within the system; and (6) where necessary, the inherent precision of surface plates and rotary tables (i.e., spindles) are used to simplify assembly.

[†] Terms in brackets added.

The manufacture of instruments with modular subassemblies is somewhat more complex than the equivalent nonmodular versions because of the added requirement for interchangeability without compromising performance. Adjustments may, in some cases, be required within the module during assembly to meet this requirement. In other cases, mounting surfaces are machined to specific orientations or locations with respect to optical axes and image planes. The assembly of instruments with modular subassemblies may be enhanced by the design and fabrication of opto-mechanical fixtures specifically intended for manufacture and alignment of the modules (Vukobratovich, 1999; Erickson et al., 1992).

Many photographic and video camera lenses, microscope objectives, and telescope eyepieces are really opto-mechanical modules. An example is the microscope objective described in Section 5.6. In photographic applications, a variety of modular lens assemblies can be interchanged on a single camera body or moved from one camera to another of similar type. These lens modules are usually parfocalized so their image planes automatically coincide with the camera's film plane or eyepiece object plane.

14.3.1 INJECTION-MOLDED PLASTIC MODULES

Injection-molding techniques allow complex opto-mechanical assemblies to be fabricated from plastic materials in modular form. Figure 14.21 shows such a module designed for use in an automatic coin-changer mechanism. It is made of polymethyl-methacrylate (acrylic) and has two lens elements (one aspheric) molded integrally with a mechanical housing having prealigned mounting provisions and interfaces for attaching two detectors. Another all-plastic subassembly, made with injection-molded components and attached together to form a module, is shown in Figure 4.78.

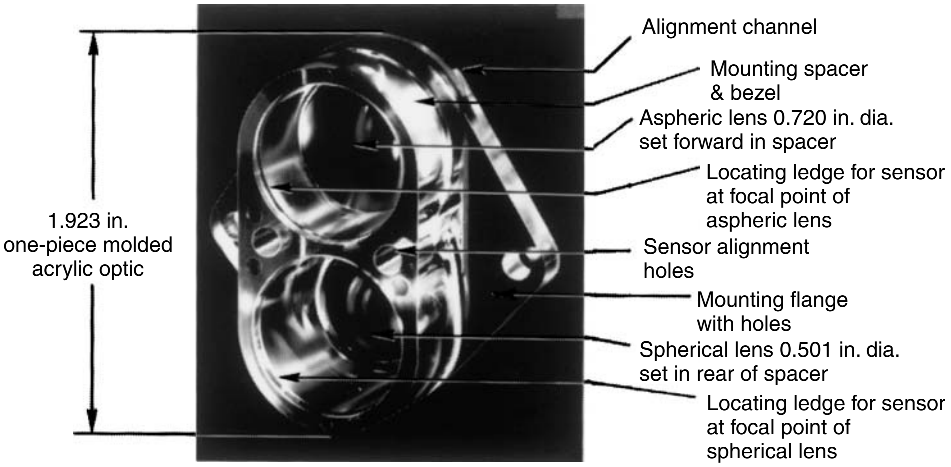
Alignment channel
Mounting spacer & bezel
Aspheric lens 0.720 in. dia. set forward in spacer
Locating ledge for sensor at focal point of aspheric lens
1.923 in. one-piece molded acrylic optic
Sensor alignment holes
Mounting flange with holes
Spherical lens 0.501 in. dia. set in rear of spacer
Locating ledge for sensor at focal point of spherical lens

FIGURE 14.21 One-piece injection-molded plastic module for an automatic coin changer. Two integral lenses, interfaces for sensors, and a mounting flange are provided. (Courtesy of 3M Precision Optics, Cincinnati, OH.)

When manufactured in large quantities, these types of modules are inexpensive. Since they require no adjustments, they are easy to install and are virtually maintenance free.

14.3.2 A MODULAR MILITARY BINOCULAR

Many thousands of military binoculars with the basic construction described in Section 14.2.1 have been produced for military and nonmilitary applications. As may be noted from Figure 14.1, each instrument has many individual parts to be assembled, adjusted, and inventoried as spare parts. A typical binocular uses >250 parts and also requires many special tools for maintenance purposes. A different approach to military binocular design was adopted during the 1970s, when the U.S. Army entered into production of the 7 × 50 Binocular M19 (see Figure 1.21). It provided improved optical performance over the prior standard 7 × 50 instruments in a smaller, lighter package (see Figure 1.19). The M19 instrument featured modular opto-mechanical design with replaceable subassemblies. Since modular construction was proven successful in this binocular and, subsequently, in other optical instruments, here we describe some of its key attributes. This description has been adapted largely from Trsar et al. (1981).

As indicated in Figure 14.22, the M19 binocular consisted primarily of five types of opto-mechanical modules. Each module was designed to be nonmaintainable, i.e., replaceable as a unit. The modules were two identical eyepieces, two identical objectives, left and right body housings (identical castings, machined differently), and a hinge pin subassembly. Each module was manufactured with tight intermodule interface tolerances in order to establish correct optical focus and angular alignment at assembly without adjustment. Only a few items of hardware (screws and O rings) were used in assembly. The seats and threads on the housings for the objective and eyepiece modules were machined after the bonded and optically cemented Porro prism assemblies were installed.

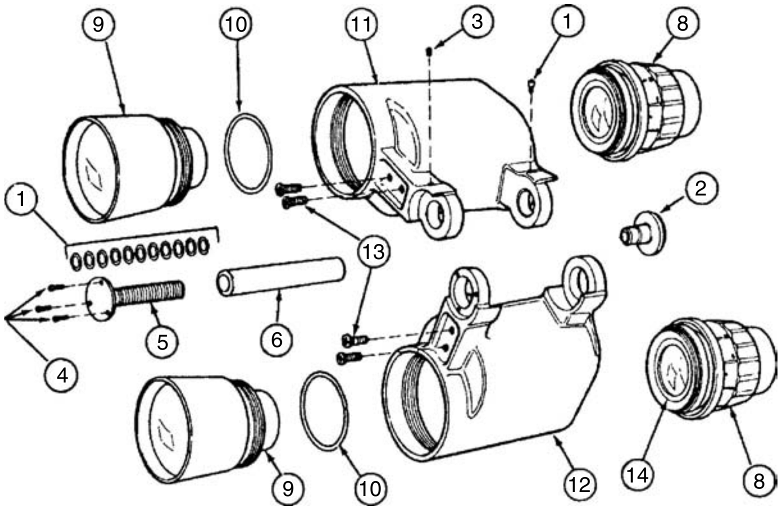

1. Screw 10547104
2. Interpupillary scale 10547103–1
3. Setscrew MS51963–21
4. Screw MS51957–2B
5. Shaft 10547101
6. Hinge sleeve 10547102
7. Preformed packing MS9021–010
8. Eyepiece assembly 10547083
9. Objective assembly 10547054
10. Preformed packing MS9021–031
11. Housing assembly R.H. 10547071
12. Housing assembly L.H. 10547079–1
13. Screw MS3212–21
14. Eyepiece bellows

FIGURE 14.22 Exploded view of the 7 × 50 Binocular M19 showing its modular construction. (Courtesy of the U.S. Army.)

Figure 14.23 shows the internal construction of this instrument. Sealing of the binocular against the environment was accomplished in two ways. Internal glass-to-metal elastomeric seals were used at each end of the objective and eyepiece modules. The objective modules were sealed to the housings with O rings. The eyepiece focus motion differed from that of prior military designs in that it translated axially by thread motion without rotating (see Figure 5.30 and accompanying description). This allowed the dynamic seal to be a highly reliable, collapsible rubber bellows of the type described by Quammen et al. (1966). See Figure 5.30. An integral bead on the bellows served to seal the eyepiece to the instrument body. After assembly, the body housings were flushed with dry nitrogen and the gas access holes closed with standard seal-screws.

The objective module of the binocular is shown in Figure 14.24. It was an air-spaced triplet of telephoto design with a focal length of 6.012 in. (152.70 mm) and an aperture of 1.969 in. (50 mm). It operated at *f*/3.05. The triplet was made of types 517647 (first two elements) and 689309 glasses. The lens diameters were 2.067 in. (52.50 mm), 1.909 in. (48.49 mm), and 1.457 in. (37.01 mm), respectively. Each OD was held to tolerances of +0, −0.001 in. (+0, −0.025 mm). The objective housing was wrought aluminum. The crown lenses were mounted directly into the housing with an intermediate tapered spacer. A threaded retainer provided axial preload on these elements through an O ring that sealed the outermost lens to the housing. A thin annular metal pressure ring protected the O ring from shearing as the retainer was tightened. The flint lens was mounted into a focusable cell that threaded into the housing. That lens was sealed into the cell with an O ring compressed axially through a thin pressure ring by a retainer that also served as a light baffle. This cell was adjusted axially as it was installed into the objective to tune the objective EFL. After adjustment, it was sealed into the objective housing with injected elastomeric sealant.

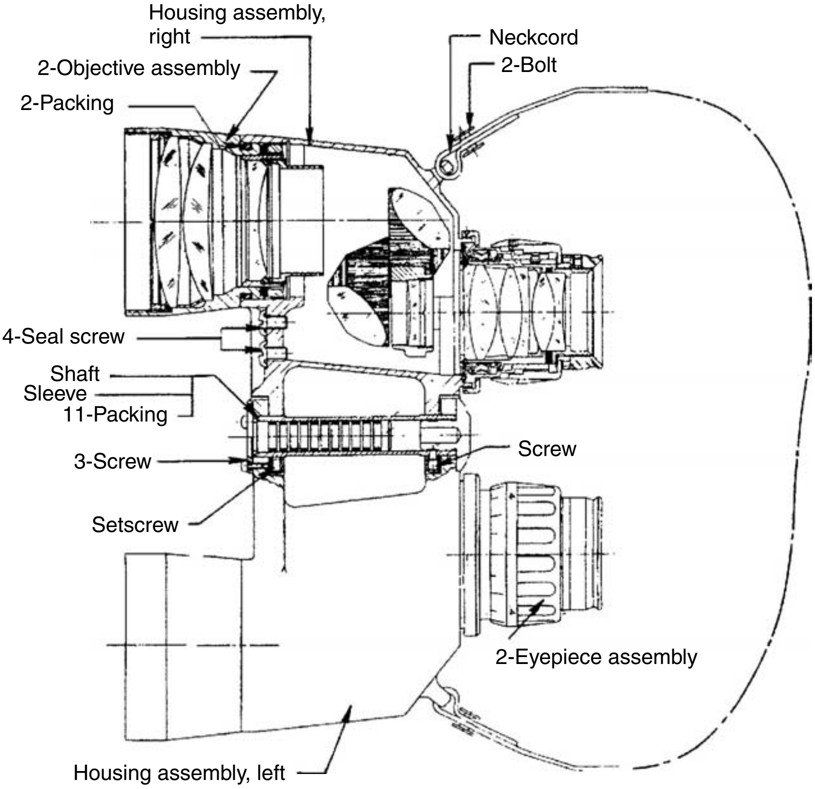

FIGURE 14.23 Sectional view of the 7 × 50 Binocular M19. (Courtesy of the U.S. Army.)

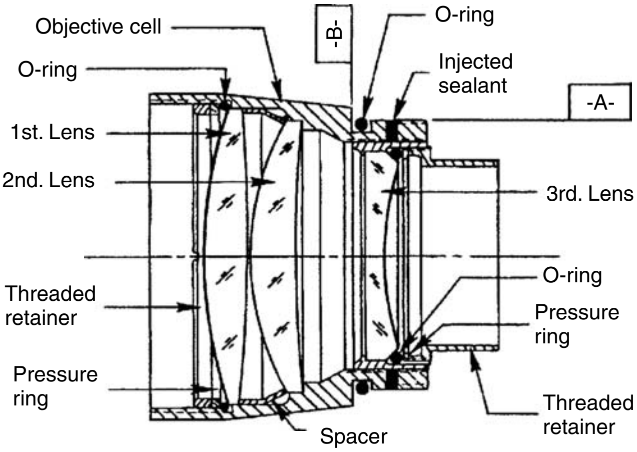

FIGURE 14.24 Sectional view of the modular objective assembly for the M19 binocular. (Adapted from Trsar, W.J., Benjamin, R.J., and Casper, J.F., *Opt. Eng.*, 20, 201, 1981.)

After all the parts of the objectives and eyepieces were assembled and before their retaining rings were tightened, these modules were placed in a vacuum chamber, evacuated, and backfilled with dry nitrogen. They were then sealed. Centration of the lenses to the system optical axis and focus were accomplished by machining the registration OD and shoulder of the module (see Figure 5.30 and Figure 14.24) to close tolerances using sophisticated optical alignment techniques to position the modules in holding and transfer fixtures. A master eyepiece was used in a test fixture to establish the optical axis and infinity focus for the objective assembly. The cell (in its fixture) was precision machined on a computer numerically controlled (CNC) lathe. The concentricity of surface -A- to the objective's optical axis was held to ±0.010 mm, while the tolerance on flange focal distance from surface -B- was ±0.038 mm.

The Porro prisms that erect the image in each telescope were cemented and bonded subassemblies, as shown in Figure 14.25. The prisms were made of high-index (type 649338) glass to ensure TIR over the full field of view and were tapered to have minimal weight without vignetting. The prisms were assembled into the housings and those housings machined to accept the objective and eyepiece as follows:

One Porro prism was bonded to a die-cast aluminum bracket with adhesive per MIL-A-4866 (such as Summers Milbond) in a fixture built to exacting tolerances and carefully maintained throughout use. After the bond had cured, the prism and bracket subassembly was mounted in a second precision fixture including a master objective and a master eyepiece in their proper locations and orientations. UV-curing optical cement (Norland 61) was applied to the appropriate portion of the prism's hypotenuse surface. The second prism was positioned with respect to the first prism so that the input and output optical axes were parallel and displaced by the proper distance. In addition, the prism was rotated in the interface plane to correct the tilt of the image around the optical axis. A video camera and monitor were used to display to the operator the pointing and tilt relationships for the prism assembly. The operator first adjusted the free prism laterally until the image of a reticle projected through the system was positioned within a prescribed rectangular tolerance envelope on the monitor screen. Then, while the image was maintained inside this rectangle, the prism was rotated slightly to align the tilt reference indicators also displayed on the monitor screen. Once adjusted, the prism was clamped in position in the fixture. Curing of the adhesive took place under a bank of UV lamps adjacent to the setting station. Multiple setting and curing fixtures were necessary to support the required production rate. After curing, the same optical alignment apparatus was used as a test device to ensure that the desired prism setting was retained through the curing process.

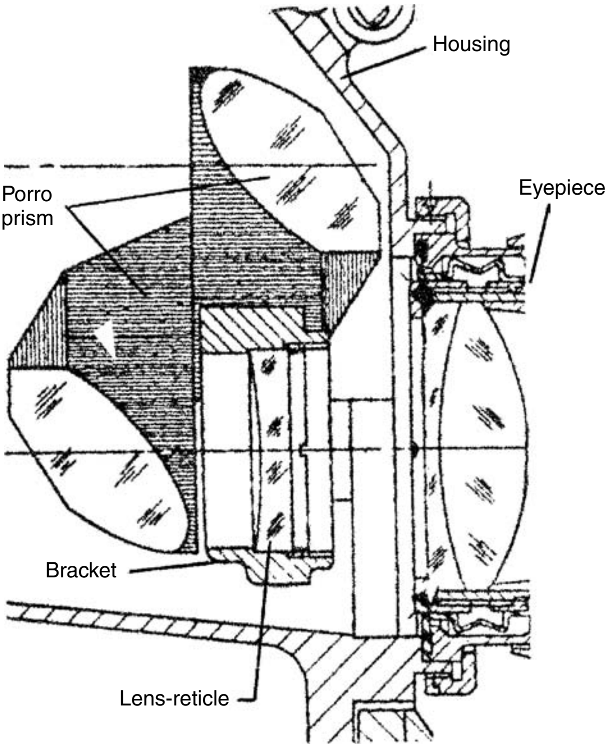

FIGURE 14.25 Portion of the opto-mechanical layout of the M19 binocular (from Figure 14.23) showing details of the erecting prism assembly, its mounting bracket, and the lens/reticle mounting. (Adapted from a U.S. Army drawing.)

Both binocular housings started out as identical thin-walled aluminum investment castings; they were machined differently to form their unique left and right shapes. The wall thickness was nominally 1.524 mm. Over this, a 0.38-mm-thick coating of soft vinyl was applied prior to machining of the critical mounting seats for the eyepiece, prism assembly, and objective. The locations of the eyepiece and prism assembly seats were established mechanically during the machining process. Normally, with a rigid, stable part, these would not have presented unusual problems despite the very demanding tolerances required. However, the structural flexibilities of the thin-walled housings posed a serious handicap. In addition, owing to the soft vinyl coating, it was not possible to reliably locate the housings from any of the vinyl-clad surfaces or to clamp on them without causing cosmetic damage. Elaborate fixtures relying upon a few previously machined surfaces that were not vinyl clad had to be developed before acceptable production yields and rates could be attained.

The prism subassembly was attached with three screws to lugs cast into the housing. It was not mechanically pinned in place. No adjustments were provided since all mechanical interfaces with optical components would be machined with the prism in place. Small errors in prism location or orientation resulting from clearances in the mounting holes over screw diameters would be compensated for during these machining operations.

Machining of the housing with the prism assembly installed was the critical step in obtaining the module precision required to permit interchangeability. Horizontal and vertical collimation requirements (divergence and dipvergence, respectively) for the monocular's optical axis with respect to the hinge pin centerline were such that the bore for the objective had to be properly located radially within 0.0127 mm. The requirement for perpendicularity between the objective seat and the optical axis was 0.0051 mm measured across the objective seat. In addition, the objective seat had to be located axially to obtain the proper flange focal distance. To obtain these accuracies, it was necessary to use optical alignment techniques to position the housing for machining.

The production approach applied here was to place the housing in a transferable setting and machining fixture. The housing was positioned using optical alignment instrumentation and locked in place in the fixture at an offline setting station. Then the fixture was transferred to the spindle of a CNC, multitool lathe for final machining. Multiple transferable fixtures were provided so that setting and machining operations could proceed in parallel.

The fixture and the optical alignment technique used at the setting station are shown schematically in Figure 14.26. The fixture base was designed to mate precisely with the lathe spindle so that the fixture centerline was coincident with the rotational axis of the spindle during machining. In this way, the mounting seat for the objective could be machined concentric with the fixture centerline. On top of the fixture base was a sliding plate that could be translated laterally. This plate carried a post simulating a binocular hinge pin. The post centerline was always parallel to the fixture centerline.

A collimator optical system in the setting station (not shown in Figure 14.26) provided an image of a target at infinity along the input optical axis, which was coincident with the fixture axis. A master objective was mounted at a fixed location in the setting station and centered on this axis. This objective formed an image of the target at an image plane inside the housing. This image was then viewed through a master eyepiece (temporarily attached to the housing) by a video camera, with the output being displayed on a video monitor. The proper flange focus position for machining the objective lens seat in the housing was obtained by moving the housing along the simulated hinge pin until the best focus was obtained on the video monitor. The housing was then clamped to the post and sliding plate. Axial positioning of the housing on the fixture was now completed, but lateral adjustment to obtain collimation was still needed.

The collimation requirements for each monocular were that the output optical axis be parallel to the hinge pin centerline within ±5 arcmin in the dipvergence plane (normal to the plane of Figure 14.26) and be diverging by 5 to 17 arcmin in the plane of the figure. Since the hinge pin and fixture centerlines were parallel, the collimation requirement was referenced to the fixture's centerline. After focus adjustment, the housing and sliding plate assembly were adjusted laterally (in two directions)

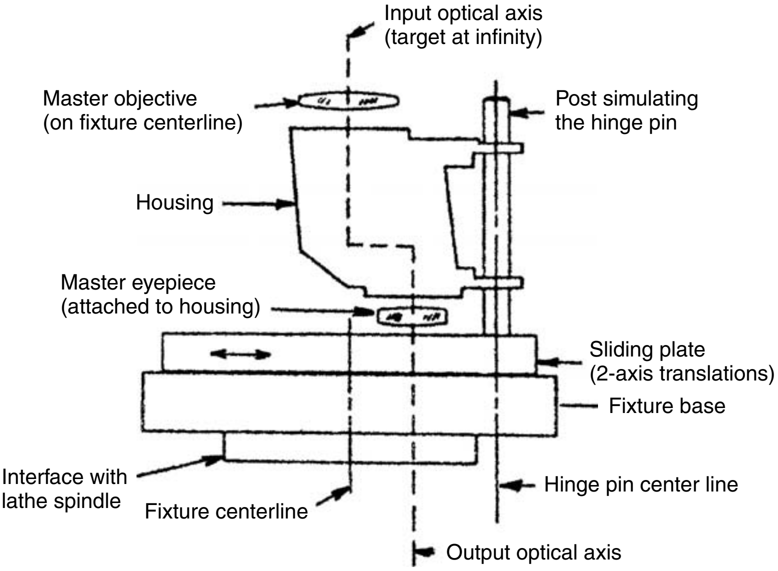

FIGURE 14.26 Schematic of the prism adjusting and holding fixture used to machine the M19 body housing with a prealigned prism installed. (Adapted from Trsar, W.J., Benjamin, R.J., and Casper, J.F., *Opt. Eng.*, 20, 201, 1981.)

with respect to the fixture base and the master objective until the required collimation conditions were achieved. This was indicated by a predetermined positioning of the target image on the video monitor. The sliding plate was then locked to the fixture base and the assembly transferred to the CNC lathe for machining of the objective mounting seat.

A similar procedure was used to orient the housing for machining the eyepiece interface. The result was a body housing with a prealigned prism assembly that would mate properly with any objective module and any eyepiece module to form one half of the binocular instrument. The left and right housing assemblies were also properly aligned to fit together at the hinge without adjustment.

For quantity production of any modular instrument, it is essential that the modules be assembled randomly without selection of parts or alignment after assembly. By machining mating surfaces between modules to close tolerances in fixtures, some with optical references, the required final instrument performance can be achieved. The initial expense of modular construction in terms of production tooling and detailed manufacturing procedure preparation presents a financial problem that, at least in large-quantity production, may be overcome by savings in production and maintenance costs as well as increased hardware reliability. In the case of the M19 Binocular, only two special tools were required to assemble or disassemble the instrument. These were an adapter plug that threaded into the front end of the objective to interface with a standard torque wrench, and a spanner wrench made to engage the retaining ring that held the eyepieces to the housings. A conventional strap wrench was used to grasp the objective during disassembly. Threaded adapters, hoses, and valves for purging and backfilling plus a tank of dry nitrogen were also needed for all but emergency repair on the front lines of combat. In an emergency, the modules would be replaced with new or cannibalized units without complete cleaning or purging the housings. Performance and useful lifetime would probably be compromised in this case.

Seeger (1996) indicated that the M19 Binocular suffered from the obvious deficiency that serious damage to an instrument would undoubtedly result in internal misalignment that could not be corrected by interchanging modules. Without provision for collimation adjustment, damaged units would probably have to be discarded or cannibalized to provide spare parts for other instruments. The present author has observed that some of the M19 Binoculars sold as military surplus have damaged (i.e., chipped) prisms that apparently broke loose at some point during their lifetimes and that have been reattached to their mounts with epoxy. One might seriously question the perfection of collimation of such units since it is unlikely that they could have been readjusted to their original condition.

14.3.3 A Modular Spectrometer for Space Application

A good example of a more complex optical instrument utilizing both modular design and SPDT techniques to advantage was the Short-Wavelength Spectrometer (SWS) designed for use in the European Space Agency's Infrared Space Observatory (ISO). This spectrometer was one of four experimental packages located at the focal plane of the observatory's 60-cm (23.6-in.)-diameter, 9-m (354-in.) focal length, liquid-helium-cooled Cassegrainian telescope. It was intended to measure stellar spectra in wavelength bands of 2.5 to 13 μm and 12 to 45 μm using dual-optical systems (see Visser and Smorenburg, 1989).

Figure 14.27 illustrates the optical system that was located behind the *f*/15 focal plane of the telescope. Dichroic beam splitters fed two functionally identical grating spectrometers outputting to multiple detector arrays. The longer-wavelength channel also fed two tunable Fabry Perot detectors. Many mirrors used here were aspheric or anamorphic to provide the necessary beam sizes at the gratings while fitting within the allowable package space. Several radiant sources were included for calibration purposes.

Front and back views of the machined main housing for the spectrometer are shown in Figure 14.28. This was machined from one piece of 6082 aluminum alloy to obtain maximum uniformity of CTE. This housing was attached with screws to the satellite structure through one rigid foot and two flexible (i.e., flexure) feet. As illustrated in Figure 14.29, various modular mirror subassemblies protruded through openings in the housings and were secured with screws from the outside. The optical surfaces of these modules (see a typical one in Figure 14.30) were

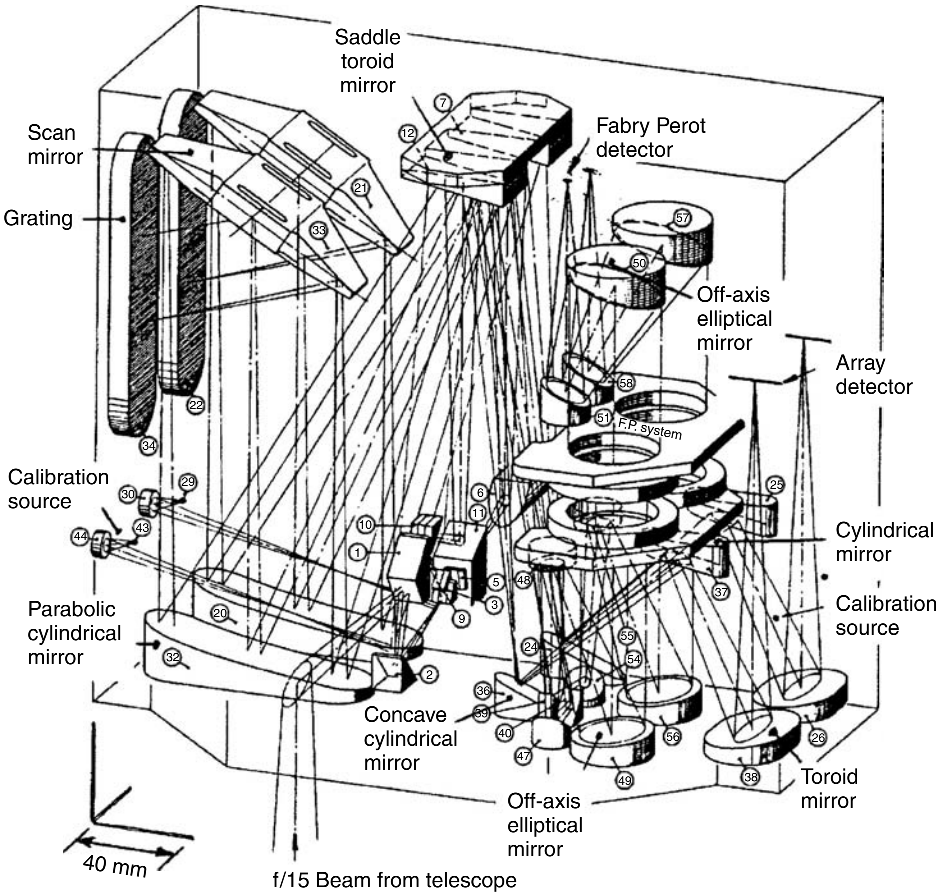
Saddle toroid mirror
Scan mirror
Grating
Fabry Perot detector
Off-axis elliptical mirror
Array detector
F.P. system
Calibration source
Cylindrical mirror
Calibration source
Parabolic cylindrical mirror
Concave cylindrical mirror
Off-axis elliptical mirror
Toroid mirror
40 mm
f/15 Beam from telescope
7
12
21
33
57
50
58
51
22
34
29
30
43
44
6
11
10
1
5
48
3
9
20
32
2
25
37
24
55
54
36
39
40
47
56
49
38
26

FIGURE 14.27 Optical system of the modular Short Wavelength Spectrometer (SWS) instrument package that analyzes the beam from a cryogenically cooled telescope (not shown). (From Visser, H. and Smorenburg, C., *Proc. SPIE*, 1113, 65, 1989.)

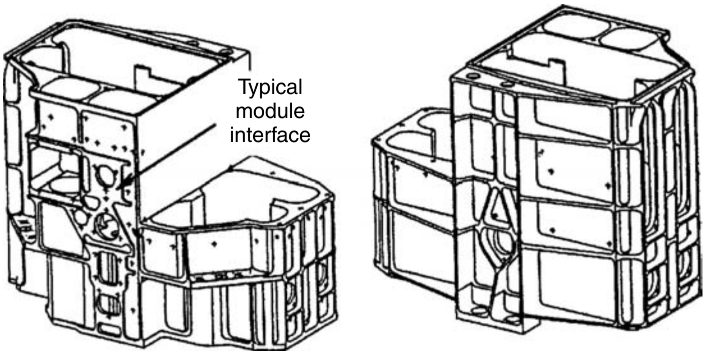
Typical module interface

FIGURE 14.28 Front and back views of the main housing of the SWS instrument showing cutouts for mounting opto-mechanical and electro-optical subassemblies to the rigid structure. (From Visser, H. and Smorenburg, C., *Proc. SPIE*, 1113, 65, 1989.)

manufactured by SPDT, so the optical surfaces were figured to better than one wavelength of visible light and with microroughness better than 15 nm. The inner surface of the flange interfaced at assembly with a machined surface on the instrument housing. Only minor adjustment (with shims) would be required during installation. This construction facilitated assembly and ensured that the

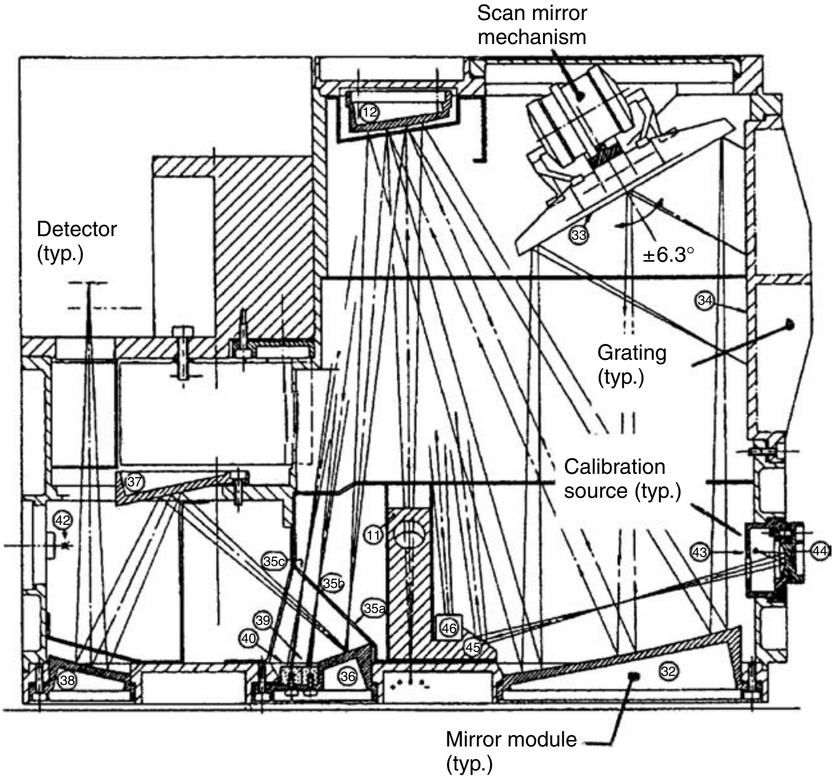
Scan mirror mechanism
Detector (typ.)
12
33
±6.3°
34
Grating (typ.)
Calibration source (typ.)
37
42
11
35c
35b
35a
39
40
38
36
46
45
32
43
44
Mirror module (typ.)

FIGURE 14.29 Partial opto-mechanical assembly views of the SWS showing interfaces between the main housing and several of the mirror modules and one grating module. (From Visser, H. and Smorenburg, C., *Proc. SPIE*, 1113, 65, 1989.)

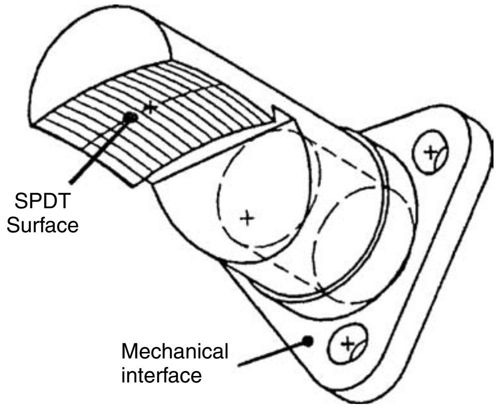
SPDT Surface
Mechanical interface

FIGURE 14.30 Diagram of one precision diamond machined toroidal modular mirror subassembly for the SWS. (From Visser, H. and Smorenburg, C., *Proc. SPIE*, 1113, 65, 1989.)

component alignment would be retained over a long time period. If necessary, replacement of a mirror would be a simple operation. The same aluminum alloy (type 6082) as the housing was used in these mirrors and in the gratings to equalize system thermal properties and enhance stability. The mirrors were gold-coated to enhance reflectivity in the IR. The gratings were ruled directly into coated aluminum blanks.

14.3.4 A Dual-Collimator Module

A variation on the theme of modular instrument design was illustrated in a paper by Stubbs et al. (2003, 2004). Their device was a compact and stable refractive dual collimator that accepted laser light from two fiber optic cables and generated two parallel 5.6-mm (0.220-in.)-diameter beams of collimated light separated by 36.27 mm (1.428 in.) (see Figure 14.31). The instrument was designed to be aligned and focused in fixtures so that it would become an interchangeable module identical in configuration, opto-mechanical interfaces, and performance with similar modules made in the same manner. Multiple units (or modules) could then be stacked together to form a row or 2D matrix of collimators. Simplicity, minimum number of parts, ease of assembly and alignment, and long-term thermal stability were inherent features of the design.

Overall dimensions of the assembly were 53 mm (2.087 in.) width, 38 mm (1.496 in.) height, and 74 mm (2.913 in.) length. Total weight was 0.74 kg (1.63 lb). It was not required by the application that the weight be minimized, so conventional machining techniques were employed, wall thicknesses were generous, and materials were selected for low CTEs rather than low densities. Figure 14.32 shows a

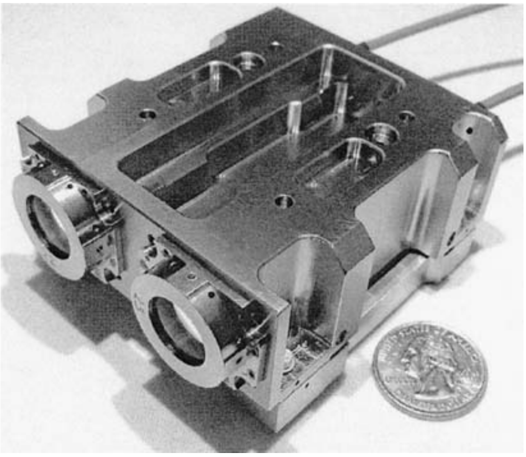

FIGURE 14.31 A dual refractive laser collimator module. (From Stubbs et al., 2003.)

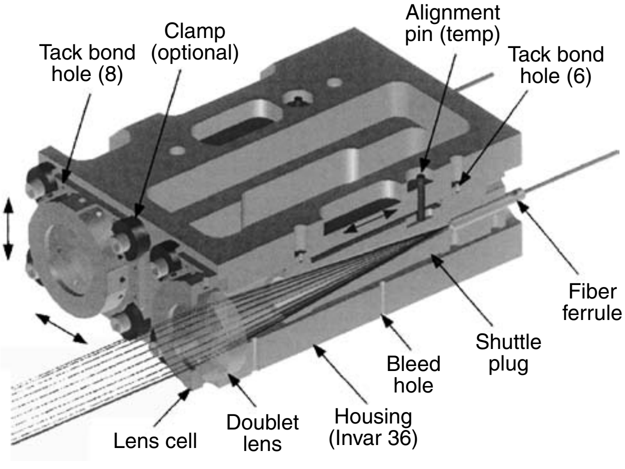

FIGURE 14.32 Opto-mechanical configuration of the collimator module of Figure 14.31. (From Stubbs et al., 2003.)

partially cut-away view of the assembly. The metal parts were Invar 36. The lenses were commercially available cemented doublets. Their performances in terms of p-v OPDs of the projected wavefront over the operating temperature range of 20 ± 1°C were acceptable at ≤ 0.010 wave. The lenses were mounted into cells and tack bonded in place with Dow Corning 6-1104 silicone sealant through eight access holes in the cell walls. These holes were inclined slightly with respect to the lens axes so that shrinkage of the sealant would draw the lenses towards the axial registration surface. The cells were held against the housing with spring clamps during alignment then tack bonded with epoxy at eight places. The output end of each fiber bundle carried a ceramic ferrule that was tack bonded with epoxy through six access holes into a shuttle plug. The plugs slipped into two precision bores in the housing and were tack bonded in place after focusing. Epibond 1210 A/9861 epoxy was used for all these bonds.

Optical fixtures were used in alignment of the fiber bundle to the shuttle plug and alignment of the lens cells to the housing. These fixtures included precision stages and goniometers to move the optical parts transversely and angularly, respectively, and clamps to hold those parts while the adhesive joints cured. Figure 14.33 and Figure 14.34 show the fixtures used for these adjustments. Assembly and align-

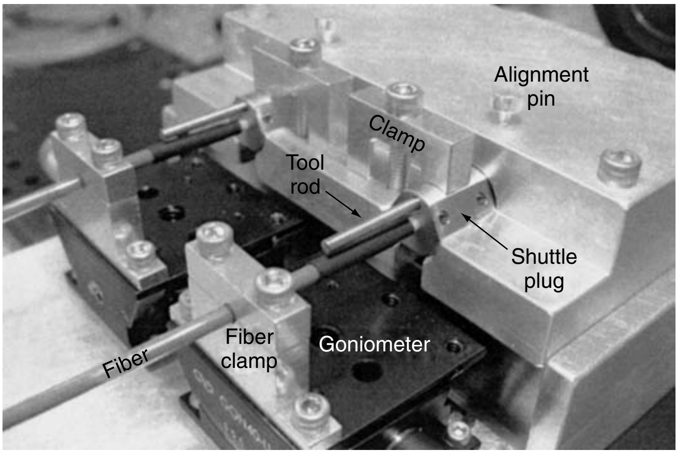

FIGURE 14.33 Fiber bundle assembly, alignment, and focusing fixture for the collimator module. (From Stubbs et al., 2003.)

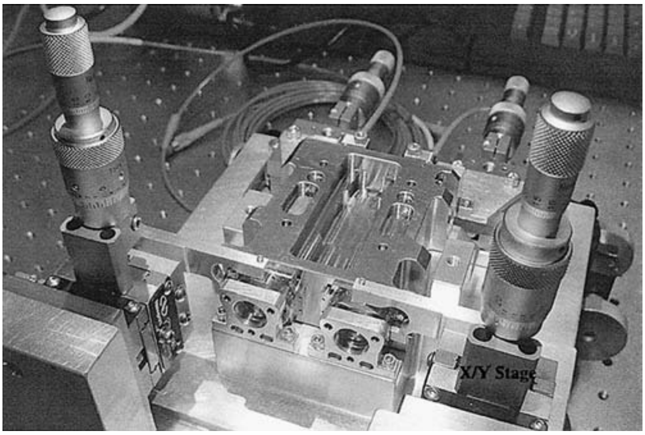

FIGURE 14.34 Objective lens subassembly alignment fixture for the collimator module. (From Stubbs et al., 2003.)

ment were conducted in a Class 1000 clean room. Reproducible diffraction-limited performance was achieved in all assemblies produced.

14.4 A STRUCTURAL DESIGN FOR HIGH SHOCK LOADING

This instrument was described in Section 5.3.6. Because it represents a solution to a structural design problem, that description is repeated here for the convenience of the reader. Figure 14.35 shows a sectional view of a lens assembly developed for use as part of a military flight motion simulator. It had air-spaced Si and Ge lens groups: the front group was a doublet with an average diameter of 9 in. (22.9 cm), while the rear group was a triplet with an average diameter of about 1.5 in. (3.8 cm). The overall dimensions of the assembly were 24.179 in. (61.41 cm) long and 12.43 in. (31.57 cm) diameter at the largest end (neglecting the larger mounting flange). It weighed approximately 80 lb (356 kg).

Palmer and Murray (2002) reported that because of the high cost of the larger lenses, the end user of the assembly specified that those optics should survive without damage a failure on the part of the simulator system that caused severe impact. Rather than designing the entire assembly to withstand the shock, the assembly was designed so that the mechanical supports for the costly components would fail at a load of $a_G = 30$, and those lenses would be constrained in a safe manner, even under much higher shock loads. The lenses would then not be damaged; they could be salvaged and reused. This unique design created an instrument that would fail gracefully under extreme environments.

The designers determined that severe impact would occur only in a direction transverse to the axis of the assembly. To make the assembly mechanically stiff under bending forces, the main housing was made of 6061-T6 aluminum and configured with a unique cross-section over most of its length. This construction may be seen in Figure 14.36(a), which is a photograph showing the exterior of the assembly. Between the lens groups that occupied the cylindrical portions of the housing, the structure was that of a "paddle wheel" with six ribs of full external diameter supporting conformal wall portions that enclosed the internal light beam emerging from the smaller lenses and expanding to fill the apertures of the larger lenses (see Figure 14.36[b]). These ribs enhanced assembly stiffness while minimizing weight.

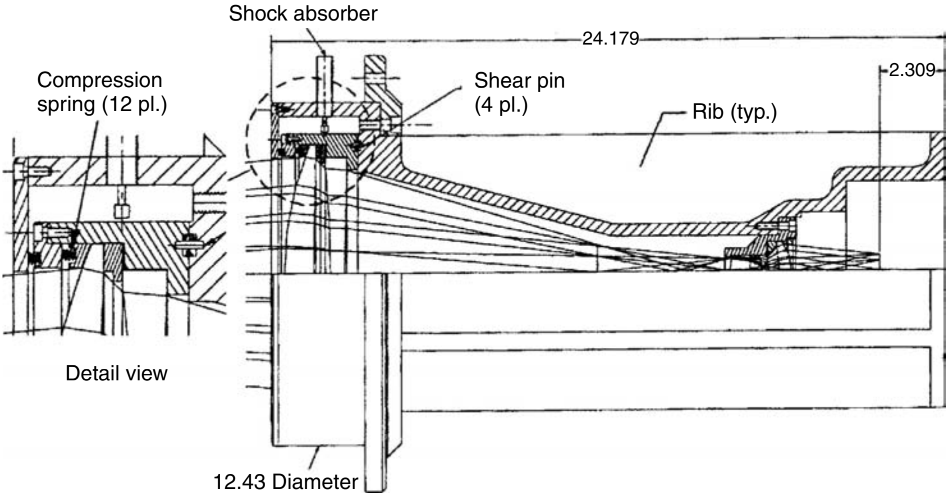

FIGURE 14.35 Sectional view of a collimating lens assembly designed to withstand high shock loading with minimal damage. Dimensions are in inches. (Courtesy of Janos Technology, Inc., Keene, NH.)

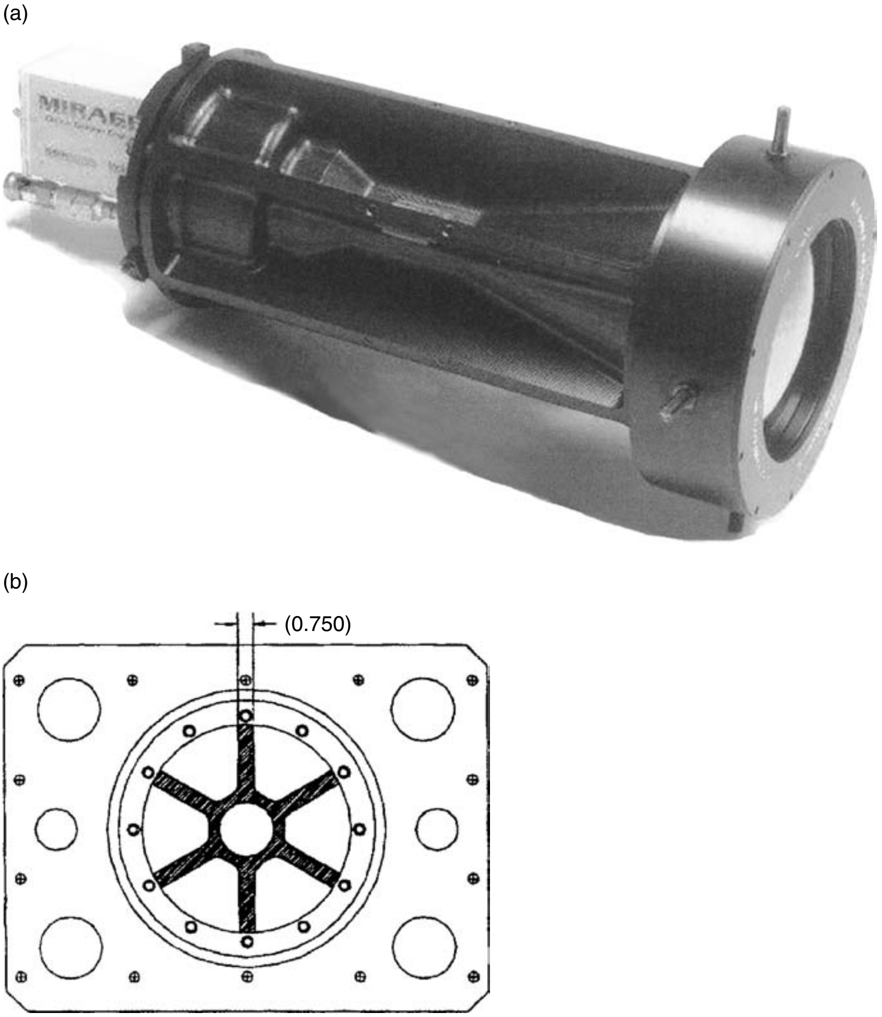

FIGURE 14.36 (a) Photograph of the collimating lens assembly of Figure 14.35 without the mounting flange. (b) Sectional view through the midpoint of the housing. (Courtesy of Janos Technology, Inc., Keene, NH.)

The cell for the large lenses was designed with a retaining flange that pressed multiple axially oriented compression springs against a pressure ring contacting the first lens. The preload so introduced pressed a spacer against the second lens, which in turn registered against a shoulder. The cell was constrained radially in the housing by three axially oriented aluminum shear pins that engaged stainless steel inserts pressed into the lens cell and the housing. Without these pins, the cell would be able to slide laterally within clearances provided all around the rim of the cell. At assembly, the pins located the cell and its lenses radially. The cell was pressed firmly against a shoulder in the housing by additional axially oriented compression springs that pushed against the outermost flange.

The pins were designed to shear under the prescribed shock load, allowing the cell to move. This cell motion would be dampened by shock absorbers oriented radially at four points around the periphery of the assembly. Three of these are shown in the photograph and one is indicated in the section view. The shock absorbers were nonlinear; they became stiffer under higher accelerations.

14.5 ATHERMALIZED STRUCTURAL DESIGNS

Athermalization is defined as the process of stabilizing an instrument's optical performance by designing the optics, mounts, and structures to compensate for temperature changes. We limit our considerations here to axial defocus effects that can be approached passively by choices of materials and dimensions or actively using mechanisms that respond to temperature changes.

14.5.1 INSTRUMENTS MADE FROM A SINGLE MATERIAL

One technique for designing thermal expansion compensation into an opto-mechanical assembly is to make all its critical parts from the same material. This allows optics and mechanical parts to expand and contract uniformly (if we assume homogeneous materials and no gradients), thereby tending to keep the system aligned and in focus. This approach can be followed only with reflecting systems since refractive index variations with temperature do not occur with mirrors.

14.5.1.1 The IRAS Telescope

A historically important example of an optical instrument built from one type of material is the IRAS Telescope as described by Schreibman and Young (1980) and by Young and Schreibman (1980). Its opto-mechanical configuration is shown schematically in Figure 14.37. All major structural parts and all optical parts comprising the imaging system were made of beryllium to minimize adverse effects of temperature changes from room temperature to the cryogenic temperature of operation. A drawing of the telescope's 24.4-in. (62.0-cm)-diameter primary mirror was shown in Figure 13.62, while details of one of the beryllium flexures that supported the mirror from the Be base plate were shown in Figure 13.63. The telescope was of Ritchey-Chretien optical design, operated in the 8 to120 μm spectral region, and was cooled to approximately 2 K.

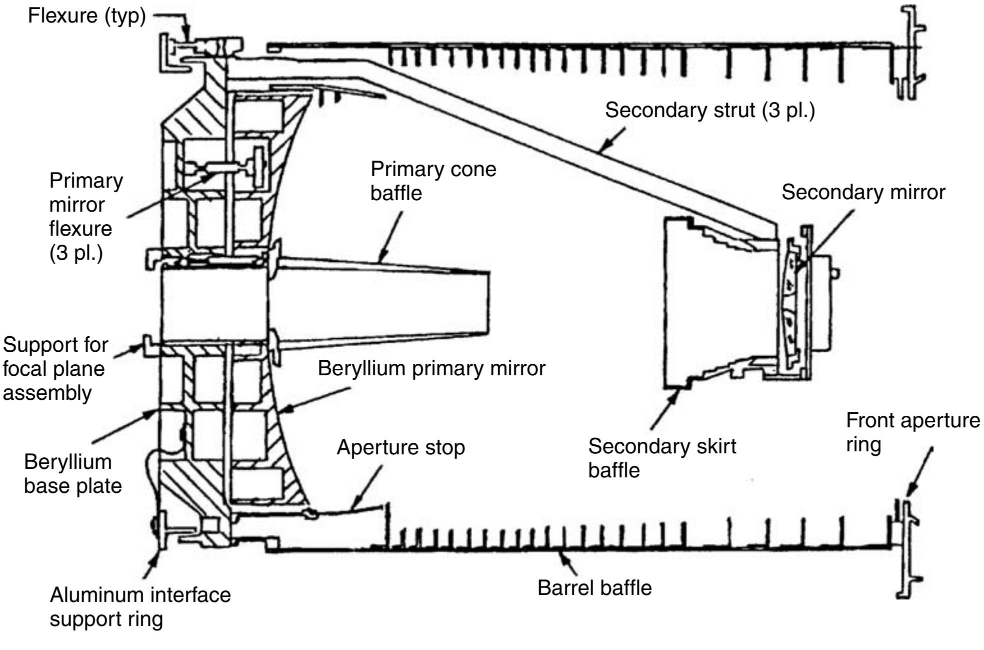
Flexure (typ)
Secondary strut (3 pl.)
Primary mirror flexure (3 pl.)
Primary cone baffle
Secondary mirror
Support for focal plane assembly
Beryllium primary mirror
Beryllium base plate
Aperture stop
Secondary skirt baffle
Front aperture ring
Aluminum interface support ring
Barrel baffle

FIGURE 14.37 Opto-mechanical configuration of the 24 in. (61 cm) aperture, cryogenically cooled, all beryllium infrared astronomical telescope (IRAS). (Adapted from Schreibman, M., and Young, P., *Proc. SPIE*, 250, 50, 1980.)

14.5.1.2 The Spitzer Space Telescope

A newer space-borne IR observatory featuring a telescope designed from a single material is the Spitzer Space Telescope (formerly known as the Space Infrared Telescope Facility [SIRTF]) (see Fanson et al., 1998; Gallagher et al., 2003). It has an 85-cm (33.5-in.)-diameter, *f*/12 lightweight all-beryllium telescope as shown in Figure 14.38. The primary mirror is a hub-mounted, single-arch design. Optical parameters of the telescope at cryogenic and room temperatures, as given by Chaney et al. (1999), are listed in Table 14.1. Note that the relative aperture, angular field of view, spectral band pass, and obscuration ratio are unchanged with temperature, as one would expect from a "same-material" design. Schwenker et al. (2003a, 2003b) describe the optical performance testing of the system and the results of that testing, respectively.

Launched by NASA in August 2003, this observatory operates in a 1 AU heliocentric orbit trailing the Earth, where it benefits from reduced thermal inputs from the Earth, shielding of solar heat inputs by the observatory's solar panels, and its ability to radiate heat from most of the instrument's surface into space. Because of its unique thermal design, here we concentrate on those aspects of the system. Publications dealing with the thermal design and its performance verification include Lee et al. (1998), Hopkins et al. (2003) and Finley et al. (2003).

In the Spitzer Observatory, only the science instruments are enclosed in the cryostat. Earlier Infrared observatories, such as IRAS, had both the telescope and its instruments enclosed in vacuum cryostats and required a large volume of cryogen to be carried. In this new observatory, the majority of the instrument remained at ambient temperature and pressure until reaching orbit where it rapidly cooled passively to about 40 K and enjoyed a vacuum environment. These advantages greatly reduced the need for cryogen (superfluid He). The cryogen supply at launch of 360 L is expected to further cool the instruments to ~5.5 K and the focal plane detectors to 1.5 K for at least 2.5 yr.

Figure 14.39 shows a cutaway view of the Spitzer Observatory indicating the telescope, scientific instruments, cryostat, cryogen supply, spacecraft bus, solar panels, shields, and associated equipment. The Multiple Instrument Chamber (MIC) contains the cold portions of four instruments (see Figure 14.40). According to Lee et al. (1998), this chamber has a diameter of 84 cm and a height of 21 cm. It is attached to the forward dome of the helium tank. Inside the MIC, pickoff mirrors send the light beam to the respective detector arrays. Signals from the detectors are preprocessed inside

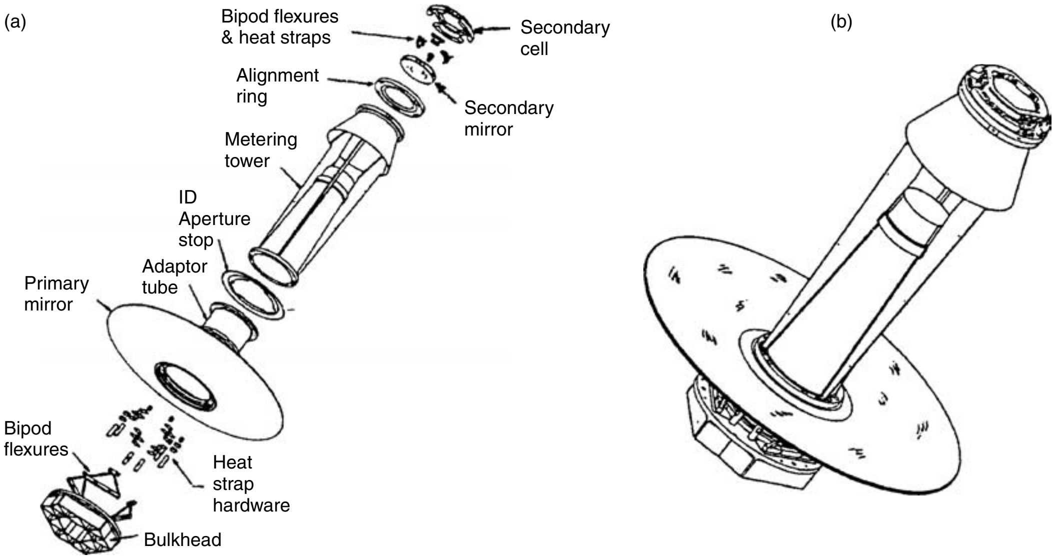

FIGURE 14.38 (a) Exploded view of the optical components of the Spitzer Space Telescope. (b) The assembled telescope optics. (From Chaney, D., Brown, R.J., and Shelton, T., *Proc. SPIE*, 3785, 48, 1999.)

TABLE 14.1
Spitzer Space Telescope Optical Parameters and their Variations with Temperature

	Cryogenic Value (~5 K)	Warm Value (~300 K)
System Parameters		
Focal length (cm)	1020.0	1021.3
Relative aperture	*f*/12	*f*/12
Back focal length (cm)	43.700	43.758
Field diameter (arcmin)	32.0	32.0
Spectral band pass (μm)	3 to 180	3 to 180
Aperture stop location	at primary rim	at primary rim
Aperture stop OD (cm)	85.000	85.111
Aperture stop ID (cm)	32.000	32.042
Obscuration ratio	0.3765	0.3765
Primary to secondary spacing (cm)	88.7545	8.8708
Radius of curved field (cm)	14.05	14.07
Focus adjustment (cm)	±2.5	±2.5
Image quality	Diffraction-limited	–
Primary Mirror Parameters		
Shape	Hyperbolic	Hyperbolic
Radius of curvature (concave) (cm)	204.000	204.265
Conic constant	−1.003548	−1.003548
Clear aperture (cm)	85.000	85.111
Relative aperture	1.20	1.20
Coating	None	None
Secondary Mirror Parameters		
Shape	Hyperbolic	Hyperbolic
Radius of curvature (convex) (cm)	29.434	29.472
Conic constant	−1.531149	−1.531149
Clear aperture (cm)	12.000	12.016

Source: Chaney, D., Brown, R.J., and Shelton, T., *Proc. SPIE*, 3785, 48, 1999.

the cold region and then transferred through miniature ribbon cables to the electronics packages within the spacecraft bus. The helium tank is supported from the spacecraft bus by a truss made of alumina/epoxy for low thermal conductivity.

The scientific instruments in the observatory are as follows:

(a) The infrared array camera (IRAC), which provides wide field imaging over two adjacent 5 × 5 arcmin fields. These fields are divided by beam splitters into separate images at 3.6 and 5.8 μm wavelengths and 4.5 and 8.0 μm wavelengths. The arrays all have 256 × 256 pixels. The detectors for the 3.6 and 4.5 μm channels are indium antimonide, while those for the 5.8 and 8.0 μm channels are arsenic doped silicon.

(b) The infrared spectrograph (IRS) has 4 separate spectrograph modules: two low-resolution channels operating over the 5.3 to 14 μm band and the 14 to 40 μm band, respectively, with resolving power of 60 to 120 and high-resolution channels operating over the 10 to 19.5 and 19.5 to 37 μm band, respectively, with resolving power of 600. The sensors are arsenic-doped silicon for the shorter wavelengths and antimonide-doped silicon for the longer wavelengths.

(c) The multiband imaging photometer (MIPS) for SIRTF provides imagery and photometry centered at 24, 70, and 160 μm wavelengths. The detector used at 24 μm is a 128 × 128

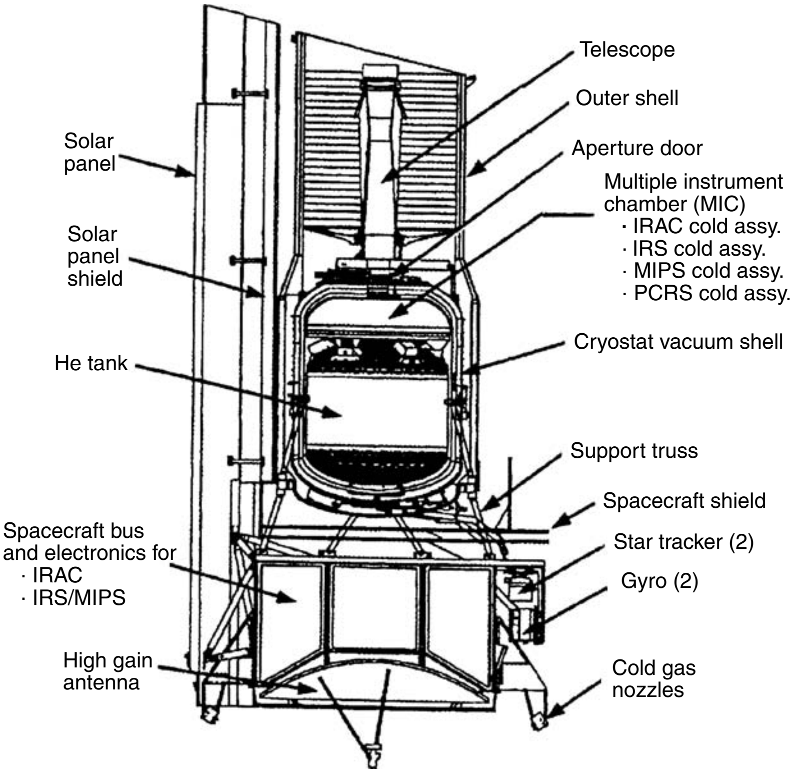
Telescope
Outer shell
Aperture door
Multiple instrument chamber (MIC)
· IRAC cold assy.
· IRS cold assy.
· MIPS cold assy.
· PCRS cold assy.
Cryostat vacuum shell
Support truss
Spacecraft shield
Star tracker (2)
Gyro (2)
Cold gas nozzles
Solar panel
Solar panel shield
He tank
Spacecraft bus and electronics for
· IRAC
· IRS/MIPS
High gain antenna

FIGURE 14.39 Cutaway view of the Spitzer Observatory. (From Fanson, J., Fazio, G., Houck, J., Kelly, T., Rieke, G., Tenerelli, D., and Whitten, M., *Proc. SPIE*, 3355, 478, 1990. With permission.)

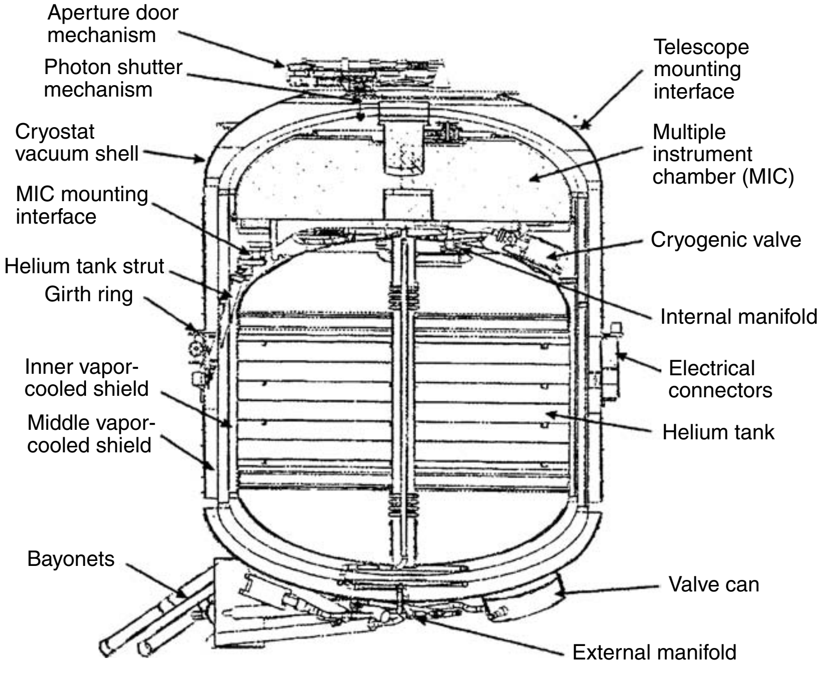
Aperture door mechanism
Photon shutter mechanism
Cryostat vacuum shell
MIC mounting interface
Helium tank strut
Girth ring
Inner vapor-cooled shield
Middle vapor-cooled shield
Bayonets
Telescope mounting interface
Multiple instrument chamber (MIC)
Cryogenic valve
Internal manifold
Electrical connectors
Helium tank
Valve can
External manifold

FIGURE 14.40 Cutaway view of the cryostat for the Spitzer Observatory. (From Lee, J.H., Blalock, W., Brown, R.J., Volz, S., Yarnell, T., and Hopkins, R.A., *Proc. SPIE*, 3435, 172, 1998. With permission.)

pixel array of arsenic-doped silicon, that used at 70 μm is a 32 × 32 pixel array of gallium-doped germanium, and that used at 160 μm is a 2 × 20 pixel array of stressed gallium-doped germanium. All three sensors observe the sky simultaneously.

A pointing calibration and reference sensor (PCRS) is provided within the MIC to calibrate thermomechanical drift errors between the telescope, the star trackers, and the gyroscopes with a radial 1-σ accuracy of 0.14 arcsec; to link the Observatory's coordinate system to the absolute J2000 Astrometric Reference Frame, and to define starting attitudes for high-accuracy absolute offset maneuvers (Mainzer et al., 1998). By simultaneously observing a reference star from the Tyco Star Catalog and the externally mounted star tracker, the relative alignment of these systems is established. An offset is then accomplished to center a target of interest in the selected science instrument's field of view.

All these cold assemblies are located, as indicated schematically in Figure 14.41, on an aluminum baseplate that serves as a stable optical bench. A thin-ribbed aluminum dome forms a light-tight cover for the MIC. A photon shutter is attached to the top center of the cover. It is normally open, but was closed during ground testing of detector dark currents. High-purity copper thermal straps were attached between the instruments and the top of the helium tank to carry heat away from those temperature-sensitive units. These straps pass through light-tight seals.

14.5.1.3 A Telescope with Optical and Inter-Component Interfaces Processed by SPDT

Erickson et al. (1992) described another example of a telescope system athermalized by making all opto-mechanical components of the image-forming system from the same material. This telescope is shown schematically in Figure 14.42. SPDT played an important part in its development by facilitating assembly and eliminating the need for alignment. The primary and secondary mirrors were designed with integral spherical reference surfaces whose nominal optical centers of curvature coincided with the system's focal point. The order of machining operations was carefully established

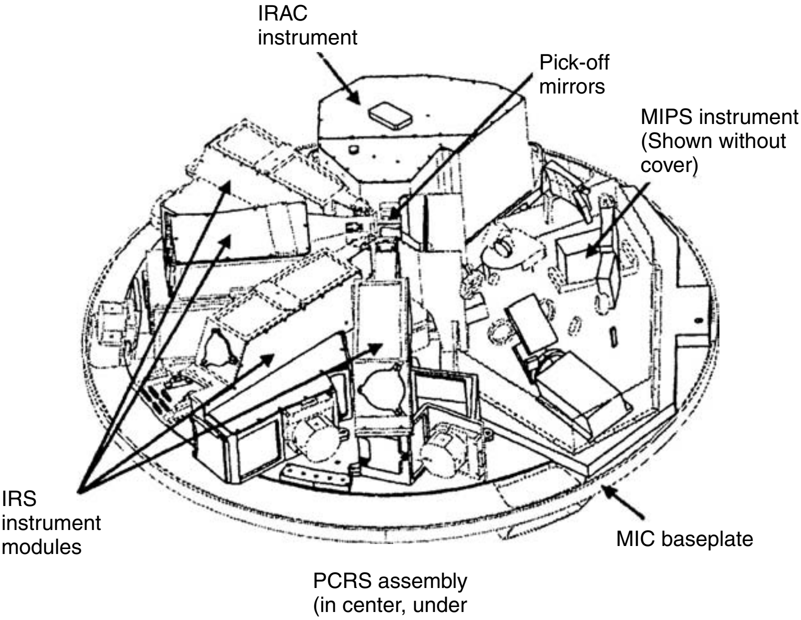
IRAC instrument
Pick-off mirrors
MIPS instrument (Shown without cover)
IRS instrument modules
MIC baseplate
PCRS assembly (in center, under instruments)

FIGURE 14.41 Arrangement of scientific instruments in the multiple instrument chamber of the Spitzer Observatory. (From Fanson, J., Fazio, G., Houck, J., Kelly, T., Rieke, G., Tenerelli, D., and Whitten, M., *Proc. SPIE*, 3356, 478, 1998.)

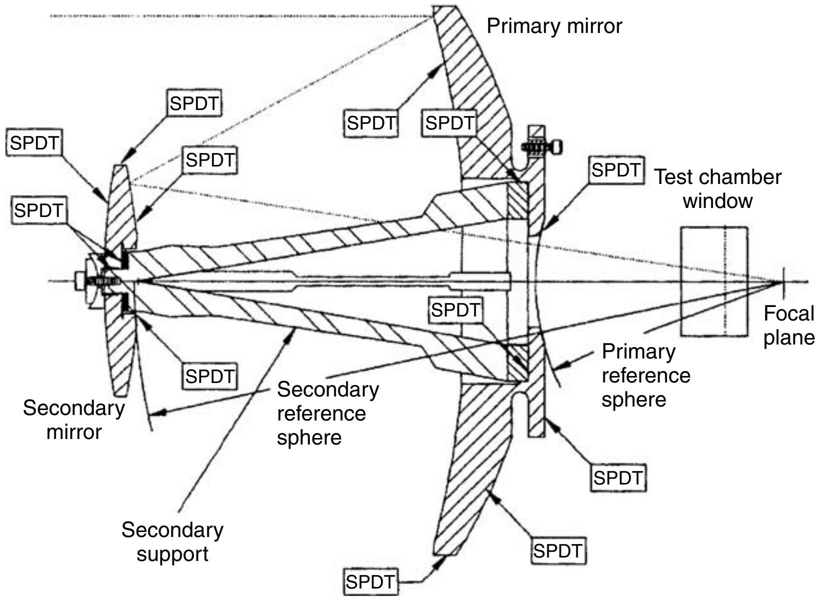

FIGURE 14.42 Schematic diagram of an all-aluminum telescope showing surfaces machined by SPDT methods. (From Erickson, D.J., Johnston, R.A., and Hull, A.B., *Proc. SPIE*, CR43, 329, 1992.)

during the design phase. Specific part diameters and surfaces were designed so they could be utilized for support and registration when flipping the mirrors over for opposite side machining. The authors provided details as to the sequence of operations during fabrication, assembly, and alignment confirmation. The latter aspect of the process proved the success of the design by showing that the expected performance could be achieved without adjustment.

14.5.2 ACTIVE CONTROL OF FOCUS

A possible means for athermalizing the focus of optical systems is active control of the location(s) of one or more optic, whereby the temperature distribution within the system is measured and motor-driven mechanisms are used to drive the mirror separation or final image distance to optimum values in accordance with preestablished algorithms. From the systems viewpoint, a better (but more complex) means would be to sense the sharpness of focus or quality of the image and actively servo control the location(s) of one or more components to optimize performance. Both techniques require an expenditure of energy that may not be easily available.

One example of an active temperature compensation system was described by Fischer and Kampe (1992). The system was a 5:1 afocal zoom attachment for a military FLIR sensor operating in the spectral range from 8 to 12 μm. Requirements for the system are listed in Table 14.2. The optical system developed to meet these requirements is shown in Figure 14.43. The first element is fixed, as are the smaller lenses so indicated. The moveable lenses are designated Groups 1 (air-spaced doublet) and 2 (singlet). All of these lenses are made of germanium as is the second small fixed lens. The other small fixed lens is zinc selenide. Its purpose is primarily to correct chromatic aberration. There are four aspherics in the design. Image quality of this design met all requirements over the specified temperature and target distance ranges when the locations of the moveable lens groups were optimized.

Achievement of athermalization was accomplished by mounting the moveable groups on guide rods through linear bearings (see Figure 14.44) and driving them independently with two stepper motors acting through appropriate spur gear trains as shown schematically in Figure 14.45.

TABLE 14.2
Requirements for an Actively Athermalized Zoom Attachment

Parameter	**Requirement at Temperature**	
	Ambient	**0 and 90°C**
Magnification range	0.9× to 4.5×	
Relative aperture	*f*/2.6	
Spectral range	8.0 to 11.7 μm	
Full excursion magnification change speed	≤2 sec	
MTF (relative to the diffraction limit)		
On axis	≥85%	≥77%
0.5 field	≥75%	≥68%
0.9 field	≥50%	≥45%
Size		
Length	5.19 in.	
Diameter	5.50 in.	—
Weight goal	≤5 lb	
Narcissus		
at magnifications ≤3×	≤0.25°C	
at magnifications ≥3×	≤0.15°C	
Athermalization	Focus maintained 0 to 50°C	
Distortion	≤5%	
Target range	500 ft to infinity	
Vignetting	None	
Coatings	≤0.3% reflectivity per surface	

Source: Fischer, R.E. and Kampe, T.U., *Proc. SPIE*, 1690, 137, 1992.

The motors were controlled either by a local microprocessor (during operation) or an external personal computer (during test). The operator commanded the magnification to be provided and the target range. The electronics then referred to a look-up table stored in a built-in *erasable programmable read only memory* (EPROM) to determine the appropriate settings for the moveable lenses at room temperature. Two thermistors bonded to the lens housing sensed the actual temperature of the assembly. Signals from these sensors were used by the electronics to select, from a second look-up table stored in the EPROM, the required changes to the lens settings to correct for temperature effects on system focus. The corrected signals were then used to drive the motors to position the lenses for best imagery at the measured temperature. The lens group motions varied as functions of magnification and target range as indicated in Figure 14.46.

14.5.3 INSTRUMENTS ATHERMALIZED WITH METERING SRUCTURES

If the thermal expansions and contractions of the rigid housing of an optical instrument with changing temperature are too large for the optics in an instrument to remain properly spaced during operation, and active control of the spacings is not provided, some form of passive athermalization might be employed. One possible arrangement uses a metering structure. The principle here is to allow one or more optical components, such as the secondary mirror of a Cassegrain-type telescope, to float axially with respect to the main housing and to control the mirror spacing with three or more rods or a truss structure made of material with a specific, usually low, CTE. Invar and fused silica are common materials for metering rods. Compound metering rods comprising specific lengths of different materials (such as aluminum and Invar) with different CTEs used in series or opposition

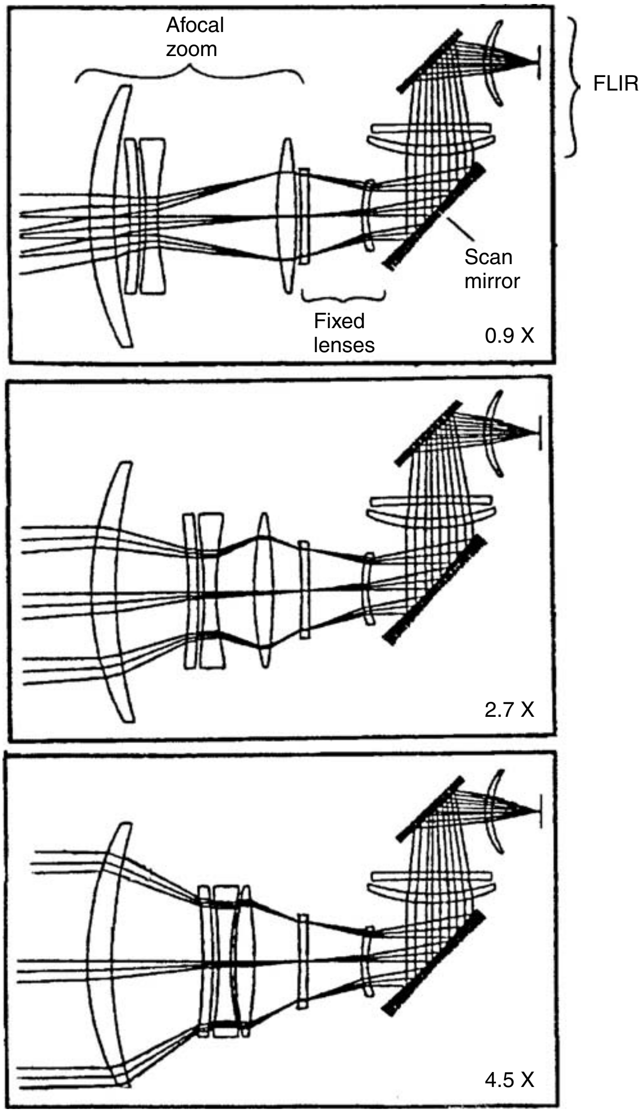

FIGURE 14.43 Optical system configurations of an afocal zoom lens at three magnifications. (From Fischer, R.E. and Kampe, T.U., *Proc. SPIE*, 1690, 137, 1992.)

have been employed successfully to create a thermal response that cannot be obtained from a length of one material alone. Composite materials can also be used to advantage as metering rods since their CTEs can be customized for the particular application.

14.5.3.1 The Orbiting Astronomical Observatory

As a classic example of the metering rod athermalization principle, we consider the 80 cm (31.5 in.) aperture, 16 m (53 ft) focal length Cassegrain objective used in the Orbiting Astronomical Observatory, Copernicus (OAO-C). This instrument was launched into a 740-km (460-mi)-high circular. Earth orbit by NASA in 1972. Equipped with a high-resolution grating spectrometer, the telescope made quantitative observations of interstellar absorption spectra in the 0.07 to 0.33 μm (UV) wavelength region throughout its long useful life in orbit.

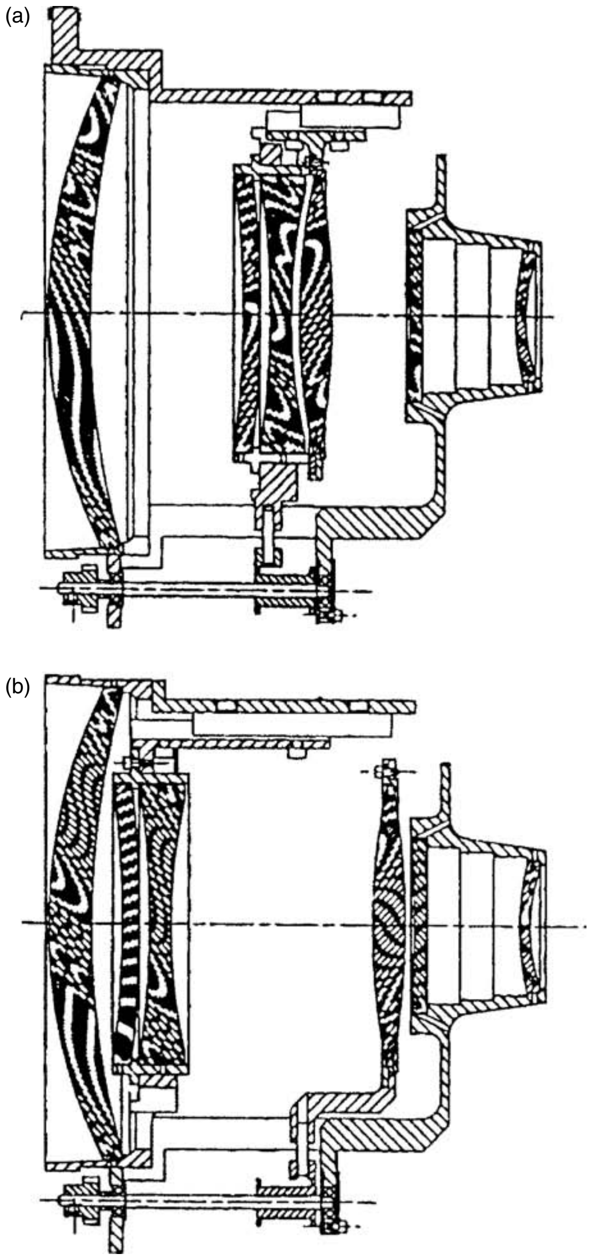

FIGURE 14.44 Section views through the zoom lens opto-mechanical system at (a) narrow field of view (4.53×) and (b) wide field of view (0.93×). (From Fischer, R.E. and Kampe, T.U., *Proc. SPIE*, 1690, 137, 1992.)

Figure 14.47 shows a sectional view and an end view of the opto-mechanical telescope assembly. The main housing of the assembly was a dual-wall, welded, stress-relieved aluminum tube of the configuration illustrated in Figure 14.48. The primary-to-secondary separation of approximately 250 cm (98.4 in.) was maintained by spring loading the mirror mounts against the ends of three, fused silica metering rods. One of these rods may be seen in Figure 14.49, which also shows part of the thermal insulation provided in the design.

To maintain centering, the primary mirror was supported by three tangential flexures. The design of the lightweighted mirror to interface with these flexures was shown in Figure 9.8 and Figure 9.9.

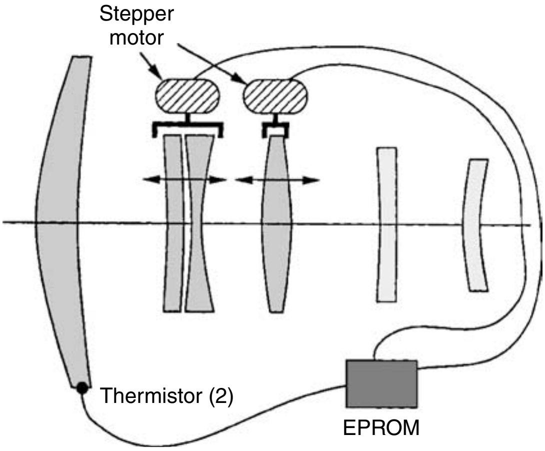

FIGURE 14.45 Schematic diagram of the temperature sensing and motor drive system used to athermalize the zoom lens of Figure 14.43. (From Fischer, R.E. and Kampe, T.U., *Proc. SPIE*, 1690, 1992.)

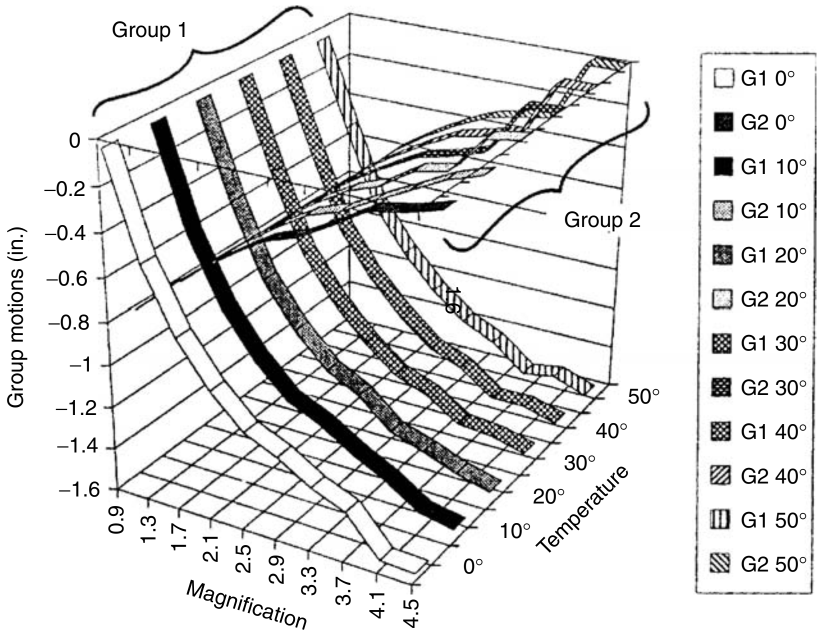

FIGURE 14.46 Motions of the afocal zoom lens groups as functions of magnification and temperature over the 0 to 50°C range. (From Fischer, R.E. and Kampe, T.U., *Proc. SPIE*, 1690, 1992.)

During launch, the primary was held away from the metering rods by a vibration isolation caging mechanism. After reaching orbit, the mirror was released electromechanically and moved into registry against the rods. The springs then maintained axial contact throughout the useful life of the instrument.

14.5.3.2 The Geostationary Operational Environmental Satellite

The 12.25 in. (31.1 cm) aperture Cassegrain telescope of the Geostationary Operational Environmental Satellite (GOES) (see Figure 14.50) also utilized metering rods to control the primary-to-secondary spacing (Zurmehly and Hookman, 1989). The telescope structure is shown

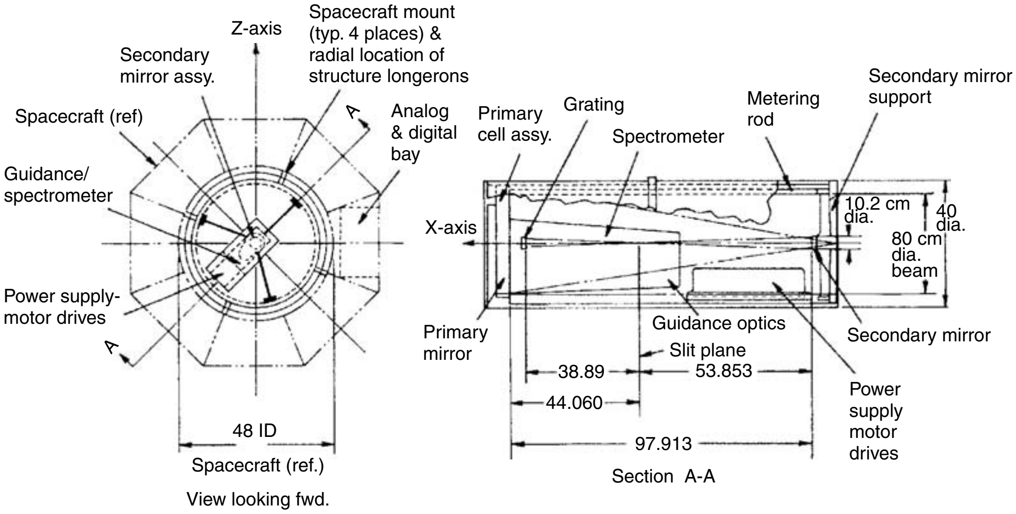
Z-axis
Secondary mirror assy.
Spacecraft mount (typ. 4 places) & radial location of structure longerons
Spacecraft (ref)
A
Analog & digital bay
Guidance/ spectrometer
Power supply- motor drives
A
48 ID
Spacecraft (ref.)
View looking fwd.
Primary cell assy.
Grating
Spectrometer
Metering rod
Secondary mirror support
X-axis
10.2 cm dia.
40 dia.
80 cm dia. beam
Primary mirror
Guidance optics
Slit plane
Secondary mirror
38.89
53.853
44.060
97.913
Power supply motor drives
Section A-A

FIGURE 14.47 Sectional views of the Orbiting Astronomical Observatory, Copernicus (OAO-C) telescope/spectrometer assembly. All dimensions are in inches except as noted. (Courtesy of Goodrich Corporation, Danbury, CT.)

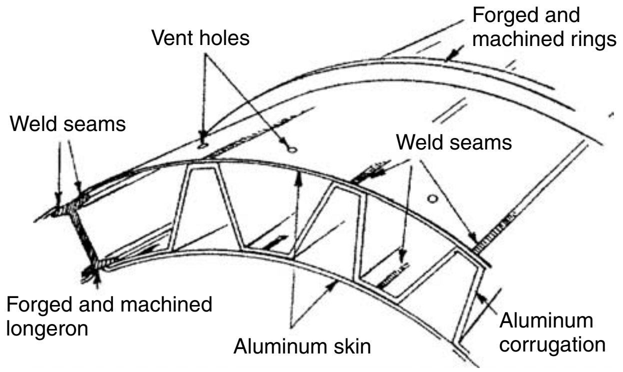
Forged and machined rings
Vent holes
Weld seams
Weld seams
Forged and machined longeron
Aluminum skin
Aluminum corrugation

FIGURE 14.48 Constructional concept for the welded dual-wall tube that formed the rigid main structure for the OAO-C telescope. (Courtesy of Goodrich Corporation, Danbury, CT.)

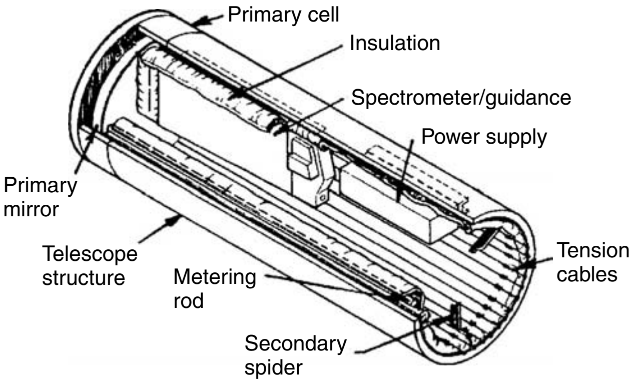
Primary cell
Insulation
Spectrometer/guidance
Power supply
Primary mirror
Telescope structure
Metering rod
Tension cables
Secondary spider

FIGURE 14.49 Sketch showing the thermal insulation and locations of major assemblies in the OAO-C telescope. One of the fused silica metering rods is visible. (Courtesy of Goodrich Corporation, Danbury, CT.)

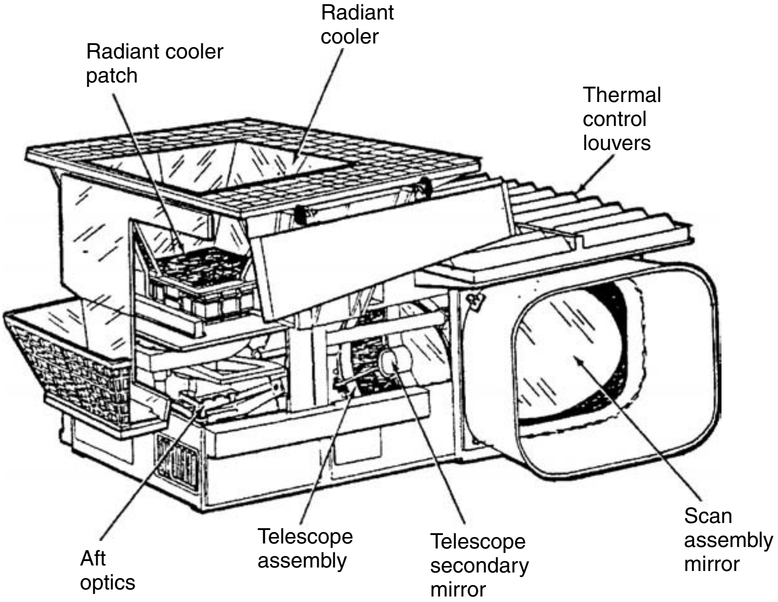

FIGURE 14.50 External view of the Geostationary Operational Environmental Satellite (GOES). (From Zurmehley, G.E. and Hookman, R., *Proc. SPIE*, 1167, 360, 1989.)

schematically in Figure 14.51. Six thin-wall Invar tubes connect the primary mirror cell to the spider supporting the secondary mirror. The primary mount, secondary spider, and secondary cell are made of aluminum. The instrument design is axially athermal because the lengths of the dissimilar structural metals have been chosen such that the axial separation between the mirrors remains constant when the temperature changes from ~1°C (~34°F) to ~54°C (~129°F) as the satellite orbits through the Earth's shadow.

Figure 14.52 shows schematically how this is accomplished. The materials involved have low or high CTEs, as indicated by the legend. The mirrors are located as indicated in the drawing. The plus and minus signs indicate how an increase in temperature affects the central air space between these mirrors. The direction of an individual change is determined by which end of the component is attached to its neighboring components. The algebraic summation of contributions, each consisting of the individual component length times its CTE times the temperature change for the various structural members, defines the mirror separation. The material for one spacer in the secondary mount is selected at assembly to accommodate minor variations in component parameters. The net result is that the air space remains fixed throughout the temperature excursion. To help regulate temperature, aluminum heat shields painted black on the outside surfaces to maximize thermal emissivity and gold plated on the inside surfaces to minimize emissivity are placed over the major mechanical components, including the metering tubes. These shields are not structural members, so they do not enter directly into the temperature compensation mechanism. Gradients as large as 8°C (46°F) were expected to occur during orbit, but no means was provided to compensate for these gradients.

The structural design of the mounting for the secondary mirror was described by Hookman (1989) and summarized in Section 8.3. This 1.53 in. (38.9 mm) aperture, convex ULE mirror was mounted into an Invar housing as illustrated in Figure 8.28. Slightly compressed buttons of RTV-566 elastomer preloaded the mirror axially and radially. These elastomer buttons were sufficiently resilient to accommodate the slight CTE differences between the mirror and mount materials.

Since the Invar secondary housing was attached to an aluminum spider structure, flexure blades integral to the housing were used to bridge the gap between these components as shown in Figure 8.29. These flexures were compliant in the radial direction but stiff in the tangential and

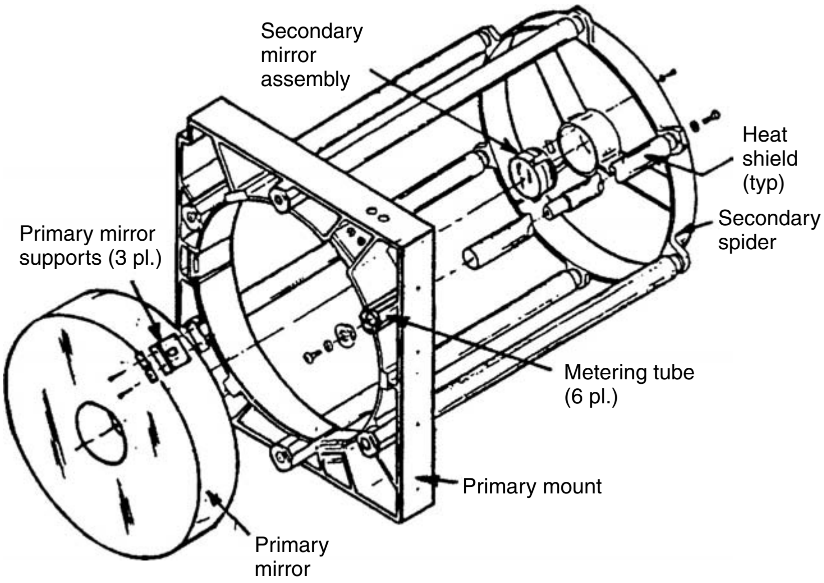
Secondary mirror assembly
Heat shield (typ)
Secondary spider
Primary mirror supports (3 pl.)
Metering tube (6 pl.)
Primary mount
Primary mirror

FIGURE 14.51 Diagram of the passively athermalized structure of the GOES telescope. (From Hookman, R., *Proc. SPIE*, 1167, 368, 1989.)

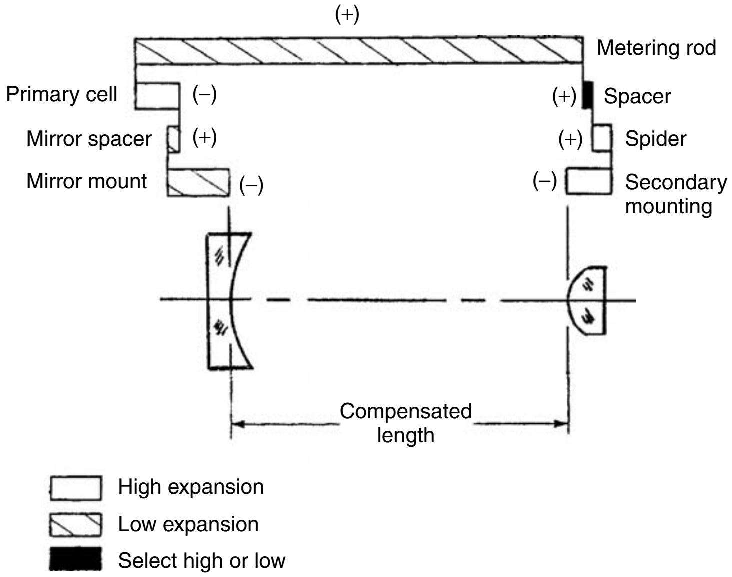
(+)
Metering rod
Primary cell
(−)
(+)
Spacer
Mirror spacer
(+)
(+)
Spider
Mirror mount
(−)
(−)
Secondary mounting
Compensated length
High expansion
Low expansion
Select high or low

FIGURE 14.52 Schematic diagram of the passive thermal compensation mechanism (metering rods) used to stabilize the axial spacing between the GOES telescope primary and secondary mirrors. (From Zurmehly, G.E. and Hookman, R., *Proc. SPIE*, 1167, 360, 1989.)

axial directions. The radial stiffness of the flexures was adjusted to give a first natural frequency mode of 832 Hz so that externally applied vibrations of lower frequency would not excite resonances.

In their 1989 paper, Zurmehly and Hookman also described a test facility used to test the effects of simulated temperature changes in focus, pointing, and pointing error repeatability. Figure 14.53 shows a portion of the facility. The test item was mounted rigidly inside a thermal vacuum chamber (dotted line) on a vibration isolation table. A back-illuminated pinhole light source was placed at the

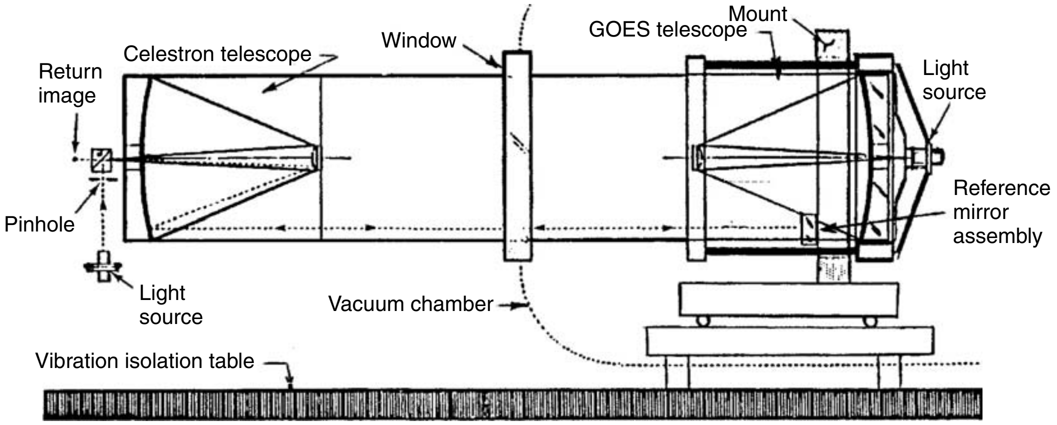

FIGURE 14.53 Schematic diagram of the test setup for thermal/vacuum testing of the GOES telescope. (From Zurmehly, G.E. and Hookman, R., *Proc. SPIE*, 1167, 360, 1989.)

focal point of the GOES telescope (at right in the figure). The collimated beam from the telescope passed through a window in the chamber wall into a modified commercial (14 in. aperture Celestron) telescope where it was focused through a beam splitter cube to the focal point of the latter telescope. The image was viewed through a microscope (not shown). The microscope was mounted on a three-axis adjustable stage equipped with means for measurement of all three motions. When the focus of the GOES telescope varied or the image wandered laterally because of temperature changes, the microscope was used to measure those shifts. From the known longitudinal and lateral magnifications of the combination of telescopes, the corresponding errors for the test item were calculated.

Because the test took place over an extended time period, provision was made for system calibration before each measurement. The microscope and Celestron telescope were mounted on a stage with transverse rails so that they could be moved laterally into alignment with a full-aperture optically flat mirror (not shown). The true focus of the Celestron telescope was determined by autocollimating the beam projected from the pinhole/light source shown below the beam splitter from that mirror. Shifts of this return image were recorded and used to correct the apparent focus shifts of the GOES telescope.

Instrumental pointing errors were removed by autocollimating the Celestron telescope/microscope system from a 2-in.-diameter flat mirror attached to the structure of the GOES telescope. This mirror was oriented so as to define the true boresight of the optical axis of the test telescope. The reference mirror was attached to the telescope on flexures so as to negate tilts from temperature changes.

The test item's temperature was varied by enclosing it (except for the optical aperture) in a noncontacting aluminum shroud that could be cooled with flowing brine at −34°C or heated with electrical resistance heaters. Heat transfer was completely by radiation. The temperature of the telescope was monitored at 72 points with thermocouples reading at 3-min intervals. Steady-state temperature was indicated when no thermocouple registered a rate of change no greater than 0.1°C/h. To prevent radiative coupling of the shroud to the room temperature vacuum chamber walls, the external surface of the shroud was covered by multilayer insulation.

14.5.3.3 The Deep Imaging Multi-Object Spectrograph

A more complex, passive, temperature-compensation mechanism utilizing a metering structure made of different materials was used in the deep imaging multi-object spectrograph (DEIMOS) camera lens assembly described by Mast et al. (1999). The assembly, discussed previously (Section 5.8) in connection with its application of fluid coupling between lens elements, was shown in Figure 5.59. The same figure is also shown here, with additional component designations, as Figure 14.54.

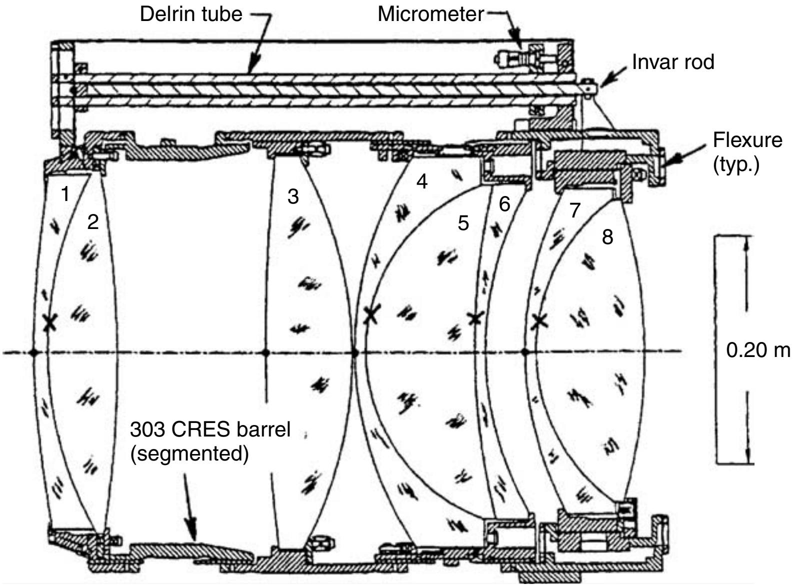

FIGURE 14.54 Opto-mechanical design layout for the DEIMOS camera assembly. (Adapted from Mast, T., Faber, S.M., Wallace, V., Lewis, J., and Hilyard, D., *Proc. SPIE*, 3786, 499, 1999.)

The need for this mechanism resulted from a requirement that the scale of the image produced by the camera was to be constant with temperature change over the operating range of ±5°C to 0.17 pixel diameter over the maximum image height of 4096 pixels. This corresponds to $\delta p/p$ of 42×10^{-6}. Calculations for the uncompensated design from the known thermal properties of the components of the assembly indicated an intolerable temperature sensitivity of $\delta p/p$ of 136×10^{-6}. The required performance would then be achieved only within a temperature range of ±0.31°C of nominal.

To solve this problem, the mechanical design of the assembly provided a passive means to move the fourth lens doublet (elements 7 and 8) axially as the temperature varies. This would refine the lens focal length and, hence, the scale factor of the image. The lens cell was supported on radially oriented flexures to permit axial movement. Force to move the cell was delivered by connecting it to the right end of an Invar rod that was fixed at its left end to a Delrin tube concentric with the rod, and attached at its right end to the lens barrel. Both the rod and tube were 440 mm long. The nominal location of the moveable lens was initially established with the micrometer indicated in the figure. Differential expansion of the rod and tube provided a length change of 0.036 mm/°C within ±3%, which was sufficient to compensate the image scale factor.

14.5.3.4 Athermalization of the Multiangle Imaging Spectro-Radiometer

In Section 14.2.4, we discussed the nine cameras used in the MISR in terms of the design of their rigid housing configurations. In order for those lenses to function properly in orbit, each back focal length (BFL), or the distance from the last lens surface to the detector plane, needed to be kept constant throughout the operating temperature range of 0 to 10°C. A passive approach was chosen in which the detector was moved as a function of temperature to keep it at the optimum location of the image formed by each lens.

The adopted temperature compensation mechanism is shown in Figure 14.55. One of these assemblies was attached to the end of each lens housing as indicated in Figure 14.56. Optimization of the detector location relative to the image was achieved in this design with a set of concentric tubes made of different materials connected at alternate ends so that their length variations with

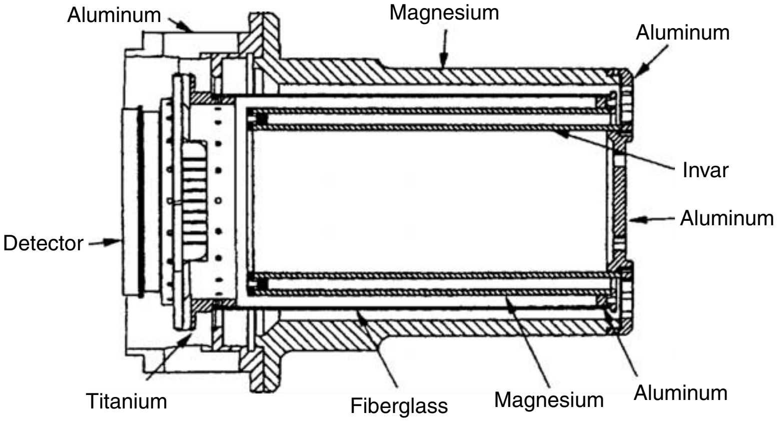
Aluminum
Magnesium
Aluminum
Invar
Aluminum
Detector
Titanium
Fiberglass
Magnesium
Aluminum

FIGURE 14.55 Schematic of the temperature compensator used with each MISR lens assembly. (From Ford, V.J., White, M.L., Hochberg, E., and McGown, J., *Proc. SPIE*, 3786, 264, 1999.)

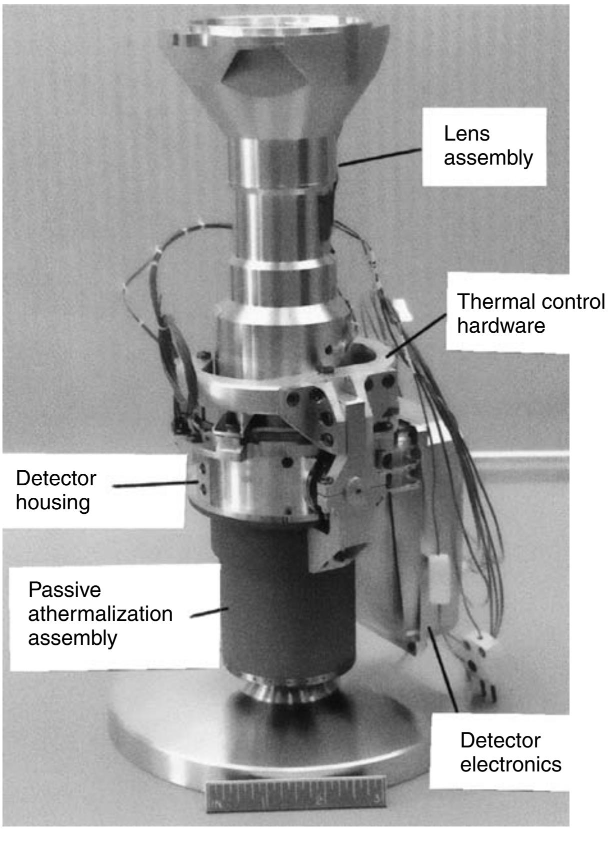
Lens assembly
Thermal control hardware
Detector housing
Passive athermalization assembly
Detector electronics

FIGURE 14.56 Photograph of an engineering model of the MISR Type D camera. (From Ford, V.J., White, M.L., Hochberg, E., and McGown, J., *Proc. SPIE*, 3786, 264, 1999.)

temperature add and subtract in a predictable manner. In this design, the materials used in the components tending to reduce the total length with increasing temperature were made of low-CTE materials (Invar and fiberglass), while those tending to increase that length were made of high-CTE materials (aluminum and magnesium). It was found that identical compensator designs would not provide complete compensation at all temperatures for all types of lenses, but that the performance degradation resulting from the use of one compromise design would be acceptable.

The detectors were cooled with thermoelectric coolers to −50 ± 0.1°C. They were thermally insulated from the surrounding structure. The detector housings were gold coated to reduce emissivity, the cold structures were mounted on a thin, fiberglass tube (selected for its low thermal conductivity), and the fiberglass tube was covered with low-emissivity aluminized Mylar. The other tubes in the assembly were metallic to obtain high thermal conductivity. The detector head for one camera is shown in Figure 14.57(a). The associated electronics assembly, thermal electric cooler, and passive athermalization assembly can be seen in this figure. Figure 14.57(b) shows a close-up view of the detector attached to its electronics.

It was expected that thermal gradients between the camera and the lens assembly would cause the temperature compensator subsystem to correct the focus at the wrong temperature. Of particular concern was the joint between the lens housing and the camera assembly, which was connected through a spacer that did not have good thermal conductivity. Additionally, heat had to be removed

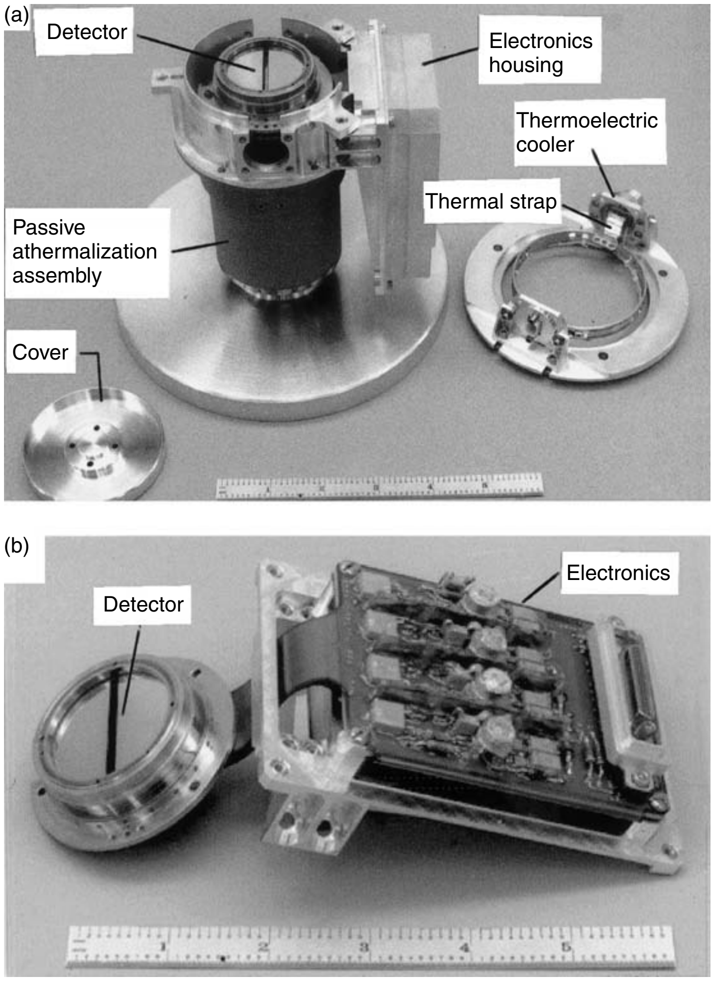

FIGURE 14.57 (a) Photograph of a MISR camera head consisting of a detector housing, electronics, and passive athermalization assembly. (From Ford, V.G., White, M.L., Hochberg, E., and McGown, J., *Proc. SPIE*, 3786, 264, 1999.) (b) Close-up photograph of the MISR detector and electronics assembly (without cover). (Courtesy of NASA/JPL/CALTECH.)

from the thermal electric cooler and the detector preamplifier. To stabilize the temperature, special thermal control hardware (indicated in Figure 14.56) was designed and added to the system. This hardware, made of highly conductive type 7073 aluminum alloy, bridged the joint between the lens and camera housings and clamped onto a conductive finger that removed heat from the electronics and the cooler. Soft, pure aluminum shims were provided in all joints of this hardware to maximize conduction of heat through those joints. Heat was then conducted from the lens housing to the structure of the instrument, where it was radiated away.

14.5.3.5 Athermalization of the Hubble Space Telescope Truss Structure

Triangular trusses have been used for many years as the main structures of large astronomical telescopes. A diagram of a typical installation for a modern ground-based telescope is shown in Figure 14.58. In general, these are not designed to athermalize the mirror separation. Material selection is usually based on availability, cost, and weight considerations. The effects of temperature changes are usually compensated for elsewhere in the opto-mechanical system.

The structural design of the optical telescope assembly (OTA) of the HST (see Figure 14.59) includes a sophisticated truss that serves the same purpose as metering rods. It was designed to maintain precise axial spacing, relative centering, and parallelism of the secondary and primary mirrors in orbit.

If the HST could operate in a totally constant environment, axial thermal stability would not be a particular concern in such a design. In practice, however, it circles the Earth about every 93 min and experiences a “day” and “night” on each orbit. Temperature swings of up to 30°C (54°F) can result.

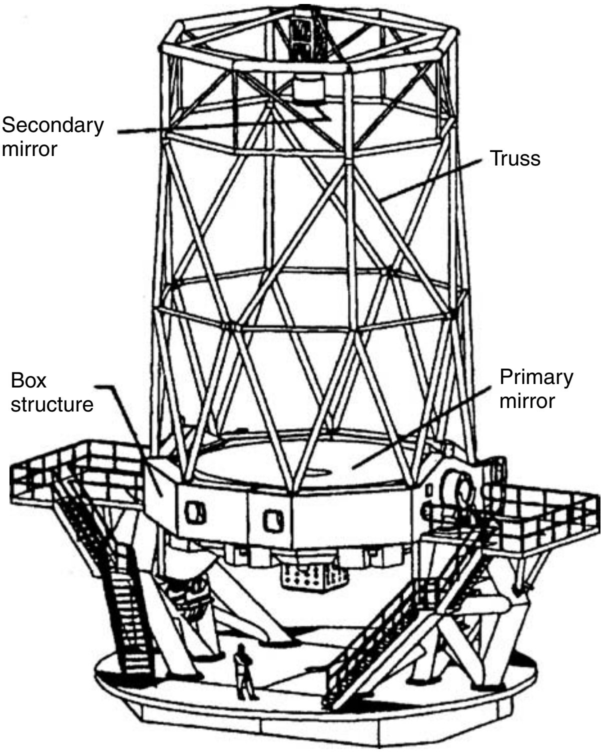

FIGURE 14.58 Artist’s representation of the structure for the Gemini telescope showing a typical triangular truss used to support the secondary mirror. (From Raybould, K., Gillet, P., Hatton, P., Pentland, G., Sheehan, M., and Warner, M., *Proc. SPIE*, 2199, 376, 1994.)

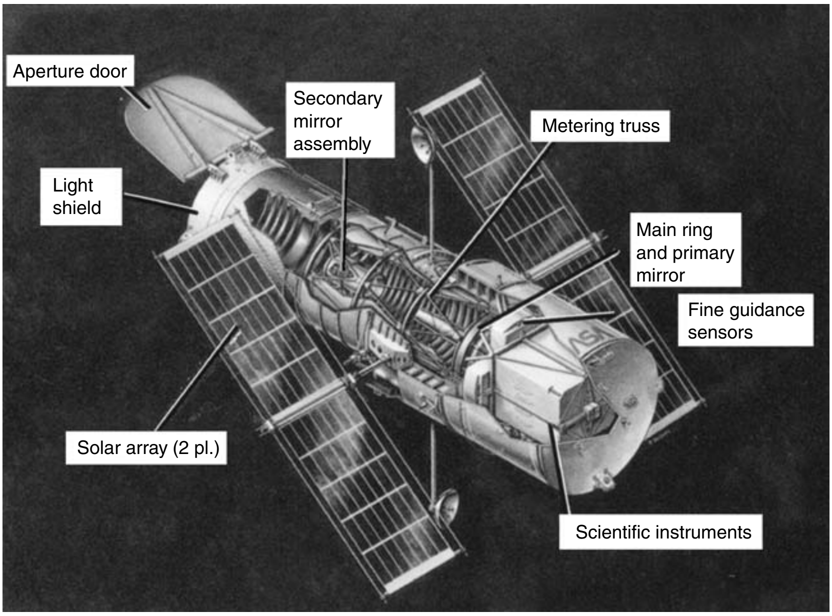

FIGURE 14.59 Cutaway view of the Hubble Space Telescope with solar arrays deployed and aperture door open. The metering truss structure that supports the secondary mirror from the main telescope ring structure is indicated. (From McCarthy, D.J. and Facey T.A., *Proc. SPIE*, 330, 139, 1982.)

Under these conditions, thermal expansion and contraction and their effects on the structure supporting the primary and secondary mirrors must be considered. In the hope of providing guidance for future designs based on this principle, we summarize some of the key considerations of the OTA truss design.

This truss was designed to hold the alignment of the two mirrors to 3 μm (1.18×10^{-4} in.) despace, 10 μm (3.94×10^{-4} in.) decenter, and 2 arcsec tilt. The manufacturer was faced with predictably variable temperatures and temperature ranges over the 4.9 m (193 in.) length of the structure, and the virtual impossibility of producing three "I" cross-section rings over 2.4 m (94 in.) in diameter plus 48 tubular elements 2.13 m (84 in.) long, all with identical (small) coefficients of expansion. Stiffness of the overall structure was also critical. A first-mode resonant frequency of 24 Hz was specified for the assembled truss.

Clearly, conventional lightweight metals such as aluminum or titanium could not provide the low-expansion characteristics needed, so the chosen approach was to develop very stable graphite fiber-reinforced epoxy struts and rings, assemble them into the required structural configuration, and verify by analysis and test that the completed truss would meet the stringent stability specifications in the operating environment.

Thermal-sensitivity analyses reported by Smith and Jones (1978) indicated that the CTE of the strut material should be $0.025 \pm 0.035 \times 10^{-6}\ °\text{F}^{-1}$, whereas that of the truss ring material should be $0.25 \pm 0.15 \times 10^{-6}\ °\text{F}^{-1}$. According to McMahan (1982), the cross-sectional dimensions and hybrid fiber lay-up materials used for the struts and truss rings were as indicated in Figure 14.60. All fibers were impregnated with 934 epoxy resin and cured in accordance with processes developed especially for this application. The construction of each strut was a multiple lay-up of two types of graphite fibers. T50 fibers (two plies) were oriented parallel to the tube's longitudinal axis, while T300 fibers (one ply) were oriented at ±59° to that axis. The ring design had webs made of three plies of T300/934 fabric, each 0.013 in (0.33 mm) thick. The caps of the rings were multiple lay-ups of T50 fibers (two plies) at 0° and T300 fibers (one ply) at ±40°.

The development of the composite material design and manufacturing processes included analysis and experimental evaluation of CTE sensitivity to (1) resin content (found to be $0.019 \times 10^{-6}\ °\text{F}^{-1}$ per

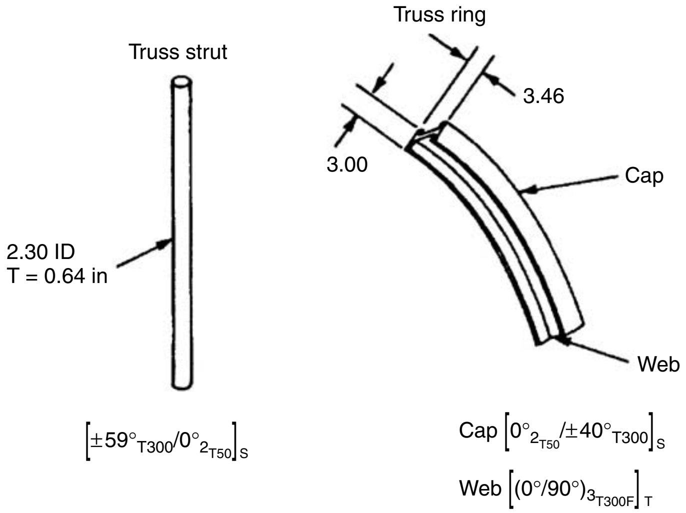
Truss strut
Truss ring
3.46
3.00
Cap
2.30 ID
T = 0.64 in
Web
$[\pm 59°_{T300}/0°_{2_{T50}}]_S$
Cap $[0°_{2_{T50}}/\pm 40°_{T300}]_S$
Web $[(0°/90°)_{3_{T300F}}]_T$

Item	Sizing	
	Geometry	Material
Struts	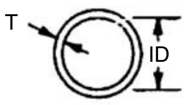 ID = 2.30 in T = 0.064 in A = 0.457 in^2 I = 0.332 in^4	Graphite/ epoxy
Rings	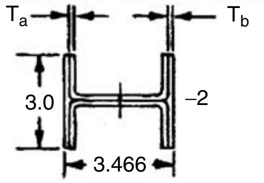 A = 0.899 in^2 I_1 = 1.909 in^4 I_2 = 0.463 in^4 T_a = 0.039 in T_b = 0.064 in	Graphite/ epoxy

FIGURE 14.60 Cross-sectional dimensions and hybrid fiber lay-up materials used in the Hubble Space Telescope metering truss structure. (From McMahan, L. L., Space Telescope Optical Telescope Assembly structural materials characterization, *Proceedings of AIIA/SPIE/OSA Technology Space Astronautics Conference: The Next 30 Years*, Danbury, CT, 1982.)

1% volume change of fiber or resin by analysis and 0.016×10^{-6} °F^{-1} by test), (2) ply orientation (found to be 0.019×10^{-6} °F^{-1} per angular degree by analysis and 0.012×10^{-6} °F^{-1} by test), and (3) cure and thermal cycling conditioning. The chosen process cured the material at a temperature of 270 °F (132 °C) and cycled it five times between −150 and +120 °F (−101 and +49 °C).

Mechanical properties tests on specimens indicated tensile strength and tensile modulus values compatible with predicted strength and stiffness requirements (~71,800 Ib/in.^{2} [500 Mpa] and 15×10^6 [1.0×10^5 MPa], respectively) for structural integrity. The effects of humidity were found not to materially affect either of these parameters. Microyield stress was also found to be in excess of 20,000 lb/in.^{2} (140 MPa); this is approximately 5000 lb/in.^{2} (30 MPa) above the allowable minimum value. Tests of the composites indicated that they met the vacuum outgassing requirements of 1.0% total weight loss and 0.1% vacuum-condensable materials established by NASA (McMahan, 1982).

McCarthy and Facey (1982) described how the CTE of each individual strut manufactured for use in the OTA metering truss was measured and the parts selectively placed after analysis in different bays of the truss to minimize the overall thermal distortion. For example, higher CTE struts were placed in the bay adjacent to the primary mirror where the operational temperature change would be the least (see Figure 14.61). Golden and Spear (1982) reported that all 52 struts manufactured had the required 0.25×10^{6} °F^{-1} CTE within the specified tolerance ($\pm 0.15 \times 10^{6}$ °F^{-1}).

Assembly verification tests were conducted to determine stiffness, vibrational mode characteristics, and thermal vacuum performance of the completed truss. Stiffness was well within design requirements. The primary frequency for rotation of the secondary mirror relative to the mounting interface at the primary mirror (predicted as 26.02 Hz) was measured as 25.96 Hz. Higher modes were also as predicted. Thermal performance values for despace, decenter, and tilt were approximately 50% smaller than the allowable tolerances stated earlier in this section. Accuracy of these measurements was ±2.5% or better. Wada and DesForges (1978) reported on other tests conducted on this truss by Boeing in which the structural damping was measured and found to be "fairly low" at all resonances. The significance of such structural damping was discussed by Richard (1990). Figure 14.62 shows the completed truss being installed into the OTA at the Perkin-Elmer Corporation facility in Danbury, CT.

Although it is recognized that this telescope represents a very special, high-precision and high-cost application, the material property development cited here provides one basis for generic application of advanced composites to other structural trusses, and a variety of applications in optical instruments and other devices requiring precision structures.

14.5.3.6 Athermalization of the Galaxy Evolution Explorer

NASA's Galaxy Evolution Explorer (GALEX) is an Earth-orbiting space telescope that will collect information on star formation by observing galaxies and stars in UV wavelengths. It was launched on April 23, 2003 on a Pegasus rocket.

As described by Ford et al. (2004), the GALEX payload consists of three major subsystems: Telescope, optical wheel assembly, and back focal assembly. They were integrated on a single structure called the telescope support plate. This plate mounts to a support base that interfaces to the spacecraft. The base supports electronics packages and a star tracker. Figure 14.63 shows these components.

The telescope is of the Cassegrain form. Its secondary mirror is supported by a composite spider that is connected to a hub passing through the center of the primary mirror. The primary mirror is supported from this hub. The hub is connected to the telescope support plate through three bipods.

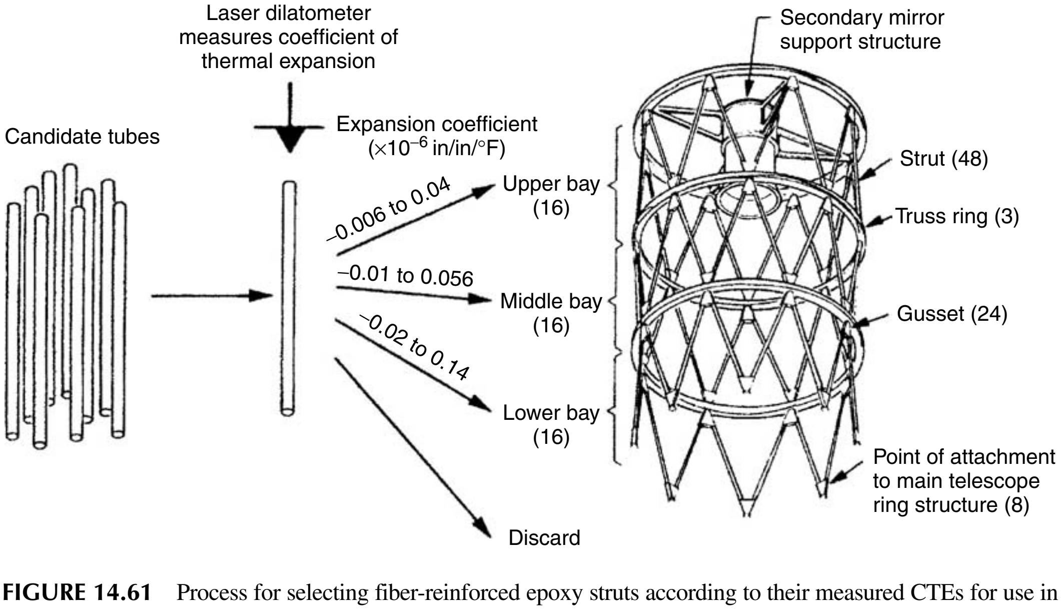
Laser dilatometer measures coefficient of thermal expansion
Candidate tubes
Expansion coefficient (×10⁻⁶ in/in/°F)
−0.006 to 0.04
Upper bay (16)
−0.01 to 0.056
Middle bay (16)
−0.02 to 0.14
Lower bay (16)
Discard
Secondary mirror support structure
Strut (48)
Truss ring (3)
Gusset (24)
Point of attachment to main telescope ring structure (8)

FIGURE 14.61 Process for selecting fiber-reinforced epoxy struts according to their measured CTEs for use in the Space Telescope metering truss structure. (From McCarthy, D.J. and Facey, T.A., *Proc. SPIE*, 330, 139, 1982.)

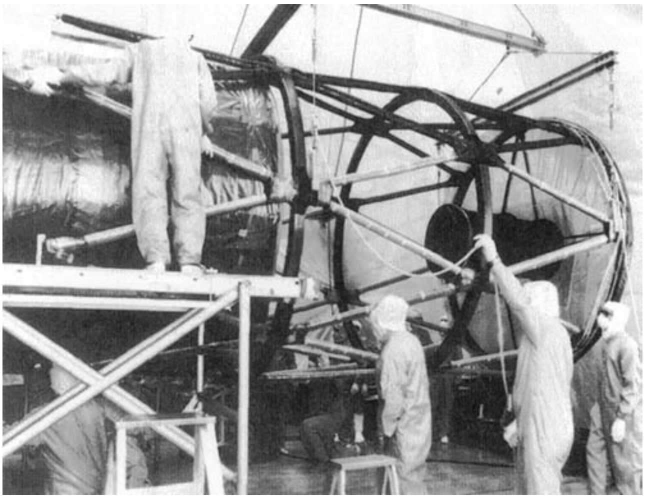

FIGURE 14.62 Photograph of the metering truss of the Hubble Space Telescope being assembled into the optical telescope assembly. The secondary mirror assembly and main telescope baffle (at left inside truss) are shown. (Courtesy of Goodrich Corporation, Danbury, CT.)

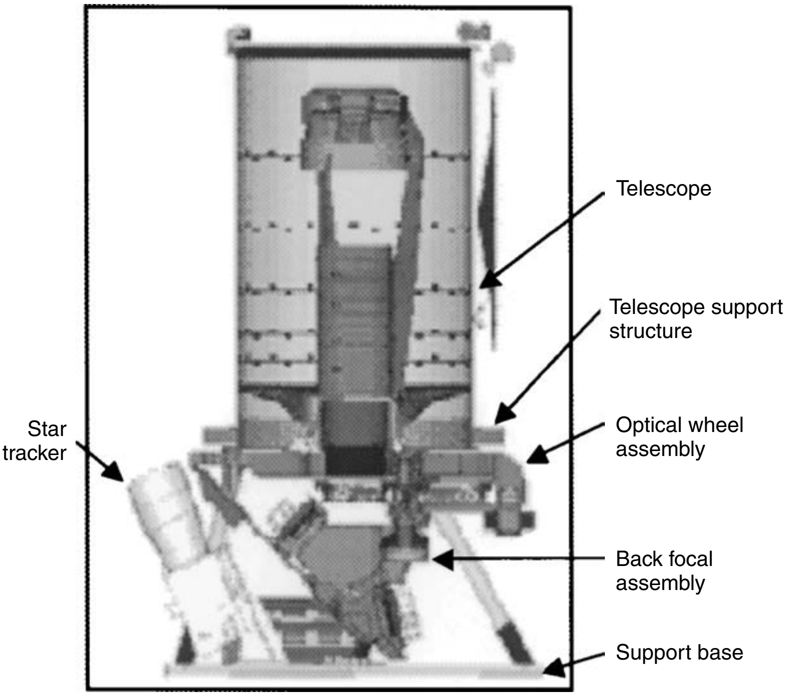
Telescope
Telescope support structure
Star tracker
Optical wheel assembly
Back focal assembly
Support base

FIGURE 14.63 Exterior view of the GALEX payload. (From Ford, V.G., Parks, R., and Coleman, M., *Proc. SPIE*, 5528, 171, 2004.)

The optical wheel assembly has a rotating plate that moves either a grism or an optical path compensating window into the image-forming beam. The grism consists of a prism with a diffraction grating, splits the light into wavebands for spectral data collection. The optical wheel assembly is attached directly to the telescope support plate.

The back focal assembly comprises the optical and electro-optical components shown in Figure 14.64. The beam from the telescope enters this assembly after it has passed through the optical

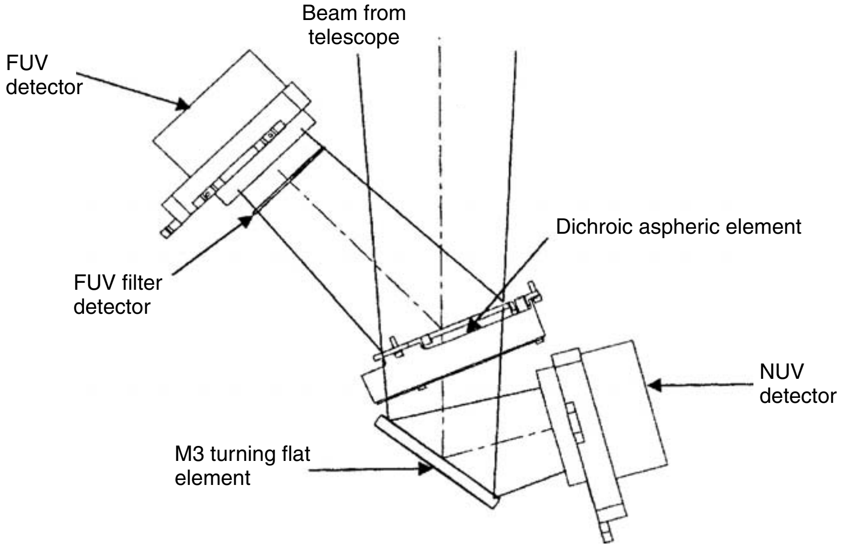
Beam from telescope
FUV detector
Dichroic aspheric element
FUV filter detector
NUV detector
M3 turning flat element

FIGURE 14.64 Components of the GALEX back focal assembly. (From Ford, V.G., Parks, R., and Coleman, M., *Proc. SPIE*, 5528, 171, 2004.)

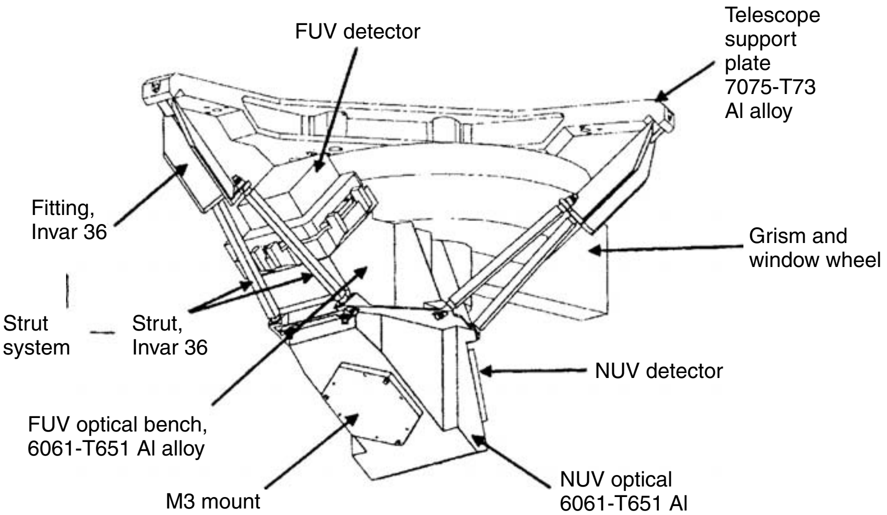
FUV detector
Telescope support plate 7075-T73 Al alloy
Fitting, Invar 36
Grism and window wheel
Strut system
Strut, Invar 36
NUV detector
FUV optical bench, 6061-T651 Al alloy
M3 mount
NUV optical 6061-T651 Al

FIGURE 14.65 Structural configuration of the GALEX back focal assembly. (From Ford, VG., Parks, R., and Coleman, M., *Proc. SPIE*, 5528, 171, 2004.)

wheel assembly. The beam encounters a slightly aspheric, dichroic beam splitter, which reflects the far-UV light toward the far-UV detector and transmits the near-UV light toward a flat mirror and thence into the near-UV detector. The structure supporting this assembly uses a passive technique to compensate for thermally induced changes in image distance (back focal length) of the optical system. Ford et al. (2004) described this thermal compensation design as follows.

The thermal requirement driving the athermalization design was that the system should stay in focus from room temperature alignment to flight operational temperatures. It was specified that the telescope and back focal assembly should operate between −15 to +25°C. To maintain focus, the back focal assembly was supported from the telescope support plate on three identical bipod subassemblies as indicated in Figure 14.65. Each bipod leg was designed as two main parts in series to allow different materials to be used in its construction as a means for tuning total length change with temperature if necessary. Spherical washers were provided at both ends of each strut to minimize transfer of moments. The struts were attached symmetrically to the telescope support plate. Thermal analysis showed that Invar 36 could be used for all parts of the struts.

The support structure (see Figure 14.66) has the following as variable parameters: R, the radius of strut attachment to the telescope support plate; r, the radius of strut attachment to the back focal assembly; and the lengths of the struts (required to be equal). Given the choices of materials indicated in Figure 14.65, these lengths were determined by successive approximations to minimize the change in focus length Z with temperature and thus maintain required optical performance of the payload. The result was an inexpensive, workable design that fully considered on-orbit thermal environment predictions. Flight performance has demonstrated that the athermalization system works as predicted.

14.5.4 ATHERMALIZATION OF REFRACTING OPTICAL SYSTEMS

Refractive and catadioptric systems present more complex athermalization problems than all-reflecting systems because of refractive index variations that occur along with dimensional variations within structural and transmissive materials when the temperature changes. Because the traditional approach is to establish an optical design with minimal adverse effects of temperature changes and then to design a mechanical structure that compensates the residual thermal effects, we include this technology with our considerations of structural designs. The treatment here is a first-order approximation to the athermalization design task. It is intended to show an approach and is not a detailed design procedure.

Key parameters here are the CTEs of all materials and the optical material's refractive indices n_G, and the rate of change of those indices with temperature. Unless the surrounding medium is a vacuum, the variation with temperature of the refractive index of that medium (usually air) must be considered. To separate these refractive variations, the absolute index for glass $n_{G,ABS}$ is obtained

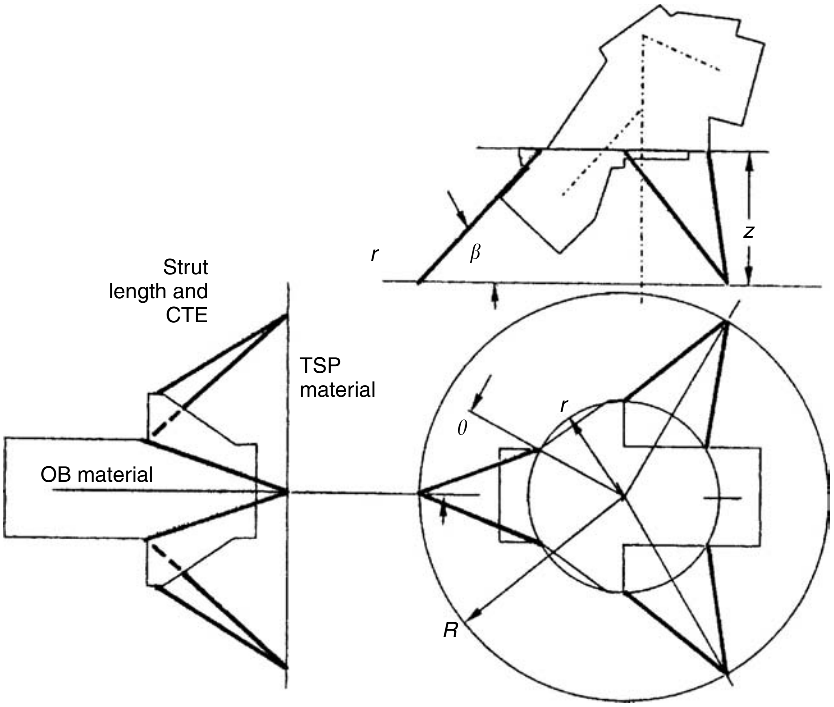

FIGURE 14.66 Geometry of the athermalization system for the GALEX back focal assembly. (From Ford, V.J., Parks, R., and Coleman, M., *Proc. SPIE*, 5528, 171, 2004.)

from the $n_{G,REL}$ value relative to air as listed in glass catalogs at a given temperature and wavelength using the following equation:

$$n_{G,ABS} = (n_{G,REL})(n_{AIR}) \tag{14.1}$$

where n_{AIR} at 15°C is calculated from an equation due to Edlen (1953) as follows:

$$(n_{AIR,15} - 1) \times 10^8 = 6432.8 + \frac{2{,}949{,}810}{146-(1/\lambda)^2} + \frac{25{,}540}{41-(1/\lambda)^2} \tag{14.2}$$

and λ is in micrometers.

The index of air varies with temperature at a rate derived from the following equation for n_{AIR} from Penndorf (1957):

$$\mathrm{d}n_{AIR}/\mathrm{d}T = (-0.003861)(n_{AIR,15} - 1)/(1 + 0.00366T)^2 \tag{14.3}$$

where T is expressed in °C. At 20°C, $\mathrm{d}n_{AIR}/\mathrm{d}T$ and $(n_{AIR} - 1)$ have the values at selected wavelengths shown in Table 14.3.

Jamieson (1992) has defined the following expression for the change in focal length of a thin, single-element lens with a change in temperature:

$$\Delta f = -\delta_G f \Delta T \tag{14.4}$$

where f is the lens focal length in air at a given wavelength and temperature and δ_G is the glass coefficient of thermal defocus given by

$$\delta_G = [\beta_G/(n_G - 1)] - \alpha_G \tag{14.5}$$

$$\beta_G = dn_G/dT \tag{14.6}$$

Equation (14.4) has the same form as the temperature variation of a length L of a material with a CTE of α, which is $\Delta L = \alpha L \Delta T$. The parameter δ_G depends only on physical properties and wavelength. Some authors refer to it as the "thermo-optic coefficient" for the glass. The value of α_G is positive for all refracting materials. For optical glasses, it ranges from ~3.2×10^{-5} to ~2.2×10^{-5}. Those glasses with small δ_G values are those for which the increase in focal length due to

TABLE 14.3
Values for dn_{AIR}/dT and $(n_{AIR}-1)$ for Various Wavelengths at a Temperature of 20°C

Wavelength (nm)	dn_{AIR}/dT	$(n_{AIR}-1)$
400	-9.478×10^{-7}	2.780×10^{-4}
550	-9.313×10^{-7}	2.732×10^{-4}
700	-9.245×10^{-7}	2.712×10^{-4}
850	-9.211×10^{-7}	2.701×10^{-4}
1000	-9.190×10^{-7}	2.696×10^{-4}

Source: Adapted from Yoder, P.R. Jr., *Mounting Optics in Optical Instruments*, SPIE Press, Bellingham, 2002a.

rising temperature and the resultant expansion of surface radii is nearly balanced by a corresponding decrease because of a reduced index of refraction. The δ_G values for optical plastics and IR materials are more extreme than those of optical glasses. Jamieson (1992) listed δ_G values for 185 Schott glasses, 14 IR crystals, four plastics, and four index-matching liquids. These are given in Table 3.12.

Consider a thin singlet lens having a positive value for δ_G and focal length f mounted as shown in Figure 14.67 in a simple (uncompensated) barrel made of a metal with a CTE = α_M and length $L = f$. A change in temperature $+\Delta T$ will lengthen the barrel by $\alpha_M L\Delta T = f\Delta T$. At the same time, the lens focal length will lengthen by $\delta_G f\Delta T$. If the materials could be chosen so $\alpha_M = \delta_G$, the system would be athermal and the image would remain at the end of the barrel at all temperatures. If $\alpha_M \neq \delta_G$, temperature changes will cause defocus. Choosing materials for this system that have nearly the same CTEs does not necessarily make them athermal.

We illustrate the defocus that occurs in a simple, uncompensated, thin-lens system as follows. Assume that a thin BK7 lens with $f = 100$ mm (3.937 in.) is mounted in (a) a 6061 aluminum or (b) a 416 stainless-steel barrel configured as shown in Figure 14.67. Let the temperature change by +40°C (+72°F). What is the defocus for each metal? From Table 3.18, $\alpha_{Al} = 23.6 \times 10^{-6}$ °C^{-1} (13.1×10^{-6} °F^{-1}) and $\alpha_{CRES} = 9.9 \times 10^{-6}$ °C^{-1} (5.5×10^{-6} °F^{-1}). Then, $\Delta L_{AL} = (23.6 \times 10^{-6})(100)(40) = 0.0944$ mm (0.0037 in.) and $\Delta L_{CRES} = (8.5 \times 10^{-6})$ (100)(40) = 0.0396 mm (0.0016 in.). From Table 3.12, δ_G for BK7 glass = 2.41×10^{-6} °F^{-1} (4.33×10^{-6} °C^{-1}). Then, from Eq. (14.4), $\Delta f = (4.33 \times 10^{-6})(100)(40) = 0.0174$ mm (0.0006 in.). Hence, defocus$_{AL}$ = 0.0944 − 0.0174 = 0.0770 mm (0.0030 in.) and defocus$_{CRES}$ = 0.0396 − 0.0174 = 0.0222 mm (0.0008 in.). The advantage of the lower CTE of the steel material for this application is apparent.

Jamieson (1992) explained how, under isothermal conditions, to determine the values for δ_G and the change in focal length Δf of a thin doublet and a thin, achromatic doublet. His equation for δ_G for the thin doublet case is:

$$\delta_{G\,DBLT} = (f/f_1)(\delta_{G1}) + (f/f_2)(\delta_{G2}) \tag{14.7}$$

where f is the focal length of the doublet, f_1 and f_2 the focal lengths of the elements, and δ_{G1} and δ_{G2} the coefficients of thermal defocus of the elements. Once $\delta_{G\,DBLT}$ is known, Δf can be calculated from Eq. (14.4).

Jamieson's equation for δ_G for the thin achromatic doublet case is

$$\delta_{G\,ACH\,DBLT} = (v_{G1}\delta_{G1} - v_{G2}\delta_{G2})/(v_{G1} - v_{G2}) \tag{14.8}$$

where v_{G1} and v_{G2} are the Abbe numbers for the elements and the other terms are as previously defined.

One means for athermalizing thick-lens systems is to design the lenses for the required image quality and, through proper choice of glasses, as independent of temperature as possible when properly focused. We then design a mount from multiple materials combining different CTEs so as to make the

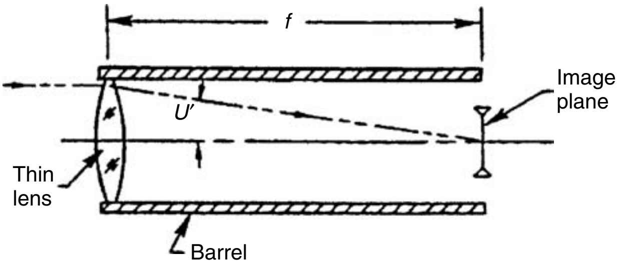

FIGURE 14.67 Schematic of a thermally uncompensated single thin lens and simple mount. (From Yoder, P.R., Jr., *Mounting Optics in Optical Instruments*, SPIE Press, Bellingham, 2002.)

change in key dimensions of the mount equal to the change in back focal length (i.e., image distance). Structures based on the design principles of Figure 14.68 can create positive or negative changes in overall length from specific lengths of different materials such as Invar, aluminum, titanium, stainless steel, composites (typically graphite epoxy), fiberglass, or plastics (such as Teflon, Nylon, or Delrin).

Vukobratovich (1993) gave equations (here slightly rewritten) for the design of these dual-material structures to thermally compensate an optical system with a coefficient of thermal defocus δ_G, CTEs α_1 and α_2, and focal length f:

$$\delta_G f = \alpha_1 L_1 + \alpha_2 L_2 \tag{14.9}$$

$$L_1 = f - L_2 \tag{14.10}$$

$$L_2 = f(\alpha_1 - \delta_G)/(\alpha_1 - \alpha_2) \tag{14.11}$$

where the geometric parameters are as defined in Figure 14.68.

Yoder (2002) gave the following example of a closely air-spaced thin lens achromat with $f_1 = 60$ mm (2.362 in.), $f_2 = -150$ mm (-5.905 in.), and axial separation $d = 0$. Lens 1 is made of BK7 glass while Lens 2 is made of SF2 glass. The effective focal length f of the combination $= f_1 f_2 /(f_1 + f_2 - d) = 100$ mm (3.937 in.). The lenses are mounted in a barrel of the reentrant type shown in Figure 14.68(a) made of Invar 36 and 6061 aluminum with $\alpha_1 = 1.26 \times 10^{-6}$ °C^{-1} and $\alpha_2 = 23.6 \times 10^{-6}$ °C^{-1}, respectively. The appropriate lengths L_1 and L_2 are calculated in the following manner. From Table 3.12, δ_{G1} (BK7) $= -4.33 \times 10^{-6}$ °C^{-1} and δ_{G2}/(SF2) $= -3.33 \times 10^{-6}$ °C^{-1}. From Eq. (14.8), $\delta_G = (100/60)(-4.33 \times 10^{-6}) + (100/-150)(-3.33 \times 10^{-6}) = -4.997 \times 10^{-6}$ °C^{-1}. From Eq. (14.9), $L_2 = (100)[1.26 \times 10^{-6} - (-4.997 \times 10^{-6})]/(1.26 \times 10^{-6} - 23.6 \times 10^{-6}) = -28.008$ mm (-1.103 in.). From Eq. (14.10), $L_1 = 100 - (-28.008) = 128.008$ mm (5.040 in.). The changes in the two tube lengths, the net changes in the barrel length, and the change in the lens's focal length for a 20°C temperature change are $\Delta L_1 = \alpha_1 L_1 \Delta T = (1.26 \times 10^{-6})(128.008)(20) = 0.0032$ mm (0.0001 in.). $\Delta L_2 = \alpha_2 L_2 \Delta T = (23.6 \times 10^{-6})(-28.008)(20) = -0.0132$ mm (0.0005 in.). The total change in barrel length $= \Delta L = \Delta L_1 + \Delta L_2 = -0.0100$ mm (-0.0004 in.). The change in focal length $= \Delta f = \delta_G f \Delta T = (-4.997 \times 10^{-6})(100)(20) = -0.0100$ mm (-0.0004 in.). Since $\Delta L = \Delta f$, the image is at the proper location after the temperature change and the design is athermal.

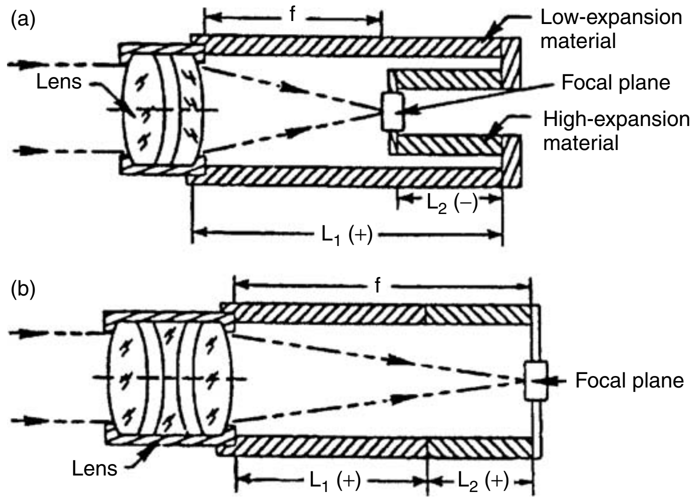

FIGURE 14.68 Schematic diagrams of simple dual-material mounts that athermalize focus of lenses. (From Vukobratovich, D., SPIE Short Course SC014, 1993. With permission.)

Modern lens design programs, such as Code V,[‡] are capable of athermalization with little intervention by the designer. The programs include thermal modeling features and stored thermal-mechanical properties of a variety of commonly used optical and mechanical materials (including mirror materials). The nominal design is typically known at a specific design temperature such as 20°C. According to Yoder (2002), the athermalization design process generally involves (1) calculation of the refractive index of air at the desired extreme high and low temperatures, (2) conversion of the catalog values for refractive indices relative to air into absolute values by multiplying them by the air index, (3) calculation of the absolute glass refractive indices at the extreme temperatures using the *dn*/*dT* values from the manufacturer's data, (4) calculation of the surface radii at the extreme temperatures using the known CTEs and dimensions of the optical materials, (5) calculation of the air spaces and component thicknesses at the extreme temperatures using the known CTEs and dimensions of the mechanical and optical materials, (6) evaluation of the system's performance at the best focus locations for the extreme temperatures, (7) design of the mechanical structure and mechanisms as needed to adjust selected component spacings or to bring the image to the proper location at each extreme temperature, and, finally, (8) assessment of the compensated system's performance at the extreme temperatures. Presumably, if the opto-mechanical design is proper, the performance degradation that is due to the specified temperature changes will be acceptable.

A detailed example of the opto-mechanical design of an athermalized aerial camera lens was given by Friedman (1981). Comprehensive summaries of mechanisms that have been used to varying degrees of success in providing component motions for athermalization purposes were given by Povey (1986), Rogers (1990), and Ford et al. (1999). The approach for focus compensation described in the latter paper was summarized in Section 14.5.3.3. As discussed in Section 14.5.2, zoom lenses that require the movement of components to achieve focal-length changes can also incorporate thermal compensation of image quality and focus as small adjustments in the locations of those components in response to temperature changes.

14.6. GEOMETRIES FOR TELESCOPE TUBE STRUCTURES

14.6.1 THE SERRURIER TRUSS

Figure 14.58 shows one example of a tube truss structure typically used to support the primary and secondary mirrors of an astronomical telescope from a "box" structure located at the elevation axis of the telescope mount. Basically, trusses of triangular members project forward and backward from the box to ring-shaped members at the outer and inner ends of the telescope. Although built to different scales and proportions, this structure and those of many other telescopes are based on the principles established by Serrurier (1938) for the structure of the telescope tube in the 200 in. (5 m) Hale Telescope on Mt. Palomar. Figure 14.69(a) shows a schematic isometric view of that structure, whereas Figure 14.69(b) illustrates it in a schematic side view. In the ideal case, points A and B of view (b) deflect under gravitational load normal to the axis of the tube (line AB) by equal amounts (d_A and d_B) if the diagonal struts have the proper cross-sectional dimensions. Mathematically, with AB horizontal,

$$\begin{aligned} d_A &= \left(\frac{P_A b}{4Ea_A}\right)\left[\left(\frac{4L_A^2}{b^2}\right)+1\right]^{3/2} \\ &= d_B = \left(\frac{P_B b}{4Ea_B}\right)\left[\left(\frac{4L_B^2}{b^2}\right)+1\right]^{3/2} \end{aligned} \qquad (14.12)$$

[‡] Code V is a product of Optical Research Associates, Pasadena, CA.

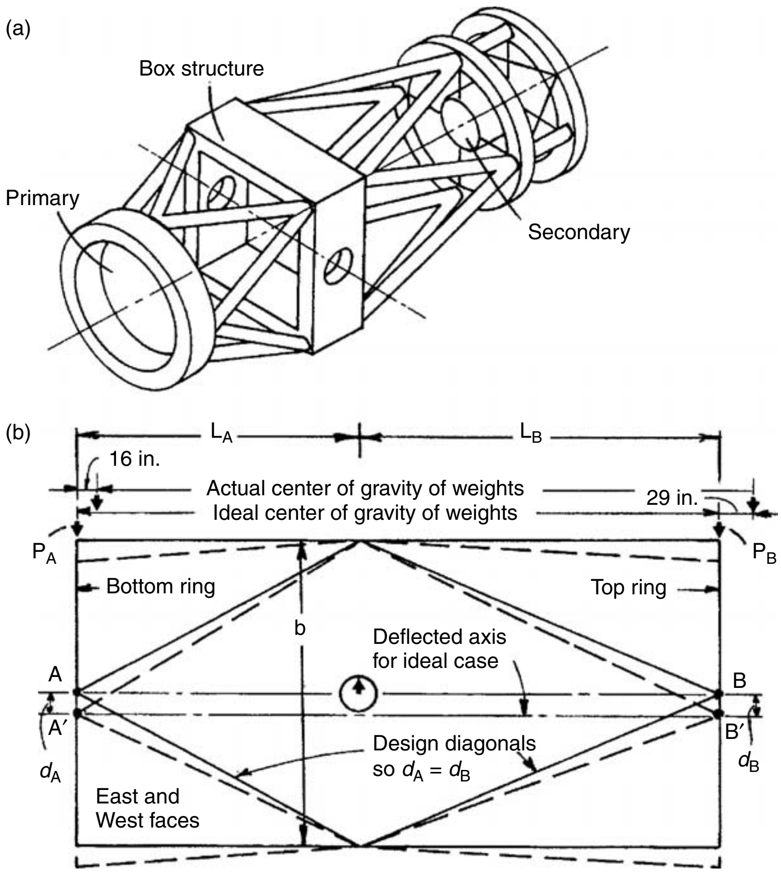
(a)
Box structure
Primary
Secondary
(b)
L_A
L_B
16 in.
Actual center of gravity of weights
Ideal center of gravity of weights
29 in.
P_A
P_B
Bottom ring
Top ring
b
Deflected axis
for ideal case
A
B
A′
B′
d_A
d_B
Design diagonals
so d_A = d_B
East and
West faces

FIGURE 14.69 Geometry of the truss structure designed by Serrurier for the Hale Telescope: (a) isomeric view, (b) side elevation view. (Adapted from Serrurier, M., *Civil Eng*., 8, 524, 1938.)

where P is the applied load at A or B, b the height of the box structure, E Young's modulus, a the cross-sectional areas of the truss struts supporting A or B, and L the cantilevered length of the structure at A or B. Ideally, the loads should be applied at the vertices of the isosceles triangles forming the truss, but generally, additional structures are placed there to support the primary and secondary mirrors, so corrections must be applied. Relationship (14.12) holds at all elevations of the telescope axis if a cosine elevation-angle factor is added to both sides of the equation. The vertical deflection obviously reduces to zero at the zenith.

A top view of the square-based Serrurier truss appears essentially the same as the side view of Figure 14.69(b), and Eq. (14.12) can be made to apply with regard to sideways deflections by adjusting the strut areas appropriately. The lengths of the struts in the top and bottom faces remain constant, so the end rings remain parallel at all orientations of the tube relative to gravity. This is highly desirable to maintain alignment of the mirrors.

The classical Serrurier truss is not a complete solution to all gravity deflection problems in telescope structures because (1) stiffness-to-weight of that truss is lower than that of other types of trusses (Meinel and Meinel, 1986), (2) a multiple-bay truss is stiffer than a Serrurier truss of the same weight when the ratio of truss length to width exceeds about 1.4 (Lubliner, 1981), and (3) low fundamental frequencies of a low-stiffness Serrurier truss (typically about 4 to 5 Hz) may lead to vibration effects (Thomas et al., 1987).

To reduce the severity of these problems for one specific instrument, Doyle and Vukobratovich (1992) developed a design for a modified Serrurier truss for a Gregorian-type beam-reducing telescope to be used with an interferometer and siderostat in a ground-based astrometric application. The telescope comprised a 30-in.-diameter *f*/2.7 primary mirror and a 4.6-in.-diameter secondary mirror separated axially by 92 in. This system reduced (or collapsed) the beam diameter by a ratio of 6.5:1. The truss was to maintain mirror separation to 2μm, centration to 25μm, and tilts of the primary and secondary mirrors to within 3 arcsec, and 6 arcsec, respectively, under gravity (at 10° static elevation) and wind loading, thermal loads, and earthquake effects. The fundamental frequency was to be $>$10 Hz.

To meet these requirements, those authors developed a set of closed-form equations for the truss sectional areas and the mirror deflections with axis horizontal. These led to a preliminary mechanical design. The truss strut areas were found to closely correspond to those of standard pipe sizes so those sizes were adopted. An FEA model of the telescope then revealed that additional braces centrally located at the top and bottom of the primary were needed to correct a slight mirror tilt resulting from the 10° inclination. A slight defocus was also noted. This would easily be corrected at installation. With these modifications, the design met all static requirements at nominal temperature. The fundamental frequency was well above the specified value, and stresses under reasonable earthquake loading were tolerable. Thermal analyses with unit temperature gradients along each axis and a 20°C temperature soak indicated defocus exceeding tolerance. With the addition of metering rods between the mirrors, this error could be eliminated. The design was then judged to be acceptable. Figure 14.70 shows the configuration.

The success of the design effort reported by Doyle and Vukobratovich (1992) indicates that with careful and thorough analysis, and minor design modifications to optimize performance, a Serrurier truss can be successfully employed in a variety of telescope applications.

14.6.2 THE NEW MULTIPLE-MIRROR TELESCOPE

During redesign of the MMT to replace the array of six primary mirrors with a single 6.5-m (256.5-in.)-diameter *f*/1.25 spin-cast mirror, various forms of forward truss structures were evaluated. The two forms most seriously considered are shown in Figure 14.71. In view (a), we see a cross-braced truss (designated XBT) while in view (b) we see an inverted Serrurier truss (designated IST). In all cases, the design task was made more complex by a requirement that a vacuum chamber be attached to the front of the mirror cell periodically to allow the mirror to be realuminized in place.

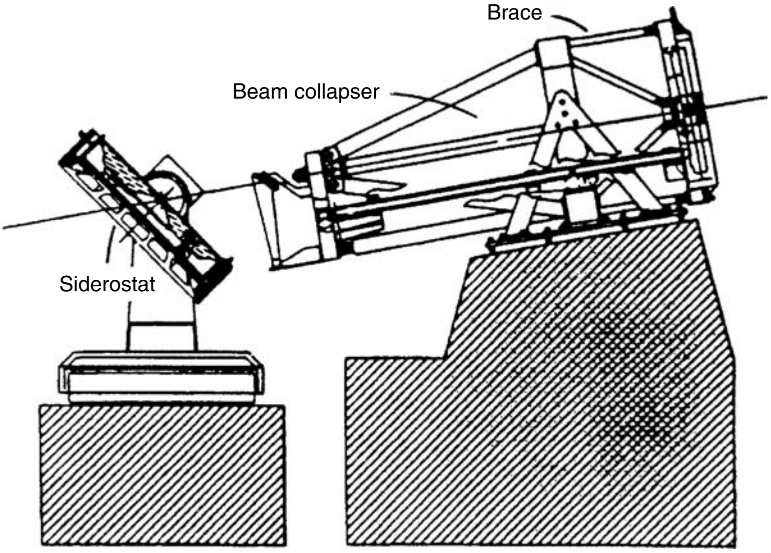

FIGURE 14.70 Configuration of a modified Serrurier truss-mounted beam reducer telescope and siderostat for use with an interferometer for astrometric applications. (From Doyle, K. and Vukobratovich, D., *Proc. SPIE*, 1690, 357, 1992.)

Antebi et al. (1998) described these alternatives as follows. In the XBT, the struts attach to the extreme corners of the trunnion beam that supports the primary mirror cell (see sectional view in Figure 14.72)* to create the widest possible base on each truss face. This maximizes stiffness. It was noted that the tilt of the forward frame from gravity loading could be controlled passively by

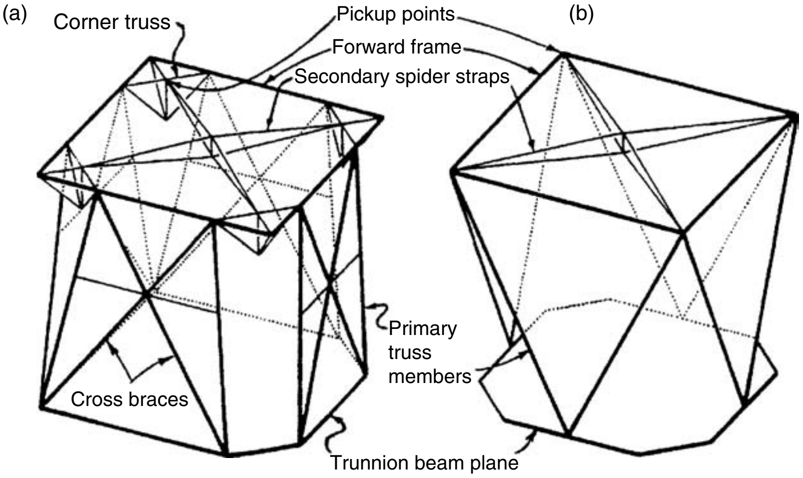
(a)
Corner truss
Pickup points
Forward frame
Secondary spider straps
(b)
Primary truss members
Cross braces
Trunnion beam plane

FIGURE 14.71 Candidate forward truss configurations for the modified MMT with 6.5 m single primary mirror: (a) cross-braced truss (XBT), (b) inverted Serrurier truss (IST). (From Antebi, J., Dusenberry, D.O., and Liepins, A.A., *Proc. SPIE*, 1303, 148, 1990.)

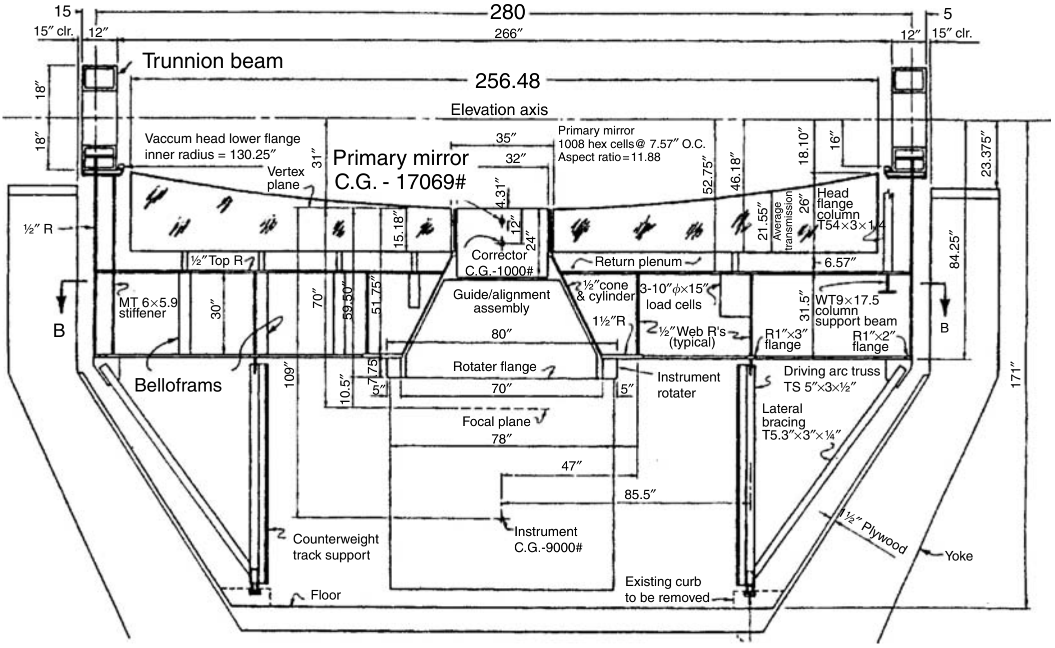
15
15″ clr.
12″
280
266″
12″
5
15″ clr.
Trunnion beam
256.48
18″
18″
Elevation axis
Vaccum head lower flange
inner radius = 130.25″
31″
Primary mirror
C.G. - 17069#
Vertex plane
35″
32″
Primary mirror
1008 hex cells@ 7.57″ O.C.
Aspect ratio = 11.88
52.75″
46.18″
18.10″
16″
23.375″
4.31″
12″
24″
15.18″
21.55″
Average transmission
26″
Head flange column
T54×3×1/4
½″ R
½″Top R
Corrector
C.G.-1000#
Return plenum
6.57″
84.25″
MT 6×5.9 stiffener
30″
70″
59.50″
51.75″
Guide/alignment assembly
½″cone & cylinder
3-10″ϕ×15″ load cells
31.5″
WT9×17.5 column support beam
B
B
1½″R
80″
½″Web R's (typical)
R1″×3″ flange
R1″×2″ flange
Bellofram
109″
10.5″
7.75
5″
Rotater flange
70″
5″
Instrument rotater
Driving arc truss
TS 5″×3×½″
171″
Focal plane
78″
Lateral bracing
T5.3″×3″×¼″
47″
85.5″
½″ Plywood
Counterweight track support
Instrument
C.G.-9000#
Yoke
Existing curb to be removed
Floor

FIGURE 14.72 Schematic diagram of the 6.5 m primary mirror for the new MMT as it would be mounted in its cell. Dimensions are in inches. (From Antebi, J., Dusenberry, D.O., and Liepins, A.A., *Proc. SPIE*, 1303, 148, 1990.)

---

[*] This figure duplicates Fig. 12.31 and is shown here for convenience of the reader.

varying the ratio of the truss members. Short corner trusses provide convenient pick-up points for the secondary mirror spiders. These "hard" point locations allow the spider legs to be shorter, and the inclination of those legs would be smaller than would result with the IST truss configuration. This tends to increase the efficiency of the spider support of the XBT design as compared with the IST design. In the IST, the struts extend from the corners of the forward frame to the centers of the trunnion beam. This allows the latter as well as the primary mirror cell to be circular, and facilitates design and attachment of the vacuum chamber. The feature inherent in the Serrurier truss design that stiffness is equal in all directions is not as important here since the telescope is on an altitude-over-azimuth mount. This feature would be important if a more conventional equatorial telescope mount were used.

As reported by Antebi et al. (1998), the final design of the new MMT combines good features of both the XBT and IST configurations. It is shown in Figure 14.73. It is a cross braced inverted Serrurier truss made of 30-in. (76.2-cm)-diameter steel pipes with 0.5-in. (1.27-cm)-thick walls. Eight "hard" points are provided on corner trusses on the front frame as in the XBT. For recoating the primary, portions of two forward truss struts are removed and the affected spider members are moved to stowed positions. The vacuum chamber head can then be lowered into the cavity within the truss and attached to the mirror cell (see Figure 14.74). All joints disturbed for recoating are designed to be reassembled in repeatable fashion. These joints are preloaded when attached to maintain stiffness.

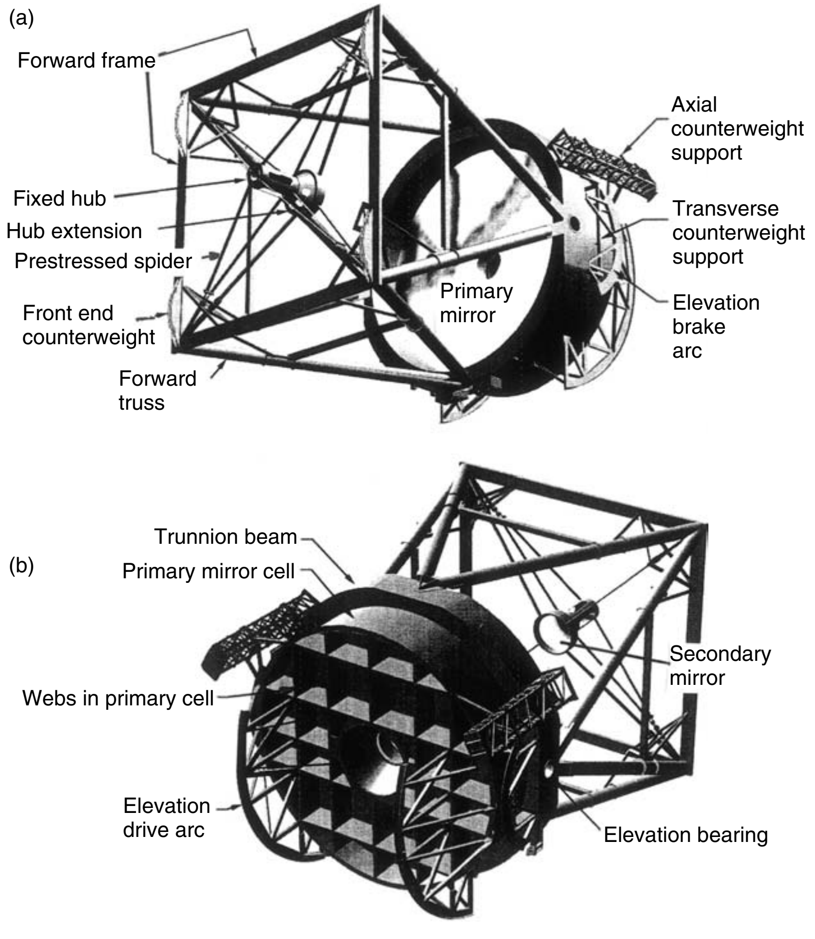
(a)
Forward frame
Fixed hub
Hub extension
Prestressed spider
Front end counterweight
Forward truss
Primary mirror
Axial counterweight support
Transverse counterweight support
Elevation brake arc
(b)
Trunnion beam
Primary mirror cell
Webs in primary cell
Elevation drive arc
Secondary mirror
Elevation bearing

FIGURE 14.73 (a) Front view of the optics support structure of the new MMT. (b) Rear view of the structure. (From Antebi, J., Dusenberry, D.O., and Liepins, A.A., *Proc. SPIE*, 3352, 513, 1998.)

14.6.3 THE *N*-TIERED TRUSS

Multiple tiers of trusses can and have been designed and used successfully for telescope tubes. The metering truss of the HST discussed in detail in Section 14.5.3.5 is an example. Lubliner (1981) showed that when member areas are optimized, an *N*-tiered structure of the general type shown in Figure 14.75 has the highest stiffness for given weight and is superior to a simple triangular structure if

$$[N(N-1)]^{1/2} < 1/b < [N(N+1)]^{1/2} \tag{14.13}$$

This type of design with $N = 2$ was used in the structures of the Keck telescopes. It was adapted to accommodate the hexagonal shape of the mount for the 10 m (32.8 ft) aperture primary. That structure (except for the secondary spider) was made of steel pipe with cross-sectional areas chosen as a compromise between total weight and gravitational deflection using pipe of standard, commercially available dimensions.

14.6.4 THE CHANDRA TELESCOPE

Composites are attractive materials for use in many other structural applications (such as trusses, masts, large reflector supporting frames, and housings and optical benches for instruments) and have been the subject of considerable research and development in recent years. Numerous

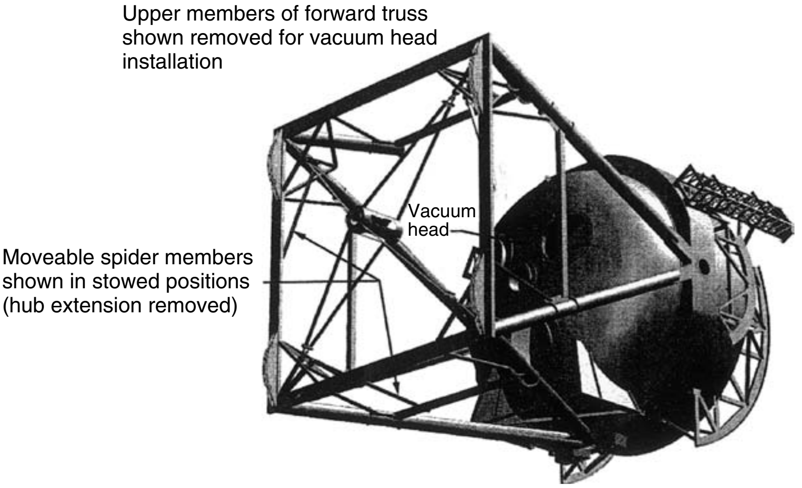
Upper members of forward truss shown removed for vacuum head installation
Vacuum head
Moveable spider members shown in stowed positions (hub extension removed)

FIGURE 14.74 Sketch showing the MMT optics structure adapted to allow realuminizing of the primary mirror in place. (From Antebi, J., Dusenberry, D.O., and Liepins, A.A., *Proc. SPIE*, 3352, 513, 1998.)

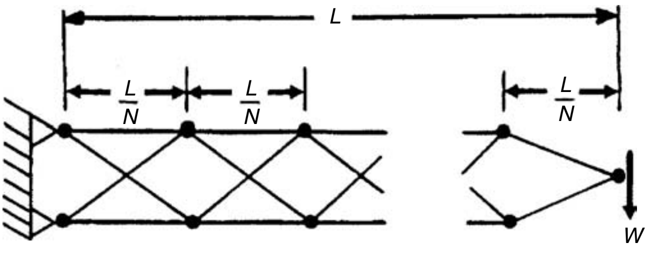

FIGURE 14.75 Geometry of a *N*-tiered truss supporting a load W as might be used in an astronomical telescope tube. (Adapted from Lubliner, J., *Keck Observatory Report 50.*, Univ. of California, Berkeley, 1981.)

publications discuss their advantages and disadvantages in optical instrumentation applications. The in-plane coefficient of thermal expansion of manufactured samples can be tailored for a particular application. As mentioned in conjunction with the HST truss, a potential disadvantage is the susceptibility of most composites to dimensional change with moisture content. Telkamp and Derby (1990), Bruner et al. (1990), Krumweide (1991) and Zweben (2002) have discussed this and some other important sources of macro- and microdimensional instabilities in these materials. Moisture barriers have proven effective. In spite of the potential problems, composites are seriously considered when weight limitations and needs for stiffness and dimensional stability under varying temperatures impose severe design constraints. Zweben (2002) listed mechanical properties of a variety of composite materials.

The preliminary configuration for the optical bench (OB) structure of the Chandra x-ray telescope was a multiple-tier truss as shown in Figure 14.76. Multiple trusses of different configurations were to be employed to accommodate the various modules and attachments, and to retain alignment of the high-resolution mirror assembly (HRMA) and the detectors in the aft-end science instrument package during many phases of manufacture, assembly, test, and shipment on Earth before reaching orbit (see Cohen et al., 1990).

The OB structure actually used in the telescope is a 26-ft (7.92-m)-long truncated conical composite tube (Olds and Reese, 1998). It is shown in Figure 14.77. Its application in Chandra is as shown in Figure 14.78. The OB is made of laminated M60J graphite-reinforced fiber and 954-3 cyanate ester resin. Parts are bonded with Hysol EA9330.3 room temperature curing two-part epoxy. Characteristics of the laminate material are listed in Table 14.4. The same materials are used in six 2.7-in. (6.86-cm)-diameter composite struts that support the HRMA from the OB. Titanium fittings bonded into both ends of the struts enable them to carry the imposed loads.

The OB cone was fabricated from three full-length 120° composite panels spliced together lengthwise as shown in Figure 14.77. These are constructed as thin inner and outer face sheets separated by a 0.31-in. (7.9-mm)-thick aluminum honeycomb core. Thicknesses of the face sheets vary as indicated in the latter figure. Axial stiffness of the structure was obtained by angling the layers as given in Table 14.4. The face sheets have negative CTEs that compensate for the positive CTEs of the core and adhesive. Six titanium 6Al-4V fittings tie the OB forward bulkhead to the

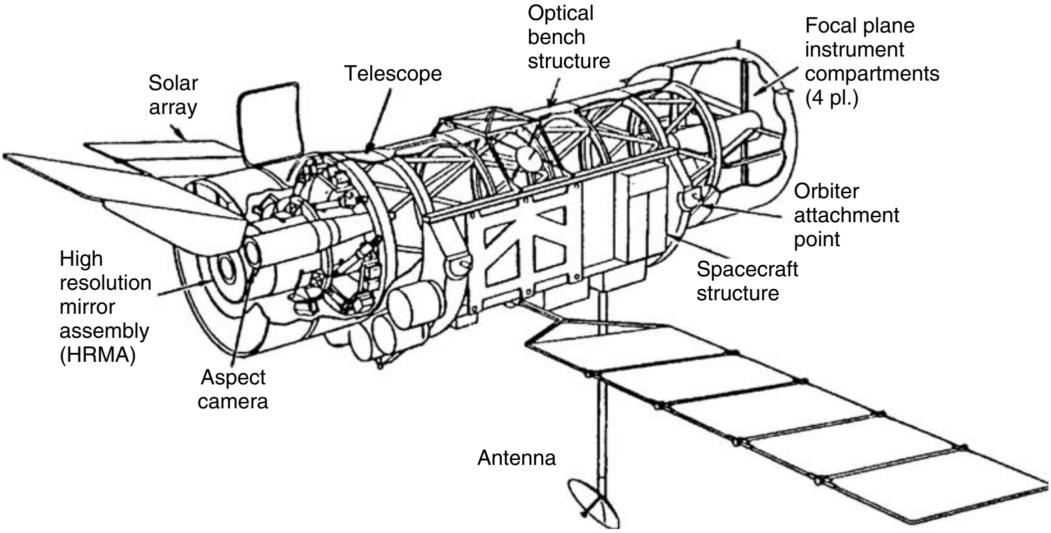

FIGURE 14.76 Early configuration of the AXAF (now Chandra) X-ray observatory showing a preliminary design using a multitiered truss to connect the high-resolution mirror assembly of cylindrical mirrors (HRMA) to the focal plane instruments. (From Spina, J.A., *Proc. SPIE*, 1113, 2, 1989.)

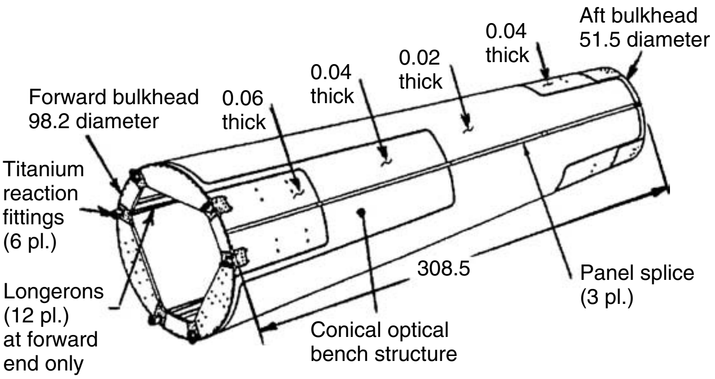
Aft bulkhead
51.5 diameter
0.04
thick
0.02
thick
0.04
thick
Forward bulkhead
98.2 diameter
0.06
thick
Titanium
reaction
fittings
(6 pl.)
Longerons
(12 pl.)
at forward
end only
308.5
Panel splice
(3 pl.)
Conical optical
bench structure

FIGURE 14.77 Configuration of the composite conical optical bench as used in the Chandra telescope. Dimensions are in inches. (From Olds, C.R. and Reese, R.P., *Proc. SPIE*, 3356, 910, 1998.)

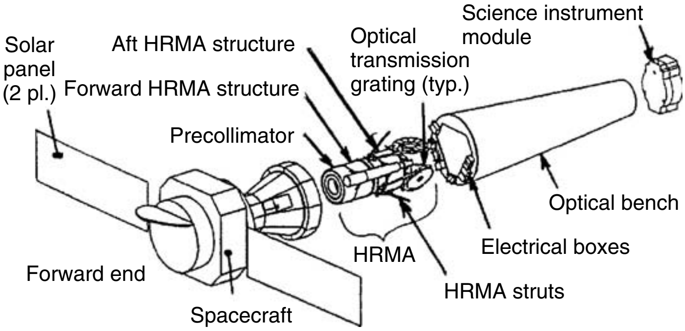
Solar
panel
(2 pl.)
Aft HRMA structure
Forward HRMA structure
Precollimator
Optical
transmission
grating (typ.)
Science instrument
module
Optical bench
Electrical boxes
HRMA
HRMA struts
Forward end
Spacecraft

FIGURE 14.78 Exploded view of the Chandra telescope showing its major assemblies. (From Olds, C.R. and Reese, R.P., *Proc. SPIE*, 3356, 910, 1998.)

TABLE 14.4
Laminates and Key Properties for the Optical Bench

Application	Laminate Description	Property E_x (Msi)	$F_{x\ \mathrm{Compression}}$ (ksi)	CTE_x (μin./in./°F)	CME_x (μin./in/°F)
Cone panel skins	M60J/954-3 $[(30/\text{-}30/0/90/0)\mathrm{s}]_{\mathrm{nT}}$	28.4	78	−0.50	59
Forward and aft bulkheads	M60J/954-3 $[(45/\text{-}45/0/90)\mathrm{s}]_{\mathrm{nT}}$	16.3	57	−0.22	90
HRMA struts	M60J/954-3 $[(5/\text{-}5)\mathrm{s}]_{\mathrm{nT}}$	45.5	98	−0.76	14

Source: Olds, C.R. and Reese, R.P., *Proc. SPIE*, 3356, 910, 1998.

spacecraft. The bulkhead is a built-up structure with thin face sheets and a ribbed core. A composite honeycomb-core bulkhead interfaces the aft end of the OB to the instrument package. Internal composite longerons at the fore and aft ends of the OB help to transfer loads effectively through the interfaces.

14.6.5 TRUSS GEOMETRIES FOR MINIMAL GRAVITATIONAL AND WIND DEFLECTIONS

Meinel and Meinel (1986) reported on their investigation of various truss configurations with regard to gravitational and wind-induced deflections. They considered the geometries sketched in Figure 14.79. The numbers in parentheses indicate the number of struts. We briefly summarize below the relative merits of the various geometries:

Serrurier truss: parallel deflections compensated; poor stiffness-to-weight since top and bottom struts merely act as spacers yet use up a significant portion of the weight budget.

Octopod: not deflection-compensated; poor stiffness-to-weight because of the small base for the eight trusses and the reduced area of the larger number of struts for given weight.

Quad-tripod: not deflection-compensated (no parallelograms); good stiffness-to-weight since all tripods carry equal portions of the total weight.

Double truss: not deflection-compensated; fair stiffness-to-weight due to increased base span of corner tripods, but with longer diagonal struts of reduced area for given weight.

Athermal truss: Design due to McGraw et al. (1982) may be deflection-compensated and made athermal axially by using aluminum in the square midframe and steel in the rest of the truss; poor stiffness-to-weight because of reduced support for nodes of the midframe.

Two-tier truss: Essentially a Serrurier truss on top of a stiff box; not deflection-compensated; fair stiffness-to-weight because areas of struts must be reduced for given total weight; can be athermalized if corner struts of box have zero CTE.

In their 1986 paper, the Meinels also considered the effects of wind striking the projected area of the truss members in the upper structure. Reducing the length of the truss reduces the wind deflections, but requires the primary optics to work at a faster relative aperture. Comparing *f*/2 and *f*/1.4 designs for a 300 in. (7.6 m) aperture telescope then being considered for the McDonald

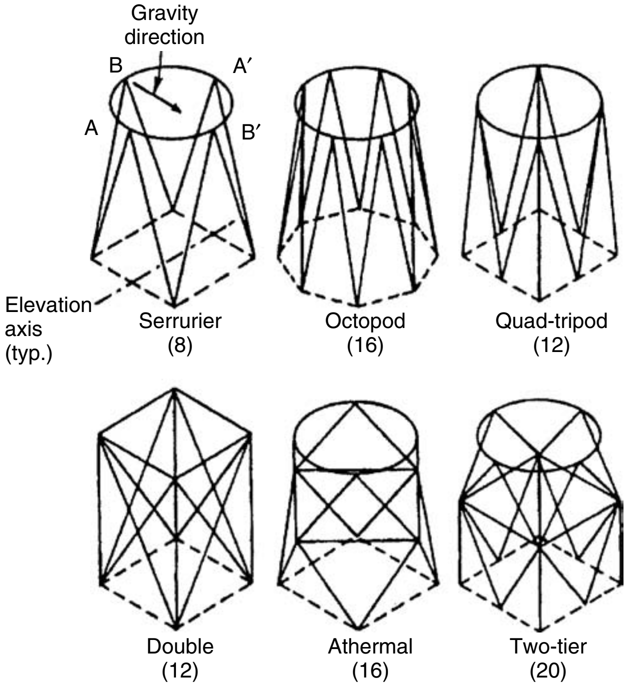

FIGURE 14.79 Geometries of various trusses considered in a comparative evaluation for a 300 in. (7.6 m) aperture telescope proposed for the McDonald Observatory. (From Meinel, A. and Meinel, M., *Proc. SPIE*, 628, 403, 1986.)

Observatory, they established the relationships shown in Figure 14.80. The secondary cage mass was assumed to be fixed at 3180 kg and wind load was assumed to be equivalent to 180 kg. The more compact and stiffer *f*/1.4 system obviously has reduced wind deflections.

Meinel and Meinel (1984) discussed the compensation of coma due to decentration or tilt of the secondary mirror of a Cassegrain telescope as might result from gravitational or wind-induced deflection of the telescope truss. In their 1986 paper, they outlined design guidelines for accomplishing this compensation in the proposed McDonald Observatory telescope. Studies of wind effects on large astronomical telescopes were referenced at the end of Section 12.3.2.

14.6.6 DETERMINATE SPACE FRAMES

Bigelow and Nelson (1998) defined a 3D truss structure in which all DOF are constrained and in which there are no redundant elements (i.e., no strut constrains the same DOF that another strut or combination of struts has already constrained) as a *determinate* space frame. This type of structure is useful in many optical system applications because it offers an opportunity for efficient and economical use of material, can be easily analyzed, and ensures that uncontrolled forces are not transferred through the joints (called nodes) into optical components such as mirrors. In the absence of gravity, a determinately supported optic will experience small motions but no stresses, even when the temperature changes and the struts change dimensions, or if the struts have been incorrectly sized during manufacture. When gravity is considered, the forces acting on the optic can be determined by static analysis of the given geometry.

According to Bigelow and Nelson (1998), a necessary condition for determinacy in a 3D truss is that the number of struts must equal the number of DOFs of the nodes. The relationship between the number of struts (S) and the number of nodes (N) is $S = 3N - 6$, where the factor 6 accounts for the six rigid body motions of the structure. Struts experience compressive or tensile axial loads as well as transverse (bending) loads due to self-weight deflections from gravity. Theoretically, nodes are pinned joints, but in practice, it is more practical to use rigid joints in which struts (typically tubes)

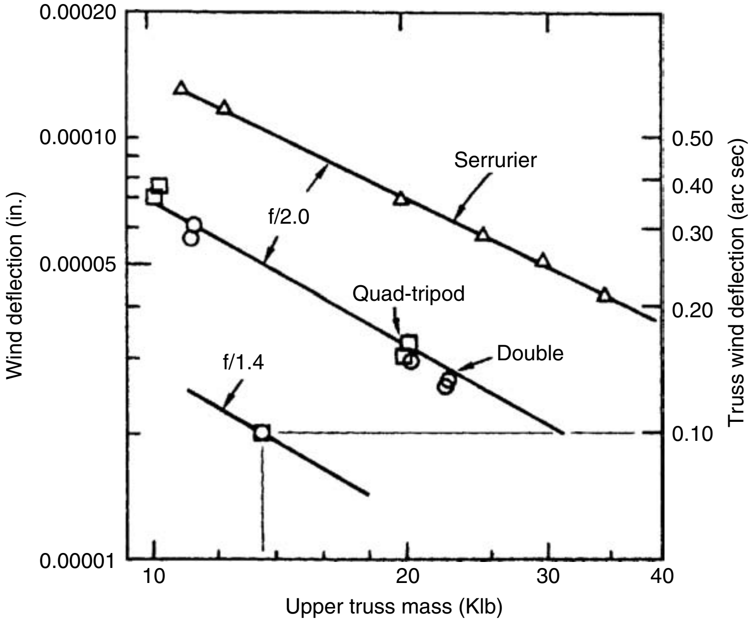

FIGURE 14.80 Linear and angular wind deflection for three truss geometries and two relative apertures as functions of upper truss mass for a proposed McDonald Observatory telescope. (From Meinel, A. and Meinel, M., *Proc. SPIE*, 628, 403, 1986.)

are welded together or attached to flanges. In astronomical telescope applications, the dynamic response of the structure must be evaluated because of the effects of the necessary motions of the optics during operation and the influences of external disturbances.

The challenge to the designer of such a structure is to create a design that allows only motions of each component and of combined groups of optics so that the combined set of possible errors is smaller than the tolerances prescribed by the error budget. To do this, the mechanical designer must work very closely with the optical designer to establish the predicted performance of the system under anticipated conditions prior to actual construction.

One example of the use of a determinate structure is the Echellette Spectrograph/Imager (ESI) developed for use at the Cassegrain focus of the Keck II 10 m telescope. This instrument has been described in detail by Sheinis et al. (1998). The spectrograph's optical system was described by Epps and Miller (1998) and by Sutin (1998). Another example can be found in the description by Radovan et al. (1998) of the active collimator used for tilt correction of the ESI. The aforementioned paper by Bigelow and Nelson (1998) described the space frame that provides the backbone for the entire instrument.

Major components of the ESI are shown in Figure 14.81. Included are two large (approximately 25 kg each) prisms that provide cross dispersion. In order to maintain optical stability during operation, these prisms must maintain a fixed orientation relative to the nominal spectrograph optical

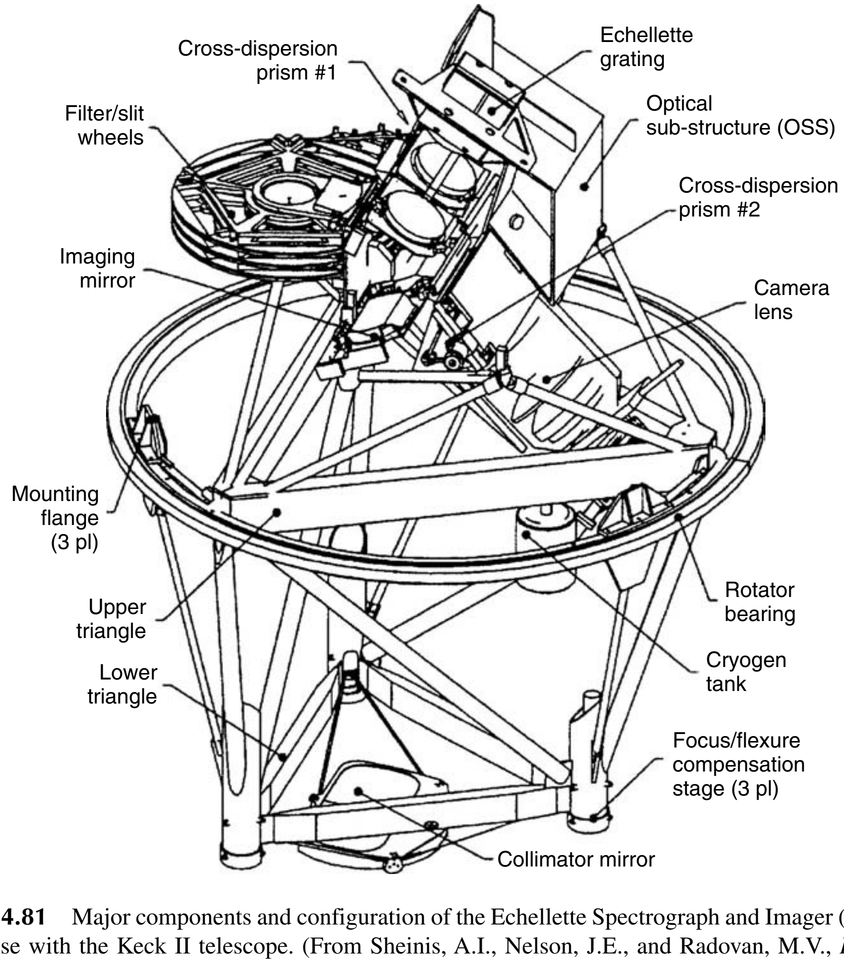
Cross-dispersion prism #1
Echellette grating
Filter/slit wheels
Optical sub-structure (OSS)
Cross-dispersion prism #2
Imaging mirror
Camera lens
Mounting flange (3 pl)
Upper triangle
Rotator bearing
Lower triangle
Cryogen tank
Focus/flexure compensation stage (3 pl)
Collimator mirror

FIGURE 14.81 Major components and configuration of the Echellette Spectrograph and Imager (ESI) developed for use with the Keck II telescope. (From Sheinis, A.I., Nelson, J.E., and Radovan, M.V., *Proc. SPIE*, 3355, 59, 1998.)

axis under a variety of gravity- and thermally-induced disturbances. Motions of the other optical elements, stress-induced deformations of the optical surfaces, and thermally induced changes in the refractive index of the materials making up the components also need to be minimized.

The ESI operates in three scientific modes: medium-resolution echellette mode, low-resolution prismatic mode, and imaging mode. To switch from one mode to another, one prism must be moved out of the beam, as shown in Figure 14.82. This prism is mounted on a single-axis stage. A mirror is moved into the beam to switch to the direct imaging mode.

The cross-dispersing prisms of the ESI are in collimated light; therefore, to a first order, small translations of the prisms will produce pupil motion only and no corresponding image motion. Tilts of the prisms in either of the two axes will produce combinations of image motion, change of the cross-dispersion direction, change in the amount of cross-dispersion, change in the anamorphic magnification factor, and increased distortion. The most important stability criterion for the prisms is control of tip and tilt, with almost no requirement for displacement stability. The computed sensitivities for ESI are ±0.013, ±0.0045, and ±0.014 arcsec of image motion for ±1 arcsec of prism tilt about the *X*-, *Y*-, and *Z*-axis, respectively. The desired spectrograph performance is ±0.06 arcsec of image motion without flexure control and ±0.03 arcsec of image motion with flexure control for a 2 h integration. These sensitivities result in a requirement of less than ±1.0, ±2.0, and ±1.0 arcsec rotation about the *X*-, *Y*-, and *Z*-axis. The normal operating temperature range for the Keck instruments is 2 ± 4°C, and the total range seen at the summit of Mauna Kea is minus 15 to 20°C. The instrument must maintain all the above translational and rotational specifications over the entire working temperature range. Therefore, the prism mounts need to be designed to be athermal with respect to tilts over this working temperature range, and must keep stresses below the acceptable limits over the complete temperature range of the site as well as extremes experienced during shipping.

In addition, attention must be paid to the stresses induced in the prisms. Not only is the potential for fracture of the bond joint or of the glass a cause for concern, but also stress induced in the glass will induce a corresponding local change in the index of refraction of the glass (i.e., birefringence), causing a possible wavefront distortion. Equally important requirements of the mounting design are (1) minimization of measurable hysteresis, which limits the accuracy of the open-loop flexure control system; (2) the ability to make a one-time alignment adjustment of the prism tilts over a 30 arcmin range during the initial assembly; and (3) the ability to remove the prisms for recoating, with a repeatable alignment position upon reassembly.

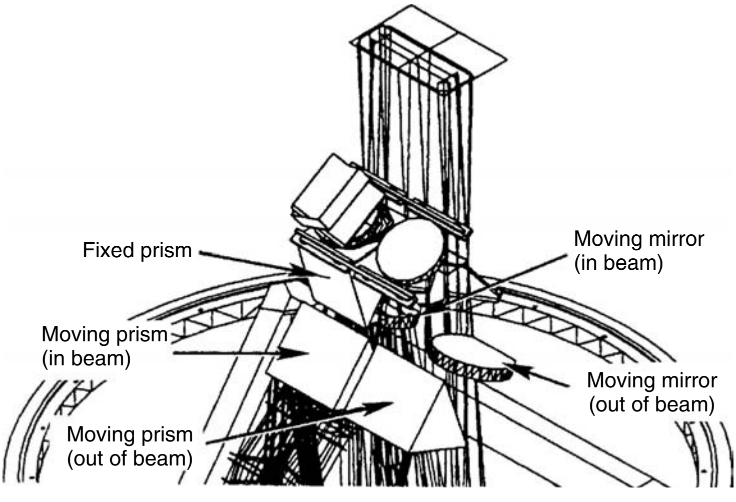

FIGURE 14.82 Partial view of the ESI showing the fixed and moveable dispersing prisms and mirrors. (From Sutin, B.M., *Proc. SPIE*, 3355, 134, 1998.)

During design of the ESI, it was found that it was easiest and adequate to build the central structure on which all of the optical elements and assemblies (except the collimator mirror) were mounted as a plate, called the optical substructure (OSS). The prisms were attached to the OSS through six struts. The actual attachment to the prism consisted of two parts: a pad that was permanently bonded to the prism, and a mating, detachable part that was permanently attached to the ends of the struts. This allowed the prism to be readily and repeatably installed and removed from its determinate support system.

The fixed and movable prism mounting designs are shown in Figure 14.83 and Figure 14.84, respectively. Joined pairs of struts are connected to each prism in one point on each of the three non-illuminated faces via a bonded tantalum pad. The CTE of tantalum ($6.5 \times 10^{-6}\ {}^{\circ}\text{C}^{-1}$) closely matches that of the BK7 prisms ($7.1 \times 10^{-6}\ {}^{\circ}\text{C}^{-1}$). The struts attach either directly to the OSS (in the case of the fixed prism) or to the translation stage (in the case of the movable prism), which in turn is bolted to the OSS. The largest refracting faces of the fixed and movable prisms measure 36.0 × 22.8 and 30.6 × 28.9 cm, respectively. The glass path is long (>80 cm), so it was necessary for the refractive

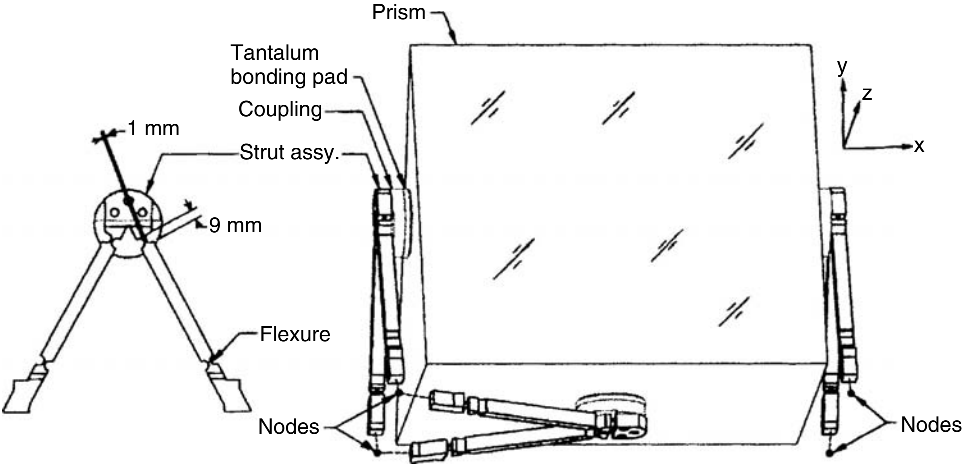
Prism
Tantalum bonding pad
Coupling
1 mm
Strut assy.
9 mm
Flexure
Nodes
Nodes
y
z
x

FIGURE 14.83 Diagram of the fixed prism assembly in the ESI showing its six-strut mounting. (From Sheinis, A.I., Nelson, J.E., and Radovan, M.V., *Proc. SPIE*, 3355, 59, 1998. With permission.)

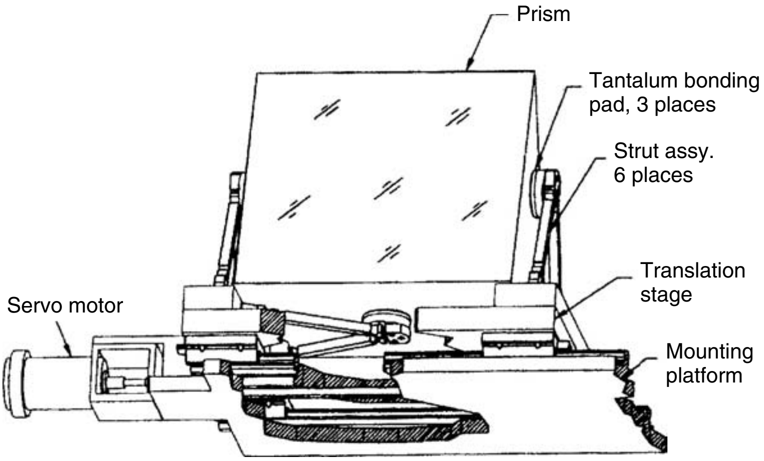
Prism
Tantalum bonding pad, 3 places
Strut assy. 6 places
Translation stage
Servo motor
Mounting platform

FIGURE 14.84 Diagram of the moveable prism assembly in the ESI showing its six-strut mounting and its translation stage. (From Sheinis, A.I., Nelson, J.E., and Radovan, M.V., *Proc. SPIE*, 3355, 59, 1998.)

index to be unusually uniform throughout the prisms. These were made of Ohara BSL7Y glass with a measured index homogeneity better than 2×10^{-6}. This achievement is believed to represent the state of the art for prisms of this size.

Each pair of struts was milled from a single piece of ground steel stock. Since each strut should constrain only one DOF of the prism, crossed flexures were cut into each end of each strut to remove four DOF (one rotation and one translation per flexure pair). The fifth DOF, axial rotation, is removed by the low torsional stiffness of the strut and flexure combination. Flexure thicknesses and lengths were designed to impart less stress than the self-weight loading of the prism into the prism pad connection, and to be significantly below the flexure material's elastic limit over the full range of adjustment, while keeping the strut as stiff as possible. Pad areas were chosen to give a self weight-induced stress of 125,000 Pa. If we consider the tensile strength of glass to be ~6.9 MPa (1000 lb/in.^{2}), this gives a safety factor of 55. The glass-to-metal bond adhesive used here was Hysol 9313 and the thickness was chosen to be the same (0.25 mm) as that developed by Iraninejad et al. (1987) during development of the bonded connections for the Keck primary segments.

To confirm these choices, extensive stress testing over various temperature ranges was performed for BK7-to-tantalum and BK7-to-steel bonds. Several samples of BK7 were fabricated with the same surface finish as specified on the prisms. These were bonded to tantalum and steel pads mechanically similar to the actual bonding pads for the prism mounts. These assemblies were subjected to tensile and shear loads up to ten times the expected loading in the instrument. The test jigs were then cycled 20 to 30 times through the expected temperature excursion range on the Mauna Kea summit. None failed. The joints were then examined for stress birefringence under crossed polarizers. The level of wavefront error was calculated to be less than the limit prescribed by the error budget in the case of the tantalum pad, but not for the steel pad. Hence, tantalum was designated for use in all the bonding pads. Note that the CTE difference between tantalum and BK7 is $0.6 \times 10^{-6}\ ^{\circ}\mathrm{C}^{-1}$. This is smaller than the CTE difference for BK7 to 6Al-4V titanium, which is $1.7 \times 10^{-6}\ ^{\circ}\mathrm{C}^{-1}$.

REFERENCES

Antebi, J., Dusenberry, D.O., and Liepins, A.A., Conversion of the MMT into a 6.5-m telescope — the optics support structure, *Proc. SPIE*, 1303, 148, 1990.

Antebi, J., Dusenberry, D.O., and Liepins, A.A., Conversion of the MMT into a 6.5-m telescope: the optics support structure and the enclosure, *Proc. SPIE*, 3352, 513, 1998.

Bigelow, B.C., and Nelson, J.E., Determinate space-frame structure for the Keck II Echellete Spectrograph and Imager (ESI), *Proc. SPIE*, 3355, 164, 1998.

Bridges, R. and Hagan, K., Laser tracker maps three-dimensional features, *The Industrial Physicist*, August/September, 28, 2001.

Bruner, M.E., Bahnsen, E.B., Cruz, T., Hong, L., and Jurcevich, B., Moisture induced dimensional changes in hydrophobic graphite-resin laminates, *Proc. SPIE*, 1335, 92, 1990.

Chaney, D., Brown, R.J., and Shelton, T., SIRTF prototype telescope, *Proc. SPIE*, 3785, 48, 1999.

Cohen, L.M., Cernoch, L.J., Matthews, G., and Stallcup, M.A., Structural considerations for fabrication and mounting of the AXAF HRMA optics, *Proc. SPIE*, 1303, 162, 1990.

DeAngelis, D.A., Designing thermally stable optical structures using strain gage technology, *Proc. SPIE*, 3786, 523, 1999.

Doyle, K. and Vukobratovich, D., Design of a modified Serrurier truss for an optical interferometer, *Proc. SPIE*, 1690, 357, 1992.

Edlin, B., The dispersion of standard air, *J. Opt. Soc. Am.*, 43, 339, 1953.

Epps, H.W., and Miller, J.S., Echellette spectrograph and imager (ESI) for Keck Observatory, *Proc. SPIE*, 3355, 48, 1998.

Erickson, D.J., Johnston, R.A., and Hull, A.B., Optimization of the optomechanical interface employing diamond machining in a concurrent engineering environment, *Proc. SPIE*, CR43, 329, 1992.

Fanson, J., Fazio, G., Houck, J., Kelly, T., Rieke, G., Tenerelli, D., and Whitten, M., The Space Infrared Telescope Facility (SIRTF), *Proc. SPIE*, 3356, 478, 1998.

Finley, P.T., Oonk, R.L., and Schweickart, R.B., Thermal performance verification of the SIRTF cryogenic telescope assembly, *Proc. SPIE*, 4850, 72, 2003.

Fischer, R.E. and Kampe, T.U., Actively controlled 5:1 afocal zoom attachment for the common module FLIR, *Proc. SPIE*, 1690, 137, 1992.

Ford, V.G., Parks, R., and Coleman, M., Passive thermal compensation of the optical bench of the Galaxy Evolution Explorer, *Proc. SPIE*, 5528, 171, 2004.

Ford, V.G., White, M.L., Hochberg, E., and McGown, J., Optomechanical design of nine cameras for the Earth Observing System Multi-Angle Imaging Spectro-Radiometer, TERRA Platform, *Proc. SPIE*, 3786, 264, 1999.

Friedman, I., Thermo-optical analysis of two long-focal-length aerial reconnaissance lenses, *Opt. Eng*., 20, 161, 1981.

Gallagher, D.B., Irace, W.R., and Werner, M.W., Development of the Space Infrared Telescope Facility (SIRTF), *Proc. SPIE*, 4850, 17, 2003.

Golden, C.T. and Spear, E.E., Requirements and design of the graphite/epoxy structural elements for the Optical Telescope Assembly of the Space Telescope, *Proceedings of AIAA/SPIE/OSA Technology Space Astronautics Conference: The Next 30 Years*, Danbury, CT, 1982, p. 144.

Hookman, R., Design of the GOES telescope secondary mirror mounting, *Proc. SPIE*, 1167, 368, 1989.

Hopkins, R.A., Finley, P.T., Schweickart, R.B., and Volz, S.M., Cryogenic/thermal system for the SIRTF cryogenic telescope assembly, *Proc. SPIE*, 4850, 42, 2003.

Jamieson, T.H., Athermalization of optical instruments from the optomechanical viewpoint, *SPIE Critical Review*, CR43, 131, 1992.

Krumweide, G.C., Attacking dimensional instability problems in graphite/epoxy structures, *Proc. SPIE*, 1533, 252, 1991.

Lee, J.H., Blalock, W., Brown, R.J., Volz, S., Yarnell, T., and Hopkins, R.A., Design and development of the SIRTF cryogenic telescope assembly (CTA), *Proc. SPIE*, 3435, 172, 1998.

Lubliner, J., Preliminary design of tube for TMT, *Keck Observatory Report 50*., Univ. of California, Berkeley, 1981.

Mainzer, A.K., Young, E.T., Greene, T.P., Acu, J., Jamieson, T., Mora, H., Sarfati, S., and VanBezooijen, R., The pointing calibration & reference sensor for the Space Infrared Telescope Facility, *Proc. SPIE*, 3356, 1095, 1998.

Mast, T., Faber, S.M., Wallace, V., Lewis, J., and Hilyard, D., DEIMOS cmera assembly, *Proc. SPIE*, 3786, 499, 1999.

McCarthy, D.J. and Facey, T.A., Design and fabrication of the NASA 2.4-Meter Space Telescope, *Proc. SPIE*, 330, 139, 1982.

McGraw, J.T., Stockman, H.S., Angel, J.R.P., and Williams, J.T., The CCD Transit Instrument (CTI) deep photometric and polarimetric survey, *Proc. SPIE*, 331, 137, 1982.

McMahan, L.L., Space Telescope Optical Telescope Assembly structural materials characterization, *Proceedings of AIAA/SPIE/OSA Technology Space Astronautics Conference: The Next 30 Years*, Danbury, CT, 1982, p. 127.

Meinel, A. and Meinel, M., Zero-coma condition for decentered and tilted secondary mirror in Cassegrain/Nasmyth configuration, *Opt. Eng*., 23, 801, 1984.

Meinel, A. and Meinel, M., Wind deflection compensated, zero-coma telescope truss geometries, *Proc. SPIE*, 628, 403, 1986.

Olds, C.R. and Reese, R.P., Composite structures for the Advanced X-ray Astrophysics Facility (AXAF) telescope, *Proc. SPIE*, 3356, 910, 1998.

Palmer, T.A. and Murray, D.A., private communication, 2002.

Penndorf, R., Tables of the refractive index for standard air and the Rayleigh scattering coefficient for the spectral region between 0.2 and 20 μ and their application to atmospheric optics, *J. Opt. Soc. Am*., 47, 176, 1957.

Povey, V., Athermalization techniques in infrared systems, *Proc. SPIE*, 655, 142, 1986.

Quammen, M.L., Cassidy, P.J., Jordan, F.J., and Yoder, P.R. Jr., U.S. Patent 3,246,563, 1966.

Radovan, M.V., Nelson, J.E., Bigelow, B.C., and Sheinis, A.I., Design of a collimator support to provide flexure control on Cassegrain instruments, *Proc. SPIE*, 3355, 155, 1998.

Raybould, K., Gillet, P., Hatton, P., Pentland, G., Sheehan, M., and Warner, M., Gemini telescope structure design, *Proc. SPIE*, 2199, 376, 1994.

Richard, R., Damping and vibration considerations for the design of optical systems in a launch/space environment, *Proc. SPIE*, 1340, 82, 1990.

Rogers, P.J., Athermalized FLIR optics, *Proc. SPIE*, 1354, 742, 1990.

Schreibman, M., and Young, P., Design of Infrared Astronomical Satellite (IRAS) primary mirror mounts, *Proc. SPIE*, 250, 50, 1980.

Schwenker, J.P., Brandl, B.R., Burmester, W.L., Hora, J.L., Mainzer, A.K., Quigley, P.C., and Van Cleve, J.E., SIRTF-CTA optical performance test, *Proc. SPIE*, 4850, 304, 2003a.

Schwenker, J.P., Brandl, B.R., Hoffmann, W.F., Hora, J.L., Mainzer, A.K., Mentzell, J.E., and Van Cleve, J.E., SIRTF-CTA optical performance test results, *Proc. SPIE*, 4850, 30, 2003b.

Scott, R.M., Optical engineering, *Appl. Opt.*, 1, 387, 1962.

Seeger, H., *Ferngläser und Fernrohre in Heer, Luftwaffe und Marine*, H. T. Seeger, Hamburg, 1996.

Seil, K., Progress in binocular design, *Proc. SPIE*, 1533, 48, 1991.

Seil, K., private communication, 1997.

Serrurier, M., Structural features of the 200-inch telescope for Mt. Palomar Observatory, *Civil Eng.*, 8, 524, 1938.

Sheinis, A.I., Nelson, J.E., and Radovan, M.V., Large prism mounting to minimize rotation in Cassegrain instruments, *Proc. SPIE*, 3355, 59, 1998.

Smith, D.D. and Jones, R.E., A statistical evaluation of space stable optical support structure, *J. SAMPE* 14, 4, 1978.

Spina, J.A., Design, fabrication, and assembly of the High Resolution Mirror Assembly for NASA's Advanced X-Ray Astrophysics Facility, *Proc. SPIE*, 1113, 2, 1989.

Stubbs, D., Smith, E., Dries, L., Kvamme, T., and Barrett, S., Compact and stable dual fiber optic refracting collimator, *Proc. SPIE*, 5176, 192, 2003.

Stubbs, D.M. and Bell, R.M., Fiber Optic Collimator Apparatus and Method, U.S. Patent No. 6,801,688, 2004.

Sutin, B.M., What an optical designer can do for you AFTER you get the design, *Proc. SPIE*, 3355, 134, 1998.

Telkamp, A.R. and Derby, E.A., Design considerations for composite materials used in the Mars Observer Camera, *Proc. SPIE*, 1303, 416, 1990.

Thomas, B.H., Neville, W., and Snodgrass, J., Assessment and control of vibrations affecting large astronomical telescopes, *Proc. SPIE*, 732, 130, 1987.

Trsar, W.J., Benjamin, R.J., and Casper, J.F., Production engineering and implementation of a modular military binocular, *Opt. Eng.*, 20, 201, 1981.

Visser, H. and Smorenburg, C., All reflective spectrometer design for Infrared Space Observatory, *Proc. SPIE*, 1113, 65, 1989.

Vukobratovich, D., Binocular performance and design, *Proc. SPIE*, 1168, 338, 1989.

Vukobratovich, D., Introduction to Optomechanical Design, SPIE Short Course SC014, 1993.

Vukobratovich, D., Modular optical alignment, *Proc. SPIE*, 3786, 427, 1999.

Vukobratovich, D., private communication, 2003.

Vukobratovich, D., private communication, 2004.

Wada, B.K. and DesForges, D.T., Spacecraft damping considerations in structural design, *Proceedings of the 48th Meeting of the AGARD Structures and Materials Panel (AGARD Proc. 277)*, Williamsburg, VA. April 2–3, NATO Advisory Group for Aerospace Research and Development, Neuilly-Sur-Seíne, France, 1979.

Yoder, P.R., Jr., *Mounting Optics in Optical Instruments*, SPIE Press, Bellingham, 2002.

Young, P., and Schreibman, M., Alignment design for a cryogenic telescope, *Proc. SPIE*, 251, 171, 1980.

Zurmehly, G.E. and Hookman, R., Thermal/optical test setup for the Geostationary Operational Environmental Satellite telescope, *Proc. SPIE*, 1167, 360, 1989.

Zweben, C.H., Advanced Composite Materials for Optomechanical Systems, SPIE Short Course SC218, 2002.

15 Analysis of the Opto-Mechanical Design

15.1 INTRODUCTION

Several types of analyses that can and frequently should be accomplished during the design of any opto-mechanical system are addressed in this chapter. Although very important, optical system performance analyses are intentionally omitted because they are adequately considered in many other places, such as Kingslake (1983), Shannon (1997), Smith (2000, 2004), Fischer and Tadic-Galeb (2000), and Laikin (2001). The details of how to accomplish structural design and evaluation by FEA and thermal analysis techniques are not discussed either. These subjects have been summarized nicely by such publications as Hatheway, (1991, 1992a), Pearson (1992), Genberg (1997a, 1997b), and Doyle et al. (2002), to cite but a few. We concentrate on topics that have received less widespread attention in the literature. These include how stresses and strains are introduced into an optic and its mount, statistical prediction of component failure from stress, and some key aspects of thermal effects in optical instruments.

We begin with basic considerations of mounting strains and stresses and how tolerable levels of stress can be established statistically for optics to be used in different environments. We then show how peak and average compressive stress and the associated tensile stress depend upon the magnitudes of constraining force, the contours of the surfaces in contact, the sizes of the deformed contact areas between the optical and mechanical bodies (both considered to be elastic), and the pertinent mechanical properties of the contacting materials. Closed-form equations adapted from Roark (1954) and from Timoshenko and Goodier (1970) are used to estimate the magnitudes of the contact stresses (compressive and tensile) induced at a variety of types of glass-to-metal interfaces commonly used for mounting lenses, windows, small mirrors, and prisms. We show how to estimate the bending stresses and gross optical surface deformations resulting from the generation of moments when axial clamping forces are applied to opposite sides of small rotationally symmetric components at different radial distances from the axis.

Summaries of the effects of temperature changes on the focus of simple optical systems (and some ways to athermalize these systems), on the radial and hoop stresses in rim-contact lens and mirror mounts, on axial preloads (which largely determine contact stresses), and on radial and axial mechanical clearances are presented. Important effects of radial and axial thermal gradients are also summarized briefly. The chapter closes with a discussion of ways to estimate thermally induced stresses in cemented and bonded joints.

The analytical models underlying the theories given here are all believed to be conservative representations of real-life situations.

15.2 FAILURE PREDICTIONS FOR OPTICS

15.2.1 General Considerations

In the preceding chapters, we considered a variety of ways to constrain lenses, prisms, windows, and small mirrors using such means as threaded retaining rings, flanges, cantilevered spring clips, and straddling springs. Each of these designs uses uniquely shaped mechanical surfaces at the interfaces with the glass components. The actual glass-to-metal contacts are "points," "lines," or small areas of specific shapes through which forces are transferred so as to constrain the optic. These forces also deform (i.e., strain) the glass and the metal elastically. Strain is dimensionless and expressed as $\Delta d/d$, where d represents deflection. Strains develop both at the interface where the force is applied and at the opposing interface where restoring force is provided in order to constrain the optic. Ideally, but not necessarily, the interfaces are directly opposite each other, so the force vectors applied normal to the respective surfaces pass through the opposing interfaces. This minimizes deformations of optical surfaces.

The well-known Hooke's Law demands that these strains produce proportional stresses within the deformed regions of the optic and the mount. Stress is expressed as force per unit area with units of $\mathrm{lb/in.}^2$ or Pa. For example, a prism pressed by a straddling spring bearing a cylindrical pad against three small coplanar locating pads arranged in a triangular pattern would experience compressive and tensile stresses at the four interfaces with the pads. In this case, the preload provided by the spring cannot be aimed toward all the pads; it might well be aimed toward the centroid of the triangular pattern. Bending moments thus introduced do not cause a problem if both the prism and the baseplate carrying the three pads are sufficiently stiff. Another example would be a lens preloaded against a cell shoulder by a retaining ring that presses against an annular area on the polished glass surface outside the clear aperture. Compressive and tensile stresses are generated in the glass within and adjacent to this area.

In this section, we are concerned with the effects of stress buildup in optical components such as lenses, small mirrors, windows, and prisms. These stress values can then be compared with damage thresholds for the materials involved. Figure 15.1 shows graphs of stress vs. strain for a brittle material and a more ductile material. The former is characteristic of glasses while the latter applies to some ceramics and crystals such as sapphire at high temperatures. In both cases, when the stress becomes high enough, the material fails.

As discussed by Vukobratovich (1993), Fuller et al. (1994), Pepi (1994a, 1994b), Harris (1999), and Doyle and Kahan (2003), rigorous assessments of stress-related damage utilize statistics to determine the probability of failure — immediate or delayed — under specified conditions. Use of these methods requires knowledge of the quality of finish (i.e., existence of defects and the shapes, sizes, orientations, and locations of those defects) of the optical surfaces. Defects are produced during grinding and polishing operations as well as during handling, mounting, and use of the optic. Manufacturing defects can be minimized by ensuring that the depths of material removal for each

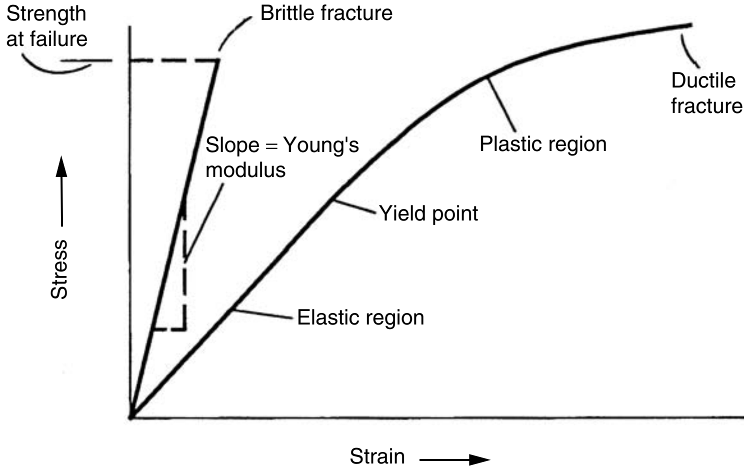

FIGURE 15.1 Responses of brittle and ductile materials to tensile stress. Drawings are not to scale.

TABLE 15.1
Typical Schedules for Conventional and Controlled Grinding of Optical Materials

		Average Particle Size		Material Removal			
				Conventional		Controlled	
Operation	**Abrasive**	**(mm)**	**(in.)**	**(mm)**	**(in.)**	**(mm)**	**(in.)**
Milling	150 grit diamond	0.1016	0.004	—	—	—	—
Fine grind	2F $A1_2O_3$	0.0304	0.0012	0.0381	0.0015	0.3048	0.0120
Fine grind	3F $A1_2O_3$	0.0203	0.0008	0.0177	0.0007	0.0914	0.0036
Fine grind	KH $A1_2O_3$	0.0139	0.0005	0.0127	0.0005	0.0609	0.0024
Fine grind	KO $A1_2O_3$	0.0119	0.0005	0.0076	0.0003	0.0406	0.0016
Polish	Barnsite rouge	—	—	—	—	—	—

Source: Adapted from Pepi, J.W., *Allowable stresses for window Design*, Internal Report, Itek Optical Systems, Lexington, MA, 1994a.

of a series of grinding and polishing operations with progressively smaller grit sizes is at least three times the average diameter of the preceding abrasive (Stoll et al., 1961). This process is called *controlled grinding*. Table 15.1, lists typical schedules for grinding and polishing an optical glass using conventional and controlled grinding. Surface damage can, ofcourse, occur after polishing.

Optics with defect-free surfaces are much more durable than damaged ones. For example, carefully made glass windows with their rims chemically polished with hydrofluoric acid to remove residual microscopic damage after edging have demonstrated tensile strengths in excess of 10^6 lb/in.^{2} (6895 MPa), whereas the commonly accepted rule-of-thumb tensile strength of typical glassy materials ranges from 1000 to 1500 lb/in.^{2} (6.89 to 10.34 MPa) (Doyle and Kahan, 2003).

15.2.2 Testing to Determine Component Strength

If a glass component is expected to experience significant tensile stress, its actual strength can be determined by testing several samples at, or above, the anticipated stress level. This gives confidence, but not proof, that the item will not fail when exposed to that level of stress. Ideally, the test should simulate the conditions of use. If it is not possible to test the actual item or items, the next best course of action would be for tests to be accomplished using multiple identical coupons made of the same material as the component of concern and that have been manufactured and handled in the same manner as that component. This data can be scaled to the size of the actual optic as an indication of the capability of that part to withstand a specified level of stress. Testing of the coupons can be accomplished by methods such as three-point, four-point, or ring-on-ring bending as illustrated schematically in Figures 15.2 (a), (b) and Figure 15.3. The latter method is preferred for optical glasses because the sample is a disk that can be polished to the same specification as the actual component. Coupon testing can also be accomplished by indenting the surface with the square pyramidal point of a crystalline diamond tool on a Vickers indenter (see Figure 15.4) or the elongated rhomboid point on a Knoop indenter. The dimension *c* is representative of the depth of the crack extending into the material under applied load *P*. These tests have been described and illustrated by many authors, including Adler and Mihora (1992) and Harris (1999). In the absence of any measured data on the actual optic or coupons, a considerably less-reliable lifetime prediction can be based on surface quality assumptions based on prior experience with typical manufacturing and handling methods for materials similar to the actual optic.

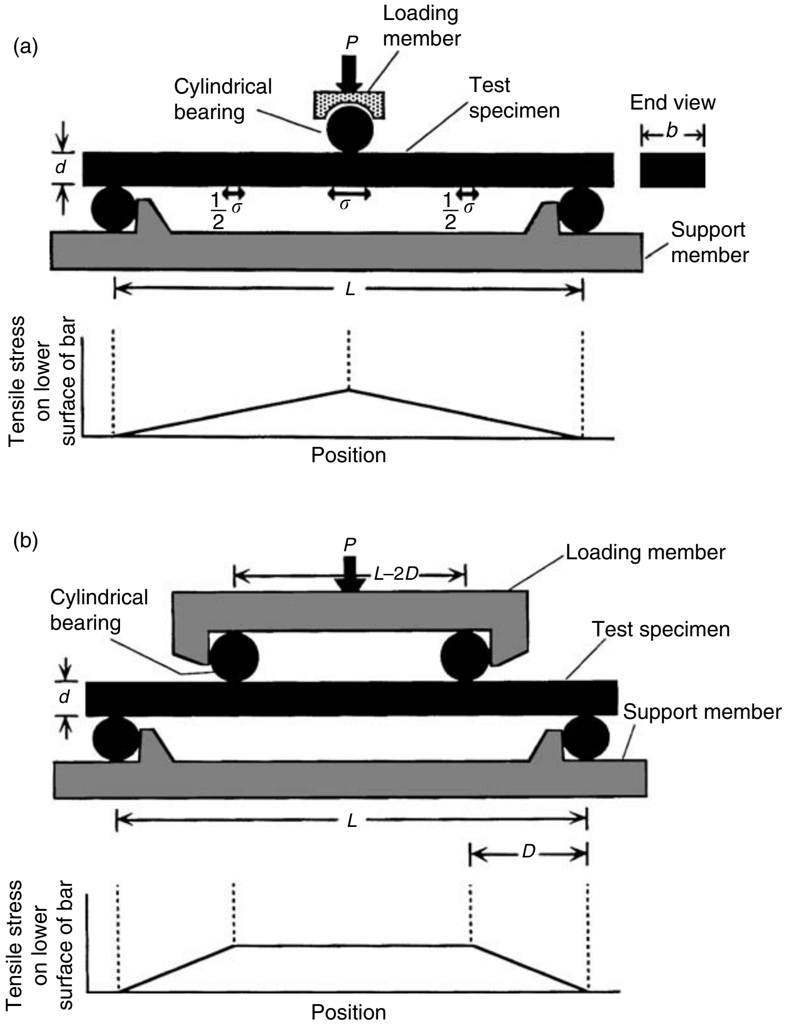
(a)
P
Loading member
Cylindrical bearing
Test specimen
End view
b
d
$\frac{1}{2}\sigma$
σ
$\frac{1}{2}\sigma$
Support member
L
Tensile stress on lower surface of bar
Position
(b)
P
L–2D
Loading member
Cylindrical bearing
Test specimen
d
Support member
L
D
Tensile stress on lower surface of bar
Position

FIGURE 15.2 Apparatuses for flexure strength measurement by (a) three-point bending and (b) four-point bending. Black circles are ends of cylinders. Note that stress is constant within the central region of (b). (From Harris, D.C., *Materials for Infrared Windows and Domes*, SPIE Press, Bellingham, 1999.)

As indicated schematically in Figure 15.1, failure of brittle materials occurs when the maximum tensile stress equals the material's strength. Harris (1999) listed approximate strengths of several IR window materials at room temperature. A portion of his list was presented in Table 6.1. Using a single value for a material's strength to predict whether a component will survive a given amount of stress can lead to errors because of uncertainty as to the pertinent physical characteristics of the particular component of concern. A better way is to utilize a fracture mechanics approach utilizing (1) the tendency of the material when stressed to growth of existing surface flaws or cracks, (2) known or assumed characteristics of those defects, and (3) the anticipated level of stress to predict if and when failure of the part will occur under that stress. Fracture of a brittle material is distinguished from elastic deformation by the breaking of atomic bonds rather than by simply stretching them. The resistance of a material to crack growth is commonly called its *fracture toughness* and is symbolized as K_C. This material parameter plays a major role in loose abrasive grinding or lapping of optical materials so much of what is currently known about it derives from ongoing research in the micromechanics of those processes (see, for example, Lambropoulos et al., 1996a, 1996b, 1997).

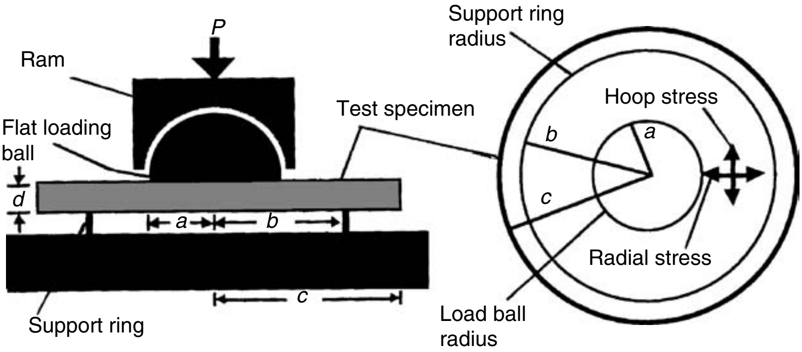
P
Ram
Flat loading ball
d
a
b
c
Support ring
Test specimen
Support ring radius
Hoop stress
Radial stress
Load ball radius

FIGURE 15.3 Apparatus for ring-on-ring flexure test. Radial stress is along the radius and hoop stress is tangential. Within the area defined by a, the radial and hoop stresses are equal. Hence, this is known as an *equibiaxial* test. (Adapated from Harris, D.C., *Materials for Infrared Windows and Domes*, SPIE Press, Bellingham, 1999.)

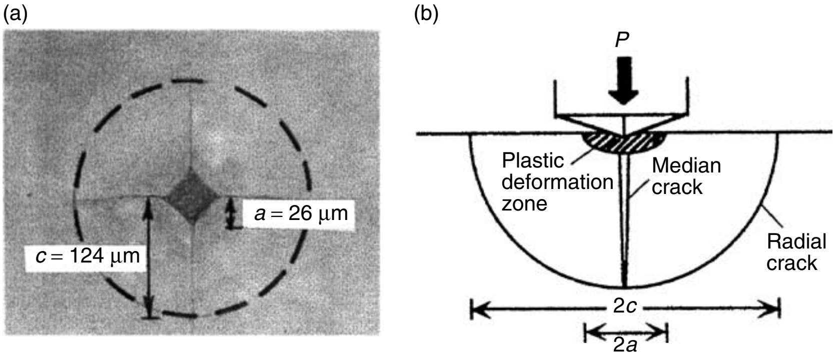
(a)
a = 26 μm
c = 124 μm
(b)
P
Plastic deformation zone
Median crack
Radial crack
2c
2a

FIGURE 15.4 (a) Micrograph of a Vickers indentation pattern in a test sample. Dashed line was added to show extent of radial crack. (b) Idealized cross section of crack system. (Adapted from Harris, D.C., *Materials for Infrared Windows and Domes*, SPIE Press, Bellingham, 1999.)

Table 15.2 lists values of K_C for selected optical materials of interest here. Values for more than 70 optical glasses from Schott, Hoya, and Russian manufacturers may be found in Schulman et al. (1996). Lambropoulos and Varshneya (2004) gave values for 11 Ohara glasses.

Measurement of the resistance of a material to cracking typically involves microindentation fracture testing of samples, which is one of the techniques discussed in the last section. According to Schulman et al. (1996), data from Vickers or Knoop tests can be applied to an analytical model attributed to Evans (1979) to derive K_C of brittle materials. This model is expressed as

$$K_C = H(D/2)^{1/2}(E/H)^{0.4}10^{f(x)} \tag{15.1}$$

where H is the Vickers hardness, D the indentation diagonal, E Young's modulus, c the half-crack size, and

$$x = \log_{10}(2c/D) \tag{15.2}$$

$$f(x) = -15.9 - 0.34x - 2.20x^2 + 11.23x^3 - 24.97x^4 + 16.32x^5 \tag{15.3}$$

Growth of a flaw such as a microscopic crack in the surface or within the volume of a glass part results from the tendency for tensile stress to be concentrated at the tip of the crack. In Figure 15.5, we show a schematic representation from Harris (1999) of a typical crack as an elongated ellipsoidal

TABLE 15.2
Approximate Fracture Toughness, K_C, for Selected Optical Materials

	Data	K_C	
Material	**Source**	**(lb/in.$^{3/2}$)**	**(Pa$^{3/2}$ × 10^5)**
Corning 7940 fused silica	(a)	674	7.41
Corning 7900 96% silica	(b)	645	7.09
Corning 7913 Vycor	(b)	679	7.46
Corning 1723 aluminosilicate	(b)	761	8.36
Corning 7740 Pyrex	(e)	692	7.6
Corning 7971ULE	(e)	683	7.5
BK1	(d)	747	8.2
BK7	(a)	774	8.5
UBK7	(b)	823	9.04
K3	(d)	719	7.9
K7	(d)	865	9.5
ZKN7	(d)	646	7.1
SK7	(d)	792	8.7
SK11	(d)	710	7.8
SK16	(a)	710	7.80
BaK2	(d)	656	7.2
BaF3	(d)	610	6.7
F2	(d)	501	5.5
F5	(d)	610	6.3
SF1	(b)	585	6.43
SF7	(d)	610	6.7
SF58	(a)	346	3.80
LaK10	(a)	865	9.50
KzF6	(d)	938	10.3
ZnSe	(c)	455	5
ZnS	(c)	910	10
Ge (single crystal)	(c)	637	7
Si	(c)	819	9
ALON	(c)	1274	14
Sapphire	(c)	1820	20
Y_2O_3	(c)	637	7
SiC	(c)	3640	40
Diamond (single crystal)	(c)	3094	34

Sources: (a) Doyle, K.B. and Kahan, M., *Proc. SPIE*, 5176, 14, 2003; (b) in vacuum by 3-point bend per Pepi, 1994; (c) Harris, D.C., *Materials for Infrared Windows and Domes*, SPIE Press, Bellingham, 1994; (d) Lambropoulos, J.C. et al., *Appl. Opt.*, 36, 501, 1997; (e) Schulman, J. et al., *COM Glass Database*, Center for Optics Manufacturing, Rochester, 1996.

cavity within a much larger volume of glass. The cavity has dimensions $2b$ and $2c$ in the plane of the figure, and is aligned with its long axis perpendicular to the tensile stress field σ_{applied} as shown. The lateral stress σ_Y at the tip of the cavity is given by

$$\sigma_Y = \sigma_{\text{applied}}\,[1 + (2c/b)] = \sigma_{\text{applied}}\,[1 + 2(c/\rho)^{1/2}] \tag{15.4}$$

where ρ is the radius of curvature at either tip of the cavity. It is approximated as

$$\rho = b^2/c \tag{15.5}$$

Equation (15.5) shows that as the crack elongates and dimension c grows, ρ gets smaller. Then, from the second form of Eq. (15.4), σ_Y increases. When this concentrated stress exceeds the material's K_C, failure would be expected to occur.

The velocity with which a crack propagates has been shown to correlate well with the intensity of the applied stress and with the size of the crack. In a dry environment (vacuum or cryogenic temperature), a flaw may not propagate until a threshold stress is reached. For a constant stress larger than the threshold, the flaw would grow until the part fails. If moisture is present, the crack growth velocity increases in direct proportion to the relative humidity of the environment surrounding the optic and within the crack (Wiederhorn, 1967; Wiederhorn et al., 1982; Freiman, 1992). The flaw grows under constant stress at a predictable rate until it reaches a critical dimension, when the optic probably fails. A typical velocity vs. stress graph for three common glasses with unspecified-sized cracks from Doyle and Kahan (2003) is shown as Figure 15.6. The graph is semi-logarithmic to

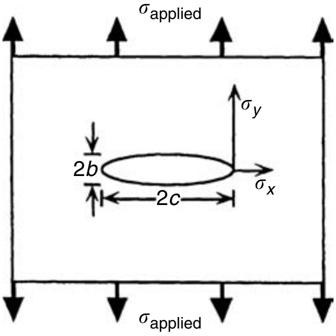

FIGURE 15.5 Schematic of an elliptical cavity in a brittle material. Semi-axes are b and c. The applied tensile stress is along the Y-axis. (From Harris, D.C., *Materials for Infrared Windows and Domes*, SPIE Press, Bellingham, 1999.)

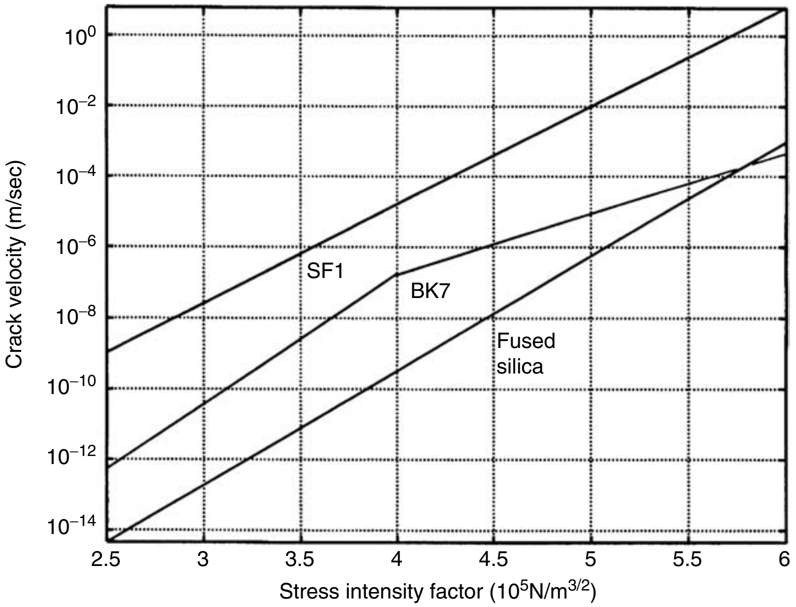

FIGURE 15.6 Plots of crack propagation velocity vs. stress intensity for three optical materials. (From Doyle, K.B. and Kahan, M., *Proc. SPIE*, 5176, 14, 2003.)

cover a large dynamic range of velocities. Lawn (1993) and Wechtman (1996) reported that growth of a so-called Griffith-type crack is related to the surface energy per unit area of the exposed surfaces within the crack.

Fuller et al. (1994) wrote that "the processes that engender defects and cracks in glass can also give rise to localized residual stresses that influence the propagation of the ensuing cracks." This residual stress field is characterized, in part, by a parameter r that equals 3.0 for a Vickers point-type indentation and 1.0 for a line-type indentation. We will encounter this parameter again in Section 15.2.5.

15.2.3 The Weibull Failure Prediction Method

Weibull (1951) established a theoretical method for expressing a statistical probability of the occurrence of an event that is particularly useful in defining the survivability of an optical component under stress. The component may be thought of as a continuum of N elements, any of which can fail. The probability of failure P_F of an optic when the weakest element of that optic fails is

$$P_F = 1 - \exp(-\varphi) \tag{15.6}$$

where φ is either $\theta = [(\sigma - \sigma_U)/\varphi_0]^m$ or $\varphi = (\sigma/\sigma_0)^m$ and σ, σ_U, and φ_0 the actual stress level in an element, the critical stress level (threshold) below which failure will not occur, and a scaling factor, respectively. The exponent m is called the Weibull modulus. The first expression for φ is a three-parameter function involving the stress threshold, whereas the second expression is a two-parameter version that assumes failure to be possible even with an extremely low level of stress, i.e., no threshold exists. We here concentrate on the more conservative two-parameter case.

In our current application of Weibull theory to the failure of stressed optics, the values of σ and σ_0 are chosen to fit a particular set of experimental data defining the stress at fracture for a given material. For such a data set, we redefine these parameters as S and S_0, respectively. Equation (15.6) then becomes

$$P_F = 1 - \exp(-S/S_0)^m \tag{15.7}$$

where S_0 is the scaling factor and m the modulus.

A component's stress level at failure S_C, determined from this equation on the basis of sample failure stresses S_S with loaded area A_S, must be scaled to the area A_C of the actual component of interest by the relationship

$$S_C/S_S = (A_S/A_C)^{1/m} \tag{15.8}$$

Further, if a stress level at failure S_1 is known for one flaw depth D_1, the equivalent stress level at failure S_2 for a different flaw depth D_2 is

$$S_2/S_1 = (D_2/D_1)^{1/2} \tag{15.9}$$

To simplify calculations, we can rewrite Eq. (15.7) as the following equivalent form:

$$\ln\{\ln[1/(1 - P_F)]\} = m(\ln S) - m(\ln S_0) \tag{15.10}$$

To illustrate the use of this theory, let us assume test results from Harris (1999) as listed in Table 15.3 for a series of 13 samples of ZnS tested to failure under stress by the ring-on-ring method. Sample dimensions are indicated. The ln{[1/(1-P_F)]} data from the fourth column of the table can be plotted on linear scales against that from the fifth column (ln *S*) as shown in Figure 15.7(a). A straight line is fitted to the data. The slope of the line is the Weibull modulus *m*. It can most easily be evaluated in this case by noting that points 2 and 13 lie on the line. Substituting the coordinates for these points from Table 15.3 into two versions of Eq. (15.10) and solving simultaneously, we obtain $m = 5.4485$ and $\ln(S_0) = 4.6192$. S_0 then equals $e^{4.6192}$ or 101.4 MPa. Figure 15.7(b) shows the corresponding plot of P_F vs. applied tensile stress. This is also a linear scale diagram. An extremely high probability of failure occurs for a stress >130 MPa.

TABLE 15.3
Example of Measured Data for Weibull Determination of ZnS Strength from Ring-on-Ring Tests of 13 Samples

Sample Number *i*	Stress at Failure *S* (MPa)	Probability of Failure $P_i = (i - 0.5)/N$	Terms from Eq. (15.10): $\ln\{\ln[1/1-P_i]\}$	ln *S*
1	62	0.0385	−3.2375	4.1271
2	69	0.1154	−2.0987	4.2341
3	73	0.1923	−1.5438	4.2905
4	76	0.2692	−1.1596	4.3307
5	87	0.3462	−0.8558	4.4659
6	89	0.4231	−0.5977	4.4886
7	90	0.5000	−0.3665	4.4998
8	93	0.5769	−0.1507	4.5326
9	100	0.6538	0.0590	4.6052
10	107	0.7308	0.2718	4.6728
11	110	0.8077	0.5000	4.7005
12	125	0.8846	0.7698	4.8283
13	126	0.9615	1.1806	4.8363

Source: Adapted from Harris, D.C., in *Materials for Infrared Windows and Domes*, SPIE Press, Bellingham, 1999.

Note: Sample Diameters are 25.4 mm, Thicknesses are 1.96 mm, Load Ring Diameter is 10.72 mm, Support Ring Diameter is 20.26 mm, and $N = 13$.

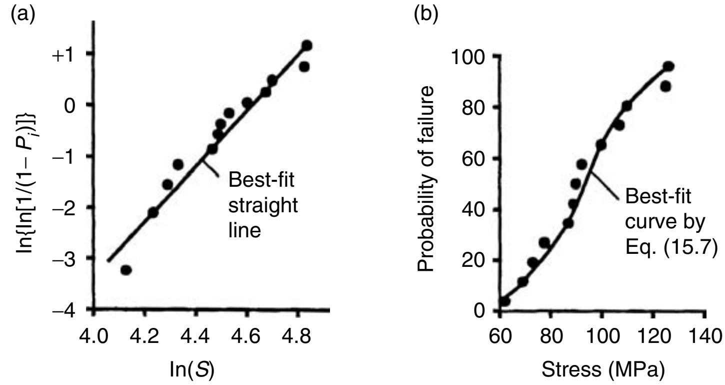

FIGURE 15.7 Plots of data from Table 15.3 for 13 ZnS samples: (a) relationship of terms from Eq. (15.10), (b) variation of failure probability P_F with stress. (Adapted from Harris, D.C., *Materials for Infrared Windows and Domes*, SPIE Press, Bellingham, 1999.)

Once again relying on theory explained by Harris (1999), we note that the mean strength of a series of identical samples of a material can be established from the calculated S_0 by the equation

$$S_{\text{mean}} = (S_0)(\Gamma) \tag{15.11}$$

where the gamma function*(Γ) is interpolated from Table 15.4 for the applicable value of m. For the example just considered, $m = 5.4485$, $\Gamma=0.9225$, and $S_{\text{mean}} = (101.42)(0.9225) = 93.5$ MPa. We next scale this stress in accordance with Eq. (15.8) to the actual component area A_C. Let us assume a component diameter of 76.2 mm. The sample diameters are 25.4 mm as indicated in Table 15.3. Then $A_C = 4560.37$ mm^2 and $A_S = 506.71$ mm^2. Using Eq. (15.8), S_{mean} for the component is $93.5(506.71/4560.37)^{1/5.4485} = 62.5$ MPa (9,064 lb/in.^{2}). This stress level can be considered as an approximate tolerance for ZnS optics of diameter 76.2 mm. Note that we have assumed here that the worst-case flaw in the actual component has the same dimensions as the worst-case flaw in the samples tested. If this is not the case, Eq. (15.9) must be employed to further adjust the tolerance.

15.2.4 The Safety Factor

When we apply a tolerance developed as explained in the last section to a particular design, we should apply an appropriate (conservative) safety factor f_S. Harris (1999) suggested that $f_S = 4.0$ is appropriate for ceramic optics displaying a Weibull modulus of about 5.0 and a scaling factor of about 100 MPa. This corresponds approximately to a 0.1% probability of failure or ~ 99% reliability. If m is larger, this safety factor can be smaller. For instance, if $m = 20$ and S_0 remains about 100 MPa, the same reliability results with a safety factor of 1.4. As a rule of thumb, we suggest a range of $2 \leq f_S \leq 4$ for application to optics in general.

Note that if failure of the optic might result in injury or loss of life (as in the case of a window in the skin of a manned aircraft or spacecraft), a much lower probability of failure and a correspondingly higher safety factor should be applied. An example of such a situation was discussed in Section 6.7 in connection with a dual-pane window for an airborne photographic system to be used in a commercial aircraft. The design of that hardware was based on a three-parameter Weibull failure probability prediction utilizing numerous tests of pristine and intentionally flawed samples of BK7 glass (Fuller et al., 1994; Pepi, 1994a). The studies reported in these papers support a tensile stress tolerance of about 1250 lb/in.^{2} (8.62 MPa) for carefully manufactured BK7 optics.

Figure 15.8 shows P_F vs. applied tensile stress curves for five types of optical glass as presented by Doyle and Kahan (2003). Values for Weibull factors S_0 and m are indicated for each glass. These curves apply to samples polished with loose 9 μm SiC abrasive subjected to double ring testing over stressed surface areas of 113 mm^2 at room temperature.

TABLE 15.4
The Gamma Function Used in Weibull Failure Predictions

m	Γ	M	Γ	m	Γ	m	Γ
3	0.8930	6.5	0.9318	10	0.9514	17	0.9693
3.5	0.8997	7	0.9354	11	0.9551	18	0.9708
4	0.9064	7.5	0.9387	12	0.9583	19	0.9722
4.5	0.9126	8	0.9417	13	0.9611	20	0.9735
5	0.9182	8.5	0.9445	14	0.9635	22	0.9757
5.5	0.9232	9	0.9470	15	0.9657	25	0.9784
6	0.9277	9.5	0.9493	16	0.9676	30	0.9818

Source: Harris, D.C., in *Materials for Infrared Windows and Domes*, SPIE Press, Bellingham, 1999.

---

*The gamma function used in statistical analysis is $\Gamma(z) = \int_0^\infty t^{z-1}e^{-t}\,dt$.

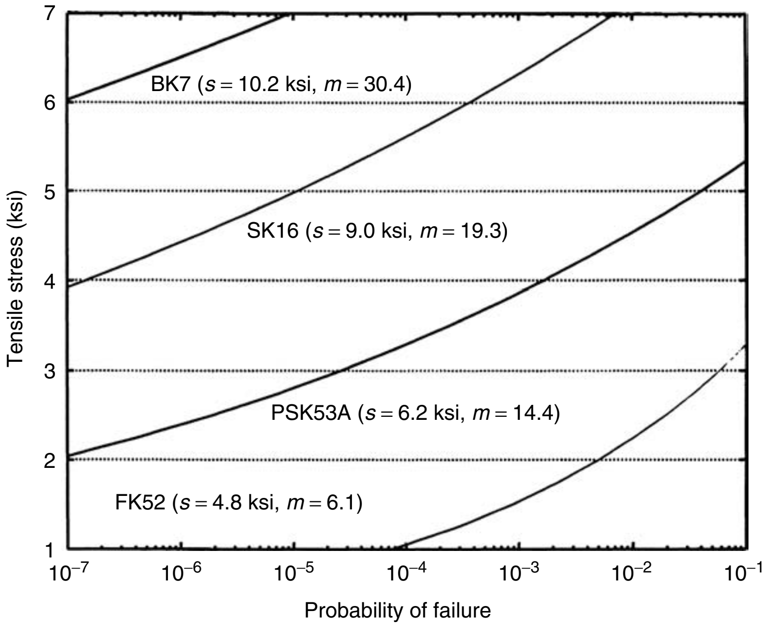

FIGURE 15.8 Probability of failure vs. applied tensile stress relationships for several Schott glasses. (From Doyle, K.B. and Kahan, M., *Proc. SPIE*, 5176, 14, 2003.)

15.2.5 Time-to-Failure Prediction

As indicated earlier, cracks in a material such as glass can grow, or propagate, when subjected to stress for an extended period of time. The velocity of propagation for flaws of particular sizes in a particular material can be determined from observations of the growth rates of visible cracks in samples under constant stress. To speed up data collection, tests are frequently conducted dynamically. The stress in this case increases at some predetermined rate. As the rate increases, the time available for cracks to grow becomes progressively shorter, so failure occurs at a somewhat higher level of stress than would occur in the static-stress case.

Pepi (1994a) gave a general equation for estimating the lifetime T_L, or time to failure, for an optic subjected to tensile stress. This lifetime is determined by the maximum stress σ_A applied to the optic, the critical stress intensity factor K_{IC}, a nondimensional shape geometry factor Y, a constant V_0 dependent upon both the environment and the material, and the residual stress character r. This equation is

$$T_L = [(r+1)^{N-3}/r^{N'-2}][\Gamma'_{(r,N)}][2K_{IC}^2/(Y^2V_0)][S^{N'-2}][\sigma_A^{-N'}] \tag{15.12}$$

where N the flaw growth susceptibility factor in the absence of a residual stress field, N' the reduced value of that factor with residual stress and

$$N' = (rN+2)/(r+1) \tag{15.13}$$

For the Griffith-type crack of prime interest here, $r = 3$, so

$$N' = (3N+2)/4 \tag{15.13a}$$

Pepi (1994a) provided a graph of T_L for BK7 glass windows in the presence of moisture for 99% reliability with 95% confidence (see the top curve in Figure 15.9. The surfaces of the optics were polished to 60-10 scratch and dig surface quality per U.S. military specification MIL-O-13830A. Data for these figures were obtained as explained in Fuller et al. (1994). The latter paper utilized a more

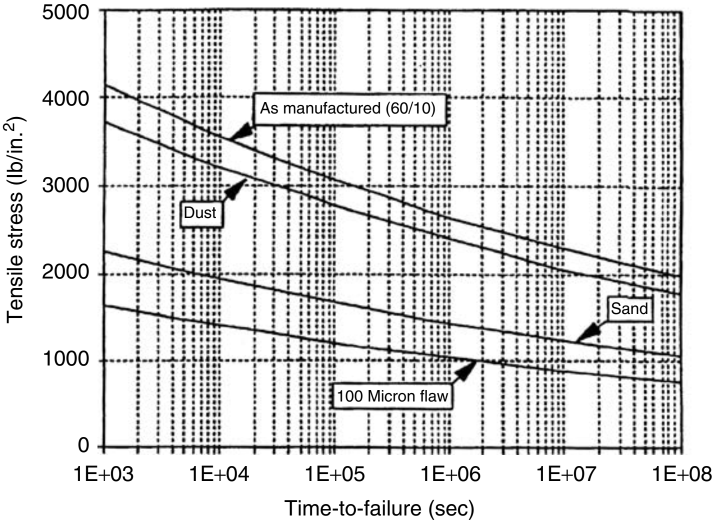

FIGURE 15.9 Plots of time-to-failure vs. applied tensile stress for BK7 glass with different degrees of surface damage for 99% reliability with 95% confidence. (From Pepi, J.W., *Proc. SPIE*, 2286, 431, 1994b.)

complex form of Eq. (15.12) that was solved using a bootstrap analysis procedure and applied to the same windows and conditions as discussed by Pepi.

The lower curves in Figure 15.9 depict the lifetimes of the BK7 windows with intentional damage from (1) erosion by airborne dust traveling at 234 m/sec (768 ft/sec) and impacting the surface at 15°; (2) erosion by windblown sand traveling at 29 m/sec (95 ft/sec) and impacting the surface at 90°; and (3) presence of a single, centrally located scratch 50–100 μm wide 20–25 μm long produced with a Vickers diamond. The reductions in lifetimes for optics with these defects are representative of anticipated worst-case environments for the windows of interest to Pepi. It is this author's opinion that, in the absence of corresponding information pertinent to other specific optics, these curves may also be applied, in general, to optics made from other optical glasses used in a typical natural (unfriendly) environment.

The variation of time-to-failure T_L vs. applied tensile stress for SF1 optical glass with three different sizes of initial flaws was predicted by Doyle and Kahan (2003). This relationship is shown in Figure 15.10. Figure 15.11 shows variations of time-to-failure T_L vs. applied tensile stress for BK7 glass as functions of the assumed probability of failure P_F ranging from 10^{-1} to 10^{-5}. These relationships are based on a Weibull S_0 of 10^4 lb/in.^{2} (68.9 MPa) and a modulus m of 30.4.

Doyle and Kahan (2003) applied the above-discussed methods to predict the lifetime to failure of a 10-in. (25.4-cm)-diameter, 0.75-in. (1.90-cm)-thick BK7 corrector plate for a Schmidt telescope that was mounted in an aluminum cell by means of 6 titanium tangential flexures bonded to the rim of the plate. The characteristic strength S_0 and modulus m of the plate were established by scaling sample test data to be 9700 lb/in.^{2} (66.88 MPa) and 30.4, respectively. The graphs of Figure 15.12 were then derived. For a desired 10 year lifetime (the vertical dashed line) and a desired probability of failure of 10^{-5} (lowest curve), a design tensile stress of 1850 lb/in.^{2} (12.75 MPa) (the horizontal dashed line) was established for each of the bonds between the flexures and the plate rim.

15.2.6 Rule-of-Thumb Stress Tolerances

Because the actual qualities of an optic's surfaces are usually unknown in real life, statistical failure analysis methods cannot always be applied with confidence. We will here apply rule-of-thumb values for the stress levels in glass that are likely to cause problems. For many years, these were based on guidance from Shand (1958) as 50,000 lb/in.^{2} (345 MPa) for compressive stress and

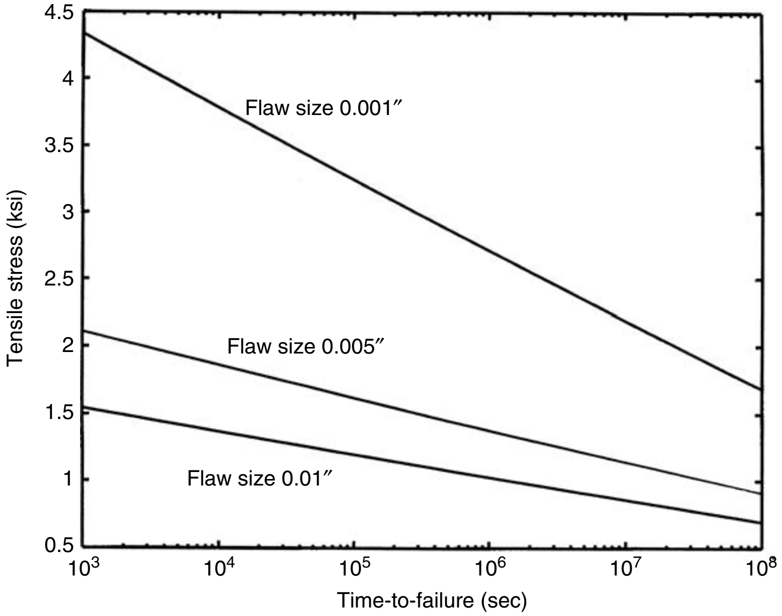

FIGURE 15.10 Time-to-failure curves for SF1 glass vs. applied tensile stress with three sizes of initial surface flaws. (From Doyle, K.B. and Kahan, M., *Proc. SPIE*, 5176, 14, 2003.)

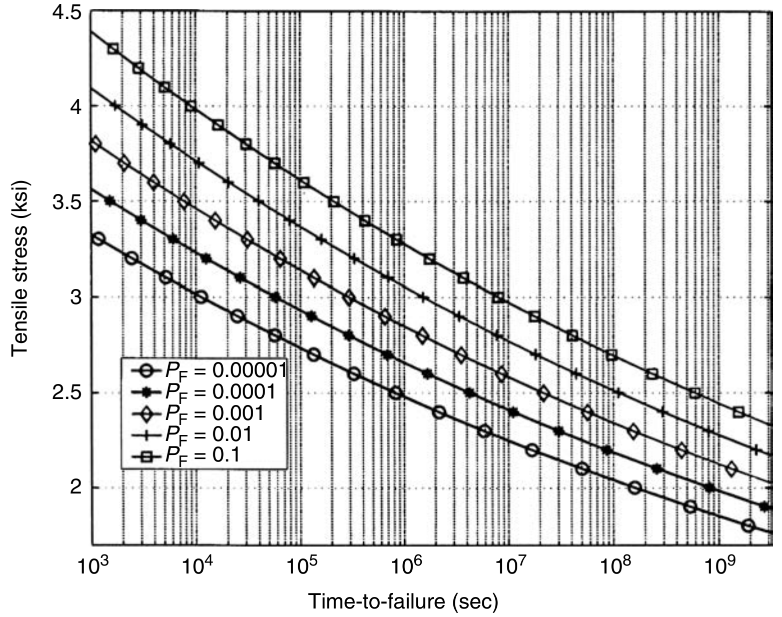

FIGURE 15.11 Time-to-failure curves for BK7 glass vs. applied tensile stress with five levels of failure probability P_F. (From Doyle, K.B. and Kahan, M., *Proc. SPIE*, 5176, 14, 2003.)

1000 lb/in.^{2} (6.9 MPa) for tension. In the immediately preceding sections, we have shown that failure of brittle materials most often occurs in tension. It would then seem appropriate to base our design decisions on estimated tensile stress rather than compressive stress. As indicated in Section 15.2.1, Doyle and Kahan (2003) suggested a rule-of-thumb tensile stress tolerance for glass of

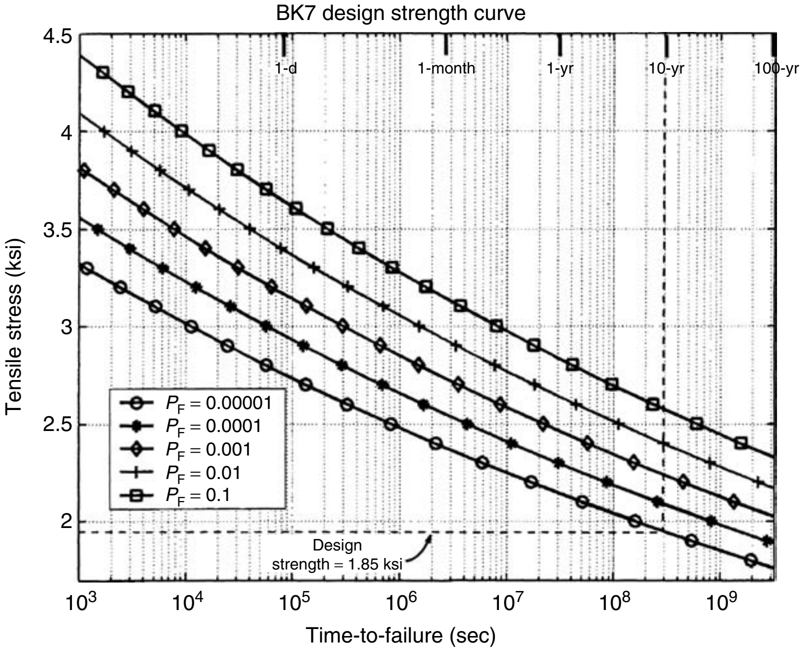

FIGURE 15.12 Time-to-failure curves for a 10-in. (25.4-cm)-diameter BK7 Schmidt telescope corrector plate vs. applied tensile stress with five levels of failure probability P_F. The allowable design stress level for bonding the plate to flexures for 10 yr lifetime is 1850 lb/in.^{2} (12.75 MPa). (From Doyle, K.B. and Kahan, M., *Proc. SPIE*, 5176, 14, 2003.)

1000 to 1500 lb/in.^{2} (6.9 to10.34 MPa). Thinking conservatively, we recommend the 1000 lb/in.^{2} (6.9 MPa) value as a generic glass survival tensile stress tolerance.

Most of the stress calculations that follow lead to compressive stress (S_C) values at glass-to-metal interfaces. Timoshenko and Goodier (1970) pointed out that compressive contact stress at these interfaces is accompanied by tensile stress in both materials. This stress occurs at the boundary of the region elastically compressed by the applied preload and is directed radially. Those authors gave the following equation for this tensile stress S_T:

$$S_T = (1 - 2v_G)(S_C)/3 \tag{15.14}$$

In Table 15.5, this equation is applied to selected optical glasses, crystals, and mirror materials. The glasses represent those from the 49 glasses in Table 3.2 having the smallest and largest v_G values as well as the ubiquitous BK7. The crystals are ones frequently used for IR optics (from Tables 3.7, 3.8, 3.10, and 3.11), whereas the mirror materials are the most common types of nonmetallics (from Table 3.13). We see from the right-hand-side column of Table 15.5 that S_T is typically S_C divided by a number ranging from a low of 4.54 to a high of 9.55 for these materials. Crompton (2004) indicated that some members of the optical industry use a S_T/S_C ratio of 0.167 or 1/6 as a rule-of-thumb value for stress analysis of opto-mechanical interfaces. Roark (1954) and Young (1989) gave no equation for this relationship, but specified $S_T \approx 0.133S_C \approx S_C/7.52$ for mechanical structures. According to Eq. (15.14), this corresponds to a v of 0.4335. Vukobratovich (2004) offered the opinion that Eq. (15.14) is extremely conservative. Slocum (1992) gave an almost identical equation to relate Hertzian (i.e., compressive) stress to flexural stress for brittle materials using a factor of 2 in the denominator instead of 3. While experts in the field do not agree as to the validity of Eq. (15.14), it is suggested for use as the best currently available approximation for "back-of-the-envelope" estimation of the significance of contact stress in glasses. We will use Eq. (15.14) for tensile contact stress estimation in this chapter. If v is not specified, we assume that a factor of 1/6 applies.

TABLE 15.5
Ratio of Tensile to Compressive Contact Stress for Selected Optical Materials per Eq. (15.14)

Material	Poisson's ratio	S_T/S_C	S_C/S_T
Optical Glasses			
K10	0.192	0.205	4.87
BK7	0.208	0.195	5.14
LaSFN30	0.293	0.138	7.25
IR Crystals			
BaF_2	0.343	0.105	9.55
CaF_2	0.290	0.140	7.14
KBr	0.203	0.198	5.05
KC1	0.216	0.189	5.28
LiF	0.225	0.183	5.45
MgF_2	0.269	0.154	6.49
ALON	0.240	0.173	5.77
$A1_2O_3$	0.270	0.153	6.52
Fused Silica	0.170	0.220	4.54
Ge	0.278	0.148	6.76
Si	0.279	0.147	6.79
ZnS	0.290	0.140	7.14
ZnSe	0.280	0.147	6.82
Mirror Materials			
Pyrex	0.200	0.200	5.00
Ohara E6	0.195	0.203	4.92
ULE	0.170	0.220	4.54
Zerodur	0.240	0.173	5.77
Zerodur M	0.250	0.167	6.00

As a further approximation, we assume that the 1000 lb/in.^{2} (6.9 MPa) tensile stress tolerance applies to nonmetallic mirror materials and optical crystals. For simplicity, we refer to all optical materials as glass and all mechanical ones as metal. In general, application of a safety factor of at least two and preferably four is advisable.

Since operational conditions are invariably less stringent than survival conditions, damage is not a concern. Mounting forces imposed under operating conditions may, however, cause optical surfaces to deform. These deformations may affect optical performance. No meaningful general tolerances for surface deformations can be given since they depend upon the level of performance required and the location of the surface in the system (surfaces are less sensitive to distortions near an image and more sensitive near a pupil). Only in a few cases are simple equations for estimating surface deformations as functions of force applied to optical components available. For the general case, these calculations are best done by FEA methods. Such methods are beyond the scope of this work.

The stresses induced by operational levels of strain can degrade the performance of optical components used in applications involving polarized light through the introduction of birefringence. This is a localized change in refractive index of the material that creates an optical path difference between two orthogonal polarized components of the radiation transmitted through the stressed region. Tolerances on birefringence are usually expressed in terms of the permitted optical path difference (OPD) for the parallel (||) and perpendicular ($\perp$) states of polarization of transmitted light at a specified wavelength. According to Kimmel and Parks (1995), birefringence of components for various instrument applications should not exceed 2 nm/cm for polarimeters or interferometers, 5 nm/cm for precision applications such as photolithography optics and astronomical telescopes, 10 nm/cm for camera, visual telescope, and microscope objectives, and 20 nm/cm for eyepieces and viewfinders. Higher birefringence can be tolerated in condenser lenses and most illumination systems. In all cases, the material's stress optic coefficient K_S determines the relationship between the applied stress and the resulting OPD. Equation (3.8) applies. It is repeated here for easy reference:

$$\mathrm{OPD} = (n_{\parallel} - n_{\perp})t = K_s St \tag{3.8}$$

where t is the path length in the material in cm, K_S is expressed in mm^2/N, and S the stress in N/mm^2. Table 3.3 lists the values of K_S at a wavelength of 589.3 nm and a temperature of about 21°C for the optical glasses listed in Table 3.2. Knowing this factor, the path length, and the tolerable birefringence, it is a simple task to establish a limit for stress in an optic.

It should be noted that surface deformations and related birefringence effects from mounting forces are seen primarily in the local regions where those forces are applied (Sawyer, 1995). Typically, these regions are near, but outside the optic's clear aperture, so the effects may not be significant over most of that aperture.

Stress also builds up within the mechanical members that compress the glass. This is usually compared with the yield strength of that metal (generally taken as that stress resulting in a dimensional change of two parts per thousand) to see if an adequate safety margin exists. In critical applications (such as those demanding extreme long-term stability), stress in mechanical components may be limited to the microyield stress value (1/ppm) for the material.

15.3 STRESS GENERATION AT OPTO-MECHANICAL INTERFACES

15.3.1 Point Contacts

Point contacts occur when spherical pads touch lightly against curved or flat optical surfaces. Figure 15.13(a) shows a flat mirror held against lapped pads by three cantilevered spring clips, each having a spherical pad. Deflections of the springs in accordance with Eq. (4.22) create the needed preload. The pad interfaces with convex and concave optical surfaces are depicted in the detail views (b) and (c) of the figure. Note that any of these surface contours could exist on any type optic. Prisms typically have flat optical surfaces. Interfaces with flat surfaces are also found at bevels adjacent to the rims of some concave optical surfaces or at step bevels used with convex optical surfaces.

When spherical optical and mechanical surfaces are pressed together, they both deform elastically creating circular contact areas $A_{\mathrm{C\ SPH}}$[†] of diameter $2r_{\mathrm{C}}$ as shown in Figure 15.14(a). The magnitudes of these areas depend upon the shapes and radii of the surfaces, the material characteristics, and the preload. The following equations, adapted from Roark (1954), apply:

$$A_{\mathrm{C\ SPH}} = \pi r_{\mathrm{C}}^2 \tag{15.15}$$

$$r_{\mathrm{C}} = 0.721(P_{\mathrm{i}}K_2/K_1)^{1/3} \tag{15.16}$$

$$K_1 = (D_1 + D_2)/(D_1D_2) \quad \text{for a convex optical surface} \tag{15.17a}$$

$$K_1 = (D_1 - D_2)/(D_1D_2) \quad \text{for a concave optical surface} \tag{15.17b}$$

$$K_2 = K_{\mathrm{G}} + K_{\mathrm{M}} = [1 - \nu_{\mathrm{G}}^2)/E_{\mathrm{G}}] + [(1 - \nu_{\mathrm{M}}^2)/E_{\mathrm{M}}] \tag{15.18}$$

[†] The "SPH" in the subscript for A_{C} identifies a spherical contact. Other terms used in other applications are "CYL," "SC," "TAN," and "TOR" representing cylindrical, sharp corner, tangent, and toroidal contacts, respectively.

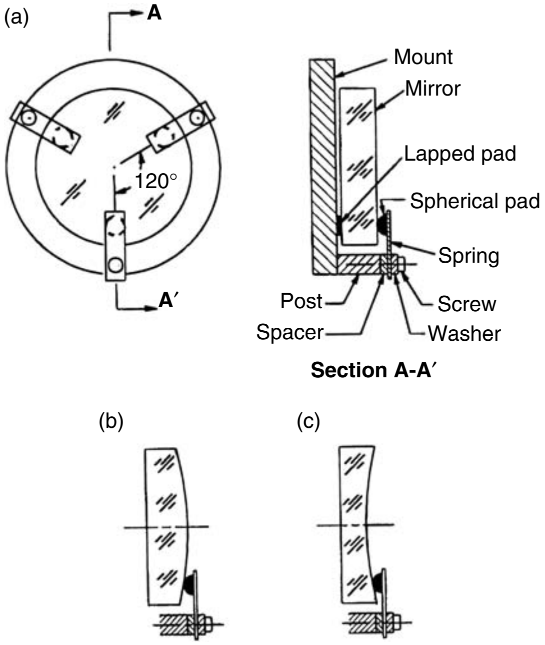
(a)
A
120°
A′
Mount
Mirror
Lapped pad
Spherical pad
Spring
Post
Screw
Spacer
Washer
Section A-A′
(b)
(c)

FIGURE 15.13 (a) Sketches of a flat mirror constrained against flat coplanar pads by three cantilevered springs with spherical pads. Detail views (b) and (c) show how one of the same pads can contact convex and concave surfaces, respectively.

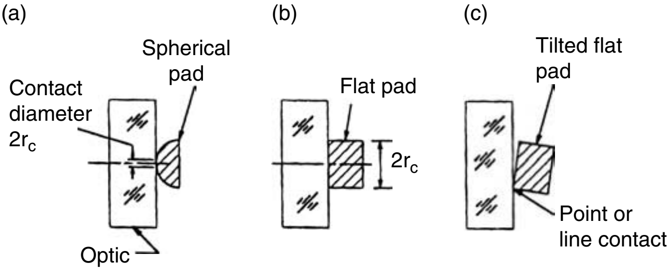
(a)
Spherical pad
Contact diameter 2r_c
Optic
(b)
Flat pad
2r_c
(c)
Tilted flat pad
Point or line contact

FIGURE 15.14 Areas of elastically deformed regions at a pad-to-flat optic interface with (a) a spherical pad and (b) a flat pad intimately contacting the optic. View (c) shows how a misaligned flat pad can cause localized stress concentration.

where P_i is the preload per spring; D_1 is twice the radius of the optical surface; D_2 is twice the radius of the contacting pad; and E_G, E_M, ν_G, and ν_M are Young's modulus and Poisson's ratio for the glass and metal, respectively.

Figure 15.15 illustrates the terms D_1 and D_2 as applied to convex, concave, and flat optical surfaces. Note that, in general, either body in this figure can be the optic (glass) and the other body the mechanical pad (metal). Usually, D_1 and D_2 are the larger and smaller body diameters, respectively. Although theoretically possible, concave pads are usually not used on convex optical surfaces.

For the geometric case shown in Figure 15.14(a), the average compressive stress in the contact region is

$$S_{\text{avg}} = P_i / A_{\text{C sph}} \tag{15.19}$$

In the case shown in Figure 15.14(b), intimate contact between two flat surfaces is assumed to exist. The stressed area A_C is still given by Eq. (15.15), but r_C is equal to one half the diameter of the pad

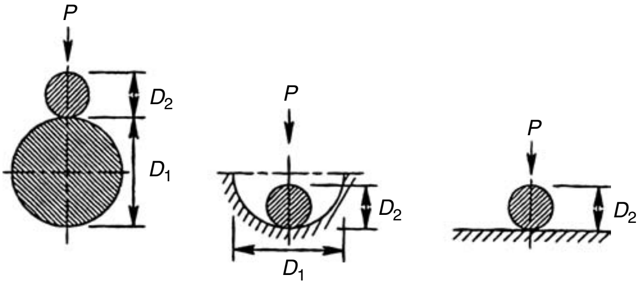

FIGURE 15.15 Key dimensions related to point contacts between elastic bodies. Shown are convex spherical pads touching (a) a convex optic, (b) a concave optic and (c) a flat optic. The force P represents the preload. (From Yoder, P.R., Jr., *Mounting Optics in Optical Instruments*, SPIE Press, Bellingham, 2002a.)

(assumed to be circular in the figure). Equation (15.19) gives the average stress across the contact area. It is obviously much smaller value for a flat pad than for a spherical pad. As shown in Figure 15.14(c), a misaligned (i.e., tilted) pad will contact the optical surface asymmetrically, leading to stress concentration in a localized region.

The compressive stress is not uniform across the contact area with a spherical pad. The peak contact stress occurs at the center of the area and decreases toward the edges of that area. Equation (15.20) is used to estimate the peak value. We will call this $S_{\mathrm{C\,SPH}}$:

$$S_{\mathrm{CSPH}} = 0.918(K_1^2 P_i / K_2^2)^{1/3} \tag{15.20}$$

where all terms are as previously defined.

Illustration of the use of Eqs. (15.14) – (15.20) for a spherical pad interface with an optic is appropriate. Let us assume that convex spherical pads made of 6061 aluminum and having radii of 2.000 in. (50.800 mm) are attached to the ends of three cantilevered springs. The pads press against the polished curved surface of a large-diameter, BK7 plano-convex lens. The total applied axial preload is 12.500 lb (55.603 N). The radius of curvature of the lens surface is 16.000 in. (406.400 mm). We want to estimate (a) the peak and (b) average compressive stresses in the glass as well as (c) the tensile stress associated with the elastic deformation of the glass.

From Tables 3.2 and 3.18: $E_G = 1.17 \times 10^7$ lb/in.^{2} (1.10 × 10^5 MPa), $\nu_G = 0.208$, $E_M = 9.9 \times 10^6$ lb/in.^{2} (6.82 × 10^4 MPa), and $\nu_M = 0.332$. For the lens, $D_1 = (2)(16.000) = 32.000$ in. (812.800 mm) and for the pad, $D_2 = (2)(2.000) = 4.000$ in. (101.600 mm). At each spring, $P_i = 12.500/3 = 4.167$ lb (18.534 N). Then, from Eq. (15.17a), $K_1 = (32.000 + 4.000)/[(32.000)(4.000)] = 0.281$ in.$^{-1}$ (0.0111 mm^{-1}). From Eq. (15.18), $K_2 = [(1 - 0.208^2)/1.17 \times 10^7] + [(1 - 0.332^2)/9.9 \times 10^6] = 1.716 \times 10^{-7}$ in.^{2}/lb (2.489 × 10^{-11} Pa^{-1}). We now have all the data needed to analyze the design.

(a) From Eq. (15.20), $S_{\mathrm{C\,sph}} = 0.918[(0.281)^2 (4.167)/(1.716 \times 10^{-7})^2]^{1/3} = 20{,}529$ lb/in.^{2} (141.55 MPa).
(b) From Eq. (15.16), $r_C = 0.721[(4.167)(1.716 \times 10^{-7})/0.281]^{1/3} = 0.0098$ in. (0.250 mm). From Eq. (15.15), $A_C = \pi(0.0098)^2 = 3.045 \times 10^{-4}$ in.^{2} (0.196 mm^2). From Eq. (15.19), $S_{\mathrm{AVE}} = 4.167/3.045 \times 10^{-4} = 13{,}683$ lb/in.^{2} (94.3 MPa).
(c) From Eq. (15.14), $S_{\mathrm{T\,SPH}} = [1 - (2)(0.208)][20{,}529]/3 = 3396$ lb/in.^{2} 27.55 MPa).

This tensile stress is too large in comparison with the above-suggested survival tolerance of 1000 lb/in.^{2} (6.9 MPa). Possible design modifications that would tend to reduce this tensile stress would be to increase the pad radius and to increase the number of springs. Increasing the pad radius by a factor of 15 to 30.0 in. (762.0 mm) and doubling the number of springs would reduce the tensile stress at each interface to 975 lb/in.^{2} (6.72 MPa) and make the design much safer.

15.3.2 Short Line Contacts

Instead of using spherical pads on springs that hold an optic in place, we could provide convex cylindrical pads as the mechanical interface. Typically, such a pad would be oriented crosswise on the end of the spring and its axial length would equal the width *b* of the spring. Alternatively, the cylindrical axis could be oriented at any convenient angle to the cantilevered length of the spring. A cylindrical pad cannot be used with a concave optical surface. Point contact between the cylinder and a convex spherical optical surface would occur under light axial loading. With greater preload, the elastic bodies would deform and contact would occur over a small area.

From the viewpoint of contact stress, the advantage of a cylindrical pad over a spherical one is slight when the optical surface is convex. This advantage increases when that surface is flat, so the primary uses of the cylindrical pad are to provide preload against the outer edges of the faces of flat lens, mirror, or window surfaces; against flat or step bevels on curved lens or mirror surfaces; or against prism surfaces. Figure 15.16 shows two examples of the latter case: (a) a cylindrical pad on a straddling spring preloading a prism vertically and (b) interfaces at posts or pins that locate a prism on a baseplate. Preload is applied in view (b) near the bottom of the hypotenuse surface by a spring (not shown).

The contact stress in a cylindrical pad interface with a flat optical surface can be modeled as shown in Figure 15.17. The pad length is *b* and its radius is R_{cyl}. D_2 is twice R_{CYL}. The surfaces are pressed together by the total preload per spring P_{i} so the preload per unit length p_{i} is P_{i}/b. The peak stress $S_{\text{C CYL}}$ that occurs along the short line contact is given by the following equation:

$$S_{\text{C CYL}} = 0.564[p_{\text{i}}/(R_{\text{CYL}}K_2)]^{1/2} \tag{15.21}$$

where K_2 is as given by Eq. (15.18).

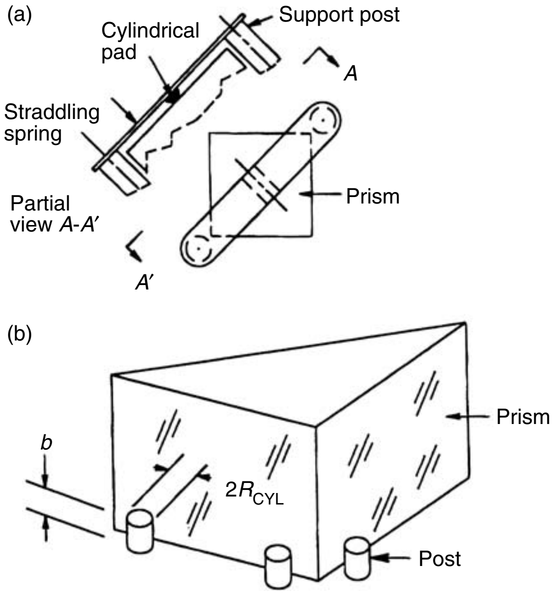

FIGURE 15.16 (a) A prism constrained by a straddling spring with a cylindrical pad. (b) A prism located on a baseplate by three cylindrical posts or pins.

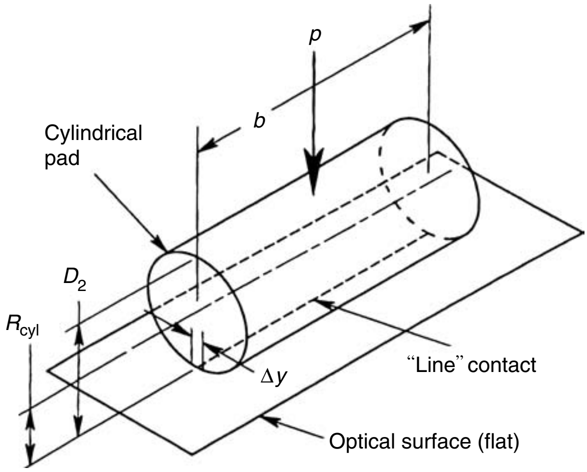

FIGURE 15.17 Analytical model for the interface between a cylindrical spring pad of length b and a flat optical surface. The parameter p is the preload per unit length of contact.

To illustrate this case, let us repeat the last example changing the spherical pad to a cylinder of length $b = 0.125$ in. (3.175 mm) and sectional radius R_{cyl} of 2.000 in. (50.800 mm). The preload per spring of 4.167 lb (18.534 N) is applied over the length b so $p_i = 4.167/0.125 = 33.336$ lb/in. (3.766 N/mm). As before, K_2 is 1.716×10^{-7} in.^{2}/lb (2.489×10^{-11} Pa^{-1}). Applying Eq. (15.21), $S_{C\ CYL} = 0.564\{33.336/[(2.000)(1.716 \times 10^{-7})]\}^{1/2} = 5560$ lb/in.^{2} (38.3 MPa). This compressive contact stress is 27% of that produced with the same preload by contact with a spherical pad of the same radius. Tensile stress would be $5560/5.137 = 1082$ lb/in.^{2} (7.46 MPa). This is almost tolerable, but if the sectional radius of the pad were to be increased to 4.000 in. (101.600 mm), the latter stress could be reduced to an even more reasonable 765 lb/in.^{2} (5.28 MPa).

The width Δy of the deformed area between the cylindrical pad and the flat optical surface as shown in Figure 15.17 is given by the equation

$$\Delta y = 1.600(K_2 p_i / K_1)^{1/2} \tag{15.22}$$

where K_1 from Eq. (15.17a) is $1/D_2$ because D_1 is infinite for a flat optical surface. Since $D_2 = 2R_{CYL}$, we can rewrite Eq. (15.22) as

$$\Delta y = 2.263(K_2 p_i R_{CYL})^{1/2} \tag{15.22a}$$

The deformed area $A_{C\,cyl}$ at the interface shown in Figure 15.17 is

$$A_{C\,CYL} = b\Delta y = 2.263b(K_2 p_i R_{CYL})^{1/2} \tag{15.23}$$

Applying this last equation to the cylindrical contact version of the last example with $R_{cyl} = 4.000$ in., we obtain $A_{C\,CYL} = (2.263)(0.125)[(1.716 \times 10^{-7})(33.336)(4.000)]^{1/2} = 1.353 \times 10^{-3}$ in.^{2}. The average compressive stress in that area is, by analogy to Eq. (15.19), equal to $P_i/A_{cyl} = 4.167/1.353 \times 10^{-3} = 3080$ lb/in.^{2} (21.2 MPa). The average tensile stress is then 600 lb/in.^{2} (4.13 MPa).

The contact stress at each locating pin of designs such as that of Figure 15.16(b) can be estimated in the same manner as just described. Generally, the stress in the prism face touching one pin will be larger than that in the face touching two pins. Yoder (2002a) showed how to estimate these stresses for a particular example. That example involved a penta prism constrained in the plane of reflection (X–Y plane) as shown in Figure 15.18(a). The locating pins were positioned just outside

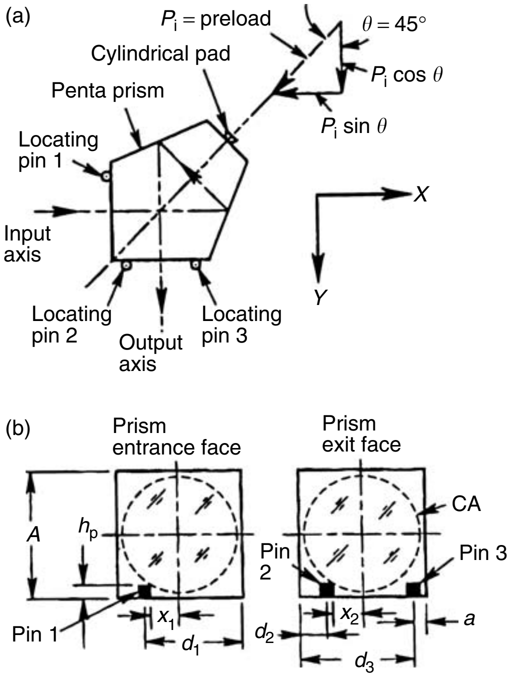
(a)
P_i = preload
$\theta = 45°$
Cylindrical pad
$P_i \cos\theta$
Penta prism
$P_i \sin\theta$
Locating pin 1
X
Input axis
Y
Locating pin 2
Output axis
Locating pin 3
(b)
Prism entrance face
Prism exit face
CA
A
h_p
Pin 2
Pin 3
Pin 1
x_1
d_1
d_2
x_2
a
d_3

FIGURE 15.18 (a) Constraints in the plane of reflection applied to a penta prism in a numerical example considered in the text. (b) Arrangement of locating pins outside the clear apertures of the prism. (From Yoder, PR., Jr., *Proc. SPIE*, 4771, 173, 2002b.)

the clear aperture (CA) as shown in Figure 15.18(b). The following equations apply to such a design:

$$x_i = [(0.5\text{CA})^2 - (0.5A - h_{pi})^2]^{1/2} \tag{15.24}$$

$$d_1 = 0.5A + x_1 + 0.5\phi_P \tag{15.25}$$

$$d_2 = 0.5A - x_2 - 0.5\phi_P \tag{15.26}$$

$$d_3 = A - \text{a} \tag{15.27}$$

$$P_1 = P_i \sin\theta \tag{15.28}$$

$$P_2 = \frac{P_i(d_1 \sin\theta - d_3 \cos\theta)}{d_2 - d_3} \tag{15.29}$$

$$P_3 = P_1 \cos\theta - P_2 \tag{15.30}$$

Equations (15.28) and (15.30) result from the geometry of the design while Eq. (15.29) results from equating the clockwise and counterclockwise moments about an axis parallel to Z through a reference point arbitrarily chosen as the corner of the prism between the refracting surfaces.

We set $\theta = 45°$ and assume the prism edge A to be 1.250 in.; dimension a to be $A/10$; the pin contact lengths to be $h_{P1} = 0.250$ in., $h_{P2} = 0.125$ in., and $h_{P3} = 0.271$ in.; the pin diameters = $2R_{CYL} = 0.125$ in.; the pins to be 416 CRES; the prism to be BK7 glass; its CA to be 0.9/A or 1.125 in.; and the total preload P_i to be 3.200 lb. We then determine the values for x_1, x_2, d_1, d_2, and d_3

from Eqs. (15.24) – (15.27) to be 0.419, 0.258, 1.107, 0.305, and 1.125 in., respectively. The preloads at each pin then are $P_1 = 2.263$ lb, $P_2 = 0.050$ lb, and $P_3 = 2.213$ lb. Dividing these values by the lengths of contact with the pins, we find the linear preloads to be $p_1 = 9.052$ lb/in., $p_2 = 0.400$ lb/in., and $p_3 = 8.165$ lb/in. From Table 3.2, $K_G = 8.05 \times 10^{-8}$ in.^{2}/lb and from Table 3.18, $K_M = 3.17 \times 10^{-8}$ in.^{2}/lb. Hence, from Eq. (15.18), $K_2 = 1.122 \times 10^{-7}$ in.^{2}/lb. Applying Eq. (15.21), we find $S_{C\ CYL}$ at pin 1 to be $0.564\{9.052/[(0.0625)(1.122 \times 10^{-7})]\}^{1/2} = 20{,}264$ lb/in.^{2}. Similarly, we find that the peak compressive stresses at pins 2 and 3 are 4260 and 19,245 lb/in.^{2}. Noting from Table 15.5 that $S_T/S_C = 1/5.14$, we find that the equivalent tensile stresses are 3942, 829, and 3744 lb/in.^{2}, respectively.

The values just calculated are not acceptable in comparison to our assumed tensile stress tolerance of 1000 lb/in.^{2}, so design changes are in order. Before addressing that issue, let us consider how we might make these stresses more equal. Yoder (2002b) addressed this issue for the prism mounting of Figure 15.18. Figure 15.19 illustrates the approach followed. The straddling spring was moved to allow the preload to be applied through a curved pad bonded to the corner of the prism just above its base and outside the clear aperture of the reflecting surface. The angle θ at which the preload was applied was then varied. Equations (15.24) – (15.30) determined the preloads at each pin interface for selected values of θ. Then, using Eq. (15.21), the compressive stresses at those interfaces were estimated. Note that friction was neglected in this computation.

Table 15.6 lists the values of the preload components and the compressive stresses at each pin for $35° < \theta < 40°$ while Figure 15.20 shows graphically how the stresses vary with angle. There is no single θ value that produces the same stress at all three pins. The best compromise toward equality for this example is indicated as 37.36°. For this angle, the stresses are equalized to within about 6% of the average value of 17,600 lb/in.^{2} (121.35 MPa).

Techniques for reducing the stress at the pins include increasing the contact lengths h_P and the pin radii R_{cyl}. These changes are limited by the need to avoid vignetting of the prism aperture. Adding more pins is not a viable change because the design would depart from the desired kinematic approach. Reducing the required preload would help, but requires a reduction in the a_G specification.

Figure 15.21 shows the approximate compressive stresses at the three pins for the design configuration of Figure 15.19 and the numerical example considered just above with various lengths of contact on the pins. The values of θ corresponding to the points plotted in Figure 15.21 range from 37.10° for $h_P = 0.1250$ in. to 29.07° for $h_P = 0.2710$ in. If we require that no pin shall be closer than 0.125 in. from the edge of a prism face and that no vignetting occur, this limiting length is

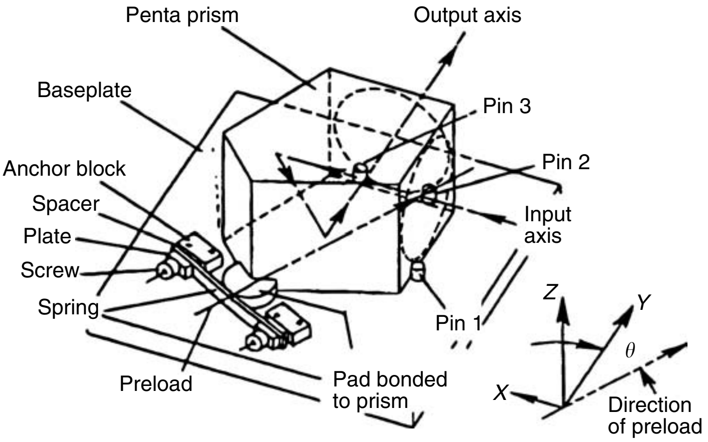

FIGURE 15.19 Spring arrangement preloading a penta prism in the X–Y plane at an angle θ to the Y-axis. One tilt and two translations are constrained semikinematically by these interfaces. (From Yoder, PR., Jr., *Proc. SPIE*, 4771, 173, 2002b.)

TABLE 15.6
Variations of Preload Components and Compressive Contact Stresses with Preload Angle θ for the Penta Prism Mounting Shown in Figure 15.19 and Discussed in the Text.

	Preload Components (lb)			Contact Stresses (lb/in.^{2})		
θ (°)	Pin 1	Pin 2	Pin 3	Pin 1	Pin 2	Pin 3
40.0	2.060	0.588	1.867	19,222	14,519	17,565
38.0	1.973	0.801	1.723	18,812	16,957	16,877
37.36[a]	1.944	0.870	1.677	18,677	17,664	16,649
37.0	1.928	0.908	1.651	18,600	18,049	16,518
36.0	1.883	1.014	1.578	18,382	19,076	16,149

[a] Values were Determined Graphically as a "Best Fit" for All Pins (See Figure 15.20).

Source: Yoder, P.R., Jr., *Proc. SPIE*, 4771, 173, 2002b.

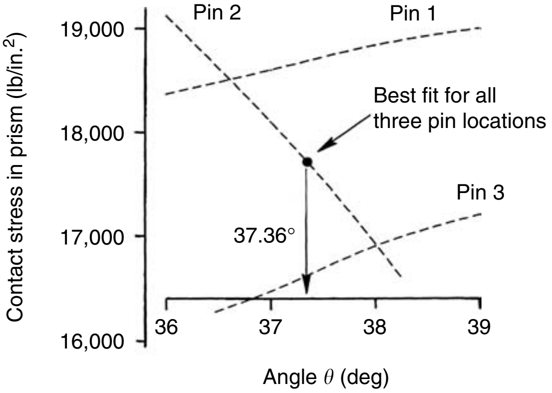

FIGURE 15.20 Variations with preload angle θ of contact stresses in the penta prism of Figure 15.19 at the locating pins 1 through 3. The "best fit" angle equalizes the stresses within about 6%. (From Yoder, PR., Jr., *Proc. SPIE*, 4771, 173, 2002b.)

0.271 in. For that condition, the stresses can be made equal within ~ 5%. This represents a slight improvement over the results cited above for $\theta = 45°$.

In all mounting arrangements wherein a prism is located against cylindrical pins, it is essential that the pin axes be parallel to the prism face. Otherwise, localized stress concentration could occur at point contacts on tilted pins with the glass surfaces. Yoder (2002b) suggested the use of locating pins designed in general as shown in Figure 15.22(b). This pin is configured as a cylinder centered at the top of a cylindrical post. One end of the cylinder has a convex spherical radius that touches the prism face. The post can be pressed into a locating hole in the baseplate of the mount as would be done with a conventional locating pin. The spherical radius is chosen to give an acceptable stress under the given preload. The configuration of Figure 15.22(a) differs from that in view (b) only in that the geometrical shape of the body attached to the post has a rectangular (cube) shape.

Stress in the glass at the sphere-to-flat interfaces with these special pins would be estimated by the technique described in the preceding section for a spherical pad contact. For example, if the mounting design of Figure 15.19 were to utilize pins with spherical radii of 14.7 in. (37.34 mm), the tensile stresses at pins 1 – 3 with the preload components for $\theta = 37.36°$ could be reduced to 999, 764, and 951 lb/in.^{2}, respectively. Longer radii would reduce these stresses even more.

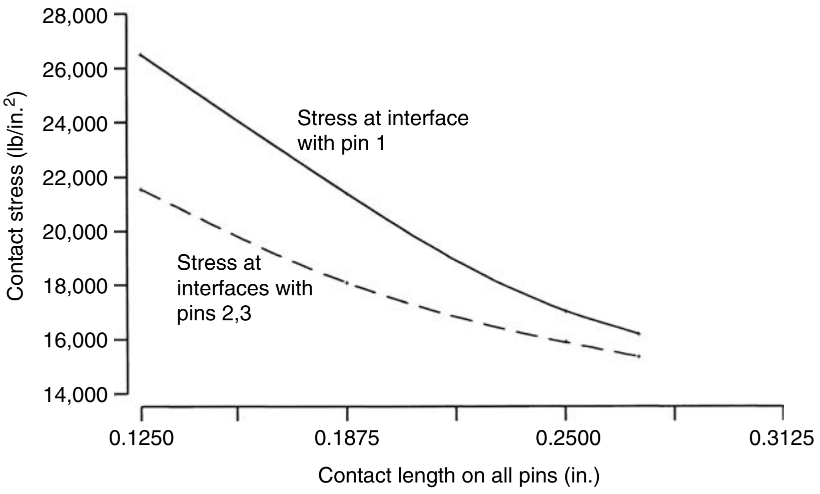

FIGURE 15.21 Variations of compressive contact stresses at the locating pins of the prism mount shown in Figure 15.19 as functions of lengths of contacts on the pins.

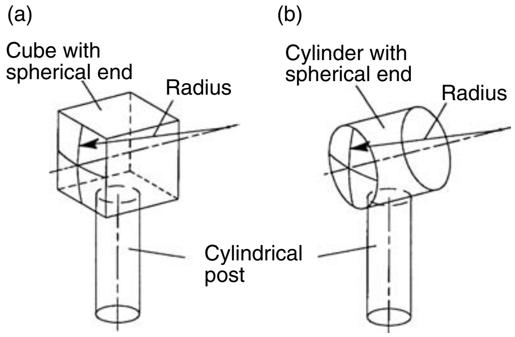

FIGURE 15.22 Configurations of special locating pins: (a) with cube-shaped top element, (b) with cylindrical top element. Each pin has one spherical face that can replace the commonly used cylindrical pin and thereby reduce criticality of pin alignment. (Adapted from Yoder, PR., Jr., *Proc. SPIE*, 4771, 173, 2002b.)

Note that a flat locating surface (a sphere of infinite radius) could be produced on the cylinder or cube atop the locating pin. This would tend to minimize contact stress if that surface is truly flat, and intimate contact can be achieved with the optic over a significant area. This configuration would be practical only if the contacting surfaces created on the pads on pin 2 and pin 3 are coplanar and the pad on pin 1 is orthogonal to the plane containing the dual pads to the same degree as the prism surfaces are orthogonal. Machining these pad surfaces *in situ* by SPDT would be one way to produce this arrangement.

Figures 15.23(a) and (b) show the same basic mounting concept as suggested for the penta prism, but applied to a beam splitter cube and to a right angle prism, respectively. The concept can be applied to other prism types as well.

15.3.3 Annular Contacts

The contact stress developed within a circular lens, window, or small mirror in a surface-contact mounting configuration from an axial force applied around the edge of the polished surface by

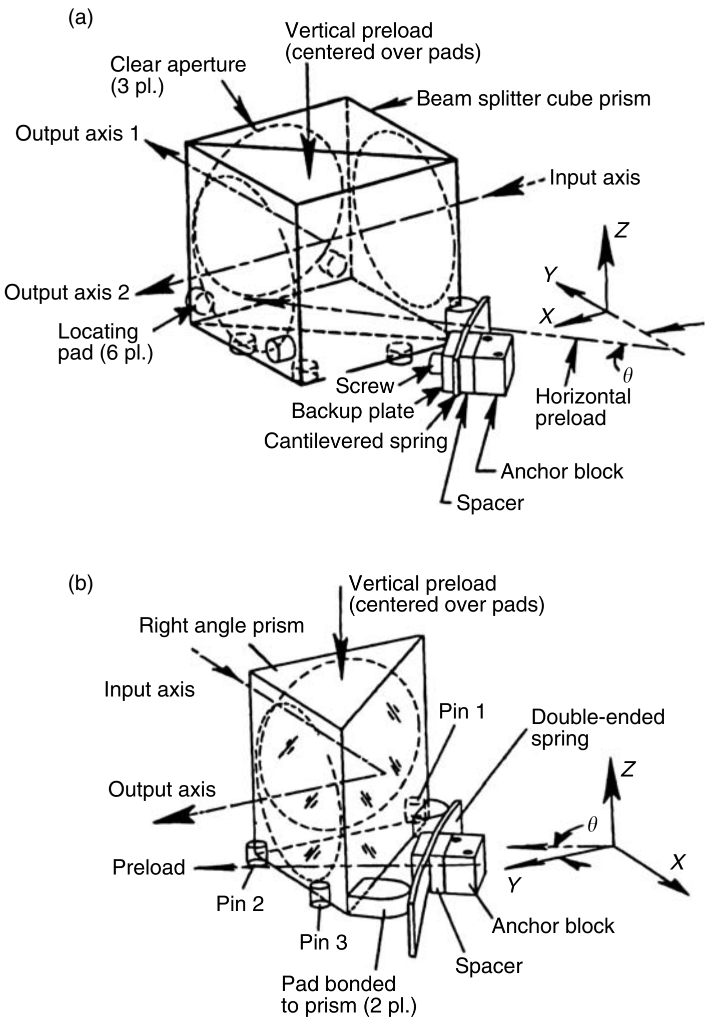
(a)
Vertical preload (centered over pads)
Clear aperture (3 pl.)
Beam splitter cube prism
Output axis 1
Input axis
Z
Y
X
θ
Output axis 2
Locating pad (6 pl.)
Screw
Backup plate
Cantilevered spring
Horizontal preload
Anchor block
Spacer
(b)
Vertical preload (centered over pads)
Right angle prism
Input axis
Pin 1
Double-ended spring
Z
Output axis
θ
X
Y
Preload
Pin 2
Pin 3
Anchor block
Spacer
Pad bonded to prism (2 pl.)

FIGURE 15.23 (a) A beam splitter cube prism constrained semikinematically with the preload in the X–Y plane provided by a cantilevered spring at an angle $\theta = 37.4°$ to the Y-axis. (b) A right-angle prism constrained semikinematically with a centrally fixed straddling spring. (From Yoder, PR., Jr., *Proc. SPIE*, 4771, 173, 2002b.)

means such as a threaded retainer (see Figure 4.33) or a circular flange (see Figure 4.40) depends on the preload, the radius of the optical surface, the geometric shape of the mechanical interface, and the physical properties of the materials involved. The force generally varies with temperature. The consequences of this variation are considered in Section 15.6.3.

Because the materials in the lens and the mount are both elastic, axial stress has a peak value S_C along the centerline of the narrow annular deformed area of contact between the metal and glass around the outer edge of the optical surface. This centerline is at a radius of y_C from the axis. The stress decreases at points within the lens progressively farther away radially from this centerline, i.e., toward and away from the lens axis. Figure 15.24 shows an analytical model of the interface. The larger cylinder of diameter D_1 represents the optical surface while the smaller cylinder of diameter D_2 represents the mount interface. Both cylinders have lengths equal to the perimeter of a circle of radius y_C or $2\pi y_C$. The cylinders are pressed against each other by the linear preload force p (i.e., preload per unit length of contact) as indicated in the figure. The annular width of the elastically deformed region is indicated as Δy; it is given by Eq. (15.22). The optical surface in Fig. 15.24

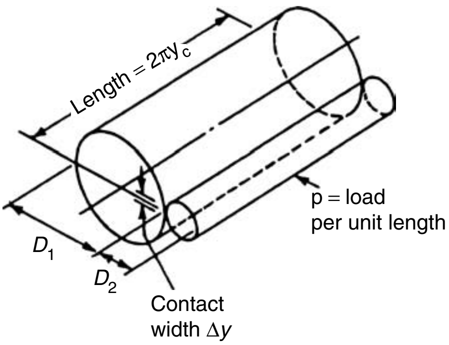

FIGURE 15.24 General analytical model of the surface contact interface between a convex mechanical constraint (small cylinder) and a convex lens or mirror surface (large cylinder).

is shown as convex. If the surface were to be concave, the smaller cylinder of the figure would contact the inside surface of the larger cylinder (as in Figure 15.15[b]). Otherwise the geometry would be unchanged.

The average contact stress within this rectangular deformed area can be calculated using

$$S_{\mathrm{ave}} = P/A_{\mathrm{C}} = P/(2\pi y_{\mathrm{C}}\Delta y) \tag{15.31}$$

The peak contact stress is given by the following equation:

$$S_{\mathrm{C}} = 0.798(K_1 p/K_2)^{1/2} \tag{15.32}$$

where K_1 is derived from Eq. (15.17a) or (15.17b) depending on whether the optical surface is convex or concave, p is the preload per unit length of the contact or $P/2\pi y_{\mathrm{C}}$, and K_2 is determined from Eq. (15.18). The parameter K_1 is discussed in the following subsections in conjunction with various possible mechanical interface shapes. Computed values of K_{G} and K_{M} are listed for selected glasses, crystals, and metals in Tables 3.2, 3.7, 3.8, 3.10, 3.11, and 3.18.

If one divides Eq. (15.32) by Eq. (15.31) it can easily be shown that $S_{\mathrm{C}}/S_{\mathrm{avg}} = (0.798)(1.600)$, so the peak axial contact stress for a lens or mirror surface constrained axially near its rim is always 1.277 times the average value. Once again, the tensile stress just outside the deformed area is given by Eq. (15.14).

15.3.3.1 The Sharp Corner Interface

The sharp-corner interface was described in Section 4.7.5.1 as one in which the intersection of flat and cylindrical machined surfaces on the metal part has been burnished to a radius of the order of 0.002 in. (0.051 mm) (see Delgado and Hallinan, 1975). This small-radius mechanical edge contacts the glass at height y_{C}, as shown schematically in Figure 15.25. The angle between the intersecting machined surfaces can be 90° (as shown) or, preferably, $> 90°$. An obtuse angle edge between the machined surfaces can usually be made smoother and with fewer defects (pits or burrs) that might cause stress concentrations than an edge with a smaller included angle. The analytical model of Figure 15.24 applies.

Assuming that D_2 for the sharp corner interface is always 0.004 in. (0.102 mm), substitution of this value into Eqs. (15.17a) or (15.17b) gives $K_{1\ \mathrm{SC}} = (D_1 \pm 0.004)/0.004D_1$ (in USC units) and $K_{1\ \mathrm{SC}} = (D_1 \pm 0.102)/0.102D_1$ (in metric units). For a convex or concave optical surface radius larger than 0.200 in. (5.080 mm), D_2 can be ignored and the value of K_1 is constant at 250/in. (10/mm). The error from this approximation does not exceed 2%.

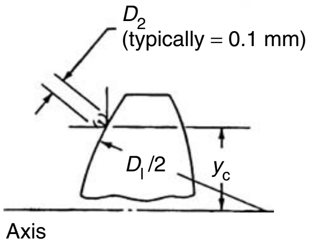

FIGURE 15.25 Sectional view through the interface between a sharp corner mechanical surface and a convex optical surface.

To help the reader understand the analysis of stresses at this type interface, we consider the following example from Yoder (2002a). A biconvex germanium lens has the following dimensions: $D_G = 3.100$ in., $R_1 = 18.000$ in. and $R_2 = 72.000$ in. The lens is mounted in an aluminum cell with sharp-corner interfaces at $y_C = 1.500$ in. on both surfaces. We want to know what contact compressive stress $S_{C\ SC}$ and the corresponding tensile stress $S_{T\ SC}$ are developed at each interface if the axial preload is 20.000 lb. From Table 3.10, $K_G = 6.13 \times 10^{-8}$ in.^{2}/lb and from Table 3.18, $K_M = 8.99 \times 10^{-8}$ in.^{2}/lb so $K_2 = 1.51 \times 10^{-7}$ in.^{2}/lb. The linear preload is $p = 20.000/[(2\pi)(1.500)] = 2.122$ lb/in. Because R_1 and R_2 both exceed 0.200 in. (5.080 mm), $K_{1\ SC} = 250$/in. for each surface. From Eq. (15.31), $S_{C\ SC} = 0.798[(250)(2.122)/1.51 \times 10^{-7}]^{1/2} = 47{,}268$ lb/in.^{2} at each surface. From Table 15.5, $S_T/S_C = 1/6.76$ for germanium, so $S_{T\ SC}$ is 6992 lb/in.^{2}. This stress level is too large in comparison with our rule-of-thumb tolerance of 1000 lb/in.^{2}, so the design is not satisfactory. A simple design change that alleviates this problem is discussed in the next section.

15.3.3.2 The Tangential Interface

The tangential interface is depicted in the sectional view (a) and analytical model (b) of Figure 15.26. It was described in Section 4.7.5.2 as an interface in which a convex spherical lens surface contacts a conical mechanical surface. This interface type cannot be used with a concave optical surface. Equation (15.32) is used to calculate $S_{C\ TAN}$. K_1 is $1/D_1$ where D_1 is twice the optical surface radius while p and K_1 are the same as for the sharp corner case.

Let us repeat the peak stress calculation for R_1 in the last example substituting a tangential mechanical interface for the sharp corner one. We know that $K_{1\ TAN} = 1/[(2)(18.000)] = 0.0277$ in.$^{-1}$. All other parameters in Eq. (15.32) are unchanged. Hence, $S_{C\ TAN} = 0.798[(0.0277)(2.122)/1.51 \times 10^{-7}]^{1/2} = 499$ lb/in.^{2}.

If we compare this result with the corresponding compressive stress with a sharp corner interface, we see that the stress with the tangential interface is significantly reduced. From examination of the pertinent equations for contact stress for the two cases, we would expect the ratio $S_{C\ SC}/S_{C\ TAN}$ to be $[(250)(2R_1)]^{1/2} = 94.9$. Not too surprisingly, this is almost exactly what we obtain from 47,268/499. Applying the S_C/S_T ratio for germanium from Table 15.5, we find that the corresponding peak tensile stress is $499/6.76 = 74$ lb/in.^{2}. For a given design, the advantage of the tangential interface over the sharp-corner interface from the viewpoint of peak contact stress is apparent. The average stress with this interface is 528/1.277 or 413 lb/in.^{2}.

15.3.3.3 The Toroidal Interface

In Section 4.7.5.3, toroidal (or donut-shaped) mechanical surfaces contacting spherical lens surfaces were described. Figure 15.25 again applies, and K_1 for interfaces on convex or concave surfaces is given by Eq. (15.17a) or (15.17b), respectively, with D_1 set equal to twice the optical surface radius and D_2 set equal to twice the sectional radius (R_T) of the toroid. Toroidal mechanical surfaces contacting optical surfaces are almost always convex. The limiting case for small values of R_T

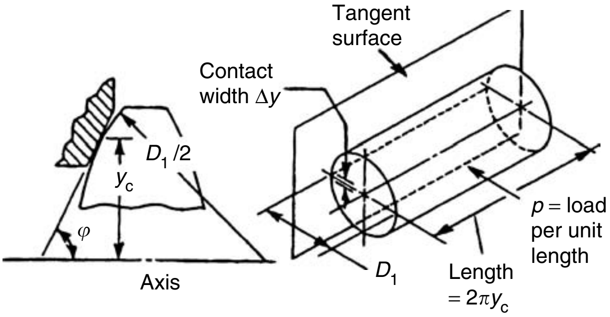

FIGURE 15.26 (a) Sectional view through the interface between a tangential (conical) mechanical surface and a convex optical surface. (b) An analytical model for that type interface.

would be equivalent to a sharp corner. If R_T increases to infinity and the lens surface is convex, the limiting case is the same as with a tangential interface. Only a convex toroid can contact a concave lens surface. The limiting case for a large R_T is then a radius equaling that of the optical surface. This is equivalent to a spherical interface (see Section 4.7.5.4).

Let us change the shape of the 3.100-in.-diameter germanium lens in the example of Section 15.3.3.1 to a meniscus with R_1 convex and R_2 concave and see what happens to the stress values. The magnitudes of the radii are unchanged at $R_1 = 18.000$ in. and $R_2 = 72.000$ in. D_1 at the convex surface is then 36.000 in. and D_1 at the concave surface is 144.000 in. We want to estimate the peak and average contact stresses $S_{C\ TOR}$ and S_{AVE} under 20.000 lb preload from a toroidal mechanical surface on a retaining ring. The contact height is once again $y_C = 1.500$ in. For reasons given in Section 15.4, we will assume $R_T = 10R_1 = 180.000$ in. at the convex surface, and $R_T = 0.5R_2 = 36.000$ in. at the concave surface. At the convex lens surface, $D_2 = (2)(180.000) = 360.000$ in. while, at the concave surface, $D_2 = (2)(36.000) = 720$ in. From Eq. (15.17a), $K_1 = (36.000 + 360.000)/[(36.000)(360.000)] = 0.0306$ in.$^{-1}$. As before, the linear preload p is 2.122 lb/in. and $K_2 = 1.51 \times 10^{-7}$ in.$^{-2}$ /lb. From Eq. (15.32), $S_{C\ TOR} = 0.798[(0.0306)(2.122)/1.512 \times 10^{-7}]^{1/2} = 522$ lb/in.^{2}. At the concave lens surface, from Eq. (15.17b), $K_1 = (144.000 - 72.000)/[(144.000)(72.000)] = 6.944 \times 10^{-3}$ in.$^{-1}$. From Eq. (15.32), $S_{C\ TOR} = 0.798[(6.944 \times 10^{-3})(2.122)/1.512 \times 10^{-7}]^{1/2} = 249$ lb/in.^{2}. The tensile stresses are now 77.2 and 36.8 lb/in.^{2} at R_1 and R_2, respectively.

Note that the peak compressive contact stresses at both surfaces in this example using toroidal interfaces are reduced significantly from those with a sharp corner interface and that, for the convex surface, they are almost the same as result with the tangential interface. The average and tensile stresses would also be very nearly the same as with the tangential interface. Since a toroid also works well with a concave optical surface, it is seen to be a favorable type of interface for the opto-mechanical interface in any surface-contact mounting design.

Although it is not common, a concave toroid could be used with a convex lens surface. It will not work with a concave lens surface. The lower limit for R_T for the convex surface case is the matching radius (i.e., a spherical interface) while the upper limit for R_T is infinity (i.e., a tangential interface). Figure 15.27(a) shows schematically a convex lens surface with convex toroidal, tangential, and concave toroidal mechanical interfaces. The latter is the dashed line. Its center is at C_T on the surface normal, but below the axis at distances h and k from the lens surface center of curvature. Note that this toroid is not normal to the axis at its intersection with that axis. Its cross-sectional shape resembles that of one side of a classical Gothic Arch as used in architectural applications (see Figure 15.27[b]). The circular curved surfaces have centers at the points C.

The applicability of this configuration and its potential for reducing contact stress below that provided by a tangential interface was pointed out by Sullivan (2004). The contact stress at the lens interface of Figure 15.27(a) is given by calculating D_2, assigning it a negative sign, and substituting it into Eq. 15.17(a) for K_1. Using the appropriate value for K_2, Eq. (15.32) then gives the compressive stress,

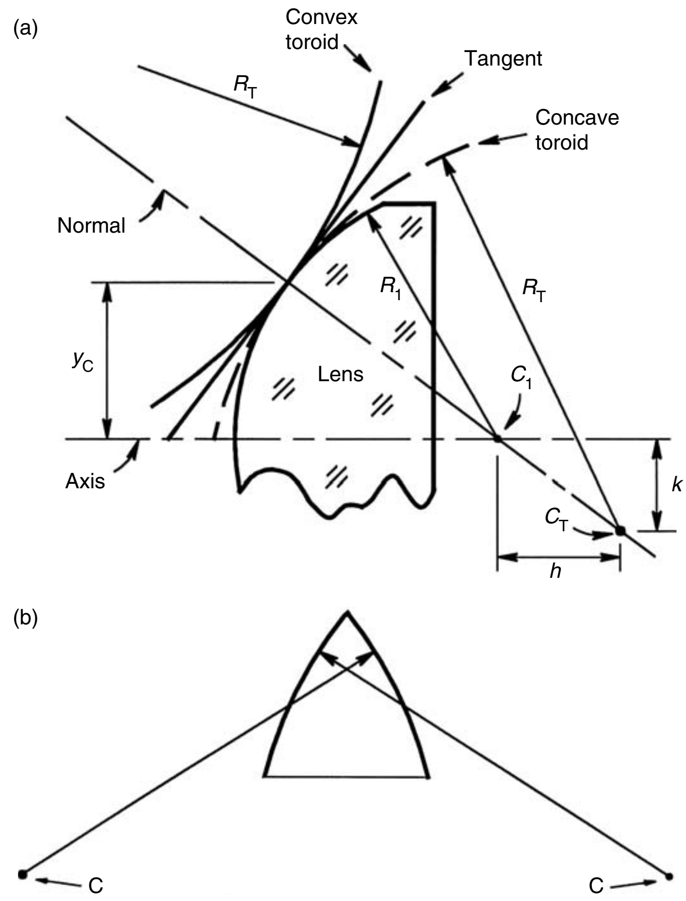

FIGURE 15.27 (a) Schematic representation of a concave toroidal interface (dashed line) with a convex lens surface. The conventional convex toroidal and tangential interfaces also are shown. (b) Representation of a classical Gothic arch, which bears a distinct resemblance to the concave toroidal interface on a lens surface.

which we convert to tensile stress by dividing by the number from Eq. (15.14) appropriate to the optical material type.

Once again considering the 18.000 in. radius convex surface (R_1) of the same 3.100-in.-diameter germanium lens and mounting design as in the last two examples, but with a concave toroidal interface, we can easily estimate the contact stress. Let us assume $R_T = 10R_1 = 180.000$ in. so $D_2 = -2R_T = 360.000$ in. and K_1 is 0.0250 in.$^{-1}$. K_2 is 1.512×10^{-7} in.^{2}/lb and $p = 2.122$ lb/in. as before. Then, $S_C = 0.798[(0.0250)(2.122)/1.512 \times 10^{-7}]^{1/2} = 473$ lb/in.^{2}. We divide this by 6.76 to obtain 70 lb/in.^{2} as the tensile contact stress. This stress is very slightly smaller than the 74 lb/in.^{2} value obtained with a tangential interface. Using a longer radius for the concave toroid would reduce the stress. For example, for $R_T = -45$ in., $S_T = 57$ lb/in.^{2} and for $R_T = -22.5$ in., $S_T = 33$ lb/in.^{2}. Note that the lower limit on $R_T = R_1$ or 18 in. for this example. In that case, the stress would be essentially zero as the interface would be, as described in the next section.

15.3.3.4 The Spherical Interface

Spherical mechanical contact by a retainer on a convex or concave optical surface (discussed in Section 4.7.5.4) distributes axial preloads over large annular areas and hence can be essentially stress free. If the surfaces match closely (i.e., within a few wavelengths of light) in radius and contour, the contact stress equals the total preload divided by the annular area of contact in accordance with Eq. (15.19). Since the area is relatively large, the stress is almost always small enough to be ignored. If the surfaces do not match closely, the contact can degenerate into a small annular area or even a line (i.e., a sharp-corner interface). Either of these alternatives would be unfavorable because of the potential for high stress generation. For this reason and because the cost of making the mechanical part to the necessary accuracy is high, the spherical interface is not often used.

15.3.3.5 The Flat Bevel Interface

In Section 4.7.5.5 we discussed flat bevel interfaces. As in the case of the spherical interface, the contact stresses that are due to axial preloads (total preload/contact area) are inherently small because the area of contact is so large. Therefore, these stresses may be ignored. However, if the contacting surfaces are not truly flat and parallel, contact will occur at the high points and stresses will increase at these locations. If these surfaces are not accurately oriented, line contact (i.e., a sharp-corner interface) can occur. This could lead to high localized stress.

15.4 PARAMETRIC COMPARISONS OF ANNULAR INTERFACE TYPES

Figure 15.28(a) shows the variation of axial tensile contact stress with radius of the contacting mechanical surface for a particular design having a convex lens surface with $R = 10.000$ in. (254.000 mm), a lens diameter of 1.500 in. (38.100 mm), and a mechanical linear preload p of 1.000 lb/in. (0.175 N/mm) on an annular area near the lens rim. The lens is made of BK7 glass and the mount is made of 6061 aluminum. Both the stress and the mechanical surface radius are plotted logarithmically to cover large ranges of variability. At the left is the short radius characteristic of the sharp corner interface (at the dashed vertical line) while at the right, the tangential interface case is approached asymptotically. Between these extremes are an infinite number of toroidal interface designs. The small circle indicates a "preferred" minimum toroidal radius ($R_T = 10R$) for which the stress is within 5% of the value that would exist with a tangential interface (see Yoder, 1991).

Figure 15.28(b) shows a similar relationship for a concave lens surface example. All other parameters are the same as in view (a). The dashed vertical line at the left again represents the sharp corner case. As the toroidal corner radius increases toward the matching radius limit (which is equivalent to a spherical interface), the stress decreases. The circle represents an arbitrarily chosen "preferred" minimum toroidal radius of $0.5R$ at which the stress will approximate the value that would prevail at the same preload on a convex surface of the same radius using a $10R$ toroidal interface. The relationships indicated in these figures demonstrate conclusively that the axial contact stress is always significantly higher with a sharp corner interface than with any other type of interface.

Figure 15.29(a) shows what happens to the axial contact stress for the same lens as in the last example if the linear preload p (and, hence, the total preload) is changed by factors of 10 from 0.001 to 10 lb/in. (1.75×10^{-4} to 1.75 N/mm). View (b) shows a similar relationship for a concave surface with all other parameters unchanged. In general, if the total axial preload P on an optic with any type of interface and any surface radius increases from P_1 to P_2 while all other parameters remain fixed, the resulting axial contact stress changes by a factor of $(P_2/P_1)^{1/2}$. A tenfold increase in preload therefore increases the stress by a factor of $\sqrt{10} = 3.162$.

Figures 15.30(a) and (b) show how the axial tensile contact stress for the same example as in Figure 15.29 varies as the surface radius of the lens is changed by successive factors of 10 for convex and concave surface cases, respectively. The preload is held constant ($p = 1.0$ lb/in. [0.175 N/mm]). The stress is seen to be independent of the surface radius or its algebraic sign (i.e., convex or concave) for a sharp corner interface (vertical dashed line on the left side of each graph). The greatest changes occur for long radii toroids on either type of surface. The limits are the tangential interface and the matching radii interface for the convex surface and the concave surface cases, respectively. Once again, the toroids indicated by the circles on each curve (toroid radius $= 10R$ for convex surfaces and $0.5R$ for concave surfaces) are the recommended minimum sectional radii for

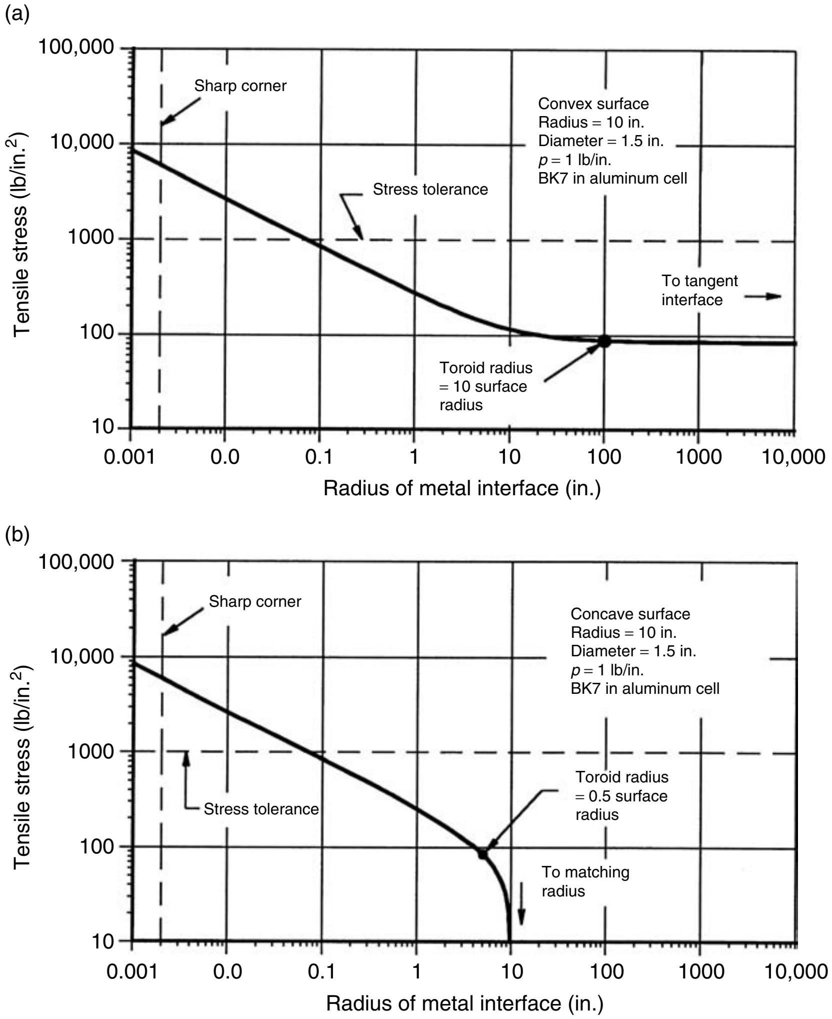

FIGURE 15.28 Variation of tensile contact stress as a function of the sectional radius of the mechanical contacting surface for (a) a typical preloaded convex lens surface and (b) a typical preloaded concave lens. The design dimensions and characteristics are as indicated.

the mechanical component. Use of toroids with longer radii than these recommended minimums would, of course, cause the contact stresses to decrease. The positive tolerance on R_T can therefore be quite loose. This simplifies inspection of such parts. Because the tangent interface is slightly easier to manufacture than a toroid, it is recommended that tangential interfaces be used on all convex lens surfaces. Further, we recommend that toroidal interfaces of radius $R_T \sim 0.5R$ be used on all concave surfaces of radius R. Both these interface shapes will significantly reduce axial contact stresses as compared to those resulting from use of sharp corner interfaces.

If the surface radius changes from R_i to R_j with all other parameters unchanged, the corresponding contact stress with long radius toroidal interfaces changes by $(R_i/R_j)^{1/2}$. Hence, for the 10:1 step increases in surface radius depicted in Figure 15.30(a) and (b), the stress decreases by a factor of $\sqrt{(1/10)} = 0.316$ between steps.

When both a convex and a concave toroidal mechanical interfaces are considered as alternative contacts on convex lens surface, the variation of tensile contact stress is as indicated in Figure 15.31. The design is for the 3.100-in.-diameter germanium lens mounting examples considered earlier. In the figure, Curve A represents the usual behavior of the design with increasing convex toroid interface

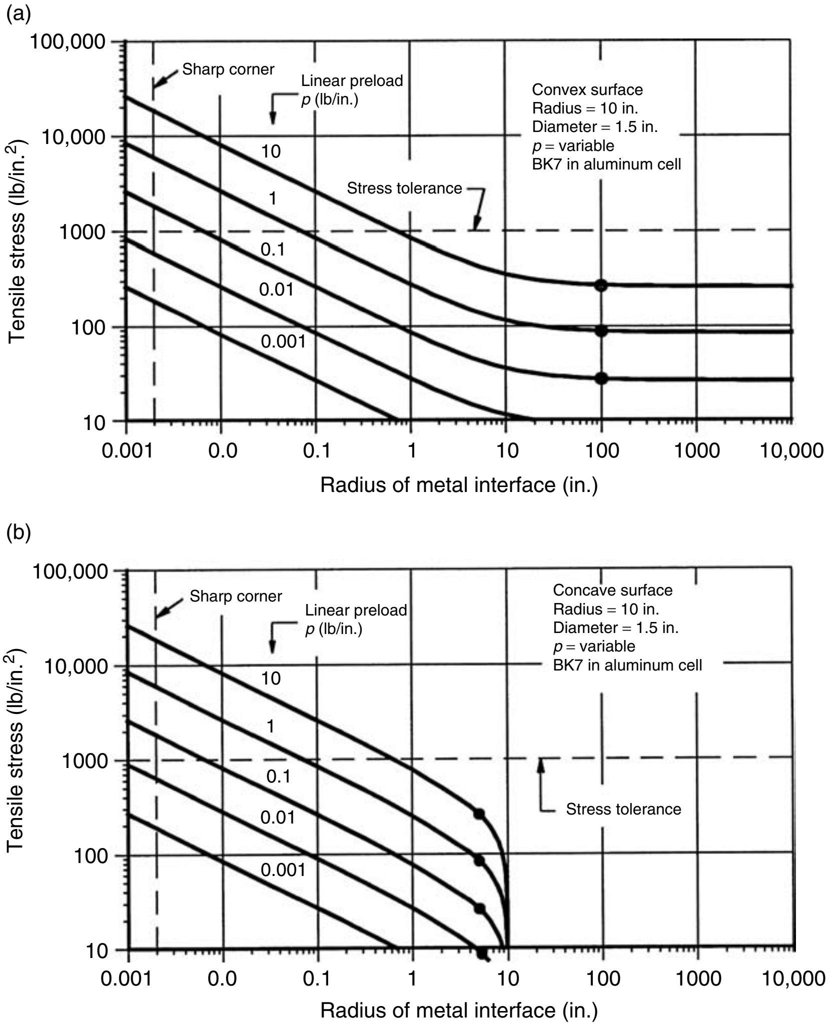

FIGURE 15.29 Variation of tensile contact stress as a function of the sectional radius of the mechanical contacting surface and linear preload for (a) a typical preloaded convex lens surface and (b) a typical preloaded concave lens. The design dimensions and characteristics are as indicated.

radius in the region where the stress levels off en route to the tangential interface represented by the square symbol. Curve B shows how the stress decreases as the concave toroidal radius approaches the spherical interface where the stress essentially goes to zero. Note that if a concave toroidal interface is employed, the design should specify a nominal radius sufficiently removed from the lens surface radius so as to allow for a reasonable tolerance on the mechanical surface radius without creating intimate contact with the glass or a sharp edge contact (as could occur if the toroid radius is too small). Whether providing a concave toroidal interface to reduce stress is worth the added cost over that of the simpler conical interface cannot be judged here.

15.5 BENDING EFFECTS DUE TO OFFSET ANNULAR CONTACTS

If, in the mounting of a circular optic (lens, window, or small mirror), the axial clamping force exerted by a retainer or flange and constraint provided by the mount are not directly opposite (i.e., at the same height from the axis on both sides), a bending moment is created within the optic. This

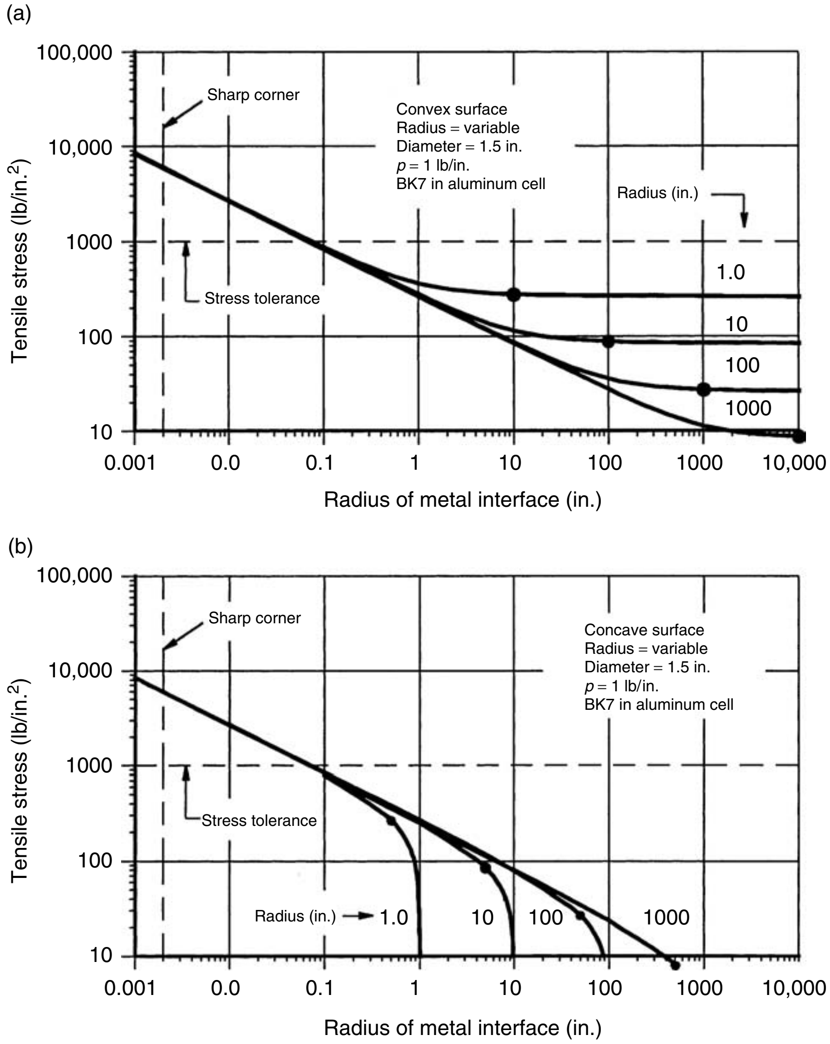

FIGURE 15.30 Variation of tensile contact stress as a function of the sectional radius of the mechanical contacting surface and lens surface radius for (a) a typical preloaded convex lens surface and (b) a typical preloaded concave lens. The design dimensions and characteristics are as indicated.

moment tends to deform the optic so that one surface becomes more convex and the other surface becomes more concave as illustrated schematically in Figure 15.32. This deformation of the optical surface(s) may adversely affect the performance of the component. The same effect occurs in noncircular optics clamped asymmetrically by springs or flanges.

When bent, the surface that becomes more convex is placed in tension. The other surface is compressed. Since glass-type materials break much more easily in tension than in compression (especially if the surface is scratched or has subsurface damage) catastrophic failure may occur if the bending effect is large. The "rule-of-thumb" tolerance for tensile stress given earlier (1000 lb/in.^{2} [6.89 MPa]) applies here.

15.5.1 Bending Stress in the Optical Component

Bayar (1981) indicated that an analytical model that uses an equation from Roark (1954) based upon a thin plane parallel plate (as shown in Figure 15.32) also applies to simple lenses. We here

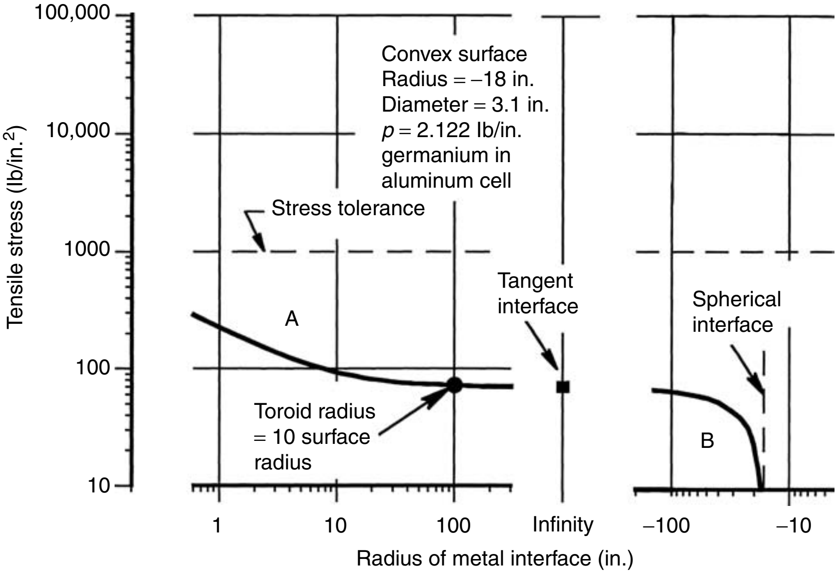

FIGURE 15.31 Variations of tensile contact stress as a function of the sectional radius of the mechanical contacting surface for a convex lens surface. Curve A represents a convex toroidal interface while Curve B represents a concave toroidal interface. The tangential interface is shown as an infinite toroidal interface radius. The design dimensions and characteristics are as indicated.

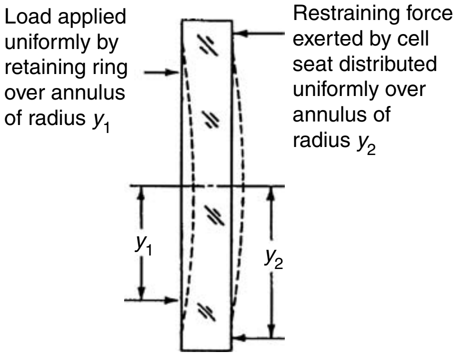
Load applied
uniformly by
retaining ring
over annulus
of radius y_1
Restraining force
exerted by cell
seat distributed
uniformly over
annulus of
radius y_2
y_1
y_2

FIGURE 15.32 Geometry allowing the estimation of the effects of bending moments from axial preload and constraining force applied at different radial heights on opposite sides of a plane parallel plate. (Adapted from Bayar, M., *Opt. Eng.*, 20, 181, 1981.)

extend the analogy to include circular windows and small circular, unperforated mirrors. The degree of approximation depends, in part, on the curvature of the surfaces. Greater curvature decreases the accuracy of the calculation because the component is stiffer.

The tensile stress S_T in a surface made more convex by bending is given approximately by

$$S_T = K_6 K_7 / t_E^2 \tag{15.33}$$

$$K_6 = 3P/(2\pi m) \tag{15.34}$$

$$K_7 = 0.5(m - 1) + (m + 1)\ln\left(\frac{y_2}{y_1}\right) - (m - 1)\left(\frac{y_1^2}{2y_2^2}\right) \tag{15.35}$$

where P is the total axial preload, m is 1/Poisson's ratio ν_G for the glass, t_E the edge or axial thickness of the optic (whichever is the smaller), y_1 the smaller contact height, and y_2 the larger contact height. To decrease the probability of breakage from this bending moment, the contact heights should be made as equal as possible. Increasing the optic's thickness also tends to reduce this danger.

Let us consider the following example. A 20.000-in. (50.800-cm)-diameter, plane-parallel, solid fused silica mirror with a thickness of 2.500 in. (6.350 cm) is contacted on one side by a toroidal shoulder at $y_1 = 9.50$ in. (24.13 cm) and on the opposite side by a toroidal clamping flange at $y_2 = 9.88$ in. (25.09 cm). The applied preload is 2000 lb (8.90×10^3 N) at low temperature. From Table 3.8, $\nu_G = 0.17$ so $m = 1/\nu_G = 5.882$. From Eq. (15.34), $K_6 = (3)(2000)/[(2\pi)(5.882)] = 162.348$ lb while from Eq. (15.35), $K_7 = [(0.5)(5.882 - 1)] + [(5.882 + 1)\ln(9.88/9.50)] - \{(5.882 - 1)(9.50^2)/[(2)(9.88^2)]\} = 0.454$. The tensile stress created is, from Eq. (15.33), equal to $(162.348)(0.454)/(2.500^2) = 11.793$ lb/in.^{2} (0.081 MPa). This is well under the survival tolerance for glasses.

15.5.2 Change in Surface Sagittal Depth of a Bent Optic

The following equation for the change in sagittal depth at the center of a plate such as that shown in Figure 15.32 that is due to the bending moment exerted by an unsymmetrical annular mounting interface was derived from Roark (1954):

$$\Delta_{SAG} = K_8 K_9 / t_E^3 \tag{15.36}$$

$$K_8 = 3P(m^2 - 1)/(2\pi E_G m^2) \tag{15.37}$$

$$K_9 = \frac{(3\,m + 1)y_2^2 - (m - 1)y_1^2}{2(m + 1)} - y_1^2 \ln\left(\frac{y_2}{y_1} + 1\right) \tag{15.38}$$

and all terms are as defined earlier. To see if this deformation of the surface is acceptable, it can be compared with the tolerance (such as $\lambda/2$ or $\lambda/20$) corresponding to the required system performance level of the system and the location of the optic in that system.

We continue with the last example to illustrate the use of these equations. From Table 3.8 for fused silica, $E_G = 1.06 \times 10^7$ lb/in.^{2} (7.3×10^4 MPa). From the prior example, $m = 5.882$, $t_E = 2.500$ in. (6.350 cm), and $P = 2000$ lb (8.90×10^3 N). From Eqs. (15.36)–(15.38)

$$K_8 = (3)(2000)(5.882^2 - 1)/[(2\pi)(1.06 \times 10^7)(5.882)^2] = 8.748 \times 10^{-5}\text{in.}^2$$

$$K_9 = \{[(3)(5.882) + 1][9.88^2] - [(5.882 - 1)(9.50)^2]\}/[(2)(5.882 + 1)]$$

$$- \{9.50^2[\ln(9.88/9.50) + 1]\} = 6.437 \text{ in.}^2$$

$$\Delta_{SAG} = (8.748 \times 10^{-5})(6.437)/(2.500^3) = 3.604 \times 10^{-5} \text{ in. } (9.1154 \times 10^{-4} \text{ mm}) = 1.45\lambda$$

for $\lambda = 0.633$ mm.

This mirror mounting design is probably unsatisfactory for any practical application even though the stress level (from the prior example) is quite low. The design could be improved significantly by making y_1 and y_2 equal.

15.6 EFFECTS OF TEMPERATURE CHANGES

When the temperature changes, corresponding changes occur in optical surface radii, air spaces and lens thicknesses, the refractive indices of optical materials and of the surrounding air, as well as the physical dimensions of structural members. Any of these effects will tend to defocus and misalign the system. The techniques for athermalizing optical instruments described in Section 14.5 can be used to minimize these effects. They are not repeated here. Temperature gradients, axial and radial, can also exist in the system. These may cause effects similar to decentrations or tilts of the optics (affecting imagery) and develop line-of-sight pointing errors. Further, optical surfaces may become distorted and materials may become less homogeneous in their optical and mechanical properties. Gradients are very significant in systems involving refractive optics. Dimensional changes of optical and mechanical parts forming assemblies usually cause changes in clamping forces (preloads); these changes affect contact stresses at opto-mechanical interfaces. Although these problems may be serious if they are not attended to, most can be eliminated or drastically reduced in magnitude by careful opto-mechanical design. Giessen and Folgering (2003) pointed out a series of pertinent guidelines for successful thermal design of optical instruments. We here discuss ways to solve some common temperature-related problems that apply in radial and axial directions. The possibility of optical component misalignment caused by loss of contact with the mount at higher temperatures, axial and radial stress buildup at lower temperatures, and shear stresses in bonded joints caused by temperature changes are also discussed.

15.6.1 Radial Effects at Reduced Temperature

Changes in temperature cause differential expansion or contraction of circular-aperture optics (lenses, windows, filters, and mirrors) with respect to mounting materials in both the axial and radial directions. In the following discussion of the effects of changes in radial dimensions, we assume rotational symmetry of the optics and of the pertinent portions of the mount; that the clearance between the optic OD and the ID of the mount (or of hard radial locating pads, if used) is small; that all components are at a uniform temperature before and after each temperature change; that the CTEs of the optical materials (glass, ceramic, metal, or composite) and of the mount (usually metal) are α_G and α_M, respectively; and that the temperature changes are ΔT.

The CTE of the mount usually exceeds that of the optic mounted in it. An exception would be if Invar were used in the mount and a higher CTE material such as glass were used in the optic. In the usual case, a drop in temperature will cause the mount to contract radially toward the optic's rim. Any radial clearance between these components will decrease in size and, if the temperature falls far enough, the ID of the mount will contact the OD of the optic. Any further temperature decrease will then cause radial force to be exerted upon the rim of the optic. This force compresses (i.e., strains) the optic radially and creates radial stress. To the degree of approximation applied here, the strain and stress are symmetrical about the axis. If the stress is large enough, the performance of the optic will be adversely affected. Extremely large stresses may cause failure of the optic and plastic deformation of the mount.

If $\alpha_M > \alpha_G$, temperature increases will cause the mount to expand away from the optic, thereby increasing any existing radial clearance or creating such a clearance. Significant increases in radial clearance may allow the optic to shift under external forces such as shock or vibration; alignment may then be affected.

15.6.1.1 Radial Stress in the Optic

The magnitude of the radial stress, S_R, in a rim contact mounted optic for a given temperature drop, ΔT, can be estimated as

$$S_R = -K_4 K_5 \Delta T \tag{15.39}$$

where

$$K_4 = \frac{\alpha_M - \alpha_G}{\dfrac{1}{E_G} + \dfrac{D_G}{2E_M t_C}} \tag{15.40}$$

$$K_5 = 1 + \frac{2\Delta r}{D_G \Delta T(\alpha_M - \alpha_G)} \tag{15.41}$$

where D_G is the optic OD, t_C the mount wall thickness directly outside the rim of the optic, and Δr the radial clearance.

Note that ΔT is negative for a temperature decrease. Also, $0 < K_5 < 1$. If Δr exceeds $[D_G \Delta T(\alpha_M - \alpha_G)/2]$, the optic will not be constrained by the mount ID and radial stress will not develop within the temperature range ΔT as a result of rim contact.

An example of this type of analysis (from Yoder, 2002a) is as follows. An SF2 lens of diameter 2.384 in. (60.554 mm) is mounted in a 416 CRES cell machined to provide 0.0002 in. (5.08×10^{-3} mm) of radial clearance for assembly at 68°F (20°C). The cell wall thickness is 0.125 in. (3.175 mm). We need to know what radial stress is developed in the lens at $T_{MIN} = -80$°F (-62°C). From Tables 3.2 and 3.18, $E_G = 7.98 \times 10^6$ lb/in.^{2} (5.50×10^4 MPa), $\alpha_G = 4.7 \times 10^{-6}$/°F ($8.4 \times 10^{-6}$/°C), $E_M = 2.9 \times 10^7$ lb/in.^{2} (2.15×10^5 MPa), $\alpha_M = 5.5 \times 10^{-6}$/°F ($9.9 \times 10^{-6}$/°C). $\Delta T = -80 - 68 = -148$°F ($-82.2$°C). From Eqs. (15.40) and (15.41),

$$K_4 = \frac{(5.50\times10^{-6} - 4.70\times10^{-6})}{(1/7.98\times10^6) + \{2.384/[(2)(2.90\times10^7)(0.125)]\}} = 1.762 \text{ lb/in.}^2\ ^\circ\text{F}$$

$$K_5 = 1 + \frac{(2)(0.0002)}{(2.384)(-148)(5.5\times10^{-6} - 4.7\times10^{-6})} = -0.417$$

From Eq. (15.39), the radial compressive stress $S_R = -(1.762)(-0.417)(-148) = -108.6$ lb/in.^{2} °F (-0.75 MPa °F). This negative radial stress at low temperature results from the fact that the CTE difference is insufficient to cause lens rim-to-cell ID contact at T_{MIN}. No radial stress is developed. This condition occurs whenever K_5 is negative.

As another example (also from Yoder, 2002a), we consider a mirror made of Ohara E6 glass with a diameter of 20.000 in. (50.800 cm) mounted in a 6061 aluminum cell machined to provide 0.0002 in. (5.08 μm) of radial clearance for assembly at 68°F (20°C). The cell wall thickness is 0.25 in. (6.350 mm) outside the mirror rim. We want to estimate the radial stress developed in the mirror at $T_{MIN} = -80$°F (-62°C). From Tables 3.12 and 8.17, $E_G = 8.50 \times 10^6$ lb/in.^{2} (5.86×10^{10} Pa), $\alpha_G = 1.5 \times 10^{-6}$/°F ($2.7 \times 10^{-6}$/°C) and $E_M = 9.90 \times 10^6$ lb/in.^{2} (6.82×10^{10} Pa), $\alpha_M = 13.1 \times 10^{-6}$/°F ($23.6 \times 10^{-6}$/°C). $\Delta T = -80 - 68 = -148$°F ($-82.2$°C). From Eqs. (15.40) and (15.41),

$$K_4 = \frac{(13.1\times10^{-6} - 1.5\times10^{-6})}{(1/8.5\times10^6) + \{20/[(2)(9.9\times10^6)(0.25)]\}} = 2.79 \text{lb/in.}^2\ ^\circ\text{F}$$

$$K_5 = 1 + \frac{(2)(0.0002)}{(20)(-148)(13.1\times10^{-6} - 1.5\times10^{-6})} = 0.988$$

From Eq. (15.39), $S_R = -(2.79)(0.988)(-148) = 408$ lb/in.^{2} (2.81 MPa). This stress would create no threat of damage to the mirror.

15.6.1.2 Tangential (Hoop) Stress in the Mount Wall

Another consequence of differential contraction of the mount relative to the rim contact optic is that stress is built up within the mount in accordance with the following equation:

$$S_M = S_R D_G/(2t_C) \tag{15.42}$$

where all terms are as defined earlier. With this expression, we can determine if the mount is strong enough to withstand the force exerted upon the optic without causing plastic deformation or failure. If the yield strength of the mount material exceeds S_M, a safety factor exists. Note that if K_5 is negative, there can be no stress in the cell wall.

We will illustrate with a typical case using the same design as analyzed in the last example where $S_R = 408$ lb/in.^{2}, $D_G = 20.00$ in., and $t_C = 0.25$ in. By Eq. (15.42), $S_M = (408)(20.000)/[(2)(0.250)] = 16{,}320$ lb/in.^{2} (112.53 MPa). From Table 3.18, we find that the yield strength of the 6061 aluminum lies between 8000 and 40,000 lb/in.^{2}. The lower value applies to the T0 tempered version while the T6 tempered version has strength of about 38,000 lb/in.^{2}. We conclude that the wall might distort if made of T0 tempered metal. We could substitute a stronger material (such as 6061-T6 aluminum or CRES) for the mount and achieve a much better design. Note that the stress in the mirror must be recomputed if such a change is made.

15.6.2 Radial Effects at Increased Temperature

The increase, ΔGAP_R , in nominal radial clearance, GAP_R , between an optic and its mount that is due to a temperature increase of ΔT from that at assembly can be estimated by

$$\Delta GAP_R = (\alpha_M - \alpha_G)(D_G/2)\Delta T \tag{15.43}$$

where all terms are as defined previously.

If there is no axial constraint (as might be the case at high temperature), any radial clearance Gap_R existing between the optic OD and the mount ID would allow the optic to roll (i.e., tilt about a transverse axis) under vibration until its rim touches the mount ID at diametrically opposite points of the edge thickness t_A. This roll angle can be estimated by the equation

$$\text{Roll} = \arctan(2GAP_R/t_E) \tag{15.44}$$

Let us determine the increase in radial clearance at $T_{MAX} = 160°F$ (71.1°C) for the 20.00 in. diameter E6 mirror opto-mechanical assembly analyzed just above. The nominal radial clearance at assembly is 0.0010 in. (2.54×10^{-2} mm) and the mount is 6061 aluminum. $\Delta T = 160 - 68 = 92°F$ (33.3°C). By Eq. (15.43), $\Delta Gap_R = (13.1 \times 10^{-6} - 1.5 \times 10^{-6})(20)(92)/2) = 0.0107$ in. (0.2711 mm). The radial gap at T_{MAX} is then $0.0010 + 0.0107 = 0.0117$ in. (0.297 mm).

We should now determine the maximum roll angle that the mirror of this example can experience under vibration at maximum survival temperature. We will assume that the mirror has an edge thickness t_E of 2.500 in. (63.500 mm). The expanded radial gap around the mirror at T_{MAX} is 0.0117 in. (0.297 mm). By Eq. (15.44), the angular roll = arctan $[(2)(0.0117)/2.500] = 0.536°$. This angle may exceed the tolerance for mirror tilt.

In the common case where the CTE of the mount exceeds that of the optic, we can determine the appropriate nominal radial clearance GAP_R between the mount ID and the lens OD at assembly temperature by applying Eq. (15.3) and the specified tolerance on decentration of the optic. We define the latter parameter as ε. Then, the design should require that

$$GAP_R = (ID_{CELL} - OD_{LENS})/2 = \varepsilon - \Delta GAP_R \tag{15.45}$$

If we apply a decentration tolerance of 0.020 in (0.508 mm) to the case of the above mentioned E6 mirror, a temperature rise to 160°F would not allow the mirror to decenter more than the tolerance if the radial gap at assembly is no greater than 0.0093 in. (0.236 mm). Note once again that axial constraint might limit mirror decentration at elevated temperatures.

15.6.3 Changes in Axial Preload Caused by Temperature Changes

15.6.3.1 General Considerations

Optical and mounting materials usually have dissimilar CTEs, so temperature changes of ΔT cause changes in total axial preload P. Equation (15.46) from Yoder (1992) quantifies this relationship.

$$\Delta P = K_3 \Delta T \tag{15.46}$$

where K_3 is the rate of change of preload with temperature for the design. This factor is sometimes called the design's "temperature sensitivity factor." Knowledge of the value of K_3 for a given opto-mechanical design would be advantageous because it would allow the estimation of actual preload at any temperature by adding ΔP to the assembly preload. In the absence of friction, this preload is the same at all surfaces of all lenses clamped by a single retaining ring. The applicable value of K_2 at each of these interfaces can be estimated by Eq. (15.18), using the material properties at that interface. Finally, knowing the type of mechanical interface and optical surface radius at each interface, the value for K_1 can be calculated using the proper form of Eq. (15.17). The compressive stress S_C at that surface can be estimated through use of Eq. (15.32) and the tensile stress from Eq. (15.14). In general, the stresses at the two surfaces of a given lens element will differ if they have different radii and different algebraic signs or if the mechanical interface shapes are different. This is because those variables are used to determine K_1. In multiple lens assemblies, the elastic and thermal properties of the various lenses may differ, thereby giving different values for K_2.

If α_M exceeds α_G (as is usually the case), the metal in the mount expands more than the optic for a given temperature increase ΔT. Any axial preload existing at assembly temperature T_A (typically 20°C [68°F]) will then decrease. If the temperature rises sufficiently, that preload will disappear. If the lens is not otherwise constrained axially (as by an elastomeric sealant), it will be free to move within the mount in response to externally applied forces. We define the temperature at which the axial preload goes to zero as T_C. This temperature is

$$T_C = T_A - (P_A/K_3) \tag{15.47}$$

The mount maintains contact with the lens until the temperature rises to T_C. A further temperature increase introduces an axial gap between the mount and lens. This gap should not exceed the design tolerance for despace of this lens.

The increases in axial gap ΔGAP_A created in a single-element lens subassembly, a cemented doublet lens subassembly, an air-spaced doublet subassembly, and a general multilens subassembly as the temperature rises by ΔT above T_C can be approximated, respectively, as

$$\Delta GAP_A = (\alpha_M - \alpha_G)(t_E)(T - T_C) \tag{15.48}$$

$$\Delta GAP_A = [(\alpha_M - \alpha_{G1})(t_{E1}) + (\alpha_M - \alpha_{G2})(t_{E2})][T - T_C] \tag{15.49}$$

$$\Delta GAP_A = [(\alpha_M - \alpha_{G1})(t_{E1}) + (\alpha_M - \alpha_S)(t_S) + (\alpha_M - \alpha_{G2})(t_{E2})][T - T_C] \tag{15.50}$$

$$\Delta GAP_A = \sum_1^n (\alpha_M - \alpha_1)(t_i)(T - T_C) \tag{15.51}$$

where all terms are as defined earlier. In all cases, if the preload applied at assembly is large, the calculated value for T_C may exceed T_{MAX}. In this case, ΔGAP_A will be negative, indicating that glass-to-metal contact is never lost within the range $T_A \leq T \leq T_{MAX}$.

In nearly all applications, small changes in position and orientation of a lens within axial and radial gaps created by differential expansion are tolerable. However, high accelerations (vibration or shock) applied to the lens assembly when clearance exists between the lens and its mounting surfaces may cause damage to the lens from glass-to-metal impacts. Such damage (called "fretting") of glass surfaces under sustained vibrational loading has been reported by Lecuyer (1980) and has been experienced on many other occasions. To minimize this threat, it is advisable to design the lens assembly to have sufficient residual preload at T_{MAX} to hold the lens firmly against the mechanical interface under the maximum expected acceleration. As indicated earlier, the preload (in pounds) needed to constrain a lens of weight W under axial acceleration a_G is simply W times a_G. In the SI system, this preload (in newtons) is $9.807Wa_G$ where W is in kilograms. In order for either of these preloads to exist at T_{MAX}, the preload at assembly would be the sum of the needed minimum preload plus the preload decrease that is caused by the temperature increase from that at assembly (T_A) to that at T_{MAX}.

For example, a lens weighing 3 lb (1.3608 kg) is to be held in contact with its mount by a flange at a maximum temperature of 160°F (71.1°C) under acceleration of 25 times gravity in the axial direction. Assume that K_3 is -20.00 lb/°F (-159.91 N/°C) and assembly takes place at 68°F (28°C). The temperature change ΔT is 160 – 68 = 92°F (51.1°C). The preload needed to overcome acceleration is (3)(25) = 75 lb (333.62 N). The preload dissipated from T_A to T_{MAX} is $(-20.00)(92) = -1840$ lb (-8184.7 N). The total preload needed at assembly is then 75 + 1840 = 1915 lb (8.52 × 103 N).

The factor K_3 that makes these types of estimations possible depends upon the opto-mechanical design of the subassembly and the pertinent material characteristics. It is difficult to quantify, even for a simple lens/mount configuration. For example, consider the design shown schematically in Figure 15.33(a). Here, a biconvex lens is clamped axially in a cell between a shoulder and a retainer with some nominal preload. The glass-to-metal interfaces are shown as sharp corners, but conical (tangent) interfaces would be more appropriate in an actual design. The contact stress developed within the lens by the preload is distributed approximately as indicated in Figure 15.34. This is an FEA representation from Genberg (2004). Hatheway (2004) and this author identified the following mechanical changes that can occur in this design and that contribute to the magnitude of its K_3:

- bulk compression of the glass at height y_C
- bulk elongation of the cell wall of thickness t_C at the lens rim
- elongation of the (weaker) threaded and undercut regions of the cell
- local deformations of the glass surfaces R_1 and R_2 at the mechanical interfaces
- local deformations of the retainer and shoulder surfaces at those same interfaces
- diaphragm-like deflections of the retainer and of the shoulder
- "pincushion" deformation of the cell wall at the lens rim from an imposed moment
- flexibility within the threaded joint
- radial dimension changes of the lens and the mechanical parts
- uncertainties caused by asperities on mechanical and glass surfaces, and
- frictional effects

Designs, such as those for cemented doublet lenses (see Figure 15.33[b]) or multiple air-spaced lenses with intermediate spacers (see Figure 15.33[c]), would add components that further increase complexity and provide additional elastic variables. In prior discussions of K_3 (see Yoder, 1992, 1993, 1994, 2002a), this author considered only the first two of these contributing factors (bulk glass compression and cell wall stretching). That theory, which may be considered a first approximation of K_3, is summarized in the following section.

15.6.3.2 Approximation of K_3 Considering Bulk Effects Only

For a single-element lens, a cemented doublet, and an air-spaced doublet clamped axially in a simple mount as shown in Figure 15.33, K_3 is given approximately as

$$K_3 = \frac{-(\alpha_M - \alpha_G)t_E}{\dfrac{2t_E}{E_G A_G} + \dfrac{t_E}{E_M A_M}} \tag{15.52}$$

$$K_3 = \frac{-(\alpha_M - \alpha_{G1})(t_{E1}) - (\alpha_M - \alpha_{G2})(t_{E2})}{\dfrac{2t_{E1}}{E_{G1} A_G} + \dfrac{2t_{E2}}{E_{G2} A_G} + \dfrac{t_{E1} + t_{E2}}{E_M A_M}} \tag{15.53}$$

$$K_3 = \frac{-(\alpha_M - \alpha_{G1})(t_{E1}) - (\alpha_M - \alpha_S)(t_S) - (\alpha_M - \alpha_{G2})(t_{E2})}{\dfrac{2t_{E1}}{E_{G1} A_G} + \dfrac{t_S}{E_S A_S} + \dfrac{2t_{E2}}{E_{G2} A_{G2}} + \dfrac{t_{E1} + t_{E2}}{E_M A_M}} \tag{15.54}$$

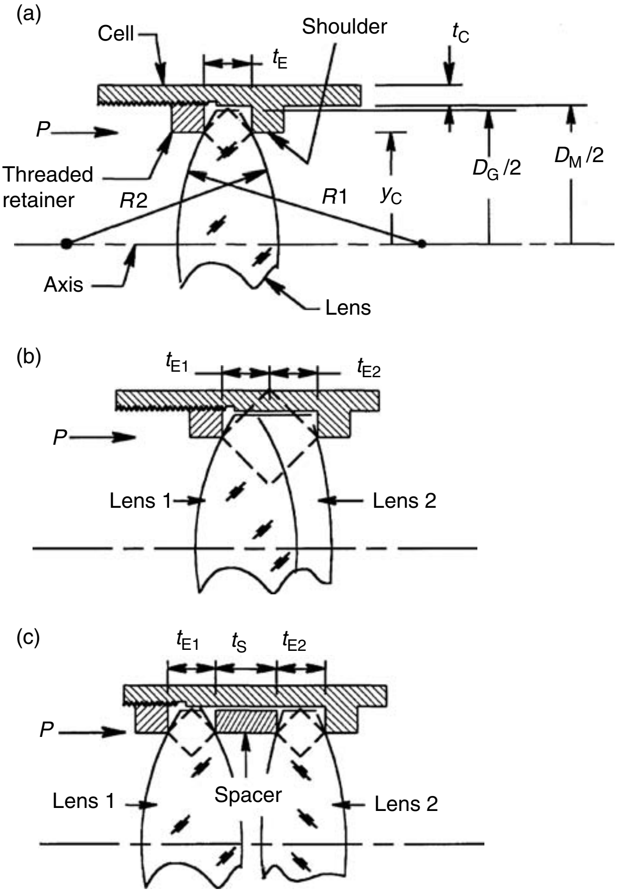
(a)
Cell
Shoulder
t_E
t_C
P
Threaded retainer
R2
R1
y_C
$D_G/2$
$D_M/2$
Axis
Lens
(b)
t_{E1}
t_{E2}
P
Lens 1
Lens 2
(c)
t_{E1}
t_S
t_{E2}
P
Lens 1
Spacer
Lens 2

FIGURE 15.33 Schematics of lens mounting configurations for (a) a single lens element, (b) a cemented doublet lens, and an air-spaced doublet.

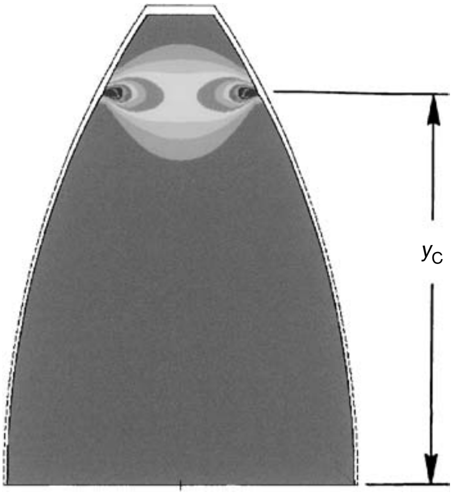

FIGURE 15.34 FEA representation of stress distribution within a lens when preloaded as in Figure 15.33(a). (Adapted from Genberg, V.L., private communication, 2004.)

where E_G, E_M, α_M, and α_G are Young's modulus and CTE values for the glass and metal, and A_G and A_M are cross-sectional areas of the stressed regions in the lens and cell wall. Note that Eq. (15.52) has been rewritten from that given in Yoder (1992) to follow the format of Eqs. (15.53) and (15.54).

The pertinent geometric parameters for the cell wall and the lens are shown in Figure 15.35 and Figure 15.36. Equation (15.55) defines A_M for the cell:

$$A_M = 2\pi t_C[(D_M/2) + (t_C/2)] \tag{15.55}$$

Here D_G is the OD of the lens, D_M the ID of the mount at the lens rim, and t_C the radial thickness of the mount wall adjacent to the lens rim. For the lens, either of the following two cases can apply: if $(2y_C + t_E) < D_G$, the stressed region (the diamond-shaped regions‡ in Figure 15.36) lies within the lens rim. Then

$$A_G = 2\pi y_C t_E \tag{15.56a}$$

If $(2y_C + t_E) > D_G$, the stressed region is truncated by the lens rim. Then

$$A_G = (\pi/4)(D_G - t_E + 2y_c)(D_G + t_E - 2y_c) \tag{15.56b}$$

In both equations, t_E is the edge thickness of the lens element at the contact height y_C. The factors of 2 included in the denominator terms pertaining to lenses in Eqs. (15.52) – (15.54) serve to average the area A_G that varies from zero at the contact to t_E at the center of the lens.

Sectional schematic views of two types of simple lens spacers are shown in Figure 15.37. Both are solids with cylindrical ODs fitting into the ID of the lens cell (not shown). The small clearances between the spacer rims and the cell IDs are ignored. The spacer version shown in view (a) has a

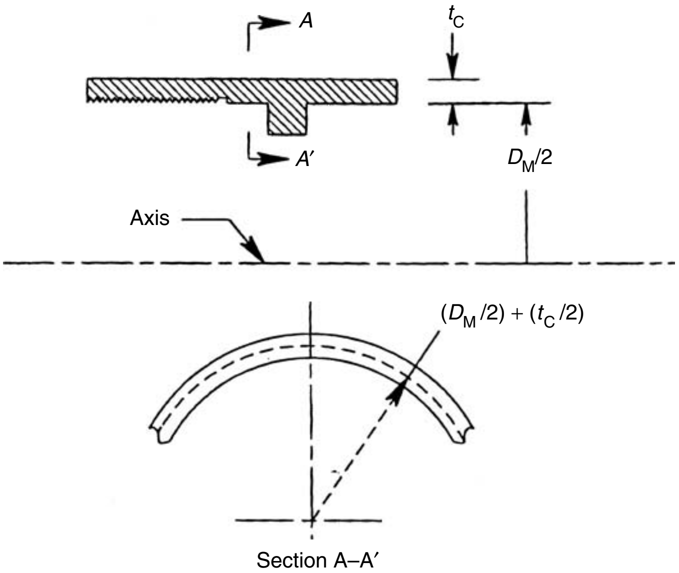

FIGURE 15.35 Geometric relationships used to approximate the cross-sectional area of the stressed region within a lens mount. (From Yoder, P.R., Jr., *SPIE Critical Review*, CR 43, 305, 1992.)

---

‡The ±45° diamond shape for the stress region within the glass was suggested by Hatheway (1992b) on the basis of its similarity to a model for heat transfer within solids.

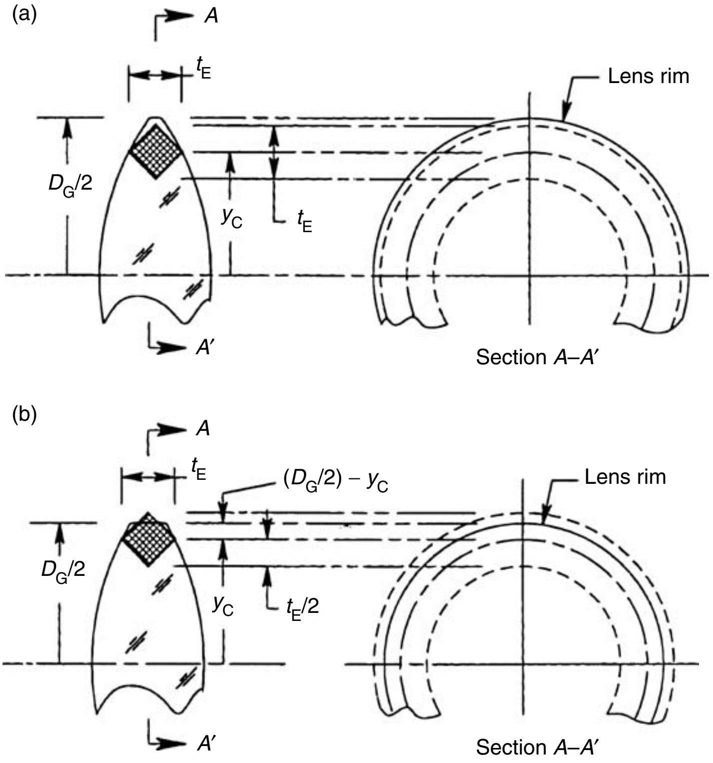
(a)
A
t_E
Lens rim
$D_G/2$
y_C
t_E
A′
Section A–A′
(b)
A
t_E
$(D_G/2) - y_C$
Lens rim
$D_G/2$
y_C
$t_E/2$
A′
Section A–A′

FIGURE 15.36 Geometric relationships used to approximate the cross-sectional area of the stressed region within a lens. (a) When completely within the lens rim, (b) when truncated by the rim. (From Yoder, P.R., Jr., *SPIE Critical Review*, CR43, 305, 1992.)

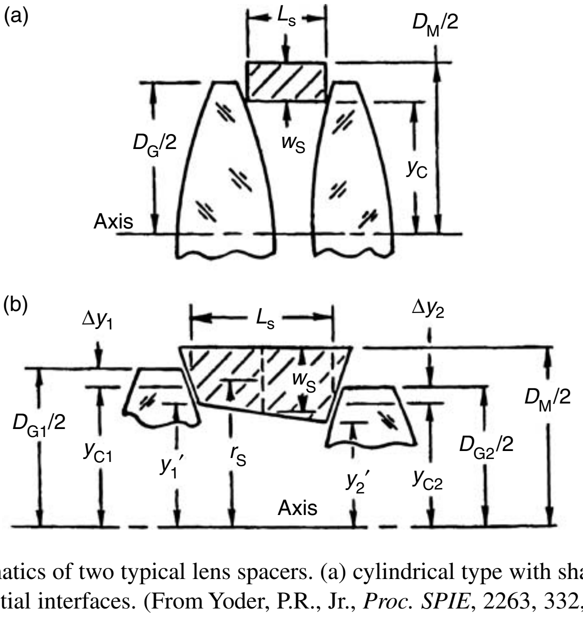
(a)
L_s
$D_M/2$
$D_G/2$
w_S
y_C
Axis
(b)
Δy_1
L_s
Δy_2
w_S
$D_M/2$
$D_{G1}/2$
y_{C1}
y_1'
r_S
y_2'
y_{C2}
$D_{G2}/2$
Axis

FIGURE 15.37 Schematics of two typical lens spacers. (a) cylindrical type with sharp-corner interfaces, (b) tapered type with tangential interfaces. (From Yoder, P.R., Jr., *Proc. SPIE*, 2263, 332, 1994.)

constant wall thickness w_S while that in view (b) has a conical ID to accommodate different heights of contact with the lenses. The wall thickness of the latter spacer is approximated as its average annular thickness. In view (a), the interfaces are shown as sharp corners while in view (b), the spacer presents conical interfaces to the lenses. Equations (15.57) – (15.62) allow the annular area A_S to be estimated for each of these spacers. Appropriate modifications of the equations should be made if conical or toroidal interfaces are used in view (a) or if one or more lens surfaces is concave. For the simple cylindrical spacer,

$$W_{S,CYL} = (D_M/2) - y_C \tag{15.57}$$

For the simple tapered spacer,

$$\Delta y_i = [(D_G)_i/2] - (y_C)_i \tag{15.58}$$

$$y_i' = (y_C)_i - \Delta y_i \tag{15.59}$$

$$w_s = (D_M/2) - [(y_1' + y_2')/2] \tag{15.60}$$

In both cases,

$$r_S = (D_M/2) - (w_s/2) \tag{15.61}$$

$$A_S = 2\pi r_S w_S \tag{15.62}$$

Similar equations can be formulated to represent other spacer designs. Drawings of actual spacers may be found in Figure 5.3 and Figure 5.6.

Equation (15.63) allows the factor K_3 of a generic single or multiple-component lens design to be estimated. The numerator of this equation is the sum of negative terms representing the axial thicknesses $(t_E)_i$ and $(t_S)_i$ of each lens element and of the spacer(s) at the applicable heights of contact multiplied by the pertinent differences in CTEs for those parts relative to the CTE of the mount. The denominator is the sum of the compliances C_i[§] for each part of the subassembly. Some terms in the denominator represent parts in compression while others represent parts in tension.

$$K_3 = \frac{-\sum_1^n (\alpha_M - \alpha_1) t_i}{\sum_1^n C_i} \tag{15.63}$$

where C_i for a lens is approximated as $[2t_E/(E_G A_G)]_i$, that for the cell wall is $[t_E/(E_M A_M)]_i$, and that for a spacer is approximated as $[t_S/(E_S A_S)]_i$.

A study conducted by Crompton (2004) suggested a possible alternative approach to determining the cross-sectional stressed area A_G within an equi-biconvex lens. He considered the stressed volume within the lens to be equivalent to a stack of infinitesimally thin annular rings. The smallest rings are located at the glass-to-metal interfaces and are assumed to be of width w equivalent to that of the region elastically deformed under axial preload previously defined as Δy by Eq. (15.22). The rings grow progressively larger following a ±45° contour to the midpoint of the lens volume then decrease in size to the opposite mechanical interface. The following equation gives the compliance per unit length of the stack of rings along the circle defined by the radius y_C:

$$C = (2/E_G) \int_0^{t_E/2} [1/(t + w)]dt \tag{15.64}$$

[§] Compliance is the reciprocal of the spring constant for a component under tension or compression. It represents displacement per unit applied force and is expressed as in./lb or m/N.

where the parameters are as indicated schematically in Figure 15.38. Integrating this equation gives

$$C = (2/E_G)\ \ln(t_E/2w) + 1 \tag{15.65}$$

Since $t_E/(2w)$ usually is much larger than unity, Eq. (15.65) can be simplified to

$$C = (2/E_G)\ \ln(t_E/2w) \tag{15.66}$$

This compliance per unit length is set equal to that of a single annular ring of constant width w_{EFF} and that width is

$$w_{EFF} = t_E/\,[2\ln(t_E/(2w))] \tag{15.67}$$

The effective area A_G is then

$$A_G = 2\pi y_c w_{EFF} \tag{15.68}$$

Because this derivation is based on knowledge of the width w of the elastically deformed glass region at the interface, it is a linear approximation of what is actually a nonlinear relationship since w is dependent upon the magnitude of the preload, which varies with temperature. The degree of approximation of the method was estimated in Crompton (2004) by comparison with the results of a limited axisymmetric FEA study that indicated differences of the order of 10% for design examples having contact widths greater than about 0.005 in. (0.127 mm).

For purposes of comparison, let us calculate K_3 for a typical example using both Yoder's and Crompton's methods for estimating A_G. We assume that the lens mounting is as shown in Figure 15.39, the lens is made of SK15 glass, and that it is mounted in a 6061-T6 aluminum cell with tangential interfaces. We wish to estimate K_3 for this design. The material properties are $E_G = 1.22 \times 10^7$ lb/in.^{2} (8.41×10^4 MPa), $\nu_G = 0.275$, $\alpha_G = 3.80 \times 10^{-6}$/°F ($6.84 \times 10^{-6}$/°C), $E_M = 9.90 \times 10^6$ lb/in.^{2} (6.83×10^4 MPa), $\nu_M = 0.332$, and $\alpha_M = 1.31 \times 10^{-5}$/°F ($2.36 \times 10^{-5}$/°C). The dimensions are: $y_C = 3.1020$ in. (78.7908 mm), $t_E = 0.2590$ in. (6.5786 mm), $D_G = 6.5350$ in. (165.9890 mm), $t_C = 0.1960$ in. (4.9784 mm), and $D_M = 6.5358$ in. (166.0093 mm). Utilizing Yoder's method, $(2y_C + t_E) = (2)(3.102) + 0.259 = 6.463$ in. (164.160 mm), which is smaller than D_G, so the stressed region lies within the lens rim. By Eq. (15.56a), $A_G = (2\pi)(3.1020)(0.2590) = 5.0480$ in.^{2} (3256.7833 mm^2).

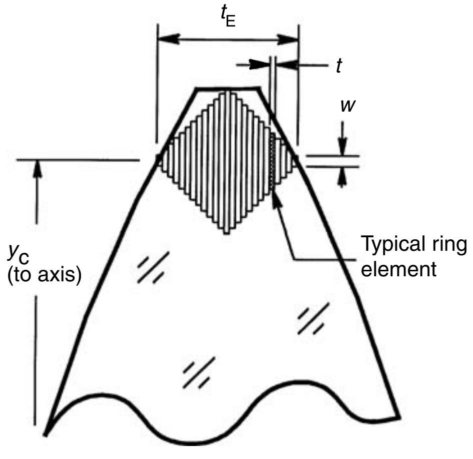

FIGURE 15.38 Schematic diagram of Crompton's model for approximating the cross sectional area A_G in an axially stressed lens element. (Adapted from Crompton, D., private communcation, 2004.)

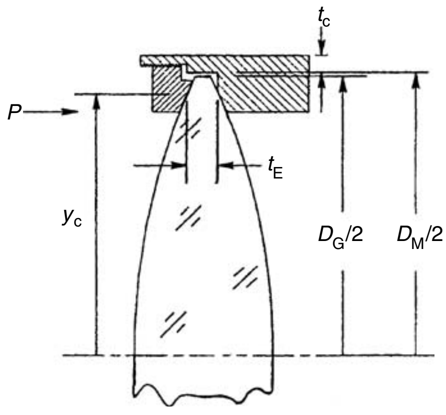

FIGURE 15.39 Schematic diagram of an axially constrained single-element lens used to compare two methods for approximating the cross sectional area A_G in an axially stressed lens element.

By Eq. (15.55), $A_M = (2\pi)(0.1960)[(6.5358/2) + (0.1960/2)] = 4.1451$ in.^{2} (2674.2659 mm^2). From Eq. (15.52)

$$K_3 = \frac{-(1.31\times10^{-5}-3.80\times10^{-6})(0.259)}{\dfrac{(2)(0.259)}{(1.22\times10^{7})(5.0480)}+\dfrac{(0.259)}{(9.9\times10^{6})(4.1451)}} = -163.6\ \text{1b/°F}(-1309.9\text{N/°C})$$

Assuming that R_1 of the lens is 7.883 in. (200.221 mm) and the axial preload is 120 lb (533.78 N), we utilize Crompton's method to estimate K_3 as follows. By Eq. (15.18), $K_2 = [(1 - 0.275^2)/1.22 \times 10^7] + [(1 - 0.332^2)/9.90 \times 10^6] = 7.577 \times 10^{-8} + 8.988 \times 10^{-8} = 1.656 \times 10^{-7}$ in.^{2}/lb and, as indicated in Section 15.3.3.2, $K_1 = 1/D_1 = 1/[(2)(7.883)] = 0.0634$. Then, $p = 120/[(2\pi)(3.1020)] = 6.157$ lb/in., and by Eq. (15.22), $w = \Delta y = 1.6[(6.157)(1.656 \times 10^{-7})/0.0634)]^{1/2} = 0.0064$ in. (0.1620 mm). By Eq. (15.67), $w_{EFF} = 0.259/\{2 \ln[0.259/((2)(0.0064))]\} = 0.0431$ in. (1.094 mm). Then, by Eq. (15.68), $A_G = (2\pi)(3.102)(0.0431) = 0.839$ in.^{2} (541.464 mm^2) and, by Eq. (15.52) (after deleting the factor of 2 in the compliance for the lens),

$$K_3 = \frac{-(1.31\times10^{-5}-3.80\times10^{-6})(0.259)}{\dfrac{(0.259)}{(1.22\times10^{7})(0.839)}+\dfrac{(0.259)}{(9.9\times10^{6})(4.1451)}} = -76.2\text{1b/°F}(-6.1\text{N/°C})$$

It is apparent from these examples that Crompton's method leads to decidedly different values for A_G and, hence, for the temperature sensitivity factor K_3, than the method previously proposed by this author. It is believed that Crompton's method gives a somewhat less conservative (and perhaps more accurate) approximation of K_3.

15.6.3.3 Approximation of K_3 Considering Effects other than Bulk Effects

Omission of the other key factors that affect K_3 (see earlier discussion related to Figure 15.33[a]), some perhaps equally or more influential than bulk glass compression and cell wall elongation, undoubtedly tends to make K_3 appear to be larger than it really is. This makes Eq. (15.46) predict greater changes in preload with temperature than would actually occur in real life. Although conservatism is usually desired during opto-mechanical design, the other above-listed design variables should not be ignored. Yoder and Hatheway (2005) suggested a theoretical method for estimating the potential impacts on K_3 from considering the above-discussed bulk compression/elongation effects in the lens and cell wall plus four additional effects for which closed form equations were available. We will next summarize that theory and illustrate its use with design examples.

15.6.3.3.1 Glass and Metal Surface Deflection Effects

Young (1989) gave the following equation for the reduction Δx in the distance between the centers of two parallel cylinders of cross-sectional diameters D_1 and D_2 when forced together by a preload P so both surfaces deform elastically:

$$\Delta x = \frac{2p(1-\upsilon^2)}{\pi E}\left(\frac{2}{3}+\ln\frac{2D_1}{\Delta y}+\ln\frac{2D_2}{\Delta y}\right) \tag{15.69}$$

This equation is based on the model for annular contact between a lens and its mount as depicted in Figure 15.24. It assumes that Young's modulus and Poisson's ratio of the two materials are equal. This is obviously not the case in mounting optics. To the level of accuracy required here, it is appropriate to use the averages of the material values. The linear preload p was defined in Section 15.3.3 as $P/(2\pi y_C)$, where y_C is the height of metal contact with the lens surface. The width Δy of the deformed areas in the interface is given by Eq. (15.22). Surface deformations occur at the interfaces on both sides of the lens. They act as two "springs" in series, with the compliance of each spring equal to

$$C_D = \Delta x/P \tag{15.70}$$

This compliance would be added to the denominator of Eq. (15.52) along with the compliances corresponding to bulk effects in the glass and metal to derive a better approximation for K_3.

15.6.3.3.2 Retainer Deflection Effects

If we assume that a threaded retainer is rigidly attached to the cell wall by its thread, it can deflect in the manner of a continuous circular flange as described in Section 4.7.3. We repeat Eqs. (4.18), (4.19a), and (4.19b) here for convenience:

$$\Delta = (K_A - K_B)(P/t^3) \tag{4.18}$$

where

$$K_A = 3(m^2 - 1)[a^4 - b^4 - 4a^2b^2 \ln(a/b)]/(4\pi m^2 E_M a^2) \tag{4.19a}$$

$$K_B = \frac{3(m^2-1)(m+1)[2\ln(a/b)+(b^2/a^2)-1][b^4+2a^2b^2\ln(a/b)-a^2b^2]}{4\pi m^2 E_M[b^2(m+1)+a^2(m-1)]} \tag{4.19b}$$

where Δ is the deflection, K_A and K_B constants, P the preload, t the axial thickness of the retainer section, a the outer radius of the cantilevered section, b the inner radius of the cantilevered section, m the reciprocal of Poisson's ratio (ν_M) of the flange material, and E_M Young's modulus of the flange material. The compliance C_R of the retainer acting as a flange is

$$C_R = \Delta/P = (K_A - K_B)/t^3 \tag{15.71}$$

The value obtained from Eq. (15.71) would be added to the denominator of Eq. (15.52) to obtain a better approximation of K_3.

Note that the deflection of the retainer causes bending stress to develop within the deflected portion of the retainer. This can, and should, be evaluated using Eqs. (4.20) and (4.21), which are

$$S_B = K_C P/t^2 = S_Y/f_s \tag{4.20}$$

where

$$K_C = \left[\frac{3}{2\pi}\right]\left[1 - \frac{2mb^2 - 2b^2(m+1)\ln(a/b)}{a^2(m-1)+b^2(m+1)}\right] \tag{4.21}$$

The bending stress must not exceed the yield stress of the material. A safety factor of two with regard to that limit might be appropriate.

15.6.3.3.3 Shoulder Deflection Effects

A shoulder within a lens cell acts in the same manner as just described for a retainer. Eqs. (4.19a), (4.19b), and (15.71) are used to define its compliance. This value would be added to the denominator of Eq. (15.52) to obtain a new K_3.

15.6.3.3.4 Radial Dimension Change Effects

Figure 15.40 shows schematically how the interfaces for a double convex lens between the retainer and the lens and between the shoulder and the lens change when the temperature rises by a ΔT of 1°F. The locations of the interfaces move radially outward by Δy_C because of differential expansion with $\alpha_M > \alpha_G$. Because the lens surface is inclined by the angle φ at the interface, the contact interfaces each move axially toward each other by Δx. The following relationships apply:

$$\varphi = 90° - \arcsin(y_C/R) \tag{15.72}$$

$$\Delta y_C = (\alpha_M - \alpha_G)y_C \tag{15.73}$$

$$\Delta_x = -\Delta y_C/\tan\varphi \tag{15.74}$$

These dimensional changes occur at each lens-to-mount interface so, for a biconvex lens, Δx for each surface must be added to the numerator of Eq. (15.52) for K_3 because they represent axial dimension changes due to differential expansion under a unit temperature change. They do not depend upon preload. Note that Δx would be negative for a concave surface and would therefore tend to reduce the magnitude of K_3. Also, Δx is zero for a flat lens surface (or flat bevel) so would not affect K_3.

15.6.3.4 Illustrative Examples of K_3 Estimation

Two examples are given in this section to illustrate the estimation of K_3 with all six of the above-discussed temperature-related effects considered. The first example, Example A, involves a single-element

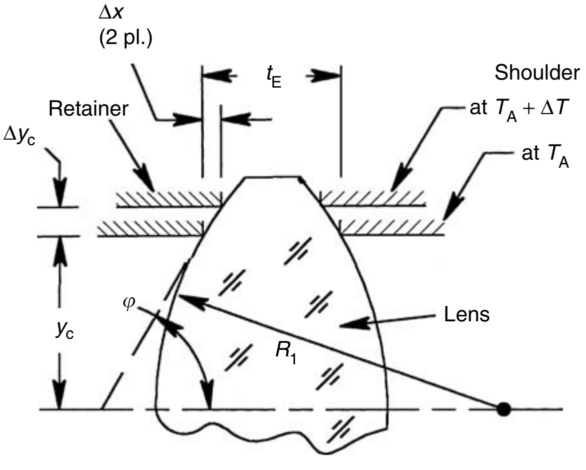

FIGURE 15.40 Diagram modeling the radial dimensional changes in the lens mounting of Figure 15.39 with increasing temperature. (From Yoder, P.R., Jr. and Hatheway, A.E., *Proc. SPIE*, 5877, 2005.)

biconvex BK7 lens with diameter $D_G = 2.5000$ in. (63.5000 mm) clamped axially by a threaded retainer in a simple 6061-T6 aluminum mount as shown in Figure 15.39. The design parameters of Table 15.7 apply. In a second example, Example B, the cell and retainer material are changed to 6Al4V titanium, so the CTEs of the glass and metal are more nearly equal. All dimensions and the temperatures given in Table 15.7 remain the same in all examples. The mechanical interfaces with the lens' spherical surfaces are assumed to be toroidal.

It may be noted from the equations given above that some of the temperature-related effects on K_3 depend upon the magnitude of the axial preload. In order to derive a mounting design that provides residual preload at T_{MAX} sufficient to maintain lens-to-mount contact under worst-case specified acceleration, we assume an initial assembly preload P_A then apply a computer spreadsheet-type computational method to estimate K_3 and the resulting axial preload P' at T_{MAX}. We next subtract P' from Wa_G to obtain the error in P_A and iterate that preload until the error is reduced to zero. The value for P_A in Example A is 2568 lb (11,423 N) while that in Example B is 334.4278 lb (1488 N). Both of these preloads are high, but we can see the advantage of choosing a mount material whose CTE approximates that of the glass.

Table 15.8 gives the results of these calculations for both designs. The applicable equation is noted for each parameter. Included are the values for K_3 obtained as each temperature-related effect is added to the previously considered effects until all five effects have been cascaded.

15.6.4 Estimation of Tensile Contact Stresses in the Lens at Various Temperatures

Once the preload on a lens in a mounting arrangement with known dimensions, materials, and mechanical interface shapes is known at a given temperature, it is a simple task to estimate the peak

TABLE 15.7
Design Parameters for Example A, a Bi-convex Singlet Lens Mounted as Shown in Figure 15.39

Parameter	Lens	Cell and Retainer
Material	BK7	6061-T6 aluminum
E_G, E_M	1.17×10^7 lb/in.^{2} (6.83×10^4 MPa)	9.90×10^6 lb/in.^{2} (8.41×10^4 MPa)
v_G, v_M	0.275	0.332
α_G, α_M	3.90×10^{-6}/°F (2.36×10^{-5}/°C)	1.31×10^{-5}/°F (6.84×10^{-6}/°C)
D_G, D_M	2.5000 in. (63.5000 mm)	2.5020 in. (63.5508 mm)
Contact height y_C		1.1500 in. (29.2100 mm)
Surface radii (2 pl.) |R|	4.000 in. (101.6000 mm)	
Lens edge thickness t_E at y_C	0.2500 in. (6.3500 mm)	
Cell wall thickness t_C		0.1000 in. (2.5400 mm)
Axial length of retainer t_R		0.2500 in. (6.3500 mm)
Axial length of shoulder t_S		0.2500 in. (6.3500 mm)
OD/2 of retainer and shoulder a		1.1800 in. (29.9720 mm)
ID/2 of retainer and shoulder $= b = y_C$		1.1500 in. (29.2100 mm)
Acceleration factor $= a_G$		15[a]
Lens weight	0.2019 lb (91.5818 g)	
T_A	68°F (20°C)	
T_{MAX}	160°F (71°C)	
T_{MIN}	–80°F (–62°C)	

[a] This acceleration level is generally considered to correspond to shipping of an optical instrument.

TABLE 15.8
Evaluation of Temperature-Related Effects for Examples A and B

Parameter	Units	Equation (number)	Value for Example A[a]	Value for Example B[b]
P_A	lb/in.^{2}	—	2568.2561[c]	334.4278[c]
1. Bulk Compression/Elongation of Glass and Metal				
$(2y_C + t_E)$	in.	—	2.5500	2.5500
A_G	in.^{2}	(15.56*a*)	1.6081	1.6081
C_G	in./lb	$2t_E/(E_G A_G)$	2.6575E-8	2.6575E-8
A_M	in.^{2}	(15.55)	0.4829	0.4829
C_M	in./lb	$t_E/(E_G A_G)$	5.2291E-8	3.1374E-8
K_3	lb/°F	(15.52)	−29.1636	−4.3141
2. Surface Deformations				
Average E	lb/in.^{2}	—	1.0800E+7	1.4100E+7
Average v	none	—	0.2700	0.2740
$K_{1\text{ TOROID}}$	in.$^{-2}$	(15.17*a*)	0.1375	0.1375
K_2	in.^{2}/lb	(15.18)	1.7165E-7	1.3537E-7
Δy	in.	(15.22)	3.3703E-2	1.0801E-2
Δx	in.	(15.69)	2.9709E-4	3.3961E-5
C_D	in.lb	(15.70)	1.1568E-7	1.0155E-7
K_3	lb/°F	(15.52)	−7.4141	−0.9577
3. Retainer Deflection				
K_A	in.^{4}/lb	(4.19*a*)	1.2925E-12	7.7083E-13
K_B	in.^{4}/lb	(4.19*b*)	3.3242E-14	1.9948E-14
Δx	in.	(4.18)	2.0699E-7	1.6071E-8
C_R	in./lb	(15.71)	8.0594E-11	4.8056E-11
K_3	lb/°F	(15.52)	−7.4122	−0.9575
4. Shoulder Deflection				
Δx	in.	(4.18)	2.0699E-7	1.6071E-8
C_S	in./lb	(15.71)	8.0594E-11	4.8056E-11
K_3	lb/°F	(15.52)	−7.4102	−0.9573
5. Radial Dimension Changes				
Angle φ	deg.	(15.72)	73.2904	73.2904
Δy_C	in.	(15.73)	1.0580*E*-5	1.1500E-6
Δx	in.	(15.74)	3.1772*E*-6	3.4534E-7
Final K_3	lb/°F	(15.52)	−27.8829	−3.6022

[a] BK7/Al design per Table 15.7.

[b] As in Example A except titanium mount.

[c] After iteration

contact stress resulting in the glass at those interfaces. The methods described in Section 15.3.3 give the peak compressive stress as:

$$S_C = 0.798(K_1 p/K_2)^{1/2} \tag{15.32}$$

where:

$$K_1 = \begin{cases} 0.50/\mathrm{R} & \text{for a tangential interface on a convex lens surface} \\ 0.50/\mathrm{R} & \text{for a torodial interface on a convex lens interface} \\ 0.50/\mathrm{R} & \text{for a torodial interface on a concave lens interface} \end{cases} \tag{15.75a,b,c}$$

and R is the absolute value of the lens surface radius of curvature and K_2 is given by Eq. (15.18). The tensile stress in the glass S_T is derived from the compressive stress S_C by Eq. (15.14), which is

$$S_T = (1 - 2y_G)(S_C)/3 \tag{15.14}$$

Table 15.9 summarizes stress estimations for Examples A and B at the three temperatures of interest T_{MIN}, T_A, and T_{MAX}. The assembly preloads are derived from Table 15.8. Neither design displays tensile stresses over the specified temperature range that meet the 1000 lb/in.^{2} (6.89 MPa) rule-of-thumb tolerance stated earlier as applicable to optical glasses. Steps that could lead to a viable design include relaxation of the temperature and acceleration specifications, selection of materials with more nearly equal CTEs, and addition of axial compliance into the mount configuration. We will explore the latter approach in the next section.

The reader is reminded that the variation of axial preload with temperature depends significantly upon the degree of sophistication of the model used to estimate K_3. We have demonstrated that significant changes in K_3 (mostly reductions) occur as more of the contributing factors defined earlier are considered. Unfortunately, techniques for incorporating the remaining factors that contribute to K_3 have not, as yet, been developed. Further investigation is needed before a complete technique for predicting the effects of temperature changes on axial preloads applied to lenses and mirrors can be adopted for general design use. Until advanced techniques are available, application of the techniques outlined in this section should allow this important design parameter to be estimated.

TABLE 15.9
Estimation of Tensile Contact Stresses at Various Temperatures for Examples A and B

Parameter	Units	Equation (number)	Value for Example A[a]	Value for Example B[b]
1. Preload Applied at Various Temperatures:				
Preload P' at T_{MAX}	lb	$P_A + K_3 (T_A - T_{MAX})$	3.0285	3.0285
Preload P_A at T_A	lb	—	2568.3	334.4
Preload P'' at T_{MIN}	lb	$P_A + K_3(T_{MIN}-T_A)$	6694.9	867.5
2. Estimation of Tensile Stress at T_{MIN}:				
Linear preload, p	lb/in.	$P''/2\pi y_C$	926.5484	120.0649
Compressive stress, S_C	lb/in.^{2}	(15.32)	21,740	8812
Ratio, tensile/compressive stress		(15.14)	0.1947	0.1947
Tensile stress	lb/in.^{2}	(S_C)(ratio)	4233	1716
3. Estimation of Tensile Stress at T_A:				
Linear preload, p	lb/in.	$P_A/2\pi y_C$	355.4354	46.2833
Compressive stress, S_C	lb/in.^{2}	(15.32)	13,465	5471
Tensile stress	lb/in.^{2}	(S_C)(ratio)	2621	1065
4. Estimation of Tensile Stress at T_{MAX}:				
Linear preload, p	lb/in.	$P'/2\pi y_C$	0.4191	0.4191
Compressive stress, S_C	lb/in.^{2}	(15.32)	462	521
Tensile stress	lb/in.^{2}	(S_C)(ratio)	90	101

[a] BK7/Al design per Table 15.7.

[b] As in Example A except titanium mount.

15.6.5 Advantages of Providing Controlled Axial Compliance in the Lens or Mirror Mount

A design technique that is frequently applied by opto-mechanical design engineers might well be considered and applied as appropriate if the value of K_3 determined as described in the last section is too large. Temperature changes might then be expected to pose problems with a specific design. To alleviate this potential problem, an axially compliant feature can be provided in the design that deliberately dominates K_3 and relegates bulk glass compression, surface deflections, cell wall stretching, etc., to secondary roles. This feature might be styled in any of the forms illustrated in Figure 15.41 or some other form that provides predictable compliance. The selected configuration should provide preload to constrain the lens axially at all survival temperatures. Designs of the general type shown in view (d) are depicted in Figure 4.40, where deflection of a continuous flange creates preload in accordance with Eq. (4.18).

Important aspects of the design of an axially compliant feature are that the compliance of the feature should, if possible, be linear, and that dimensional changes caused by changes in temperature should not significantly alter the axial preload applied at assembly. The continuous flange discussed earlier satisfies the former concern over a significant range of deflections. To illustrate how an opto-mechanical assembly can be configured to provide a specific compliance, let us consider again the design of Table 15.7. If the retainer has the general form of Figure 15.41(d), the deflection of the annular flexure over its free annular width ($a - b$) of Table 15.7 will produce preload in accordance with Eq. (4.18). This is a linear relationship over a significant range of deflection. Its linearity over a large temperature range is, of course, affected by variations of Young's modulus. We will here neglect this variation.

As pointed out by Yoder and Hatheway (2005), a device used to determine the actual deflection of the compliant part will typically be able to measure that deflection to at least the nearest 0.0005 in. (12.7 μm). To control preload to, say, ±10%, we should design the part to provide a deflection of 10 times 0.0005 in. or 0.0050 in. (0.1270 mm). The compliance C_R of the retainer in USC units will then be $0.0050/P_A$. This value would replace the compliances of the retainers for Examples A and B as given in Table 15.8 and would have a large effect in reducing the K_3 factors for the lens assemblies. Table 15.10 repeats the calculations of Table 15.8 with these changes for what are now called Examples C and D. These examples differ from Examples A and B only with regard to the C_R terms. The resulting

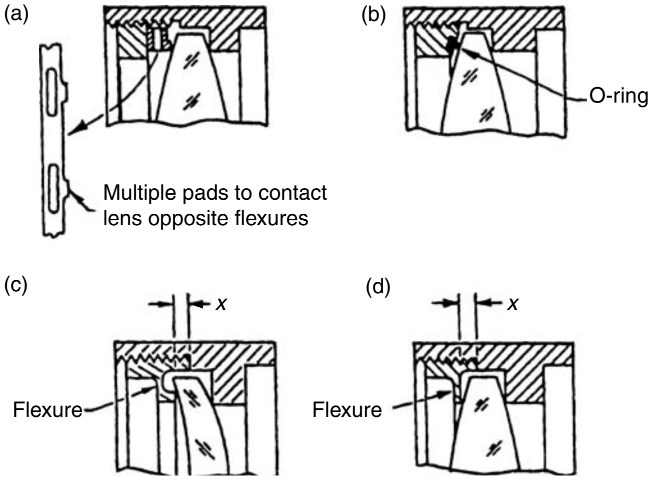

FIGURE 15.41 Four techniques for providing axial compliance in a lens mounting. (a) multiple flexures, (b) O-ring contact, (c) flexure retainer contacting a concave surface, and (d) flexure retainer contacting a convex surface. (From Yoder, P.R., Jr., *Mounting Optics in Optical Instruments*, SPIE Press, Bellingham, 2002a.)

TABLE 15.10
Evaluation of Temperature-Related Effects for Examples C and D

Parameter	Units	Equation (number)	Value for Example C	Value for Example D
P_A	lb/in.^{2}	—	3.6019	3.0818
1. Bulk Compression/Elongation of Glass and Metal				
$(2y_C+t_E)$	in.	—	2.5500	2.5500
A_G	in.^{2}	(15.56*a*)	1.6081	1.6081
C_G	in./lb	$2t_E/(E_GA_G)$	2.6575E-8	2.6575E-8
A_M	in.^{2}	(15.55)	0.4829	0.4829
C_M	in./lb	$t_E/(E_GA_G)$	5.2291E-8	3.1374E-8
K_3	lb/°F	(15.52)	−29.1636	−4.3141
2. Surface Deformations				
Average E	lb/in.^{2}	—	1.0800E+7	1.4100E + 7
Average v	none	—	0.2700	0.2740
$K_{1\ \mathrm{TOROID}}$	in.$^{-2}$	(15.17*a*)	0.1375	0.1375
K_2	in.^{2}/lb	(15.18)	1.7165E-7	1.3537E-7
Δy	in.	(15.22)	1.2622E-3	1.0368E-3
Δx	in.	(15.69)	5.9562E-7	3.9644E-7
C_D	in./lb	(15.70)	1.6536E-7	1.2864E-7
K_3	lb/°F	(15.52)	−5.6153	−0.7931
3. Retainer Deflection				
Δx	in.		0.0050[a]	00050[a]
C_R	in./lb	(15.71)	1.3882E-3	1.6224E-3
K_3	lb/°F	(15.52)	−0.0017	−0.0002
4. Shoulder Deflection				
K_A	in.^{4}/lb	(4.19*a*)	1.2925E-12	7.7083E-13
K_B	in.^{4}/lb	(4.19*b*)	3.3242E-14	1.9948E-14
Δx	in.	(4.18)	2.9029E-10	1.4810E-10
C_S	in./lb	(15.71)	8.0594E-11	4.8056E-11
K_3	lb/°F	(15.52)	−0.0017	−0.0002
S. Radial Dimension Changes				
Angle φ	deg.	(15.72)	73.2904	73.2904
Δy_C	in.	(15.73)	1.0580E-5	1.1500E-6
Δx	in.	(15.74)	3.1772E-6	3.4534E-7
Final K_3	lb/°F	(15.52)	−0.0062	−0.0006

[a] Assumed value.

reductions in P_A and K_3 for both examples are quite significant. Table 15.11 shows the tensile contact stress estimations for these new examples. The stress levels for these examples at all three critical temperatures are well below the allowable tolerance, so the lenses are mounted in a nearly stress-free manner. Note that the advantage from a stress viewpoint of choosing the metal for the mount so that its CTE approaches that of the associated glass (such as titanium rather than aluminum to mount a BK7 lens) is much less significant when axial compliance is properly provided in the design. This is fortunate because the CTEs of the various optical materials used in instruments differ considerably, the number of suitable mount materials is quite limited, and the use of multiple materials in a single mounting design adds unwanted complexity.

Although the engineering design of the retainers for Examples C and D have not been fully optimized, it is of interest to see if obtaining the desired deflections and acceptable bending stress might

TABLE 15.11
Estimation of Tensile Contact Stresses at Various Temperatures for Examples C and D

Parameter	**Units**	**Equation (number)**	**Value for Example C**	**Value for Example D**
1. Preload Applied at Various Temperatures				
Preload P' at T_{MAX}	lb	$P_{\mathrm{A}} + K_3\,(T_{\mathrm{A}} - T_{\mathrm{MAX}})$	3.0285	3.0285
Preload P_{A} at T_{A}	lb	—	3.6019	3.0818
Preload P'' at T_{MIN}	lb	$P_{\mathrm{A}} + K_3(T_{\mathrm{MIN}} - T_{\mathrm{A}})$	4.5243	3.1676
2. Estimation of Tensile Stress at T_{MIN}				
Linear preload, p	lb/in.	$P''/2\pi y_{\mathrm{C}}$	0.6261	0.4384
Compressive stress, S_{C}	lb/in.^{2}	(15.32)	565	532
Ratio, tensile/compressive stress		(15.14)	0.1947	0.1947
Tensile stress	lb/in.^{2}	(S_{C})(ratio)	110	104
3. Estimation of Tensile Stress at T_{A}				
Linear preload, p	lb/in.	$P_A/2\pi y_{\mathrm{C}}$	0.4985	0.4265
Compressive stress, S_{C} lb/in.^{2}		(15.32)	504	525
Tensile stress	lb/in.^{2}	(S_{C})(ratio)	98	102
4. Estimation of Tensile Stress at T_{MAX}				
Linear preload, p	lb/in.	$P'/2\pi y_{\mathrm{C}}$	0.4191	0.4191
Compressive stress, S_{C}	lb/in.^{2}	(15.32)	462	521
Tensile stress	lb/in.^{2}	(S_{C})(ratio)	90	101

pose potential problems for the retainers. Using Eqs. (4.18), (4.20), and (4.21), assuming that the yield stress S_{Y} for 6061-T6 aluminum is 42,000 lb/in.^{2}, and applying parameter values from Tables 15.7 and 15.8, we estimate these characteristics as follows for Example C:

$$t = [(1.2925 \times 10^{-12} - 3.3242 \times 10^{-14})(3.6019)/0.0050]^{1/3} = 0.0010 \text{ in.}$$

$$K_{\mathrm{C}} = \left[\frac{3}{2\pi}\right]\left[1 - \frac{(2)(3.0120)(1.1500^2)-(2)(1.1500^2)(4.0120)\ln(1.1800/1.1500)}{(1.1800^2)(2.0120)+(1.1500^2)(4.0120)}\right] = 2.4377 \times 10^{-2}$$

$$f_{\mathrm{s}} = (0.0010^2)(42{,}000)/(2.4377 \times 10^{-2})(4.5243) = 0.38 \text{ at } \mathrm{T_{MIN}}$$

This safety factor is decidedly low, so the retainer for Example C might be redimensioned to give a higher factor. Changing the retainer material to a stiffer material such as 416 CRES would give a higher f_{s}.

A similar calculation for Example D with S_{Y} for the 6Al4V titanium assumed to be 120,000 lb/in.^{2} and deriving needed parameter values from Tables 15.7 and 15.10 and Eq. (4.18) gives

$$K_{\mathrm{C}} = \left[\frac{3}{2\pi}\right]\left[1 - \frac{(2)(2.9412)(1.1500^2)-(2)(1.1500^2)(3.9412)\ln(1.1800/1.1500)}{(1.18002)(1.9412)+(1.15002)(3.9412)}\right] = 2.4351 \times 10^{-2}$$

$$t = [(7.7083 \times 10^{-13} - 1.9948 \times 10^{-14})(3.0818)/0.0050]^{1/3} = 0.0008 \text{ in.}$$

$$f_{\mathrm{s}} = (0.0008^2)(120{,}000)/(2.4351 \times 10^{-2})(3.1676) = 1.00 \text{ at } \mathrm{T_{MIN}}$$

This factor is acceptable, so the design should be successful.

A lens assembly that could benefit from simple design improvements is the air-spaced triplet relay lens assembly shown in Figure 15.42. To show why this is true, we first evaluate key axial dimensional changes of a temperature increase from an assembly temperature T_A of 68°F to a maximum survival temperature T_{MAX} of 160°F ($\Delta T = +92°F$). Next, we assess those changes for a temperature decrease from T_A to a minimum survival temperature T_{MIN} of −80°F ($\Delta T = -148°F$). The radial dimension changes from the same temperature changes are then calculated. The significances of both sets of dimensional changes are then defined. Similar calculations are then made for two revised designs in which configuration, material, and dimensional changes reduce the potential problems revealed with regard to the original design.

The axial length from point A to point B of Figure 15.42(a) can be expressed as $L_{AB} = t_{E1} + t_{S1} + t_{E2} + t_{S2} + t_{E3}$ where the thicknesses t_{Ei} are the edge thicknesses of the lenses at the height of contact with the metal y_C. The thicknesses t_{Si} are the thicknesses of the spacers at the same height y_C. At assembly, these dimensions are as indicated in the third column of Table 15.12. Note that showing the dimensions to six decimal places does not mean that each must be controlled to that accuracy. This number of significant figures is provided to reduce round-off errors in computations involving subtraction of small numbers to illustrate the principle of the theoretical design. The total length L_{AB} for the original design at the assembly temperature T_A, is 1.064000 in. When the temperature increases by $\Delta T = T_{MAX} - T_A = 92°F$, each component lengthens by $(t_i)(\alpha_i)(\Delta T)$, where the α terms are as listed in the fourth column of the table. We note that L_{AB} by the glass path grows by 0.000523 in. The portion of the cell wall extending from A to B also grows as the temperature rises. At T_{MAX}, its length is $L_{AB} + (L_{AB})(\alpha_{CELL})(\Delta T) = 1.065282$ in., so it grows by 0.001282 in. Assuming each component to be stiff, differential expansion then causes an axial gap of +0.000759 in. to occur. This gap can exist at any single interface in the assembly or it can be distributed among the various components. The designer cannot control this distribution. When such an axial gap exists, the preload imposed at assembly no longer constrains the components, so they are free to move under acceleration.

When the temperature drops to T_{MIN}, the components in the assembly of Figure 15.42(a) contract as indicated in the last column of Table 15.12. A difference in length L_{AB} of 0.001222 in., with the path through the cell changing length more than the path through the lenses and spacers, occurs from differential contraction. This would be expected to result in both compression of the lenses and spacers and stretching of the cell wall. The method described by Yoder and Hatheway (2005)

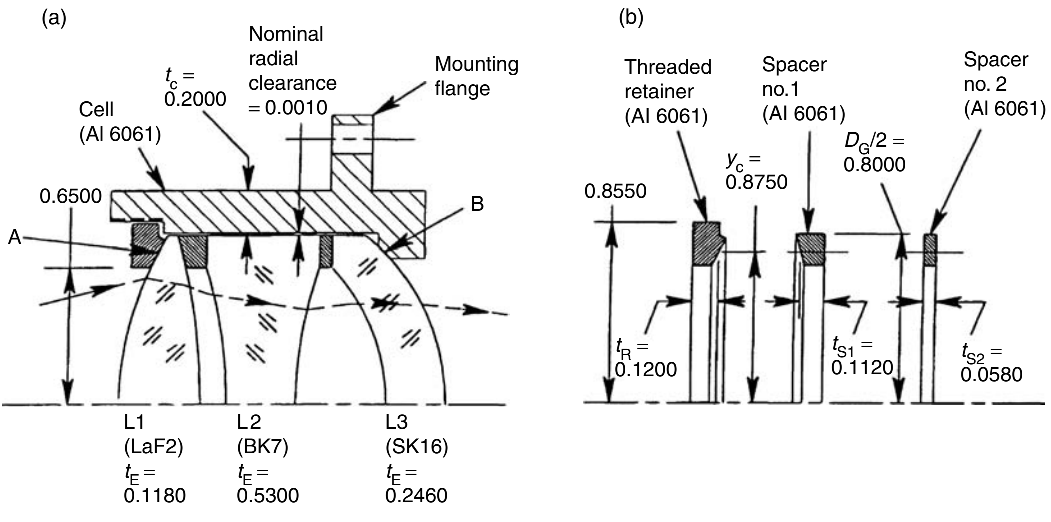

FIGURE 15.42 (a) Opto-mechanical layout of a hard-mounted triplet lens assembly discussed in the text. (b) Details of the retainer and spacers. Dimensions are in in.

TABLE 15.12
Axial Dimensions at T_A, T_{MAX}, and T_{MIN} of the Lenses, Spacers, and Cell Wall for the Assembly of Figure 15.42

Component	Material	Component Length t_i at T_A (in.)	Component CTE (in./in. × 10^{-6})	Component Length t_i at T_{MAX} (in.)	Component Length t_i at T_{Min} (in.)
Lens L_1	LaF2	0.118000	4.5	0.118049	0.117921
Spacer S_1	A16061	0.112000	13.1	0.112135	0.111783
Lens L_2	BK7	0.530000	3.9	0.530190	0.529694
Spacer S_2	A16061	0.058000	13.1	0.058070	0.057888
Lens L_3	SK16	0.246000	3.5	0.246079	0.245873
L_{AB} (lenses and spacers)	—	1.064000	—	1.064523	1.063158
L_{AB} (cell wall)	A16061	1.064000	13.1	1.065282	1.061937
ΔL (lenses and spacers)	—	—	—	+0.000523	−0.000842
ΔL (cell wall)	—	—	—	+0.001282	−0.002063
$\Delta(\Delta L)$	—	—	—	+0.000759	−0.001221

Note: T_A = 68°F, T_{MAX} = 160°F, T_{MIN} = −80°F.
Dimensions are in in.

and summarized above, one can estimate the factor K_3 of Eq. 15.63 and predict how the assembly preload changes with temperature. Space constraints do not allow that analysis to be included here, so it is left for the interested reader to perform.

The analytical process just described for axial temperature effects in the assembly of Figure 15.42(a) can be applied as well to its radial dimension changes. When the temperature increases, radial clearances around the lenses and spacers tend to increase while, as the temperature decreases, the radial clearances shrink. As pointed out in Section 15.6.1.1, if those clearances are small at assembly, they may disappear completely at some lower temperature. Radial stresses would then develop in the lenses because of compressive forces imposed in that direction. Tensile (hoop) stresses would develop in the wall of the cell as it shrinks around the resisting internal components (see Section 15.6.1.2).

Table 15.13 lists the radial dimensions and the changes in those dimensions for the assembly of Figure 15.42(a) at the three temperatures of interest. In the sixth column we find the differences between (component diameter)/2 and the (cell ID)/2 at T_{MAX}. These differences are the radial clearances; the component can decenter by this amount if not constrained by axial preload. The nominal clearance of 0.001000 in. at assembly is increased significantly at all lenses. The radial clearances for the two spacers do not change, because they are made of the same material as the cell. Since we learned earlier that axial preload no longer exists at T_{MAX} with this design, lens decentrations would be expected. Fretting of the glass surfaces may also occur under vibration. When the temperature returns to the operating range, the preload will return and the lenses may be constrained in decentered conditions. The optical performance of the system may be degraded if these decentrations exceed the allowable limits for the design.

Table 15.13 also indicates, in the eighth column, that the assembly's internal components do not decenter when the temperature drops to T_{MIN}. The negative signs for all three lens decentrations indicate that the cell compresses the glasses. Once again, the clearances for the spacers are unchanged because they and the cell are made of the same material.

There are several ways in which the design of Figure 15.42 can be improved. We will examine two of these. The first modification is depicted in Figure 15.43. Here, the metals used in some components are selected so that their CTEs more closely match those of the glasses, thereby reducing the tendency to create axial and radial gaps in the assembly at high temperatures. The critical changes are to substitute CRES 416 for the cell and CRES 303 for the second spacer. In order that

TABLE 15.13
Radial Dimensions at T_{MAX} and T_{MIN} of the Lenses, Spacers, and Cell Wall for the Example of Figure 15.42

Component	Material	Component Diameter/2 at T_{ASSY} (in.)	Component CTE (in./in. × 10^{-6})	Component Diameter/2 at T_{MAX} (in.)	Possible Decentration at T_{MAX} (in.)	Component Diameter /2 at T_{MIN} (in.)	Possible Decentration at T_{MIN} (in.)
Lens L_1	LaF2	0.800000	4.5	0.800331	0.001634	0.799467	−0.000020
Spacer S_1	A16061	0.800000	13.1	0.800964	0.001001	0.798449	0.000998
Lens L_2	BK7	0.800000	3.9	0.800287	0.001678	0.799538	−0.000091
Spacer S_2	A16061	0.800000	13.1	0.800964	0.001001	0.798449	0.000998
Lens L_3	SK16	0.800000	3.5	0.800258	0.001707	0.799586	−0.000139
Cell ID	A16061	0.801000	13.1	0.801965	—	0.799447	—

Note: T_{ASSY} = 68°F, T_{MAX} = 160°F, T_{MIN} = −80°F.
Dimensions are in in.

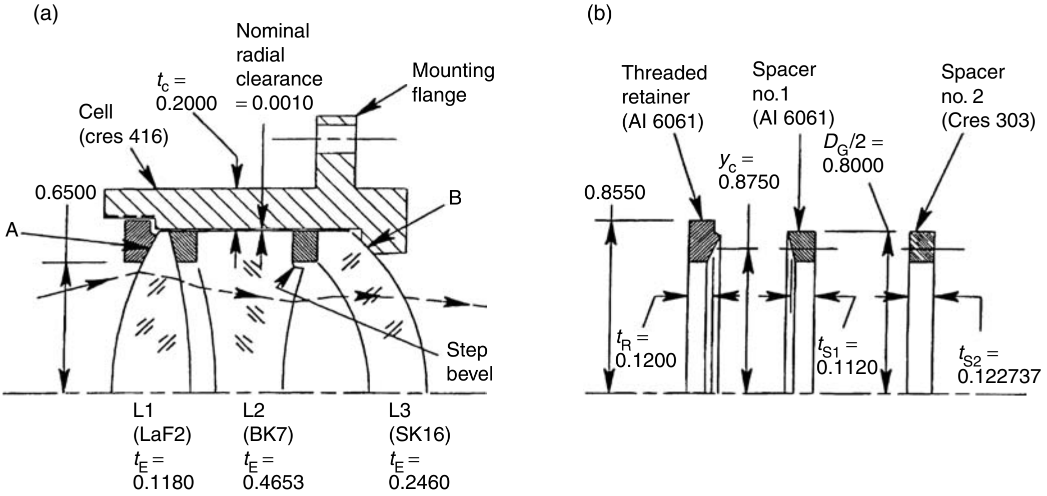
(a)
Nominal radial clearance = 0.0010
t_c = 0.2000
Cell (cres 416)
Mounting flange
0.6500
A
B
Step bevel
L1 (LaF2) t_E = 0.1180
L2 (BK7) t_E = 0.4653
L3 (SK16) t_E = 0.2460
(b)
Threaded retainer (Al 6061)
Spacer no.1 (Al 6061)
Spacer no. 2 (Cres 303)
$D_G/2$ = 0.8000
y_c = 0.8750
0.8550
t_R = 0.1200
t_{S1} = 0.1120
t_{S2} = 0.122737

FIGURE 15.43 (a) Modified design for the triplet lens mounting of Figure 15.42 to make it more nearly athermal axially. (b) Details of the retainer and spacers. Dimensions are in in.

the length L_{AB} be the same for the cell as for the stack of lenses and spacers, the axial length of the second spacer must be increased from 0.058000 in. to 0.122737 in. In order to accommodate the added length of the second spacer without changing the axial thicknesses of the lenses or the axial separations thereof, the right side of lens 2 is provided with a step bevel. Step bevels could have been placed on both lens 2 and 3 to achieve the same end results, but with minor increased cost. It would not be wise to retain the full t_E of lens 2 and provide the full step bevel on lens 3 because that would reduce the strength of the outer region of that lens. As indicated in the last two columns of Table 15.14, the $\Delta(\Delta L)$ parameter is zero at both T_{MAX} and T_{MIN}, so the design is axially athermal at both extreme temperatures.

Table 15.15 shows the radial dimensional changes that occur as the temperature changes for the revised design of Figure 15.43. The possible lens decentrations at T_{MAX} are slightly reduced from those of the original design because of the lower CTE of the CRES cell material. At T_{MIN}, radial clearances for the revised design are only slightly increased from the values at T_{ASSY}. Clearances persist to T_{MIN}, so radial stresses never develop in the lenses, and tensile stresses are not introduced

TABLE 15.14

Axial Dimensions at T_A, T_{MAX}, and T_{MIN} of the Lenses, Spacers, and Cell Wall for the Assembly of Figure 15.42

Component	Material	Component Length t_i at T_A (in.)	Component CTE (in./in. × 10^{-6})	Component Length t_i at T_{MAX} (in.)	Component Length t_i at T_{MIN} (in.)
Lens L_1	LaF2	0.118000	4.5	0.118049	0.117921
Spacer S_1	A1 6061	0.112000	13.1	0.112135	0.111783
Lens L_2	BK7	0.465263	3.9	0.465430	0.464994
Spacer S_2	CRES 303	0.122737	9.6	0.122845	0.122563
Lens L_3	SK16	0.246000	3.5	0.246079	0.245873
L_{AB} (lenses and spacers)	—	1.064000	—	1.064538	1.063134
L_{AB} (cell wall)	CRES 416	1.064000	5.5	1.064538	1.063134
ΔL (lenses and spacers)	—	—	—	+0.000538	−0.000866
ΔL (cell wall)	—	—	—	+0.000538	−0.000866
$\Delta(\Delta L)$	—	—	—	0.000000	0.000000

Note: T_A = 68°F, T_{MAX} = 160°F, T_{MIN} = −80°F.
Dimensions are in in.

TABLE 15.15

Radial Dimensions at T_{MAX} and T_{MIN} of the Lenses, Spacers, and Cell Wall for the Example of Figure 15.43

Component	Material	Component Diameter/2 at T_{ASSY} (in.)	Component CTE (in./in. × 10^{-6})	Component Diameter/2 at T_{MAX} (in.)	Possible Decentration at T_{MAX} (in.)	Component Diameter/2 at T_{MIN} (in.)	Possible Decentration at T_{MIN} (in.)
Lens L_1	LaF2	0.800000	4.5	0.800331	0.001074	0.799467	0.000881
Spacer S_1	A1 6061	0.800000	13.1	0.800964	0.000441	0.798449	0.001899
Lens L_2	BK7	0.800000	3.9	0.800287	0.001118	0.799538	0.000810
Spacer S_2	CRES 303	0.800000	9.6	0.800707	0.000699	0.798863	0.001485
Lens L_3	SK16	0.800000	3.5	0.800258	0.001148	0.799586	0.000762
Cell ID	CRES 416	0.801000	5.5	0.801405	—	0.800348	—

Note: T_{ASSY} = 68°F, T_{MAX} = 160°F, T_{MIN} = −80°F.
Dimensions are in in.

into the cell wall. Since axial preload can be preserved at all temperatures with this design, there is little danger of lens decentration at any temperature within the survival range unless the accompanying acceleration level is quite high.

Figure 15.44 shows a second revised configuration for the lens assembly of Figure 15.42. Here, the cell and spacer materials stay the same as in the original design, but the solid (i.e., axially stiff) threaded retaining ring is replaced with a compliant flange. Therefore, assembly preload can be applied by deflecting the portion of the ring that extends toward the lens L_1. The thickness t of the compliant portion of the retainer and the annular dimension of that portion are chosen to give the required axial force with a reasonable deflection while not introducing excessive stress into the bent flange.

To see how this revised design might work, let us assume that the design requires a deflection of the compliant retainer equaling 0.020000 in. As noted earlier, in the design of Figure 15.42, a temperature change from T_A to T_{MAX} produces a differential expansion for the lens-plus-spacers path of +0.000759 in. as compared to the path through the cell. This change in length is about 4%

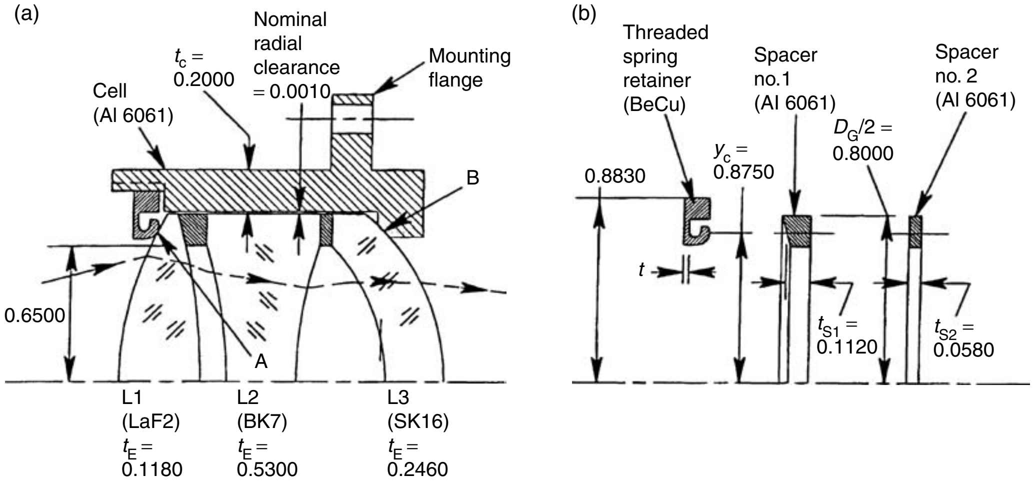

FIGURE 15.44 (a) Variation of the design of Figure 15.42 to provide axial compliance at the retaining ring. (b) Details of the retainer and spacers. Dimensions are in in.

of the retainer deflection; therefore, so the preload will be reduced approximately by this amount at T_{MAX}. Similarly, at T_{MIN}, differential expansion will change the retainer deflection by –0.001221 in. as compared to the path through the cell. This change in length is about 6% of the flange deflection, so the preload will be increased by about this amount at T_{MIN}. These changes are probably not very significant for the intended application of the lens assembly.

In Section 14.2.4, we described the opto-mechanical design of the Multiangle Imaging Spectro-Radiometer (MISR) lens assemblies. These had Vespel SP-1 spacers under each lens retainer. The thicknesses of these high-CTE spacers were determined so that, at extreme temperatures, the total axial lengths through the lenses were essentially equal to the corresponding lengths through the housing. This design feature rendered those assemblies axially athermal in the manner just described for the assembly of Figure 15.43.

Figure 15.45 shows a hardware implementation of a compliant axial constraint for a single lens that also provides compliance in the radial direction. This design, from Barkhouser et al. (2004), is to be used in a high-resolution IR camera for the Wisconsin, Indiana, Yale, National Optical Astronomical Observatory (WIYN) 3.5-m (138-in.)-diameter telescope on Kitt Peak. Axial differential expansion effects are compensated for by flexure of a disk spring (similar to the continuous flange of Figure 4.40[a]). Six screws secure this spring. The floating ring acts as a spacer between the spring and the lens. Its thickness determines the spring deflection that provides axial preload.

Radial differential expansion effects are compensated in this lens assembly by a series of six “roll-pin” flexures as detailed in view (b) of the figure. These flexures are machined into the ID of the aluminum centering ring by an electrical discharge milling (EDM) process in much the same manner as the radial flexures shown in Figure 4.54. In this case, however, the lens rim is not bonded to the flexures, but is constrained symmetrically with predetermined radial preload applied to the lens rim. The magnitude of this preload is determined by dimensional control during machining. The function of these flexures is similar to that of the centering ring described by Ford et al. (1999) and shown in Figure 14.13.

Another lens mounting that provides both radial and axial compliance has been designed at the Instituto de Astrofisica de Canarias in Tenerife, Spain, for use as a camera objective in EMIR, a cryogenic near-IR multiobject spectrograph for the 10 m class Gran Telescopio Canarias (GTC) telescope. It was described by Barrera et al. (2004a). The telescope was described by Alvarez and Rodriguez-Espinosa (1998).

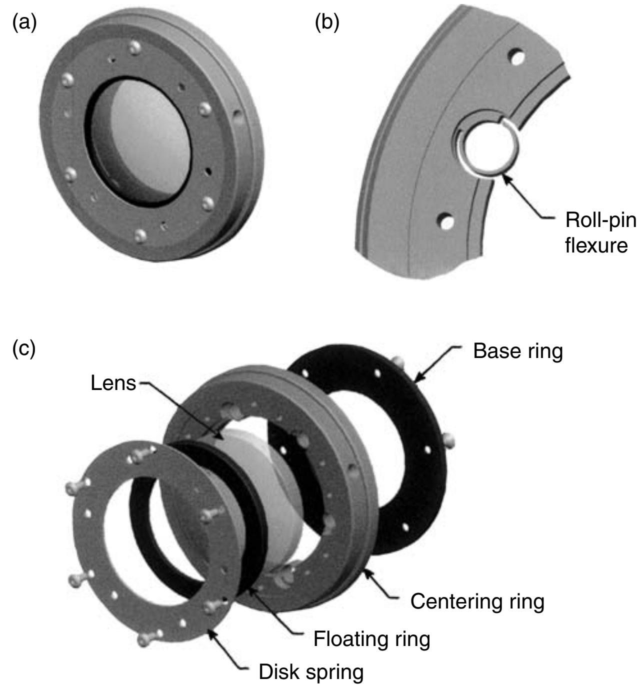

FIGURE 15.45 A lens mount with axial and radial compliance. (a) assembly, (b) detail view of radial flexure, (c) exploded view. (Adapted from Barkhouser, R.H. et al., *Proc. SPIE*, 5492, 921, 2004.)

A partially cut-away view of the objective is shown in Figure 15.46. Glass types are indicated, as is one of the flanges that provide axial preloads to the lens elements. The radial aspect of the mounting for one element is illustrated conceptually in Figure 15.47. A spring subassembly preloads the lens radially against two fixed supports. All three supports are made of aluminum and have PTFE pads that contact the lens rim. Details of the spring assembly are shown in Figure 15.48(a). All supports are precision-machined to ensure centration of the lens at assembly with radial constraints at 120° intervals around the lens rim. The dimensions of the supports, including the pads, were chosen to make the nominal design radially athermal. Small residual differential expansion effects through the anticipated temperature range cause the radial preload to vary slightly. Symmetry of the design ensures that the lens will remain centered within an allowable tolerance of ±75 μm at the 77 K operating temperature.

Axial compliance is provided in this assembly by an annular spring made of BeCu that is attached to the lens mount by several screws penetrating through a steel stiffening ring (see Figure 15.48[b]). The outer portion of the spring is slit radially to form 12 independently acting cantilevered springs. Deflections of these springs preload the lens against a shoulder in the same manner as the flange of Figure 4.40(a). The magnitude of each deflection is adjusted by machining the thickness of an aluminum ring (spacer) located between the spring and the mount housing. The spring thickness is 0.380 mm (0.015 in.). Nominally, the spring deflection is 1.000 mm (0.039 in.) and the applied axial force per spring at room temperature is 40.5 N (9.10 lb). As the temperature changes, the spring deflection changes slightly so as to maintain nearly constant axial preload on the lens. At the operating temperature of 77 K, the preload increases to 43.8 N (9.85 lb). The worst-case stress in each spring is 253.8 MPa (36,809 lb/in.^{2}). This gives a factor of safety of about 3 with respect to the yield stress of the material (Barrera, 2004b).

Contact with the lens surface at its spring-loaded side is through a PTFE ring that reduces friction at the interface and distributes the preload on the lens surface. The surface of the shoulder that

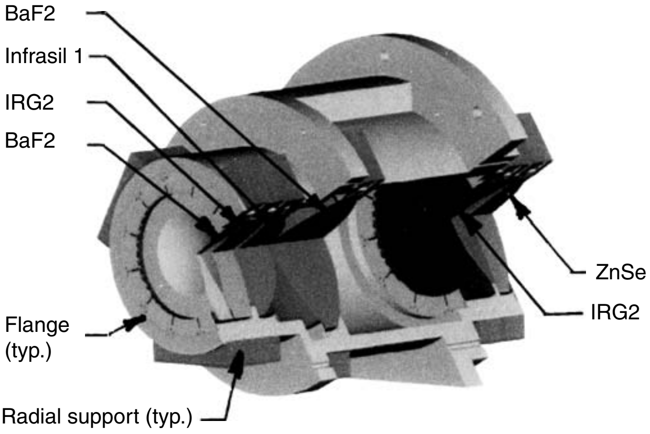
BaF2
Infrasil 1
IRG2
BaF2
ZnSe
IRG2
Flange (typ.)
Radial support (typ.)

FIGURE 15.46 An infrared camera objective assembly featuring spring-loaded radial and axial lens element constraints. (From Barrera, S. et al., *Proc. SPIE*, 5495, 611, 2004a)

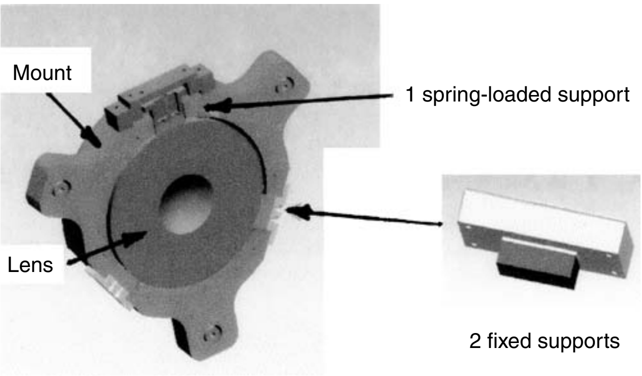
Mount
1 spring-loaded support
Lens
2 fixed supports

FIGURE 15.47 Concept for the radially compliant lens mounting used in the objective of Fig. 15.46. (Adapted from Barrera, S. et al., *Proc. SPIE*, 5495, 611, 2004a.)

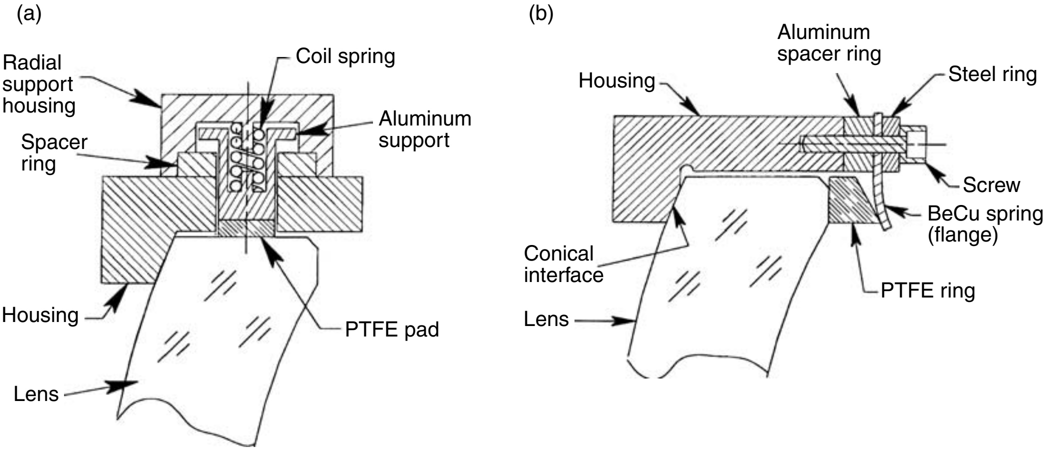
(a)
Radial support housing
Coil spring
Aluminum support
Spacer ring
Housing
PTFE pad
Lens
(b)
Aluminum spacer ring
Housing
Steel ring
Screw
BeCu spring (flange)
Conical interface
PTFE ring
Lens

FIGURE 15.48 Schematics of the compliant constraints for the objective of Figure 15.46. (a) radial support, (b) axial support. Note diagrams not necessarily to scale. (Adapted from Barrera, S., et al., *Proc. SPIE*, 5495, 2004a and Barrera, S., private communication, 2004b.)

contacts the other lens surface is covered with thin Kapton tape for the same reasons. As indicated in Figure 15.48(b), the PTFE ring is tapered, so the spring always touches the inner rim of the ring's face. This ensures that the cantilevered length of each spring is constant at 17 mm (0.669 in.).

Yet another lens mounting that provides axial compliance at cryogenic temperature was described by Stevanovic and Hart (2004). It was designed at the Research School of Astronomy and Astrophysics, Australian National University, in Canberra, Australia, and is to be used in the Gemini South Adaptive Optics Imager (GSAOI). This is a near-IR camera that will serve as the main science instrument in the Multi-Conjugate Adaptive Optics (MCAO) system in Chile. The lens mounting is depicted schematically in the exploded view of Figure 15.49. A stiff flange-type retaining ring with a conical interface to the outermost lens clamps the two lens elements axially against a conical shoulder in the lens cell. A wave washer located along with a conventional spacer between the lenses provides predetermined axial compliance. The lenses in this assembly are Infrasil and CaF_2 and have diameters of 170 mm (6.69 in.). These are the largest elements in the camera. The mountings for the smaller lenses are similar to this configuration. The lenses have the correct radial clearance at the time of assembly at room temperature to provide zero theoretical clearance at the operating temperature of 70 K.

An interesting feature of the mounting design of Figure 15.49 is that the alignment of the lens cell is adjustable within the lens mount. Four setscrews are provided to allow the lateral position of the cell to be adjusted in two axes at assembly. Holes are provided in the walls of the mount for micrometer measurements of cell location to be made.

The referenced paper by Stevanovic and Hart gives a detailed analysis of the effects of transient dimensional changes within the lens mount as the system cools to operating temperature. All components do not cool at the same rate, so differential dimensional effects occur. The analysis shows that the design is conservatively adequate to prevent damage to the optics during expected temperature variations.

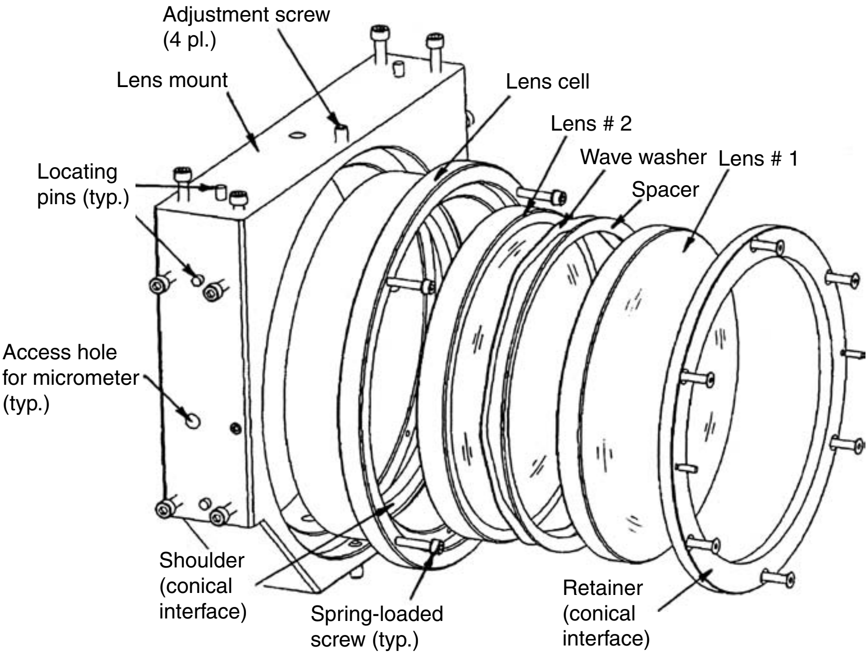

FIGURE 15.49 Exploded view of a lens mounting with compliant axial support and adjustable centration. (Adapted from Stevanovic, D. and Hart, J., *Proc SPIE*, 5495, 305, 2004.)

15.7 EFFECTS OF TEMPERATURE GRADIENTS

Temperature gradients exist in optical and mechanical components when all points within an optical instrument are not at the same temperature. These may be axial or radial and both types may occur simultaneously within the same component. Gradients result from changes in ambient conditions, movement of the instrument from one temperature environment to another, varying heat load from the sun or from more local heat sources, etc. If an optical instrument is held in a constant temperature environment for a long time (a process called "soaking"), the temperatures tend to equalize and all gradients reduce in severity. Experience based on analysis and tests with military, industrial, and consumer optical equipment indicates that a moderate-sized instrument may need several hours at constant temperature to stabilize. Under some conditions, the instrument never really reaches equilibrium, particularly if exposed to a varying temperature environment.

Some optical instruments are exposed to rapidly changing temperatures as part of their intended application. An example is an optical assembly that must survive thermal shock and perform to specification after being cooled rapidly from room temperature to cryogenic temperatures. One such assembly was described by Stubbs and Hsu (1991). This was an IR sensor objective designed to cool $\sim$ 150°C from room temperature to < 120 K within 5 min. It contained a 26 mm (1.02 in.) aperture germanium singlet that was cooled by conduction of heat through annular interfaces with a multicomponent brazed molybdenum TZM mount. Figure 15.50(a) is a schematic sectional view of the objective while Figure 15.50(b) is an exploded view thereof.

The mount was made of molybdenum TZM (CTE $= 5.5 \times 10^{-6}$/K) to closely match the CTE of the germanium (CTE $= 4.9 \times 10^{-6}$/K). The rate of heat flow out of the lens was maximized by establishing intimate contact between a flat bevel on the front (concave) lens surface and a brass spacer, and between the spherical rear (convex) lens surface and a matching concave spherical mechanical interface. The latter surface was ground and polished using optical test plates made to match the radius of the lens when at 120 K within $\sim$ 11 fringes at 0.633 μm wavelength. An assembly preload of 55 lb (245 N) was provided by three stainless-steel wave spring washers in series with a bolted-on, flange-type retainer. The authors indicated that the room-temperature axial preload was 113 lb/in.^{2} (0.78 MPa), so the contact area probably was about 0.5 in.^{2} (322 mm^2). With such large surface contacts, stress within the lens from the preload would be minimal.

Three flow channels were machined into the housing's outer cylindrical surface and a cylindical plenum cover was brazed over these exposed channels. Fill and vent tubes were then brazed radially onto the cover. The chamber labeled "simulated PCM cavity" in Figures 15.50(a) and (b) is a region reserved for a phase-change material to be used to stabilize the temperature of the assembly for about 25 min during operation after cool down with LN_2 flow through the three channels. Coolant lines were epoxied to the radial tubes using Epibond epoxy type 1210A/9615-10 supplied by CIBA-Geigy Furane Aerospace Products.

Interferometric tests of a model of the lens assembly showed that the lens would survive the imposed thermal shock and its surfaces would not be excessively distorted by gradients or compressive forces during operation. Laboratory tests of thermal behavior of the assembly showed that temperatures measured as a function of time after cryogen flow was initiated followed predictions reasonably well. Further, it was determined that the lens' temperature could be stabilized at about 100 K for the desired 25 min time period.

Another situation involving rapid temperature change and the possibility of thermal shock is an aerial camera moved from a warm environment on a flight tarmac to a frigid environment at a high altitude above the Earth. Proper operation of the camera's mechanisms and full optical performance may not be realized in the severe operational environment for a long time, if ever. Orbiting scientific optical payloads typically pose severe thermal design problems. In some such cases, excess heat may be radiated into outer space during part of a mission.

Refracting components such as lenses, windows, filters, and prisms are usually temperature stabilized by blowing conditioned air across their surfaces, by flowing current through electrically

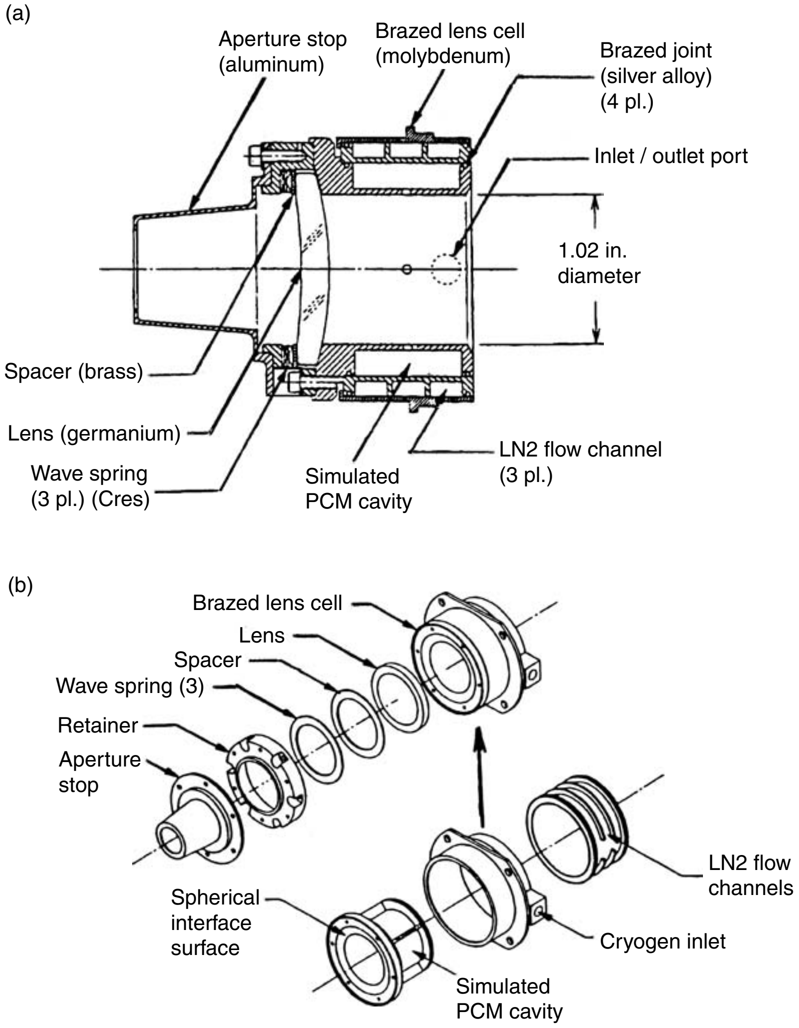
(a)
Aperture stop (aluminum)
Brazed lens cell (molybdenum)
Brazed joint (silver alloy) (4 pl.)
Inlet / outlet port
1.02 in. diameter
Spacer (brass)
Lens (germanium)
Wave spring (3 pl.) (Cres)
Simulated PCM cavity
LN2 flow channel (3 pl.)
(b)
Brazed lens cell
Lens
Spacer
Wave spring (3)
Retainer
Aperture stop
Spherical interface surface
Simulated PCM cavity
Cryogen inlet
LN2 flow channels

FIGURE 15.50 (a) Cross section view of a lens assembly designed for rapid cooling to cryogenic temperature by conduction through the lens surfaces near the rim. (b) Exploded diagram of the lens assembly (From Stubbs, D.M. and Hsu, I.C., *Proc. SPIE*, 1533, 36,1991.)

conducting coatings on one or more surface(s), or by conduction from the mount. Cooled window and filter examples were described in Sections 6.3 and 6.6. Typically, small and moderate-sized mirrors are cooled (or heated) by conduction through their mounts or by heat-transfer devices attached to their back surfaces. Mirrors used in high-energy laser applications are generally temperature controlled by flowing coolant through heat-exchange channels within their substrates. Large ground-based astronomical telescope mirrors are usually temperature stabilized with attached heaters or coolers or by airflow across the front and back surfaces. An example of the latter approach is the new MMT telescope primary described in Section 12.3.3. Components whose temperatures are controlled by heat flow through their mounts around the peripheries of their apertures tend to suffer from radial gradients and may have nonsymmetrical temperature gradients.

Hatheway (2000) described how an argon ion laser was cooled by flowing air through a heat exchanger contacting the OD of the laser cavity wall. Figure 15.51 shows the natural air convection flow around a hot horizontal laser cavity. A vertical temperature gradient then develops, the structure warps, and the end mirrors of the cavity tilt, thereby causing the beam to deflect in the vertical plane, as indicated in Figure 15.52. For the laser to be stable and usable in any orientation relative to gravity, the temperature gradient must be minimized. Cooling the assembly with flowing air accomplishes this goal and maintains the integrity of the brazed and frit bonded seals in the cavity.

Figure 15.53 schematically shows the configuration of the laser. It is built around a beryllium oxide rod that has a 1.0-mm-diameter hole bored through along the centerline. Argon gas from the reservoir fills the cavity between the end mirrors and lases when electrically excited between the

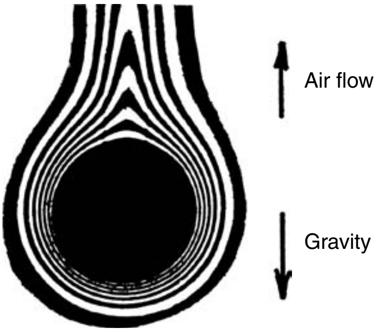
Air flow
Gravity

FIGURE 15.51 The natural vertical flow of air due to convection around a heated cylinder (gas laser cavity). (From Hatheway, A.E., *Proc. SPIE*, 4198, 141, 2000.)

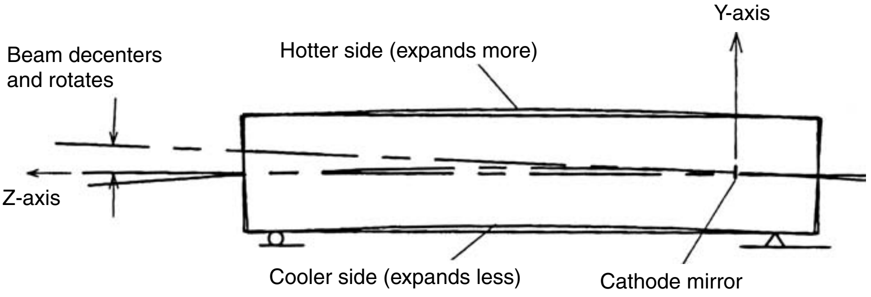
Y-axis
Beam decenters and rotates
Hotter side (expands more)
Z-axis
Cooler side (expands less)
Cathode mirror

FIGURE 15.52 Effect of natural heat convection on beam location and direction with natural convective heat flow. (From Hatheway, A.E., *Proc. SPIE*, 4198, 141, 2000.)

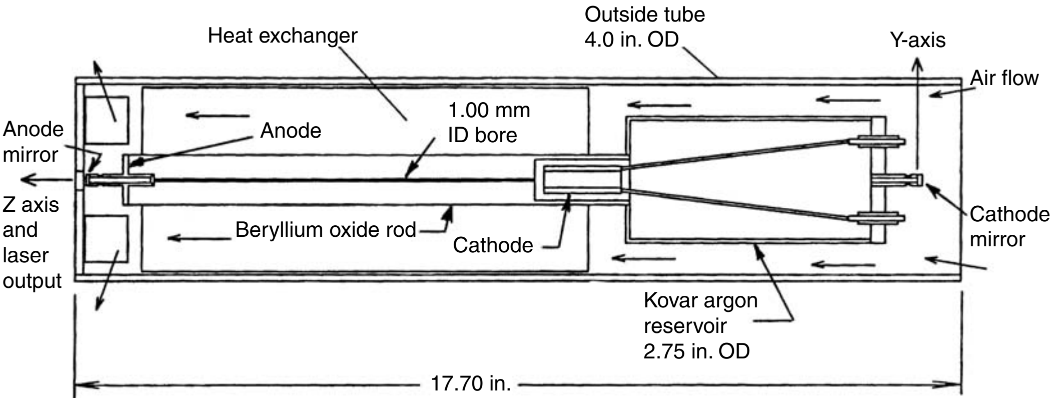
Heat exchanger
Outside tube 4.0 in. OD
Y-axis
Air flow
Anode mirror
Anode
1.00 mm ID bore
Z axis and laser output
Beryllium oxide rod
Cathode
Cathode mirror
Kovar argon reservoir 2.75 in. OD
17.70 in.

FIGURE 15.53 Schematic configuration of an argon ion laser with forced air cooling. (Adapted from Hatheway, A.E., *Proc. SPIE*, 4198, 141, 2000.)

cathode and anode. The laser design called for dissipation of about 2500 watts along the cavity bore plus about 100 watts of cathode heater power. From the outset, it was known that the laser would not function without cooling.

A high-efficiency aluminum heat exchanger was designed to fit within the available space around the rod and inside the outside tube ID. Figure 15.54 shows an end view of this exchanger. A centrifugal fan was chosen to provide airflow equivalent to about 0.5 in. water pressure head. Analysis of the thermal and structural design models was accomplished using a Unified Analysis technique as described by Hatheway (1991). The element displacements and temperatures were determined to within 2% error. The study indicated that the beam wander would be approximately 17 μrad or 0.0066 μrad/W of heat dissipation in the laser.

15.7.1 Radial Temperature Gradients

Figure 15.55 shows a generic radial gradient in a simple lens. The lens is in air and is subjected to a radial gradient in which the glass near the rim is warmer than that near the axis by an amount Δ*T*.

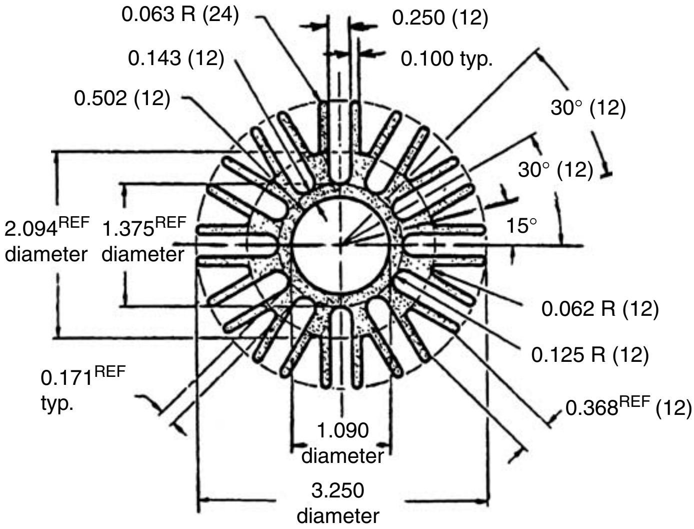
0.063 R (24)
0.250 (12)
0.143 (12)
0.100 typ.
0.502 (12)
30° (12)
30° (12)
15°
2.094^REF diameter
1.375^REF diameter
0.062 R (12)
0.125 R (12)
0.171^REF typ.
0.368^REF (12)
1.090 diameter
3.250 diameter

FIGURE 15.54 End view of the heat exchanger used to cool the laser shown in Figure 15.53. (Adapted from Hatheway, A.E., *Proc. SPIE*, 4198, 141, 2000.)

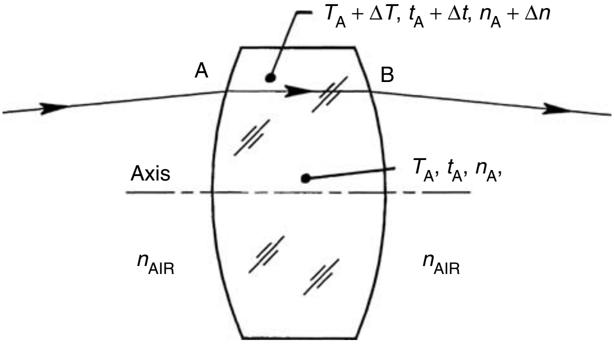
$T_A + \Delta T$, $t_A + \Delta t$, $n_A + \Delta n$
A
B
Axis
T_A, t_A, n_A,
n_{AIR}
n_{AIR}

FIGURE 15.55 Illustration of a radial temperature gradient in a simple lens. (From Yoder, P.R., Jr., *Mounting Optics in Optical Instruments*, SPIE Press, Bellingham, 2002a.)

The temperature, lens thickness, and refractive index of the axial region remain essentially constant at T_A, t_A, and n_A, while those parameters at the rim increase as indicated to $T_A + \Delta T$, $t_A + \Delta t$, and $n_A + \Delta n$. Jamieson (1992) indicated that, neglecting temperature gradients along the axis, the OPD between the arbitrary ray shown passing between the points A and B compared with the corresponding ray along the axis is approximated by the expression OPD $= [(n - 1) + \Delta n(t + \Delta t) - (n - 1)(t)$. Since $\Delta n = \beta_G \Delta T$ and $\Delta t = \alpha_G\, t\, \Delta T$, we obtain OPD $= [(n - 1)(a) + \beta] t_A\, \Delta T$. From this we derive these working equations:

$$\text{OPD} = (n_G - 1)\gamma_G t_A \Delta T \tag{15.76}$$

$$\gamma_G = \alpha_G + [\beta_G/(n_G - 1)] \tag{15.77}$$

The parameter γ_G is a thermo-optical coefficient for the glass that describes its sensitivity to spatial temperature variations. Jamieson (1992) indicated that γ_G for most optical glasses lies between 5×10^{-6}/°C and 25×10^{-6}/°C. Exceptions are fluor crown (FK) and phosphate crown (PK) glasses from Schott and Ohara, and some glasses from Hoya. Table 3.12 lists γ_G values for a variety of refractive materials. A few glasses with small or negative values are available. These reduce the sensitivity of lens systems to temperature gradients. Optical plastics and some IR-transmitting materials (notably germanium) have larger values of γ_G than glasses. The thermal conductivities and heat capacities of plastics are low, so these materials tend to be quite sensitive to spatial temperature gradients. Germanium has a high conductivity and heat capacity, so lenses made from that material might not suffer much when the temperature is not uniform. Germanium is, however, subject to thermal runaway, meaning that the hotter it gets, the more it absorbs radiation. Pronounced transmission degradation starts at about 100°C and degrades rapidly between 200°C and 300°C. Absorption may result in catastrophic failure of the optic. Combinations of materials with high and low γ_G tend to reduce gradient sensitivity. The liquids listed in Table 3.12 are sometimes used to fill the air spaces between lenses to make the system more athermal (Jamieson, 1992, Andersen, 1993).

To illustrate the use of Eqs. (15.76) and (15.77), consider the following example from Yoder (2002a). Thin lenses made of (a) BK7 glass, (b) SF11 glass, and (c) germanium are all 3.500 mm (0.137 in.) thick and have radial temperature gradients causing their rims to be 2°C hotter than at the axis. What OPDs are created in each case? We assume $\lambda = 0.546$ µm for the glass lenses and 10.6 µm for the Ge lens. Let $n_{\lambda\,\text{BK7}} = 1.5187$, $n_{\lambda\,\text{SF11}} = 1.7919$, and $n_{\lambda\,\text{Ge}} = 4.0000$. From Table 3.12, $\gamma_{G\,\text{BK7}} = 9.87 \times 10^{-6}$/°C, $\gamma_{G\,\text{SF11}} = 20.21 \times 10^{-6}$/°C , and $\gamma_{G\,\text{Ge}} = 136.3 \times 10^{-6}$/°C. We use Eq. (15.76) for each case.

(a) OPD $= (0.5187)(3.500)(9.87 \times 10^{-6})(2) = 3.58 \times 10^{-5}$ mm $= 0.07\ \lambda$ @ 0.546 µm for BK7
(b) OPD $= (0.7919)(3.500)(20.21 \times 10^{-6})(2) = 1.12 \times 10^{-4}$ mm $= 0.20\ \lambda$ @ 0.546 µm for SF11
(c) OPD $= (3.0000)(3.500)(136.3 \times 10^{-6})(2) = 2.86 \times 10^{-3}$ mm $= 0.27\ \lambda$ @ 10.6 µm for Ge.

These OPDs would all be large enough to be of concern in high-performance applications.

Jamieson (1992) indicated that Eq. (15.76) is quite helpful in making general choices of optical materials for a preliminary design or in estimating the significance of anticipated temperature gradients, but is not sufficiently accurate for final design purposes because it is based on thin-lens approximations. Final design requires that ray traces be conducted using realistic input temperature distributions to determine the index and thickness values as functions of zonal locations within the lens apertures and their effects upon lens performance.

Since there is no refraction, radial temperature gradients will affect reflecting optical components by changing the radii of optical surfaces and surface sagittal depths as functions of height from the axis. Surface deformations may also result from spatial gradients. Lens design programs may evaluate the effects of these changes by considering the surfaces to be aspheric. The resulting effects upon the image are quite easily determined using such programs.

15.7.2 Axial Temperature Gradients

An axial temperature gradient can be created in an optical component such as a window, lens, or prism by absorption of an incident heat flux such as solar or laser radiation. The gradient so created will cause changes in bending of the optic. Barnes (1966) gave a classic treatment of thermal effects on space optics. With uniform axial irradiation, a plane-parallel window becomes a shallow, concentric meniscus. Its mean radius of curvature R is given by $1/R = \alpha q/k$, where α is the linear thermal expansion coefficient, q the heat flux per unit area, and k the material's thermal conductivity. If the thickness t is small compared with R, the optical power P of this bowed window is given by

$$P = 1/f = \frac{(n-1)}{n}\left(\frac{tq}{k}\right)^2 \tag{15.78}$$

With this equation, Barnes (1966) showed that for an optical system at 300 K in LEO, the axial thermal gradient in a 2.5-cm (1.0-in.)-thick crown glass window caused by the ~15% of incident solar radiation absorbed may be negligible for apertures smaller than 2.9 m (9.5 ft) since the focal shift introduced would be smaller than the Rayleigh $\lambda/4$ tolerance. This critical aperture varies inversely as the square root of the window thickness for a given heat flux absorbed.

Temperature gradients introduced through the edge mounting for a window or corrector plate introduce differences in optical path length at various radial zones. This is due to changes in mechanical thickness of the material as well as changes in the refractive index of the optical material. In general, stresses are built up in the glass and birefringence is introduced. These effects are small.

To illustrate the use of the analytical tools discussed in his paper, Barnes (1966) gave an example of an edge-insulated, single-glazed, nominally plane-parallel crown glass window 3.0 cm (1.2 in.) thick and 61 cm (24 in.) in aperture. When used in an Earth-oriented satellite at 960 km (600 mi) altitude, this window was found to become a shallow negative lens and to have an optical path difference distribution of zero on axis and at a zonal radius of 0.9, but a zonal aberration peaking at a zonal radius of 0.6 to 0.7 that is equivalent to ~ 0.5 wave p-v at visible wavelengths during operation. If used in an *f*/5 optical system of 55 cm (21.7 in.) aperture, this deformation would cause the system focus to shift about 42 μm; this is nearly twice the Rayleigh quarter-wave tolerance for that system. The zonal aberration would reduce the system's performance even if it were to be refocused. Barnes concluded that the use of a window with an aperture significantly (about 25%) larger than that of this particular optical system would reduce the error to a much more tolerable magnitude without resorting to complex on-board thermal controls. Reducing the window thickness or decreasing the thermal coupling between the mount and the window by increasing the degree of thermal insulation provided would tend to reduce the effects of such a radial thermal gradient.

Vukobratovich (1993) indicated that the change in curvature of a mirror if exposed to a steady-state linear axial thermal gradient is given by

$$(1/R_0) - (1/R) = (\alpha q/k) \tag{15.79}$$

where R_0 and R are the original and new radii of curvature, respectively, a the mirror CTE, k its thermal conductivity, and q the heat flux absorbed per unit surface area. The ratio of a/k in Eq. (15.79) is the steady-state thermal distortion coefficient listed in Table 3.16 for a variety of mirror materials. A preferred material from the viewpoint of resistance to a thermal gradient has a low value for this coefficient.

15.8 STRESSES IN CEMENTED AND BONDED OPTICS DUE TO TEMPERATURE CHANGES

Three major sources of stress in cemented optics and bonded joints between optics and their mounts are shrinkage of the adhesive during curing, acceleration in a direction that tends to pull the optic from the mount, and differential expansion and contraction at high and low temperatures. FEA methods can be used to predict all of these effects, but they are beyond the scope of this book. In this section, we consider each of these effects briefly. Doyle et al. (2002) summarize the fundamentals of adhesive bond modeling. Hatheway (1998) and Genberg (1997a) give more detailed treatments of this subject.

During curing, most adhesives shrink by a few percent of each dimension of the adhesive layer. The resultant stresses in the adhesive layer and in the bonded components may persist throughout the life of the device. This stress is usually small, but will tend to bend the optic and the mount. If the optic is too thin, this may change the figure(s) of optical surface(s) sufficiently to degrade performance. Corrective actions during design include making sure that the optic stiffness is as large as reasonably possible, choosing an adhesive with minimal curing shrinkage, and minimizing the lateral dimensions of the bond. Using an optical material with a large Young's modulus contributes to the stiffness of mirrors, but this option is not generally available with refractive optics. In cemented doublets, triplets, and prisms, the size of the joint is not a variable; it is determined by the aperture requirements.

Figure 15.56 shows the result of an experiment involving a proposed design for a 9-cm (3.54-in.)-diameter cemented doublet lens for a particular military application. The lens designer wanted to use FK51 and KzFS7 glasses for optical performance reasons, but concern was expressed that the disparity in CTEs would be a problem in the extreme low-temperature environment of −62°C. The CTEs of the materials were 13.3×10^{-6}/°C and 4.9×10^{-6}/°C, respectively. With $\Delta T = -82$°C from assembly temperature, one glass would shrink 0.098 mm and the other 0.036 mm across the cemented diameter. The thicknesses of the plates were 22 mm (0.866 in.) and 28 mm (1.102 in.), respectively, so they were quite stiff. Severe distortion of the surfaces was not expected, but stress would undoubtedly build up in the joint when cold.

Rather than risk making the required number of doublets and having them fail during testing, a less expensive model was made. Two plane-parallel plates of the chosen glasses with thicknesses equal to the element axial thicknesses were cemented together conventionally with standard optical cement. This model was cooled toward the specified low temperature and failed the test as shown

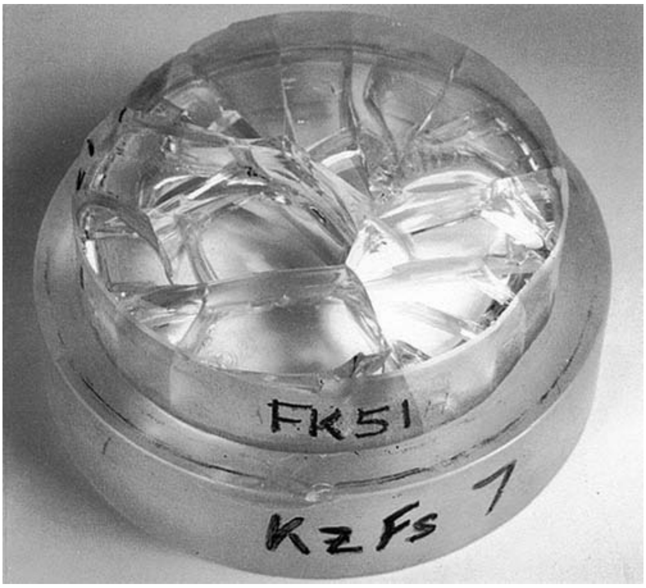

FIGURE 15.56 Photograph of a pair of thick glass plates optically cemented together to simulate a cemented doublet lens and subjected to low temperature. Fractures occurred due to differential thermal expansion effects from the widely differing CTEs of the materials involved.

in the photograph. Rather than redesign the lens system to use other glasses, a variety of other adhesives were considered. A transparent elastomeric sealing compound, Sylgard XR-63-489 (formerly manufactured by Dow Corning), was chosen because it could be used in a thicker layer and forms a softer joint than the conventional optical cement. Tests with additional plates indicated this adhesive to be acceptable over all the specified temperature extremes and from the optical performance viewpoint, so the manufacture of the lenses proceeded successfully.

Differential contraction or expansion of materials and acceleration forces can place a bonded prism-to-mount joint in tension with sufficient force to weaken or break the bond. Because the strength of the adhesive joint is often greater than the tensile strength of the optical material, the latter material may fracture. Thermal effects in bonded joints that are due to a mismatch of glass, adhesive, and metal CTEs obviously have their greatest impacts at extreme survival temperatures. Usually, $\alpha_e \gg \alpha_M > \alpha_G$. Shear stresses across the joint tend to bend both the optic and the mount. If small, these effects are temporary and reversible. If large, damage may result.

Vukobratovich (2002, 2003) presented an analytical method, based on work by Chen and Nelson (1979), for estimating the shear stress developed in a bonded joint as a result of differential dimensional changes at temperatures other than that at assembly. The pertinent equations are as follows:

$$S_S = \frac{(\alpha_M - \alpha_G)\Delta T S_e \tanh(\beta L)}{\beta t_e} \tag{15.80}$$

$$S_e = \frac{E_e}{2(1+\nu_e)} \tag{15.81}$$

$$\beta = \left[\left(\frac{S_e}{t_e}\right)\left(\frac{1}{E_M t_M} + \frac{1}{E_G t_G}\right)\right]^{1/2} \tag{15.82}$$

where S_S is the shear stress in the joint; α_M and α_G the CTEs of the metal and glass, respectively; ΔT the temperature change from assembly temperature; S_e the shear modulus of the adhesive; tanh the hyperbolic tangent function; L the largest dimension (length, width, or diameter) of the bond; t_e is the thickness of the bond; E_M and E_G Young's modulus for the metal and glass, respectively; ν_e the Poisson's ratio for the adhesive; and t_M and t_G the thicknesses of the metal and glass components, respectively.

We illustrate the use of these equations with the following example. The cube-shaped prism shown in Figure 15.57 was made of fused silica and was bonded to a titanium base with 3M 2216 epoxy. The face width of the prism was 1.378 in. (35 mm). The metal base was 1.051 in. (26.695 mm) thick. The bond was 0.004 in. (0.102 mm) thick, and covered the entire glass-to-metal interface. Assuming that the stress in the prism equaled the shear stress in the adhesive, what was that stress for a temperature drop ΔT of 90°F? From Table 3.2, $\alpha_G = 0.32 \times 10^{-6}$/°F, $E_G = 10.6 \times 10^6$ lb/in.^{2}, and $\nu_G = 0.17$. From Table 3.17, $\alpha_M = 4.90 \times 10^{-6}$/°F, $E_M = 16.5 \times 10^6$ lb/in.^{2}, and $\nu_M = 0.31$. From Table 3.26, $E_e = 1.00 \times 10^5$ lb/in.^{2} and $\nu_e = 0.43$. From Eq. (15.81), $S_e = 1.0 \times 10^5/[(2)(1 + 0.43)] = 3.50 \times 10^4$ lb/in.^{2}. From Eq. (15.82),

$$\beta = \left\{\left(\frac{3.50\times10^4}{0.004}\right)\left[\frac{1}{(16.5\times10^6)(1.051)} + \frac{1}{(10.6\times10^6)(1.378)}\right]\right\}^{1/2} = 1.050 \text{ in.}^{-1}$$

From Eq. (15.80) with $\beta L = (1.050)(1.378) = 1.447$,

$$S_S = (4.90 \times 10^{-6} - 0.32 \times 10^{-6})(90)(3.50 \times 10^4)(\tanh 1.447)/[(1.050)(0.004)] = 3074 \text{ lb/in.}^2$$

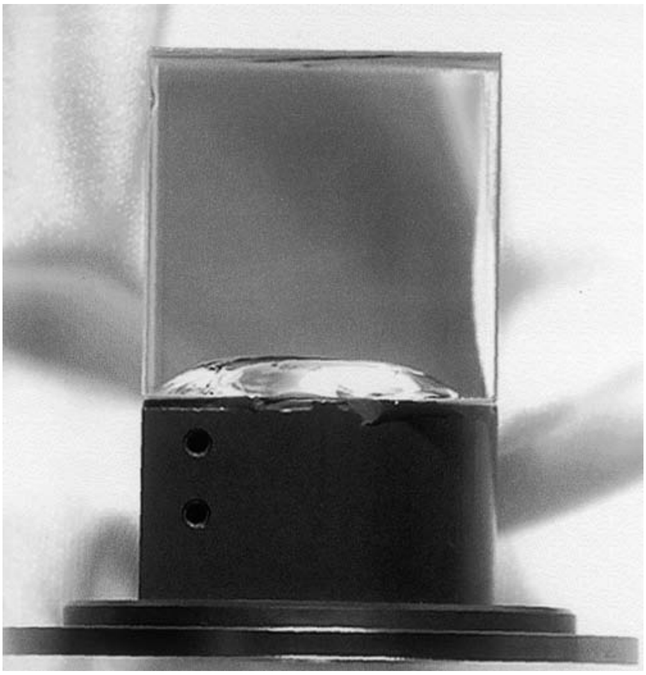

FIGURE 15.57 Photograph of a fused silica cube beamsplitter prism with face width $A = 35$ mm bonded across its fine ground bottom surface to a titanium mount with epoxy. Failure occurred at a low temperature because of differential expansion of the glass, adhesive, and metal. (From Yoder, P.R., Jr., *Mounting Optics in Optical Instruments*, SPIE Press, Bellingham, 2002a.)

This stress significantly exceeded the 1000 lb/in.^{2} rule-of-thumb tolerance established earlier for tensile stress in glass, so breakage of the prism was to be expected at the specified low temperature. As shown in the photograph, failure did indeed happen.

It was suggested that a bond area comprising three equal circles of 0.250 in. diameter could replace the larger single bond. Using the Chen and Nelson theory, what would be the stress in each of these bonded areas for $\Delta T = 90°\text{F}$? From Eq. (15.80) with $\beta L = (1.050)(0.250) = 0.262$,

$$S_S = (4.90 \times 10^{-6} - 0.32 \times 10^{-6})(90)(3.50 \times 10^4)(\tanh 0.262)/[(1.050)(0.004)] = 880 \text{ lb/in.}^2$$

The stress at low temperature would be reduced to a much more acceptable value and the prism should survive low temperature if the bonded glass surface was free of defects. Tests with these smaller bond areas indicated this to be the case.

15.9 SOME EFFECTS OF TEMPERATURE CHANGES ON ELASTOMERICALLY MOUNTED LENSES

In Chapter 4, we described a method for mounting a lens in a cell by encapsulating the lens rim in an annular ring of elastomer such as an RTV compound (see Figure 4.51). This method offers potential benefits of relative simplicity, athermalization in the radial direction, and a small degree of mechanical resiliency over the equivalent mechanically clamped mountings. Equations (4.25) and (4.26) were cited previously as appropriate means for "optimizing" the thickness of the annular layer of elastomer to make it just fill the radial space between the lens rim and the cell ID at all temperatures within the range where the material CTEs can be considered constant. This supposedly creates a stress-free mounting for the lens.

Miller (1999) reported an FEA of this type of lens mounting in which three germanium lenses of the same diameter (~ 2 in. [~ 51 mm]) having meniscus, biconcave, and biconvex shapes were mounted in elastomeric rings of differing thicknesses within 6061 aluminum cells (see Figure 15.58). The stresses in the lens and cell wall at a temperature 30°C (54°F) above assembly temperature were predicted as the elastomer ring thickness t_e was reduced from the nominal 0.077 in. (1.956 mm) value derived from Eq. (4.25) to 0.005 in. (0.127 mm). Figure 15.59 depicts the distributions of stresses within the cell, elastomer, and lens for the "athermal" ring thicknesses as well as thicknesses of 0.010 in. (0.254 mm). The maximum stress levels (darkest ends of gray scales) are indicated for each case. The contours of the lenses and the elastomer layers have been emphasized in the figures to make those shapes more visible. Definite changes in stress patterns are visible. The highest stresses are found for the thinner elastomer layers. Note that the elastomer bulges outward, indicating compression, at the elevated temperature. One would expect the elastomer layer to have straight sides if truly "athermal." It is apparently in tension, as shown by its concave boundaries, at the 0.010 in. (0.254 mm) elastomer thickness. We observe that the elastomer does not exactly fill the available space between the lens and the cell wall at the elevated temperature.

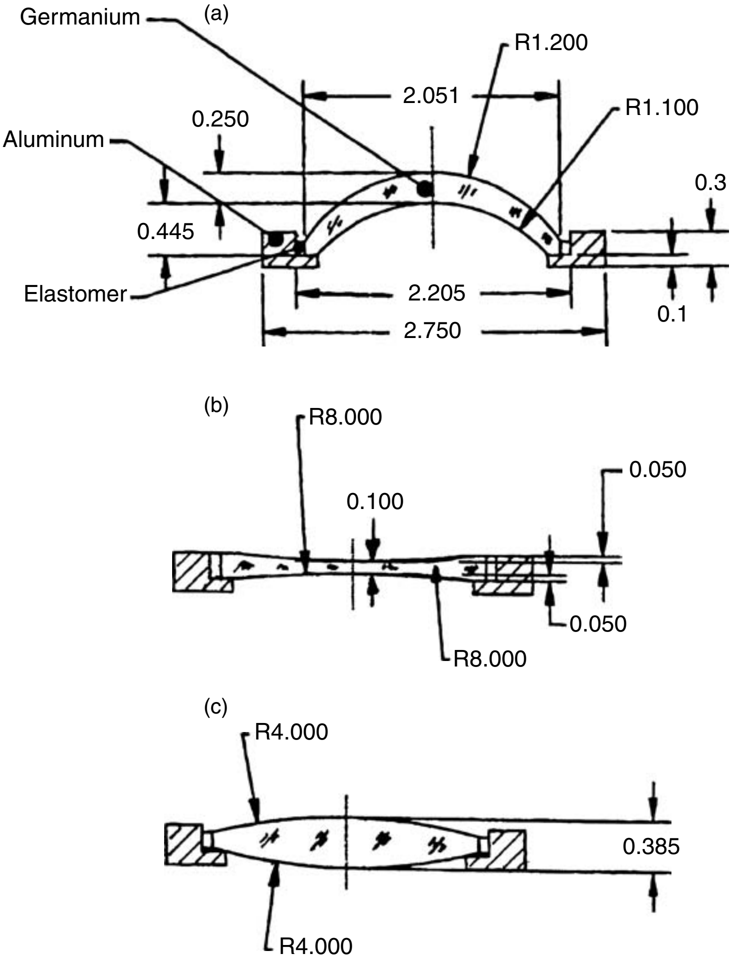

FIGURE 15.58 Schematics of lens configurations analyzed by finite element methods: (a) meniscus, (b) biconcave, and (c) biconvex shapes. (From Miller, K.A., *Proc. SPIE*, 3786, 506, 1999.)

Figure 15.60 shows the variations with t_e of maximum stresses at elevated temperature for all three lens types. We observe that reducing the thickness by as much as a factor of two has little effect on stress; Eq. (4.25) does not give the lowest stress; and the stress is dependent upon lens shape. Miller assumed ν_e to be 0.49 in his analysis and may not have computed the effective CTE for the elastomer as discussed in Section 4.8. If this was the case, use of α_e^* would reduce his "athermal" t_e considerably. Although Miller does not specifically discuss it, increasing t_e from the "athermal" value might be expected to decrease thermally induced stress and increase the flexibility of the joint. From a stress viewpoint, the tolerance for the thickness of the elastomer layer can obviously be quite large.

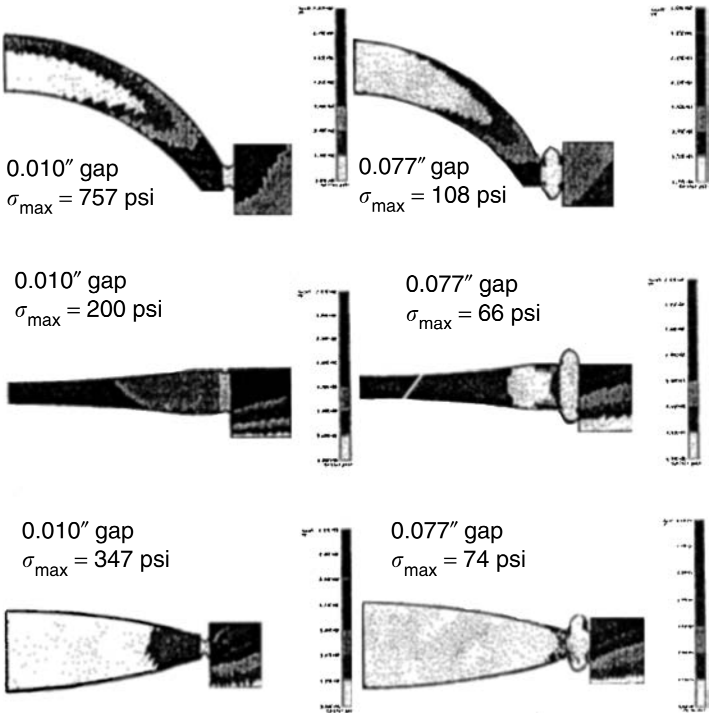
0.010″ gap
σ_{max} = 757 psi
0.077″ gap
σ_{max} = 108 psi
0.010″ gap
σ_{max} = 200 psi
0.077″ gap
σ_{max} = 66 psi
0.010″ gap
σ_{max} = 347 psi
0.077″ gap
σ_{max} = 74 psi

FIGURE 15.59 Stress magnitudes and distributions for the lenses of Figure 15.58 at 30°C (54°F) above assembly temperature for elastomer layers with approximately "athermal" radial thicknesses of 0.077 in. (1.956 mm) and 0.010 in. (0.254 mm). (From Miller, K.A., *Proc. SPIE*, 3786, 506, 1999.)

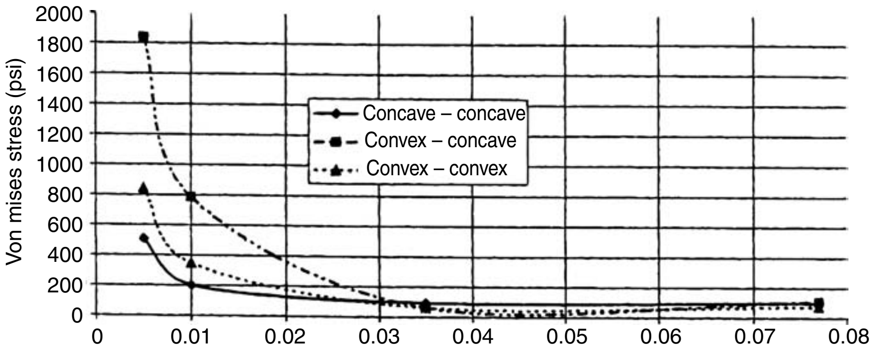

FIGURE 15.60 Variations of the maximum stress with thickness of the elastomer layer in the lenses of Figure 15.58 at elevated temperature. (From Miller, K.A., *Proc. SPIE*, 3786, 506, 1999.)

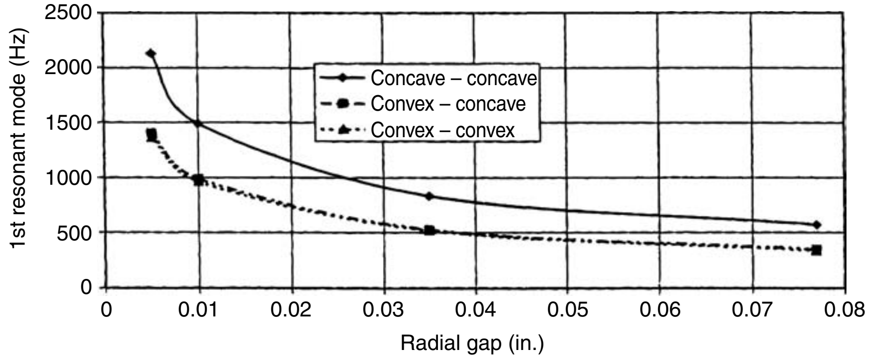

FIGURE 15.61 Variations of the resonant frequency with thickness of the elastomer layer in the lens assemblies of Figure 15.58 at elevated temperature. (From Miller, K.A., *Proc. SPIE*, 3786, 506, 1999.)

Figure 15.61 shows the variation in the lowest resonant frequency of the lens and cell assemblies as functions of lens shape and elastomer thickness. Again, we see small changes for rather large decreases in layer thickness and dependence on lens shape. The expected increase in frequency for thinner (i.e., stiffer) layers is apparent. The biconvex and biconcave lenses have essentially the same resonant characteristics, while the meniscus-shaped lens shows a greater variation.

REFERENCES

Adler, W.F. and Mihora, D.J., Biaxial flexure testing: analysis and experimental results, in *Fracture Mechanics of Ceramics*, Vol. 10 Bradt, R.C., Hasselman, D.P.H., Munz, D., Sakai, M., and Ya Shevchenko, V., Eds., Plenum, New York, 1992.

Alvarez, P. and Rodriguez-Espinosa, J.M., The Gran Telescopo CANARIAS project. Project status, *Proc. SPIE*, 3352, 70, 1998.

Andersen, T.B., Multiple-temperature lens design optimization, *Proc. SPIE*, 2000, 2, 1993.

Barkhouser, R.H., Smee, S.A., and Meixner, M., Optical and optomechanical design of the WIYN high resolution infrared camera, *Proc. SPIE*, 5492, 921, 2004.

Barnes, W.P., Jr., Some effects of aerospace thermal environments on high-acuity optical systems, *Appl. Opt.*, 5, 701, 1966.

Barrera, S., Villegas, A., Fuentes, F.J., Correa, S., Pérez, J., Redondo, P., Restrepo, R., Sánchez, V., Tenegi, F., Garzón, F., and Patrón, J., EMIR optomechanics, *Proc. SPIE*, 5495, 611, 2004a.

Barrera, S., private communication, 2004b.

Bayar, M., Lens barrel optomechanical design principles, *Opt. Eng.*, 20, 181, 1981.

Chen, W.T. and Nelson, C.W., Thermal stress in bonded joints, *IBM J. Res. Develop.*, 23, 179, 1979.

Crompton, D., private communication, 2004.

Delgado, R.F. and Hallinan, M., Mounting of optical elements, *Opt. Eng.*, 14, S-11, 1975. Reprinted in *SPIE Milestone Series*, 770, 173, 1988.

Doyle, K.B. and Kahan, M., Design strength of optical glass, *Proc. SPIE*, 5176, 14, 2003.

Doyle, K.B., Genberg, V.L., and Michels, G.J., *Integrated Optomechanical Analysis*, Tutorial Text TT58, SPIE Press, Bellingham, 2002.

Evans, A.G., Fracture toughness: the role of indentation techniques, in *Fracture Mechanics Applied to Brittle Materials*, ASTM STP 678, Freiman, S.W., Ed., American Society for Testing and Materials, 112, 1979.

Fischer, R.E. and Tadic-Galeb, B., *Optical System Design*, McGraw-Hill, New York, 2000.

Ford, V.G., White, M.L., Hochberg, E., and McGown, J., Optomechanical design of nine cameras for the Earth observing system multi-angle imaging spectro-radiometer, TERRA platform, *Proc. SPIE*, 3786, 264, 1999.

Freiman, S., *Stress Corrosion Cracking*, Jones, R., Ed., ASM International, Materials Park, OH, 1992.

Fuller, E.R., Jr., Freiman, S.W., Quinn, J.B., Quinn, G.D., and Carter, W.C., Fracture mechanics approach to the design of glass aircraft windows: a case study, *Proc. SPIE*, 2286, 419, 1994.

Genberg, V.L., Structural analysis of optics, in *Handbook of Optomechanical Engineering*, Ahmad, A., Ed., CRC Press, Boca Raton, FL, 1997a, chap. 8.

Genberg, V.L., Thermal and thermoelastic analysis of optics, in *Handbook of Optomechanical Engineering*, Ahmad, A., Ed., CRC Press, Boca Raton, FL, 1997b, chap. 9.

Genberg, V.L., private communication, 2004.

Giessen, P. and Folgering, E., Design guidelines for thermal stability in opto-mechanical instruments, *Proc. SPIE*, 5176, 126, 2003.

Harris, D.C., *Materials for Infrared Windows and Domes*, SPIE Press, Bellingham, 1999.

Hatheway, A.E., An overview of the finite element method in optical systems, *Proc. SPIE*, 1532, 2, 1991.

Hatheway, A.E., Review of finite element analysis techniques: capabilities and limitations, *Proc. SPIE*, CR43, 367, 1992a.

Hatheway, A.E., private communication, 1992b.

Hatheway, A.E., Analysis of adhesive bonds in optics, *Proc. SPIE*, 1998, 2, 1998.

Hatheway, A.E., Thermo-elastic stability of an argon ion laser cavity, *Proc. SPIE*, 4198, 141, 2000.

Hatheway, A.E., private communication, 2004.

Jamieson, T.H., Athermalization of optical instruments from the optomechanical viewpoint, *Proc. SPIE*, CR43, 131, 1992.

Kimmel, R.K. and Parks, R.E., *ISO 10110 Optics and Optical Instruments—Preparation of Drawings for Optical Elements and Systems: A User's Guide*, 2nd ed., Optical Society of America, Washington DC, 2004.

Kingslake, R., *Optical System Design*, Academic Press, Orlando, 1983.

Laikin, M., *Lens Design, Third Edition, Revised and Expanded*, Marcel Dekker, Inc., New York, 2001.

Lambropoulos, J.C., Fang, T., Funkenbusch, P.D., Jacobs, S.D., Cumbo, M.J., and Golini, D., Surface microroughness of optical glasses under deterministic microgrinding, *Appl. Opt.*, 35, 4448, 1996a.

Lambropoulos, J.C., Xu, S., Fang, T., and Golini, D., Twyman effect mechanics in grinding and microgrinding, *Appl. Opt.*, 35, 5704, 1996b.

Lambropoulos, J.C., Xu, S., and Fang, T., Loose abrasive lapping hardness of optical glasses and its interpretation, *Appl. Opt.*, 36, 501, 1997.

Lambropoulos, J.C. and Varshneya, R., Glass material response to the fabrication process: example from lapping, *Optical Fabrication and Testing Workshop, Rochester*, Optical Society of America, Washington, 2004.

Lawn, B., *Fracture of Brittle Solids*, 2nd ed., Cambridge University Press, Cambridge, 1993.

Lecuyer, J.G., Maintaining optical integrity in a high-shock environment, *Proc. SPIE*, 250, 45, 1980.

Miller, K.A., Nonathermal potting of optics, *Proc. SPIE,* 3786, 506, 1999.

MIL-O-13830A, *Optical Components for Fire Control Instruments: General Specification Governing the Manufacture, Assembly and Inspection of*, U.S. Department of the Army, 1975.

Pearson, E.T., Thermo-elastic analysis of large optical systems, *Proc. SPIE*, CR43, 123. 1992.

Pepi, J.W., *Allowable Stresses for Window Design*, Internal Report, Itek Optical Systems, Lexington, MA, 1994a.

Pepi, J.W., Failsafe design of an all BK-7 glass aircraft window, *Proc. SPIE*, 2286, 431, 1994b.

Roark, R.J., *Formulas for Stress and Strain*, 3rd ed., McGraw-Hill, New York, 1954.

Sawyer, K.A., Contact stresses and their optical effects in biconvex optical elements, *Proc. SPIE*, 2542, 58, 1995.

Schulman, J., Fang, T., and Lambropoulos, J., Brittleness/ductility database for optical glasses, *COM Glass Database*, v. 2, Oct. 10, 1996, Center for Optics Manufacturing, Rochester, 1996.

Shand, E.B., *Glass Engineering Handbook,* 2nd ed., McGraw-Hill, New York, 1958.

Shannon, R.R., *The Art and Science of Optical Design*, Cambridge University Press, Port Chester, 1997.

Slocum, A.H., *Precision Machine Design*, Society of Manufacturing Engineers, Dearborn, 1992.

Smith, W.J., *Modern Optical Engineering*, McGraw-Hill, New York, 2000.

Smith, W.J., *Modern Lens Design*, McGraw-Hill, New York, 2004.

Stevanovic, D. and Hart, J., Cryogenic mechanical design of the Gemini south adaptive optics imager (GSAOI), *Proc. SPIE*, *5495,* 305, 2004.

Stoll, R., Forman, P.F., and Edelman, J., The effect of different grinding procedures on the strength of scratched and unscratched fused silica, *Proceedings of the Symposium on the Strength of Glass and Ways to Improve It*, Union Scientifique Continental du Verre, Florence, 1961.

Stubbs, D.M. and Hsu, I.C., Rapid cooled lens cell, *Proc. SPIE*, 1533, 36, 1991.

Sullivan, M.T., private communication, 2004.

Timoshenko, S.P. and Goodier, J. N., *Theory of Elasticity*, 3rd ed., McGraw-Hill, New York, 1970.

Vukobratovich, D., Optomechanical Systems Design, in *The Infrared & Electro-Optical Systems Handbook,* Vol. 4, ERIM, Ann Arbor and SPIE, Bellingham, 1993, chap. 3.

Vukobratovich, D., private communication, 2002.

Vukobratovich, D., Introduction to optomechanical design, *SPIE Short Course SC014*, 2003.

Vukobratovich, D., private communication, 2004.

Wechtman, J.B., *Mechanical Properties of Ceramics*, Wiley, New York, 1996.

Weibull, W., A statistical distribution function of wide applicability, *J. Appl. Mech.*, 13, 293, 1951.

Wiederhorn, S.M., Influence of water vapor on crack propagation in soda-lime glass, J. Am. Ceram, Soc., 50, 407, 1967.

Wiederhorn, S.M., Freiman, S.W., Fuller, E.R., Jr., and Simmons, C.J., Effects of water and other dielectrics on crack growth, J. Mater., Sci., 17, 3460, 1982.

Yoder, P.R., Jr., Axial stresses with toroidal lens-to-mount interfaces, *Proc. SPIE*, 1533, 2, 1991.

Yoder, P.R., Jr., Advanced considerations of the lens-to-mount interface, *SPIE Critical Review*, CR43, 305, 1992.

Yoder, P.R., Jr., Parametric investigations of mounting-induced contact stresses in individual lenses, *Proc. SPIE*, 1998, 8, 1993.

Yoder, P.R., Jr., Estimation of mounting-induced axial contact stresses in multi-element lens assemblies, *Proc. SPIE*, 2263, 332, 1994.

Yoder, P.R., Jr., *Mounting Optics in Optical Instruments*, SPIE Press, Bellingham, 2002a.

Yoder, P.R., Jr., Improved semikinematic mounting for prisms, *Proc. SPIE*, 4771, 173, 2002b.

Yoder, P.R., Jr. and Hatheway, A.E., Further considerations of axial preload variations with temperature and the resultant effects on contact stresses in simple lens mountings, *Proc. SPIE*, 2005, (in press).

Young, W.C., *Roark's Formulas for Stress & Strain*, 6th ed., McGraw-Hill, New York, 1989.

Appendix A

UNITS AND THEIR CONVERSION

In this book, we utilize the metric (Systèm International [SI]), and U.S. Customary (USC) systems of units, depending on the context of the particular discussion or the precedent of the references quoted. Whenever practical, quantities are expressed in both systems of units by enclosing the converted value in parentheses. In the few cases where one system is almost always used (such as wavelength), the appropriate system is employed without conversion.

To facilitate conversion from one system of units to the other in cases where equivalent values are not given, we tabulate below the standard formulas for changing a value of some frequently encountered parameters from the USC system to the alternative system. In most cases, this involves multiplication by an appropriate factor. Conversion in the reverse direction is, of course, achieved by dividing by the listed factor.

To change length in:
    inches (in.) to meters (m), multiply by 0.0254
    inches (in.) to millimeters (mm), multiply by 25.4
    inches (in.) to nanometers, multiply by 2.54×10^{7}
    feet (ft) to meters (m), multiply by 0.3048
To change mass in:
    pounds (lb) to kilograms (kg), multiply by 0.4536
    ounces (oz) to grams (g), multiply by 28.3495
To change force or preload in:
    pounds (lb) to newtons (N), multiply by 4.4482
    kilograms (kg) to newtons (N), multiply by 9.8066
To change linear force in:
    lb/in. to N/mm, multiply by 0.1751
    lb/in. to N/m, multiply by 175.1256
To change spring compliance in:
    in./lb to m/N, multiply by 5.7102×10^{-3}
To change temperature dependence of preload in:
    lb/in. to N/°F, multiply by 8.0068
To change pressure, stress, or units for Young's modulus in:
    lb/in.^{2} (psi) to N/m^2 or pascals, multiply by 6894.757
    lb/in.^{2} (psi) to megapascals (MPa), multiply by 6.895×10^{-3}
    lb/in.^{2} (psi) to N/mm^2, multiply by 6.895×10^{-3}
    atmospheres to lb/in.^{2}, multiply by 14.7
    atmospheres to MPa, multiply by 0.1103
    torr to lb/in.^{2}, multiply by 1.933×10^{-2}
    torr to pascals, multiply by 133.3
To change torque or bending moment in:
    lb-in. to N-m, multiply by 0.11298
    oz-in. to N-m, multiply by 7.0615×10^{-3}
    lb-ft to N-m, multiply by 1.35582
To change volume in:
    in.^{3} to cm^3, multiply by 16.387

To change density in:
    lb/in.^{3} to g/cm^3, multiply by 27.6799
To change acceleration in:
    gravitational units (g) to m/sec^2, multiply by 9.80665
    ft/sec^2 to m/sec^2, multiply by 0.30480
To change specific heat in:
    Btu/lb-°F to J/kg-K, multiply by 4184
    cal/g-°C to J/kg-K, multiply by 4184
To change thermal diffusivity in:
    ft^2/h to m^2/sec, multiply by 2.5806×10^{-5}
To change thermal conductivity in:
    BTU/h ft-°F to W/m-K, multiply by 1.7296
To change temperature in:
    °F to °C, subtract 32 and multiply by 5/9
    °C to °F, multiply by 9/5 and add 32
    °C to K, add 273.1

Appendix B

SUMMARY OF METHODS FOR TESTING OPTICAL COMPONENTS AND OPTICAL INSTRUMENTS UNDER ADVERSE ENVIRONMENTAL CONDITIONS*

B.1 COLD, HEAT, HUMIDITY TESTING

The following methods of conditioning in a test chamber are specified:

Method 10, Cold: Condition for 16 h to 1 of 10 degrees of severity with temperature ranging from 0 to −65°C.

Method 11, Dry heat: Condition for 16 h to 1 of 4 degrees of severity with temperature ranging from 10 to 63°C and <40% RH. Two additional 6-h conditionings may apply with temperatures of 70 or 85°C and <40% RH.

Method 12, Damp heat: Condition at 40°C and 92% RH to 1 of 5 degrees of severity ranging from 16 h to 56 d. Two additional 6- or 16-h conditionings at 55°C and 92% RH may apply.

Method 13, Condensed water: Condition at 40°C and approximately 100% RH for 1 of 6 degrees of severity ranging from 6 h to 16 d.

Method 14, Cycling exposure conditions, slow temperature change: Condition for 5 cycles to 1 of 9 degrees of severity ranging from 40°C high and −65°C low to 85°C high to −65°C low, with a rate of change between 0.2 and 2°C/min.

Method 15, Cycling exposure conditions, rapid temperature change (thermal shock): Condition for 5 cycles to 1 of 5 degrees of severity ranging from 20°C high and −10°C low to 70°C high to −65°C low within 20 sec for equipment to 10 kg and within 10 min for larger equipment. Dwell at extreme temperatures until stabilized.

Method 16, Cycling exposure conditions, damp heat: Condition for 5 to 20 cycles at specified rates of change to 1 of 3 degrees of severity ranging from a low of 23°C with 82% RH and a high of 40°C with 92% RH to a low of 23°C and a high of 70°C with unspecified RH.

B.2 MECHANICAL STRESS TESTING

The following methods of conditioning at ambient atmospheric conditions on a shock machine, acceleration facility, or electrodynamic shaker are specified:

Method 30, Shock: Condition with 3 shocks in each direction along each axis to 1 of 8 degrees of severity ranging from 10 to 500g acceleration with half-sine wave pulse durations of 0.5 to 18 msec.

Method 31, Bump: Condition with 1000 to 4000 shocks in each direction along each axis to 1 of 8 degrees of severity ranging from 10 to 40g acceleration with half-sine wave pulse durations of 6 to 16 msec.

Method 32, Drop and topple: Condition with 1 of 3 degrees of severity involving 25 to 100 mm drops on each corner plus topple about each edge.

Method 33, Freefall: Condition in transport container or unprotected (if so designed) with 2 to 50 falls ranging in severity from 25 to 1000 mm, depending on mass of specimen.

Method 34, Bounce: Condition to 1 of 3 degrees of severity ranging from 15 to 180 min with double amplitude 25.5 mm and 4.75 Hz frequency on an approved bounce table.

---

[*] Based on preliminary draft of ISO 9022.

Method 35, Steady-state acceleration: Condition to 1 of 3 degrees of severity ranging from 5 to 20g for 1 to 2 min in each direction along each axis.

Method 36, Vibration, sinusoidal sweep frequencies: Condition at ambient conditions to 1 of 10 degrees of severity involving displacements ranging from 0.035 to 1.0 mm and accelerations of 0.5 to 5g sweeping at 1 octave/min within frequency bands ranging from (lowest) 10 to 55 Hz for equipment used on ships, near heavy machinery, or in general industrial applications to (highest) 10 to 2000 Hz for equipment used in aircraft and missiles. This test may be followed by conditioning for 1 of 3 degrees of severity ranging from 10 to 90 min vibration along each axis at characteristic frequencies indentified under sweep frequency tests or identified in the applicable specification.

Method 37, *Vibration*, *random*: Condition to 1 of 26 degrees of severity ranging from a power spectral density of 0.001 to 0.2 g^2/Hz with random frequencies of 20 to 2000 Hz and conditioning times of 9 to 90 min.

B.3 SALT MIST TESTING

Representative samples of components or materials to be used in optical instruments that will experience exposure to salt atmosphere are to be tested. Complete instruments are tested only in exceptional cases. The tests are not considered reliable representations of actual exposure, but serve only as indications of suitability or unsuitability. Method 40 specifies the following:

The test chamber shall have a volume of at least 400 L and be heated to 30°C during the test. Precautions are taken to prevent direct impingement of spray onto specimens or condensate from dripping onto them. The salt mist is injected pneumatically through plastic nozzles at a rate that delivers a prescribed volume of 5% aqueous solution of sodium chloride/h. The purity of ingredients must be high and the pH of the solution must be controlled.

Conditioning is to 1 of 7 degrees of severity ranging from 2 h to 8 d duration.

B.4 COLD, LOW AIR PRESSURE TESTING

Method 50 specifies that the hardware shall be conditioned in a chamber to low pressure with and without exposure to condensation and freezing of moisture to simulate exposure in unheated aircraft or missiles or operation/transport in high mountainous regions. Conditioning is for 4 h to 1 of 8 degrees of severity ranging from -25°C and 60 kPa pressure (3500 m altitude) to -65°C and 1 kPa pressure (31,000 m altitude).

B.5 DUST TESTING

This test, Method 52, evaluates the resistance of the specimen to blowing dust that may impair function of moving parts or cause unacceptable wear of surfaces. Unless otherwise specified, optical surfaces are covered during exposure. The dust consists of sharp-edged particles, not less than 97% silicon dioxide. Particle size ranges from 0.045 to 0.1 mm, with the majority (90%) smaller than 0.071 mm.

Conditioning is to 1 of 3 degrees of severity involving 6- to 34-h exposure to 8 to 10 m/sec velocity air containing 5 to 15 g/m^3 sand. Temperature is held at 18 to 28°C and RH controlled at $<25\%$.

B.6 DRIP, RAIN TESTING

The following methods of conditioning in a test chamber are specified:

Method 72, Drip testing: Means shall be provided for decalcified or de-salted water to drip through a perforated plate (0.35 mm holes) onto the specimen from a distance >1 m. The specimen shall be rotated in the chamber. Condition to 1 of 9 degrees of severity ranging from 1 to 30 min exposure to 1.5 to 5.5 mm/min.

Method 73, Steady rain: Shower heads shall be arranged within the test chamber so as to distribute simulated rainfall to the rotating specimen at 5 or 20 mm/min rate for 30 min.

Method 74, Driving rain: Wind-driven water shall be directed onto the specimen at velocities of 18 or 33 m/sec for 1 of 6 degrees of severity corresponding to exposure times of 10 to 30 min. Rainfall shall be at 2 or 10 mm/min.

B.7 HIGH-PRESSURE, LOW-PRESSURE, IMMERSION TESTING

The following methods of conditioning are specified:

Method 80, Internal high pressure: Conditioning for 10 min to 1 of 13 degrees of severity involving either 100- or 400-Pa pressure difference with associated allowable drops in the internal pressure ranging from 75% (least severe) to 2% (most severe).

Method 81, Internal low pressure: Identical to the above test except with higher pressure outside the specimen.

Method 82, Immersion: Conditioning by submersion of the specimen 1 to 400 m under water for 2 h.

B.8 SOLAR RADIATION

Under Method 20, a specimen is tested in a heated test chamber having a source capable of irradiating the specimen to a specified level (in W/m^2) within each of six spectral bands representative of solar energy. Removal of ozone, if generated, is required. Two degrees of conditioning severity expose the specimen to about 1 kWh/m^2 for 1 to 5 24 h cycles with chamber temperature varying between 25 and 55°C and <25% RH. Two additional degrees of conditioning apply to representative samples tested for longer periods of time (to 240 h) to evaluate photochemical influences and achieve artificial aging.

B.9 COMBINED SINUSOIDAL VIBRATION, DRY HEAT, OR COLD TESTING

The following methods of conditioning are specified:

Method 61, Combined sinusoidal vibration, dry heat: Condition to 1 of 13 degrees of severity involving three elevated test chamber temperatures (40 to 63°C) with RH <40% and displacements ranging from 0.035 to 1.0 mm and accelerations of 0.5 to 5g sweeping at 1 octave/min within frequency bands ranging from (lowest) 10 to 55 Hz to (highest) 10 to 2000 Hz. This test may be followed by conditioning for 1 of 3 degrees of severity ranging from 10 to 30 min vibration along each axis at characteristic frequencies identified under sweep frequency tests or identified in the applicable specification.

Method 62, Combined sinusoidal vibration, cold: Condition to 1 of 17 degrees of severity involving six reduced test chamber temperatures (−10 to −65°C) with RH <40% and displacements, accelerations, and frequencies per Method 61. This test may be followed by conditioning for either 10 or 30 min vibration along each axis at characteristic frequencies identified under sweep frequency tests or identified in the applicable specification. Guidance for choice of test severity is given in terms of application of the instrument to astronomical, industrial, ground vehicle, naval vessel, or aircraft/missile/special applications.

B.10 MOLD GROWTH TESTING

Method 85 specifies that representative samples such as mounted optics, materials samples, or surface coatings be conditioned for 28 or 84 d in a closed test chamber, with a temperature of approximately 29°C and high humidity. Complete instruments are tested only if required by the specification. Tests require innoculation of the test samples with mixed viable spores of ten specified types of fungi. Control strips of sterilized filter paper are innoculated and placed in the test chamber along with the test samples. Mold growth on the control strips must be visible 7 d into the test period for the test to be considered valid. At the conclusion of the test, all samples are examined for mold growth and physical damage (such as coating damage, etching, or corrosion). If the specification requires evaluation of possible effects on optical performance, control samples are exposed for the same time period at the same temperature and humidity conditions, but without mold spores. These are compared with the innoculated samples at the conclusion of the test.

Note that the sequence of environmental testing can have an effect on results. Fungus testing should not follow salt mist or sand/dust exposure because salt tends to supress mold growth and sand/dust may provide nutrients for mold growth.

B.11 CORROSION TESTING

Condition representative samples such as mounted optics, material samples, or surface coatings for specified time periods in contact with felt pads saturated with specified substances at ambient atmospheric conditions. Complete instruments are tested only if required by the specification. Post-test evaluation classifies specimens to five levels of damage ranging from no visible degradation to heavy degradation and structural damage. Basic test methods follow.

Method 86, Basic cosmetic substances and artificial hand sweat: Condition in contact with paraffin oil, glycerine, vasoline, lanolin, cold cream, and artificial hand sweat for 1 to 30 d and inspect.

Method 87, Laboratory agents: Condition in contact with various agents including sulfuric, nitric, hydrochloric, and acetic acids and potassium hydroxide in various dilutions with water for 10 to 120 min as well as agents like ethanol, acetone, and xylene for 5 to 60 min and inspect.

Method 88, Production plant resources: Condition in contact with hydraulic oil, synthetic oil, cooling lubricant, and general-purpose detergent for 2 to 16 h and inspect.

Method 89, Fuels and resources for aircraft, naval vessels, and land vehicles: Condition in contact with specified materials including gasoline, fuel oil, lubricating oil, hydraulic oil, brake fluid, deicing fluid, antifreeze agent, fire extinguishing agent, detergent, alkaline, and acid battery electrolyte, etc. and inspect.

B.12 COMBINED SHOCK, BUMP, OR FREE FALL, DRY HEAT, OR COLD TESTING

The following methods of conditioning at elevated or reduced temperatures on a shock machine, acceleration facility, or electrodynamic shaker are specified:

Method 64, Shock, dry heat: Condition with 3 shocks in each direction along each axis to 1 of 15 degrees of severity ranging from 15 to 500g acceleration with half-sine wave pulse durations of 1 to 11 msec. Four temperatures ranging from 40 to 85°C and <40% RH apply.

Method 65, Bump, dry heat: Condition with 1000 to 4000 shocks in each direction along each axis to 1 of 8 degrees of severity ranging from 10 to 25g acceleration with half-sine wave pulse durations of 6 msec. Three temperatures ranging from 40 to 63°C and <40% RH apply.

Method 66, Shock, cold: Condition with 3 shocks in each direction along each axis to 1 of 25 degrees of severity ranging from 15 to 500g acceleration with half-sine wave pulse durations of 1 to 11 msec. Six temperatures ranging from −10 to −65°C apply.

Method 67, Bump, cold: Condition with 1000 to 4000 shocks in each direction along each axis to 1 of 14 degrees of severity ranging from 10 to 25g acceleration with half-sine wave pulse durations of 6 msec. Six temperatures ranging from −10 to −65°C apply.

Method 68, Freefall, dry heat: Condition in transport container or unprotected (if so designed) with 2 to 50 falls ranging in severity from 100 to 1000 mm, depending on mass of specimen. Three temperatures ranging from 40 to 85°C and <40% RH apply.

Method 69, Freefall, cold: Condition in transport container or unprotected (if so designed) with 2 to 50 falls ranging in severity from 100 to 1000 mm, depending on mass of specimen. Five temperatures ranging from −25 to −65°C apply.

B.13 DEW, HOARFROST, ICE TESTING

Exposure to dew (Method 75), hoarfrost (Method 76), or ice (Method 77) results from rapid change in environmental conditions in a chamber or from transfer of the specimen from a cold chamber to a conditioned room. Instrument parts normally protected from frost or ice should be protected during the test. Each test is conducted in three steps:

1. Stabilization at temperatures ranging from 10 to −25°C in accordance with 5 degrees of severity
2. Exposure to 30°C and 85% RH (dew formation) or −5 to −25°C with water spray (ice formation) until temperature is stabilized or ice has reached thickness up to 75 mm, as applicable
3. Exposure to 30°C and 85% RH to stabilize.

Appendix C

HARDNESS OF MATERIALS

Jastrzebski (1976), Symonds (1987), Lines (1991), and Tropf et al. (1994) each summarized briefly the characteristic hardness of materials and the general means used for measurement of this property. Typically, hardness is quantified by measuring resistance to mechanical abrasion (scratching) or by measuring the characteristics of indentations made by a shaped diamond tool under fixed load. Because no fundamental theory exists for establishing hardness, the various scales of hardness in use are arbitrary. In one technique, the well-known Mohs hardness test, the scratch resistance of a given sample of material is matched with that of one of ten minerals ranked in order of their increasing hardness from 1 (for talc) to 10 (for diamond). The Knoop hardness test is more quantitative and consists of pushing a penetrator into the material under test and measuring the effect in some way. The geometric form of the penetrator and the load mechanism vary with the different tests, as does the technique for measuring the magnitude of the indentation. Other methods measure Brinell hardness or Rockwell hardness.

Hardness measurements made by one method cannot be converted directly to the hardness measured by another method. An approximate empirical conversion can, however, be made between scales. One such comparison for four of the more commonly used scales is shown in Figure Cl. Hardness correlates well with Young's modulus and with strength for many materials, particularly glasses. Its measurement helps to quantify the vulnerability of a material to surface damage. It also is an indicator of the ease with which a surface can be polished on the material. Those with Knoop hardness < 100 kg/mm^2 are very soft, difficult to polish, and vulnerable to damage during handling. Materials with Knoop hardness > 750 kg/mm^2 are quite hard. The hardness of crystals depends upon the geometric orientation of the crystal axes with respect to the surface being tested. Measured values for several optical materials are tabulated in the tables of Chapter 3.

REFERENCES

Jastrzebski, Z.D., *The Nature and Properties of Engineering Materials*, Wiley, New York, 1976.

Lines, M.E., Physical properties of materials: theoretical overview, in *Handbook of Infrared Optical Materials*, Klocek, P., Ed., Marcel Dekker, New York, 1991, chap. 1, p. 30.

Symonds, J., Mechanical properties of materials, in *Marks Standard Handbook for Mechanical Engineers*, 9th ed., Sec. 5.1, Avallone, E. A. and Baumeister, P., III, Eds., McGraw-Hill, New York; 1987, pp. 5–12.

Tropf, W.J., Thomas, M.E., and Harris, T.J., Properties of crystals and glasses, in *Handbook of Optics*, 2nd ed., Vol. II, Bass, M., Van Stryland, E.W., Williams, D.R., and Wolfe, W.L., Eds., Optical Society of America, Washington, DC, 1994, chap. 33.

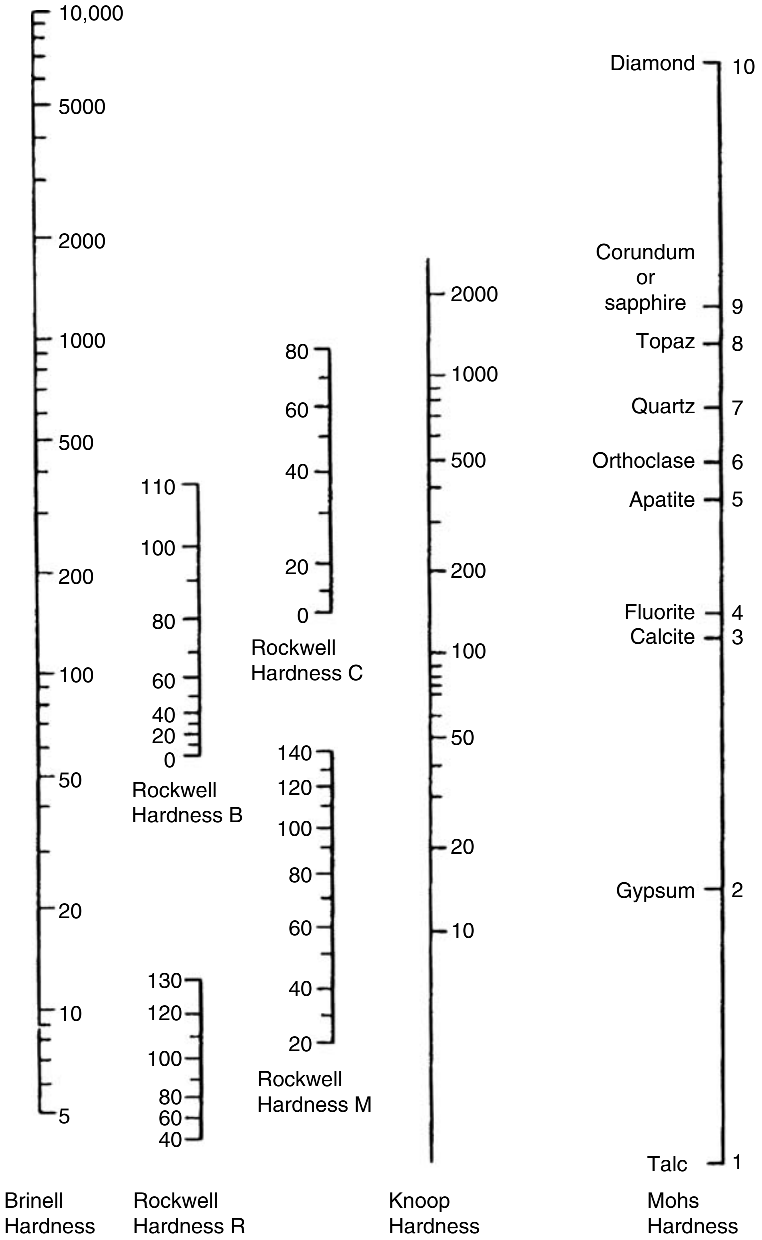

FIGURE C1 An approximate comparison of hardness scales. (Adapted from Jastrzebski, Z.D., *The Nature and Properties of Engineering Materials*, Wiley, New York, 1976.)

Appendix D

GLOSSARY

The following pages provide a glossary of terms and symbols intended to help the reader understand the shorthand language of the various technical topics involved in the opto-mechanical design process and in the analysis of designs as well as acronyms used in instrument descriptions. Common usage in the field of opto-mechanics has, in many cases, dictated the use of a specific term to represent a parameter. The Greek symbol α is a good example. It is used to represent the coefficient of thermal expansion for a material in equations when the common abbreviation *CTE* is not appropriate. There are occasions when the same term or symbol has more than one meaning. Multiple definitions are then indicated. Subscripts are frequently used to identify the specific application of a symbol to a specific material. Included in the tables are fundamental parameters and their units of measure, frequently used prefixes, Greek symbol applications, acronyms, abbreviations, and other terms as may be found in the text.

D.1 UNITS OF MEASURE AND ABBREVIATIONS USED

Parameter	SI or metric	U.S. and Canadian
Angle	radian (rad)	degree (^{o})
Area	square meter (m^2)	square inch ($in.^2$)
Conductivity, thermal	watt/meter-kelvin (W/m-K)	British thermal unit per hour-foot-degree Fahrenheit (Btu/h-ft-^{o}F)
Density	gram per cubic meter (g/m^3)	pound per cubic inch ($lb/in.^3$)
Diffusivity, thermal	meter squared per second (m^2/sec)	inch squared per second ($in.^2/sec$)
Force	newton (N)	pound (lb)
Frequency	hertz (Hz)	hertz (Hz)
Heat	joule (J)	British thermal unit (Btu)
Length	meter (m)	inch (in.)
Mass	kilogram (kg)	pound (lb)
Moment of force (torque)	newton-meter (N-m)	pound-foot (lb-ft)
Poisson's ratio	none	none
Pressure	pascal (Pa)	pound per square inch ($lb/in.^2$)
Specific heat	joule/kilogram-Kelvin (J/kg-K)	British thermal unit per pound-degree Fahrenheit (Btu/lb-^{o}F)
Strain	micrometer/meter (μm/m)	microinch per inch (μin./in.)
Stress	pascal (Pa)	pound per square inch ($lb/in.^2$)
Temperature	kelvin (K) degree Celsius (^{o}C)	degree Fahrenheit (^{o}F)
Time	second (sec)	second (s or sec), hour (h)
Velocity	meter/second (m/sec)	mile per hour (mph)
Viscosity	poise (P), centipoise (cP)	pound-sec per square foot ($lb\text{-}sec/ft^2$)
Volume	cubic meter (m^3)	cubic inch ($in.^3$)
Young's modulus	pascal (Pa)	pound per square inch ($lb/in.^2$)

D.2 PREFIXES

mega, M	million	milli, m	thousandth
kilo, k	thousand	micro, μ	millionth
centi, c	hundredth	nano, n	billionth

D.3 GREEK SYMBOL APPLICATIONS

α	material CTE; angle
β	angle; term used in equation for shear stress in a bonded optic
β_{G}	rate of change in refractive index with change in temperature (dn/dT)
γ	shape factor for a resilient pad in a prism mounting
γ_{G}	thermo-optical coefficient for a glass
Γ	gamma factor in statistical analysis
δ	decentration of an elastomeric-supported optic; ray angular deviation
δ_{G}	glass coefficient of thermal defocus
Δ	spring deflection; finite difference (change) for a given parameter
Δ_{E}	eyepiece focus motion per diopter
ΔP_{W}	pressure differential through a window
Δy	deflection
θ	angle
λ	wavelength; thermal conductivity in Schott catalog
λ_{TK}	average effective resonance wavelength (in μm) in Sellmeier equation for dn/dT
μ	Poisson's ratio in Schott catalog
μ_{M}, μ_{G}	coefficient of sliding friction of metal-to-metal, glass-to-metal contact
ξ	ratio of shortest to longest dimensions of a rectangular mirror
π	3.14159
ρ	density, radius of curvature of cavity tip in brittle material
σ	standard deviation, stress
Σ	summation
σ_i	tensile yield strength of components in a bonded joint
ν, ν_{G}, ν_{M}	Poisson's ratio, for glass, for metal
φ	angle
ψ	cone half-angle

D.4 ACRONYMS, ABBREVIATIONS, AND OTHER TERMS

Å	Angstrom unit
A	aperture, area
a, b, c, etc.	dimensions
-A-, -B-, etc.	reference (datum) surface designation
A/R	antireflection (type of coating)
a_{a}	absorption coefficient for a refractive medium
A_{C}	area of elastically deformed region at an interface
a_{G}	acceleration factor (interpreted as "times ambient gravity")
ANSI	American National Standards Institute
AR	Schott code for alkaline resistance of glass
A_{P}	mechanical interface pad area
a_{s}	scatter coefficient for a refractive medium
AMSD	Advanced Mirror System Demonstrator (for JWST)
ASC/OP	American Standards Committee, Optics and Electro-Optical Instruments
ASCII	American Standard Code for Information Exchange
ASME	American Society of Mechanical Engineering
A_{T}	annular area of a single thread

AU	astronomical unit
AVG	as subscript, indicates average value
A_{W}	unsupported area of a window
AWJ	abrasive water jet (at Corning facility)
AXAF	Advanced X-ray Astrophysical Facility
B	Schott code for bubble class of glass
b	spring width, cylindrical pad length
BDTF	bidirectional transmittance distribution function
BRDF	bidirectional reflectance distribution function
BTU	British thermal unit
B_λ, C_λ	constant in Sellmeier equation for n_λ.
C	center of curvature, Celsius temperature, as subscript, indicates circular shape
C, d, D, e, F, g, s	as subscripts, refer to wavelengths of Fraunhofer absorption lines
CA	clear aperture
CAD	computer aided design
CAM	computer aided manufacturing
CCC	carbon/carbon matrix composite
CCD	charge coupled device
CG	center of gravity
C_κ	mirror mount type factor used to determine gravitational effect
CLAES	Cryogenic Limb Array Etalon Spectrometer
CMC	carbon matrix composite
CNC	computer numerically controlled
C_p	specific heat
cP	centipoise
CR	Schott code for climatic resistance of glass
C_{R}, C_{T}	spring constants in radial, tangential directions
CRES	corrosion-resistant (stainless) steel
C_{S}	compressive stress in pad
C_{T}	center of curvature of a toroidal surface
CTE	coefficient of thermal expansion
CVD	chemical vapor-deposited
CW	continuous wave (laser)
CWA	chemical warfare agent
C_{X}, C_{Y}	spring constants in X, Y directions
CXT	cross braced truss (modified MMT truss concept)
CYL	as subscript, indicates cylindrical shape
d	major diameter of an internal screw head
D	thermal diffusivity; diopter, major diameter of an external thread
D_1, D_2	twice radius of optical surface or mechanical surface at interface
D_{B}	diameter of a bolt circle
DBM	data base manager
D_{G}	OD of a circular optic
D_{i}, E_{i}	coefficient in Sellmeier equation for $\mathrm{d}n/\mathrm{d}T$
DEIMOS	Deep Imaging Multi-Object Spectrograph
DIN	Deutsches Institut für Normung
DLC	diamond like coating
D_{M}	ID of a metal component
D_{P}	pad width or diameter
$\mathrm{d}n/\mathrm{d}T$	rate of change of refractive index with temperature
DOF	degree of freedom
D_{P}	diameter of a resilient pad
D_{R}	OD of a compressed snap ring
D_{T}, d_{t}	pitch diameter of a thread, external or internal
E, E_{G}, E_{M}, E_{e}	Young's modulus, for glass, for metal, for elastomer
E/ρ	specific stiffness

ECM	electro chemical milling (process for contouring metal)
EDM	electric discharge milling (process for contouring metal)
EFL	effective focal length (as of a lens or mirror)
ELN	electroless nickel plating
EN	electrolytic nickel plating
EPROM	erasable programmable read only memory
ESO	European Southern Observatory
EOS	Earth Observing System
EUV	extreme ultraviolet radiation
f	focal length
F	force, Fahrenheit temperature
f_E, f_O	focal length of an eyepiece, objective
FEA	finite element analysis
FED-STD	U.S. Federal Standard
FIM	full indicator movement
FLIR	forward looking infrared sensor
F_{MIN}	minimum force needed to constrain motion
FR	Schott code for stain resistance of glass
f_S	factor of safety
FUSE	Far Ultraviolet Spectroscopic Explorer
$\boldsymbol{g}$	acceleration due to gravity
GALEX	Galaxy Evolution Explorer
GAP_R, GAP_A	radial and axial gaps between an optic and its mount at the interface
GEO	Geosynchronous Earth orbit (~ 35,800 km)
GOES	Geostationary Operational Environmental Satellite
grism	diffraction grating on a prism face
GSAOI	Gemini South Adaptive Optics Imager
GTC	Gran Telescopio Canarias
Gy	abbreviation for unit of radiation dose (gray)
H	thread crest-to-root height, Vickers hardness of a material
HeNe	helium-neon laser
HG	Schott code for "grindability" of glass
HIP	hot isostatic pressing
HK	Knoop hardness
HRMA	high-resolution mirror assembly (in the Chandra telescope)
HST	Hubble Space Telescope
i	paraxial value for plane parallel plate tilt angle, as subscript denotes "i^{th}" component
I, I'	angle of incidence, refraction
I, I_0	beam intensity after and before interface
ICO	International Commision for Optics
ID	inside diameter
IEC	International Electrotechnical Commission
IMC	image motion compensation
IPD	interpupillary distance in binocular systems
IR	infrared
IRAS	Infrared Astronomical Satellite
ISIM	Integrated Science Instrument Module
ISO	International Organization for Standards, Infrared Space Observatory
IST	inverted Serrurier truss (modified MMT truss concept)
J	strength of an adhesive bond
JWST	James Webb Space Telescope
K, K_S	Kelvin temperature, stress optic coefficient
k	thermal conductivity
K_C	fracture toughness of a brittle material
K_1, K_A, K_G, K_M, etc.	constant term in an equation
KAO	Kuiper Airborne Observatory

k_W	support condition constant in window stress equation
L	length of a spring that is free to bend; width or diameter of a bond
L1, L2	Lagrange points No. 1 and No. 2 (Sun/Earth/Moon orbit)
LAGEOS	Laser Geodynamic Satellite
LAMA	Large Active Mirror in Aluminum
LEO	Low Earth orbit (200 to 700 km)
LID	laser induced damage
LIDT	laser induced damage threshold
$L_{j,k}$	axial length of a lens spacer
LLTV	low light-level television
$\ln(x)$	natural logarithm of x
LOS	line of sight
lp	line pair (element for resolution measurement as in lp/mm)
LRR	lower rim ray at maximum semifield angle
M	Mach number
m	reciprocal of Poisson's ratio, modulus of a Weibull function
MEO	middle Earth orbit (700 to 35,000 km)
MIL-STD	U.S. Military Standard
MISR	Multiangle Imaging Spectro-Radiometer
MLI	multilayer insulation
MMC	metal matrix composite
MMT	Multiple Mirror Telescope
MOCVD	metal organic chemical vapor deposition
MTF	modulation transfer function
n_λ	refractive index for a specific wavelength
N	number of springs or truss section; as prefix in Schott glass name, indicates "new"
N'	flaw growth susceptibility factor
n, n_{ABS}, n_{REL}	refractive index, refractive index in vacuum, refractive index in air
$n_\parallel$, $n_\perp$	refractive index for parallel polarized light component, perpendicular component
NASA	National Aeronautics and Space Administration
NDM	neutral data model
N_E, N_1, N_2	number of threads per unit length of differential thread
NGST	Next-Generation Space Telescope
NIST	National Institute of Standards and Technology
nu, v	Abbe number for a glass
OAO-C	Orbiting Astronomical Observatory-Copernicus
OB, OBA	optical bench, optical bench assembly
OD	outside diameter
OEOSC	Optics and Electro-Optics Standards Council
OFHC	oxygen-free high-conductivity
OPD	optical path difference
OSA	Optical Society of America
OTA	optical telescope assembly of the Hubble Space Telescope
OTF	optical transfer function
P	preload force; optical power; free stream air pressure on a moving window, probability
P_F,P_S	probability of failure, of survival
p	thread crest-to-crest pitch; linear preload
PACVD	plasma-aided chemical vapor deposition
P_i	preload per spring, preload at surface "i"
PMC	polymer (resin) matrix composite
ppm	parts per million
PR	Schott code for phosphate resistance of glass
PSD	power spectral density
PTFE	polytetrafluoroethylene
p-v	peak to valley (surface or wavefront distortion)
q	heat flux per unit of area

Q	torque; bonding area
Q_{MAX}	maximum bonding area within face dimensions
Q_{MIN}	minimum bonding area for strength of joint
r	snap ring cross-sectional radius
R	surface radius
r_{C}	radius of elastically deformed region at an interface
RH	relative humidity
rms	root mean square
roll	component tilt about transverse axis
r_{S}	radius to center of a spacer
R_{S}	reflectance of a coated surface
R_{T}	cross-section radius of toroidal surface
RT	as a subscript, means racetrack shape
RTV	room-temperature vulcanizing (sealant type)
R_{λ}	reflectance of a surface at wavelength λ
S_{AVG}	average contact stress in an interface
S_{B}	stress in a bent component such as a spring
SBMD	Subscale Beryllium Mirror Demonstrator (for JWST)
S_{C}	compressive contact stress at an optic-to-mount interface
$S_{\mathrm{C\ CYL}}$, $S_{\mathrm{C\ SPH}}$, $S_{\mathrm{C\ SC}}$	peak contact stress in glass with cylindrical, spherical, or sharp corner metal interface
SC	subcommittee (within ISO TG), SPIE short course
S_{e}	shear modulus of an elastomer
S_{f}	fracture strength of a window material
S_{F}	material yield strength
SIRTF	Space Infrared Telescope Facility (now Spitzer Space Telescope)
S_{j}, S_{k}	sagittal depth of surface j, k
S_{M}	tangential tensile (hoop) stress in a mount's wall
S_{MY}	microyield strength
SOFIA	Stratospheric Observatory for Infrared Astronomy
S_{PAD}	average stress in a pad-to-optic interface
SPDT	single-point diamond turning
SPH	as subscript, indicates spherical interface
S_{R}	radial stress at an optic-to-mount interface
SR	Schott code for acid resistance of glass
S_{S}	shear stress developed in a bonded joint from a temperature change
S_{T}	tensile stress
S_{W}	yield strength for window material
SWS	Short Wavelength Spectrometer
SXA	proprietary aluminum metal matrix composite
S_{Y}	yield strength
t	path length in a refractive medium; thickness (as of spring or flange)
t_0	reference temperature in Sellmeier equation for $\mathrm{d}n/\mathrm{d}T$
T	temperature
T_{A}, T_{MAX}, T_{MIN}	assembly temperature, maximum, minimum temperature
TAG	Technical Advisory Group (within ISO TC)
TAN	as subscript, indicates a tangential interface
tanh	hyperbolic tangent function
t_{C}	cell wall thickness
TC	Technical Committee (within ISO)
T_{C}	temperature at which assembly preload reduces to zero, i.e., mechanical contact is lost
t_{E}	edge thickness of a lens
t_{e}	thickness of an annular elastomer layer
TERRA	name of EOS satellite payload (Latin for "land")
T_{G}	glass transformation temperature
TIR	total internal reflection; total indicator runout

TIS	total integrated scatter
T_L	lifetime, time to failure
TOR	as subscript, indicates a toroidal interface
t_P	uncompressed thickness of a resilient pad
tpi	threads per inch
t_W	thickness of a window
T_λ	transmittance of a surface at wavelength λ
U, U'	angles of marginal ray with respect to the axis in object, image space
ULE	Corning's ultra-low expansion material
UNC, UNF	unified coarse or fine thread
URR	upper rim ray at maximum semifield angle
USC	United States customary system of units
UV	ultraviolet
v_λ	Abbe number for a specific wavelength
V	volume; lens vertex
V/H	velocity-to-height ratio for an aerial camera system
VLT	Very Large Telescope
w	unit applied load
W	weight
WG	Working Group (within ISO)
WWII	World War Two
w_S	wall thickness of a spacer
X, Y, Z	coordinate axes, dimensions
y_C	contact height on an optical surface
y_S	ID/2 for a lens mounting

INDEX

Abbe
  erecting system, 344, 665
  number, 80
  version of the Porro prism, 399
Aberration
  from prisms, 332
  compensator, 286–289
Abrasion (see Erosion)
Absorption
  of high-energy radiation, 63, 64
  of light, 54, 56, 59, 63, 64, 66, 77, 78, 92, 100, 105, 130, 132, 312, 320, 323, 410, 415, 586, 696, 799
  of water, by plastics, 95, 96, 131
  thermal, 39, 42, 142, 312, 800
Acceleration factor (a_G), defined, 820
Acceptance testing, 33, 70
Acrylic (see Polymethylmethacrylate)
Adaptive optics, 472, 571, 574–576, 794
Adhesives, optical (see Optical cements)
Adhesives, structural (see Epoxy, Cyanoacrylate, Elastomer, Urethane)
Advanced Electro-Optical System (AEOS), 574
a_G [see Acceleration factor (a_G)]
Air bag/bladder mirror support (see Mirror mounts, air bag/bladder)
Al_2O_3 (see Sapphire),
Albedo, 39
AlBeMet162®, 128
Alignment
  by lathe assembly (see Lathe assembly)
  clocking/phasing, 234, 287, 427, 570
  of cylindrical lenses, 234, 236
  of microscope objectives, 264, 294–296
  of multiple lenses, 282–297
  of reflecting systems, 297, 298
  of single lenses, 208–222
  plastic/liquid pinning after, 213, 214, 293
  with alignment telescope, 282–284
Allyl diglycol carbonate (CR39), 96, 222
  properties of, 96
ALON (see Aluminum oxynitride)
Aluminum (Al), 116–118
  properties of, 101, 111
Aluminum matrix (see SXA)
Aluminum oxynitride (ALON), 97, 101, 312–314, 324, 738, 747
  properties of, 97, 101, 738, 747
AlumiPlate®, 143, 623,
American National Standards Institute (ANSI), 8–11
American Society of Mechanical Engineers (ASME), 9, 150, 188
Amici prism, 338, 340, 342, 343, 349, 351, 359, 383, 397
Amici/penta erecting system, 349, 351
AMTIR ($Ge_{33}As_{12}Se_{55}$), 97, 106, 172
  properties of, 106
Analysis,
  dynamic relaxation, 491, 499, 500, 527
  finite element (FEA), 15, 20, 40, 61, 143, 207, 243, 245, 427, 442, 499, 611, 623, 642, 644, 659, 804
  maintainability, 21
  structural, 17
  thermal, 17, 427, 712, 733
Antireflection (A/R) coating (see Coating, antireflection)
Aperture requirement, estimation of for prisms, 334–336
Arsenic trisulfide (As_2O_3), 106, 132
  properties of, 106
Articulated telescope, prism mounting for, 389–391
As2O3 (see Arsenic trisulfide)
Athermalization techniques, 42, 105, 659, 669, 689, 694–696, 703–706, 709, 711, 712, 716, 803
Atomic oxygen, effects of, 57, 142, 609
AXAF (see Chandra telescope)
Axicon, 359, 362, 363, 631, 635, 648

BaF_2 (see Barium Fluoride)
Barium fluoride (BaF_2), 97, 98, 132, 793
  properties of, 98
Bauernfeind 45° prism, 357–359
Be (see Beryllium)
Beamsplitter, 164, 165, 211, 212, 213, 214, 290, 295, 296, 376, 803
Bearing
  flexure, 513, 514
  spherical, 516, 552, 558, 580
Beryllium (Be), 111, 113, 115, 116, 118, 121, 128, 143, 144, 450, 476, 586, 587, 594, 598–601, 603–606, 623, 624, 628, 630, 633, 637, 638, 642–644, 646, 689, 690
  grades, 111, 121
  properties of, 111,120, 587, 628
Binocular
  Leica, 664
  M17, 28, 660
  M19, 28, 29, 662, 677–682
  Steiner, 661
  Swarovski, 252, 383, 663
  T14/Tl4EI, 28, 29
  Zeiss, 252, 662
Biocular prism, 365, 366
Birefringence
  natural, 12, 79, 84, 87, 100
  stress-related, 9, 11, 12, 82, 84, 87, 90, 243, 727, 729
Bladder mirror support (see Air bag/bladder mirror support)

Bonding, glass-to-metal,
  for prism mounting, 130, 338, 387–394, 679, 727–729, 801–803
  for mirror mounting, 130, 425–427, 432, 435, 442, 465, 801–803
Boresight adjustment (see Prism types, Risley wedge)
Bosses, attachment, for mirrors, 430–433, 533, 536, 537
Brass, 122, 148, 179, 180, 216, 247, 249, 284, 285, 795, 796
  properties of, 119, 628
Breathing ports, 239, 240
Burnishing lenses into cells, 179, 180, 181, 247, 249, 284, 320

C (see Diamond)
$CaAl_2O_3$ (see Calcium aluminosilicate)
Cadmium telluride (CdTe), 219, 628
  properties of, 109
CaF_2 (see Calcium fluoride)
Calcium aluminosilicate ($CaAl_2O_3$) properties of, 101
Calcium fluoride (CaF_2), 69, 95, 100, 270, 316, 794
  properties of, 68, 95, 98, 172, 324, 747
Calcium lanthanum sulfide ($CaLa_2S_4$), 61
Catadioptric systems, 272–282
  Baker-Nunn “Satrack” camera, 277, 278
  infrared catadioptric objective, 274–276
  motion picture camera objective, 278–282
  solid catadioptric objective, 272, 273
  star sensor objective, 273, 274
Cement, optical (see Optical cement)
Center of gravity location, 6, 157, 177, 178, 244, 261, 374, 388, 431, 488, 492, 495, 527, 556, 717
Centering of optics (see also Decentration), 9, 11, 22, 133, 161–165, 167, 171, 207, 209, 214–218, 220, 221, 239, 261, 264, 265, 270, 274, 276, 280, 284, 418, 524, 538, 601, 602, 630, 631, 642, 649, 650, 669, 671, 672, 697, 706, 791, 792
Cerium oxide (CeO_2) (see Glass, radiation resistant)
Cer-Vit, 113, 115, 434, 436, 467, 516, 523, 550, 551
  properties of, 110, 115, 116, 587
Cesic®, 618–623
  properties of, 112, 120, 619,
Chalcogenide materials, 69
  properties of, 106, 628
Chandra telescope, 1, 579–581, 721–723
Coatings,
  antireflection (A/R), 41, 55, 56, 60, 63, 68, 87, 141, 284, 304–306, 402,412
  conductive, 304
  low-emissivity, 307, 705
  optical black, 141–143
  protective, 140, 141
  reflecting, 402, 594
  sputtered, 111, 113, 603, 604, 608, 609
Coatings, nickel (see Plating, electroless/electrolytic nickel)
Coefficient
  of friction, 186, 190
  of thermal defocus (β_G), 105, 107–109, 713–715
  of thermal expansion (CTE, α), 15, 42, 127, 186, 387, 425, 450, 455, 458, 463, 586–588, 637, 709, 722
Compliance
  axial, 397, 783, 784, 785, 791, 792, 794
  radial, 421, 431, 556, 792
Composites, 1, 44, 54, 57, 77, 124–127, 619, 673, 709,715, 721, 722
  manufacture of, 128, 149, 150, 707–709, 722, 723
  properties of, 112, 118, 119, 126, 127, 708
Computer-aided
  design, 2, 17, 19, 34, 336, 405
  engineering, 2, 30, 34
  manufacturing, 2, 17, 18, 30, 34
Conceptualization, 2, 3, 14
Conduction/conductivity, thermal, 42, 66, 79, 84, 96, 118, 122, 124, 137, 450
Conical interface (see Tangent interface)
Constraint, design, 5, 722
Contact stress (see Stress)
Contamination, 39, 44, 55–59, 66, 69, 132, 137, 151, 213, 266, 516, 581, 605
Controlled grinding, 67, 306, 318, 601, 608, 735
Convective heat transfer, 39, 545, 796, 797
Copper (Cu), 115, 116, 121, 122, 123, 144, 313, 350, 408, 450, 586, 587, 601, 603, 607, 608, 623, 630, 636, 693
  properties of, 111, 116, 119, 628
Corner-cube prism (see Cube-corner prism)
Corrosion, 6, 39, 44, 54, 55, 116, 118, 121, 123, 140, 141, 310, 326, 438, 586, 618, 623
CR39 (see Allyl diglycol carbonate)
Crystals, optical, 95–105, 747
  alkali and alkaline earth halides, 97–100
  chalcogenides, 105, 106
  glasses and other oxides, 100–103
  semiconductors, 100, 103, 104
Cu (see Copper)
Cube-corner prism, 331, 359–361, 363, 364, 437, 439
Cyanoacrylate adhesive, 132,137
  properties of, 136

Damage threshold, laser, 67, 609, 623
Data Base Manager (DBM), 18
Decentration, (see also Centering of optics), 24, 180, 186, 205, 426, 707, 709, 770, 788
  of lens with elastomeric mounting, 203, 204
Deep Imaging Multi-Object Spectrograph (DIMOS), 270, 702, 703
Deformations of surfaces of bent optic, 767
Delta prism, 350–352, 355–357, 403
Density, mass, 1, 43, 44, 48, 54, 79, 82–86, 96, 98, 99, 100–102, 104, 106, 110–112, 115, 118–120, 123–127, 131, 175, 272, 312, 328, 338, 450
Design reviews, 12, 14, 20, 30–32, 146
Diamond (C) 40, 55, 61, 71, 113, 144, 161, 162, 215, 318, 324 441, 467, 468, 552, 585, 609, 612, 625, 629, 630, 639, 735, 744
  properties of, 97, 104
Diamond-like coatings, 55
Differential thread, 247, 248
Dispersing prism, 368

Dispersion,
  optical, 78–80, 82, 83, 93, 105, 301, 366–368, 726, 727
  mechanical, 122, 126, 608
Documentation, design, 34, 260
Dome,
  optical 301, 302, 310–315, 317, 319, 320, 323, 325–327, 454
  astronomical, 545, 575
Double-Dove prism, 341, 346–348, 352, 385, 386
Dove prism, 346–348, 385
Drop-in assembly, 178
Duran 50 (see also Pyrex), properties of, 110, 116
Dynamic relaxation analysis (see Analysis, dynamic relaxation)

E6 (see Ohara E6 glass)
Earth orbit classifications, 37, 38, 42, 43
Echellette spectrograph/imager (ESI), 726–728
Edge-contacted lenses, 224
Elastomer, 137, 183, 202–204, 209, 217, 219, 221, 222, 236, 239, 243–245, 264, 270, 271, 274, 302, 308, 310, 311, 321, 323, 324, 385, 426–428, 438, 536, 551, 700, 803–806
  properties of, 138, 139
Emission,
  planetary, 39, 41
  spectral, 80, 312
Engineering testing, 33
Environmental specifications, 41, 50, 52, 70, 597, 707, 783
Environmental testing, 11, 28, 69, 620
Epoxy/liquid pinning, 213, 214, 293
Epoxy, properties of, 135, 136
Erosion, 6, 39, 60–63, 302, 305, 310, 744
Error budget, 21–25, 542, 545, 646, 726, 729
ESO Very Large Telescope, 596–598, 600, 602
Expansion, thermal (see Thermal expansion)
Eyepiece,
  diopter adjustment, 248–252
  Erfle, 13
  fixed focus, 235, 236
  focusing, 249, 250
  Kellner, 13, 249, 662
  Ploessl, 235
  sealing of, 237, 250, 251, 678

Far Ultraviolet Spectroscopic Explorer (FUSE) spectrograph, 441–443
Films, thin (see Coatings)
Filter, optical 63, 65, 178, 179, 221, 225, 244, 246, 247, 254, 255, 263, 270–273, 302, 320–323, 328, 329, 405, 558, 665, 670, 711, 726, 796
Finite element analysis (see Analysis, finite element)
Flexure
  bearing (pivot) (see Bearing, flexure)
  supports, 204–208, 396–399, 563, 498, 642–647
Fluoride glass, 89
  properties of, 98, 101
Fluorite (see Calcium fluoride (CaF))
Fluorophosphate glass (IRG9)
  properties of, 101
Flushing (see Purging)
Focus adjustment, 22, 248, 249, 258, 484, 663, 681, 691
Fracture toughness, 125, 646, 736, 738
Fresnel reflection, 78, 87, 105, 132, 272, 284, 301, 373, 410, 415
Friction, (see Coefficient of friction)
Frit bonding (see Mirror, nonmetallic, frit bonded)
Fungus, 6, 39, 59, 60, 310, 384
Fused silica (SiO_2), 62, 64, 67, 69, 87, 100, 113, 271, 292, 301, 306, 308, 360, 364, 402, 412, 426, 432, 433, 441, 450, 455, 456, 458, 461, 466, 473, 475, 481, 495, 504–507, 532, 553, 556, 586, 611, 637, 638, 695, 697, 699, 739, 767, 802, 803
  properties of, 65, 68, 102, 103, 110, 115, 116, 117, 172, 324, 587, 738, 747

Galaxy Evolution Explorer (GALEX), 709–712
Gallium arsenide (GaAs),
  properties of, 97, 104, 109
$Ge_{33}AS_{12}Se_{55}$ (see AMTIR)
Gemini telescopes, 508, 537, 540–545, 706, 794
Geostationary Orbiting Environmental Satellite (GOES) telescope, 423, 424, 698, 700–702
Germanate,
  properties of, 101
Germanium (Ge), 40–42, 55, 60, 63, 103, 132, 203, 221, 241, 246, 258, 275, 307, 311, 317, 628, 630, 631, 634, 687, 693, 694, 759–761, 763, 766, 795, 796, 799, 804
  properties of, 104, 109, 172, 219, 324, 628
Glass
  optical, 4, 10, 12, 78–80, 82–84, 94, 222, 301, 384, 415, 735, 742
  map, 80, 81, 88, 92
  properties of, 86, 89
  radiation resistant, 92
Glidcop™, 122, 586
  properties of, 111, 117, 120
Graphite epoxy, 1, 57, 116, 127, 450, 580, 673, 708, 715
  properties of, 112
Gratings, mountings for [see Far Ultraviolet Spectrographic Explorer (FUSE) spectrograph]
Gravitational effects on optics, (see Acceleration factor, Self-weight deflection)

Hale Telescope, 453, 466, 530, 531, 533, 716, 717
Hall's criterion/equation/, 506, 637, 638
Hardness, 79, 84, 96, 98, 99, 101, 102, 104, 106, 110–112, 123, 124, 131, 138, 139, 171, 234, 516, 623, 625, 630, 737, 817, 818
Hindle/whiffletree mounting for mirrors, 450, 481, 489, 490, 503, 512–515, 533, 538, 546, 560–563, 570, 573, 597, 637, 638
Hoop stress (see Stress, tangential in cell wall)
Housing,
  rigid, 659, 674, 695, 703
  semimonocoque, 670
Hubble Space Telescope, 1
  axial/radial supports for primary mirror, 577–580
  primary mirror manufacture/test, 27, 56, 519, 525
  truss assembly, 126, 706–510

Humidity, 37, 39, 54, 55, 59, 70, 78, 137, 445, 708, 739, 811
Hyperhemisphere (see Dome, optical)

Image/beam displacement, 332, 333, 370
Image,
  ghost, 41, 339, 401, 402, 411–415, 445
  left/right handed/orientation, 6, 17, 331, 335, 336, 401–406
Indium antimonide (InSb), 575, 576
  properties of, 104
Indium, as a window seal, 307–309
Infrared Astronomical Satellite (IRAS) Telescope, 604–606, 646, 647, 689, 690
Infrared Multi-Object Spectrograph (IRMOS), 638
Interface
  cylindrical pad, 196, 379, 380–382, 433, 734, 751–753
  elastomeric, 184, 202–204, 216, 239, 240, 243, 245, 307, 308, 320, 376, 426, 427, 437, 804
  flat bevel, 194, 201, 241, 256, 280, 281, 419, 762, 780, 795
  kinematic, 373, 374, 422, 423, 438, 558, 638, 643, 674, 675, 754,
  nonkinematic, 384, 542
  rim contact, 160, 161, 165, 166, 183, 202, 669, 733, 768, 769
  semikinematic, 194, 373, 374, 375–379, 415, 420–423, 445, 491, 542, 544, 644
  sharp-corner, 184, 189, 197, 198, 235, 237, 260, 380, 748, 758, 759, 760, 762, 763-765, 775
  spherical pad, 194, 381, 382, 748, 749, 750, 752, 755
  spherical, 198–200, 760, 761, 762, 764, 766, 796,
  step bevel, 194, 200, 201, 669, 789
  surface contact, 161, 184, 186, 187, 200, 229, 756, 758, 760
  tangential, 197, 198, 229, 232, 237, 239, 261, 282, 418, 419, 669, 759–764, 766, 775, 777, 782
  toroidial, 198–200, 209, 210, 214, 229, 233, 235, 282, 284, 310, 418, 419, 649, 748, 759–767, 776, 781
Interface drawing, example, 5, 6
Interference, electromagnetic, 6
Interference fit, 141, 181, 182, 244, 245, 268, 313, 314, 549, 635
International Standards Organization (ISO), 8–12, 50–52, 69, 70
Invar, 1, 122, 123, 210, 245, 274, 397, 423, 424, 432–434, 437, 442–444, 498, 532, 534, 538, 546, 549, 556, 560, 567, 568, 570, 572, 577, 579, 685, 686, 695, 700, 703, 704, 711, 712, 715, 768,
  properties of, 114, 115, 117, 120
IRAS telescope [see Infrared Astronomical Satellite (IRAS) Telescope]
Irtran, 100, 132
ISO (see International Standards Organization)

Keck Telescopes, 114, 270, 566, 567, 569–574, 629, 721, 726, 729
Kinematic mounting (see Interface, kinematic)
Kitt Peak National Laboratory/Observatory, 507, 509, 516, 530, 531, 538, 791
KRS5 (see Thallium bromoiodide)
Kuiper Telescope (KAO), 594, 595, 640, 642

Laser damage to optics, 11, 12, 66, 67
Lathe assembly of lenses, 229, 259, 260, 261, 262, 272
Lens cone, 3–5, 262, 670, 672, 673
Lens mount
  burnished, 179, 180, 197, 247, 249, 284, 320
  cantilevered spring, 179, 194, 195, 196, 197
  continuous ring (flange), 184, 192-194, 242, 274, 280, 310, 311, 323, 325, 419, 420, 688, 757, 764, 767, 772, 779, 784, 790–795
  elastomeric, 202–204, 209, 217, 219, 221, 222, 243–245, 270, 536, 551, 803–806
  flat bevel, 194, 201, 241, 256, 280, 281, 419, 762, 780, 795
  flexure, 204–208
  pressed-in ring, 182, 183, 243–245
  nonsymmetrical, 194–196
  rim contact, 160, 161, 165, 166, 183, 202, 669, 733, 768, 769
  snap ring, 180–182
  surface contact, 161, 184, 186, 187, 200, 229, 756, 758, 760
  threaded retainer, 184, 188–190, 194, 201, 214, 230, 237, 241, 303, 418, 419, 660, 669, 678, 679, 757, 773, 779, 781, 787, 789,
Lens, spherical/crowned rim, 183, 262
Lens-to-mount interface (see Interface)
Lick Observatory, 55, 530
LiF (see Lithium fluoride)
Liquid coupling of lenses, 229, 270, 271
Liquid pinning (see Epoxy pinning)
Lithium fluoride (LiF), 97, 442
  properties of, 97, 98, 172, 747
Locating pin/post, application of, 375, 376, 379, 380, 382, 397, 398, 416, 568, 681, 749, 751–753, 755, 756

Magnesium (Mg), 55, 123, 141, 662, 704
  properties of, 120, 144
Magnesium fluoride (MgF_2), 62, 219, 402, 408, 628
Magnesium oxide (MgO), 40, 141
Management, configuration/project, 1, 30
Manufacture,
  of composite parts, 149, 150
  of mechanical parts, 146–149
  of optical parts, 143–146
Metal matrix (see SXA)
Methylmethacrolate (see Polymethylmethacrylate)
Methylmethacrolate styrene copolymer (NAS), 94, 222
  properties of, 96
Mg (see Magnesium)
MgF_2 (see Magnesium fluoride)
Micrometeorites, effects of, 57, 63, 66,
Microscope objective,
  assembly/alignment of, 264, 294–296
  correction collar, 265, 266
  high-performance, 292–297

  reflecting, 266, 267
  resilient mount, 266
Microyield strength, 121, 586, 598, 708, 748
Mirror,
  aluminum, 55, 111–113, 116, 117, 587–598, 641, 643
  beamprint on, 405–408
  beryllium, 116–121, 599, 604, 606, 637, 638, 642–644
  built up
    brazed/welded, 595–598
    egg crate/slotted strut, 456, 507
    frit bonded, 463–465
    monolithic, 454–462, 464, 473, 519, 533, 545, 560, 561, 566, 577, 601, 604
    Hextek process 461–463
    low temperature bonded, 465
  cast, 453–456, 593
  contoured-back, 470–474
  copper, 122, 587, 607
  first-surface, 397, 402, 408, 409, 413–415, 417, 420, 425–427, 440, 548
  foam core, 450, 451, 474, 475, 612, 613, 615–619
  ion figured, 570, 571, 607
  lateral constraint during polishing, 524, 525
  machined core/back, 465, 466–470
  Mangin, 414
  materials, characteristics for, 110, 111
  molybdenum, 111, 115–117, 316, 450, 586, 587, 607, 609, 623
  neutral surface of, 451, 452, 461, 466, 481, 600, 643
  penta, 433–436
  Porro, 436, 437
  retroreflector,
    hollow corner (HCR), 437–441
    lateral transfer (LTR), 440, 441
    spherically mounted (SMR), 438–441
  rigidity of, 115, 415, 416, 466, 515, 564, 565, 578, 595
  roof penta, 435, 436, 401
  sandwich, 126, 127, 450–454, 473–475, 481, 557, 601
  scaling relationships for lightweight, 451, 473–477
  second-surface, 105, 354, 401, 402, 408–414, 418, 419, 445
  segmented, 401, 545, 561–573, 596, 597
  smoothness of, 105, 110–113, 143, 190, 587, 589, 594, 607, 608, 623, 632
  specific stiffness of (see Specific stiffness)
  spin cast, 454, 456, 593, 718
  stability of, 113, 115, 118, 128, 434, 441, 449, 450, 455, 463, 495, 507, 523, 558, 586, 593, 595, 603, 608–613, 617, 624, 651, 684
  thin face sheet, 561, 566, 568
Mirror mounts
  adaptive, 472, 571, 574, 575, 576, 794
  air bag/bladder, 450, 491, 503, 506–511, 555, 556
  bipod, 432, 433, 541, 542, 551, 557–560, 563, 602, 690, 711
  bonded, 389, 427, 463, 464
  center-mounted/hub, 279, 280, 469, 548–553, 576, 640, 642, , 690, 709, 720
  clamped, 415–424
  double-arch, 553–557
  elastomeric, 427–429
  flexure, 428–433, 642–647
  Hindle/whiffletree (see Hindle/whiffletree mounting for mirrors)
  horizontal axis, 481–502
  ideal, 486, 491, 492
  integral, 638–641
  lever, counterweighted, 450, 489, 491, 515, 516, 527–534
  mercury tube, 481, 492, 493
  metrology, 27, 503, 516, 518–525, 577
  multiple-point see Hindle/whiffletree mounting for mirrors)
  parallel post (V-block), 482–489
  pneumatic/ hydraulic, 503, 516–522
  push-pull, 498–481, 498, 499, 527, 528
  ring support, 474, 475, 503, 505, 507, 556
  single-arch, 548–553
  strap/chain, 481, 486, 493–500, 493–497
  thin face sheet, 472, 473, 561, 566, 568
  variable orientation, 527–581
  vertical axis, 503–525
MMT (see Multiple-Mirror telescope)
Mo (see Molybdenum)
Modeling,
  computer, 14, 29
  experimental, 27
Modular construction,
  dual collimator example, 685
  principles, 659
  molded plastic example, 225, 676
  binocular example, 28, 29, 662, 677–682
  space borne spectrometer example, 682–684
Modulation/optical transfer function (MTF/OTF)/image quality,
  of an athermalized lens, 695
  with double-Dove prism, 346
Modulus of elasticity (see Young's modulus)
Molybdenum (Mo) 115, 316, 318, 450, 586, 587, 607, 609, 623, 795, 796
  properties of, 111, 116, 117
  use in lens cell, 795, 796
Multiangle Imaging Spectro-Radiometer (MISR), 666, 668, 669
Multiple-lead thread, 249
Multiple-Mirror telescope (MMT), 507, 508, 545–551, 575, 576, 718–721, 796

NaCl (see Sodium chloride)
NAS (see Methylmethacrylate styrene copolymer)
National Ignition Facility, (NIF), 56

Ohara E6 glass, 454, 546, 769
  properties of, 637, 747
Optical cement, 321, 434, 679, 801, 802
  properties of, 131, 132
Optical path difference (OPD) due to radial gradient, 799
Optics and Electro-Optics Standards Council (OEOSC), 9, 11
Orbiting Astronomical Observatory Copernicus) (OAO-C), 696, 699
Outgassing, 57, 134, 137, 142, 240, 561, 618, 708

Pechan prism (see Prism types, Pechan)
Pellicle, 401, 444, 445, 446
Penta prism (see Prism types, penta)
Periscope, 4, 13, 29, 43, 60, 231, 261, 262, 345, 347, 385, 388, 389, 403–405, 612, 663–665
Pinning (see Epoxy/liquid pinning)
Plastic windows, deep-submersible, 325
Plastic materials, optical,
  map, 94
  properties of, 94, 96
Plastic optics, 92, 93, 95, 132, 141, 157, 222–225, 229, 267–270, 298, 301, 311, 320, 412, 662, 676
Plating/coating,
  aluminum, 589, 623, 624
  chrome, 141, 143
  electroless nickel, 113, 128, 143, 145, 172, 585, 589, 590, 597, 613, 623–625, 643
  electrolytic nickel, 141, 143, 145, 172, 585, 595, 623, 624
  gold, 143, 306, 408, 409, 434, 594, 623, 684, 700, 705,
  silver, 409
PMMA (see Polymethylmethacrylate)
Polycarbonate, 92, 94, 222, 628, 661, 662
  properties of, 96, 109
Polymethylmethacrylate (PMMA)/acrylic, 92, 94, 140, 222, 224, 270, 325, 628, 676
  properties of, 94, 96, 109
Polystyrene, 92, 662
  properties of, 94, 109, 628
Porro prism (see Prism types, Porro)
Porro prism erecting system (see Prism types, Porro erecting system)
Potassium bromide (KBr), 100
  properties of, 97, 98, 109, 747
Potassium chloride (KCl), 95, 97
  properties of, 98, 109, 747
Power spectral density, vibration, 48, 49, 812, 823
Precision diamond machining (see Single point diamond turning)
Preload, axial, 165, 182, 184, 186–190, 194, 200, 233, 418, 421, 422, 669, 678, 750, 759, 762, 766, 767, 770, 771, 776, 778, 781, 783, 784, 788, 790–792, 795
Pressure,
  aerodynamic, 326
  atmospheric, 37, 43, 150, 264, 308, 508, 511, 604, 634
  differential, 44, 301, 304, 314, 321, 322–328
  hydrodynamic, 44
  pumping, 43, 56
  testing, 44, 303, 812
  variation with altitude, 43
Prism mounts,
  athermal, 727–729
  bonded, 387–396
  clamped, 375
  flexure, 396
  in articulated telescope, 389–392
  kinematic, 373, 374
  nonkinematic, 384–387
  semikinematic, 373–375–384
  with elastomeric pad, 376–379
Prism tunnel diagram, 333, 334, 338, 339, 343
Prism,
  45° Bauernfeind , 357– 359
  Abbe erecting system, 344, 345
  Abbe version of Porro, 339, 340, 344
  acromatic dispersing, 366–368
  Amici, 338, 340, 342, 343, 349, 351, 359383, 397
  Amici/penta erecting system, 349, 351
  anamorphic, 371–373
  axicon, 359, 362, 363
  beamsplitter (or beamcombiner) cube, 338, 340, 342, 376
  biocular, system, 365, 366
  constant deviation, 367
  cube-corner, 331, 359–361, 363, 364, 375, 437, 439
  delta, 350, 352, 353, 355356, 385, 403
  dispersing, 366–368
  double-Dove, 341, 346, 347, 348, 352, 385, 386
  Dove/Harting-Dove, 341, 346, 347, 352, 385, 386, 387
  focus-adjusting wedge system, 370, 371
  Frankford Arsenal Nos. 1 & 2, 358–360
  Leman, 359, 361, 362
  ocular prism for rangefinder, 351, 362, 364, 365
  Pechan, 352, 356–358, 385–389, 393, 395, 663, 664
  penta, 347–349, 351, 361, 365, 378, 379, 433, 434, 752–756
  Porro erecting system, 333, 335, 340, 342, 345, 359, 384, 394, 396, 663
  Porro, 331, 334–336, 339, 340, 343–345, 375–377, 383, 387–392, 394, 396, 405, 436, 660–662, 665, 667, 679, 680
  reversion, Abbe Type A/B, 349, 350, 353–355, 359
  rhomboid, 341, 345, 346, 365, 394, 396
  right-angle, 333, 334, 336–340, 344–346, 349, 351, 365, 375–378, 391, 392, 397, 757
  right-angle/roof penta erecting system, 349, 351
  Risley wedge system, 368–370
  roof penta, 348, 349, 350, 351, 388, 389
  Schmidt, 355–358, 392, 393, 395
  sliding wedge, 370
  thin wedge, 368–371
Probability of failure (P_F), 740, 741, 742, 744, 745, 746
Purging, 59, 682
Pyrex, (see also Duran 50), 100, 178, 270, 437, 450, 453, 461, 487, 488, 532, 535
  properties of 110, 117, 172, 637, 738, 747

Quartz, crystalline (SiO_2), (see also Fused silica), 61, 78, 95, 100, 552, 553, 818

Radial gap, 207, 770, 805, 806
Radial preload, 421, 791, 792
Radiation resistant glass (see Glass, optical, radiation resistant)
Radiation,
  high energy, 63, 64, 65, 129, 636
  laser, 69, 89, 131, 308, 408, 800
  solar, 39, 40, 581, 800, 813
Rain erosion (see Erosion)
Rectangular lens mounting (see Mounting techniques, lens, nonsymmetrical)

Reflection,
  law of, 331
  ghost, 412–415
  total internal (TIR), 336, 337, 346, 350, 352, 354–356, 358, 359, 366, 367, 373, 384, 679
Refraction, law of/Snell's law, 79, 331, 336, 337, 367
Refractive index,
  absolute, 78, 79, 712, 716
  relative, 78, 79
  variation with temperature, 80
  variation with wavelength (dispersion), 79, 80
Relative humidity (see Humidity)
Resonance, mechanical/fundamental frequency, 46–48, 428, 556, 718, 612
Retaining ring,
  configuration of, 184, 187–191
  stress in, 190, 191
  thread fit, 188, 189
  applied torque relationship, 189, 190
Reversion prism (see Prism types, reversion)
Rhomboid prism (see Prism types, rhomboid)
Right-angle prism (see Prism types, right-angle)
Rim, lens, crowned/spherical, 183, 184
Risley wedge system (see Prism types, Risley wedge)
Roof penta prism (see Prism types, roof penta)
RTV (see Sealants)
Rule of thumb stress tolerance for glass, 84, 742, 745–747, 754, 763–766

Salt content in atmosphere, 54
Salt, rock (see Sodium chloride)
SAN (see Styrene acrylonitrile)
Sapphire (Al_20_3), 40, 61, 62, 69, 225, 245, 312, 314, 318, 319, 324, 468, 734, 818
  properties of, 97, 172, 313, 324, 738
Schmidt prism (see Prism types, Schmidt)
Sealants
  room temperature vulcanizing (RTV), 137, 140, 183, 184, 202, 210, 217, 239, 247, 259, 272–275, 279, 302, 304, 324, 328, 385, 423, 424, 427, 428, 523, 551, 560, 700, 803
  polysulfide, 139, 140, 302, 313, 314, 661, 673
Self-weight deflection,
  lens, 203, 204, 205
  mirror, 117, 426, 449–451, 454, 464, 470, 473, 475, 504, 505, 515, 518, 527, 553, 554, 564, 566, 612, 637, 646, 670, 725
Semiconductor materials, 67, 100, 104
Semikinematic mounting (see Interface, semikinematic)
Sharp-corner interface (see Interface, sharp-corner)
Shell, optical (see Domes, optical)
Shock,
  mechanical, 14, 15, 38, 40, 44, 45, 52–54, 70, 89, 142, 180, 184, 185, 202, 204, 205, 237, 256, 272, 374, 375, 377, 384, 387, 388, 397, 415, 416, 425, 429, 435, 436, 577, 636, 642, 659, 665, 669, 768, 771
  lens assembly designed for, 241, 242, 687, 688
  testing, 52, 54, 71, 811, 814,
  thermal (see Thermal shock)
Short-Wavelength Spectrometer (SWS), 682, 683, 684
Si (see Silicon)
SiC (see Silicon carbide)
Silicon (Si), 100, 115, 145, 614, 615, 617
  properties of, 97, 104, 109, 111, 117, 172, 588, 589, 616, 738, 747
Silicon carbide (SiC), 115, 124, 142, 442, 450, 454, 455, 594, 604, 607–612, 617–620, 623, 742
  properties of, 97, 111, 112, 116–118, 120, 125, 127, 144, 588, 610, 619, 637, 738
Silicon dioxide (see Quartz, crystalline and Fused silica)
Single point diamond turning (SPDT), 25, 32, 144, 145, 209, 210, 213, 215–220, 224, 225, 285, 286, 318, 585, 589, 625–644, 648–652, 682–684, 693, 694, 756
SIRTF (see Spitzer Space Telescope)
Snap ring (see Mounting techniques, lens, snap ring)
Snell's law (see Law of refraction)
Sodium chloride (NaCl), 54, 95, 308, 310, 812
  properties of, 97, 99, 109, 219, 628
Stratospheric Observatory for Infrared Astronomy (SOFIA) Telescope, 468, 469, 560–563
Space Shuttle, 1, 38, 48, 49, 557, 578, 581
Space Station Freedom, 57
SPDT (see Single-point diamond turning)
Specific heat, 42, 79, 84, 131, 586, 587, 589, 598, 637
Specific stiffness, 116, 124, 150, 450
Specification, 4, 5, 7, 9, 19, 48, 52, 53, 82, 96, 130, 134, 140, 163, 169, 170, 225, 302, 303, 318, 327, 388, 427, 465, 518, 521, 524, 670, 735, 743, 754, 795, 812–814
  definition per Walker, 7
Spectrograph, FUSE (see Far Ultraviolet Spectroscopic Explorer spectrograph)
Spherical-seat mirror mounting (see Interface, spherical)
Spinel ($MgOA1_2O_3$), 62, 312
  properties of, 97, 313
Spring,
  cantilevered, 194, 379–381, 416, 418, 733, 748, 757
  straddling, 376, 378, 379, 381–383, 734, 751, 754, 757
Spring mounting for lenses (see Mounting techniques, lens, spring)
Spitzer Space Telescope, 552, 556, 690–693
Stabilization of image, 254, 255, 256
Standards,
  international, 8, 9, 19, 37, 69
  national, 8, 9
Star test, 265, 295
Steel, carbon, 123, 600
  properties of, 120
Steel, corrosion resistant (CRES), 4, 15, 55, 115, 123, 141, 189, 205, 230, 232, 233, 237, 240–242, 245, 254, 263, 271, 290, 302–304, 308, 309, 388, 392, 393, 425, 426, 437, 438, 444, 445, 550, 513, 551, 556, 560, 568, 577, 586, 587, 607, 641–644, 670, 672, 714, 715, 795
  properties of, 117, 120, 588, 703, 714, 753, 769, 770, 786, 788, 789, 790, 796
Steel, stainless [see Steel, corrosion resistant (CRES)]
Stiffness, specific, of mirror materials (see Specific stiffness)
Strain, 44, 52, 121, 125, 127, 129, 180, 396, 465, 570, 581, 599, 638, 639, 643, 674, 675, 734, 747, 768

Stratoscope II Telescope, 532, 534
Stray light, 17, 140, 141, 225, 233, 242, 269, 273, 276, 339, 384, 414, 649, 687
Stress birefringence (see Birefringence)
Stress,
  contact, 82, 194, 198, 384, 418, 419, 503, 660, 733, 746, 747, 750–752, 755, 756. 758–768,772, 781–783, 785, 786
  average,
    in threads, 190
    in contact area, 749
  conversion from compressive to tensile, 733, 746
  in bonded/cemented interface, 800–803
  tangential (hoop) in cell wall, 769, 770
  tensile in bent optic, 765–767
  tolerance for glass-type materials, 84, 742, 745–747, 754, 763–766
Stress optic coefficient, 84, 87, 88, 243, 748
Structures,
  modular, 28, 29, 59, 579, 659, 662, 675–679, 682–685
  multiple-tier truss, 721
  rigid housing, 659, 669, 674, 695, 703
  semimonocoque, 670
  Serrurier truss, 716–720, 724, 725
Styrene (see Polystyrene)
SXA, 126–128, 475, 586
  properties of, 112, 116, 120
Sylvite, (see Potassium chloride)

Tangential interface (see Interface, tangential)
Temperature compensation (see Athermalization)
Temperature
  effect on axial preload, 770–783
  gradients, 39, 105, 481, 587, 718, 768, 795–800
  testing, 42, 621, 811–814
  transformation, 79, 84
  variation with altitude, 42, 43, 312, 315, 795
Thallium bromoiodide (KRS5), 100
  properties of, 99, 109
Thermal
  conductivity, 42, 66, 79, 84, 96, 118, 122, 124, 137, 450, 587, 589, 610, 614, 618, 637, 691, 705, 800
  emissivity, 42, 56, 57, 140, 306, 312, 700, 705
  expansion coefficient (see Coefficient of thermal expansion)
  runaway in germanium, 799
  shock, 40, 41, 129, 308, 312, 795
Thermo-optic coefficient (see Coefficient of thermal defocus)
Ti (see Titanium)
Time to failure prediction, 743–746
TIR (see Reflection, total internal)
Titanium (Ti), 1, 55, 123, 124, 141, 193, 197, 204, 205, 243, 244, 261, 307, 313–316, 444, 556, 561, 579, 600, 607, 643, 644, 646, 669, 670–673, 704, 707, 715, 722, 723, 729, 744, 781–786, 802, 803
  properties of, 120, 145, 148, 672
Tolerances,
  birefringence, 84, 87
  relative cost impacts of, 167–173
  stress (see Stress, tolerance for glass-type materials)
  typical values for glass optics, 22
  typical values for plastic optics, 95,
Toroidal interface (see Interface, toroidal)
Torque applied to a retainer (see Retaining ring, torque applied)
Transmittance, light, (see Absorption of light)
Truss/structure,
  for Chandra Telescope, 722, 723
  determinate space frame, 725–728
  for Hubble Space Telescope, 1, 127, 706–710
  for New MMT, 718–721
  N-tiered, 721, 722
  Serrurier (see Structures, Serrurier truss)

ULE, 113, 114, 402, 423, 450, 458, 459, 463, 465, 487, 488, 519, 520, 523, 532, 533, 537, 557, 566, 577, 586, 604, 610, 700
  properties of, 110, 114–117, 145, 456, 473, 587, 610, 611, 637, 747
Units, conversion factors, 809, 810
Urethane adhesive, 134, 394–396
  properties of, 135

Very Large Telescope (VLT), 596, 597, 600, 602
Vibration,
  fundamental/natural/resonant frequency, 45, 185, 374, 552, 599
  periodic, 45, 46, 50, 57
  random, 47, 48, 374
  testing, 48,241, 442, 687
Vibration criteria (VC) for facilities, 49–52

Weight estimation for lenses, 174–176
Weibull statistics, use of, 442, 74–744
Weight reduction in mirrors (see Lightweighting of mirrors)
Whiffletree mounting (see Hindle mounting for mirrors)
Window deformation,
  from pressure differential, 44, 301, 304, 323–326
  from temperature gradient, 800
  from radially offset axial forces, 764–767
Window/filter,
  brazed, 313, 314
  composite, 321–323
  conformal, 306, 307, 315–320
  deep submergence, 325
  heated, 304, 305, 321–323
  laminated, 304, 305, 321, 323
  multiaperture, 305, 306, 320, 321
  segmented, 321–323
  shell/dome, 310–320
  vacuum, 307–310

Yield strength, 45, 121, 191, 196, 197, 307, 383, 419, 586, 748, 769, 770

Zernike polynomials, 17, 18, 105, 287, 288, 499, 501, 507, 553
Zerodur, 113–115, 145, 397, 402, 426, 437, 450, 451, 454, 455, 465, 468, 487, 488, 492, 498, 532, 560, 565, 567, 568, 572, 577, 579, 596, 637
  delayed elastic deformation of, 114
  properties of, 110, 114–117, 172, 747
Zerodur M, 113
  properties of, 110, 114, 116, 117, 747
Zinc selenide (ZnSe), 55, 63, 132, 694
  properties of, 106, 219, 628
Zinc sulfide (ZnS), 55, 132
  properties of, 219, 628
Zoom lens, 252–259, 405, 664–667, 694–698, 716